

**ELEVENTH INTERNATIONAL CONFERENCE  
ON COMPOSITE MATERIALS**

**Gold Coast, Queensland, Australia  
14th - 18th July 1997**

**PROCEEDINGS**

**VOLUME II**

**FATIGUE, FRACTURE AND  
CERAMIC MATRIX COMPOSITES**

**Editor  
Murray L. Scott**

**AUSTRALIAN COMPOSITE STRUCTURES SOCIETY  
WOODHEAD PUBLISHING LIMITED**

# TABLE OF CONTENTS

## ***Damage Tolerance***

<b>Compression After Impact (CAI) Properties of Hat Stiffened CF/PEEK Panels Fabricated through a Route without Autoclave</b>	<b>1</b>
<i>Takashi Ishikawa, Masamichi Matsushima</i>	
<b>Damage Tolerance of Biomimetic Laminates</b>	<b>10</b>
<i>Patrick Kim, Toshio Tanimoto</i>	
<b>Effect of Loading Parameters on Compression Dominated Fatigue Behavior of Impact Damaged Composite Laminates</b>	<b>17</b>
<i>Milan Mitrovic, H. Thomas Hahn, Greg P. Carman</i>	
<b>RTM Carbon Composites - Influence of Process Parameters on Compression Strength After Impact</b>	<b>27</b>
<i>Florentin Berthet, Pierre Devos, Thierry Ansart</i>	

## ***Dynamic Response Behaviour***

<b>Free Vibration of Delaminated Composite Plates with Contact Analysis</b>	<b>36</b>
<i>Meng-Kao Yeh, Ren-Cheng Lai</i>	
<b>The Dynamic Response of Inelastic, Delaminated Composite Plates</b>	<b>47</b>
<i>Todd O. Williams, Frank L. Addessio</i>	
<b>Vibration Analysis of Thick Laminated Trapezoidal Plates</b>	<b>55</b>
<i>C.C. Chen, C. W. Lim, S. Kitipornchai, K.M. Liew</i>	
<b>Dynamic Responses of Orthotropic Annular Composite Plates</b>	<b>64</b>
<i>C.L.D. Huang</i>	
<b>The Dynamic Response of a Pultruded Fiberglass Tube Subjected to Lateral Loading</b>	<b>74</b>
<i>Louis J. Brunet, James A. Nemes</i>	
<b>Vibration Analysis for Composite Cylindrical Shells with a Rectangular Cutout</b>	<b>84</b>
<i>Young-Shin Lee, Young-Wann Kim</i>	
<b>An Analysis of Vibration Damping in Composite Plates Using Complex Frequency Equations</b>	<b>94</b>
<i>S. Kalyanasundaram, D.H. Allen, M. Cardew-Hall, A.E. Lowe</i>	
<b>Vibrations of a Laminated Composite Beam Elastically Supported at One End and Carrying a Tip Mass at the Other</b>	<b>103</b>
<i>T. Yokoyama, Z.M. Yang</i>	

## ***Fatigue***

<b>Fatigue Behaviour of Commingled CF/PEEK Composite</b>	<b>114</b>
<i>Lin Ye, Xiaoxue Diao, Yiu-Wing Mai</i>	
<b>Effect of Load Frequency on the Tensile Fatigue Behaviour of Angle-Ply AS4/PEEK</b>	<b>124</b>
<i>X.R. Xiao, I. Al-Hmouz</i>	

<b>Residual Strength of GRP at High Cycle Fatigue</b>	<b>135</b>
<i>J. Andersons, J. Korsgaard</i>	
<b>A Stochastic Cumulative Damage Model for the Fatigue Response of Laminated Composites</b>	<b>145</b>
<i>R. Ganesan, S.V. Hoa, S. Zhang, M. El-Karmalawy</i>	
<b>Progressive Fatigue Modeling of Laminated Composite Pinned/Bolted Connections</b>	<b>156</b>
<i>Mahmood M. Shokrieh, Larry B. Lessard</i>	
<b>Prediction of Flexural Fatigue Life for Unidirectional CFRP Laminates</b>	<b>167</b>
<i>Masayuki Nakada, Takeshi Ishiguro, Yasushi Miyano</i>	
<b>Fatigue Behavior of the Carbon/Epoxy and the Carbon/PEEK Composites Subjected to Low-Energy Impact</b>	<b>177</b>
<i>Nyan-Hwa Tai, Ming-Chuen Yip, Chih-Ming Tseng, Hui-Chia Yu</i>	
<b>Initiation of Free-Edge Delamination in a Composite Laminate Under Fatigue Loading</b>	<b>185</b>
<i>Ran Y. Kim, Allan S. Crasto</i>	
<b>Fatigue Crack Growth Behavior of a Random Fiber Sheet Molding Compound Composite</b>	<b>194</b>
<i>D.R. Atodaria, S.K. Putatunda, P.K. Mallick</i>	
<b>Damage Based Fatigue Life Modeling for Brittle Composites</b>	<b>203</b>
<i>G.M. Newaz, N. Bonora,</i>	
<b>Fatigue Damage in Nicalon SiC(f)/Al Composite Wires</b>	<b>211</b>
<i>Yue Zhuo, Hong Wan, Jin Pan, Deming Yang</i>	
<b><i>Fracture</i></b>	
<b>The Mode-I Fracture Toughness of IM7/LARC-RP46 Composites at High Temperatures</b>	<b>215</b>
<i>W.X. Wang, F.G. Yuan, B.D. Potter, R.H. Pater, Y. Takao</i>	
<b>Intralaminar Fracture Behaviour and Microstructural Characteristics of Unidirectional T300/914</b>	<b>225</b>
<i>Adrian Lowe, Shankar Kalyanasundaram</i>	
<b>Rate Effects on Mode I Interlaminar Fracture Toughness in Carbon-Fibre/Epoxy and Carbon-Fibre/Toughened-Epoxy Composite Laminates</b>	<b>234</b>
<i>Takayuki Kusaka, Masaki Hojo, Tomoaki Kurokawa, Shojiro Ochiai</i>	
<b>Toughness of Marine Composites: Delamination Resistance Under Static Loading</b>	<b>244</b>
<i>P. Compston, P.-Y. B. Jar, P.J. Burchill, G.J. Simpson</i>	
<b>Improved Interlaminar Fracture Toughness for Vinyl Ester Resin - Fibre Glass Composites</b>	<b>254</b>
<i>Peter J. Burchill, Gary J. Simpson</i>	
<b>Dynamic Crack Propagation and Perforation of Laminated Composites Using a Split Hopkinson Pressure Bar</b>	<b>263</b>
<i>Sylvanus N. Nwosu, Gregory J. Czarnecki</i>	
<b>Evaluation of Multiaxial Test Data of UD-Laminate by So-Called "Fracture-Type Strength Criteria" and By Supporting Probabilistic Means</b>	<b>273</b>
<i>Ralf G. Cuntze</i>	

<b>A Singular Hybrid Finite Element Analysis of Interlaminar Crack Problems</b>	<b>290</b>
<i>Kyohei Kondo, Kazuhiro Yagi</i>	
<b>Failure Behavior and Morphology of Hybrid Short-Fibers Reinforced Composite Under Thermal and Mechanical Loadings</b>	<b>301</b>
<i>Kh. G. Schmitt-Thomas, Zhen-Guo Yang, R. Malke</i>	
<b>Debonding and Fracture Mechanisms of Particulate Filled Polypropylene</b>	<b>312</b>
<i>I.L. Dubnikova, D.K. Muravin, V.G. Oshmyan</i>	
<b>Effects of Pores and Voids on the Interlaminar Delamination Toughness of a Carbon/Epoxy Composite</b>	<b>322</b>
<i>Leif E. Asp, Fredrik Brandt</i>	
<b>A Statistical Model for Crack Growth in Composite Materials</b>	<b>332</b>
<i>Biao Wang, Jin Dai, Shanyi Du</i>	
<b>Modelling Problems of Damage and Fracture of Notched Fibre Composites</b>	<b>342</b>
<i>R.A. Dimant, H.R. Shercliff, P.W.R. Beaumont</i>	
<b>Improved Fracture Mechanics Predictions for Delamination of Composites Accounting for Yield Zones</b>	<b>353</b>
<i>Z. Petrossian, Michael R. Winsom</i>	
<b>Damage Mechanics of Reinforcement Cracking in Particle or Short-Fiber Reinforced Composites</b>	<b>364</b>
<i>Keiichiro Tohgo, Young-Tae Cho, Hitoshi Ishii</i>	
<b>Parallel Computing and Damage in Composite Structures</b>	<b>374</b>
<i>F. Devries, F. L��n��, G. L'Hostis, D. Soulat</i>	
<b>A Proper Treatment of Interfacial Cracks in the Presence of Friction</b>	<b>387</b>
<i>C.T. Sun, W. Qian</i>	
<b>An Effective Method for Modeling the Tension Fracture of Composite Structures</b>	<b>397</b>
<i>Khanh Trinh, Fu-Kuo Chang</i>	
<b>Effect of Strain Rate on Tensile Fracture Behaviour of Fibre Reinforced Polyamide Composites</b>	<b>405</b>
<i>M. Todo, K.Takahashi, Ph. B��guelin, H.H. Kausch</i>	
<b>Fibre Orientation Effects on Interlaminar Fracture Toughness of Marine Composites</b>	<b>415</b>
<i>P. Compston, P.-Y. Jar, P. Davies</i>	
<b>Improving of the Fracture Toughness of MG-Alloy Composites Produced by Powder Metallurgical Technique</b>	<b>424</b>
<i>P. Abachi, B.L. Mordike, K.U. Kainer</i>	
<b>Study on the Mode I Interlaminar Fracture Toughness of Multi-Directional Laminates</b>	<b>431</b>
<i>Li Yong, Li Shunling, Xiao Jun, Tao Jie</i>	
<b>Experimental Delamination Behavior of Anisotropic Layered Plates with Different Internal Artificial Delaminations Under Compression Loading</b>	<b>438</b>
<i>M. Sczepanik-Weinmann, U. Stoll, F.J. Arendts</i>	
<b>Effect of Fabric Orientation on Fracture Toughness of Glass Fabric/PC Composite</b>	<b>447</b>
<i>J.B. Wang, Y.Q. Sun, S.R. Zheng, X.T. Jing</i>	
<b>Interface Modelling in Laminate Composites for Free-Edge Effects Analysis</b>	<b>453</b>
<i>Mohamed Haboussi, H��l��ne Dumontet, Jean Louis Bill��t</i>	



## **Impact**

<b>Behavior of Gradient Designed Composite Under Ballistic Impact</b>	<b>464</b>
<i>Frank K. Ko, Amotz J. Geshury, John W. Song</i>	
<b>Hypervelocity Impact Damage to Composite Materials</b>	<b>474</b>
<i>R.C. Tennyson, G.D. Shortliffe</i>	
<b>Results from Testing of the Helicopter Tail Rotor Blade Made of Composite Laminated Materials After Ballistic Damages</b>	<b>485</b>
<i>Boško Rašuo</i>	
<b>Low Velocity Impact Failure Analysis of Sandwich Beam</b>	<b>495</b>
<i>Ya-Jung Lee, Yau Shyu</i>	
<b>Influence of Water Absorption on Delamination Induced by Low-Velocity Impact and CAI Strength of FRPs</b>	<b>503</b>
<i>Kenjiro Komai, Kohji Minoshima, Kazuto Tanaka</i>	
<b>Low Velocity Impact Damage of Organic Foam Core Sandwich Composites</b>	<b>513</b>
<i>William J. Craft, Derke R. Hughes, Ajit D. Kelkar</i>	
<b>Perforation Characteristics Prediction of Multi-Layered Composite Plates Subjected to High Velocity Impact</b>	<b>522</b>
<i>Hideaki Kasano, Kenichi Abe</i>	
<b>Finite Element Analysis of the Ballistic Impact Response of Composite Helmet Materials</b>	<b>532</b>
<i>J. Van Hoof, M. J. Worswick, P.V. Straznicky, M. Bolduc, S. Tylko</i>	
<b>Perforation Characteristics of Fabrics Made of High Strength PE Fibers</b>	<b>542</b>
<i>K. Takahashi, H. Komatsu</i>	
<b>Using a Homogenization Procedure for Prediction of Material Properties and the Impact Response of Unidirectional Composite</b>	<b>552</b>
<i>A.D. Resnyansky, E.I. Romensky</i>	
<b>Impact Damage and Failure Mechanisms in Structure Relevant Composite Specimens</b>	<b>562</b>
<i>J.F.M. Wiggendaad, L.C. Ubels</i>	
<b>Impact Damage Growth and Failure of Carbon-Fibre Reinforced Plastic Skin-Stringer Panels</b>	<b>573</b>
<i>Emile Greenhalgh, Sunil Singh, Donald Roberts</i>	
<b>Simulation of Impact Deformation, Damage &amp; Fracture in Composite Laminates</b>	<b>583</b>
<i>Da-Xhi Jiang, Wei Shen, Xing-Ye Wang</i>	

## **Ceramic Matrix Composites**

<b>Fabrication and Mechanical Properties of Glass Matrix Composites with Different Fibre Architectures</b>	<b>593</b>
<i>Heinrich Kern, Volker Winkler, Aldo R. Boccaccini</i>	
<b>Thermoelectric Properties of B<sub>4</sub>C-Based Composite Ceramics Prepared by Arc-Melting</b>	<b>603</b>
<i>Takashi Goto, Jianhui Li, Toshio Hirai</i>	
<b>Formation and Characterisation of Fibre-Matrix Interfaces in Continuous Fibre Reinforced Silicon Carbide</b>	<b>613</b>
<i>Pamela M. Farries, Jean-Bernard Veyret</i>	

<b>Structural Analysis of Ceramic-Matrix Composites</b>	<b>621</b>
<i>Alain Burr, Francois Hild, Frederick A. Leckie</i>	
<b>Failure Mechanism of a Multi-Layer Coating for the Oxidation Protection of C/C Composites</b>	<b>630</b>
<i>Laifei Cheng, Litong Zhang, Yongdong Xu</i>	
<b>Subsurface Damage Measurement on Carbon Carbon Composite Materials in Braking Applications</b>	<b>638</b>
<i>Yves Remond, Christiane Wagner</i>	
<b>Microstructural Characterisation of 3D Woven SiC/SiC-based Composites after Tensile Testing at Room and Elevated Temperature in Different Atmospheres</b>	<b>646</b>
<i>Ian J. Davies, Takashi Ishikawa, Masaki Shibuya, Tetsuro Hirokawa</i>	
<b>The Mechanical Properties of 3D Woven Carbon Fibers Reinforced Ceramic Matrix Composites</b>	<b>658</b>
<i>Wenwei Zheng, Xingye Wang, Jiayu Xiao, Fengrong Liu, Dazhi Jiang, Zhaohui Chen</i>	
<b>Effects of Temperature and Layup on the Mixed-Mode Delamination Toughness of a Ceramic Matrix Composite Material</b>	<b>665</b>
<i>Jonathon J. Polaha, Tor W. Sherwood, Barry D. Davidson</i>	
<b>Toughening of Silicon Nitride Matrix Composites by the Addition of Si-C-N Nanometer Particles</b>	<b>675</b>
<i>Xingui Zhou, Changrui Zhang, Zhaohui Chen, Kai Xie, Anchen Zhou</i>	
<b>Non Linear Behavior of Two Woven Ceramic Matrix Composites Under Cyclic Loading</b>	<b>682</b>
<i>Jean-Marie Morvan, Stéphane Baste</i>	
<b>Fracture in Off-Axis and Angle-Ply Fiber Reinforced Ceramics</b>	<b>694</b>
<i>Alex S. Selvarathinam, Y.J. Weitsman</i>	
<b>The Research of Self-Reinforced HP Silicon Nitride</b>	<b>703</b>
<i>Li Fengmei</i>	
<b>Microstructural Study of the Sintered Composite Composed of TiN and Ni</b>	<b>709</b>
<i>Shujie Li, Yuping Li, J.H. Maas, J. Boeijmsma, B.H. Kolster</i>	
<b>Structural Evolution of C/C-SiC Composites Through the Main Production Steps on the Liquid Silicon Infiltration (LSI) Route</b>	<b>717</b>
<i>Herbert Mucha, Akira Kamiya, Bernhard Weilage</i>	
<b>The Fabrication of Two Dimensional Carbon Fiber Reinforced Alumina Composites by Pressure Infiltration</b>	<b>725</b>
<i>Hsien-Kuang Liu, Bor-Horng Lin</i>	
<b>Application of Pre-ceramic Polymer For Shape-Forming of Multiphase SiC/Si<sub>3</sub>N<sub>4</sub> Ceramic Parts</b>	<b>735</b>
<i>Yongqing Li, Zhaohui Chen, Changrui Zhang, Haifeng Cheng, Ancheng Zhou, Xiaoheng Bao</i>	
<b>Key Components of High Temperature Stable High Oxidation Resistant Ceramic Matrix Composites of SiC/SiC Type Working Out and Technological Ways of their Making</b>	<b>741</b>
<i>A.M. Tsirlin, V.G. Gerlivanov, N.A. Popova, Yu E. Pronin, E.K. Florina, S.P. Gubin</i>	
<b>Microstructure of the TZP Particulate Composites</b>	<b>751</b>
<i>Marek Faryna, Zbigniew Pedzich, Lidia Litynska, Krzysztof Haberkowicz</i>	
<b>FEM Analysis of Micro-Indentation Test for C/C Composites</b>	<b>759</b>
<i>H. Serizawa, S. Sato, H. Tsunakawa, A. Kohyama</i>	

<b>Preparation and Properties of 3D-Carbon Fiber Woven Preform Reinforced SiC and Al<sub>2</sub>O<sub>3</sub> Hybrid Matrix Composites</b>	<b>769</b>
<i>Jiayu Xiao, Fengrong Liu, Wenwei Zheng, Xingye Wang, Dazhi Jiang, Zhaohui Chen</i>	
<b>Continuous Fibre Reinforced Composites with Mullite Matrix Derived from Colloidal Precursors</b>	<b>775</b>
<i>Jaili Wu, Frank R. Jones, Peter F. James</i>	
<b><i>New and Non-Traditional Materials</i></b>	
<b>Mechanical Properties of Spider Silk</b>	<b>785</b>
<i>Sueo Kawabata, Frank K. Ko, Mari Inoue, Masako Niwa, John W. Song</i>	
<b>Natural-Fibre-Mat-Reinforced Thermoplastic Composites Based on Flax Fibres and Polypropylene</b>	<b>794</b>
<i>S. Garkhail, R. Heijenrath, M. van der Oever, H. Bos, T. Peijs</i>	
<b>Mechanical Properties of Woven Fabric Carbon/Magnesium-Composites</b>	<b>804</b>
<i>O. Öttinger, W. Schäff, C. Hausmann, T. Heyne, R.F. Singer</i>	
<b>Modelling Stress Transfer in a Wood Composite</b>	<b>813</b>
<i>Rowan Paton</i>	
<b>Microcellular Graphitic Foam Processing</b>	<b>825</b>
<i>Kristen M. Kearns, David P. Anderson</i>	
<b>Development and Characterisation of a New High Damping Composite: Mg<sub>2</sub>Si/Mg</b>	<b>833</b>
<i>Christine Mayencourt, Robert Schaller</i>	
<b>Interface Study of Composite Bands Formed by Powders Plating and Rolling (PPR)</b>	<b>845</b>
<i>Sun Yong, Zhang Shuhong, Zhang Daiming, Qian Tiancai, Gao Yun, Li Bin</i>	
<b>Mechanical Performance of Compression Molded and Injection Molded Blends of LaRC Polyimide with Polyetherimide (PEI)</b>	<b>851</b>
<i>David Olivero, Donald Radford, Sarah Hummel, Charles Smith, Betty Tung</i>	
<b>Engineering Composite Electret Materials</b>	<b>859</b>
<i>L.S. Pinchuk, V.A. Goldade, I.M. Vertyachikh, V.N. Kestelman</i>	
<b>Multi-Axial Warp Knitted Layers - a Textile for Reinforcing Concrete</b>	<b>870</b>
<i>Gerd Franzke, Peter Offermann, Thomas Bischoff, Burkhard Wulfhorst</i>	
<b>Processing and Electrical Properties of PTCR Composite Materials</b>	<b>881</b>
<i>Z.X. Xiong, K.Z. Baba-Kishi</i>	

# COMPRESSION AFTER IMPACT (CAI) PROPERTIES OF HAT STIFFENED CF/PEEK PANELS FABRICATED THROUGH A ROUTE WITHOUT AUTOCLAVE

**Takashi Ishikawa and Masamichi Matsushima**

*Airframe Division, National Aerospace Laboratory  
6-13-1 Ohsawa, Mitaka, Tokyo 181, Japan*

**SUMMARY:** Compression after impact (CAI) properties in composite structure levels were experimentally obtained and examined. A remarkable feature in the fabrication technology of the test piece panels was the fusion bonding process without autoclave. This route was pursued for possible low cost fabrication methodology of carbon fiber (CF)/thermoplastic composites exhibiting an excellent damage tolerance property. Used test specimens were stiffened panels with hat shaped stiffeners regarded as optimal for CF/thermoplastic, CF/PEEK being chosen here. Two kinds of panels in size were tested in compression loading after drop weight impact for creating delamination. The results are compared with the previous similar CAI tests for T-stiffened panels of CF/PEEK where the present results exhibit higher CAI values. A potential of this fusion bonding technology without autoclave is indicated. Numerical analysis for predicting initial buckling stress was also conducted with a favorable agreement with experiments.

**KEYWORDS:** experiments, impact, delamination, thermoplastic composites, fusion bonding, ultrasonic C-Scan, buckling, finite element analysis

## INTRODUCTION

Damage tolerance properties of composites are considered to be important design criticals in their application to aircraft structures. Particularly, importance of compression after impact (CAI) values have been recognized in strength design of composite wing or fuselage in recent years. Therefore, NAL of JAPAN has been conducting a long term research project [1] for development of tough composite structures to aircraft component. A chosen material system in this project was CF/PEEK. After basic material properties including compression after impact (CAI) strengths for NASA type thick plates [2] were obtained, stiffened panels with four T-shaped stiffeners were tested [3,4] as structural level CAI evaluations. Based on such achievement, two model wing box structures of CF/PEEK were built and tested [1,5] in fatigue loading followed by residual static strength tests. The results of these boxes exhibited high delamination propagation resistance and excellent strength properties. In summary, a possibility of 35 % weight reduction by CF/PEEK from a baseline metal structure was verified [1] even in a conservative estimate.

However, one major disadvantage of CF/PEEK was also revealed through this work. Since it requires high temperature and pressure during fabrication procedure, its autoclave processing may lead to high cost because of expensive autoclave itself and tooling. This fact could be an obstacle for rapid spreading of CF/PEEK material into aerospace composite community. Based on such a background, a fabrication technique without an autoclave has been pursued by NAL and Fuji Heavy Industries Inc. (FHI) in JAPAN for realizing low cost thermoplastic composite structures. A possible solution might be non-traditional hot-pressing where an appropriate shape of stiffeners is also a key point of concern. The present paper describes recent results of this research program. A detailed description of fabrication process [6] will be minimized and the focus will be placed on presentation and discussion of experimental CAI properties. Numerical analysis of them with locally delaminated hat stiffeners at skin-stiffener interface was also conducted using a commercially available finite element code.

### DESCRIPTION OF TEST SPECIMENS

As stated before, material employed was CF/PEEK (AS4/APC-2). Shape and dimensions of a smaller test panel stiffened by single hat are shown in Fig.1, which is considered to be a prototype of larger panels. The larger panel dimensions stiffened by three hats are shown in Fig.2. A hat shaped stiffener was chosen for its compatibility with secondary fusion bonding to a flat skin and anti-buckling properties. A key point of the fusion bonding technique without autoclave is a development of a mold-platen containing line heaters. At first, a technique with PEEK film was established and two smaller panels were fabricated with this route, designated as CPA03 and 04. A problem of non-uniform thickness distribution in skin-stiffener attachment flanges remained unsolved in this phase probably due to re-softening mentioned later. Next, several thermoplastic films with lower melting point than PEEK and methods for fusion promotion into CF/PEEK substrate structure were tried in their combinations. Some screening interlaminar toughness and strength tests were conducted and a combination of PEI and pre-fusion to a substrate was selected [6]. A benefit of this technique is that re-softening and deformation in the previously formed region can be minimized during fusion bonding. One larger panel designated as CPB02 was fabricated through this method, whereas a larger panel CPB01 was also

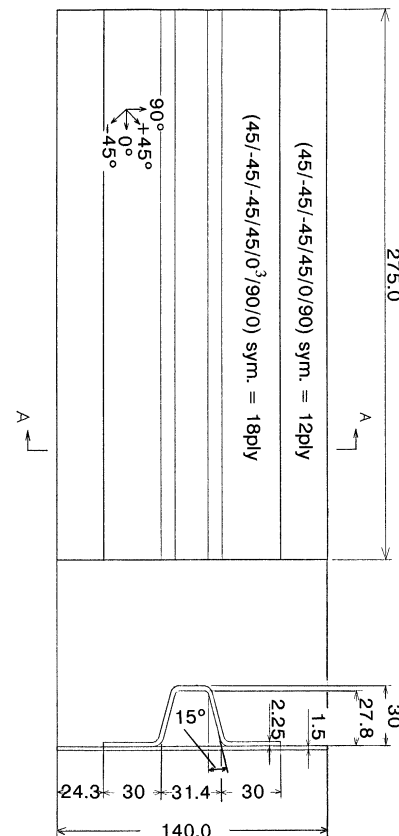


Fig.1: Single hat panel: shape and dimensions

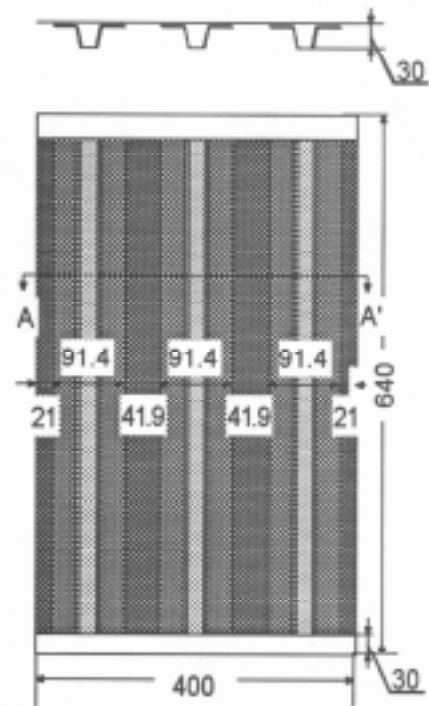


Fig. 2: Three hat panel: shape and dimensions



fabricated through an established PEEK film with autoclave technique for comparison. Stacking sequences were  $(45/-45/-45/45/0/90)_{sym}$ :12 plies and  $(45/-45/-45/45/0/90)_{sym}$ :18 plies for skin and stiffener, respectively, regardless of panel sizes. Aluminum end platens were adhered with a epoxy potting agent for compression tests for both loading edges of the panel.

### OUTLINE OF IMPACT TESTS AND FORMED DELAMINATION

All the panels were subjected to drop weight impact tests on a skin-stiffener bonding region with the following normalized energy levels (Unit: J/mm) by thickness at a impact point: CPA03= 2, CPA04= 4, CPB01=6.7 (with Autoclave) , CPB02=6.7 (with PEI film). These levels were determined so as to create barely visible indentation according to the previous results [3,4] and preliminary impacts. The reason why the larger panel required greater energy is supposed that some amount of impact energy was consumed in elastic deformation under a longer supporting span. Impact points were located on a mid-line parallel to the loading ends. The panels were supported on a very stiff steel table and hold by C-cramps at impact as shown in a photo of Fig. 3.

The panels were C-scanned after impact and projection area of delamination was measured by a ultrasonic C-scanner. A typical delamination image taken through a C-scanner, SDS 3300 by Krautkraemer Japan Co., is shown in Fig. 4 for CPA04 panel. It can be seen that delamination occurred almost along fusion bonding interface in this case.



Fig. 3: Photo of impact test by drop weight impactor

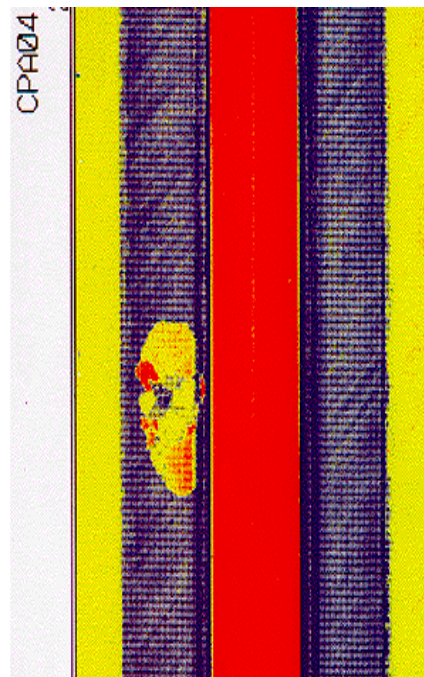


Fig.4: Delamination image for CPA04

Although an indication is omitted here, delamination also took place within skin and stiffener in cases of CPB01 and 02, which is similar to one shot thick plate cases [2]. Relationships between normalized impact energy and the delamination area in projection are indicated in Fig. 5 with the previous T-stiffened panel results [3,4]. A general tendency of the present impact results seems to be reasonable, although larger panels show smaller areas due to the

above reason. It can be understood that the present fusion bonding technique without autoclave worked out well from a standpoint of impact delamination.

**OUTLINE OF COMPRESSION TESTS AFTER IMPACT AND DISCUSSIONS**

Compression tests were conducted after 12 strain gages were glued onto the smaller panels. For the larger panes, 88 strain gages were used whereas a description of results is omitted in this paper because tests are undergoing now. For the smaller panel, a strain gage map is shown in Fig.6 where even number gages were glued back to back of odd ones on a stiffener side with some exceptions. A gage #3 was placed on an impact indentation. A number of gages, 12, was limited by 16 channel capacity of a data logger, . Thus, these strains, a load and 3 points of deflections were recorded into this data-logger, DAA 100A by Kyowa Co. JAPAN. Loading edge conditions were close to clamped due to aluminum end platens. Stainless steel tubes with sharpened slits acting as knife edges were installed along both side edges so that simply supported conditions were approximately realized. Compression load was introduced by Instron 1128 screw driven machine directly through a glued platen. A photo taken during a compression test is shown in Fig.7.

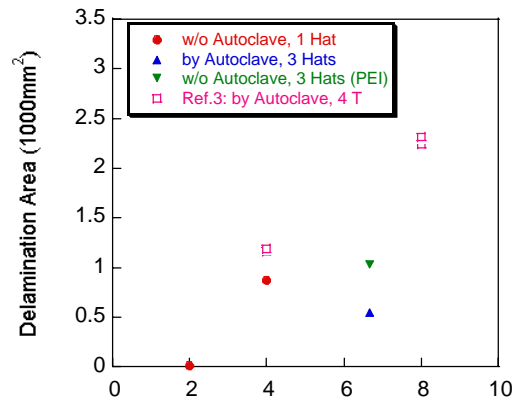


Fig.5: Relationships between normalized impact energy and delamination area

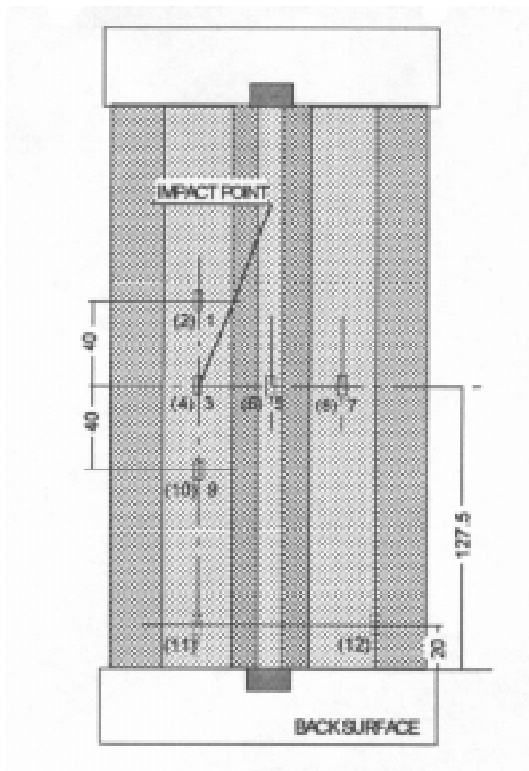


Fig. 6: Strain gage map for CPA panel

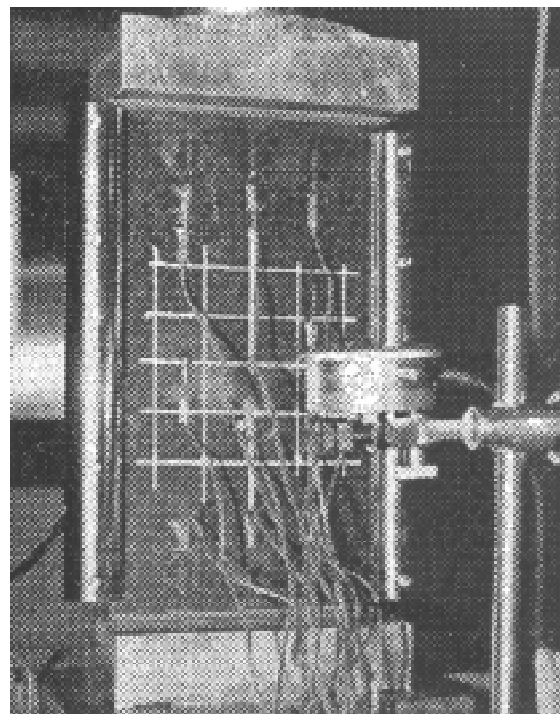


Fig. 7: Photo of compression test for CPA

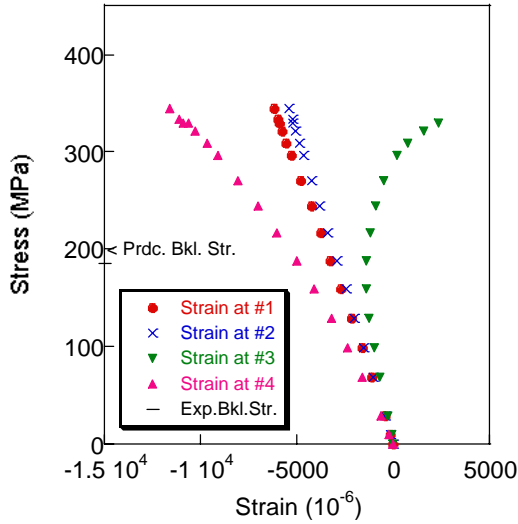


Fig. 8: Stress-strain behavior for panel CPA04 (4J/mm)

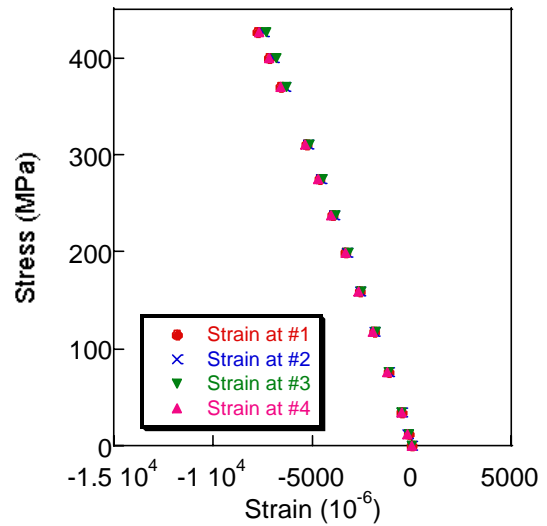


Fig. 9: Stress-strain behavior for panel CPA03 (2J/mm)

Stress-strain behavior for the case where impact delamination affects the final strength, CPA04 with 4 J/mm, is shown in Fig.8. Note that delamination of this panel was already shown in Fig. 4. In Fig.8, a back-to-back pair of strain gages, #3 and #4 on the delamination, clearly indicates the behavior of delamination buckling far prior to the final failure. Such behavior is basically similar to that of a CF/PEEK T-stiffened panel in Ref. 4. It should be noted that an inflection point of stress-average strain curve for this pair provides an experimental initial buckling stress, being determined as 185MPa for CPA04. A comparison of this value with a numerically predicted initial buckling stress will be discussed later.

For CPA03 panel with 2J/mm impact, a delamination area measured by C-scan was 1/50of CPA04. Therefore, its stress-strain behavior shown in Fig. 9 does not indicate any symptom of delamination buckling before the final failure. All curves are almost straight up to the failure and coincide with each other.

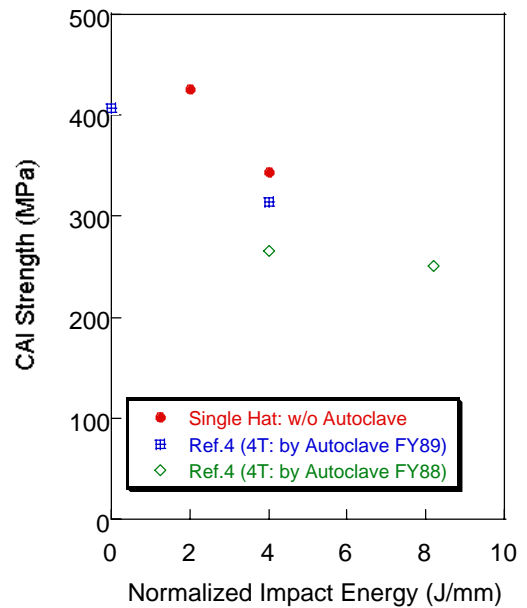
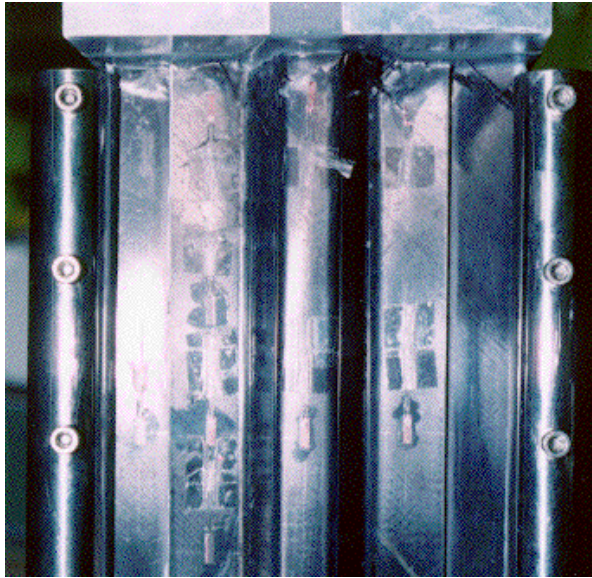


Fig. 10: CAI strengths vs. impact energy

CAI strengths of the smaller hat stiffened panels without autoclave fabrication are shown in Fig.10 with comparison data of CF/PEEK panels stiffened by four T-shaped stiffeners and fabricated by autoclave technology in FY 1988 and 1989 [3,4]. Although single stiffener panels exhibit a disadvantage in terms of CAI strength comparing with multi-stiffener panels [4], the present hat-stiffened panels show excellent CAI strengths. If we take a note for 4



J/mm data of 344MPa, the present fusion bonding quality without autoclave can be regarded as excellent.



*Fig. 11: Final Failure Mode of CPA 04 panel fabricated without autoclave and impacted with 4J/mm*

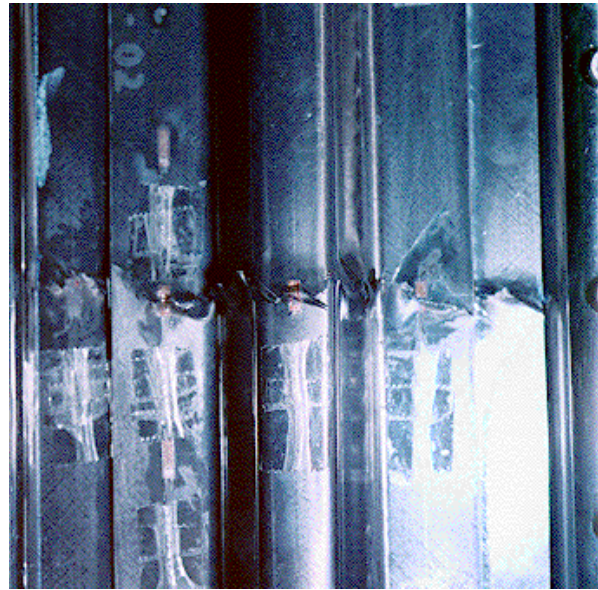


*Fig. 12: Final Failure Mode of CPA 03 panel fabricated without autoclave and impacted with 2J/mm*

The reason why even a strength at 2 J/mm (CPA03) exceeds no impact strength of 4-T panel can be ascribed to a good anti-buckling property of hat stiffeners and a small delamination area by virtue of an excellent fusion bonding quality without autoclave.

Final failure modes of these panels are indicated in photos of Fig.11 and 12 taken from the stiffener side for panels CPA04 and 03, respectively. In Fig.11 with larger delamination area, a transverse failure band formation to the introduced loads can be observed which was observed in flat plate CAI tests [7] without any exception. Although this failure band formation can be well correlated experimentally with the transverse delamination penetration in the case of flat plates, ambiguous mechanism remains unexplained in the detail in the present stiffened panels. At least, the delamination buckling behavior must be a trigger of the final failure in the present case. In Fig.12 with a very small size of delamination, the final failure occurred along the loading end platen and it was not influenced by delamination. This finding is in accordance with the stress-strain behavior indicated in Fig.9. Therefore, this CAI value of 426 MPa is estimated to be close to the compression strength of the present panel without delamination. A failure mode similarity to the NASA or SACMA plates with small delamination radius was verified in Fig.12.

CAI results for three stiffener panels are being obtained now and they would be demonstrated at the presentation. Thus, a description in the current text is skipped.

## **PREDICTION OF BUCKLING BEHAVIOR BY FINITE ELEMENT ANALYSIS**

Numerical analysis by a finite element method was conducted with simplified delamination location between skin and stiffener. A commercially supplied code, NISA-II, capable of handling laminate elements was used here. The used elements were 4 or 8 nodes isoparametric shell elements composed of assigned stacking sequence of unidirectional plies.

Outside of delaminated regions, skin-stiffener attachment flange was merely modeled as a thicker plate with total number of plies of both constituents where the thickness of fusion bonding film was neglected. This treatment implies that a slight local bending-stretching coupling may exist according to an unsymmetrical stacking sequence. In order to idealize a delaminated panel, a single delamination was assumed to exist between a skin and a hat stiffener. A projection shape of delamination was simplified into a rectangle nevertheless the true shape was the one as shown in Fig. 4. An important point of difference from the reality may be the following: Delamination edges along the fusion bonded region were considered to be free against opening deflection whereas narrow but tight bonded area remained along these edges according to a C-scan image. Boundary conditions along the loaded and the side edges were assumed to be fixed and simply supported, respectively, under consideration of potting material as discussed in Ref. 3 and tubular knife edges. Buckling under flat compression loading was simulated in the following manner. A static analysis was done first under the same specified end shortening at all the nodes along the loading edge and reaction forces at these nodes were obtained. Linear buckling analysis was done next using corresponding nodal forces along the loading line.

The employed elastic moduli for unidirectional CF/PEEK lamina are as follows:  $E_L = 117.3$  GPa,  $E_T = 10.3$  GPa,  $G_{LT} = 4.62$  GPa,  $\nu_L = 0.38$ , and  $\nu_{TT} = 0.5$  which are compatible with the experimental values adopted in Ref. 3. Ply thickness values for skin and stiffener regions were determined as 0.125mm and 0.13mm, respectively, from each measured thickness divided by ply number. An example of a numerical deformation pattern in the buckled state is shown in Fig.13 where absolute value of deflection has no meaning according to the nature of the eigenvalue problem. Because the delaminated area are assumed to be a rectangle as stated above, skin deformation pattern looks more square than reality. Initial buckling stress of 201 MPa was obtained and plotted by a symbol of < in Fig.8, whereas experimental buckling stress of 185 MPa determined through back-to-back strain gages was also plotted by — on the left axis in Fig.8. Note that stresses are merely plotted on the vertical axis. A correlation between these predicted and experimental buckling stress is shown to be very favorable. However, because the shape and area of the delaminated region, and geometrical structure of delamination were simplified very much in a finite element modeling, this good agreement is not considered to be a perfect description of this sort of complicated problem but some coincidence makes the agreement favorable. A discussion about this point may be summarized conservatively as follows: The present modeling of delaminated stiffened structure can predict a trend in deformation pattern of initial buckling and an approximate value of its initial buckling stress.

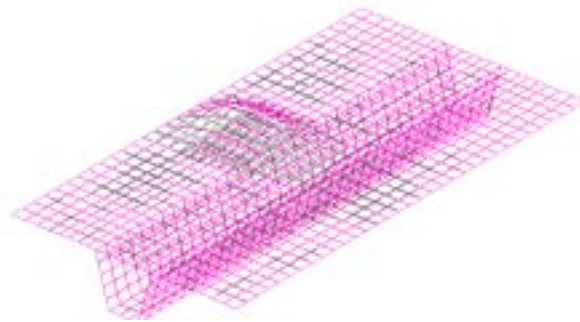


Fig. 13: Deformation Pattern in a Buckled Single Hat Panel under Flat Compression

## **CURRENT CONCLUSIONS**

A fabrication technology of stiffened panels using secondary fusion bonding without autoclave was pursued with a considerable success. Two key factors in the technology consist of a development of a mold with embedded heaters and adaptation of fusion bonding film to a thermoplastic composite substrate. A goal of this technology is to realize an affordable CF/thermoplastic structure for future civil transport aircraft. A stiffener shape of a hat was chosen so as to optimize buckling load and compatibility for fusion bonding. Single and three hat stiffener panels were fabricated of CF/PEEK (AS4/APC-2) material system. Both panels exhibited similar or superior delamination resistance under impact loading to panels of CF/PEEK containing four T-stiffeners which were fabricated and tested previously. CAI strengths of the present single stiffener panels are greater than those obtained for the 4-T panels. Thus, the present fusion bonding technology is proven as a potential fabrication method for an affordable thermoplastic composite component. Some part of the reason why the present no impact strength is higher than that of the 4-T panels can be attributed to a better buckling resistance of hat stiffeners than T's. Numerical predictions by finite element analysis were conducted for a simplified mechanical model of a delaminated panel. In terms of an initial buckling stress, correlation between the predicted and experimental values was favorable. Further effort will be required for complete prediction of the behavior in the postbuckling region.

Because a baseline technology for low cost thermoplastic composite structures is established, NAL of JAPAN is seeking to find an application route of heat-resistant thermoplastic composites to future high speed commercial transport where weight reduction is a crucial technological barrier. A candidate resin there is not PEEK but PIXA, semi-crystalline polymer by Mitsui-Toatsu Co. JAPAN. Fortunately, the present fusion bonding technology for CF/PEEK can be directly transferred to CF/PIXA material system. Structural test results for this new system will be presented in the future.

## **ACKNOWLEDGEMENT**

The authors owed a great deal of the present work to those who dedicated themselves to fabrication technology development in Fuji Heavy Industries LTD, e.g., Mr. Shigeru Machida and Hiroyuki Nakamura. The authors express their sincere gratitude to Mr. Kenji Matsui of JAMCO Co. LTD, Japan, (Student of Nihon University at moment) for his effort to conduct most of experiments. They also wish to thank Mr. Hee-Jun Kim of a student of Seoul National University, and Dr. Ik-Hyeon Choi of a senior researcher of KARI (Korean Aerospace Research Institute) for their assistance in some parts of the experiments. Their stay in JAPAN is supported by Japan-Korea Foundation and JISTEC. Fabrication expense of the panel specimens was funded by STA of Japanese Government for Future Supersonic Transport Technology Program.

## REFERENCES

1. Ishikawa, T., Hayashi, Y., Sugimoto, S., Matsushima, M., and Amaoka, K., "Development and Test Results of Full CF/PEEK (APC-2) Horizontal Stabilizer Models - Basis for SST Structure", *Proceedings 1st AIAA Aircraft Engineering, Technology, and Operations Congress*, Los Angeles, CA, USA, September 19-21, 1995, also AIAA Paper 95-3931
2. Ishikawa, T., Matsushima, M., Hayashi, Y., and Noguchi, T., "Comparison of Tensile and Compressive Properties of Some Structural Elements between Carbon/PEEK and Carbon/Epoxy Composites", *Proceedings 5th Japan-US Conference on Composite Materials*, Tama-City, Tokyo, Japan, June 24-27, 1990, Kobayashi, A., Ed., pp.445-452.
3. Ishikawa, T., Matsushima, M., and Hayashi, Y., "Improved Correlation of Predicted and Experimental Initial Buckling Stresses of Composite Stiffened Panels", *Composite Structures*, Vol.26, No.1, 1993. pp.25-38.
4. Ishikawa, T., Hayashi, Y., and Matsushima, M., "Compression after Impact Strengths of Stiffened Panels Made of CF/PEEK and CF/Epoxy (in Japanese)", *Journal of the Japan Society for Aeronautical and Space Sciences*, Vol. 42, No.484, 1994, pp. 319-328
5. Ishikawa, T., Hayashi, Y., Sugimoto, S., and Matsushima, M., "Development of Full CF/PEEK (APC-2) Horizontal Stabilizer Models and Their Strength Test Results", *Proceedings 10th International Conference on Composite Materials*, Whistler, British Columbia, Canada, August 14-18, 1995, Vol.III: Processing and Manufacturing, Poursartip, A., Street, K.N., Eds., pp. 693-700.
6. Machida, S., Nakamura, H., Kawakami, M., Akiba, K., and Ishikawa, T., "Development of Fusion Bonding Technology of Thermoplastic Composites with Focused Heating Method (in Japanese)", *Proceedings 37th JSASS/JSME Structures Conference*, Fukuoka-shi, Fukuoka, Japan, July 12-14, 1995, pp.249-252.
7. Ishikawa, T., Sugimoto, S., Matsushima, M., and Hayashi, Y., "Some Experimental Findings in Compression-after-Impact (CAI) Tests of CF/ PEEK (APC-2) and Conventional CF/Epoxy Flat Plates", *Composite Science and Technology*, Vol.55, No.4, 1995. pp.349-363.
8. Engineering Mechanics Research Corporation, "Users Manuals of NISA-II, Version 91", Troy, MI, April 1991.



# DAMAGE TOLERANCE OF BIOMIMETIC LAMINATES

Patrick Kim<sup>1</sup> and Toshio Tanimoto<sup>2</sup>

<sup>1</sup>*School of Engineering and*

<sup>2</sup>*Department of Materials Science and Ceramic Technology*

*Shonan Institute of Technology, 1-1-25 Tsujido Nishikaigan, 251 Fujisawa, Kanagawa, Japan*

**SUMMARY:** The strength of a biomimetic CFRP laminate with a stacking sequence similar to that found in many animal hard tissues is examined. The static strength of the biomimetic laminate with holes of different diameters is compared to that of a standard quasi-isotropic and a cross-ply laminate. The first two have similar elastic moduli and strengths without a hole. The ratio of notched to unnotched strength is also nearly the same, while the cross-ply laminate has the lowest ratio. This difference is explained in terms of the extent of an equivalent damage zone, which depends on the laminate's architecture. The implications of the findings for the design of damage-tolerant laminates are discussed.

**KEYWORDS:** biomimetic composite, damage tolerance, notched sample, strength ratio, fracture, fiber orientation distribution

## INTRODUCTION

Biological materials derive remarkable mechanical properties from their composite nature and reinforcement architecture. Many biological composites are fiber-reinforced laminates similar to plywood, with a fiber orientations that varies through their thickness in relatively constant angle steps [1-3]. As these composites often have a protective or structural function, such as in insect cuticles, it has been assumed that this fiber architecture may give them a particularly good strength or damage tolerance. If this should be the case, a biomimetic microstructure would be a way to make improved composites [3, 4]. Tests have shown that the quasi-static moduli and unnotched strength of a biomimetic and a conventional quasi-isotropic laminate are nearly the same. Gunderson and Whitney however showed that the impact resistance of the biomimetic laminate, in terms of energy and force to initiate delamination, was better than that of a standard quasi-isotropic laminate [3]. To examine the post-impact performance, this paper presents results on the quasi-static behavior of a biomimetic laminate including some damage. It examines the sensitivity of a biomimetic laminate to the presence of a damaged area, here modeled as an open hole, and compares the residual strength and the fracture patterns to those of conventional quasi-isotropic and a cross-ply laminates.

## THEORETICAL BACKGROUND

Various authors, including Neville [1], Giraud et al. [2], and Gunderson and Whitney [3] have shown examples of biological laminates with a fairly regular angle difference of about 78°

between successive plies (Fig. 1). This lamination scheme, selected for the biomimetic laminate in the present study, gives a double helical lay-up with angle steps of  $24^\circ$  for each helix. For a 16-ply laminate, the outermost plies are oriented at  $90^\circ$  with respect to each other, and the laminate is nearly quasi-isotropic.

The damage tolerance as related to the ratio of strength of a laminate with and without a hole was analyzed by the Damage Zone Criterion (DZC) approach developed by Eriksson and Aronsson [5]. The actual, two-dimensional damage in the laminate is modeled as a fictitious crack extending from the hole perpendicularly to the applied load. The residual stress acting on this crack of length  $d$  representing the damage zone is assumed to be constant. The stresses ahead of this crack correspond to a linear elastic stress distribution for an anisotropic plate:

$$\begin{aligned} \sigma_r &= \sigma_o, \quad x \leq d \\ \sigma_r &= \frac{\sigma_a}{2} \left\{ 2 + R^2 + 3R^4 - (K_T^\infty - 3)[5R^6 - 7R^8] \right\} \quad x \geq d \\ R &= D/2x \end{aligned} \tag{1}$$

where  $\sigma_a$  is the applied stress,  $\sigma_r$  is the stress on the reduced section,  $\sigma_o$  is the strength of the laminate without hole, and  $D$  is the diameter of the hole. The stress concentration factor  $K_T^\infty$  for an infinitely wide plate depends on the laminate's elastic properties:

$$K_T^\infty = 1 + \left[ \frac{2}{A_{22}} \left( \sqrt{A_{11}A_{22}} - A_{12} + \frac{A_{11}A_{22} - A_{12}^2}{2A_{66}} \right) \right]^5 \tag{2}$$

where  $A_{ij}$  are the laminate stiffnesses. The elastic properties of the laminates were calculated using classical lamination theory [6]. A correction was made for the finite width of the samples. This however gives a negligible calculated difference for the sample dimensions used here and is thus not absolutely necessary. The integral of the stresses on the net section must equal the applied load:

$$\frac{\sigma_a w t}{2} = \sigma_o t d + \int_{D/2+d}^{w/2} (\sigma_o + \sigma_r - \sigma_r|_{x=D/2+d}) dx \tag{3}$$

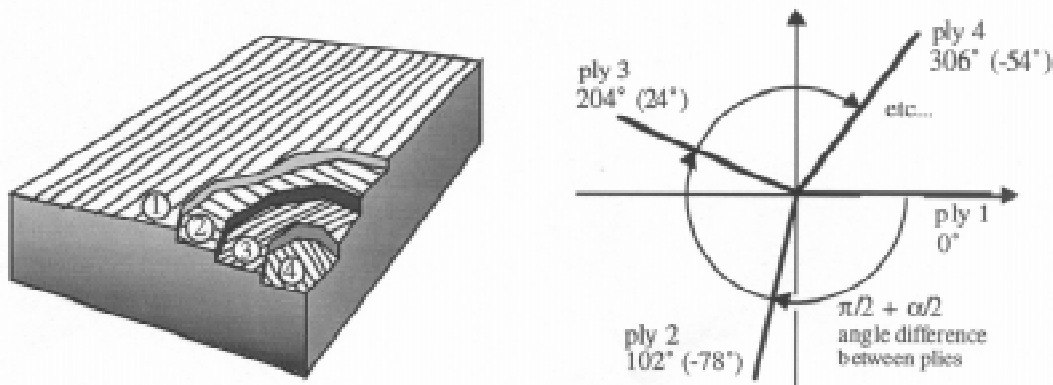


Fig. 1: Lay-up of the biomimetic composite laminate

The critical damage zone size  $d^*$  can be calculated from this equation at the ultimate load  $\sigma_N$  of the sample with a hole [5]. This damage zone size is taken as an indicator of the damage

tolerance of the laminate. A larger damage zone at failure would point to a higher damage tolerance, as it gives a higher ratio of strength with a hole to strength without a hole.

## EXPERIMENTAL

The samples were made from unidirectional (UD) AT400/EP carbon fiber-reinforced epoxy prepregs (Asahi Kasei Corporation, Japan). The cured material had a longitudinal modulus of 117Gpa and a transverse modulus of about 11GPa. Laminated plates consisting of 16 plies of prepreg were cured in an autoclave at a pressure of 6bar and 130°C for two hours. The samples were slow cooled under pressure by turning off the heat in the autoclave, in order to minimize internal stresses. The resulting laminates had a thickness of 1.98mm,  $\pm 0.06$ mm. The cured plates were cut into 20mm wide samples with a water-cooled rotary diamond saw. The samples were then left to stabilize at room temperature and humidity for at least one week. The lay-ups of the samples for this study are given in Table 1. Samples were tested without hole and with a central 4mm or 5mm diameter hole corresponding to a ratio of hole diameter to sample width of 1/5 and 1/4. The CFRP samples were clamped between two 5mm thick acrylic plates during drilling, in order to keep damage around the hole during machining to a minimum. The samples without and with a hole had a gauge length of 120mm and 80mm, respectively. Tapered GFRP tabs were bonded to the sample ends to reduce the likelihood of damage or slippage in the grips.

The tensile tests were conducted monotonically up to failure at a cross-head velocity of 1mm/min. For the samples without holes the extension was measured by strain gauges bonded to both sides of the samples. Strength results were accepted only for samples in which failure damage did not extend into the gripping areas. For the samples with holes, the load-extension curve and the peak force were recorded. The stress was calculated based on the full section of the sample.

*Table 1: Definition of sample types*

Sample	Lam. type	Laminate lay-up
CP	Cross-ply	$(0^\circ / 90^\circ)_{4s}$
QI	Quasi-isotropic	$(0^\circ / 45^\circ / 90^\circ / -45^\circ)_{2s}$
BM	Biomimetic	$(0^\circ / -78^\circ / 24^\circ / -54^\circ / 48^\circ / -30^\circ / 72^\circ / -6^\circ // -84^\circ / 18^\circ / -60^\circ / 42^\circ / -36^\circ / 66^\circ / -12^\circ / 90^\circ)$

## RESULTS AND DISCUSSION

The biomimetic and the standard quasi-isotropic laminates had nearly the same elastic modulus, while the cross-ply laminate was much stiffer (Table 2). The experimental moduli of the plain laminates are all within 5% of the predictions. The symmetric quasi-isotropic and cross-ply laminates had no extension/flexural coupling. The transverse strains on opposing surfaces of the biomimetic laminate, however, differed significantly, as the axial stress led to a bending about the longitudinal axis.

Table 2: Elastic properties of the unnotched laminates (calculated values in parentheses)

Sample	$E_l$ [GPa]	$\nu$	$\sigma_o$ [MPa]
CP	66.47 (64.4)	0.065	901
QI	48.84 (50.8)	0.335	676
BM	49.38 (52.0) / 47.98 (52.0)*	0.320 / 0.333*	654 / 619 *

\* in two normal directions, parallel to surface fibers

The unnotched laminates had a linear stress strain curve until failure. All samples failed on the free length, away from the grips. The strength of the biomimetic samples was 3-8% lower than that of the quasi-isotropic laminate. The cross-ply sample's strength was about one third higher, as a result of the higher proportion of strong 0° plies. The fractured zones had different appearances in all three samples. The cross-ply samples broke along a straight, slightly jagged line, perpendicular to the sample's axis, and damage was localized in the vicinity of the fracture. On the other hand, the damaged area in the quasi-isotropic and biomimetic laminates extended over a length corresponding to more than twice the tensile sample's width, with extensive delamination and splitting. The biomimetic laminate samples also failed in compression in the longer half of the broken sample, upon recoil at tensile failure. This happened for none of the two other laminate types, and may be due to a lower apparent compressive strength of the unsymmetric biomimetic laminate.

The notched strength, the notched-to-unnotched strength ratio, and the equivalent damage zone size calculated from the strength ratio are reported in Table 3, for laminates with two different hole diameters. The strengths of the biomimetic and quasi-isotropic laminates with a ø4mm hole were about the same. With a ø5mm hole, the biomimetic laminate had a clearly higher strength. Its strength ratio with a ø4mm or ø5mm hole was slightly over 4% higher and nearly 15% higher, respectively, than that of the quasi-isotropic laminate. Its strength was also less variable than that of the latter. Although the cross-ply laminate had a much higher unnotched strength than the others, its notched strength was just 11% higher than that of the quasi-isotropic and biomimetic laminates, and its strength ratio was almost 20% lower for a ø4mm hole. From these results, it would seem that the biomimetic laminate is slightly more tolerant to damage in the form of a hole than the quasi-isotropic laminate, and that this characteristic is more pronounced for larger hole diameters. Further tests are planned with other hole sizes, to verify this.

Table 3: Failure loads of the laminates with holes and calculated critical length of the representative damage zone. Standard deviation given in parentheses

Sample	$D$ [mm]	$\sigma_N$ [MPa]	$\sigma_N / \sigma_o$	$d^*$
CP	4.0	459.1 (14.1)	0.510	0.45
QI	4.0	407.3 (49.3)	0.603	0.89
	5.0	351.1 (26.4)	0.519	0.72
BM	4.0	399.8 (19.7)	0.628	1.01
	5.0	379.4 (18.1)	0.596	1.13

The calculated equivalent damage zone  $d^*$  at failure for the samples with the ø4mm hole was about 13% larger in the biomimetic than in the standard quasi-isotropic laminate. For a ø5mm hole, it was over 50% larger. The size of  $d^*$  for the cross-ply laminate was by far the



lowest, at less than half the value for the biomimetic laminate. The higher value of  $d^*$  indicates a more extensive lateral propagation of the damage before failure of the sample. The dependence of the extent of the damage on the laminate lay-up has been modeled by Chang et al. [6]. The present results concord with the analytical results of that group for the cross-ply and quasi-isotropic laminates: whereas the cross-ply samples failed suddenly, without prior sign, the development of damage in the quasi-isotropic samples was signaled by sharp, high-pitch sounds as failure approached. Although the biomimetic laminate had a similar calculated extent of damage at impending failure,  $d^*$ , as the quasi-isotropic laminate, its different reinforcement geometry is expected to lead to a different spatial distribution of the damage. The broader distribution of angles between plies and the loading direction is expected to lead to a wider range of interlaminar shear stresses near the edge and the hole, and thus to a more progressive evolution of damage. This will be investigated in the future. The stress distribution in the reduced section calculated by the DZC approach for a hole of  $\varnothing 4\text{mm}$  is shown in Fig. 2 for the three sample types. The distributions for the quasi-isotropic and biomimetic laminates are nearly the same, with the former having a higher stress in the damage zone, corresponding to the higher unnotched strength.

Fig. 3 illustrates the fracture observed in the samples with a  $\varnothing 4\text{mm}$  hole. The pictures are also fairly representative of the different fracture patterns observed in the samples with the  $\varnothing 5\text{mm}$  hole. The notched cross-ply laminate, like the unnotched sample, broke along a straight line, and the damage, involving mainly fiber breakage, was very localized. The locations of the fracture in the two legs of the reduced section were somewhat staggered. In the quasi-isotropic sample, the fracture ran at  $45^\circ$  from the hole, leading to a  $90^\circ$  V-shape. This was accompanied by delamination exposing mainly  $45^\circ$  layers and some loose debris of pulled-out delaminated layers. When the surface fibers were parallel to the sample's axis, extensive splitting occurred, while some spalling occurred for  $0^\circ$  surface layers. In the biomimetic laminate, the angle of the V-shaped fracture was larger, and much less splitting was observed in the surface layer with longitudinal fibers. Delamination exposed mainly layers with fibers at angles above  $45^\circ$ , leading to the conclusion that the other layers, at angles closer to  $0^\circ$ , failed by fiber breakage. The fact that more fiber breakage could be achieved at fracture for the biomimetic lay-up may explain the higher relative strength of the notched samples.

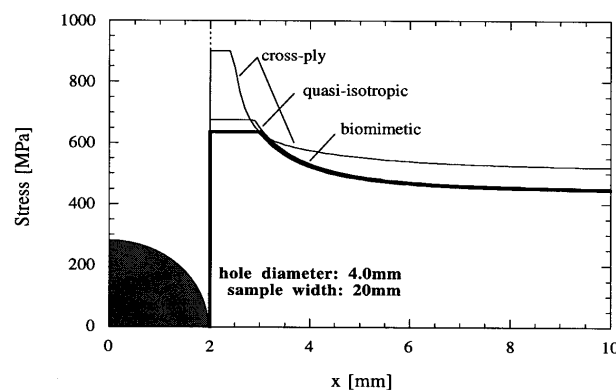


Fig. 2: Calculated stress profile at failure of samples with a 4mm diameter circular hole.

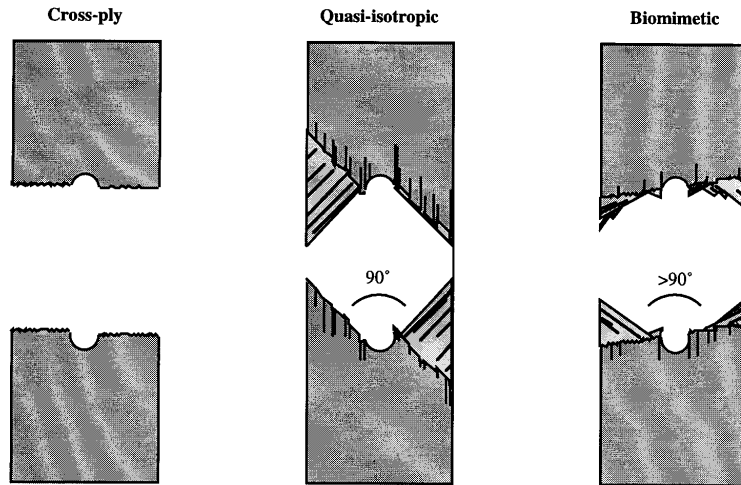


Fig. 3: Features of fracture in (from L to R) the cross-ply, quasi-isotropic, and biomimetic laminates with a central  $\phi 4\text{mm}$  hole.

Keeping in mind its higher resistance to impact damage initiation [3], the higher notched strength ratio of the biomimetic laminate further contributes to its better overall damage tolerance compared to the standard quasi-isotropic laminate. The tradeoff for this increase in performance is the higher complexity of the lay-up, requiring more care during production. With current automated, computer-controlled manufacturing methods, this should however be a minor problem when increased damage tolerance is really desired.

## CONCLUSIONS

The plain and notched strength of a biomimetic laminate with a reinforcement architecture similar to that used in biological composites has been examined and compared to the strength of conventional quasi-isotropic and cross-ply laminates. For plain samples without a hole, the modulus of the biomimetic laminate is about the same as that of the quasi-isotropic one, and its strength is only slightly lower. Both have a lower strength than the cross-ply laminate. When a hole is introduced into the laminate, the strength of the biomimetic laminate is decreased less than that of the quasi-isotropic, and much less than for the cross-ply laminate. This higher strength ratio and the larger size of a calculated equivalent damage zone indicates a somewhat superior damage tolerance of the biomimetic laminate under tension. This quality is more pronounced for the larger hole size in the present investigation. It is proposed to be a result of the broader distribution of fiber angles leading to a wider range of interlaminar stresses near the edges and hole. As the biomimetic laminate is also more impact resistant, its overall damage tolerance is clearly better than the conventional quasi-isotropic laminate.

## ACKNOWLEDGMENTS

We thank Ms. M. Taguchi for her contribution to the experimental work for this study.

## REFERENCES

1. Neville, A.C., *The Biology of Fibrous Composites: Development Beyond the Cell Membrane*, Cambridge University Press, 1993.

2. Giraud, M.M., Castanet, J., Meunier, F.J., Bouligand, Y., The fibrous structure of coelacanth scales: a twisted 'plywood', *Tissue and Cell*, Vol. 10, No. 4, pp. 671-686, 1978.
3. Gunderson, S.L., Whitney, J.M., A controlled unsymmetric ply orientation for improved isotropic properties, *Advances in Experimental Mechanics*, ASME Vol. AMD-146, pp. 99-109, 1992.
4. Li, S., Zhang, R., Fu, S., Chen, X., Zhou, B., Zeng, Q., A biomimetic model of fiber-reinforced composite materials, *Journal of Materials Science and Technology*, Vol. 10, No. 1, pp. 34-38, 1994.
5. Eriksson, I., Aronsson, C.-G., Strength of tensile-loaded graphite/epoxy laminates containing cracks, open and filled holes, *Journal of Composite Materials*, Vol. 24, No. 5, pp. 456-482, 1990.
6. Chang, K.-Y., Liu, S., Chang, F.-K., *Journal of Composite Materials*, Vol. 25, pp. 274-301, 1991.

# EFFECT OF LOADING PARAMETERS ON COMPRESSION DOMINATED FATIGUE BEHAVIOR OF IMPACT DAMAGED COMPOSITE LAMINATES

Milan Mitrovic, H. Thomas Hahn & Greg P. Carman

*Mechanical & Aerospace Engineering Department,  
University of California, Los Angeles, CA 90095-1597, USA*

**SUMMARY:** In this paper work aimed at characterizing the influence of low-velocity impact damage and loading parameters on fatigue response of AS4/3501-6 quasi-isotropic laminates is presented. Constant amplitude compression-compression fatigue tests indicate that the impact induced delamination does not growth in the absence of local buckling effects and for the load levels below 50% of the CSAI (Compressive Strength After Impact). In the presence of overloads maximum compressive strain that these laminates can sustain without damage growth is reduced substantially, and block loading tests indicate that the high/low sequence is more damaging than the low/high loading sequence. Constant amplitude tension-compression fatigue of impacted laminates shows negligible differences in terms of life and damage propagation modes when compared to the undamaged specimens. Results of this study suggest that clearly defined damage tolerance criteria for impacted composite laminates can be derived from a limited number of tests.

**KEYWORDS:** impact damage, post-impact fatigue, damage tolerance

## INTRODUCTION

In aircraft applications composite panels are routinely subjected to both low-velocity impacts and long term mechanical loading (fatigue). These loading events cause damage to develop in the form of fiber breakage, matrix micro-cracking, and delaminations which lead to material property degradation with the most severe being compression strength. This reduction represents one of the major issues for satisfying the safety requirements of the aircraft structures. Strength reduction of impacted composite panels has been studied extensively over the past decades, and it has been shown that it depends both on the type and extent of damage.

The post-impact fatigue behavior has been studied by a number of researchers on different materials, lay-ups, and for different loading conditions. Stellbrink [1] studied the fatigue behavior under the tension-compression loading of T300/69 and T300/914 quasi-isotropic laminates. From S-N curves, it was concluded that the rate of life reduction is higher for undamaged than for damaged specimens, and that test data agree better with the sudden death model than with the degradation model. Influence of impact damage on fatigue behavior of AS4/3501-6 laminates under tension-tension (T-T), tension-compression (T-C), and compression-compression (C-C) loading was studied by Ramkumar [2]. Fatigue testing was performed at stress levels above 60% of the ultimate strength, and while most of the specimens subjected to T-T loading survived 1 million cycles, all specimens loaded in T-C

and C-C failed well before. The author concluded that tensile loading, static or fatigue, represents the least severe mode to cause additional damage in impacted laminates. In another experimental study by Ramkumar [3], the effect of imbedded (idealized) delaminations on the compression behavior of three different stacking sequence of quasi-isotropic T300/5208 graphite/epoxy laminates was investigated. From the S-N data, it was concluded that the threshold value of the maximum compressive stress, at which failure is not expected to occur, depends on the location and shape of the implanted delamination. Also, the occurrence of delamination growth and its direction is shown to be dependent of the laminate stacking sequence and its through-the-thickness location, and the failures were induced predominantly by the propagation of imbedded delaminations to the tab region. Blaricum et al., [4], studied the compression dominated loading based on the modified FALSTAFF flight by flight sequence on a [+45/-45/0/0]<sub>7S</sub> XAS-914C impacted specimens. Fatigue testing is performed under the maximum compressive strain of 0.36%, a value close to the design strain used in military aircraft. It is reported that for this type of material and lay-up, the low load levels can be deleted from the testing sequence with no significant effect on fatigue life, and that the duration effect of high-level loads does not influence fatigue life significantly. Some researchers have suggested the fatigue damage tolerance criteria for impacted composite structures that require only static loading [5]. This is based on observations that the impacted composite panels have very flat compression *S-N* curves, and that although compression strength is greatly influenced by the impact damage, any subsequent reduction under fatigue loading is minimal.

While the real service loads are usually kept much lower than the ultimate failure loads, most of the research work on fatigue of composite laminates with impact induced damage has focused on the final failure. The objective of this study is to determine the influence of loading parameters on impact induced delamination growth during fatigue loading, and the fatigue design limits (delamination growth thresholds) for composite laminates containing barely visible low-velocity impact damage. Specifically the effects of load type, load level, load sequence, and the effect of overloads, their magnitude and place in the load spectrum are of interest in this study. Method to accelerate fatigue testing is suggested by extending the results of compression dominated constant amplitude and block loading tests to random fatigue loading.

## **EXPERIMENTAL SETUP**

Quasi-isotropic [0/+45/-45/90]<sub>S4</sub> laminates made from an AS4/3501-6 graphite/epoxy material system were used in this study. Gage length of the coupons for static and fatigue tests of 38.1 x 38.1 mm was chosen to prevent the occurrence of buckling effects in the presence of compressive loads. Impact tests are performed on a Dynatup 8200 drop weight impact testing machine with a 6.35 mm and 12.7 mm tup diameters and 4.3 kg impactor weight (cross-head and tup). A modified SACMA SRM 2-88 impact fixture was used to provide the necessary support for the specimens. Modifications were made to accommodate specimens dimensions used in this study, and consisted of a smaller 25.4 x 25.4 mm square cutout instead of the recommended 76.2 x 127 mm cutout. In conjunction with the Dynatup 8200 drop weight impact testing machine, the model 730-I data acquisition and analysis system was used which can provide complete records of impact energy and force as a function of time. Static compression tests are performed on a 50 kN capacity Instron test frame. The specimens were loaded at a displacement rate of 1.27 mm/min, per ASTM D3410-75 standard. An end-loaded compression testing fixture was used, which is similar to NASA

short block compression fixture. The test fixture was placed in the test frame upon a spherical seat which provided alignment of the specimen during compression. Following static tests, the fatigue was performed on a 10 kN capacity Instron test frame. Monitoring damage progression during fatigue loading, via X-ray radiography, was done periodically to assess the change of the damaged area as a function of loading parameters.

**IMPACT DAMAGE EVALUATION AND COMPRESSIVE STRENGTH AFTER IMPACT (CSAI)**

Initial impact tests were performed to determine the influence of impact test parameters on damage development. Impact energies were adjusted to produce barely visible impact damage for subsequent fatigue loading. The overall impact damage area, in the form of a delamination, has been determined via X-ray radiography, and the observed damage size is plotted versus the incident impact energy in Figure 1.a. Caution should be taken when interpreting results for the maximum damage diameter of 25.4 mm achieved in these tests, since it coincides with the 25.4 x 25.4 mm square cutout of the clamping fixture. That is, the damaged area might have been larger if the boundary conditions in these tests were different (i.e., for the larger unsupported area).

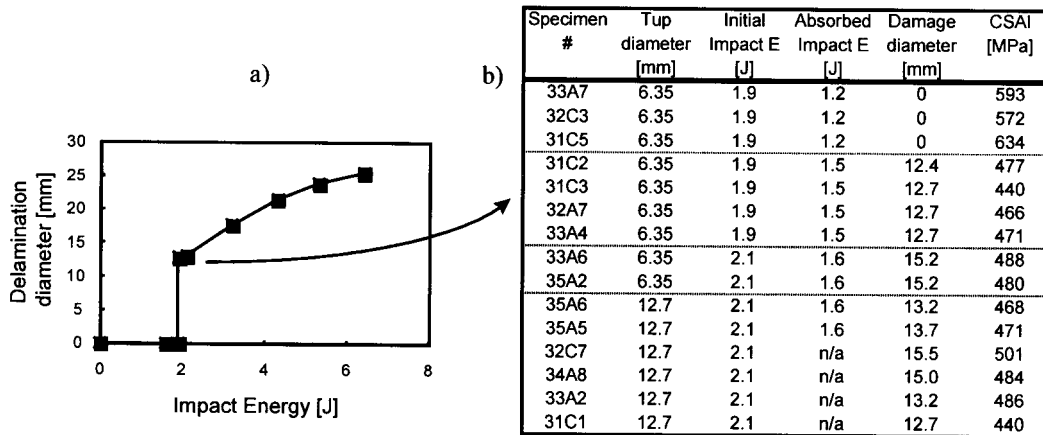


Fig. 1. a) Damage area vs. the incident impact energy  
 b) CSAI as a function of impact test parameters

As can be seen from Figure 1.a, some specimens that were impacted with the same incident energy of 1.9 Joules, displayed different damage patterns. That is, some specimens contained delaminations 12.7 mm in diameter, while others showed no damage at all. Even sectioning and microscopic examination of these specimens revealed the absence of any damage in the form of matrix cracking or delamination, suggesting that there exists an impact energy threshold below which damage cannot be found (~ 2 J for this material system and lay-up). Above this threshold energy, significant damage occurred, corresponding to 12.7 mm diameter of damaged area and resulting in a damage diameter to specimen width ratio (d/w) of 0.33. Other researchers have also reported the existence of the minimum energy required to cause an impact damage. Choi et al. [6] reported that an impact energy threshold exists for T300/976 graphite epoxy cross-ply composites. The study also showed that stacking sequence

significantly influences the impact energy required to initiate impact damage. Reported values range from 0.52 to 3.1 J, which is similar to the values obtained for our material system. In another study [7] various lay-ups of the carbon fiber reinforced thermoplastic toughened epoxy (IM7/977-2) were investigated, including cross-ply and quasi-isotropic. The normalized energy at the onset of incipient damage was found to be on the average 1.5 J/mm (or 9.75 J, if expressed in the total impact energy). These values are much higher than observed in our investigation, which is as expected for 977-2 toughened epoxy system.

Since the objective of this research is to investigate the fatigue growth of barely visible impact damage, an incident impact energy producing a repeatable damage pattern was chosen (2.1 J). A summary of static compression tests of these specimens is presented in Figure 1.b, including all relevant test parameters and associated compressive strengths. As can be seen from the figure, samples that did not contain visible damage showed negligible degradation in the compressive strength with respect to the undamaged specimens. That is, the average CSAI of these specimens (600 MPa) is very close to the value of 621 MPa obtained on undamaged samples. It can be concluded that the compressive strength of impacted specimens is only function of the damage present, agreeing well with the results of Cairns and Lagace [8]. That is, the damage was caused by different impactor mass, velocity and boundary conditions, but for the equivalent damage an equivalent compressive strength is measured. Furthermore, while subjected to slightly different impact energies and different impactors, samples with approximately same delamination of 12.7 mm in diameter experienced very similar compressive strength reduction (Figure 1.b). Average CSAI of these samples is 470 MPa (with a small standard deviation of 18 MPa), which corresponds to 25% reduction when compared to the undamaged specimens. Stellbrink [1] has reported compressive strength reduction of ~50% for impacted T300/69 and T300/914 quasi-isotropic laminates with d/w ratios of 0.32 - 0.44, while Ramkumar [2] investigated the behavior of impacted AS4/3501-6 laminates and observed ~65% reduction in compressive strength. While the ratio of the damaged area with respect to the overall specimen's dimensions in Ramkumar study is almost the same as in current study (i.e., d/w of 0.33), the strength reductions are substantially different. It seems that more accurate qualification of the impact damage, rather than the overall damaged area, is needed in order to compare different test results. Furthermore, compression test method, gage length of the specimen (buckling effects), and definition of the final failure are also parameters which are important in defining the CSAI. The actual 'delamination failure' of the coupons in this study occurs at ~380 MPa, while the final collapse of the specimens occurs much later at ~470 MPa, which is defined as the compressive strength after impact.

### **POST-IMPACT FATIGUE BEHAVIOR**

Summary of fatigue test results including the type of loading, load levels, test frequency and the number of cycles for each specimen is outlined in Table 1. Two specimens were tested per each load level which were chosen between 30 and 70% of CSAI. It should be noted that the variable test frequency (smaller for higher stress levels) was dictated by the limitations of the test frame capacity.



Table 1. Test matrix for constant amplitude and block loading

Specimen #	Test frequency [Hz]	Load level [% of CSAI]	N # of cycles
Constant Amplitude Compression-Compression			
32A6	7.5	40 %	1,000,000
32A7	7.5	40 %	1,000,000
33B1	7.5	50 %	1,000,000
33B4	7.5	50 %	1,000,000
34A8	5	60 %	>500,000
35A5	5	60 %	>400,000
33B2	4	70 %	141,607*
35A6	4	70 %	100,000*

Specimen #	Test frequency [Hz]	Load level [% of CSAI]	N # of cycles
Compression Block Loading (High/Low)			
33B3	4	70 %	100
	10	30 %	1,000,000
33B5	4	70 %	100
	7.5	40 %	1,000,000
Compression Block Loading (Low/High)			
31C7	7.5	40%	1,000,000
	4	70%	>100,000
32A6	7.5	40 %	1,000,000
	4	70 %	45,296*
Constant Amplitude Tension-Compression			
32C5	7.5	30 %	1,000,000
32C6	7.5	30 %	1,000,000
31C5	5	40 %	>600,000
33A6	5	40 %	376,602*
33A5	5	50 %	70,500*
31C4	5	50 %	110,000*

\* indicates cycles to final failure

### CONSTANT AMPLITUDE (C.A.) COMPRESSION-COMPRESSION (C-C) LOADING

The extent and mode of delamination growth under compression loading varied significantly depending on the applied load level. For specimens cycled at 40 and 50% of CSAI, the impact induced damage did not grow under cyclic loading up to  $10^6$  cycles. At higher load levels corresponding to 60% of CSAI only minor growth of impact damage was observed. Moderate delamination growth initiated after 2,000 cycles, and it reached the tab region of the specimen after 50,000 cycles. Schematic representation of this damage pattern, as observed by X-ray radiography, is presented in Figure 2. Growth of this thin delaminated region occurred on the rear impacted side of the specimen, along the lines of impact induced matrix cracks in the outer  $0^\circ$  ply, and is attributed to local buckling of the outer plies. At higher load levels (70% of CSAI) different and more severe type of damage growth was observed, as can be seen from Figure 3. Although there are some variations between specimens, delamination



extended throughout the entire gage section at ~10,000 cycles. This was a consequence of 'delamination failure' which occurred between 100 and 1,000 cycles. Microscopic examination of specimens tested at 70% CSAI indicate more severe damage which spans few outer plies on the rear impacted side of the specimen. However, catastrophic failure of these specimens occurred much later, at more than 100,000 cycles. Again, buckling of the outer plies on the rear impact side was the major factor governing delamination growth at this stress level.

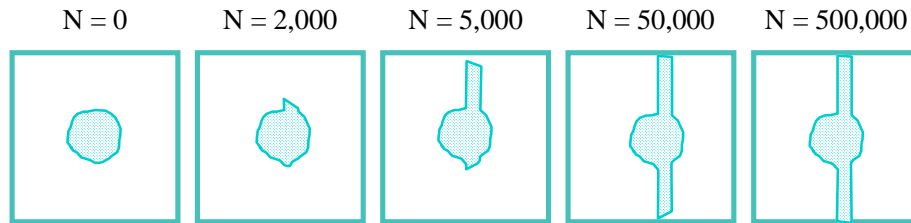


Fig. 2. Growth of impact damage under compression-compression fatigue (60% of CSAI)

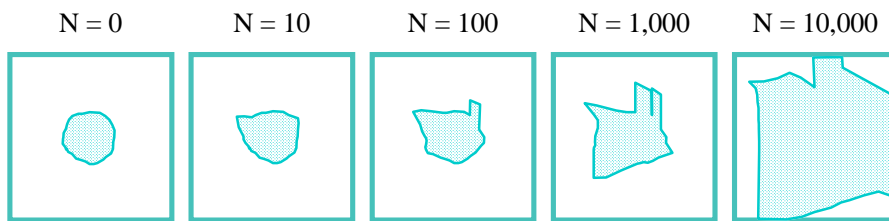


Fig. 3. Growth of impact damage under compression-compression fatigue (70% of CSAI)

S-N curves of impacted and previously [9] tested undamaged specimens are presented in Figure 4.a. Stress levels in this figure are normalized with respect to the ultimate compressive strength (UCS) of undamaged specimens, where 100% of CSAI corresponds to 75% of UCS. It is evident that the fatigue life of impacted specimens is reduced when compared to undamaged coupons, especially at higher load levels (> 60% of CSAI or 45% of UCS) where local buckling and damage growth due to delamination failure govern the fatigue response. At lower load levels for which damage did not grow in fatigue, similar performance in terms of life is observed.

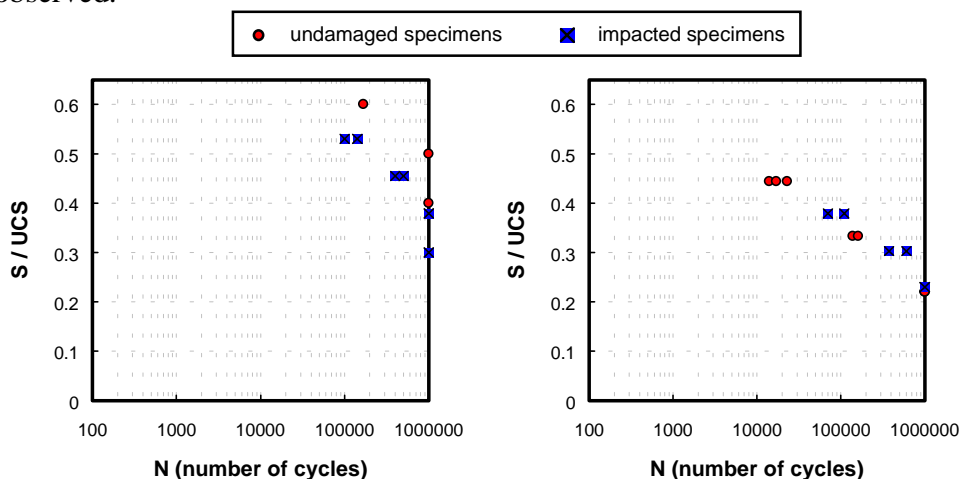


Fig. 4. Strength vs. number of cycles (S-N) curve for undamaged and impacted specimens  
 a) C-C loading, b) T-C loading. Note: stress levels are normalized with respect to the ultimate compressive strength (UCS) of undamaged specimens

### CONSTANT AMPLITUDE (C.A.) TENSION-COMPRESSION (T-C) LOADING

The damage growth under the tension-compression loading resembled the fatigue behavior of undamaged specimens. Specimens cycled at  $\pm 30$  of CSAI revealed only ply cracking, and no growth of impact damage up to  $10^6$  cycles. At higher load levels of  $\pm 40$  and  $\pm 50$  of CSAI both ply cracking and edge delamination are observed, together with the minor impact damage growth. Schematic representation of the damage pattern at  $\pm 50$  of CSAI is presented in Figure 5. While the growth of very thin delaminated region occurs prior to the growth of delamination from the edges, it is the edge delamination that actually governs the fatigue life as in the case of non-impacted specimens. Furthermore, comparison of S-N curves of impacted and previously [9] tested undamaged specimens (Figure 4.b) reveals no differences between the two. Due to the most damaging nature of T-C loading, failure of the laminates occurs at lower load levels than in C-C loading. Therefore, the delamination failure, as observed in constant amplitude C-C loading at 70% of CSAI has no practical importance in T-C loading, and can not influence the damage growth modes for this type of loading. These results suggest that long and costly testing of impacted composite laminates is not necessary for T-C loading as long as the life of non-impacted laminates is known.

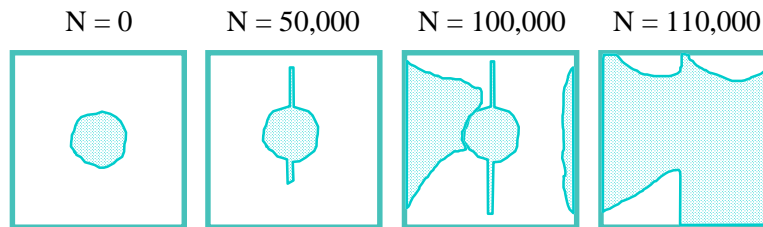


Fig. 5. Growth of impact damage under tension-compression fatigue ( $\pm 50\%$  of CSAI)

### COMPRESSION-COMPRESSION BLOCK LOADING - EFFECT OF OVERLOADS

In order to determine the damage tolerance criteria for impacted composite laminates, constant amplitude tests can provide useful information about the damage growth parameters at different load levels. Based on the results of C.A. tests the fatigue design limit without impact damage growth for this material system and type of initial impact damage corresponds to load levels less than 50% of CSAI (0.5% strain) in the presence of only compressive loads, and  $\pm 30\%$  of CSAI (0.32% strain) in tension-compression loading. However, it has been suggested that delamination in composite materials may grow very rapidly for a small load range, and that small uncertainties in the applied load may lead to large uncertainties in delamination growth [10]. This is especially important if the service loads are greater than anticipated. Therefore, the influence of overloads that might occur during the real service conditions on damage growth and fatigue life is investigated next. Since only minor damage growth was observed for specimens tested below 60% of CSAI, emphasis was placed on the sequence of occurrence of high load levels (i.e. 70%).

Two specimens were subjected to low/high block loading to assess the influence of this type of load sequence on damage propagation. After one million cycles at 40% of CSAI (with no visible damage growth) fatigue was continued at 70% until the final failure. Observed delamination growth for these specimens was very similar to the coupons that were tested only at 70% load level. Comparison of normalized delamination area (area of damage / gage section area) for constant amplitude and 40/70 block loading is presented in Figure 6.a. As

can be seen from the figure, for the same number of cycles at 70% the same trend in delamination growth is observed. Also, the number of cycles (at 70%) to final failure of these specimens is comparable to the coupons fatigued at constant amplitude loading (see Table 1). For other fatigue damage modes in composite materials (like ply cracking in tension dominated fatigue) blocked tests have shown that low/high load sequence results in a greater damage [9]. For that case the low loads by itself may not be damaging, but they may aid the subsequent high load to produce greater damage than would otherwise occur without it. For the type of damage in this study the exact opposite behavior is observed.

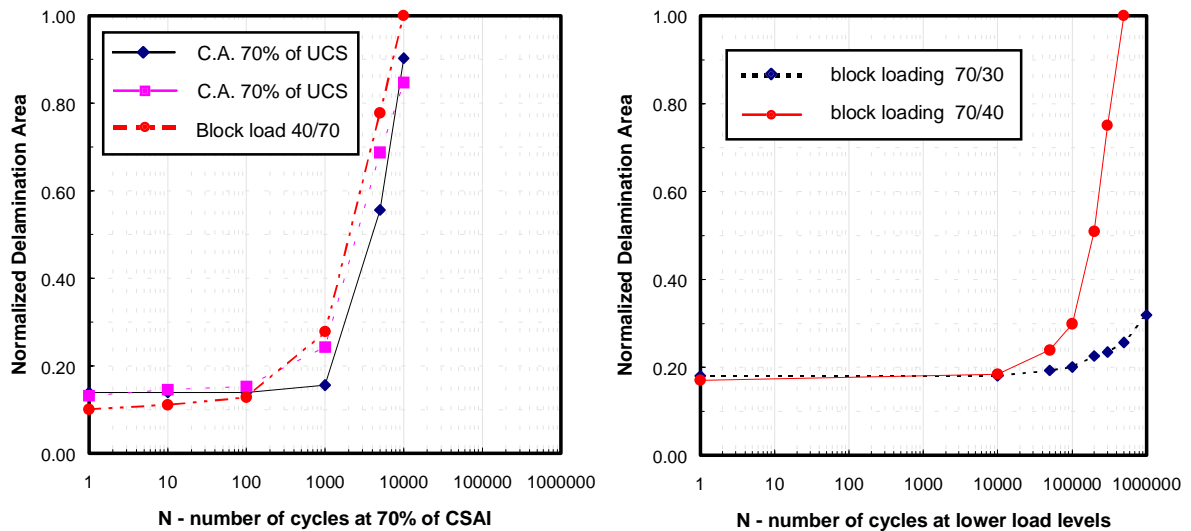


Fig. 6. Delamination growth as a function of number of cycles  
 a) at 70% of CSAI for constant amplitude (70%) and low/high block loading (40/70%)  
 b) at 30 and 40% of CSAI for high/low block loading (70/30 and 70/40%)

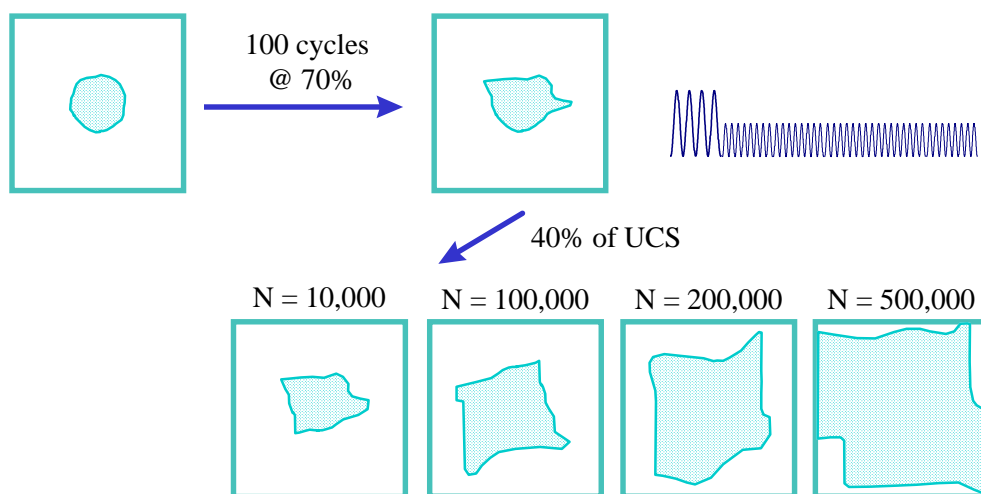


Fig. 7. Growth of impact damage under block compression-compression loading

Effect of overloads that occur at the beginning of the load spectrum (high/low test sequence) was investigated on two coupons which were initially exposed to 100 cycles at 70%, and subsequently fatigued at lower stress levels (i.e. 30% and 40% of CSAI). Schematic representation of the damage pattern for the second case, as observed by X-ray radiography, is presented in Figure 7. As indicated in this figure, following the overloads that cause 'delamination failure', delamination growth occurs even at these low load levels (for which no growth of impact damage is observed in constant amplitude tests). Normalized delamination area is plotted versus the number of cycles for these two load sequences in Figure 6.b. Examination of these data indicate that delamination growth threshold, for laminates subjected to overloads, is even below 30% of CSAI. Results also suggest that the high/low test sequence for impact damaged composite laminates is more damaging than the low/high sequence.

Based on the results of constant amplitude and block loading some conclusions about the influence of higher load levels on damage progression during random spectrum loading can be inferred. Since high load levels represent less than 0.05% of the total number of cycles in the transport wing spectrum test [11], their magnitude and sequence of occurrence is very important for the appropriate design of standardized certification procedures for impact damaged composite materials. Since a full flight-by-flight spectrum test is long and costly, a method of accelerating this test through truncation of either low or high loads is beneficial [11]. Based on the results of this study, the damage progression modes are expected to be the same for the baseline and truncated load spectrum as long as the highest load levels are kept below the levels that cause 'delamination failure' (i.e., <60% of CSAI). On the other hand, if these high load levels are included in the test spectrum the truncation of either high or low load levels (following a high load level) might lead to unreasonable estimates of fatigue life. However, it should be pointed out that these suggestions apply only for the type of initial damage as used in this study, that is, barely visible low-velocity impact damage.

## **CONCLUSIONS**

Results of impact tests show that a correlation exists between the energy absorbed by the composite during impact and damage induced in it. Furthermore, static compression tests demonstrate that the compressive strength is a function of the damage state only (i.e. absorbed impact energy), and is relatively independent of other impact test parameters. For the laminates impacted close to the impact damage threshold (resulting in a damage-diameter-to-width ratio of 0.33), a 25% reduction in compressive strength was measured. Subsequent constant amplitude compression-compression fatigue tests of these specimens indicate that the delamination does not grow for load levels below 50% of the CSAI. On the other hand, coupons tested at 70% of CSAI and above, exhibited significant delamination growth even after a few cycles. The growth was caused by the delamination failure of the plies located on the rear impact side of specimens. Local buckling of delaminated plies was the reason for delamination growth even when the load levels were reduced to 30% and 40% of CSAI. Furthermore, block loading tests indicate that the high/low sequence is more damaging than the low/high load sequence for compression-compression loading. Fatigue behavior under the constant amplitude tension-compression loading of impacted laminates shows negligible differences in terms of life and damage propagation modes when compared to the undamaged specimens, suggesting that the damage tolerance criteria for this type of loading can be defined from a limited number of tests.

## ACKNOWLEDGMENTS

The authors of this paper gratefully acknowledge the support of the Federal Aviation Administration under grant number 95-G-021. We would also like to thank Peter Shyprykevich and Joseph Soderquist of FAA for their guidance.

## REFERENCES

1. Stellbrink, K.K.U., "Influence of Low-Velocity Impact on the Fatigue Behaviour of CFRP Laminates", *Fatigue and Creep of Composite Materials, Third International Symposium on Metallurgy and Material Science*, M. Lilholt and R. Talreja, Eds., 1982, pp. 319-327.
2. Ramkumar, R.L., "Effect of Low-Velocity Impact Damage on the Fatigue Behavior of Graphite/Epoxy Laminates", *Long-Term Behavior of Composites, ASTM STP 813*, T.K. O'Brien, Ed., American Society for Testing and Materials, Philadelphia, 1983, pp. 116-135.
3. Ramkumar, R.L., "Compression Fatigue Behavior of Composites in the Presence of Delaminations", *Damage in Composite Materials, ASTM STP 775*, K.L. Reifsnider, Ed., American Society for Testing and Materials, 1982, pp. 184-210.
4. Blaricum, T.J., D.S. Saunders, G. Clark and T.E. Preuss, "Damage Tolerance of Impact Damaged Carbon Fibre Composite Wing Skin Laminates", *New Materials and Fatigue Resistant Aircraft Design, Symposium*, D.L. Ed., 14th CAF, 1989, pp. 537-556.
5. Demuts, E., R.S. Whitehead, and R.B. Deo, "Assessment of Damage Tolerance in Composites", *Composite Structures*, Vol. 4, 1985, pp. 45-58.
6. Choi, H.Y., H.S. Wang and F.-K. Chang, "Effect of Laminate Configuration and Impactor's Mass on the Initial Impact Damage of Graphite/Epoxy Composite Plates Due to Line-Loading Impact", *Journal of Composite Materials*, 26 (6), (1992), pp. 804-827.
7. Strait, L.H., M.L. Karasek and M.F. Amateau, "Effects of Stacking Sequence on the Impact Resistance of Carbon Fiber Reinforced Thermoplastic Toughened Epoxy Laminates", *Journal of Composite Materials*, 26 (12), (1992), pp. 1725-1740.
8. Cairns, D.S. and P.A. Lagace, "Residual Tensile Strength of Graphite/Epoxy and Kevlar/Epoxy Laminates with Impact Damage", *Composite Materials: Testing and Design (Ninth Volume)*, ASTM STP 1059, S.P. Garbo, Ed., ASTM, Philadelphia, 1990, pp. 48-63.
9. Hahn, H.T., J. Bartley-Cho, and S.G. Lim, "The Effect of Loading Parameters on Fatigue of Composite Laminates: Part II", *DOT/FAA/AR-95/79 Report*, 1996.
10. O'Brien, T.K., "Towards a Damage Tolerance Philosophy for Composite Materials and Structures", *Composite Materials: Testing and Design (Ninth Volume)*, ASTM STP 1059, S.P. Garbo, Ed., ASTM, Philadelphia, 1990, pp. 7-33.
11. Phillips, E. P., "Effect of Truncation of a Predominantly Compression Load Spectrum on the Life of a Notched Graphite/Epoxy Laminate", *Fatigue of Fibrous Composite Materials, ASTM STP 723*, 1981, pp. 197-212.

# RTM CARBON COMPOSITES: INFLUENCE OF PROCESS PARAMETERS ON COMPRESSION STRENGTH AFTER IMPACT

Florentin Berthet<sup>1</sup>, Pierre Devos<sup>1</sup>, Thierry Ansart<sup>2</sup>

<sup>1</sup> *École des Mines d'Albi Carmaux, Centre de recherche matériaux,  
Campus Jarlard-route de Teillet, 81013 Albi Ct Cedex 09, France*

<sup>2</sup> *Centre d'Essais Aéronautique de Toulouse, Division matériaux et structures,  
Département structures et matériaux cellule,  
23 avenue Henri Guillaumet, 31056 Toulouse, Cedex, France*

**SUMMARY:** By using the Taguchi method of experimental design, it has been possible to demonstrate the influence of some processing factors on compression strength after impact of carbon/epoxy composite materials processed by resin transfer molding. The parameters studied were injection and holding pressure, mold temperature, fiber bundle size, tackifier level, injection type and the interaction between injection pressure and mold temperature. Statistical analysis of results leads to the conclusion that temperature and pressure conditions modify the interface properties. Moreover, fiber bundle size, pressure, temperature and most likely tackifier level affect the post impact compressive behavior of the materials. Nevertheless, RTM can be considered as tolerant to process conditions variations.

**KEYWORDS:** resin transfer molding, experimental design, processing, quality, compression strength after impact

## INTRODUCTION

Use of advanced composite materials in defense and aeronautics increased dramatically in the last 30 years because these sectors could bear extra costs of production provided there was a reduction in the component weight. The challenge which now has to be faced by aerospace manufacturers is to reduce their costs. For this reason, the Resin Transfer Molding Process (R.T.M.) currently provides new interest for the aeronautics industry.

Numerous studies have been performed to simulate flow of resin through preforms with applications in mold design. A new requirement has arisen: the identification of the relationship between process parameters and mechanical properties of the molded component.

Compression strength after impact is one of the most significant mechanical properties for aerospace requirements. Resin transfer molding has been identified as a process through which it is possible to improve impact resistance.

Therefore a study had been conducted experimentally to fill a part of the gap. Compression strength after impact (C.S.A.I.) has been evaluated.



## BACKGROUND

### Taguchi Method

Experimental design using the Taguchi method is well adapted to evaluate influence of processing conditions on mechanical properties of RTM CFRP because the potential parameters are numerous. Experimental design makes it possible to simultaneously minimize the number of tests necessary and maximize the quality of results.

A test on assumed equality of variance between samples and in samples leads to a separation of factors in three categories: very significant (VS), significant (S), not significant (NS). The greater the variance between two levels, the more significant the factor concerned.

An effect is associated with a factor  $i$  and a level  $j$ . It represents what should theoretically be added to the average value if the component has been molded at level  $j$  of the factor  $i$ . That is to say the effect  $E_{ij}$  of having been molded at level  $j$  instead of at average level. This effect is defined as Eqn 1.

$$E_{ij} = \text{average at level } j - \text{general average} \quad (1)$$

More details can be found in M.Pillet's book (1).

The main difficulty in this kind of problem is to establish a relationship between what happens microscopically and macroscopically. It is all the more complicated because the involved mechanisms are multiple. Moreover the expected effects are small at room temperature.

## RTM

RTM is a process in which a dry fibrous preform is impregnated by a thermoset to produce a composite. In a prior stage called preforming the fibre layup is made to the shape of the component to produce a preform. The role of the tackifier is to keep the shape of the component and to make it stiff enough to be handled prior to injection.

It is now widely accepted, that in RTM, resin flow is governed by Darcy's law:Eqn 2.

$$\vec{v} = - \frac{[K]}{\mu \varepsilon} \text{grad}(p) \quad (2)$$

$v$ : front velocity in porous media,  $\mu$ : viscosity,  $\varepsilon$ : porosity (volume left free by fibers divided by total volume),  $p$ : applied pressure  $K$ : permeability tensor.

In RTM porous media for impregnation are heterogeneous. In a component there are two levels of heterogeneity, microscopic (fiber level) and macroscopic (fabric level). This implies that there are two types of flow (around bundles and in bundles) and permeability.

Available studies of the influence of process parameters on mechanical properties are rare. Nevertheless Hayward and Harris [2] Dockum and Shell [3], Steenkamer [4], Young [5] and Michaeli [6] have done some work in this area. But their conclusions are contradictory.

## Impact Testing

### *Impact test procedure*

The impact tests were performed using a drop weight tester. The specimens were clamped at all corners with a rectangular window (75x125 mm), in agreement with Airbus Industrie test method AITM 1-0010. The drop weight was released at a predetermined height to impact the center of the specimen with a given energy. Restrike of the drop weight was prevented by capturing it after first impact.

### *Non destructive control*

Damage areas were measured with C-SCAN.

### *Compression after impact test procedure*

Specimens (150x100 mm) were subjected to a compressive load using an antibuckling C.A.I. test fixture. The compression tests were conducted at a constant cross head speed of 1mm/mn.

## DESCRIPTION OF EQUIPMENT AND PROCESS

Our equipment consisted of:

- A square steel mold allowing fabrication of plates 400\*400mm in different thicknesses. With this mold we can do peripheral injection (using the whole feeder as indicated on Fig. 1) or directional injection (by filling the side feeders).
- An heated 20T hydraulic press
- An RTM machine (pressurized pot) allowing injection up to 4 bars
- A vacuum pump
- A data recorder (pressures, temperatures, vacuum)

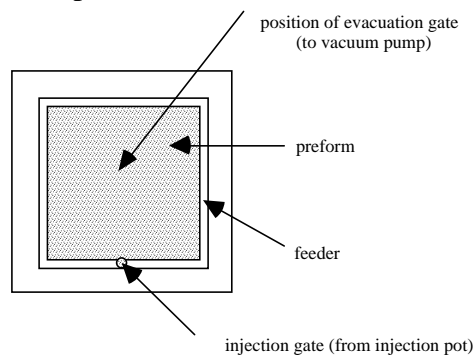


*Fig. 1: Top view of half mold with preform*

The typical resin transfer molding cycle is as follows

- 1) cutting out of reinforcements
- 2) assembly of reinforcements



- 3) preforming 5 min at 120°C under 2 bars (cohesion of reinforcements is achieved by a tackifier that is a thermoplastic or a re-actifiable uncatalysed thermoset).
- 4) mold closure, vacuum application, resin degassing, and injection until mold is filled
- 5) holding pressure until no more material enters the mold
- 6) cure 75 min at 160°C
- 7) mold opening
- 8) post cure in autoclave following a programmed cycle (120 min at 180°C)

## DESCRIPTION OF EXPERIMENT

### Parameters

Parameters chosen for this study are: mold temperature, injection pressure, holding pressure, fiber bundle size, tackifier level, injection type and interaction between mold temperature and injection pressure. These parameters are varied between two values according to L8 taguchi table (Table 1).

*Table 1: L8 Taguchi table applied to RTM*

specimen no.	mold temp. (°C)	injection pressure (bars)	Temp.-pressure Interaction	holding pressure (bars)	tackifier level (g/m <sup>2</sup> /face)	injection type	fiber bundle size (filaments)
1	100	1	1	2	5	directional	3000
2	100	1	1	3	15	peripheral	6000
3	100	2	2	2	5	peripheral	6000
4	100	2	2	3	15	directional	3000
5	140	1	2	2	15	directional	6000
6	140	1	2	3	5	peripheral	3000
7	140	2	1	2	15	peripheral	3000
8	140	2	1	3	5	directional	6000

We discount the effects of cure and post cure because these two steps are not characteristics of RTM.

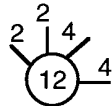
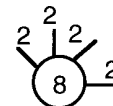
What is specific to RTM is the fiber/matrix interface formation with defect creation during injection caused by unknown mechanisms. From this one assumes that processing influences fiber/matrix bonding and thus the mechanical properties of the composite.

### Materials

Four fabrics were used, the fabric style was the same (balanced fabric), but fabrics are woven from fiber bundles of different sizes (3K 400g/m<sup>2</sup> or 6K 600g/m<sup>2</sup>), and contained two possible levels of tackifier (5g/m<sup>2</sup>/face or 15g/m<sup>2</sup>/face). When different fiber bundle size are used, different layups had to be used to achieve comparable bending stiffness (Table 2).

The injected resin is a special RTM single component epoxy resin .

Table 2: Layups used for different fiber bundle size

	3K	6K
C.S.A.I.	 Kvf=59% 4,5mm [0/45/90/-45/0/45] <sub>s</sub>	 Kvf=59% 4,5mm [0/45/90/-45] <sub>s</sub>

**PRESENTATION OF DATA AND RESULTS**

For each of the processing conditions, one plate is produced and in each plate six rectangular samples were cut (150 (in O° direction)x100mm ). Specimens were impacted at 5J(x2), 10J, 15J, 25J, 35J.

Table 3: Mass and energy impact conditions

Impact energy (J)	Drop weight (kg)
5	2,55
10	2,55
15	2,55
25	6,69
35	6,69

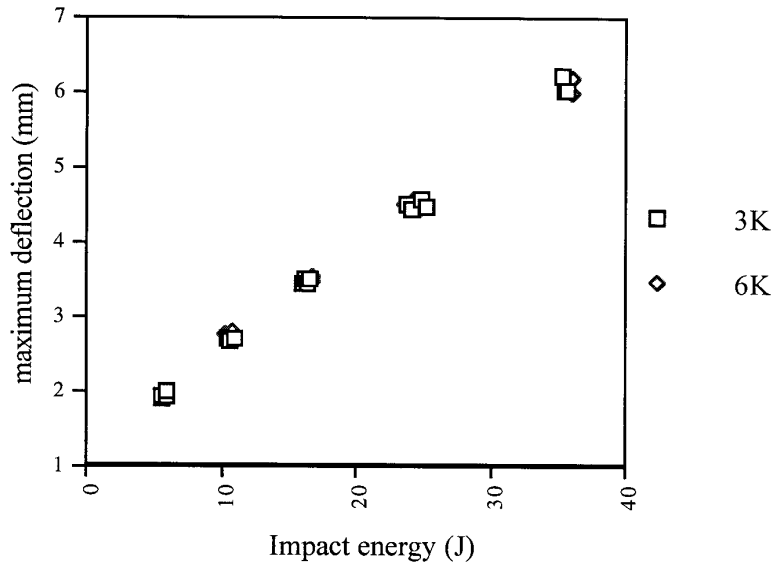


Fig.2: Maximum deflection at the centre of RTM plates during impact testing

As shown in Fig.2 different fiber bundle sizes do not lead to different maximum deflections. It proves that working at the same bending stiffness [8] is justifiable and that the change in properties is a consequence of processing and not a consequence of layup.

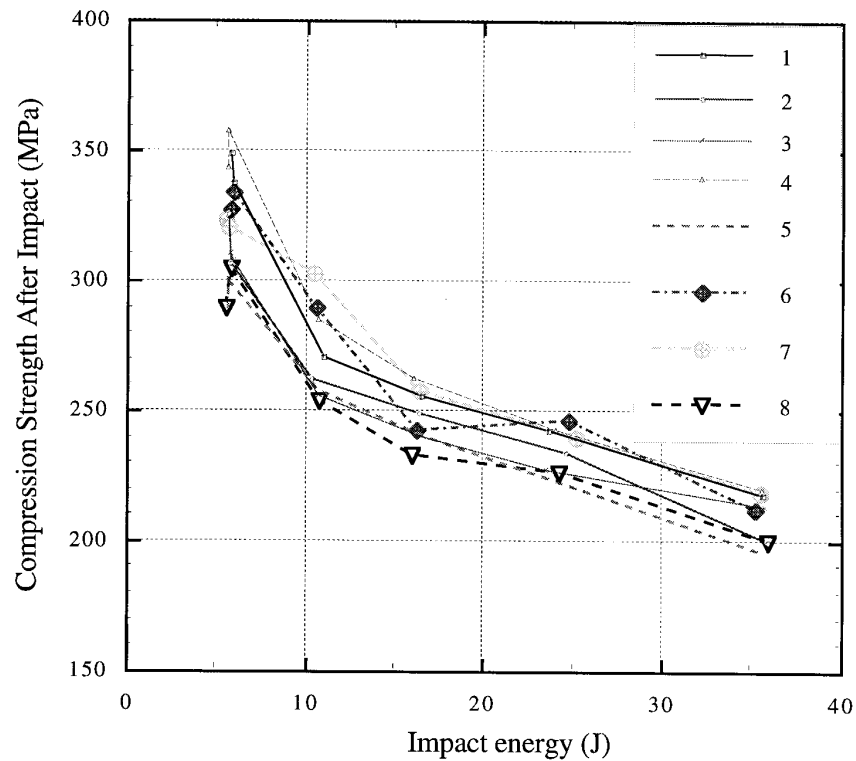


Fig.3: Compression strength after impact in resin transfer molding

The plates produced with different materials can be easily differentiated on Fig.3 by bundle size: 1,4,6,7 small (3K), 2,3,5,8 large (6K). But as presented in Fig.3 the data are not easy to interpret and some more work is required .

## INTERPRETATION OF DATA

### Damage Surface at 5J Impact

For an impact event damage initiation first appears at the fiber/matrix interphase at low levels of impact energy. There is an energy threshold at which microcracks appear at the fiber/matrix interface. Then cracks propagate in the matrix and at the interface between two plies. Thus the damage surface (measured by C.SCAN), for a low impact energy, will reflect the level of fiber and matrix bonding. Results of variance analysis in agreement with Taguchi method appear in Table 4.

The calculated value  $F_{exp}$  is more important than the tabulated value  $F_{theo95}$  for mold temperature and  $F_{theo99}$  for fiber bundle size. Mold temperature and fiber bundle size have a significant effect, and very significant respectively on damage area at 5J. For example, a mold temperature increase from 100°C to 140°C is associated with a reduction of the damaged area of 40 mm<sup>2</sup> that is to say a variation of twice the effect (19.9 mm<sup>2</sup>).

Table 4: variance analysis table for damage surface at low impact energy

	Effect (mm <sup>2</sup> )	F <sub>exp</sub>	F <sub>theo95</sub> nu1=1,nu2=8	F <sub>theo99</sub> nu1=1,nu2=8	sign.
mold temperature	-19,9	6,21	5,32	11,26	S
injection pressure	6,63	0,69	5,32	11,26	NS
holding pressure	-0,38	0	5,32	11,26	NS
tackifier level	-11,63	2,13	5,32	11,26	NS
injection type	-1,88	0,06	5,32	11,26	NS
fiber bundle size	46,38	33,8	5,32	11,26	VS
P-T interaction	13,63	2,92	5,32	11,26	NS

Increasing mold temperature favours fiber/matrix bonding (damage area reduction with increasing temperature as indicated by the negative sign of mold temperature effect).

Influence of fiber bundle size is due to a structure effect (although laminates have bending stiffness as similar as possible) and also a difference of impregnation induced by fiber mismatch. The bigger the fiber bundle the more difficult to impregnate the bundle and the more important the damage area.

Kittelson and al. [7] have shown influence of tackifier compatibility with the resin. At higher temperatures tackifier level influences compression strength. In our study this parameter had an effect, but was not statistically significant. It is likely that tackifier (level) is also important (if temperature has to be considered ).

### Compression Strength after Impact

A least square fit of experimental data points leads to an equation of CAIS as a function of impact energy summarized in Table 5. Data are fitted to a power law : Eqn 3.

$$C.S.A.I. = K.(E_i)^n \tag{3}$$

K: coefficient, n:exponent, E<sub>i</sub>: incident energy

Analysis of coefficient and exponent by the taguchi method is shown in Table 6 and in Table 7. Pooling method was used to artificially increase the degree of freedom (D.O.F. to 3) of the residual so as to draw conclusions more easily.

Fiber bundle size, mold temperature and holding pressure have a (very) significant effect on coefficient (Table 6).

Holding pressure has a positive effect on coefficient of C.S.A.I.. For example, increasing the holding pressure from 2 to 3 bars is associated with a variation of twice the effect (+8.5 MPa) that is to say an increase of coefficient of 17 MPa.

Table 5: equations for different process conditions

Plate n°	equation
1	$y=521x^{-0,2478} R^2=0,967$
2	$y=468x^{-0,2301} R^2=0,96$
3	$y=438x^{-0,2082} R^2=0,97$
4	$y=532x^{-0,2503} R^2=0,987$
5	$y=426x^{-0,2106} R^2=0,983$
6	$y=501x^{-0,2379} R^2=0,955$
7	$y=469x^{-0,2092} R^2=0,97$
8	$y=421x^{-0,2052} R^2=0,97$

Table 6: Variance analysis for coefficient y:C.S.A.I. x:E<sub>i</sub>

	Effect	sum of squares	DOF	Var.	Fexp	Ftheo95 v1=1,v2=3	Ftheo99 v1=1,v2=3	sign.
Holding pressure	8,5375	583,1	1	583,1	12,60587	10,1	34,1	S
injection pressure	-2,99	406,4	1	406,4	8,785889	10,1	34,1	NS
Mold Temp.	-17,8075	2537	1	2537	54,84249	10,1	34,1	VS
Fiber bundle size	-33,7625	9119	1	9119	197,1426	10,1	34,1	VS
residual		138,8	3	46,26				

Table 7: variance analysis for exponent

source	Effect	sum of squares	DOF	Var.	Fexp	Ftheo95 v1=1,v2=3	Ftheo99 v1=1,v2=3	sign.
Holding pressure	0,005963	0,0003	1	3E-04	6,629955	10,1	34,1	NS
injection pressure	-0,00669	0,0004	1	4E-04	8,340294	10,1	34,1	NS
Mold Temp.	-0,00919	0,0007	1	7E-04	15,74159	10,1	34,1	S
Fiber bundle size	-0,01139	0,001	1	0,001	24,18302	10,1	34,1	S
residual		0,0001	3	4E-05				

Finally mold temperature and fiber bundle size have rather a negative effect on compression strength after impact. Higher temperatures and fiber bundle size lead to a reduction of compression strength of the material (Fig.4), and residual property also decreases faster with impact energy. Different temperature and pressure conditions during injection influence the mechanical property of the resin. It was proved that fiber bundle size, temperature and pressure conditions have a statistically significant effect on compression strength after impact.

These process parameters are supposed to act through modifying the resin's capacity to prevent fiber microbuckling and energy release rate ( $G_{IIC}$ ).

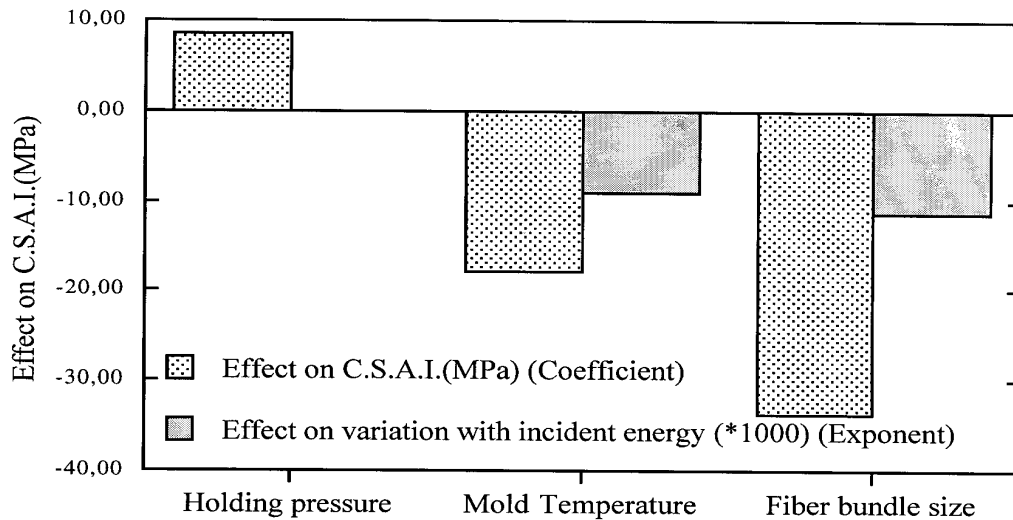


Fig.4: Effects of statistically significant process conditions on after impact compression behavior.

## CONCLUSION

Experimental design made it possible to demonstrate the effect of some processing factors on mechanical properties of RTM CFRP. We established the (limited) effect of temperature and pressure conditions during injection on the final quality of composites. The initiation of cracks is favoured by large fiber bundles and low injection temperature. The compression and residual compression resistance are influenced by pressure, temperature and fiber bundle size. The most significant effect found was fiber bundle size. Nevertheless, RTM can be considered as tolerant to process condition variations.

## REFERENCES

1. Pillet, M. "Introduction aux plans d'expériences par la méthode taguchi", 2nd edition, les éditions de l'organisation, 1994.
2. Hayward, J.S. and Harris, B. "Effects of process variables on the quality of RTM moldings", SAMPE journal, Vol. 26, n°3, May/June 1990, pp.39-46.
3. Dockum, J.F.Jr. and Schell, P.L. "Fiber directed preform reinforcement: factor that may influence mechanical properties in liquid composite molding", proceeding of the ASM/ED conference, 1990, pp.393-406.
4. Steenkamer, D.A. "The influence of preform design and manufacturing issues on the processing and performance of the resin transfer molded composites", Thesis of the University of Delaware, 1994.
5. Young, W.B., Tseng, C.W., "Study on the preheated temperatures and injection pressures of the RTM process", J.of Reinf.Plast.and Comp., Vol.13-May 1994, pp.467-482.
6. Michaeli, W., Dickhoff, J., "Production of fibre reinforced components with high surface quality using a modified RTM technique", SAMPE 39, April 1994, pp.145-153.
7. Kittelson, J.L. and Hackett, S.C., "Tackifier/resin compatibility is essential for aerospace grade resin transfer molding", SAMPE 39, April 1994, pp.82-96.
8. Bucinell, R.B., Nuismer, R.J., Koury, J.L., "Response of composite plates to quasistatic impact events", Composite materials : fatigue and fracture (third volume), ASTM STP 1110, T.K. O'Brien, Ed., American Society for Testing Materials, Philadelphia, 1991, pp.528-549.



# FREE VIBRATION OF DELAMINATED COMPOSITE PLATES WITH CONTACT ANALYSIS

Meng-Kao Yeh and Ren-Cheng Lai

*Department of Power Mechanical Engineering  
National Tsing Hua University, Hsinchu 30043 Taiwan, ROC*

**SUMMARY:** The free vibration of composite laminated plates with through-the-width delamination was investigated analytically and experimentally. In analysis, Hamilton's principle and the finite element method were extended to derive the free vibration equation for the delaminated composite plates. The transformation method, which reduced the degrees of freedom of the plate, was applied to deal with the geometric compatibility between the contact surfaces of upper and lower sublaminates in the delaminated region. The free vibration of the delaminated composite plate was treated as a two-dimensional plane-strain eigenvalue problem. In experiment, a shaker system was used to determine the natural frequencies and the corresponding mode shapes for the delaminated plates. The delamination becomes significant to affect the natural frequencies as its size exceeds 50% of the laminate length. The natural frequencies of the delaminated plates decrease with increasing values of fiber orientation and also decrease as the delaminated region located toward the center of the composite plates.

**KEYWORDS:** free vibration, natural frequency, composite plate, delamination

## INTRODUCTION

Owing to high strength/weight ratio, composite materials have been widely used in the aerospace, automobile, defense and civil industries. However, there is occasionally some defects in our daily used materials. Composite materials have defects as well. Delamination is one of the defects encountered in most composite laminated plates. It results from low velocity impact, fatigue loads and manufacturing defects. Therefore, study of influence of delamination on the composite laminates is rather important.

The dynamic characteristics of composite laminates were investigated by Rayleigh-Ritz method [1], Galerkin Method [2, 3], and finite element method [4-10]. Among them, Bhimaraddi [2] studied the effect of initial imperfection on the nonlinear dynamic response of composite laminates; Bicos and Springer [4] derived the free vibration equation of composite laminates with damping by Hamilton's principle; Dhanaraj and Palaninathan [5] and Ju et al. [6] discussed the influence of initial stress on the dynamic characteristics of composite laminates. Shen and Grady [7], Tracy and Pardoen [8] and Ju et al. [9, 10] assessed the dynamic characteristics of composite laminates with delamination. Ju et al. [10] analyzed the contact phenomenon at the delamination; however, they dealt with the case with node pairing only.

Among the methods related to contact mechanics, there are transformation matrix method [11-13], penalty method [14, 15], Lagrangian multiplier [16, 17] and flexibility matrix method [18]. The solution accuracy and stability of penalty method is determined by the magnitude of penalty number and structural stiffness. The Lagrangian multiplier method needs additional parameters. When using the flexibility matrix method, the node pairing on both sides of contacting surfaces is required. The transformation matrix method satisfies the geometric compatibility between the contacting surfaces and reduces the number of degrees of freedom of the problem. It deals with both sticking and sliding conditions on the contacting surfaces, which was not discussed before for the composite laminates; therefore, it was used in this study to obtain the dynamic response of the composite laminates.

In analysis, Hamilton's principle and the finite element method were used to derive the system equation of the composite laminates. The governing equation omitted the damping due to its small effects on the composite laminates [19-21]. For the contact points, the transformation matrix method was used and the contacting conditions were iterated. The free vibration of composite laminates was treated by a two-dimensional plane strain eigenvalue problem to find the natural frequencies and mode shapes. The material properties used in the analysis were obtained from experiment. In experiment, a shaker system was used to obtain the dynamic characteristics of the composite laminates. The size and the position of delamination and the fiber orientation were varied and compared with results obtained from analysis.

### HAMILTON'S PRINCIPLE

The contact effects on the free vibration response of composite laminates with through-the-width delamination was investigated in this study. Fig. 1 shows schematic of a cantilever composite laminated plate with through-the-width delamination. Hamilton's principle is expressed as [22]

$$\int_{t_1}^{t_2} \delta(T - U) dt + \int_{t_1}^{t_2} \delta W_{nc} dt = 0 \quad (1)$$

where  $T$  is the total kinetic energy of the laminate system;  $U$  is the potential energy of the system;  $\delta W_{nc}$  is the virtual work done by nonconservative forces;  $\delta(\bullet)$  is a variation symbol;  $t_1, t_2$  are the times at which the system configuration is known. Here

$$T = \int_V \frac{1}{2} \rho \dot{\underline{u}}^T \dot{\underline{u}} dv \quad (2)$$

$$U = \int_V \frac{1}{2} \underline{\tau}^T \underline{\epsilon} dv = \int_V \frac{1}{2} \underline{\epsilon}^T [E] \underline{\epsilon} dv \quad (3)$$

$$W_{nc} = W_F + W_C \quad (4)$$

$$W_F = \int_V \underline{u}^T \underline{f} dv + \int_S \underline{u}^T \underline{F} dS \quad (5)$$

$$W_C = \int_{S_c} \underline{u}_A^T \hat{\underline{F}}_{CA} dA + \int_{S_c} \underline{u}_B^T \hat{\underline{F}}_{CB} dA \quad (6)$$

where  $\underline{u}$  is the displacement vector;  $\dot{\underline{u}}$  is the velocity;  $\rho$  is the density;  $\underline{\tau}$  is the stress;  $\underline{\epsilon}$  is the strain;  $[E]$  is the matrix of material constants;  $W_F$  is the work done by the nonconservative external force;  $W_C$  is the work done by the contact force;  $\underline{f}$  is the body force;  $\underline{F}$  is the surface tractions;  $\underline{F}_{CA}, \underline{F}_{CB}$  and  $\underline{u}_A, \underline{u}_B$  are the contact forces and displacements on the surfaces above and below the delamination;  $V = V_A + V_B$  and  $S = S_A + S_B$  are the volume and surface of the composite laminate;  $S_c$  is the contact area.

The contact force  $\hat{\mathbf{F}}_C$  must be in equilibrium as  $\hat{\mathbf{F}}_C = \hat{\mathbf{F}}_{CA} = -\hat{\mathbf{F}}_{CB}$ . Eqn 6 is expressed as

$$W_C = \int_{S_C} (\underline{\mathbf{u}}_A - \underline{\mathbf{u}}_B)^T \hat{\mathbf{F}}_C dA \quad (7)$$

### Transformation Matrix

The displacement  $\underline{\mathbf{a}}_A$  of an arbitrary contact point p on the surface above delamination is divided into three parts [11, 12] as: (i)gap displacement  $\underline{\mathbf{a}}_{p \rightarrow q}$ , (ii)sticking displacement  $\underline{\mathbf{a}}_{q \rightarrow r}$ , (iii)relative sliding displacement  $\underline{\mathbf{a}}_{r \rightarrow s}$ , as shown in Fig. 2.

$$\underline{\mathbf{a}}_A = \underline{\mathbf{a}}_{p \rightarrow s} = \underline{\mathbf{a}}_{p \rightarrow q} + \underline{\mathbf{a}}_{q \rightarrow r} + \underline{\mathbf{a}}_{r \rightarrow s} = [\mathbf{N}] \underline{\mathbf{a}}_B + \underline{\mathbf{t}} a_s + \underline{\mathbf{h}} = [\mathbf{G}] \underline{\mathbf{a}} + \underline{\mathbf{h}} \quad (8)$$

where  $\underline{\mathbf{h}}$  is the gap displacement;  $[\mathbf{N}]$  is the matrix of shape function;  $\underline{\mathbf{a}}_B$  is the displacement vector of point q below delamination;  $\underline{\mathbf{t}}$  is the tangent vector of contact point below delamination;  $a_s$  is the magnitude of relative displacement. Eqn 8 is the constraint condition of the contact surface above delamination.  $[\mathbf{G}]$  includes  $[\mathbf{N}]$  and  $\underline{\mathbf{t}}$  and is called the transformation matrix.  $\underline{\mathbf{a}}$  is a combination of  $\underline{\mathbf{a}}_B$  and  $a_s$ . If point p doesn't contact with point on surface below delamination,  $[\mathbf{G}]$  is a unity matrix, and  $\underline{\mathbf{a}} = \underline{\mathbf{a}}_A$ ,  $\underline{\mathbf{h}} = \underline{\mathbf{0}}$ .

### Finite Element Method

The two-dimensional isoparametric quadratic element was used in analysis. The laminate is divided into two parts; part A is above the delamination, part B includes regions below the delamination and area without delamination (see Fig. 3). In Eqn 7,  $\underline{\mathbf{u}}_A - \underline{\mathbf{u}}_B$  is the relative displacement of points above and below delamination; they can be expressed as  $\underline{\mathbf{a}}_{p \rightarrow s} - \underline{\mathbf{a}}_{q \rightarrow r}$ , as shown in Fig. 2. After finite element discretization, the work done by the contact force  $W_C$  is

$$W_C = \sum_{j=1}^J (\underline{\mathbf{a}}_{p \rightarrow s} - \underline{\mathbf{a}}_{q \rightarrow r})^T (\hat{\mathbf{R}}_C) = \sum_{j=1}^J ((\underline{\mathbf{t}}^T \hat{\mathbf{a}} + \underline{\mathbf{h}})^T (\hat{\mathbf{R}}_C)) \quad (9)$$

where  $J$  is the element number above the delamination;  $\hat{\mathbf{R}}_C = \int_{S_C} \mathbf{1}^{\mathbf{N}} \mathbf{r}_C dA$  is the contact nodal force to be determined;  $\hat{\mathbf{a}}$  is the nodal displacement produced by contact force  $\hat{\mathbf{R}}_C$ . Both  $\hat{\mathbf{a}}$  and  $\hat{\mathbf{R}}_C$  are to be determined. The total kinetic energy, potential energy and work done by nonconservative external force can be expressed in terms of  $[\mathbf{G}]$  and  $\underline{\mathbf{a}}$  as

$$T = \sum_{j=1}^{J_A} \frac{1}{2} ([\mathbf{G}] \dot{\underline{\mathbf{a}}} + \dot{\underline{\mathbf{h}}})^T [\mathbf{M}_A] ([\mathbf{G}] \dot{\underline{\mathbf{a}}} + \dot{\underline{\mathbf{h}}}) + \sum_{j=1}^{J_B} \frac{1}{2} (\dot{\underline{\mathbf{a}}})^T [\mathbf{M}_B] (\dot{\underline{\mathbf{a}}}) \quad (10)$$

$$U = \sum_{j=1}^{J_A} \frac{1}{2} ([\mathbf{G}] \underline{\mathbf{a}} + \underline{\mathbf{h}})^T [\mathbf{K}_A] ([\mathbf{G}] \underline{\mathbf{a}} + \underline{\mathbf{h}}) + \sum_{j=1}^{J_B} \frac{1}{2} (\underline{\mathbf{a}})^T [\mathbf{K}_B] (\underline{\mathbf{a}}) \quad (11)$$

$$W_F = \sum_{j=1}^{J_A} ([\mathbf{G}] \underline{\mathbf{a}} + \underline{\mathbf{h}})^T (\underline{\mathbf{Q}}_A) + \sum_{j=1}^{J_B} (\underline{\mathbf{a}})^T (\underline{\mathbf{Q}}_B) \quad (12)$$

where  $J_A$  and  $J_B$  are the element numbers of part A and part B;  $[\mathbf{M}_A]$  and  $[\mathbf{M}_B]$  are mass matrices;  $[\mathbf{K}_A]$  and  $[\mathbf{K}_B]$  are stiffness matrices;  $\underline{\mathbf{Q}}_A$  and  $\underline{\mathbf{Q}}_B$  are external forces. Since there is only contact force, no external force, on the contact surface,  $\underline{\mathbf{Q}}_A = \underline{\mathbf{0}}$ ,  $\underline{\mathbf{Q}}_B = \underline{\mathbf{0}}$ , the nodal contact force can be expressed by the nodal force equilibrium above the delamination as  $\hat{\mathbf{R}}_C = [\mathbf{K}_A] \hat{\underline{\mathbf{a}}}_A + [\mathbf{M}_A] \hat{\underline{\mathbf{a}}}_A$ . The frictional force on the contact surface is expressed according to Coulomb's law as

$$\underline{t}^T \hat{\underline{R}}_C = \text{sign} \cdot \mu_d \cdot \underline{n}^T \hat{\underline{R}}_C \quad (13)$$

where  $\mu_d$  is the frictional coefficient;  $\underline{t}$  and  $\underline{n}$  are the tangential and normal vectors on the contact surface. If  $\underline{a}$  is replaced by global parameter  $\underline{a}^*$ , after substituting Eqns 9 to 13 into Hamilton's principle and rearrangement for zero gap displacement at contact point  $\underline{h}^* = 0$  and no external forces  $\underline{Q}_A^* = \underline{Q}_B^* = 0$ . The system governing equation can be obtained as

$$[[G^*]^T - \mu_d \cdot \text{sign} \cdot [n^*]^T \quad [I]] \left( \begin{bmatrix} [M_A^*] [G^*] \\ [M_B^*] \end{bmatrix} \ddot{\underline{a}}^* + \begin{bmatrix} [K_A^*] [G^*] \\ [K_B^*] \end{bmatrix} \underline{a}^* \right) = 0 \quad (14)$$

### Material Properties

The material property of each layer of the composite laminate is assumed as transversely isotropic. There are total of five material constants: Longitudinal modulus  $E_1$ , transverse modulus  $E_2$ , shear modulus  $G_{12}$  and Poisson's ratios  $\nu_{12}$  and  $\nu_{23}$ , which result in the stress-strain relation of each layer in the fiber principal direction. The material property in the natural coordinate can be obtained by a transformation matrix between the fiber principal direction and the natural coordinate. For simplicity, assume that the composite laminate is under plane strain condition. The stress-strain relation in Cartesian coordinate can be obtained by a transformation matrix between the natural coordinate and Cartesian coordinate.

The Gaussian quadrature was used in numerical integration. For composite laminate, each layer may have different fiber orientation; therefore, the material properties are integrated through layers in the thickness direction. The elemental stiffness matrices  $[K_A]$ ,  $[K_B]$  can be obtained through the use of material property matrix in Cartesian coordinate and are assembled to be the global stiffness matrices  $[K_A^*]$ ,  $[K_B^*]$  in Eqn 14.

### Free Vibration of Laminated Plates

Assuming that  $\underline{a}^*$  has the following form.

$$\underline{a}^* = \underline{\Phi} e^{-i\omega t} \quad (15)$$

where  $\underline{\Phi}$  is the displacement vector which is not a function of time. After substituting Eqn 15 into Eqn 14, for  $\underline{\Phi}$  to have nontrivial solution, let

$$\det\left( [[G^*]^T - \mu_d \cdot \text{sign} \cdot [n^*]^T \quad [I]] \left( \begin{bmatrix} [M_A^*] [G^*] \\ [M_B^*] \end{bmatrix} \omega^2 + \begin{bmatrix} [K_A^*] [G^*] \\ [K_B^*] \end{bmatrix} \right) \right) = 0 \quad (16)$$

Eqn 16 is the standard eigenvalue problem, in which the eigenvalue  $\omega$  is the natural frequency of the system. The composite laminates studied have one end fixed and the other end free. The following boundary conditions were applied to the system.

$$u_i = 0, \quad v_i = 0, \quad dv_i / dx = 0 \quad (17)$$

where  $u_i$ ,  $v_i$  are the displacements in the x- and y-direction at the fixed end, respectively. From the solution obtained from Eqn 16, the eigenvector  $\underline{\Phi}$  can be found to represent the natural mode shapes of laminated plate.

## EXPERIMENT

In addition to the finite element analysis, the shaker vibration experiments were performed to verify the analytical results. The size and location of delamination and the fiber orientation were varied to assess their effects on the dynamic response of the laminated plate. The composite specimens were made from graphite/epoxy prepregs (0.12mm thick per ply) with required size and stacking sequence. They were put in an aluminum mold on a temperature-controlled hot press. In the upper region of the aluminum mold air pressure was applied on top of the specimen; while a vacuum pump was used to empty the gas produced during the curing process. For the delaminated specimens, a Teflon piece (0.1 mm thick) was imbedded to form an artificial delamination.

The material property of a single composite layer is assumed as transversely isotropic. Five material constants  $E_{11}$ ,  $E_{22}$ ,  $G_{12}$ ,  $\nu_{12}$ ,  $\nu_{23}$  are needed, in which  $\nu_{23} = \nu_{12}$  is assumed as conventional [23, 24]. The rest four material constants were measured on a tensile testing frame according to ASTM D3039 [25]. Each constant was obtained by the average of three experiments as  $E_{11} = 147.27 \pm 6.09$  Gpa,  $E_{22} = 13.89 \pm 1.04$  Gpa,  $G_{12} = 4.87 \pm 0.15$  Gpa,  $\nu_{12} = 0.320 \pm 0.032$ .

### Shaker Vibration Experiment

The specimens used in shaker vibration experiment had length 200 mm, width 40 mm and 8 layers. One end of specimen was fixed for 50 mm, the test section had 150 mm long. Before the experiment, proper position for force sensor and sampling points for output signal were layout on surface of the laminate specimen. The specimens were then fixed on the test fixture and shaker, amplifier, signal analyzer, force sensor, accelerometer connected as arranged in Fig. 4. The force sensor was glued on the specimen. The accelerometer was used to measure the dynamic response at each sampling point. During the experiment, an excitation was generated by the signal analyzer, amplified and connected to the shaker. The shaker forced the specimen to vibrate. The signals from force sensor and the accelerometer on the laminate specimen were amplified and fed into the signal analyzer to obtain the frequency response function by fast Fourier transform (FFT). The response function was directed into a personal computer in which the STAR Modal System was used to calculate the natural frequencies and mode shapes.

## RESULTS AND DISCUSSION

In this study, the free vibration of composite laminates with through-the-width delamination was analyzed by the finite element method and was verified by shaker vibration experiment. The position and size of delamination and the fiber orientation were varied to evaluate their influence on the dynamic response of the laminated plates. Fig. 5 shows three-dimensional mode shapes obtained from shaker vibration experiment for specimen ( $w=40$  mm,  $L=150$  mm,  $D=1.1$  mm,  $a/L=2/3$ ,  $d/D=1/8$ ,  $[0^\circ]_8$ ). The first and third mode shapes are bending types. The second mode shape is a torsional one which can't be obtained from plane strain analysis. Fig. 6 shows the corresponding two-dimensional bending mode shapes from the middle section. Fig. 7 shows the corresponding natural modes obtained from the finite element analysis. The analytical first mode shows a bulge-up separation in the middle delaminated region, while it is not shown in the experimental results due to counter effect of

the weight of accelerometer on the weaker upper delaminated region. The second bending modes agree well in both analytical and experimental results. Because of high noise and poor signal acquisition at higher frequency, the third bending mode was unable to found in experiment; however, the analytical third bending mode showed a contact point in the middle of delamination.

### Variation of Delamination Size

The size of delamination was varied for laminated specimens to find its influence on the dynamic response of composite laminates. The sizes of delamination were  $a/L=1/4$ ,  $1/2$ ,  $2/3$  and  $5/6$ . The separate movement of the delaminated region occurs for delamination size larger than 50% of laminate length. Figs. 8 and 9 show the relation between the bending natural frequencies and delamination size for laminated specimens ( $w=40$  mm,  $L=150$  mm,  $D=1.1$  mm,  $d/D=1/8$ ,  $[0^\circ]_8$ ). In Fig. 8, the natural frequencies of the first bending mode decrease with the delamination size. Larger reduction can be seen for delamination size larger than  $2/3$ . The trend of analytical results was consistent with the experimental ones. In Fig. 9, the natural frequency of the second bending mode for  $a/L=1/2$  and  $2/3$  were larger than those of laminates without delamination, since separating movement occurred for the delaminated region. The bulge-up of delaminated region increases the bending rigidity of laminate which results in higher natural frequency for  $a/L=1/2$  and  $2/3$ . As the length of delamination increases, the upper delaminated region becomes weaker; therefore, the additional rigidity obtained from the bulge-up movement was smaller and natural frequencies decrease as also observed in experiment.

### Variation of Delamination Position

The position of the delamination in the thickness direction of specimens was varied to evaluate its effect on the dynamic response of the laminate plates. The positions of delamination are  $d/D=1/8$ ,  $2/8$  and  $4/8$ . Figs. 10 and 11 show the relation between the natural frequencies and delamination position for laminated specimens ( $w=40$  mm,  $L=150$  mm,  $D=1.1$  mm,  $a/L=2/3$ ,  $[0^\circ]_8$ ). The natural frequencies of the first bending modes decrease as the delamination position toward the center of specimen. The experimental natural frequencies for specimens with  $d/D=1/8$  is lower than those of the specimens with  $d/D=2/8$  due to the difficulty in manufacturing the former specimens. The specimens with  $d/D=1/8$  probably changed their local thickness at the delaminated region. For the second bending modes, the natural frequencies for specimens with  $d/D=1/8$  and  $d/D=2/8$  are higher than those of specimens without delamination. This can be explained from separating movement for mode shapes of specimens at the delaminated region. The bulge-up delamination gave extra bending rigidity for the composite laminates. For the case with delamination position at the mid-thickness  $d/D=4/8$ , no separating movement found in the bending mode; thus, the bending rigidity decrease and natural frequencies decrease as well.

### Variation of Fiber Orientation

The delaminated plate specimens ( $w=40$  mm,  $L=150$  mm,  $D=1.1$  mm,  $a/L=2/3$ ,  $d/D=1/8$ ) were used with variation of fiber orientation  $\theta$  to evaluate its effect for laminates with  $[\pm\theta]_{2S}$  stacking sequence. The stacking sequences were  $[0^\circ]_8$ ,  $[\pm 30^\circ]_{2S}$ ,  $[\pm 45^\circ]_{2S}$ ,  $[\pm 60^\circ]_{2S}$  and



$[\pm 90^\circ]_{2S}$ . Figs. 12 and 13 show bending natural frequencies for specimens with different fiber orientation. The bending natural frequencies decrease with fiber orientation for both first and second bending modes. The natural frequencies decrease more quickly for  $\theta$  between  $0^\circ$  and  $45^\circ$ . The plane strain finite element method can only predict reasonable results for cross-ply laminated plates which is symmetric about the middle section in the longitudinal direction.

## CONCLUSIONS

In this study, the free vibration of composite laminates with through-the-width delamination was investigated analytically and experimentally. The two-dimensional finite element analysis was used to calculate the natural frequencies and mode shapes for the delaminated composite plates. The shaker vibration experiment was carried out to verify the analytical results. The following conclusions can be made:

- (1) The natural frequencies of the delaminated plates decrease as delamination size increases. This effect is more significant for cases with delamination near upper surface of specimen and size larger than  $a/L=2/3$ .
- (2) For laminated plates with small delamination, no local separating movement at delaminated region occurs and their natural frequencies are close to composite plates without delamination.
- (3) The natural frequencies of the delaminated plates usually are smaller than those of laminated plates without delamination; however, for some cases e.g.,  $a/L=2/3$ ,  $d/D=1/8$ , the local separating movement adds bending rigidity which increases the natural frequencies to a higher value than those of laminates plates without delamination.
- (4) When the delamination position is at mid-thickness of the laminated plate, no local separating movement occurs and the natural frequencies are much lower than those laminated plates without delamination.
- (5) The natural frequencies of the delaminated plates decrease as the fiber orientation increases for laminates with stacking sequence  $[\pm\theta]_{2S}$ .

## REFERENCES

- 1 Baharlou, B. and Leissa, A. W., "Vibration and Buckling of Generally Laminated Composite Plates with Arbitrary Dage Conditions," International Journal of Mechanical Sciences, Vol. 29, No. 8, pp. 545-555, 1987.
2. Bhimaraddi, A., "Non-Linear Free-Vibration Analysis of Composite Plates with Initial Imperfections and Inplane Loading," International Journal of Solids and Structures, Vol. 25, No. 1, pp. 33-43, 1989.
3. Bowlus, J. A., Palazotto, A. N. and Whitney, J. M., "Vibration of Symmetrically Laminated Rectangular Plate Considering and Rotatory Inertia," AIAA Journal, Vol. 25, No. 11, pp. 1500-1511.
4. Bicos, A. S. and Springer, G. S., "Analysis of Free Damped Vibration of Laminated Composite Plates and Shells," International Journal of Solids and Structures, Vol. 25, No. 2, pp. 129-149, 1989.

5. Dhanaraj, R. and Palaninathan, "Free Vibration of Initially Stressed Composite Laminates," *Journal of Sound and Vibration*, Vol. 142, pp. 365-378, 1990.
6. Ju, F., Lee, H. P. and Lee, K. H., "Free-Vibration Analysis of Composite Beams with Multiple Delaminations," *Composites Engineering*, Vol. 4, pp. 715-730, 1994.
7. Shen, M. H. H. and Grady, J. E., "Free Vibration of Delaminated Beams," *AIAA Journal*, Vol. 30, No. 5, pp. 1361-1370, 1992.
8. Tracy, J. J. and Pardoan, G. C., "Effect of Delamination on the Natural Frequencies of Composite Laminate," *Journal of Composite Materials*, Vol. 23, pp. 1200-1215, 1988.
9. Ju, F., Lee, H. P. and Lee, K. H., "Finite Element Analysis of Free Vibration of Delaminated Composite Plates," *Composites Engineering*, Vol. 5, pp. 195-209, 1995.
10. Ju, F., Lee, H. P. and Lee, K. H., "Dynamic Response of Delaminated Composite Beams with Intermittent Contact in Delaminated Segments," *Composites Engineering*, Vol. 4, pp. 1211-1224, 1995.
11. Chen, W. H. and Yeh, J. T., "Finite Element Analysis of Finite Deformation Contact Problems with Friction," *Computers & Structures*, Vol. 29, pp. 423-436, 1988.
12. Chen, W. H. and Yen, J. T., "Three-dimensional Finite Element Analysis of Static and Dynamic Contact Problems with Friction," *Computers & structures*, Vol. 35, No. 5, pp. 541-552, 1990.
13. Chen, W. H., Chang, C. M. and Yeh, J. T., "An Incremental Relaxation Finite Element Analysis of Viscoelastic Problems with Contact and Friction," *Computer Methods in Applied Mechanics & engineering*, Vol. 109, pp. 315-329, 1993.
14. Pascoe, S. R. and Mottershead, J. E., "Two New Finite Element Contact Algorithms," *Computers & Structures*, Vol. 32, No. 1, pp. 137-144, 1989.
15. Wanxie, Z. and Suming, Z., "A Finite Element Method for Elasto-plastic Structures and Contact Problems by PQP," *International Journal for Numerical Method in Engineering*, Vol. 26, pp. 2723-2738, 1988.
16. Gallego, F. J. and Anza, J. J., "A Mixed Finite Element Model for the Elastic Contact Problem," *International Journal for Numerical Method in Engineering*, Vol. 28, pp. 1249-1264, 1989.
17. Pascoe, S. K. and Mottershead, J. E., "Linear Elastic Contact Problems Using Curved Element and Including Dynamic Friction," *International Journal for Numerical Method in Engineering*, Vol. 26, pp. 1631-1643, 1988.
18. Francavilla, A. and Zienkiewicz, O. C., "A Note on Numerical Computation of Elastic Contact Problem," *International Journal of Numerical Method in Engineering*, Vol. 9, pp. 913-924, 1975.
19. Zabararas, N. and Pervez, T., "Viscous Damping Approximation of Laminated Anisotropic Composite Plates Using the Finite Element Method," *Computer Method in Applied Mechanics and Engineering*, Vol. 81, pp. 291-316, 1990.
20. Maaskant, R. and Gibson, R. F., "Analysis of Damping in Composite Laminates," *AIAA Journal*, Vol. 30, No. 7, pp. 1912-1915, 1991.
21. Hwang, S. J. and Gibson, R. F., "The Use of Strain Energy-Based Finite Element Techniques in the Analysis of Various Aspects of Damping of Composite Materials and Structures," *Journal of Composite Materials*, Vol. 17, pp. 2585-2605, 1992.
22. Craig, R. R., Jr., *Structural Dynamics: An Introduction to Computer Methods*, Wiley, New York, 1981.

23. Kim, K. S. and Hong, C. S., "Delamination Growth in Angle-Ply Laminated Composites," *Journal of Composite Materials*, Vol. 20, pp. 423-438, 1986.
24. Whitcomb, J. D., "Parametric Analytical Study of Instability-Related Delamination Growth," *Composites Science and Technology*, Vol. 25, pp. 19-48, 1986.
25. ASTM, "General Products, Chemical Specialties, and End Use Products," D3039, *Annual Book of ASTM Standards Standard Test Method for Tensile Properties of Fiber-Resin Composites*, Section 3, Vol. 15.03, pp. 162-165, 1983

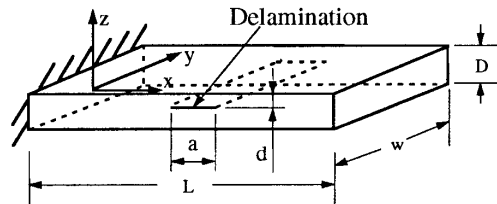


Fig. 1: Schematic of a cantilever composite plate with through-the-width delamination.

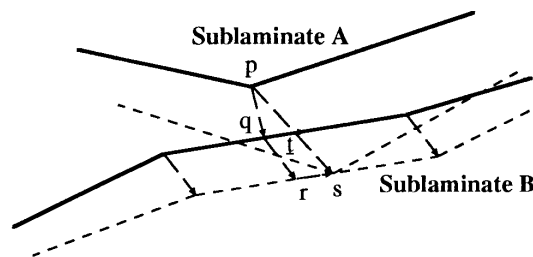


Fig. 2: Schematic of contact nodal displacement.

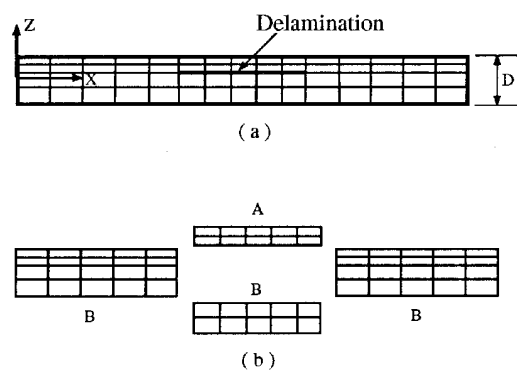


Fig. 3: Schematic of finite element mesh for delaminated plate.

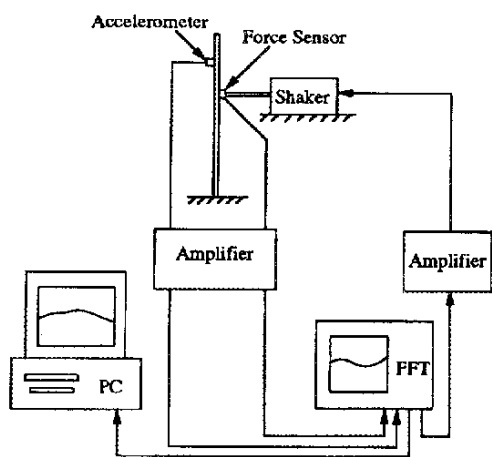


Fig. 4 Arrangement of shaker vibration experiment.

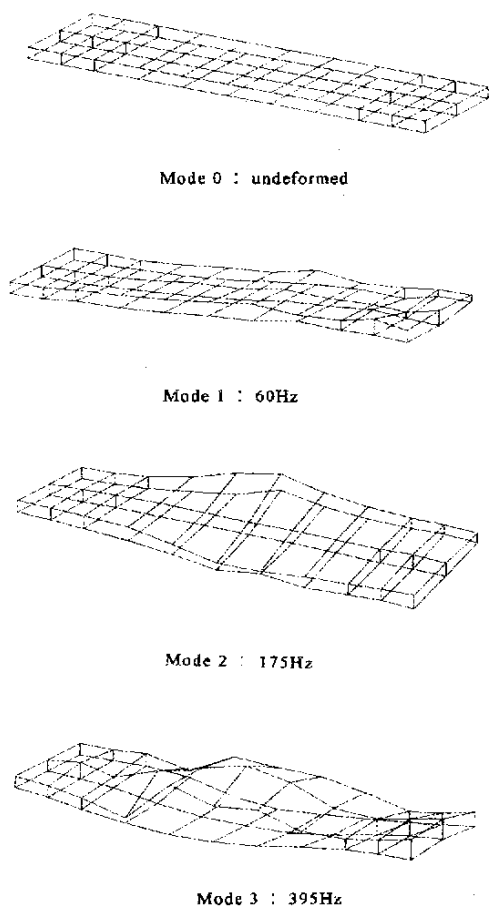


Fig. 5 Experimental three-dimensional mode shapes for specimen with  $w=40$  mm,  $L=150$  mm,  $D=1.1$  mm,  $a/L=2/3$ ,  $d/D=1/8$  and  $[0^\circ]_8$ .

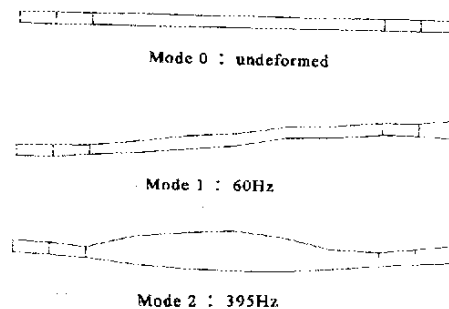


Fig. 6 Experimental two-dimensional mode shapes for specimen with  $w=40$  mm,  $L=150$  mm,  $D=1.1$  mm,  $a/L=2/3$ ,  $d/D=1/8$  and  $[0^\circ]_8$ .

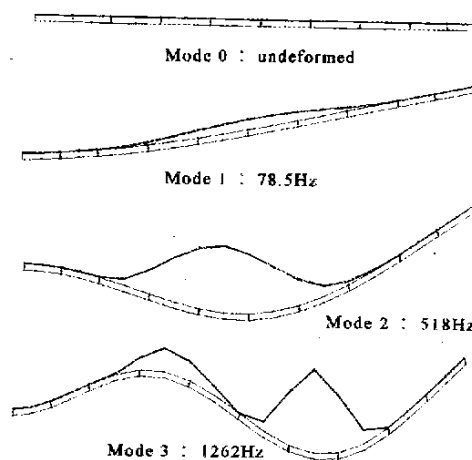


Fig. 7 Analytical mode shapes for specimen with  $w=40$  mm,  $L=150$  mm,  $D=1.1$  mm,  $a/L=2/3$ ,  $d/D=1/8$  and  $[0^\circ]_8$ .

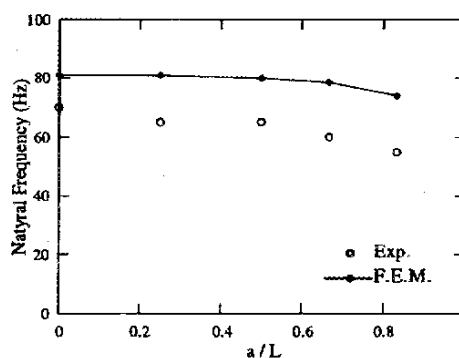


Fig. 8 First bending natural frequencies for laminated specimens ( $w=40$  mm,  $L=150$  mm,  $D=1.1$  mm,  $a/L=2/3$ ,  $d/D=1/8$ ,  $[0^\circ]_8$ ) with different delamination size.

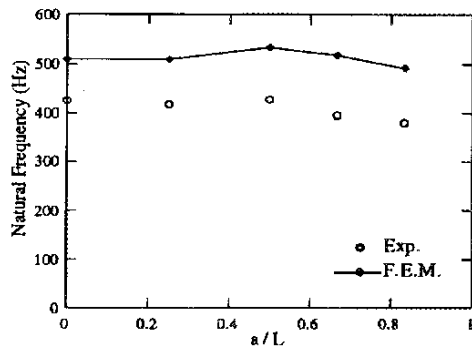


Fig. 9 Second bending natural frequencies for laminated specimens ( $w=40$  mm,  $L=150$  mm,  $D=1.1$  mm,  $a/L=2/3$ ,  $d/D=1/8$ ,  $[0^\circ]_8$ ) with different delamination size.

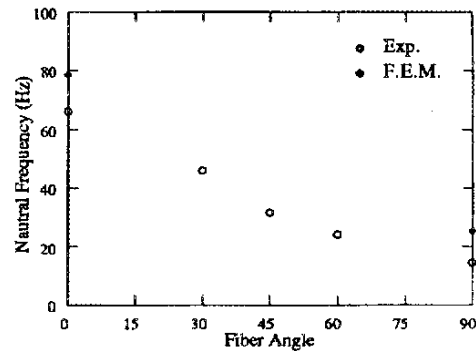


Fig. 12 First bending natural frequencies for laminated specimens ( $w=40$  mm,  $L=150$  mm,  $D=1.1$  mm,  $a/L=2/3$ ,  $d/D=1/8$ ) with different fiber orientation.

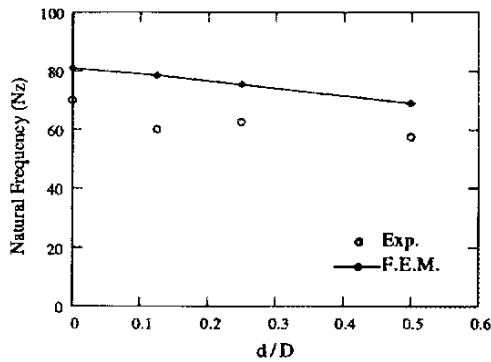


Fig. 10 First bending natural frequencies for laminated specimens ( $w=40$  mm,  $L=150$  mm,  $D=1.1$  mm,  $a/L=2/3$ ,  $[0^\circ]_8$ ) with different delamination position.

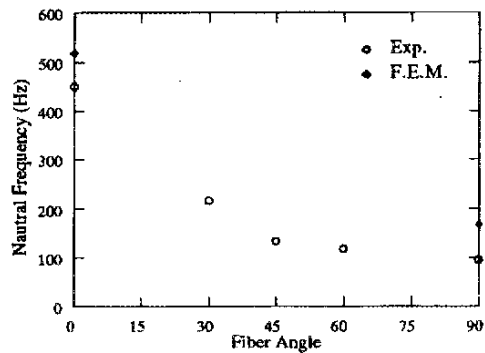


Fig. 13 Second bending natural frequencies for laminated specimens ( $w=40$  mm,  $L=150$  mm,  $D=1.1$  mm,  $a/L=2/3$ ,  $d/D=1/8$ ) with different fiber orientation.

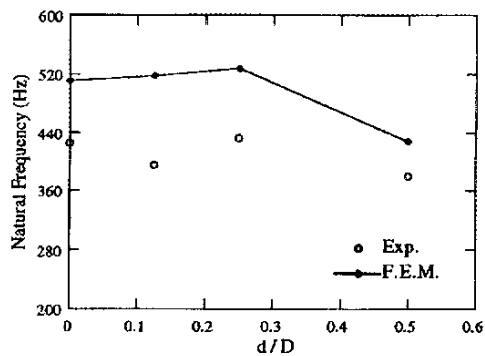


Fig. 11 Second bending natural frequencies for laminated specimens ( $w=40$  mm,  $L=150$  mm,  $D=1.1$  mm,  $a/L=2/3$ ,  $[0^\circ]_8$ ) with different delamination position.

# THE DYNAMIC RESPONSE OF INELASTIC, DELAMINATED COMPOSITE PLATES

Todd O. Williams and Frank L. Addessio

*T-3 Theoretical Division  
Los Alamos National Laboratory  
Los Alamos, New Mexico 87545, USA*

**SUMMARY:** The dynamic behavior of metal matrix composite (MMC) plates is considered. In particular, the influence of inelastic deformations and delamination at the interfaces of the lamina on the macroscopic and local response of  $Al_2O_3/Al$  plates are studied. The work is carried out using a recently developed plate theory which models both delamination and localized history-dependent effects such as inelasticity. A linear debonding model for the interface is employed for the current work. The theory models both the initiation and growth of delaminations without imposing any restrictions on the location, size, or direction of growth of the delamination. In the current work the response of the individual lamina in the plate are modelled using the Method of Cells (MOC) micromechanical model. The inelastic behavior in the matrix is modelled using the unified viscoplastic theory of Bodner and Partom.

The behavior of a  $Al_2O_3/Al$  plate under dynamic cylindrical bending subjected to a ramp and hold type of loading is examined. For simplicity, the plate is assumed to be composed of a cross-ply layup. It is shown that both inelastic deformations and delamination have a strong influence on dynamic plate behavior. The inelastic deformations have stronger effect on the axial displacement while delamination has greater influence on the deflection.

**KEYWORDS:** delaminated composite plates, interfacial constitutive laws, dynamic plate behavior, micromechanics, method of cells, viscoplasticity

## INTRODUCTION

Laminated composite structures have many potential applications in a variety of engineering fields. However, laminated structures are susceptible to delaminations between layers. The presence of delaminations can cause significant degradation of the structural response characteristics, as compared to perfectly bonded structures. Additionally, it must be recognized that history-dependent inelastic deformations evolve in composite plates under many loading situations. Furthermore, these mechanisms can be highly interactive. Therefore, it is necessary that analytical tools which can accurately predict these effects must be developed and subsequently employed in the design and analysis process.

A review of work which considers the inelastic dynamic behavior of homogeneous plates is given in [1]. More recently, work has been done to study the inelastic behavior of composite plates [2]. To date, relatively little work has been done considering the dynamic behavior of inelastic delaminated composite plates.

One potential method for analyzing delamination initiation and growth is through the use of interfacial constitutive models [3-6] The general form of such constitutive relations are given by

$$\Delta_i = f_i(\Delta_i, t_i) \quad (1)$$

where  $\Delta_i$  are the displacement jumps and  $t_i$  are the interfacial tractions. The relationship of these types of models to fracture mechanics is provided in [6].



A recently developed plate formulation is employed to study the dynamic behavior of inelastic delaminated composite plates [7,8]. The plate theory is based on an approximate higher-order discrete layer analysis. The theory is capable of incorporating any general nonlinear interfacial model behavior in an internally consistent fashion. No assumptions concerning the location, direction of growth, or number of delaminations are made in the theory. The plate theory is sufficiently general that any inelastic constitutive model can be employed. The plate theory has been shown to provide excellent agreement with both exact static elastic solutions and approximate dynamic solutions [7,8].

### PLATE THEORY FORMULATION

Consider a single layer. It is assumed that the displacement field within this layer is approximated by

$$u_i(x, y, z, t) = V_i^j(x, y, t) \phi^j(z) \quad (2)$$

where  $j = 1, 2, \dots, N$ .  $N$  is the order of the polynomial expansion. The functions  $\phi^j(z)$  are specified functions of the transverse coordinate  $z$  and the  $V_i^j(x, y, t)$  are the associated displacement coefficients. The governing equations for the layer are obtained by substituting the above displacement field into the principle of virtual work

$$\tau_i^j + N_{i\alpha, \alpha}^j - R_i^j + F_i^j = I^{mj} \dot{v}_i^m \quad (3)$$

where  $m, j = 1, 2, \dots, N$ . The corresponding inplane boundary conditions are

$$V_i^j = \text{specified on } \partial\Omega_1 \quad (4a)$$

$$T_i^j = N_{i\alpha}^j n_\alpha \quad \text{on } \partial\Omega_2 \quad (4b)$$

where  $\partial\Omega = \partial\Omega_1 + \partial\Omega_2$  and  $\partial\Omega$  is the plate boundary. Explicit satisfaction of both the continuity of the interfacial tractions and the jump conditions on the interfacial displacements are utilized to couple the equations governing the behavior of different layers to obtain the governing equations for the laminate. These interfacial conditions are given by

$$(V_i^l)^{k+1} - (V_i^N)^k = \Delta_i^k = f_i(\Delta_i^k, \tau_i^k) \quad (5a)$$

$$\left(\tau_i^j\right)^k + \left(\tau_i^j\right)^{k+1} = 0 \quad (5b)$$

The above results are completely general and the displacement jumps are expressed in a direct and consistent fashion as a function of the fundamental unknowns in the theory,  $V_i^j$  and  $\tau_i^j$ . Additionally, the interfacial delamination relations can easily incorporate the constraint that the layers cannot interpenetrate.

The above formulation has been carried out in a sufficiently general fashion that any constitutive law for the behavior of the layer or interface may be incorporated and, therefore, any evolution laws for the local effects can be consistently incorporated into the formulation.

The general theory has been implemented in an explicit finite element (FE) code. In the FE code it is assumed that the temporal gradient in the equation of motion is approximated as

$$\dot{v} = \frac{v - v_0}{\Delta t} \quad (6)$$

where  $v_0$  and  $\Delta t$  are the velocity at the preceding time and the time increment, respectively. Also the left hand side of the equation of motion is evaluated at the previous time step. It is noted that the gradient terms are evaluated using the Mean-Value Theorem.

$$\left\langle \frac{\partial \sigma_{ix}}{\partial x} \right\rangle_m \int \Psi^m d\Omega = \sum_n \left( \int \Psi^m \frac{\partial \Psi^n}{\partial x} d\Omega \right) \sigma_{iz}^n \quad (7)$$

Use of these expressions in the definitions of the force resultants,  $N_{i\alpha}^j$  and  $R_i^j$ , then using these results in the governing equations as known forcing terms allows the new velocities for the layers

to be determined. The new velocities are used to update the rate-of-deformation tensor using an expression based on the Mean-Value theorem similar to the above expression. The stresses throughout the plates are then updated by substituting the new rate-of-deformation tensor into the constitutive model for the materials within each layer. Once the stresses are computed, the boundary conditions for the plate are updated and the algorithm pursues advancing the velocities at the next time step. This process is continued until the problem is complete. Further details of the dynamic implementation of the theory are given in [8].

### METHOD OF CELLS MODEL

The Method of Cells [3] represents an efficient and accurate micromechanical model for predicting the inelastic behavior of composite materials. The analysis considers the behavior of a composite composed of a doubly periodic array of fibers which implies that it is only necessary to model the behavior of a unit cell, Fig. 1. The unit cell is subsequently considered to consist of four subcells. A linear velocity expansion is used to model the behavior in each subcell.

$$\dot{u}_i^{(\alpha,\beta)} = \dot{u}_i^{(\alpha,\beta)} + \bar{x}_2 \phi_i^{(\alpha,\beta)} + \bar{x}_3 \psi_i^{(\alpha,\beta)} \quad (8)$$

where  $\alpha$  and  $\beta$  are used to denote the subcells and  $\bar{x}_2$  and  $\bar{x}_3$  denote local subcell coordinates. Using the strain displacement relations the infinitesimal strains within each subcell can be expressed as functions of the  $\phi_i^{(\alpha,\beta)}$  and the  $\psi_i^{(\alpha,\beta)}$ . Imposing the velocity and traction continuity conditions between subcells

$$\begin{aligned} h_1 l_\beta \dot{\epsilon}_{i2}^{(1,\beta)} + h_2 l_\beta \dot{\epsilon}_{i2}^{(2,\beta)} &= h \dot{\epsilon}_{i2}^o \quad \text{for } i=1,3 \\ h_\alpha l_1 \dot{\epsilon}_{i3}^{(\alpha,1)} + h_\alpha l_2 \dot{\epsilon}_{i3}^{(\alpha,2)} &= l \dot{\epsilon}_{i3}^o \quad \text{for } i=1,3 \\ \sum_{\alpha,\beta=1}^2 v_{(\alpha,\beta)} \dot{\epsilon}_{23}^{(\alpha,\beta)} &= V \dot{\epsilon}_{23}^o \quad (9) \\ \sigma_{i2}^{(1,\beta)} &= \sigma_{i2}^{(2,\beta)} \\ \sigma_{i3}^{(\alpha,1)} &= \sigma_{i3}^{(\alpha,2)} \end{aligned}$$

in conjunction with the periodicity of the velocity fields provides closed form expressions for the effective macroscopic constitutive relations for a composite.

$$\dot{\bar{\sigma}} = \mathbf{C}^{eff} \dot{\epsilon}^o - \Gamma^{eff} \quad (10)$$

### BODNER-PARTOM VISCOPLASTIC MODEL

The simplest form of the unified viscoplastic theory of Bodner and Partom [9] is used to model the inelastic behavior of the matrix phase in the composite. The fiber is assumed to be elastic. A Prandtl-Reuss type flow rule is used in this theory.

$$\dot{\epsilon}_{ij}^I = \Lambda s_{ij} \quad (11)$$

where

$$\begin{aligned} \Lambda &= \left( \frac{D_2^I}{J_2} \right) \\ D_2^I &= D_o^2 \exp \left[ - \left( \frac{A^2}{J_2} \right)^n \right] \quad (12) \\ A^2 &= \frac{1}{3} Z^2 \left( \frac{n+1}{n} \right)^{\frac{1}{n}} \\ Z &= Z_1 - (Z_1 - Z_o) \exp(-mW_p/Z_o) \end{aligned}$$

where  $\dot{\epsilon}_{ij}^I$  is the inelastic strain rate,  $W_p$  is the plastic work, and  $J_2 = \frac{1}{2} s_{ij} s_{ij}$  and  $s_{ij} = \sigma_{ij} - \frac{1}{3} \sigma_{kk} \delta_{ij}$ . The material viscoplastic response is characterized by the constants  $n$ ,  $m$ ,  $D_o$ ,  $Z_o$ , and  $Z_1$ . The Bodner-Partom theory as presented models the inelastic material behavior using isotropic hardening only.

## RESULTS

For this work the dynamic response of a cross-ply (0/90) composite plate subjected to cylindrical bending is examined. The aspect ratio of the plate is 5. Thus the plate can be considered to be a thick plate. In such a plate significant transverse stresses are observed. The plate is composed of alumina fibers  $Al_2O_3$  embedded in an aluminum matrix. The fiber is elastic and the matrix supports inelastic deformation. The material properties of the constituent phases are given in Table 1. A fiber volume fraction of 64% is used to generate the results. The plate is subjected to a ramping half sine load for 1  $\mu s$  where the peak value changes from 0 to  $q_0 = 1$  GPa. The load is subsequently held at this peak value for 4  $\mu s$ .

**TABLE 1. Material properties for  $Al_2O_3/Al$  constituents.**

Material	$E$ (GPa)	$\nu$	$\rho$ (g/cm <sup>3</sup> )	$D_o(1/s)$	$Z_0$ (MPa)	$Z_1$ (MPa)	m	n
$Al_2O_3$	398.7	0.236	3.97	—	—	—	—	—
Al	72.0	0.345	2.70	$10^5$	340	435	300	10

Three cases are considered. In the first case the plate is modelled as inelastic but perfectly bonded (PB). In case 2 both inelastic behavior and debonding (DB) are modelled. For this case, a linear interfacial constitutive model is employed for simplicity, ( $\Delta_i = R\tau_i$ ), where the  $\tau_i$  are the appropriate interfacial stresses obtained directly from the theory. The interfacial model parameters for the debonded analysis are  $R_n = R_s = 0.1$  cm/GPa where the subscripts n and s denote the normal and shearing responses. Initially the laminate in case 2 is perfectly bonded. The final case models the plate as elastic and perfectly bonded.

The transverse displacement as a function of time for the three cases is given in Fig. 1. The following discussion is based on simple 1D wave propagation arguments considering the effects of the internal waves. The quoted times apply to case 3 (the elastic, perfectly bonded case). The transverse sound speed in the lamina is about 0.8. The transverse sound speed of the lamina is about 0.8 cm/ $\mu s$ . Initially, the top surface of the plate is rapidly accelerated by the applied loading. Both the interface and the bottom surface remain at rest. At approximately 1.2  $\mu s$  the maximum amplitude of the wave reaches the interface. The presence of the interface results in a reflected wave in the top lamina and a transmitted wave in the bottom lamina. The initial transmitted waves due to the beginning of the applied loading reach the outer surfaces of the plate at this time. This begins a rapid acceleration of the back surface. The reflected waves at the top surface begin to cause some deceleration of this surface. At approximately 2  $\mu s$  the initial wave reflections from the outer surfaces reach the interface. The midsurface of the plate then begins to accelerate. Additionally, at this point in time, the maximum wave amplitude has reached the outer surfaces of the plate. This results in the greatest acceleration at the bottom surface and rapid deceleration of the top surface. Similar wave reflection and interaction process continues throughout the rest of the calculations and corresponding interpretations of the wave effects can be made.

Incorporating inelastic deformations into the calculation, case 1, results in similar effects in the deflection versus time response. However, the trends occur at delayed times as compared to case 3. The delays in the trends are due to the fact that the inelastic deformations mitigate the effects of the elastic waves. The presence of the inelastic deformations "soften" the plate and result in larger deformation magnitudes. The amount of delay in case 1 as compared to case 3 is relatively small due to the relatively large volume fraction of the elastic fiber. If the fiber were inelastic or a lower fiber volume fraction were considered then the delays in the effects due to the presence of inelastic deformations would be larger.

Consideration of the response for case 2 (debonding and inelastic deformations) shows that the presence of delamination results in the same trends as cases 1 and 2. Similar to case 1, the trends

are delayed as compared to case 1. These delays are greater than those observed in case 1. The presence of the debonding at the interface results in an impedance mismatch. This impedance results in stronger reflected wave effects within the top lamina and weaker transmitted wave effects in the bottom lamina. As the value of  $R$  increases the impedance becomes larger and the reflected wave effects become stronger. Large values of  $R$  result in the plate approaching the debonded state with the top lamina being ejected as a solid body. In general, the displacement magnitudes are larger for case 2 than for cases 1 and 3. This is consistent with the "softer" behavior induced by the presence of both the inelastic deformations and the debonding. It is evident from these results that the presence of delamination results in displacement jumps across the interface which are significant in comparison with the variation of the displacement change across the laminate at various times. Examination of all three sets of results indicates that for the current laminate debonding has a larger effect on the response than plasticity.

The distributions of the axial displacement through the thickness at the end of the plate for all three cases are given in Fig. 2. It is evident from these results that both plasticity and debonding have a strong impact on the plate deformation at the local level. The largest deviations due to the presence of these effects occur in the region around the midplane of the plate. The maximum deviation between cases 2 and 3 does occur at the midplane and represents about 61% of the total variation in the distribution. The presence of plasticity has a relatively stronger influence on the axial displacement than does the presence of delamination. Consideration both plasticity and delamination only results in an additional variation, as compared to case 1, of about 13%. The displacement jump in case 2 due to delamination represents about 10% of the overall variation in the distribution.

The transverse displacement distributions through the thickness of the plate at the middle of the plate for all three cases are given in Fig. 3. The presence of plasticity has a much smaller effect on the deflection than was seen in the axial displacements. The maximum deviation from distribution of case 3 is 5%. The presence of the delamination has a more significant impact on the deflection than observed for the axial displacement. In this case, the maximum deviation from the case 3 distributions is about 30%. The jump due to delamination represents about 22% of the variation in the deflection distribution.

Finally, the transverse stress distributions through the thickness of the plate for all three cases at the middle of the plate are given in Fig. 3. As was observed in the deflection distributions, the presence of plasticity has a much smaller influence on the transverse stress as compared to the presence of the delamination. The maximum deviations between the distributions for cases 1 and 3 is about 0.07 while a maximum deviation of about 0.57 is observed between cases 2 and 3.

## CONCLUSIONS

A discrete layer plate theory has been used to consider the relative influence of both inelastic deformations and delamination on the dynamic behavior of a 0/90  $Al_2O_3/Al$  plate. The inelastic deformations of the composite were modelled using the Bodner-Partom viscoplastic theory in the micromechanical models known as the Method of Cells. A simple linear debonding model for the interfacial behavior was used in this study.

It was seen that the presence of plasticity and delamination have a significant effect on both the macroscopic and local behavior of the plate. Consideration of the macroscopic behavior indicated that the delamination had a stronger influence than the inelastic deformations. This was in part due to the fact that the debonding at the interface acted as an impedance which results in stronger wave effects in the top lamina as compared to the bottom lamina. Consideration the effects of delamination and plasticity on the local behavior indicated that these phenomena had different influences. The presence of inelasticity had a stronger influence on the axial displacement than did the presence of delamination. Alternatively, the presence of the delamination had a much stronger influence on the deflection and the transverse stress than did inelasticity.

## REFERENCES

1. Jones, N. "Recent Studies on the Dynamic Plastic Behavior of Structures", *Appl. Mech. Rev.*, Vol. 42, pp 95
2. Gilat and Aboudi, "Dynamic Buckling of Metal Matrix Composite Plates and Shells under Cylindrical Bending", *Comp. Struct.*, Vol. 28, 1994, pp 459
3. Aboudi, J. "The Mechanics of Composite Materials: A Unified Micromechanics Approach", Elsevier Science Publishers B.V., Amsterdam, The Netherlands, 1991
4. Needleman, A. "A Continuum Model for Void Nucleation by Inclusion Debonding", *J. Appl. Mech.*, Vol. 54, 1987, pp 525
5. Needleman, A. "An Analysis of Decohesion along an Imperfect Interface", *Int. J. Fract.*, Vol. 42, 1990, pp 21
6. Corigliano, A. "Formulation, Identification, and Use of Interface Models in the Numerical Analysis of Composite Delaminations", *IJSS*, Vol. 30, 1993, pp 2779
7. Williams, T.O. and Addessio, F.L. "A General Theory for Laminated Plates with Delaminations", *IJSS*, (in press), 1997 (also available as a LANL internal report, LA-UR-96-2593)
8. Williams, T.O. and Addessio, F.L. "Dynamic Behavior of Laminated Plates with Delaminations", *IJSS*, (in submission), 1997 (also available as a LANL internal report, LA-UR-96-3110)
9. Bodner, S.R. and Partom, Y. "Constitutive Equations for Elastic-Viscoplastic Strain Hardening Materials", *J. Appl. Mech.*, pp 385

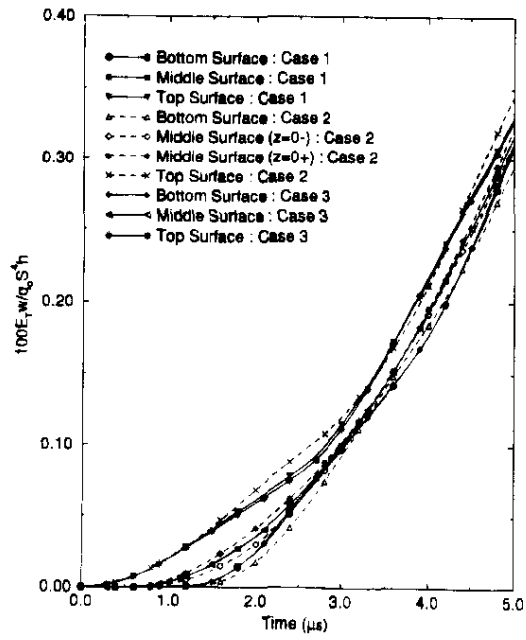


Figure 1 Transverse displacement at the middle of the plate as a function of time.

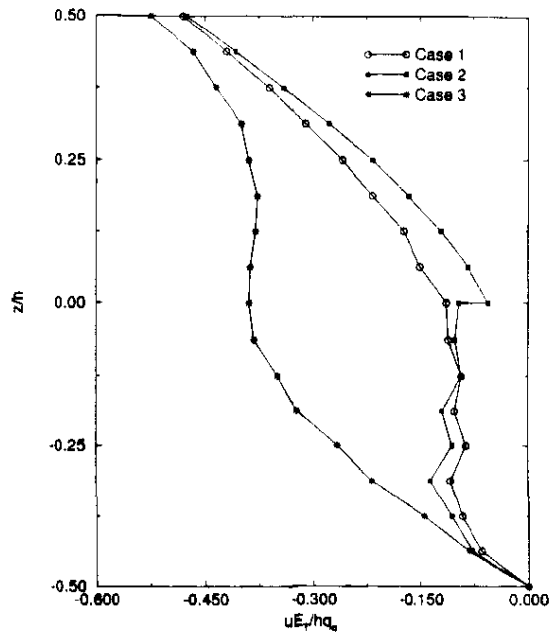


Figure 2. Through the thickness distributions of the axial displacement at the end of the plate.

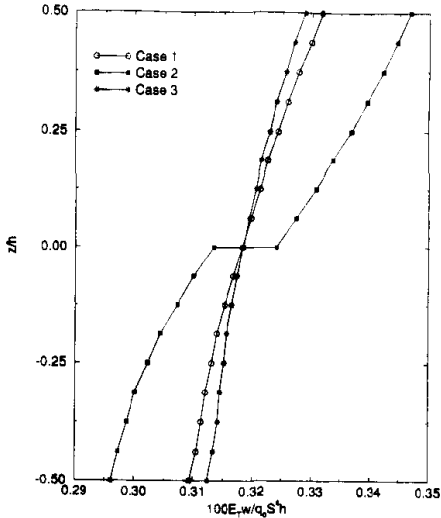


Figure 3. Through the thickness distributions of the deflection at the middle of the plate.

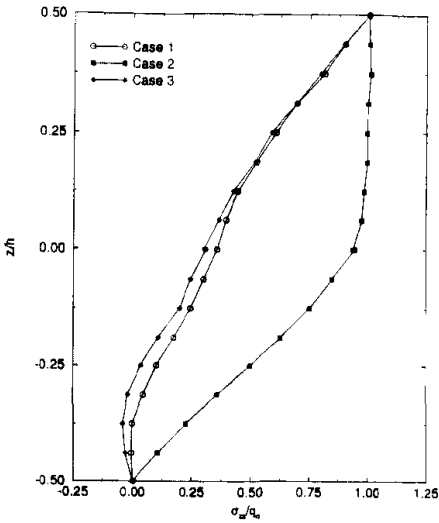


Figure 4. Through the thickness distributions of the transverse stress at the middle of the plate.



# VIBRATION ANALYSIS OF THICK LAMINATED TRAPEZOIDAL PLATES

C.C. Chen<sup>1</sup>, C.W. Lim<sup>1</sup>, S. Kitipornchai<sup>1</sup>, and K.M. Liew<sup>2</sup>

<sup>1</sup> *Department of Civil Engineering, The University of Queensland, Qld 4072, Australia*

<sup>2</sup> *Division of Engineering Mechanics, School of Mechanical and Production Engineering, Nanyang Technological University, Singapore 639798*

**SUMMARY:** To account for the effect of transverse shear deformation, the  $p$ -Ritz method incorporating Reddy's third-order shear deformation theory has been developed for the free vibration analysis of thick, laminated, cantilever, trapezoidal plates. In the proposed  $p$ -Ritz method, sets of uniquely defined polynomial functions are used as the admissible trial displacement and rotation functions. The admissible function consists of the product of a two-dimensional function and a basic function which is defined by multiplying the equations of the plate's prescribed boundary. The total energy is derived by using Reddy's third-order shear deformation theory which is able to predict the vibration characteristics of thick laminates more accurately. A convergence study has been carried out to verify the accuracy of the results. The results, wherever possible, are compared with published solutions to demonstrate the versatility and applicability of the proposed method.

**KEYWORDS:** free vibration, laminate, plate, higher-order shear deformation theory,  $p$ -Ritz method

## INTRODUCTION

The characteristics of high tensile strength and light weight has made the laminated plates gained their popularity in aerospace and marine engineering applications. Therefore, the ability to accurately determine the structural behavior of these panels is of paramount importance. The use of shear deformation theories for the analysis of thick laminated composite plates has emerged because of the inadequacy of the classical laminated plate theory [1] based on the Kirchhoff-Love hypothesis. The most popular shear deformation theory is the first-order shear deformation theory [2] which was extended to laminates by Yang *et al.*[3] In this theory, a shear correction factor is assumed a priori and it doesn't account for surfaces free of transverse shear strains. In an effort to circumvent the drawbacks of the first order shear deformation, various second and higher-order shear deformation theories have been proposed. The most common higher-order theory was pioneered by Levinson [4] and Reddy [5,6] which assumes transverse inextensibility. The present method adopts the simple higher-order theory based on the pioneering work of Reddy [5].

The need of wing-type structures has facilitated the development of trapezoidal laminates. Not much research in this topic have been done so far. Lee and Lee [7] applied the finite element method incorporating the first-order theory to investigate the vibration problem of moderately thick, cantilevered, trapezoidal laminates. Kapania and Lovejoy [8] used Chebychev

polynomials as displacement functions in the Rayleigh-Ritz method and utilized the first-order theory to study the free vibration of moderately thick, generally laminated, cantilevered, quadrilateral plates. Liew and Lim [9] integrated the classical theory and  $p$ -Ritz method for the problem of thin trapezoidal laminates. The  $p$ -Ritz method which developed by Liew [10] avoids the difficulty of mesh generation and continuity conditions required in discretization methods and is applicable to laminates with free, simply supported and clamped edge conditions. In this study, the  $p$ -Ritz method incorporating Reddy's third-order shear deformation theory is proposed for the vibration analysis of cantilevered, thick, laminated, trapezoidal plates. Convergence of frequency parameters has been carried out to ensure adequate terms in the displacement and rotation functions. The effects of aspect ratio, taper ratio, plate geometry and stacking angle on the thick, cantilevered, trapezoidal laminate are also investigated. The results, wherever possible, are compared with published solutions to evaluate the validity and to demonstrate the applicability of the proposed method.

## MATHEMATICAL FORMULATIONS

### Preliminary Definitions

Fig. 1 illustrates a thick, cantilever, laminated, trapezoidal plate composed of  $N$  orthotropic laminae oriented at angle  $\theta_k$  with respect to the  $x$ -axis and with the geometric configuration of

length-to-thickness ratio  $a/h$ , aspect ratio  $a/b$ , taper ratio  $c/b$ , skew angle  $\gamma$ , and total thickness  $h$ . The reference Cartesian coordinate system is located at the mid-plane of the laminated plate. The angle  $\gamma$  which measures positive in the clockwise direction, is the degree of skewness of the trapezoidal laminate. Another two definitions of the skew angles,  $\alpha$  and  $\beta$ , are also used for the convenience of comparison. The laminae are cross-plyed or stacked symmetrically with respect to the middle surface of the laminated plate. The interior angles of laminate geometries are assumed to be no larger than 90 degrees. The vibration frequencies of the trapezoidal laminate subjected to a variety of skewness angles, aspect ratios, taper ratios, and stacking angles are to be determined.

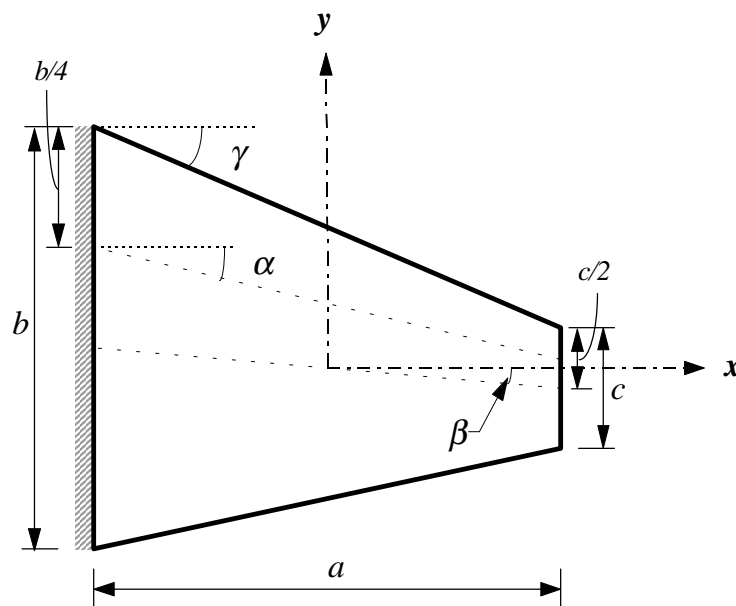


*Fig. 1: Laminated trapezoidal plate geometry*

## Energy Expressions

For a thick trapezoidal laminate undergoing small-amplitude vibration, the spatial displacement at a general point may be resolved into  $u$ ,  $v$  (in-plane motion) and  $w$  (out-of-plane motion) components, respectively. By using Reddy's higher-order shear deformation theory, the displacement field along the  $x$ -,  $y$ -,  $z$ -axis can be expressed in the following form:

$$\begin{aligned} u(x, y, z, t) &= u_0(x, y, t) + z\phi_x(x, y, t) - \frac{4z^3}{3h^2} \left( \phi_x(x, y, t) + \frac{\partial w(x, y, t)}{\partial x} \right) \\ v(x, y, z, t) &= v_0(x, y, t) + z\phi_y(x, y, t) - \frac{4z^3}{3h^2} \left( \phi_y(x, y, t) + \frac{\partial w(x, y, t)}{\partial y} \right) \\ w(x, y, z, t) &= w_0(x, y, t) \end{aligned} \quad (1)$$

where  $(u_0, v_0, w_0, \phi_x, \phi_y)$  are the displacement components of the mid-plane along the  $x$ -,  $y$ -, and  $z$ -directions and rotations of the mid-plane about the  $y$ - and  $x$ -direction, respectively. For free vibration problem, the deflection and rotation functions of the laminate mid-plane are sinusoidal in time, that is

$$\begin{aligned} u_0(x, y, t) &= U(x, y) \sin \omega t \\ v_0(x, y, t) &= V(x, y) \sin \omega t \\ w_0(x, y, t) &= W(x, y) \sin \omega t \\ \phi_x(x, y, t) &= \Theta_u(x, y) \sin \omega t \\ \phi_y(x, y, t) &= \Theta_v(x, y) \sin \omega t \end{aligned} \quad (2)$$

If the laminated plate is made of elastic materials, the strain energy for each ply is given by

$$U_k = \frac{1}{2} \int_{V_k} \boldsymbol{\varepsilon}_k^T \boldsymbol{\sigma}_k dV_k \quad (3)$$

where  $U_k$  and  $V_k$  are the strain energy and the volume of the  $k$ th lamina, respectively. Neglecting normal stress  $\sigma_k$ , the total strain energy for the entire laminated plate is

$$U = \frac{1}{2} \sum_{k=1}^N \iint_A \int_{h_{k-1}}^{h_k} (\sigma_x \varepsilon_x + \sigma_y \varepsilon_y + \sigma_{xz} \varepsilon_{xz} + \sigma_{yz} \varepsilon_{yz} + \sigma_{xy} \varepsilon_{xy})_k dz dA \quad (4)$$

Also, the total kinetic energy  $T$  associated with the vibration of laminated plate is

$$T = \frac{h}{2} \sum_{k=1}^N \iint_A \rho_k \left[ \left( \frac{\partial u}{\partial t} \right)^2 + \left( \frac{\partial v}{\partial t} \right)^2 + \left( \frac{\partial w}{\partial t} \right)^2 \right] dA \quad (5)$$

in which  $\rho_k$  is the mass density of the  $k$ th lamina.

The energy components  $U$  and  $T$  can be further simplified by introducing the equivalent modulus for a multidirectional lamina

$$(A_{ij}, B_{ij}, D_{ij}, E_{ij}, F_{ij}, H_{ij}) = \sum_{k=1}^N \int_{h_k}^{h_{k+1}} (\bar{Q}_{ij})_k (1, z, z^2, z^3, z^4, z^6) dz \quad (6)$$

in which,  $(\bar{Q}_{ij})_k$  are obtained by transforming the stacking angle  $\theta_k$  and the stiffness constants,  $(Q_{ij})_k$ , which are related to the material properties,  $E_1, E_2, \nu_{12}, \nu_{21}, G_{12}, G_{13}, G_{23}$ , of each ply. Eqns (4) and (5) can be further expanded in terms of  $(U, V, W, \Theta_u, \Theta_v)$  by substituting the strain-displacement relationship, stress-strain relationships and Eqn (2). As the vibration is periodic in time, we are able to obtain the maximum strain energy  $U_{\max}$  and maximum kinetic energy  $T_{\max}$  in a vibratory cycle. Finally, the total energy functional  $\Pi$  for the free vibration of laminated plate is defined as

$$\Pi = U_{\max} - T_{\max} \quad (7)$$

which is to be minimized by the Rayleigh-Ritz method to obtain the frequency.

### ***p*-Ritz Method**

The displacement and rotation components,  $U(x, y)$ ,  $V(x, y)$ ,  $W(x, y)$ ,  $\Theta_u(x, y)$ , and  $\Theta_v(x, y)$ , can be further simplified by using the non-dimensional expressions

$$\xi = \frac{x}{a}, \eta = \frac{y}{b} \quad (8)$$

In the Rayleigh-Ritz method, the displacement and rotation functions should be expressed in the form of a series containing unknown coefficients,

$$\begin{aligned} U(\xi, \eta) &= \sum_{i=1}^m c_i^u \varphi_i^u(\xi, \eta) \\ V(\xi, \eta) &= \sum_{i=1}^m c_i^v \varphi_i^v(\xi, \eta) \\ W(\xi, \eta) &= \sum_{i=1}^m c_i^w \varphi_i^w(\xi, \eta) \\ \Theta_u(\xi, \eta) &= \sum_{i=1}^m c_i^{\theta_u} \varphi_i^{\theta_u}(\xi, \eta) \\ \Theta_v(\xi, \eta) &= \sum_{i=1}^m c_i^{\theta_v} \varphi_i^{\theta_v}(\xi, \eta) \end{aligned} \quad (9)$$

where  $c_i^u, c_i^v, c_i^w, c_i^{\theta_u}, c_i^{\theta_v}$  are the unknown coefficients.

Now, using the *p*-Ritz method, we assumed the *p*-Ritz shape functions,  $\varphi_i^u, \varphi_i^v, \varphi_i^w, \varphi_i^{\theta_u}, \varphi_i^{\theta_v}$  to be the products of two-dimensional polynomial series and basic functions. The two-dimensional polynomial series  $f_i(\xi, \eta)$  are defined as

$$\sum_{i=1}^m f_i(\xi, \eta) = \sum_{q=0}^p \sum_{i=0}^q \xi^{q-i} \eta^i \quad (10)$$

where  $p$  is the highest degree of the set of two-dimensional polynomials.

To ensure automatic satisfaction of geometric boundary conditions, the basic functions are assumed to be consist of products of boundary expressions of the laminated plate raised to their associated basic powers. Thus, for the trapezoidal laminated plate shown in Fig. 1, the basic functions can be structured as shown below

$$\begin{aligned} \varphi_b^\kappa = & \left( \xi + \frac{1}{2} \right)^{\Omega_1^\kappa} \left\{ \eta + \left[ \frac{a}{b} \tan \beta - \frac{1}{2} \left( 1 - \frac{c}{b} \right) \right] \xi + \frac{1}{4} \left( 1 + \frac{c}{b} \right) \right\}^{\Omega_2^\kappa} \left( \xi - \frac{1}{2} \right)^{\Omega_3^\kappa} \\ & \times \left\{ \eta + \left[ \frac{a}{b} \tan \beta + \frac{1}{2} \left( 1 - \frac{c}{b} \right) \right] \xi - \frac{1}{4} \left( 1 + \frac{c}{b} \right) \right\}^{\Omega_4^\kappa} \end{aligned} \quad (11)$$

where  $\Omega_s^\kappa$  denotes the associated basic power. If the cantilevered plate clamped at  $\xi = -1/2$ , the basic powers  $\Omega_s^\kappa$  are defined as follows,

$$\begin{aligned} \Omega_s^\kappa &= 0, \text{ for } \kappa = u, v, w, \theta_u, \theta_v \text{ and } s = 2, 3, 4 \\ \Omega_1^\kappa &= 1, \text{ for } \kappa = u, v, w, \theta_u, \theta_v \\ \Omega_1^w &= 2, \end{aligned} \quad (12)$$

The total energy functional  $\Pi$  derived in equation (7) are minimized with respect to the unknown coefficients leading to the following governing equation,

$$\frac{1}{D_0} \begin{bmatrix} K^{uu} & K^{uv} & 0 & 0 & 0 \\ & K^{vv} & 0 & 0 & 0 \\ & & K^{ww} & K^{w\theta_u} & K^{w\theta_v} \\ & & & K^{\theta_u\theta_u} & K^{\theta_u\theta_v} \\ & sym. & & & K^{\theta_v\theta_v} \end{bmatrix} - \lambda \begin{bmatrix} M^{uu} & 0 & 0 & 0 & 0 \\ & M^{vv} & 0 & 0 & 0 \\ & & M^{ww} & M^{w\theta_u} & M^{w\theta_v} \\ & & & M^{\theta_u\theta_u} & 0 \\ & sym. & & & M^{\theta_v\theta_v} \end{bmatrix} \begin{Bmatrix} c^u \\ c^v \\ c^w \\ ac^{\theta_u} \\ bc^{\theta_v} \end{Bmatrix} = 0 \quad (13)$$

with

$$D_0 = \frac{Q_{11} h^3}{12(1 - \nu_{12} \nu_{21})} \quad (14)$$

Details of the stiffness and mass matrices can be found in [11]. If the laminae are made of the same material with mass density per unit volume  $\rho$  and the same thickness  $h$ , the non-dimensional eigenvalue  $\lambda$  becomes

$$\lambda = \omega ab \sqrt{\frac{\rho h}{D_0}} \quad (15)$$

The vibration frequencies and mode shapes of trapezoidal laminates are obtained by solving  $\lambda$ .

## NUMERICAL STUDIES AND DISCUSSION

Numerical computation has been carried out in double precision on a *SGI PowerChallenge* computer. The results have been compared with available solutions of first-order shear deformation theory. Excellent agreement exists between the present method and previous solutions. In all examples, laminates have been assumed to be equal thickness and made of non-dimensional material properties,  $E_1/E_2 = 25$ ,  $G_{12}/E_2 = 0.5$ ,  $G_{23}/E_2 = 0.2$ ,  $G_{13} = G_{12}$ , and  $\nu = 0.25$ .

*Table 1: Convergence of frequency parameters  $\lambda$  of 6-ply trapezoidal laminates with  $a/b = 1.0$ ,  $c/b = 0.3$ , stacking sequence  $[30_2/0]_s$ ,  $a/h = 5$ , and  $\gamma = 0$*

$p$	Mode sequence number							
	1	2	3	4	5	6	7	8
8	2.3576	4.6118	7.1591	7.5668	9.7511	10.8658	13.4282	15.3492
10	2.3575	4.6110	7.1582	7.5668	9.7488	10.8596	13.4223	15.3365
11	2.3575	4.6108	7.1581	7.5667	9.7486	10.8584	13.4218	15.3344
12	2.3575	4.6108	7.1580	7.5667	9.7484	10.8578	13.4215	15.3337
13	2.3575	4.6107	7.1580	7.5667	9.7483	10.8573	13.4213	15.3332
14	2.3575	4.6107	7.1580	7.5667	9.7483	10.8571	13.4213	15.3330
15	2.3575	4.6107	7.1579	7.5667	9.7483	10.8569	13.4212	15.3328

The trapezoidal laminated plates with aspect ratio 1, taper ratio 0.3, length-to-thickness ratio 5,  $\gamma = 0$ , and stacking sequence  $[30_2/0]_s$  were solved in the first example. Convergence studies have been carried out to check the numerical accuracy of this method. The degree of polynomial  $p$  was increased from 8 to 15 to study its effect on the non-dimensional frequency parameters  $\lambda$ . As shown in Table 1, the difference between the results for  $p = 11$  and  $p = 15$  are less than 0.02%. Apparently, the degree of polynomial  $p = 15$  is enough to ensure the convergence of the results and it is used in all subsequent examples.

The effects of aspect ratio, taper ratio and stacking angle on the frequency parameters of moderately thick symmetric laminates have been investigated in the second example. The present method is further verified by comparing the results for frequency parameters with the solutions from Kapania and Lovejoy[8] who applied Chebychev polynomials and first-order shear deformation theory. As shown in Table 2, the results are in excellent agreement with previous solutions. It is noted that the frequency parameter decreases with increasing aspect ratio or taper ratio. The influence of aspect ratio indicates that cantilevered plates with higher  $a/b$  are structurally weaker than those with lower  $a/b$ . As for the effect of taper ratio, the authors believe that the reduction in mass for lower  $c/b$  leads to the increase of the frequency.

In the previous example, the increase in stacking angle caused different change in frequency parameter. Therefore, a cursory examination of the influence of stacking angles and taper ratios on the vibration of thick trapezoidal laminates is required. In the third example, the laminates are assumed to be stacked symmetrically with stacking sequence  $[-\theta/\theta]_s$ , a length-to-thickness ratio of 5, and plate geometry  $\beta = 0$ . By comparing the lowest four frequency results  $\lambda$ , the effects of taper ratio and stacking angle for laminates with different geometry have been shown in Fig.2. Again, it confirms that a lower taper ratio results in higher frequency parameter. Also note that the fundamental frequencies decrease as stacking

angle increases. For all modes except the fundamental mode, higher frequencies are likely to occur with the stacking angle between 15 and 45 degrees.

Table 2: Effects of aspect ratio, taper ratio and stacking angle on the four lowest frequency parameters,  $\lambda_1 = \omega a^2 / h\sqrt{\rho / E_2}$ , of laminated trapezoidal plates with  $\alpha = 0$ , stacking sequence  $[-\theta / \theta / 0]_s$  and  $a/h = 10$

a/b	c/b	$\theta$	Mode sequence number								
			1		2		3		4		
			Ref. 8	Present	Ref. 8	Present	Ref. 8	Present	Ref. 8	Present	
1	0.25	0	6.85	6.904	11.9	12.029	14.9	14.901	22.5	23.091	
		30	5.21	5.224	16.4	16.431	19.5	19.704	32.4	32.141	
		45	3.7	3.704	14.9	14.826	17.3	17.402	32.8	32.319	
	0.50	0	6.20	6.252	9.05	9.136	13.5	13.451	18.7	18.896	
		30	4.59	4.603	12.7	12.681	18.3	18.402	27.1	26.967	
		45	3.20	3.206	13.2	13.160	14.3	14.227	29.2	28.816	
	1.00	0	5.58	5.628	6.10	6.153	9.53	9.592	11.6	11.574	
		30	4.01	4.023	8.21	8.218	14.2	14.250	19.4	19.481	
		45	2.75	2.759	8.45	8.444	13.1	13.116	20.1	20.026	
	2	0.25	0	2.05	2.052	4.93	4.945	7.14	7.131	8.67	8.761
			30	1.34	1.343	5.85	5.829	8.24	8.259	12.1	12.091
			45	0.885	0.884	4.04	4.021	8.65	8.634	10.0	10.886
0.50		0	1.80	1.803	3.53	3.536	6.41	6.399	8.32	8.408	
		30	1.16	1.155	5.58	5.557	6.19	6.209	10.9	10.895	
		45	0.755	0.754	3.86	3.849	6.50	6.489	9.87	9.852	
1.00		0	1.55	1.547	2.10	2.106	5.46	5.455	6.93	6.935	
		30	0.987	0.987	3.85	3.852	5.35	5.345	9.49	9.470	
		45	0.640	0.639	3.72	3.712	4.08	4.072	8.73	8.709	
5		0.25	0	0.361	0.361	1.46	1.461	1.75	1.753	2.24	2.176
			30	0.201	0.201	0.957	0.955	2.18	2.119	2.46	2.442
			45	0.128	0.128	0.621	0.619	1.61	1.597	1.92	1.853
	0.50	0	0.308	0.308	1.05	1.050	1.63	1.633	2.03	1.969	
		30	0.170	0.170	0.910	0.908	1.98	1.933	2.39	2.387	
		45	0.108	0.108	0.588	0.586	1.60	1.589	1.75	1.694	
	1.00	0	0.255	0.255	0.614	0.614	1.54	1.544	1.73	1.713	
		30	0.143	0.143	0.877	0.876	1.47	1.467	1.78	1.760	
		45	0.0901	0.0900	0.566	0.564	1.57	1.548	1.58	1.576	

Consideration is now given to the effect of taper ratios and plate geometry on the 8-ply anti-symmetrically cross-plyed trapezoids. Numerical results have been illustrated in Fig. 3. As anticipated, an increase in taper ratio leads to a decrease in the frequency parameter. The fundamental frequency parameter decreases as the plate geometry  $\beta$  increases. However, for the rest of the modes, the effect of plate geometry on the frequency parameter is significant. From the numerical results of the third and fourth examples, we may conclude that an increase in aspect ratio or taper ratio results in an decrease in frequency parameter. As for the effect of stacking angle on the frequency parameters, no theoretical explanation is available, to the authors' knowledge. However, from the results of this study, we may conclude that: 1)

for the bending modes, the frequency parameter decreases when stacking angle increases; 2) for other modes except torsional modes, the frequency parameter decreases when stacking angle approaches 0 or 75 and maximum frequency values are most likely to occur when stacking angle is between 15 and 45; 3) for the torsional modes, the change of frequency parameter is influenced by the plate geometry.

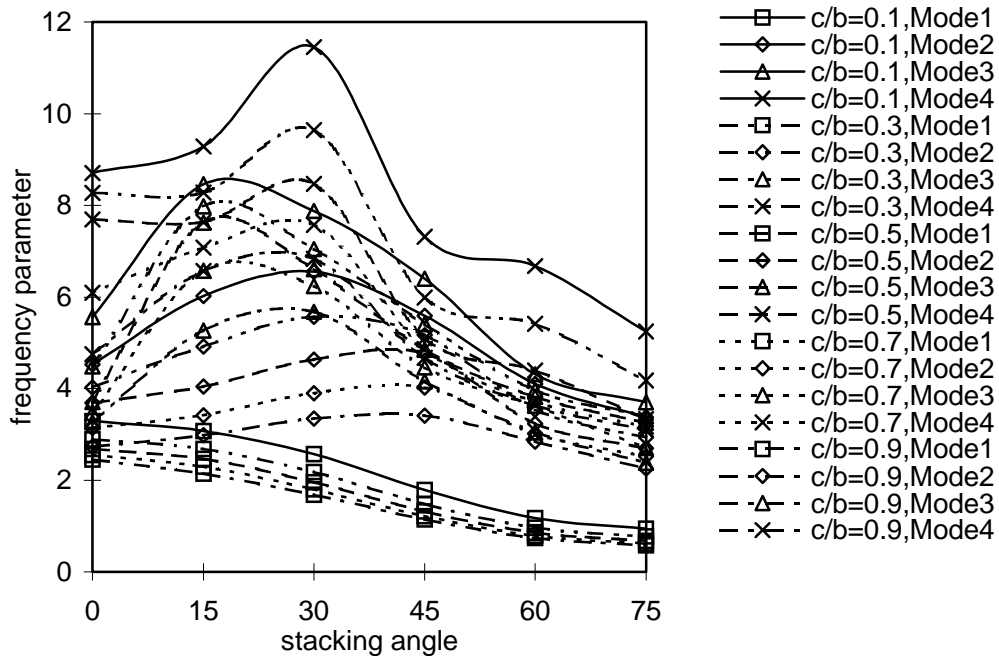


Fig. 2: Effects of taper ratio  $c/b$  and stacking angle  $\theta$  on the first four non-dimensional frequency parameters  $\lambda$  of laminated trapezoidal plates with stacking sequence  $[-\theta/\theta]_s$ ,  $\beta = 0$  and  $a/h = 5$

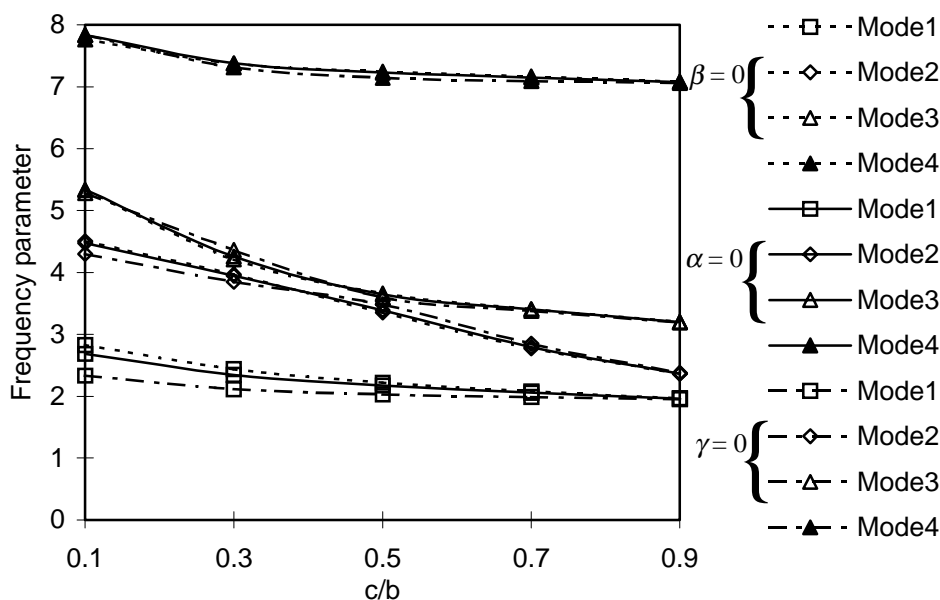


Fig. 3: Effects of taper ratio  $c/b$  on the first four non-dimensional frequency parameters  $\lambda$  of laminated trapezoidal plates with stacking sequence  $[0/90]_4$  and  $a/h = 5$



## CONCLUSIONS

This paper presents an approximate method based on the Rayleigh-Ritz energy approach for the vibration analysis of thick, cantilevered, stacked symmetrically or cross-plyed trapezoidal laminates. In this method, sets of two-dimensional  $p$ -Ritz shape functions are employed as the admissible displacement and rotation functions. Since the boundary conditions have been formulated as the intrinsic components of the  $p$ -Ritz functions, the boundary conditions are automatically satisfied at the outset. Several examples have been verified and the results are in close agreement with available published literature. It can be concluded that an increase in aspect ratio or taper ratio results in a decrease in frequency parameter. In addition, both plate geometry and stacking angle should be considered as their influence on the frequency parameter are significant.

## REFERENCES

1. Leissa, A.W., *Vibration of Plates*, NASA SP-160, Scientific and Technical Information Division, Office of Technology Utilization, NASA, Washington D. C., 1969.
2. Reissner, E., "The Effect of Transverse Shear Deformation on The Bending of Elastic Plates", *Journal of Applied Mechanics*, Vol. 12, 1945, pp. A69-A77.
3. Yang, P.C., Norris, C.H., and Stavsky, Y., "Elastic Wave Propagation in Heterogeneous Plates", *International Journal of Solids and Structures*, Vol. 2, 1966, pp. 665-684.
4. Levinson, M., "An Accurate Simple Theory of The Statics and Dynamics of Elastic Plates", *Mechanical Research Communications*, Vol. 7, 1980, pp. 343-350.
5. Reddy, J.N., "A Simple Higher-Order Theory for Laminated Composite Plates", *Journal of Applied Mechanics*, Vol. 51, 1984, pp. 745-752.
6. Reddy, J.N. and Phan, N.D., "Stability and Vibration of Isotropic, Orthotropic and Laminated Plates According to A Higher-Order Shear Deformation Theory", *Journal of Sound and Vibration*, Vol. 98, 1985, pp.157-170.
7. Lee, I., and Lee, J.J., "Vibration Analysis of Composite Plate Wing", *Computers and Structures*, Vol. 37, No. 6, 1990, pp. 1077-1085.
8. Kapania, R.K., and Lovejoy, E.L., "Free Vibration of Thick Generally Laminated Cantilever Quadrilateral Plates", *AIAA Journal*, Vol. 34, No. 7, 1996, pp.1474-1486.
9. Liew, K.M., and Lim, C.W., "Vibratory Characteristics of General Laminates, I: Symmetric Trapezoids", *Journal of Sound and Vibration*, Vol. 183, No. 4, 1995, pp. 615-642
10. Liew, K.M., *The Development of 2-D Orthogonal Polynomials for Vibration of Plates*, Ph.D. Thesis, National University of Singapore, Singapore, 1990.
11. Chen, C.C., Liew, K.M., Lim, C.W., and Kitipornchai, S., "Vibration Analysis of Symmetrically Laminated Thick Rectangular Plates Using the Higher-Order Theory and  $p$ -Ritz Method", *Journal of the Acoustical society of America*, in press, 1997.

# DYNAMIC RESPONSES OF ORTHOTROPIC ANNULAR COMPOSITE PLATES

C.L.D. Huang

*Department of Mechanical Engineering, Durland Kansas State University Manhattan,  
Kansas 66506-5106 USA*

**SUMMARY:** Using Hamilton's principle, the nonlinear partial differential for large oscillations and the associated boundary conditions, for thick circular composite plates, have been derived. A high-order shear deformation thick plate theory rather than a first-order shear deformation plate theory is implemented in the basic equations. The applications of the finite element method to the dynamic problems rely on the use of a variational principle to derive the necessary element properties and motion equations. The assembled equations for an eigenvalue problem. A numerical technique of using an incremental and iterative scheme is utilized for calculating frequency responses. The HSG-PRD-HSG and PRD-HSG-PRD annular composite plate with free-clamped boundary conditions are studied as examples and their dynamic responses are obtained.

**KEYWORDS:** non-linear dynamic response, thick annular composite plates

## INTRODUCTION

Composite plates are made of laminae, the plates can be layers of isotropic or anisotropic materials which material properties may or may not depend on orientation. The plates are heterogeneous in thicknesswise because of difference material layers. Also the thickness of plates may be thick enough for which the "thin" plate theory might not be sufficient to describe the physical models. Thus, the equations of motion of a heterogeneous anisotropic thick plate are needed. Using Hamilton's principle, the nonlinear partial differential equations for large oscillations and the associated boundary conditions have been derived. A higher-order shear deformation plate theory (the inplane displacements are expressed as a cubic polynomial functions of thickness coordinate and the transverse deflection is assumed to be a constant) rather than a first-order shear deformation plate theory is implemented in the basic equations. The applications of the finite element method to the dynamic problems rely on the use of a variational principle to derive the necessary element properties and equations. The assembled finite-element equations for the plate are formed by summing each element equation obtained in consideration of a single element. Then, the boundary conditions are imposed on the vector of nodal field variables, so that the appropriate boundary conditions are satisfied. The assembled equations form an eigenvalue problem. The developed model is then applied to study an axisymmetric large vibration of heterogeneous orthotropic annular composite plate. A numerical technique of using an incremental and iterative scheme is utilized for calculating frequency responses. The HSG-PRD-HSG (High-Strength-Graphite epoxy sandwiched with two filaments of PRD-49-III developed by E.I. DuPont de Nemours and Company, Inc.) and PRD-HSG-PRD annular composite plates with free-clamped boundary conditions, are used as examples, and their dynamic responses are obtained. The effects of thickness of plate which are due to the shear deformation, rotatory inertia, inplane deformation and inplane inertia, are examined and discussed.

## EQUATIONS OF MOTION IN FINITE ELEMENT FORM

According to the higher order shear deformation plate theory (Reddy, 1984) [1], the displacements of an axisymmetric polar orthotropic annular plate can be expressed as:

$$u_r = u_r^0 + z \left[ \Psi_r - \frac{4}{3} \left( \frac{z}{h} \right)^2 (\Psi_r + w_{,r}) \right], \quad (1a)$$

$$u_z = w(r, t), \quad (1b)$$

where  $u_r$  and  $u_z$  are respectively the inplane displacements in the radial and transverse directions,  $u_r^0$  and  $w$  are the midplane displacements in the radial and transverse directions, respectively,  $w_{,r}$  (partial derivative of  $w$  with respect to  $r$ ) is the slope of the midplane, and  $\Psi_r$  is the rotation of the normal to the midplane.

Following the Von Karman theory of flat plates, the strain-displacement relations are:

$$\varepsilon_{rr} = \frac{\partial u_r}{\partial r} + \frac{1}{2} \left( \frac{\partial w}{\partial r} \right)^2, \quad \varepsilon_{\theta\theta} = \frac{u_r}{r}, \quad \gamma_{rz} = \frac{\partial w}{\partial r} + \frac{\partial u_r}{\partial z}. \quad (2)$$

For polar orthotropic material, the stress-strain relations are:

$$\begin{Bmatrix} \sigma_{rr} \\ \sigma_{\theta\theta} \\ \sigma_{rz} \end{Bmatrix} = \begin{bmatrix} Q_{11} & Q_{12} & 0 \\ Q_{12} & Q_{22} & 0 \\ 0 & 0 & Q_{55} \end{bmatrix} \begin{Bmatrix} \varepsilon_{rr} \\ \varepsilon_{\theta\theta} \\ \gamma_{rz} \end{Bmatrix}, \quad (3)$$

where the reduced plane-stress elastic constants,  $Q_{ij}$ , are in terms of the moduli and Poisson's ratios,

$$Q_{11} = \frac{E_r}{1 - \nu_{r\theta}\nu_{\theta r}}, \quad Q_{12} = \frac{\nu_{r\theta}E_r}{1 - \nu_{r\theta}\nu_{\theta r}}, \quad (4)$$

$$Q_{22} = \frac{E_\theta}{1 - \nu_{r\theta}\nu_{\theta r}}, \quad Q_{55} = E_{rz}.$$

The following nondimensional parameters are introduced:

$$\chi = w/r_0, \quad \Psi_\xi = \Psi_r, \quad u_\xi^0 = u_r^0/h, \quad u_\xi = u_r/h, \quad (5)$$

$$\xi = r/r_0, \quad R = r_i/r_0, \quad \zeta = z/h.$$

The energy approach is used in this paper for solving the problem considered. Since the plate is axisymmetric, ring elements are chosen. The normalized region of the plate  $[R, 1]$  is

divided into  $n$  finite elements, each having a width  $2s$ , where  $s = (1 - R)/2n$ . Each element has three nodes (two exterior nodes and one interior node) and each nodal point has four degrees of freedom,  $u_\xi^0$ ,  $\Psi_\xi$ ,  $\chi_\xi$ , and  $\chi_{,\xi}$ .

The kinetic and strain energy of an annular plate subjected to axisymmetric vibrations can be expressed as:

$$T = \frac{1}{2} \rho \int_0^{2\pi} \int_{-1/2}^{1/2} \int_1^R \left[ \left( h \frac{\partial u_\xi}{\partial t} \right)^2 + \left( r_0 \frac{\partial \chi}{\partial t} \right)^2 \right] h r^2 d\xi d\zeta d\theta, \quad (6a)$$

$$V = \frac{1}{2} \int_0^{2\pi} \int_{-1/2}^{1/2} \int_1^R \{ \varepsilon \}^T [Q] \{ \varepsilon \} h r^2 d\xi d\zeta d\theta. \quad (6b)$$

The nondimensional inplane displacements for a finite element are expressed as:

$$u^0_{\xi}(\xi, t) = \sum_{i=1}^3 N_i(\xi) U_i(t), \quad (7a)$$

$$\Psi_{\xi}(\xi, t) = \sum_{i=1}^3 \phi_i(\xi) W_i(t), \quad (7b)$$

$$\chi(\xi, t) = \sum_{i=1}^3 \phi_i(\xi) W_i(t), \quad (7c)$$

where  $U_i$ ,  $V_i$  and  $W_i$  are nodal variable vectors, defined as:

$$\{U_i\} = [U_1 \ U_2 \ U_3]^T, \quad (8a)$$

$$\{V_i\} = [V_1 \ V_2 \ V_3]^T, \quad (8b)$$

$$\{W_i\} = [W_1 \ W_{1,\xi} \ W_2 \ W_{2,\xi} \ W_3 \ W_{3,\xi}]^T, \quad (8c)$$

and the shape functions  $\rho_i$  and  $N_i$  are (Huang and Huang, 1989):

$$\{\phi_i\} = \begin{bmatrix} 0.75 & -0.5 & -1.25 & 1 & 0 & 0 \\ 0.25 & -0.25 & -0.25 & 0.25 & 0 & 0 \\ 0 & 1 & 0 & -2 & 0 & 1 \\ 1 & 0 & -2 & 0 & 1 & 0 \\ -0.75 & -0.5 & 1.25 & 1 & 0 & 0 \\ 0.25 & 0.25 & -0.25 & -0.25 & 0 & 0 \end{bmatrix} \begin{Bmatrix} \eta^5 \\ \eta^4 \\ \eta^3 \\ \eta^2 \\ \eta \\ 1 \end{Bmatrix}, \quad (9a)$$

$$\{N_i\} = \begin{bmatrix} 0.5 & -0.5 & 0 \\ -1 & 0 & 1 \\ 0.5 & 0.5 & 0 \end{bmatrix} \begin{Bmatrix} \eta^2 \\ \eta \\ 1 \end{Bmatrix}. \quad (9b)$$

The strain vector  $\{\epsilon\}$  in eqn (6b) can be separated into a linear part and a nonlinear part as:

$$\{\epsilon\} = \{\epsilon^L\} + \{\epsilon^{NL}\} = \begin{Bmatrix} \{\epsilon^L_p\} \\ \{\epsilon^L_b\} \\ \{\epsilon^L_s\} \end{Bmatrix} + \begin{Bmatrix} \{\epsilon^{NL}_p\} \\ 0 \\ 0 \end{Bmatrix}, \quad (10)$$

where superscripts  $L$  and  $NL$  denote linear and nonlinear, respectively, and subscripts of  $p$ ,  $b$  and  $s$  represent inplane, bending and shear strains, respectively. The linear strain components are:

$$\{\varepsilon^L_p\} = \frac{h}{r_0} \begin{Bmatrix} \partial u^0_\xi / \partial \xi \\ u^0_\xi / \xi \end{Bmatrix}, \quad (11a)$$

$$\{\varepsilon^L_b\} = \frac{z}{r_0} \begin{Bmatrix} \Psi_{\xi,\xi} \\ \Psi_{\xi\xi} \end{Bmatrix} - \frac{4}{3h^2} \frac{z^3}{r_0} \begin{Bmatrix} \Psi_{\xi,\xi} + \chi_{,\xi\xi} \\ (1/\xi) (\Psi_\xi + \chi_{,\xi}) \end{Bmatrix}, \quad (11b)$$

$$\{\varepsilon^L_s\} = (1 - 4\zeta^2) (\Psi_\xi + \chi_{,\xi}), \quad (11c)$$

and the nonlinear inplane component is expressed as:

$$\varepsilon^{NL}_p = \frac{1}{2} (\chi_{,\xi})^2 = f(\chi_{,\xi}), \quad (11d)$$

where  $f$ , the linearized function, is defined as:

$$f = \frac{1}{2} \chi_{,\xi}. \quad (12)$$

Substituting eqn (7) into (11), strain components are expressed in terms of shape functions:

$$\{\varepsilon^L_p\} = \frac{h}{r_0} \begin{bmatrix} \frac{\partial N_i}{\partial \xi} & 0 & 0 \\ N_i & 0 & 0 \end{bmatrix} \begin{Bmatrix} U_i \\ V_i \\ W_i \end{Bmatrix}, \quad (13a)$$

$$\{\varepsilon^L_b\} = \frac{z}{r_0} \begin{bmatrix} 0 & \frac{\partial N_i}{\partial \xi} & 0 \\ 0 & \frac{N_i}{\xi} & 0 \end{bmatrix} \begin{Bmatrix} U_i \\ V_i \\ W_i \end{Bmatrix} - \frac{4}{3h^2} \frac{z^3}{r_0} \begin{bmatrix} 0 & \frac{\partial N_i}{\partial \xi} & \frac{\partial^2 \phi_i}{\partial \xi^2} \\ 0 & \frac{N_i}{\xi} & \frac{1}{\xi} \frac{\partial \phi_i}{\partial \xi} \end{bmatrix} \begin{Bmatrix} U_i \\ V_i \\ W_i \end{Bmatrix}, \quad (13b)$$

$$\{\varepsilon^L_s\} = (1 - 4\zeta^2) \begin{bmatrix} 0 & N_i & \frac{\partial \phi_i}{\partial \xi} \end{bmatrix} \begin{Bmatrix} U_i \\ V_i \\ W_i \end{Bmatrix}, \quad (13c)$$

$$\{\varepsilon^{NL}_p\} = f \begin{bmatrix} 0 & 0 & \frac{\partial \phi_i}{\partial \xi} \\ 0 & 0 & 0 \end{bmatrix} \begin{Bmatrix} U_i \\ V_i \\ W_i \end{Bmatrix}. \quad (13d)$$

The kinetic and strain energies of a ring element of the plate subjected to harmonic

oscillations are:

$$T^{(e)} = \frac{1}{2} 2\pi\rho \int_{-1/2}^{1/2} \int_{\xi_i}^{\xi_{i+1}} \left[ \left( h \frac{\partial u \xi}{\partial t} \right)^2 + \left( r_0 \frac{\partial \chi}{\partial t} \right)^2 \right] h r^2 \xi d\xi d\zeta, \quad (14a)$$

$$V^{(e)} = \frac{1}{2} 2\pi \int_{-1/2}^{1/2} \int_{\xi_i}^{\xi_{i+1}} \{\varepsilon\}^T [Q] \{\varepsilon\} h r^2 \xi d\xi d\zeta. \quad (14b)$$

The strain energy is separated into two parts, namely the linear strain energy  $V_L^{(e)}$  and the nonlinear strain energy  $V_{NL}^{(e)}$ . They are as follows:

$$V_L^{(e)} = \pi \int_{-1/2}^{1/2} \int_{\xi_i}^{\xi_{i+1}} \{\varepsilon^L\}^T [Q] \{\varepsilon^L\} h r^2 \xi d\xi d\zeta, \quad (15a)$$

$$V_{NL}^{(e)} = \pi \int_{-1/2}^{1/2} \int_{\xi_i}^{\xi_{i+1}} \left[ \{\varepsilon^{NL}\}^T [Q]^k \{\varepsilon^L\} + \{\varepsilon^L\}^T [Q]^k \{\varepsilon^{NL}\} \right. \\ \left. + \{\varepsilon_{NL}\}^T [Q]^k \{\varepsilon_{NL}\} \right] h r^2 \xi d\xi d\zeta. \quad (15b)$$

Applying Hamilton's principle and carrying out the first variation of the energy functional:

$$\delta \int_{t_1}^{t_2} (T^{(e)} + V^{(e)}) dt = 0, \quad (16)$$

one obtains the basic equation of motion in the finite element from:

$$([K]^{(e)} - \omega^2 [M]^{(e)}) \{\Delta\}^{(e)} = 0, \quad (17)$$

where the element stiffness matrix  $[K]^{(e)}$  and element mass matrix  $[M]^{(e)}$  are:

$$[K]^{(e)} = [K]^{(e)}_L + [K]^{(e)}_{NL} \\ = \begin{bmatrix} [K^{11}]_L & [K^{12}]_L & [K^{13}]_L \\ [K^{12}]^T_L & [K^{22}]_L & [K^{23}]_L \\ [K^{13}]^T_L & [K^{23}]^T_L & [K^{33}]_L \end{bmatrix}^{(e)} + \begin{bmatrix} 0 & 0 & [K^{13}]_{NL} \\ 0 & 0 & 0 \\ [K^{13}]^T_{NL} & 0 & [K^{33}]_{NL} \end{bmatrix}^{(e)}, \quad (18)$$

$$[M]^{(e)} = \begin{bmatrix} [M^{11}] & [M^{12}] & [M^{13}] \\ [M^{12}]^T & [M^{22}] & [M^{23}] \\ [M^{13}]^T & [M^{23}]^T & [M^{33}] \end{bmatrix}^{(e)}. \quad (19)$$

The details of stiffness coefficients  $[K^{\hat{ij}}]$  and mass coefficients  $[M^{\hat{ij}}]$  are listed in the Ref [2].

The global form of the equation of motion is:

$$([K] - \omega^2 [M]) \{\Delta\} = 0, \quad (20)$$

where  $[K]$  and  $[M]$  represent global stiffness matrix and mass matrix, respectively. The boundary conditions for Free-Clamp Case are:

$$\{U\} = [U_1, U_2, \dots, U_n, 0]^T, \quad (21a)$$

$$\{V\} = [V_1, V_2, \dots, V_n, 0]^T, \tag{21b}$$

$$\{W\} = [W_1, W_{1,\xi}, W_2, W_{2,\xi}, \dots, W_n, W_{n,\xi}, 0, 0]^T. \tag{21c}$$

With the boundary conditions, for linear vibrations, eqn (20) can be solved directly by numerical computation to obtain the frequencies  $\omega$  by using a standard algorithm. For nonlinear vibrations, the nonlinear part of element stiffness matrix  $[K]^{(e)}_{NL}$  contains the unknown function  $f$  in eqn (17), and an iterative procedure (Raju and Rao, 1982) [3] must be used to find their frequency responses. A computer code is written for the purpose of obtaining numerical results.

### NUMERICAL RESULT AND DISCUSSION

In the numerical calculations, the total thickness of the plate  $h$  is chosen as 6.35 mm, and the ratio of outer radius-thickness ( $r_0/h$ ) is taken as 10 and 25, as the thick and thin annular sandwich plates, (see Figure 1) respectively. Two interior hole sizes are used, i.e.  $R = r_0/r_0 = 0.1$  and 0.3. The material properties of HSG and PRD-49 III are listed below:

Material	density $\rho$ $\text{kg/m}^3 \times 10^3$	$E_{11}$ $\text{N/m}^2 \times 10^{10}$	$E_{22}$ $\text{N/m}^2 \times 10^{10}$	$E_{55}$ $\text{N/m}^2 \times 10^{10}$	$\nu_{12}$	$\nu_{21}$
High-strength graphite epoxy (HSG)	1.558	12.40	1.03	0.55	0.27	0.0224
PRD-490 III epoxy (PRD)	1.391	7.93	0.41	0.21	0.30	0.0155

With these material properties, the element matrices in equations (18) and (19) and the basic equation (20), the frequency responses are obtained and plotted in Figures.

Figures 2 and 3 show the linear frequency, affected by the variation of sandwiched thickness ratio of annular sandwich plates, comprised of PRD 49-III and HSG with  $r_0/h=25$  (thin plate) and 10 (thick plate), respectively. Both show that, for a given sandwiched thickness ratio value of  $2h_f/h$ , the linear frequency response of a HSG-PRD-HSG annular sandwich plate is higher than that of a PRD-HSG-PRD annular sandwich plate. The homogeneous HSG annular plate ( $2h_{f(\text{PRD})}/h=0$  or  $2h_{f(\text{HSG})}/h=1$ ) has a higher frequency response than the homogeneous PRD annular plate ( $2h_{f(\text{HSG})}/h=0$  or  $2h_{f(\text{PRD})}/h=1$ ). The frequency response of a annular sandwich plate comprised of PRD core with HSG facings is higher than that of a homogeneous PRD plate. On the contrary, the frequency response of an annular sandwich plate with HSG core and PRD facing is lower than that of a homogeneous HSG plate. Figure 2 shows the frequency of HSG-PRD-HSG annular sandwich plates increases with an increase of the sandwiched thickness ratio. The maximum frequency occurs approximately at  $2h_f/h=0.8$  for both hole sizes  $R=0.1$  and 0.3. The frequency decreases slightly when the ratio  $2h_f/h$  is greater than 0.8. The frequency at  $2h_f/h=0$  is the frequency of a homogeneous HSG plate. In Figure 3, the frequency of HSG-PRD-HSG annular sandwich plate increases monotonically with an increase of the sandwiched thickness ratio, and reaches the maximum

value, which is the frequency of the homogeneous plate made of HSG. In comparison of Figures 2 and 3, the characteristics of frequency curves with respect to sandwiched thickness ratio are similar with some variations. This phenomena is due to the effects of shear deformation and rotatory inertia which must be included in the thick plate theory.

Figure 4 shows the frequency ratio  $\omega_{NL}/\omega_L$  versus the sandwiched thickness ratio  $2h_f/h$  at the finite amplitude of  $w_{max}/h=1.0$ . The PRD-HSG-PRD annular sandwich plate has higher frequency ratio than that of HSG-PRD-HSG annular sandwich plate for  $0 < 2h_f/h < 0.7$ . The maximum frequency ratio  $\omega_{NL}/\omega_L$  occurs approximately at  $2h_f/h=0.4$  for the annular sandwich plate comprised of HSG core with PRD facings. At the highest frequency ratio, the frequencies of nonlinear vibrations are 5.2% and 1.81% higher than those of linear vibrations, respectively.

### REFERENCES

1. Reddy, J.N., "A Refined Nonlinear Theory of Plate with Transverse Shear Deformation", *J. Non-Linear Mech.*, Vol.20 (9/11), 1984, pp.881-896.
2. Huang, C.L.D. and Lu, H.Y., "Nonlinear Vibrations of Orthotropic Thick Annular Plates Using Higher Order Shear Deformation Theory", *Composites Engineering*, Vol. 1, No. 10, pp. 985-994.
3. Raju, K.K. and Rao, G.V., "Large Amplitude Asymmetric Vibration of Some Thin Shells Revolution." *Journal of Sound and Vibration*. Vol.44, 1982, pp.327-333

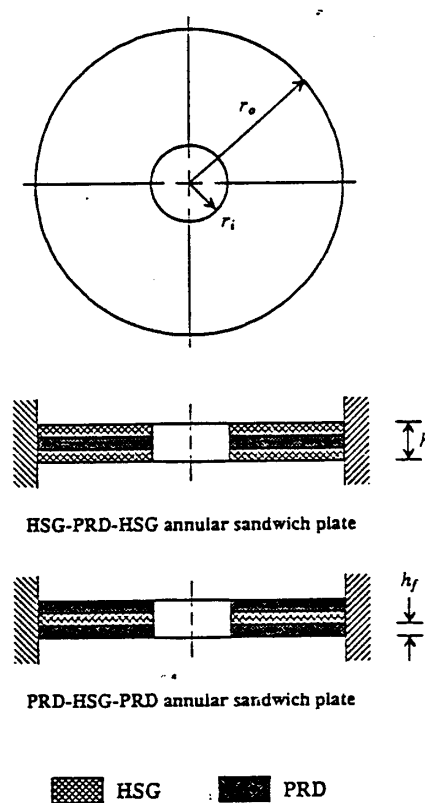


Figure 1



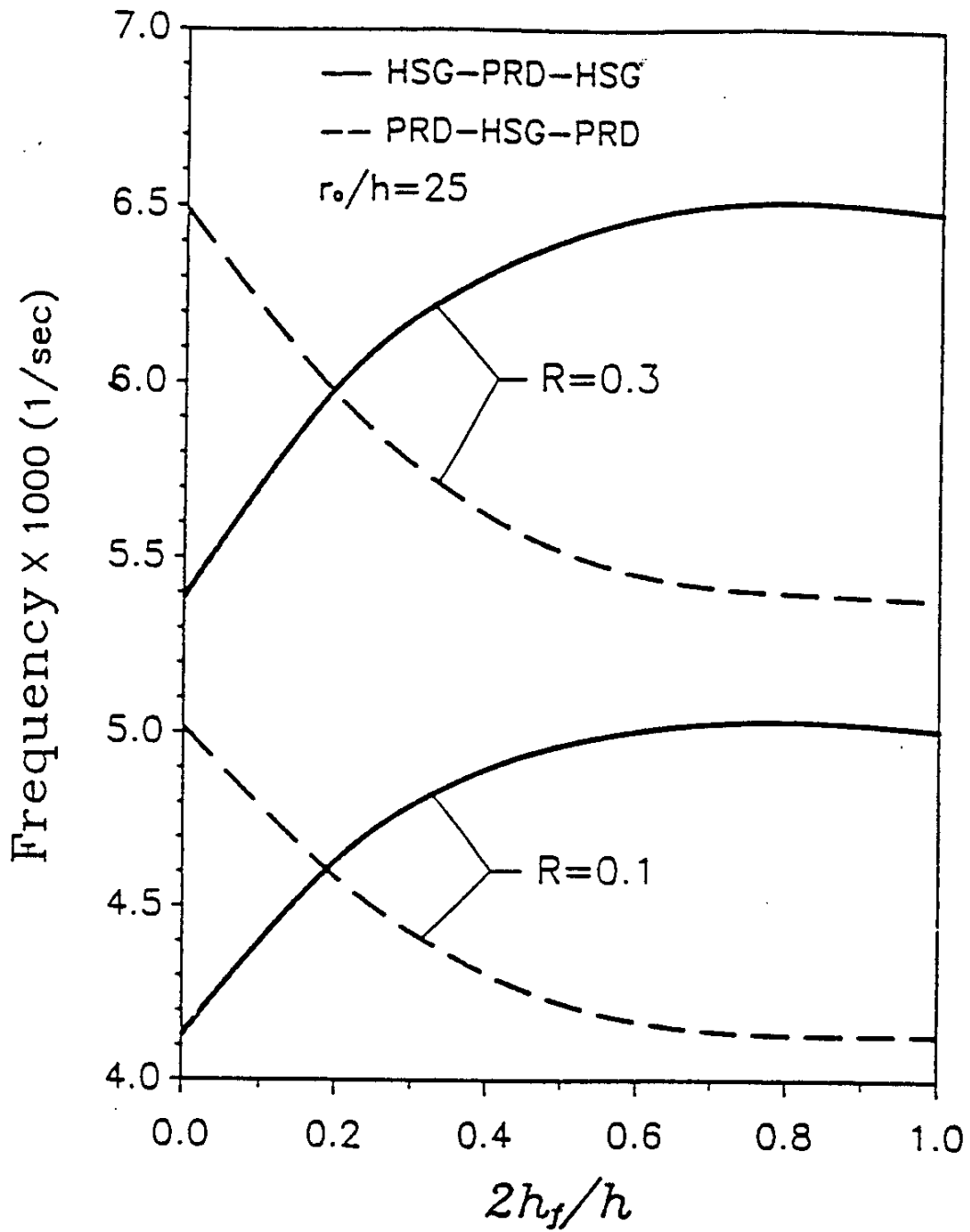


Figure 2: Linear Frequency Responses for Various Thickness Ratios of Thin Plates

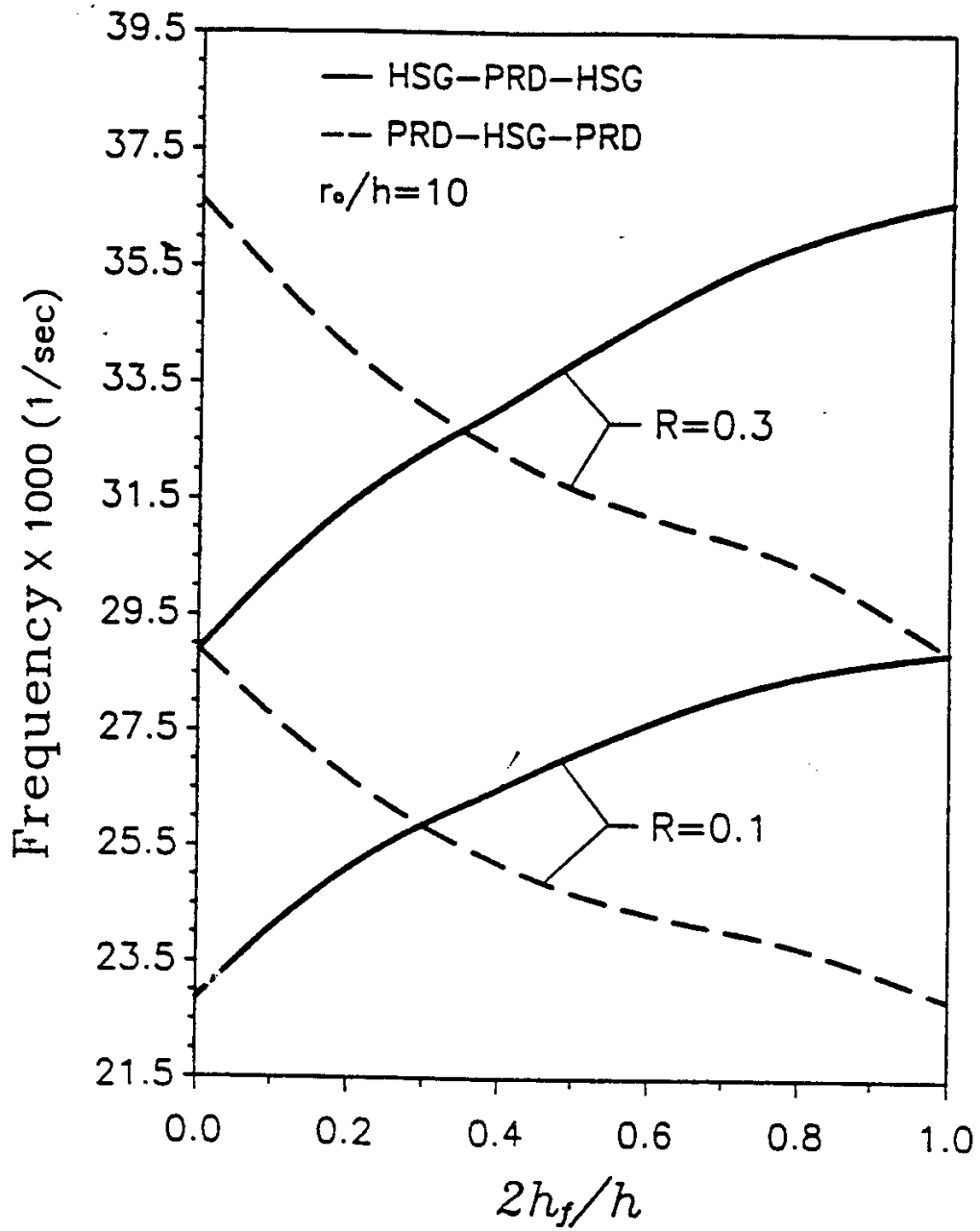


Figure 3. Linear Frequency Response for Various Sandwiched Thickness Ratio of Thick Plates

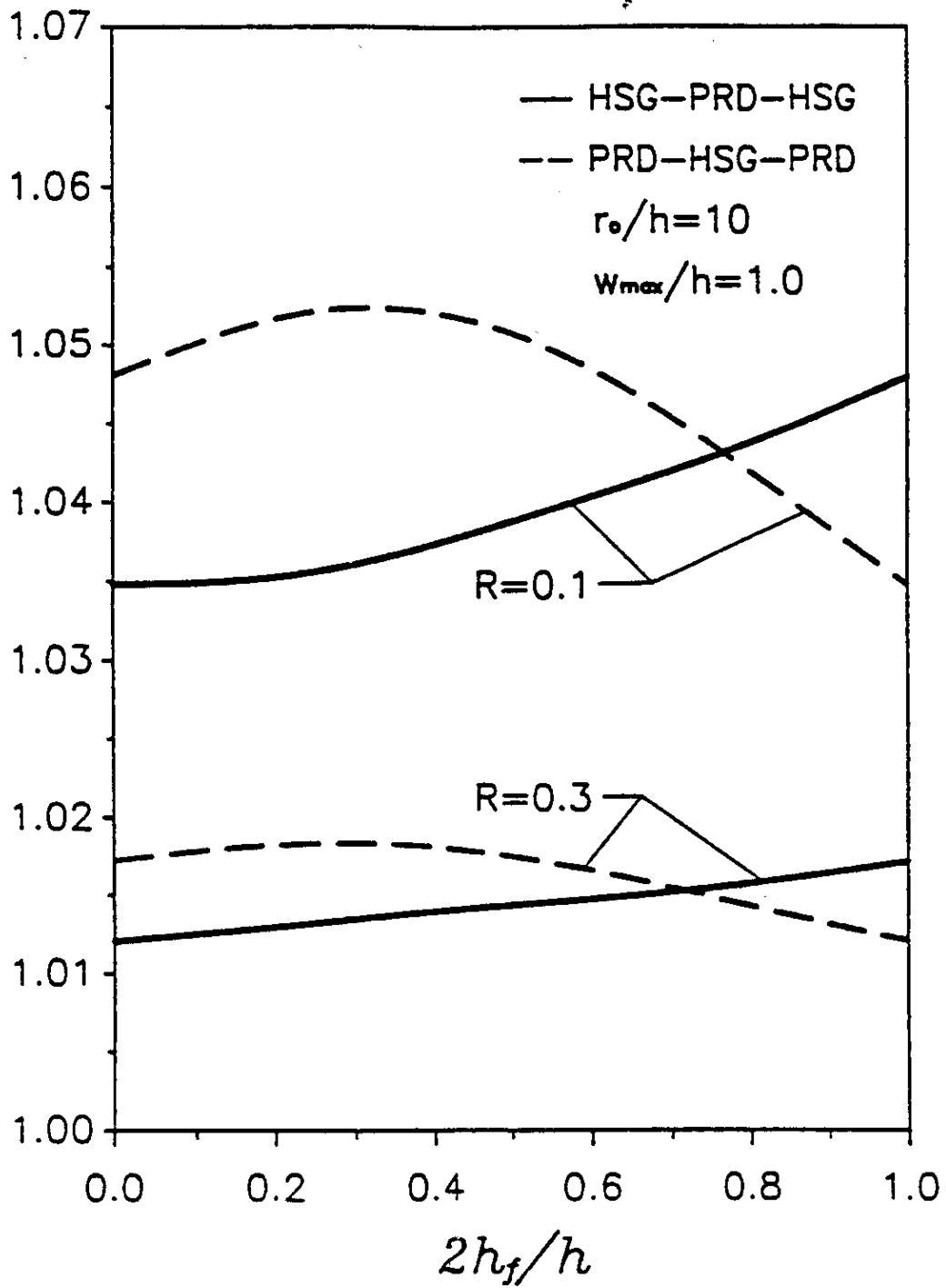


Figure 4. Nonlinear Frequency Response for Various Thickness Ratio of Thin Plates

# THE DYNAMIC RESPONSE OF A PULTRUDED FIBERGLASS TUBE SUBJECTED TO LATERAL LOADING

Louis J. Brunet and James A. Nemes

*Mechanical Engineering Department,  
McGill University 817, rue Sherbrooke ouest, Montréal QC Canada, H3A 2K6*

**SUMMARY:** This paper is an investigation of the large deflection response of a double fixed-end pultruded fiberglass tube subjected to lateral loading, in both quasi-static and dynamic conditions. A test fixture has been designed to achieve the desired end-conditions. The experiments yield a two mode response of the tubing to loading, with the first mode, referred to as the local mode, dominated by crushing of the cross-section, and the second mode, referred to as the global mode, consisting of beam flexure and shear. An analytical model has been developed to predict the response of the tubing under quasi-static loading conditions. The same two modes are generated. Model results are promising and computation time is minimal. Dynamic tests demonstrate a significant rate dependency of the system. The rate dependency is more pronounced in the globally dominated portion of the behavior. A finite element model incorporating a rate dependent continuum damage model has demonstrated rate dependence of the tubing's response, as well as the two mode behavior of the system, but the global mode of the response of the tubing is underestimated. The deformed geometry of the finite element model is in good agreement with experiment.

**KEYWORDS:** pultruded tubing, impact, quasi-static modeling, lateral loading, large deflection

## INTRODUCTION

The dynamic behavior of composite materials has been investigated by numerous authors, with much of that research focused on basic dynamic properties of composites. Other authors [1] have investigated the interaction between materials and structure, in the hope of developing lightweight energy absorbing structures. The behavior of pultruded sections, particularly I-beams subjected to quasi-static loading, has also been investigated [2]. Some dynamic testing of composite tubing has been done, but this work has been concerned primarily with the onset of damage [3], rather than with large deflection to failure. Those who have investigated the large scale deflection of tubing due to transverse loading have been focused mainly on the behavior of traditional materials subjected to such loading [4,5]. In this paper, the large deflection behavior of a pultruded fiberglass tube subject to quasi-static and dynamic loading will be investigated.

## EXPERIMENTAL CONFIGURATION

The experiment consists of a double fixed-end pultruded fiberglass tube subjected to a centrally applied lateral load (Fig. 1). The tube has a total span of  $L$ , varying from 203.2 mm to 508.0 mm, inside diameter,  $R_i$ , of 9.53 mm, and an outside diameter,  $R_o$ , of 12.7 mm; thus, an average radius,  $R$ , of 11.1 mm, and a wall thickness,  $t$ , of 3.175 mm. The material

properties are directional with moduli in the longitudinal and circumferential direction,  $E_x$  and  $E_y$ , of 17.2 GPa and 5.5 GPa respectively. The shear modulus,  $G$ , is 2.9 GPa.

The material used, commercially available from MMFG, is an isophthalic polyester / glass fiber composite. Specifically, the Extren Series 500 was used in the tests. Loads were applied quasi-statically and dynamically using a standard hydraulic test machine and a drop weight impact tower. The drop weight impact tower is a model designed and built at McGill University. The tower houses a piezoelectric load sensor that generates an impact load history recorded on a Nicolet Pro40 digital oscilloscope. Experiments are performed with an impactor mass much greater than that of the tube, such that the impact response can be approximated by a single degree-of-freedom system.

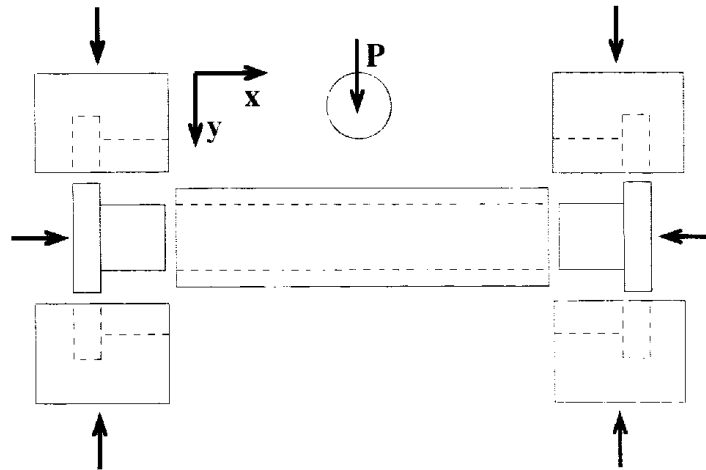


Fig. 1: Fixture assembly.

The double fixed-end condition is achieved using a newly designed fixture (Fig. 1). The fixture consists of sockets inserted in the tubing to prevent crush damage from extending to the ends of the tubing. The socketed tube ends are then clamped to prevent end rotation of the tubing.

The tube is impinged upon by a cylindrical steel impactor of the same radius as that of the tube,  $R$ , machined to be fitted to a tup. The length of the impactor is chosen to exceed  $\pi R$ , such that tube puncture does not occur, which is a failure mechanism not considered in the analysis developed in the following section.

Dynamic tests are performed on samples of length  $L = 203.2$  mm. The drop weight impact tower's carriage was loaded to 15.1 kg, and was dropped from a height of 1.13 m. Using the calibration of the drop tower this will yield an impact velocity of 4.46 m/s; thus, an input energy of approximately 150 joules. Since the impact mass is much greater than that of the tube, the test can be considered to have a single degree-of-freedom allowing the load history, obtained from the load cell, to be twice integrated with respect to time to obtain a displacement history, and subsequently a load displacement curve.

### ANALYTICAL MODEL

The model accounts for three types of deformation. The first of these is the local deformation, which is the deformation of the tube's cross-section below and adjacent to the contact area with the tup (Fig. 2.) The second and third types of deformation are the beam flexural deformation and the beam shear deformation, which are considered global modes of deformation.

The local deformation is used to compute the load, and the global deflection of the beam in response to this load is determined. Once local deformation has been exhausted, the stiffness for both global components are maintained and further load may be applied with its accompanying deflection.

Material properties are considered constant in this model, with change of sectional properties alone being responsible for the decrease in stiffness of the tubing.

The model is limited by a minimum beam length, such that the damage zone must not extend to the fixture sockets.

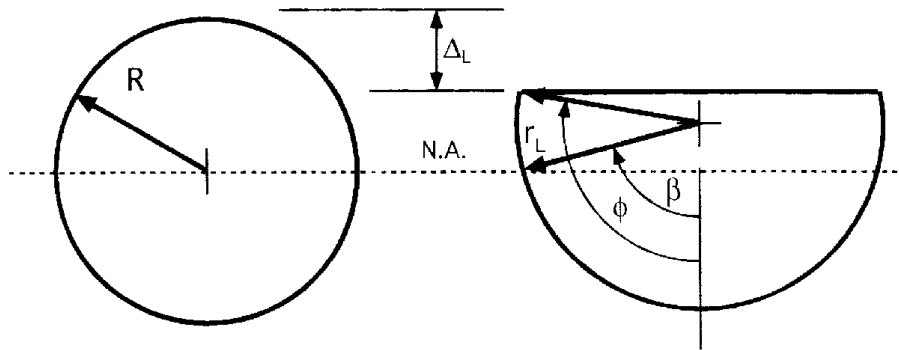


Fig. 2: Deformed cross-section of the tube.

**Local Deformation**

The cross-section of the tubing is assumed to deform under the impactor as shown in Fig. 2. This deformation is further assumed to be inextensional, such that the circumferential length of the tubing is maintained. These assumptions permit the deformed geometry of the tubing to be determined from the local deformation,  $\Delta_L$ .

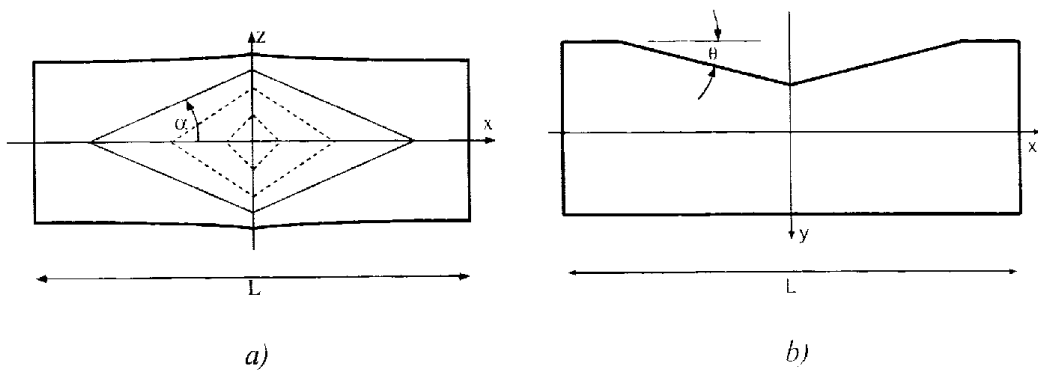


Fig. 3: Local damage zone, a) evolution of damage zone as seen from above, and b) seen from the side.

The circumference of the deformed section and the original section must remain the same; thus;

$$2\pi R = 2r_L(\phi + \sin \phi) \tag{1}$$

where  $r_L$  is the radius of the deformed cross-section, and  $\phi$  is the arc angle of the circular segment of the deformed section. With  $\beta$  defined as the angle to the neutral axis, the following must also hold.

$$\pi R = 2r_L \beta \quad (2)$$

From Eqns 1 and 2, it follows that,

$$\beta = \frac{(\phi + \sin \phi)}{2}. \quad (3)$$

The deflection of the cross-section may be defined based on the previous angular relationships. Based on the projection of the radius, the deflection can be determined:

$$\Delta_L = R + r_L \cos \phi - r_L \cos \beta. \quad (4)$$

Substituting Eqn 2 into Eqn 4, the local deflection becomes,

$$\Delta_L = R \left[ 1 + \frac{\pi}{2\beta} (\cos \phi - \cos \beta) \right]. \quad (5)$$

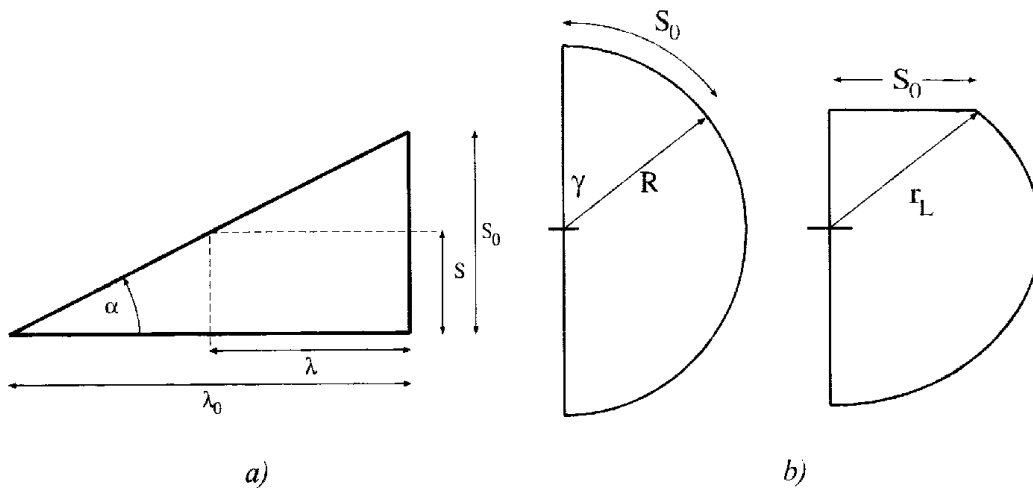


Fig. 4: a) quadrant of damage zone, and b) damage zone arc angle

The damage zone has been assumed to be diamond-shaped (see Fig. 3a). It is characterized by an angle  $\alpha$  determined from the damage width and length,  $S_0$  and  $\lambda_0$  (see Fig. 4a).

$$\tan \alpha = \frac{S_0}{\lambda_0}. \quad (6)$$

The angle  $\alpha$  is known to vary with the size of the damage zone [4] and the adopted relationship is:

$$\alpha = \alpha_i \left[ 1 - \frac{C_1 S_0}{C_2 S_{\max}} \right] \quad (7)$$

Where  $C_1$ ,  $C_2$  and  $\alpha_i$  would need to be experimentally determined. These terms are certainly dependent on the material properties and on the tube diameter to thickness ratio. The relationship used for the purposes of this tubing is:

$$\alpha = \frac{\pi}{10} \left[ 1 - \frac{6S_0}{11S_{\max}} \right]. \quad (8)$$

$S_0$  was defined previously, and  $S_{\max}$  is the maximum damage width, or  $\pi R/2$ .  $S_0$  may also be defined as the horizontal projection of the deformed radius of the tubing (see Fig. 2, and Eqns 2 and 3).

$$S_0 = r_L \sin \phi \quad (9)$$

The damage zone would be expected to be curvilinear as seen from the side, though as a simplification, the surface is assumed to vary linearly (see Fig. 3b.) The off-axis length and deflection of the damage zone,  $\lambda$  and  $\Delta$ , are defined based on an off-axis position in the damage zone,  $S$ , and the associated arc angle  $\gamma$  (see Fig. 4).  $S$  is a segment of  $S_0$ , and the angle  $\gamma$  is defined as the arc angle from the vertical to  $S$  in the undeformed configuration. Fig. 4 shows the arc angle for  $S = S_0$ . This leads to,

$$\gamma = \frac{S}{R} \quad (10)$$

$$\lambda = \frac{(S_0 - S)}{\tan \alpha} \quad (11)$$

$$\Delta = \Delta_L + R(\cos \gamma - 1), \quad (12)$$

with the center line chosen as the origin. The deflection angle,  $\theta$ , may be determined for a given position based on the above quantities.

$$\theta = \arccos \frac{\lambda}{[\lambda^2 + \Delta^2]^{\frac{1}{2}}}. \quad (13)$$

### Load

The load resulting from the above deformation is based on the strain of the material in the damage zone of the tubing, initially along the axial direction of the tube. The strain in a given linear element is expressed as,

$$\varepsilon = \frac{[\lambda^2 + \Delta^2]^{\frac{1}{2}} - \lambda}{\lambda}. \quad (14)$$

The resultant vertical force, exploiting symmetry, is,

$$F = 4E_x t \int_0^{S_0} \varepsilon(S) \sin \theta(S) dS. \quad (15)$$

### Global Deflection

Flexural deflection of the tube is determined by solving the beam flexure equation considering the variable moment of inertia and redistribution of moment as the cross-section is changed due to the local deformation. The experimental observations indicate that a true fixed end condition is not maintained during the later stages of the experiment. As a result, both fixed and simply supported end conditions are considered as lower and upper bounds for the



flexural displacement. Results presented, here, are obtained simply as the numerical average of the results for the two end conditions. Shear displacement for the beam is calculated using the constant cross-sectional area, with a uniform shape factor for simplicity.

## EXPERIMENTAL AND ANALYTICAL RESULTS

### Quasi-Static Test Results

Quasi-static tests were performed for four beam lengths; 203.2 mm (8 in), 304.8 mm (12 in), 406.4 mm (16 in) and 508.0 mm (20 in). The length of the beam has a significant effect on the load displacement curve of the beam due to the flexural displacement component (see Fig. 5a). A locally dominated initial mode of displacement is observed in all specimens, followed by a global mode dominated by beam flexure. With the more pronounced beam deformation comes a decrease in the load for the longer tube lengths, as expected.

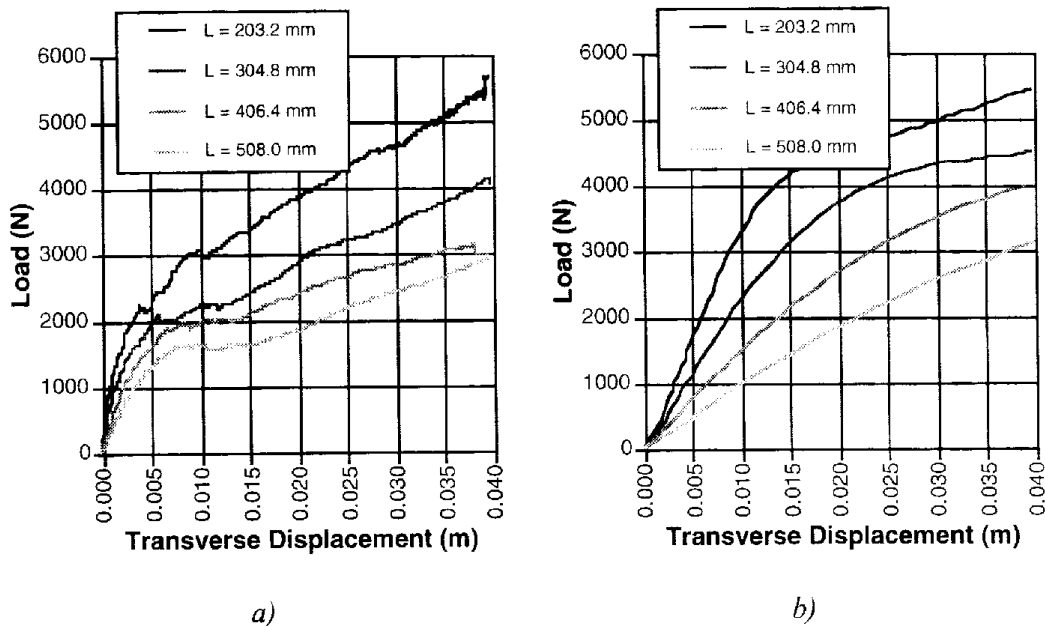


Fig. 5: a) Quasi-static test results, and b) model results

### Model Results

The above analytical model was solved using MatLab as the programming environment, and the chosen incremented quantity was the local displacement. The load is calculated followed by the flexural and shear deflections. The code was run on a desktop computer, and the required computation time was less than five minutes to generate on the order of 50 data points. The results of the model are compared to the experimental quasi-static tests in Fig. 6. As is the case with the experiments, the model yields data that corresponds to a two mode system. The first mode is locally dominated, and the second mode is globally dominated. The model results compare well to the experimental results. The model has some difficulty in generating abrupt transitions in the tubing response. The result is a somewhat softened response in the locally dominated mode of deformation as the tube length is increased.

### Dynamic Test Results

Fig. 7 shows a comparison of the quasi-static and impact experimental results for a beam of 203.2 mm (8 in) in length. The two mode deformation persists in the dynamic test results. The initial portion, corresponding to the locally dominated behavior, of the two experiments is

essentially indistinguishable, while the second portion of the curve, corresponding to the globally dominated behavior, displays a significant load increase. Conclusions regarding the cause of this load increase are not drawn here. Further investigation may reveal that the cause is related to material properties or it may be related to structure. The consequences of this increased load will manifest themselves in the high-rate energy-absorption of the system.

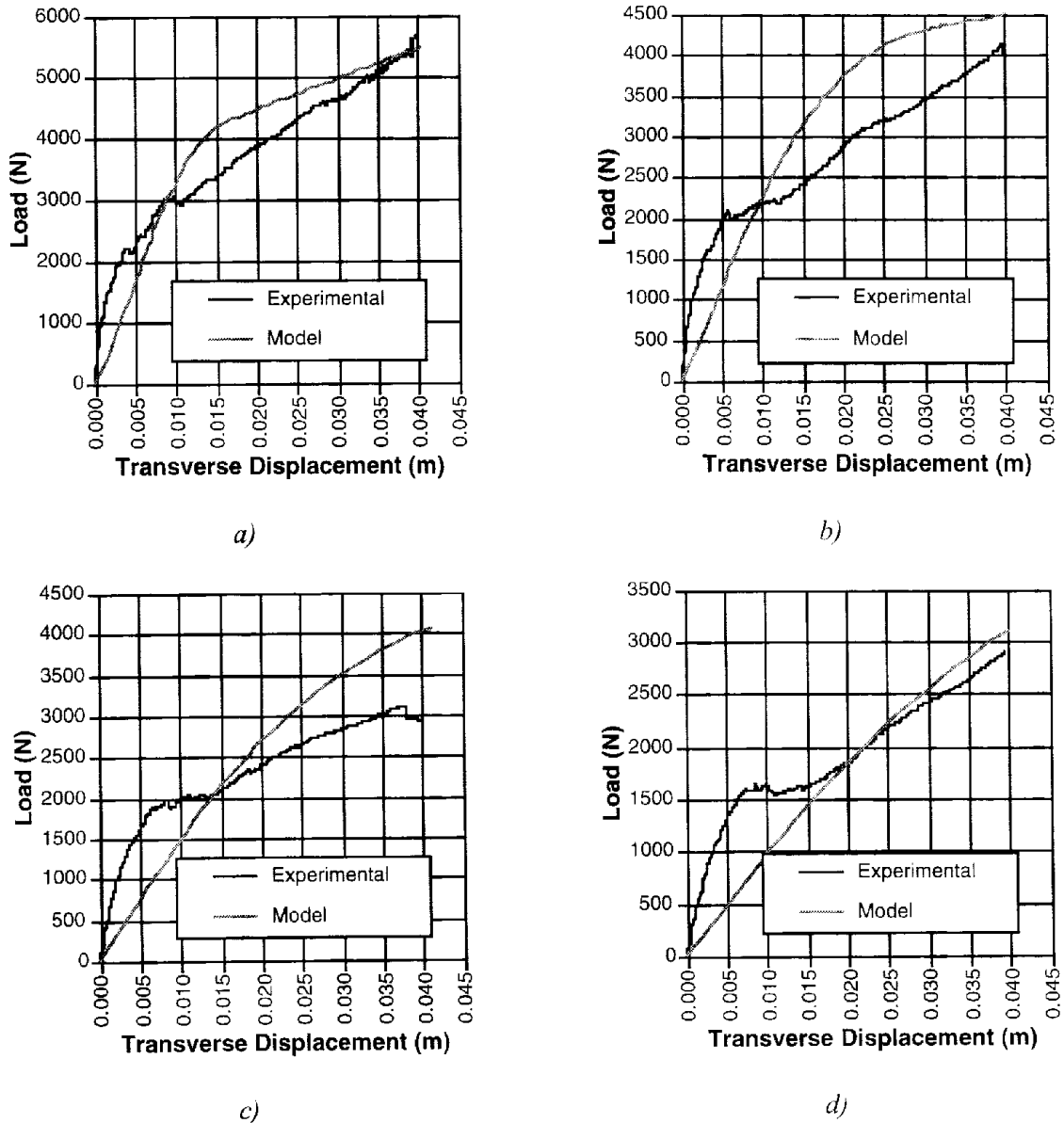


Fig. 6: Experimental and model results for:  
 a)  $L = 203.2$  mm, b)  $L = 304.8$  mm, c)  $L = 406.4$  mm, and d)  $L = 508.0$  mm.

### FINITE-ELEMENT ANALYSIS

The quasi-static and impact experiments on the 203.2 mm (8 in) long tube were also simulated by finite element analysis, using a continuum damage model, implemented in the code ABAQUS/Explicit. The model used is similar to that given by Nemes and Bodelle [6], which describes rate-dependent response through the damage evolution equations. Based on the experimental observations, the damage parameter,  $V$ , represents matrix cracking along the

direction of the fibers and is taken to vary between 0 and 1. The three dimensional stress-strain relations are written in terms of local material axes  $r$ ,  $\theta$  and  $z$  as:

$$\begin{pmatrix} \sigma_{rr} \\ \sigma_{\theta\theta} \\ \sigma_{zz} \\ \sigma_{r\theta} \\ \sigma_{rz} \\ \sigma_{\theta z} \end{pmatrix} = \begin{bmatrix} C_{11} & C_{12} & C_{13} & 0 & 0 & 0 \\ C_{21} & C_{22} & C_{23} & 0 & 0 & 0 \\ C_{31} & C_{32} & C_{33} & 0 & 0 & 0 \\ 0 & 0 & 0 & C_{44} & 0 & 0 \\ 0 & 0 & 0 & 0 & C_{55} & 0 \\ 0 & 0 & 0 & 0 & 0 & C_{66} \end{bmatrix} \begin{pmatrix} e_{rr} \\ e_{\theta\theta} \\ e_{zz} \\ e_{r\theta} \\ e_{rz} \\ e_{\theta z} \end{pmatrix} \quad (16)$$

where  $\sigma_{ij}$  are the components of Cauchy stress,  $e_{ij}$  are the finite strain components, obtained from time integration of the rate of deformation tensor components, and  $C_{ij}$  are the components of the symmetric elasticity tensor, which are taken to be a function of damage. Taking the material to be transversely isotropic, these components are assumed to be degraded in the following manner:

$$\begin{aligned} C_{11} &= C_{22} = (1 - \sqrt{V})C_{11}^0 \\ C_{33} &= (1 - \mu\sqrt{V})C_{33}^0 \\ C_{12} &= (1 - \sqrt{V})C_{12}^0 \\ C_{13} &= C_{23} = (1 - \sqrt{V})C_{13}^0 \\ C_{44} &= (1 - \sqrt{V})C_{44}^0 \\ C_{55} &= C_{66} = (1 - \sqrt{V})C_{55}^0 \end{aligned} \quad (17)$$

where the superscript '0' denotes virgin properties, and the parameter  $\mu$  is included in  $C_{33}$  to allow stiffness in the fiber direction to be retained even with  $V$  going to 1.

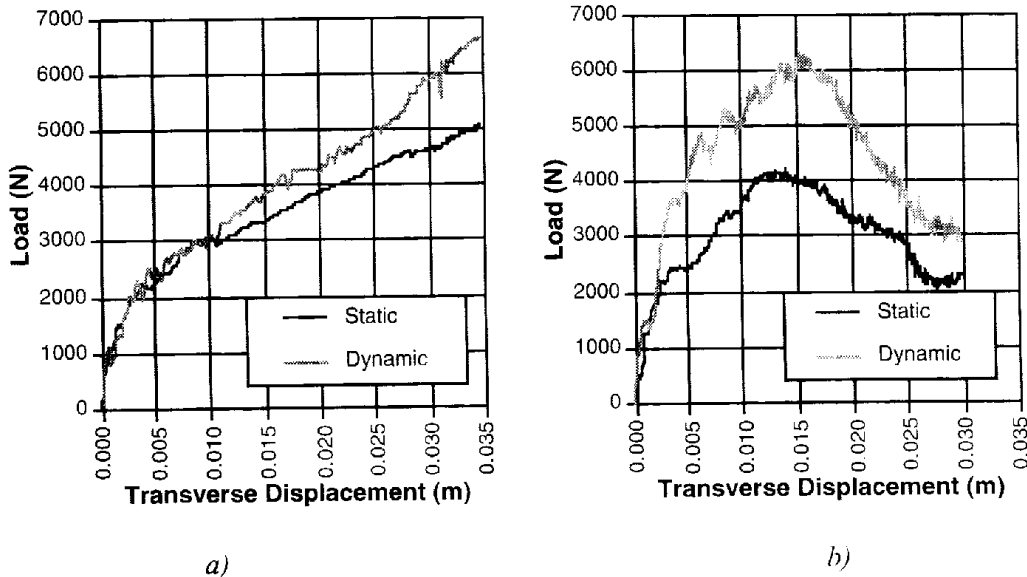


Fig. 7: Quasi-static vs. dynamic a) test results, and b) finite element model results.

Damage evolution is taken to be dependent on the  $\sigma_{\theta\theta}$  component according to the following:

$$\dot{V} = 0, \quad |\sigma_{\theta\theta}| < \sigma_G \quad (18)$$

$$\dot{V} = \frac{1}{\eta} \left( \frac{|\sigma_{\theta\theta}| - \sigma_G}{\sigma_{G_0}} \right)^n, \quad |\sigma_{\theta\theta}| \geq \sigma_G \quad (19)$$

$$\text{with} \quad \sigma_G = (1 - V^2)\sigma_{G_0} \quad (20)$$

where  $\sigma_{G_0}$  is the initial damage threshold stress and  $\eta$  and  $n$  are material parameters related to the rate-dependence of damage evolution.

The tube is modeled using 3-D solid elements with three elements through the thickness and a total of 3122 elements for one quarter of the tube. For the quasi-static case, the evolution of the damage parameter and deformed shape are shown in Fig. 8, and compared to photographs from the experiment at three instants during the experiment. The predicted deformed geometry and extent of damage agree quite well with the experiment. Computed load vs. displacement results for quasi-static and impact rates are shown in Fig. 7b. As can be seen in the figure the model has the capability of predicting the rate-dependent response. However, when comparing these results to those obtained experimentally in Fig. 7a, it can be seen that both the magnitude of load for the local mode as well as the degree of rate-dependence are both over-predicted by the model. In addition the model predicts softening behavior, which is not observed in the experiments. Nevertheless, based on the limited material data for determining the parameters appearing in the continuum damage model the results appear promising, although it should be noted that the finite element analysis required on the order of 10 CPU hours on an HP 720 computer.

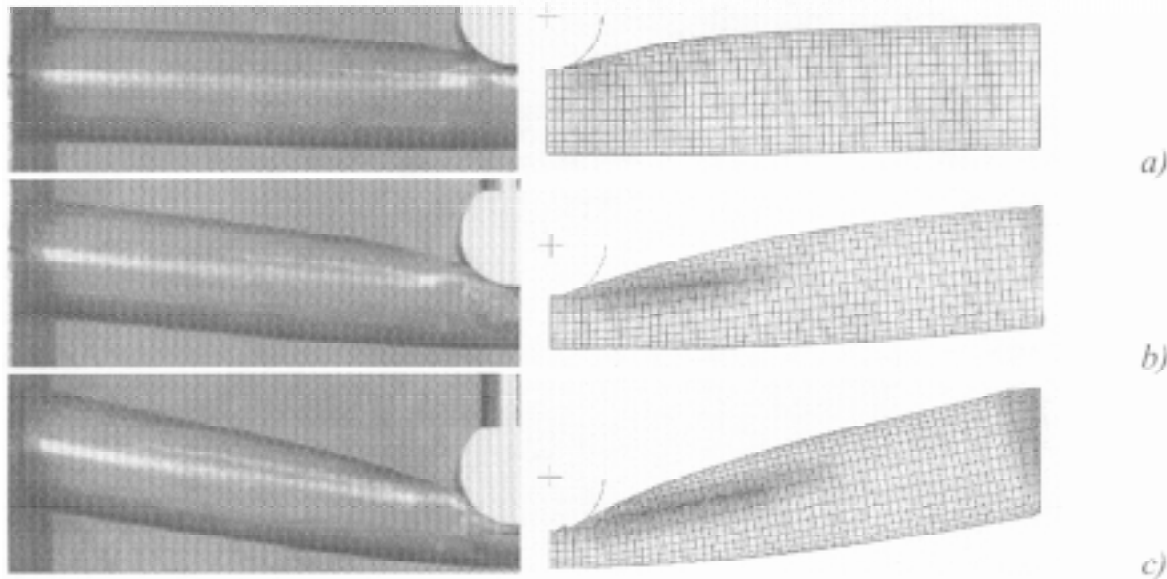


Fig. 8: Experimental photographs and finite element contours showing damage in dark gray at a) 10 mm, b) 20 mm and c) 30 mm total transverse displacement.

## CONCLUSION

A test method and fixture has been developed to determine the impact and quasi-static response of a simple composite structure. To accompany this test method, finite element and analytical models have been developed that predict the load displacement curve for a given structure.

The fixturing used has been quite successful; however, the end conditions stipulated have not been maintained as strictly as desired or required during the later stages of deformation. This required some approximation in the analytical model.

The model offers significant time savings in computation and less computing power than the finite element analysis model. The model could be improved by determining more precisely the parameters controlling the deformation zone angle,  $\alpha$ , and the end moment sustained by the beam. More significantly, however, constitutive models accounting for damage could be incorporated to predict the cracking of the tubing that is observed.

The dynamic response of the tubing displays rate sensitivity in the global regime. It may also be possible to adapt the model to be rate-dependent, as the rate-dependent regime has been identified.

The material studied benefits from relatively low linear density and low cost. This will render it an attractive option to many, and this model may assist in design of structures making use of them. This is of relevance in a market where synthetic materials are replacing traditional structural materials. Transport industries will also find this of particular interest as crashworthiness has become one of their primary concerns.

### ACKNOWLEDGMENTS

The authors wish to thank Morrison Molded Fiber Glass Inc. for providing the material used in the experiments, and for the partial financial support of the Natural Sciences and Engineering Research Council (NSERC) of Canada.

### REFERENCES

1. Mammalis, A.G., Manolakos, D.E., Demosthenous, G.A. and Ioannidis, M.B., "Analysis of Failure Mechanisms Observed in Axial Collapse of Thin-Walled Fibreglass Structures", *Thin-Walled Structures*, Vol. 24, 1996, pp. 335-352.
2. Bank, L.C., Gentry, T.R. and Nadipelli, M., "Local Buckling of Pultruded FRP Beams - Analysis and Design", *Journal of Reinforced Plastics and Composites*, Vol. 15, 1996, pp. 283-294.
3. Pang, S.S. and Kailasam, A.A., "A Study of Impact Response of Composite Pipe", *Transactions of the ASME*, Vol. 113, 1991, pp. 182-188.
4. Jones, N. and Shen, W.Q., "A Theoretical Study of the Lateral Impact of Fully Clamped Pipelines", *Proceedings of the Institution of Mechanical Engineers, Part E: Journal of Process Mechanical Engineering*, Vol. 206, 1992, pp. 129-146.
5. Wang, X.D., Yu, T.X. and Meguid, S.A., "On the Dynamic Analysis of an Ideally-Plastic Softening Beam", *International Journal of Impact Engineering*, Vol. 15, 1994, pp. 297-309.
6. Nemes, J.A. and Bodelle, G., "Simulation of Vehicle Impact on Steel and Composite Highway Guardrail Structures", *Symposium on Crashworthiness and Occupant Protection in Transportation Systems*, San Francisco CA, Nov. 12-17, 1995, Eds. J.C. Reid, et. al., pp. 179-190.

# VIBRATION ANALYSIS FOR COMPOSITE CYLINDRICAL SHELLS WITH A RECTANGULAR CUTOUT

Young-Shin Lee and Young-Wann Kim

*Department of Mechanical Design Engineering,  
Chungnam National University, 200 Kung-dong, Yousung-ku, Tae-jon, 305-764, Korea*

**SUMMARY** : The free vibration of the stiffened composite cylindrical shells with a rectangular cutout is investigated using analytic method and experiment. The stiffened composite cylindrical shells are stiffened with uniform interval. The Love's shell theory is used to derive the governing equation of the shell and the discrete stiffener theory is used to consider the ring stiffening effect. Two sets of boundary condition, clamped-clamped and clamped-free, are considered. The cylindrical shells are laminated with plain weave glass/epoxy or CFRP composite, and the stiffeners are unidirectionlly laminated.

**KEYWORDS**: rectangular cutout, ring stiffened composite cylindrical shell, discrete stiffener theory, plain weave

## INTRODUCTION

The cylindrical shells are used in many industrial applications, such as aircraft, space, submarines, missiles, and nuclear reactors. The information of the dynamic behavior of these structures subjected to external dynamic loads that might cause the undesirable vibrations, fracture, and buckling is essential to design engineer to ensure safety, operational requirement in the analysis. There are some limitations, such as size, weight, stiffness, etc., to supply these structures into field application. Many researchers should reinforce these structures to obtain the higher stiffness in given size. In recent year, as the composite materials have advantages of high strength-to-weight ratio and high stiffness-to-weight ratio, the composite materials have been used in many engineering fields to obtain higher stiffness, less weight. Using these advanced composite materials one can make thin walled structure. If, however, these thin walled structures are undergone the dynamic load, the undesirable problem may be caused more easily. In real structures, openings, cutouts, and other discontinuities are necessary for such functional requirements as inspection, branch connections, visibility and weight reduction. These discontinuities cause structural weakness. The weakened structure is to fracture more easily than the unweakened by external dynamic loads. There are many researches for the stiffened structure. Most of previously published literature is concerned on the isotropic stiffened shell. In recently, there are some papers for the composite stiffened shell.

Reddy and Starnes[1] presented the analytic solution for buckling loads of composite cylindrical shells with axial and circumferential stiffeners, where stiffeners are isotropic. Schokker *et al.*[2] investigated the dynamic behavior for the ring stiffened composite

cylindrical shell. Starnes *et al.*[3] studied the postbuckling and fractural behavior for the stiffened composite plate and panel subject to compressive load by experiment. Lee and Kim[4] analyzed the free vibration for the stringer stiffened composite cylindrical shell using smeared stiffener theory. There are few researches for the cylindrical shell with a cutout, but some researches on the plate with cutout are published. Rajamani and Paramasivan[5] studied the effect of rectangular cutout in natural frequency for the rectangular plate using finite difference method. They[6] investigated the vibration characteristics for the anisotropic plate with a rectangular cutout. They considered the various boundary conditions and material properties. Reddy[7] researched large amplitude vibration of the plate with rectangular cutout using finite element method. Lee *et al.*[8] reported the vibration characteristics of the rectangular composite plate with a rectangular cutout using Rayleigh principle. For the cylindrical shell, Toda and Komatsu[9] analyzed the vibration with the circular cutout using experiment. Bicos and Springer[10] investigated the free vibration for the rectangular plate and cylindrical panel with a circular cutout using finite element method, and they[11] presented the more information for the vibration characteristics of the composite plate and panel with a circular cutout using finite element method.

All mentioned researches are mainly concerned with isotropic material structures. In this paper the frequency equation for the stiffened composite cylindrical shell with a rectangular cutout is obtained by applying the Rayleigh-Ritz procedure. The love's thin shell theory based on the discrete stiffener theory is used to derive the frequency equation. For the ring stiffened plain weave composite cylindrical shell, it is compared with experiment and analytic result to check the validity of analytic procedure.

### FORMULATION

Figure 1 shows the considered the stiffened composite cylindrical shell with a rectangular cutout, where  $R$ ,  $L$  and  $h$  are the radius, length and thickness of the shell. The arbitrary point in middle plane is taken by axial, circumferential and radial axis( $x, \phi, z$ ), and the origin of coordinate system is located on the edge of the shell. The height and width of the stiffeners are symbolized by  $d_{s(r)}$ ,  $b_{s(r)}$ . Subscripts  $s$  and  $r$  are indicated the axial(stringer), and circumferential(ring) stiffeners, respectively. The rectangular cutout with axial length  $a$  and circumferential cutout angle  $\phi_0$  is located on the center of the shell.

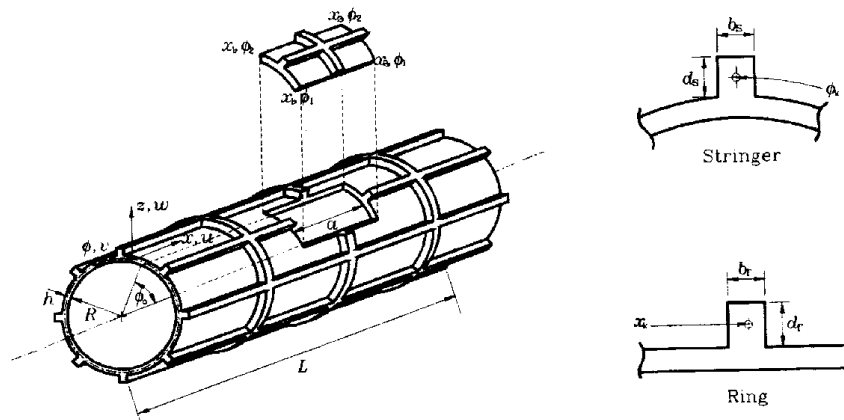


Fig. 1: Coordinate system for the orthogonally stiffened cylindrical shell with a rectangular cutout

For the symmetrically laminated composite shell the strain energy can be expressed by following equation in terms of stiffness coefficients,  $A_{ij}$  and  $D_{ij}$ .

$$U_c = \frac{1}{2} \int_0^L \int_0^{2\pi} \left( A_{11} \varepsilon_x^2 + 2A_{12} \varepsilon_x \varepsilon_\phi + A_{22} \varepsilon_\phi^2 + A_{66} \varepsilon_{x\phi}^2 + D_{11} \kappa_x^2 + 2D_{12} \kappa_x \kappa_\phi + D_{22} \kappa_\phi^2 + D_{66} \kappa_{x\phi}^2 \right) R dx d\phi \quad (1)$$

From Love's thin shell theory, the strain  $\varepsilon_i (i = x, \phi, x\phi)$  and curvature  $\kappa_i (i = x, \phi, x\phi)$  are follows:

$$\varepsilon_x = u_{,x} \quad \varepsilon_\phi = \frac{1}{R} (u_{,\phi} + w) \quad \varepsilon_{x\phi} = \frac{u_{,\phi}}{R} + v_{,x} \quad (2a)$$

$$\kappa_x = -w_{,xx} \quad \kappa_\phi = -\frac{1}{R^2} (w_{,\phi\phi} - v_{,\phi}) \quad \kappa_{x\phi} = -\frac{1}{R} (2w_{,x\phi} - v_{,x}) \quad (2b)$$

where  $(,)$  means the differentiation for the in given space. The symbols  $u, v, w$  are displacement fields for each direction. The deformation of a point at distance  $z$  from the shell middle plane for the stiffener is given by:

$$u_{s(r)} = u - zw_{,x} \quad v_{s(r)} = v - \frac{z}{R} w_{,\phi} \quad w_{s(r)} = w \quad (3)$$

The strain energy for the stiffeners can be written following forms from discrete stiffener's theory.

$$U_s = \sum_{k=1}^{N_s} \frac{E_{xs}}{2} \int_0^L \int_{A_s} \varepsilon_{xs}^2 dA_s dx + \sum_{k=1}^{N_s} \frac{(GJ)_s}{2} \int_0^L \left( \frac{w_{s,x\phi}}{R} \right)^2 dx \quad (4)$$

$$U_r = \sum_{k=1}^{N_r} \frac{E_{x\phi r}}{2} \int_0^{2\pi} \int_{A_r} \varepsilon_{\phi r}^2 R dA_r d\phi + \sum_{k=1}^{N_r} \frac{(GJ)_r}{2} \int_0^{2\pi} \frac{1}{R} w_{r,\phi} d\phi \quad (5)$$

$$\varepsilon_{xs} = u_{s,x} = u_{,x} - z w_{,xx} \quad (4a)$$

$$\varepsilon_{\phi r} = \frac{1}{R} (v_{r,\phi} + w_r) = \frac{1}{R} \left( v_{,\phi} - \frac{z}{R} w_{,\phi\phi} + w \right) \quad (5a)$$

where  $N_s$  and  $N_r$  are number of stiffeners, and  $\varepsilon_{xs}, \varepsilon_{\phi r}$  are longitudinal strain for the stringer and circumferential strain for the ring, and  $(GJ)_{s(r)}$  and  $A_{s(r)}$  are torsional stiffness and cross sectional area for the stiffener.

Assuming the behavior of cutout depends on the shell, the strain energy for the rectangular cutout part relates to the energy for the shell and stiffeners. Therefore the strain energy for the cutout can be expressed by following form:

$$U_o = \frac{1}{2} \int_{x_1}^{x_2} \int_{\phi_1}^{\phi_2} \left( A_{11} \varepsilon_x^2 + 2A_{12} \varepsilon_x \varepsilon_\phi + A_{22} \varepsilon_\phi^2 + A_{66} \varepsilon_{x\phi}^2 + D_{11} \kappa_x^2 + 2D_{12} \kappa_x \kappa_\phi + D_{22} \kappa_\phi^2 + D_{66} \kappa_{x\phi}^2 \right) R dx d\phi + \sum_{k=1}^{N_s} \delta_k \frac{E_{xs}}{2} \int_{x_1}^{x_2} \int_{A_s} \varepsilon_{xs}^2 dA_s dx + \sum_{k=1}^{N_s} \delta_k \frac{(GJ)_s}{2} \int_{x_1}^{x_2} \frac{1}{R^2} (w_{s,\phi})^2 dx \quad (6)$$



$$+ \sum_{k=1}^{N_r} \delta_k \frac{E_{sr}}{2} \int_{\phi_1}^{\phi_2} \int_{A_r} \varepsilon_{\phi}^2 R dA_r d\phi + \sum_{k=1}^{N_r} \delta_k \frac{(GJ)_r}{2} \int_{\phi_1}^{\phi_2} \frac{1}{R} (\dot{w}_{r,\phi})^2 d\phi$$

where

$\delta_k = 1$ , if the stiffener cross the cutout

$\delta_k = 0$ , otherwise.

The kinetic energy for the cylindrical shell is given by:

$$T_c = \frac{1}{2} \rho_t \int_0^{2\pi} \int_0^L [\dot{u}^2 + \dot{v}^2 + \dot{w}^2] R dx d\phi \quad \rho_t = \sum_{k=1}^N \rho_k h_k \quad (7)$$

where  $(\dot{\phantom{x}})$  is the differentiation to time.  $\rho_k$  and  $h_k$  are density and thickness to  $(k)$ -th layer.

The kinetic energy for the stringer and ring stiffener have similar expression to kinetic energy for the shell.

$$T_s = \frac{1}{2} \sum_{k=1}^s \rho_s \int_0^L \int_{A_s} [\dot{u}_s^2 + \dot{v}_s^2 + \dot{w}_s^2] dA_s dx \quad (8)$$

$$T_r = \frac{1}{2} \sum_{k=1}^r \rho_r \int_0^{2\pi} \int_{A_r} [\dot{u}_r^2 + \dot{v}_r^2 + \dot{w}_r^2] R dA_r d\phi \quad (9)$$

Where  $\rho_{s(r)}$  is the density of the stiffener.

The kinetic energy for the cutout is expressed following form as the behavior of cutout depends on that of the shell.

$$T_c = \frac{1}{2} \rho_t \int_{x_1}^{x_2} \int_{\phi_1}^{\phi_2} [\dot{u}^2 + \dot{v}^2 + \dot{w}^2] R dx d\phi + \frac{1}{2} \sum_{k=1}^s \delta_k \rho_s \int_{x_1}^{x_2} \int_{A_s} [\dot{u}_s^2 + \dot{v}_s^2 + \dot{w}_s^2] dA_s dx \\ + \frac{1}{2} \sum_{k=1}^r \delta_k \rho_r \int_{\phi_1}^{\phi_2} \int_{A_r} [\dot{u}_r^2 + \dot{v}_r^2 + \dot{w}_r^2] R dA_r d\phi \quad (10)$$

The beam modal function is used for the axial vibration mode satisfying the considered boundary conditions. The general expression can be written following form:

$$\psi(x) = \left( \cosh \frac{\lambda_m x}{L} - \cos \frac{\lambda_m x}{L} \right) - \sigma_m \left( \sinh \frac{\lambda_m x}{L} - \sin \frac{\lambda_m x}{L} \right) \quad (11)$$

where  $\sigma_m$  is the value determined from boundary condition, and  $\lambda_m$  is the number(not necessary integer) related to axial vibration mode. The considered boundary conditions in this study are that one edge is clamped, the other edge is clamped or free. The clamped condition prohibits transverse displacement and rotation. The free condition is free of bending moment and transverse shear force. For the mentioned boundary condition, the mathematical expressions in using beam function are given by:

- clamped (C)  $\psi = \psi' = 0$
- free (F)  $\psi'' = \psi''' = 0$

The characteristic equation and coefficient  $\sigma_m$  for the considered boundary conditions are

given in Table 1.

Table 1: Characteristic equations and  $\sigma_m$  for various boundary conditions

B.C.	Characteristic Equation	Formula for $\sigma_m$
C-C	$\cos \lambda_m \cosh \lambda_m - 1 = 0$	$\sigma_m = \frac{\cosh \lambda_m - \cos \lambda_m}{\sinh \lambda_m - \sin \lambda_m}$
C-F	$\cos \lambda_m \cosh \lambda_m + 1 = 0$	$\sigma_m = \frac{\cosh \lambda_m + \cos \lambda_m}{\sinh \lambda_m + \sin \lambda_m}$

The admissible displacement functions for freely vibrating cylindrical shell with different boundary conditions can be written by

$$\begin{aligned}
 u &= U_{mn} \varphi(x) \cos n \phi \cos \omega_{mn} t \\
 v &= V_{mn} \psi(x) \sin n \phi \cos \omega_{mn} t \\
 w &= W_{mn} \psi(x) \cos n \phi \cos \omega_{mn} t
 \end{aligned} \tag{12}$$

$$\varphi(x) = \frac{L}{\lambda_m} \psi'(x)$$

where  $U_{mn}$ ,  $V_{mn}$  and  $W_{mn}$  are the amplitudes for each direction,  $n$  is the circumferential wave number, and  $\omega_{mn}$  is the angular natural frequency for  $(m, n)$  vibration mode.

Substituting the admissible displacement functions into energy equation and integrating these result to domain, one can obtain the energy in term of amplitudes. The first the strain energy for the cylindrical shell is as follows:

$$\begin{aligned}
 U_c &= \left[ \alpha_{11}^c U_{mn}^2 + \alpha_{22}^c V_{mn}^2 + \alpha_{33}^c W_{mn}^2 \right. \\
 &\quad \left. + 2\alpha_{12}^c U_{mn} V_{mn} + 2\alpha_{13}^c U_{mn} W_{mn} + 2\alpha_{23}^c V_{mn} W_{mn} \right]
 \end{aligned} \tag{13}$$

where the coefficient  $\alpha_{ij}^c$  is the value in terms of stiffness coefficients  $A_{ij}$ ,  $D_{ij}$  and shell's geometric parameters. Also, the strain energy for the stringer and ring stiffener are as follows:

$$U_s = \alpha_{11}^s U_{mn}^2 + \alpha_{33}^s W_{mn}^2 + 2\alpha_{13}^s U_{mn} W_{mn} \tag{14}$$

$$U_r = \alpha_{22}^r V_{mn}^2 + \alpha_{33}^r W_{mn}^2 + 2\alpha_{23}^r V_{mn} W_{mn} \tag{15}$$

Using the same scheme, the strain energy for the cutout is given by:

$$\begin{aligned}
 U_o &= \left[ \alpha_{11}^o U_{mn}^2 + \alpha_{22}^o V_{mn}^2 + \alpha_{33}^o W_{mn}^2 \right. \\
 &\quad \left. + 2\alpha_{12}^o U_{mn} V_{mn} + 2\alpha_{13}^o U_{mn} W_{mn} + 2\alpha_{23}^o V_{mn} W_{mn} \right].
 \end{aligned} \tag{16}$$

Next, we must obtain the kinetic energy for each element. The kinetic energy for the composite cylindrical shell is obtained as follows:

$$T_c = \omega_{mn}^2 \left( \beta_{11}^c U_{mn}^2 + \beta_{22}^c V_{mn}^2 + \beta_{33}^c W_{mn}^2 \right) \tag{17}$$

The kinetic energies for the stringer and ring stiffeners are as follows:

$$T_s = \omega_{mn}^2 \left[ \beta_{11}^s U_{mn}^2 + \beta_{22}^s V_{mn}^2 + \beta_{33}^s W_{mn}^2 + 2\beta_{13}^s U_{mn} W_{mn} + 2\beta_{23}^s U_{mn} W_{mn} \right] \quad (18)$$

$$T_r = \omega_{mn}^2 \left[ \beta_{11}^r U_{mn}^2 + \beta_{22}^r V_{mn}^2 + \beta_{33}^r W_{mn}^2 + 2\beta_{13}^r U_{mn} W_{mn} + 2\beta_{23}^r U_{mn} W_{mn} \right] \quad (19)$$

The kinetic energy for the cutout is as follows:

$$T_o = \omega_{mn}^2 \left( \beta_{11}^o U_{mn}^2 + \beta_{22}^o V_{mn}^2 + \beta_{33}^o W_{mn}^2 + 2\beta_{13}^o U_{mn} W_{mn} + 2\beta_{23}^o V_{mn} W_{mn} \right) \quad (20)$$

The total energy for the stiffened composite cylindrical shell with a cutout can be obtained by adding the energy for the stiffener and eliminating the energy for the cutout.

The frequency matrix is taken easily by using the Rayleigh-Ritz procedure given in below.

$$\frac{\partial}{\partial X_i} (T_i - U_i) = 0, \quad X_i = U_{mn}, V_{mn}, W_{mn} \quad (21)$$

where  $T_i = T_c + T_s + T_r - T_o$ ,  $U_i = U_c + U_s + U_r - U_o$ .

Sequentially the frequency matrix for the stiffened composite cylindrical shell with a cutout is as follows:

$$\begin{bmatrix} K_{11} & K_{12} & K_{13} \\ K_{21} & K_{22} & K_{23} \\ K_{31} & K_{32} & K_{33} \end{bmatrix} \begin{bmatrix} U_{mn} \\ V_{mn} \\ W_{mn} \end{bmatrix} - \omega_{mn}^2 \begin{bmatrix} M_{11} & M_{12} & M_{13} \\ M_{21} & M_{22} & M_{23} \\ M_{31} & M_{32} & M_{33} \end{bmatrix} \begin{bmatrix} U_{mn} \\ V_{mn} \\ W_{mn} \end{bmatrix} = 0 \quad (22)$$

where  $K_{ij}, M_{ij}$  are stiffness and mass element like follows:

$$K_{ij} = \alpha_{ij}^c + \alpha_{ij}^s + \alpha_{ij}^r - \alpha_{ij}^o, \quad M_{ij} = \beta_{ij}^c + \beta_{ij}^s + \beta_{ij}^r - \beta_{ij}^o \quad (23)$$

Eqn.(22) is simplified by follows:

$$\begin{bmatrix} C_{11} & C_{12} & C_{13} \\ C_{21} & C_{22} & C_{23} \\ C_{31} & C_{32} & C_{33} \end{bmatrix} \begin{Bmatrix} U_{mn} \\ V_{mn} \\ W_{mn} \end{Bmatrix} = 0 \quad (24)$$

where the coefficient  $C_{ij}(i,j=1,2,3)$  is the summation of each element in Eqn.(22). To obtain the non-trivial solution on Eqn.(24), the determinant of the matrix must be zero.

$$\begin{vmatrix} C_{11} & C_{12} & C_{13} \\ C_{21} & C_{22} & C_{23} \\ C_{31} & C_{32} & C_{33} \end{vmatrix} = 0 \quad (25)$$

Expanding Eqn.25), a polynomial equation for the natural frequency can be obtained as following form:

$$\alpha_6 \omega_{mn}^6 + \alpha_4 \omega_{mn}^4 + \alpha_2 \omega_{mn}^2 + \alpha_0 = 0 \quad (26)$$

### RESULTS AND DISCUSSION

To check the validity of the present analytic results, the experimental and analytic results are compared. In experiment, impact exciting method is used and the composite material is the plain woven by glass fiber.

$$E_1=E_2=25\text{Gpa}, G_{12}=4.1\text{GPa}, \nu_{12}=0.15, \rho=1866\text{kg/m}^3$$

The plain weave composite cylindrical shell with 4 ring stiffener is laminated with [60<sub>2</sub>/-60<sub>3</sub>/60<sub>2</sub>]. Table 2 shows the results from experiment and theory, where  $L=0.31\text{m}$ ,  $R=.08\text{m}$ ,  $h=3\text{mm}$ . The maximum discrepancy between two results is 15%. Usually the discrepancy is less than 10%. The vibration mode from 1st to 4th are given in Fig. 2.

Table 2: The frequencies for the ring stiffened GFRP composite cylindrical shell

Method \ Mode	Frequencies(Hz)	
	Experiment	Analysis
1st	460(1,2)	494(1,2)
2nd	745(1,1)	831(1,1)
3rd	925(1,3)	949(1,3)
4th	1265(2,3)	1310(2,3)
5th	1420(2,2)	1653(2,2)
6th	1505(1,4)	1721(1,4)

Table 3: The frequencies for the ring stiffened GFRP composite cylindrical shell with a rectangular cutout

Method \ Mode	Natural Frequencies(Hz)	
	Experiment	Analysis
1st	455(1,2)	479(1,2)
2nd	720(1,1)	823(1,1)
3rd	920(1,3)	914(1,3)
4th	1255(2,3)	1281(2,3)
5th	1375(2,2)	1601(2,2)
6th	1500(1,4)	1661(1,4)

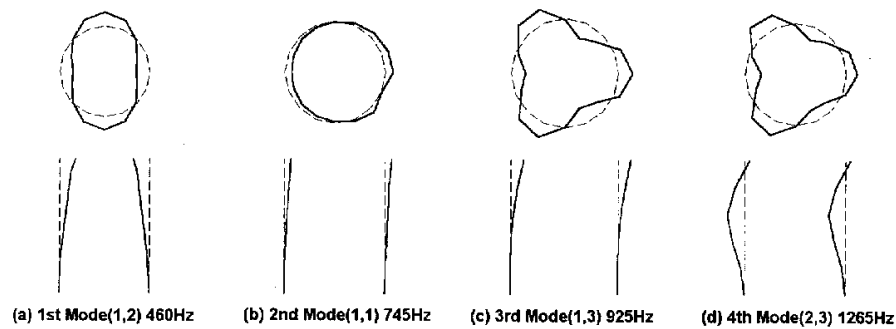


Fig. 2: Mode shapes from experiment for the plain weave GFRP composite shell

Table 3 gives the experiment and theoretical results for the ring stiffened plain weave composite cylindrical shell with  $\alpha \times \phi_0 = 0.13L \times 34^\circ$  cutout. As shown in Table 3, the discrepancy between two methods is less than 10%. The vibration mode shapes for the weakened shell in Fig. 3 are similar to those of unweakened shell. But the relative amplitude around cutout region is larger than other region for the 4th vibration mode which axial mode number is 2.

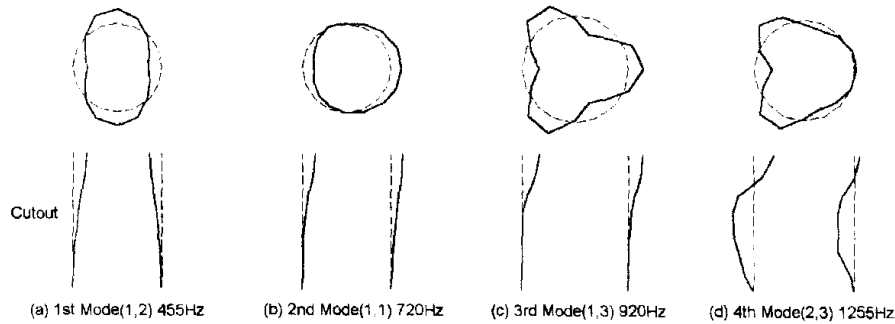


Fig. 3: Mode shapes from experiment for the GFRP composite shell with a rectangular cutout

The composite material for the following numerical examples is carbon fiber reinforced (CFRP:T300/LY556/HY917). The material properties are followings:

$$E_1=139.4\text{Gpa} \quad E_2=8.7\text{Gpa} \quad G_{12}=3.1\text{Gpa} \quad \nu_{12}=0.268 \quad \rho=1542\text{kg/m}^3.$$

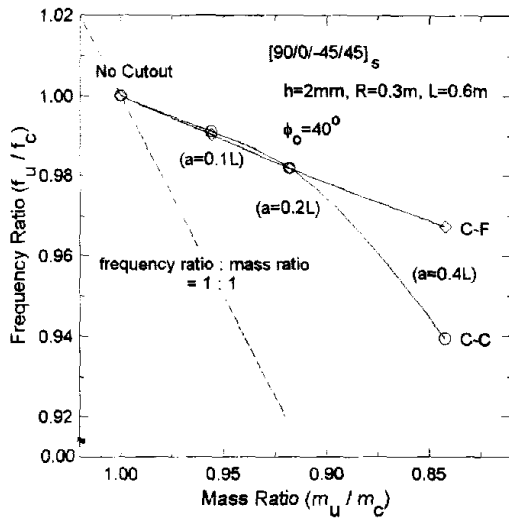


Fig. 4: Effect of axial cutout size on the frequency for unstiffened CFRP composite shell

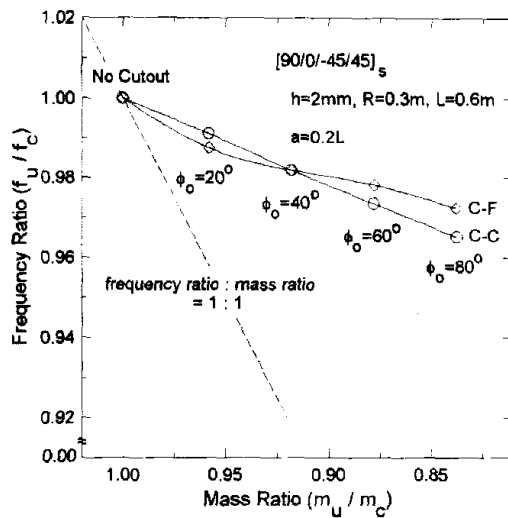


Fig. 5: Effect of circumferential cutout size on the frequency for unstiffened CFRP composite shell

Fig. 4 shows the fundamental frequency ratio of the unstiffened composite cylindrical shell with a rectangular cutout, where the circumferential cutout angle  $\phi_0$  is  $40^\circ$  and the axial cutout sizes vary  $0.1L$  to  $0.4L$ . The x-axis indicates the mass ratio that is the ratio of unweakened shell-to-weakened shell mass and the y-axis is the frequency ratio. It is the dashed line that the frequency ratio-to-mass ratio is matching one-to-one. As shown in figure, the size of cutout decreases the frequency. The frequency reduction is less than mass reduction. For the C-F boundary conditions, the frequency decreases monotonically with cutout size except

the C-C boundary condition. For the C-C- boundary condition, the frequency decreases sensitively.

Fig. 5 indicates the fundamental natural frequency behavior with circumferential cutout size variation, where circumferential cutout angle  $\phi_0$  varies  $20^\circ$  to  $80^\circ$  and axial cutout size  $a$  is  $0.2L$ . As shown in Fig. 4 and 5, the frequency decrease is less than mass reduction. The axial cutout size effects more sensitively on the fundamental frequency than circumferential cutout size.

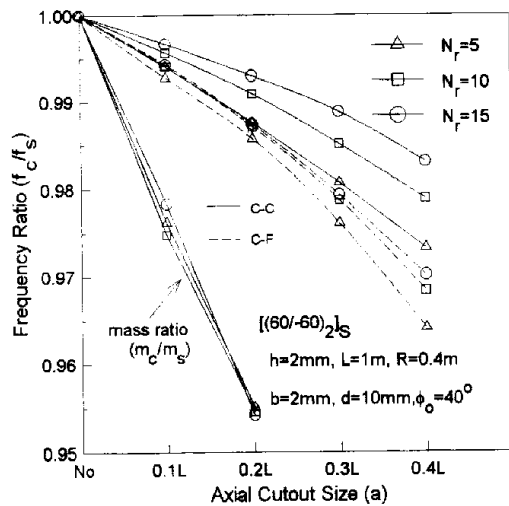


Fig. 6: Effect of stiffener number on the frequency for orthogonally stiffened CFRP composite shell

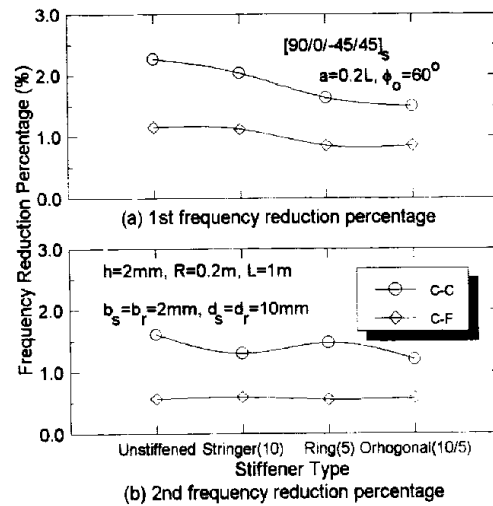


Fig. 7: Frequency ratio for the CFRP composite shell with the various stiffening types

Fig. 6 shows the effect of stiffener number on frequency for the ring stiffened composite cylindrical shell with a cutout, where circumferential cutout size  $\phi_0$  is  $40^\circ$  and axial cutout size varies from  $0.1L$  to  $0.4L$ . From the figure, the frequency for the shell with many stiffeners decreases less than that with few stiffeners. Unlike the unstiffened shell, the frequency for the shell with C-F boundary condition varies more sensitively than that for the shell with C-C boundary condition.

Fig. 7 shows the frequency reduction percentage for the cylindrical shell with various stiffening type. For the 1st and 2nd fundamental frequency of unstiffened shell, the maximum frequency reduction percentage is about 2.0%~2.5% for the shell with C-C boundary condition. For the orthogonally stiffened shell, the frequency reduction is the least among the shells with other stiffener type. Ring, stringer stiffened shell are followed. From this result, as being stiffened, the effect of cutout on frequency is less than unstiffened shell.

## CONCLUSION

In this paper, the effect of rectangular cutout on natural frequency for the stiffened composite cylindrical shell with clamped-clamped and clamped-free boundary conditions presented by theoretical method. In the admissible displacement functions, one-term trigonometric function is used for the circumferential mode and beam modal function is used

for the axial mode satisfying various boundary conditions. Love's thin shell theory combined with discrete stiffener theory is adopted to formulate the theoretical model. Theoretical results are obtained through the Rayleigh-Ritz procedure based on energy method and compared with experimental results.

## REFERENCES

1. J.N. Reddy and J.H. Starnes, Jr, 1993, "General Buckling of Stiffened Circular Cylindrical Shells According to a Layerwise Theory", *Computers & Structures*, Vol.49, No.4, pp.605-616.
2. A. Schokker, A. Kasagi and S. Sridharan, 1995, "Dynamic Interactive Buckling of Ring-Stiffened Composite Shells", *AIAA J.*, Vol.33, No.10, pp.1956-1962.
3. J.H. Starnes Jr., N.F. Knight Jr. and M. Rouse, 1985, "Postbuckling Behavior of Selected Flat Stiffened Graphite-Epoxy Panels Loaded in Compression", *AIAA J.*, Vol.23, No. 8, pp.1236-1246.
4. Y.S. Lee and Y.W. Kim, "Free Vibration of the Composite Laminated Cylindrical Shells Stiffened with the Axial Stiffeners," *Trans. of KSME(in Korean)*, Vol.20(A), No.7, 1996, pp.2223-2233.
5. A. Rajamani and R. Prabhakaran, 1977, "Dynamic Response of Composite Plates with Cut-outs, Part I: Simply-Supported Plates", *J. of Sound and Vibration*, Vol.54, No.4, pp.549-564.
6. A. Rajamani and R. Prabhakaran, 1977, "Dynamic Response of Composite Plates with Cut-outs, Part II: Clamped-Clamped Plates", *J. of Sound and Vibration*, Vol.54, No.4, pp.565-576.
7. J. N. Reddy, 1982, "Large Amplitude Flexural Vibration of Layered Composite Plates with Cutouts", *J. of Sound and Vibration*, Vol.83, No.1, pp.1-10.
8. H. P. Lee, S. P. Lim and T. Chow, 1987, "Free Vibration of Composite Rectangular Plates with Rectangular Cutouts", *Composite Structures*, Vol.8, pp.63-81.
9. S. Toda and K. Komatsu, 1977, "Vibrations of Circular Cylindrical Shells with Cutouts", *J. of Sound and Vibration*, Vol.52, No.4, pp.497-510.
10. A. S. Bicos and G. S. Springer, 1989, "Vibrational Characteristics of Composite Panels with Cutouts", *AIAA J.*, Vol.27, No.8, pp.1116-1122.
11. A. S. Bicos and G. S. Springer, 1989, "Analysis of Free Damped Vibration of Laminated Composite Plates and Shells", *Int. J. Solids Structures*, Vol.25, No.2, pp.129-149.

# AN ANALYSIS OF VIBRATION DAMPING IN COMPOSITE PLATES USING COMPLEX FREQUENCY EQUATIONS

S. Kalysanasundaram\*, D. H. Allen\*\*, M. Cardew-Hall\*, A.E. Lowe\*

*\*Department of Engineering, Australian National University, Australia*

*\*\*Department of Aerospace Engineering, Texas A & University, U.S.A.*

## Summary

Correspondence principle of viscoelasticity has been used to derive the complex frequency equations and vibration damping in orthotropic plates. Vibration damping has been found to be sensitive to the mode of vibration, lamination schemes and aspect ratio of the plates. Increasing the aspect ratio of the plate leads to cylindrical bending. Comparison of the results obtained from this study with the model developed by Adams illustrates that this model captures the physical phenomenon of cylindrical bending in orthotropic plates accurately.

**KEYWORDS:** vibration damping, viscoelasticity, complex frequency equations, specific damping capacity, cylindrical bending

## 1. Introduction

The use of composite materials in many structural applications due to their high specific stiffness and strength has attracted interest in methods for improving the damping performance of these structures. It has been found that the damping of composites depends on the micromechanical properties of the constituent materials and the lamination schemes. The composite damping exhibits an opposing trend to stiffness and strength, being minimum in the direction of fibers and maximum in the transverse and shear directions. Structural damping is also found to be strongly dependent on the structural geometry and deformation modes. Thus there is a need to develop integrated mechanics models for the analysis of structural components which are capable of describing the global structural response by correlating the damping characteristics of the structural components to the parameters of the basic constituent materials, laminate configuration and geometry of the structure. A variety of analytical models have been developed for predicting the damping in composites at the micromechanical and macromechanical levels [1-5]. In this paper, two basic analytical approaches will be considered for predicting damping in orthotropic plates:

1. The use of elastic-viscoelastic correspondence principles in combination with elastic solutions from solid mechanics and laminate theory will be used to derive the complex frequency equations and vibration damping in orthotropic plates.
2. The results from the above model will be compared with the approach taken by Adams [5] in estimating the vibration damping by defining a specific damping capacity.



## 2. Development of Complex Frequency Equations

There are number of assumptions made in the theory of thin plates in order to reduce three dimensional equations to a two-dimensional set that can be solved. In this paper a thin plate theory consistent with the classical assumptions of Kirchoff will be used where the terms involving transverse shear strains and rotary inertia are assumed to be negligible. The displacements in the standard  $x, y, z$  coordinate system are denoted by  $u, v, w$  respectively and given by

$$\begin{aligned} u &= u^o(x, y, t) - z \frac{\partial w}{\partial x} \\ v &= v^o(x, y, t) - z \frac{\partial w}{\partial y} \\ w &= w(x, y, t) \end{aligned} \quad (1)$$

The strain displacement relationships are given by

$$\begin{aligned} \epsilon_x &= \epsilon_x^o + z \kappa_x \\ \epsilon_y &= \epsilon_y^o + z \kappa_y \\ \epsilon_{xy} &= \epsilon_{xy}^o + z \kappa_{xy} \end{aligned} \quad (2)$$

where  $\epsilon_x^o, \epsilon_y^o$  and  $\epsilon_{xy}^o$  are the midplane strains and  $\kappa_x, \kappa_y$  and  $\kappa_{xy}$  are the plate curvatures.

The equations of motion for the  $k^{th}$  layer of the laminate are given by

$$\frac{\partial \sigma_x^{(k)}}{\partial x} + \frac{\partial \sigma_{xy}^{(k)}}{\partial y} + \frac{\partial \sigma_{xz}^{(k)}}{\partial z} = \rho_o^{(k)} \frac{\partial^2 u}{\partial t^2} \quad (3)$$

$$\frac{\partial \sigma_{xy}^{(k)}}{\partial x} + \frac{\partial \sigma_y^{(k)}}{\partial y} + \frac{\partial \sigma_{yz}^{(k)}}{\partial z} = \rho_o^{(k)} \frac{\partial^2 v}{\partial t^2} \quad (4)$$

$$\begin{aligned} \frac{\partial}{\partial x} (\sigma_{xz}^{(k)} + \sigma_x^{(k)} \frac{\partial w}{\partial x} + \sigma_{xy}^{(k)} \frac{\partial w}{\partial y}) + \frac{\partial}{\partial y} (\sigma_{yz}^{(k)} + \sigma_{xy}^{(k)} \frac{\partial w}{\partial x} + \sigma_y^{(k)} \frac{\partial w}{\partial y}) + \\ \frac{\partial}{\partial z} (\sigma_z^{(k)} + \sigma_{xz}^{(k)} \frac{\partial w}{\partial x} + \sigma_{yz}^{(k)} \frac{\partial w}{\partial y}) = \rho_o^{(k)} \frac{\partial^2 w}{\partial t^2} \end{aligned} \quad (5)$$

Equations (3-5) are derived from the nonlinear equations of motion by retaining only the nonlinear terms involving products of stresses and plate slopes. Integrating equations (3) and (4) with respect to  $z$  and neglecting the rotary inertia term results in

$$\begin{aligned} \frac{\partial N_x}{\partial x} + \frac{\partial N_{xy}}{\partial y} &= \rho \frac{\partial^2 u_o}{\partial t^2} \\ \frac{\partial N_{xy}}{\partial x} + \frac{\partial N_y}{\partial y} &= \rho \frac{\partial^2 v_o}{\partial t^2} \end{aligned} \quad (6)$$

where  $N_x, N_y$  and  $N_{xy}$  are the stress resultants. Integrating equation (5) with respect to  $z$  and neglecting higher order terms yields

$$N_x \frac{\partial^2 w}{\partial x^2} + 2N_{xy} \frac{\partial^2 w}{\partial x \partial y} + N_y \frac{\partial^2 w}{\partial y^2} + \frac{\partial Q_x}{\partial x} + \frac{\partial Q_y}{\partial y} + q = \rho \frac{\partial^2 w}{\partial t^2} \quad (7)$$

where

$$\begin{bmatrix} Q_x \\ Q_y \end{bmatrix} = \begin{bmatrix} \int_{-\frac{h}{2}}^{\frac{h}{2}} \sigma_{xz}^{(k)} dz \\ \int_{-\frac{h}{2}}^{\frac{h}{2}} \sigma_{yz}^{(k)} dz \end{bmatrix}$$

and

$$q = \sigma_z^{(k)} \left( \frac{h}{2} \right) - \sigma_z^{(k)} \left( -\frac{h}{2} \right)$$

Multiplying equations (3) and (4) with  $z$  and integrating over the plate thickness and differentiating the resulting equations with respect to  $x$  and  $y$ , respectively, results in

$$\begin{aligned} \frac{\partial Q_x}{\partial x} &= \frac{\partial^2 M_x}{\partial x^2} + \frac{\partial^2 M_{xy}}{\partial x \partial y} \\ \frac{\partial Q_y}{\partial y} &= \frac{\partial^2 M_{xy}}{\partial x \partial y} + \frac{\partial^2 M_y}{\partial y^2} \end{aligned} \quad (8)$$

Where  $M_x$ ,  $M_y$  and  $M_{xy}$  are the moment resultants.

Substituting the expressions for moment resultants into Equation (7) gives:

$$\frac{\partial^2 M_x}{\partial x^2} + 2 \frac{\partial^2 M_{xy}}{\partial x \partial y} + \frac{\partial^2 M_y}{\partial y^2} + N_x \frac{\partial^2 w}{\partial x^2} + 2N_{xy} \frac{\partial^2 w}{\partial x \partial y} + N_y \frac{\partial^2 w}{\partial y^2} + q = \rho \frac{\partial^2 w}{\partial t^2} \quad (9)$$

Equations (6) and (9) constitute the equations of motion in terms of moment and force resultants and is identical for elastic and viscoelastic plate problems. The harmonic stress-strain relationship for the viscoelastic problem for any layer  $k$  in the plate can be written as

$$\begin{bmatrix} \sigma_x^{*(k)} \\ \sigma_y^{*(k)} \\ \sigma_{xy}^{*(k)} \end{bmatrix} = \begin{bmatrix} Q_{11}^{*(k)} & Q_{12}^{*(k)} & Q_{16}^{*(k)} \\ Q_{12}^{*(k)} & Q_{22}^{*(k)} & Q_{26}^{*(k)} \\ Q_{16}^{*(k)} & Q_{26}^{*(k)} & Q_{66}^{*(k)} \end{bmatrix} \begin{bmatrix} \epsilon_x^{*(k)} \\ \epsilon_y^{*(k)} \\ \epsilon_{xy}^{*(k)} \end{bmatrix} \quad (10)$$

where the reduced complex stiffness terms  $Q_{ij}^*$  are given by

$$Q_{ij}^* = C_{ij}^* - \frac{C_{i3}^* C_{j3}^*}{C_{33}^*}$$

Using Equation (10) and strain-displacement relations in the definition of stress and moment resultants yields

$$\begin{bmatrix} N_x^* \\ N_y^* \\ N_{xy}^* \\ M_x^* \\ M_y^* \\ M_{xy}^* \end{bmatrix} = \begin{bmatrix} A_{11}^* & A_{12}^* & A_{16}^* & B_{11}^* & B_{12}^* & B_{16}^* \\ A_{12}^* & A_{22}^* & A_{26}^* & B_{12}^* & B_{22}^* & B_{26}^* \\ A_{16}^* & A_{26}^* & A_{66}^* & B_{16}^* & B_{26}^* & B_{66}^* \\ B_{11}^* & B_{12}^* & B_{16}^* & D_{11}^* & D_{12}^* & D_{16}^* \\ B_{12}^* & B_{22}^* & B_{26}^* & D_{12}^* & D_{22}^* & D_{26}^* \\ B_{16}^* & B_{26}^* & B_{66}^* & D_{16}^* & D_{26}^* & D_{66}^* \end{bmatrix} \begin{bmatrix} \epsilon_x^{*0} \\ \epsilon_y^{*0} \\ \epsilon_{xy}^{*0} \\ \kappa_x^* \\ \kappa_y^* \\ \kappa_{xy}^* \end{bmatrix} \quad (11)$$

where  $A_{ij}^*$ ,  $B_{ij}^*$  and  $D_{ij}^*$  are functions of the reduced complex stiffness terms  $Q_{ij}^*$ . The transformations of  $A_{ij}^*$ ,  $B_{ij}^*$  and  $D_{ij}^*$  from a known coordinate system  $x, y, z$  to a rotated coordinate system  $x', y', z'$  follows the transformation for an elastic problem [6].

The equations of motion in terms of displacements can be found by substituting the stress and moment resultant expressions into equations of motion (6) and (9). For a simply-supported rectangular plate undergoing free vibrations these equations reduce to:

$$D_{11}^* \frac{\partial^4 w}{\partial x^4} + 2(D_{12}^* + 2D_{66}^*) \frac{\partial^4 w}{\partial x^2 \partial y^2} + D_{22}^* \frac{\partial^4 w}{\partial x^4} + \rho \frac{\partial^2 w}{\partial t^2} = 0 \quad (12)$$

In this work, laminates will be considered which are symmetric and for which the bending-twisting coupling terms vanish. The definition of damping used in this work is defined as  $Tan\phi$ . A physical explanation for this definition can be offered by considering the phase difference between sinusoidally varying stress and strain for uniaxial loading:

$$\begin{aligned} \epsilon^* &= \epsilon_A e^{i\omega t} \\ \sigma^* &= \sigma_A e^{i(\omega t + \phi)} \end{aligned} \quad (13)$$

where  $\phi$  is the phase difference between stress and strain. The complex modulus can be written as

$$E^* = \frac{\sigma^*}{\epsilon^*}$$

or

$$E^* = \frac{\sigma_A}{\epsilon_A} (\cos\phi + i\sin\phi) \quad (14)$$

The physical meaning of the complex modulus is gained by studying the energy dissipated in a cycle of uniaxial sinusoidal motion given by the integral

$$\Delta U = \int_0^{2\pi} \sigma^* \frac{d\epsilon^*}{d(\omega t)} d(\omega t) \quad (15)$$

In order to obtain meaningful expressions for energy dissipation the real part of  $\sigma^*$  and  $\epsilon^*$  should be used in the evaluation of (15). This leads to

$$\Delta U = \pi E'' \epsilon_A^2 \quad (16)$$

The strain energy stored during the peak displacement is given by

$$U = \frac{E' \epsilon_A^2}{2} \quad (17)$$

The present definition of damping as  $Tan\phi$  is thus a measure of the ratio of the energy dissipated to the peak stored strain energy in a cycle of sinusoidal motion and is given by

$$Tan\phi = \frac{\Delta U}{2\pi U} \quad (18)$$

There are several other definitions of damping used in the literature. The specific damping capacity  $\psi$  is defined as

$$\psi = \frac{\Delta U}{U} = 2\pi Tan\phi \quad (19)$$

Other related damping definitions include logarithmic decrement  $\Lambda$  measured in a free vibration decay experiment and resonance peak width  $\frac{\Delta f_n}{f_n}$  measured in a resonant experiment. The relationships between different measures are as follows:

$$\frac{\Delta U}{U} = 2\pi Tan\phi = 2\Lambda = 2\pi \frac{\Delta f_n}{f_n} \quad (20)$$

The solution for free vibrations which occur after the removal of a harmonic exciting force can be written in the following separable form

$$w = W(x, y)e^{i\omega_n t} \quad (21)$$

where  $W(x, y)$  is the spatial displacement function at any point in the plate. Here it is assumed that for sufficiently low loss viscoelastic materials ( $Tan\phi$  less than about 0.1), the free vibrations are also approximately harmonic with an exponential decay. For a plate simply-supported on all four sides, Equation(21) must satisfy the following boundary conditions

$$\begin{aligned} w &= 0 \quad \text{at } x = 0, a \text{ and } y = 0, b \\ M_x^* &= -D_{11}^* \frac{\partial^2 w}{\partial x^2} - D_{12}^* \frac{\partial^2 w}{\partial y^2} = 0 \text{ at } x = 0, a \\ M_y^* &= -D_{12}^* \frac{\partial^2 w}{\partial x^2} - D_{22}^* \frac{\partial^2 w}{\partial y^2} = 0 \text{ at } y = 0, b \end{aligned} \quad (22)$$

The solution to equation(21) which satisfies the above boundary conditions is given by

$$w(x, y, t) = A_{mn} \text{Sin} \frac{m\pi x}{a} \text{Sin} \frac{n\pi y}{b} e^{i\omega_{mn} t} \quad (23)$$

where  $m$  and  $n$  are integers. Substituting equation(23) in (12) leads to the complex frequency equation

$$D_{11}^* \frac{m^4 \pi^4}{a^4} + 2(D_{12}^* + 2D_{66}^*) \frac{m^2 n^2 \pi^4}{a^2 b^2} + D_{22}^* \frac{n^4 \pi^4}{b^4} = \rho \omega_{mn}^2 \quad (24)$$

The frequency  $\omega_{mn}$  is complex and is given by

$$\omega_{mn} = \omega'_{mn} + i\omega''_{mn}$$

and

$$\omega_{mn}^2 = \omega_{mn}^{\prime 2} \left(1 - \frac{\omega_{mn}^{\prime\prime 2}}{\omega_{mn}^{\prime 2}}\right) + 2i\omega'_{mn}\omega''_{mn} \quad (25)$$

For low loss viscoelastic materials,  $\left(\frac{\omega''_{mn}}{\omega'_{mn}}\right)^2 \ll 1$  and  $\omega_{mn}^2$  can be written as

$$\omega_{mn}^2 \simeq \omega_{mn}^{\prime 2} + 2i\omega'_{mn}\omega''_{mn} \quad (26)$$

Equating the real part of the complex frequency equation( 24) leads to

$$D_{11}' \frac{m^4 \pi^4}{a^4} + 2(D_{12}' + 2D_{66}') \frac{m^2 n^2 \pi^4}{a^2 b^2} + D_{22}' \frac{n^4 \pi^4}{b^4} = \rho \omega_{mn}^{\prime 2} \quad (27)$$

Equating the imaginary part of the complex frequency equation( 24) results in

$$D_{11}'' \frac{m^4 \pi^4}{a^4} + 2(D_{12}'' + 2D_{66}'') \frac{m^2 n^2 \pi^4}{a^2 b^2} + D_{22}'' \frac{n^4 \pi^4}{b^4} = \rho 2\omega'_{mn}\omega''_{mn} \quad (28)$$

Damping for the plate is obtained by

$$\text{Tan}\phi = \frac{2\omega''_{mn}}{\omega'_{mn}} \quad (29)$$

$Tan\phi$  provides a measure of the decay of the displacement per cycle of vibration and is related to the logarithmic decrement  $\Lambda$  obtained from a free vibration decay experiment by

$$Tan\phi = \frac{\Lambda}{\pi} \quad (30)$$

### 3. Specific Damping Capacity of Orthotropic Plates

The theory developed in this work uses the correspondence principle of linear viscoelasticity to develop a complex frequency equation for a free vibration problem. Solution of the complex frequency equation leads to the prediction of damping. This approach is general and can be extended to predict damping in complicated structures. Adams has taken a different approach in estimating the damping in beam and plate structures [4,7]. Good correlation between theory and experiments has been reported for beam problems. This model has not been applied to specially orthotropic plates and it is useful to compare the present model with this approach. The specific damping capacity in Adams model is defined by

$$\psi = \frac{\Delta U}{U} \quad (31)$$

where  $\Delta U$  is the strain energy dissipated during a strain cycle and  $U$  is the maximum strain energy in the laminate. Taking an element of the  $k^{th}$  layer at a distance  $z$  from the mid-plane, the energy dissipation of the plate is separated into three components associated with  $\sigma_x$ ,  $\sigma_y$  and  $\sigma_{xy}$

$$\Delta U = \Delta U_x + \Delta U_y + \Delta U_{xy} \quad (32)$$

$\Delta U_x$ ,  $\Delta U_y$  and  $\Delta U_{xy}$  are given by

$$\begin{aligned} \Delta U_x &= \frac{1}{2} \int \int \int \psi_L \sigma_x \epsilon_x dx dy dz \\ \Delta U_y &= \frac{1}{2} \int \int \int \psi_T \sigma_y \epsilon_y dx dy dz \\ \Delta U_{xy} &= \frac{1}{2} \int \int \int \psi_{LT} \sigma_{xy} \epsilon_{xy} dx dy dz \end{aligned} \quad (33)$$

$\psi_L$ ,  $\psi_T$  are the specific damping capacities of  $0^\circ$  and  $90^\circ$  beam specimens, which are tested in flexure and  $\psi_{LT}$  is the specific damping capacity of a  $0^\circ$  specimen tested in longitudinal shear from a torsion experiment. The energy dissipated,  $\Delta U$ , can be expressed in terms of the plate displacements by substituting strain-displacement relationships(2) into (33) and integrating with respect to  $z$ .

### 4. Discussion of Results

The material system used for the study of plate damping is an epoxy matrix reinforced with E-glass fibers (Scotch ply 1002). The material properties were obtained from [8]. The volume fraction of the fibers is 0.44. The effective complex properties  $E_a^*$ ,  $E_t^*$ ,  $G_a^*$  were obtained from the matrix and fiber properties by using the micromechanical analysis from [5]. The plate is a square plate and simply-supported on all four sides.

Figure 1 illustrates the effect of aspect ratio  $R(a/b)$  on damping for the  $[15^\circ / -15^\circ]_m$  laminated plate. The first mode of vibration is used. Damping increases with increasing aspect ratio. This increase is due to the behavior of cylindrical bending in the plate. Increasing the aspect ratio makes the plate behave in a manner having a large dimension

in the x-direction and the deflected surface is cylindrical in the y-direction. The plate deformation may then be considered to be independent of the x-direction. Thus, increasing the aspect ratio tends to deform the plate in a direction normal to the fiber direction for this lamination scheme. The cylindrical bending leads to an increase in damping as the aspect ratio is increased. Whitney [9] has shown that the maximum deflection under transverse loading rapidly approaches cylindrical bending for laminates of the class  $[0^\circ/90^\circ]_m$ . For an aspect ratio of 3, the center deflection was within 4 percent of the center deflection of an infinite strip.

Figures 2,3 and 4 illustrate the effect of aspect ratio on plate damping for a  $[0_4^{\circ}/90_4^{\circ}]_s$  laminate. In Figure 2 damping in the first mode is considered ( $m = 1, n = 1$ ). For aspect ratios of less than 1, the damping in the plate predicted by the Adams' model is less than the present theory. For aspect ratios greater than 1 the damping predicted by Adams model is higher than the present theory and it approaches the damping value of the transverse modulus  $E_T^*$ . Figure 3 exhibits a similar trend. The value for m is 1 and the value for n is 2 in this case. There is more bending in the y-direction for this mode and both models approach cylindrical bending faster with increasing aspect ratio. In Figure 4 the value of m is 2 and the value of n is 1. There is comparatively less bending in the y-direction for this mode shape and both models approach cylindrical bending less rapidly.

Figures 5( $m=1, n=1$ ) and 6( $m=2, n=1$ ) depict the effect of aspect ratio on damping for a  $[0_2^{\circ}/90_2^{\circ}/0_2^{\circ}/90_2^{\circ}]_s$  laminate. The difference in the two models is large for increasing aspect ratio for this lamination scheme. Damping values for Adams' model approach the value of  $E_T^*$  for aspect ratios greater than 2. Figures 7( $m=1, n=1$ ) and 8( $m=2, n=1$ ) illustrate the effect of aspect ratio on damping for a  $[[0/90]_{4s}]_s$  laminate. The differences in the two models are largest for this lamination scheme. Damping from Adams' model approaches the value of  $E_T^*$  for increasing aspect ratio. The present theory predicts damping to be different for different lamination schemes as cylindrical bending is approached. Adams' model predicts the damping to be the value of  $E_T^*$  for all lamination schemes as cylindrical bending is approached. In the expressions for dissipation of energy (32), the coupling term  $D_{12}$  is multiplied by  $\psi_T$  and this seems to contribute to the overprediction of damping in Adams' model. A better approach might be to define a new specific damping capacity  $\psi_{12}$  corresponding to the term  $D_{12}$  as a function of  $\psi_L, \psi_T$  and  $\psi_{LT}$ .

## 5. Conclusions

The use of elastic-viscoelastic correspondence principle in combination with elastic solutions from thin orthotropic plate theory has been used to derive the complex frequency equations and vibration damping. This procedure has been found to be physically intuitive and mathematically rigorous. Comparison of the results obtained from this investigation with the model developed by Adams illustrates that this model captures the physical phenomenon of cylindrical bending in plates accurately. This approach is general and can be extended to predict damping in complicated structures.

## 6. References

1. Gibson, R.F. 1992. "Damping characteristics of Composite Materials and Structures," *Journal of Materials Engineering Performance*, 1:11-20.
2. Saravanos, D.A., and C. C. Chamis. 1991. "Computational Simulation of Damping in composite Structures," *Journal of Reinforced Plastics and Composites*, 10:256-278.
3. Bert, C.W.1980. "Composite Materials: A Survey of the Damping Capacity of Fiber-Reinforced composites," *Damping Application for Vibration Control*, ASME, AMD Vol. 38: 53-63.

4. Lin, D.X., Ni, R.G., and R. D. Adams. 1984. "Prediction and Measurement of the Vibrational Damping parameters of Carbon and Glass Fibre-Reinforced Plastic Plates," *Journal of Composite Materials*, 18:132-152.

5. Kalyanasundaram, S. 1994. "An Investigation of Damping Behavior in Composite Materials," PhD Dissertation, Texas A & M University, May 1994.

6. Whitney, J.M. 1987. "Structural Analysis of Laminated Anisotropic Plates," Technomic Publishing Company, PA, 1987.

7. Ni, R.G., and R. D. Adams. 1984. "The Damping and Dynamic Moduli of Symmetric Laminated Composite Beams-Theoretical and Experimental Results," *Journal of Composite Materials*, 18:104-121.

8. Gibson, R.F. 1975. "Elastic and Dissipative Properties of Fiber-Reinforced Composite Materials in Flexural Vibrations," PhD Dissertation, University of Minnesota, December 1975.

9. Whitney, J.M. 1969. "Bending-Extensional Coupling in Laminated Plates under Transverse Loading," *Journal Of Composite Materials*, 3:20-28.

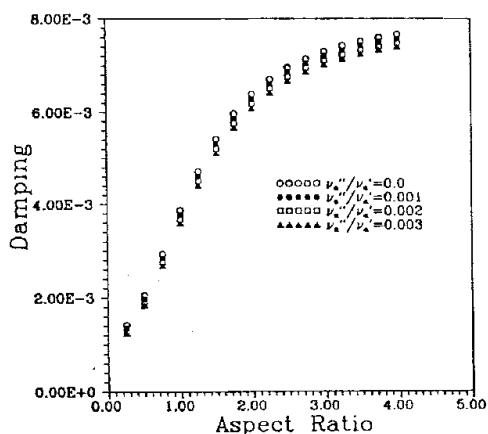


Figure 1

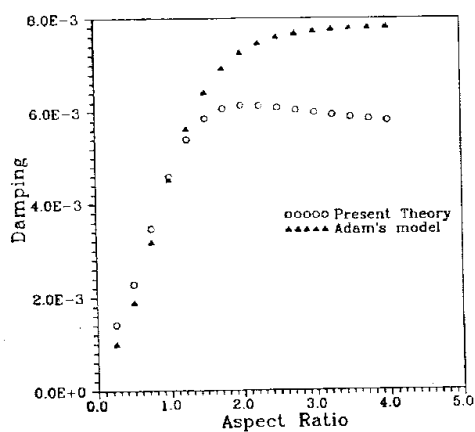


Figure 2

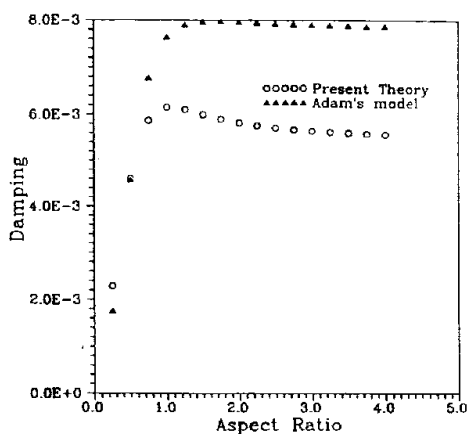


Figure 3

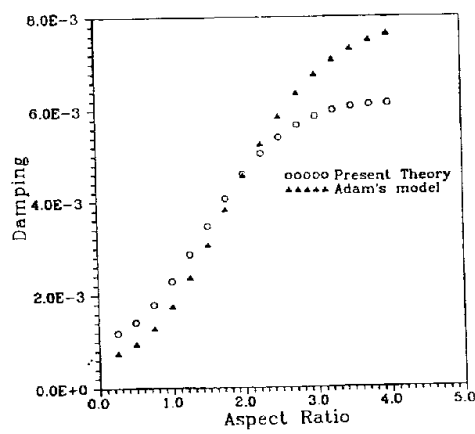


Figure 4

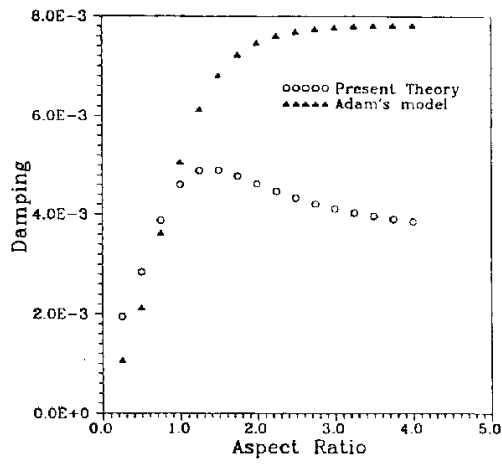


Figure 5

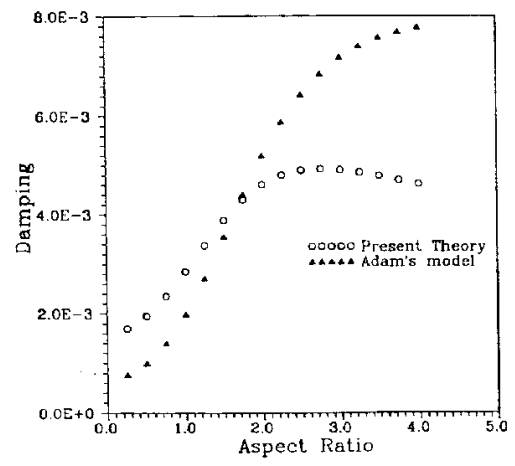


Figure 6

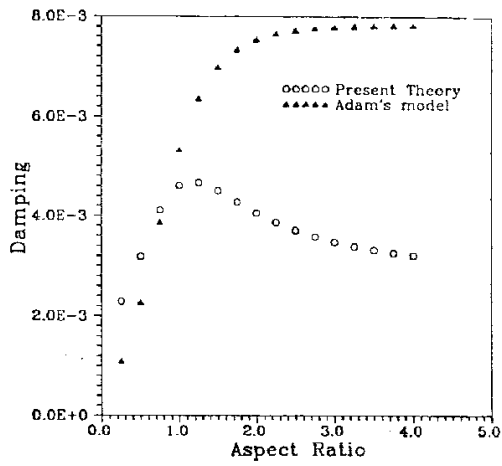


Figure 7

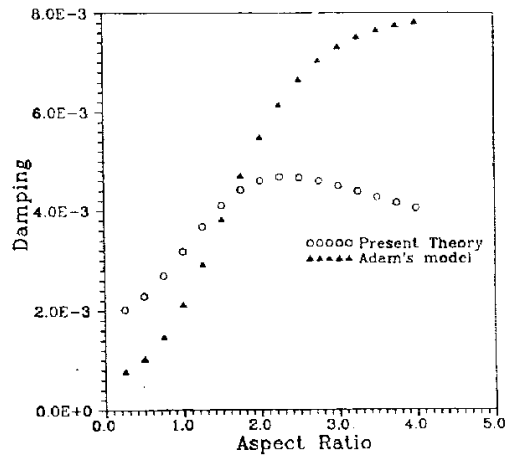


Figure 8



# VIBRATIONS OF A LAMINATED COMPOSITE BEAM ELASTICALLY SUPPORTED AT ONE END AND CARRYING A TIP MASS AT THE OTHER

T. Yokoyama and Z. M. Yang

*Department of Mechanical Engineering  
Okayama University of Science, 1-1 Ridai-Cho, Okayama 700, Japan*

**SUMMARY:** The present work deals with the free vibration analysis of a symmetrically laminated composite beam with one end elastically supported and having a tip mass at the other free end. The governing equations for free vibrations of the composite beam are derived from Hamilton's principle accounting for the effects of shear deformation and rotatory inertia. The individual influences of ply orientation, beam end constraint, tip mass and distance between the tip mass centroid and the point of attachment on the natural frequencies of the composite beam are examined and presented in three-dimensional graphs. It is shown that the increase in the (tip mass)/(beam mass) ratio, the (radius of gyration of the tip mass)/(beam length) ratio and the (distance between the tip mass centroid and the point of attachment)/(beam length) ratio yields the decrease in the fundamental frequencies. The validity of the analysis is verified by comparison with the frequency results available in the literature.

**KEYWORDS:** laminated composite beam, natural frequency, beam end constraint, tip mass, ply orientation, coupling effect, timoshenko beam theory

## INTRODUCTION

The increasing use of laminated composite beams as robot arms or rotating blades requires a deeper understanding of vibration characteristics of these beam structures. A beam theory based on the classical lamination theory [1] is inadequate for accurate prediction of the natural frequencies of laminated composite beams, because the effects of shear deformation are pronounced for composites due to the high ratio of extensional modulus (in-plane modulus) to transverse shear modulus. The bending-torsion coupled vibrations of generally orthotropic beams have been studied by several authors [2-5] including the effects of shear deformation and rotatory inertia. The same vibration problem of symmetrically laminated composite beams was solved by Chen and Yang [6] using finite element approach. A similar study of orthotropic beams was subsequently performed by Suresh *et al.* [7] including cross-sectional warping effects, neglecting rotatory inertia and shear deformation effects. The free bending vibrations of symmetrically laminated composite beams were discussed by Chandrashekhara *et al.* [8] and Abramovich [9]. Later on, the influence of tip mass on the natural frequencies of laminated composite beams was considered by Chandrashekhara and Bangera [10]. Recently, the free vibrations of unsymmetrically laminated composite beams were analyzed by Krishnaswamy *et al.* [11], Abramovich and Livshits [12] and Abramovich *et al.* [13].

The present paper is concerned with the free vibrations of a laminated composite beam elastically supported at one end and carrying a tip mass at the other free end as a basic model for a single-joint flexible robot arm or a rotor blade. The governing equations for free vibrations of the composite beam are derived from Hamilton's principle accounting for the effects of shear deformation and rotatory inertia. A parametric study is carried out to elucidate the individual effects of ply orientation, beam end constraint, tip mass and distance between the tip mass centroid and the point of attachment on the natural frequencies of the composite beam.

## FORMULATION OF PROBLEM

### Laminate Analysis

A laminated composite beam is considered, referred to a system of Cartesian co-ordinates ( see Fig.1 ) with the origin on the midplane of the beam and the x-axis being coincident with the beam axis. The length, width and height of the beam are denoted by  $L$ ,  $b$  and  $h$ , respectively. In an effort to include the coupling effects among bending stiffness, twisting stiffness and shearing stiffness of the composite beam, the linear elastic plate theory is applied in this study. Neglecting the in-plane displacements compared with the flexure-induced displacements, the displacement field for the composite beam can then be assumed as:

$$u(x,y,z,t) = z \psi(x,y,t), \quad v(x,y,z,t) = z \varphi(x,y,t), \quad w(x,y,z,t) = w^0(x,y,t) \quad (1)$$

where  $u$ ,  $v$  and  $w$  are the displacement components in the  $x$ ,  $y$  and  $z$  directions, respectively,  $w^0$  is the lateral displacement of a point on the midplane, and  $\psi$  and  $\varphi$  are the rotations of the normals to the cross-sections. The strain-displacement relations are given by

$$\varepsilon_x = z \kappa_x, \quad \varepsilon_y = z \kappa_y, \quad \gamma_{xy} = z \kappa_{xy}, \quad \gamma_{xz} = \psi + \frac{\partial w^0}{\partial x}, \quad \gamma_{yz} = \varphi + \frac{\partial w^0}{\partial y} \quad (2)$$

The curvatures ( $\kappa_x, \kappa_y, \kappa_{xy}$ ) can be written as

$$\kappa_x = \frac{\partial \psi}{\partial x}, \quad \kappa_y = \frac{\partial \varphi}{\partial y}, \quad \kappa_{xy} = \frac{\partial \psi}{\partial y} + \frac{\partial \varphi}{\partial x} \quad (3)$$

The laminate beam constitutive relations are derived based on the laminate plate theory as

$$\begin{pmatrix} M_x \\ M_y \\ M_{xy} \end{pmatrix} = \begin{bmatrix} D_{11} & D_{12} & D_{16} \\ D_{12} & D_{22} & D_{26} \\ D_{16} & D_{26} & D_{66} \end{bmatrix} \begin{pmatrix} \kappa_x \\ \kappa_y \\ \kappa_{xy} \end{pmatrix} \quad (4)$$

$$\begin{pmatrix} Q_{xz} \\ Q_{yz} \end{pmatrix} = \begin{bmatrix} A_{55} & A_{45} \\ A_{45} & A_{44} \end{bmatrix} \begin{pmatrix} \gamma_{xz} \\ \gamma_{yz} \end{pmatrix} \quad (5)$$

where  $(M_x, M_y, M_{xy})$  are the moments,  $(Q_{xz}, Q_{yz})$  are the shear force resultants, and  $(\gamma_{xz}, \gamma_{yz})$  are the transverse shear strains. The laminate stiffness coefficients in Eqs (4) and (5) are defined by

$$D_{ij} = b \int_{-\frac{h}{2}}^{\frac{h}{2}} \bar{Q}_{ij} z^2 dz \quad i, j = 1, 2 \text{ and } 6, \quad A_{ij} = b k \int_{-\frac{h}{2}}^{\frac{h}{2}} \bar{Q}_{ij} dz \quad i, j = 4, 5 \quad (6,7)$$

where  $k$  is the shear correction factor dependent on the shape of the cross-section [14], and  $\bar{Q}_{ij}$  are the transformed material coefficients from the principal material coordinate system to the  $x$ - $y$ - $z$  coordinate system. For the laminated composite beam under study, the couples  $(M_y, M_{xy})$  and the resultant  $Q_{yz}$  can be assumed to be zero. However, the curvatures  $(\kappa_y, \kappa_{xy})$  and the shear strain  $\gamma_{yz}$  are assumed to be non-zero. Thus, Eqs (4) and (5) can be rewritten as

$$M_x = \bar{D}_{11} \kappa_x, \quad Q_{xz} = \bar{A}_{55} \gamma_{xz} \quad (8,9)$$

where

$$\bar{D}_{11} = D_{11} - \frac{D_{12}^2}{D_{22}} + \frac{(D_{12}D_{26} - D_{16}D_{22})^2}{D_{22}(D_{26}^2 - D_{22}D_{66})} \quad (10)$$

$$\bar{A}_{55} = A_{55} - \frac{A_{45}^2}{A_{44}} \quad (11)$$

Note that the  $D_{12}$  term denotes bending-bending stiffness, the  $D_{16}$  and  $D_{26}$  terms refer to bending-twisting stiffness, and the  $A_{45}$  term represents shearing-shearing stiffness of the laminated composite beam.

## Governing Equations

The kinetic energy  $T$  of the laminated composite beam can be written as

$$T = \frac{1}{2} \int_0^L \left[ I_1 \left( \frac{\partial w^0}{\partial t} \right)^2 + I_3 \left( \frac{\partial \psi}{\partial t} \right)^2 \right] b dx \quad (12)$$

where  $I_1$  and  $I_3$  are the translational and rotary inertia of the cross section of the composite beam, defined by

$$I_1 = b \int_{-\frac{h}{2}}^{\frac{h}{2}} \rho dz, \quad I_3 = b \int_{-\frac{h}{2}}^{\frac{h}{2}} \rho z^2 dz \quad (13)$$

and  $\rho$  being the mass density of the composite beam material. The strain energy  $V$  is given by

$$V = \frac{1}{2} \int_0^L \left( M_x \kappa_x + Q_{xz} \gamma_{xz} \right) b \, dx \quad (14)$$

The governing equations for free vibrations of the composite beam can be derived from Hamilton's principle, *i.e.*

$$\int_{t_1}^{t_2} \delta (T - V) \, dt = 0 \quad (15)$$

where  $t_1$  and  $t_2$  are two arbitrary time variables and  $\delta$  denotes the first variation. Substituting Eqs (12) and (14) into Eqn (15) and integrating by parts leads to

$$\bar{A}_{55} \left( \frac{\partial \psi}{\partial x} + \frac{\partial^2 w^0}{\partial x^2} \right) - I_1 \frac{\partial^2 w^0}{\partial t^2} = 0, \quad \bar{D}_{11} \frac{\partial^2 \psi}{\partial x^2} - \bar{A}_{55} \left( \psi + \frac{\partial w^0}{\partial x} \right) - I_3 \frac{\partial^2 \psi}{\partial t^2} = 0 \quad (16)$$

### Solution Procedure

The harmonic solutions to Eqn (16) can be assumed in the form

$$w^0(x, t) = W(x) e^{i\omega t}, \quad \psi(x, t) = \Psi(x) e^{i\omega t} \quad (17)$$

where  $W(x)$  is the lateral vibration mode,  $\Psi(x)$  is the rotational vibration mode and  $\omega$  is the circular frequency. Substitution of Eqs (17) into Eqs (16) yields

$$\frac{d^2 W}{d\xi^2} + p^2 s^2 W + L \frac{d\Psi}{d\xi} = 0, \quad s^2 \frac{d^2 \Psi}{d\xi^2} - (1 - p^2 r^2 s^2) \Psi - \frac{1}{L} \frac{dW}{d\xi} = 0 \quad (18)$$

where

$$p^2 = \frac{I_1 L^4 \omega^2}{\bar{D}_{11}}, \quad r^2 = \frac{I_3}{I_1 L^2}, \quad s^2 = \frac{\bar{D}_{11}}{\bar{A}_{55} L^2}, \quad \xi = \frac{x}{L} \quad (19)$$

By eliminating  $W(\xi)$  and  $\Psi(\xi)$ , Eqs (18) can be transformed into two uncoupled differential equations as

$$\begin{aligned} \frac{d^4 W}{d\xi^4} + p^2 (r^2 + s^2) \frac{d^2 W}{d\xi^2} - p^2 (1 - p^2 r^2 s^2) W &= 0 \\ \frac{d^4 \Psi}{d\xi^4} + p^2 (r^2 + s^2) \frac{d^2 \Psi}{d\xi^2} - p^2 (1 - p^2 r^2 s^2) \Psi &= 0 \end{aligned} \quad (20)$$

The solutions to Eqs (20) can be expressed as

Case (I)  $\left| (r^2 - s^2)^2 + \frac{4}{p^2} \right|^{\frac{1}{2}} > (r^2 + s^2)$  or  $\omega^2 < \bar{A}_{55} / I_3$

$$\begin{aligned} W(\xi) &= A_1 \cosh p\alpha\xi + A_2 \sinh p\alpha\xi + A_3 \cos p\beta\xi + A_4 \sin p\beta\xi \\ \Psi(\xi) &= B_1 \sinh p\alpha\xi + B_2 \cosh p\alpha\xi + B_3 \sin p\beta\xi + B_4 \cos p\beta\xi \end{aligned} \quad (21)$$

where

$$\frac{\alpha}{\beta} = \frac{1}{\sqrt{2}} \left\{ \begin{array}{l} - (r^2 + s^2) + \left[ (r^2 - s^2)^2 + 4 / p^2 \right]^{1/2} \\ + (r^2 + s^2) + \left[ (r^2 - s^2)^2 + 4 / p^2 \right]^{1/2} \end{array} \right\}^{1/2} \quad (22)$$

Case (II)  $\left| (r^2 - s^2)^2 + \frac{4}{p^2} \right|^{\frac{1}{2}} < (r^2 + s^2)$  or  $\omega^2 > \bar{A}_{55} / I_3$

$$\begin{aligned} W(\xi) &= A_1 \cos p\alpha' \xi + i A_2 \sin p\alpha' \xi + A_3 \cos p\beta\xi + A_4 \sin p\beta\xi \\ \Psi(\xi) &= i B_1 \sin p\alpha' \xi + B_2 \cos p\alpha' \xi + B_3 \sin p\beta\xi + B_4 \cos p\beta\xi \end{aligned} \quad (23)$$

where  $\alpha' = \alpha / i$ . The constants are related by the coupled Eqs (18) as

$$\begin{aligned} B_1 &= -\frac{p}{L} \frac{(\alpha^2 + s^2)}{\alpha} A_1, & B_2 &= -\frac{p}{L} \frac{(\alpha^2 + s^2)}{\alpha} A_2 \\ B_3 &= \frac{p}{L} \frac{(\beta^2 - s^2)}{\beta} A_3, & B_4 &= -\frac{p}{L} \frac{(\beta^2 - s^2)}{\beta} A_4 \end{aligned} \quad (24)$$

Boundary conditions and frequency equation

The associated boundary conditions for the composite beam under consideration may be written as

$$\text{at } x = 0, \quad \bar{D}_{11} \frac{\partial \psi}{\partial x} = k_r \psi \quad (25a)$$

$$\bar{A}_{55} \left( \psi + \frac{\partial w^0}{\partial x} \right) = k_t w^0 \quad (25b)$$

$$\text{at } x = L, \quad \bar{D}_{11} \frac{\partial \psi}{\partial x} = -(J + M d^2) \frac{\partial^2 \psi}{\partial t^2} + M d \frac{\partial^2 w^0}{\partial t^2} \quad (25c)$$

$$\bar{A}_{55} \left( \psi + \frac{\partial w^0}{\partial x} \right) = -M \frac{\partial^2 w^0}{\partial t^2} + M d \frac{\partial^2 \psi}{\partial t^2} \quad (25d)$$

where  $\bar{k}_r$  and  $\bar{k}_t$  are the rotational and translational spring stiffnesses, respectively.  $J$  is the rotational moment of inertia of the tip mass,  $M$  is the tip mass, and  $d$  is the distance between the center of gravity of the tip mass and the point of attachment. Using Eqs (17) and the non-dimensional variable  $\xi$ , Eqs (25) may be rewritten as

$$\text{at } \xi = 0, \quad \frac{\partial \Psi}{\partial \xi} = \frac{L k_r}{\bar{D}_{11}} \Psi \quad (26a)$$

$$\Psi + \frac{1}{L} \frac{\partial W}{\partial \xi} = \frac{k_t}{\bar{A}_{55}} W \quad (26b)$$

$$\text{at } \xi = 1, \quad \frac{\bar{D}_{11}}{L} \frac{\partial \Psi}{\partial \xi} = (J + M d^2) \omega^2 \Psi - M d \omega^2 W \quad (26c)$$

$$\bar{A}_{55} \left( \Psi + \frac{1}{L} \frac{\partial W}{\partial \xi} \right) = M \omega^2 W - M d \omega^2 \Psi \quad (26d)$$

With the help of relations of integration constants in Eqs (24), inserting the solutions Eqs (21) into the boundary conditions Eqs (26) gives four homogeneous linear algebraic equations. In order that the solution other than zero exists, the coefficients  $A_i$  ( $i = 1, 2, \dots, 4$ ) must be equal to zero. This leads to the determinantal equation as

$$\begin{vmatrix} k_{11} & k_{12} & k_{13} & k_{14} \\ k_{21} & k_{22} & k_{23} & k_{24} \\ k_{31} & k_{32} & k_{33} & k_{34} \\ k_{41} & k_{42} & k_{43} & k_{44} \end{vmatrix} = 0 \quad (27)$$

The coefficients  $k_{ij}$  in Eqn (27) are omitted because of space limitations. For a given beam, the frequency coefficients  $p_i$  ( $i = 1, 2, 3, \dots$ ) can be found by solving the frequency equation (27), and the corresponding natural frequencies  $\omega_i$  ( $i = 1, 2, 3, \dots$ ) can then be calculated from Eqs (19). The roots of Eqn (27) are obtained by applying the false position method [15] with a tolerance of  $\varepsilon = 10^{-8}$ .

## NUMERICAL RESULTS AND DISCUSSION

In order to verify the validity of the present formulation, we analyze the free vibrations of a laminated composite beam made of AS/3501-6 graphite-epoxy with the following material properties [8] :

$$\begin{aligned} E_1 &= 144.79 \text{ GPa}, \quad E_2 = 9.65 \text{ GPa}, \quad G_{23} = 3.45 \text{ GPa} \\ G_{12} &= G_{13} = 4.14 \text{ GPa}, \quad \nu_{12} = 0.3, \quad \rho = 1389.23 \text{ kg / m}^3 \end{aligned}$$

The short-thick beam ( $L/h = 15$  or  $r = 0.019$ ) is considered for the purpose of comparison with the available exact solutions. The beam width  $b$  is taken as unity for all the problems. The shear correction factor  $k$  is taken as  $5/6$  for the rectangular cross-section. The frequency results are given in the non-dimensional form

$$\bar{\omega} = \omega L^2 \sqrt{\rho / E_1 h^2} \quad (28)$$

For computational convenience, the following non-dimensional parameters are introduced :

$$\bar{k}_r = k_r L / E_1 I, \quad \bar{k}_t = k_t L^3 / E_1, \quad \bar{M} = M / m, \quad \bar{d} = d / L, \quad \bar{R} = R / L \quad (29)$$

where  $I$  is the second moment of area of the beam cross-section,  $m$  is the mass of the beam and  $R$  is the radius of gyration, which is directly related to  $J = MR^2$ .

Table 1 shows the first five natural frequencies of a cross-ply laminated composite beam with different degrees of constraint at one end. It is seen that the natural frequencies of the composite beam increase with increasing  $\bar{k}_r$  and  $\bar{k}_t$  and approach those of a cantilever composite beam from Ref.[8]. Figure 3 displays the effect of ply orientation on the fundamental frequency of the composite beam with a rotational and translational constraint at one end. It is important to note that the fundamental frequency of the composite beam becomes smallest at the ply orientation  $[49.4/-40.6]_s$ . Although not shown here, the same

tendency is observed for the higher mode frequencies. This may be due to the fact that the shear deformation parameter  $s$  in Eqs (19) for the composite beam has a minimum at this ply orientation in the region  $0^\circ < \theta < 90^\circ$ .

The influences of the various parameters are presented in three-dimensional graphs of the non-dimensional natural frequency. Figure 4 shows that the tip mass  $M$  reduces significantly the fundamental frequency of the composite beam more than the radius of gyration of the tip mass  $R$ . Figure 5 indicates the effects of the tip mass  $M$  and the distance  $d$  between the tip mass centroid and the point of attachment on the fundamental frequency. As with Fig.4, the tip mass  $M$  has a greater effect on the fundamental frequency than the distance  $d$ . Figure 6 represents the influences of  $R$  and  $d$  on the fundamental frequency of the composite beam with a constant tip mass at the free end. Obviously the effect of  $d$  on the fundamental frequency is higher than that of  $R$ .

### CONCLUSIONS

The natural frequencies of a symmetrically laminated composite beam with one end elastically supported and carrying a tip mass at the other free end have been calculated and plotted. A parametric study was conducted to examine the individual effects of ply orientation, beam end constraint, tip mass and distance between the center of gravity of the tip mass and the point of attachment on the natural frequencies of the composite beam. The accuracy of the numerical results was confirmed by comparison with the available frequency results. The present results show that the increase in the (tip mass)/(beam mass) ratio, the (radius of gyration of the tip mass)/(beam length) ratio and the (distance between the center of gravity of the tip mass and the point of attachment)/(beam length) ratio yields the decrease in the fundamental frequencies.

### REFERENCES

1. Vinson, J.R. and Sierakowski, R.L., *The Behavior of Structures Composed of Composite Materials*, Kluwer Academic Publishers, Dordrecht, 1987, p.119-147.
2. Abarcar, R.B. and Cunniff, P.F., "The Vibration of Cantilever Beams of Fibre Reinforced Material", *Journal of Composite Materials*, Vol.6, 1972, pp.504-517.
3. Teoh, L.S. and Huang, C.C., "The Vibration of Beams of Fibre Reinforced Material", *Journal of Sound and Vibration*, Vol.51, No.4, 1977, pp.467-473.
4. Teh, K.K. and Huang C.C., "The Vibrations of Generally Orthotropic Beams, A Finite Element Approach", *Journal of Sound and Vibration*, Vol.62, No.2, 1979, pp.195-206.
5. Teh, K.K. and Huang, C.C., "The Effects of Fibre Orientation on Free Vibrations of Composite Beams", *Journal of Sound and Vibration*, Vol.69, No.2, 1980, pp.327-337.
6. Chen, A.T. and Yang, T.Y., "Static and Dynamic Formulation of a Symmetrically Laminated Beam Finite Element for a Microcomputer", *Journal of Composite Materials*, Vol.19, 1985, pp.459-475.

7. Suresh, J. K., Venkatesan, C. and Ramamurti, V., "Structural Dynamic Analysis of Composite Beams", *Journal of Sound and Vibration*, Vol.143, No.3, 1990, pp.503-519.
8. Chandrashekhara, K., Krishnamurthy, K. and Roy, S., "Free Vibration of Composite Beams Including Rotary Inertia and Shear Deformation", *Composite Structures*, Vol.14, 1990, pp.269-279.
9. Abramovich, H., "Shear Deformation and Rotary Inertia Effects of Vibrating Composite Beams", *Composite Structures*, Vol.20, 1992, pp.165-173.
10. Chandrashekhara, K. and Bangera, K. M., "Vibration of Symmetrically Laminated Clamped-Free Beam with a Mass at the Free End", *Journal of Sound and Vibration*, Vol.160, No.1, 1993, pp.93-101.
11. Krishnaswamy, K., Chandrashekhara, K. and Wu, W.Z.B., "Analytical Solutions to Vibration of Generally Layered Composite Beams", *Journal of Sound and Vibration*, Vol.159, No.1, 1992, pp.85-99.
12. Abramovich, H. and Livshits, A., "Free Vibrations of Non-Symmetric Cross-Ply Laminated Composite Beams", *Journal of Sound and Vibration*, Vol.176, No.5, 1994, pp.597-612.
13. Abramovich, H., Eisenberger, M. and Shulepov, O., "Vibrations and Buckling of Cross-Ply Nonsymmetric Laminated Composite Beams", *AIAA Journal*, Vol.34, No.5, 1996, pp.1064-1069.
14. Cowper, G.R., "The Shear Coefficient in Timoshenko's Beam Theory", *Journal of Applied Mechanics*, Vol.33, 1966, pp.335-340.
15. Conte, S.D. and de Boor, C., *Elementary Numerical Analysis: An Algorithmic Approach*, 3rd Ed., McGraw-Hill, 1981, p.72.



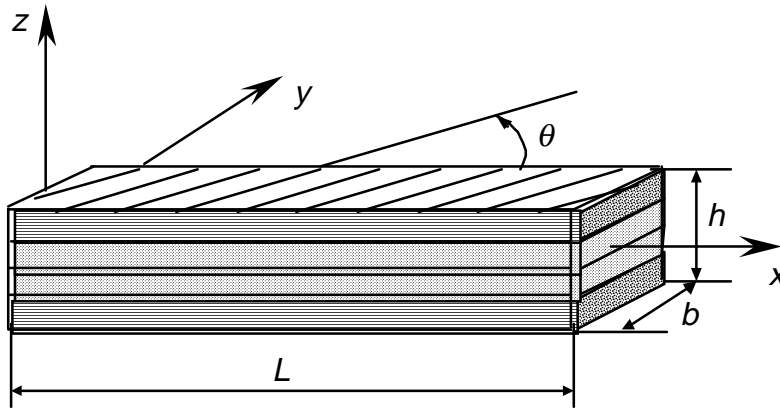


Fig.1. Coordinate system and dimensions of a laminated composite beam.

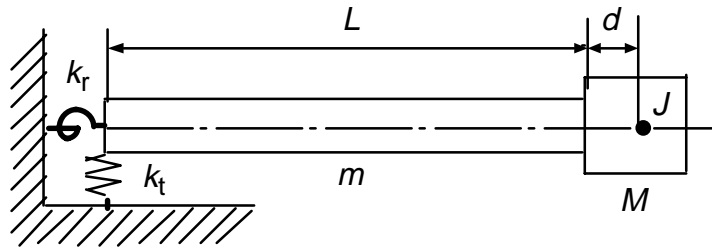


Fig. 2. A laminated composite beam with a rotational and translational constraint at one end and carrying a tip mass at the other free end.

Table 1. Non-dimensional natural frequencies of a cross-ply laminated composite beam with different degrees of constraint at one end ( $L/h = 15$ )

$$(\bar{M} = \bar{d} = \bar{R} = 0) \quad [0/90/90/0]$$

Mode No. \ $\bar{k}_r = \bar{k}_t$	$10^0$	$10^2$	$10^4$	$10^6$	cantilever (Ref. 8)
1	0.2492	0.8800	0.9226	0.9231	<b>0.9241</b>
2	0.9568	3.6710	4.8739	4.8888	<b>4.8925</b>
3	5.9228	8.1904	11.3731	11.4345	<b>11.4400</b>
4	13.0597	14.8569	18.5699	18.6920	<b>18.6972</b>
5	20.9092	22.3594	26.0309	26.2082	<b>26.2118</b>

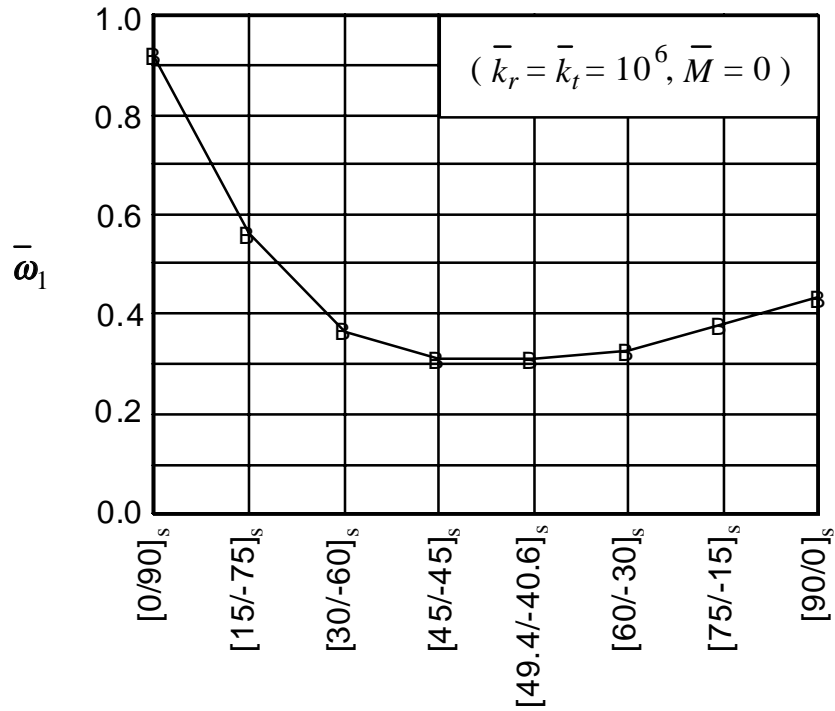


Fig.3. Effect of ply orientation on fundamental frequency of a laminated composite beam with a rotational and translational constraint at one end.

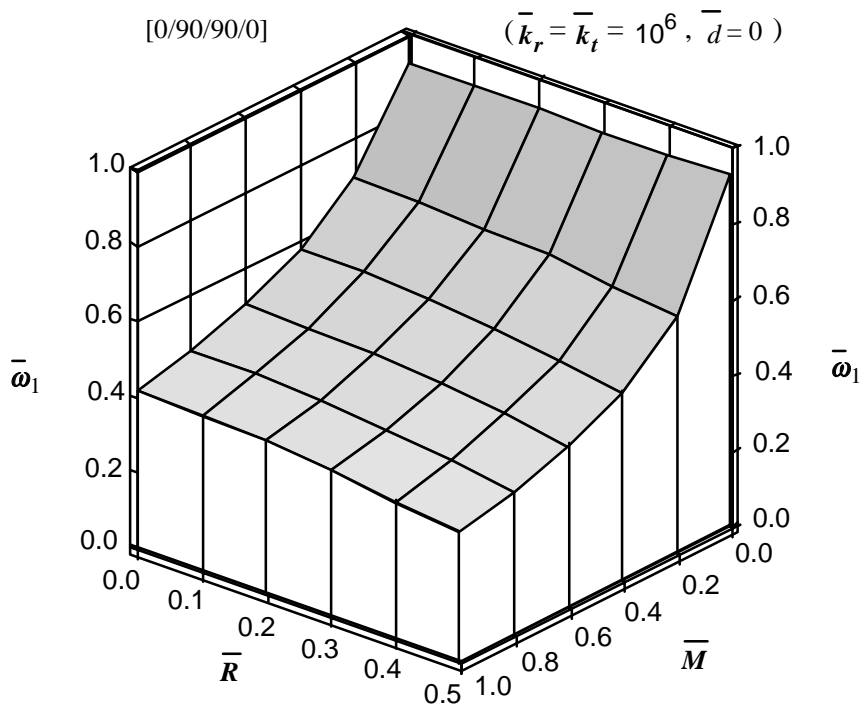


Fig.4. Non-dimensional fundamental frequency versus  $\bar{R}$  and  $\bar{M}$  for a cross-ply laminated composite beam with a rotational and translational constraint at one end.

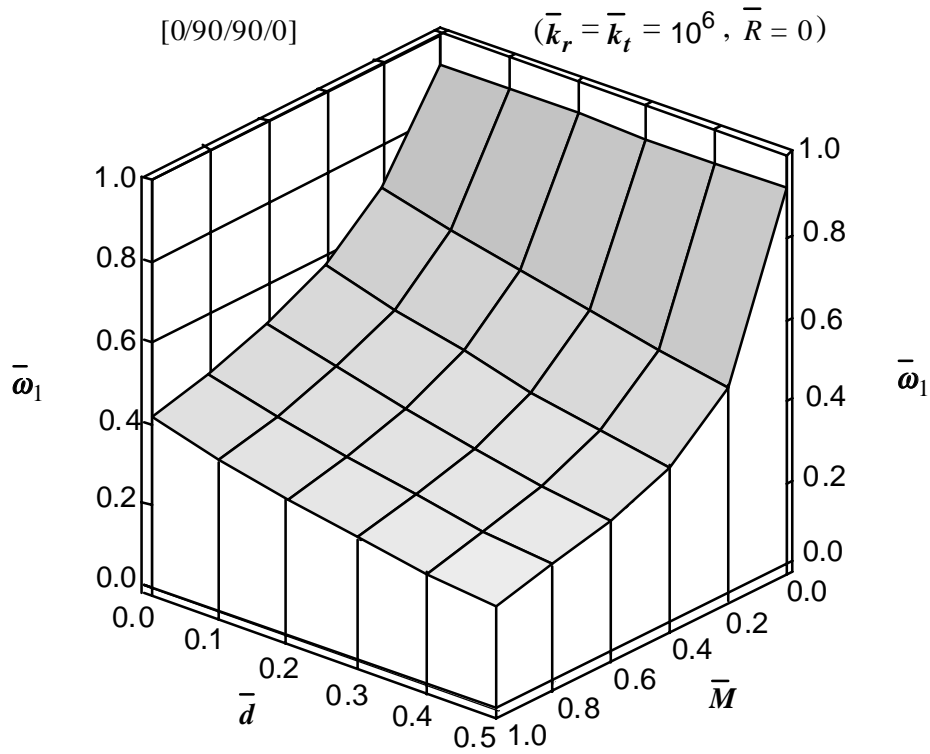


Fig.5. Non-dimensional fundamental frequency versus  $\bar{d}$  and  $\bar{M}$  for a cross-ply laminated composite beam with a rotational and translational constraint at one end.

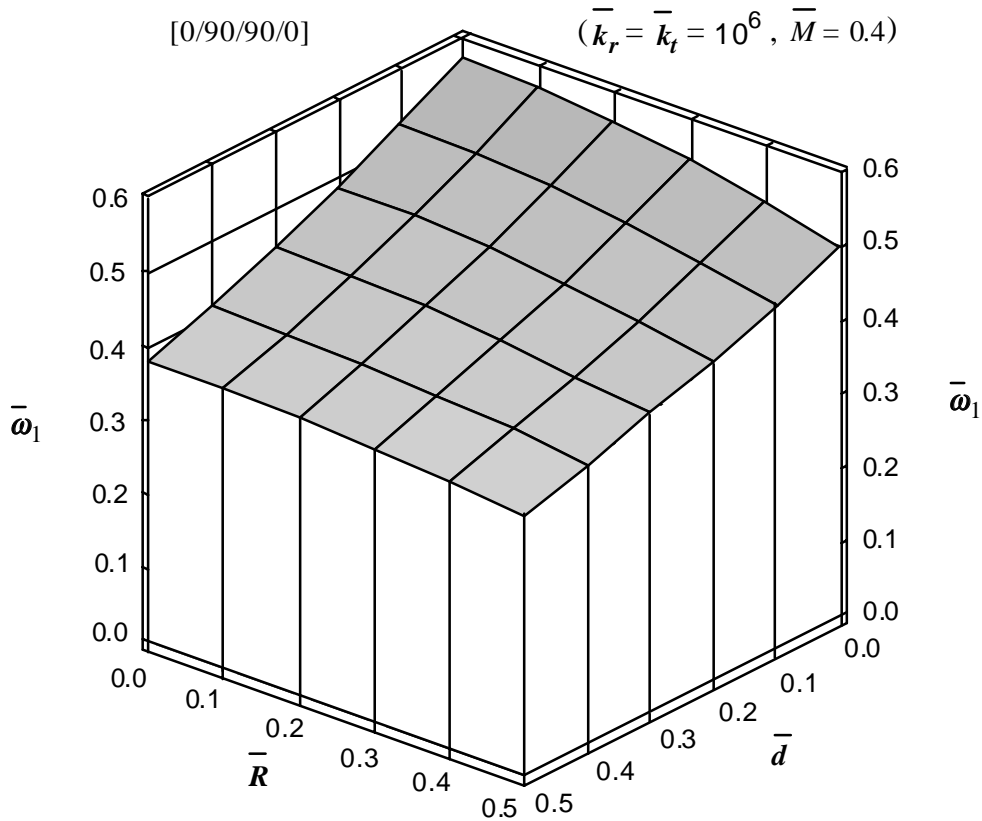


Fig.6. Non-dimensional fundamental frequency versus  $\bar{R}$  and  $\bar{d}$  for a cross-ply laminated composite beam with a rotational and translational constraint at one end and having a constant tip mass at the other free end.

# FATIGUE BEHAVIOUR OF COMMINGLED CF/PEEK COMPOSITES

Lin Ye, Xiaoxue Diao and Yiu-Wing Mai

*Centre for Advanced Materials Technology, Department of Mechanical & Mechatronic Engineering, The University of Sydney, NSW 2006, Australia*

**SUMMARY:** The static and fatigue properties of continuous AS4 carbon fibre (CF) reinforced polyetheretherketone (PEEK) composite laminates made from commingled unifabric prepreg were investigated under static tension and tension-tension fatigue loading. Three different lay-ups were studied, namely  $[0]_{16}$ ,  $[90]_{16}$  and  $[0_2/90_2]_{2S}$ . The results for static stiffness and strength as well as fatigue life and residual strength under different fatigue stress amplitudes were evaluated, and the damage and failure mechanisms of the composite laminates were discussed. The wear-out model was applied to fit the S-N curves and estimate residual strength of composite laminates, and good correlation was obtained. Compared to composite laminates made from pre-impregnated tape prepreg (e.g. APC-2), the commingled CF/PEEK composite laminates are more sensitive to fatigue loading because of imperfect fibre bundle alignment.

**KEYWORDS:** fatigue behaviour, CF/PEEK composites, commingled prepreg, tension-tension fatigue, damage mechanisms

## INTRODUCTION

Fatigue behaviour of a composite structure is an important property for engineering applications. For many years the primary matrix materials used in polymer-based composites have been thermosets. High performance thermoplastics have been introduced as matrix materials in recent years, which have many advantages over their thermosetting counterparts. In particular, thermoplastic matrices offer the potential for simpler, less time-consuming manufacturing cycles [1,2]. Continuous carbon fibre (CF) reinforced polyether-ether-ketone (PEEK) composites constitute one group of the most competitive materials in the aerospace and defence industries. CF/PEEK prepreg is usually supplied in a form of pre-impregnated tapes (e.g. APC-2). However, more recently CF/PEEK prepreg has been available in form of a woven fabric, consisting of unidirectional and continuous carbon fibres mingled with continuous PEEK fibres, which are interwoven with continuous PEEK fibres in the transverse direction. This type of prepreg is particularly suitable for manufacturing components of complex geometry. The fatigue behaviour of CF/PEEK composites produced from this type of prepreg has not been studied comprehensively. The main objectives of this work are to investigate the static and fatigue properties of commingled unifabric CF/PEEK composite laminates under static tension and tension-tension fatigue loading and to compare them with those of continuous CF/PEEK composite laminates made from the pre-impregnated tape prepreg (e.g. APC-1, APC-2). The damage and failure mechanisms in the composite laminates are discussed and the fatigue performance of the laminates is evaluated using the wear-out model.

## MATERIAL PREPARATION AND EXPERIMENTAL PROCEDURE

The material used in this study was commingled continuous carbon fibre reinforced PEEK unifabric (UD AS4 3K/PEEK) supplied by the Polymer Research Division, BASF. A diagram of the commingled unifabric system is shown in Fig. 1. The diameter of PEEK fibres is approximately 130  $\mu\text{m}$  in the cross-weave and 30  $\mu\text{m}$  in the longitudinal direction, where PEEK fibres were mingled with carbon fibres. The global weight percentage of PEEK polymer in the preform is 32%. With a density of 1.265  $\text{g}/\text{cm}^3$  for non-crystallised PEEK [3], the fibre volume fraction amounts to 55% in a fully consolidated composite.

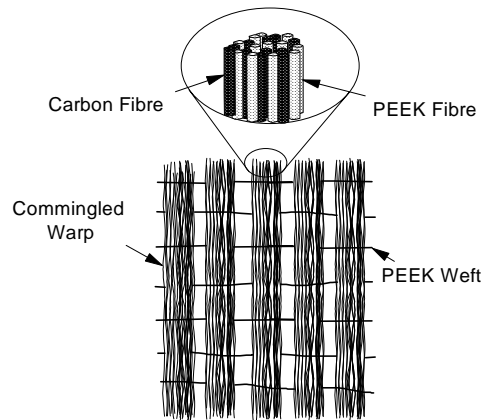


Fig. 1 Schematics of commingled CF/PEEK composite unifabric prepreg.

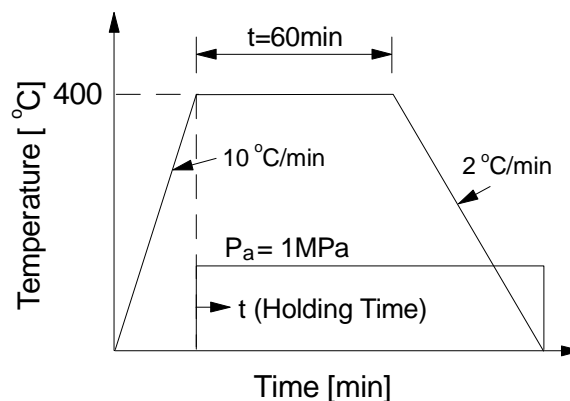


Fig. 2 Processing cycle of CF/PEEK laminates from commingled unifabric prepreg.

Unidirectional prepreg layers were produced through “edge-welding” the unifabric with a soldering iron into 199×199 mm sheets, with subsequent cutting. The prepreg layers were then placed in a steel mould of a 200×200 mm square cavity in specified stacking sequences and consolidated using a laboratory hot press. Two different lay-ups were chosen in manufacturing the panels, i.e. unidirectional  $[0]_{16}$  and  $[0_2/90_2]_{2S}$ . The 16 layers of prepreg gave a subsequent panel thickness of approximate 2.2 mm after consolidation. Upilex® polyimide films (50  $\mu\text{m}$  in thickness) coated with Frekote®-FRP release agent were used between the prepreg stack and the mould surface to ensure easy removal of the panels after consolidation. The processing cycles of the composite laminates are outlined in Fig. 2.

Two different geometries of specimens were chosen, i.e. “straight-side” for static tests and “dog-bone shape” for fatigue tests, shown in Fig. 3. The specimens were end-tabbed for

testing, bonding aluminium tabs of 40 mm in length and 2 mm in thickness with a CIBA-GEIGY Araldite superstrength adhesive.

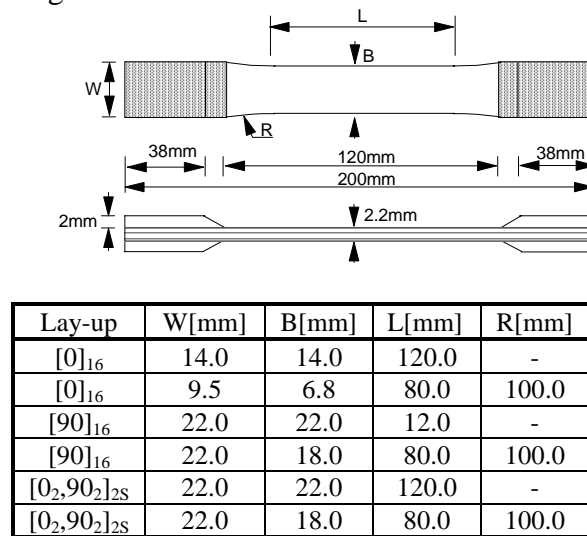


Fig. 3 Geometrical dimensions of coupon specimens.

The static tensile tests were performed using Instrons 1195 and 5567 respectively at a constant cross-head rate of 1.0 mm/min. A clip gauge with a gauge length of 25 mm was attached to the middle part of specimens during testing to measure the strain response and consequently determine the stiffness. The fatigue tests were conducted on an Instron 8501 hydraulic serve machine under load control at a frequency of 8 Hz with a stress ratio of 0.1. Some tests were continued until the specimen failed in order to establish S-N curves, the rest tests were terminated at specified stages of fatigue life for measurements of residual-tensile stiffness and strength as well as investigations of damage mechanisms.

## RESULTS AND DISCUSSION

### Static Properties

From the stress-strain response, the static strength and stiffness of laminates with three different lay-ups are determined, listed in Table 1, which are compared with the corresponding properties of XAS/PEEK (APC-1,  $V_f=55\%$ ) [4], AS4/PEEK (APC-2,  $V_f=60\%$ ) [1] and AS4/Epoxy ( $V_f=68\%$ ) [5] laminates as well as those of a pure PEEK resin [3] in Fig. 4. The longitudinal tensile strength of the CF/PEEK commingled unidirectional composite laminate is 17% higher than that of APC-1 composite which is of the same fibre volume fraction as the former, but is clearly lower than those of APC-2 and AS4/Epoxy composites because these are of higher fibre volume fractions. In principle, the longitudinal tensile strength of the CF/PEEK commingled composite laminates should be lower than that of composites of the same fibre volume fraction made from the pre-impregnated tape prepreg, because in the former the fibres are not stretched out as in the latter so that the fibre reinforcement is not as effective as in the latter. However, the reason why the CF/PEEK commingled composite is of higher static tensile strength than APC-1 is probably due to the fact that the strength of AS4 fibres is about 16% higher than that of XAS fibres [6]. The longitudinal stiffness of the CF/PEEK commingled composite is about 10% lower than those of APC-2 and AS4/Epoxy because of higher fibre volume fractions in both composites.

The average transverse tensile strength of the CF/PEEK commingled composite is almost the same to that of APC-2 [1] but is 28% higher than that of AS4/Epoxy composites, indicating that the failure strength of unidirectional composites under transverse tension is controlled by the matrix strength. The transverse strengths of all PEEK matrix composites are lower than that of the pure PEEK resin as shown in Fig. 6. Unlike the longitudinal tensile strength which is determined almost entirely by the fibre strength, the transverse tensile strength is governed by many factors including properties of the fibre and matrix, the interface bond strength, the presence and distribution of voids, the residual stress and interactions between these mechanisms. The transverse stiffnesses of CF/PEEK, APC-2 and AS4/Epoxy are quite close to each other, and they are all much higher than that of the pure PEEK resin.

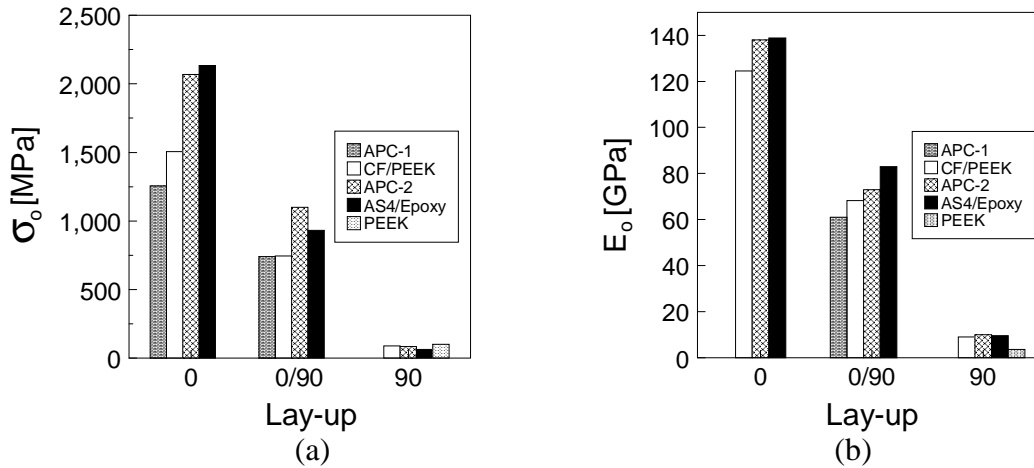


Fig. 4. Static strength (a) and stiffness (b) of CF/PEEK commingled laminates in comparison with those of other composite materials.

Table 1 Properties of commingled CF/PEEK composite laminates

Lay-up	Strength $\sigma_o$		Stiffness $E_o$		Ultimate Strain	
	Mean [MPa]	CV[%]	Mean [MPa]	CV[%]	Mean [MPa]	CV[%]
[0] <sub>16</sub>	1507.05	7.20	124.57	3.43	1.17	17.20
[90] <sub>16</sub>	88.61	9.58	9.03	1.56	1.31	7.57
[0 <sub>2</sub> /90 <sub>2</sub> ] <sub>2S</sub>	744.17	8.87	68.27	4.73	1.18	6.15

The static uniaxial strength of the CF/PEEK [0<sub>2</sub>/90<sub>2</sub>]<sub>2S</sub> cross-ply laminate is very close to that of APC-1 [7] laminate with 11 plies (six in the axial direction and five in the transverse direction) because of the higher strength of AS4 fibres although a [0<sub>2</sub>/90<sub>2</sub>]<sub>2S</sub> laminate contains a less percentage of 0° plies. The uniaxial stiffness of CF/PEEK [0<sub>2</sub>/90<sub>2</sub>]<sub>2S</sub> laminate is 7% lower than APC-2 and 13% lower than AS4/Epoxy, but about 10% higher than APC-1.

### Fatigue Properties

The experimental S-N data for the CF/PEEK composites with three different lay-ups are shown in Figs. 5-7 with comparison with those of unidirectional and cross-ply APC-1 [4] as well as the best fit curve of the pure PEEK resin [3], respectively. Compared with APC-1,

the S-N data of the unidirectional CF/PEEK commingled composite exhibit quicker degradation in Fig. 4, indicating that this material is more fatigue sensitive.

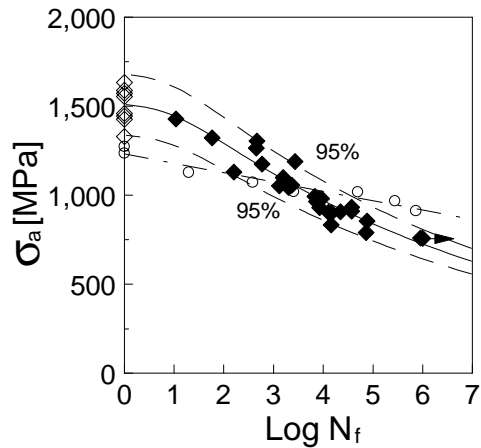


Fig. 5 S-N curve of unidirectional  $[0]_{16}$  CF/PEEK laminate ( $\diamond$ : static data,  $\blacklozenge$ : fatigue data) in comparison with APC-1 ( $\circ$ ).

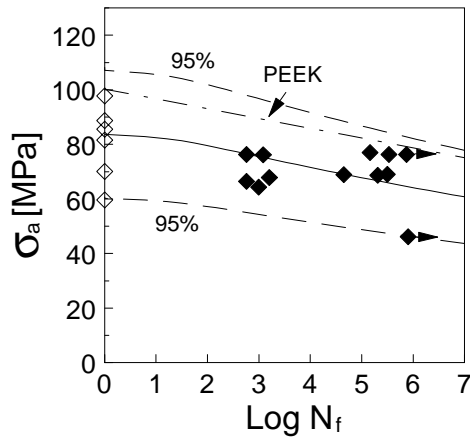


Fig. 6 S-N curve of unidirectional  $[90]_{16}$  CF/PEEK laminate ( $\diamond$ : static data,  $\blacklozenge$ : fatigue data) in comparison with PEEK resin.

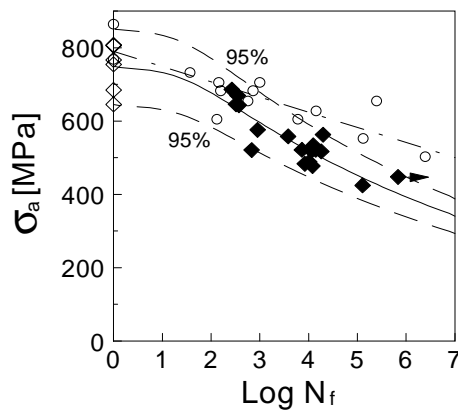


Fig. 7 S-N curve of cross-ply  $[0_2/90_2]_{2S}$  CF/PEEK laminate ( $\diamond$ : static data,  $\blacklozenge$ : fatigue data) in comparison with APC-1 ( $\circ$ ).



The data of cross-ply laminates shown in Fig. 5 exhibit the same trend, and the experimental results of APC-1 cross-ply laminates are almost always above those of CF/PEEK laminates because of a higher percentage of  $0^\circ$  plies. The data of the CF/PEEK  $[90]_{16}$  laminates are much more scattered. The best fit curve of S-N data for the pure PEEK resin is above all the data of the CF/PEEK laminates shown in Fig. 6.

### Performance Degradation

A series of tests for measurements of residual-tensile stiffness and strength were conducted on the unidirectional  $[0]_{16}$  and cross-ply  $[0_2,90_2]_{2S}$  CF/PEEK composite laminates which had been fatigued for some specified cycles. The residual strength degradation with cycle number for the CF/PEEK  $[0]_{16}$  and  $[0_2,90_2]_{2S}$  composite laminates subjected to different fatigue stress levels is plotted in Fig. 8, which exhibit large scatter in experimental data. There is globally little degradation in residual strength during most part of fatigue life for both laminates until the final stage of fatigue damage which causes dramatic degradation in residual strength followed by catastrophic failure of the laminates.

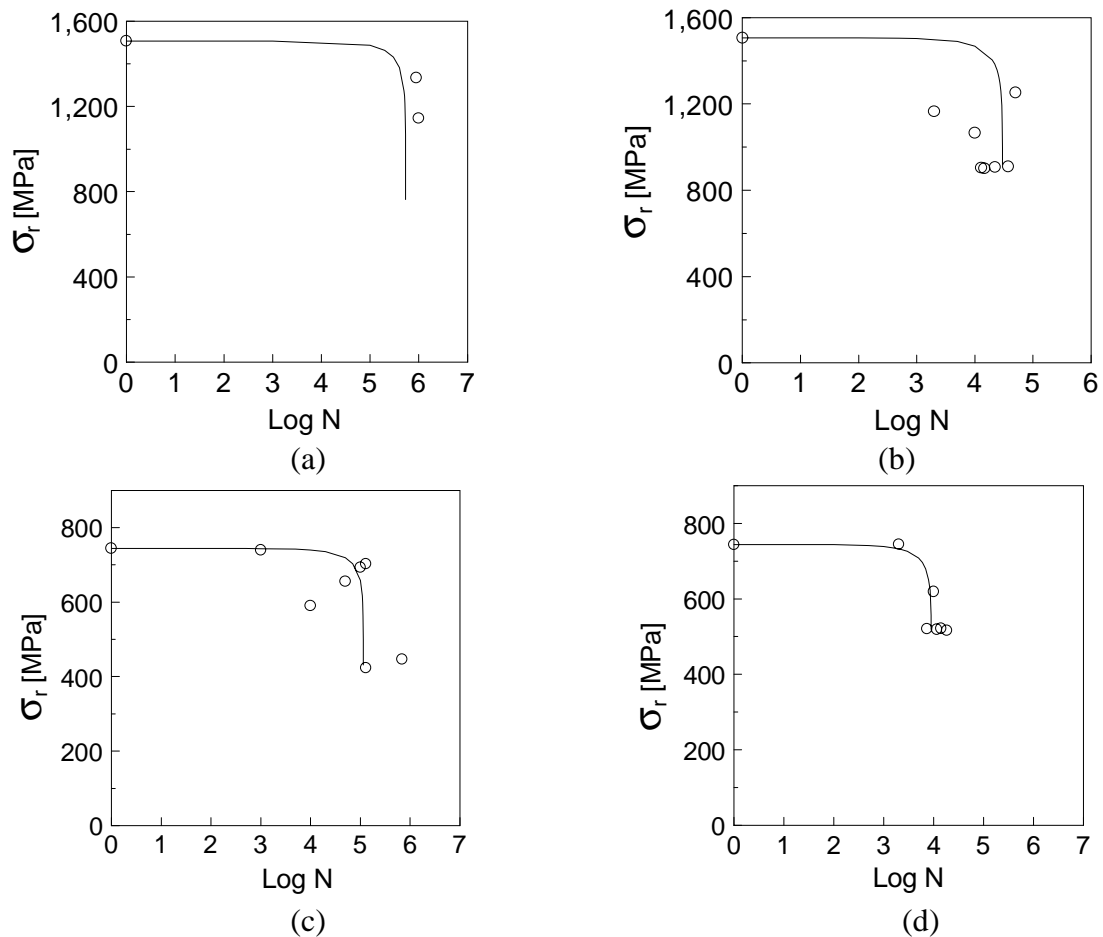


Fig. 8 Residual strength for  $[0]_{16}$  unidirectional laminate (a)  $\sigma_a=50\%\sigma_o$ , (b)  $\sigma_a=60\%\sigma_o$  and  $[0_2/90_2]_{2S}$  cross-ply laminate (c)  $\sigma_a=60\%\sigma_o$ , (d)  $\sigma_a=70\%\sigma_o$ , ——— wear-out model, o: experimental data.

## Failure Mechanisms

Under both static and fatigue loading, fibre breakage is the main micro-damage mode for the unidirectional laminate, which occurs either individually or in the form of bundles as shown in Fig. 9. In the areas where fibres are stretched out, fibres usually break or fragment randomly, while in the areas where fibre bundles are misaligned, fibre bundles fracture occurs because of local stress concentration (Fig. 9b). With the increase of fatigue cycle the fibre bundle fracture occurs continuously. This probably is the reason why the CF/PEEK commingled laminates is much more fatigue sensitive than APC-1. The fibre/matrix interfacial adhesion appeared to be quite good because the isolated and broken fibres are almost never stripped but always coated with the PEEK matrix, shown by the scanning electron microscopy (Fig. 9c).

The  $[0_2/90_2]_{2S}$  cross-ply laminate exhibits multiple damage modes including transverse matrix cracking in the  $90^\circ$  plies in the first stage of damage development and delamination growth along the interfaces between  $0^\circ$  and  $90^\circ$  plies originated from the tips of transverse matrix cracks at the late stage of damage development, and final fibre breakage in  $0^\circ$  plies. Fig. 10 shows the polished edge of a failed specimen under static loading, illustrating transverse matrix cracks and extensive delamination. When the laminate is subjected to fatigue loading, damage usually starts in  $90^\circ$  plies in the form of matrix cracking, which multiplies in number and extends in length with the increase of fatigue cycle. Delamination then initiates at the tips of transverse matrix cracks and propagates through the  $0/90$  interface (Fig. 11), causing the continuous load transfer from  $90^\circ$  plies to  $0^\circ$  plies until the massive fibre breakage occurs in  $0^\circ$  plies, which results in the catastrophic failure of the specimen. However, although numerous transverse matrix cracks and large delaminations are observed in the post-failed specimens, the damage in the CF/PEEK composite laminates appears fairly late at the present fatigue stress levels. This phenomenon is different from that of carbon/epoxy laminates [5], in which transverse matrix cracks appear quickly because of brittle characteristics of epoxy resins. In the CF/PEEK composite laminates the tough characteristics of PEEK matrix delay the damage initiation to a late stage of the fatigue life.

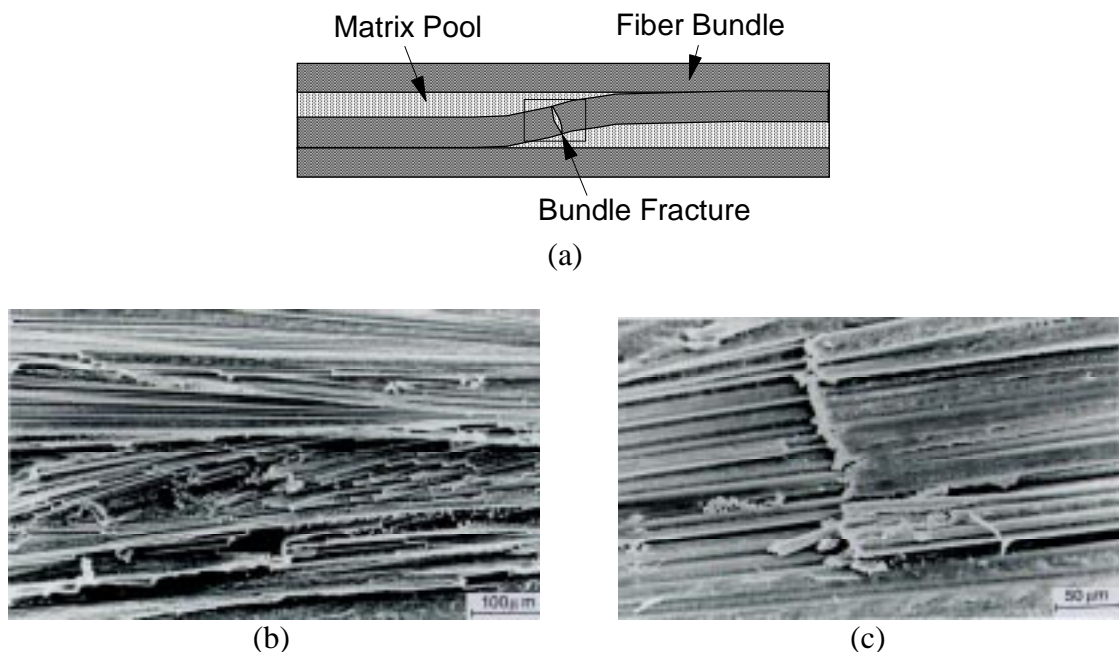


Fig. 9 Schematic of misaligned fibre bundle (a), SEM photography of fracture of misaligned bundles (b) and fibre/matrix adhesion (c).



Fig. 10 Photography of the polished edge of a failed  $[0_2/90_2]_{2S}$  specimen under static loading.

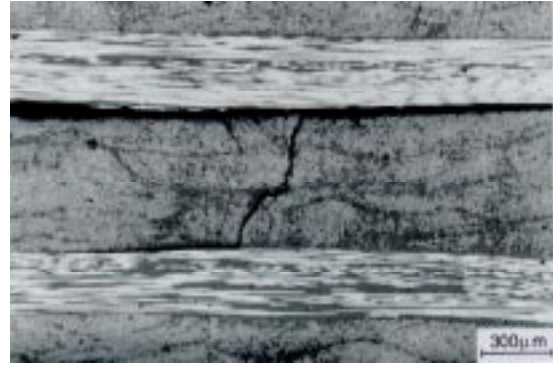


Fig. 11 Photography illustrating micro-fracture modes in  $[0_2/90_2]_{2S}$  laminate subjected to cyclic stress  $\sigma_a=60\%\sigma_o$  for  $N=684,000$  cycles

### WEAR-OUT MODEL ANALYSIS

To evaluate the fatigue behaviour of the CF/PEEK laminates of different lay-ups, the wear-out model of residual strength proposed by Halpin et al. [8] is applied. The degradation of residual strength of composites under fatigue loading is assumed to be in the form of

$$\sigma_r^\gamma = \sigma_o^\gamma - A\sigma_a^\gamma(N-1) \quad (1)$$

where  $\sigma_r$ ,  $\sigma_o$ ,  $\sigma_a$  are the residual strength, the static strength and the maximum applied cyclic stress, respectively,  $\gamma$  and  $A$  are material constants to be determined. This equation means that the strength of a composite laminate decreases from the initial value  $\sigma_o$  to  $\sigma_r$  after  $N$  cycles of fatigue loading with the maximum cyclic stress  $\sigma_a$ . When the residual strength equals to the maximum applied stress, i.e.  $\sigma_r=\sigma_a$ , Eq. (1) is reduced to the S-N relation of the laminate,

$$\sigma_e = \sigma_a [1 + A(N-1)]^S, \quad S = \frac{1}{\gamma} \quad (2)$$

where  $\sigma_e$  is the equivalent static strength. The formulation of the wear-out model is completed assuming that the equivalent static strength obeys a two-parameter Weibull distribution, and the probability of the static strength higher than  $\sigma_e$ , or the reliability, is given by

$$P(\sigma_e) = \exp\left\{-\left(\frac{\sigma_e}{\beta}\right)^\alpha\right\} \quad (3)$$

where  $\alpha$  and  $\beta$  are the Weibull shape and scale parameters, respectively. To evaluate fatigue behaviour of composite laminates, these four parameters  $\gamma$ ,  $A$ ,  $\alpha$  and  $\beta$  can be determined, fitting the wear-out model to the experimental data.

The model parameters, calculated with the maximum likelihood method [9, 10], are obtained for the CF/PEEK laminates of three different lay-ups, listed in Table 2. The S-N curve of each composite laminate calculated from Eq. (2), with the equivalent static strength determined by

$\sigma_e = \beta \Gamma (1 + 1/\alpha)$ , is shown as a solid line in Figs. 5-7, respectively. The dashed lines denote the 95% confidence level. It can be seen that the wear-out model provides a good estimation to the experimental data.

*Table 2. Parameters of fatigue model for CF/PEEK commingled composite laminates.*

Lay-up	S	A	$\alpha$	$\beta$ [MPa]
[0] <sub>16</sub>	0.0630	0.1117	21.80	1549.25
[90] <sub>16</sub>	0.0237	0.0629	8.78	88.19
[0 <sub>2</sub> /90 <sub>2</sub> ] <sub>2S</sub>	0.0604	0.0409	17.69	769.66

The residual strength degradation behaviour is simulated for both unidirectional [0]<sub>16</sub> and cross-ply laminates [0<sub>2</sub>/90<sub>2</sub>]<sub>2S</sub> at different fatigue stress levels using the model parameters in Table 2, which is shown as a solid line in Fig. 8. The difference between the wear-out model and experimental data for the [0]<sub>16</sub> laminate at a fatigue stress level of 50% static strength is clearly visible. While for other stress levels, the wear-out model is correlated with the experimental data very well for both [0]<sub>16</sub> and [0<sub>2</sub>/90<sub>2</sub>]<sub>2S</sub> laminates.

## CONCLUSIONS

Based on the present study, the following points can be highlighted:

1. The static properties of the CF/PEEK composite laminates made from commingled unifabric prepreg are higher than those of APC-1 because of the higher tensile strength of AS4 fibres, but are clearly lower than those of APC-2 due to a lower fibre volume fraction.
2. The composite laminates exhibit higher fatigue sensitivity under tension-tension fatigue loading than APC-1 because of fibre bundle breakage at the locations where fibre bundles are misaligned.
3. The matrix cracking in transverse plies and extensive delaminations between 0° and 90° plies initiated from the tips of transverse matrix cracks are two main damage mechanisms in the cross-ply laminate. Compared with carbon/epoxy composite laminates, the damage in the CF/PEEK laminates appears relatively late, because the tough characteristics of the matrix delay the initiation of damage.
4. The wear-out model shows good correlation with the experimental data for both S-N curve and residual strength.

## ACKNOWLEDGMENT

L. Ye wishes to thank the Polymer Research Division, BASF, Germany, for supplying the testing materials. X. X. Diao is supported by an Overseas Postgraduate Research Scholarship and a Sydney University Postgraduate Research Award. The partial support from the Australian Research Council (ARC) on this project is appreciated

## REFERENCES

1. Thermoplastic Composite Materials Handbook, ICI Thermoplastic Composites, 1992, pp.1
2. Henaff-Gardin, C. and Lafie-Frenot, M. C., "Fatigue Behaviour of Thermoset and Thermoplastic Cross-Ply Laminates", *Composites*, 23(1992)358-303
3. Rigby, R. B., "Polyetheretherketone", in *Engineering Thermoplastics, Properties and Applications*, Margolis, J. M., Ed., Marcel Dekker, Inc. (1995), pp. 299-314
4. Maekawa, Z., Hamada, H., Lee, K. and Kitagawa, T., "Reliability Evaluation of Mechanical Properties of AS4/PEEK Composites", *Composites*, 25(1994)37-45
5. Charewicz, A. and Daniel, I. M., "Damage Mechanisms and Accumulation in Graphite/Epoxy Laminates", in *Composite Materials: Fatigue and Fracture, ASTM STP 907*, Hahn, H. T., Ed., American Society for Testing and Materials, Philadelphia, 1986, pp.274-297
6. *Engineering Materials Handbook, Vol.1, Composites*, ASM International, 1987, pp.112-113
7. Dickson, R. F., Jones, C. J., Harris, B., Leach, K. C. and Moore, D. R., "The Environmental Fatigue Behaviour of Carbon Fibre Reinforced Polyether Ether Ketone", *Journal of Materials Science*, 20(1985)60-70
8. Halpin, J. C., Jerina, K. L. and Johnson, T. S., "Characterisation of Composites for the Purpose of Reliability Evaluation, in *Analysis of the Test Methods for High Modulus Fibres and Composites*", ASTM STP 521, Whitney, J. M., Ed., American Society for Testing and Materials, Philadelphia, 1973, pp.5-64
9. Sendeckyj, G. P., "Fitting Models to Composite Materials Fatigue Data", in *Test Methods and Design Allowable for Fibrous Composites, ASTM STP 734*, Chamis, C. C., American Society for Testing and Materials, Philadelphia, pp.245-260
10. Diao, X. X., Ye L. and Mai, Y. W., "Fatigue Behaviour of CF/PEEK Composite Laminates Made from Commingled Prepreg Part I - An Experimental Study", *Composites*, in revision

# EFFECT OF LOAD FREQUENCY ON THE TENSILE FATIGUE BEHAVIOUR OF ANGLE-PLY AS4/PEEK

X. R. Xiao, I. Al-Hmouz

*Concordia Center For Composites, Concordia University, Dept. of Mechanical Engineering  
1455 de Maisonneuve Blvd. W., Montreal, Quebec H3G 1M8*

**SUMMARY:** This paper presents the results of a study aimed at understanding the load frequency effect on fatigue life of thermoplastic composites. The tensile fatigue behaviour ( $R=0.13$ ) of straight sided angle-ply  $[\pm 45]_4s$  AS4/PEEK was investigated at three frequencies. The cyclic stress-strain data and temperature variation during fatigue tests were recorded. A model correlating the thermal effect to the load frequency on the fatigue life of the thermoplastic composite was proposed.

**KEYWORDS:** fatigue, load frequency, thermoplastic, hysteresis loop, thermal effect

## INTRODUCTION

The load frequency is known to have a substantial effect on fatigue performance of polymer composites, especially on laminates dominated by the matrix properties [1-8]. Literature data indicate that the load frequency has a two-fold effect on fatigue of polymer composites: the creep effect and the thermal effect. Due to the viscoelastic nature of polymeric matrices, matrix dominated laminates tend to creep during low frequency fatigue testing and, hence, decreasing load frequency tends to reduce the fatigue strength of the material. On the other hand, the viscoelastic dissipation under cyclic loading leads to autoheating of the matrix material. The friction at damaged sites also generates heat. Since the heat generation is proportional to load frequency, increasing frequency would increase the temperature rise and, thus, result in softening of the material. Depending on the material system, the level and wave form of cyclic stress, increasing load frequency may either increase or decrease the fatigue life determined by the balance between the creep and thermal effects.

Fatigue failures associated with large-scale hysteretic heating have been observed in polymers [9,10] and in glass fiber reinforced epoxy [1] where fatigue life decreased as load frequency increased. The effect of hysteretic heating was less substantial in graphite/epoxy and consequently fatigue life increased as load frequency increased [3]. The same trend was observed in Boron/epoxy [6].

Several studies on fatigue of thermoplastic composite AS4/PEEK have shown that hysteretic heating in AS4/PEEK is much more pronounced as compared to that in thermoset composites [4,5,11] and the fatigue life decreases remarkably with increasing load frequency [4,5]. Dan-Jumbo et al [5] have developed a model to account for the load frequency effect on fatigue life. Their study, however, was conducted with notched specimens where the thermal effect is restricted as compared to that in smooth specimens because the heat generated at notch areas can dissipate into a much larger surrounding materials at lower stresses.

The present work is aimed at understanding the thermal effect associated with load frequency on fatigue life of thermoplastic composite AS4/PEEK. To emphasize the thermal effect, straight sided angle-ply  $[\pm 45]_{4s}$  specimens were used. Tensile-tensile fatigue tests were conducted at three frequencies. The cyclic stress-strain data and temperature variation during fatigue tests were recorded. A model correlating the thermal effect to the load frequency on the fatigue life of the thermoplastic composite was proposed.

## **EXPERIMENTAL**

### **Specimens**

AS4/PEEK  $[0/90]_{4s}$  panels of 12x12 inches were made from prepreg using a WABASH hot press following ICI's procedure. The straight sided  $[\pm 45]_{4s}$  specimens were then cut from the laminates. The nominal dimensions of the specimens were 200x18x2 mm with 38 mm long aluminum end tabs, which follows the specification of ASTM D3479. The ultimate tensile strength of the  $[\pm 45]_{4s}$  laminates was measured to be 338 MPa, which was very close to the value reported in literature. Fig.1 shows the typical stress-strain curve obtained by static tensile tests.

### **Fatigue Test**

The tensile-tensile fatigue tests were carried out using a MTS machine under load controlled mode with sinusoidal load wave form. The stress ratio in fatigue was  $R=0.13$ . Three load frequencies were investigated: 1 Hz, 5 Hz and 10 Hz. At each frequency, fatigue tests were conducted at three stress levels: 60%, 70% and 80% of the ultimate tensile strength. To complete the S-N curve, few more fatigue tests were conducted at other stress levels.

During fatigue tests, the load level was monitored from the signal of the load cell while the axial strain was measured using an extensormeter. The cyclic stress-strain data were collected at selected cycles. The temperatures were measured during the test using thermocouples attached to the center region of the specimen surface and recorded by a computer data acquisition system.

## **RESULTS AND DISCUSSION**

### **S-N Data**

The data on fatigue strength - number of cycle to failure (S-N) obtained are presented in Table 1. The values of the equilibrium or the maximum temperature recorded during fatigue tests are also listed in Table 1. The S-N curves for three frequencies are plotted in Fig.2, where symbols are the test data. It is evident that increasing frequency reduced the fatigue life and this life reduction effect appeared to be larger at lower stress levels.



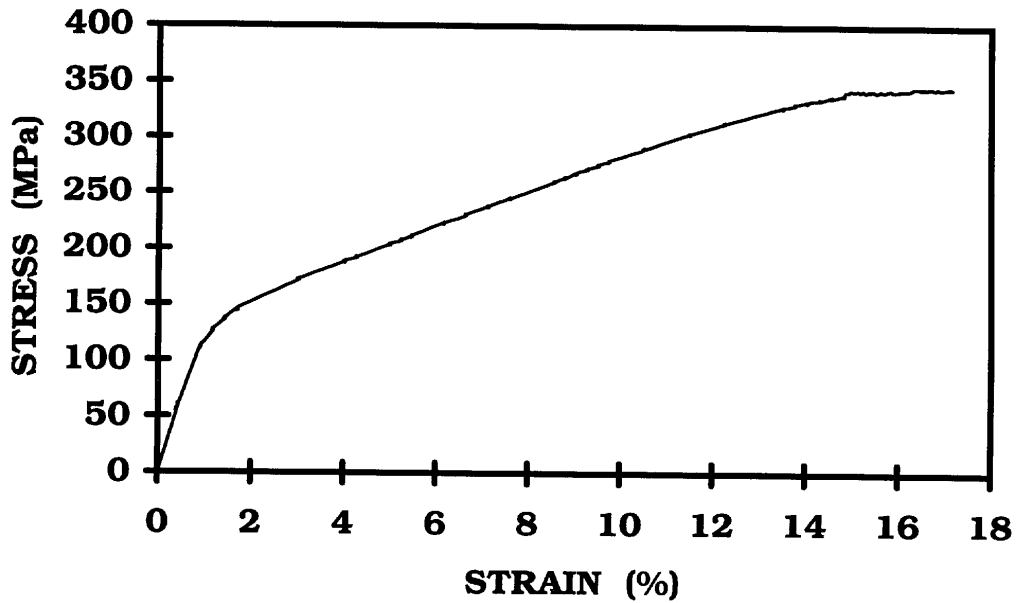


**Fig.1 STRESS-STRAIN BEHAVIOR OF ANGLE-PLY APC2/AS-4 UNDER STATIC LOADING**

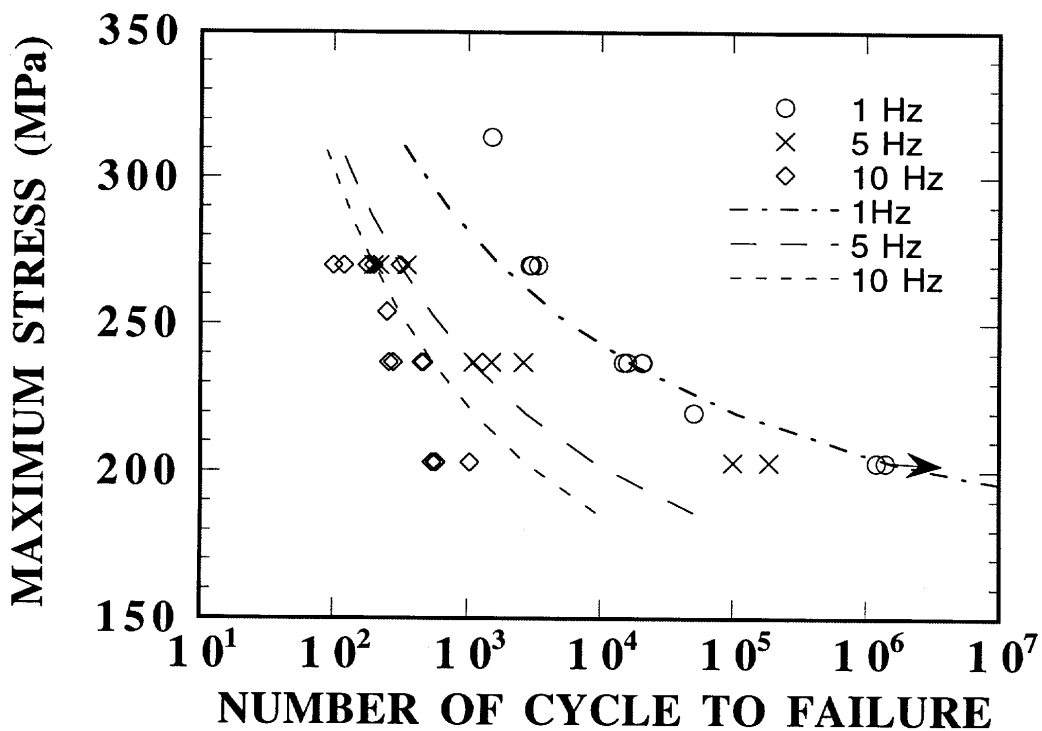


**Fig.2 S-N curves of AS4/PEEK [±45]4s laminates.**  
The symbols are test data and the dashed lines are the predictions by Eq.8.



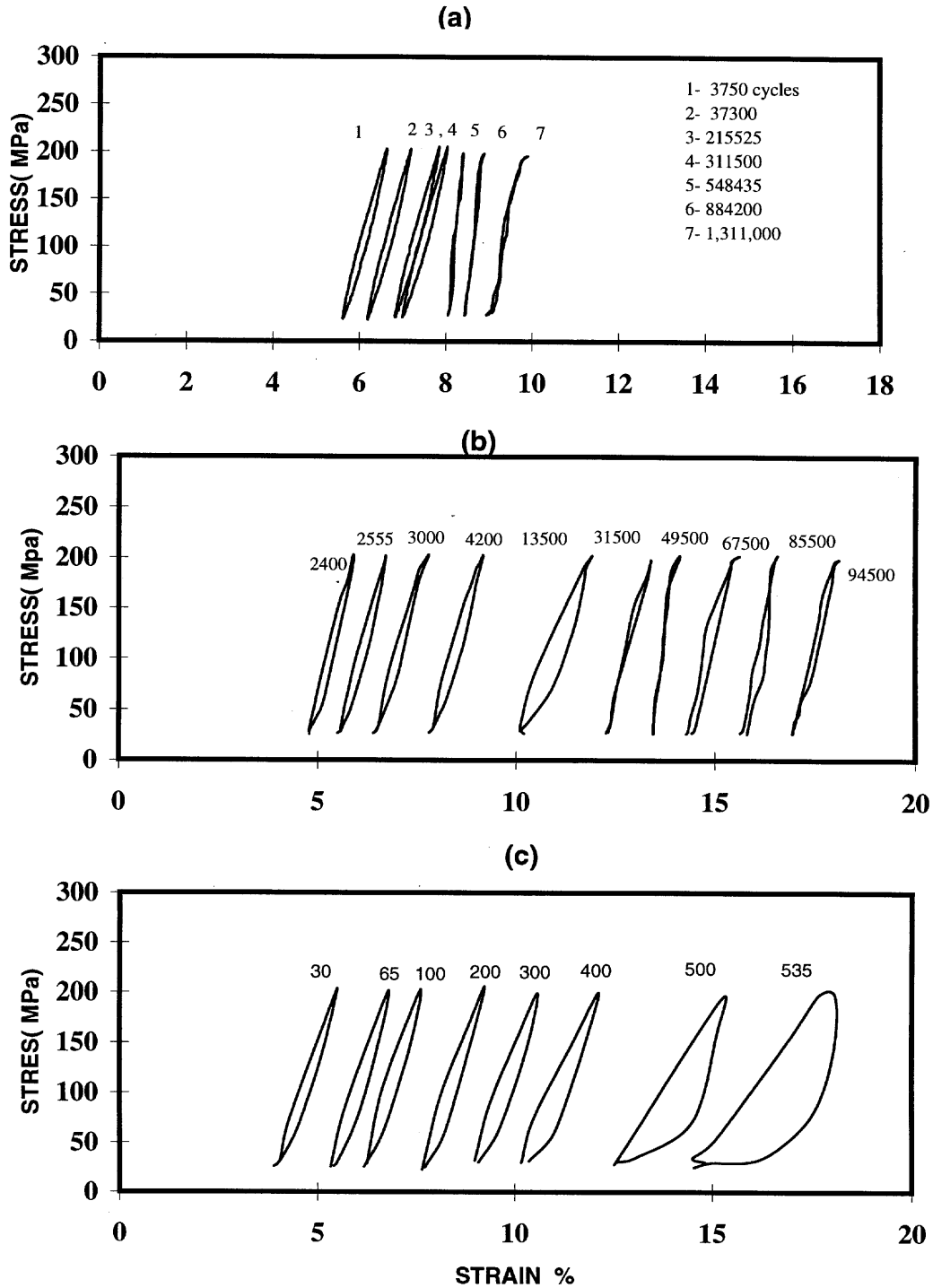


Fig.3 Hysteresis loops during fatigue at 60% of the ultimate strength and

(a)1Hz, (b)5Hz, (c)10Hz at selected numbers of cycles

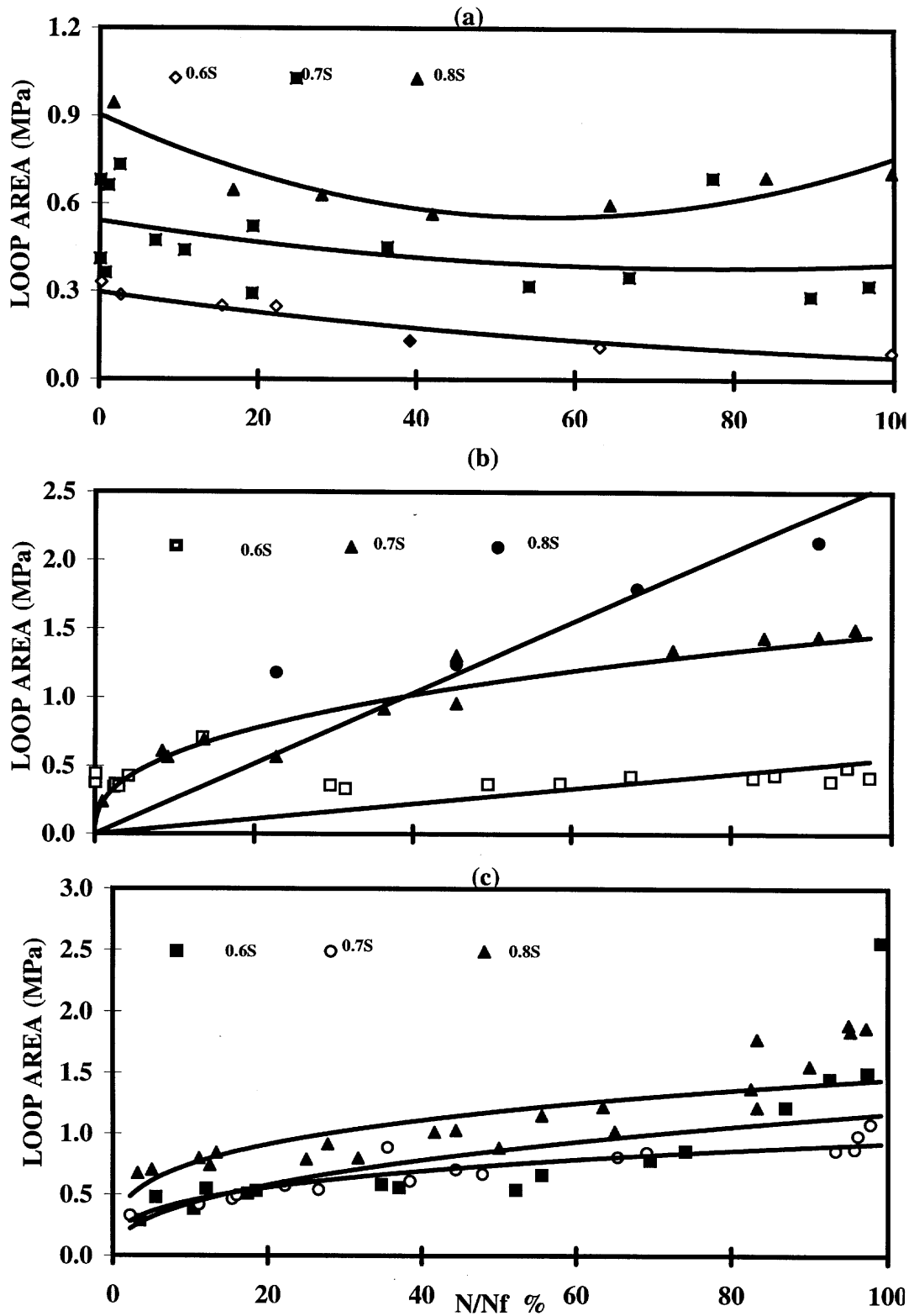
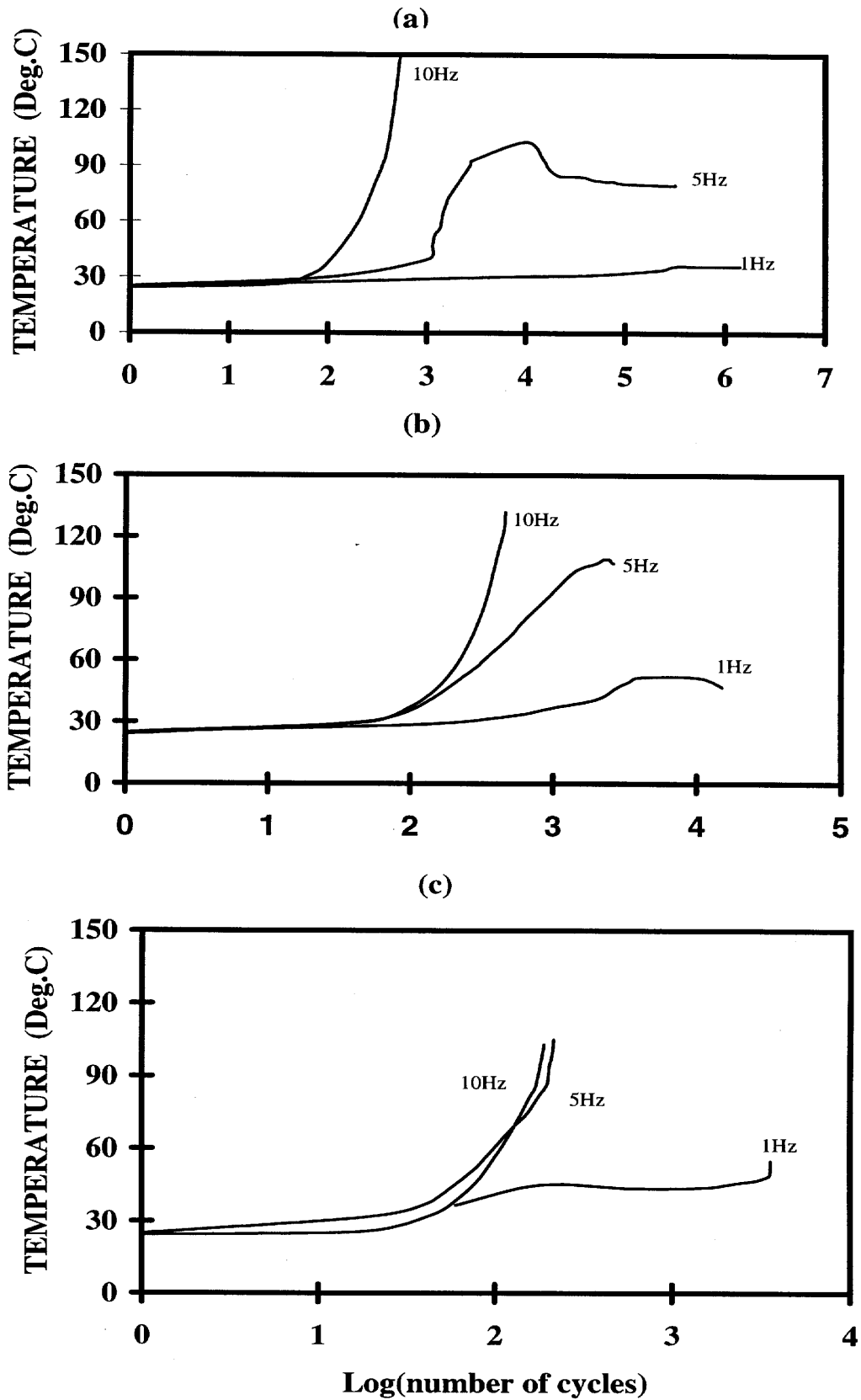


Fig.4 Hysteresis loop area vs. normalized fatigue life at (a)1Hz, (b)5Hz, and (c)10Hz



**Fig.5 Temperature variation during fatigue at (a)60%, (b)70%, and (c)80% of the ultimate strength**

## Hysteresis Loop

Fig.3 shows the typical hysteresis loops recorded during fatigue tests at 60% stress level for the three load frequencies. As seen the shape of the hysteresis loops changed gradually during fatigue and the way of its change depended upon load frequency. Initially the hysteresis loop had a shape of slim ellipse and was symmetric to its center, which may be approximated by two triangles placed base to base as observed by other researchers [1]. With increasing the number of cycle, the loop nearly collapsed in Fig. 3a and Fig. 3b (1 Hz and 5 Hz, respectively) but expanded in Fig 3c (10 Hz).

At other stress levels, the evolution of hysteresis loop also appeared to depend upon frequency. To compare the effect of frequency and stress level on the evolution of hysteresis loop, the area of hysteresis loop is plotted versus the normalized number of cycle  $N/N_f$  in Fig.4, where  $N_f$  is the fatigue life. At 1 Hz (Fig.4a), the area of hysteresis loop decreased as the number of cycles increased whereas at 5 Hz and 10 Hz (Fig.4b and Fig.4c) the trend reversed and this trend became stronger at higher stress levels.

The evolution of hysteresis loop correlated well with the damage extent observed on specimen surfaces. The main type of damage observed on fatigue failed specimens was matrix cracking. It was found that, with increasing load frequency and stress level, the intensity of the matrix cracks increased. The additional energy dissipation as reflected by the expanded hysteresis loops is likely due to friction at these damaged sites.

Another noticeable point in Fig.4 is the accumulation of creep strain. Regardless of the load frequency and stress level used, all specimens failed by fatigue exhibited a total maximum strain in the range of 18-20%, which is in the range of failure strain obtained by static tests.

## Temperature Rise

The typical temperature variations during fatigue tests are shown in Fig.5 for the three load frequencies at three stress levels. At 1 Hz, temperature rise reached the equilibrium for fatigue tests conducted at all stress levels and the equilibrium temperature increased with stress levels. At 5 Hz, a peak in temperature rise curve, which is similar to that reported by [4], was observed at tests conducted at 60% level. At higher stress levels, monotonic temperature rises were recorded. At 10 Hz, continuously rising temperatures were measured at all stress levels. The values of the equilibrium or the maximum temperature recorded during fatigue tests have been given in Table 1.

It should be noticed that the temperature measured at specimen surfaces for samples tested at 10 Hz sometimes exhibited a lower value than those tested at 5 Hz at the same stress level. This is believed due to the delay in thermal conduction. During fatigue tests at higher load frequencies and higher stress levels, the temperature differences between the center and the surfaces of the specimens are much higher and the specimens may fail before the temperature rises are reflected at their surfaces. Indeed, continuous temperature rises were recorded on specimens tested at 10 Hz even after the fatigue test had been halted upon failure .

Taking this factor into consideration, we may conclude that the decrease in fatigue life of AS4/PEEK  $[\pm 45]_{4s}$  laminates with increasing load frequency is directly related to the temperature rise associated with hysteretic heating. This is to say that the effect of load frequency on fatigue life is mainly thermal nature.

Table 1 Results of fatigue tests for  $[\pm 45]_{4s}$  APC2/AS-4 samples

Sample#	Frequency (Hz)	Load level % $\sigma_{ult}$	Number of cycles	Temperature (°C)
2-B-3	1	60	1,400,000*	34 E
4-B-93	1	60	1,200,000*	32 E
2-C-4	1	65	50700	—
1-A-3	1	70	20650	43 E
1-B-1	1	70	16000	40 E
1-B-8	1	70	21000	45 E
1-B-6	1	70	18800	46 E
3-C-4	1	80	2900	45 E
3-C-22	1	80	3000	45 E
-C-32	1	80	3850	—
1-L-6	1	80	3570	45 E
2-C-2	1	93	1500	—
2-B-2	5	60	100,000	84 F
1-A-4	5	60	186,000	84 F
3-B3	5	70	2200	127 F
3-B-1	5	70	1500	—
1-K-2	5	70	1100	135 F
1-S-5	5	70	2600	152 F
1-A-9	5	70	2620	127 F
1-K-3	5	75	350	100 F
4-B-8	5	80	200	110 F
4-B-7	5	80	220	97 F
1-B-4	5	80	200	108 F
2-D-5	10	60	540	152 F
1-S-1	10	60	575	140 F
1-K-7	10	60	1040	—
1-S-2	10	60	580	—
1-S-8	10	70	450	136 F
1-S-9	10	70	260	95 F
1-K-1	10	70	280	—
1-L-2	10	70	470	119 F
2-D-4	10	75	450	80 F
2-D-2	10	80	200	110 F
2-D-3	10	80	180	102 F
1-S-6	10	80	315	135 F
1-S-7	10	80	120	—
1-A-7	10	80	100	90 F

Sample did not fail after this number of cycles.

E : equilibrium temperature.

F : failure temperature.

### A MODEL FOR THERMAL EFFECT ON FATIGUE LIFE

Literature data and our experimental results have shown that thermal degradation associated with hysteretic heating is the dominant frequency effect on fatigue life of thermoplastic composite AS4/PEEK.

For viscoelastic materials, the rate of hysteretic heating is determined by the hysteretic energy dissipated under fatigue loading [9].

$$w = \pi f D''(f, T) \sigma^2 \quad (1)$$

where  $w$  = energy dissipated,  $f$  = frequency,  $D''$  = the loss compliance,  $\sigma$  = the peak stress.

The hysteretic heating can also be measured directly from the area of hysteretic loop. Hanh and Kim [2] have shown that the hysteretic energy can be approximated by

$$w = C(1-R)^2 \sigma(\sigma - \sigma_t) \quad (2)$$

where  $C$  is a parameter related to the mid-width of the hysteretic loop,  $R$  is the stress ratio of the fatigue test and  $\sigma_t$  is the threshold stress below which no hysteretic heating is measured. The hysteretic heating rate is given by

$$q = C(1-R)^2 \sigma(\sigma - \sigma_t) f \quad (3)$$

From heat transfer analysis, the equilibrium temperature is found to be proportional to  $q$  and hence may be predicted by

$$T = T_0 + \eta' [(1-R)^2 \sigma(\sigma - \sigma_t) f]^\beta \quad (4)$$

where  $\eta'$  and  $\beta$  are parameters,  $T_0$  is the environment temperature.

An observation of S-N curves suggests that these curves may be described by the following function

$$\text{Log}(N)(\sigma - \sigma_0') = C \quad (5)$$

where  $\sigma_0'$  is the fatigue limit,  $C$  is a parameter. The strength of viscoelastic materials is sensitive to temperature, so is the fatigue limit. Assuming that the effect of temperature on fatigue limit  $\sigma_0'$  follows an exponential function

$$\sigma_0' = \sigma_0 \exp[-\eta''(T - T_0)] \quad (6)$$

With Eq.4, Eq.6 becomes

$$\sigma_0' = \sigma_0 \exp\{-\eta''[(1-R)^2 \sigma(\sigma - \sigma_t) f]^\beta\} \quad (7)$$

Substitute Eq.7 into Eq.5 and introduce stress parameters  $p=\sigma/\sigma_{ult}$ ,  $p_0=\sigma_0/\sigma_{ult}$  and  $p_t=\sigma_t/\sigma_{ult}$  we obtain the mathematics model for thermal effect on fatigue life of materials

$$\text{Log}(N)\{p-p_0\exp[-\eta((1-R)^2p(p-p_t)f)^\beta]\}=C \quad (8)$$

Eq.8 is actually a variation of the model presented by Dan-Jumbo et al [5] but, instead of employing the temperature rise data, here the thermal effect is directly related to the stress level and load frequency. In addition, the model in [5] is based on crack growth in viscoelastic media, whereas Eq.8 is based on the assumption of a general strength degradation of the material and hence it is suitable for smooth composite samples.

By curve fitting the data given in Table 1 and with  $p_0=0.55$ ,  $p_t=0$  and  $R=0.13$ , the values of the parameters in Eq.8 were determined as follows:  $C=1.7$ ,  $\eta=1$  and  $\beta=0.5$ . The S-N curves predicted by Eq.8 are presented in Fig.2 by dashed lines to compare with the test data. In general, the model predicted the trend of load frequency effect except for 5 Hz at 60% stress level.

## CONCLUSIONS

Tensile fatigue tests of  $[45]_{4s}$  AS4/PEEK laminates were carried out at three frequencies: 1 Hz, 5 Hz and 10 Hz. Substantial temperature rises were recorded during fatigue tests, especially at higher frequencies and stress levels. Fatigue life reduced significantly as load frequency increased. The results clearly indicate that the effect of load frequency on fatigue life was dominated by thermal effect. A model correlating thermal effect with load frequency and stress level was proposed. The prediction by the model agreed reasonably well with the test data.

## ACKNOWLEDGMENT

This work is supported by National Science and Engineering Research Council of Canada. We also like to thank Mr.J.Dufour of IMI, National Research Council of Canada for the assistance in fabrication of composite plates, Mr.P.Oullette and Mr.M.El-Karmalawy of Concordia Center for Composites for their assistance in fatigue tests.

## REFERENCES

1. J.W.Dally and L.J.Broutman, "Frequency effects on the fatigue of glass reinforced plastics", J. Composite Materials, Vol.1, 1967, 424-442.
2. H.T.Hahn, R.Y.Kim, "Fatigue behaviour of composite laminate", J. Composite Materials, Vol.10, 1976, 156-180.
3. C.T.Sun, W.S.Chan, "Frequency effect on the fatigue life of a laminated composite", Composite Materials: Testing and Design, ASTM STP 674, Ed. S.W.Tsai, 1979, 418-430.

4. D.C.Curtis, D.R.Moore, B.Slater, N.Zahlan, "Fatigue testing of multi-angle laminates of CF/PEEK", *Composites*, Vol.19, No.6, 1988, 446-452.
5. E.Dan-jumbo, S.G.Zhou, C.T.Sun, "Load-frequency effect on fatigue life of IMP6/APC-2 thermoplastic composite laminates", *ASTM STP 1044*, G.M.Newaz, Ed., 1989, 113-132.
6. K.L.Reifsnider, W.W.Stinchcomb, T.K.O'Brien, "Frequency effects on a stiffness based fatigue criterion in flawed composite specimens", *Fatigue of Filamentary Composite Materials. ASTM STP 636*, K.L.Reifsnider and K.N.Lauraitis, Eds., ASTM, 1977, 171-184.
7. D.Kujawski, F.Ellyin, "Rate/frequency-dependent behaviour of fibreglass/epoxy laminates in tensile and cyclic loading", *Composite*, Vol.26, 1995, 719-723.
8. J.F.Mandell, U.Meier, "Effect of stress ratio, frequency, and loading time on the tensile fatigue of glass-reinforced epoxy", *Long-Term Behaviour of Composites, ASTM STP 813*, ASTM, 1983, 55-77.
9. R.W.Hertzberg, J.A.Manson, *Fatigue of Engineering Plastics*, Academic Press, New York, 1980.
10. S.Suresh, *Fatigue of Materials*, Cambridge University Press, New York, 1991.
11. C.C.M.Ma, S.H.Lin, N.H.Tai, J.F.Wu, G.Y.Wu, C.L.Ong, Y.C.Chang, M.F.Sheu, Y.R.Yang, "Fatigue behaviour of carbon fiber reinforced thermoplastic and thermoset polymer composites (I)  $[\pm 45]_4s$  laminates under tension-tension loading, *Proceedings of ICCM10, Vol.I*, 1995, 569-576.



# RESIDUAL STRENGTH OF GRP AT HIGH CYCLE FATIGUE

J. Andersons<sup>1</sup>, J. Korsgaard<sup>2</sup>

<sup>1</sup>*Institute of Polymer Mechanics, 23 Aizkraukles iela, Riga LV-1006, Latvia*

<sup>2</sup>*LM Glasfiber A/S, Denmark*

**SUMMARY:** Residual strength degradation of glass-fiber reinforced polyester composite of a lay-up typical for wind rotor blade material is studied at low-cycle fatigue. Gradual reduction of remaining strength is observed as expected for GRP, accompanied by increasing scatter. Residual strength model based on strength-life equal rank assumption yields accurate approximation of experimental data. Strength reduction at stress level corresponding to high-cycle fatigue ( $N > 10^6$  cycles) appears to correlate well with higher stress level test results indicating that strength degradation at design stress level can be evaluated using low-cycle tests. Assuming that strength degradation model parameters do not depend on applied stress level, residual strength data obtained at low stress level tests of comparatively short duration can be used to estimate the average fatigue life at the same stress thus considerably reducing total test time.

**KEYWORDS:** fatigue, residual strength, glass/polyester composite

## INTRODUCTION

Fail-safe strength design of engineering composite structures has to ensure that appropriate residual static strength level is maintained during design life. The latter is typically too long to allow conventional fatigue and residual strength tests to be performed at the desired low design stress level. Hence fatigue test data are usually extrapolated to low stress levels of interest. In order to improve the accuracy of remaining strength and life estimates, a model of composite fatigue behavior during high-cycle fatigue verified by experimental data is necessary.

Residual strength models have been developed for prediction of residual strength and life distribution under constant amplitude, block [1], and spectrum loading [2]. Modifications taking into account mean stress effect [3], competing failure modes [4], degradation mechanism change [5] have been proposed. In [6] residual strength model is used to extrapolate experimentally derived S-N curves. The model predictions satisfactorily agree with experimental data in the stress range covered, which in most investigations is limited by that corresponding to fatigue life of about  $10^6$  cycles. Less research is dedicated to strength degradation at lower cyclic stress levels which are of primary significance for long-term applications.

With this aim residual strength degradation at a range of stress levels has been studied experimentally, and a method of fatigue life estimation based on limited amount of residual strength tests at the stress level of interest is proposed.

## MATERIAL AND TESTS

Glass fiber reinforced polyester used as a blade material for wind turbines was tested. The material was produced by hand lay-up, and comprised chopped strand mat, unidirectionally reinforced, and fabric layers in the following sequence: /CSM, fabric,(CSM, UD)<sub>2</sub>/ s. The resin used was an orthophthalic polyester (Norpol 410M910). The average fiber volume fraction was 41 %. Longitudinal modulus and tensile strength were correspondingly  $E = 30 \pm 2$  GPa and  $S = 672 \pm 21$  MPa.

Dog-bone shape specimens were used for tensile static strength and fatigue tests. Static strength distribution is shown in Fig. 1, and fatigue diagram - in Fig. 2. Fatigue tests were run at ambient conditions. Loading frequency was 17 Hz, stress ratio  $r = 0.1$ . Residual tensile strength degradation was studied at a number of stress levels. The results are shown in Table 1.

*Table 1: Residual strength*

Maximum stress, MPa	Duration of loading, cycles	Duration of loading, fraction of nominal life*	Number of specimens tested	Average residual strength, MPa	Standard deviation of residual strength, MPa
284	$2.5 \cdot 10^4$	.17	7	604	27
	$5 \cdot 10^4$	.33	9	555	35
	$1 \cdot 10^5$	.66	7	507	53
	$1.24 \cdot 10^5$	.82	8	493	82
235	$2 \cdot 10^5$	.15	6	628	27
	$4 \cdot 10^5$	.30	7	598	30
221	$4 \cdot 10^5$	.16	5	628	31
206	$4 \cdot 10^5$	.08	5	634	28
186	$8 \cdot 10^5$	.07	7	635	35
167	$1.6 \cdot 10^6$	.06	5	617	3

\*life fraction reported in the Table is calculated with respect to linear approximation of  $\lg N$  vs.  $\sigma$  diagram

## MODELING OF RESIDUAL STRENGTH DEGRADATION

Majority of residual strength  $R$  degradation models can be derived from the following rate equation:

$$\frac{dR}{dn} = f(\sigma, r, S)g(R)h(n) \quad (1)$$

supplemented by initial condition  $R(0) = S$  and failure criterion  $R(N) = \sigma$ , where  $R$  - residual strength,  $S$ - static strength,  $N$ - fatigue life at cyclic stress with maximum value  $\sigma$ ,  $n$  - current number of loading cycles. Non-linearity of strength reduction is accounted for by appropriate choice of functions  $g$  and  $h$ . Models derived assuming that strength degradation rate does not explicitly depend on either  $n$  (i.e.  $h=1$ ) or  $R$  are commonly used. Since there is little physical background for favoring any of these approaches, both of them are considered below.

### Statistical Model

Taking  $g = \frac{1}{v} R^{-v+1}$ ,  $h \equiv 1$  and  $f = -\frac{S^v - \sigma^v}{S^c - \sigma^c} \frac{1}{N^*}$ , residual strength model [7] is recovered,

and residual strength  $R$  of a specimen with initial static strength value  $S$  after fatigue loading of  $n$  cycles at a constant maximum stress level  $\sigma$  is:

$$R^v = S^v - \frac{S^v - \sigma^v}{S^c - \sigma^c} \frac{n}{N^*} \quad (2)$$

Residual strength distribution is derived in [7] assuming Weibull distribution function for static strength  $S$ :

$$F_S(S) = 1 - \exp[-S^\alpha] \quad (3)$$

and fatigue life (at constant maximum stress level  $\sigma$ ):

$$F_N(n) = 1 - \exp\left[-\left(\sigma^c + \frac{n}{N^*}\right)^{\alpha/c}\right] \quad (4)$$

All variables with stress dimension are normalized by Weibull scale parameter  $\beta$  of static strength distribution;  $N^*$  - characteristic fatigue life at stress level  $\sigma$ . It follows from (4) that it is related to the mean life  $\bar{N}$ :

$$\bar{N} = N^* \Gamma\left(1 + \frac{c}{\alpha}\right) + \sigma^c \quad (5)$$

Residual strength distribution is given by Eqn 6:

$$F_R(R) = 1 - \exp[S_0^\alpha - S(R)^\alpha] \quad (6)$$

where by  $S(R)$  is denoted the static strength value corresponding to residual strength  $R$  and obtained solving (2) for  $S$ . Parameter  $S_0$  accounts for the fact that residual strength can be determined only for the specimens that have survived fatigue loading, i.e. for which  $R(n) > \sigma$ . Therefore  $S_0$  is calculated from (2) replacing  $R$  by  $\sigma$ .

The model described comprises five material parameters. They were estimated by maximum likelihood method as corresponding distribution function parameters in the following order. First, strength distribution scale and shape parameters  $\beta$  and  $\alpha$  were evaluated fitting (3) to static strength test results (see Fig. 1), then parameter  $c$  characterizing fatigue life scatter and characteristic S-N curve  $\lg N^* = A - B\sigma$  parameters  $A$  and  $B$  were determined approximating constant amplitude fatigue data (Fig. 2) by (4), and the remaining residual strength degradation rate parameter  $\nu$  - fitting (6) to residual strength data at  $\sigma = 284$  MPa (Fig. 3). Parameter values are shown in Table 2.

Table 2: Model parameter values

$\alpha$	$\beta$ , MPa	$c$	$A$	$B$ , MPa <sup>-1</sup>	$\nu$
35.1	683	10.8	10.7	.019	2.45

### Deterministic Model

If  $h(n) = \gamma \cdot n^{\gamma-1}$  and  $g(R) \equiv 1$  are taken in Eqn 1, it follows that residual strength degrades under constant amplitude cyclic loading according to relation (7):

$$R = S - (S - \sigma) \left( \frac{n}{N} \right)^\gamma \quad (7)$$

Although the model allows statistical treatment, strength and fatigue life in Eqn 7 are normally substituted by their average values therefore making model deterministic (see e.g. [8]).

Deterministic model, unlike the statistical one, cannot account for apparent slowing down of strength reduction at  $n$  approaching mean fatigue life  $N$  (and caused by failure of weaker specimens during cycling). Therefore average residual strength values at  $\sigma = 284$  MPa obtained at loading duration up to  $.66N$  only were used for parameter  $\gamma$  determination, resulting in  $\gamma = 1.33$  (see Fig. 4).

## RESULTS AND DISCUSSION

Residual strength data apparently form a mastercurve (Fig. 5), when plotted as a function of nominal life fraction spent under cyclic load. It makes it possible to roughly estimate residual strength reduction at low cyclic stress level using high stress level data. Variation of remaining strength for small to medium loading duration in terms of life fraction ( $n/N < .35$ ) is very close to that of static strength with the exception of the lowest stress level considered  $\sigma = 167$  MPa. Standard deviation of residual strength for the latter was almost an order of magnitude less than that of static strength.

In order to check whether strength degradation model parameters are stress dependent, they were determined from two residual strength data sets obtained at  $\sigma = 284$  MPa (corresponding fatigue life  $N = 1.9 \cdot 10^5$ ) and  $\sigma = 235$  MPa ( $N = 1.7 \cdot 10^6$ ). Stress levels were chosen so that they lay within the stress range at which fatigue tests were performed, so that reliable estimate of

corresponding fatigue lives was available. Model parameters for data generated at  $\sigma = 284$  MPa are listed above, while for  $\sigma = 235$  MPa they are  $\nu = 2.36$  (statistical model) and  $\gamma = 1.28$  (deterministic model). The difference in parameter values determined at different stress levels is negligible for both models, therefore they can be considered material parameters. Prediction of residual strength distribution at  $\sigma = 235$  MPa by statistical model (Fig. 6, 7) and mean strength degradation by deterministic model (Fig. 4) using model parameters determined at  $\sigma = 284$  MPa show very good agreement with test data.

Assuming that further reduction of cyclic stress level will not influence model parameters, low stress residual strength data can be used for estimation of the corresponding fatigue life. For deterministic model, relation for mean life estimate at stress  $\sigma$  follows from Eqn 7:

$$N = n \left( \frac{S - \sigma}{S - R} \right)^{1/\gamma} \quad (8)$$

For statistical model, maximum likelihood method was used for determining the value of  $N^*$  in Eqn 2 that yields the best fit of distribution function (6) to residual strength data obtained at the corresponding maximum cyclic stress  $\sigma$ . Theoretical residual strength distributions are plotted in Fig. 8-10. This method allows to calculate also standard deviation of  $N$ , thus allowing to evaluate the accuracy of prediction. For the lowest cyclic stress value considered estimated variation of  $N$  was of the same order as  $N$  clearly indicating that statistical model is not applicable in this case.

Predicted fatigue life at low stress is shown in Fig. 2. Fatigue life estimates by both residual strength models are very close to each other, and slightly below extrapolation line of experimental S-N data.

## CONCLUSIONS

Residual strength data vs. life fraction of GRP under load form a mastercurve, from which a rough estimate of strength reduction at the cyclic stress level of interest can be obtained.

Strength degradation model parameters appear not to depend on cyclic stress level. It permits to estimate fatigue life of composite at a given stress level from a limited amount of residual strength test results at the same test level.

## ACKNOWLEDGMENTS

This work was partially supported by CEC contract JOU2-CT93-0277 - Advanced Flexible Composite Rotor for Large Wind Turbines.

## REFERENCES

1. Yang, J. N. and Jones, D.L., "The effect of load sequence on statistical fatigue of composites", *AIAA Journal*, 1980, Vol. 18, N 12, pp. 1525-1531.
2. Yang, J. N. and Shanyi Du, "An exploratory study for fatigue of composite under spectrum loading", *Journal of Composite Materials*, 1983, Vol. 17, Nov., pp. 511-526.
3. Kim, R.Y., "Effect of mean stresses on fatigue behavior of composite laminates", *Proc. ICCM 7*, 1982, pp. 621-626.
4. Whitney, J.M., "A residual strength degradation model for competing failure modes", *Long-Term Behavior of Composites, ASTM STP 813*, 1983, pp. 225-245.
5. Talreja, R., *Fatigue of Composite Materials*, 1985, 125 p.
6. Donaldson, S.L., and Kim, R.Y., "Life prediction of glass/vinylester and glass/polyester composites under fatigue loading", *Proc. of ICCM-10, Vol. I: Fatigue and Fracture*, 1995, pp. 577-584.
7. Yang, J.N., and Jones, D.L., "Load sequence effects on the fatigue of unnotched composite materials", *Fatigue of Fibrous Composite Materials, ASTM STP 723*, 1981, pp. 213-232.
8. Reifsnider, K.L., and Stinchcomb, W.W., "A critical element model of the residual strength and life of fatigue-loaded composite coupons", *Composite Materials: Fatigue and Fracture, ASTM STP 907*, 1986, pp.298-313.

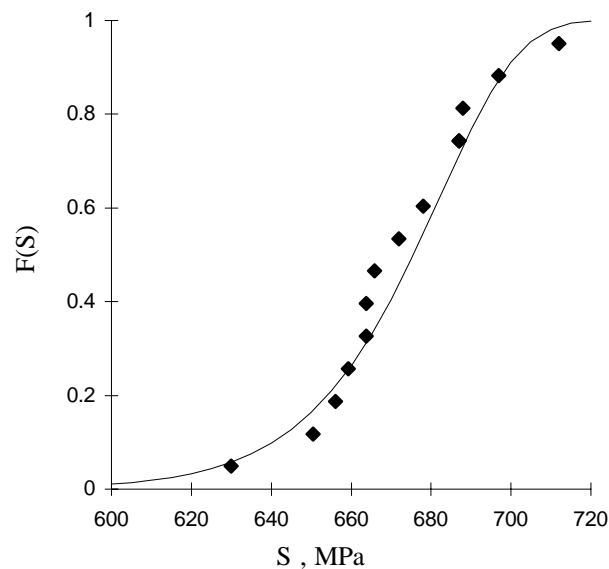


Fig. 1: Static tensile strength distribution of GRP

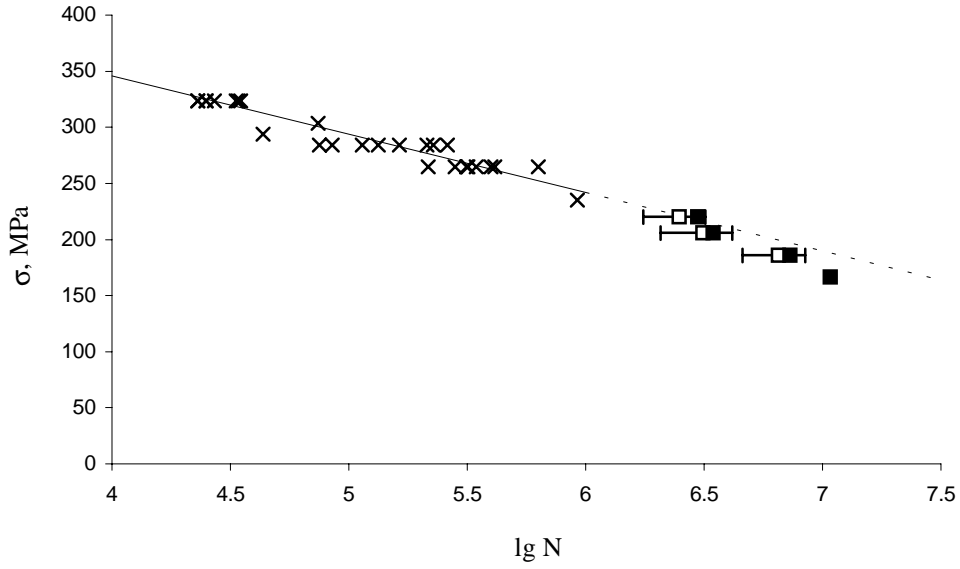


Fig. 2: Fatigue diagram  
 (x) - S-N data; mean life predicted by statistical (□) and deterministic (■) models

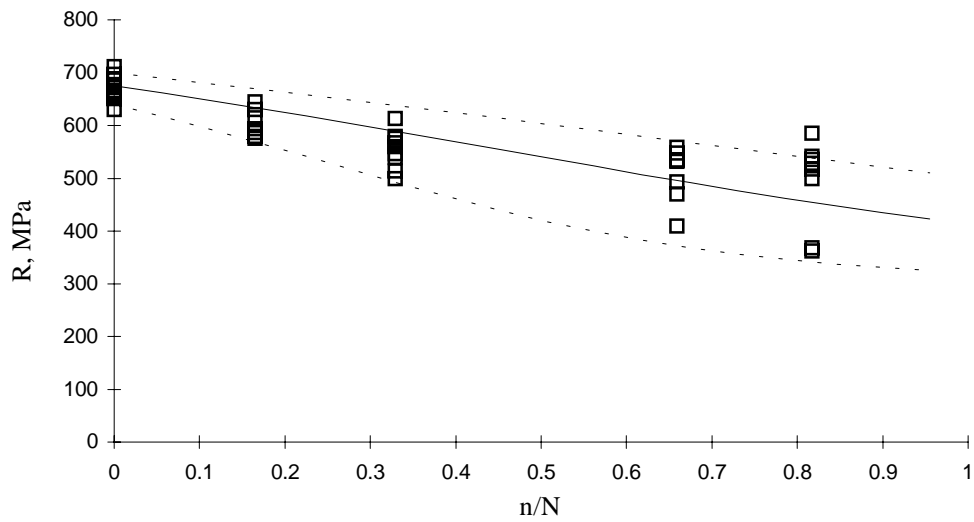


Fig. 3: Residual strength reduction at  $\sigma = 284 \text{ MPa}$   
 Statistical residual strength model prediction for failure probabilities .5 (—) ;  
 .1 and .9 (- - -)

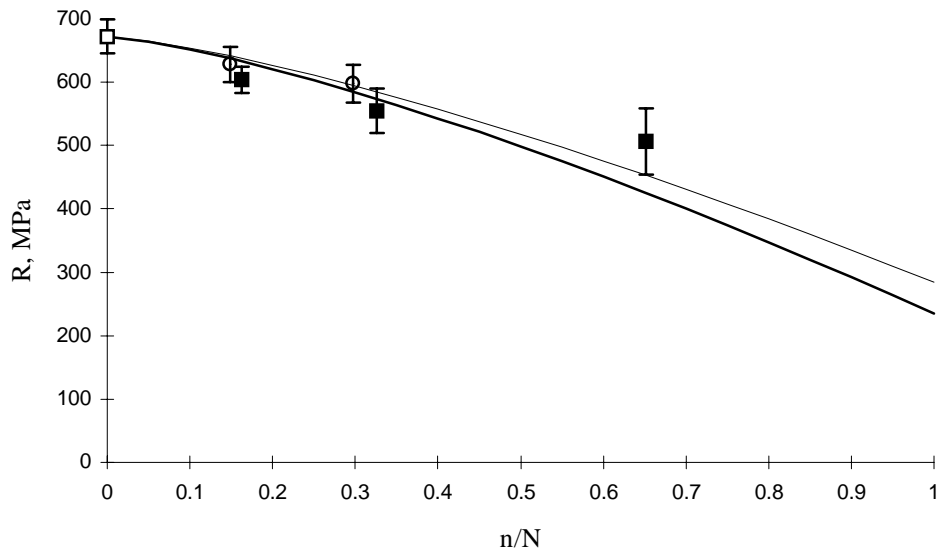


Fig. 4: Mean strength degradation at  $\sigma = 284$  MPa (■) and  $\sigma = 235$  MPa (○)  
Lines -deterministic model prediction

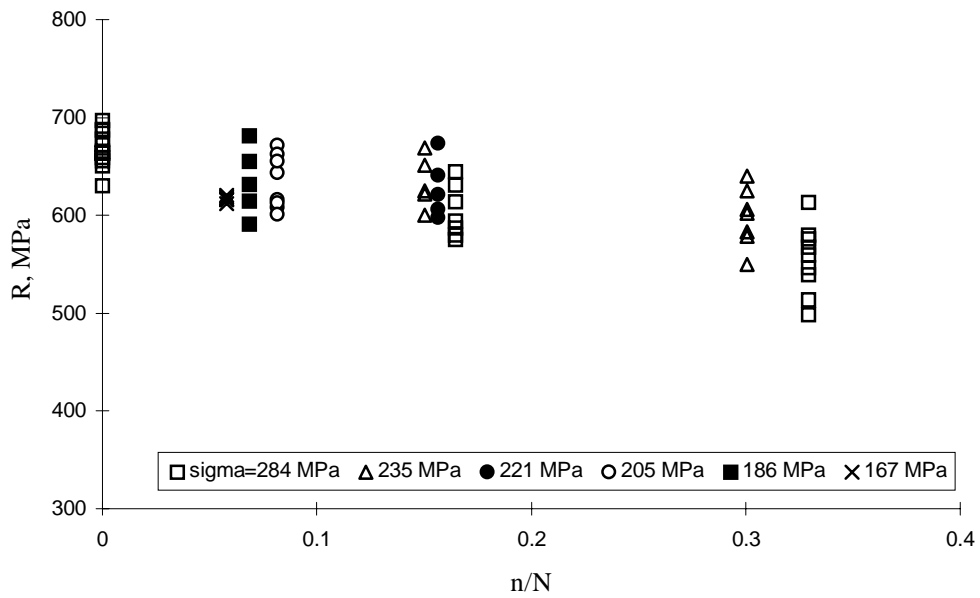


Fig. 5: Residual strength vs.nominal life fraction for different cyclic stress levels



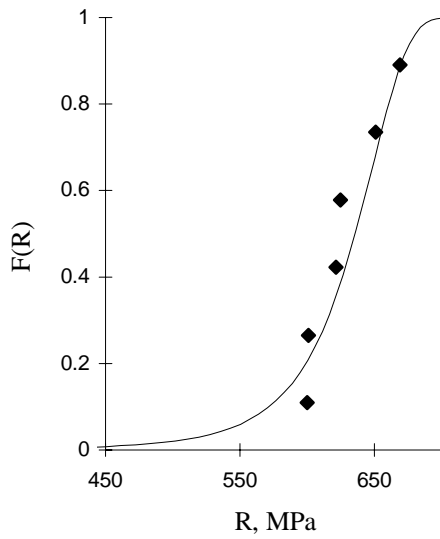


Fig. 6: Residual strength distribution after 200000 cycles at  $\sigma = 235$  MPa

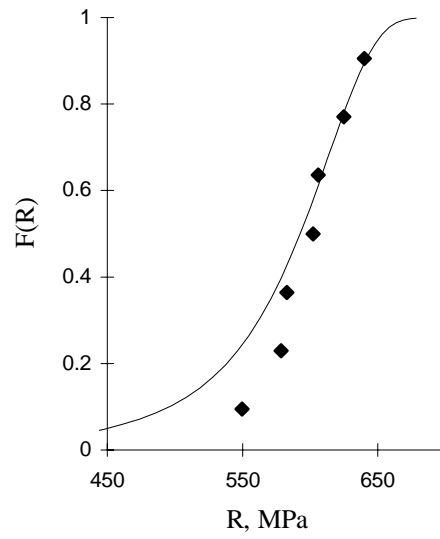


Fig. 7: Residual strength distribution after 400000 cycles at  $\sigma = 235$  MPa

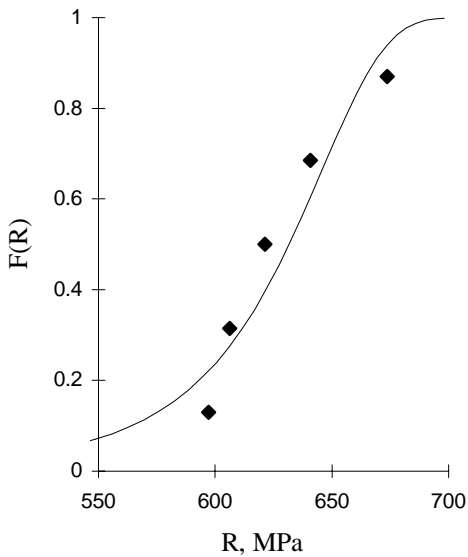


Fig. 8: Residual strength distribution after 400000 cycles at  $\sigma = 221$  MPa

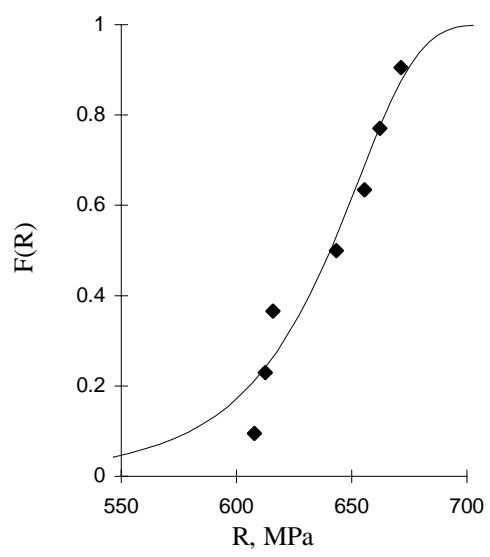
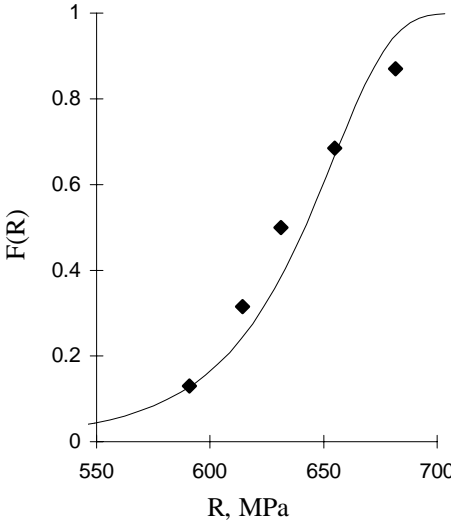


Fig. 9: Residual strength distribution after 400000 cycles at  $\sigma = 206$  MPa



*Fig. 10: Residual strength distribution after 800000 cycles at  $\sigma = 186$  MPa*

# A STOCHASTIC CUMULATIVE DAMAGE MODEL FOR THE FATIGUE RESPONSE OF LAMINATED COMPOSITES

R. Ganesan, S.V. Hoa, S. Zhang and M. El-Karmalawy

*Concordia Centre for Composites, Department of Mechanical Engineering  
Concordia University, Montreal, Quebec, Canada.*

**SUMMARY:** Polymer-matrix fibre-reinforced laminated composites display considerable variability in their fatigue response. Existing works on the quantification of fatigue response of composite laminates have deployed statistical and probabilistic approaches. These approaches are however inadequate for the prediction of the fatigue response as well as its probabilistic characteristics, and for the determination of reliability for use in design. In the present paper, a new cumulative damage model is developed based on a stochastic approach. The damage evolution in the composite laminate is quantified through the compliance increase in the laminate based on the embedded Markov process theory. The prediction of increase in compliance and the associated probabilistic characteristics is carried out based on this model. The fatigue response of a graphite epoxy composite laminate is then analyzed based on the new model using the test data. The composite material considered is AS 4/3501-6 graphite epoxy cross ply lay up  $[0/90]_{4s}$ .

**KEYWORDS:** fibre-reinforced polymer-matrix laminated composites, fatigue behaviour, stochastic process modelling and analysis, markov chains

## INTRODUCTION

Laminated composites are known for the high degree of variability in their mechanical properties. In particular, the behaviour and engineering properties of polymer-matrix laminated composite materials are significantly affected by the technological process defects, design errors at both material and structural level, and environmental effects which are random in nature. However, for quantifying the fatigue behaviour of composite laminates, so far only a deterministic approach has in most cases been deployed. This deterministic approach has resulted in disagreement between theory and practice.

Weibull [1] introduced into fatigue failure studies a probability distribution function in order to account for the variations in the life data of mechanical components made of metallic materials. Reliability analyses have been developed for metallic structures based on this distribution function. The Weibull distribution function has also been used to model the fatigue life data of composites [2-4].

The Weibull distribution function frequently provides a reasonable fit to the probability distributions of life times that have been obtained from fatigue tests or service operation. Some aspects of variability in life time can be assessed and accounted for. However, (i) the probability distribution function of life times has not been related to the fatigue damage process, (ii) it is not possible to separate and account for the major sources of variability in material response, (iii) the

correlation characteristics of test data are not accounted for, and (iv) the nature of physical process is not reflected. Further, there are only two limiting states of the material in the Weibull distribution based fatigue model, that are (i) satisfactory (no damage) and (ii) failure (completely damaged). This imposes severe limitations on the validity and applications of this model. For instance, one can not incorporate the initial damage distribution (for a composite, this refers to the fluctuations in the initial elastic modulus) nor it is possible to trace the damage accumulation during service using the Non-Destructive Testing (NDT) techniques. A rigorous stochastic approach can take into account all sources of variability in material response and lead to a reliable prediction of material response.

Fundamental to the design of composite structures is a model that can be deployed for the prediction of fatigue damage accumulation. The development of a cumulative damage model based on a rigorous stochastic approach and the associated prediction scheme is the objective of the present work.

### **MARKOV PROCESS MODELLING OF COMPLIANCE**

The model developed here considers the "Cumulative Damage (CD)" due to fatigue, which is the irreversible accumulation of fatigue damage in the composite material. A "Stochastic Phenomenological Model" is developed, since the experimental data display considerable randomness. The central idea is that in a suitably defined "Duty Cycle (DC)" a random amount of fatigue damage is accumulated in the composite laminate. This fatigue damage in turn results in the reduction of the elastic modulus of the laminate.

It is quite natural and reasonable to assume that the increment of damage at the end of a DC depends in a probabilistic manner on the amount of damage present at the start of the DC, on that DC itself, and is independent, in the probabilistic sense, of how (i.e. the damage development path) the damage was accumulated up to the start of that DC. This corresponds to the Markov assumption in the stochastic process theory.

It may be noted here that the Markov assumption is consistent with the system theory concepts that are well established. The laminate specimen can be viewed as a dynamic system. At any instant of time (or equivalently the load cycles), the compliance of the laminate is analogous to a variable system parameter. The input to the system, i.e. the excitation, is the loading during a DC. The increase in the compliance of the sample (i.e. damage increment) can be viewed as an output (i.e. response). The Markov assumption then simply implies that the response of the system (which is the increase in compliance at the end of a DC) is a function of the system parameter (i.e. the fatigue damage that has been present in the laminate before the DC was applied which is indicated by the laminate compliance at the start of the DC), and the excitation, and is independent of the way with which the value of the system parameter (i.e. the fatigue damage in the laminate at the start of DC) has been arrived at.

It is well known that (i) unlike the metals in a composite laminate various damage mechanisms become simultaneously active, and (ii) the viscoelastic response of the laminate is path-dependent. However, the fatigue damage in a laminate is not quantified in terms of the length of the fatigue crack or any other physically-observable variables (for which the path dependency is an important consideration) as in the case of metals. Rather, a material parameter such as compliance that is sensitive to, reflective of and representative of whatever forms of fatigue damage is deployed as a "system descriptor" or "damage development indicator". Also, this

parameter is determined from the instantaneous response of the laminate and not from the transient response.

Test data regarding the elastic modulus are collected using nominally-identical composite specimens that are subjected to fatigue loading. The compliance, which is the reciprocal of elastic modulus, increases as the fatigue damage sets in. The compliance is denoted here by  $C$  and the number of load cycles is denoted by  $n$ . The values of the stress ratio and the stress amplitude of the fatigue loading are denoted by  $R$  and  $S$  respectively.

For each test specimen, the  $C - n$  curve can be plotted. Due to the inherent variability associated with the accumulated damage, this curve varies from specimen to specimen. Typical sample realizations are depicted in Figure 1. The stochastic process modelling the compliance is denoted as  $\{C(n, S, R), n \in N, S \in A, R \in B\}$ , where  $N, A$  and  $B$  are the respective sample spaces of the number of load cycles, the stress amplitude and the stress ratio. The sets  $N, A$  and  $B$  are the index sets of the stochastic process  $\{C(n, S, R)\}$ .

The discrete set of damage states is determined based on the following procedure. The entire range of compliance values is calculated from the sample test data. This range is then divided into  $m$  number of equal or non-equal intervals,  $(C_2 - C_1), (C_3 - C_2), \dots, (C_{i+1} - C_i), \dots, (C_{m+1} - C_m)$ , where  $C_{m+1}$  is the maximum value of the compliance.

### Finite Markov Chain

The compliance process is viewed as a Markov process. The compliance process is non-homogeneous because the compliance is a continuous function of the number of load cycles. The index set  $N$  of this non-homogenous Markov process is  $(n_0, n_1, n_2, \dots, n_{j-1}, n_j, \dots, n_{max})$  and the state space is  $(1, 2, 3, \dots, j-1, j, \dots, m)$ . Both these index sets are discrete. A Markov process that has discrete index sets is called as Markov Chain (MC). Since the index sets are finite, the compliance becomes a Finite Markov Chain.

### Transition Probability Function (TPF)

As a result of the Markovian property and non-homogeneity of the stochastic process,

$$p_{ij}(n_{k-1}, n_k) = P[C(n_j) = j | C(n_{j-1}) = i]; n_k \in n_{k-1} \quad (1)$$

where  $p_{ij}(n_{k-1}, n_k)$  is the Transition Probability Function (TPF), which is the probability of the composite specimen entering a new damage state  $j$  at loading cycle  $n_k$ , given that it is currently in damage state  $i$  at loading cycle  $n_{k-1}$ . Based on the definition of the conditional probability density function, joint probability density function and Bayes' theorem [5] this equation can be recast into

$$p_{ij}(n_{k-1}, n_k) = P\{[C_j < C(n_k) \leq C_{j+1}] \cap [C_i < C(n_k) \leq C_{i+1}]\} / P[C_i < C(n_k) \leq C_{i+1}] \quad (2)$$

The individual probability density functions of random variables  $C_{k-1}$  and  $C_k$  are denoted by  $f_{C_{k-1}}(c_{k-1})$  and  $f_{C_k}(c_k)$  respectively. The joint probability density function corresponding to these two

correlated random variables is denoted by  $f_{C_{k-1} C_k} (c_{k-1}, c_k)$ . The TPF between damage states  $i$  and  $j$ , can be determined according to

$$p_{ij} (n_{k-1}, n_k) = \int_{C_j}^{C_{j+1}} \int_{C_i}^{C_{i+1}} f_{C_{k-1} C_k} (c_{k-1}, c_k) dc_{k-1} dc_k / \{ \int_{C_i}^{C_{i+1}} f_{C_{k-1}} (c_{k-1}) dc_{k-1} \} \quad (3)$$

### Transition Probability Matrix (TPM)

Generalizing Eq. (2) for all possible damage states included in the state space, the Transition Probability Matrix (TPM) of the composite specimen, denoted by  $[[[ (n_{k-1}, n_k) ]]$ , when the load cycle is increased from  $n_{k-1}$  to  $n_k$ , can be obtained. Since all damage states are mutually exclusive and collectively exhaustive, the sum of the probabilities in any row of the TPM that has non-zero probabilities is equal to unity. When the load cycle is  $n_{k-1}$ , the compliance is  $C(n_{k-1}) = i$ . Now, if the load cycle is increased to  $n_k$ , the compliance is  $C(n_k) = j$ . It is also possible that  $C(n_k) = C(n_{k-1})$  so that  $j = i$ . However, the system can not make a transition from a higher state to a lower state, i.e.  $C(n_k) < C(n_{k-1})$  so that  $j < i$ . The final state  $m$  is the "absorbing state" and so  $p_{mm} (n_{k-1}, n_k) = 1$ .

### M-Step Transition Probability Matrix

The transition probability matrix of the composite specimen corresponding to any initial load cycle  $n_0$  and any final load cycle  $n_m$  can be determined in terms of the transition probability matrices, based on the stochastic process theory. The resulting matrix of order  $m \times m$  is called as the "M-Step Transition Probability Matrix (M-Step TPM)" and is denoted by  $[[[ (n_0, n_m) ]]$ . In order to determine this matrix, use is made of the Chapman-Kolmogorov Theorem [5]. The product equation for the M-Step TPM is obtained as

$$[[[ (n_0, n_m) ]] = [[[ (n_0, n_1) ]] \times [[[ (n_1, n_2) ]] \times [[[ (n_2, n_3) ]] \times \dots \times [[[ (n_{m-1}, n_m) ]] \quad (4)$$

In order to determine the unconditional probabilities of the damage states of the specimen, given the initial damage state distribution, when the load cycle is increased from  $n_0$  to  $n_m$ , the following equation is derived.

$$\{ \prod^U (n_0, n_m) \} = \{ \prod (0) \} \times [[[ (n_0, n_1) ]] \times [[[ (n_1, n_2) ]] \times \dots \times [[[ (n_{m-1}, n_m) ]] \quad (5)$$

In this equation,  $\{ \prod (0) \}$  denotes the initial damage state (row) vector of the specimen which consists of the probabilities of the specimen in different damage states at load cycle  $n_0$ .

### Prediction of Damage States at any Load Cycle

The initial and final values of load cycles that have been included in the test program are first considered. This duty cycle is expressed in terms of  $m$  number of smaller duty cycles. For each smaller duty cycle, the transition probability matrix is determined according the procedure given in the foregoing. This way,  $m$  number of transition matrices will be available. For each entry in the transition probability matrix,  $m$  number of values will be available. For instance, consider any transition probability  $p_{ij}$ . If 10 steps (smaller duty cycles) are considered, ten values of this transition probability viz.,  $1p_{ij}, 2p_{ij}, 3p_{ij}, \dots, 10p_{ij}$  will be available. These ten values are considered as constituting a random variable. Further, it is assumed here that this random variable, denoted by  $p_{ij}$  has a Gaussian distribution.

The ten sample values are used as a basis for predicting the value of transition probability  $p_{ij}$  that corresponds to the duty cycle defined by the final load cycle value of the 10-th (smaller) duty cycle and the value of the load cycle at which the prediction is to be made. The relevant rationale and procedure are outlined in the following.

(i) For the random variable  $p_{ij}$ , a Gaussian probability density function is fitted using the ten sample values available. The parameters of this Gaussian density function,  $\mu_{ij}$  and  $\sigma_{ij}$ , can be determined following the standard parameter estimation techniques [6]. A suitable statistical analysis program is available in the MATLAB software, and this program was used in the present work.

(ii) A standardized random variable  $z_{ij}$  is defined according to the relationship  $z_{ij} = (p_{ij} - \mu_{ij}) / \sigma_{ij}$ . This standardized random variable will also have Gaussian distribution because the Gaussian nature of probability distribution does not change when a linear transformation of normal random variable is performed.

(iii) Now, the concepts of reliability theory and failure probabilities [7] are deployed. It can be proved using the probability theory and system reliability theory that a value of  $p_{ij}$  that corresponds to a reliability  $R$  (say 90%) can be obtained by first determining the value of  $z_{90}$  such that the area bounded by the density function curve of  $z_{ij}$  between the range  $-\infty$  to  $z_{90}$  is 0.9, and then calculating the value of  $p_{ij}$  according to the relationship  $(z_{90} \sigma_{ij}) + \mu_{ij}$ . For instance, when the reliability is 90%, the value of  $z_{90}$  is approximately equal to 1.3. Now consider a transition probability, say  $p_{33}$ . By fitting a Gaussian distribution, the parameters of Gaussian density function for  $p_{33}$  can be obtained and say, they are equal to, 0.4819 and 0.2843 (it is worthwhile to note the magnitude of randomness in the values of  $p_{33}$ , which is approximately 60% in the above example). The value of  $p_{33}$  which will have a reliability of 90% (i.e. the probability that this value will be exceeded in actual test results is 10%) is  $\{[1.3 (0.2843)] + 0.4819\}$  which is equal to 0.8515. This is the predicted value of  $p_{33}$ . This procedure is followed to determine the predicted values of all the transition probabilities. This way, the complete transition probability matrix is determined.

Now, the (10+1) - step duty cycle defined by the initial value of the load cycle in the test program and the value of the duty cycle at which the prediction is to be made, is considered. Ten transition probability matrices can be determined from test data and the eleventh transition probability matrix is predicted. The unconditional probabilities of damage states corresponding to the load cycle at which prediction is to be made can be determined using Eqs. (4) and (5). The value of  $m$  is equal to 11. These unconditional probabilities define the histogram of damage states corresponding to the load cycle where prediction is to be made.

### Analytical Probability Density Functions

The probability density function of the compliance at load cycle  $n_{k-1}$ , which is denoted as  $f_{C_{k-1}}(c_{k-1})$  is determined based on the Maximum Entropy Method [7]. Based on this method, the analytical form of the probability density function  $f_{C_{k-1}}(c_{k-1})$  is taken to be

$$f_{C_{k-1}}(c_{k-1}) = \exp \left[ \lambda_0 + \sum_{i=1}^p \lambda_i c_{k-1}^i \right] \quad (6)$$

The values of the parameters  $\lambda_i$ ,  $i = 0, 1, 2, \dots, p$  are determined such that the entropy of the random variable  $c_{k-1}$  given by

$$S = - \int_R f_{C_{k-1}}(c_{k-1}) \ln [ f_{C_{k-1}}(c_{k-1}) ] dc_{k-1} \quad (7)$$

where  $R$  denotes the range of the random variable  $c_{k-1}$ , is maximum, subject to the following constraints: (i) the total probability is unity, i.e.

$$\int_R f_{C_{k-1}}(c_{k-1}) dc_{k-1} = 1 \quad (8)$$

and (ii) the probabilistic moments of the random variable  $c_{k-1}$  defined in terms of the probability density function  $f_{C_{k-1}}(c_{k-1})$  are equal to the corresponding statistical moments obtained from the compliance data, i.e.

$$\int_R c_{k-1}^i f_{C_{k-1}}(c_{k-1}) dc_{k-1} = M_i, \quad i = 1, 2, \dots, q \quad (9)$$

where  $M_i$  is the  $i$ -th statistical moment about the origin of the compliance values  $c_{k-1}$ .

Further details regarding the Maximum Entropy Method can be found in Ref. 7. The above problem should be solved based on the techniques of optimization. The optimization technique that is best suited to this problem is the Nonlinear Programming Technique proposed by Jacobson and Oksman [8].

### Joint Probability Density Functions

The joint probability density function is determined based on the relative frequency approach [6], in the form of a three-dimensional histogram.

## EXPERIMENTAL INVESTIGATION

The composite material considered is AS 4/3501-6 Graphite Epoxy cross ply lay up  $[0/90]_{4s}$ . Plates made up of this material and of dimensions 280 mm x 250 mm x 1 mm were manufactured. The manufacturing conditions are as follows: Each plate is first heated for 1 hour at a temperature of 116° C and at a pressure of 586 kPa (full vacuum), then it is heated for 2 hours at a temperature of 176° C and at a pressure of 655 kPa (full vacuum). Each plate was then used to produce 10 specimens each of dimensions 280 mm x 25 mm x 1 mm. Aluminium plates 30 mm x 30 mm x 0.2 mm were attached to the gripping regions of the specimens, using the ASTM D 3039/D 3039-93 test procedure. The effects of relaxation stresses induced during manufacturing usually disappear about six months after fabrication, as described in [9]. In order to minimize the effects of stress relaxation, all the tests for a batch of specimens were carried out at a fixed time, that is one month after conditioning, after which 90% of the recovery has taken place.

The environmental conditions can seriously affect the damage properties of composites. In particular, the internal stress caused by machining and the moisture induced during machining can change the value of the damage measure, and so the specimens must be conditioned before testing. The method previously used in Ref. 9 has been employed in the present work, in this regard. It consists of (i) heating the specimens at 100° C in an oven for 2 hours, (ii) raising the



temperature to 170° C and holding it for two hours, and (iii) leaving the specimen at room temperature for at least one week before testing. All the plates were tested for defects using C-scanning technique and using microscopic inspection for voids, and only those plates that met the required quality were chosen for static and fatigue tests.

### Static Testing

In the experimental investigation, considerable attention has been paid to ensure the quality of the composite specimens and test procedures. Two specimens were chosen from each plate to be tested for static properties and strength, and those specimens were chosen from a random position in the plate. The specimens were tested for their tensile properties in accordance with the ASTM D 3039/D 3039-93 standard test method for tensile properties of polymer matrix composite materials. Only those plates with specimens having tensile strength and modulus within 10% variation of the average tensile strength and average modulus of all tested specimens, were accepted. All other specimens were rejected. The (statistical) average tensile strength of the tested specimens was 614 MPa with a standard deviation of 49.5 MPa. The (statistical) average Young's modulus of the tested specimens has been 61.151 GPa with a standard deviation of 2.27 GPa.

### Fatigue Testing

Tests were conducted at room temperature on an MTS hydraulic machine. Specimens were clamped to the machine grips using Al tabs as outlined in the ASTM D 3039/D 3039-93 test procedure. An on-axis T-T fatigue load at 5 Hz frequency and with a load ratio R of 0.1 was applied. The maximum load is chosen to be that required to induce gradual failure to the specimens. The value chosen corresponds to 70% of the average specimen strength. This value represents a realistic value used in the design of composite structures. The fatigue/static strength ratio for uniaxial CFRP is widely quoted [10] as being about 70% for endurance of about  $10^7$  cycles. The stress level selected is at a middle level between the higher applied stress levels resulting in higher stiffness at failure and shorter fatigue lives, and the lower stress levels which induce more total damage than higher stress levels (as evident by the greater amount of stiffness reduction at failure). The fatigue modulus was obtained by dividing the maximum applied stress by the corresponding strain. The values were monitored continuously during load cycling. The values of fatigue compliance at different number of load cycles were plotted in Figure 1.

## NUMERICAL RESULTS FOR THE MARKOV CHAIN

**Step 1:**Determination of the damage states: The largest value in the state space i.e. the largest value of the compliances of all test specimens, is  $1.7831 \times 10^{-11} \text{ Pa}^{-1}$  and the lowest value is  $1.6114 \times 10^{-11} \text{ Pa}^{-1}$ , as can be seen from Figure 1. This range of compliance values is then divided into seventeen damage states of same size.

**Step 2:**Generate Probability Density Functions for Each Compliance Value Set  $C(n_{k-1})$ : The first four statistical moments, i.e.  $M_1$ ,  $M_2$ ,  $M_3$  and  $M_4$ , of each compliance value set  $C(n_{k-1})$  are determined and are used as constraints in the determination of  $f_{C_{k-1}}$ . The maximum entropy method yields the values of the five parameters viz.,  $\lambda_i$ ,  $i=0, 1, 2, \dots, 4$ , for each  $f_{C_{k-1}}$ . The values of these parameters are listed in Table 1.

Table 1: List of the values of  $\lambda_i$  at five load cycles

	$\lambda_0$	$\lambda_1$	$\lambda_2$	$\lambda_3$	$\lambda_4$
0 cycle	-59.75927	12.11768	-0.976104	0.0350279	-0.000468
101 cycles	-52.95307	4.758957	-0.163753	0.0024078	-0.000013
151 cycles	-10.20866	0.032665	0.0168172	-0.000467	0.0000034
201cycles	11.63882	-1.913443	0.0765457	-0.001223	0.0000067
251 cycles	-1.021048	-0.437083	0.0163917	-0.000210	0.0000008

**Step 3:**Determination of Joint Probability Density Functions: Five three-dimensional histograms that correspond to five smaller duty cycles (0, 101), (101, 151), (151, 201), (201, 251) and (251, 301) are determined.

**Step 4:**Evaluation of Transition Probability Matrices: The transition probability matrices can now be evaluated using Eq. (3). The single-variable integration is performed using a subroutine available in MATLAB software. At this stage, the sum of the non-zero transition probabilities in each row of the transition probability matrix is calculated. Theoretically, the sum must be equal to unity. However, for practical purposes, a tolerance margin of  $\pm 10\%$  is used in the present work. If the sum of the transition probabilities is more than 1.1 or less than 0.9, suitable modifications have to be made as to the bounding compliance values of the damage states  $C_i$ ,  $i = 1, 2, \dots, 18$  and/or the bounds used for the single-variable distributions. An iterative procedure is hence called for. The five transition probability matrices each of order  $17 \times 17$  corresponding to the five duty cycles (0, 101), (101, 151), (151, 201), (201, 251) and (251, 301) are obtained using the above procedure. The matrices  $[\Pi(0, 101)]$  and  $[\Pi(101, 151)]$  are considered for illustrative purposes and those parts of the rows and columns of these matrices that have non-zero entries are given below:

$[\Pi(n_0, n_1)] = [\Pi(0, 101)]:$   
 Row 1 0.0 0.4369 0.2496 0.1872 0.1248 0.0 0.0  
 Row 2 0.0 0.2003 0.5342 0.1335 0.0668 0.0668 0.0

$[\Pi(n_1, n_2)] = [\Pi(101, 151)]:$   
 Row 2 0.0 0.3064 0.7149 0.0 0.0 0.0 0.0  
 Row 3 0.0 0.0 0.5243 0.5243 0.0 0.0 0.0  
 Row 4 0.0 0.0 0.0 0.3935 0.5902 0.0 0.0  
 Row 5 0.0 0.0 0.0 0.0 0.2792 0.5583 0.0  
 Row 6 0.0 0.0 0.0 0.0 0.0 0.9089 0.0

**Step 5:**Calculation of  $m$ -step Transition Probability Matrices: The 5-step transition probability matrix  $[\Pi(n_0, n_5)]$ , which is  $[\Pi(0, 301)]$  can be determined using Eq. (4). The entries in the first two rows and first six columns of the transition probability matrices have non-zero values and they are given below:

$[\Pi(n_0, n_5)] = [\Pi(0, 301)] =$   
 Row 1 0.0 0.4369 0.2496 0.1872 0.1248 0.0  
 Row 2 0.0 0.2003 0.5342 0.1335 0.0668 0.0668

**Step 6:** Calculation of the Unconditional Probabilities of Compliances at Load Cycle 301: This step is carried out using Eq. (5) to determine the probability density function of compliances at the end of duty cycle (0, 301). The row vector  $\{\Pi(0)\}$  consists of the probability distribution of initial damage states of the specimens and is determined from the distribution of  $C(0)$ . For the present case the row vector  $\{\Pi(0)\}$  is given by:  $\{\Pi(0)\} = \{0.516129, 0.483871, 0, 0, 0, 0, 0, 0, 0, 0, 0, 0, 0, 0, 0\}$ . The unconditional probabilities of the compliances at  $n_5=301$  is given below:

$$\{\Pi^U(0, 301)\} = \{0.0 \ 0.0967 \ 0.0967 \ 0.3870 \ 0.2580 \ 0.1290 \ 0.0322 \ 0 \dots\dots 0\}$$

**Prediction of Damage State Probabilities at Load Cycle 351**

Now, the duty cycle (301, 351) is considered. Using the transition probability matrices  $[\Pi(0, 101)]$ ,  $[\Pi(101, 151)]$ ,  $[\Pi(151,201)]$ ,  $[\Pi(201, 251)]$ , and  $[\Pi(251, 301)]$ , the transition probability matrix  $[\Pi(301, 351)]$  is predicted with a reliability of 90%. All the non-zero transition probabilities are located within the first six rows and six columns of predicted matrix  $[\Pi(251, 301)]$ :

$[\Pi(301, 351)] :$

Row 1	0.0	0.3414	0.1950	0.1463	0.0975	0.0
Row 2	0.0	1.1415	0.7022	0.1043	0.0522	0.0522
Row 3	0.0	0.0	0.8515	0.6060	0.0	0.0
Row 4	0.0	0.0	0.0	1.0259	0.5545	0.0
Row 5	0.0	0.0	0.0	0.0	1.2590	0.4752
Row 6	0.0	0.0	0.0	0.0	0.0	1.2924

The unconditional probability matrix is given by  $\{\Pi^U(0, 351)\} : \{0.0 \ 0.0709 \ 0.0965 \ 0.2989 \ 0.3494 \ 0.0899 \ 0.0944 \ 0 \ 0 \dots\dots 0\}$ , and the corresponding histogram is plotted in Figure 2. From the test data, the histogram of compliances at load cycle 351 is determined (Figure 3). They are:  $\{0.0 \ 0.0968 \ 0.0968 \ 0.3548 \ 0.2581 \ 0.0968 \ 0.0968 \ 0 \ 0 \dots\dots 0\}$ . A reasonable agreement can be observed.

**CONCLUSIONS**

The fatigue behaviour of laminated composites is considered and a stochastic approach to model and analyze this behaviour is developed. The following major sources of variability in cumulative damage process are incorporated in the stochastic model: (i) Initial damage state, (ii) Severity and order of both the load cycles as well as the material damage, (iii) State of damage at the failure of the test specimen. The severity of load cycle and the material damage (including the changes in the material properties) is specified in the model in terms of the probability transition matrix. The variations in the severity of repetitive load cycles and the material damage are incorporated through the non-homogeneous nature of the damage evolution process. The randomness in the initial damage due to manufacturing errors, technological process defects, design errors etc., is specified by the initial damage state vector. The stochastic model developed in the present work possesses the capability of prediction.

## REFERENCES

1. Weibull, W. 1951. A Statistical Distribution Function of Wide Applicability. *Transactions of the ASME: Journal of Applied Mechanics*, 1951, Vol. 18, pp. 293-297.
2. Hahn, H. T. and Kim, R. Y. 1975. Proof Testing of Composite Materials. *Journal of Composite Materials*, Vol. 9, pp. 297-311.
3. Ramani, S. V. and Williams, D. P. 1977. Notched and Unnotched Fatigue Behaviour of Angle-Ply Graphite/Epoxy Composites. In: *Fatigue of Filamentary Composite Materials*, ASTM STP 636. Eds.: K. L. Reifsnider and K. N. Lauraitis, pp. 27-46.
4. Talreja, R. 1987. *Fatigue of Composite Materials*. Technomic publishing Company, Lancaster.
5. Cox, D. R. and Miller, H. D. 1965. *The Theory of Stochastic Processes*, Methuen and Co, London.
6. Bendat, J. S. and Piersol, A. G. 1986. *Random Data: Analysis and Measurement Procedures*, Wiley Interscience, New York.
7. Siddall, J. N. 1983. *Probabilistic Engineering Design: Principles and Applications*. Marcel Dekker, New York.
8. Siddall, J. N. 1982. *Optimal Engineering Design*. Marcel Dekker, New York.
9. Ni, R. G. and Adams, R. D. 1984. The Damping and Dynamic Moduli of Symmetric Laminated Composite Beams - Theoretical and Experimental Results. *Journal of Composite Materials*, Vol. 18, pp. 104-121.
10. Cardrick, A. W. and Smith, M. A. 1974. An Approach to the Development of Meaningful Design Rules for Fatigue-Loaded CFRP Components, *Composites*, Vol. 5, pp. 96-100.

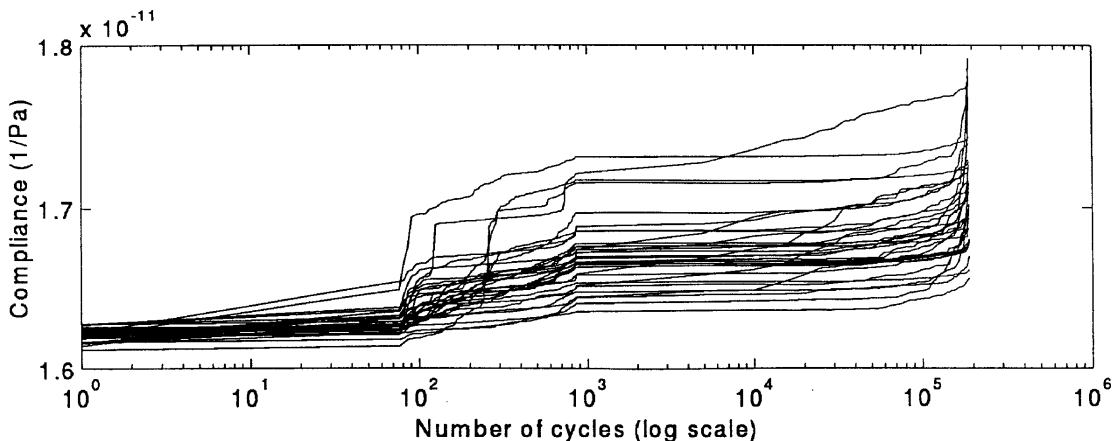


Fig. 1 Typical Sample Realizations of Specimen Compliance

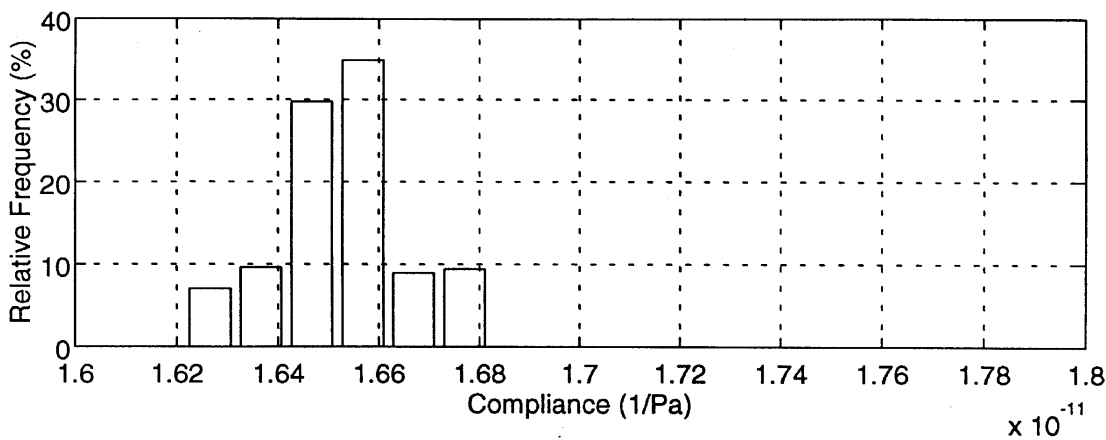


Fig. 2 Predicted Probability Distribution for the Compliance at Load Cycle 351

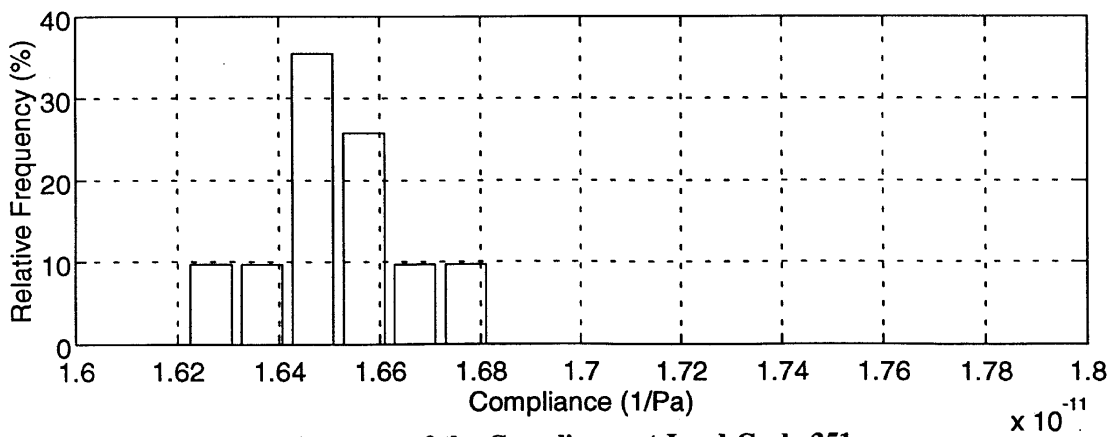


Fig. 3 Histogram of the Compliance at Load Cycle 351

# PROGRESSIVE FATIGUE MODELING OF LAMINATED COMPOSITE PINNED/BOLTED CONNECTIONS

Mahmood M. Shokrieh<sup>1</sup> and Larry B. Lessard<sup>2</sup>

<sup>1</sup> *Department of Mechanical Engineering, Iran University of Science and Technology  
Tehran, Iran*

<sup>2</sup> *Department of Mechanical Engineering, McGill University, 817 Sherbrooke St. West  
Montréal, Québec, H3A 2K6, Canada*

**SUMMARY:** In this research, a deterministic model for predicting the behaviour of laminated composite pinned/bolted connections under fatigue loading is described. A phenomenological modeling technique, called *progressive fatigue damage modeling*, is established which is capable of predicting the residual strength, residual stiffness, and fatigue life of composite laminates. Stress analysis, failure analysis, and material property degradation rules are the three major components of the model. A three dimensional, nonlinear, finite element technique is proposed for the stress analysis. Based on the state of stress, different failure modes are detected by a set of fatigue failure criteria. To remove the requirement of the large experimental data base for the failure analysis a normalization technique is established. By using this technique the restriction of the application of the failure criteria to limited states of stresses is overcome. Material properties of each element are degraded by using *sudden* and *gradual* material property degradation rules. For this purpose an analytical technique is established to predict the degradation of material properties of a unidirectional ply under multiaxial fatigue loading. Based on the *model*, a computer code is developed that simulates cycle by cycle behaviour of composite laminates under fatigue loading.

**KEYWORDS:** fatigue, pin, bolt, progressive modeling, failure criteria

## INTRODUCTION

One of the earliest papers in fatigue of composite laminates with stress concentrations was published by Owen and Bishop [1]. Today, there are several experimental [2-5] and analytical [6-8] research papers in this field. However, the present state of knowledge is still in the stage of development and improvement. Among the existing models, the semi-empirical model of Kulkarni *et al.* [6], the critical element model of Reifsnider *et al.* [7], and the damage growth model of Spearing *et al.* [8] are all systematic and methodological, therefore they are worthwhile for discussion. The semi-empirical model of Kulkarni *et al.* [6] was developed based on a mechanistic wearout [9] framework. The wearout philosophy treats fatigue damage as the growth of pre-existing flaws or discontinuities in a material. By growing the flaws, the strength of the material decreases and reaches to the level of the state of stress and finally, catastrophic fatigue failure occurs. The semi-empirical model was evaluated by experimental techniques, but little correlation between the theory and

experiments was found. Although the semi-empirical model of Kulkarni *et al.* [6] never showed a correlation with experimental results, there are however many interesting points and valuable information in their work. The critical element model of Reifsnider *et al.* [7] was developed based on a mechanistic approach. Their mechanistic approach is based on micromechanical representations of strength. Sendekyj [10] listed some of the weaknesses of this model. In the critical model, it is assumed that failure occurs suddenly and everywhere in the lamina, which is not consistent with the experimental observations. Also in the model, the dependence of lamina failure stresses on the lamina thickness in laminates is not properly considered. Moreover, the model does not properly account for delamination between the laminae in the laminate. The damage growth model of Spearing *et al.* [8] is based on quantification of notch tip damage by the extent of the individual failure processes, such as splitting in the 0° plies and delamination between the 0° ply and off-axis plies. There are some limitations in the damage growth model which are listed here. The model is laminate geometry dependent, i.e., by changing the lay-up of the laminate, the model must be modified. Moreover, the existence of transverse ply cracks, which is an important failure mode, is ignored in their model. Furthermore, they assume that the damage pattern is similar in all plies and delamination shape is the same at all interfaces which is not a general assumption. Also, the shape of the notch is pre-defined. In addition, their model is only capable of considering cyclic tensile loading. Thus all existing models for fatigue analysis of composites have limitations which make them unsuitable for general use.

### **PROBLEM STATEMENT**

Consider a composite plate with a hole under fatigue pin/bolt loading. The coordinate axes, dimensions, and variables are shown in Fig. 1. At the start of cyclic loading, the strength of the material is greater than the stress state, therefore there is no static mode of failure anywhere on the plate. By increasing the number of cycles from zero, based on the stress states at each point of the plate, material properties at those points are degraded as a function of number of cycles. By increasing number of cycles with more degradation of the material properties and redistribution of stresses, failure begins in regions where the strength of the material is less than the stress state at that point. After failure initiation, stresses are redistributed around failed regions. By further increasing the number of cycles, failure propagates in different directions. Finally after a certain number of cycles the laminate cannot tolerate additional cycles. At this point the maximum number of cycles is reached and the laminate has failed completely.

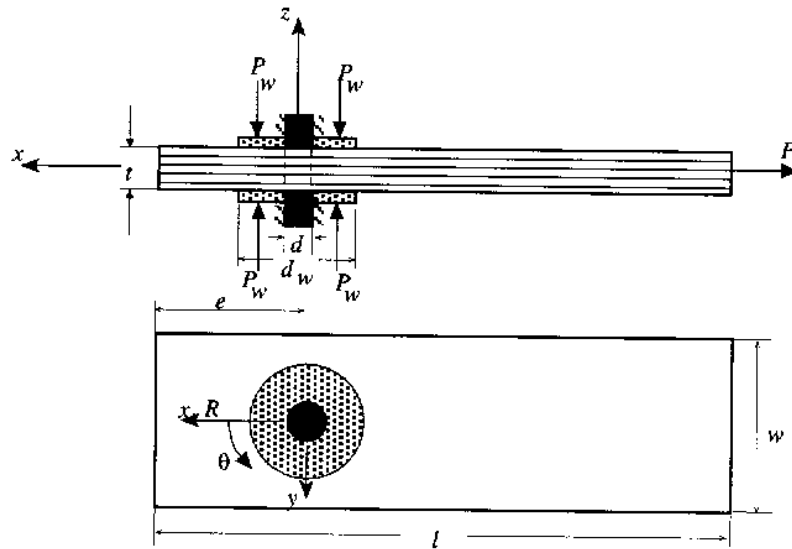


**Fig. 1: Composite plate under pin/bolt load**

## COMPONENTS OF THE MODEL

Progressive fatigue damage model is an integration of three major components. These are stress analysis, failure analysis, and material property degradation rules. There are some similarities between static and fatigue progressive damage modeling. However, there are many features in fatigue progressive damage modeling that make this technique quite different from static progressive damage modeling. Details of these differences will be more clear in the next sections. In the following, after a brief explanation of each component, the model is established by the integration of the three components.

### Stress Analysis

By considering edge effects, delamination, out-of-plane buckling, and stacking sequence effects that are fully three dimensional phenomena, and because of material nonlinearity, a three dimensional nonlinear finite element technique is used for the stress analysis. Assuming symmetric geometry, loading, and ply lay-up, suitable boundary conditions are used (Fig. 2). Radial fixed displacement boundary conditions have been applied on nodes around the hole at the load region to simulate the pin load. To simulate a fully tightened bolt, a uniform pressure is applied on the washer region. Moreover, to simulate friction between the washer and the plate, fixed displacement boundary conditions in radial and tangential directions are applied on nodes on the surface of the composite plate and under the washer region. The material properties of a unidirectional ply are assumed to be transversely isotropic. By this assumption, in three dimensions, the number of material parameters (strengths, stiffnesses, and Poisson's ratios) is reduced from eighteen to eleven. To achieve high accuracy, the isoparametric quadratic 20-node brick element was used. Also by using a large number of elements near the edge of the hole and at layer interfaces, stress singularities have been considered.



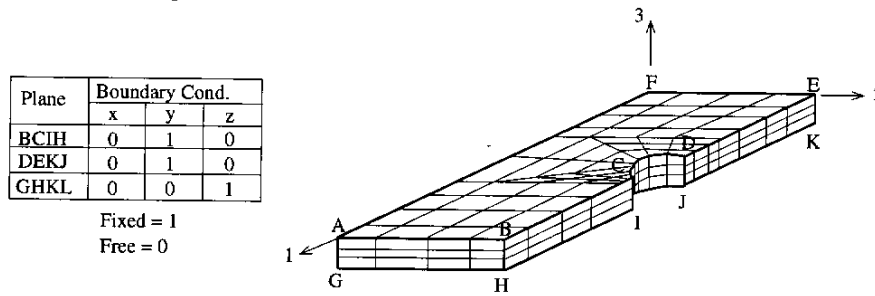


**Fig. 2: Finite element model**

**Failure Analysis**

Despite the existence of an extensive amount of research on biaxial/multi-axial fatigue of metals [11], research in the same field on composite materials [12,13] is less complete. Literature reviews on multi-axial and biaxial fatigue loading of composite materials presented by Found [12], and Chen and Matthews [13] state that further research in this field is needed.

In this research, seven different failure modes for the unidirectional ply under multi-axial state of stress are considered which are: fiber tension, fiber compression, fiber-matrix shearing, matrix tension, matrix compression, normal tension and normal compression failure modes. Suitable stress-based failure criteria for detecting these modes of failure under static and fatigue loading conditions are derived. The effect of material nonlinearity on the mathematical form of the failure criteria is also considered. Difficulties and limitations of application of such failure criteria, in traditional forms, for unidirectional plies under multi-axial fatigue loading conditions for general stress state and stress ratios are discussed. Under fatigue loading conditions, the material is loaded by a stress state which is less than the maximum strength of the material, therefore there is no static mode of failure. However, by increasing the number of cycles, the material properties degrade and eventually lower to the level of the stress state and, at this point, catastrophic failure occurs. The idea of using polynomial failure criteria to predict the life of a composite ply under multi-axial fatigue loading has been utilized by many investigators [14-16]. They used the fatigue strength, as a function of number of cycles, in the denominators of failure criteria instead of the static strength of the material. This strategy is potentially beneficial, however in practice, the application of their models are restricted to very specific conditions.

To show the restriction of application of fatigue failure criteria in traditional forms, consider the following fatigue failure criterion introduced by Hashin [15] for fiber tension fatigue failure mode of a unidirectional ply under a two-dimensional state of stress (biaxial fatigue),

$$\left( \frac{\sigma_{xx}}{X_t(n, \sigma, \kappa)} \right)^2 + \left( \frac{\sigma_{xy}}{S_{xy}(n, \sigma, \kappa)} \right)^2 = g_{f+}^2 \quad (\text{if } g_{f+} > 1, \text{ then failure}) \quad (1)$$

where  $X_t(n, \sigma, \kappa)$  is the residual longitudinal tensile strength of a unidirectional ply under uniaxial fatigue loading, and  $S_{xy}(n, \sigma, \kappa)$  is the residual in-plane shear strength of a unidirectional ply under uniaxial shear fatigue loading conditions. Both  $X_t$  and  $S_{xy}$  are functions of  $n$ ,  $\sigma$  and  $\kappa$ , which are number of cycles, stress state and stress ratio, respectively. In practice, designers must deal with a wide range of states of stress, varying from low to high. Therefore, in order to apply Eq. 1, the residual longitudinal tensile fatigue strength and

residual in-plane shear fatigue strength of a unidirectional ply ( $X_{i,(n,\sigma,\kappa)}$  and  $S_{xy,(n,\sigma,\kappa)}$ ) must be fully characterized under different stress levels and stress ratios. This requires a large quantity of experiments just to predict the fiber in tension fatigue failure mode of a unidirectional ply under simple biaxial fatigue loading conditions. By considering the other modes of failure and the multiaxial states of stress which are encountered in the real fatigue design of composite structures, the proposed method is faced with severe difficulties.

To overcome the difficulties arising from the large quantity of experiments required at different stress states and stress ratios to characterize the material, many investigators [14-16] restricted their models to specific stress ratios. This assumption is too restrictive for general cases. For example, in the analysis of a pin/bolt fatigue loaded composite laminate, using a constant stress ratio leads to incorrect results. Clearly, for this problem there are different states of stress at different points in the material. Also, after applying fatigue load on a notched composite laminate, failure initiates near the stress concentrations and the material property degrades, therefore the stress ratio and the state of stress are not constant at different points. This means that in practice, stresses redistribute during the fatigue loading. By considering the different behaviour of a unidirectional ply for each combination of the stress state and stress ratio, an infinite number of experiments would be required in order to fully characterize the residual properties of a unidirectional ply under arbitrary state of stress and stress ratio. To eliminate the aforementioned obstacle of using the quadratic polynomial failure criteria for a wide range of stress state and stress ratio, a novel technique (generalized residual material property degradation model) which has been explained in detail in other articles [17,18] published by authors. The fatigue failure criteria for different modes of failure are similar to static failure criteria, except that the material properties are not constants but functions of number of cycles, stress state, and stress ratios. It should be added that the effects of material nonlinearity on the fatigue failure criteria are also considered. A list of different fatigue failure criteria suitable for detecting various modes of failure is explained elsewhere [19] and for brevity is not repeated in this paper.

### **Material Property Degradation**

As failure occurs in a ply of a laminate, material properties of that failed ply are changed by the material property degradation rules. For each mode of failure, there exists an appropriate *sudden* material property degradation rule. Some of the failure criteria are catastrophic and some of them are not. Thus for each failure mode a suitable rule exists. For instance, after detecting fiber tension failure mode, which is a catastrophic mode, all of the stiffnesses and Poisson's ratios of the failed ply are reduced abruptly to zero. As another example, for matrix tension failure mode, only the transverse stiffness and Poisson's ratios are changed to zero. Moreover in fatigue loading, after each number of cycles, material properties of each ply (strengths, stiffnesses, and Poisson's ratios) are degraded, even though failure is not detected by any of the above mentioned failure criteria. For this purpose an analytical technique is established to predict the *gradual* degradation of material properties of a unidirectional ply under multiaxial fatigue loading.

The residual strength of a unidirectional ply under arbitrary uniaxial state of stress and stress ratio is calculated using the following equation:

$$R(n, \sigma, \kappa) = \left[ 1 - \left( \frac{\log(n) - \log(.25)}{\log(N_f) - \log(.25)} \right)^\beta \right]^{\frac{1}{\alpha}} (R_s - \sigma) + \sigma \quad (2)$$

where,  $R(n, \sigma, \kappa)$  = residual strength,  $R_s$  = static strength,  $n$  = number of applied cycles,  $\sigma$  = magnitude of applied maximum stress,  $N_f$  = fatigue life at  $\sigma$ ,  $\kappa$  = stress ratio, and  $\alpha$  and  $\beta$  = experimental curve fitting parameters. The residual stiffness of a unidirectional ply under arbitrary uniaxial state of stress and stress ratio is calculated using the following equation:

$$E(n, \sigma, \kappa) = \left[ 1 - \left( \frac{\log(n) - \log(.25)}{\log(N_f) - \log(.25)} \right)^\lambda \right]^{\frac{1}{\gamma}} \left( E_s - \frac{\sigma}{\epsilon_f} \right) + \frac{\sigma}{\epsilon_f} \quad (3)$$

where,  $E(n, \sigma, \kappa)$  = residual stiffness,  $E_s$  = static stiffness,  $\epsilon_f$  = average strain to failure, and  $\gamma$  and  $\lambda$  = experimental curve fitting parameters. The normalized fatigue life of a unidirectional ply under arbitrary uniaxial state of stress and stress ratio is calculated using the following equation:

$$u = \frac{\ln(a/f)}{\ln[(1-q)(c+q)]} = A + B \log N_f \quad (4)$$

where,  $f$  and  $u$  = curve fitting parameters,  $\sigma_a = (\sigma_{\max} - \sigma_{\min})/2$  = alternating stress,  $\sigma_m = (\sigma_{\max} + \sigma_{\min})/2$  = mean stress,  $q = \sigma_m/\sigma_t$ ,  $a = \sigma_a/\sigma_t$ ,  $c = \sigma_c/\sigma_t$ ,  $\sigma_t$  = tensile strength,  $\sigma_c$  = compressive strength. For the shear loading condition Eq. 4 must be modified. For a unidirectional ply under shear, the definitions of tensile strength and compression strength are meaningless, i.e., there is no difference between positive and negative shear. Therefore, the word strength is used instead. By considering this, the parameter “c” in Eq. 4 is equal to one ( $c=1$ ) for shear fatigue conditions. Also, the experimental results for unidirectional plies under in-plane shear loading conditions show that a better curve fitting is achieved by adding a “ $\log_{10}$ ” to the left-hand side of Eq. 4. Therefore, Eq. 4 is changed to the following form for the simulation of fatigue life of the unidirectional ply under shear loading conditions. The left-hand side of Eq. 5 is still denoted by “u” for brevity.

$$u = \log_{10} \left( \frac{\ln(a/f)}{\ln[(1-q)(1+q)]} \right) = A + B \log N_f \quad (5)$$

### **PROGRESSIVE FATIGUE DAMAGE MODEL**

The model is explained by means of a flowchart shown in Fig. 3. As shown in this figure, the finite element model must first be prepared. In this step, material properties, geometry, boundary conditions, maximum and minimum fatigue load, maximum number of cycles, incremental number of cycles, etc., are defined. Then the stress analysis, based on the maximum and minimum fatigue load, is performed. Consequently, the maximum and minimum induced on-axis stresses of all elements are calculated. It should be emphasized that on-axis stresses for each ply of each laminate of each element at Gauss points are

calculated and averaged. Therefore, the stress ratio ( $\kappa = \sigma_{\min}/\sigma_{\max}$ ) for each element is determined. In the next step, failure analysis is performed and the maximum stresses are examined by the set of fatigue failure criteria. If there is a sudden mode of failure, then the material properties of the failed plies are changed according to appropriate *sudden* material property degradation rules. The stiffness matrix of the finite element model is rebuilt and the stress analysis is performed again. New stresses are examined by the set of fatigue failure criteria. In this step, if there is no sudden mode of failure, an incremental number of cycles are applied (e.g.,  $\delta n = 100$ ). If the number of cycles is greater than a preset total number of cycles, then the computer program stops. Otherwise, material properties of all plies of all elements are changed according to *gradual* material property degradation rules using the *generalized material property degradation technique*. Then stress analysis is performed again and the above loop is repeated until catastrophic failure occurs, or the maximum number of cycles (pre-defined by the user) is reached. If catastrophic failure is reached, then fatigue life and the mechanisms of failure due to fatigue loading have been achieved. It should be noted that if the maximum number of cycles is selected as a large number, such as  $10^9$ , then the fatigue life of the problem can be obtained by the algorithm. If the computer program stops because the user-chosen maximum number of cycles is reached, then the mechanisms of failure due to fatigue loading are found by examining the final state of damage. Furthermore, in the latter case, residual strength of the composite laminate is obtainable by performing a progressive static damage modeling on the final results of *progressive fatigue damage model*.

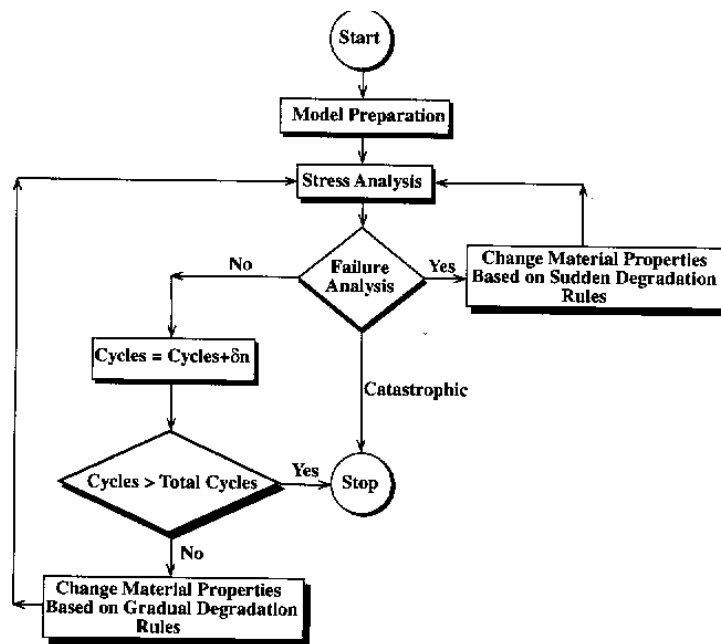


**Fig. 3: Flowchart of progressive fatigue damage model**

In order to verify the *fatigue progressive damage model*, a complete knowledge of material properties (stiffness, strength, and fatigue life) of a unidirectional ply under static and fatigue loading conditions is required. Hence, to run the computer program developed for *progressive fatigue modeling* of laminated composites, the mechanical behaviour of a unidirectional ply under uniaxial static and fatigue loading conditions must be fully characterized. For this purpose, the material properties of a unidirectional composite laminate in static and fatigue loading conditions; in the fiber and matrix directions; under tensile, compressive, in-plane-shear and out-of-plane-shear loading are required.

## RESULTS

To verify the fatigue simulation capability of the *model*, fatigue life and residual strength tests are performed for different ply configurations and load levels. To show the generality of the *model*, simulated results for fatigue life of the pin/bolt-loaded composite laminates are also compared with independent experimental results available in the literature. Also, the residual fatigue life of the pin-loaded composite laminates under two consecutive load levels (low and high) is measured experimentally and the results are compared with simulated results by the *model*. In the following some of the typical results obtained are presented. Additional results are published by the authors elsewhere [17-19]. The results of the fatigue life of pin-loaded  $[0_4/90_4]_s$  and  $[90_4/0_4]_s$  cross-ply laminates made of AS4/3501-6, are shown in Fig. 4. As shown, similar to the static strength behaviour, the pin-loaded  $[90_4/0_4]_s$  laminate shows a higher fatigue life than the  $[0_4/90_4]_s$  cross-ply laminate for the same fatigue loading conditions. The main reason for this behaviour is explained by the lower singular stress state for the  $[90_4/0_4]_s$  cross-ply laminate near the edge of the hole.

To evaluate the *progressive fatigue damage model* by independent experimental data, the fatigue life of a pin-loaded quasi-isotropic  $[0/90/\pm 45]_s$  laminate made of AS4/3501-6 is simulated and compared with the experimental results of Herrington and Sabbaghian [20]. The fatigue life of the pin-loaded quasi-isotropic laminate is simulated by the *progressive fatigue damage model* and compared with the experimental results (Fig. 5).

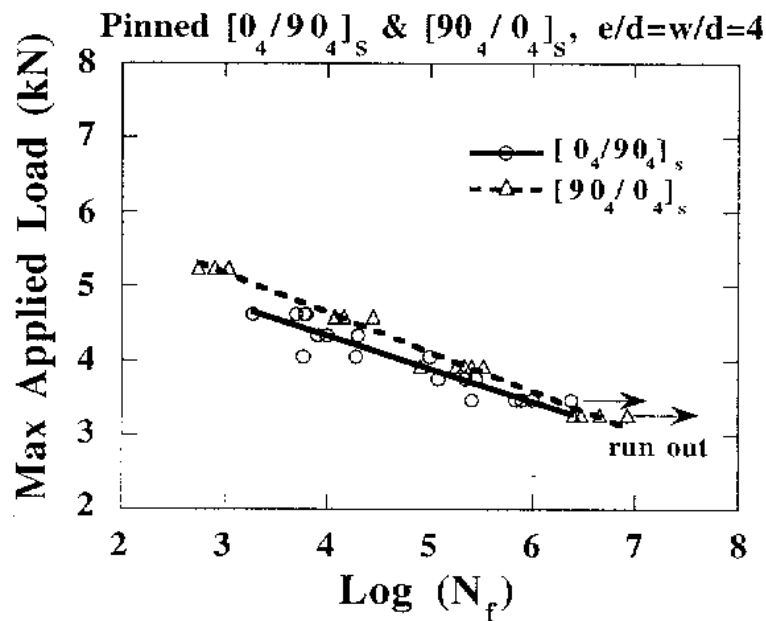


*Fig. 4: Fatigue life curves of pin-loaded  $[0_4/90_4]_s$  and  $[90_4/0_4]_s$  laminates*

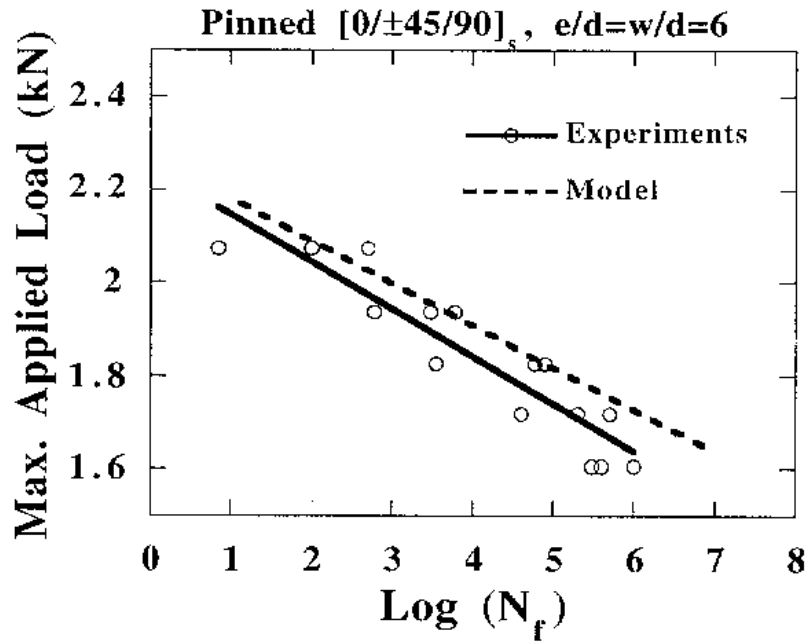
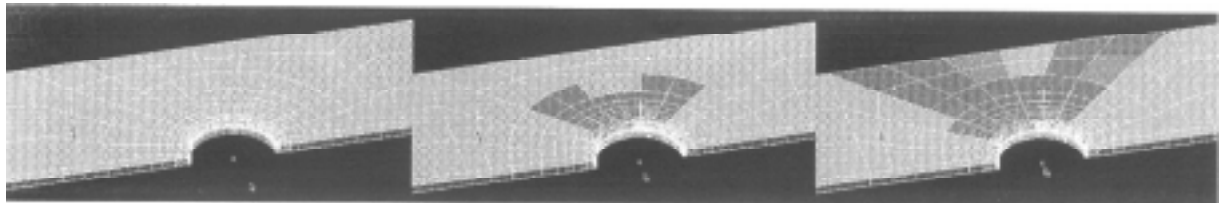
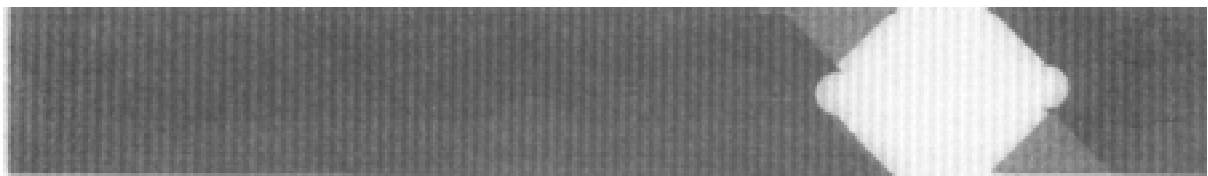


*Fig. 5: Fatigue life of pin-loaded quasi-isotropic  $[0/\pm 45/90]_s$  laminates (simulation by the model and experiments by Herrington and Sabbaghian [20])*

The progression of damage in a pin-loaded angle-ply  $[+45_4/-45_4]_s$  laminate at different number of cycles is shown in Fig. 6. The simulated number of cycles to failure is 25000 cycles, while the experiments show a range of 15000 to 26900 cycles. As shown, an excellent agreement between the simulated and experimental results is achieved for mode of failure.



*simulated by the model after 0, 18000 and 25000 fatigue loading cycles*



*experiment at final failure*

*Fig. 6: Progression of damage in a pin-loaded angle-ply  $[+45_4/-45_4]_s$  laminate*

## SUMMARY

The present research establishes a new modeling approach to simulate the behaviour of composite laminates under general fatigue loading conditions. Using the idea of the traditional progressive damage model which is capable of simulating of static behaviour of composite laminates, the *progressive fatigue damage model* is developed. The *model* consists of three major components: stress analysis, failure analysis and material property degradation rules. The *model* determines the state of damage at any load level and number of cycles, from failure initiation and propagation to catastrophic failure. The *model* is able to predict the residual strength, residual life, final failure mechanisms and final fatigue life of composite laminates under general fatigue loading conditions. Based on the *model*, a computer code is developed which simulates the cycle-by-cycle behaviour of composite laminates under fatigue loading conditions. The capabilities of the model are examined by simulation of a pin/bolt-loaded composite laminates as a complicated example.

## REFERENCES

1. Owen, M. J. and Bishop, P. T., "Fatigue Properties of Glass-Reinforced Plastics Containing a Stress Concentrator," *Journal of Physics - D: Applied Physics*, Vol. 6, (1973), pp. 2057-2069.
2. Simonds, R. A. and Stinchcomb, W. W., "Response of Notched AS4/PEEK Laminates to Tension/Compression Loading," *Advances in Thermoplastic Matrix Composite Materials*, ASTM STP 1044, G. M. Newaz, Ed., (1989), pp. 133-145.
3. Bakis, C. E., Simonds, R. A. and Stinchcomb, W. W., "A Test Method to Measure the Response of Composite Materials Under Reversed Cyclic Loads," *Test Methods for Design Allowables for Fibrous Composites*, ASTM STP 1003, C. C. Chamis and K. L. Reifsnider, Eds., (1989), pp. 93-110.
4. Xiao, J. and Bathias, C., "Fatigue Behaviour of Unnotched and Notched Woven Glass/Epoxy Laminates," *Composites Science and Technology*, 50, (1994), pp. 141-148.
5. Xiao, J. and Bathias, C., "Fatigue Damage and Fracture Mechanism of Notched Woven Laminates," *Journal of composite Materials*, Vol. 28, No. 12, (1994), pp. 1127-1139.
6. Kulkarni, S. V., McLaughlin Jr., P. V., Pipes, R. B. and Rosen, B. W., "Fatigue of Notched Fiber Composite Laminates: Analytical and Experimental Evaluation," *Composite Materials: Testing and Design (Fourth Conference)*, ASTM STP 617, (1977), pp. 70-92.
7. Reifsnider, K. L., "The Critical Element Model: A Modeling Philosophy," *Engineering Fracture Mechanics*, Vol. 25, Nos. 5/6, (1986), pp. 739-749.
8. Spearing, S. M. and Beaumont, P. W. R. and Kortschot, M. T., "The Fatigue Damage Mechanics of Notched Carbon Fibre/PEEK Laminates," *Composites*, Vol. 23, No. 5, (Sept., 1992), pp. 305-311.
9. Halpin, J. C., Jerina, K. L. and Johnson, T. A., "Characterization of Composites for the Purpose of Reliability Evaluation," *Analysis of the Test Methods for High Modulus Fibers and Composites*, ASTM STP 521, (1973), pp. 5-64.

10. Sendeckyj, G. P., "Life Prediction for Resin-Matrix Composite Materials," *Fatigue of Composite Materials*, Ed. by K. L. Reifsnider, (1990), pp. 431-483.
11. Garud, Y. S., "Multiaxial Fatigue: A Survey of the State of the Art," *Journal of Testing and Evaluation*, JTEVA, Vol. 9, No. 3, (May 1981), pp. 165-178.
12. Found, M. S., "A Review of the Multiaxial Fatigue Testing of Fiber Reinforced Plastics," *Multiaxial Fatigue*, ASTM STP 853, K. J. Miller and M. W. Brown, Eds., (1985), pp. 381-395.
13. Chen, A. S. and Matthews, F. L., "A Review of Multiaxial Biaxial Loading Tests for Composite Materials," *Composites*, Vol. 24, No. 5, (1993), pp. 395-406.
14. Sims, D. F. and Brogdon, V. H., "Fatigue Behavior of Composites under Different Loading Modes," *Fatigue of Filamentary Materials*, ASTM STP 636, K. L. Reifsnider and K. N. Lauraitis, (1977), pp. 185-205.
15. Hashin, Z., "Fatigue Failure Criteria for Unidirectional Fiber Composites," *Journal of Applied Mechanics*, Vol. 48, (Dec. 1981), pp. 846-852.
16. Ryder, J. T. and Crossman, F. W., "A Study of Stiffness, Residual Strength and Fatigue Life Relationships for Composite Laminates," NASA Contract Report CR-172211, 1983.
17. Shokrieh, M. M., and Lessard, L. B., "Multiaxial Fatigue Behaviour of Unidirectional Plies Based on Uniaxial Fatigue Experiments: Part I. Modeling," *International Journal of Fatigue*, accepted, 1996.
18. Shokrieh, M. M., and Lessard, L. B., "Multiaxial Fatigue Behaviour of Unidirectional Plies Based on Uniaxial Fatigue Experiments: Part II. Experimental Evaluation," *Int. Journal of Fatigue*, accepted, 1996.
19. Shokrieh, M. M., "Progressive Fatigue Damage Modeling of Composite Materials," Ph. D. Thesis, McGill University, Department of Mechanical Engineering, Montreal, Quebec, Canada, 1996.
20. Herrington, P. D. and Sabbaghian, M., "Fatigue Failure of Composite Bolted Joints," *Journal of Composite Materials*, Vol. 27, No. 5, (1993), pp. 491-512.



# PREDICTION OF FLEXURAL FATIGUE LIFE FOR UNIDIRECTIONAL CFRP LAMINATES

Masayuki Nakada<sup>1</sup>, Takeshi Ishiguro<sup>2</sup> and Yasushi Miyano<sup>1</sup>

<sup>1</sup> *Materials System Research Laboratory, Kanazawa Institute of Technology,  
Ohgigaoka Nonoichi, Ishikawa 921, Japan*

<sup>2</sup> *Graduate School, Kanazawa Institute of Technology,  
Ohgigaoka Nonoichi, Ishikawa 921, Japan*

**SURMMARY:** A prediction method of fatigue strength of polymer composites for an arbitrary frequency, stress ratio and temperature was proposed. The method is based upon the four hypotheses, (A) same failure mechanism for static, creep and fatigue failure, (B) same time-temperature superposition principle for all failure strengths, (C) linear cumulative damage law for monotone loading and (D) linear dependence of fatigue strength upon stress ratio. Flexural static, creep and fatigue tests at various temperatures were conducted in the longitudinal direction of unidirectional CFRP laminates. The validity of the prediction method and the applicability of the hypotheses for the flexural fatigue strength in the longitudinal direction of unidirectional CFRP laminates were discussed.

**KEYWORDS:** fiber reinforced plastics, static strength, creep strength, fatigue strength, time-temperature superposition principle

## INTRODUCTION

It is well known that the mechanical behavior of polymer resins exhibits time and temperature dependence, called viscoelastic behavior, not only above the glass transition temperature  $T_g$  but also below  $T_g$ . Thus, it can be presumed that the mechanical behavior of polymer composites also significantly depends on time and temperature. It has been confirmed that the viscoelastic behavior of polymer resins as matrices is a major influence on the time and temperature dependence of the mechanical behavior of FRP [1-8].

In previous papers, we proposed a prediction method for the fatigue strength of polymer composites for an arbitrary frequency, stress ratio and temperature from the data measured by static tests at several constant loading-rates and various temperatures, and fatigue tests at a

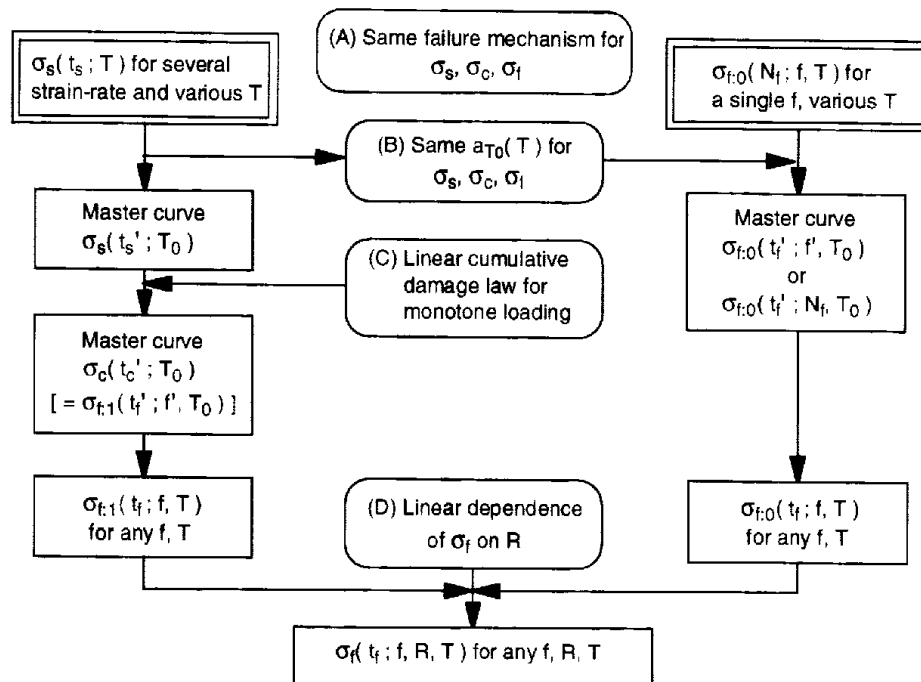
single frequency and various temperatures. The validity of this method was proven for the case of flexural behavior of satin-woven CFRP laminates [9].

In this paper, the validity of the prediction method is discussed for the case of flexural behavior in the longitudinal direction of unidirectional CFRP laminates.

### PREDICTION PROCEDURE OF FATIGUE STRENGTH

We proposed a prediction method for fatigue strength of polymer composites for an arbitrary frequency, stress ratio and temperature from the data measured by static tests at several constant loading-rates and various temperatures, and fatigue tests at a single frequency and various temperatures. The method rests on the four hypotheses, (A) same failure mechanism for static, creep and fatigue failure, (B) same time-temperature superposition principle for all failure strengths, (C) linear cumulative damage law for monotone loading and (D) linear dependence of fatigue strength upon stress ratio.

When these hypotheses are met, the fatigue strength for an arbitrary combination of frequency,



- $T, T_0$  : temperature, reference temperature
- $f, f'$  : frequency, reduced frequency
- $t_s, t_c, t_f$  : time to failure under constant strain-rate, creep and fatigue loadings
- $t_s', t_c', t_f'$  : reduced time to failure
- $a_{T_0}(T)$  : time-temperature shift factor ( $a_{T_0}(T) = t_s'/t_s' = t_c'/t_c' = t_f'/t_f' = f'/f$ )
- $R$  : stress ratio ( $R = \sigma_{min}/\sigma_{max}$ )
- $N_f$  : number of cycles to failure ( $N_f = f t_f$ )
- $\sigma_s, \sigma_c, \sigma_f$  : static, creep, and fatigue strengths
- $\sigma_{f,0}, \sigma_{f,1}$  :  $\sigma_f$  for  $R=0$  and  $R=1$

Fig.1 Prediction procedure of fatigue strength for polymer composites

stress ratio and temperature can be determined based on the following test results: (a) master curve of static strength and (b) master curve of fatigue strength for stress ratio of zero. The master curve of static strength is constructed from the test results at several constant loading-rates for various temperatures. On the other hand, the master curve of fatigue strength for zero stress ratio can be constructed from tests at a single frequency for various temperatures using the time-temperature superposition principle for the static strength.

The outline of this method is shown schematically in Fig.1 together with definitions of some notations. The detail of the method will be presented with experimental results.

### EXPERIMENTAL PROCEDURE

#### Preparation of Specimen

Unidirectional CFRP laminates were prepared. The PAN based carbon fiber is T300 (Toray, brand name Torayca). The matrix resin is thermosetting epoxy resin 2500. The glass transition temperature  $T_g$  of 2500 is 130°C. The prepreg sheet made from these fiber and resin, which were T300/2500, was hot pressed into 3mm thick laminates. The fiber volume fraction of T300/2500 was approximately 55% .

#### Test Procedure

Three point bending static tests were conducted by using an Instron type testing machine with a constant temperature chamber. The CFRP specimen's constitutions are shown in Fig.2. The nominal dimensions of the test specimens were 80x10x3 mm (length, width, thickness). The span of the test fixture was 60 mm. The test conditions are shown in Table1. The tests were conducted at three loading- rates  $V=0.02, 2, 200$  mm/min at 7 steps of testing temperature from  $T=50$  to 180°C.

Specimens with the same dimensions were used for three point bending creep and fatigue tests. The creep tests were conducted at 3 uniform temperatures by using creep testing machine. The fatigue tests were conducted by using an electro-hydraulic servo testing machine with a constant temperature chamber. The tests were conducted at two loading frequencies of  $f=2$  and 0.02Hz at several steps of testing temperature. Stress ratio  $R$  (minimum stress/maximum stress) was 0.05. Additionally, the fatigue tests were also conducted at  $T=50, 100, 140^\circ\text{C}$ ,  $f=2\text{Hz}$  and  $R=0.5$ .

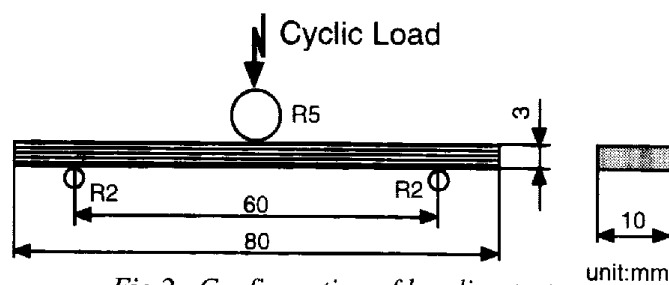


Fig.2 Configuration of bending tests

Table 1 Test conditions of static, creep and fatigue tests

Loading type	Deflection rate [mm/min]	Frequency [Hz]	Stress ratio $\sigma_{\min}/\sigma_{\max}$	Temperature [°C]
Static	0.02, 2, 200	—	—	50, 80, 100, 120, 140, 160, 180
Creep	—	—	1	50, 100, 140
Fatigue	—	0.02	0.05	31.5, 80.5, 128.8
		2	0.05, 0.5	50, 80, 100, 140

## RESULTS AND DISCUSSION

### Fractographs

Side-view of flexural failure under static, creep and fatigue loadings at various temperatures are shown in Fig.3. All of static, creep and fatigue failure occur in the surface layer on the compression side of specimen. All these failed specimens are similar regardless of loading patterns. Therefore, we consider that the failure mechanisms are the same for static, creep and fatigue loadings.

### Master Curve of Static Strength

The left side of Fig.4 shows the flexural static strength  $\sigma_s$  versus time to failure  $t_s$  at various temperatures  $T$ , where  $t_s$  is defined as the time period from initial loading to maximum load in constant loading-rate tests. From the graphs on the left side, it is shown that the  $\sigma_s$  depends on  $t_s$  and  $T$ . The master curve was constructed by shifting  $\sigma_s$  at various constant temperatures along the log scale of  $t_s$  so they overlapped each other as shown in the right side of Fig.4. The time-temperature shift factor  $a_{T0}(T)$  is defined by

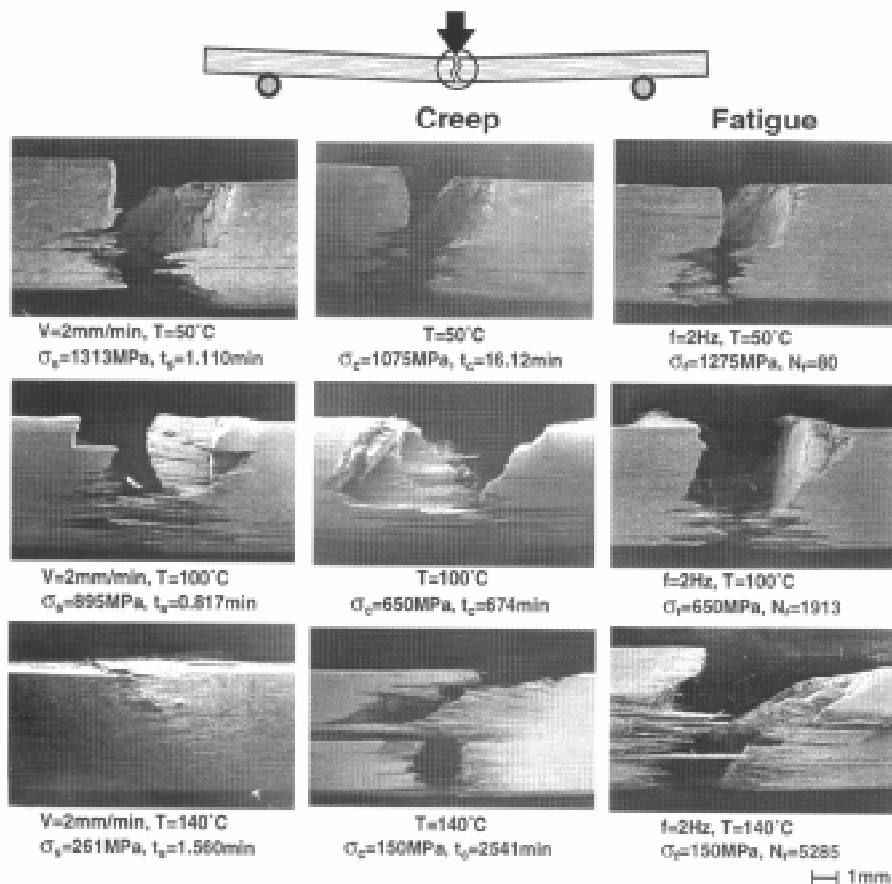


Fig.3 Side-view of flexural failure under static, creep and fatigue loadings at various temperatures

$$a_{T_0}(T) = \frac{t_s}{t_s'} \tag{1}$$

Where,  $t_s'$  is reduced time to failure,  $T_0$  is reference temperature.

Since  $\sigma_s$  at various temperatures can be superimposed smoothly, the time-temperature superposition principle is applicable for  $\sigma_s$ .

Fig.5 shows the time-temperature shift factors  $a_{T_0}(T)$  obtained experimentally for the master curve of the flexural static strength. All of these shift factors are quantitatively in good agreement with two Arrhenius' equation with different activation energies.

$$\log a_{T_0}(T) = \frac{\Delta H}{2.303R} \left( \frac{1}{T} - \frac{1}{T_0} \right) \tag{2}$$

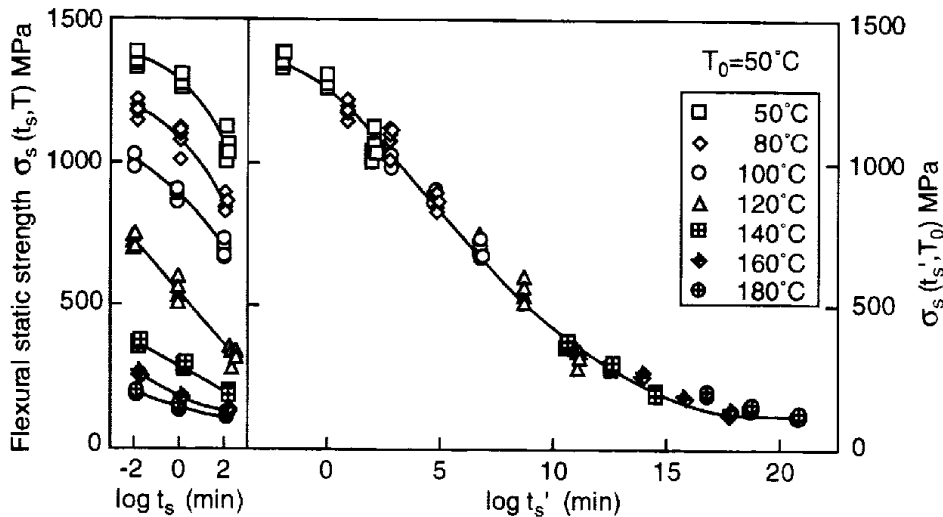


Fig.4 Master curve of flexural static strength

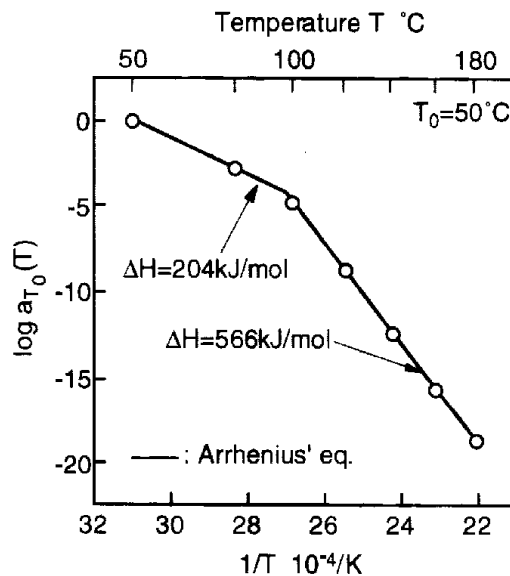


Fig.5 Time-temperature shift factors for flexural static strength

where,  $\Delta H$  is activation energy [kJ/mol],  $R$  is gas constant  $8.314 \times 10^{-3}$  [kJ/(K.mol)].

### Master Curve of Creep Strength

A prediction method of creep strength  $\sigma_c$  from the master curve of static strength using the linear cumulative damage law was proposed. Let  $t_s(\sigma)$  and  $t_c(\sigma)$  be the static and creep failure time for the stress  $\sigma$ . Suppose that the material experiences a monotone stress history  $\sigma(t)$  for  $0 \leq t \leq t^*$  where  $t^*$  is the failure time under this stress history. The linear cumulative damage law states

$$\int_0^{t^*} \frac{dt}{t_c[\sigma(t)]} = 1 \quad (3)$$

When  $\sigma(t)$  is equal to constant stress  $\sigma_0$ , the above formula implies  $t^* = t_c(\sigma_0)$ .

Fig.6 displays the creep strength  $\sigma_c$  versus time to failure  $t_c$ ; the left side shows the experimental data, while the right side exhibits the data shifted to the reference temperature  $T_0=50^\circ\text{C}$  using the shift factors for the static strength. Since  $\sigma_c$  at various temperatures can be superimposed smoothly, the time-temperature superposition principle is also applicable for  $\sigma_c$ .

The right side of this figure also displays the static strength master curve drawn by a dotted line. The creep strength prediction curve calculated by equation (3) using the static strength master curve is shown by a solid line. The  $\sigma_c$  can be predicted using the master curve of static strength based on the linear cumulative damage law because the predicted  $\sigma_c$  agrees well with the experimental data.

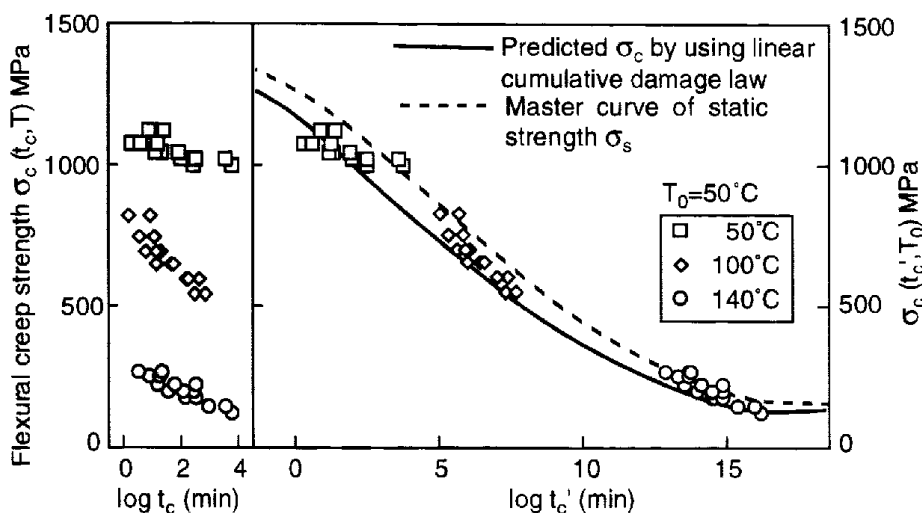


Fig.6 Master curve of flexural creep strength

### Master Curve of Fatigue Strength

We regard the fatigue strength  $\sigma_f$  either as a function of the number of cycles to failure  $N_f$  or of

the time to failure  $t_f=N_f/f$  for a combination of  $f, R, T$  and denote them by  $\sigma_f(N_f; f, R, T)$  or  $\sigma_f(t_f; f, R, T)$ . Further, we consider that the static strength  $\sigma_s(t_f; T)$  is equal to the fatigue strength at  $N_f=1/2$  and  $R=0$  by choosing  $t_f=1/(2f)$ . At this point, we introduce special symbols for fatigue strength at zero and unit stress ratios by  $\sigma_{f,0}$  and  $\sigma_{f,1}$  where the latter corresponds to creep strength.

To describe the master curve of  $\sigma_{f,0}$ , we need the reduced frequency  $f'$  in addition to the reduced time  $t_f'$ , each defined by

$$t_f' = \frac{t_f}{a_{T_0}(T)} = \frac{N_f}{f} \quad , \quad f = f \cdot a_{T_0}(T) \quad (4)$$

Thus, the master curve has the form,  $\sigma_{f,0}(t_f'; f', T_0)$ . An alternative form of the master curve is possible by suppressing the explicit dependence on frequency in favor of  $N_f$  as  $\sigma_{f,0}(t_f'; N_f, T_0)$ . Recall that the master curve of fatigue strength at  $N_f=1/2$  reduces to the master curve of static strength.

The fatigue strength  $\sigma_f$  versus the number of cycles to failure  $N_f$  ( $\sigma_f-N_f$  curve) at 2 frequencies  $f=2$  and  $0.02\text{Hz}$  are shown in Fig.7. The  $\sigma_f$  depends remarkably on temperature and frequency as well as  $N_f$ . The temperature conditions of  $T=50,100$  and  $140^\circ\text{C}$  at  $f=2\text{Hz}$  can be converted

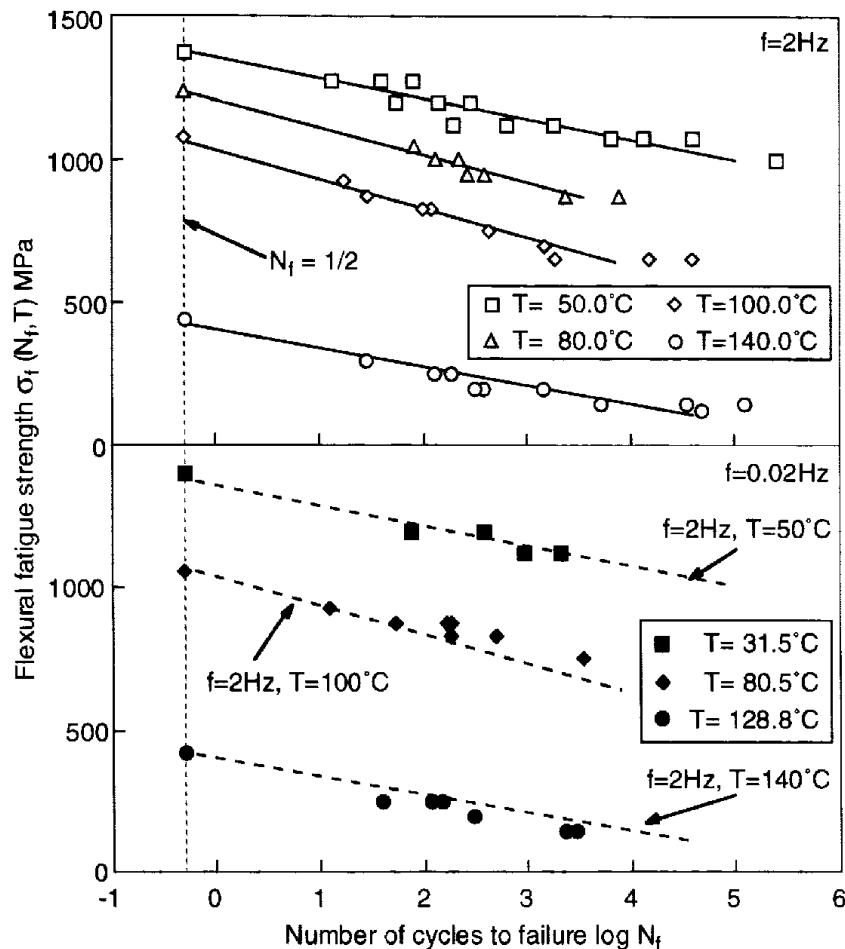


Fig.7 Flexural fatigue strength versus the number of cycles to failure  $N_f$

into the conditions of  $T=31.5, 80.5$  and  $128.8^\circ\text{C}$  at  $f=0.02\text{Hz}$  by using the time-temperature superposition principle which holds for the static strength. The  $\sigma_f-N_f$  curves at  $f=0.02\text{Hz}$  agree well with those at  $f=2\text{Hz}$ . Therefore, the time-temperature superposition principle for the static strength also holds for the fatigue strength, and the hypothesis (B) is valid for fatigue strength.

The upper portion of Fig.8 shows  $\sigma_f$  versus the reduced time to failure  $t_f'$ . On the other hand, each point on the master curves of constant reduced frequency represents a number of cycles to failure. Connecting the points of the same  $N_f$  with these curves, the master curves of  $\sigma_f$  for constant  $N_f$  are constructed as shown in the lower side of Fig.8. The  $\sigma_f$  for a given number of cycles to failure at an arbitrary temperature and frequency can be determined by using the master curves of  $\sigma_f$  as shown in this figure.

### Prediction of Fatigue Strength for Arbitrary Frequency, Stress Ratio and Temperature

We have the master curve for creep strength  $\sigma_c(t_c'; T_0)$  from which follows the creep strength at any temperature  $T$ . The creep strength, in turn, may be regarded as the fatigue strength  $\sigma_{f,1}(t_f'; f, T)$  at unit stress ratio  $R=1$  and arbitrary frequency  $f$  with  $t_c'=t_f'$ . Further, from the master curve for fatigue strength at zero stress ratio, we can deduce the fatigue strength  $\sigma_{f,0}(t_f'; f, T)$  at zero stress ratio for any frequency  $f$  and temperature  $T$ .

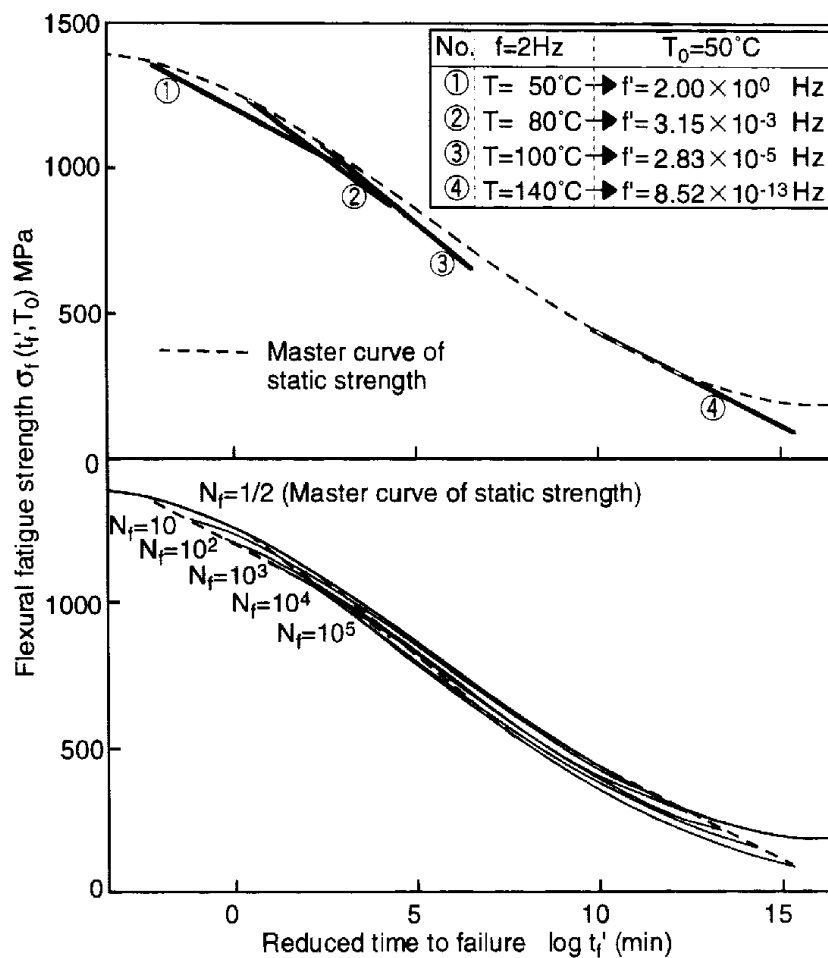


Fig.8 Master curves of flexural fatigue strength



Implementing hypothesis (D), we propose a formula to estimate the fatigue strength  $\sigma_f(t_f; f, R, T)$  at an arbitrary combination of  $f, R, T$  by

$$\sigma_f(t_f; f, R, T) = \sigma_{f,1}(t_f; f, T)R + \sigma_{f,0}(t_f; f, T)(1-R) \quad (5)$$

Fig.9 shows the experimental data of  $\sigma_f-t_f$  for  $f=2\text{Hz}$ ,  $R=0.05, 0.5, 1.0$  and  $T=50, 100, 140^\circ\text{C}$ . The curves of  $R=0.05$  and  $R=1$  respectively represent the least squares fit for experimental data of fatigue test of  $R=0.05$  and creep test. The curve of  $R=0.5$  is calculated from equation (5) on the basis of the curves for  $R=0.05$  and  $R=1$ . As can be seen, the predictions correspond with the experimental data. We can predict  $\sigma_f-t_f$  relation for given  $R, f$  and  $T$  from equation (5) if  $\sigma_{f,1}(t_f; f, T)$  and  $\sigma_{f,0}(t_f; f, T)$  are known.

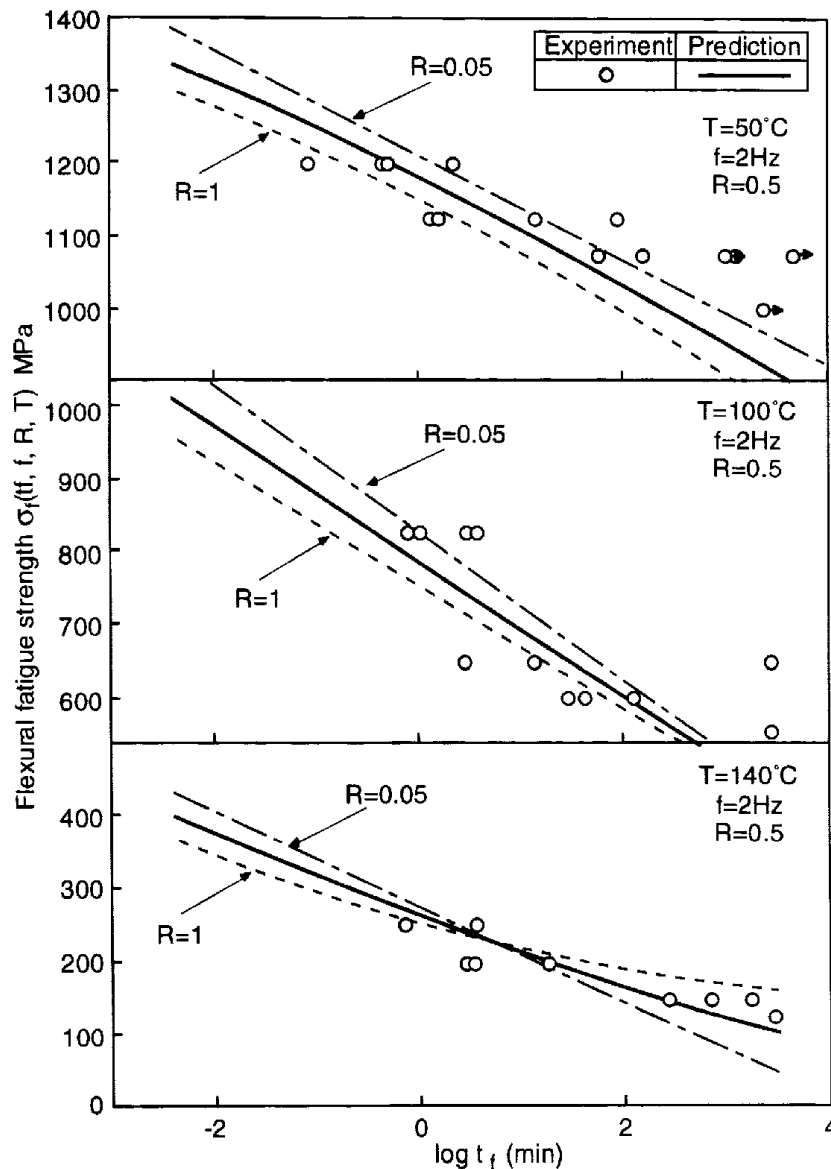


Fig.9 Flexural fatigue strength versus time to failure curves for various stress ratios

## CONCLUSION

We had proposed a prediction method for the fatigue strength of polymer composites for an arbitrary frequency, stress ratio and temperature in previous papers. The method is based upon the four hypotheses, (A) same failure mechanism for static, creep and fatigue failure, (B) same time-temperature superposition principle for all failure strengths, (C) linear cumulative damage law for monotone loading and (D) linear dependence of fatigue strength upon stress ratio. Flexural static, creep and fatigue strength tests at various temperatures were conducted in the longitudinal direction of unidirectional CFRP laminates, which is T300/2500. The test results indicated the validity of the prediction method and the applicability of the hypotheses for this material.

## REFERENCES

1. Aboudi, J. and Cederbaum G., *Composite Structures*, 12, 243 (1989).
2. Ha, S.K. and Springer, G.S., *J. Composite Materials*, 23, 1159 (1989).
3. Sullivan, J.L., *Composite Science and Technology*, 39, 207 (1990).
4. Gates, T.S., *Experimental Mechanics*, 68 (1992).
5. Miyano, Y., Kanemitsu, M., Kunio, T. and Kuhn, H., *J. Composite Materials*, 20, 520 (1986).
6. Miyano, Y., McMurray, M.K., Enyama, J. and Nakada, M., *J. Composite Materials*, 28, 1250 (1994).
7. Miyano, Y., McMurray, M.K., Kitade, N., Nakada, M. and Mohri, M., *Advanced Composite Materials*, 4, 87 (1994).
8. Miyano, Y., Nakada, M. and McMurray, M.K., *J. Composite Materials*, 29, 1808 (1995).
9. Miyano, Y., McMurray, M.K. and Muki, R., *Numerical Methods in Structural Mechanics*, ASME AMD-204, 69 (1995).

# FATIGUE BEHAVIOR OF THE CARBON/EPOXY AND THE CARBON/PEEK COMPOSITES SUBJECTED TO LOW-ENERGY IMPACT

Nyan-Hwa Tai<sup>1</sup>, Ming-Chuen Yip<sup>1,2</sup>, Chih-Ming Tseng<sup>2</sup> and Hui-Chia Yu<sup>2</sup>

<sup>1</sup> *Materials Science Center and* <sup>2</sup> *Department of Power Mechanical Engineering  
National Tsing-Hua University, Taiwan, R.O.C.*

**SUMMARY:** Fatigue behaviors of carbon fiber reinforced thermosetting and thermoplastic composites with and without subjecting low-energy impact were investigated. The [0/45/90/-45]<sub>2S</sub> T300/976 carbon/epoxy and AS-4/PEEK laminates were used in this study. The impact response of these two laminates shows a linear force-deformation relationship in the initial penetration impact loading, which implies an elastic behavior of these two composites; the following zigzag peaks indicate fracture initiation and arrest. The fatigue tests were performed at various stress levels under tension-tension loadings with a fatigue frequency of 3 and stress ratio of 0.1. The median rank method and Weibull distribution were applied to predict the fatigue probabilities of the specimen under static and fatigue tests. The S-N curves for the undamaged and low-energy impact damaged laminates are compared.

**KEYWORDS:** low-energy impact, fatigue behavior, T300/976 carbon/epoxy, AS-4/PEEK, Weibull distribution, S-N curve

## INTRODUCTION

Although fiber reinforced composite shows many remarkable features such as lower specific strength and modulus, better corrosion resistance, and precise tailoring, the inherent anisotropic property of fiber reinforced composites results in much more complicated fracture mode than that of the conventional materials. During the past two decades, carbon/epoxy composites have been adopted in many applications, and numerous studies on the fatigue properties of the laminates have been reported[1,5]. On the other hand, carbon fiber reinforced thermoplastic composite such as Gr/PEEK laminate is a relatively new material; only a few studies were performed on the topic of fatigue behavior for Gr/PEEK laminates[6-8]. Besides fatigue behavior, impact behavior is also a very important property for composites in engineering applications[9]. On the applications of composites in transportation vehicles, the damages can be introduced during maintenance such as dropped tool and during service such as debris rebound; all these damages result in reduction of performance. However, very few articles were published to investigate the effects of the combined loading, fatigue and impact, on the performance of the Gr/epoxy and Gr/PEEK composites. The purposes of this work are to study the fatigue behavior of the low-energy impacted composites and to compare the performance of the quasi-isotropic thermosetting (Gr/epoxy) and thermoplastic (Gr/PEEK) composites.

## EXPERIMENTAL

P3051F Gr/epoxy and AS-4/PEEK prepregs were supplied by Toray in Japan and Imperial Chemical Industry (I.C.I.) in U.K., respectively. The Gr/epoxy and Gr/PEEK laminates were fabricated in autoclave and hot press, respectively. Specimens were cut from fabricated panels through a water-cooled diamond table saw. The dimensions of the test coupons are 227mm x 19.1 mm x 2mm with a gage length of 127 mm. Non-tapered glass/epoxy end tabs with dimensions of 50 mm x 19.1 mm x 1.6 mm were used.

The cross-section area of the test specimens for penetration impact was 100 mm x 100 mm. The impact procedure was conducted using a steel impactor of cylindrical shape with a hemispherical nose 19.0 mm in diameter and 17.01 kg in weight. The diameter of the support ring is 76 mm.

Low-velocity impact tests were conducted using a Dynatup/GRC drop weight impact tester. The specimens were firmly fixed between flat circular rings with a support ring 18 mm in diameter. The impact machine is equipped with a hemispherical nose 12.7 mm in diameter and a rebound apparatus to prevent multiple impacts. Various energies for low-energy impact tests were employed by changing the hammer height.

## THEORETICAL ANALYSIS

The two-parameter Weibull distribution function, which is shown in Eq. (1), was adopted to analyze strength, residual strength after impact, and fatigue life.

$$R_i (X_i) = 1 - \exp \left[ - \left( \frac{X_i}{X_o} \right)^{\alpha_s} \right] \quad (1)$$

The median rank is employed in Eq. (2) for failure probability,  $R(X_i)$  at  $X_i$ ,  $1 < i < m$ ,

$$R (X_i) = \frac{i - 0.3}{m + 0.4} \quad (2)$$

where  $X_i$  denotes the test strength of fatigue life of the  $i^{\text{th}}$  specimen.

Based upon the data of fatigue cycles to failure under various stress levels, the S-N curves were plotted using linear regression method.

## RESULTS AND DISCUSSION

Figures 1a and 1b show the relationship among force, deformation, and energy during penetration impact loading for both Gr/epoxy and Gr/PEEK laminates, respectively. Although the differences in energies required to penetrate these two laminates are not obvious, the responses during impact loading of these two composites are different. A linear relation between force and deformation for these two laminates can be observed during the initial penetration process, which implies an elastic behavior of the composites. After the linear region, a force relaxation which indicates the formation of a fracture surface is detected for

Gr/epoxy laminates only. On the other hand, no obvious peak can be detected before reaching the peak load for Gr/PEEK laminates. As compared the deformation at which the peak load is reached of these two laminates, Gr/PEEK composites show greater deformation than Gr/epoxy composites, which implies better damage tolerance of the Gr/PEEK laminates. Further verification can be made by comparing the response of the composites after peak load; a sharp drop in force is detected, which indicates the formation of a large fracture surface in Gr/epoxy composites. However, only slightly reduction in force can be observed for Gr/PEEK laminates, which implies less force relaxation and fracture surface formation. The total energy to penetrate the laminate is denoted as  $E_i$ .

Figure 2 shows the strengths of the unimpacted specimens and the impact-damaged specimens loaded under various impact energies. The strength is reduced with increasing impact energy for both composites. Moreover, the rate of decrease in tensile strength for Gr/PEEK is higher than that of the Gr/epoxy laminates. After impact loading, a wider distribution in tensile strength is also detected.

The failure probabilities of the unimpacted and the 25%  $E_i$  impacted Gr/epoxy laminates were compared in Figure 3a; a slight difference in failure probability can be observed; and the impact damage results in a broader distribution in strength is also detected. However, nearly no difference in failure probability predicted by Weibull function can be observed for Gr/PEEK laminates (Figure 3b), although some experimental data have a significant deviation from theoretical prediction.

Figure 4a shows the S-N curves of unimpacted and impacted Gr/epoxy composites. A linear stress-fatigue life relationship is obtained. The shift of the curve implies that low-energy impact results in lower fatigue life, however, no significant variation in slope is observed, which indicates both composites (unimpacted and impacted) having similar fatigue sensitivity. Figure 4b shows the S-N curves of the unimpacted and 25%  $E_i$  impacted Gr/PEEK composites, and it reveals that low-energy impact loading results in the reduction of fatigue life for Gr/PEEK composites. A linear S-N curves were obtained using linear regression analysis. In our previous study, the Gr/PEEK composite shows two-segment S-N curves[6]; the difference between these two results may be due to different testing conditions and analytical methods. Furthermore, it is also observed that fatigue life distribution becomes less spread at lower stress level when the Gr/PEEK composites were subjected to a low-energy impact.

## CONCLUSIONS

Penetration impact loadings were applied to Gr/epoxy and Gr/PEEK laminates; Gr/epoxy shows a brittle fracture behavior, whereas Gr/PEEK shows a plastic fracture mode. The tensile strength reduces with increasing impact energy for both Gr/epoxy and Gr/PEEK laminates. A good correlation between experimental data and theoretical analysis for failure prediction in tensile strength is achieved. The data of fatigue life to failure indicate that the fatigue life is reduced when the specimens were subjected to a low-energy impact, and the distribution becomes less spread for both Gr/epoxy and Gr/PEEK composites.

## ACKNOWLEDGEMENT

This work was supported by the National Science Council of the Republic of China, under Contract No. NSC 86-2212-E-007-037.

## REFERENCES

1. Yang, J.N., Jones, D.L., and, S.H. and Meskini, A., "A Stiffness Degradation Model for Graphite/Epoxy Laminates", *J. Composite Materials*, Vol. 24,1990, pp. 753-769.
2. Hahn, H.T. and Hwang, D.G., "Failure Characterization of a Graphite/Epoxy Laminate Through Proof Testing", *Composite Materials: Testing and Design (Sixth Conference)*, ASTM STP 787, I.M. Daniel, Ed., American Society for Testing and Materials, 1982, pp. 247-273.
3. Whitney, J.M., "Fatigue Characterization of Composite Materials", *Fatigue of Fiber Composite Materials*, ASTM STP 723, American Society for Testing and Materials, Philadelphia, 1981, pp. 133-151.
4. Rotem, A. and Nelson, H.G., "Residual Strength of Composite Laminates Subjected to Tensile-Compressive Fatigue Loading", *J. Composites Technology and Research*, Vol. 12, No. 2, 1990, pp.76-84.
5. Spearing, S.M. and Beautmont, P.W. R., "Fatigue Damage Mechanisms of Composite Materials Part III: Prediction of Post-Fatigue Strength", *Composites Science and Technology*, Vol. 44, 1992, pp. 299-307.
6. Tai, N.H. Ma, C.C.M., and Wu, S.H., "Fatigue Behavior of Carbon Fiber/PEEK Laminates Composites", *Composites*, Vol. 28,No. 8, 1995, pp.551-559.
7. Curtis, D.C., Moore, D.R., Slater, B., and Zahlan, N., "Fatigue Testing of Multi-angle Laminates of CF/PEEK ", *Composites*, Vol.19, No. 6, 1988, pp. 446-452.
8. O'Brien, T.K., "Fatigue Delamination Behavior of PEEK Thermoplastic Composite Laminates", *J. Reinf. Plast. Compos.* Vol. 4, No. 4, 1988, pp.341-359.
9. Cantwell, W.J. and Morton, J., "The Impact Resistance of Composite Materials - A Review", *Composites*, Vol. 22, No. 5, 1991, pp. 347-362.

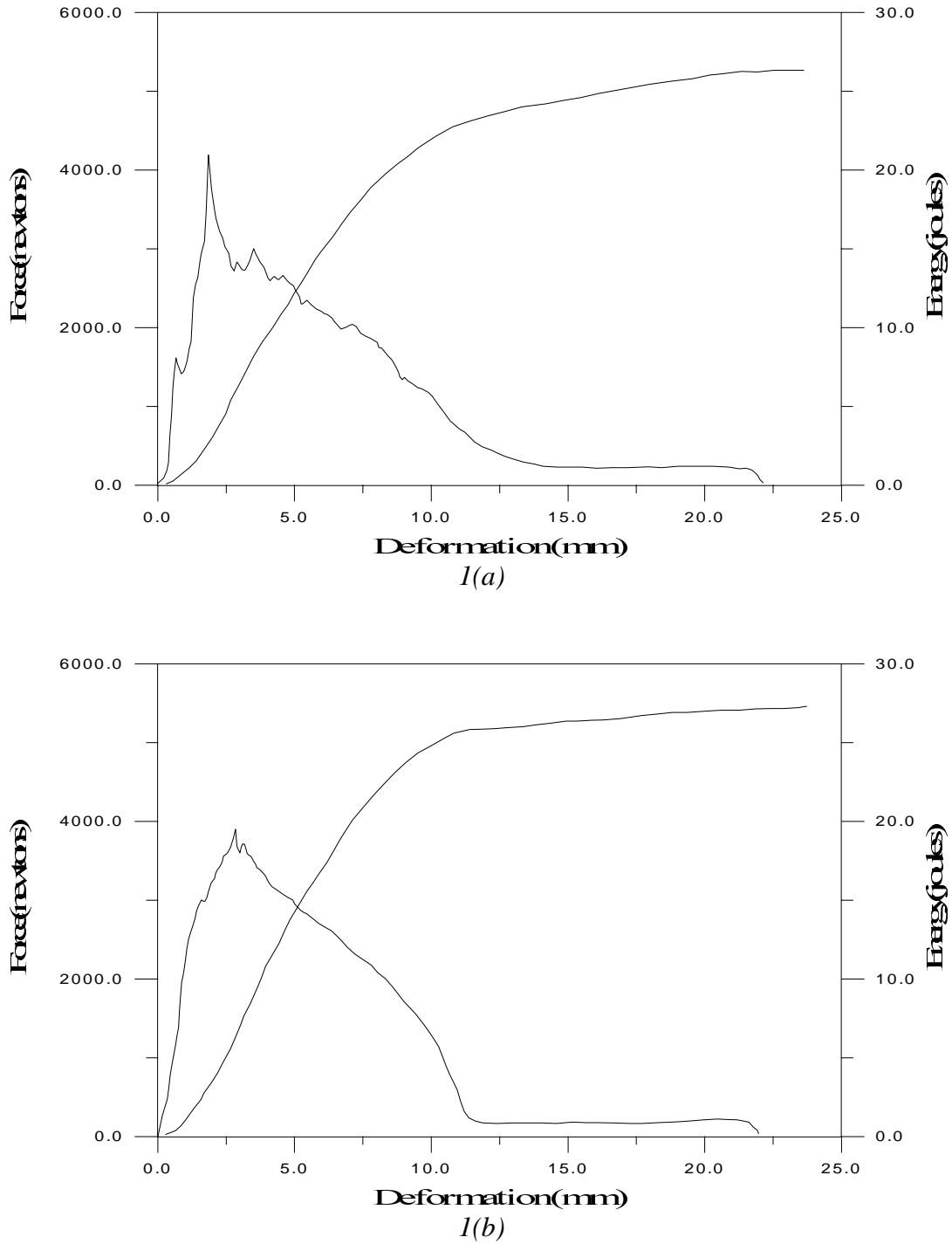
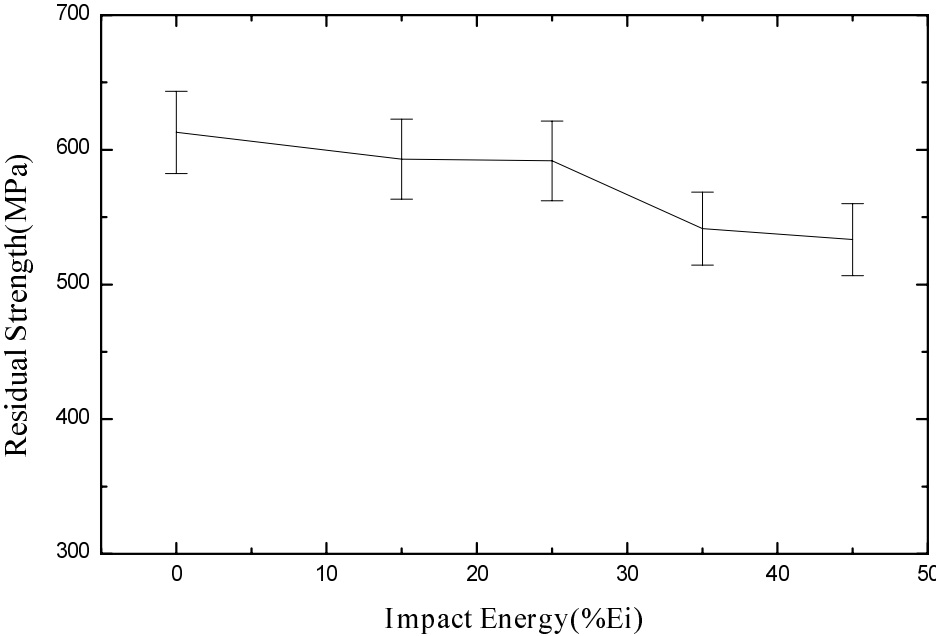
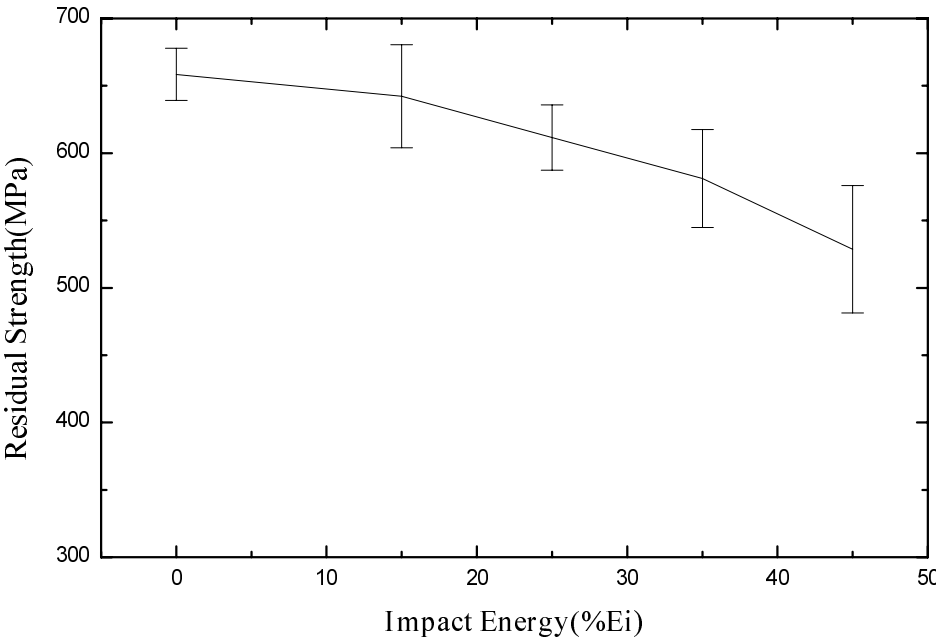


Fig. 1: Relationship among deformation, force, and energy during penetration impact loadings for (a) Gr/epoxy and (b) Gr/PEEK laminates



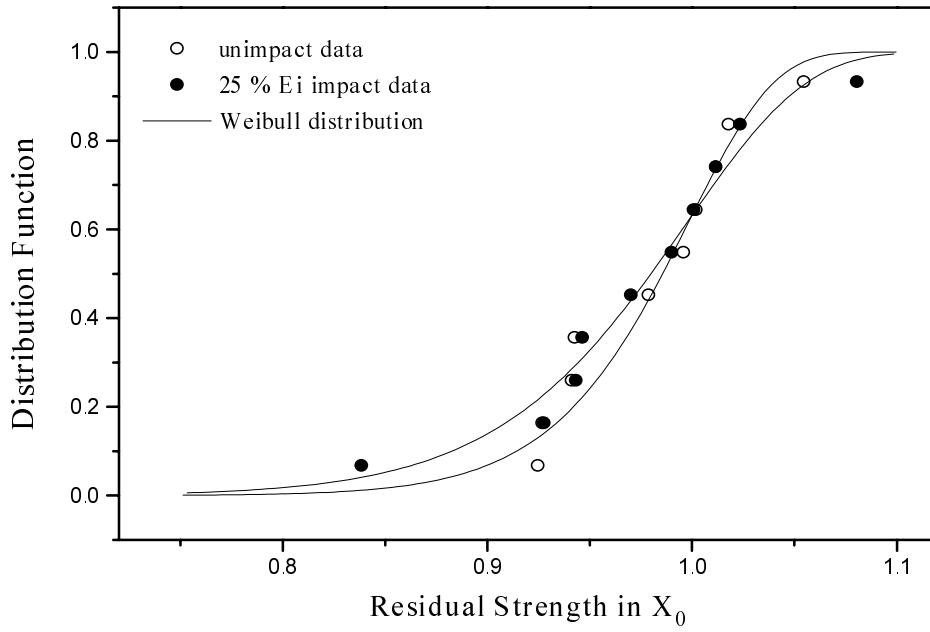
2(a)



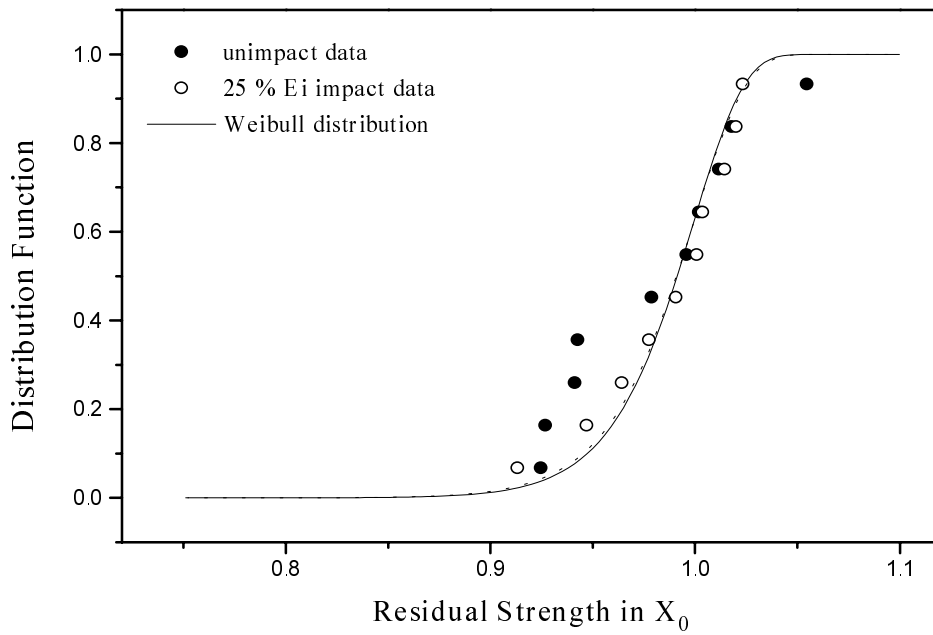
2(b)

Fig. 2: Residual strength of the specimens after being subjected to various impact energies for (a) Gr/epoxy and (b) Gr/PEEEK laminates



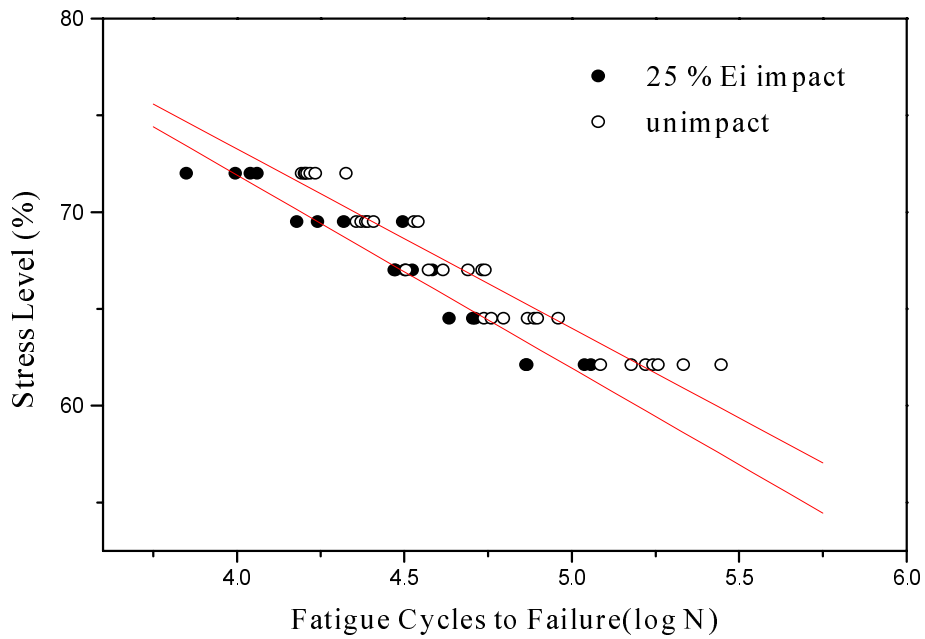


3(a)

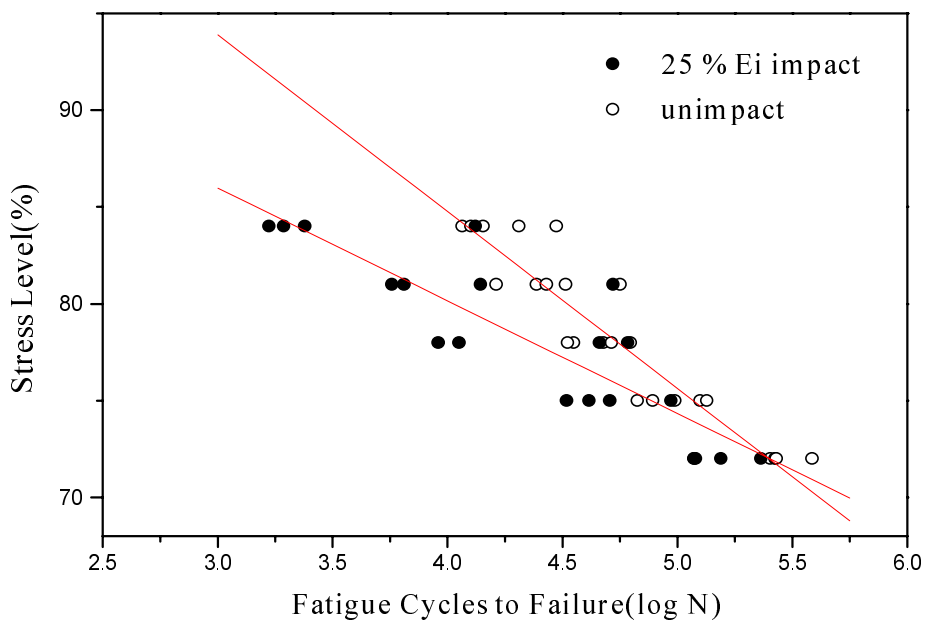


3(b)

Fig. 3: Weibull distribution of the composites without and with subjected to 25%  $E_i$  impact loading for (a) Gr/epoxy and (b) Gr/PEEK laminates



4(a)



4(b)

Fig. 4: S-N curves of the composites without and with subjected to 25%  $E_i$  impact loading for (a) Gr/epoxy and (b) Gr/PEEK laminates

# INITIATION OF FREE-EDGE DELAMINATION IN A COMPOSITE LAMINATE UNDER FATIGUE LOADING

Ran Y. Kim and Allan S. Crasto

*University of Dayton Research Institute, Dayton, OH 45469, USA*

**SUMMARY:** This paper is concerned with the onset of free-edge delamination in composite laminates subjected to fatigue loading. The material system investigated was a carbon fiber-reinforced toughened bismaleimide (IM7/5250-4). A quasi-isotropic laminate with a  $[90_2/\pm 30]_s$  lay-up was employed and the onset of free-edge delamination determined under static loading and compression-compression fatigue loading. The interlaminar stresses in the free-edge region were calculated using an analytical model, taking into consideration residual curing stresses. The stress for the onset of delamination under static compression and the cycles for the onset of delamination under fatigue loading at various fatigue stress levels were experimentally determined. Delamination occurred at the 30/-30 interface for all specimens under both static and fatigue loadings. The critical component of the interlaminar stresses was found to be the interlaminar shear stress  $\tau_{xz}$  at the 30/-30 interface due to mechanical loading and curing residual stresses. This stress  $\tau_{xz}$  was therefore used to predict the onset of delamination in conjunction with the S-N relationship for in-plane shear, which was obtained from the fatigue testing of  $[\pm 45]_{2s}$  specimens. The experimental data for both static and fatigue loadings compare well with the analytical prediction.

**KEYWORDS:** delamination onset, interlaminar shear stress, fatigue, bismaleimide.

## INTRODUCTION

Free-edge delamination of composite laminates under in-plane static loading has been extensively studied since the early 1970's [1-5]. From the results of these studies, for example [2, 4, 5], the nature of the interlaminar stress components is well understood and the onset of delamination under static loading is reasonably well predicted. However, little work has been reported on the onset of delamination under fatigue loading. The objective of this study was to develop the capability to predict the onset of free-edge delamination in composite laminates subjected to fatigue loading. The material system investigated was a carbon fiber-reinforced toughened bismaleimide (IM7/5250-4). A quasi-isotropic laminate with a  $[90_2/\pm 30]_s$  lay-up was employed and the onset of delamination determined under compression-compression fatigue loading. Applied compressive loading was chosen, to eliminate the interaction of transverse cracks which usually occurs prior to delamination under applied tension. A laminate was designed to produce an interlaminar normal tensile stress under applied uniaxial compression. When this laminate is subjected to an axial compressive stress, delamination occurs due to interlaminar stresses in the free-edge region prior to the formation of transverse cracks. The interlaminar stresses at the free-edge region were calculated using an analytical model [4], taking into consideration curing residual stresses. The maximum-stress failure theory was applied to predict the initiation of

delamination. Because of the presence of a severe stress gradient along the free edge of the specimen, the concept of an effective stress, the average stress over a distance from the free edge equivalent to the thickness of one ply, was utilized. The thermomechanical properties required for the analytical calculations were determined experimentally in a complementary study. The stress-free temperature was also determined from the deflection of an unsymmetric laminate strip as a function of temperature to calculate the residual interlaminar stresses due to curing. The stress for the onset of delamination under static compression and the cycles for the onset of delamination under fatigue loading at various fatigue stress levels were experimentally determined. Acoustic emission was employed to detect the onset of delamination, and the result was confirmed visually using a microscope. Delamination occurred at the 30/-30 interface for all specimens under both static and fatigue loadings. The critical component of the interlaminar stresses was found to be the interlaminar shear stress  $\tau_{xz}$  at the 30/-30 interface due to mechanical loading and curing residual stresses. This stress,  $\tau_{xz}$ , was therefore used to predict the onset of delamination in conjunction with the S-N relation for in-plane shear which was obtained from fatigue testing of  $[\pm 45]_{2s}$  specimens. The experimental data for both static and fatigue loadings compare well with analytical predictions.

## **EXPERIMENTAL**

The material system selected for this study was a graphite/bismaleimide, IM7/5250-4, obtained in the form of unidirectional prepreg tape. A laminate with a stacking sequence of  $[90_2/\pm 30]_s$  was fabricated according to the manufacturer's recommended cure cycle and postcured at 227°C for five hours. The panel was cut into rectangular specimens 15 cm long and 2 cm wide using a diamond-impregnated saw blade. Glass/epoxy end-tabs, 5 cm long, were bonded at each end leaving a gage section of 5 cm, and the specimen edges were polished to enhance microscopic detection of delamination. Unidirectional laminates were also fabricated to determine the necessary thermoelastic properties for calculation of the interlaminar stresses in the free-edge region and to measure the appropriate strengths required for the prediction of the onset of delamination. The average fiber content was determined to be 64 percent by volume. The Poisson's ratio  $\nu_{yz}$  was determined from the tensile loading of a  $[90]_{16T}$  specimen with strains measured in y- and z-directions and utilized to calculate  $G_{yz}$ .

A device was designed and built to provide side support to the specimen and thereby prevent premature failure due to specimen buckling under compressive load. This side support has a central opening to accommodate an acoustic emission transducer to detect the onset of delamination under static as well as fatigue loading. An acoustic emission transducer was mounted on the flat face of the specimen using high-temperature vacuum grease to monitor the onset of delamination. A brittle white coating was applied to one of the free edges for the visual observation of the onset of delamination during loading. At the first indication of delamination, the specimen was unloaded and the delamination confirmed by microscopic examination of the specimen edge.

Of all the interlaminar stress components, the interlaminar shear stress  $\tau_{xz}$ , was found to be responsible for the free-edge delamination under applied compressive loading. Therefore, to predict the onset of delamination under fatigue loading, an S-N curve must be generated for interlaminar shear loading. Fatigue strength for in-plane shear loading was assumed to be equivalent to fatigue strength for interlaminar shear loading, and fatigue life data were generated from the uniaxial tension-tension fatigue of the  $[\pm 45]_{2s}$  specimens. Five stress levels were chosen with a minimum of five replicates at each stress level. All specimens were

fatigued to final failure on an MTS test machine in the displacement-control mode. The fatigue tests were conducted at a frequency of 10 Hz and a stress ratio of  $R= 0.1$ .

Fatigue life data were reduced by employing a statistical procedure which allows the generation of S-N curves with some statistical value without resorting to an extremely large data base. The details of this procedure can be found in [6]. The outline of this procedure is as follows:

- (a) The fatigue life data at each stress level are fitted to a two-parameter Weibull distribution

$$X(n) = \exp[-(n/N)^a] \quad (1)$$

where  $a$  is the shape parameter and  $N$  is the scale parameter (characteristic fatigue life). These parameters are estimated using a maximum-likelihood method.

- (b) All the fatigue life data for each stress level are normalized with respect to the characteristic life estimated in step (a). Then the common shape parameter is determined by pooling the normalized data for all stress levels, and the characteristic life for each stress level is re-estimated using the common shape parameter.

- (c) The estimated characteristic lives are fitted to a classical power law of the S-N relationship

$$S(n) = aN^b \quad (2)$$

where  $a$  and  $b$  are material constants which are determined by least-square regression analysis.  $N$  is the characteristic fatigue life estimated in step (b).

The fatigue cycles at the onset of delamination were determined under compression-compression fatigue with a frequency of 5 Hz and  $R= 1$ , using a  $[90_2/\pm 30]_S$  specimen with the same dimensions as those used in the static tests. Specimens were fatigued until the onset of delamination and unloaded to confirm the delamination under a microscope. A total of 12 specimens were tested at six different stress levels with 1 to 3 replicates at each stress level. The location of the interface where delamination occurred was identified for each specimen under a microscope.

## RESULTS AND DISCUSSION

The thermomechanical properties of the material system determined for calculation of interlaminar stresses and prediction of the onset of free-edge delamination are listed in Table 1.

### Interlaminar Stresses in the Free-Edge Region

Interlaminar stresses at each interface in the free-edge region were calculated using the variational model developed by Pagano [4]. The distribution of interlaminar stresses,  $\sigma_z$ ,  $\tau_{yz}$ , and  $\tau_{xz}$ , at the 30/-30 interface and the midplane due to an applied compression of 1 MPa and due to thermal loading alone (from curing residual stresses) are shown in Figures 1-4. There is only an interlaminar normal tensile stress present at the midplane under either mechanical loading or thermal loading due to curing residual stresses. All three interlaminar stress components exist at the 30/-30 interface. Interlaminar stresses at the other ply interfaces were

found to be insignificant compared to those at the midplane and the 30/-30 interface. There is a large gradient in the interlaminar stress components in the vicinity of the free edge. At both the midplane and the 30/-30 interface, the interlaminar normal stress is tensile due to mechanical loading, whereas it is compressive due to residual curing stresses. This compressive interlaminar normal stress increases the applied stress for the onset of delamination at these interfaces. A large interlaminar shear stress  $\tau_{xz}$  exists at the 30/-30 interface and is negative for both applied mechanical loading and curing residual stresses.

*Table 1: Thermomechanical properties of IM7/5250-4 under ambient conditions*

Longitudinal modulus, $E_x$ , GPa	165
Transverse modulus, $E_y=E_z$ , GPa	10.3
Shear modulus, $G_{xy}=G_{xz}$ , GPa	5.8
Transverse shear modulus, $G_{yz}$ , GPa	3.3
Major Poisson's ratio, $\nu_{xy}=\nu_{xz}$	0.31
Minor Poisson's ratio, $\nu_{yz}$	0.56
Coefficient of thermal expansion	$10^{-6}/^{\circ}\text{C}$
Longitudinal, $\alpha_x$	0.45
Transverse, $\alpha_y=\alpha_z$	24.7
Stress-free temperature, $^{\circ}\text{C}$	177
Fiber volume, $V_f$ , %	64
Cured ply thickness, mm	0.127
Shear strength, MPa	122
Transverse strength, MPa	61.3

The subscript x refers to the fiber direction and y and z refer to directions perpendicular to the fiber direction.

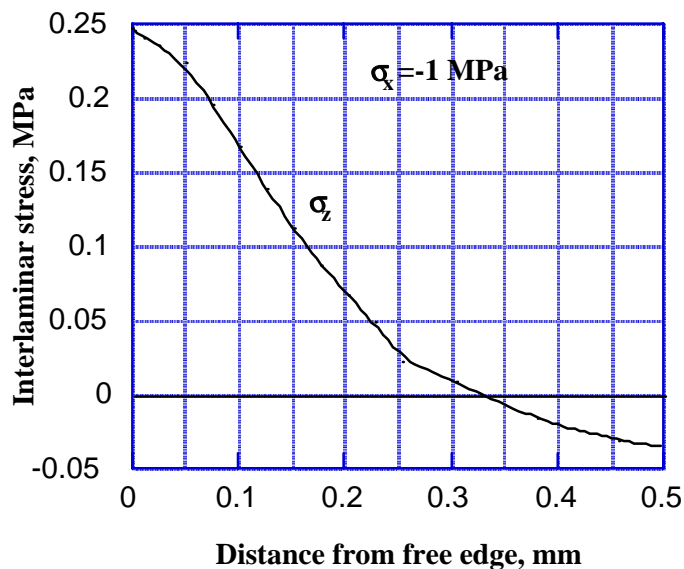


*Fig. 1: Interlaminar normal stress distribution at the midplane due to applied compression*

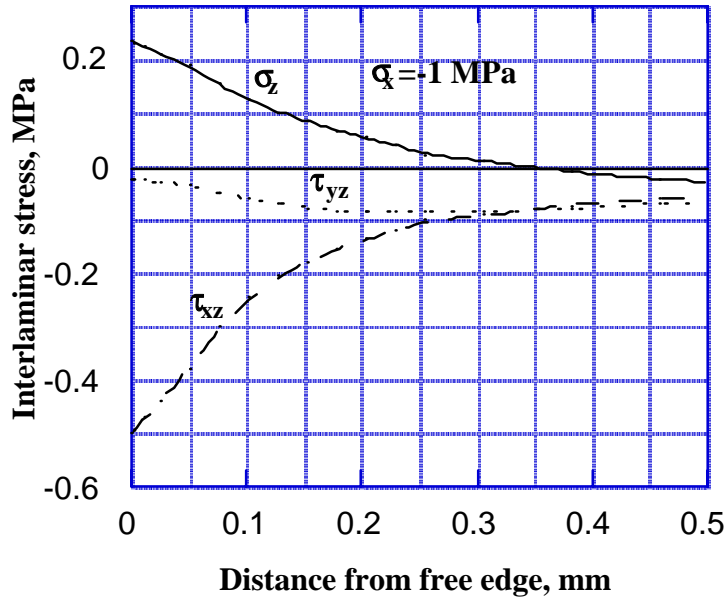


Fig. 2: Interlaminar stress distributions at the 30/-30 interface due to applied compression

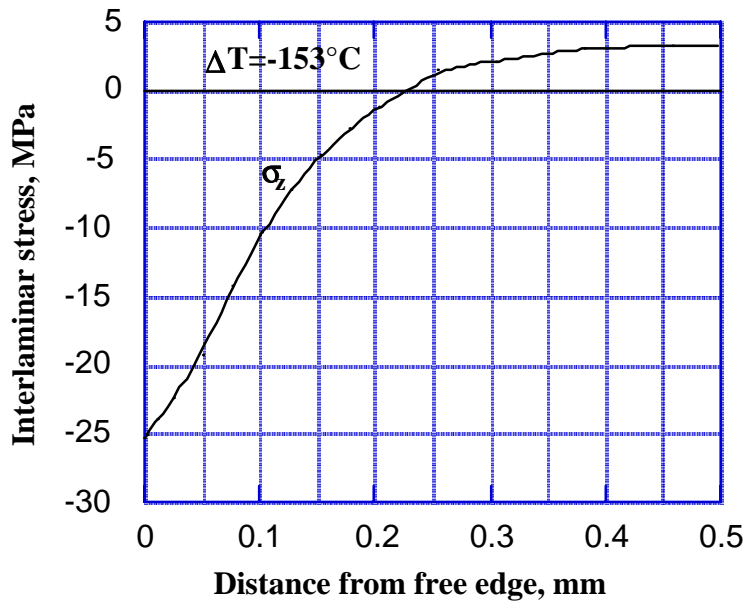


Fig. 3: Interlaminar normal stress distribution at the midplane due to curing residual stress

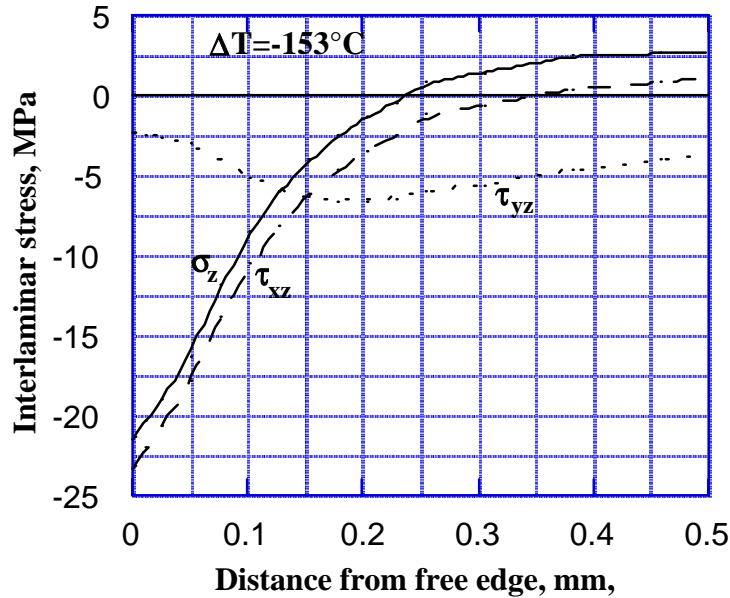


Fig. 4: Interlaminar stress distributions at the 30/-30 interface due to curing residual stress

### Prediction of the Onset of Delamination Under Static Loading

The results of the interlaminar stress analysis were applied to the prediction of the onset of delamination in conjunction with a failure theory [7]. The average value of each stress component at the free edge, instead of the maximum value, was assumed to be the effective stress level, i.e. that stress which is responsible for failure. The effective stress is obtained by averaging the interlaminar stress components over a fixed distance  $h_0$  from the free edge along the width of the laminate at the interface in question and is given by

$$\bar{\sigma}_I(z) = \frac{1}{h_0} \int_0^{h_0} \sigma_I(y,z) dy \quad (3)$$

The fixed distance  $h_0$  was taken as a thickness of one ply in all cases.

For prediction of the stress level at the onset of delamination and its location (interface), the maximum stress criterion was applied. Failure via delamination was assumed to occur when any of the effective stresses,  $\bar{\sigma}_I(z)$ , at each interface first reached the corresponding strength. By comparison of all interlaminar stresses with the corresponding strengths at the 30/-30 interface and the midplane for the laminate used in this study, the critical effective stress component was found to be the interlaminar shear stress,  $\tau_{xz}$ , at the 30/-30 interface. Thus, the onset of delamination was predicted when this effective stress reached the interlaminar shear strength. The interlaminar shear strength of the laminate was assumed to be equal to the in-plane shear strength of the material system. Results from [8] demonstrate that the difference between the interlaminar shear strength and in-plane shear strength is less than two percent for the graphite/epoxy AS4/3501-6 composite system.

The predicted stress for the onset of delamination compares fairly well with the experimental value as shown in Table 2. The experimental value is an average of four specimens with a coefficient of variation, ( $C_v$ ), of 4.5 percent.



Table 2: Comparison of prediction and experiment for onset of delamination under static loading

	Onset stress, MPa		Delaminated interface	
	Prediction	Experiment	Prediction	Experiment
$[90_2/\pm 30]_s$	346	312	30/-30	30/-30
$C_v, \%$	-	4.5	-	-

Delamination occurred at the 30/-30 interfaces for all specimens, as shown in Figure 5. The exact location of the delamination with respect to the ply interface could also be identified from these micrographs. No transverse crack was found to occur prior to delamination.

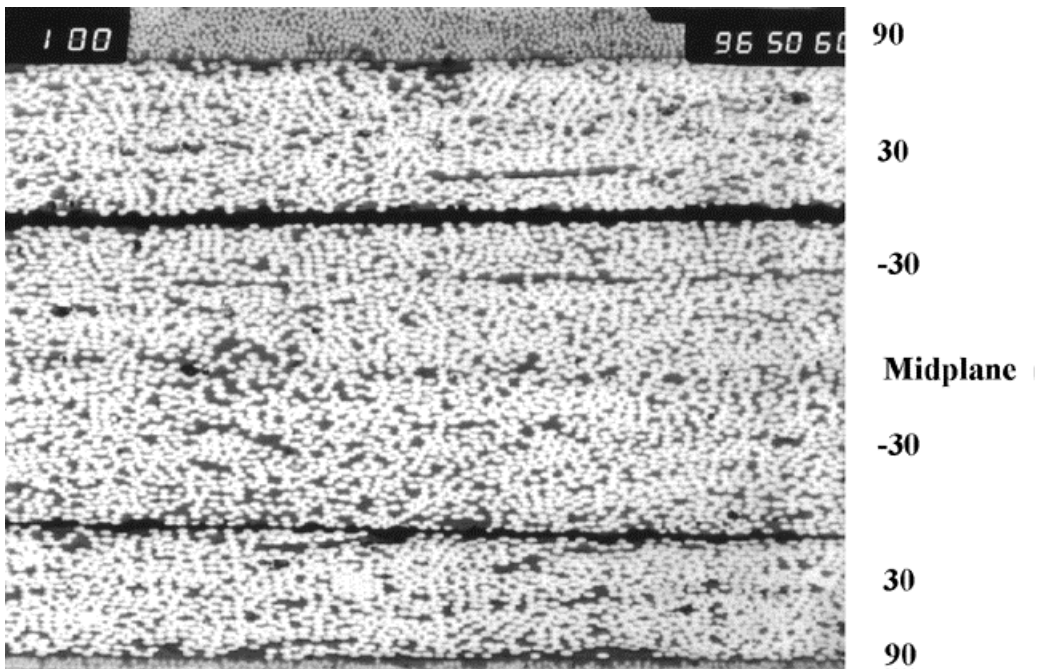


Fig. 5: Micrograph showing the onset of delamination for the  $[90_2/\pm 30]_s$  specimen

This is consistent with the analytical prediction of the stress to first-ply failure being greater than the stress for the onset of delamination under these conditions.

**Onset of Delamination Under Fatigue Loading**

Since  $\tau_{xz}$  is responsible for the free-edge delamination, the inplane shear S-N relationship and the calculated  $\tau_{xz}$  under a given load (including curing residual stress) were utilized to predict the onset of delamination under fatigue loading. Fatigue failure was assumed to occur when the fatigue interlaminar shear stress,  $\tau_{xz}$ , reached the fatigue shear strength of the material system. Figure 6 shows the shear S-N relationship determined under tension-tension fatigue from the  $[\pm 45]_{2s}$  laminate.

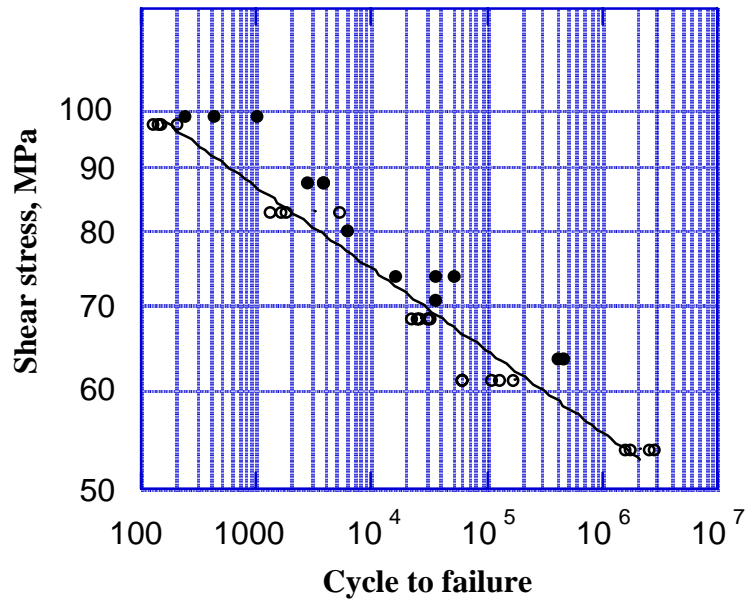


Fig. 6: S-N relationship for shear and fatigue data of  $[90_2/\pm 30]_s$  laminates in terms of the calculated effective stress  $\tau_{xz}$  at the 30/-30 interface. Solid line: shear S-N relation from  $[\pm 45]_{2s}$  laminate; open circle: fatigue data from  $[\pm 45]_{2s}$  laminate; and solid circle: fatigue data from  $[90_2/\pm 30]_s$  laminate

The open circles are the fatigue data obtained from experiment, and the solid line represents the regression line which was fitted to Eqn 2 using the data reduction scheme described previously. The material constants  $a$  and  $b$  in Eqn 2 determined from the regression analysis are 135.7 and -0.065, respectively. For a given interlaminar shear stress the number of cycles for the onset of delamination can then be predicted from Eqn 2. The interlaminar shear stress generated in the fatigue loading of any laminate can be calculated using the global-local model. The fatigue data at the onset of delamination for the  $[90_2/\pm 30]_s$  specimen under compression-compression fatigue are plotted (solid circle) in Figure 6. The shear stresses in the ordinate are obtained from the applied fatigue stress on the  $[90_2/\pm 30]_s$  laminate using the global-local model. The experimental data appear to fit the predicted S-N relation reasonably well with a little higher trend. This higher trend may be partially attributed to the difficulty in determining the exact number of cycles for the onset of delamination under cyclic loading. It may also be due to the inability of the acoustic emission system to capture a very small signal from the initiation of delamination. Further work is needed to refine the technique.

## CONCLUSIONS

An investigation was conducted to determine the initiation of free-edge delamination in IM7/5250-4 graphite/epoxy laminates under static and fatigue loading. Predictions regarding stress level and location (interface) for the onset of delamination agree very well with experimental results under static loading. The approach used in this work appears to be promising for prediction of onset of delamination under fatigue loading. In both static and fatigue loading no transverse ply failure was observed prior to free-edge delamination for this laminate. The absence of any damage prior to delamination might be helpful for prediction of

the delamination. The onset of delamination in this laminate can be accurately determined experimentally by monitoring strains in the axial and thickness directions and the use of acoustic emission. Further study is required to obtain confidence in this approach using a variety of laminates and different loading conditions.

### REFERENCES

1. R.B. Pipes and N.J. Pagano, "Interlaminar Stresses in Composite Laminates under Uniform Axial Extension", *J. Composite Materials* (1970), v4, 538-548.
2. N. J. Pagano and R.B. Pipes, "The Influence of Stacking Sequence on Laminate Strength", *J. Composite Materials* (1971), v5, 50-57.
3. J.M. Whitney and C.E. Browning, "Free-Edge Delamination of Tensile Coupons", *J. Composite Materials* (1973), v6, 300-303.
4. N.J. Pagano, "Stress Fields in Composite Laminates", *Int. J. Solids & Struct.* (1978), v14, 385-400.
5. N.J. Pagano and S.R. Soni, "Global-Local Laminate Variation Model", *Int. J. Solids & Struct.* (1983), v19, 207.
6. W. J. Park and R. Y. Kim, "Statistical Analysis of Composite Fatigue Life", *Progress in Science and Engineering of Composites*, T. Hayashi, et al., ICCM-IV, Tokyo, Japan, October, (1982),v1, 709-716.
7. R.Y. Kim and S.R. Soni, "Experimental and Analytical Studies on the Onset of Delamination in Laminated Composites", *J. Composite Materials* (1984), v18, 70-79.
8. R. Y. Kim, F. Abrams, and M. Knight, Mechanical,"Characterization of a Thick Composite Laminate", *Proc. of American Society for Composites*, Technomic Publishing (1988), 711-718.

### ACKNOWLEDGMENT

This work was performed under U.S. Air Force Contract No. F33615-95-D-5029. The authors wish to express their appreciation to Mr. Ron Esterline of the University of Dayton Research Institute for his help in the preparation and testing of specimens.

# FATIGUE CRACK GROWTH BEHAVIOR OF A RANDOM FIBER SHEET MOLDING COMPOUND COMPOSITE

D. R. Atodaria<sup>1</sup>, S. K. Putatunda<sup>1</sup> and P. K. Mallick<sup>2</sup>

<sup>1</sup> *Department of Materials Science and Engineering, Wayne State University,  
Detroit, Michigan 48202, USA*

<sup>2</sup> *Department of Mechanical Engineering, University of Michigan-Dearborn,  
Dearborn, Michigan 48128, USA*

**SUMMARY:** The purpose of this study is to investigate the fatigue crack growth behavior of a random fiber sheet molding compound (SMC-R) composite and to examine the applicability of a new fatigue crack growth rate model to this material. In this study, the fatigue crack growth rate of SMC-R was measured using a compliance approach. The new fatigue crack growth rate model is based on a power law equation and takes into account not only the effect of the stress intensity factor range, but also the effect of crack growth at various stages of loading using a weight average stress intensity factor. It was observed that this new model can represent the fatigue crack growth rate of this SMC-R at three different load ratios in a single unifying curve.

**KEYWORDS:** random fiber composites, sheet molding compounds, fatigue crack growth, compliance, power law equation

## INTRODUCTION

Randomly oriented short fiber reinforced sheet molding compound (SMC-R) composites are finding increasing use in many structural applications, including automotive structures and bridge structures. Many of these structures experience repeated loading in service and fatigue failure must be considered as one of the critical failure modes in their design. Use of SMC in these structures requires that a better understanding of the fatigue failure process and a suitable fatigue life prediction technique be developed for this class of composite materials.

There is now a significant number of publications on the fatigue behavior of continuous fiber reinforced laminated composites; however, publications on the fatigue behavior of random fiber composites are extremely limited. In an earlier work [1], we proposed a new empirical model to characterize the fatigue crack growth behavior of random fiber composites. In the present work, we have studied the fatigue crack growth rate of a random fiber SMC composite at three different load ratios and extended the application of our model to the fatigue life prediction of this material.

## PROPOSED MODEL

An understanding of fatigue behavior is important for any material that experiences repeated loading during service. There are basically two approaches for generating information and knowledge of the fatigue behavior of materials: (1) the S-N curve or the  $\epsilon$ -N curve approach, and (2) the fracture mechanics approach. The fracture mechanics approach assumes the presence of inherent cracks or flaws in the material and attempts to predict its life using empirical models of fatigue crack growth rate. The most commonly used Mode I fatigue crack growth rate model is based on the Paris power law equation [2]

$$\frac{da}{dN} = A(\Delta K)^m \quad (1)$$

where,  $da/dN$  = fatigue crack growth rate

$\Delta K$  = difference in the maximum and minimum Mode I stress intensity factors

A, m = curve-fitted power law constants for the material

Eqn. (1) has been used extensively for metals and to some extent, with composite materials as well. Wang et. al. [3] employed Eqn. (1) to establish fatigue crack growth rate in an SMC. They found the value of A and m to be  $7.58 \times 10^{-8}$  and 9.65, respectively. Similar attempts have also been made to fit Eqn. (1) to fatigue crack growth rate of other random fiber composites, such as injection molded thermoplastic composites [4].

The Paris model, given by Eqn. (1), assumes that the fatigue crack growth rate depends only on the stress intensity factor range,  $\Delta K$ . For a fatigue test with zero load ratio,  $K = K_{max}$ , and thus, according to Eqn. (1), the fatigue crack growth rate depends only on  $K_{max}$ , regardless of the mean load imposed during cycling. Furthermore, for any given value of stress intensity factor range, the fatigue crack growth rate is independent of other values of K within this range. For many composites, it is observed that crack growth occurs at stress levels that are lower than the maximum stress imposed in the fatigue cycle and, therefore, stress intensity factors lower than the  $K_{max}$  will also have some effect on the fatigue crack growth rate of such composites. In each cycle, the crack may grow in a very slow and progressive manner as the stress increases from the minimum to the maximum value; however, the extent of damage growth may not be equal at each stress level. It is expected that the crack growth rate will be slower at low stress levels and will be faster as the stress increases toward the maximum value. Based on this assumption, we have proposed a modified power law model which takes into account this progressive crack propagation process by including a weight average value of K in addition to the stress intensity range that is already present in the Paris model. According to this modified model, the fatigue crack growth rate can be expressed as

$$\frac{da}{dN} = A_0 (\Delta K^\alpha \cdot K_{average}^\beta)^\gamma \quad (2)$$

$$\text{where, } K_{average} = \left[ \frac{1}{n} \sum_{K_{th}}^{K_{max}} K^w \right]^{1/w}$$

n = number of divisions by which the range of  $K_{th}$  to  $K_{max}$  is equally divided (Fig. 1)

w = weighting factor

$A_0, \alpha, \beta, \gamma$  = constants

$K_{th}$  = threshold stress intensity factor below which no crack propagation occurs

Note that the constants  $A_0$ ,  $\alpha$ ,  $\beta$ ,  $\gamma$  and the weighting factor  $w$  are determined by iteration to fit the experimental data. In Ref. 1, we assumed  $\alpha = \beta = 0.5$  and found that Eqn. (2) fits the experimental data for random carbon fiber reinforced PEEK with  $A_0 = 5.43 \times 10^{-20}$ ,  $w = 16.9$  and  $\gamma = 17.4$ . The powers  $\alpha$  and  $\beta$  may not have the same value, since, depending on the material,  $\Delta K$  and  $K_{\text{average}}$  may have different influences on the fatigue crack growth rate of the material.

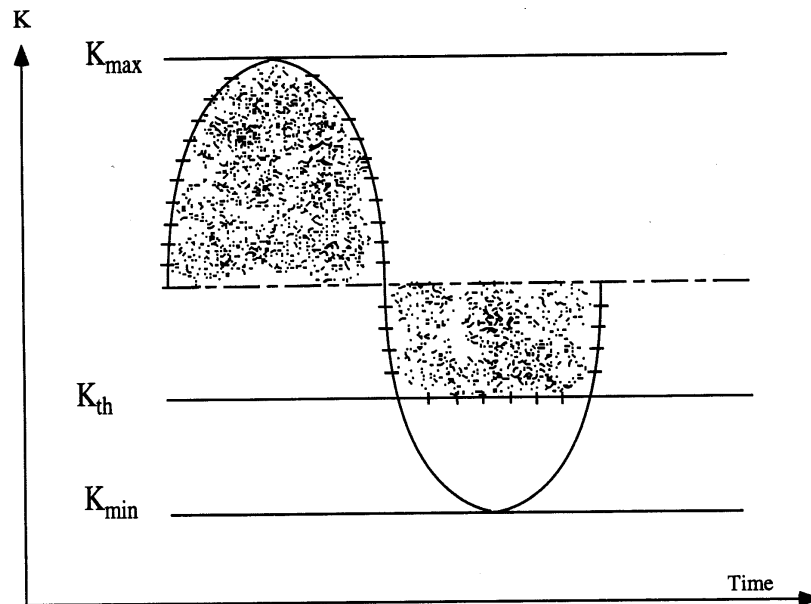


Fig. 1: Partition from  $K_{th}$  to  $K_{max}$  in 'n' divisions for calculating  $K_{average}$

In the present work, we have used the proposed model for a random fiber sheet molding compound composite. However, unlike the carbon fiber reinforced PEEK, the fatigue failure does not occur by the enlargement of a single visible crack. In the first few fatigue tests performed with SMC specimens, it was observed that the fatigue crack in this material does not follow a well defined path. As the fatigue loading is continued, a number of small cracks appear in the vicinity of the original notch tip. These cracks are oriented at different angles with the notch plane. With a traveling microscope focused on the specimen surfaces, the opening and closing of these cracks can be clearly seen; however it was difficult to judge whether these cracks are only at the surfaces or also extend deep into the thickness of the specimen. Eventually one of these cracks extends in length, but stops after a slight extension. With continued cycling, multiple small cracks appear in the vicinity of the extended crack and the whole process of stop-and-go crack growth process is repeated. Another point to note is that the crack extension occurs in SMC in a zigzag manner, often deviating from the plane of the original notch. This created a problem in that the crack length could not be accurately measured during the fatigue test. This has led us to use the increase in specimen compliance as an indirect measure of the fatigue crack growth in SMC. The compliance measurement technique is described in the next section.

## EXPERIMENTAL PROCEDURE

The material used in this study is a sheet molding compound (SMC) composite containing 25 mm long chopped E-glass fibers randomly oriented in a thermosetting polyester resin. The fiber weight fraction is estimated to be 30 percent. In addition to the randomly oriented fibers and the matrix, the other major ingredient in the material is a calcium carbonate filler which is randomly dispersed in the matrix. The nominal thickness of compression molded SMC plate was 3.6 mm.

The fatigue experiments were conducted in an MTS servohydraulic testing machine using a 18 kN load cell cartridge. Compact tension specimens with the dimensions shown in Fig. 2 were used in all fatigue tests. The crack opening displacement during the fatigue tests were measured using a clip gauge, which was inserted at the notch mouth in the beginning of each test. Fatigue cycling was performed in a load-controlled mode at room temperature using a frequency of 2 Hz. Three different load ratios,  $P_{min}/P_{max}$ , were used, namely 0.1, 0.3 and 0.5.

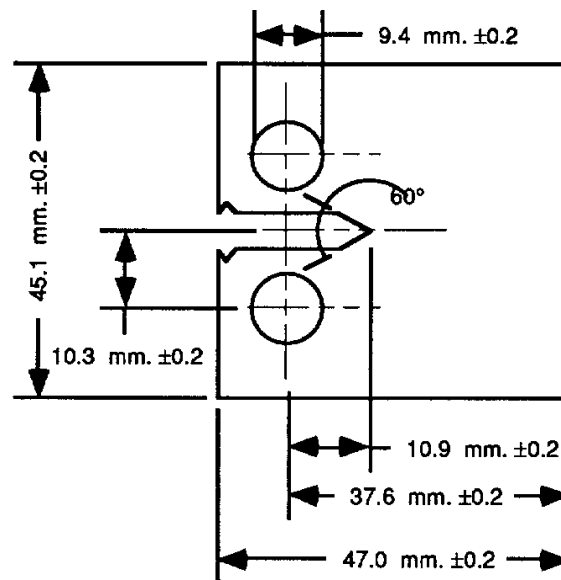


Fig. 2: Compact tension specimen

In order to use the compliance measurement as an indirect measure of fatigue crack growth, we had to first establish a compliance calibration equation which relates the specimen compliance to an equivalent crack length. The calibration curve was obtained using 10 specimens with different initial notch lengths, varying in length from 12 to 20 mm. Each of these specimens was cycled once between 0.67 kN and 1.33 kN at 0.1 Hz. The specimen compliance, defined as the ratio of crack opening displacement (COD) to load, is determined from the loading portion of the load vs. COD diagram obtained during this test.

The specimen compliance during the fatigue test was measured at regular intervals. Instead of applying the full load in the first cycle, the load was increased in steps. After reaching the end of each load step, the specimen was allowed to fatigue for a few cycles at 2 Hz. before recording the hysteresis loop depicting the load vs. the crack opening displacement at 0.1 Hz. The load was then increased to the next step. This process was continued until the full load

was reached and the specimen was subsequently allowed to cycle between the maximum and minimum loads for the duration of its life. The specimen compliance was calculated from the digital data of load and crack opening displacement using the Excel software. A function called ‘linest’ in the Excel software was used in to calculating the slope of the loading portion of the hysteresis loop.

### RESULTS

The compliance calibration diagram for the SMC material considered is shown in Fig. 3. Following equation was obtained relating the compliance to the crack length :

$$C = 5.903 \times 10^{-7} a^{1.276} \tag{3}$$

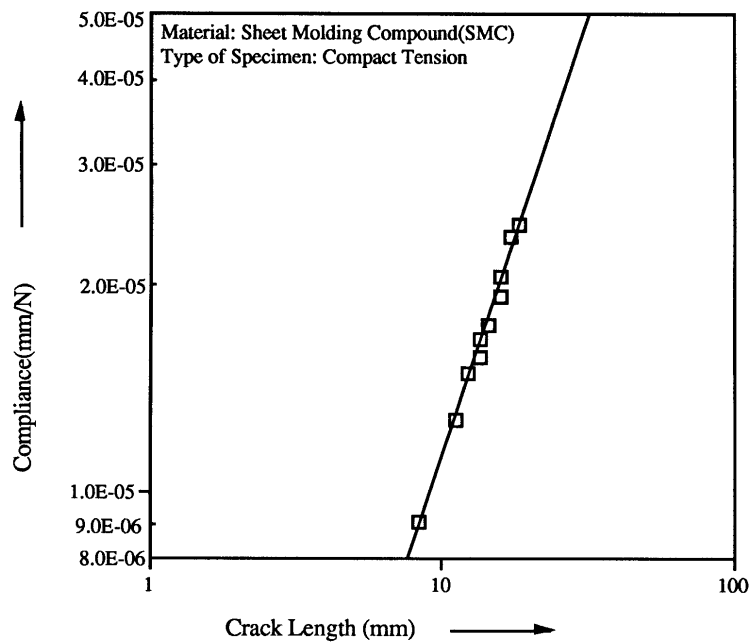


Fig. 3: Compliance Calibration Diagram for Estimating Fatigue Crack Length

The stress intensity factor for the compact tension specimen was calculated using the following equation [5]:

$$K = \frac{P}{B \sqrt{W}} f \left( \frac{a}{W} \right) \tag{4}$$

where, P = applied load on the specimen, B = specimen thickness,  
 W = width of the specimen from the center of the loading point,  
 a = crack length measured from the center of the loading point, and  
 for a compact tension specimen,



$$f\left(\frac{a}{W}\right) = \frac{2 + \frac{a}{W}}{\left(1 - \frac{a}{W}\right)^{3/2}} \left[ 0.886 + 4.64\left(\frac{a}{W}\right) - 13.32\left(\frac{a}{W}\right)^2 + 14.72\left(\frac{a}{W}\right)^3 - 5.60\left(\frac{a}{W}\right)^4 \right]$$

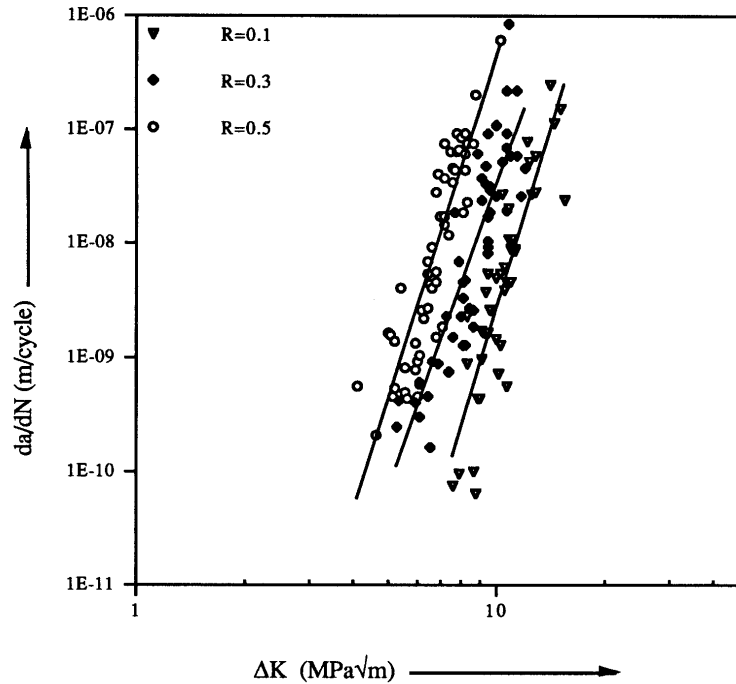


Fig. 4 : Fatigue crack growth rate vs.  $\Delta K$

Fig. 4 shows the fatigue crack growth rate vs.  $\Delta K$  for three different load ratios considered in this study. This figure shows that the fatigue crack growth rate of the SMC increases with increasing load ratio. If the Paris equation is used to model the fatigue crack growth rate, there will be different constants for different load ratios. Similar observation can be made if the fatigue crack growth rate is plotted as a function of  $K_{\text{average}}$  (Fig. 5); however, the distinction between the load ratios is much narrower in this figure. Next, the effects of  $K$  and  $K_{\text{average}}$  are combined using different values of  $\alpha$  and  $\beta$  for the powers of these two parameters, and as shown in Fig. 6, the fatigue crack growth data for all three load ratios fall in a very narrow band for  $\alpha = 0.15$  and  $\beta = 0.85$ . This indicates that Eqn. (2) can be used to unify the load ratio effect in the SMC. The best fit line drawn through the data points for all three load ratios has the equation given by

$$\frac{da}{dN} = 2.06 \times 10^{-20} (\Delta K^{0.15} K_{\text{average}}^{0.85})^{11.2} \quad (5)$$

The experimental fatigue crack growth rate for each load ratio was compared with the fatigue crack growth rate predicted by Eqn. (5). One such comparison is shown in Fig. 7 for load ratio  $R=0.1$ . As can be seen in Fig. 7, there is a close agreement between the experimentally

determined values and predicted values. Similar agreement was also observed for the other two load ratios.

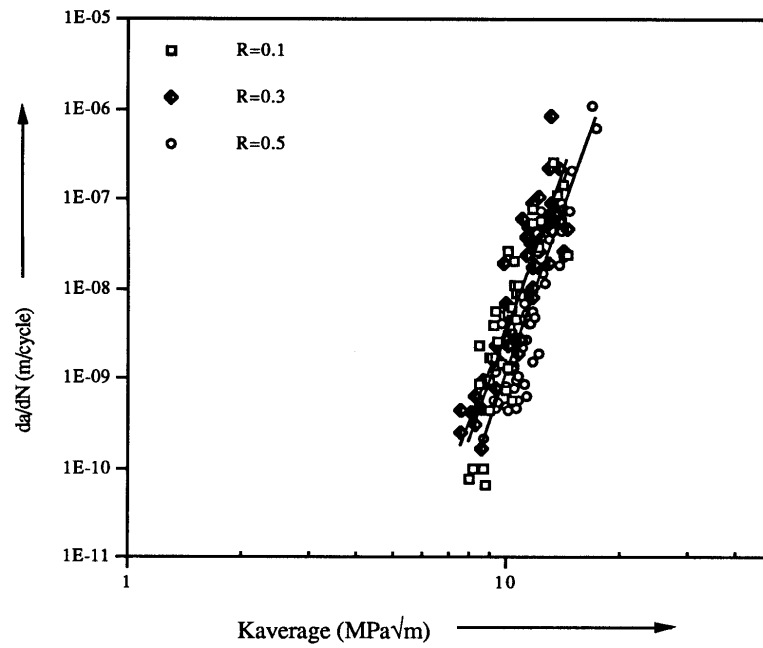


Fig. 5 : Fatigue Crack Growth Rate vs.  $K_{average}$

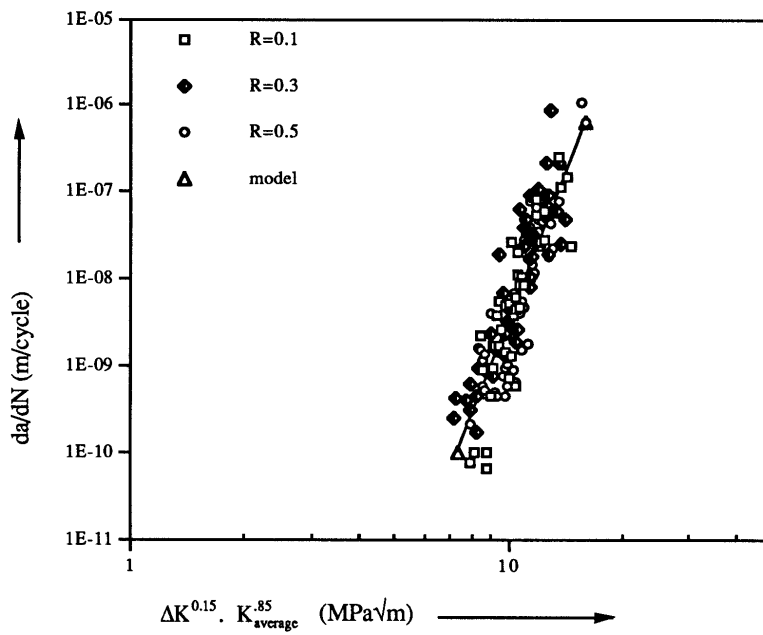


Fig. 6 : Fatigue crack growth rate vs. combined  $\Delta K$  &  $K_{average}$  as per model

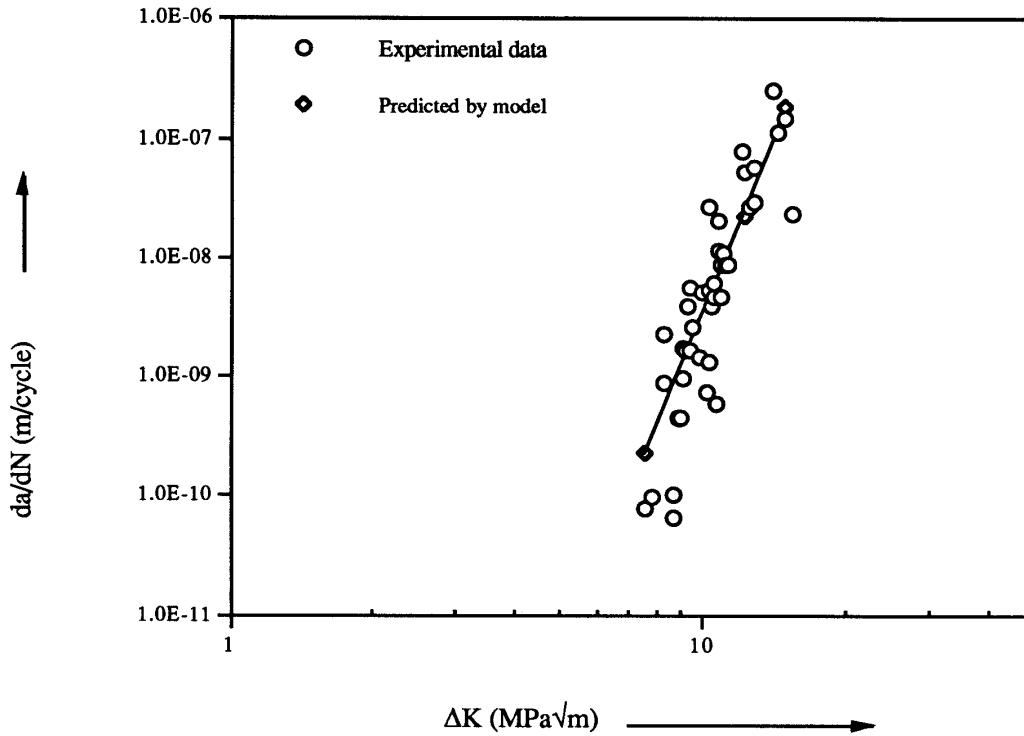


Fig. 7 : Comparison of experimental fatigue crack growth rate with the one predicted by model

### CONCLUSIONS

1. The compliance measurement approach was shown to be an effective method for monitoring the fatigue crack growth in random fiber SMC composites.
2. The proposed model is capable of unifying the fatigue crack growth rate at three load ratios considered into a single power law equation:

$$\frac{da}{dN} = 2.06 \times 10^{-20} (\Delta K^{0.15} K_{\text{average}}^{0.85})^{11.2}$$

3. Good agreement was found between predicted fatigue crack growth rate using the proposed model and the experimentally measured fatigue crack growth rate in a random fiber SMC composite.

### REFERENCES

1. Atodaria, D.R., Putatunda, S.K. and Mallick, P.K., "A Fatigue Crack Growth Model for Random Fiber Composites," *Journal of Composite Materials*, Vol. 31, No.8, 1997 (in print).
2. Paris, P.C. and Erdogan, F., "A Critical Analysis of Crack Propagation Laws," *Trans. ASME Journal of Basic Engineering*, Vol. D85, 1963, pp. 528-534.

3. Wang, S.S., Chim, E.S.-M., and Zahlan, N.M., "Fatigue Crack Propagation in Random Short-Fiber Composite," *Journal of Composite Materials*, Vol. 17, 1983, pp. 251-266.
4. Karger-Kocsis, J. and Friedrich. K., "Fatigue Crack Propagation in Short and Long Fibre-Reinforced Injection Moulded PA 6.6 Composites," *Composites*, Vol. 19, No. 2, 1988, pp. 105-114.
5. Hertzberg, R.W., *Deformation and Fracture Mechanics of Engineering Materials*, 4th Edition, John Wiley and Sons, Inc., New York, 1996, pp. 757.

# DAMAGE BASED FATIGUE LIFE MODELING FOR BRITTLE COMPOSITES

G. M. Newaz<sup>1</sup> and N. Bonora<sup>2</sup>

<sup>1</sup>*Mechanical Engineering Department, Wayne State University,  
505 Anthony Wayne Drive, Detroit, MI 48202, USA*

<sup>2</sup>*Industrial Engineering Department, University of Cassino,  
Via G. De Biasio 43, 03043 Cassino (FR), Italy*

**SUMMARY:** Fiber reinforced composites are usually notch insensitive. Damage in composite, under static loading is usually due to several concurrent fracture modes as fiber failure, matrix cracking, fiber-matrix debonding, fibre pull-out and delamination. These mechanisms reduce the material load carrying capability. In fatigue this situation can be even more complicated. In brittle composite systems where all constituents have brittle behavior with no dissipation processes other than the creation of new fracture surfaces - they exhibit a strong connection between the first damaging fatigue cycle and the subsequent damage evolution. In addition, damage produced during the first cycle can be directly related to the one produced due to monotonic loading. In the present paper a fatigue damage model for brittle composites is presented. The effect of complex damage state was examined in terms of stiffness loss as a function of the accumulated strain during cycling. The model, developed on phenomenological basis, has been verified on several composite systems such as unidirectional ceramic matrix and cross-ply polymeric composites.

**KEYWORDS:** fatigue life model, brittle composite, stiffness loss, damage

## INTRODUCTION

Prediction of fatigue life in brittle composites where only microcracks dominate the overall dissipation characteristics remains an important challenge as growth laws based on fracture mechanics for single cracks are inadequate. Due to the complex damage modes that occur in a composite material under static or cycling loading, it is appropriate to address the complex damage states where several basic fracture types such as matrix cracks, fibre breaks, delamination, and fibre-matrix disbonds and their mutual interactions are accounted for, particularly, in developing life models. The best way to investigate fatigue effects on composite materials is to assess the degradation of the material properties such as elastic moduli as a function of the number of cycles [1-3]. A direct consequence of distributed microcrack-type damage is tensorial stiffness property change in composites.

There is an important connection between the first cycle damage and subsequent damage evolution in fatigue in laminated composites. The damage that occurs in the first cycle is no different than that which occurs during monotonic response. In order to clearly understand the implication of this initial damage, it is important to develop the link between monotonic damage and fatigue damage to develop proper fatigue life models. Monotonic response of unidirectional CMCs have been studied extensively by a number of researchers [4-12].

Proportional limit of unidirectional CMCs have been associated with matrix cracking and subsequent nonlinear behavior has been identified to be due to progressive fiber failure [9,10]. Matrix cracking in CMCs has been the subject of in-depth investigation by researchers as well [12,13]. Continuum damage mechanics models can be used to predict the stiffness loss in these composites due to the presence of damage which are typically microcrack entities such as matrix cracks, fiber matrix disbonds and fiber cracks [3]. Monotonic damage evolution and subsequent modeling of the stiffness changes using continuum approaches were investigated for the hybrid composite [14]. Cyclic damage has been characterized by a number of researchers for glass matrix composites which confirm that a combination of damage such as matrix cracking, fiber-matrix debonding and fiber fracture depending on the lay-up of the composite [15]. Polymeric composites (PMCs) brittle matrices such as epoxy also can be categorized as brittle composites because of the nature of dissipation characteristics due to distributed matrix cracks. Other PMCs also show brittle characteristics as plastic deformation is suppressed at the microstructural level as much of the load is carried by carbon fibers. Microcracking in toughened epoxies and in thermoplastic matrices are also dominant dissipation mechanisms precluding plastic deformation that occurs readily in bulk matrices. As far as distributed microcracking is concerned in PMCs during fatigue, they can be categorized as brittle where energy dissipation is primarily controlled by free surface creation.

### **MODELING ASPECTS**

Fig. 1 shows the data scatter for several fatigue tests performed with ceramic matrix composites [16] at room temperature with the same R-ratio and frequency and  $\sigma_{\max}$ . In order to arrange experimental data in a more meaningful way, the number of cycles has been normalized by  $N_f$ . This representation allows one to separate the scatter relative to  $N_f$  and to underline the main feature of the fatigue damage evolution law. In this case, it is possible to identify a lower bound for the degradation of the moduli.

The fact that brittle composites are very sensitive, in terms of accumulated damage, to the very first cycle is indicative of a high sensitivity to the applied strain. It has been seen that it is more appropriate to approach composites in terms of strain instead of stress, since due to the non-homogeneity of the micro-structure, strains have to be the same while stresses are different in matrix and in the fiber.

If the strains applied in the first few cycles are high enough to introduce damage in the microstructure, this will lead to stiffness loss. The subsequent cycles will see a progressive evolution of the initiated damage state that will develop more gradually up to the moment of final fracture. It is very difficult to develop an accurate model, defined on micro-mechanical basis that is able to predict the physical evolution of complex damage states. The main features can be obtained from the fatigue tests in terms of the shape of the stiffness reduction trend. Many authors pointed out that brittle materials such as glass or glass-ceramic materials show practically no range of fatigue behavior that results in a crack of the order of an existing flaw size growing instantaneously. A number of authors [15,17] suggested that fatigue cycling does not lead to new damage modes in the composites.

If fatigue cycling does not introduce additional damage modes other than the growth of the already existing complex damage state, it follows that the evolution features related to the fatigue process are all contained in the shape of the distribution of the fatigue data. Furthermore, cyclic damage measurements taken at different cycles should fall on the same

static damage curve shown in Fig.2. The last observation has been verified by plotting damage measurements taken at different number of cycles versus the total strain applied during the cycling. When a specimen is cycled in stress control, due to creation of new surfaces, the true applied strain increases with the number of cycles as shown in Fig. 3. The progressive material damage is illustrated in Fig. 4. The applied strain is partially recovered elastically in the cycle but there is a contribution that accumulates as ratchetting, due to incomplete closure of cracked surfaces during unloading.

The relation that describes the damage evolution via modulus reduction in the applied loading direction,  $E_D/E_0$ , as a function of the number of cycles, have to be bounded between 0 and 1 for a number of cycles comprised between 1 and  $N_f$ . The following relation :

$$\frac{E_D}{E_0} = B(\varepsilon) \cdot \left[ 1 - \frac{\ln(N)}{\ln(N_f)} \right]^{\frac{1}{\beta}} \quad (1)$$

seem to be appropriate to describe the experimental data trend. When the number of cycle reaches  $N_f$ , i.e. the number of cycles at fracture, the ratio  $E_D/E_0$  goes to zero.  $E$  with subscripts D and 0 represent current and initial stiffnesses, respectively. Note that  $D = 1 - E_D/E_0$ . When  $N=1$ , then the amount of damage at the first cycle is determined by the imposed strain field in the material. In fact only if the strain level is high enough to produce damage in the first place, then further damage will develop during cycling.

To determine the amplitude constant B, it is sufficient to observe that the first cycle, if the strain rate is not extremely high, is similar to a static load ramp up to the imposed maximum strain. For this reason, the amount of damage produced in the first cycle have to be related to the static damage curve as suggested by the authors [14]:

$$B(\varepsilon) = (1 - D_0) - (D_{cr} - D_0) \left[ 1 - \frac{\ln(\varepsilon / \varepsilon_{th})}{\ln(\varepsilon_f / \varepsilon_{th})} \right]^{\frac{1}{m}} \quad (2)$$

that substituted in Eqn. 1 leads to:

$$\frac{E_D}{E_0} = \left( (1 - D_0) - (D_{cr} - D_0) \frac{\ln[e / e_{th}]}{\ln[e_f / e_{th}]} \right)^{\frac{1}{m}} \left[ 1 - \frac{\ln[N]}{\ln[N_f]} \right]^{\frac{1}{\beta}} \quad (3)$$

In addition to CMCs, the model can be applied to PMCs as the fatigue damage process in these materials is dominated by matrix cracking which manifests as stiffness loss as a function of fatigue cycles. As in the case of CMCs, the damage in PMCs in terms of matrix cracks and/or fiber cracks are the energy dissipation events that are completely controlled by creation of new surfaces only. Consequently, based on damage processes at work in fatigue, both types of composites exhibit brittle behavior. Working with data from literature [18-19] and analyzing them using the approach discussed earlier, the proposed fatigue damage model can predict the trend in damage evolution as shown in Figures 5-6.

## CONCLUSIONS

Damage in CMCs as well as PMCs are strain controlled. More particularly, magnitude of damage as manifested by stiffness loss is dependent on the strain experienced by the composite as described by Eqn. 3. The fatigue life model presented requires the evaluation of a number of parameters such as  $\varepsilon_{th}$ ,  $\varepsilon_{cr}$  and  $m$  which can be obtained through a static test. Only two parameters, exponent  $\beta$  and the number of cycle at fracture  $N_f$ , have to be determined using fatigue data. Anyway, only few tests performed at two or three different stress levels will be sufficient to identify the parameters in a proper way. The nature of damage evolution as dictated by stiffness loss during fatigue can be cast in a functional form that captures the essence of strain controlled damage. Fatigue life for a given reduction in stiffness can be estimated from the functional form if nominal final life is known from limited experimental data. This approach seems to work well for both CMCs and PMCs. Hence, this basic life prediction model for fatigue that captures the essence of the trend in fatigue data in brittle composites shows significant promise.

## ACKNOWLEDGEMENT

The authors acknowledge the funding for this research work from the IHPTET program support from the Propulsion and Materials Laboratory of Wright Laboratories. Mr. Larry Zawada of the Materials Directorate was the program monitor.

## REFERENCES

1. Highsmith, A. L. and Reifsnider, K. L., "Stiffness-Reduction Mechanisms in Composite Laminates," in *Damage in Composite Materials*, ASTM STP 775, American Society for Testing and Materials, Philadelphia, PA, 1982, pp.103.
2. Laws, N., Dvorak, G.J., and Hejazi, M., "Stiffness Changes in Unidirectional Composites Caused by Crack Systems," *J. Mechanics of Materials*, vol.2, 1983, p.123
3. Talreja, R., *Fatigue of Composite Materials*, Technical University of Denmark, 1985.
4. Prewo, K.M., "Tension and Flexural Strength of Silicon Carbide Fiber-reinforced Glass Ceramics", *Journal of Materials Science*, Vol. 21, 1986, p. 3590.
5. Prewo, K. M., "Advanced Characterization of SiC Fiber reinforced Glass Matrix Composites", Office of Naval Research Contract N00014-81-C-0571, Interim report, June, 1983.
6. Zawada, L.P., Butkus, L.M. and Hartman, G.A., "Room Temperature Tensile and Fatigue properties of SiC Fiber-Reinforced Aluminosilicate Glass", *Ceramic Engineering Science and Proceedings*, Vol. 11, 1990, p. 1592.
7. Nardone, V.C. and Prewo, K.M., "Tensile Performance of Carbon Fiber-Reinforced Glass", *Journal of Materials Science*, Vol. 23, 1988, p. 168.
8. Newaz, G.M., Brust, F.W., Jarmon, D.C. and Cairo, R.R., "Deformation, Failure and Mechanical Response Modeling in Dual Fiber CMC", Presented at the Annual ACS Meeting, Cocoa beach, Florida, January, 1994.
9. Rousseau, C.Q., "Monotonic and Cyclic Behavior of a SiC/CAS Composite", ASTM STP 1080, J.M. Kennedy, H.M. Mouller, and W.S. Johnson Eds., 1990, p. 136.



10. Prewo, K.M., Johnson, B. and Starett, S., "Silicon Carbide Fiber-Reinforced Glass-Ceramics", *Journal of Materials Science*, Vol.24, 1989, p.1373.
11. Sbaizero, O. and Evans, A.G., "Tensile and Shear properties of Laminated Ceramic Matrix Composites", *Journal of American Ceramic Society*, Vol. 69, # 6, 1986, p. 481.
12. Aveston, and J.Kelly, "Theory of Multiple Fracture of Fibrous Composites", *Journal of Materials Science*, 1973, Vol.8, p. 352.
13. Budiansky, B., Hutchinson, J.W., and Evans, A.G., "Matrix Fracture in Fiber-Reinforced Ceramics", *Journal of Mechanics and Physics of Solids*, Vol. 34. p. 35.
14. Bonora, N. and Newaz, G., "Modeling Damage Evolution in a Hybrid Ceramic Matrix Composite Under Static Tensile Loading", accepted for publication in *J. Engineering Materials and Technology*, ASME, Nov., 1996.
15. Karandikar, P.G. and Chou, T.W., "Microcracking and Elastic Moduli Reductions in Unidirectional Nicalon-CAS Composites Under Cyclic Fatigue Loading", *Proceeding of the 16th Annual Conference on Composites and Advanced Ceramics*, Cocoa Beach, Florida, Jan., 1992.
16. Newaz, G.M. and Bonora, N., "Fatigue Life Modeling in Hybrid CMCs," in *Thermal and Mechanical Test methods and Behavior of Continuous Fiber Ceramic Composites*, ASTM STP 1309, M.G.Jenkins, S.T. Gonczy, E. Lara-Curizio, N.E Ashbaugh and L.P. Zawada, Eds., American Society for Testing and Materials, 1996.
17. Evans, A.G. and Fuller, E.R., "Crack Propagation in Ceramic Materials under Cyclic Loading Conditions", *Metall. Trans.* 5, (1974), p.27.
18. Charewicz A. and I.M. Daniel, "Damage Mechanisms and Accumulation in Graphite/Epoxy Laminates," in *Composite Material: Fatigue and Fracture*, ASTM STP 907, H.T.Hahn Ed., 1986, pp. 274-297.
19. Bonora, N., Marchetti, M. and Millela, P.P., "Theoretical Forecasting and Experimental Validation of Damage Tolerance and Accumulation in Glass/Epoxy laminates", *J. of reinforced Plastics and Composites*, Vol II, 1992, pp. 56-81.

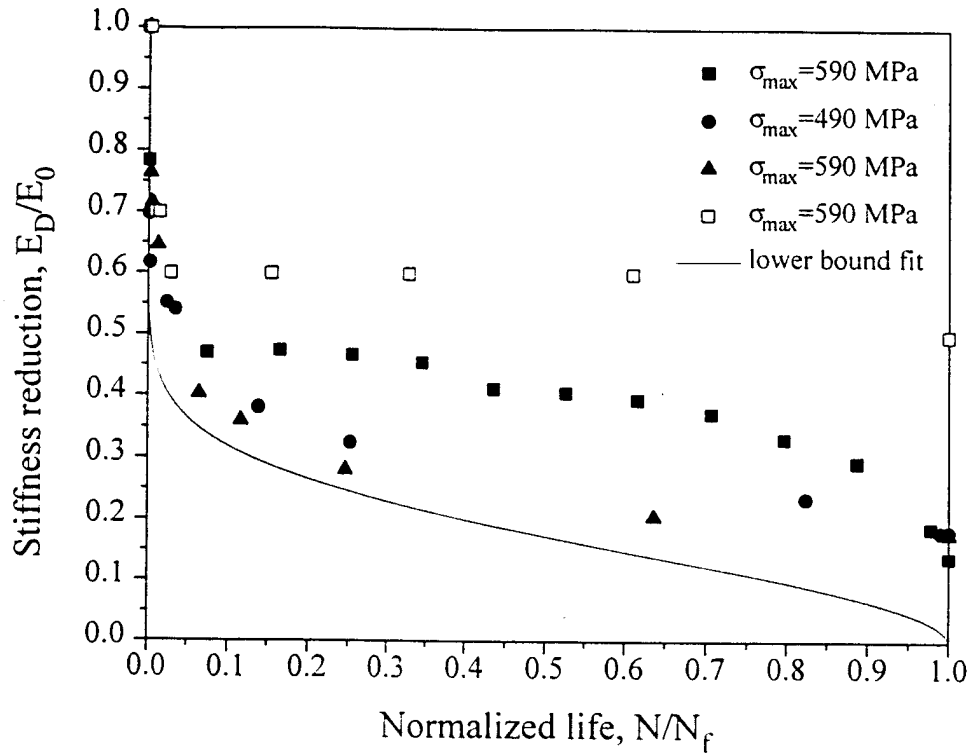


FIG. 1 -- Different stiffness loss versus number of cycle for similar maximum applied cyclic stress

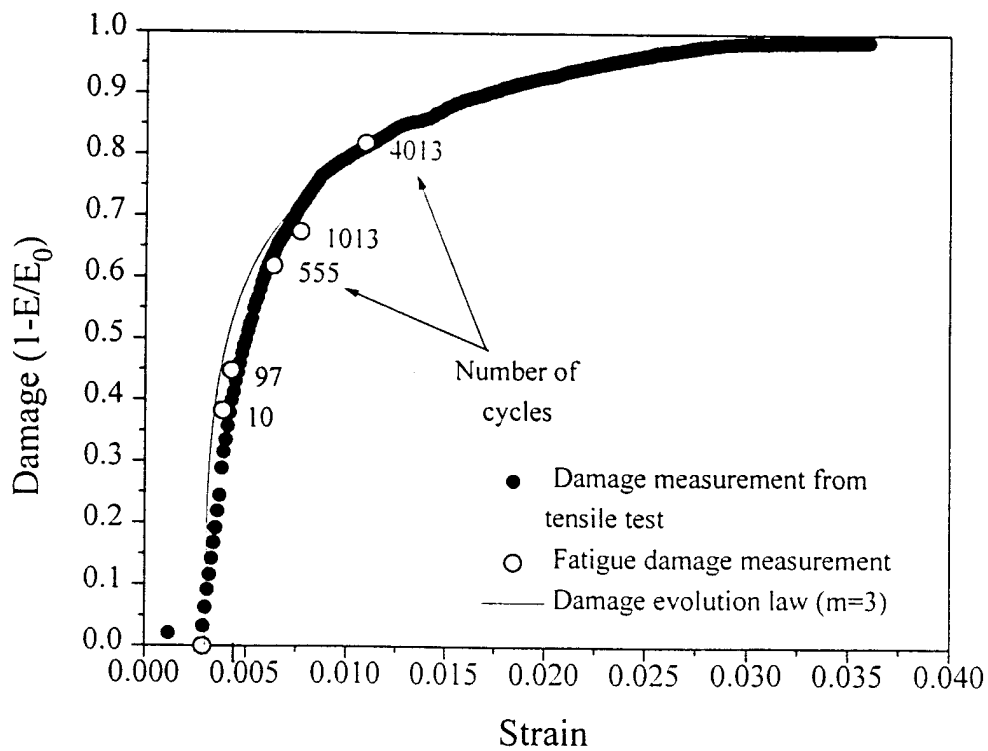


FIG. 2 -- Comparison between static and fatigue damage and proposed law.

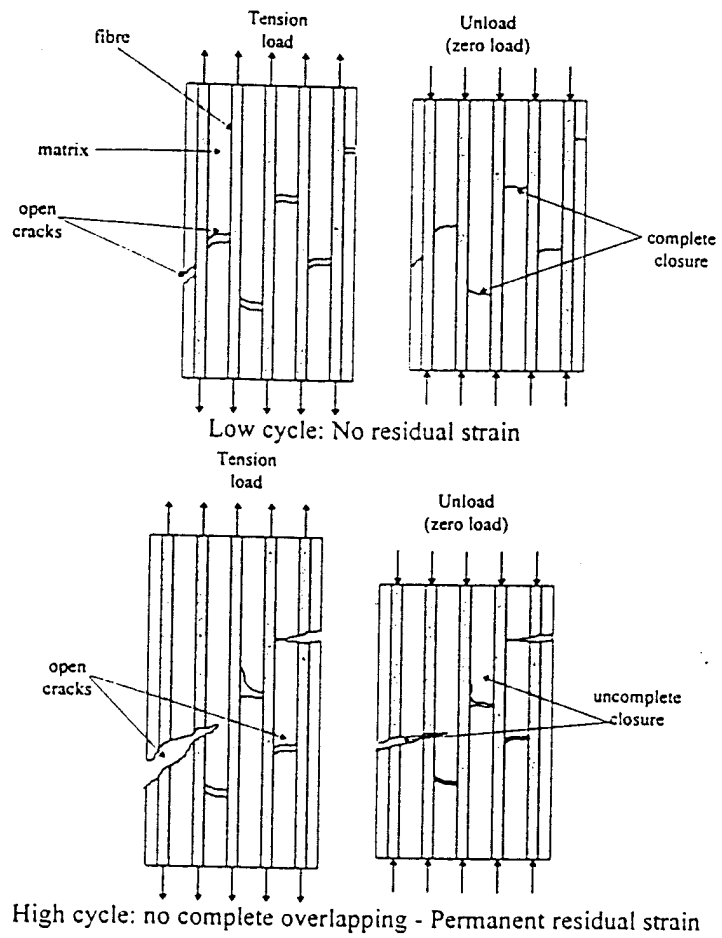


FIG. 3 -- Scheme of residual strain, due to damage, accumulation process under fatigue loading.

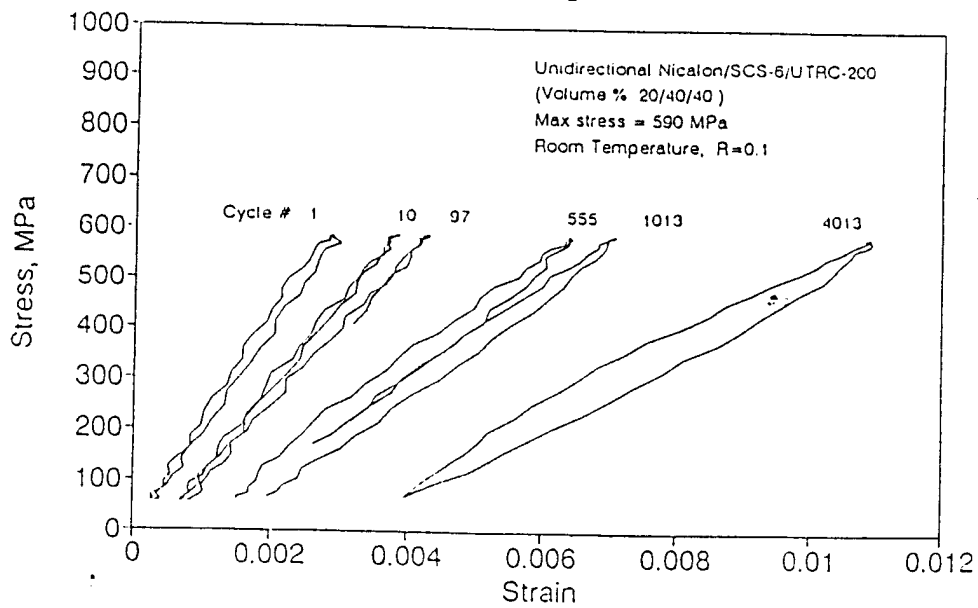


FIG. 4 -- Stress-strain material data curves during cycling.

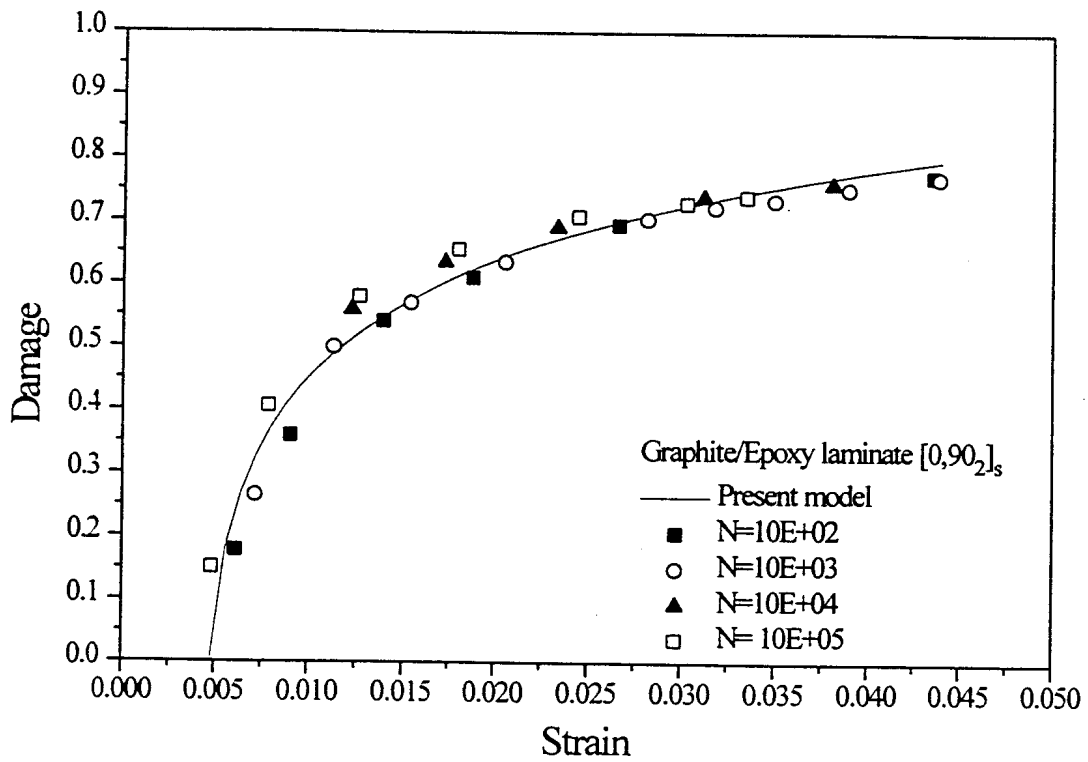


Fig. 5 - Damage in Graphite/Epoxy  $[0,90_2]_s$  laminate under fatigue loading: comparison between experimental data and the present model, (data from Charewicz and Daniel, 1986)

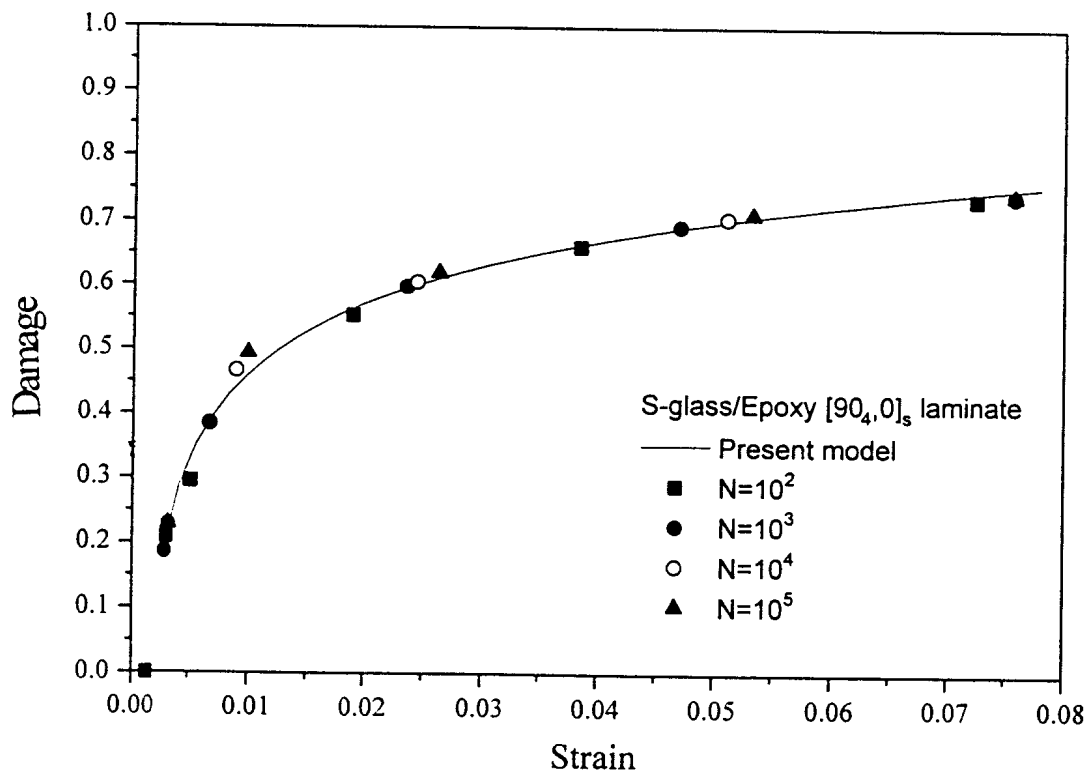


Fig. 6 - Damage in S-Glass/Epoxy  $[90_4,0]_s$  laminate under fatigue loading: comparison between experimental data and the present model, (data from Bonora et al., 1992).

# FATIGUE DAMAGE IN NICALON SiC(f)/AL COMPOSITE WIRES

Yue Zhuo, Hong Wan, Jin Pan and Deming Yang

*State Key Laboratory for Fatigue and Fracture of Materials  
Department. of Materials Engineering and Applied Chemistry  
National University of Defense Technology  
Changsha, Hunan, 410073, China .*

**SUMMARY:** To understand the fatigue damage mechanism in Nicalon SiC(f)/Al composite, the wires of SiC(f)/Al were fabricated by ultrasonic liquid infiltration method. Tensile -- tensile fatigue test on the composite wires was carried out at stress ratio  $R=0.1$  at room temperature and at 573 K . Tests show that the dominant damage model in the wire is progressive fiber fracture and the progressive fiber fracture is due to the deorientation of fiber to the stress axis. Test at 573 K shows no evident differences in the fatigue property between room temperature and 573 K . The wires after exposure at 873 K for 30 minutes, through the interface bonding force has been increased by interface reaction, are of lower fatigue property than those unexposed.

**KEY WORDS:** metal-matrix composite, silicon carbide fiber, fatigue damage

## INTRODUCTION

Despite its evident importance in numerous engineering application, few published investigation exist on the fatigue properties and damage of SiC multifilaments reinforced Aluminum composite. The specimens used in this paper are composite wires with the fibers uniaxially oriented in the loading direction. Its fatigue failure mode is different from the fatigue crack growth mode in short fibers reinforced aluminum composite[1]. The fatigue failure mode in continuous fiber reinforced metal matrix composites (MMC) is controlled by the following three constituents of the system: fiber, matrix, and fiber/matrix interface. W.S.Jonson basing on the relative strain to fatigue failure grouped possible failure modes of MMC into three categories[2]--- matrix dominated, fiber dominated and self-similar damage growth. The purpose of this paper is to find the failure mode and damage process in this composite wires. The experiment results also provide a method to improve the fatigue properties of SiC fiber/Al composite.

## EXPERIMENTAL MATERIALS & METHODS

The composite wire used here is reinforced by a bind of 500 Nicalon SiC fibers produced by NIPPON Carbon Co. Ltd. The matrix is industrial pure Al 1100 infiltrated by ultrasonic liquid infiltration method. Total wire length of a batch is 200 to 500 meters and the fibers are oriented in the length direction. Specimen cut from the same batch of wire are 50 mm and have the same mechanical properties. The main properties of the fiber and composite wire are listed in table 1. Tension-tension fatigue tests were conducted in load control on a  $1 \times 10^3$ N

EHF FB01-4LA material test machine with a stress ratio  $R=0.1$ . A sinusoidal waveform with a frequency of 20 Hz was used. The fatigue fractograph is observed by a S-360 scanning electron microscope.

Table 1: The main properties of the fiber and composite wire

materials	diameter	density ( $\text{g/cm}^3$ )	UTS (MPa)	E (GPa)	$V_f$ %
$\text{SiC}_f$	10-15 $\mu\text{m}$	2.55	2500-3000	180-200	-
wire	0.52 mm	2.60	1100-1200	110-120	40-45

Load/elongation curve was detected by a punctuation extensometer and recorded by means of an X-Y recorder. If the specimens fractured near the grips its date would not be count in. Specimens tested at 573 K were heated by a tube stove and the gips were not in the stove.

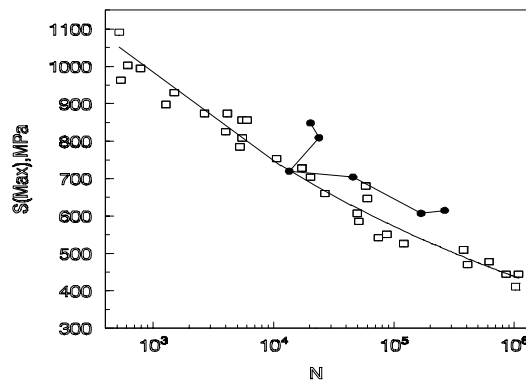


Fig. 1: S-N curve of NICALON  $\text{SiC}_f/\text{Al}$  composite wire

□ ---- at room temperature  
• ---- at 573 K

## RESULTS AND DISCUSSION

Figure 1 is the S--N curve of the composite wires. From the curve it can be known that the fatigue stress to failure is decreased quickly with the increase of cycle numbers. When the cycle index is  $10^6$  its fatigue strength is 440 MPa, less than one half of its static tensile strength. For fibers in the wire is ceramic material and its fatigue stress to failure generally has no relationship with the numbers of stress cycle. The fatigue strength of the Al matrix is more than 90% of its static tension stress while the fatigue cycle number is  $10^6$  [3]. Why does the fatigue stress of the composite wire decrease so rapidly?

To find the reason, a fatigue test at 573 K was taken on the wires. At this temperature the mechanical properties of fiber can not be influenced, but the properties of Al matrix can be changed. Test result is shown in fig. 1. The composite wire at 573 K is of the same fatigue property with its room temperature. Treated the wire at 873 K for 30 min. than test its fatigue property at  $S_{\text{max}}=700$  MPa at room temperature. The cycle index to failue is  $5 \times 10^2$ — $5 \times 10^3$  and much lower than that of untreated specimen. Nicalon  $\text{SiC}$  fibers can react with Al at 873--913 K and form  $\text{Al}_2\text{O}_3$  and  $\text{Al}_4\text{C}_3$ . This interface reaction can increase the bonding force between fibers and matrix and can decrease the mechanical properties of the fibers in the

specimens. So the fatigue damage in this composite wire must be mainly dominated by the fibers.

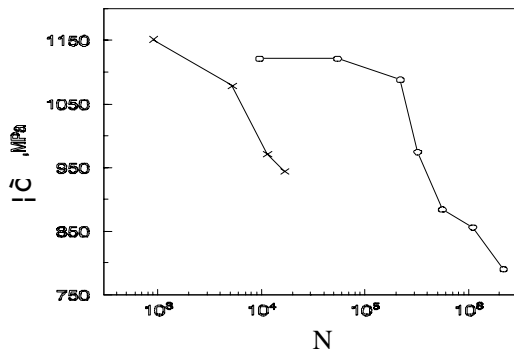


Fig. 2: The relation of static tensile strength with fatigue cycle number  
*x* ---  $S_{max}=700$  MPa      *o* ---  $S_{max}=450$  MPa



Fig. 3: The photomicrograph of the composite wire  $\times 100$

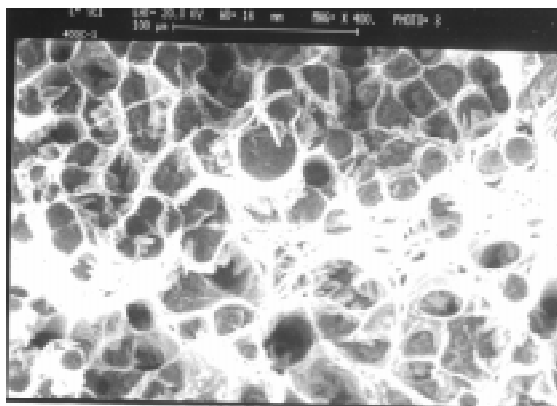


Fig 4: The SEM fatigue fractograph of the composite wire

To find the fatigue damage process in the wire, a specimen after 10<sup>6</sup> cycles on  $S_{max}=450$  MPa and a specimen fractured by static tensile test have been extracted by NaOH solution. The two specimens are of the same length (50 mm) before extracted. The fiber in the fatigue specimen become short about 5 mm, but the fiber in static test specimen is about 50 mm same with the length of fibers in untested specimen. To confirm this fiber fracture process during fatigue test, several specimens stressed on  $S_{max}=700$ MPa and  $S_{max}=450$ MPa were tested to different cycle

numbers and then tested their static tensile strength. The relation between cycle numbers and static tensile strength are shown in Fig. 2. The tensile strength is decline with the increase of fatigue cycle index. So the fibers fracture must be progressive as the fatigue test going. This fiber length after fatigue test at certain conditions can also give us some information about the bonding force between fiber and matrix.

What made the fibers in fatigue specimen fractured one by one? For the composite wire was fabricated by ultrasonic liquid infiltration method and exists the deorientation in the length direction, as shown in photomicrograph (Fig. 3). The deorientation resulted in the stress difference among the fibers during fatigue test. The Al matrix displayed a good special fatigue ductility and cooperated with the rotation of fibers while one fiber of hard orientation fractured after another. A SEM fatigue fractograph as Fig. 4 shows that the Al matrix in a specimen after  $10^6$  cycles is still appeared as a ductility fractograph characteristic. Electric conductivity of the fatigue specimen before and after fatigue test is unchanged too. The specimen elongation during the fatigue process was detected and the result is shown on Fig. 5. This specimen elongation may be caused by improving its fiber deorientation and that is the reason of the fiber fractured one by one.

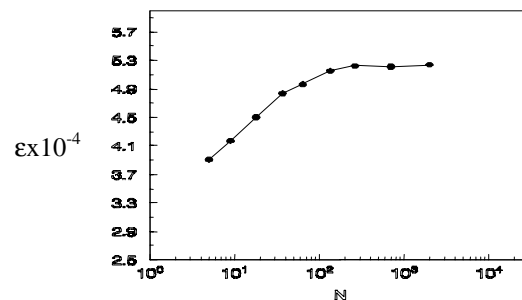


Fig. 5: The specimen elongation during the fatigue test

## CONCLUSION

1. The progressive fiber fracture is the dominant damage model in this composite wire.
2. The deorientation of the fibers to the stress axis resulted in the fibers fracture one by one and this fatigue process is with the cooperation of matrix fatigue ductility.

## ACKNOWLEDGMENTS

The authors would like to thank to Professor Wang Zhong Guang and Mr. Gong Wen Ku , Yao Ge for useful discussions and assistance with the fatigue test.

## REFERENCES

1. Xi Cong Liu and C. Bathias, "Fatigue damage development in Al<sub>2</sub>O<sub>3</sub>/Al composite", Composites, Vol.24, No. 3(1993)pp282-287
2. W.S.Johnson, "Fatigue damage accumulation in various metal matrix composites", NASA Technical Memorandum 89116, N87-18416, 1987
3. G.J.Dvorak and W.S.Johnson, International Journal of Fracture 16(1980)585-607



# THE MODE-I FRACTURE TOUGHNESS OF IM7/LARC-RP46 COMPOSITES AT HIGH TEMPERATURES

W.X. Wang<sup>1</sup>, F. G. Yuan<sup>2</sup>, B. D. Potter<sup>2</sup>,  
R. H. Pater<sup>3</sup> and Y. Takao<sup>1</sup>

<sup>1</sup> *Research Institute for Applied Mechanics,  
Kyushu University, Kasuga, Fukuoka 816, Japan*

<sup>2</sup> *Department of Mechanical and Aerospace Engineering,  
North Carolina State University, Raleigh, NC 27695, USA*

<sup>3</sup> *NASA Langley Research Center, Hampton, VA 23681, USA*

**ABSTRACT:** In this paper, DCB (double cantilever beam) static fracture tests were conducted to investigate Mode-I fracture toughness of an IM7/LaRC-RP46 composite at three high temperature levels with five different loading rates. Two types of crack growth behavior, slow crack extension and relatively fast crack propagation, were observed and the slow crack extension caused the nonlinear response of the load-displacement relation. The initial values of fracture toughness,  $G_{IC}$ , decreased slightly than that obtained at room temperature, while the propagation values increased by nearly 30% to 100%. The materials exhibited the highest fracture toughness at 288°C among the three different tested temperatures. The fracture toughness decreased drastically when tested beyond  $T_g$ . No significant effects of loading rates on the  $G_{IC}$  were observed in the range of the loading rates. However, the loading rates significantly influenced the crack growth rates.

**KEYWORDS:** fracture toughness, high temperature, mode I, energy release rate, viscoelasticity and viscoplasticity, loading rate, crack growth rate

## 1. INTRODUCTION

It is well recognized that use of two different constituents in a material often leads to a more efficient structure. With the increasing demand for high performance and efficiency of various vehicles under various environments, the use of high-temperature polymer composite materials have attracted much attention. The structural components of an aircraft that experience high Mach numbers in normal flight profile may be subjected to cyclic thermal and mechanical loads. High speed and high efficiency aircrafts require high-temperature capability of the composites and accurate life prediction of these materials. Therefore, determination of the interlaminar fracture behavior of polymer laminated composites under various high temperature becomes crucial. Russell and Street [1] investigated the effects of temperature on the fracture toughness of AS1/3501-6 composites and found that the propagation values of  $G_{IC}$  increased by nearly 50% as the temperature was raised from -50°C to 100°C. T300/934 composites were tested by Garg and Ishai [2] and a 20% increase of  $G_{IC}$  was observed for a temperature rise of 100°C. Similar trend was also noticed for T300/914 by Davies and de Charentenary [3]. Relatively large increase, up to 80%, of  $G_{IC}$  values was also observed by Heshemi et al. [4] for carbon/PEEK composites when temperature was raised from 20°C to 120°C. Only few researches (e.g., [5,6]), to the authors' knowledge, have involved the time-dependent fracture behavior, such as the effects of temperature and loading rate on the crack growth characteristics

in polymer composites. Devitt et al. [5] investigated the delamination fracture toughness of E-glass/epoxy under a wide range of loading rates (0.25-250 mm/min.) at room temperature. The time-dependent characteristics of the fracture behavior was examined and the relation between the Mode-I energy release rate and the crack growth rate was found to be a power-law type. Gillespie et al. [6] also investigated the effects of loading rates on the Mode-I fracture toughness of graphite/epoxy and graphite/PEEK composites at room temperature. The inelastic and viscoelastic effects in the process zone around the crack tip on the fracture behavior was noted. However, study focuses on the combined effects of temperatures and loading rates on the fracture behavior remains to be quantitatively established. Therefore, further research is necessary to understand the fracture behavior of polymer composites under high temperatures with different loading rates, especially the time-dependent fracture characteristics of high-temperature polymer composites.

A material, LaRC-RP46, is a low toxicity PMR type high-temperature polyimide resin developed at the NASA Langley Research Center [7,8]. It is designed to be used at high temperatures up to 300°C which is much higher than the operating temperature of conventional polymer matrices. The material also provides the same or improved characteristics of the high temperature PMR-15 resin, such as low raw material costs, superior processability, excellent processing reproducibility, and high temperature endurance. In this paper, the DCB tests were performed to investigate the interlaminar Mode-I fracture behavior of IM7/LaRC-RP46 laminated composites under high temperatures below and beyond  $T_g$  ( $\approx 310^\circ\text{C}$ ) [7]. Special attention was concentrated on the effects of temperature and loading rate on the Mode I energy release rate  $G_{IC}$  and crack growth rate  $da/dt$  due to the viscoelastic and viscoplastic behavior of the matrix at high temperatures [9].

## 2. EXPERIMENTAL

### 2.1 Materials and Specimens

The high temperature polymer composite material IM7/LaRC-RP46 [7,8] was investigated. The fiber volume fraction  $V_f$  is approximately 62%. The mechanical properties of unidirectional laminates are shown in Table 1 [10]. Unidirectional  $[0]_{24}$  panels of 152 mm by 152 mm (6 in. by 6 in.) were manufactured in a Wabash hot press by the use of prepreg sheets provided by the NASA Langley Research Center. The dry molding cure cycle recommended by the NASA Langley Research Center [8] is employed in the processing of the laminated panels. Prepreg sheets were oven B-staged at 204°C for one hour before the curing process. A 0.008 mm thick Kapton film was inserted between the plies at the mid-plane of the panel to make a pre-crack of length 50.8 mm (2 inches). The thickness of panels is 3 mm (0.12 inches).

Table 1: Mechanical properties of IM7/LaRC-RP46 Composite

Longitudinal modulus, $E_{11}$	155.8 GPa
Transverse modulus, $E_{22}$	8.8 GPa
Shear modulus, $G_{12}$	5.1 GPa
Poisson's ratio, $\nu_{12}; \nu_{21}$	0.34; 0.022

Specimens made from the panels were straight-sided, approximately 25.4 mm wide, 150 mm long and 3 mm thick. Steel hinges were used to transfer the external load into specimens. Wet prepreps of IM7/LaRC-RP46 acting as adhesive films together with small screws were used to bond the tab of steel hinges to the surfaces of specimens in order to ensure full load transfer at high temperatures. After hinges were mounted, the specimens with bonded hinges were subjected to one hour post cure at 260°C to ensure the adhesive strength between the hinges and surfaces of the specimens. In order to make a sharp and natural crack tip, initial crack extension of nearly 4 mm length was made for each specimen at room temperature. The crack length was measured from the center of the hinge pivot pin to the crack tip. Specimen edges were painted white and scaled to make an easy observation of crack growth.

## 2.2 Testing Procedures

Tests were performed on an Instron 8500 hydraulic machine and an Instron 3119 high temperature environmental chamber under three temperature levels of 232°C, 288°C and 343°C. Five specimens with the same initial crack length were tested at each temperature level by applying five different loading rates of 0.51 mm/min. (0.00033 in./sec), 1.52 mm/min. (0.001 in./sec), 3.05 mm/min. (0.002 in./sec), 4.57 mm/min. (0.003 in./sec) and 6.10 mm/min. (0.004 in./sec) to each specimen. This loading rate range (0.51-6.10 mm/min.) is close to the range (1-5 mm/min.) normally used in static DCB tests [11]. Specimens were kept in the chamber for one hour warming-up period at the testing temperature before loading starts. Then the specimens were subjected to a gradually increasing load until a crack extension,  $da$ , occurred. After the crack was extended by a  $da$  length the specimens were unloaded by applying the same crosshead rate as the loading process until the load approached zero. Prior to the next loading and unloading processes, a waiting period of about 15 minutes was taken to minimize the residual effects of stresses and strains due to viscoelasticity. The load-displacement response, as shown in Fig. 3, was recorded by means of a personal computer. The crack growth length was measured by reading the scales drawn on the edge of specimens. The crack growth time was obtained by observing the crack tip and reading the time shown on the display of the testing machine together with the load-time response curves recorded by the computer. A rapid unloading was employed to simplify the visual determination of the crack growth ending time from the load-time curves. It should be pointed out that the loading and unloading processes are basically similar to the testing process used in the area method [11]. However, the purpose of employing this process in the present testings is mainly to accurately determine the crack growth time  $\Delta t$  and crack growth length  $da$ , hence the crack growth rate.

## 2.3 Data Reduction

Conventional data reduction methods to determine the Mode-I energy release rate,  $G_{IC}$ , for DCB specimens are the compliance method and the area method [11]. The compliance method is based on the traditional beam theory and provides a conservative estimation of the fracture toughness. The area method is based on the determination of area, which represents the work done by the external load during crack extension by a  $da$ , enclosed within the loading and unloading load-displacement curves. It requires that the work done by the external load should be contributed entirely to the crack growth. In the present testings, the composites, especially the matrix phase, was observed to undergo relatively large viscoelastic and viscoplastic deformations except for crack growth. Hence, an equation resulted from compliance method [11] was employed to evaluate the Mode-I energy release rate  $G_{IC}$ .

$$G_{IC} = \frac{12P_c^2 a^2}{E_{11} B^2 h^3} \quad (1)$$

where  $P_c$  is the critical load for crack growth,  $a$  is the crack length,  $E_{11}$  is the tensile modulus in the fiber direction,  $B$  is the width of the specimen and  $h$  is the half-thickness of the specimen. A comparison between eq. (1) and a modified formula [12] by including end rotation and transverse shear effects into the  $G_{IC}$  has been made for the  $G_{IC}$  of IM7/LaRC-RP46 at room temperature [13]. The difference between the results deduced from these two formulas was found to be within 3%. Then, for a first order approximation, it seems to be appropriate to utilize the simple eq. (1) to give a relatively conservative  $G_{IC}$ .

## 3. EXPERIMENTAL RESULTS AND DISCUSSIONS

### 3.1 Load-Displacement Curves

A typical load-displacement at high temperature is shown in Fig. 1(a). All the cases at three temperature levels with five loading rates have the similar load-displacement curves, thereby only the case at 288°C and 1.52 mm/min. being presented in the figure. For comparison, the load-displacement response curve of IM7/LaRC-RP46 at room temperature (20°C) [13] is shown in Fig. 3(b). No waiting period was taken in the case at room temperature. The  $a_i$  ( $a_i = a_1, a_2, \dots, a_8$ ) represent different crack lengths.

Comparing Figs. 1(a) with 1(b), three salient characteristics at high temperature tests can be identified. Firstly, the loading portion of the load-displacement response curve related to the crack length  $a_1$  appears to be nonlinear from a relatively low load (about 64 N), while the corresponding curve at room temperature shown in Fig. 1(b) behaves linearly up to the maximum load where crack propagation occurs. The deviation from linearity reveals that the precrack initiated at room temperature begins to grow at relatively low loads due to the viscoelastic and viscoplastic deformation of the matrix near the sharp crack tip. Once the crack is extended at high temperatures, the crack tip is expected to experience blunting. From the loading curves related to crack length  $a_i$  ( $a_i > a_1$ ), it also can be seen that the deviation between the load at the onset of crack growth and the peak load decreases after a blunt crack tip is formed at high temperatures. Secondly, as shown in Fig. 1(a), the crack growth processes consist of two steps, that is, the subcritical crack growth and crack propagation at high temperatures. The crack grows slowly as the load increases from the load at the onset of crack growth to the peak value due to the viscoelastic and viscoplastic response of the matrix during the subcritical crack growth. As the plastic deformation and damage accumulation in the vicinity of the crack tip reach the critical state, the critical crack propagation occurs and a reduction in load can be observed. This crack growth behavior was also observed in graphite/PEEK composites under higher loading rates at room temperature [6]. Lastly, relatively large hysteresis loops prevailed in the load-displacement response although a waiting period of 15 minutes was taken to minimize the hysteretic effects arisen from the viscous feature of the matrix at high temperatures.

### 3.2 Energy Release Rates and Crack Growth Rates

Figures 2(a-c) present crack growth resistance curves (R-curves) described by the interlaminar Mode-I energy release rate  $G_{IC}$  as the function of crack growth length. It is seen that  $G_{IC}$  increases as the crack grows at all high temperature levels and loading rates. These R-curves are similar to the ones at room temperature [13] except that the increasing range between the initial value and the steady propagation value of  $G_{IC}$  becomes larger than that in the case at room temperature. The value of  $G_{IC}$  at the crack length = 80 mm is considered to be the steady propagation value of  $G_{IC}$  in the present testings. It is also clear that  $G_{IC}$  varies with temperatures. Especially, the steady propagation value of  $G_{IC}$  is sensitive to temperatures. However, the effects of loading rates on  $G_{IC}$  are not evident and no distinct trend can be quantified in the present loading rate range. It is understood that the scatter ranges of  $G_{IC}$  due to different loading rates are nearly the same order as the scatter ranges due to different specimens. In the present tests, the scatter ranges of  $G_{IC}$  from different specimens are found to be within  $\pm 5\%$  of the averaged value for the primary crack growth (roughly the primary 10 mm extension) and  $\pm 10$  to  $\pm 20\%$  of the averaged value for the continuing crack growth, which is roughly consistent with the occurrence and development of the fiber bridging observed in the testings. Hence, the fiber bridging is considered to be one of the major reasons which cause relatively large scatter ranges of  $G_{IC}$  during the later crack propagation. Besides the above characteristics of R-curves, a different trend of the R-curve in the case at 343°C together with 0.51 mm/min. loading rate is observed in Fig. 2(c), that is, the last two white circles seems to suddenly drop. This trend may be attributed to the physical aging effects of duration of 4 to 5 hours at 343°C.

In order to understand the effects of high temperatures on  $G_{IC}$ , the averaged energy release rates over the five loading rates are presented in Figs. 3 and 4 together with the results at room temperature [13]. The R-curves of averaged  $G_{IC}$  are shown in Fig. 3. It is seen that the steady propagation value of  $G_{IC}$  is significantly influenced by temperatures while the initial value of

$G_{IC}$  varies slightly. The crack growth behavior can be seen more clearly in Fig. 4 where the initial and propagation values of  $G_{IC}$ ,  $G_{IC-init}$  and  $G_{IC-prop}$ , are presented against the temperature. It can be seen that the propagation value of  $G_{IC}$  increases with increasing temperature, reaches its maximum value near  $T_g$  and then decreases when the temperature exceeds  $T_g$ . On the other hand, the initial value of  $G_{IC}$  shows slight reduction before  $T_g$  and relatively large reduction beyond  $T_g$ . The fracture behavior below  $T_g$  is similar to the previous results observed from conventional composites at elevated temperatures[1-4].

The effects of loading rates and temperatures on the crack growth rates are presented in Figs. 5(a-c). Figs. 5(a-c) describe the variation of crack growth rate  $da/dt$  with energy release rate  $G_{IC}$  at different loading rates and temperatures. It is clear from these figures that the crack growth rate is influenced significantly by loading rates and temperatures. Firstly, it is seen that the crack growth rate decreases with crack growth, that is, along the direction of  $G_{IC}$  increasing, except for the case of 343°C with 0.51 mm/min. loading rate. The fiber bridging may be considered to be one of the major attributes which cause the decrease of the crack growth rate. In the case of 343°C with 0.51 mm/min. loading rate, as previously described, the different behavior may be caused by the effects of physical aging. A further research is necessary to understand the effects of physical aging on the fracture toughness. Secondly, comparing these three figures, it can be found that the crack growth rate decreases with elevated temperatures. It is understood that this phenomenon may reveal the effects of the viscoelasticity and viscoplasticity which are sensitive to temperatures. Finally, it is also obvious that the crack growth rate is very sensitive to the loading rates. In general, it is easily anticipated that higher loading rates result in faster crack opening and thereby the higher crack growth rates. This direct effect of loading rates on the crack growth rate is called a proportional effect in the present paper. Besides this, the crack growth rate may also be influenced by loading rates because of the time and temperature dependent nature of the materials, especially the viscoelasticity and viscoplasticity of the matrix. Hence, it is difficult to distinguish these effects from Figs. 5(a-c).

#### 4 Concluding Remarks

DCB tests were conducted to investigate the interlaminar Mode-I fracture behavior of IM7/LaRC-RP46 composite materials at high temperatures. Specimens were tested at three high temperature levels of 232°C, 288°C (below  $T_g$ ) and 343°C (beyond  $T_g$ ) by applying five different loading rates from 0.51 mm/min. to 6.1 mm/min. Effects of temperatures and loading rates on the energy release rate  $G_{IC}$  and crack growth rate  $da/dt$  were investigated. The following conclusions are obtained.

1. The crack growth in IM7/LaRC at high temperatures is found to consist of two distinct types, that is, slowly subcritical crack growth and relatively fast crack propagation. The former causes the nonlinear load-displacement response.
2. The energy release rate  $G_{IC}$  varies with temperatures. Two parameters, that is, the initial value  $G_{IC-init}$  and the steady propagation value  $G_{IC-prop}$  of  $G_{IC}$  seems to be necessary to characterize variation of the Mode-I fracture toughness with temperatures. The  $G_{IC-init}$  decreases slightly with elevated temperatures, while the  $G_{IC-prop}$  increases by nearly 30% to 100%. Furthermore, the  $G_{IC-prop}$  firstly increases with elevated temperature and reaches its maximum value near  $T_g$  and then decreases drastically when the temperature exceeds  $T_g$ . On the other hand the effects of loading rates on  $G_{IC}$  is not evident and no distinct trend can be obtained in the present loading rate range.
3. The significant effects of temperatures and loading rates on the crack growth rate are also quantified. High temperatures cause low crack growth rates, while high loading rates cause high crack growth rates. However, it is difficult to distinguish the effects of loading rates mainly due to the time-dependent nature of the viscoelasticity and viscoplasticity. Further researches by applying higher loading rates seem to be necessary.
4. The physical aging effects of temperatures on the energy release rate and the crack growth rate were observed from the results at 343°C together with 0.51 mm/min. loading rate. Hence, physical aging effects should be considered in the use of IM7/LaRC-RP46 at high temperatures, especially at the temperature beyond  $T_g$ .

## ACKNOWLEDGMENT

This research is partly supported by the Ministry of Education, Japan under the Grant-in-Aid for Scientific Research (B) [No. 06452347]. Dr. Yuan would like to acknowledge the support from U.S. Air Force Scientific Research under Grant F49620-95-1-0256.

## REFERENCES

1. Russel, A.J. and Street, K.N., 1985, "Moisture and Temperature Effects on the Mixed-Mode Delamination Fracture of Unidirectional Graphite/Epoxy Delamination and Debonding of Materials," *ASTM STP* 876, p. 349.
2. Garg, A. and Ishai, O., 1987, *Eng. Fract. Mech.*, 22, p. 413.
3. Davies, P. and de Charentenay, F.X., 1987, *Proc. 6th Int. Conf. on Composite Materials/2nd Eur. Conf. on Composite Materials*, Vol.3, p. 284.
4. Hashemi, S., Kinloch, A.J. and Williams, J.G., 1990, "The Effects of Geometry, Rate and Temperature on the Mode I, Mode I and Mixed-Mode *II* Interlaminar Fracture of Carbon-Fiber/Poly(ether-ether ketone) Composites," *J. Composite Materials*, 24, pp. 918-939.
5. Davitt, D.F., Schapery, R.A. and Bradley, W.L., 1980, "A Method for Determining the Mode I Delamination Fracture Toughness of Elastic and Viscoelastic Composite Materials," *J. Composite Materials*, 14, pp. 270-285.
6. Gillespie Jr, J.W., Carlsson, L.A. and Smiley, A.J., 1987, "Rate-Dependent Mode I Interlaminar Crack Growth Mechanisms in Graphite/Epoxy and Graphite/PEEK," *Composites Science and Technology*, 28, pp. 1-15.
7. Pater, R.H., 1991, "The 316°C and 371°C Composite Properties of an Improved PMR Polyimide: LaRC-RP46," *36th Int. SAMPE Symposium and Exhibition*, San Diego, CA, p. 78.
8. Hou, T.H., Wilkinson, S.P., Johnston, N.J., Pater, R.H. and Schneider, T.L., 1994, "Processing and Properties of IM7/LARC-RP46 Polyimide Composites," *39th Int. SAMPE Symposium and Exhibition*, Anaheim, California, p. 1.
9. Yuan, F.G. and Potter, B.D., 1994, "Prediction of Long-Term Transverse Creep Compliance in High-Temperature IM7/LaRC-RP46 Composites," *Proc. of Ninth Technical Conference of the American Society for Composites*, pp. 275-282.
10. Pater, R. H., 1996, *Private communication*.
11. Davies, P. and Benzeggagh, M.L., 1989, "Interlaminar Mode I Fracture Testing," in *Application of Fracture Mechanics to Composite Materials*, K.Friedrich, ed., Elsevier Science, p. 81.
12. Williams, J.G., 1989, "End Corrections for Orthotropic DCB Specimens," *Composite Science and Technology*, 35, pp. 367-376.
13. Wang, W.X., Yuan, F.G., R. H. Pater and Y. Takao, 1996, "Interlaminar Mode I Fracture Toughness of High Temperature Composite Materials IM7/LaRC-RP46", *Proc. of The Annual Meeting of The Western Branch, The Japan Society for Aeronautical and Space Sciences*, pp. 83-86.

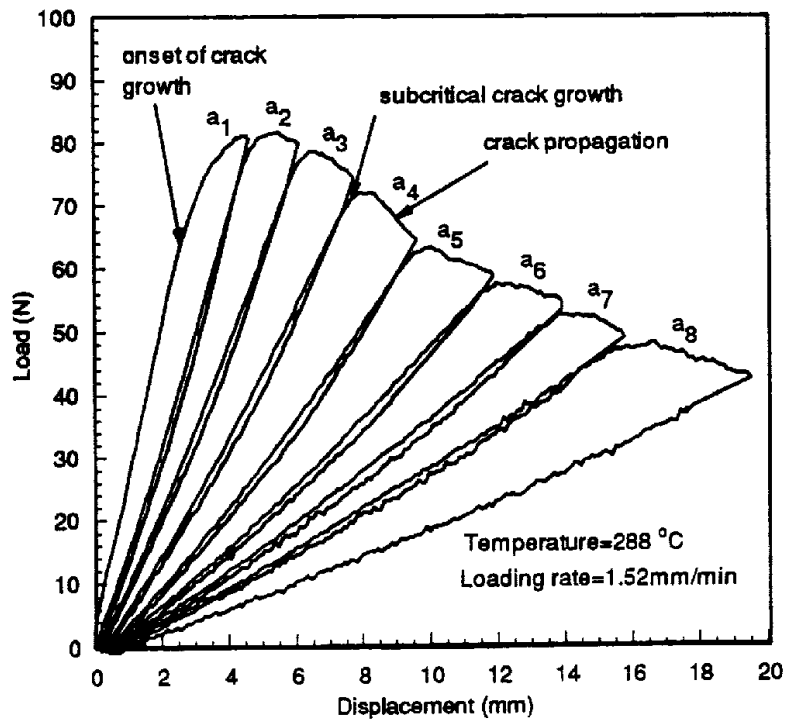


Fig. 1a Typical load-displacement response at high temperature

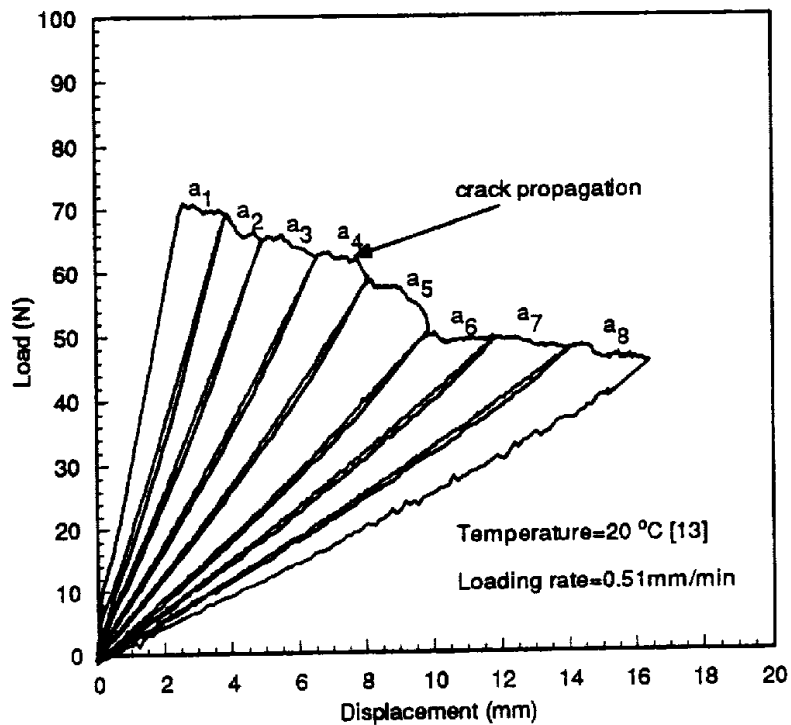
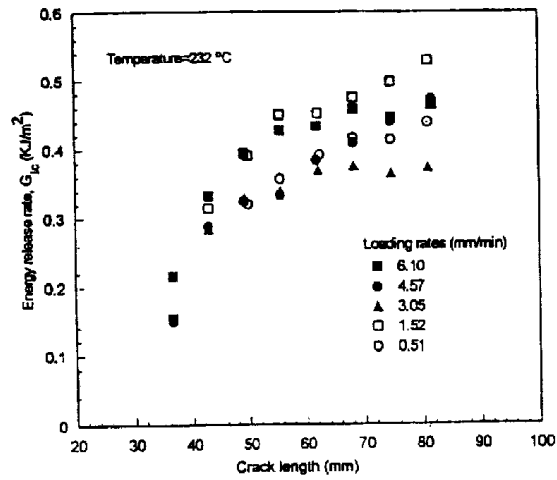
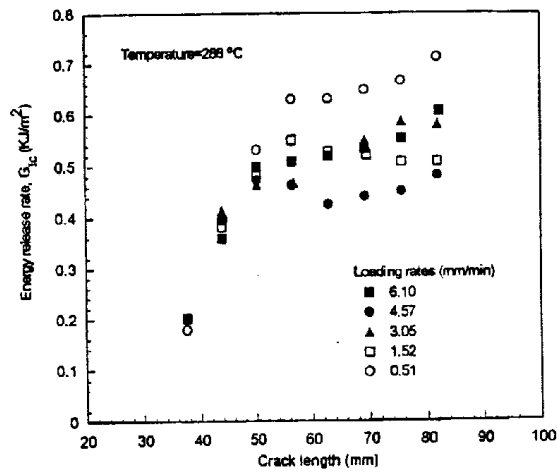


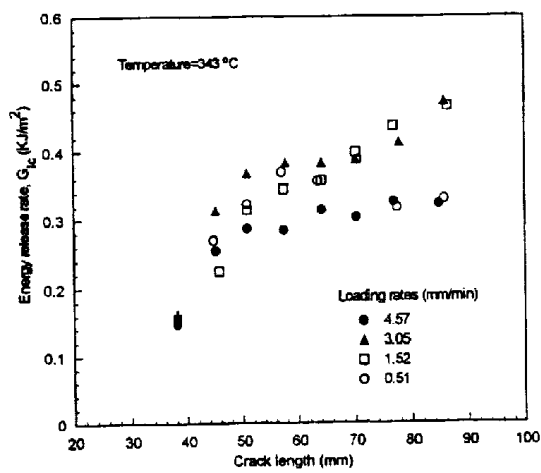
Fig. 1b Typical load-displacement response at room temperature



(a)



(b)



(c)

Fig. 2 Energy release rate versus crack length at (a) 232°C, (b) 288°C, (c) 343°C.



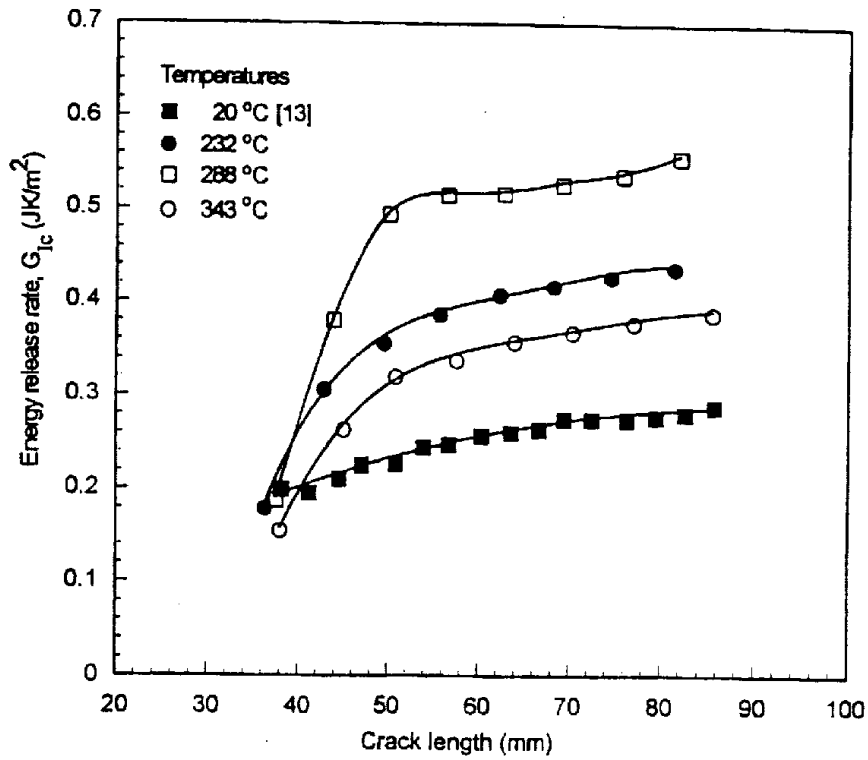


Fig. 3 Averaged energy release rate versus crack length at various temperatures

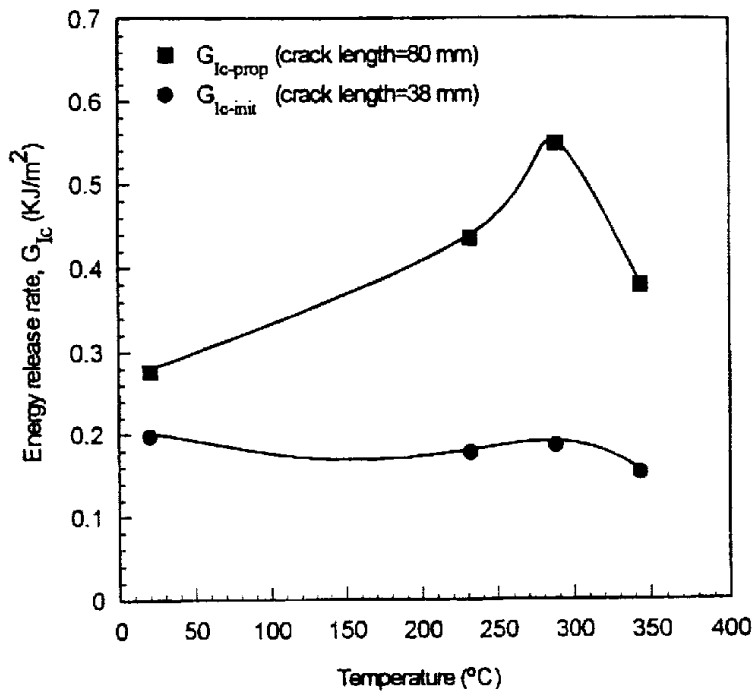
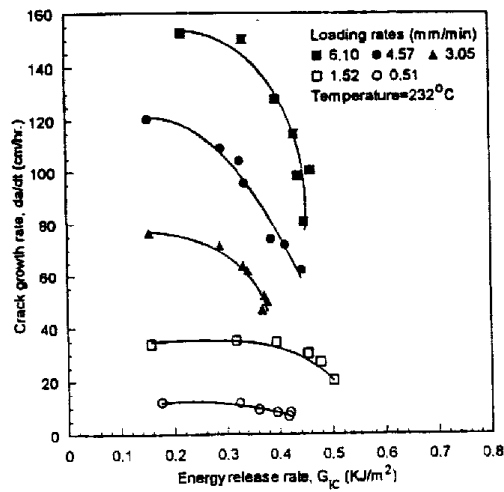
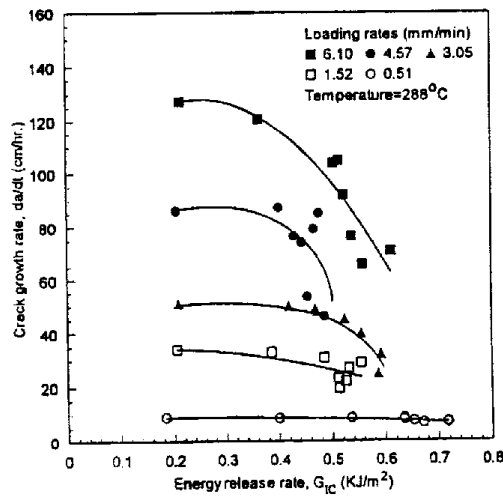


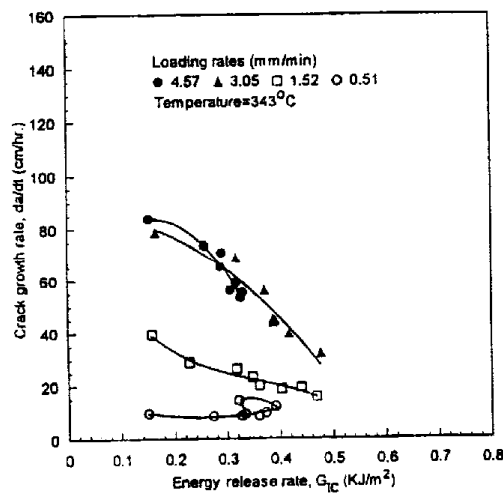
Fig. 4 Effects of temperature on the initial and propagation values of averaged energy release rate



(a)



(b)



(c)

Fig. 5 Effects of loading rates on the crack growth rate at (a) 232°C, (b) 288°C, (c) 343°C

# INTRALAMINAR FRACTURE BEHAVIOUR AND MICROSTRUCTURAL CHARACTERISTICS OF UNIDIRECTIONAL T300/914

Adrian Lowe and Shankar Kalyanasundaram

*Department of Engineering, Australian National University, Australia*

## SUMMARY

The Iosipescu shear test method has been used to determine the intralaminar shear properties of unidirectional T300/914 carbon/epoxy composite as a function of temperature and test rate. The viscoelastic response of the material in intralaminar shear was found to be greater than in tension or compression suggesting that the material is at its weakest in shear. Fractographic analysis showed that the interphase region was irregular in nature and that there is little or no bond between the interphase and the particulate phase. Closer examination revealed that the particulate structure of the resin was in fact caused by inhomogeneous regions of epoxy-rich material that failed by tearing rather than by debonding. Also, the degree of phase separation was seen to vary according to remoteness from the interphase region.

**KEYWORDS:** shear, failure mechanisms, carbon/epoxy, fractography, phase separation

## INTRODUCTION

Epoxy resins appear in many different forms and in many different applications. The main drawback of these materials used to be their inherent brittleness. However, this problem has been minimised by the application of various toughening processes. One such process is thermoplastic toughening [1, 2] whereby small amounts of thermoplastic are blended with epoxy resins to form a two phase structure. 914 resin is one such material, and its structure is known to be complex [3, 4] consisting of an epoxy-based particulate phase embedded within a thermoplastic-based connecting phase. When used as the matrix in a composite material, an interphase region forms around the fibres, affecting the mechanical properties. Information on the matrix dominated behaviour of 914 based composites over temperature and test rate ranges is limited and information pertaining to shear is extremely scarce [5, 6]. As T300/914 is a widely used structural aerospace material, this lack of information is surprising. Knowledge of a materials response under shear loading, e.g. intralaminar delamination or transverse compressive loading, is of prime importance in component design. The tensile and compressive matrix dominated behaviour of T300/914 and its microstructure have already been previously established and modelled [3, 4] and this study aims to expand this knowledge to encompass intralaminar shear fracture behaviour over predetermined temperature and test rate ranges. Additional microstructural features observed during high resolution electron microscopic analysis will also be discussed.

## EXPERIMENTAL DETAILS

The composition of, and the manufacturing processes for unidirectional T300/914 laminates, 24 plies (3.3mm) thick are detailed in [3]. Intralaminar shear fracture tests were performed using the Iosipescu 4-point bend test fixture [7-14]. The fixture was chosen in preference to other established test methods, because of its extensive use by Walrath et al. [9, 10] and its in-house use by Broughton and co-workers in Cambridge [7, 12]. The test fixture (designed by Broughton), is shown partially assembled in Figure 1. It is circular in nature with each half vertically mobile via adjustable legs and free to rotate through 360° to accommodate off-axis testing. The test specimens were rectangular coupons, 80mm long, 20mm wide, 3.3mm (24 plies) thick and centrally notched on each long side. The notch angle was 90° and the notch depth 4mm. The specimen was asymmetrically loaded between fixture halves by two pairs of loading plates, and under an applied load,  $P$ , the uniform shear force in the centre section is of magnitude  $P$  and a zero moment is produced at the mid-length. Failure during the test is a four-stage process, with splitting at the two notch roots followed by secondary shear failure and subsequent wholesale crushing of the specimen. Secondary shear failure is defined as a series of axial splits forming in the region of pure shear.

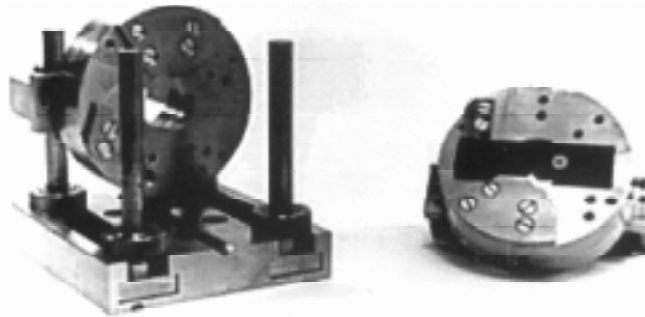


*Figure 1: Partially assembled Iosipescu asymmetric 4-point bend test fixture showing location of specimen and loading plates*

The Iosipescu test fixture has provoked continuous discussion and arguments over the years. Opinions differ as to the definition of true shear failure. Initially, it was believed to be at the first axial split i.e. shearing along the specimen at the notch root. Several authors (e.g. [10]) believe it to be at the onset of secondary failure, and that the initial axial splits are caused by relief of the stress concentrations present at the notch roots. Other aspects of the Iosipescu test such as position of the load points, notch geometry and the consistency of the data obtained have been the subject of much discussion e.g. [14]. These issues have been addressed by Ho et al. [13] who suggested that the state of strain in the centre of 0° orthotropic specimens (the type used in the current study) is not pure shear, and the use of correction factors is recommended. Further work [15] defined the correction factor (CF) for modulus calculation as according to equation (1) where  $E_x$  is the longitudinal modulus and  $E_y$  is the transverse modulus.

$$CF = 1.036 - 0.125 \log \left( \frac{E_x}{E_y} \right) \quad (1)$$

$$G_{13} = 7.555 + 0.214 \left( \frac{R}{R_0} - 1 \right) \quad (4)$$

Figure 3(a) presents the variation of  $\tau_{13}$  with temperature. The two sets of data represent the shear strength at the first axial split,  $\tau_{13p}$ , and the shear strength at the onset of secondary failure,  $\tau_{13s}$ .

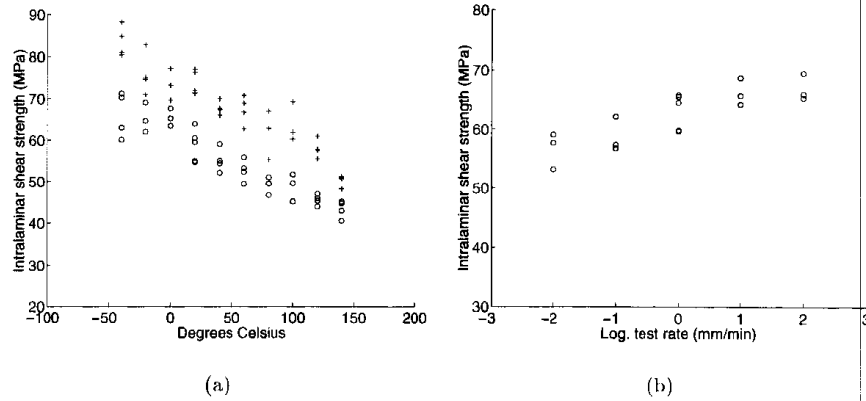


Figure 3: The variation of primary (o) and secondary (+) intralaminar shear strength with (a) temperature and (b) test rate

Again, experimental scatter was reduced at elevated temperatures. The onset of secondary failure was very often defined by a region on the stress/strain curve, rather than by a finite point, hence a specific value for  $\tau_{13s}$  was hard to define. Equations (5) define this strength behaviour with  $\tau_{13s}$  and  $\tau_{13p}$  measured in MPa.

$$\tau_{13p} = 58.922 - 3.218 \left( \frac{T}{T_0} - 1 \right) \quad \text{and} \quad \tau_{13s} = 72.111 - 3.335 \left( \frac{T}{T_0} - 1 \right) \quad (5)$$

i.e. the gradients are similar. The variation of  $\tau_{13p}$  with test rate is shown in figure 3(b) and described by equation (6):

$$\tau_{13p} = 65.159 + 2.623 \left( \frac{R}{R_0} - 1 \right) \quad (6)$$

No  $\tau_{13s}$  data are presented as secondary failure at high test rates was impossible to detect. However,  $\tau_{13s}$  data obtained at low test rates suggested that the trends observed in Figure 3(a) (equivalent  $d\tau/dT$  and  $\tau_{13s} - \tau_{13p} = \text{constant}$  at all temperatures) may be assumed to occur in this instance.

Figures 4(a) and 4(b) detail the dependence of intralaminar shear fracture strain,  $\gamma_{13s}$ , (expressed in %) with temperature and test rate respectively. The shear fracture strain is defined as the strain at the onset of secondary failure. The values are similar to compressive values presented in [4]. This was not surprising, as essentially the same deformation processes are at work. This behaviour is described by equations (7) and (8):

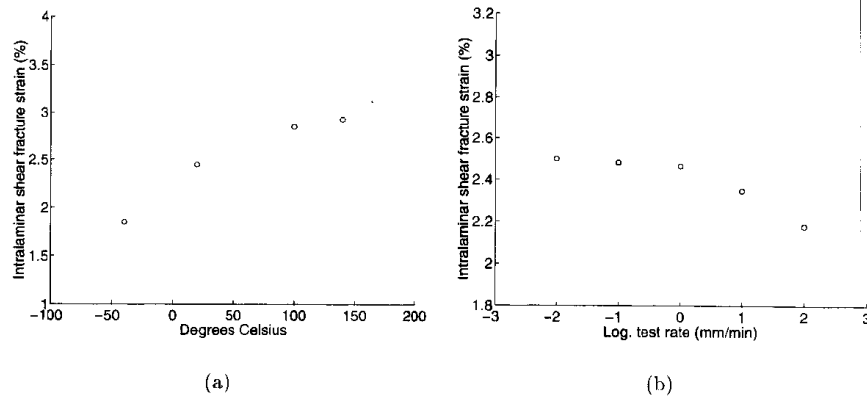


Figure 4: The variation of intralaminar shear strain with (a) temperature and (b) test rate

$$\gamma_{13s} = 2.287 + 1.108 \left( \frac{T}{T_0} - 1 \right) \quad (7)$$

$$\gamma_{13s} = 2.299 - 0.084 \left( \frac{R}{R_0} - 1 \right) \quad (8)$$

In previous work [3, 4], viscoelastic characterisation of transverse tensile and compressive properties was performed using a parameter,  $\Delta$ , that cross-related temperatures and test rates to mutual property values. A change in applied test rate of 1 (logarithmic scale) causes the same change in a given mechanical property as does a temperature change of  $\Delta^\circ\text{C}$ . For tensile and compressive modulus,  $\Delta$  was found to be approximately 14 and for the corresponding strength and strain, between 16.5 and 17.5 i.e. a well-defined difference between macro- and micro- parameters. The intralaminar shear values obtained of 11.3 (modulus), 18.8 (strength) and 18.6 (fracture strain) also show this difference. The disparity between the  $\Delta$  values in shear and in tension/compression may be due to the interphase region present in the composite [3] having its greatest influence in intralaminar shear.

The author believes that the true shear strength value is represented by  $\tau_{13s}$ , not  $\tau_{13p}$ . This is because the purpose of the notches is simply to provide a region of pure shear in the centre of the specimen, and not at the notch roots. The radius of the notch root does, however, affect the data. This phenomenon is well-known in the field of composites fracture toughness testing, suggesting that  $\tau_{13p}$  values may correspond to some form of fracture toughness parameter rather than a shear parameter. Also, the fracture strain values obtained in the compressive study [4] are similar to the secondary fracture strain values shown in Figure 4, and as transverse compression is essentially a shear process, it can therefore be assumed that secondary failure is a true shear failure.

## FRACTOGRAPHIC EXAMINATION

Figure 5(a) and Figure 5(b) were obtained from specimens fractured under shear at ambient temperature. The fibre in the centre of figure 5(a) contains an area where the interphase

where  $G_f$  and  $G_m$  are the fibre and matrix moduli respectively, and  $\nu_f$  and  $\nu_m$  are the fibre and matrix Poissons ratios. This expression was derived from classical elasticity theory and whereas previous models assumed a perfect continuum boundary between the fibre and the matrix, this one regards the interface as an interphase region of finite thickness. In the current study, equation (9) was used to determine  $G_i$  over a range of temperatures by using  $G_{13}$  values from equation (3) and matrix shear modulus values from CIBA-GEIGY [6]. The interphase thickness and volume fraction were calculated according to the structural models developed for high fibre volume fraction regions [3]. The results are presented in Figure 6 and show that the interphase possessed a modulus value between the composite and the bulk resin moduli. This is in accordance with previous tensile results and clearly shows that the mechanical influence of the interphase must be considered when designing with this composite material.

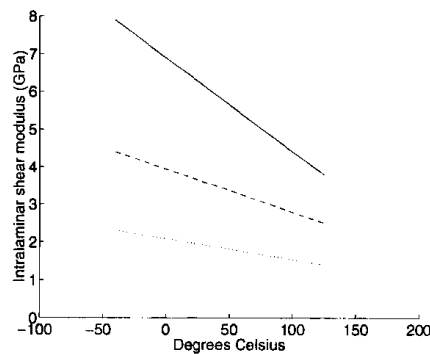
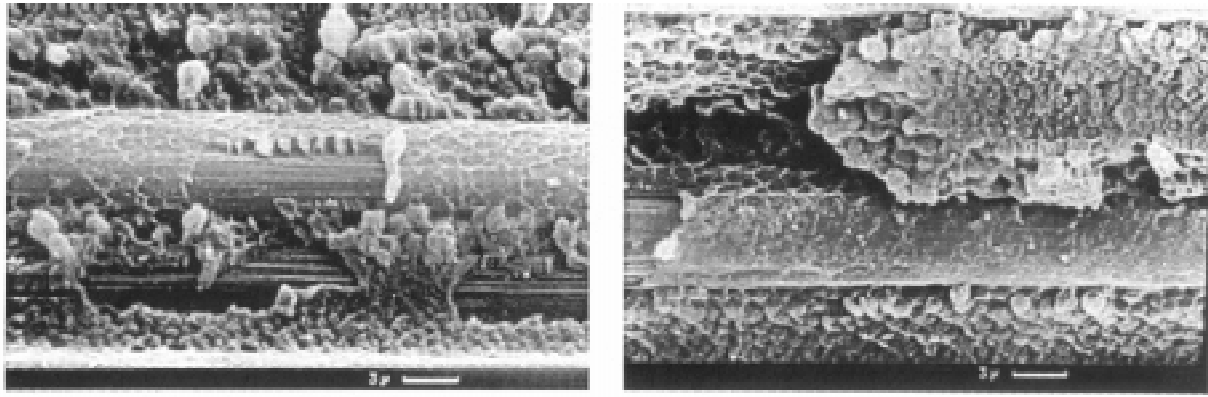


Figure 6: Variation of intralaminar shear modulus with temperature for (—) the composite, (- -) the interphase and (..) the resin

## HIGH RESOLUTION EXAMINATION

Figure 5(a) and Figure 5(b) were obtained at relatively low magnification. Therefore, any microstructure associated with individual particles or with the phases present could not be observed. Figure 7(a) and Figure 7(b) are of an interlaminar shear fracture surface obtained under standard test conditions (1mm/min at ambient) using a high resolution scanning electron microscope, and show features hitherto undetected.

Figure 7(a) is of a resin-rich region and shows that although the particulate structure is observed on the left side of the image (close to an interphase region), the matrix material on the right side of the image (remote from any interphase) is clearly different. The boundary between the interphase and the thermoplastic-based connecting phase is hard to detect, suggesting that the two phases may not be fully separated. The degree of separation appears to vary according to location i.e. it was noted that separation between particles and connecting matrix was greatest close to the interphase. Figure 7(b) shows an epoxy-based particle being torn away from within the thermoplastic-based connecting phase. The term "particle" now seems to be inappropriate, as no distinct phase boundary is observed. This tearing process is fibrillar in nature and suggests that the "particles" are merely areas of fairly distinct, roughly spherical, inhomogeneity within the matrix phase that possess different mechanical properties. The irregular surface features observed on the particle are probably remnants of fractured fibrils still adhering to the surface.



(a)

(b)

Figure 5: Unidirectional T300/914 intralaminar shear fracture surfaces obtained under standard conditions showing (a) an irregular interphase and (b) fibrillation of the matrix

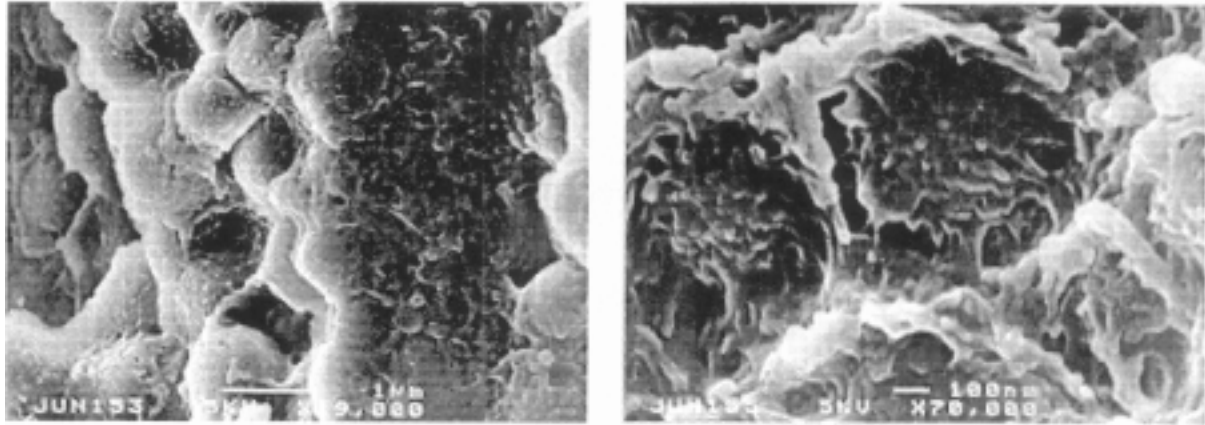
has detached from the fibre, revealing the ribbed nature of the fibre surface. Resins tend to adhere readily to such a surface, thus explaining the relatively strong interphase/fibre interface in this material. The detached area has sheared away leaving transverse cusps on the interphase region. It also shows the uneven thickness of the interphase region. The complex structure of the surrounding matrix rendered cusping in this region indistinguishable from normal fracture profiles. No pitting of the interphase region can be seen, indicating that the interphase region formed before particulation of the epoxy phase. The thermoplastic nature of the connecting phase is confirmed in figure 5(b) where areas of acute fibrillation associated with large plastic deformation can be observed. This fracture surface was obtained at a much lower test rate and as a consequence, the increased plastic deformation has resulted in the scar pattern on the interphase having completely sheared away. In the upper right corner, truncated spheres can be seen on the interphase surface, partially debonded.

## INTERPHASE STUDIES

The presence of the interphase region is known to affect macroparameters such as tensile and compressive modulus over a range of temperatures [3, 4]. It is therefore not unreasonable to assume that the intralaminar shear modulus would be affected in a similar way. The modified Halpin-Tsai expression introduced in [3] showed that the interphase region has a modulus value between that of the composite and that of the bulk resin, and also possesses a different thermal response ( $dE/dT$ ). As no T300 fibre shear data were available, this expression could not be used in shear. However, Sideridis [16] developed an expression that calculated shear modulus,  $G_{LT}$ , in terms of  $G_i$ , the interphase shear modulus, and also in terms of  $r_f$  and  $r_i$  - the fibre radius and the radius of the fibre plus interphase:

$$G_{LT} = \frac{G_m \left( 4G_m \left[ G_f \nu_f + \frac{2\nu_f}{r_f^2} \int_{r_f}^{r_i} G_i(r) r dr \right] + [(G_i^2 + G_m^2)(2 - \nu_m) + 2G_i G_m \nu_m] \nu_m \right)}{[G_i \nu_m + G_m (2 - \nu_m)]^2} \quad (9)$$





(a)

(b)

*Figure 7: Unidirectional T300/914 - high resolution images showing (a) varying degrees of phase separation and (b) a particle tearing from the connecting phase*

Figure schematically details the difference between a particulate toughened material, and T300/914. In traditional particulate toughened materials (Figure 8(a)), distinct regions exist together with a distinct interfacial boundary. Under sufficient loading, the particle and matrix invariably debond with the matrix region deforming plastically (Figure 8(b)), until final failure occurs, leaving a distinct fracture morphology (Figure 8(c)). In T300/914, the boundary between the particle and the matrix is vague and indistinct i.e. there is a gradual transition from one phase to the other (Figure 8(d)). On loading, the particulate region, being of different mechanical properties to the matrix region, will not deform in relation to the matrix region, resulting in the indistinct region between the two phases plastically deforming (Figure 8(e)), giving the characteristic fibrillation seen in figure 7(b). Final fracture (Figure 8(f)) results in a morphology significantly more incoherent than with the traditional particle toughened model. This lack of structural clarity renders any modelling attempted on this material extremely difficult.

In addition, it has been shown that the interphase may act as a “phase separation inducer” in that the degree of phase separation appears to increase with decreasing distance from the interphase region. This is possible, as it has been established in previous work that the interphase forms before phase separation in the remaining matrix occurs [3]. Local changes in solubility parameters and other growth parameters may therefore result, which effectively encourage phase separation to occur to a higher degree than in areas remote to the interphase. This high degree of phase separation close to the interphase is a structural weakness within the material, as fracture preferentially occurs in these regions. Further study on this system may result in homogenising the phase separation throughout the material, without losing the beneficial effects of the interphase. In theory, a tougher material should result.

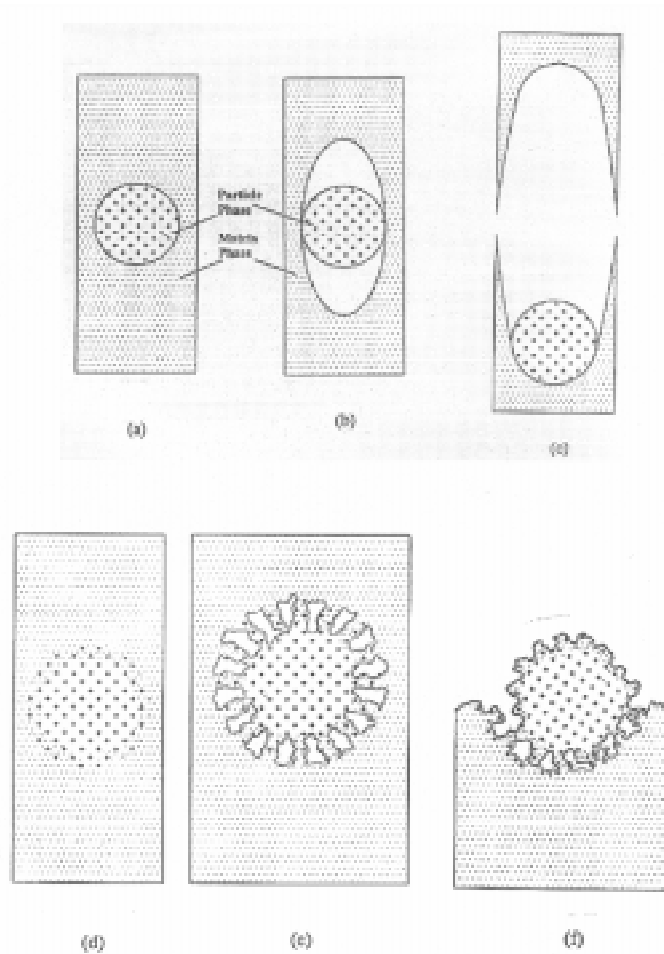


Figure 8: Detailing the debonding processes in traditional particulate toughened materials (a-c) and in T300/914 (d-f)

## CONCLUSIONS

This study has established the intralaminar shear behaviour of unidirectional T300/914 as a function of temperature and test rate. The presence of the interphase clearly affects the behaviour of the composite, and viscoelastic effects appear to be greater in shear than in tension or compression [3, 4]. Fractographically, it has been proven that there is little or no bond between the interphase and the particulate phase and that the degree of phase separation decreases with increasing distance from the interphase. The high resolution analysis has shown that the thermoset-based particles are in fact regions of high concentrations of epoxy material with an indistinct phase boundary, rather than particles of a well-defined geometry.

## ACKNOWLEDGEMENTS

Dr. Lowe wishes to express his gratitude to the Department of Materials Science, University of Cambridge, and to Professor Yiu-Wing Mai of the Department of Mechanical and Mechatronic Engineering, University of Sydney, for their assistance with this work.

## References

- [1] Yamanaka, K., Inoue, T., "Structure Development in Epoxy Resin Modified with Poly(ether sulphone)", *Polymer*, **30**, pp.662-667 (1989)
- [2] Bucknall, C.B., Partridge, I.K., "Phase Separation in Epoxy Resins Containing Poly(ethersulphone)", *Polymer*, **24**, pp.639-644 (1983)
- [3] Lowe, A., "Matrix Dominated Tensile Behaviour of Unidirectional T300/914 and Structural Modelling of the Material", *J. Mat. Sci.*, **31**, pp.983-993 (1996)
- [4] Lowe, A., "Transverse Compressive Testing of T300/914", *ibid*, pp.1005-1011 (1996)
- [5] G'sell, C., Jaques, D., Favre, P., "Plastic Behaviour Under Simple Shear of Thermosetting Resins for Fibre Composite Matrices", *J. Mat. Sci.*, **25**, pp.2004-2011 (1990)
- [6] Fischer, M., *Purchase Order EP311 484 2P Report no.1*, CIBA-GEIGY, Marley, Switzerland (1989)
- [7] Broughton, W.R., Kumosa, M., Hull, D., "Analysis of the Iosipescu Shear Test as Applied to Unidirectional Carbon Fibre Reinforced Composites", *Comp. Sci & Tech*, **38**, pp.299-325 (1990)
- [8] Iosipescu, N., "New Accurate Procedure for Single Shear Testing of Metals", *J. Materials*, **2**, no.3, pp.537-566 (1967)
- [9] Walrath, D.E., Adams, D.F., "The Iosipescu Shear Test as Applied to Composite Materials", *Exp. Mech*, **23**, May, pp.105-110 (1993)
- [10] Walrath, D.E., Adams, D.F., *Verification and Application of the Iosipescu Shear Test Method*, University of Wyoming Department Report UWME DR-401-103-1 (1984)
- [11] Kumosa, M., Hull, D., "Mixed-Mode Fracture of Composites Using Iosipescu Shear Test", *Int. J. Fracture*, **35**, pp.83-102 (1987)
- [12] Broughton, W.R., "Mixed-Mode Failure of Carbon-Fibre Reinforced Composite Materials", *PhD Thesis*, University of Cambridge (1989)
- [13] Ho, H., Tsai, M.Y., Morton, J. Farley, G.L., "An Experimental Investigation of Iosipescu Specimen for Composite Materials", *Exp. Mech.*, **31**, December, pp.328-336 (1991)
- [14] Sullivan, J.L., "The Use of Iosipescu Specimens", *Exp. Mech.*, **28**, September, pp.326-328 (1988)
- [15] Ho, H., Tsai, M.Y., Morton, J. Farley, G.L., "Numerical Analysis of the Iosipescu Specimen for Composite Materials", *Comp. Sci & Tech.*, **46**, pp.115-128 (1993)
- [16] Sideridis, E., "The In-Plane Shear Modulus of Fibre Reinforced Composites as Defined by the Concept of the Interphase", *Comp. Sci. & Tech.*, **31**, pp.35-53 (1988)

# RATE EFFECTS ON MODE I INTERLAMINAR FRACTURE TOUGHNESS IN CARBON-FIBRE/EPOXY AND CARBON-FIBRE/TOUGHENED-EPOXY COMPOSITE LAMINATES

Takayuki Kusaka<sup>1</sup>, Masaki Hojo<sup>2</sup>, Tomoaki Kurokawa<sup>3</sup> and Shojiro Ochiai<sup>2</sup>

<sup>1</sup> *Hyogo Prefectural Institute of Industrial Research,  
3-1-12, Yukihiro-cho, Suma-ku, Kobe 654, Japan*

<sup>2</sup> *Mesosopic Material Research Centre, Kyoto University,  
Yoshidahonmachi, Sakyo-ku, Kyoto 606-01, Japan*

<sup>3</sup> *Department of Mechanical Engineering, Setsunan University,  
17-8, Ikedanakamachi, Neyagawa 572, Japan*

**SUMMARY:** Rate dependence of mode I interlaminar fracture properties of unidirectional carbon-fibre/epoxy and carbon-fibre/toughened-epoxy composite laminates was investigated over a very wide range of loading rate from quasi-static to impact at room temperature. In both materials, the fracture toughness decreased stepwise interposing a transition region, where the fracture toughness decreased rapidly with increasing loading rate. The transition of the fracture toughness approximately corresponded to the transition of the microscopic fracture characteristics; the fracture surface was rougher at low loading rates than at high loading rates. Even under a geometrically stable testing condition, the crack growth behaviour was significantly unstable at low loading rates, while it was almost stable at high loading rates. This trend was the consequence of the stepwise characteristic in the fracture toughness with respect to the loading rate.

**KEYWORDS:** delamination, mode I, fracture toughness, rate effect, impact strength, crack propagation, unstable fracture, stick-slip phenomenon

## INTRODUCTION

Recently, composite materials have been widely used in structural engineering applications and consequently the assessment of damage tolerance in composite structures becomes vitally important. Especially, delaminations have been recognized to be one of the most serious defects which can lead to the catastrophic failure in laminated composite structures. The interlaminar fracture properties have been, therefore, regarded as important in the development of new composite materials [1]. Recent studies have shown that fracture mechanics is useful to deal with this kind of problem and have also clarified fairly in detail the characteristics under quasi-static loading [2–5].

On the other hand, for further understanding, the effects of temperature, moisture, loading rate, etc. on the interlaminar fracture properties must be fully characterized, because the mechanical properties of the matrix resin is much dependent on these factors, as is often the case with most polymers [6]. Concerning loading rate, some researchers in-

investigated its effects on the interlaminar fracture properties in composite laminates [7-11]. However, the characteristics at very high (impact) loading rates have not been sufficiently investigated yet [9-11]. This is partly because the accurate measurement of fracture properties is not easy under impact loading due to the inertia force both in the measuring system and in the specimen. The authors have, therefore, developed a simple method for estimating the modes I and II interlaminar fracture toughness under impact loading and investigated the rate dependence of fracture toughness in some composite materials [10,11].

In the present study, the rate dependence of mode I interlaminar fracture toughness in two different types of composite materials was investigated over a very wide range of loading rate from quasi-static to impact. In addition, the stability of crack growth behaviour was discussed in relation to the rate dependence of fracture toughness.

## EXPERIMENTAL PROCEDURE

### Materials

Carbon-fibre/epoxy (T300/2500, Toray) and carbon-fibre/toughened-epoxy (T800H/3900-2, Toray) composite laminates were examined in the present study. The T300/2500 is a first generation composite material using a brittle epoxy resin as the matrix. The T800H/3900-2 is a newly developed composite material having a tough 'interlayer' (30  $\mu\text{m}$  in thickness) containing fine polyamide particles in a epoxy resin and has excellent CAI (Compression After Impact) performance [1]. Figure 1 illustrates the microstructures and the typical crack paths in the present materials. In T800H/3900-2, the crack path is inside the interlayer during the initial stage of crack growth, however, it shifts from the interlayer to the interface between the interlayer and the base lamina or to the intralaminar during the propagation stage of crack growth. According to the transition of the crack path, the fracture toughness,  $G_{IC}$ , varies largely in T800H/3900-2; the fracture toughness,  $G_{IC}$ , is higher in the initial stage than that in the propagation stage under quasi-static loading [12]. In the present study, the fracture toughness for the interlayer fracture will be termed 'interlayer toughness',  $G_{IC}^{lay}$ , and that for the interface or intralaminar fracture will be termed 'interphase toughness',  $G_{IC}^{pha}$ , which can be easily distinguished by a visual inspection. In T300/2500, the crack grows along the mid-plane and the fracture toughness,  $G_{IC}$ , remains almost constant during crack propagation.

Unidirectional panels of 20 plies were fabricated according to the prepreg manufacturer's recommended cure cycle. The volume fraction of carbon-fibre was about 58 and 54 %, and the nominal thickness of the panels was about 2.7 and 3.1 mm for T300/2500 and T800H/3900-2, respectively. A PTFE film (25  $\mu\text{m}$  in thickness) for T300/2500 and a polyimide film treated with release agent (8  $\mu\text{m}$  in thickness) for T800H/3900-2 were

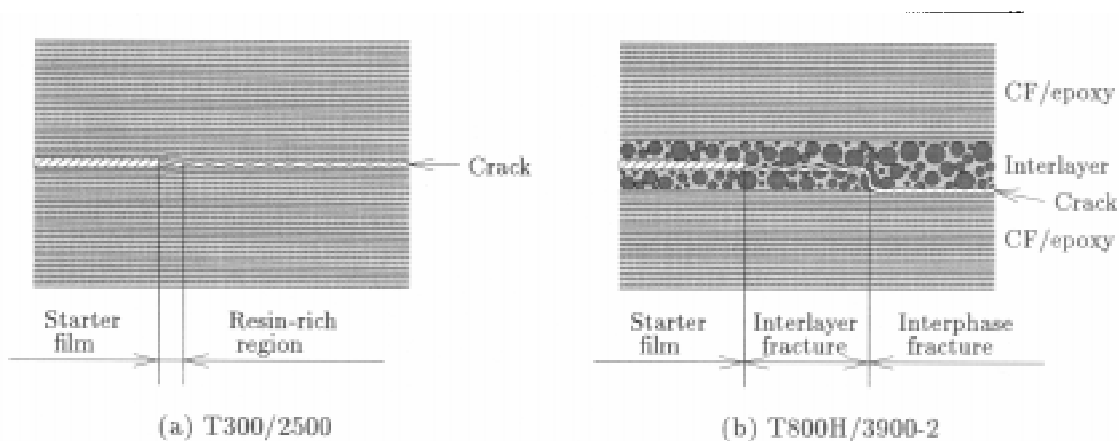


Fig. 1: Typical crack paths in mode I interlaminar fracture.

inserted between the plies at the mid-plane of the panels to introduce an artificial starter slit. The specimens of T300/2500 were precracked about 1–2 mm to diminish the effect of the resin-rich region at the film's tip. The specimens of T800H/3900-2 were not precracked because the inserted film was sufficiently thinner than the thickness of the interlayer.

### Experimental procedure

DCB (Double Cantilever Beam) method [3] was used to estimate the mode I interlaminar fracture toughness,  $G_{IC}$ , at low loading rates ( $\dot{\delta} = 0.01\text{--}500$  mm/min). Figure 2 shows the geometry of a DCB specimen, where  $P (= F_y)$  is the load applied to the specimen and  $\delta$  is the displacement of the loading point.  $b$ ,  $2h$  and  $a$  are the width, thickness and crack length of the specimen, respectively. However, the DCB method is not necessarily fitting to impact fracture tests, because the behavior of the specimen under impact loading is much complicated due to its asymmetry with respect to the loading line. Hence, WIF (Wedge Insert Fracture) method [13], which is the compressive version of the DCB method, was used to estimate the mode I interlaminar fracture toughness,  $G_{IC}$ , at high loading rates ( $\dot{\delta} = 5\text{--}15$  m/sec). Figure 3 shows the geometry of a WIF specimen, where  $F_x (= P/2)$  and  $F_y$  are the  $x$ - and  $y$ -components of the load,  $P$ .

Quasi-static DCB tests were carried out under constant crosshead speeds using a screw-driven testing machine (Instron 1175). Impact WIF tests were carried out using a SHPB (Split Hopkinson Pressure Bar) system, which can precisely estimate the load,  $P$ , and the displacement,  $\delta$ , by analyzing the stress wave propagating in elastic bars on the basis of one-dimensional wave theory [11].

### Data reduction

Assuming a DCB specimen to be a pair of cantilever beams of bending span,  $a + e$ , the mode I energy release rate,  $G_I$ , can be determined by the following equation [4].

$$G_I = \frac{\{F_y(a + e)\}^2}{bEI} \quad (1)$$

where  $E$  and  $I (= bh^3/12)$  are the Young's modulus and moment of inertia of area of the specimen, respectively.  $e$  is the correcting value for local deformation in the vicinity of the crack tip [4]. The compliance,  $C (= v/F_y \simeq \delta/P)$ , is given by the following equation [5].

$$\frac{a}{2h} = \alpha \sqrt[3]{bC} + \beta \quad (2)$$

where  $v (\simeq \delta)$  is the crack opening displacement.  $\alpha (= \sqrt[3]{E}/4)$  and  $\beta (= -e/2h)$  are the constants identified experimentally [5], which were  $12.1 \text{ N}^{1/3}/\text{mm}^{2/3}$  and  $-0.87$  for T300/2500, and  $13.5 \text{ N}^{1/3}/\text{mm}^{2/3}$  and  $-1.58$  for T800H/3900-2, respectively. Substituting Eqn. 2 to Eqn. 1, the energy release rate,  $G_I$ , can be finally determined by the following equation for a DCB specimen.

$$G_I = \frac{3}{2(2h)} \left(\frac{F_y}{b}\right)^2 \frac{\sqrt[3]{(bC)^2}}{\alpha} \quad (3)$$

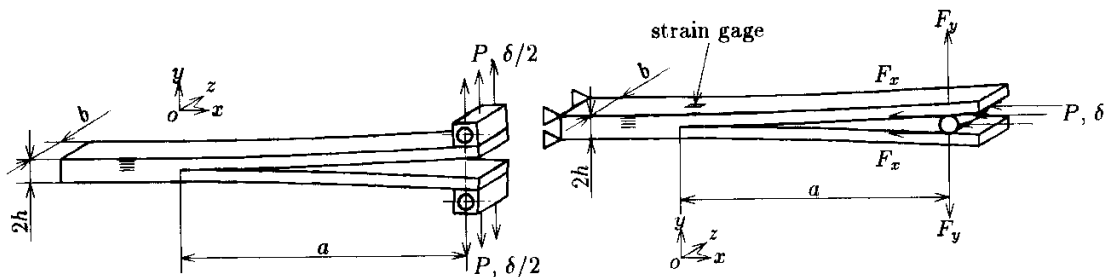


Fig. 2: DCB specimen.

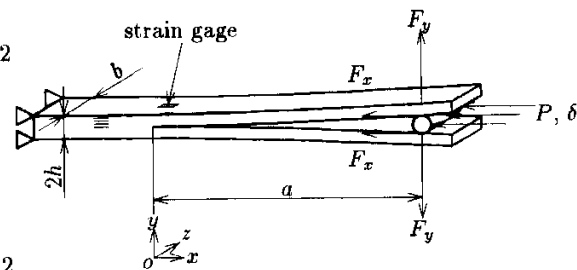


Fig. 3: WIF specimen.

Assuming a WIF specimen to be a pair of cantilever beams of bending span,  $a + e$ , the mode I energy release rate,  $G_I$ , can be determined by the following equation [13].

$$G_I = \frac{\{F_x r \cos \theta\}^2 + \{F_y(a + e)\}^2}{bEI} \quad (4)$$

where  $r$  is the radius of the wedge and  $\theta$  is the deflection angle of the specimen. When the deflection angle,  $\theta$ , is sufficiently small, the term relative to the load,  $F_x$ , can be neglected and Eqn. 4 yields to the same form as Eqn. 1. On the basis of beam theory, the surface strain of the specimen at  $(x, y) = (0, h)$ ,  $\varepsilon_{tip}$ , is given by the following equation.

$$-\frac{\varepsilon_{tip}}{F_y} = \frac{ha}{2EI} \equiv \kappa \quad (5)$$

Considering that the deflection angle,  $\theta$ , is small, the ratio,  $2r/F_z$  ( $\simeq v/F_y$ ), should be equivalent to the compliance,  $C$ , for a DCB specimen. Accordingly, the ratio,  $2r/F_z$ , will be similarly denoted by  $C$  for a WIF specimen. Now, using the compliance,  $C^*$ , and the variable,  $\kappa^*$  for a reference crack length,  $a^*$ , the compliance,  $C$ , and the variable,  $\kappa$ , for an arbitrary crack length,  $a$ , can be determined by the following equations.

$$C = \left(\frac{a + e}{a^* + e}\right)^3 C^* \quad , \quad \kappa = \frac{a}{a^*} \kappa^* \quad (6)$$

Substituting Eqns. 5 and 6 to Eqn. 3, the energy release rate,  $G_I$ , can be finally determined by the following equation for a WIF specimen.

$$G_I = \frac{3}{2(2h)} \left(\frac{\varepsilon_{tip}}{b\kappa^*}\right)^2 \frac{\sqrt[3]{(bC^*)^2}}{\alpha} \left\{ \frac{(a + e)a^*}{(a^* + e)a} \right\}^2 \quad (7)$$

Hence, the fracture toughness,  $G_{IC}$ , can be obtained by measuring the critical strain,  $\varepsilon_C$ , and the critical crack length,  $a_C$ , at the onset of crack growth, when the compliance,  $C^*$ , and the variable,  $\kappa^*$ , are determined by a preliminary DCB test. In the present study,  $a^* = 40$  mm was chosen to determine the compliance,  $C^*$ , and the variable,  $\kappa^*$ .

Though the above derivation was based on static theory, the authors confirmed that Eqn. 7 was effective even in the impact WIF test when an adequate incident stress wave was applied to the specimen [14]. This is mainly because the influence of the inertia force in the specimen can be reduced remarkably by using a slow-gradient stress wave (ramped stress wave) and consequently the deformation mode of the specimen becomes approximately equal to that in the quasi-static WIF test.

The time delivative of energy release rate,  $\dot{G}_I$ , which will be termed 'loading rate', was used in place of the strain rate,  $\dot{\varepsilon}$ , to characterize the rate dependence of fracture properties, because the estimation of the strain rate,  $\dot{\varepsilon}$ , is not easy due to its singularity at the crack tip. The loading rate,  $\dot{G}_I$ , was estimated by the following equations [6].

$$\dot{G}_I = G_I \frac{2\dot{\delta}}{\delta} \quad (\text{for DCB}) \quad , \quad \dot{G}_I = G_I \frac{4\dot{\delta}}{a} \quad (\text{for WIF}) \quad (8)$$

## RESULTS AND DISCUSSION

### Rate dependence in T300/2500

Figure 4 shows the rate dependence of the fracture toughness,  $G_{IC}$ , in T300/2500. There clearly existed a transition region (Region II) where the fracture toughness,  $G_{IC}$ , decreased rapidly with increasing the loading rate,  $\dot{G}_I$ , and regions (Regions I and III)

where the fracture toughness,  $G_{IC}$ , was not sensitive to the loading rate,  $\dot{G}_I$ , above and below the transition region. Consequently, the relationship between the loading rate,  $\dot{G}_I$ , and the fracture toughness,  $G_{IC}$ , showed a stepwise characteristic as shown in Fig. 4. The average values of the fracture toughness,  $G_{IC}$ , in Regions I and III were 272 and 203 J/m<sup>2</sup>, respectively.

Figure 5 shows typical load-displacement relations in quasi-static DCB tests. In Region I, the crack growth behaviour was significantly unstable; the crack grew discontinuously in several millimeters with accompanying high-speed growth and arrest, where the load-displacement relation showed a saw-toothed shape as shown in Fig. 5 (a). The average crack velocity during a crack jump was about 30 m/s. In Region III, to the contrary, the crack growth behaviour was stable; the crack grew continuously with the displacement,  $\delta$ , as shown in Fig. 5 (b). The crack growth behaviour was stable even in the impact WIF test. In Region II, the crack growth behaviour was unstable, however, the size of the saw-tooth became smaller with increasing loading rate. Almost any fibre-bridgings were

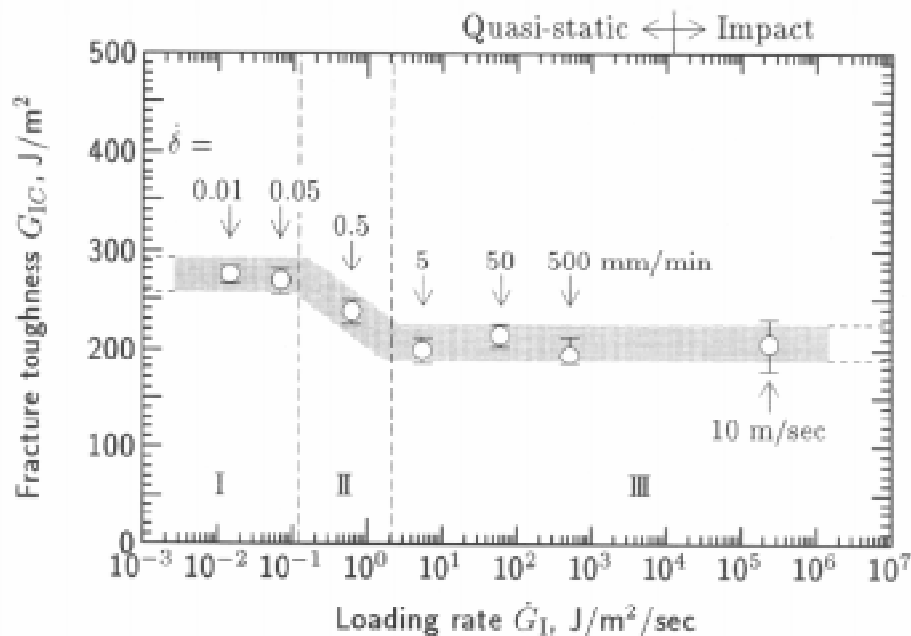


Fig. 4: Rate dependence of fracture toughness (T300/2500).

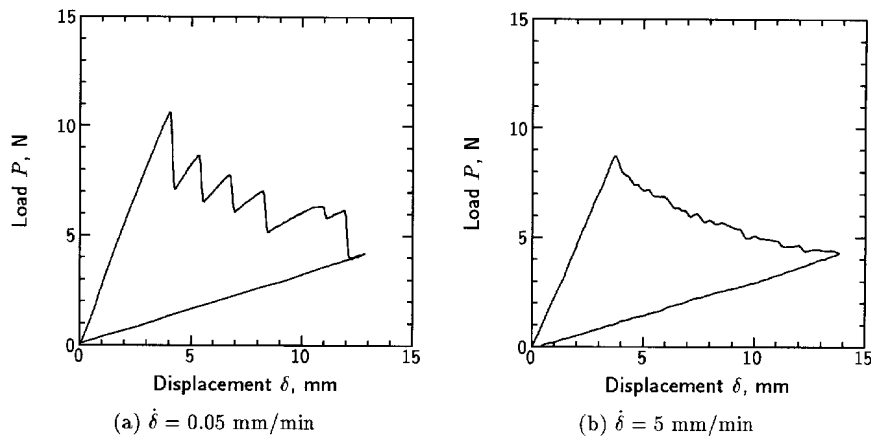


Fig. 5: Load-displacement relations in quasi-static DCB tests (T300/2500).

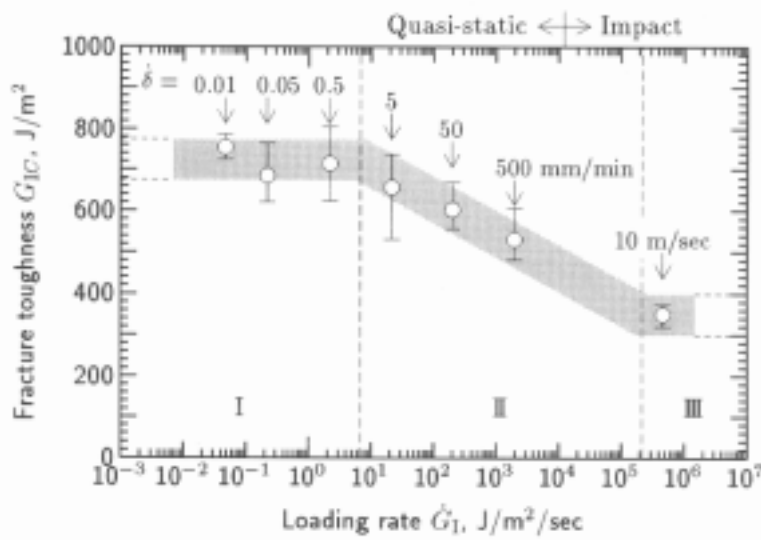


not observed in all loading rates.

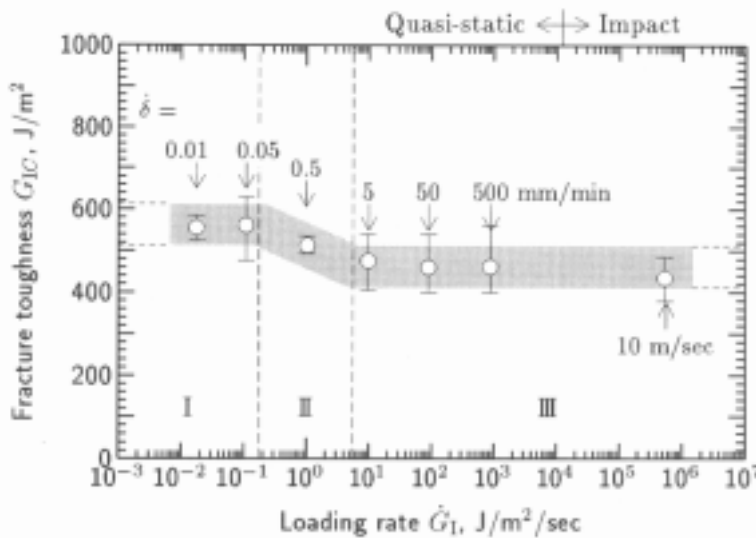
**Rate dependence in T800H/3900-2**

In T800H/3900-2, the interlayer fracture occurred in the initial stage of crack growth and the interphase fracture occurred in the propagation stage of crack growth as mentioned previously. Accordingly, the results will be discussed with classifying the interlayer fracture and the interphase fracture.

Figure 6 shows the rate dependence of the fracture toughness,  $G_{IC}$ , in T800H/3900-2. For the interphase toughness,  $G_{IC}^{pha}$ , the similar stepwise characteristic to T300/2500 was observed as shown in Fig. 6 (b). For the interlayer toughness,  $G_{IC}^{lay}$ , on the other hand, the existence of rate-insensitive region above the transition region (Region III) was not clear for lack of experimental results at higher loading rates as shown in Fig. 6 (a). However, there will probably exist the rate-insensitive region, because only stable crack growth occurred in the impact WIF test as shown in Fig. 7, though the characteristic of  $dG_{IC}/d\dot{G} < 0$  should



(a) Interlayer fracture



(b) Interphase fracture

Fig. 6: Rate dependence of fracture toughness (T800H/3900-2).

lead to unstable fracture [15]. The average values of the interlayer toughness,  $G_{IC}^{lay}$ , were 718 and 350 J/m<sup>2</sup>, and those of the interphase toughness,  $G_{IC}^{pha}$ , were 558 and 458 J/m<sup>2</sup> in Regions I and III, respectively.

The transition region of the interlayer toughness,  $G_{IC}^{lay}$ , was higher in loading rate than that of the interphase toughness,  $G_{IC}^{pha}$ . The decrease in the interlayer toughness,  $G_{IC}^{lay}$ , was much larger than that in the interphase toughness,  $G_{IC}^{pha}$ , moreover, the interlayer toughness,  $G_{IC}^{lay}$ , was even lower than the interphase toughness,  $G_{IC}^{pha}$ , at impact loading rates. As the consequence of the above rate dependence, the relationship between the crack extension,  $\Delta a$ , and the fracture toughness,  $G_{IC}$ , (R-curve) showed different shapes with respect to loading rate; the higher region in fracture toughness in the initial stage of crack growth was gradually disappeared with increasing loading rate as shown in Fig. 8. However, the cause for the difference in rate dependence between the interlayer toughness,  $G_{IC}^{lay}$ , and the interphase toughness,  $G_{IC}^{pha}$ , is still not clear.

Figure 9 show typical load-displacement relations in quasi-static DCB tests. In Region

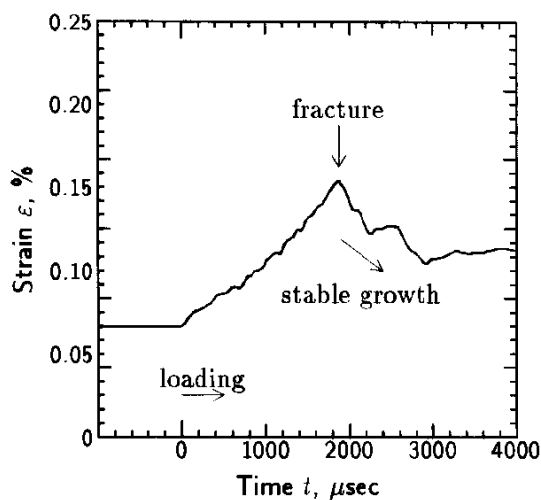


Fig. 7: History of the surface strain of the specimen in an impact WIF test.

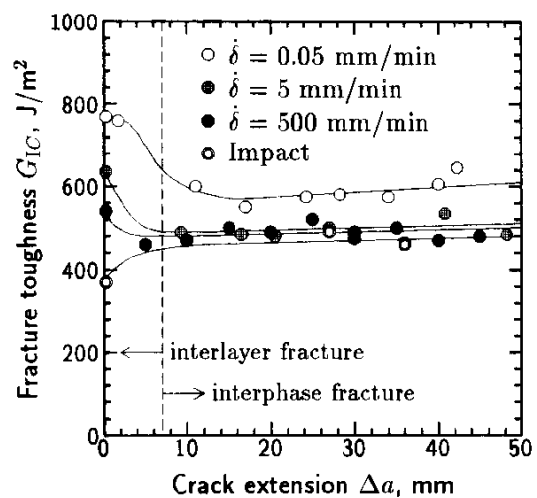


Fig. 8: Rate dependence of R-curve in T800H/3900-2.

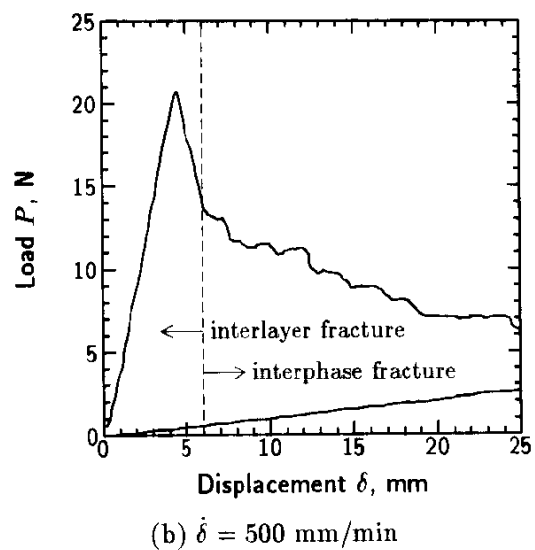
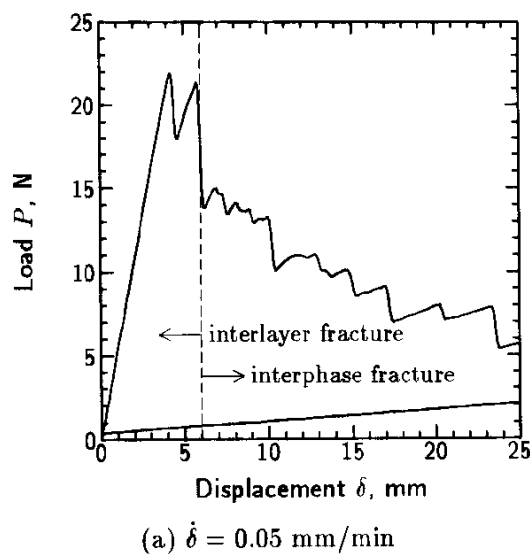


Fig. 9: Load-displacement relations in quasi-static DCB tests (T800H/3900-2).

I, the crack growth behaviour was unstable both for the interlayer fracture and for the interphase fracture as shown in Fig. 9 (a). For the interlayer fracture, the first crack jump was considered to be due to the rate dependence of fracture toughness, while the second crack jump was considered to be due to both the rate dependence of fracture toughness and the transition from the interlayer fracture to the interphase fracture. For the interphase fracture, the crack growth behaviour was somewhat different from that in T300/2500, because the average crack velocity during a crack jump was about 20 mm/s, which is much lower than that in T300/2500. This was probably caused by the fibre-bridgings, which prevented the crack from growing in high-speed. The growth and breakage of the fibre-bridgings also contributed the unstable crack growth behaviour in addition to the rate dependence of fracture toughness in T800H/3900-2. In Region III, the crack growth behaviour was almost stable both for the interlayer fracture and for the interphase fracture as shown in Figs. 7 and 9 (b).

Mai and Atkins [15] studied the criterion for crack stability, where they suggested that the material characteristic of  $dG_{IC}/da < 0$  ( $dG_{IC}/d\dot{G}_I < 0$ ) should lead to unstable fracture even under a geometrically stable testing condition as the displacement-controlled DCB test. This criterion seemed to be much likely for the present materials;  $dG_{IC}/d\dot{G}_I$  is negative when the crack initiated in Region I or II because the strain rate at the tip of a moving crack is at least one or two order of magnitude greater than that of the stationary crack loaded at the same rate [6] and consequently the fracture toughness,  $G_{IC}$ , decreases rapidly from the value corresponding to Region I or II to that corresponding to Region III, while  $dG_{IC}/d\dot{G}_I$  is almost zero when the crack initiated in Region III because the fracture toughness,  $G_{IC}$ , remains almost constant in Region III even though the strain rate increases.

### Microscopic observation

Examinations of the fracture surface were performed with a SEM (Scanning Electron Microscopy) to study the microscopic fracture mechanisms. Figures 10 and 11 show the fracture surfaces in T300/2500 and T800H/3900-2, respectively.

In T300/2500, two distinct types of fracture surface were observed in Regions I and II as shown in Figs. 10 (a), (b) and (c). The first type was a whitened zonal region corresponding to the initiation of unstable crack. The second type was a dark region corresponding to the propagation of unstable crack. In the whitened region, the roughness of the surface was larger, and the damage was extended deeply in the materials as shown in Fig. 10 (b). In the dark region, to the contrary, the surface was relatively smooth, and the damage was localized around the main crack as shown in Fig. 10 (c). The width of the whitened region was about 0.2 mm, which approximately agreed with the damaged zone size (0.4 mm) estimated by the Dugdale model [16]. In Region III, only a smooth fracture surface was observed as shown in Fig. 10 (d). No significant difference was recognized between the fracture surfaces shown in Figs. 10 (c) and (d), suggesting that the fracture mechanisms were similar between in the propagation stage of unstable crack in Region I and in the propagation stage of stable crack in Region III.

In T800H/3900-2, the crack grew inside the interlayer without respect to the loading rate in the initial stage of crack growth as shown in Figs. 11 (a) and (b), where the fracture surface in Region I was rougher than that in Region III. On the other hand, the crack grew near the interface between the interlayer and the base lamina without respect to the loading rate in the propagation stage of crack growth as shown in Figs. 11 (c) and (d), where the fracture surface in Regions I, II and III was similar to that in T300/2500, respectively. However, the whitened region was not clearly recognized in T800H/3900-2.

Assuming that the development of the damaged zone causes the effective blunting of the crack tip, the stress concentration at the crack tip is reduced by it and consequently the fracture toughness rises apparently. Hence, in the present materials, the effect of the crack blunting should be larger in Region I than in Region III because the damaged zone size was

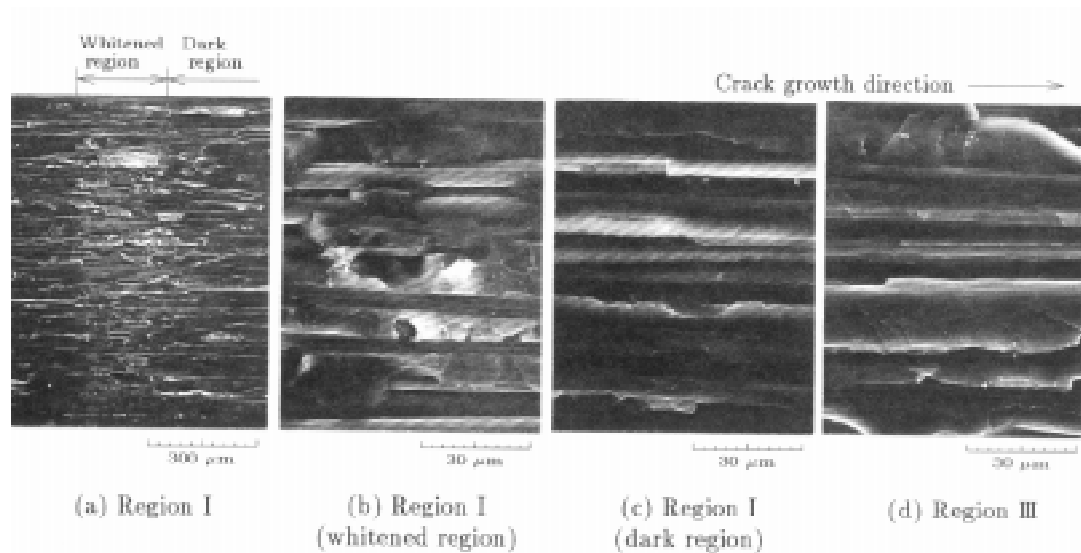


Fig. 10: Scanning electron micrographs of the fracture surface (T300/2500).

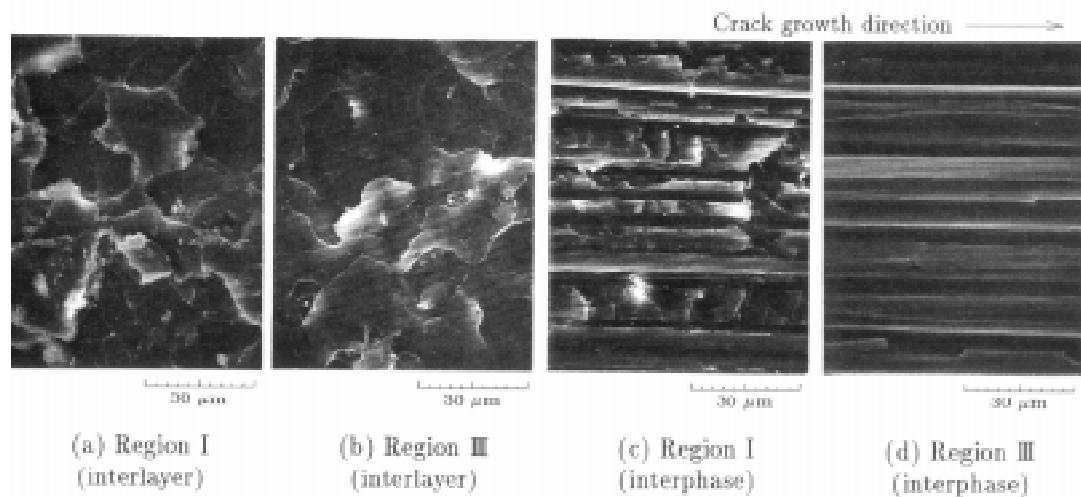


Fig. 11: Scanning electron micrographs of the fracture surface (T800H/3900-2).

larger in Region I than in Region III as shown in Figs. 10, and 11, and consequently the fracture toughness should be higher in Region I than in Region III. The above idea seems to be likely to explain the rate dependence of fracture toughness shown in Figs. 4 and 6, though it is not exact because the fracture toughness does not depend only on the stress state at the crack tip but on the material strength at the strain rate concerned. Considering that the crack growth behaviour was unstable in Region I and II, the above idea agrees with the experimental results reported by Gledhill et al. [17], which suggested that the crack blunting should lead to the unstable fracture in epoxy resin.

## CONCLUSIONS

Rate dependence of mode I interlaminar fracture properties of unidirectional carbon-fibre/epoxy and carbon-fibre/toughened-epoxy composite laminates was investigated over a very wide range of loading rate from quasi-static to impact.

The fracture toughness decreased stepwise interposing a transition region, where the

fracture toughness decreased rapidly with increasing loading rate. In T300/2500, the average values of the fracture toughness were about 272 and 203 J/m<sup>2</sup> below and above the transition region, respectively. In T800H/3900-2, the average values of the interlayer toughness were about 718 and 350 J/m<sup>2</sup>, and those of the interphase toughness were about 558 and 458 J/m<sup>2</sup> below and above the transition region, respectively.

In T800H/3900-2, the shape of R-curve varied with the loading rate because of the variation of fracture toughness with respect to both loading rate and crack extension.

The transition of the fracture toughness approximately corresponded to the transition of the microscopic fracture characteristics; larger damaged zone was developed and the fracture surface was rougher at low loading rates than at high loading rates.

The crack growth behaviour was unstable in and below the transition region but stable above the transition region. The stability of crack growth behaviour was much dependent on the rate-sensitivity of the fracture toughness when the crack initiated; the crack grew stably when the value of  $dG_{IC}/d\dot{G}_I$  was not negative but unstably when the value of  $dG_{IC}/d\dot{G}_I$  was negative.

### ACKNOWLEDGEMENTS

The authors would like to thank Dr. J. Matsui of Toray Industries, Inc. and Mr. I. Chou of Ishikawajima-Harima Heavy Industries Co., Ltd., for their help in fabricating the specimens of the T800H/3900-2.

### REFERENCES

1. Odagiri, N., Kishi, H. and Yamashita, occurrence M., *Adv. Compos. Mater.*, Vol. 5, 1996, pp. 249-252.
2. Friedrich, K., *Application of Fracture Mechanics to Composite Materials*, 1989.
3. Whitney, J.M., Browning, C.E. and Hoogsteden, W., *J. Reinf. Plast. Compos.*, Vol. 1, 1982, pp. 297-313.
4. Hashemi, S., Kinloch, A.J. and Williams, J.G., *Proc. Roy. Soc.*, Vol. A-427, 1990, pp. 173-199.
5. Hojo, M., Kageyama, K. and Tanaka, K., *Composites*, Vol. 26, 1995, pp. 243-255.
6. Atkins, A.G. and Mai, Y.W., *Elastic and Plastic Fracture*, Ellis Horwood, 1985.
7. Aliyu, A.A. and Daniel, I.M., *ASTM STP 876*, 1985, pp. 336-348.
8. Gillespie, J.W., Carlsson, L.A. and Smiley A.J., *Compos. Sci. Tech.*, Vol. 28, 1987, pp. 1-15.
9. Maikuma, H., Gillespie, J.W. and Wilkins, D.J., *J. Compos. Mater.*, Vol. 24, 1990, pp. 124-149.
10. Kusaka, T., Yamauchi, Y. and Kurokawa, T., *Journal de Physique IV*, Vol. C-8, 1994, pp. 671-676.
11. Kurokawa, T., Kusaka, T., Shimazaki, T., Yamauchi, Y. and Kawashima, T., *Proc. IUTAM Symposium*, Japan, 1995, pp. 217-224.
12. Kageyama, K., Kimpara, I., Ohsawa, I., Hojo, M. and Kabashima, S., *ASTM STP 1230*, 1995, pp. 19-37.
13. Kusaka, T. and Kurokawa, T., *J. Soc. Mat. Sci. Jpn.*, Vol. 45, 1996, pp. 445-450, (*in Japanese*).
14. Kusaka, T., Kurokawa, T., Hojo, M. and Ochiai, S., *unpublished research*.
15. Mai, Y.W. and Atkins, A.G., *J. Mater. Sci.*, Vol. 10, 1975, pp. 2000-2003.
16. Dugdale, D.S., *J. Mech. Phys. Sol.*, Vol. 8, 1960, pp. 100-108.
17. Gledhill, R.A., Kinloch, A.J., Yamini, S. and Young, R.A., *Polymer*, Vol. 19, 1978, pp. 574-582.

# TOUGHNESS OF MARINE COMPOSITES: DELAMINATION RESISTANCE UNDER STATIC LOADING

P. Compston<sup>1</sup>, P.Y.B. Jar<sup>1</sup>, P.J. Burchill<sup>2</sup> and G. Simpson<sup>2</sup>

<sup>1</sup> *Department of Engineering, The Australian National University,  
Canberra, ACT 0200, Australia*

<sup>2</sup> *Defence Science and Technology Organisation, Aeronautical and Maritime Research  
Laboratory, G.P.O. Box 4331, Melbourne, Victoria 3001, Australia*

**SUMMARY:** The effect of fibre lay-up and matrix toughness on the Mode I and Mode II static delamination resistance of glass fibre reinforced marine composites has been investigated. Woven roving and unidirectional laminates were made using two vinyl ester matrices of different toughness. Testing methods followed the ESIS Protocol for Interlaminar Fracture of Composites. Results for crack initiation in Mode I are consistent with matrix toughness but independent of fibre lay-up. Small scatter of results for unidirectional fibre suggests that this type of test specimen is more reliable than the woven roving counterpart. In Mode II, results are again consistent with matrix toughness and independent of fibre lay-up.

**KEYWORDS:** delamination resistance, marine, glass fibre, woven roving, unidirectional, vinyl ester.

## INTRODUCTION

The application of fibre-reinforced composites in marine environments is increasingly evident [1, 2]. This is attributed to the high specific strength and stiffness of the composite, and the corrosion resistance and aesthetic qualities of polymer matrices. For economic reasons, glass fibre is the preferred reinforcement in marine composites. Therefore, improvement of any composite property will be cost effective through improvement of matrix properties. Polyester resins have been the most common matrix material in the past but attention is now turned towards vinyl ester due to its superior ageing resistance [3].

Like most laminated composites, marine composites are susceptible to delamination damage [4], therefore it is important to accurately characterise their delamination resistance. Standard test methods are now available to assess Mode I and Mode II delamination

resistance of composites through measurement of  $G_c$  (critical strain energy release rate) [7, 8]. Extensive testing of carbon fibre composites has shown delamination resistance to be influenced by matrix toughness, fibre-matrix bond strength and, in Mode I, fibre bridging [9-11]. However, most studies have, in accordance with the test standards, used specimens with unidirectional fibres. While this may give a lower bound value for  $G_c$ , it does not reflect the type of fibre lay-up used in the marine industry, such as woven roving.

This paper examines the effect of fibre lay-up and matrix toughness on the Mode I and Mode II static delamination resistance of marine composites. Woven roving and unidirectional fibres with two vinyl ester matrices of different toughness were used for the study.

## MATERIALS

Woven roving E-glass fibres with a silane sizing (Colan AR106) were used for this study. The linear density of fibres in the warp and weft yarns was 1.2 and 1.8 tex (g/m) respectively. The nominal construction was 295 yarns/m in the warp direction and 158 yarns/m in the weft direction. The overall fibre density is therefore 354 g/m<sup>2</sup> and 284 g/m<sup>2</sup> for warp and weft respectively. Unidirectional plies were obtained by removing the weft yarns from the original woven roving plies. Two weft yarns were glued at either end of the ply to act as binders. A schematic of the woven roving (WR) and unidirectional (UD) plies used for laminate fabrication is shown in Fig.1.

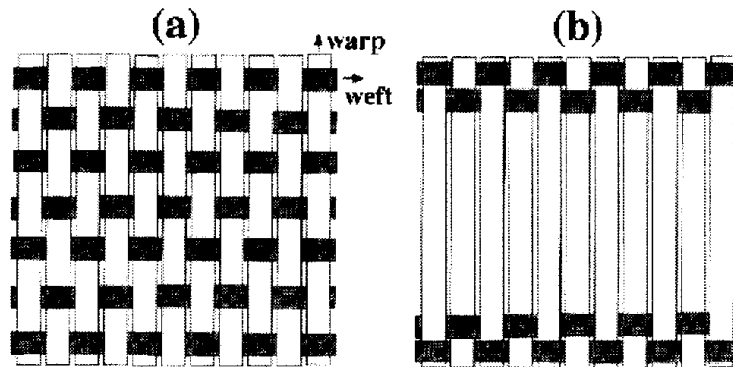


Figure 1: Schematic of E-glass fibre plies used for laminate fabrication; (a) woven roving (WR) and (b) unidirectional (UD).

Two Dow Derakane vinyl ester resins, 411-45 and 8084, were chosen as the matrix materials. The 8084 vinyl ester is elastomer-modified to increase toughness. The supplier-provided tensile properties and fracture toughness [12] of each resin are given in Table 1. It shows the toughness of the 8084 resin to be greater than the 411-45 resin. In the rest of the text, an abbreviation will be used for each composite which relates to the fibre lay-up and the matrix resin. For example, UD/411-45 refers to the composite containing unidirectional fibres and the Dow 411-45 resin.

Table 1: Matrix resin properties

Resin	Tensile strength (MPa)	Tensile Modulus (GPa)	Elongation (%)	Fracture Toughness ( $G_{Ic}$ ) (KJ/m <sup>2</sup> )
411-45	76-83	3.4	5-6	0.167
8084	69-76	3.2	10-12	0.508

Laminates were made by hand lay-up using a vacuum bag. Woven roving and quasi-unidirectional laminates were made for each matrix, producing a total of 4 laminates. The woven roving laminates contained 10 plies whereas the quasi-unidirectional laminates contained 4-ply WR regions on either side of a central, 4-ply, UD region. A piece of aluminium (Al) foil, 15 $\mu$ m thick and 75mm long, inserted at the mid-thickness of each laminate acted as a starter crack. The Al foil was oriented to facilitate crack propagation parallel to the warp direction in the woven roving composites and parallel to the UD fibres in the quasi-unidirectional composites. After an initial room temperature cure, each laminate was post-cured at 90°C for 4 hours. Fibre volume fraction in each composite was approximately 45%. Test specimens were cut from the laminates using a water-cooled diamond saw, then dried in a vacuum oven for 12 hours. The UD laminates were trimmed so that the weft binding fibres did not form part of the test specimen.

## EXPERIMENTAL PROCEDURES

Mode I double cantilever beam (DCB) and Mode II end notch flexure (ENF) tests were conducted in accordance with the ESIS Protocols for Interlaminar Fracture Testing of Composites [7]. Testing was conducted in displacement control on an Instron 4505 Universal Testing Machine. A minimum of 4 specimens from each composite were tested. The specimens were not pre-cracked from the insert film.

### Mode I DCB

The DCB specimen geometry used for Mode I testing is shown in Fig.2. The thickness ( $2h$ ) was approximately 6mm, width ( $B$ ) 20mm and length sufficient to allow at least 100mm of crack growth. Loading was introduced through aluminium blocks that were attached to the end containing the crack starter film. One edge along the specimen length was covered with a thin layer of white correction fluid and then marked at 1mm intervals. This enabled crack identification and measurement during the test. Testing speed was 2mm/min and a load/displacement plot was produced for each test. The load and displacement data were recorded for each individual crack length measurement. The Mode I critical strain energy release rate,  $G_{Ic}$ , was calculated using the corrected beam theory method [13]:

$$G_{Ic} = \frac{3P\delta}{2B(a + |\Delta|)}$$

where  $P$  is load,  $\delta$  displacement,  $B$  specimen width,  $a$  crack length and  $\Delta$  is a crack length correction factor, the value for which is given by the x-axis intercept on a plot of the cube root of compliance,  $C^{1/3}$  (where  $C = \delta/P$ ), versus crack length.



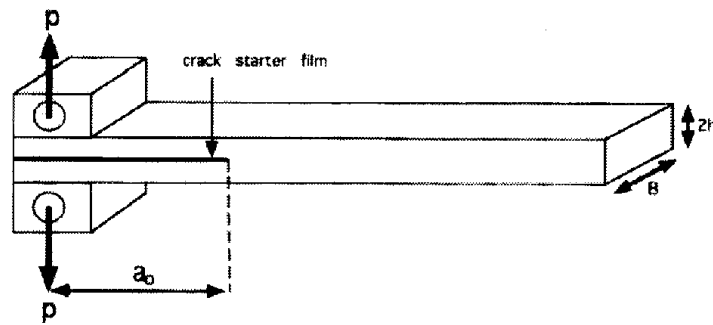


Figure 2: Mode I DCB test specimen geometry with initial crack length  $a_0$ .

Values of  $G_{Ic}$  were plotted as a function of crack length to produce a resistance (R) curve. For all composites, results were obtained for crack initiation,  $G_{Ic-imit}$ , defined as the first deviation from linearity on the load/displacement plot. Results for steady state crack propagation  $G_{Ic-prop}$ , defined by a plateau on the R-curve, were obtained for both UD composites, but not for the WR composites due to unstable crack growth. This type of behaviour was previously observed in other work [14], where an average  $G_{Ic}$  value was calculated for short periods of stable crack growth and for the onset and arrest of unstable crack growth. The same approach was taken for the WR composites in this study.

### Mode II ENF

The ENF specimen geometry used for Mode II testing is shown in Fig.3. The thickness was approximately 6mm, width 20mm and length 160mm. The specimen was placed in a 3-point bending fixture with half span length,  $L$ , set at 50mm and the ratio of crack length to half span length,  $a/L$ , maintained at 0.5.

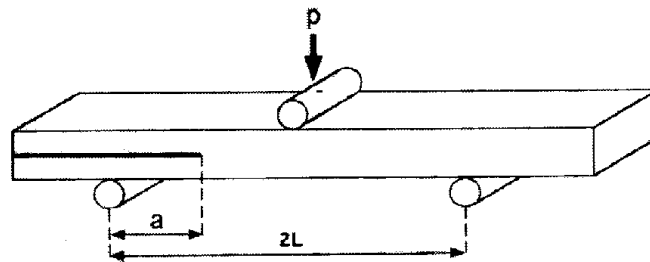


Figure 3: Mode II ENF test specimen geometry.

The Mode II critical strain energy release rate,  $G_{IIc}$ , was calculated using direct beam theory [6]:

$$G_{IIc} = \frac{9a^2 P \delta}{2B(2L^3 + 3a^3)}$$

Values for  $G_{IIc}$  at the maximum load point,  $G_{IIc-max}$ , for both the UD and WR composites were calculated. (Due to indistinct non-linear points on the load/displacement plots, values for crack initiation were not calculated).

## RESULTS AND DISCUSSION

### Mode I DCB

Typical load/displacement plots for UD/411-45 and WR/411-45 are shown in Fig.4. Their profiles are also typical for UD/8084 and WR/8084. In the UD composites crack propagation was stable and a large fibre bridging zone consisting of individual fibres was observed. In contrast, for the WR composites there were many instances of unstable fracture and few periods of stable fracture in which crack length measurements could be made. The fibre bridging zone for these composites was small and evidence of extensive fibre "nesting", involving the weft fibres, was observed on the fracture surface. These areas corresponded to the crack length at which unstable fracture occurred, indicating that simultaneous failure of the "nested" bridging fibres was responsible for the unstable crack growth.

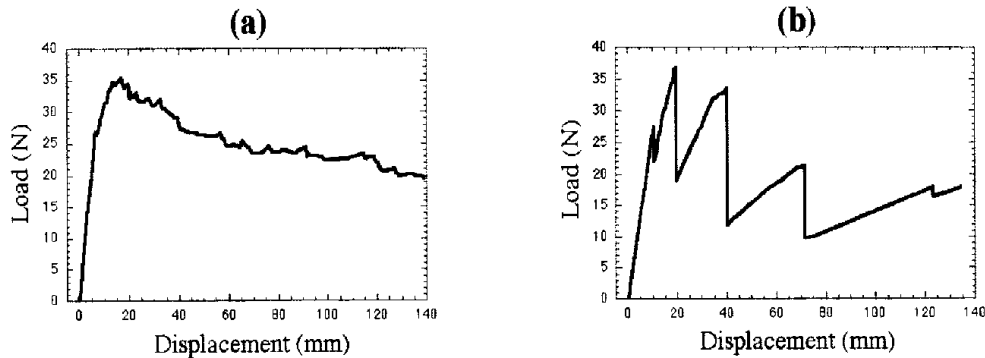


Figure 4: Mode I load/displacement plots; (a) UD/411-45 and (b) WR/411-45.

R-curves for UD/411-45 and WR/411-45 are shown in Fig.5. The profiles are again representative of the R-curves for UD/8084 and WR/8084. In each R-curve the first value signifies the onset of crack growth and is taken as the  $G_{Ic-init}$  value. For UD/411-45 there is a distinct region of steady-state crack propagation from which a  $G_{Ic-prop}$  value can be calculated. In the same region on the WR/411-45 R-curve there are only a few  $G_{Ic}$  values. The higher  $G_{Ic}$  values correspond to the onset of unstable fracture and the lower values correspond to crack arrest. The stable  $G_{Ic}$  values that could be obtained for the WR composites tend to lie in between those for onset and arrest, and do not form a distinct region of steady-state crack propagation. It is also noted that in Fig.5(b), some stable and onset  $G_{Ic}$  values occur at the same crack length. This is due to crack "sticking" behaviour after periods of stable crack growth, whereby crack length at onset points corresponded to the last recorded crack length during stable crack growth.

To facilitate comparison, bar charts with clear and shaded backgrounds have been used to present results for composites with the 411-45 and 8084 matrices respectively. Results

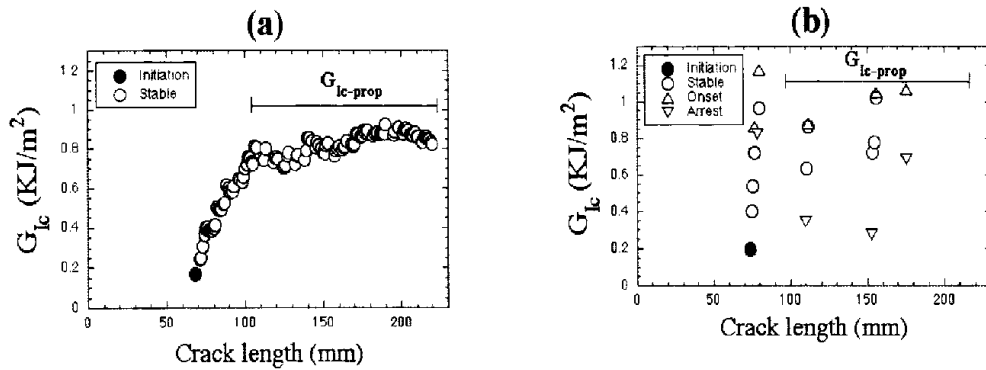


Figure 5: Mode I R-curves; (a) UD/411-45 and (b) WR/411-45.

for crack initiation,  $G_{Ic-init}$ , are shown in Fig.6(a) and Fig.6(b). The composites with the tougher 8084 matrix have a higher  $G_{Ic-init}$  than the composites with the 411-45 matrix. Where the matrix is the same, the WR composites have a marginally higher absolute  $G_{Ic-init}$  value. However, when standard deviation (represented by the error bar) is considered the results are similar. Therefore, the results mainly indicate  $G_{Ic-init}$  in these composites to be independent of fibre lay-up and dominated by matrix toughness.

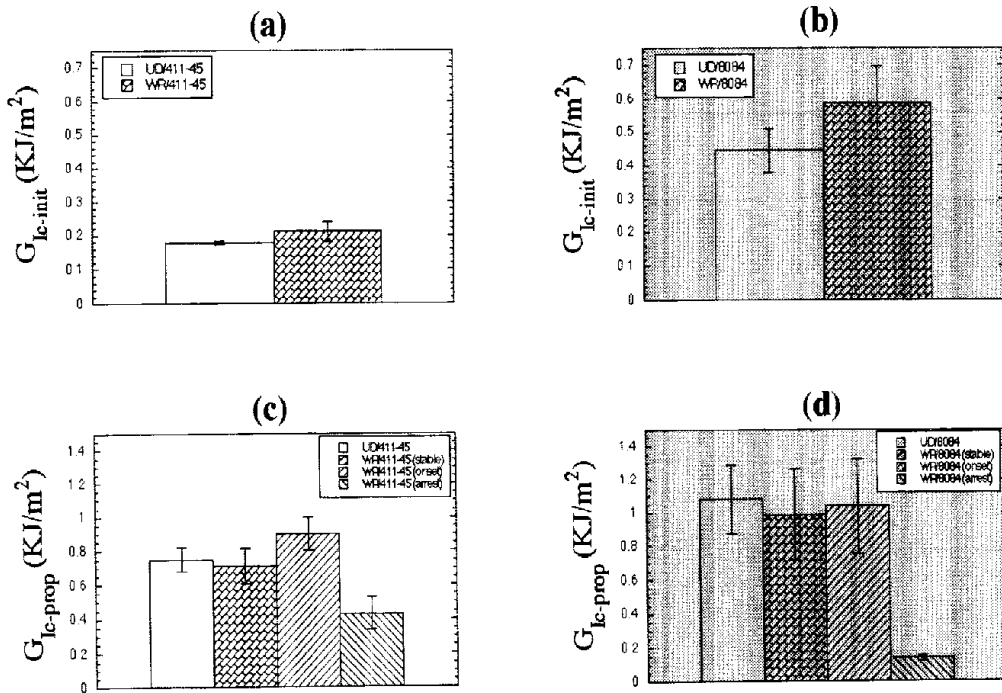


Figure 6: Mode I results for crack initiation; (a) UD-WR/411-45, (b) UD-WR/8084; and crack propagation (c) UD-WR/411-45, and (d) UD-WR/8084.

The  $G_{Ic}$  results for stable and unstable crack propagation are shown in Fig.6(c) and Fig.6(d). The  $G_{Ic-prop}$  values for UD/411-45 and UD/8084 are consistent with matrix toughness. However, due to fibre bridging the difference is not as significant as for the  $G_{Ic-init}$  results. Where the matrix is the same, the  $G_{Ic-prop}$  value for the UD composite is similar to the stable  $G_{Ic}$  value in the WR composite. However, the large standard deviation for the WR results reflects the low number of stable  $G_{Ic}$  values that could be obtained from the tests on the WR composites. There is a large variation in the results for onset and arrest of unstable crack propagation. This would also be a source of variation in any average value for stable  $G_{Ic}$  if stable crack growth occurred close to either an onset or arrest point.

Fracture surface micrographs of UD/411-45 and UD/8084 are shown in Fig.7(a) and Fig.7(b) respectively. They show greater deformation in the 8084 resin than in 411-45 and this is consistent with the matrix toughness. They also show very little matrix attached to the fibres after fracture in both composites. Therefore, since the interface characteristics are the same, the micrographs support the conclusion that both  $G_{Ic-init}$  and  $G_{Ic-prop}$  are dominated by the matrix. Fig.7(a) and Fig.7(b) are also representative of the fracture surface in the warp regions of the WR composites.

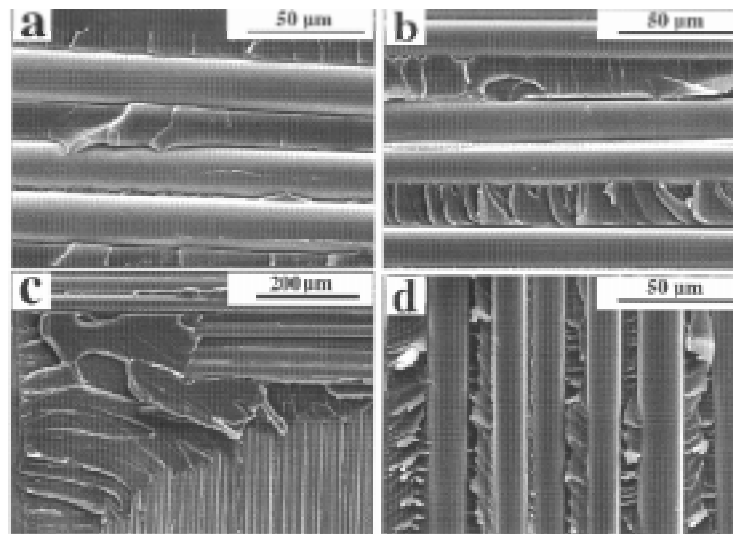


Figure 7: Mode I fracture surface micrographs; (a) UD/411-45, (b) UD/8084, (c) resin pockets in WR/8084 and (d) weft region in WR/8084.

In both the WR/411-45 and WR/8084 composites large resin pockets were observed at the intersection of the warp and weft yarns, such as that shown in Fig.7(c). These resin pockets could explain the marginally higher absolute  $G_{Ic-init}$  values, and greater scatter, obtained for the WR composites. Matrix deformation was observed to be even more extensive between the fibres in the weft yarns, as illustrated through a comparison of Fig.7(d) from WR/8084 and Fig.7(b) from UD/8084.

**Mode II ENF**

Typical load/displacement plots for UD/411-45 and WR/411-45 are shown in Fig.8. Their profiles are also typical for UD/8084 and WR/8084. At the maximum load point in the UD/411-45 composite there is only one instance of unstable fracture, after which the crack was observed to have extended to the mid-point of the span length. In the WR/411-45 unstable fracture occurred several times beyond the maximum load point until the crack reached a similar position. The  $G_{IIc-max}$  value for the WR composites was calculated using the maximum load point immediately prior to the first instance of unstable fracture, even if a higher load point was consequently reached.

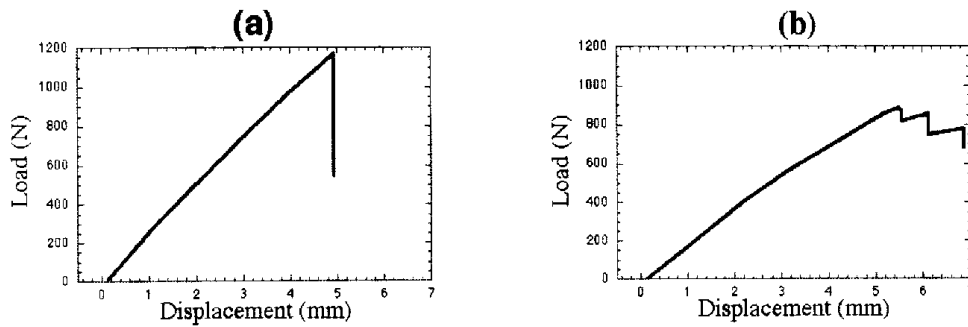


Figure 8: Mode II load/displacement plots; (a) UD/411-45 and (b) WR/411-45.

The results for  $G_{IIc-max}$  are shown in Fig.9. The composites with the tougher 8084 matrix have a higher  $G_{IIc-max}$  value than the composites with the 411-45 matrix. The results also show that, within scatter, the  $G_{IIc-max}$  is similar for both the WR and UD composites when the matrix is the same.

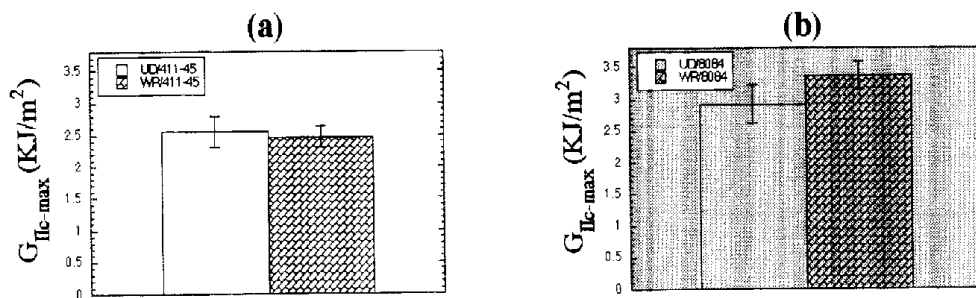


Figure 9: Mode II results for maximum load; (a) UD-WR/411-45, and (b) UD-WR/8084.

Fracture surface micrographs of UD/411-45 and UD/8084 are shown in Fig.10(a) and Fig.10(b) respectively. There is extensive hackle mark deformation in both matrices, with little matrix still attached to the fibres. The hackle mark density is marginally

higher in the 8084 resin. These observations support the conclusion that  $G_{IIc-max}$  is matrix dominated and the order of results will be consistent with matrix toughness. Broken bridging fibres were observed in both the WR/411-45 and WR/8084 composites, as illustrated in Fig.10(c). This could explain why unstable fracture in these composites occurred in steps. The influence of bridging fibres may also have had a restraining effect on matrix deformation, and so explain the lower hackle mark density observed in the warp regions of the WR composites, in contrast to the UD composites. This is illustrated when Fig.10(d) from WR/8084 is compared with Fig.10(b) which is from UD/8084.

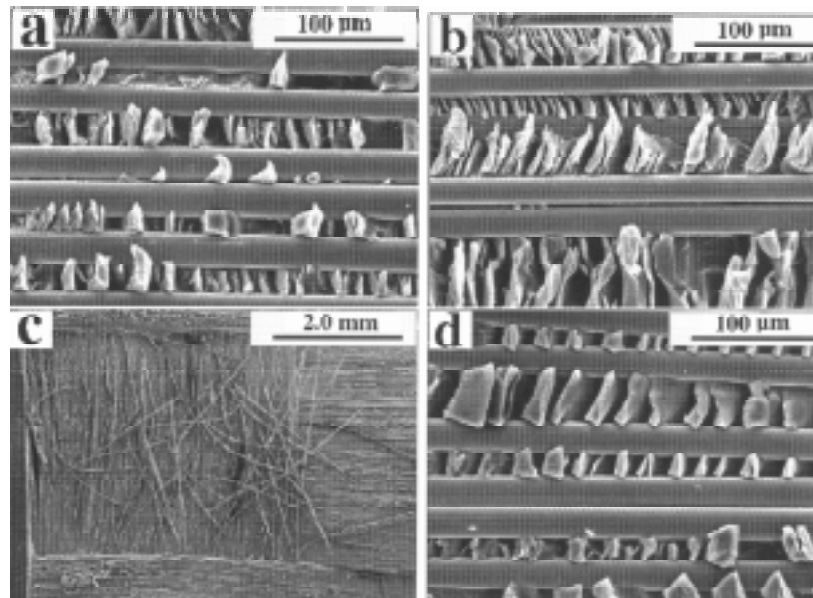


Figure 10: Mode II fracture surface micrographs, (a) UD/411-45, (b) UD/8084, (c) bridging fibres in WR/8084 and (d) warp region in WR/8084.

## CONCLUSIONS

Mode I DCB and Mode II ENF static delamination tests were conducted to study the effect of fibre lay-up and matrix resin toughness in marine composites. Results for crack initiation in Mode I were consistent with the order of matrix toughness and independent of fibre lay-up. Results for steady-state crack propagation in Mode I for the unidirectional composites were also consistent with matrix toughness, but due to fibre bridging the difference was not as significant as for crack initiation. R-curves for the woven roving composites only produced a small number of stable  $G_{Ic}$  values compared to the unidirectional composites, consequently there was greater scatter in the results. For the purposes of material comparison, results from unidirectional specimens are more reliable. Where fibre lay-up was the same, the results for the maximum load point in Mode II were consistent with matrix toughness. Where the matrix was the same, the results showed little variation due to fibre lay-up. However, for the woven roving composites there was evidence of fibre bridging, and the extent to which this may affect Mode II results requires further investigation.

## References

- [1] Nautical Construction in Composite Materials, *Proc. 3rd Ifremer conference*, eds. P. Davies and L. Lemoine, Paris, Dec. 1992.
- [2] Marine Applications of Composite Materials, *Proc. 6th international conference*, Florida, March 1996.
- [3] Gutierrez J., Le Ley F. and Hoarau P., "A Study of the Aging of Glass Fibre Resin Composites in a Marine Environment". *Int. Conf. Nautical Construction with Composite Materials*, P. Davies and L. Lemoine, eds. Paris, 1992, pp. 338-346.
- [4] Barnouin B. and Renaud P., "Damage Observed During Inspection of Composite Pleasure Boats". *Int. Conf. Nautical Construction With Composite Materials*, P. Davies and L. Lemoine, eds. IFREMER. Paris, 1992, pp. 389-393.
- [5] Davies P. & Benzeggagh M.L., "Interlaminar Mode-I Fracture Testing". Chapter 3 in *Application of Fracture Mechanics to Composite Materials*. K. Friedrich ed. Elsevier Science Publishers, B.V. 1989, 81-112.
- [6] Carlsson L.A. & Gillespie J.W., "Mode-II Interlaminar Fracture of Composites". Chapter 4 in *Application of Fracture Mechanics to Composite Materials*. K. Friedrich ed. Elsevier Science Publishers, B.V. 1989, 113-157.
- [7] European Structural Integrity Society (ESIS), *Protocols for Interlaminar Fracture Testing of Composites*, 1993.
- [8] ASTM D5528-94a Standard Test Method for Mode I Interlaminar Fracture Toughness of Unidirectional Fiber-Reinforced Polymer Matrix Composites.
- [9] Hibbs M.F., Tse M.K. and Bradley W.L., "Interlaminar Fracture Toughness and Real-Time Fracture Mechanism of Some Toughened Graphite/Epoxy Composites". *Toughened Composites* ASTM STP 937, 1987, pp. 115-130.
- [10] Madhukar M.S. and Drzal L.T., "Fiber-Matrix Adhesion and its Effects on Composite Mechanical Properties: IV. Mode I and Mode II Fracture Toughness of Graphite/Epoxy Composites". *Journal of Composite Materials* **26(7)**, 1992, pp. 936-968.
- [11] Albertsen H., Ivens J., Peters P., Wevers M. and Verpoest I., "Interlaminar Fracture Toughness of CFRP Influenced by Fibre Surface Treatment: Part I. Experimental Studies". *Composites Science and Technology* **54**(1995), pp. 133-145.
- [12] Simpson G.J., Pearce P.J. and Burchil P.J., "Tougher Vinyl Ester Resins and their Fibre Glass Composites", *20th Australian Polymer Symposium*, (RACI Polymer division), Adelaide, South Australia, February 5-9, 1995, pp. 333-334
- [13] Hashemi S., Kinloch A.J. & Williams J.G., "Corrections Needed in Double Cantilever Beam Tests for Assessing the Interlaminar Failure of Composites". *Journal of Materials Science Letters* **8**(1989) pp. 125-129.
- [14] Davies P. & Moore D.R., "Glass/Nylon-6.6 Composites: Delamination Resistance Testing". *Composites Science and Technology* **38**(1990) 211-227.

# IMPROVED INTERLAMINAR FRACTURE TOUGHNESS FOR VINYL ESTER RESIN - FIBRE GLASS COMPOSITES

**Peter J. Burchill and Gary J. Simpson**

*Ship Structures and Materials Division,  
Aeronautical and Maritime Research Laboratory, DSTO,  
PO Box 4331, Melbourne, Victoria 3001, Australia.*

**SUMMARY:** Toughening the matrix using modified acrylonitrile - butadiene copolymers improves the delamination resistance of vinyl ester resin - glass woven roving composites. Analysis of the largest (or smallest) measurements of toughness by extreme value theory shows that the improvement to the matrix resin is fully transferred to the composite. The glass content of the composite does not appear to determine the delamination resistance for contents of 38 - 70 vol%. For the composites used in this study the contribution to interlaminar fracture toughness by the reinforcement ranges from 0 to 1400 Jm<sup>-2</sup>.

**KEYWORDS:** delamination resistance, extreme value theory, vinyl ester resins, acrylonitrile / butadiene copolymers, woven glass roving reinforcement

## INTRODUCTION

Fracture in cloth - resin composites occurs most easily parallel to the reinforcement between the layers of cloth resulting in delamination of the composite and a large reduction in compressive strength. Generally tensile loading produces this delamination, and the cracks grow at the fibre-matrix interface or through failure of the matrix resin, or a combination of both. Improvement of the fracture toughness of composite structures will require the suppression of this crack growth. Most studies of fracture in composites have looked at unidirectional fibre - epoxy resin based materials [1], but vinyl ester resin composites are just as prone to delamination which is governed by the brittle nature of the matrix and the fibre - matrix bond. From previous studies, two energy absorbing mechanisms can be identified contributing to the delamination resistance; energy is absorbed by deformation of the resin or by the effects of fibres bridging the crack [2-6]. Bridging fibres absorb energy through their being pulled out of the matrix and through fracture. Another mechanism by which the fracture energy may be increased is by crack deflection which may arise due to imperfections in the composite or through local changes in fibre orientation, that will be experienced with cloth - based composites.

Vinyl ester resins (VE) are typically a mixture of methacrylate esters produced from epoxy resins diluted with other monomers such as styrene and are generally cured at room temperature to give materials with a much higher resistance than polyester resins to moisture and corrosive chemicals. A commonplace VE resin is made from the diglycidylether of bisphenol A and is the work horse of the vinyl ester resin market. A feature which gives these



resins a strong advantage over epoxy resins apart from price is that they can be formulated to provide almost any desired pot-life. Studies of the properties of bulk castings show them to be brittle, however recent work on toughening has shown that large improvements in toughness can be gained by the addition of suitable reactive liquid polymers (RLP) which yield a separated elastomeric phase upon cure [7,8]. This study will examine how well the improvement in resin bulk properties transfer to VE resin / glass fibre composites.

The hand lay-up and vacuum bagging method of composite fabrication was suspected of not being very reproducible in terms of glass to resin ratio, in addition, toughened resins have a higher viscosity which will affect resin wet-out and flow in the preparation of the composite. Hence, no attempt was made to control the glass content, but rather allow deliberate variation in the process to give a glass to resin ratio which was as wide as practicable between composites. In this way, a more confident comparison was expected of the influence different resins have on composite toughness. This approach was hoped would also provide data on the fibre bridging and weave effects of the reinforcement which were suspected of being influenced by resin content.

## **EXPERIMENTAL**

### **Materials**

Two vinyl ester resins used were: Derakane® 411 (Der 411) a standard bisphenol A epoxy based vinyl ester resin, and Derakane® 8084 (Der 8084) a toughened version of Der 411 internally modified with a reactive acrylonitrile - butadiene copolymer during manufacture. The additives were: a vinyl terminated acrylonitrile - butadiene copolymer (BF Goodrich VTBN X33) and a BF Goodrich carboxy terminated acrylonitrile - butadiene copolymer pre-reacted with an aliphatic oligomeric epoxide (S22) [9]. The reinforcement was a woven roving - AR106, Colan Products Pty. Ltd., nominal areal density 630 g/m<sup>2</sup> - with a vinyl ester resin compatible finish. The structure of the cloth was warp 29.5 yarns per 10cm, 1200 tex., and weft 15.8 yarns per 10cm, 1800 tex. All other materials were commercial chemicals used as received.

### **Resin Cure and Composite Fabrication**

The resins and their blends with the additives were cured at room temperature using the catalyst system cobalt octoate (0.3 pph, of a 41% wt/vol solution in white spirit) and methylethylketone peroxide (1.5 pph, of a 40% dimethyl phthalate solution), and the gel time was adjusted with dimethylaniline (accelerator) and 2,4-pentanedione (retarder). Curing of all resin systems was completed overnight at room temperature then for 90 minutes at 90°C. The test methods used for evaluating bulk properties were, Heat Distortion Temperature (ASTM D648), T-Peel (ASTM D1876) and fracture toughness from double torsion geometry [10].

Various techniques were used to alter the glass : resin ratio in the hand lay-up/vacuum bagging method, involving timed application of vacuum, and pot formulations to change gel times. The composite panels were assembled with 16 plies of cloth (300mm x 500mm) cut with the warp direction measuring 300mm. A thin Teflon® film was placed as a de-bond zone between the 8<sup>th</sup> and 9<sup>th</sup> plies to give an initial crack of about 50mm in the test specimens.

## Fracture Resistance

Double Cantilever Beam (DCB) specimens (25 x 190mm) with the long axis parallel to the warp direction were cut from the composite panels with the de-bond layer at one end. To load the specimen, tabs were attached to the de-bond end; and one side of the specimen was painted with whitener to aid observation of the crack and marking its length. The specimen was carefully put under a tensile load to open the de-bonded zone and pre-cracked to about 52 mm from the beginning. The specimen was then unloaded to its original position, and the Instron Testing Machine (Model 4502) set at a crosshead speed of 2 mm/min. When a pre-determined crosshead displacement was reached, the specimen was unloaded by about 5% of the displacement before marking the crack length. The first measurement was generally between 60 to 75 mm from the open end of the beam. The corresponding load and displacement before the unloading were recorded automatically by the computer. Further measurements were taken until 12 measurements (excluding the initial crack length) were recorded. After the test, the specimen was unloaded and crack lengths were measured using a travelling microscope with all measurements taken from the tab-end.

Load (P), displacement (d) and crack length (a) data were analysed by two methods, one due to Hashemi, Kinloch and Williams [11] and another due to Rosensaft [12]. Both methods of data reduction gave essentially the same values for fracture toughness and the values reported here are from analysis using equations given by Hashemi et al.

Compliance ( $C = P/d$ ) is related to specimen dimensions and material properties by:

$$C = 8N \cdot \frac{(a + \chi h)^3}{Bh^3 E_{11}} \quad (1)$$

N is a correction factor which accounts for the stiffening effects of the attachments required to load the specimen and corrections due to large displacements and attachment tilting, other symbols are: thickness 2h, width B, modulus  $E_{11}$ . The term  $\chi h$ , adjusts the measured crack length for compliance of the un-cracked part of the specimen [11,13,14].

Strain energy release rate ( $G_I$ ) is calculated from:

$$G_I = (F/N) \cdot 3P\delta / 2B(a + \chi h) \quad (2)$$

F is a factor which corrects for the shortening of the crack length due to large displacements. Equations for F and N can be found in references [11,14].

## RESULTS AND DISCUSSION

### Matrix Resins

The ability of the rubber additives to improve adhesion and crack resistance of the vinyl ester resin Der 8084 is detailed in Table 1. A marked improvement in peel strength is achieved by the addition of either rubber, and similar improvements are seen in the fracture energy of the castings. The lowering of HDT due to the rubber should also be noted, and is an unfortunate consequence of rubber toughening of any type of resin

*Table 1: Properties of the resin systems*

Resin	Additive	Fracture Energy kJ/m <sup>2</sup>	Peel Strength N/mm	HDT °C
411	NONE	0.13	0.5	101
8084	NONE	0.4	0.9	80
8084	6.86% X33	1.40	2.31	73
8084	6.86% S22	2.40	3.01	70

### Composite Properties

A minimum of five specimens was tested from each composite panel, and from each specimen generally twelve measurements of toughness were obtained as the crack propagated between the plies. Load deflection curves for these composites showed that crack growth generally progressed by stick / slip with some continuous slow crack growth regions which were greater in extent with toughened matrix resins.

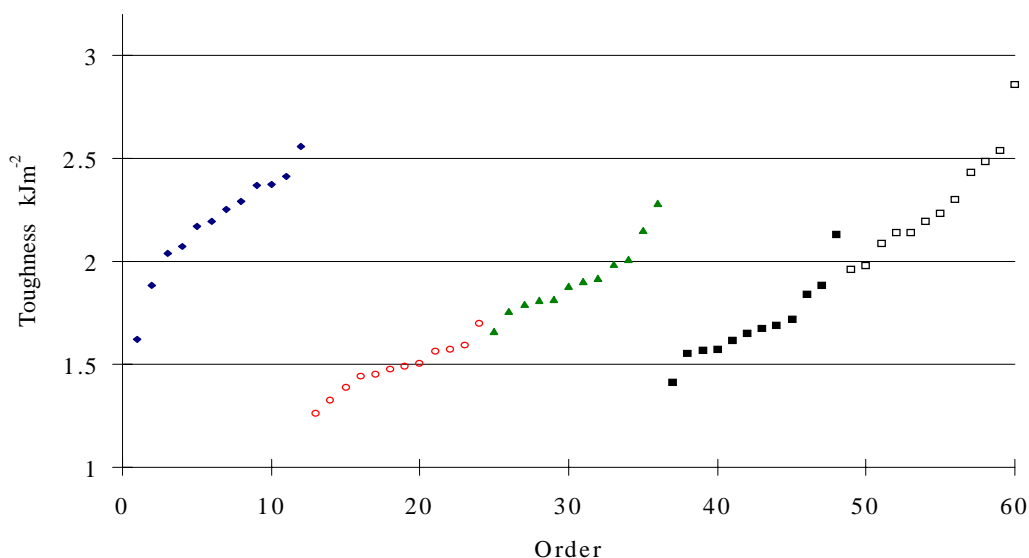


*Fig. 1: Toughness measurements on Der 8084 + X33 composite specimens*

Despite the uniformity with which a particular composite was made, it was apparent early in the project that the specimens were not the same, and there was a wide variation in calculated toughness values in one specimen associated with crack initiation and arrest. Fig. 1 gives the toughness values from the five specimens of a Der 8084 + X33 composite. The values for each specimen have been placed in serial order and is not the order in which they were determined, toughness measurements did not depend on position along the specimen.

An analysis of variance showed that the specimens were not identical, and a similar result was found for all the composite panels. Nevertheless, if the compliance measurements for each specimen are normalised for variation in thickness and width, and plotted as the cube root against crack length, all the values fall on a common line as seen in figure 2, and as expected if equation 1 was obeyed. The slope of this line is  $(8/E_{11})^{1/3}$ .

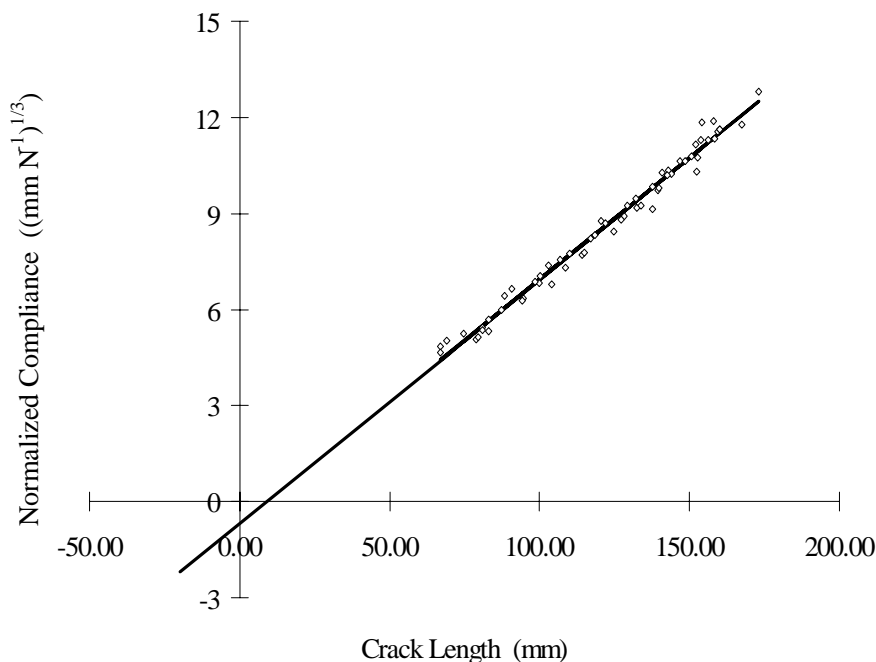


Fig. 2: Compliance data for all specimens tested from a Der 8084 + S22 composite

This agreement in modulus for the specimens from one panel indicates that the variation in toughness is not due to poor fabrication of the panel. The average toughness determined from a composite specimen was always greater than the toughness of the neat resin.

Figure 3 gives a plot for each resin type of the observed average specimen toughness against specimen thickness. Thickness is a function of the glass content which for these composites varied between 38 and 70 volume %, and each line is constructed from measurements on at least four composite panels.

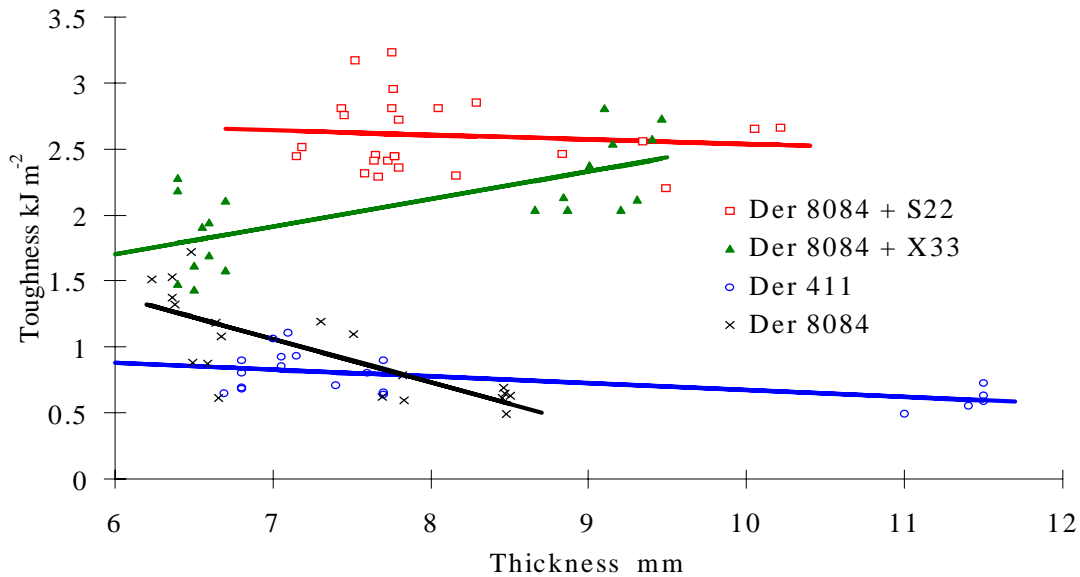


Fig. 3: Variation of toughness with specimen thickness

These results show that there is an increase in toughness of a composite with increase in resin toughness, however, the scatter makes the difference difficult to quantify. The slopes of these lines suggests that there is little or no dependence on glass content. Thus the variation in interlaminar toughness of these composites seems to be determined wholly by the conditions along the plane which the crack is forced to follow. These conditions appear not to be determined by a global glass to resin ratio. Previous work ascribes the toughness of a composite as being determined by the toughness of the resin and by fibre bridging effects [2-6]. Improvements to resin toughness have been said not to be fully transferred to a composite, and that there was a limit above which the benefits of further toughening of the matrix were marginal [3,4].

### Extreme Value Analysis

An alternate analysis of the results has been carried out applying extreme value theory [15,16]. Firstly, because of the very weak dependence on glass content the results from all the composites made from a particular resin were pooled, and the values from each specimen ordered from smallest to largest. Thus from the four composites made with Derakane 411, twenty smallest (or largest) values of toughness were obtained which were again ranked in increasing order. These values have been presented as a Gumbel plot in figure 4, in which the ordinate scale is a function of the cumulative probability ( $F(x)$ ) defined as  $i/(n+1)$  where  $i$  is the rank of a particular value, and  $n$  is the total number of values.

This figure represents the cumulative probability of observing a toughness less than or equal to a given value, and the linearity of the plot indicates a reasonable fit to the Gumbel distribution - a Type 1 asymptotic distribution of smallest or largest extremes. Data from Der 8084 composites are also displayed, and the differences between these two curves probably reflects different interactions of the resin with the reinforcement

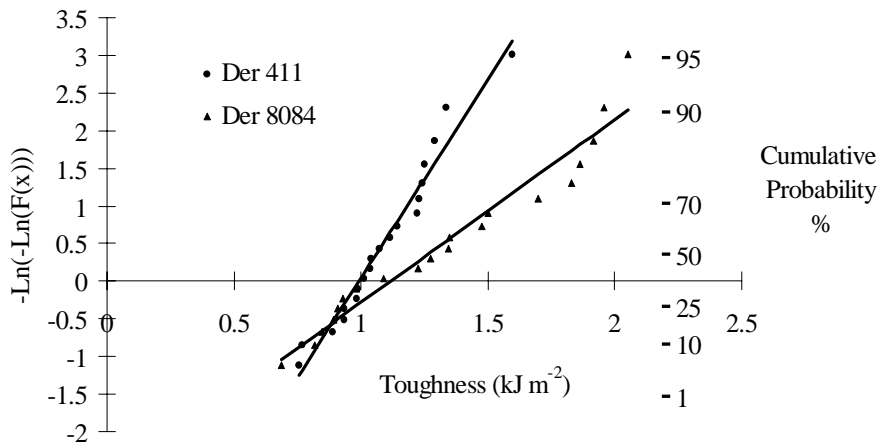


Fig 4: Probability plot of maximum toughness recorded for each specimen

Fig. 5 shows the Gumbel plot for the maximum specimen toughness values for Derakane 8084 blended with S22, and compared with the values obtained from composites with the untoughened resin. Here the advantages of toughening the resin is clearly seen, the offset between the curves is similar to the change in toughness of the neat resin when blended with the additive. Likewise, a plot for Der 8084 + X33 composites gave the improvement to the toughness as an offset of about  $1.1\text{kJm}^{-2}$ . These plots also indicate that the probability of having a toughness less than a specified value is much reduced for composites made with the modified resin.

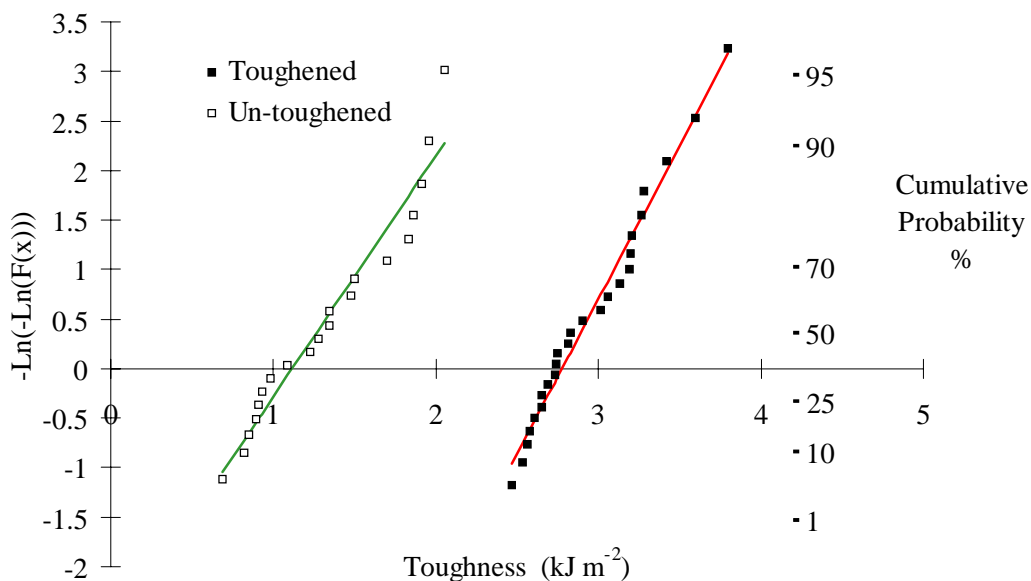


Fig. 5: Probability plot of effect of resin toughening on composite delamination

Because the crack growth behaviour in these composites was seen to be a stick - slip process, then the maximum values observed for each specimen are most likely to be for crack growth initiation. The wide range of these values would then seem to be associated with the varying effects of crack pinning by the glass filaments and from crack deflection as a result of following the undulating surface of the cloth. The smallest of these maximum values could be as a result of initiation from resin rich areas within the composite. Comparison with the largest values then gives a measure of the contribution due to glass fibres and the structure of the cloth.

Table 2 lists these smallest and largest values for the four resin systems , and from the above assumptions the difference gives how much this particular glass cloth might contribute to toughness in a composite. This contribution is thus about 0 to 1.4kJ m<sup>-2</sup> in addition to the toughness of the resin for Der 8084 based composites. Except for the Der 8084 + S22 matrix, the smallest values are much larger than the toughness of the unreinforced resins especially in the case of Der 411, and shows that these values also have a contribution from the reinforcement.

Table 2: Smallest and largest values of the observed maximum toughness

Composite Matrix	Smallest Maximum (kJ m <sup>-2</sup> )	Largest Maximum (kJ m <sup>-2</sup> )	Contribution by Glass Cloth (kJ m <sup>-2</sup> )
Der 411	0.76	1.60	0.84
Der 8084	0.69	2.05	1.36
Der 8084 + X33	1.70	3.19	1.49
Der 8084 + S22	2.47	3.80	1.33

## CONCLUSIONS

The delamination resistance of vinyl ester resin - glass woven roving composites can be greatly improved through toughening the resin. Scatter in the results and the use of average values hides the true advantage of using a toughened resin in a composite to improve interlaminar fracture resistance. However by applying extreme theory to the largest (or smallest ) toughness values recorded from each test specimen, the benefits of increased resin toughness becomes much more apparent. For the resin systems used, the improvement to the resin is clearly transferred to the composite. The reinforcement also contributes a variable amount to the delamination resistance which appears to be between 0 and 1400 Jm<sup>-2</sup>. Global variation in glass content does not appear to be a factor in determining this reinforcement contribution.

## REFERENCES

1. Martin, R.H., "Interlaminar Fracture Characterization: A Current Review", *NASA -CR-187573*, 1991.
2. Slepetz, J.M. and Carlson, L., in 'Fracture Mechanics of Composites', *ASTM Special Technical Publication 593*, 1975, p.143.
3. Bascom, W.D., Bitner, J.L., Moulton, R.J. and Siebert, A.R., "The interlaminar fracture of organic-matrix woven reinforcement composites", *Composites* 1980, 9

4. Hunston, D.L., "Composite Interlaminar Fracture: Effect of Matrix Fracture Energy", *Compos. Technol. Rev.*, Vol. 6, 1984, p. 176.
5. Huang, X.N. and Hull, D., "Effects of fibre bridging on  $G_{Ic}$  of a unidirectional glass / epoxy composite", *Compos. Sci. Technol.*, Vol 35, 1989, p. 283.
6. Briscoe, B.J. and Williams, D.R., "Interlaminar Fracture Toughness of Aramid/Epoxy Laminates", *Compos. Sci. Technol.*, Vol. 46, 1993, p. 277.
7. Pham, S. and Burchill, P.J., "Toughening of Vinyl Ester Resins with Modified Polybutadienes", *Polymer*, Vol. 36, 1995, p. 3279.
8. Burchill, P.J. and Pearce, P.J., "Epoxy Acrylate - Based Resins", *Polymeric Materials Encyclopedia*, Vol. 3, Salamone, J.C., Ed., CRC Press Inc., 1996, 2204.
9. Material synthesised by P.J. Pearce according to information provided by BF Goodrich.
10. Kies, J.A., and Clark, B.J., "Fracture propagation rates and times to fail following proof stress in bulk glass", *Fracture 1969*, Ed., Pratt, P.L., (Chapman and Hall, London, 1969), p. 483.
11. Hashemi, S., Kinloch, A.J. and Williams, J.G., "The analysis of interlaminar fracture in uniaxial fibre-polymer composites", *Proc. Royal Soc.*, Vol. A427, 1990, p. 173.
12. Rosensaft, M. and Marom, G., "A one Specimen Mode I Delamination Test for Composite Materials", *J. Comp. Tech. Res.*, Vol. 10, 1988, p. 114.
13. Kanninen, M.F., "An Augmented Double Cantilever Beam Model for Studying Crack Propagation", *Int. J. Fracture*, Vol. 9, 1973, p. 83.
14. Williams, J.G., "The Fracture Mechanics of Delamination Tests", *J. Strain Anal.*, Vol. 24, 1989, p. 207.
15. Gumbel, E.J., "Statistics of Extremes", Columbia University Press, New York, 1966.
16. Mann, N.R., Schafer, R.E. and Singpurwalla, N.D., "Methods for Statistical Analysis of Reliability and Life Data", John Wiley & Sons Inc., New York, 1974.



# DYNAMIC CRACK PROPAGATION AND PERFORATION OF LAMINATED COMPOSITES USING A SPLIT HOPKINSON PRESURE BAR

Sylvanus N. Nwosu<sup>1</sup> and Gregory J. Czarnecki<sup>2</sup>

<sup>1</sup> *Department of Physics, Dillard University, New Orleans, LA 70122, USA*

<sup>2</sup> *Wright Laboratory, Wright Patterson AFB, Ohio 45433, USA*

## ABSTRACT

A modified high-pressure split Hopkinson bar is developed for dynamic quantification of energy expended in the perforation of composite laminates. Preliminary test results using [ $\pm 45/0/90$ ]<sub>n</sub>s 8-ply, 16-ply, and 32-ply graphite/epoxy laminates demonstrate that a threshold energy exists above which a visible crack will be initiated on the laminate's rear surface. The energy dissipated in the perforation process depends on the laminate's thickness, fiber lay-up, the impact parameters, and the incident stress delivered to the laminate. Failure modes of the composite test specimens are characterized by the level of energy absorption in the perforation process. The average impact energy requirement for damage initiation within the graphite/epoxy system are  $7 \pm 1$  J/ply, 10 J/ply, and  $11 \pm 3$  J/ply for crack initiation on the rear surface, perforation, and plug push-out, respectively.

**KEYWORDS:** perforation, dynamic impact, energy, crack propagation, laminates, Hoskinson bar

## INTRODUCTION

When a projectile is launched into the end of a long bar, the impact produces a transient compressive stress wave. This incident wave travels through the bar with an amplitude defined by the projectile's velocity, a wave length defined by the projectile's length and material, and a velocity equivalent to the speed of sound in the bar. In Kolsky's experiments [1], a split Hopkinson bar was used which consisted of a pair of long axially aligned cylindrical bars of equal diameter. Test specimens were sandwiched between the bars. In the current work, the split Hopkinson bar design is modified to allow perforation of the test laminate while maintaining the ability to assess the mechanical response to high strain rate loading. As a projectile's velocity approaches the ballistic limit (defined as the critical velocity where all of the projectile's kinetic energy is transferred to the target), energy absorbed is largely in the form of damage generation. Of interest in this paper is the quantification of wave-induced damage near the ballistic limit threshold. Compared to conventional ballistic projectile experiments, the Hopkinson bar is ideally suited for examining the effects of projectile (indenter) velocity and the resulting stress wave on damage generated within laminated plates. Hopkinson bar penetration experiments allow precise positioning of the impact site, control of the damage process (through the delivered wave form), and the ability to quantify the damage process through stress wave analysis. Strain rate

sensitivity is investigated by incorporating strain rate and stress wave effects in the perforation process. A detailed review of wave theory that predicts the experimental observation is available in the literature [2,3]. For a mathematical description of material deformation under dynamic impact, it is assumed [1,4] that : 1) The composite plate is elastic and its properties remain unchanged by the impact; 2) the state of the stress over the cross sectional area is one-dimensional and uniaxial; 3) the wave is non-dispersive; 4) the state of the stress at any instant is homogenous and in equilibrium over the entire composite plate; and 5) transverse strain, lateral inertia, and body forces are all negligible. For the current test apparatus, one dimensional wave theory is valid since the wavelength of the incident pulse (610 mm) is more than three times the rod diameter (25.4 mm) and the bars are prismatic with a slenderness ratio  $d/L < 1/50$  [2]. The stress wave rise time is  $15\mu s$  compared to  $5\mu s$  to traverse the diameter of the rod (three times greater). The transient time to traverse a 32-ply composite plate is  $4.3\mu s$ , which is short compared to incident wave's  $122\mu s$  duration. Thus the state of the stress wave in the specimen is homogeneous [4]. An outline pertinent to the present investigation and a complete discussion on fulfillment of the above assumptions are given elsewhere [5].

Modes of failure exhibited by composite material systems are complex and controlled by several energy absorbing mechanisms operative during the perforation process. For the purpose of this investigation, damage is accumulated during three successive stages of *indentation*, *partial penetration*, and *perforation* (complete penetration). Indentation is characterized by a small crater at the contact site with no visible cracking on the laminate's opposite (exit) side. The partial penetration stage involves entrance of the indenter into the plate and is characterized by a deeper crater at the contact site, with visible cracks and bulging on side opposite. With penetration, the number of damaged fibers increases. This reduces the plate's local stiffness and results in decreased resistance to additional damage. Perforation on the other hand is a complete penetration of the indenter through the plate and is characterized by punch-through and plug formation (where visible light can be seen through the plugged hole). Perforation initiates when the indenter's tip emerges from the rear side of the plate. In terms of failure or fracture of the composite, such perforation is exhibited by further growth of the bulge, matrix cracking, fiber failure, plug push out, and extended delamination. Since indentation and perforation are considered special cases of the penetration process, the process will be referred to as penetration.

## EXPERIMENTAL SYSTEM

### Test Apparatus and Instrumentation

The ultimate aim of this project is to achieve a state of penetration analogous to that produced by a projectile at the ballistic limit velocity. To accomplish this, the split Hopkinson bar system is modified at the point of specimen contact. A conical hemispherical-nosed indenter is attached to the incident bar, while a fixture holding the circular test laminate is attached to the transmitter bar. The experiment proceeds by generating a high stress level in the incident bar from a longitudinal impact between a striker and the bar. Specimen failure occurs if the combination of incident stress intensity and duration exceeds a critical value for the laminate [2].

The experimental setup (described below) consists of (1) a stress generating system comprised of a split Hopkinson bar and striker, (2) special fixturing consisting of a specimen holder and

indentor, (3) a stress measuring system made up of sensors (typically resistance strain gages and PVDF sensors), and (4) a data acquisition and analysis system.

*Stress generating system.*

Fig. 1 graphically describes the modified split Hopkinson pressure bar (SHPB), the special fixture and perforation assembly. A detail description of the configuration can be found in reference 4. The modified SHPB apparatus consists of incident, transmitter, and striker bars (300 maraging AMS 6414 steel), each being 0.0254 m (1-in) in diameter. The incident and transmitter bars are 3.66 m (12 ft) in length, where the striker bar is 0.305 m (1 ft) long. The striker is housed inside a 0.610 m (2 ft) launch cylinder and is driven by compressed air of up to 1.72 MPa (250 psi). The perforation assembly system consists of the indentor and specimen support that holds the laminated plate. The fixture is sandwiched between the incident and transmitter bars as shown in the Fig. 1 insert.

*Stress measuring system*

The stress measuring system consists of resistance strain gages. Data collection is initiated through an external trigger circuit (using a 6 volt battery) which is completed by electrical contact between the striker and the incident bar.

*Data acquisition system*

The data acquisition system consist of a Nicolet Pro 42 digital oscilloscope. Incident, reflected, and transmitted waves are recorded at a rate of 20 million samples per second. Signal analysis is completed using a Nicolet Spectrum Analyzer.

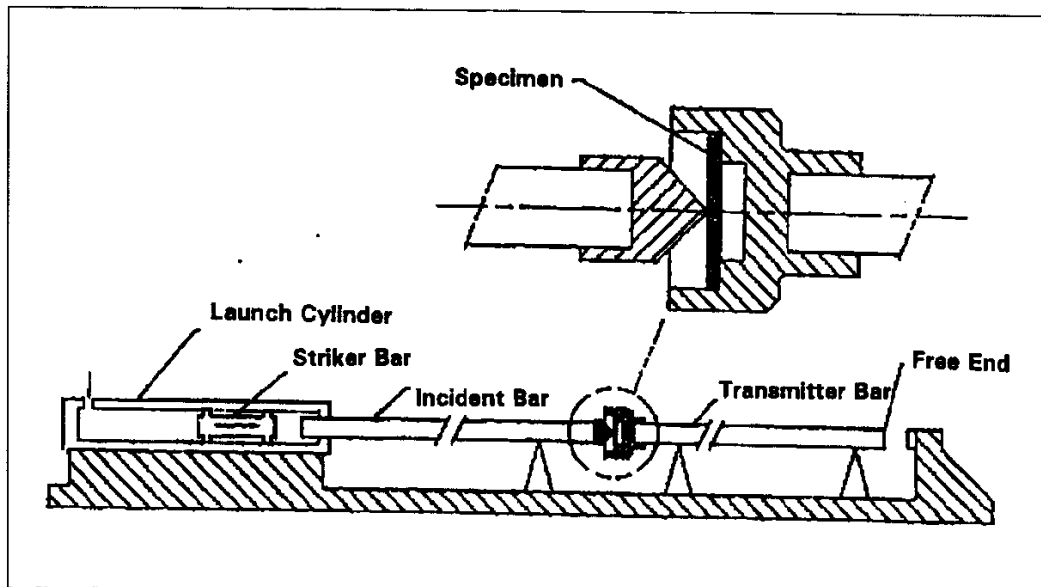


Fig. 1. Modified split Hopkinson pressure bar for perforation experiments

**Materials and Experiments**

Target laminates consisted of graphite thickness from 8 to 32-plyes. Specimens were circular in shape with a diameter of 617 mm (2.43 inches) and conformed to the lay-up described in Table 1. Test specimens were simply supported on the fixture and spanned an unsupported

region having a diameter of 5.08 cm (2.0-in). Laminates were held in place by indenter contact. Contact between the indenter and specimen was maintained using a rubber band. All laminates were subjected to transversely-applied compressive contact loads as supplied by the modified Hopkinson bar. Contact force was applied perpendicular to the plane of the panel. The major experimental objective was to characterize the damage generation (involving indentation, penetration, and perforation) in terms of energy expenditure and visible (surface) damage size.

**Table 1. Characteristics of Graphite/Epoxy Specimen**

Specimen Specifications	Parameters	Experimental Data
<u>Ply/Lay-UP</u>	<u>Thickness/Diameter</u>	<u>Maraging Steel Properties</u>
GP1: 8-ply $[\pm 45]_{2s}$	1.042mm (0.041 in)	$E_0 = 2.07 \times 10^5$ Mpa
GP2: 8-ply $[\pm 45/0/90]_s$	1.042mm (0.041 in)	Wave speed=5010 m/s
GP3: 16-ply $[\pm 45/0/90]_{2s}$	2.083 mm (0.082 in)	Bar material density=8000 kg/m <sup>3</sup>
GP4: 32-ply $[\pm 45/0/90]_{4s}$	4.064mm (0.160 in)	$E_Y = 2.03 \times 10^5$ Mpa

## RESULTS AND DISCUSSION

### Characterization of the Wave Forms

Fig. 2(a) shows a typical measured stress signal provided by incident and reflected waves. Similar and repeatable results (for 8, 16, and 32-ply samples) are obtained when uniform impact conditions were applied. The spike in the reflected wave shown in Fig. 2(a) is due to an impedance mismatch at the bar/indenter interface.

### Damage Initiation and Penetration Process Stages

Results shown in Figs. 2(b-d) illustrate the variation of force (A), particle velocity (B), energy absorption (C), and penetration (D) history for graphite/epoxy laminates contacted with a conical hemispherical-nosed indenter. Plotted values are scaled (by  $10^4$ ,  $10^8$  and  $10^5$  for energy, penetration, and particle velocity, respectively) for comparison purposes. The complete penetration process involves five interdependent damage events: compression-induced matrix cracking and fiber fracture, shear plug formation, plug separation, delamination, and perforation [2]. These damage events are completed during the five penetration stages discussed below.

#### *Stage I: Compressive Loading Stage*

Stage I is mainly compressive and is characterized by the indenter's velocity being greater than that of laminate particles. As the indenter decelerates into the plate, an energy transfer to the laminate takes place. The contact force increases and the plate is pushed or flexed forward with increasing particle velocity. The initial perforation energy can be divided into stored and absorbed components. Stored energy is elastically recoverable, whereas the absorbed energy is manifested in the form of damage and fracture propagation.

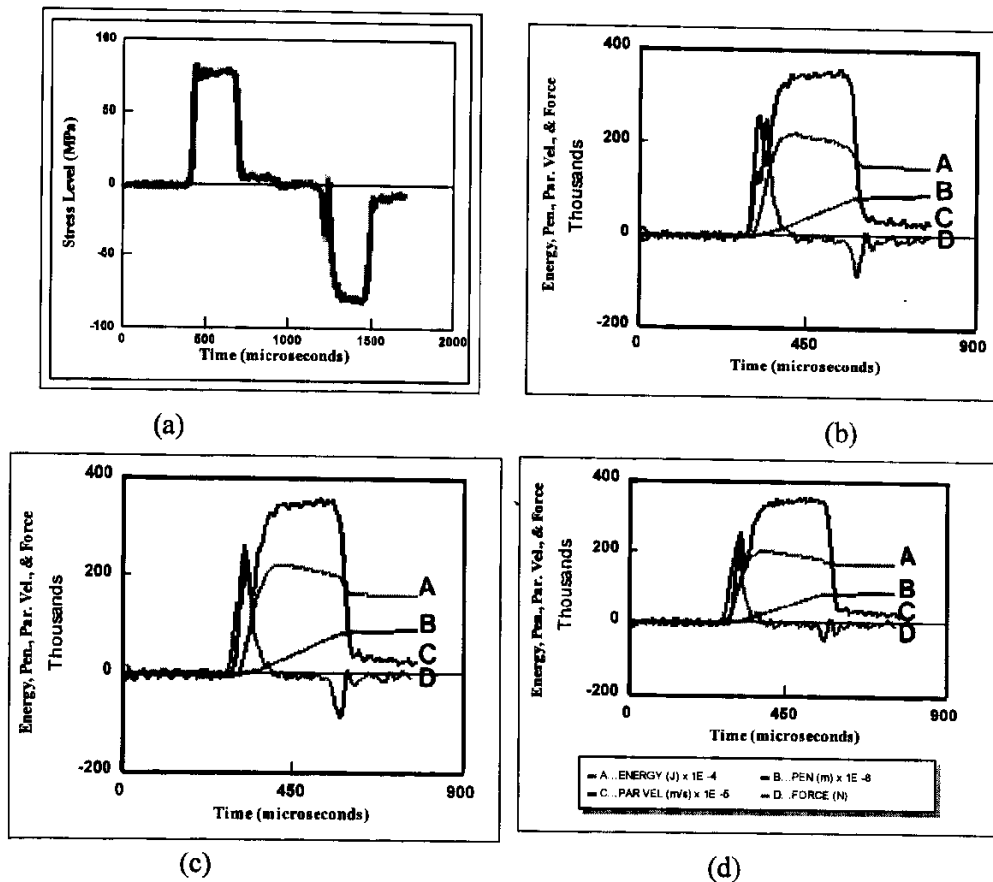


Fig. 2: (a) Condition of incident and reflected stress levels for 8-, 16-, and 32-ply graphite/epoxy samples, (b) energy, penetration, particle velocity, and force history measurements for 8-ply, (c) 16-ply, and (d) 32-ply graphite/epoxy laminates penetrated at 133J striker impact energy

*Stage II: Equilibrium Stage.*

The equilibrium stage is characterized by laminate particle velocities which match that of the indenter. Cracks and fractures created during Stage I are propagated in Stage II. In extreme cases, localized material at the impact site may shear away, yielding a shear plug roughly matching the projectile's velocity. The energy absorption rate approaches a constant value since a state of particle velocity equilibrium is formed. The indenter continues to penetrate through the plate at a nearly constant velocity while the plate's boundary is held fixed by the perforation fixture.

*Stage III: Reloading (Tensile Wave) Stage*

During the reloading stage, the compression wave is reflected off the rear surface of the specimen as a tensile wave. The stress reflection causes a sharp decrease in the rate of absorbed energy since reflected energy is subtracted from the total energy. This stage is marked by reversal of the force direction on the force-displacement curve. The decrease can also be associated with the release of elastic strain energy stored in the specimen during the loading stage.

*Stage VI: Unloading Stage*

The unloading stage is characterized by a reduction in the force applied to the laminate. As the indenter decelerates, force applied to the laminate is reduced. The plate may continue to flex forward causing a rapid drop in the contact force.

*Stage V: Vibration Stage*

This stage involves residual energy absorbed by the system. Penetration ceases and the system vibrates (as shown in the force vs displacement curve). This could partly be caused by the flexure of the panel. Studies have shown that the vibration mainly originates from elastic waves traveling back and forth in the indenter [6] and that the amplitude of such vibration increases with indenter velocity.

**Damage Process**

The damage process is not a linear function of impact energy over all regions. Figs. 3-6 describe peak energy absorbed vs incident stress, peak force, penetration, and particle velocity, respectively. Tests were performed using a consistent launch velocity. Although more experimental data are needed to confirm the observed trends, the relationship between energy absorbed, particle velocity, and amplitude of the incident stress are quadratic in form. From wave propagation theory, energy transferred to the specimen is proportional to the square of the incident wave amplitude and expressed as (6)

$$E_A = \left(\frac{AC_0}{E_0}\right) \int (\sigma_i^2(t) - \sigma_r^2(t) - \sigma_t^2(t)) dt \quad (1)$$

where  $A$  is the cross sectional of the bar,  $C_0$  is the wave velocity in the bar,  $E_0$  is Young's modulus, and  $\sigma(t)$  is the stress field written for incident (i), reflected (r) and transmitted (t) waves.

As shown in Fig. 3, the higher quadratic term in the nonlinear fit, shows that the relationship between energy absorbed and peak force is more linear for the 32-ply sample (without perforation) than for 16-ply samples (with penetration). The point of deviation appears to be an indication of transition to another damage mechanism, possibly from matrix cracking and fiber breakage, or delamination and perforation. For the same impact conditions, the 16-ply laminate approaches the perforation threshold earlier than the 32-ply. After perforation is achieved at the threshold kinetic energy for a 16-ply sample, a nonlinear relationship between impact energy and energy is expected to dominate. Most of the energy, after material failure, is returned to the indenter while energy absorbed by the specimen remains constant. This is equivalent to the energy, or load, being outside the specimen's elastic response region. The present analysis shows that threshold kinetic energy exists above which crack initiation on the rear surface will be visible.

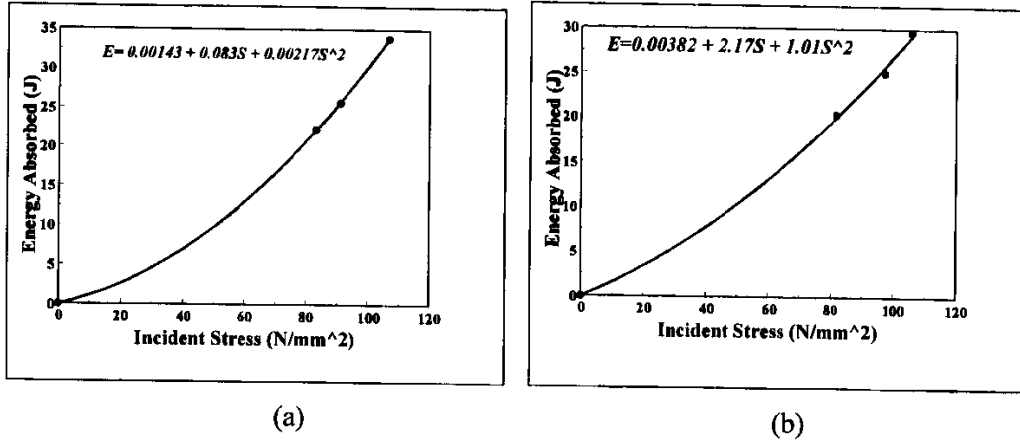


Fig. 3. Variation of energy absorption with incident stress level for (a) 16-ply and (b) 32-ply graphite/epoxy laminates

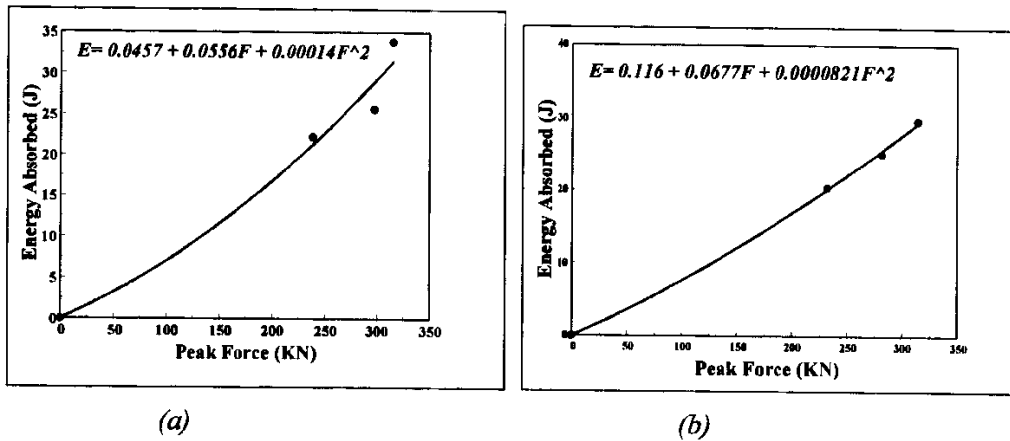


Fig. 4. Variation of energy absorption with peak force for (a) 16-ply and (b) 32-ply graphite/epoxy laminates

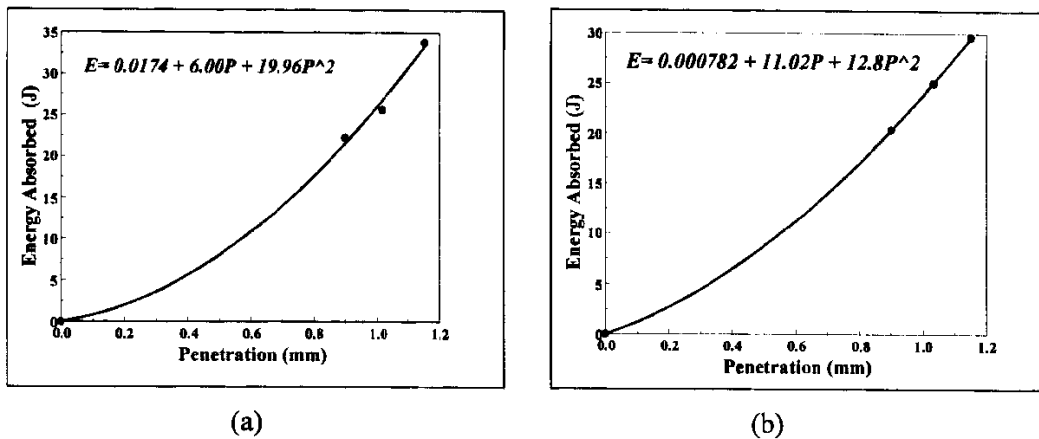


Fig. 5. Variation of energy absorption with penetration for (a) 16-ply and (b) 32-ply graphite/epoxy laminates

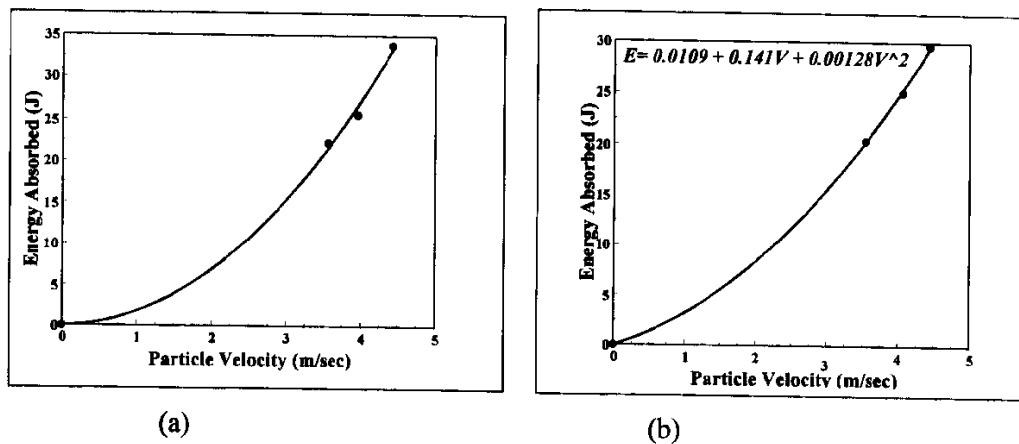


Fig. 6: Variation of energy absorption with particle velocity for (a) 16-ply and (b) 32-ply graphite/epoxy laminates

### Damage Propagation Energy

Crack propagation along the fiber direction increases with impact energy. As a further characterization of the damage process, the height ( $h$ ), delamination damage length at the rear surface ( $L_d$ ), and entrance width ( $w$ ) of 16-ply specimens, under different impact energies and same fiber lay-up were measured (Fig. 7(a)). The variation or progression of length (along the diameter) of the damaged area with impact velocity (energy) is shown in Fig. 7(b) and the associated photographs in Fig. 8. The result shows that the damage length or area propagates linearly with impact energy (velocity) as

$$L_d = GV_I + G_0 \quad (2)$$

where  $I/G$  is a measure of the rate of crack propagation and  $G_0$  is a constant. From Fig. 7(b), the threshold velocity (striker velocity) for crack initiation in the 16-ply specimen is 13.5 m/s, corresponding to a threshold impact energy of 113 J for initiation of a visible crack on the rear surface. An experimental estimate of the ballistic limit energy is in Fig. 7 (c)

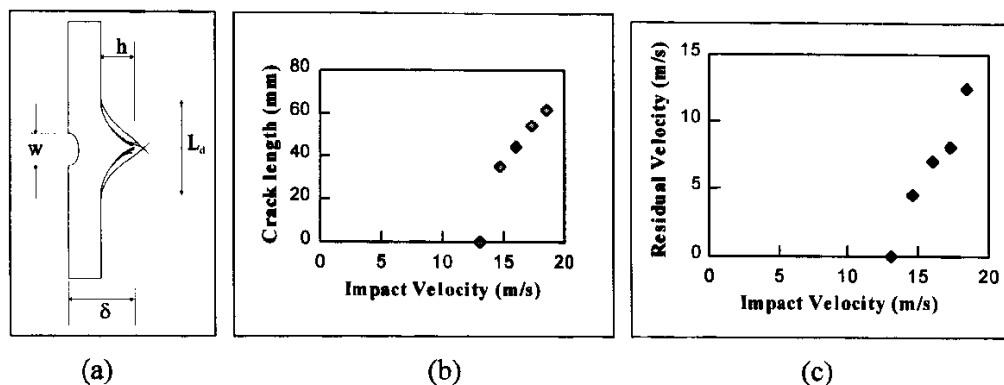
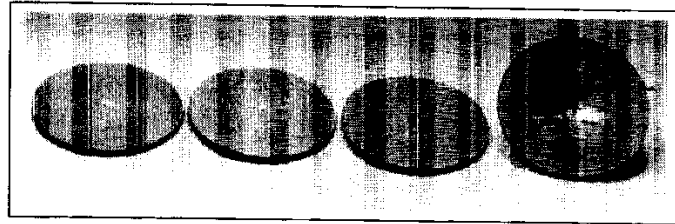


Fig. 7: (a) Schematic of perforated laminate, (b) variation of surface crack length with impact velocity, and (c) residual velocity vs impact velocity for a 16-ply specimen



### Plugging

Plugging (involving complete punch through) occurs at 186 J and 260 J for 16- and 32-ply specimens, respectively. Photographs in Figs. 8 and 9 show a difference in the level of damage, and reveal that the major event is plug push out and associated delamination. The figures show entrance and exit side damages involving matrix cracking, buckling, and fiber breakage. For the 16-ply laminate, a rear surface crack first became visible at an input energy of 106 J (not shown)



(a)



(b)

*Fig. 8: Photographs of damaged 16-ply graphite/epoxy laminates showing (a) entrance surface damage and (b) rear surface damage for varying impact energies of 133 J, 159 J, 186 J, and 212 J, respectively, as shown*

corresponding to an impact velocity of 13.1 m/s. The crack propagated as the energy increased. The critical energy for perforation equates to 159 J or 10 J/ply for the 16-ply specimen. Plug push-out was achieved at an input energy of 212 J. Rear surface cracking on the 32-ply laminate was first observed at an input energy of 233 J. The crack propagated as energy increased until complete plug push-out and failure occurred at an impact energy of 260 J. Perforation was expected below this energy but was not investigated for the 32-ply specimen. However, it appears from the visible nature of the damage that the impact energies of 212 J and 260 J had exceeded the ballistic limit of this specimen. A difference of 27 J (233 J and 260 J) of energy in the case of 32-ply specimen caused a significant difference in the propagation of the damage around the ballistic limit region.

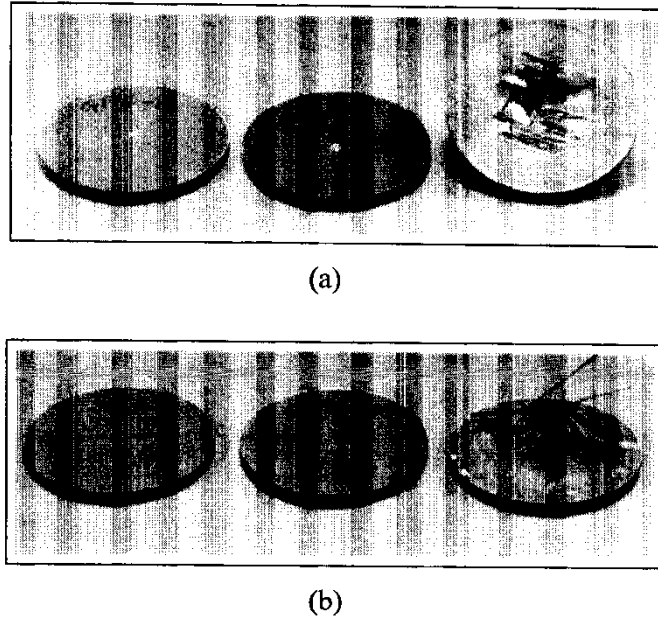


Fig. 9: Photographs of damaged 32-ply graphite/epoxy laminates showing (a) entrance surface damage and (b) rear surface damage for varying impact energies of 159 J, 233 J, and 260 J, respectively, as shown

## CONCLUSION

A threshold energy exists above which a crack will form and propagate. The threshold kinetic energy per laminate needed for damage initiation in unidirectional graphite/epoxy laminate is  $7 \pm 1$  J/ply for crack initiation at the rear surface, 10 J/ply for perforation, and  $11 \pm 3$  J/ply for plug push out. Incipient damage is noted by increased force reflection (a greater amplitude of the force reversal). Crack formation propagates linearly with impact energy. For 16-ply laminates, the striker, threshold impact velocity to initiate damage is 13.5 m/s corresponding to 113 J impact energy. The relationship between energy absorbed, particle velocity, impact velocity, and penetration during the first damage stage assumed to be matrix cracking and fiber breakage appear quadratic. Spikes in the reflected wave (Fig. 3 (a)) are due reflection caused by impedance mismatches at the incident bar/indenter interface.

## REFERENCES

1. Kolsky, H., *Stress Waves in Solids*, Clarendon Press, Oxford, 1953
2. Zukas, J.A., Nicholas, T., Swift, H., Greszczuk, L. B., and Curran, D., *Impact Dynamics*, Kreiger Publishing Co., 1992.
3. Graff, K. F., *Wave Motion in Elastic Solids*, Ohio University Press, Ohio, 1975
4. Bickle, L.W. "An Introduction of the Use of Strain Gages for the Measurement of Propagating Strain Waves", Sandia Laboratories, Albuquerque, New Mexico, 1970.
5. Nwosu, S.N., "Hopkinson Bar Perforation of Laminated Composite", *Interim Report # WL-TR-96-3080*, USAF Flight Dynamics Directorate, Wright Laboratory, Ohio, 1995.
6. Sjoblom, P.O., Hartness, T., and Cordell, T., "On Low Velocity Impact Testing of Composite Materials", *Journal of Composite Materials*, Vol. 22, 1988, pp. 30-51

# EVALUATION OF MULTIAXIAL TEST DATA OF UD-LAMINAE BY SO-CALLED "FRACTURE-TYPE STRENGTH CRITERIA" AND BY SUPPORTING PROBABILISTIC MEANS

Ralf G. Cuntze

*Division of Spacecraft, MAN Technologie AG, Liebigstr. 5a, 85757 Karlsfeld/Munich.*

**SUMMARY:** Overall objective of this elaboration is to calibrate fracture criteria resp. to define size and shape of the fracture body as cheaply as possible by executing the characteristic tests only. Based on knowledge, achieved by investigating v. *Mises*, *Mohr* - *Coulomb* and the new physically based *Hashin* - *Puck* Strength Criteria for inter fibre fracture (IFF) of brittle unidirectional laminae, a new and general concept for the derivation of fracture criteria will be proposed and applied to fibre reinforced plastics (FRP).

The fracture body derived here is basically piecewise smooth, each piece representing a single *failure mode*. As interpolation functions the *invariants* associated to the material's symmetries are utilised. Physical basis is the reference to the 2 fracture-types in a material: normal fracture (NF) and shear fracture (SF). For the subsets of failure modes "fibre fracture (FF)" and "IFF" two conditions for FF and three for IFF are derived. These five conditions describe the five failure modes or mechanisms occurring, and five failure modes are the maximum number a transversally-isotropic material, modelled a crystal, can possess.

In the transition zone of two failure modes or domains of mixed fracture, respectively, a probabilistic modelling has to be applied. This finally leads again to a smooth surface of the complete fracture body.

As the most remarkable results of the elaboration have to be pointed out: Consider micromechanics resp. real material stresses in the constituents fibre and matrix (incl. interface) which only can fail, however, formulate and visualise in lamina stresses at composite resp. macromechanical level and think in Mohr's fracture stresses.

The application of the criteria to test results is very promising. Erroneous results, possible if applying the traditional global (stress) interaction criteria, should not be achieved.

**KEYWORDS:** fibre reinforced composites, strength criteria, test data evaluation

## INTRODUCTION

"Hot spots" of load carrying isotropic structures have to be designed versus various (Fig. 1) strength failure modes including *onset of yielding* and *fracture* resp. *onset of cracking*.

In case of laminates built from brittle UD-laminae the stress man has to dimension each

lamina (ply-by-ply) versus IFF and fibre-fracture (FF). Whereas IFF indicates the onset of *fibre-parallel cracking* in one lamina of the laminate FF will indicate the onset of *fibre cracking*. First FF of a lamina usually marks the final fracture of the laminate. A reliable prediction of IFF under 3D-states of stress is mandatory for the calculation of progressive failure.

As well in the stress analysis as in the failure criterion of the strength analysis there are scattering design parameters. The uncertainty of these parameters (loads, strengths, geometrical quantities, young's module, ...) is of *physical nature* or of *statistical nature* (shortage of information due to a too small sample size of a certain design parameter measured). Besides this there is always some *uncertainty in the calculation model*.

This scatter is usually considered in the design by the use of fixed, deterministic *factors of safety*, better called *design factors of safety* (DFOS), which are based on experience with structural tests. In aerospace industry structures are dimensioned by using DFOS  $j$  which *increase* the so-called *design limit load* (DLL) to the design ultimate load (DUL) according to  $j_{ult} \cdot DLL$ . This procedure includes the idea of *proportional loading* and that the reserve factor  $f_{Res}$  is related to the external load only. Above "*load factors*" are discriminating the *onset of yield* (e.g.  $j_{po,2} = 1.1$ ) for isotropic material and *ultimate fracture* (e.g.  $j_{ult} = 1.5$ ).

The design allowables to be used as strength values are statistics-based minimum values [Cun96/2]. This might be a so-called Mil-Hdbk 17 "B-value" with 90 % reliability and 95 % confidence probability, the latter number regards the confidence in the transfer of the finite number of sample test data to the parent distribution with its infinite number of data.

*Proofs of Design* or *design verifications* done by analysing and/or testing a structure have to be given for *failure modes* such as stability, deformation, vibration and strength. Target of the designer is to achieve a margin of safety  $MS \geq 0$  for each single failure mode and - in this paper - for fracture modes as a subset of them. In order to achieve a reliable margin of safety ( $MS = f_{Res} - 1$ ) in the Strength Proof of Design the engineer should accurately know the normally non-linear 3D-state of stress in the critical material element and its separation into load-induced and residual stresses!

*Fracture* criteria as a subset of *strength* criteria should enable the engineer to perform the Strength Proof of Design for any 3-dimensional state of stress resp. combination of stresses with a *minimum* amount of test data.

*Verified* fracture criteria as a subset of strength criteria (Fig. 1) enable to do this. They can be calibrated after execution of the *basic strength* tests, only.

The traditional criteria such as Tsai/Wu have some shortcomings which forces research to correct or replace them [VDI97]. However, in the last four years heavy progress has been made in Germany with the derivation of more physically-based fracture criteria for brittle unidirectional isolated laminae. On the basis of [Has80] A. Puck developed the "Hashin-Puck (Action-Plane) Strength Criteria" for IFF [Puc92] assuming 2 modes. Additionally, tests were performed under a German grant to verify the criteria [VDI97].

Parallel, the author tried to generate strength criteria, each of which should be related to one single failure mechanism resp. fracture *mode* (not *type*) and formulated by *invariants*, thus taking the material's symmetries into account. Basis are the *types of fracture in a material*

which are normal stress induced fracture (NF) and shear stress induced fracture (SF). This fracture-type concept proposed may be applied to *any* brittle or ductile behaving material [Cun96/2].

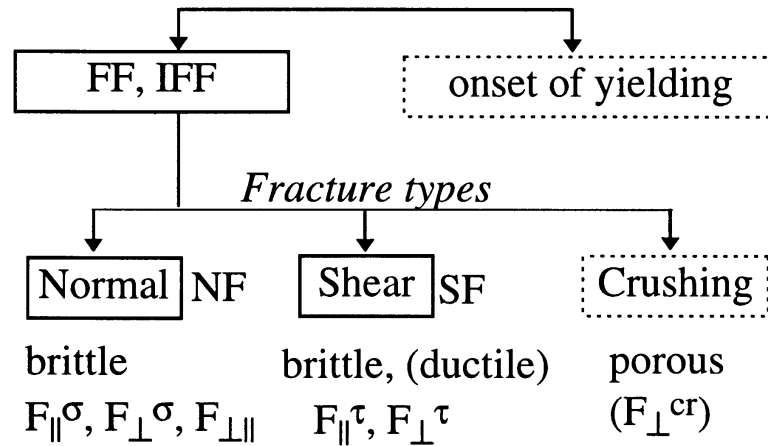


Fig. 1: Strength Failure Modes (modi) of Composites. (NF = normal fracture, SF = shear fracture.  $F_{||}^{\sigma}, \dots, F_{\perp}^{cr}$  are the UD-lamina's failure functions representing fracture modes)

In this paper brittle UD-laminae are described, only. The fracture criteria derived are *stress* criteria and have as foundations: The material is *homogeneous* (smeared or averaged material) and can be modelled an *ideal crystal* with its symmetries and mutual independent basic strengths from a meso/macromechanical point of view. However, for the in reality heterogeneous composite (is a structure not a material) the micromechanical behaviour of the constituents (real materials) fibre, matrix and interphase will be considered too.

### FRACTURE MECHANISMS IN UD-LAMINAE

Fracture is understood in this article as a separation of material, which is free of damage such as cracks but not free of defects and flaws prior to loading. In this context *crushing* of a porous material has to be seen a separate *fracture mechanism* resp. (*fracture*) *failure mode* and *type*.

Idealising a material a crystal one can draw from Table 1 the information: The number of symmetries determines the number of strengths. The higher the *structural level* of the material the more basic strengths have to be measured.

Due to the fact 5 strengths being usually measured in case of a transversally-isotropic lamina the application of the crystal model is still general practice.

Fig. 2 shall give answer to the question: How many *types of fracture* are recognised in case of isotropic and transversally-isotropic *ideal materials*? These are just two: the shear stress induced fracture SF (Mohr's stress  $\tau_n$  is acting at the "plane" of fracture) and normal stress  $\sigma_n$

induced fracture NF - as we know - for isotropic materials, but also two for the UD-material. However, the letter case comprises several SF and NF which belong to FF and IFF.

Table 1 : Number of Strengths and Fracture Types for Various Ideal Materials ( $t =$  tension,  $c =$  com-pression;  $\parallel, \perp =$  parallel, transversal to the fibre;  $W =$  warp,  $F =$  fill. Superscript  $c =$  critical)

material has	no structure	increasing structural level $\rightarrow$	
	0	1	2
allocation to crystal type	isotropic	transversally isotropic	rombically anisotropic
symmetries	2	5	9
material example	resin matrix, mono. ceramics	UD-lamina, mat	fabrics
elasticity quantities	$E, \nu$ (2)	$E_{\parallel}, E_{\perp}, G_{\parallel\perp}$ $\nu_{\perp\parallel}, \nu_{\perp\perp}$ (5)	$E_W, E_F, G_{WF}, \nu_{FW}, E_3,$ $\nu_{3W}, \nu_{3F}, G_{F3}, G_{W3}$
strength quantities ( <i>resistances</i> )	$R_{\sigma}^t, R_{\tau}^c$ or (2)	$R_{\parallel}^t, R_{\parallel}^c, R_{\perp}^t,$ $R_{\perp c}, R_{\perp\parallel}$ (5)	$R_W^t, R_W^c, R_F^t, R_F^c, R_3^t,$ $R_{3W}, R_{FW}, R_{3F}, R_3^c$ (9)
invariants	$I_1, I_2,$ or $J_2 \dots$	$I_1, \dots, I_5, \dots$	$I_1, \dots, I_7, \dots$
fracture toughnesses	$K_{Ic}^t, K_{IIc}^c$ (2)	$K_{\parallel c}^t, K_{\parallel c}^c, K_{\perp c}^t$ $K_{\perp c}^c, K_{\perp\parallel c}$ (5)	

Also the physical fracture "planes" are pointed out in the figure.

A comparison of Fig. 2 with Table 1 leads to an essential conclusion: *One strength governs one distinct fracture type.*

The characterisation of the strength of transversally-isotropic composites requires the measurement of five independent basic strengths:  $R_{\parallel}^t, R_{\parallel}^c$  (fibre parallel tensile and compressive strength) as well  $R_{\perp}^t, R_{\perp}^c$  (tensile, compressive strength perpendicular to the fibre direction) and  $R_{\perp\parallel}$  (fibre parallel shear strength).  $R_{\parallel}^t$  is determined by the strength of the constituent fibre,  $R_{\parallel}^c$  is generally governed by *shear stability*. This includes different microfailure mechanisms: The matrix may shear under loading and does not stabilise the generally somewhat misaligned fibres embedded. Hence it comes to bending and "kinking" (structure behaviour). But, the load "grasping" fibre as the well-stabilised, stiffer constituent may shear (this is material behaviour) under  $\sigma_{\parallel}^c$  and  $\tau_{\perp\parallel}$ , too.  $R_{\perp}^t$  is determined as well by the relatively low strength properties of the matrix (cohesive failure) and the interphase material in the interface fibre-matrix (adhesive failure caused by a weak fibre-matrix bond), as by the fibres acting as embedded stress risers.

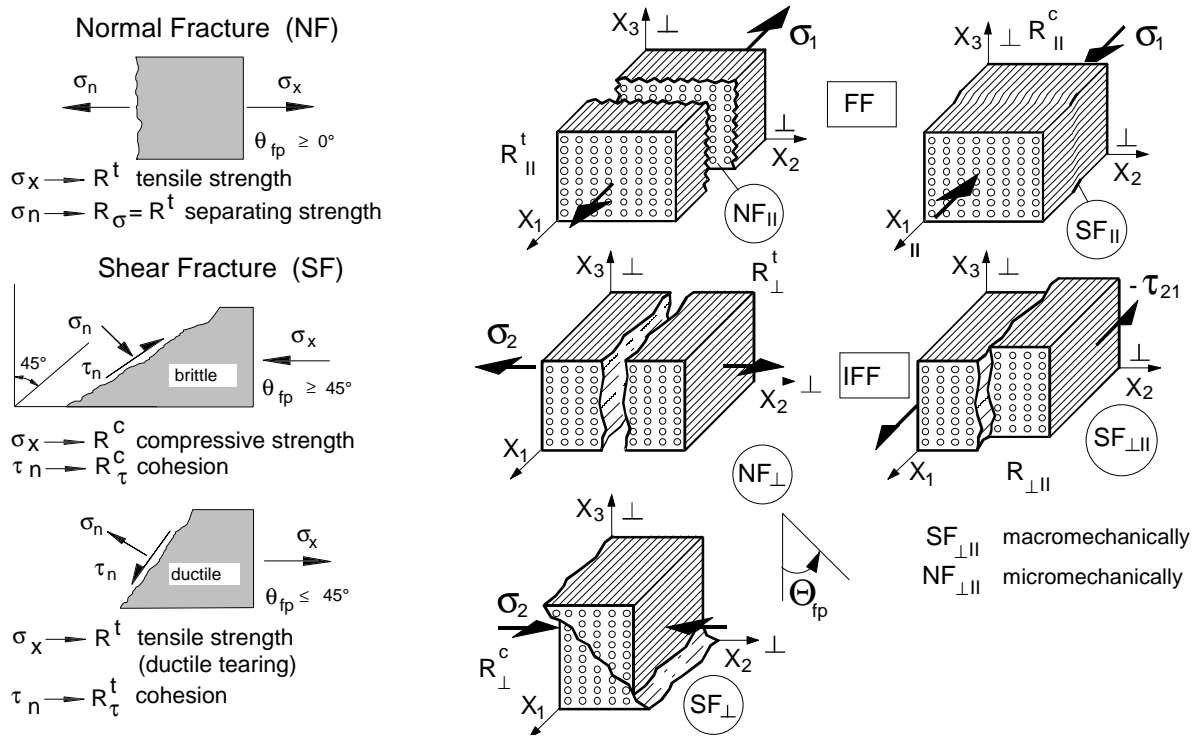


Fig. 2: Fracture Types ( $\equiv$  modes) in case of Brittle and Ductile behaving Isotropic Material and Fracture Modes in case of Transversally-isotropic Material ( $\sigma_n^A$  ( $\theta = \theta_{fp}$ ) =  $\sigma_n$ ).

Well known from literature is the shift of the fracture limit of IFF strain resp. stress to higher values the absolutely thinner the lamina is and the stiffer in comparison the embedding laminae and the laminate are. Whereas the free isolated lamina (UD-specimen) if transversally tensile loaded is underlying a weakest-link failure (resulting in a Weibull distribution for  $R_{\perp}^t$ ) the embedded lamina will be strain controlled by its neighbours. Inherent defects or microcracks as often reported can grow together to form mesocracks *only* in case they have a chance to open. However, these microcracks are arrested fracture-mechanically by the embedding laminae.

In order to consider the constraint effect on a "thin" embedded lamina following [Fla 82] and some own investigations the author recommends e.g. for CFRP ( $t_{thr} \approx 0,35$  mm) as correction formula for the design allowable  $R_{\perp}^t$  due to

$$R_{\perp}^t (t_{\perp} < t_{thr}) = R_{\perp}^t \sqrt{t_{thr} / t_{\perp}} . \tag{2.1}$$

### GENERAL FORMULATIONS OF STRENGTH CRITERIA AND CONDITIONS

Strength criteria  $F \stackrel{\geq}{<} 1$  are generally formulated as (isotropic case shown for simplicity)

$$F(\{\sigma\}; \{R\}) = F(\sigma_x, \sigma_y, \sigma_z, \tau_{zy}, \tau_{zx}, \tau_{yx}; R^t, R^c) \stackrel{\geq}{<} 1 \quad \dots \text{criterion.} \tag{3.1}$$

In the failure (here fracture) function  $F$  the vector  $\{\sigma\}$  contains the six stresses in the coordinate system of the structure - as above - or the six lamina stresses. The vector  $\{R\}$  contains all *basic strengths* to be applied such as  $R^t, R^c$  in isotropic case.

$$F(\{f_{Res} \{\sigma\}; \{R\}) = 1 \quad \dots \text{condition} \quad (3.2)$$

To achieve this, the stresses in equation 3.1 have to be multiplied by the reserve factor  $f_{Res}$ , which is usually dropped for reasons of a simpler writing.

Composites with a polymeric matrix exhibit brittle behaviour from a macroscopic point of view. Thus a formulation of strength criteria can be based on the fracture hypotheses of *Mohr* and *Coulomb*, adapted to UD-laminae. This was suggested by Hashin [Has80]. Hence, using Mohr's fracture stresses, which act together at the *same plane*, the isotropic equations read:

$$F_{\sigma} = F(\{\sigma^{Mohr}\}, R_{\sigma}) = 1 \quad \dots \text{NF} \quad (3.3a)$$

$$= \sigma_n / R_{\sigma} = 1 \quad (\text{normal stress hypothesis})$$

$$F_{\tau} = F(\{\sigma^{Mohr}\}, R_{\tau}) = 1 \dots \text{SF} \quad (3.3b)$$

$$= \tau_n / (R_{\tau} - \mu \sigma_n) = 1 \quad \text{e.g. (shear stress hypothesis, Mohr-Coulomb)}$$

With  $R_{\sigma}$ : = separating strength (resistance)  $R_{\tau}$ : = cohesion (resist.),  $\mu$ : = Coulomb friction.

This outlines: *one* condition is to be used for *each* fracture mechanism which is dominated by *one fracture resistance*  $R_{\sigma}$  or  $R_{\tau}$  (s. also [Cun96/2] for isotropic materials. A resistance (of the fracture plane) corresponds with the basic strength associated if the action plane of a distinct stress comes to be the potential (load must be high enough, too) fracture plane: e.g. in brittle case  $\max \sigma = R_{\sigma} = R^t$  (isotropic) or  $R_{\perp}^t$  (transversally-isotropic). In case of brittle behaviour only  $R_{\sigma}$  can be measured and vice versa  $R_{\tau}$  in case of ductile behaviour. Therefore,  $R_{\tau}$  principally remains undeterminable until the fracture angle  $\theta_{fp}$  is determined. This is also valid for the *fracture plane stresses*  $\{\sigma^{Mohr}\}$ .

The "curve fitting" of the course of test data can be performed much easier by not taking Mohr's stresses and the 2 resistances  $R_{\sigma}$ ,  $R_{\tau}$  but  $\{\sigma\}$  and the 2 basic strengths. However, equation (3.1) will now be used in Mohr's sense meaning one basic strength governs one fracture mechanism NF or SF

$$F_{\sigma} = F(\{\sigma\}, R^{NF}) = F(\{\sigma\}, R^t) = 1 \quad \text{and} \quad F_{\tau} = F(\{\sigma\}, R^{SF}) = 1. \quad (3.4)$$

Both, the physical basis and the numeral handling are improved by using invariants as interpolation functions, a well known and classical approach.

## DERIVATION OF "FRACTURE-TYPE STRENGTH CRITERIA"

### Description of 3D-States of Stress

Three-dimensional states of stress in a lamina may be described by lamina stresses  $\{\sigma\}$ . A further possibility is given by using *Mohr's fracture stresses* mentioned above. They are acting in the potentially physical fracture "plane" (Fig. 3) and are decisive for fracture. In case of



normal (stress induced) fracture  $\sigma_n$  will be responsible for fracture and in case of shear (stress induced) fracture  $\tau_n$  will be the fracture dominating one. Fig. 3 does also explain how

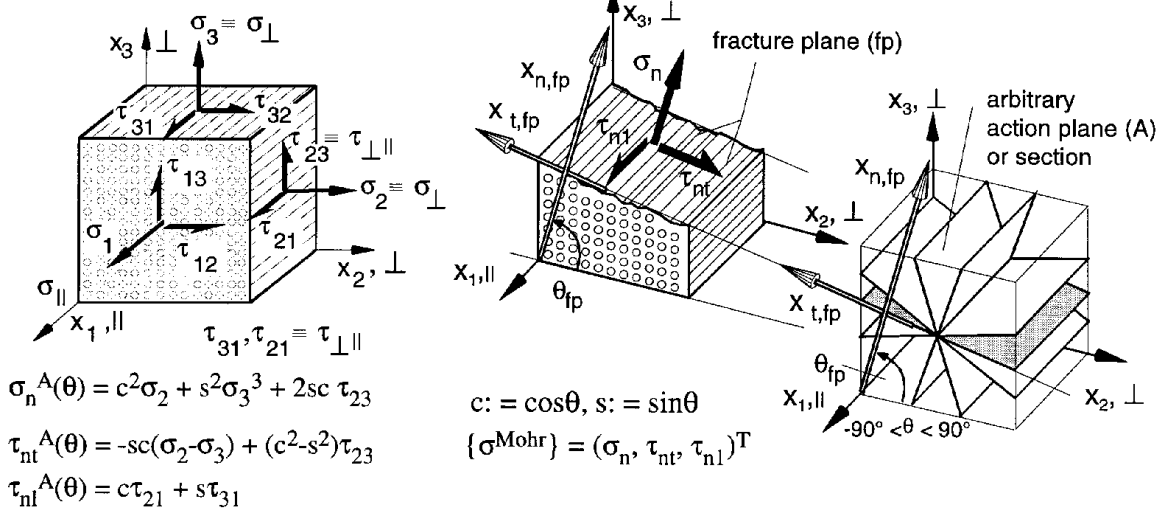


Fig. 3: 3D-states of Stress (lamina stresses and Mohr's stresses at the fracture plane)

Mohr's fracture stresses are derived by transformation of  $\{\sigma\}$  into a fibre-parallel plane  $\{\sigma(\theta)\} = [T(\theta)] \{\sigma\}$ , ([Cun94]). Fracture plane will become that plane where the effort E under  $\{\sigma(\theta)\}$  will be the maximum or  $f_{Res}$  will become a minimum, if  $\sigma_n = \sigma_n^A(\theta_{fp})$  etc.

A comprehensive way to describe states of stress is given if using invariants formed by the lamina stresses (s. [Has80], [Boe85]). Table 2 depicts the invariants for a transversally-isotropic UD-lamina ( $I_3 = \text{square of max } \tau_{\perp\parallel}, I_4 \approx \text{square of max } \tau_{\perp\parallel}$ ):

$I_{1f} = v_f \sigma_{1f}$   
 $I_2 = \sigma_2 + \sigma_3 = \sigma_n + \sigma_t = \sigma_{II} + \sigma_{III}$   
 $I_3 = \tau_{31}^2 + \tau_{21}^2 = \tau_{t1}^2 + \tau_{nl}^2, \quad I_5 = (\sigma_2 - \sigma_3) (\tau_{31}^2 - \tau_{21}^2) + 4\tau_{23} \tau_{31} \tau_{21}$   
 $I_4 = (\sigma_2 - \sigma_3)^2 + 4\tau_{23}^2 = (\sigma_n - \sigma_t)^2 + 4\tau_{nt}^2 \quad \text{or} \quad I_4 = \tau_{23}^2 - \sigma_2\sigma_3 = -\sigma_{II}\sigma_{III}$

Table 2: Invariants of a UD-lamina  
 ( $v_f = \text{fibre volume fraction; index } f \text{ for fibre}$ )

#### 4.2 Fracture-type strength conditions

Table 3 summarises the author's proposal for fracture-type strength conditions being applied later to glass fibre reinforced plastics (GFRP).

Table 3: Fracture-type Strength Conditions for Transversally-isotropic Laminae. ( $f_{Res}$  dropped in the equations; characteristic basic strength depicted;  $\tau$  and  $\sigma$  indicate the responsible stress. The correction terms for IFF considering  $\sigma_1$  are not depicted here, see [Cun96/1])

- Fibre Fracture (FF) -

$F_{\parallel\sigma}: a_{\parallel\sigma} \cdot I_{1f} = R_{\parallel\sigma}^t \quad \text{and} \quad F_{\parallel\tau}: a_{\parallel\tau} \cdot I_{1f} + b_{\parallel\tau} I_3 = R_{\parallel\tau}^c \quad \dots\dots NF_{\parallel} \text{ and } SF_{\parallel}$

- Inter Fibre Fracture (IFF) - (matrix, interface) -

$F_{\perp\sigma}: a_{\perp\sigma} I_2 + b_{\perp\sigma} \sqrt{I_4} + \dots\dots\dots + [d_{\perp\sigma} I_3 + (e_{\perp\sigma} I_2 I_3 + f_{\perp\sigma} I_5) R_{\perp\sigma}^t / R_{\perp\sigma}^t] / R_{\perp\sigma}^2 = R_{\perp\sigma}^t \quad \dots\dots NF_{\perp}$   
 $F_{\perp\parallel}: a_{\perp\parallel} I_3 + (b_{\perp\parallel} I_2 I_3 + c_{\perp\parallel} I_5) / R_{\perp\parallel} = R_{\perp\parallel}^2 \quad \dots\dots NF_{\perp\parallel}$   
 $F_{\perp\tau}: a_{\perp\tau} I_2 + b_{\perp\tau} I_4 / R_{\perp\tau}^c + \dots\dots\dots + c_{\perp\tau} I_3 R_{\perp\tau}^c / R_{\perp\tau}^2 = R_{\perp\tau}^c \quad \dots\dots SF_{\perp}$

- Crushing - (porous matrix) -

$F_{\perp cr}: a_{\perp cr} I_2 + b_{\perp cr} I_4 = R_{\perp cr} \quad \dots\dots CrF_{\perp}$

The prediction of failure - made by whichever condition - is satisfied first. Terms in table 3 enveloped by dots are *local correction* terms to approximate (fit) the mixed fracture domains. They are not *global interaction* terms as e.g. in the global fracture criteria of Tsai-Wu.

The stresses  $\tau_{21}$  and  $\sigma_1^t$  do not have a common action plane, but marginally act micromechanically together. However,  $\tau_{21}$  and  $\sigma_1^c$  almost have the same action plane in case of brittle constituents fibre and matrix.

How the stress efforts are adding, linearly or quadratically or even cubically is determined by the course of test data.

The fracture type Crushing Fracture is added in Table 3 for reasons of completeness. It belongs to a material which due to its porosity will fail by internal *voluminous* degradation under compressive stresses and not in "planes" any more.

### Determination of IFF Calibration Conditions besides the Basic Strengths

•Putting the compressive strength  $R_{\perp}^c$  into  $F_{\perp}^{\tau}$  delivers  $a_{\perp}^{\tau} = b_{\perp}^{\tau} - 1$ . (4.1)

A second equation, if using the measurable fracture angle  $\Theta_{fp}^c$  as the other obtainable information of the lateral compression test will be Mohr-Coulomb's condition ( $\hat{c} := \cos \theta_{fp}^c$ )

$$-\frac{\partial F_{\perp}^{\tau}}{\partial \sigma_n} / \frac{\partial F_{\perp}^{\tau}}{\partial \tau_n} = -\mu_{\perp\perp} = +\cot \text{an } 2\Theta_{fp}^c = 0,5 \left( \frac{\hat{c}}{\hat{s}} - \frac{\hat{s}}{\hat{c}} \right) \text{ yielding } b_{\perp}^{\tau} = 1/(4\hat{c}^2 - 1). \quad (4.2)$$

•Trials to estimate the tensile fracture stress  $\sigma_{\perp}^{tt}$  in an appropriate test had no success [VDI97]. However, a good estimation can be achieved by using the information  $R_{\perp}^c$  being Weibull distributed. Following [Awa78] easily can be derived

$$\sigma_{\perp}^{tt} = R_{\perp}^c / \sqrt[k]{2} \quad \text{with } k = \text{Weibull's module.} \quad (4.3)$$

•With respect to Fig. 6 a value for a point on the "bulge" ( $\tau_{\perp\parallel}^{2D}, \sigma_{\perp}^{2D}$ ) can be estimated or directly a value for the linearized slope  $m_{\perp\parallel} \approx (\tau_{\perp\parallel}^{2D} - R_{\perp\parallel}) / \sigma_{\perp}^{2D}$  (4.4)

### Analytical Derivation of Mohr's Envelope Curve

Resolving the fracture condition  $F_{\perp}^{\tau} = 1$  for  $\sigma_2$  delivers in case of  $\tau_{23} = 0$

$$\sigma_2 \cdot 2b_{\perp}^{\tau} = -R_{\perp}^c a_{\perp}^{\tau} + 2\sigma_3 b_{\perp}^{\tau} + \sqrt{a_{\perp}^{\tau 2} R_{\perp}^{c2} - 8a_{\perp}^{\tau} R_{\perp}^c b_{\perp}^{\tau} \sigma_3 + 4b_{\perp}^{\tau} R_{\perp}^{c2}} = f(\sigma_3) \quad (4.5)$$

$$\text{with } \tilde{c} = \sqrt{(a_{\perp}^{\tau} R_{\perp}^c - 2b_{\perp}^{\tau} \sigma_3 + 2b_{\perp}^{\tau} \sigma_2) / (4b_{\perp}^c / (\sigma_2 - \sigma_3))}, \quad \sigma_3 = \text{variable} \quad (4.6)$$

$$\text{And } \tau_{nt} = |\tilde{s} \tilde{c} (-\sigma_2 + \sigma_3)|, \quad \sigma_n = \tilde{c}^2 \sigma_2 + \tilde{s}^2 \sigma_3, \quad \tilde{s} = \sqrt{1 - \tilde{c}^2}. \quad (4.7)$$

Then the cohesion can be calculated from  $R_{\perp}^{\tau} = \tau_{nt} (\sigma_n = 0)$ . This quantity corresponds to Puck's  $R_{\perp\perp}^A$  [Puc96].

### PROBABILISTIC MODELLING OF MULTIPLE FAILURE DOMAINS

The application of probabilistics will connect adjacent modes.

The influence of the FF modes on IFF can be taken into account very simply by practical correction terms (see [Cun96/1]) in the IFF conditions *or* by probabilistics as shown now.

To estimate the *joint probability of failure* of the different IFF modes as *logical model of the failure system* the series system or union U of  $\ell = 3$  IFF failures will be taken. This delivers a failure probability  $p_f$  on the safe side (index S for sum, see [Cun96/2]), of

$$p_f \leq \sum p_{f,\ell} = 1 - (1-f_{\perp}^{\sigma S})(1-f_{\perp\parallel}^S)(1-f_{\perp}^{\tau S}) \quad (5.1)$$

since small  $p_{f,\ell}$  are expected. Correlation among the  $\ell$  (component) failures leads to a smaller (system) failure probability  $p_f$ , above expression therefore is conservative. In case of a Weibull-distributed strengths  $R_{\perp}^t, R_{\perp}^c, R_{\perp\parallel}$  as "sum" function

$$f^S = 1 - \exp\left[-\left(\frac{r}{w}\right)^k\right] \quad (5.2)$$

is valid (it represents the distribution of the extreme defects) with  $r$  = stress variable,  $k$  = Weibull's module (characterising the scatter of a strength) and  $w$  = shape parameter. A further parameter  $\tau$  characterising the position of the distribution is put zero. This is in any case permitted for very brittle materials (e.g. monolithic ceramics,  $k \geq 2$ ). An estimation of Weibull's parameter is possible [Pli95] on basis of the mean value  $m$  and the coefficient of variation of the parent distribution of each strength measured (bounds:  $cov < 25\%$ ,  $k > 4,8$ ) by

$$k \approx 1.2 / cov; \quad w = m / \Gamma(1+1/k); \quad m = \bar{R} \quad \text{with} \quad \Gamma = \text{Gamma function.} \quad (5.3)$$

As estimations for  $m, v$  the values of a well sized sample are taken *without* considering the confidence interval.

Combining (5.1) and (5.2) yields the following equation for the IFF body

$$\left(\frac{r_{\perp}^{\sigma}}{w_{\perp}^{\sigma}}\right)^{k_{\perp}^{\sigma}} + \left(\frac{r_{\perp\parallel}}{w_{\perp\parallel}}\right)^{k_{\perp\parallel}} + \left(\frac{r_{\perp}^{\tau}}{w_{\perp}^{\tau}}\right)^{k_{\perp}^{\tau}} = -\ell_n(1-p_f). \quad (5.4)$$

Instead of a uniaxial stress the *equivalent stress* as representation of the multiaxial state of stress will be put in (5.4):  $r_{\perp}^{\sigma} = \sigma_{\perp}^{\sigma}$ ,  $r_{\perp\parallel} = \sigma_{\perp\parallel}$ ,  $r_{\perp}^{\tau} = \sigma_{\perp}^{\tau}$ . It can be calculated in

case of  $F_{\perp}^{\tau}$  (shorter than for the IFF cases having cubic invariants)

$$F_{\perp}^{\tau} = f_{Res_{\perp}}^{\tau} \sigma_{\perp}^{\tau} / R_{\perp}^c = 1 \quad \text{or} \quad \sigma_{\perp}^{\tau} = R_{\perp}^c / f_{Res_{\perp}}^{\tau} \quad (5.5)$$

$$f_{Res_{\perp}}^{\tau} = [-a_{\perp}^{\tau} I_2 + \sqrt{a_{\perp}^{\tau 2} I_2^2 + 4b_{\perp}^{\tau} I_4 + 4c_{\perp}^{\tau} R_{\perp}^c / R_{\perp||}^2}] / 2[b_{\perp}^{\tau} I_4 / R_{\perp}^c + c_{\perp}^{\tau} I_3 R_{\perp}^c / R_{\perp||}^2].$$

For the IFF Proof of Design an engineering approach estimates  $f_{Res}$  in the mixed failure domain

$$(1 / f_{Res})^k = (1 / f_{Res_{\perp}}^{\sigma})^k + (1 / f_{Res_{\perp||}}^{\sigma})^k + (1 / f_{Res_{\perp}}^{\tau})^k = f(f_{Res}^{(modes)}) \quad (5.6)$$

(MFD) with  $k \approx \min k$  (safe side) causing a maximum out-smoothing.

### APPLICATION TO GLASS/EPOXIDE-FRP

#### Determination of Curve Parameters (applying MATHCAD)

For the application of the criteria achieved at first all informations on the basic strengths: The type of distribution, the mean value  $\bar{R}$  and the coefficient of variation  $cov$  have to be provided. Table 4 represents an example set of data. The sources are various investigations [Kna72], [ZTL], [VDI97], due to the fact that a real complete test series of all interesting combinations of stresses including  $\sigma_1$  for FRP is not existing.

*Table 4: Strength Properties ( $\nu_f = 0.60$ ) and data of Calibration Points (mean values)*

$$\begin{aligned} \bar{\theta}_{fp}^c &= 49^\circ; \tau_{\perp}^{\tau} = 73 \text{ MPa}; \sigma_{\perp}^{\tau} = -95 \text{ MPa} \\ \sigma_{\perp}^{\tau} &= -86 \text{ MPa}, \tau_{\perp}^{\sigma} \approx 1.05 R_{\perp||} (\sigma_2 = 0) \\ (\sigma_2, \tau_{21}) &= (40, 0), (28, 40), (0, 58), (-90, 72) \\ \bar{R}_{||}^t &: \text{Weibull, } 1500 \text{ MPa, } cov = 6 \% \\ \bar{R}_{||}^c &: \text{Weibull, } 1200 \text{ MPa, } cov = 7 \% \\ \bar{R}_{\perp}^t &: \text{Weibull, } 40 \text{ MPa, } cov = 12 \% \\ \bar{R}_{\perp}^c &: \text{Weibull, } 144 \text{ MPa, } cov = 7 \% \\ \bar{R}_{\perp||} &: \text{Weibull, } 61 \text{ MPa, } cov = 10 \% \end{aligned}$$

#### Fracture Curves: Deterministic Approach incl. Effect of Correction Terms

Fig. 4 comprises four different cross-sections of the five-dimensional IFF-body ( $\sigma_2, \sigma_3, \tau_{23}, \tau_{31}, \tau_{21}$ ): The graph  $(\tau_{21}, \sigma_2)$  represents stresses in the plane of the lamina which are of highest interest in the justification of the stress-output delivered from Classical Laminate Theory (CLT). Three curves  $F_{\perp||}^{\tau}$  (transversal SF),  $F_{\perp||}$  (transversal-parallel SF) and  $F_{\perp||}^{\sigma}$  (transversal-parallel NF) envelope the "50 % safe domain". The graph  $(\tau_{31}, \sigma_2)$  outlines by "Puck's corner" that in contrary to  $(\tau_{21}, \sigma_2^t)$  the shear stress  $\tau_{31}$  has *not* the same action plane

as  $\sigma_2^t$ . The remaining two graphs ( $\sigma_2, \sigma_3$ ) and ( $\tau_{23}, \sigma_2$ ) are well-known from isotropic materials. In these isotropic cross-sections fracture can be described excellently by the homogenised lamina stresses ( $\sigma_2, \sigma_3, \tau_{23}$ ) or artificially smeared stresses, respectively. In the hydrostatic domain  $\sigma_2^c = \sigma_3^c \approx -10 R_{\perp}^c$  the IFF curves will be closed by  $F_{\parallel}^z$ , due to Poisson's effect.

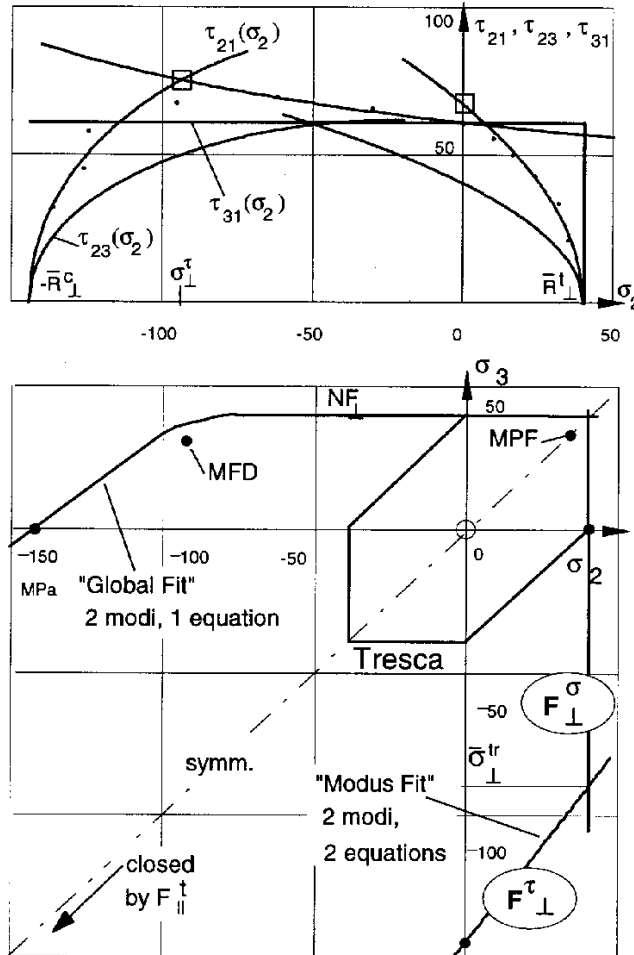


Fig. 4: IFF-curves (Glass FRP). (MFD = mixed failure domain = fracture due to 2 modes, MPF = multiplane fracture of the same mode  $NF_{\perp}$ )

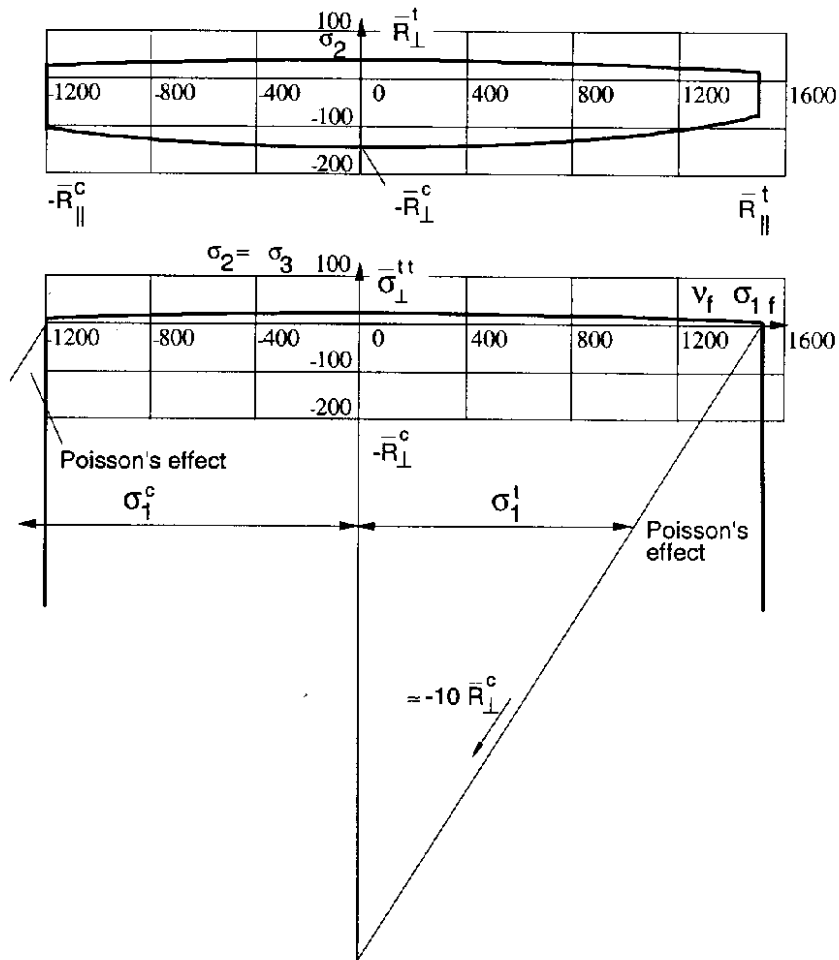


Fig. 5: FF- and IFF-curves (Glass FRP).  
(with correction terms, different scales)

Fig. 5 outlines the limited applicability of the homogenized lamina stresses. The lamina (composite) stress  $\sigma_1$  is not the fracture active stress, however, the stress  $\sigma_{1f}$  of the constituent (material) fibre. In order to nevertheless remain in the graphical display on composite level the fibre stress has to be multiplied by the fibre volume fraction  $v_f$ . This should be an acceptable approach due to the extreme difference in the stiffness and thereby in the load carrying capacity of fibre and matrix. Tests performed, see [VDI97], show the effect of Poisson: Under biaxial compression the load can be only increased until tensile fracture stress or strain of the fibre will be met.

### Simple 2D-Approximation of the $(\sigma_2, \tau_{21})$ Fracture Curve

For an improved but nevertheless simple approximation of the  $(\sigma_2, \tau_{21})$ -test results, which are mandatory for the evaluation of CLT stresses, the utilisation of the formulae

$$F_{\perp\parallel}^{\sigma}: a_{\perp}^{\sigma} \sigma_2 / R_{\perp}^t + c_{\perp}^{\sigma} \sigma_2^2 / R_{\perp}^{t2} + d_{\perp}^{\sigma} \tau_{21}^2 / R_{\perp\parallel}^2 + e_{\perp}^{\sigma} \sigma_2 \tau_{21}^2 / R_{\perp\parallel}^3 = 1 \quad (6.1a)$$

$$F_{\perp}^{\tau}: a_{\perp}^{\tau} \sigma_2 / R_{\perp}^c + b_{\perp}^{\tau} \sigma_2^2 / R_{\perp}^{c2} + c_{\perp}^{\tau} \tau_{21}^2 / R_{\perp\parallel}^2 = 1 \quad (6.1b)$$

is recommended with  $a_{\perp}^{\tau}, b_{\perp}^{\tau}$  from the equations (4.1, 4.2) and the calibration points indicated in Fig. 6 by a square. Due to micromechanical interaction caused by the matrix the author *micromechanically* combines  $NF_{\perp\parallel}$  and  $NF_{\perp}$  in his approach (Puck:  $SF_{\perp}$  and  $SF_{\perp\parallel}$  *macrome*-mechanically).

**Fracture Curves: Probabilistic Approach**

The probabilistic out-smoothing in the MFD or transition zone, resp., of the piecewise smooth fracture-type related domains of the IFF-body shall be visualised by Fig. 7.

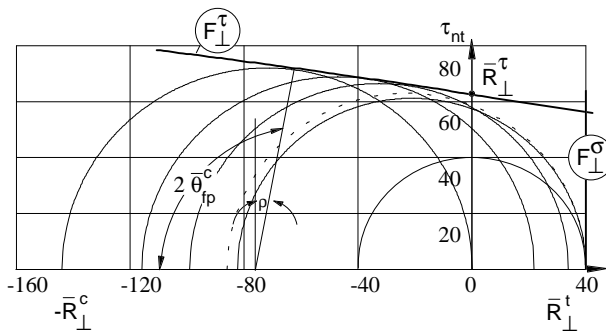


Fig. 8: An analytically derived Mohr-Coulomb "Envelope" Curve (bold) with MFD-circles and Transition Circle (dashed).

(  $R_{\perp}^{\tau}$  = friction cohesion,  $\rho = \tan \mu_{\perp\perp}$ ,

$$x_i^{NO} = (m-k) \cdot t_i - \frac{m^2 (c_N^{NO})_{x_i}}{4h_i t_i} \left( i_i \geq (c_N^{NO})_{x_i} \frac{m}{2h_i t_i} \right)$$

Further the traditional "global fit" by polynomial interaction failure models (applied by most of the traditional strength criteria) is compared with the "modus fit" proposed in this article. The application of the probabilistic out-smoothing leads again back to one equation for the description of the global course of test data. Based on the numerical investigations for Fig. 7 one further conclusion can be drawn that multiple fracture in a mode, e.g.  $NF_{\perp}$  caused by biaxial tensile stresses, will be not covered by the simple modus fit ( $c_{\perp}^{\sigma} = 0$ ). This correction term is necessary to approximate the test data in the MPF regime. Beside this, the term also has an effect in the MFD regime ( $SF_{\perp}, NF_{\perp}$ ), which is not adverse because such brittle materials with a high contents of defects show both sorts of out-smoothing.

Essential for the dimensioning of FRP-structures is the "B-value Design Curve", most often.

Fig. 8 eventually shows (probably for the first time) an analytically derived Envelope Curve. To remind us of the former enveloping procedure the compression circle and the transition (the fracture mechanism jumps from  $NF_{\perp}$  to  $SF_{\perp}$ ) circle are included. Also the relationship of

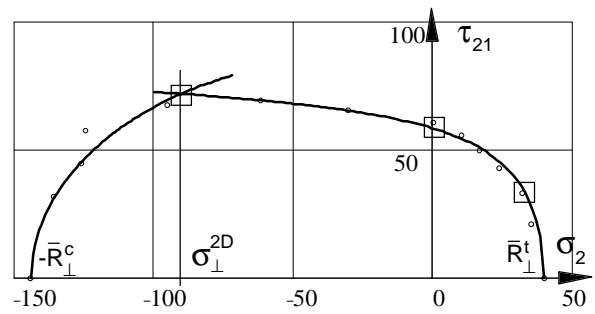


Fig. 6: 2D-Approximation (50%, Mean Curve).   
 o Test Data from [Kna72].   
 □ calibration points

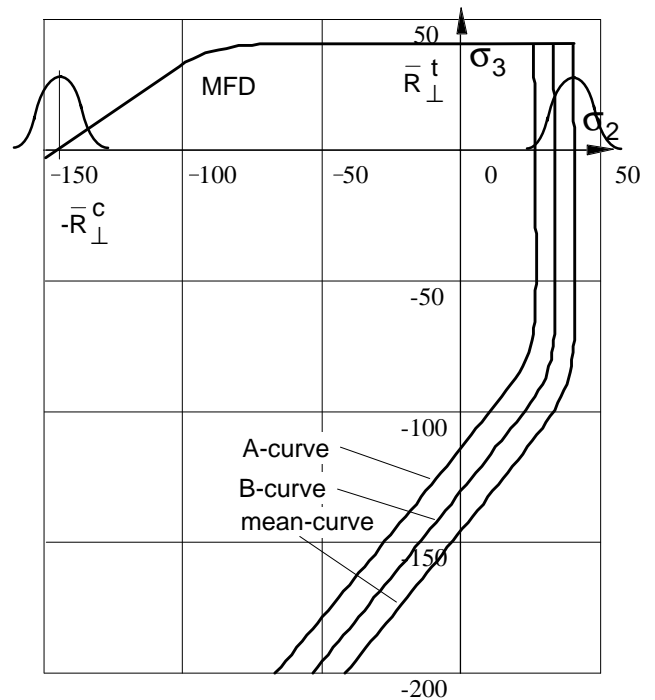


Fig. 7: "Global Fit" versus "Modus Fit".   
 Design curves showing Probabilistic Out-smoothing in the Mixed Failure Domain (MFD)

fracture angle, friction angle  $\rho$  and the local Coulomb friction coefficient  $\mu_{\perp\perp}^c$  derived from a  $R_{\perp}^c$ -loading are given.

In the MFD no realistic fracture angle will be determined. Consequently the  $\tau_{nt}(\sigma_n)$  curve again has to be an envelope of the circles  $(\sigma_2^d, \sigma_3)$  or  $(\sigma_2, \sigma_3^d)$  the values of which are the curve points of the probabilistic function (5.4) describing the transition from  $SF_{\perp}$  to  $NF_{\perp}$ . And, looking at the FEM codes the fracture conditions offered for a so-called "linear or parabolic Mohr-Coulomb Material" is nothing but a continuous mathematical description of an envelop of Mohr's circles in the MFD. It just has relation to Mohr's fracture angle outside the MFD where a "pure"  $SF_{\perp}$  or  $NF_{\perp}$  mode is dominating.

## **CONCLUSIONS, OUTLOOK AND REMARKS**

### **Test Data Fit and Failure Modes**

- The author has the same point of view as L.J. Hart-Smith: It is scientifically incorrect to employ polynomial interaction failure models whenever the (micromechanical) failure mechanism of the critical constituent of the composite changes with the state of stress. And - valid for any material - the main shortcoming of global criteria is: A change in one strength (which belongs to a distinct fracture mode) has an effect on the *whole failure surface (surface of fracture body)* which represents all modes ([Har93, Cun94]). Interactions between *different* failure modes are incorrect. Interactions between stresses affecting the *same* failure mode in the *same* constituent of the composite are permitted.
- Separate characterisations are needed for *each* failure mechanism in *each* constituent of a composite of materials. The fit has to be performed for each mode separately.
- It does not matter whether a state of stress comes from a one-, a two- or a three-dimensional stressing as long it belongs to one fracture mechanism or mode. Consequently all these states of stress can be described by the *same* fracture condition.
- In the isotropic planes test data excellently can be described by the homogenized stresses  $\sigma_2, \sigma_3, \tau_{23}$  (composite = smeared or averaged material). However, if the UD-lamina is e.g. subjected to  $(\sigma_1, \sigma^2, \sigma^3)$  the constituent (real isotropic or anisotropic material) stress  $\sigma_{1f}$  will be responsible for fracture and not the composite stress  $(\sigma_1)$ .

### **Strength Criteria:**

- There are 3 categories of failure criteria: stress-based, strain-based and energy-based. The criteria can be grouped into independent, partly (stress) interactive and globally interactive ones. Their development may be based on micromechanical (constituent level) and/or (meso/) macromechanical investigations (lamina resp. composite level).
- The author prefers stress criteria in the proof of design because: stresses fracture the material, residual stresses are taken into account and strain history is considered in the strength values.



- The concept of strength criteria presented exhibit a physical basis, a good fit of test data course, invariance with respect to coordinate transformations, a relatively easy application involving numerical stability and applicability to ductile behaving composites as well.
- From the several applications a preliminary assessment of the concept is possible:
  - the fracture conditions  $F = 1$  determine the shape of the failure surface with its five piecewise smooth areas, representing the five modes
  - a separation of mechanical and probabilistic modelling would be advantageous for an accurate interpretation of test results but is not completely possible. The probabilistic tool has to be taken to smooth-out in the mixed failure domain (MFD) resp. transition domain of two or more modes the adjacent mode-related pieces of the "failure surface"
  - the out-smoothing approximately can be done by applying correction terms instead of performing real probabilistic calculations
- The application of the concept to various isotropic test results was very successful and is very promising in case of transversally-isotropic UD-laminae, too. A big challenge will be an application to the various woven fabric laminae.
- Because "high tech" composite parts normally have notches and often have to be designed to damage tolerance they were qualified more or less by tests. So, the physical drawbacks of the traditional strength criteria applied to unnotched (and notched) structures have not been revealed.

### Design (dimensioning) and Proof of Design:

- There are 5 basic strengths (or 5 resistances, if Mohr would be strictly applied) and as much modes or fracture mechanisms, respectively.
- To establish 3D-design curves the concept just needs for the "fitting" of the 5 pure modes the 5 basic strength allowables, the fracture angle  $\theta_{fp}^c$  (pertaining Coulomb's friction) and a calibration point at the  $(\sigma_2, \tau_{21})$ -bulge. If micromechanical interaction will be taken into account 3 more calibration points have to be provided or can be assumed from experience with a FRP family in order to determine the remaining curve parameters belonging to the correction terms. The curve parameters of each failure function in this paper are computed- beside the basic strength points - from further distinct calibration points, only. Generally of course, a root mean square-fit is foreseen to achieve their values.
- For the dimensioning the designer needs the coloured contour plots or profiles of the stresses as output of the FEM stress analysis and for the Proof of Design he should get offered by the FEM codes coloured profiles of  $f_{Res}^{mode}$  too. This is indirectly still practiced when plotting the equivalent stress of v. Mises ( $3 J_2 / \sigma_{yield}^2 = 1 \rightarrow f_{Res}^{mode} = (\sigma_{yield}^2 / \sigma_{equiv}^2)^{0,5} = \sigma_{yield}^2 / 3J_2)^{0,5}$ ) plots for the mode "onset of yielding" in case of isotropic material or for NF with the principal tensile stress ( $\sigma_I / R^t = 1 \rightarrow f_{Res}^{mode} = R^t / \sigma_I$ ). The lowest  $f_{Res}^{mode}$  computed for IFF and FF drives the design.

- In the mixed failure domain equ. (5.6) delivers an estimation for  $f_{Res} = f(f_{Res}(\text{modes}))$ , therewith bypassing together with the correction terms a real probabilistic out-smoothing.
- The determination of  $f_{Res}$  in case of cubic invariants is a little more laborious. If residual stresses have to be taken into account, due of  $f_{Res} \cdot \{\sigma\}^{(load)} + \{\sigma\}^{(residual)}$ , see [VDI97].

### ACKNOWLEDGEMENTS

The author highly appreciates the excellent support of his colleague B. Szelinski, the fruitful discussions with Dr. "John" Hart-Smith and the comments of members co-operating under the German R&D contract number 03N8002 of the BMBF [VDI97].

### REFERENCES

- [1] Awaji, H. and Sato, S.: A Statistical Theory for the Fracture of Brittle Solids under Multiaxial Stresses. International Journal of Fracture 14 (1978), R13-16
- [2] *Boehler, J.P.*: Failure criteria for glass-fiber reinforced composites under confining pressure. J. Struct. Mechanics 13, 371-393
- [3] *Cuntze, R.G.*: "Fracture-type Strength Criteria" formulated by Invariants which consider the Materials Symmetries of the Isotropic/Anisotropic Material used. Conf. on Spacecraft Structures, Materials and Mechanical Testing. ESA-CNES-DARA: Noordwijk, March 1996
- [4] *Cuntze, R.G.*: Bruchtypbezogene Auswertung mehrachsiger Bruchtestdaten und Anwendung im Festigkeitsnachweis sowie daraus ableitbare Schwingfestigkeits- und Bruchmechanikaspekte. DGLR-Jahrestagung, Dresden, Sept. 96, Tagungsband 3
- [5] *Flaggs, D.L., Kural, M.H.*: "Experimental Determination of the In Situ Transverse Lamina Strength in Graphite Epoxy Laminates". J. Comp. Mat. Vol 16 (1982), S. 103-116
- [6] *Hart-Smith, L.J.*: An Inherent Fallacy in Composite Interaction Failure Curves. Designers Corner, Composites 24 (1993), 523-524
- [7] *Hashin, Z.*: Failure Criteria for Unidirectional Fibre Composites. J. of Appl. Mech. 47 (1980), 329-334
- [8] *Hufenbach, W. and Kroll, L.*: A New Failure Criterion Based on the Mechanics of 3-Dimensional Composite Materials. ICCM-10, Whistler, Canada, 1995
- [9] *Jeltsch-Fricker, R.*: Bruchbedingungen vom Mohrschen Typ für transversal-isotrope Werkstoffe am Beispiel der Faser-Kunststoff-Verbunde. ZAMM 76 (1996), 505-520

- [10] *Knappe, W. und Schneider, W.*: "Bruchkriterien für unidirektionalen Glasfaser/Kunststoff unter ebener Kurzzeit- und Langzeitbeanspruchung". *Kunststoffe*, Bd. 62 (1972), 864
- [11] *Kopp J. and Michaeli, W.*: Dimensioning of Thick Laminates using New IFF Strength Criteria and some Experiments for their Verification. Proceedings "Conf. on Spacecraft Structures Materials and Mechanical Testing", ESA, 27-29 March 1996
- [12] *Mohr, O.*: Welche Umstände bedingen die Elastizitätsgrenze und den Bruch eines Materials? *Civilingenieur* 44 (1900), 1524-1530, 1572-1577
- [13] *Paul, B.*: A Modification of the Coulomb Mohr Theory of Fracture. *J. of Appl. Mech.* (1961), 259-268
- [14] *Puck, A.*: Ein Bruchkriterium gibt die Richtung an. *Kunststoffe* 82 (1992), S. 607-610 (A failure criterion shows the Direction - Further Thoughts on the Design of Laminates - *Kunststoffe German Plastics* 82 (1992), 29-32)
- [15] *Puck, A.*: Festigkeitsanalyse von Faser-Matrix-Laminaten. (Modelle für die Praxis). München: Carl Hanser Verlag, 1996
- [16] *Rowlands, R.E.*: Strength (Failure) Theories and their Experimental Correlation. In Sih, G.C. and Skudra, A.M.: editors, *Handbook of Composites*, Vol. III, chapter 2, Elsevier Science Publisher B.V., Madison, WI, U.S.A., 1985, 71-125
- [17] *Sähn, S. und Göldner, H.*: Bruch- und Beurteilungskriterien in der Festigkeitslehre. Fachbuchverlag Leipzig-Köln, 2. Ausgabe, 1993
- [18] *Tsai, S.W. and Wu, E.M.*: A General Theory of Strength for Anisotropic Materials. *Journal Comp. Mater*, Vol. 5 (1971), 58-80
- [19] *Cuntze, R.G., et.al.*: Zum verbesserten Festigkeitsnachweis von Bauteilen aus Faser-kunststoffverbund. - Modellbildung und Experimente zu einer physikalisch begründeten Festigkeitshypothese für die unidirektionale Schicht. VDI-Fortschrittbericht, Reihe 5. BMBF-Vorhaben 03N8002 (A. Puck, adviser until 1995)
- [20] Dornier, Fokker, MBB, DLR: Investigations of Fracture Criteria for Laminae (in German). 1975-1980, Grant from Ministry of Defence, BMVg, Koblenz

# A SINGULAR HYBRID FINITE ELEMENT ANALYSIS OF INTERLAMINAR CRACK PROBLEMS

Kyohei Kondo<sup>1</sup> and Kazuhiro Yagi<sup>2</sup>

<sup>1</sup> *Department of Aeronautics and Astronautics, University of Tokyo  
7-3-1 Hongo, Bunkyo-ku, Tokyo 113, Japan.*

<sup>2</sup> *Space Systems Department, Aerospace Division, Nissan Motor Co., Ltd.  
3-5-1 Momoi, Suginami-ku, Tokyo 167, Japan.*

**SUMMARY:** Singular stress distributions near interlaminar crack in composite laminate under various loadings are analyzed by a singular hybrid element method which is developed based on the elasticity solutions and the variational principle of a hybrid functional. Asymptotic solutions for displacements and stresses near the interfacial crack between dissimilar anisotropic materials are utilized as the displacement and stress expressions within the crack element. The singular hybrid element is used in conjunction with the conventional displacement-based, quasi three-dimensional elements to study the detailed nature of the displacements and stresses in vicinity of the interlaminar crack tip.

Analyzing a small interfacial crack in a large composite under mechanical loading, we demonstrate that the present numerical solutions are in good agreement with the analytical ones for a interfacial crack in infinite composite. Then, we apply the present method for analysis of delamination cracks originating from transverse cracking in composite under various loadings. Comparisons of the present solutions with the results by the displacement finite element method show the accuracy and efficiency of the present finite element procedure.

**KEYWORDS:** delamination, stress singularity, potential energy release rate, finite element method, singular element, hybrid element, variational principle

## INTRODUCTION

Delamination is the most commonly observed failure mode in composite laminates under mechanical and hygrothermal loadings which have been extensively utilized for the lightweight structures. Onset and growth of the delamination can be characterized by the fracture mechanics based on the singular stress distributions at the crack tip. The stress field near the interfacial crack can be analyzed by the conventional displacement finite element method [1, 2] or the singular hybrid finite element method [3, 4].

In this paper, a singular hybrid element method for studying the stresses near the interfacial crack is presented. The fundamental solution for the displacements and stresses in vicinity of the crack tip is reviewed first. The singular crack element is formulated based on the elasticity solutions and a hybrid variational principle. Comparisons of the present numerical

solutions with the analytical ones or the numerical ones by the displacement finite element method demonstrate the accuracy and efficiency of the present finite element method.

### **ASYMPTOTIC SOLUTION FOR DISPLACEMENTS AND STRESSES NEAR INTERFACIAL CRACK TIP**

For the generalized plane strain state, displacements are given by

$$u_i = U_i(x_1, x_2) = U_i(x_\sigma) \quad (1)$$

We use the convention that all Latin indices take the values 1, 2, 3 and all Greek indices the values 1, 2.

#### **Two-Dimensional Anisotropic Elasticity Problem**

The equilibrium equations are

$$\sigma_{i\sigma, \sigma} = 0 \quad (2)$$

The strain-displacement relations are

$$\varepsilon_{k\ell} = \frac{1}{2}(u_{k, \ell} + u_{\ell, k}) \quad (3)$$

The constitutive equations are

$$\sigma_{i\sigma} = C_{i\sigma k\ell} \varepsilon_{k\ell} \quad (4)$$

Substituting Eqns 3 to Eqns 4 and to Eqns 2, we have

$$C_{i\sigma k\ell} u_{k, \sigma\ell} = C_{i\sigma k\rho} u_{k, \sigma\rho} = 0 \quad (5)$$

It can be assumed [5] that general solutions to Eqns 5 are given by

$$u_k = a_k f(z) \quad z = x_1 + p x_2 \quad (6)$$

where  $a_k$  and  $p$  are, respectively, the eigenvector and eigenvalue to be determined.

Inserting Eqns 6 into Eqns 5, we get

$$\{C_{i1k1} + p(C_{i1k2} + C_{i2k1}) + p^2 C_{i2k2}\} a_k f(z)_{,zz} = 0 \quad (7)$$

The condition that all  $a_k$ 's are not zero gives six eigenvalues and the associated eigenvectors, and

$$p_\alpha, p_{\alpha+3} = \bar{p}_\alpha \quad ; \quad \mathbf{a}_\alpha, \mathbf{a}_{\alpha+3} = \bar{\mathbf{a}}_\alpha \quad (\text{Im}[p_\alpha] > 0, \alpha = 1, 2, 3)$$

where Im stands for the imaginary part and the overbar denotes the complex conjugate. The displacements are expressed as

$$\mathbf{u} = \sum_{\alpha=1}^3 \{ \mathbf{a}_\alpha f_\alpha(z_\alpha) + \bar{\mathbf{a}}_\alpha f_{\alpha+3}(\bar{z}_\alpha) \} \quad z_\alpha = x_1 + p_\alpha x_2 \quad (8)$$

And the stresses take the form

$$\left. \begin{aligned} \sigma_{i1} &= - \sum_{\alpha=1}^3 \left\{ p_{\alpha} b_{i\alpha} \frac{d}{dz_{\alpha}} f_{\alpha}(z_{\alpha}) + \bar{p}_{\alpha} \bar{b}_{i\alpha} \frac{d}{d\bar{z}_{\alpha}} f_{\alpha+3}(\bar{z}_{\alpha}) \right\} \\ \sigma_{i2} &= \sum_{\alpha=1}^3 \left\{ b_{i\alpha} \frac{d}{dz_{\alpha}} f_{\alpha}(z_{\alpha}) + \bar{b}_{i\alpha} \frac{d}{d\bar{z}_{\alpha}} f_{\alpha+3}(\bar{z}_{\alpha}) \right\} \end{aligned} \right\} \quad (9)$$

where

$$\begin{aligned} b_{i\alpha} &= (C_{k1i2} + p_{\alpha} C_{i2k2}) a_{i\alpha} \\ &= -\frac{1}{b_{\alpha}} (C_{i1k1} + p_{\alpha} C_{i1k2}) a_{i\alpha} \end{aligned} \quad (10)$$

### Displacements and Stresses near Interfacial Crack Tip

If we assume a power-type eigenfunction for  $f(z)$  in Eqns 6 as

$$f(z) = \frac{cz^{\delta+1}}{\delta+1} \quad \text{Re}[\delta] > -1 \quad (11)$$

near the crack tip shown in Fig.1, we have

$$f_{\alpha} = q_{\alpha} f(z_{\alpha}) \quad f_{\alpha+3}(\bar{z}_{\alpha}) = h_{\alpha} f(\bar{z}_{\alpha}) \quad (\alpha = 1, 2, 3) \quad (12)$$

From the stress conditions on the crack surface and the continuity conditions for displacements and tractions on the interface, we get

$$\begin{aligned} \delta_n^I &= -\frac{1}{2} + n + i\gamma & \bar{\delta}_n^I &= -\frac{1}{2} + n - i\gamma & \delta_n^R &= -\frac{1}{2} + n & \delta_n^{N_1} &= \delta_n^{N_2} = \delta_n^{N_3} = n \\ & & & & & & & (n = 0, 1, 2, \dots) \end{aligned} \quad (13)$$

It follows from Eqns 8, 9, 11 and 12 that the displacements and stresses are given by

$$u_i^{(k)} = \sum_{n=0}^{\infty} \left[ s_n^{I_1} \text{Re}[\varphi_{in}^{I(k)}] + s_n^{I_2} \text{Im}[\varphi_{in}^{I(k)}] + s_n^R \text{Re}[\varphi_{in}^{R(k)}] + \sum_{j=1}^3 s_n^{N_j} \text{Re}[\varphi_{in}^{N_j(k)}] \right] \quad (k = 1, 2) \quad (14)$$

$$\left. \begin{aligned} \sigma_{i1}^{(k)} &= \sum_{n=0}^{\infty} \left[ s_n^{I_1} \text{Re}[X_{in}^{I(k)}] + s_n^{I_2} \text{Im}[X_{in}^{I(k)}] + s_n^R \text{Re}[X_{in}^{R(k)}] + \sum_{j=1}^3 s_n^{N_j} \text{Re}[X_{in}^{N_j(k)}] \right] \\ \sigma_{i2}^{(k)} &= \sum_{n=0}^{\infty} \left[ s_n^{I_1} \text{Re}[\psi_{in}^{I(k)}] + s_n^{I_2} \text{Im}[\psi_{in}^{I(k)}] + s_n^R \text{Re}[\psi_{in}^{R(k)}] + \sum_{j=1}^3 s_n^{N_j} \text{Re}[\psi_{in}^{N_j(k)}] \right] \end{aligned} \right\} \quad (15)$$

## HYBRID FINITE ELEMENT FORMULATION

The functional of the hybrid Hellinger-Reissner principle [6] is given by

$$\Pi_{Rh} = \sum_m \left[ \iint_{A_m} \left\{ \frac{1}{2} \sigma_{ij} (u_{i,j} + u_{j,i}) - U_c(\sigma_{ij}) \right\} dA - \int_{S_m} T_i (u_i - \tilde{u}_i) ds - \int_{(S_u)_m} T_i (u_i - \bar{u}_i) ds - \int_{(S_\sigma)_m} \bar{T}_i \tilde{u}_i ds \right] \quad (16)$$

where  $A_m$  is the area of element ;  $S_m$  is the interelement boundary,  $(S_u)_m$  the boundary where displacements are prescribed,  $(S_\sigma)_m$  the boundary where tractions are prescribed ; and  $\tilde{u}_i$  is displacements defined along the element boundary. If we assume that

$$\tilde{u}_i = \bar{u}_i \quad \text{on } (S_u)_m \quad (17)$$

$$u_i = \tilde{u}_i \quad \text{on } (S_\sigma)_m \quad (18)$$

and introduce Eqns 18 into Eqn 16 by adding the term

$$- \int_{(S_\sigma)_m} T_i (u_i - \tilde{u}_i) dS$$

we obtain a functional of a modified hybrid Hellinger-Reissner principle as

$$\Pi_{mRh} = \sum_m \left[ \iint_{A_m} \left\{ \frac{1}{2} \sigma_{ij} (u_{i,j} + u_{j,i}) - U_c(\sigma_{ij}) \right\} dA - \int_{\partial A_m} T_i (u_i - \tilde{u}_i) ds - \int_{(S_\sigma)_m} \bar{T}_i \tilde{u}_i ds \right] \quad (19)$$

where  $\partial A_m$  is the boundary of  $A_m$ .

If the stresses satisfy the equilibrium equations and the compatibility conditions, Eqn 19 becomes

$$\begin{aligned} \Pi_{mRh} &= \sum_m \left[ \iint_{A_m} \frac{1}{2} \sigma_{ij} u_{i,j} dA - \int_{\partial A_m} T_i (u_i - \tilde{u}_i) ds - \int_{(S_\sigma)_m} \bar{T}_i \tilde{u}_i ds \right] \\ &= \sum_m \left[ \int_{\partial A_m} T_i \tilde{u}_i ds - \frac{1}{2} \int_{\partial A_m} T_i u_i ds - \int_{(S_\sigma)_m} \bar{T}_i \tilde{u}_i ds \right] \end{aligned} \quad (20)$$

And, if the stress boundary conditions

$$\bar{T}_i = 0 \quad \text{on } (S_\sigma)_m \quad (21)$$

are satisfied, Eqn 20 takes the form

$$\begin{aligned} \Pi_{mRh} &= \sum_m \left[ \int_{\partial A_m} T_i \tilde{u}_i ds - \frac{1}{2} \int_{\partial A_m} T_i u_i ds \right] \\ &= \sum_m \left[ \int_{\partial A_m} \mathbf{T}^T \tilde{\mathbf{u}} ds - \frac{1}{2} \int_{\partial A_m} \mathbf{T}^T \mathbf{u} ds \right] \end{aligned} \quad (22)$$

### Stiffness Matrix Formulation for Singular Crack Element

If we truncate the series expansion in Eqns 14 and 15 at  $n = N$ , we have the displacements and tractions at the interelement boundary of  $A_m$  as

$$\mathbf{u} = \mathbf{U}\boldsymbol{\beta} \quad \mathbf{T} = \mathbf{R}\boldsymbol{\beta} \quad (23)$$

where

$$\boldsymbol{\beta} = [s_0^{I_1}, s_0^{I_2}, s_0^R, s_0^{N_1}, s_0^{N_2}, s_0^{N_3}; \dots; s_N^{I_1}, s_N^{I_2}, s_N^R, s_N^{N_1}, s_N^{N_2}, s_N^{N_3}] \quad (24)$$

The interelement boundary displacements are expressed in terms of the nodal displacements  $\mathbf{q}$  as

$$\tilde{\mathbf{u}} = \mathbf{L}\mathbf{q} \quad (25)$$

Substituting Eqns 23 and 25 into Eqn 22, we get

$$\begin{aligned} \Pi_{mRh}^{(m)} &= \boldsymbol{\beta}^T \left[ \int_{\partial A_m} \mathbf{R}^T \mathbf{L} ds \right] \mathbf{q} - \frac{1}{2} \boldsymbol{\beta}^T \left[ \int_{\partial A_m} \mathbf{R}^T \mathbf{U} ds \right] \boldsymbol{\beta} \\ &= \boldsymbol{\beta}^T \left[ \int_{\partial A_m} \mathbf{R}^T \mathbf{L} ds \right] \mathbf{q} - \frac{1}{2} \boldsymbol{\beta}^T \left[ \frac{1}{2} \int_{\partial A_m} (\mathbf{R}^T \mathbf{U} + \mathbf{U}^T \mathbf{R}) ds \right] \boldsymbol{\beta} \\ &= \boldsymbol{\beta}^T \mathbf{G} \mathbf{q} - \frac{1}{2} \boldsymbol{\beta}^T \mathbf{H} \boldsymbol{\beta} \end{aligned} \quad (26)$$

where

$$\mathbf{G} = \int_{\partial A_m} \mathbf{R}^T \mathbf{L} ds \quad H = \frac{1}{2} \int_{\partial A_m} (\mathbf{R}^T \mathbf{U} + \mathbf{U}^T \mathbf{R}) ds \quad (27)$$

Taking variation of  $\Pi_{mRh}^{(m)}$ , we obtain

$$\delta \Pi_{mRh}^{(m)} = \delta \boldsymbol{\beta}^T (\mathbf{G} \mathbf{q} - \mathbf{H} \boldsymbol{\beta}) = 0 \quad (28)$$

which gives

$$\boldsymbol{\beta} = \mathbf{H}^{-1} \mathbf{G} \mathbf{q} \quad (29)$$

Substituting Eqns 29 into Eqn 26, the variational functional is expressed as

$$\Pi_{mRh}^{(m)} = \frac{1}{2} \mathbf{q}^T [\mathbf{G}^T \mathbf{H}^{-1} \mathbf{G}] \mathbf{q} = \frac{1}{2} \mathbf{q}^T \mathbf{k}_s \mathbf{q} \quad (30)$$

where  $\mathbf{k}_s$  is the stiffness matrix for the hybrid singular crack tip element.

In the present finite element approach, a 17-node, hybrid crack element shown in Fig.2 with 51 degrees of freedom is constructed. The total number  $N$  of terms in the truncated series in Eqn 23 is takes as 14. Standard quadratic interpolation functions are used for the  $L$  in Eqns 25 to ensure matching of the boundary displacements of the singular hybrid element with those of adjacent 8-node, 24 degrees of freedom, isoparametric regular elements as shown in Fig.3.



## NUMERICAL RESULTS

To confirm the singular hybrid finite element solutions, we analyze a large carbon fiber reinforced plastics (CFRP)  $[0^\circ/90^\circ]$  laminate with a small central crack of length  $2a$  subjected to the uniform far field stress  $\sigma_{22}^\infty$  as shown in Fig.4. The total and singular stress distributions along the interface are shown in Fig.5. The singular stress distributions are shown in Fig.6 together with those obtained by the analytical solution for an infinite plate [7]. Comparison of the numerical solution for the interlaminar singular stresses with the analytical one is also shown in Table 1. The potential energy release rates from the two approaches are

A large CFRP  $[\theta^\circ/-\theta^\circ]$  laminate with a small central crack is also analyzed. The numerical solution for the potential energy release rates is shown in Fig.7 together with the analytical one [7].

Then, we analyze CFRP laminate with delamination originating from transverse cracking as illustrated in Fig.8. The stress distributions along the interface of CFRP laminate under tensile strain  $\varepsilon_{11}^\infty$  are shown in Fig.9 together with those obtained by the displacement finite element method [2] with fine discretization as illustrated in Fig.10.

## CONCLUSIONS

A singular hybrid interfacial crack element has been developed to study the stresses near interfacial crack combining with the conventional regular elements. The present numerical solutions for a small interfacial crack in a large composite are in good agreement with the analytical ones for a crack in an infinite composite. And comparison of the present solutions for delamination originating from transverse cracking with those by the conventional displacement-based finite element method show the accuracy and efficiency of the present finite element procedure.

## REFERENCES

1. Kondo, K. and Aoki, T., "An Energy Release Rate Approach for Free-edge Delamination Problem in Composite Laminates", Composite Structures 4, Marshall, I.H., Ed., Proceedings Fourth International Conference on Composite Structures, Paisley, Scotland, Vol. 2, 1987, pp.241-257.
2. Kondo, K. and Yasue, Y., "Transverse Crack and Delamination in Composite Laminates Subjected to Mechanical and Hygrothermal Loading", Composites '95 : Recent Advances in Japan and the United States, Kimpara, I., Miyairi, H. and Takeda, N., Eds., Proceedings of Seventh Japan-U.S. Conference on Composite Materials, Kyoto, Japan, 1995, pp.91-98
3. Wang, S.S. and Yuan, F.G., "A Singular Hybrid Finite Element Analysis of Boundary - Layer Stresses in Composite Laminates", Int. J. Solids Structures, Vol.19, No.9, 1983, pp.825-837.

4. Kim, Y. and Im, S., "Delamination Crack Originating from Transverse Cracking in Gross-ply Laminates under Various Loadings", *Int. J. Solids Structures*, Vol.30, No.16, 1993, pp.2143-2161.
5. Ting, T.C., "Explicit Solution and Invariance of the Singularities at an Interface Crack in Anisotropic Composite", *Int. J. Solids Structures*, Vol.22, No.9, 1986, pp.965-983.
6. Washizu, K., *Variational Principle in Elasticity and Plasticity*, Second Edition, Pergamon Press, 1974.
7. Qu, J. and Bassani, J. L., "Interfacial Fracture Mechanics for Anisotropic Bimaterials", *Journal of Applied Mechanics*, Vol.60, No.2, 1993, pp.422-431

Table 1 : Interlaminar singular stresses near crack tip of CFRP [0°/90°] laminate under  $\sigma_{22}^{\infty}$  ( $x_2=0, r=x_1-a$ ).

$r/a$	Analytical Solution		FEM Solution	
	$\sigma_{22} / \sigma_{22}^{\infty}$	$\sigma_{21} / \sigma_{22}^{\infty}$	$\sigma_{22} / \sigma_{22}^{\infty}$	$\sigma_{21} / \sigma_{22}^{\infty}$
0.0001	65.35043	-33.60590	64.43491	-33.12293
0.0002	46.88079	-21.78091	46.22377	-21.46717
0.0005	30.15390	-12.09209	29.73109	-11.91726
0.001	21.56054	-7.63736	21.25812	-7.52654
0.002	15.39514	-4.74804	15.17912	-4.67883
0.005	9.84300	-2.45179	9.70482	-2.41575
0.01	7.00676	-1.43630	6.90836	-1.41499
0.05	3.16682	-0.33072	3.12232	-0.32557
0.1	2.24477	-0.13838	2.21321	-0.13608
0.5	1.00473	0.03755	0.99059	0.03709
1.0	0.70922	0.05672	0.69924	0.05603

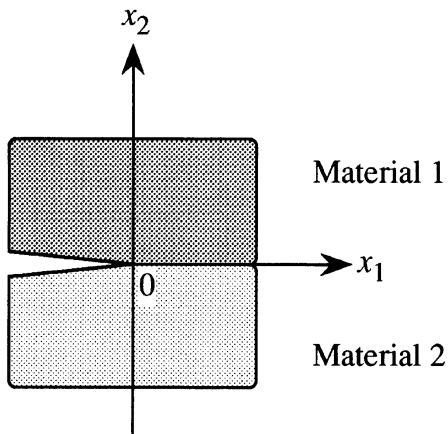


Fig. 1 : Semi-infinite crack.

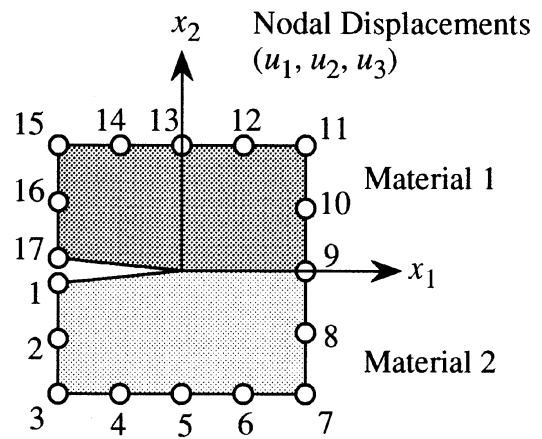


Fig. 2 : Hybrid singular crack element.

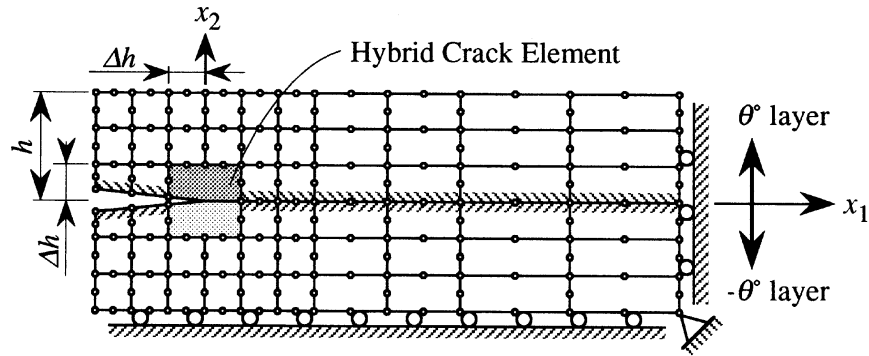


Fig. 3 : Finite element discretization.

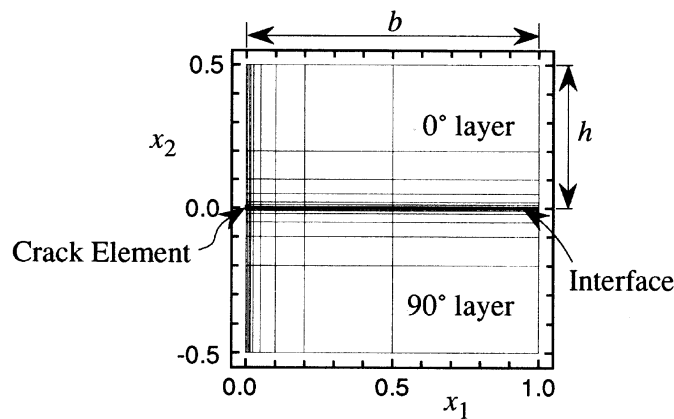


Fig. 4 : CFRP[0°/90°] laminate with central crack of length  $2a$  under  $\sigma_{22}^\infty$ .

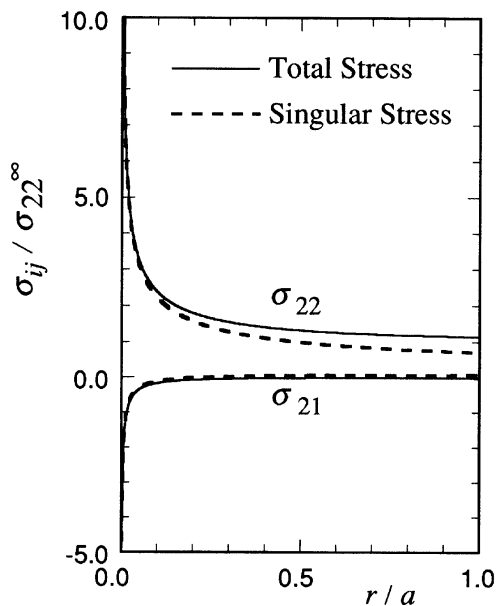


Fig. 5 : Stress distributions along interface near crack tip of CFRP [0°/90°] laminate under  $\sigma_{22}^\infty$  ( $x_2 = 0$ ,  $r = x_1 - a$ ).

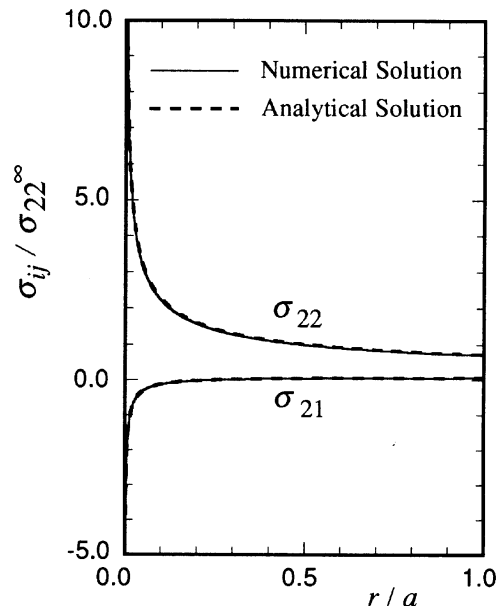


Fig. 6 : Singular stress distributions along interface near crack tip of CFRP [0°/90°] laminate under  $\sigma_{22}^\infty$  ( $x_2 = 0$ ,  $r = x_1 - a$ ).

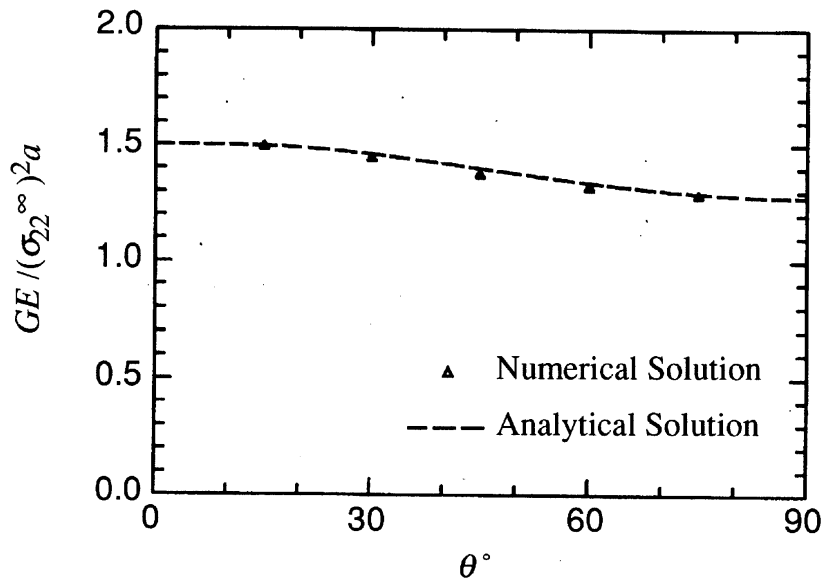


Fig. 7 : Potential energy release rates for crack of CFRP  $[\theta^\circ/\theta^\circ]$  laminate under  $\sigma_{22}^\infty$ .

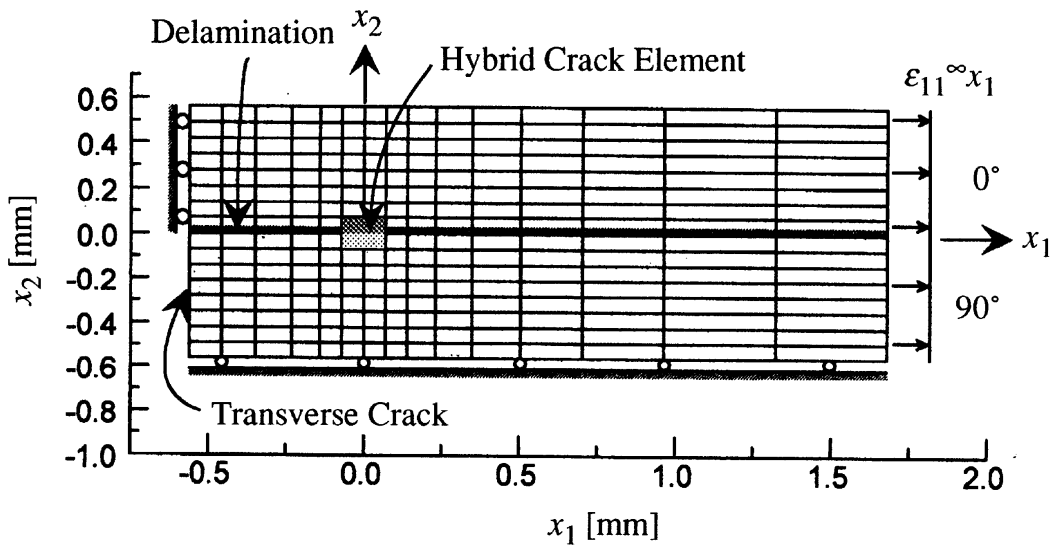


Fig. 8 : CFRP  $[0^\circ/90^\circ]_s$  laminate with delamination originating from transverse crack tip.

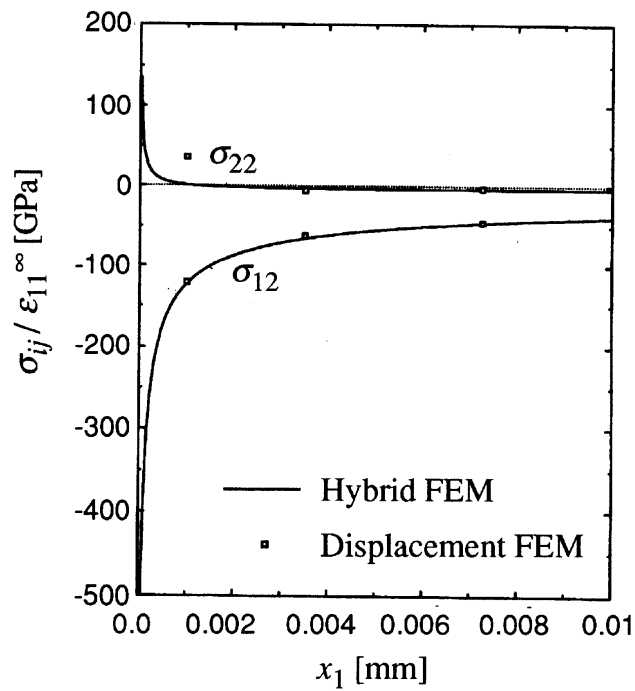


Fig. 9 : Stress distributions along interface of CFRP  $[0^\circ/90^\circ]_s$  laminate with delamination originating from transverse crack tip.

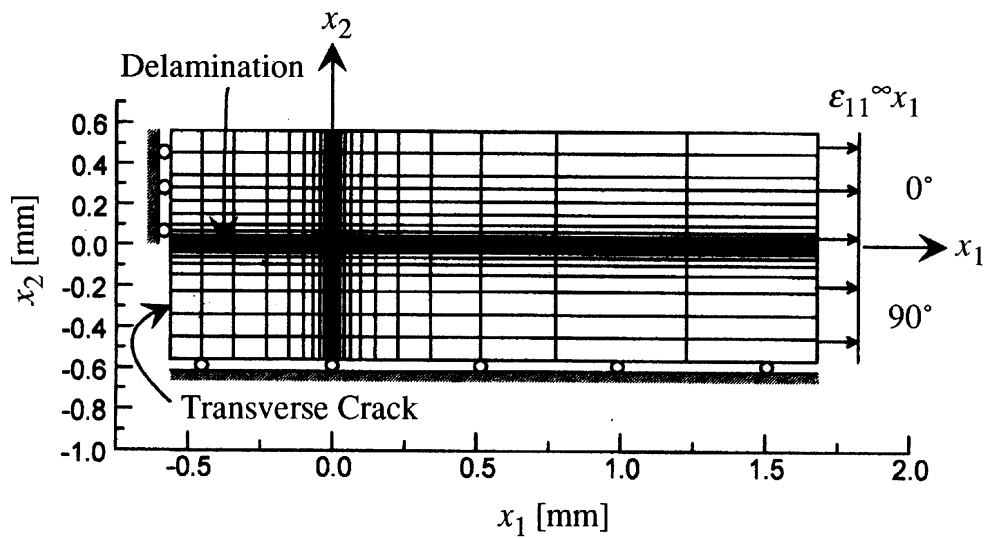


Fig. 10 : Discretization for displacement finite element analysis of CFRP  $[0^\circ/90^\circ]_s$  laminate with delamination originating from transverse crack tip.

# FAILURE BEHAVIOR AND MORPHOLOGY OF HYBRID SHORT-FIBERS REINFORCED COMPOSITE UNDER THERMAL AND MECHANICAL LOADINGS

Kh. G. Schmitt-Thomas, Zhen-Guo Yang, and R. Malke

*Institute of Applied Materials Engineering  
Technical University of Munich, Arcisstraße 21, 80333 Munich, Germany*

**SUMMARY:** The mechanical property, microstructure morphology, and failure behavior of hybrid fiber reinforced thermoplastic composite containing defects were studied under coupled thermal and mechanical loading. The system investigated was hybrid short Al/C fibers reinforced polyaryletherketon composite, in which aluminum-fiber and carbon-fiber were 30 wt.-% and 10 wt.-%, respectively. First fracture testing of specimens with different artificial defects including notch and crack-like slot subjected to thermal and mechanical loading was carried out using three-point short-beam bending test; the effect of changing temperature on mechanical strength of the composite was then discussed; next failure mode and corresponding morphology of broken samples were systematically characterized by SEM; and finally, the macroscopic and microscopic failure behavior of the composite under coupled thermal and applied loads were addressed based on experimental data. Results show that high temperature is able to significantly affect macroscopic fracture mode, microscopic failure behavior, and ruptured morphology of the composite along with its mechanical properties.

**KEYWORDS:** Hybrid short-fiber, PAEK resin, high temperature, failure behavior, notch, slot, aluminum-fiber, carbon-fiber.

## INTRODUCTION

Hybrid composite consisting of two different fibers and single matrix is often advantageous over a regular composite. With alternative choice of fiber combination, it offers improved material properties such as thermal conductivity property, fracture toughness, and mechanical strength due to mixture effect of fibers. Therefore hybrid composite has been received considerably attention in the literature. A number of investigations have been made for performance analysis and characterization of hybrid continuous-fiber reinforced composite, for instance, selected papers like static problem [1], dynamic problem [2], fracture mechanics [3], and engineering application [4]. Meanwhile people are also increasingly interested in hybrid short-fiber reinforced composite as it can be used as a secondary structure to substitute steel materials due to its high strength to weight ratio and convenience of molding geometrical complex component. But most of works concentrated on the improvement of its physical properties including thermal and electrical conductivity [5-8], and surface treatment of fibers [9-10].

Like laminated composite for structural materials, however, hybrid short-fiber reinforced composite is sometimes serviced in more complicated environment such as high temperature and coupled thermal-mechanical load. Unfortunately, an available data about the influence

of changing temperature on mechanical property and failure behavior of a given material is very seldom. Furthermore the works done were only limited to consider the effect of single short-fiber on material property regarding high temperature [11-13]. It is thus necessary to perform laboratory tests to simulate actual operation environment of the hybrid composite and further to evaluate its structural integrity under practical service condition.

This study aims to investigate the effect of changing temperature on strength performance and failure behavior of hybrid short-fiber reinforced polymeric composite. The matrix material chosen is Polyaryletherketon (PAEK); it is a kind of new high performance semi-crystalline thermoplastic resin with glass transition temperature of around 170 °C, which combines excellent high-temperature property with retaining high elastic modules and high impact strength [14]. Reinforcements used are aluminum-fiber and carbon-fiber, respectively; the former is used for improving thermal conductivity property of the composite and the latter for enhancing mechanical performance. Since this kind of hybrid composite is a typical advanced composite material, it is able to be used as secondary component in some places where local service temperature is sometimes higher than 160 °C, such as aerospace motor-casing, heating-removal fan, and power pump. Hence the present study will provide important basis for the practical use of PAEK composite as lightweight component replacement. For this purpose, three-point short beam bending test were carried out for specimens containing different artificial defects under varying temperature; then microstructure and fracture mode of the specimens were viewed by optical microscopy, and failure behavior and morphology of the broken samples were observed in detail with scanning electron microscopy.

## EXPERIMENTAL DETAILS

### Materials

The matrix used is a commercial grade PAEK resin, called Ultrapek A1000, which is provided by BASF; aluminum-fiber and carbon-fiber are supplied by Japanese company. Carbon-fiber is a 3 mm long with a diameter of 7  $\mu\text{m}$ , and aluminum-fiber, called as AlMg2.5 metallic-alloy fiber, is a length of 3 mm and its cross-section looks like a quasi triangular-shape with each side length of about 90  $\mu\text{m}$ . Based on the previous work on its thermal and electrical property [5], the hybrid composite to be considered in this study will consist of 30 wt.-% of aluminum-fiber and 10 wt.-% of carbon-fiber. According to designation of ASTM D790, rectangular specimens for three-point short-beam bending test, in which the geometrical dimensions are 80 mm long, 10 mm wide and 4 mm thick, respectively, were manufactured directly by injection molding. The fundamental properties of the relevant materials are listed in Table 1.

### Testing

Optical microscopy was utilized for the visualization of fiber alignment and orientation in the specimen and polarized light was used to view the crystallization of matrix in the composite. Fracture surface and morphology of broken samples were observed in a scanning electron microscope (SEM) and samples were previously gold coated before SEM observation. Differential scanning calorimetry (DSC) was performed for measuring glass transition temperature of the composite, and the results relevant to thermal properties of the composite with different contents of fiber measured by DSC are given in Table 2.



Table 1: Fundamental properties of constituents consisting of hybrid composite

Materials	Tensile strength (MPa)	Tensile modulus (MPa)	Density ( $g / cm^3$ )	Ultimate elongation (%)
Matrix A1000	104	4100	1.3	4
AlMg2.5 fiber	210	70000	2.68	7.5
Carbon fiber	3950	2380000	1.77	1.55
PAEK composite	106	10280	1.60	2.35

Table 2: Thermal properties for the hybrid composite with different fiber content

Sample No.	Matrix	Fiber content (wt. %)	$T_g$ [ $^{\circ}C$ ]	$T_c$ [ $^{\circ}C$ ]	$T_m$ [ $^{\circ}C$ ]
1	PAEK	0	169	339	393
2	PAEK	19.13	169	336	393
3	PAEK	40	170	327	380

Note:  $T_g$  denotes glass transition temperature,  $T_c$  initial melting temperature, and  $T_m$  melting temperature; sample 2 only contains aluminum-fiber and sample 3 contains 30 wt.-% aluminum-fiber and 10 wt.-% carbon-fiber.

Three different kinds of specimens containing different artificial defects were prepared for bending test. The artificial defects with semi-notch and crack-like slot were machined into the center on the edge of each specimen. The geometrical size and configuration of defects are described in the following: the slot is approximately 0.4mm wide and the depth from the edge is 2 mm long; the notch has a radius of  $R=2$  mm and depth from the edge is also 2mm long.

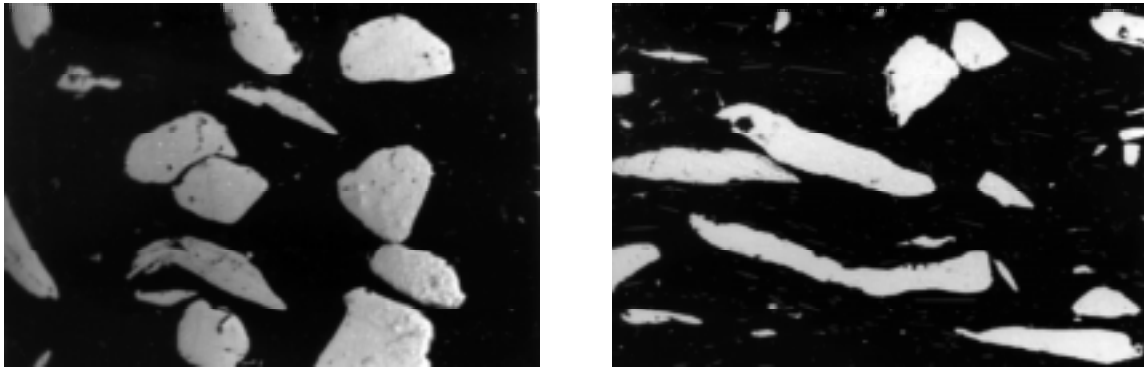
With temperature ranging from room temperature to 200  $^{\circ}C$ , short beam three-point bending test were conducted in Instron 4515 universal test machine with a temperature chamber, and loading rate was chosen to be 5 mm/min. After testing, some samples were cut from section of the fractured specimens for observing their fracture behavior and morphology.

## RESULTS AND DISCUSSIONS

### Microstructure details

In general, injection-molded hybrid short-fiber reinforced composite is fairly inhomogeneous because most of the fibers are aligned in the direction of mold-filling. Fig.1, which illustrates the fiber distribution and orientation along the transverse and longitudinal direction, shows the fibers are preferentially oriented parallel to mold-filling direction. Aluminum-fibers are tendency to the longitudinal direction, in which fiber length points to the flow direction of mold-filling. However, in the direction of transverse section, there is very seldom for fiber length to locate along this direction. As a result, the microstructure of the composite made

through injection molding displays anisotropic property, which will also influence fracture behavior of the material.



*a) along transverse direction (200x)                      b) along longitudinal direction (200x)*  
*Figure 1: Profile of fiber distribution and orientation*

**Effect of changing temperature on composite strength**

The relationship between bending stress and strain of the specimen without artificial defect subjected to different temperature is depicted in Fig. 2. From this figure, we can see that at room temperature, once the applied stress reaches yielding stress of the material, the composite breaks immediately, with no visible plastic deformation. When temperature is raised to 100 °C, the relationship of material 's stress-strain still keeps linear basically without the effect of temperature and the load-bearing capability of the composite reduces a little. The value of maximum stress at this case is only smaller than that of its counterpart at room temperature by a quarter and the magnitude of Young's modulus is almost same each other.

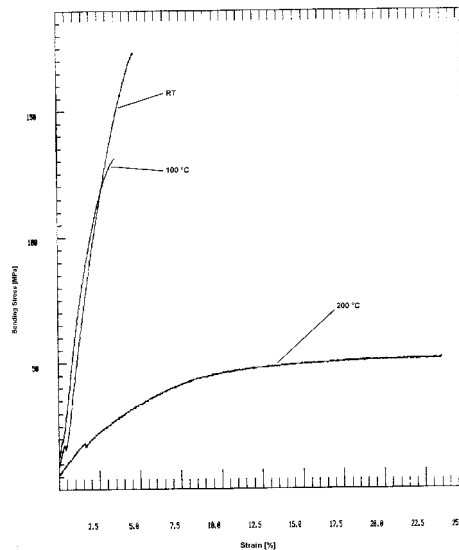


*Figure 2: The effect of changing temperature on material strength (without defect)*

For the case of 200 °C, however, the composite softens greatly and displays nonlinear plastic deformation feature for the high temperature; the whole stress-strain curve looks smooth, and the amount of plastic deformation is considerably large. Consequently, the load-bearing capability of the composite considerably reduces once temperature is above a certain value. Higher temperature makes inherent energy of the material be raised so movement of

molecular becomes more easier. When temperature is risen up to 200 °C, namely higher than glass transition temperature of the resin, the reduction in strength of the composite is extremely large, irrespective of how much of the content of reinforcement fiber; the maximum stress at this time is only half a value at room temperature. Furthermore, the Young's modulus also decreases dramatically, which is only 20% of Young's modulus at room temperature. Comparing to strength performance of the material, the influence of temperature on the composite's stiffness is significantly larger than that of its influence on composite's strength. Similar feature can also be seen from specimens with artificial defect, which will further be discussed in an another separated paper [15]. Therefore, high temperature not only influences strength of the composite but also changes the deformation behavior of the composite. Moreover, when temperature is well above glass transition temperature of resin, the effect of fiber orientation becomes less significant due to easy movement of resin molecular. So high temperature will cause resin damage and shorten residual life of the composite.

**Effect of defect type on material property**

Figure 3 shows the effect of different defect shape on the strength of the composite at room temperature and the associated mechanical properties measured are listed in Table 3.

*Table 3: The effect of defect type on composite strength at room temperature*

Defect type	Young's modulus (MPa)	Maximum load (KN)	Maximum Stress (MPa)	Displacement at break (mm)	Strain at break (%)
non-defect	5343	1.164	173.20	1.209	4.48
notch	4617	0.500	75.58	0.495	1.83
slot	4485	0.488	71.94	0.481	1.79

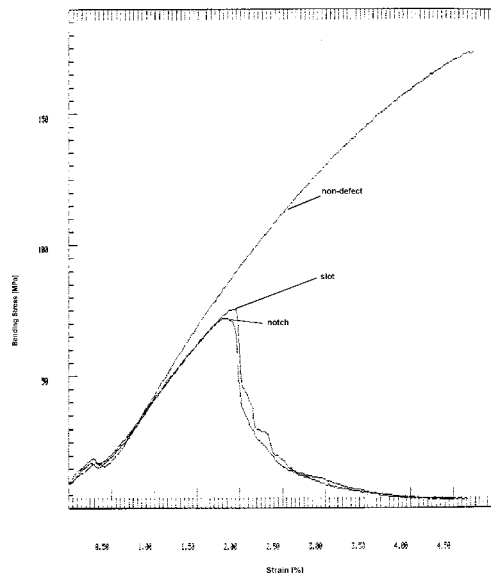


*Figure 3: The effect of defect shape on the strength of the composite (T=24°C)*

Because of stress concentration, like metal material, load-bearing capability of the composite containing defect substantially reduces. In this figure, it can be seen that the maximum stress specimen containing artificial defect can undertake is much smaller than that of specimen

without defect. Usually, their stress values are less than a half stress value of specimen without defect (see Table 3). In addition, the deformation curves of specimens with and without defect are also quite different. Regarding specimen without defect, its stress increases with the increase of strain until final fracture of specimen; whereas for the specimens with defect, their stress first increases with increasing of strain and then the stress in the specimen rapidly decreases due to resin yielding. This implies once resin material enters yielding, specimen will immediately fail without any softening-strengthening phenomena. This is also the same trend for both specimens with defect and specimen without defect. However, for the specimens with notch and slot, their stress-strain curve and tendency look very similarly. The reason is as follow: due to stress concentration, stress at the tip of the notch and slot will reach yielding stress of resin and surrounding materials are thus blunted; but stresses a little far away from the tip zone are still less than yielding stress of the resin, and the materials nearby the tip zone are surrounded by a large amount of linear-elastic material. In this instance, stress at the tip of notch and slot will be relaxed and redistributes by means of plastic deformation of the resin to let tip displacement open largely than before. Moreover, under the condition of high temperature, the material possesses larger ductility and permits bigger displacement value at the tip of defect in comparison with that at room temperature. As a result of these, local stress concentration is not critical to some extent to the magnitude of width at the tip of defect for the tough resin like PAEK. Instead the elastic-plastic behavior of resin material becomes important. Therefore if the resin is a tough material, the critical magnitude of the width at defect tip is a little dependent on the extend of stress concentration caused by defect type but be more dependent on their material's elastic-plastic behavior. This maybe the main reason why the stress-strain curves of the specimens with notch and slot resemble one another.

### Macroscopic fracture mode

For three kinds of specimens, the macro fracture mode of the composite is dependent largely upon temperature. Visual observation of the broken samples indicates that the hybrid composite dissipates fracture energy primarily by a combination of saw-tooth deflection of fracture surface, plastic deformation of specimen, as well as fiber's pull-out, debonding, and rupture (see Fig. 4, and the detailed analysis will be addressed in the following section on microscopic failure behavior).

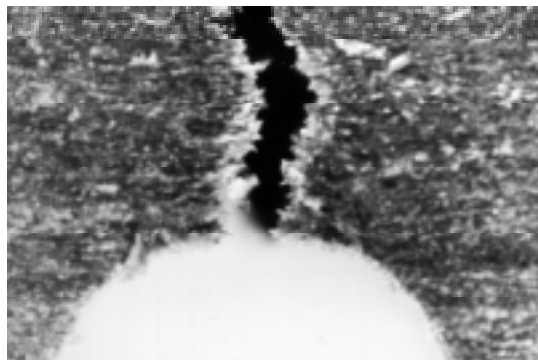
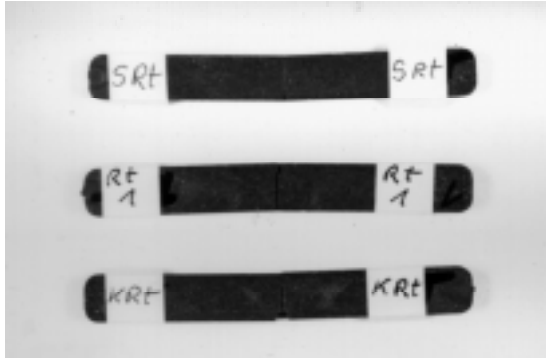


*Figure 4: The macroscopic fractography of specimens containing notch at room temperature*

Fig. 5 shows fracture profile of three kinds of specimens with varying temperature. At room temperature, the fractured specimen keeps fundamentally original shape and the fractured section of three specimens almost separates in the way of brittle. It means that for brittle fracture mode there is very little energy dissipation consumed by plastic deformation prior to

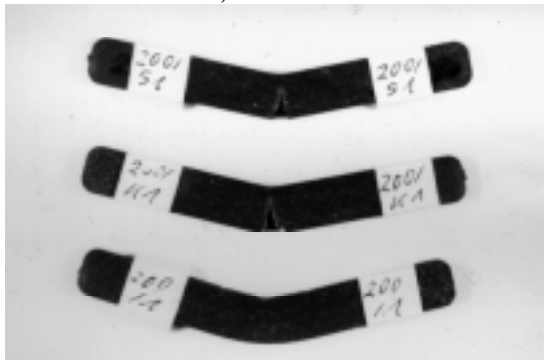
final failure. With the increase of temperature, failure manner is changed from quasi-brittle mode at room temperature to ductile mode at 100 °C. At the time when temperature is equal to 100 °C, the composite possesses more ductile behavior due to increase of inner energy and the whole specimen occurred a little plastic bending.



a)  $T=24^{\circ}\text{C}$



b)  $T=100^{\circ}\text{C}$



c)  $T=200^{\circ}\text{C}$

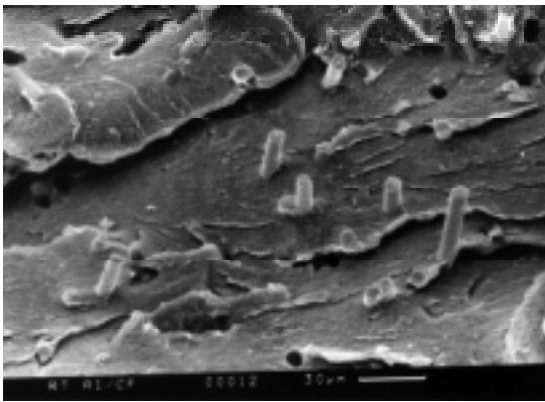
*Figure 5: Optical micrography of the fracture profiles for different temperature*

Compared to its original shape, the geometrical shape of the fractured specimen happen variation; most obviously, fracture surfaces for specimens with notch and slot still connect each other after failure. That implies ductile fracture will consume a certain amount of fracture energy before breaking through plastic deformation as specimens have undergone a larger bend plastic deformation. As temperature is risen to 200 °C, failed specimen displays large plastic deflection. In this circumstance, fracture surface of all three specimens do not break apart; furthermore, deformation process exhibits non-linear plastic flow due to viscous-plastic stretching of matrix. This means the movement and slide of polymer molecular become more easier for high temperature, and resin material tends to be viscous-plasticity behavior. Thus the characteristic of resin damage at high temperature will be viscous-plastic stretching instead of only yielding. For this reason, fracture surfaces of specimens at 200 °C keep together. All of these cases demonstrate the macro fracture feature of the composite has a great good relation with temperature.

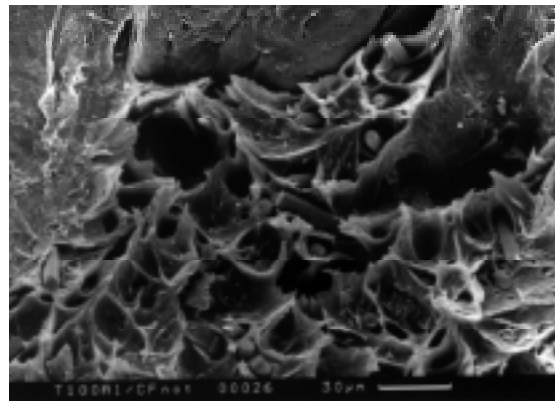
### Microscopic failure behavior

SEM photography of the fracture surface for hybrid composite with changing temperature are shown in Figs 6-8.

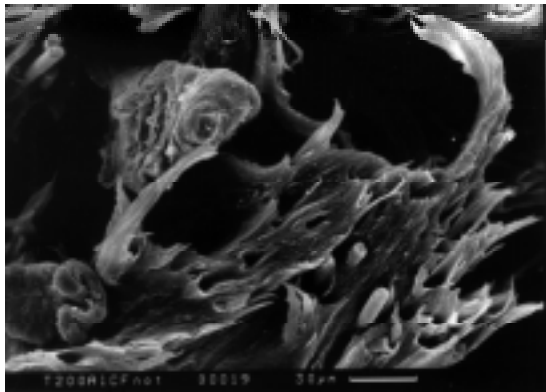
In a sense of micro-level, the fundamental failure behavior of the hybrid composite comprises fiber pull-out (Fig. 6(a)), fiber debonding (Fig. 7), fiber rupture (Fig. 8), and plastic deformation of matrix (Fig. 6 (b) and (c)). The most obvious characteristic for the failure of the composite is that morphology of the matrix is extremely quite different with changing temperature (Fig. 6). At room temperature, matrix morphology is basically flat with cusp and exists a little shear band with brittle behavior; matrix morphology at 100 °C gets rough and appears many ductile dimples, illustrating deformation is in the manner of elastic-plasticity; while  $T=200$  °C, fractography of matrix looks like a shape of mop filling with fibrils, exhibiting viscous-plastic flow deformation is caused by excessive high temperature.



a)  $T=24^{\circ}\text{C}$



b)  $T = 100^{\circ}\text{C}$

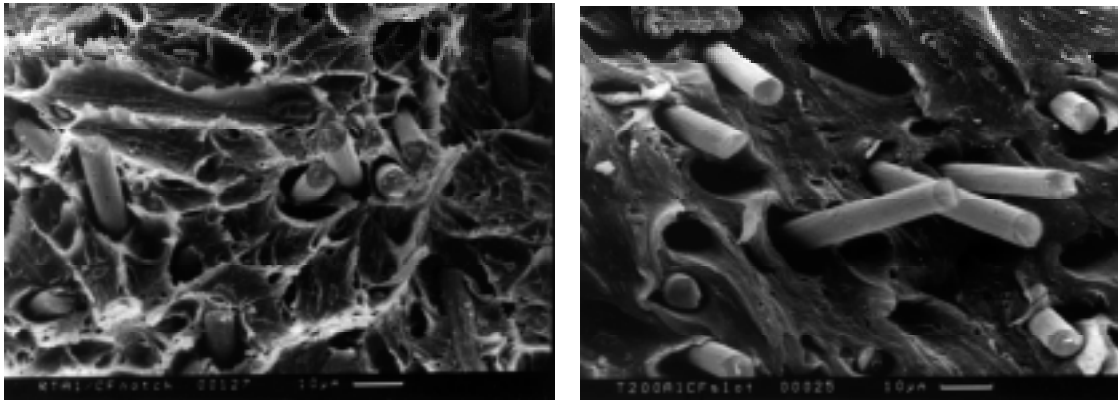


c)  $T=200^{\circ}\text{C}$

*Fig. 6: The effect of changing temperature on morphology of matrix*

Moreover, the interface of matrix and fiber becomes severe due to difference of their thermal expansion coefficients. However, there is no obvious feature to well characterize the effect of defect type on the morphology owing to insensitivity of tough matrix to defect type. The interface between carbon-fiber and matrix is dependent to great extent on their position and place. Two cases for bonding surface of carbon fibers at room temperature are depicted in Fig. 6 (a) and Fig. 7(a). Fig. 6(a) demonstrates excellent interface of carbon-fibers and Fig. 7(a) poor situation for the interface of carbon-fibers. Why is the interfacial surface of carbon-fiber fully different for the same process condition? The crystallization and extend of resin

PAEK on the surface of carbon-fiber account for this result. With reference to Fig. 6(a), there exist a very thin layer of resin film adhere to the surface of the carbon-fiber. This thin layer is resulted directly from crystallization of PAEK resin shown in Fig. 9, in which the interface between resin and carbon-fiber bonds strongly. By contrast, there is very clean on the surface of carbon-fiber shown in Fig. 7, which indicates there is no any crystallization thin layer adhesive to the surface of carbon-fiber. This event is, in fact, closely related to cooling way of the extruded reinforced pellets and molding process of the specimen when molded by injection machinery. At a time when hybrid-fiber reinforced PAEK pellets are extruded, they need to be cooled fast to fix their shape. If the resins are located inside the pellet, they are gradually cooled and thus have relatively more time to crystallize on the surface of the fibers; but if the resins situate on or near the surface of the pellet, they are immediately cooled and thus create brittle amorphous structure without any crystallization.



a)  $T = 24^{\circ}\text{C}$

b)  $T = 200^{\circ}\text{C}$

Figure 7: Carbon-fiber pull-out and debonding

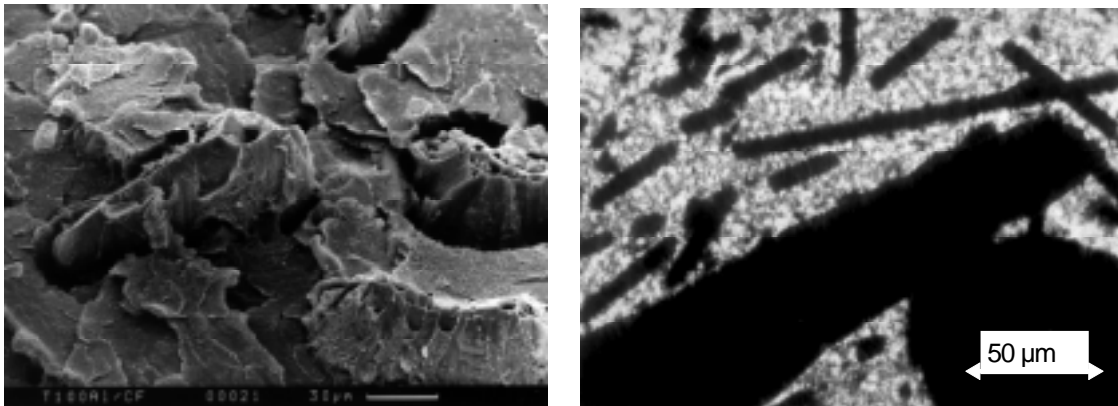


Fig. 8: The morphology of ruptured aluminum-fiber

Fig. 9: The crystallization photo of matrix on the surface of aluminum- and carbon-fiber

Similarly, when specimen is manufactured from the pellets by injection machine, cooling of molding tool also affects the crystallization of resin. Resins lying on the surface of specimen are usually not easy to crystallize for the fast cooling of tool, and resins near the center of the specimen are easy to be crystallized due to longer period of cooling so that they form crystallization morphology. It is these reasons that result in completely different interface

between carbon-fiber and matrix. Another interesting thing about interface of the carbon-fiber is worthwhile to noting there is no fracture phenomena of the fiber due to its too short.

Comparing with carbon-fiber, however, the interfacial bonding between aluminum-fiber and matrix is always relatively poor. As indicated in Table 1, elongation rate of aluminum-fiber is much larger than that of carbon-fiber, but larger than that of resin. When applied stress is above yielding stress of resin, the tensile stress will automatically transfer to aluminum-fiber, making it be elongated longitudinally and contracted transversely. With the increase of tensile stress, the cross-section of the aluminum-fiber is shrunken greatly until its final rupture ( see Fig. 8), resulting in the surface of aluminum-fiber to be separated from matrix. While this pattern is equivalent to pull-out of carbon-fiber, their ruptured section is not a smooth flat, but looks like steep rock. Besides, for the reason of high temperature, the number of pull-out of carbon-fiber at 200 °C is more than that at room temperature (see Fig. 7); furthermore, carbon-fibers seem to be moved obviously due to large viscous-plasticity stretching of matrix. These further illustrate temperature is a crucial factor to influencing both deformation morphology of matrix and fiber interface.

## CONCLUSIONS

Based on the experimental results of PAEK composite with varying temperature and failure analysis for broken samples, the following conclusions may be drawn:

- (1) Micro failure behavior of the composite is closely related to temperature. Matrix morphology at a room temperature is cusp flat with a small brittle shear bands, at 100 °C matrix surface gets rough and exists a lot of ductile dimples, and in the case of 200 °C matrix deformation looks like a mop consisting of fibrils with a characteristic of viscous-plastic flow.
- (2) The macro failure behavior of the composite is also affected by high temperature. With the increase of temperature, failure behavior is changed from quasi-brittle mode at room temperature to ductile mode at 100 °C; when temperature equals 200 °C, fracture mode becomes large plastic deflection.
- (3) The interface situation between fiber and matrix is dependent mainly upon crystalline degree of resin and service temperature. With high crystallization, the interface bonds strongly, and vice versa. Furthermore, the interface of resin and fibers becomes poor with the temperature; high temperature tends to weaken the fiber/matrix interfacial bond because of the difference in their thermal expansion coefficients.
- (4) The temperature effect on strength performance of the composite is very significant. With the increase of temperature, the strength reduction of the composite is extremely large and the strength at 200 °C is only half a value at room temperature. However, as PAEK resin is a kind of tough material, the type of defect only influences magnitude of local stress concentration, but not influences failure behavior of the material.

## REFERENCES

1. Gruber, M. B. and Chou T., *Polymer Composites*, **4**, 265-269, 1983
2. Jang, B Z. et al, *Comp. Sci. & Tech.*, **34**, 305-335, 1989
3. Aronhime, J. et al, *Comp. Sci. & Tech.*, **43**, 105-116, 1992



- 4 Johnson, W. S., Li E. and Miller J. L., in *Proceedings of ICCM-10*, **Vol.V**, 227-234, 1995
5. Schmitt-Thomas, Kh.G. and Malke R., in *Proceedings of ICCM-10*, **Vol. IV**, 449-456, 1995
6. Dunn, M. L. et al, *J. Comp. Mater.*, **27** (15), 1493-1512, 1993
7. O'Rourke, J. M., Bushby R. S. and Scott V. D., *Comp. Sci. & Tech.*, **56**, 957-965, 1996
8. Takei, T. H., Hatta H. and Taya M., *Mater. Sci. & Eng. A*, **131**, 145-152, 1993
9. Maldas, D. and Kokta B. V., *J. Reinforced Plastics and Composites*, **11**, 1093-1103, 1992
10. Maldas, D. and Kokta B. V. , *J. Comp. Mater.*, **25**, 375-390, 1991
11. Schultz, J. M. and Friedrich K. , *J. Mater. Sci.*, **19**, 2246-2258, 1984
12. Yau, S. S. and Chou T. W., in *ASTM STP 1003*, **Vol.2**, pp45-54, 1989
13. Sarasua, J, Remiro P. M. and Pouyet J., *Polymer Composite*, **17** (3), 468-477, 1996
14. BASF, User's manual for Ultrapek, Germany, 1978
15. Influence of temperature and defect on failure mechanism and properties of PAEK/hybrid short-fiber composite (in preparation, to be submitted to *Composite Science & Technology*)

# DEBONDING AND FRACTURE MECHANISMS OF PARTICULATE FILLED POLYPROPYLENE

I.L.Dubnikova, D.K.Muravin and V.G.Oshmyan

*Polymer and Composite Department, Semenov Institute of Chemical Physics,  
Russian Academy of Sciences,  
4 Kosygin street, 117977 Moscow, Russia*

**SUMMARY:** Regularities of plastic deformation and fracture of particulate-filled polypropylene are analyzed. Experimental data on elongation at break  $\epsilon_b$  of PP, filled by particles of different fraction and size are presented. Debonding and plastic flow micromechanisms are studied. The effect of micromechanisms on composite macroscopic behavior is analyzed. Two concentration regions of different debonding and flow micromechanisms were found. At low filler fraction ( $< 15 - 20$  vol. %) particles debond independently at the initial stages of drawing and a microhomogeneous flow mechanism takes place. In this region deformation occurs with necking. Above a critical filler content, debonding proceeds in a correlated way with the formation of craze-like deformation zones transverse to the stretching axes. Concentration of craze-like zones is determined by filler fraction, particle size and the level of interfacial interaction. Whether microhomogeneous or craze-like mechanisms occur essentially determines the regularities of further deformation and fracture: localized or macrohomogeneous flow, ductile or quasi-brittle fracture, the drop or the rise of ultimate strains with increase of particle diameters.

**KEYWORDS:** particulate filled polypropylene, particle size, mechanical properties, debonding, plastic flow, craze, fracture mechanism.

## INTRODUCTION

It is well established both by measurements and theoretical approaches that a level of interfacial interaction plays an important role in particulate filled composites deformation [1-5]. It is shown, in particular, that weakening of adhesion causes a diminution of composite stiffness [1,2,4] and yield stress [1,3,5]. Yield strain drops sharply with filler fraction in a case of well-bonded particles and slightly diminishes in an opposite case [3,5].

A simplified model of composite fracture was proposed in [5] in framework of deformation theory of plasticity. It is based on the numerical analysis of stress-strain distribution (SSD) and critical value criterion of maximum shear strain. The model predicts a sharp drop of ultimate elongation with an increase in filler fraction in a case of a perfect interfacial bond and a gradual decrease of the last in a case of poor adhesion. The predictions are in qualitative agreement with experimental data, however the model does not account two important factors.

An effect of the particle size is the first one. Debonding in the particulate filled polymers leads to a formation of the pores on initial stages of deformation. Further growth and confluence of the pores seems to be an adequate mechanism of ductile materials (PP, PE)

rupture [6,7]. In a case of the brittle material a dramatic drop in the strength with an increase in a defect size forms a basic point of a linear fracture mechanics. Whenever pores are the defects responsible for the fracture of high plastic materials, their size likely affects on fracture parameters in analogous manner. From the other side not only absolute size, but also concentration of the defects should determine fracture parameters. This concentration in turn is determined by a level of interfacial interaction. As was shown in [8,9], the particle diameter,  $\bar{d}$ , is responsible for this level, namely, the debonding stress,  $\sigma_d$ , decreases with an increase in  $\bar{d}$ . In accordance with a model of [5], the less is a portion of debonded particles, the less should be ultimate strain.

A second simplification of a model [5] is in a consideration of uniform SSD. High plastic polymers and composite on their basis mostly deform in heterogeneous manner with formation and growth of the neck. In this case a sharp reduction in composite deformability (ductile-brittle transition) clearly should coincide with a disappearance of a strain hardening, i.e. equality between a strength  $\sigma_b$  and a neck stress  $\sigma_n$  [10].

In the present study an effect of particle content and size on macroscopic behavior of particulate-filled PP is analyzed. An establishment of the correlation between debonding processes at the initial stage of deformation, plastic flow mechanisms and composite fracture regularities is the goal of this investigation.

## EXPERIMENTAL

Isotactic PP was used as a matrix. Polymer molecular weight characteristics, measured by a GPC method, were:  $\bar{M}_w=6.3 \times 10^5$ ,  $\bar{M}_w/\bar{M}_n=3.5$ . Aluminum hydroxide  $Al(OH)_3$  was used as the filler. Four fractions of mean,  $\bar{d}$ , minimum,  $d_{min}$ , and maximum,  $d_{max}$ , diameters were used: 1 (0.5-1.5), 2.5 (1.5-5), 8 (4-16) and 25 (5-50)  $\mu m$ .

Composites were prepared in a "Brabender" mixing chamber at  $T=190^\circ C$ , duration of mixing was 10 min. Calcium stearate (2 wt.% of the filler fraction) was added to avoid filler aggregation. Polymer degradation was prevented by Topanol (0.3 wt.%) and dilauriltiodipropionate (0.5 wt.%). Filler content was in the range 0-70 wt.% (0-47 vol.%). A filler surface treatment by octamethylcyclotetrasiloxane was used into the series of high filler content to reduce adhesive interaction.

The specimens for mechanical testing were prepared by the molding at  $T=190^\circ C$  and the pressure  $p=10 MPa$  with subsequent cooling under the pressure. The drawing of the blade shaped samples was performed on the "Instron-1122" at the room temperature and strain rate  $0.67 min^{-1}$ .

The structure of the deformed composite samples was observed by scanning electron microscopy (SEM) with the use of "JSM-35C".

## RESULTS AND DISCUSSION

### The effect of filler fraction and size on ultimate elongations of particulate-filled PP.

The dependencies of the elongations at break  $\epsilon_b$  on the filler volume fraction and particle size are shown in Fig. 1. A series of regularities is seen from these data.

1. Ultimate strains decrease with the rise of filler content. The increase of  $\epsilon_b$  in the case of large particles ( $\bar{d} = 25 \mu m$ ) in the range of filler fraction  $15\% \leq \Phi \leq 30 \text{ vol.}\%$  is an interesting exclusion from this regularity. It will be discussed below. Here we note that only two publications (Fu, Wang and Shen [11,12]) are known to us as other experimental evidence on the rise of polyolefines fracture properties with an increase of rigid filler content. Authors found brittle-ductile impact strength transition for the HDPE- $CaCO_3$  composites in the case of filler surface modification by phosphate.
2. The ductile-brittle transition is rather sharp in the case of small particles ( $\bar{d} = 1,2,5 \mu m$ ) and occurs at  $\Phi_{br} \approx 25 \text{ vol.}\%$ . The increase of  $\bar{d}$  leads to the more smooth concentration dependencies and to the shift to the right of  $\Phi_{br}$  ( $\Phi_{br} \approx 36 \text{ vol.}\%$  for  $\bar{d} = 8 \mu m$ ).
3. An increase of the particle size leads to the drop of the elongation at break at small filler fraction ( $< 15 \text{ vol.}\%$ ) and to the rise of the  $\epsilon_b$  above  $\Phi \approx 30 \text{ vol.}\%$ . Intermediate region is characterized by the extreme-type size dependencies (Fig. 2).

Three regions of volume fraction are also characterized by different modes of macroscopic deformation.

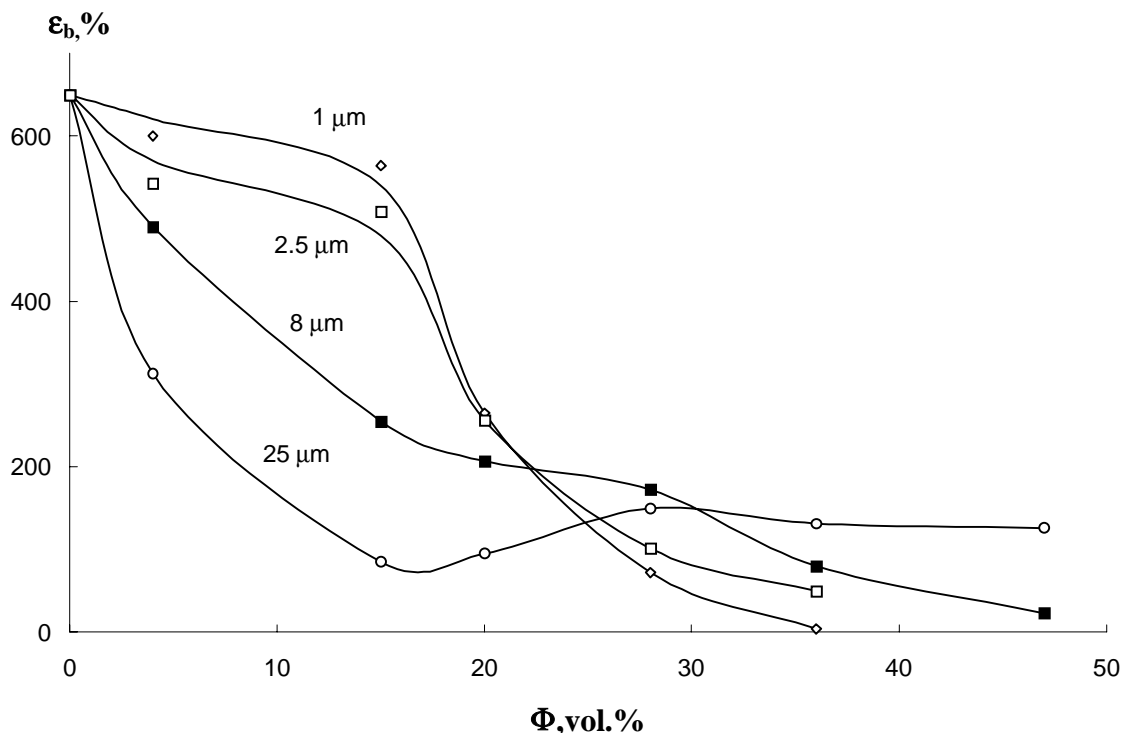


*Fig.1. The elongation at break versus filler volume fraction for different particle size*

Below  $\Phi = 15 \text{ vol.}\%$  the drawing is accompanied by formation and propagation of a neck. Strain-hardening is briefly recognized in the case of small particles. This circumstance

provides propagation of the neck all through the sample. However, the increase of the particle size causes the drop in strain-hardening. It results in the fracture of samples, filled by 14 vol.% of large inclusions ( $\bar{d} = 25 \mu m$ ), at the initial or intermediate stage of the neck propagation.

In the intermediate region ( $15 \text{ vol.}\% \leq \Phi \leq 30 \text{ vol.}\%$ ) a tendency to unstable neck propagation is observed. Formation of two or three necks is seen in the case of small particles. The increase of  $\bar{d}$  leads to the disappearance of the neck and the tendency to homogeneous flow.

Above 30 vol.%, filled by small particles ( $\bar{d} = 1,2,5 \mu m$ ) composites break in quasi-brittle manner with formation of a narrow neck. The increase of  $\bar{d}$  provides macrohomogeneous flow, but up to the certain threshold, dependent of particle size. For the composites of  $\bar{d} = 8 \mu m$  a tendency to the formation of a narrow neck and quasi-brittle fracture is revealed at  $\Phi \cong 36 \text{ vol.}\%$ .

The surface treatment of small particles by octamethylcyclotetrasiloxane rises elongation at break of composites filled by 28 vol.% and 36 vol.% (Fig. 2, dashed lines) [13]. This procedure causes the transition from localized flow and quasi-brittle failure to macrohomogeneous deformation and ductile fracture in the case of  $\bar{d} = 2.5 \mu m$ .

Experimental data on filler fraction and size dependencies of ultimate strains and microscopical observations of samples deformed demonstrate the change of debonding and flow micromechanisms at  $\Phi_{cz}$  between 15 and 20 vol.%.

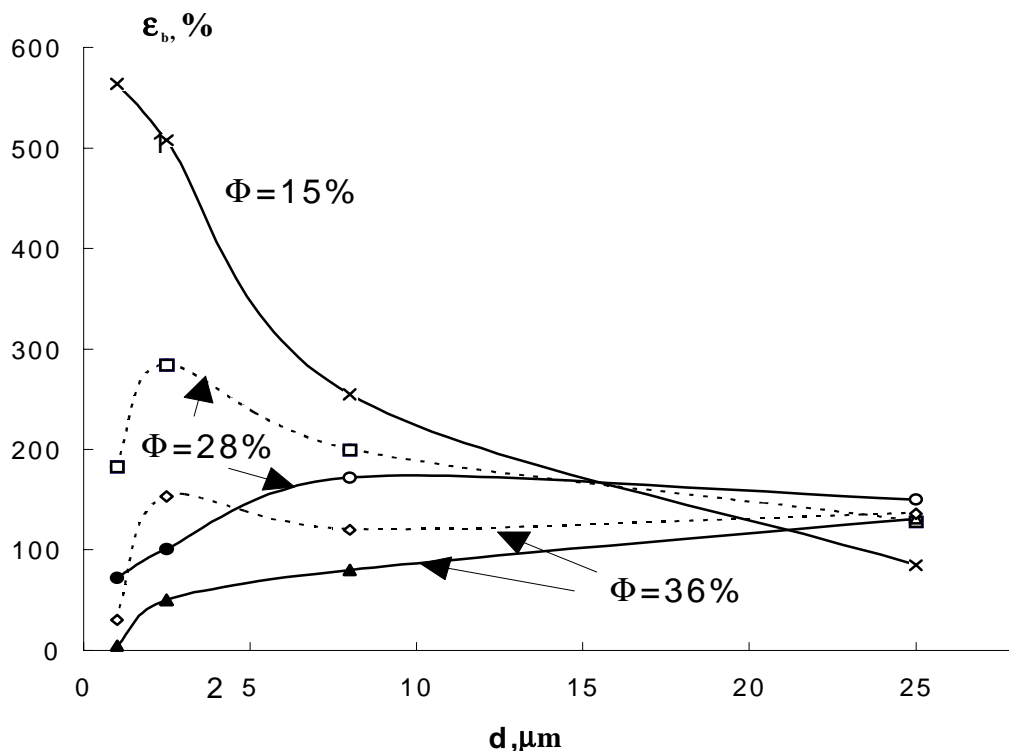


Fig.2. The elongations at break versus particle diameter. Dashed lines point to surface treatment.

### The transition of debonding and plastic flow micromechanisms with the increase of filler fraction.

Exfoliation along the surface of a single inclusion obviously results in the change of SSD in its close vicinity. So, it is natural to expect the occurrence of different debonding micromechanisms depending on particle content.

#### *Uncorrelated debonding and microhomogeneous flow mechanism.*

The change of SSD is not noticeable far from the source of this change. So, in the case of the large interparticle distance, or, equivalently, at a small filler fraction debondings of different particles should proceed independently. Uncorrelated debonding mechanism (Fig.3a) causes microhomogeneous flow (see Fig.3b, which corresponds to the region of the developed neck). A picture of this type was observed by SEM for the composite samples with  $\Phi < 15$  vol.% [14]. We underline the following features.

1. Exfoliation occurs along the surfaces of all the particles.
2. Longitudinal elongation of the every pore formed is equal, with a good precision, to the draw ratio mean elongation of the neck region (microhomogeneous deformation).

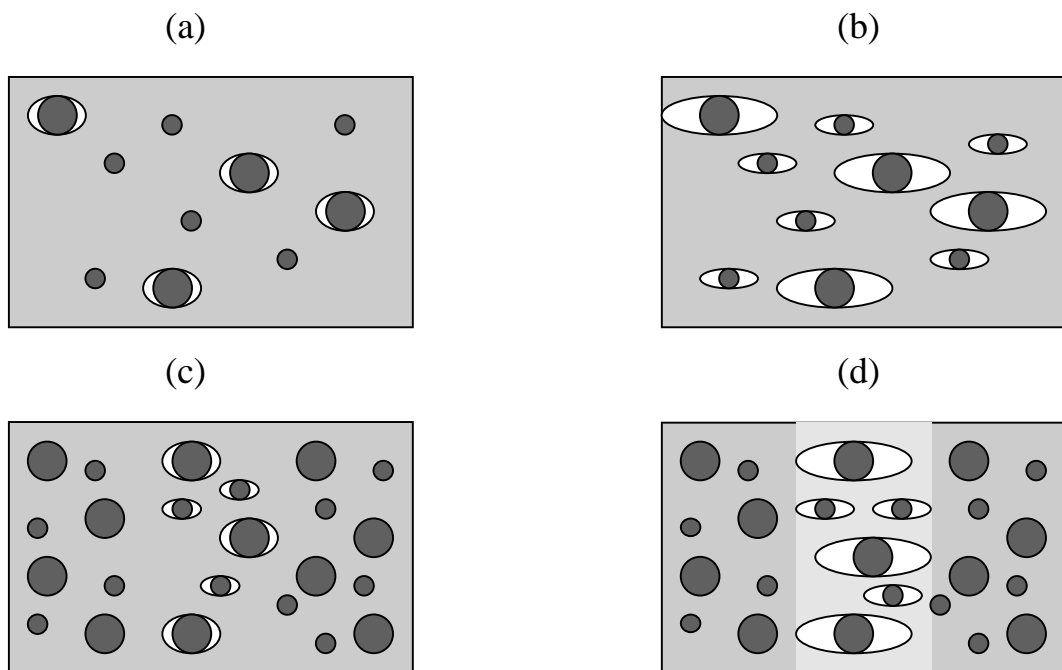


Fig.3: Scheme representation of uncorrelated (a), correlated (c) debonding micromechanisms and sequent microhomogeneous (b), and craze-like (d) plastic flow

#### *Correlated debonding and craze-like flow micromechanism.*

Quite another situation takes place in the case  $\Phi > 15-20$  vol.%. Debonding of the single inclusion considerably changes SSD of a neighbor because of the small interparticle distance. The maximum stress intensity in the uniaxially stretched composites is reached in the area of

a pore equator. It should result in correlated debondings of neighbor particles and the formation of the craze-like microporous zones, extended in the direction transverse to the stretching axes. Correlated debonding (Fig.3c) causes the craze-like flow mechanism (Fig.3d). Such picture was observed by SEM for the composite samples with  $\Phi > 20$  vol.% [14]. Contrary to the previous case, debonding is characterized by the following features. A noticeable portion of the particles outside the craze-like zones remain bonded.

Because of the sharp difference in the compliances, further deformation mainly concentrates inside the craze-like microporous zones, whenever the other regions remain weakly stretched. The first regularity may be clarified by the following estimation of the screen effect efficiency, which is in the drop of the stress in the area of craze banks, caused by formation of micropores inside. Let us denote the debonding stress (the stress value sufficient for the exfoliation along the surface of the given particle) by  $\sigma_d$  and the stress of polymer bulkhead inside the crack by  $\sigma^{bh}$ . It is natural to suggest that the pore fraction inside the craze-like zones is equal to the filler volume content  $\Phi$  and to use the minimum cross section area estimation for the calculation of the stress,  $\sigma^{cz}$ , tightening the craze-like zone banks:

$$\sigma^{cz} = \sigma^{bh} (1 - \alpha \Phi^{2/3}). \quad (1)$$

Correlation between  $\sigma_d$  and  $\sigma^{cz}$

$$\sigma^{cz} \geq \sigma_d \quad (2)$$

determines the conditions for the further debonding of the particles in the vicinities of the craze banks. It is seen that even in the case of the weak adhesive strength (low  $\sigma_d$  value, which is analyzed in the present paper) new debondings formation in the process of further stretching will be forbidden at sufficiently high filler content.

As noted, the increase of the particle size results in a drop of the debonding stress  $\sigma_d$  [8,9] and thereby in the rise of pore concentration. The surface treatment by the antiadhesive component is another route for a debonding stress decrease [9,13].

The stage of secondary debondings depends upon the state of bulkheads in the primary crazes.  $\sigma^{bh}$  and, hence,  $\sigma^{cz}$  can be raised in the process of further drawing, if the bulkheads deform in the elastic or strain hardening region.  $\sigma^{bh}$  is a fixed value, equal to the polymer matrix yield stress  $\sigma_Y$ , if the bulkheads are in the stage of plastic flow. So, if the craze-like flow mechanism is realized, debonding may occur, not only at the beginning of drawing, but at the developed or even final stages. In the case of the sample, filled by 36 vol.% of small ( $\bar{d} = 2.5 \mu m$ ) particles only few zones are seen outside the narrow neck. Inside the neck their concentration is much higher because of the strain-hardening stage of the bulkheads in deformation zones.

### **Macroscopic consequences of microhomogeneous or craze-like flow.**

#### *Localized or macrohomogeneous flow.*

Unfilled PP is characterized by a well-emphasized extreme-type engineering diagram and localized plastic flow, but the true stress increases with draw ratio. An extreme type of the engineering diagram is caused by a conservation of volume and, therefore, a drop of the cross-section area on draw.

The increase of pore concentration in the filled PP leads to a more noticeable growth of

material volume on deformation and, hence, to a less drop of the cross-section area. In the framework of a microhomogeneous mechanism ( $\Phi \leq 15$  vol.%), debonding occurs for every particle at the initial stage of deformation. However, because of the small filler fraction, the volume of the pores formed is not sufficient for the qualitative change of engineering diagrams and the samples deform with necking for the every particle size studied.

The transition to macrohomogeneous flow would take place at the further increase of filler fraction if the microhomogeneous mechanism remains valid. But the change of microhomogeneous flow mechanism by the craze-like process complicates the situation. If  $\sigma_d$  is low, debonding in accordance with (1), (2) is not forbidden and the volume of the pores formed becomes sufficient for the change of the engineering diagram from the extreme to increasing ones. This is the reason for macrohomogeneous deformation of high filled composites ( $\Phi > 20$  vol.%) in the cases of large ( $\bar{d} = 8,25 \mu m$ ) inclusions or small ones ( $\bar{d} = 2,5 \mu m$ ), treated by anti-adhesive component. In the case of untreated small particles the criterion (2) of debonding is not valid, because of the increase of the debonding stress. So, micropore concentration remains low and the samples deform with the necking.

#### *Ductile and quasi-brittle fracture.*

The fracture properties of particulate-filled ductile polymers are determined by the growth and confluence of micropores, formed in the process of debonding. So, debonding and the consequent flow mechanism are extremely important.

In the framework of microhomogeneous flow mechanism ( $\Phi < 15$  vol.%) a filler fraction can be sufficiently low for the complete adhesive failure at the initial stages of deformation (composite yield stress  $\sigma_Y$  decreases with  $\Phi$ , but can remain higher than  $\sigma_d$ ). The composites characterized by ductile fracture. The drop of  $\varepsilon_b$  with the increase of particle size (Fig. 1, the initial portions of the curves, Fig. 2,  $\Phi = 15$  vol.%) is governed by the geometric factor of rupture, which is in the aggravation of fracture parameters with the growth of the size of a defect, responsible for fracture.

In the framework of the craze-like mechanism, complete debonding is not obtained because of the screen effect discussed. In this case the main part of deformation is concentrated in the narrow microporous zones, so ultimate strains depend upon the specific amount of the last by means of at least two reasons. The first is the increase of the elongation due to the increase in the concentration of the deformed regions. The second reason is the rise of the strain at break of polymer bulkheads inside the craze, as a result of the decrease of the local strain rate, at fixed value of the last, with an increase of the crazes density. Therefore, geometric factor of fracture contradicts with the debonding one, which is in the change of degree of debonding processes completion. The influence of this contradiction on  $\varepsilon_b$  is illustrated by the intermediate and final portions of the curves in Fig. 1 and by the plots of Fig.2, corresponded to  $\Phi = 28$  and 36 vol.%.

Debonding stress distributions, ( $dV_d/d\sigma d\sigma$  is a volume fraction of the particles, debonded in the stress interval between  $\sigma$  and  $\sigma+d\sigma$ ), are schematically represented at Fig.4. The increase of filler fraction does not noticeably change the debonding stress [9], i.e., the abscissa position of the curves 1-3 in Fig. 4a, but gives a proportional increase of the ordinate. The porosity of the sample should increase due to this factor. However, the stress  $\sigma^{cz}$  in the vicinities of the



craze banks drops with  $\Phi$  in accordance with correlation (1). Competition between these two factors admits the rise or drop of craze-like zones density and, therefore, the existence of increasing or decreasing portions of ultimate strains dependencies upon filler fraction. This phenomenon is the reason of the rise of  $\varepsilon_b$  with  $\Phi$  in the region  $15 \text{ vol.}\% \leq \Phi \leq 30 \text{ vol.}\%$  in the case  $\bar{d} = 25 \mu\text{m}$  and the drop of the last in the case of small particles (Fig. 1). Dramatic diminution of the microporous zones density provides the transition from ductile to quasi-brittle fracture. The corresponding filler fraction,  $\Phi_{br}$ , depends upon the debonding stress (which is the decreasing function of  $\bar{d}$ ) and should be shifted to the higher  $\Phi$  with the increase of particle size. This regularity is experimentally confirmed by the increase of  $\Phi_{br}$  from  $\cong 25 \text{ vol.}\%$  for  $\bar{d} = 1$ , and  $2.5 \mu\text{m}$  to  $\Phi_{br} \cong 36 \text{ vol.}\%$  for  $\bar{d} = 8 \mu\text{m}$  (Fig. 1).

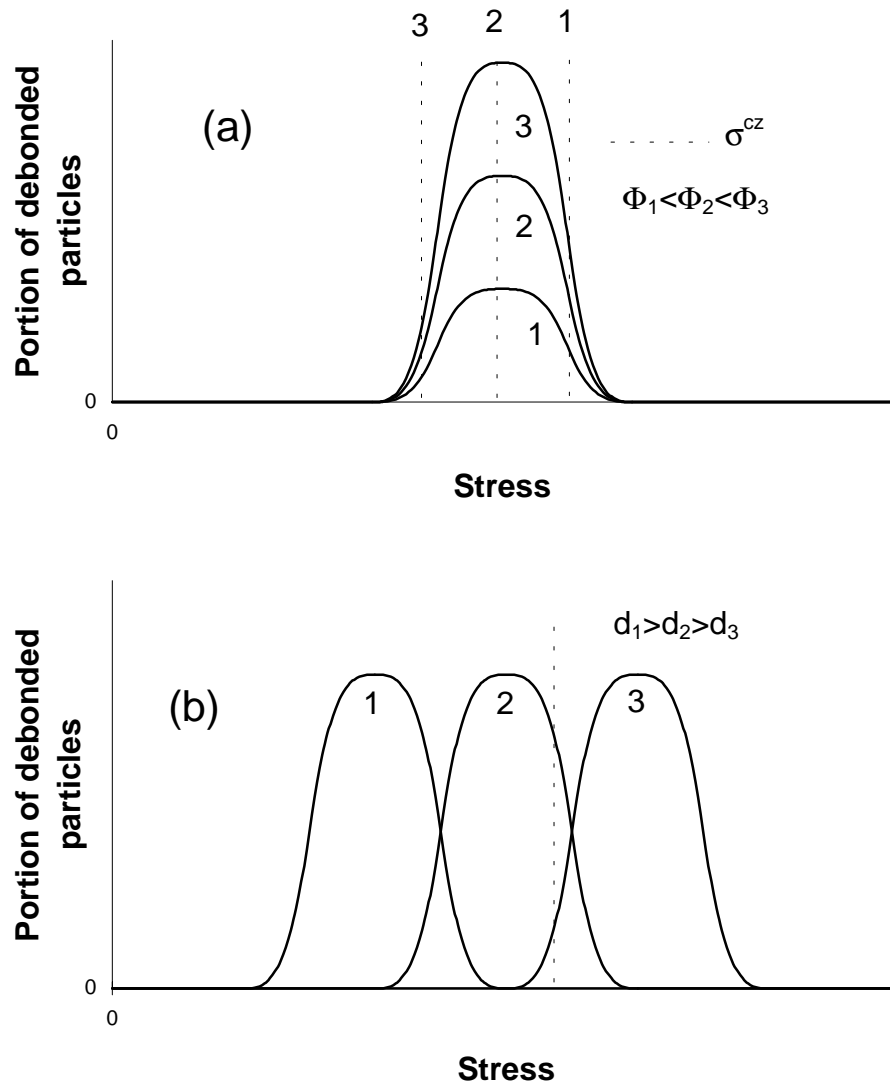


Fig.4: Scheme representation of the debonding stress distributions: (a) - for different filler fractions ( $\Phi_1 < \Phi_2 < \Phi_3$ ) and fixed particle size; (b) - for the various particle diameters ( $\bar{d}_1 > \bar{d}_2 > \bar{d}_3$ ) and fixed filler fraction. Vertical lines denote the stresses  $\sigma^{cz}$  in the vicinities of the craze banks (see formula (1))

Contrary, at the fixed filler fraction the  $\sigma^{cz}$  value remains unchanged, whenever the change of the particle size results in the horizontal shift of the debonding stress distribution (Fig4b). The surface treatment by the anti-adhesive component facilitates debonding [9] and is an alternative way to achieve such a shift. So, at the high filler content, debonding is most important and causes an increase of  $\varepsilon_b$  with the increase of inclusion size (Fig. 2,  $\Phi = 36$  vol.%, solid line). Competition between adhesive and geometric factors of fracture (the last remains valid in framework of the craze-like mechanism) is the reason of the extreme size dependence of  $\varepsilon_b$  at  $\Phi=28$  vol.% (Fig. 2, solid line) and at high filler content in the case of anti-adhesive coating of the particles (Fig. 2,  $\Phi = 28$  and 36 vol.%, dashed lines).

## CONCLUSIONS

1. Fracture properties of particulate-filled PP have been studied in the wide range of filler fraction and size.
2. Two debonding micromechanisms and the transition between them at  $\Phi_{cz} \sim 15\%$  were discovered. The first is uncorrelated debonding at the initial stages of deformation and occurs at low  $\Phi$  ( $< 15$  vol.%). The second micromechanisms is correlated debonding of neighbor particles inside the narrow zones, transverse to the loading axis.
3. Two different material flow mechanism - microhomogeneous and the craze-like one ( $\Phi > 15$  vol.%) - have been found. In the case of uncorrelated debonding the microhomogeneous deformations form in the neighborhood of the pores. The correlated debondings of neighbor particles results in the craze-like flow mechanism. In this case plastic deformation is mainly concentrated inside craze-like regions.
4. An increase of micropore fraction is the reason for the transition from localized drawing (with necking) to macrohomogeneous draw.
5. Two factors of composite failure are formulated: a geometric one, which is in the drop of fracture properties with an increase of particle (pore) size; and a debonding factor, which is in the formation of the sources of fracture in the processes of phase exfoliation and in the change of degree of debonding processes completion dependent of particle size.
6. In the framework of microhomogeneous flow mechanism, geometric factor governs the fracture, and ultimate elongations decrease with an increase of filler content and particle size.
7. In the framework of craze-like mechanism, the debonding factor of fracture plays an important role. The increase of debonding stress with the decrease of the particle size results in the drop of the craze-like zone concentration and in a decrease of  $\Phi_{br}$  of the ductile-brittle transition. Competition between geometric and debonding factors causes extreme dependence of the elongation at break upon  $\bar{d}$  in the intermediate region  $15 \text{ vol.}\% < \Phi < 30 \text{ vol.}\%$ . At  $\Phi > 30 \text{ vol.}\%$  ultimate strains increase with the rise of  $\bar{d}$ , due the increase of deformation zone concentration.

## REFERENCES

1. Nielsen, L.E., *Mechanical Properties of Polymer Blends and Composites*, Marcel Dekker, Inc., New York, 1974.
2. Manson, J.A. and Sperling, L.H., *Polymer Blends and Composites*, Plenum Press, New York, 1976.

3. Pukanszky B., Fekete E. and Tudos F., "Surface Tension and Mechanical Properties in Polyolefine Composites", *Makromolekulare Chemie, Macromoleculare Symposium*, Vol. 28, 1989, pp. 165-186.
4. Lyapunova, M.A., Knunyatz, N.N., Manevitch, L.I., Oshmyan, V.G. and Shaulov A.Yu., "Simulation of the Effect of Interfacial Bond on Elastic Properties of Particulate Composite", *Mekhanika komposithich materialov*, No. 2, 1986, pp. 231-234.
5. Gorbunova, N.V., Knunyantz, N.N., Oshmyan, Manevitch, L.I., Oshmyan, V.G. and Topolkaev, V.A., "On the Effect of Interfacial Bond on Elastic-Plastic Properties of Particulate Filled Composite", *Mekhanika komposithich materialov*, No. 2, 1990, pp. 336-339.
6. Topolkaev, V.A., Tovmasyan, Yu.M., Dubnikova, I.L., Petrosyan, A.I. Meschkova, I.N., Berlin, Al.Al., Gomza, Yu.P., Schilov, V.V., "The Effect of Particle Size on the Structure and Deformation Behaviour of Particulate Filled HDPE with Different Molecular Mass", *Mekhanika komposithich materialov*, No.4, 1987, pp.616-622.
7. Dubnikova, I.L, Topolkaev, V.A. Paramzina, T.V., Gorokhova, E.V., Dyachkovskii, F.S., "Plastic Properties of Particulate Filled PP", *Vysokomolekularnye Soedineniya*, Ser. A, Vol. 32, No 4, 1990, pp.841-847.
8. Zhuk, A.V., Knunjantz, N.N., Oshmjan, V.G., Topolkaev, V.A. and Berlin, A.A., "Regularities of Adhesive Failure in Particulate Filled Polymers", *Makromolekulare Chemie, Macromoleculare Symposium*, Vol. 44, 1991, pp. 295-299.
9. Zhuk, A.V., Knunyants, N.N., Oshmyan, V.G., V.A.Topolkaev and A.A.Berlin, "Debonding microprocesses and interface strength in particle filled polymer materials" *Journal of Material Science*, Vol. 28, 1993, pp. 4595-4606.
10. Bazhenov, S.A., "The Effect of Particles on Failure Modes of Filled Polymers", *Polymer Engineering and Science*, Vol. 35, No. 10, 1995, pp. 813-822.
11. JFu, Q., Wang, G. and Shen, J., "Polyethylene Toughened by CaCO<sub>3</sub> Particles: Brittle-Ductile Transition of CaCO<sub>3</sub> Toughened HDPE", *Journal of Applied Polymer Science*, Vol. 49, No. 4, 1993, pp. 673-682.
12. Fu, Q., Wang, G. and Shen, J., "Effect of Morphology on Brittle-Ductile Transition on HDPE / CaCO<sub>3</sub> Blends", *Journal of Applied Polymer Science*, Vol. 49, No. 11, 1993, pp. 1995-2002.
13. Dubnikova, I.L, Gorokhova, E.V., Gorenberg, A.Ya., Topolkaev, V.A., "The Effect of Small Additives of Octamethylcyclotetrasiloxane on Deformation Behaviour of the Particulate Filled Polyolefines", *Vysokomolekularnye Soedineniya*, Ser.A, Vol. 37, No 9, 1995, pp.1535-1544.
14. Dubnikova, I.L., Oshmian, V.G., Gorenberg, A.Ya, "Mechanisms of Particulate Filled Polypropylene Finite Plastic Deformation and Fracture", *Journal of Material Science*, Vol.31, 1996.

# EFFECTS OF PORES AND VOIDS ON THE INTERLAMINAR DELAMINATION TOUGHNESS OF A CARBON/EPOXY COMPOSITE

Leif E. Asp and Fredrik Brandt

*The Aeronautical Research Institute of Sweden  
P.O. Box 11021, SE-161 11 Bromma, Sweden*

**SUMMARY:** Presence of pores and voids is known to impair mechanical properties such as strengths and moduli of composite materials. At least, for aeronautical applications it is important to understand how defects such as voids affect the interlaminar delamination toughness of a composite laminate. Therefore an investigation on the influence of voids on the interlaminar delamination toughness of a carbon fiber/epoxy composite in pure modes I and II as well as mixed mode has been performed. Voids are found to have a deleterious or no effect on the critical strain energy release rate at crack growth initiation. However, at propagation in pure mode I and mixed mode load-cases presence of voids causes a R-curve behavior. The increase in  $G_c$ , which is strong in mode I and moderate in mixed mode is inherent to changes in failure mechanisms. In pure mode I, ply splits are observed to bridge the crack as the crack locally leaps between plies at propagation. In mixed mode ( $G_{II}/G \approx 0.5$ ), the crack propagates in one interface only, multilayer cracking in the crack tip region results in increased  $G_c$  at crack propagation. From the observed R-curve behavior it is concluded that pores and voids do not impair the delamination toughness of the HTA/6376C composite in static loading.

**KEYWORDS:** Voids, pores, manufacturing defects, interlaminar delamination toughness, delamination tests.

## INTRODUCTION

Poor manufacturing of laminates may cause appearance of voids and pores in and in-between plies. To date, laminates containing detectable voids are discarded. Cost will be significantly reduced if laminates containing voids can be accepted in some applications. For this reason it is important to understand the influence of voids on the mechanical properties of composite laminates. In particular, for aeronautical applications, the effect of voids on interlaminar delamination toughness is of interest. This is motivated by interlaminar delamination growth being one of the major failure modes in composite structures, such as aircraft wing skins. Interlaminar delamination or fracture may be defined as debonding of plies due to the interlaminar stresses present in the laminate.

It is well known that voids degrade mechanical properties, e.g. tensile and shear strengths, of composites. Over the years a number of studies have been presented on this matter. Comprehensive reviews on the work in this area have been given by Judd and Wright [1], and more recently by Cantwell and Morton [2]. To date, work has been focused on the effects of void content on strengths and moduli of composites. Especially, the interlaminar shear strength (ILSS) has been of concern [1-4]. Results presented on the effects of voids and pores

on mechanical properties are found to differ substantially between studies. For instance, for carbon fiber/epoxy composites, the ILSS has been reported to decrease between 1 and 21% for the first one percent voids [1]. This inconsistency is coherent with the difficulty to measure true void content reported by Ghiorse [5]. In spite of the efforts made, to the authors knowledge, no results on the influence of voids on the interlaminar delamination toughness of CF/EP composites have been reported in the literature.

The objective of this study is to investigate the influence of voids and pores on the interlaminar delamination toughness of a HTA/6376C composite laminate in pure modes I and II as well as mixed mode loading.

## EXPERIMENTAL METHODS

### Test methods

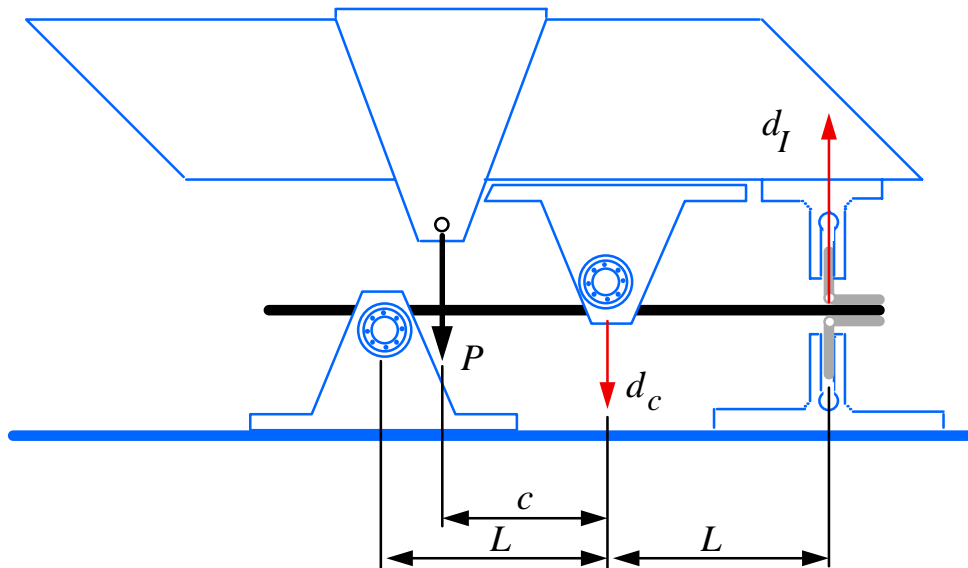


*Fig. 1: FFA's mixed mode bending rig*

To study the effects of pores and voids on delamination toughness of HTA/6376C composite laminates, several test methods were utilized. Tests in modes I and II as well as mixed mode were performed. For Mode I, the common DCB (Double Cantilever Beam) test was used. In mode II, specimens were tested in three-point bending in the ENF (End Notch Flexural) test. Finally, in the mixed mode tests, the specimens were tested under combined loads in the MMB (Mixed Mode Bending) test. Seven specimens were tested in each test method. All tests were performed in a modified version of the mixed mode rig originally suggested by Reeder and Crews [6,7]. In this study only one mixed mode ratio was investigated together with the pure mode tests. According to the analysis by Reeder and Crews [6], an expected mode ratio,  $G_{II}/G$ , of 0.5 was chosen by setting  $c=41$  mm, where  $L=50$  mm, see Fig. 1.

Three-point bending tests were performed to determine the flexural modulus of the uncracked laminates at room temperature. In these experiments the distance between support rollers was 65 mm. All experiments were performed at ambient conditions.

## Specimens

All specimens were fabricated from HTA/6376C carbon/epoxy prepreg supplied by Ciba Geigy. The laminates were cured according to the suppliers recommendations (at 6 bars pressure). However, to introduce voids in one of the laminates the applied vacuum was tampered with during cure. This was done in the following manner: General consolidation of the laminate was achieved as the vacuum-bag was evacuated prior to curing. After evacuation the vacuum pump was turned off. The laminate was heated at a rate of 2°C/min to a temperature of 175°C. As the laminate was heated the pressure inside the bag rose to 6 bar. When the laminate had been heated for one hour the bag was ventilated at 1 atmosphere pressure. Ventilation was repeated as the temperature reached the plateau value of 175°C. After one hour at 175°C the laminate was left at a pressure of 1 atmosphere.

The laminates included a 35 mm long artificial delamination as a starter crack. The artificial delamination consisted of a 7.5 µm thick Upilex 7.5S polyimide film from UBE. The thin film used reduces the resin pocket created at the film edge and hence its influence on the critical strain energy release rate [8]. After curing, the laminates were C-scanned for flaws, such as delaminations, and cut into specimens in a diamond wheel cutter. Prior to testing all specimens were dried in an oven at 70°C for two weeks. The dimensions of the rectangularly shaped specimens were; width 20 mm, length 150 mm and nominal thickness 3.3 mm. The nominal thickness of the void-free laminate was 3.1 mm. The specimen lay-up was  $[0^\circ_{12}/\text{//}(\pm 5^\circ/0^\circ_4)_s]$ , where the sign “//” refers to the interface plane, i.e. the plane of the artificial delamination. The off-axis angle of 5° was applied to reduce fiber bridging at delamination growth. In a study by Olsson et al. [8] it was concluded that an off-axis layer at the interface suppresses fiber bridging in DCB and MMB tests. Also, Olsson et al. [8] showed that the off-axis layers in the composite have a negligible effect on the local G distribution through the specimen width. To release any adhesion between the polyimide film and the composite the specimens were pre-loaded prior to testing.

Three-point bend specimens were cut to the dimensions; width 5 mm and length 75 mm with a nominal thickness of 3.3 mm.

## Measurements

The delamination beam DCB, ENF and MMB tests were performed in a screw-driven Zwick tension load machine at a constant displacement rate of 0.5 mm/min. In the DCB tests a 250 N load cell was used, while in the ENF and MMB tests a 5 kN load cell was utilized. The specimens were connected to the test rig by hinges with automatic couplings, for details see ref. 7.

Crack growth in the DCB, MMB and ENF specimens was measured manually with a traveling microscope. The microscope was equipped with an instrumented dial gauge providing continuous reading of the observed crack tip position. The dial gauge had a maximum stroke length of 20 mm. In the DCB tests, use of a 20 mm extension made it possible to measure a total crack growth length of 40 mm. Mode I opening displacement in the DCB test was measured with a string/wheel potentiometer drawn by a wire attached to the load point of the specimen. In the ENF and three point bend tests the vertical load point displacement was measured with an instrumented dial gauge. In the mixed mode MMB test, the vertical fulcrum displacement,  $d_c$ , as well as the opening displacement,  $d_I$ , were measured with instrumented dial gauges, see Fig. 1. The vertical fulcrum displacement was measured

directly on the specimen, whereas the opening displacement was measured on an extension of the upper hinge in the direction of the applied load. In the experiments loads, displacements and crack lengths were acquired with an IBM PC equipped with Labtech Notebook software.

The void content was determined by image analysis, using the OPTILAB<sup>®</sup> image analysis software of Graftek. The void content of the composite was averaged over 36 cross-sections covering the entire area (20\*3.3 mm<sup>2</sup>) of totally 20 specimens. Interlaminar void contents in 0°/+5° and +5°/-5° interlayers were determined separately in one dimension on the respective interface. The void content of the laminate was determined on specimens cut parallel as well as perpendicular to the 0°-direction, whereas interlaminar void contents were determined on specimens cut parallel to the 0°-direction, only.

### DATA REDUCTION

Here, a short description of the methods used for the data reduction is given. A more complete description was presented in ref. 7. The methods used for evaluation of the DCB and ENF are based on load, displacement and crack length measurements. The results for the strain energy release rates for MMB load cases are achieved by superposition of the pure mode I and mode II load cases, see Figs. 2 and 3.

The mode I strain energy release rate was determined using an expression by Hashemi et al. [9],

$$G_I = \frac{3}{2} \frac{P_I d_I}{b(a + \Delta)} \quad (1)$$

In Eq. (1)  $b$  is the specimen width,  $a$  is the measured crack length and  $\Delta$  is a crack length correction.  $\Delta$  is determined analytically using an expression by Olsson [10] (the shear factor is set to  $K=5/6$ ),

$$\frac{\Delta}{h} = \left( \frac{E_F}{12KG_T} + \sqrt{\frac{E_F}{6E_T}} \right) \frac{h}{a} + \sqrt[4]{\frac{E_F}{6E_T}} + \frac{1}{2\pi} \sqrt{\frac{E_F}{G_T}} \quad (2)$$

The strain energy release rate in mode II was determined using the following expression by Carlsson and Gillespie [11]

$$G_{II} = \frac{9a^2 P_{II} d_{II}}{2b} \frac{\left( 1 - C_{SH} \frac{P_{II}}{d_{II}} \right)}{(2L^3 + 3a^3)}, \text{ where } C_{SH} = \frac{6L + 3a - \frac{L^3}{a^2}}{20bhG_T} \quad (3).$$

In the equations presented,  $h$  is half the thickness of the specimen,  $E_F$  is the measured longitudinal flexural modulus.  $E_T$  and  $G_T$  are the transverse Young's and shear moduli, respectively. Here, data from the void-free laminate are used [7],  $E_T=10.5$  GPa and  $G_T=5.25$  GPa. Eqs. (1) and (3) have low sensitivity to the accuracy in estimations of these mechanical properties.

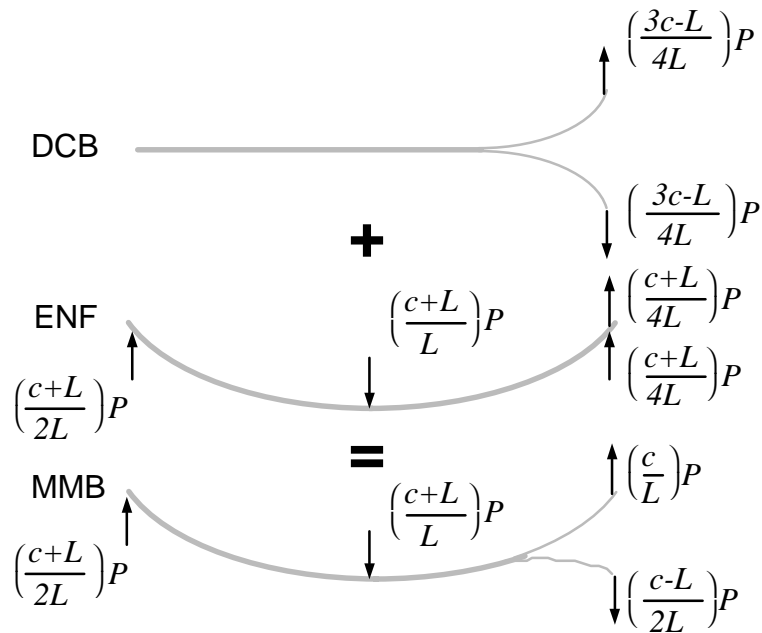


Fig. 2: Separation of modal loads in the MMB test

The results for the strain energy release rates for MMB load cases are achieved by superposition of the pure mode I and mode II load cases, see Figs. 2 and 3. The respective mode I,  $P_I$ , and mode II,  $P_{II}$ , load components, which have been worked out by Reeder and Crews [6], are proportional to the applied load,  $P$ , as:

$$P_I = \left(\frac{3c-L}{4L}\right)P \quad , \quad P_{II} = \left(\frac{c+L}{L}\right)P \quad (4)$$

where  $P$ ,  $c$  and  $L$  are defined in Fig. 1. Further, geometry determines the displacements associated with mode I opening,  $d_I$ , and mode II flexure,  $d_{II}$ . The mode I opening displacement,  $d_I$ , is measured. The mode II displacement,  $d_{II}$ , is calculated from  $d_I$  and the fulcrum displacement,  $d_c$ , as

$$d_{II} = d_c + \Delta_c \quad , \quad \text{where } \Delta_c = d_I L \frac{1}{\sqrt{16L^2 - d_I^2}} \quad (5)$$

In the analysis of the three-point bend tests, determining the flexural modulus, influence of shear deformation was taken into account.



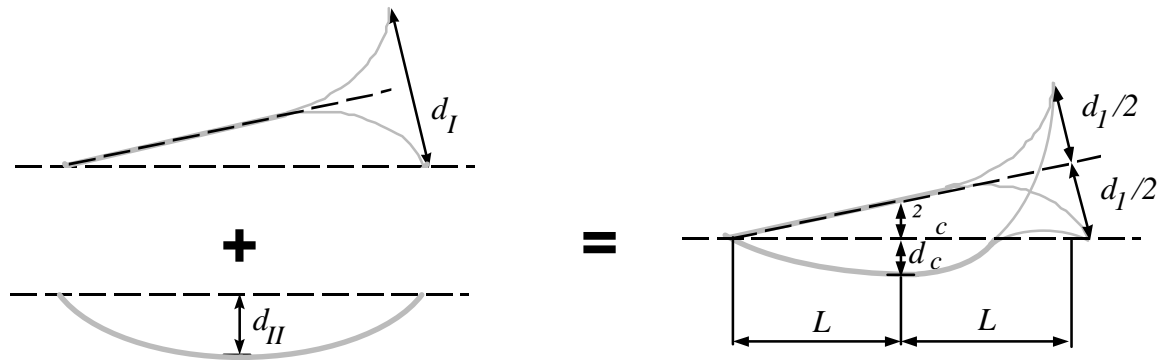


Fig. 3: Separation of modal displacements in the MMB test

## RESULTS AND DISCUSSION

The laminate void content was determined to 0.9%. The interlaminar void contents between the  $0^\circ/+5^\circ$  (the position of the starter crack) and  $+5^\circ/-5^\circ$  plies were 1.4% and 9.2%, respectively. The scatter in data is large as the voids were irregularly distributed in the laminate. For this reason some of the cross-sections contained a large amount of voids as others were void-free. The largest values for the void content of the laminate and interlaminar void content measured in one specimen were 2.2% and 25.8%, respectively. All the observed voids were needle shaped, meaning that they were long in the direction parallel to the fibers compared to their width. The length of the individual voids varied, whereas the void diameter was typically that of 1-2 fiber diameters.

The flexural modulus of the laminate containing voids was determined to 111 GPa, which is 7.5% lower than that previously measured flexural modulus of the void-free laminate [7]. This is in good agreement with results by Ghiorse [5], who reported a decrease in the flexural modulus of 5.3% for a carbon fiber/epoxy cross-ply laminate for the first one percent voids.

### Delamination tests

Table 1: The critical strain energy release rates of the tests on the void-free and voided laminates. Standard deviations are presented within brackets. All units in  $J/m^2$ .

Test method	Void-free laminate		voided laminate	
	$G_C$ (initiation)	$G_C$ (max)	$G_C$ (initiation)	$G_C$ (max)
<b>DCB</b> (mode I)	229.0 ( $\pm 17.8$ )	253.4 ( $\pm 6.6$ )	239.8 ( $\pm 9.7$ )	441.4 ( $\pm 50.8$ )
<b>ENF</b> (mode II)	883.1 ( $\pm 117.5$ )	883.1 ( $\pm 117.5$ )	811.3 ( $\pm 57.0$ )	811.3 ( $\pm 57.0$ )
<b>MMB</b> (mixed mode)	478.8 ( $\pm 43.7$ )	487.1 ( $\pm 45.5$ )	381.4 ( $\pm 47.6$ )	454.5 ( $\pm 70.3$ )

The results of the delamination tests are summarized in Table 1. In the table critical strain energy release rates,  $G_C$ , for void-free specimens and specimens containing voids, referred to as voided laminate, are presented. Table 1 lists data for  $G_C$  at crack growth initiation as well as maximum  $G_C$  at crack propagation. The maximum  $G_C$  provides information about the R-

curve behavior of the specimens, i.e. the dependency of the critical strain energy release rate on crack length. All data for void-free specimens were reported in a previous study [7]. In ref. 7 a more comprehensive description of the delamination crack growth behavior of the void-free specimens is given.

#### *DCB tests*

The presence of voids did not affect the critical strain energy release rate at crack growth initiation in pure mode I, see Table 1. However, their presence affected the crack growth behavior. Although stable crack growth was observed in both void-free specimens and specimens containing voids, their overall behavior were considerably different. For void-free specimens no R-curve behavior was found. In contrast, for specimens containing voids a very strong R-curve behavior was observed. Typical appearances of the critical strain energy release rates as a function of crack lengths are depicted in Fig. 4. For these specimens the critical strain energy release rate increased as the crack propagated. The maximum value at crack propagation was 84% higher than that at crack growth initiation, see Fig. 4. This shift in crack growth behavior is explained by a change in failure mechanism. In the void-free specimens an insignificant amount of crack bridging was established at the crack tip. In the specimens containing voids, however, ply splits (approximately 1-2 mm wide) were observed to bridge the crack. The bridged zone was measured to be 25-30 mm long. The observed crack bridging appeared as the crack tip locally leaped between plies as the crack propagated. The scatter in data for the laminate containing voids is significantly larger than for the void-free laminate, see Table 1. Thus, the irregularity in the distribution of voids affects the interlaminar delamination toughness of the composite loaded in pure mode I.

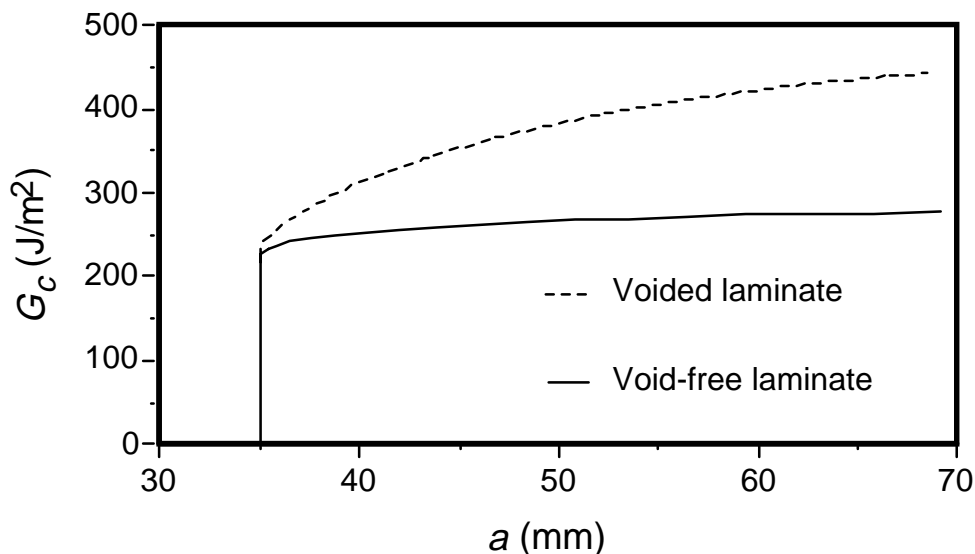


*Fig.4: Schematic of the mode I critical strain energy release rates dependence on crack length for the void-free and void containing (voided) laminates*

In a recent study, Hou et al. [12] reported results on the influence of voids on the interlaminar delamination toughness for CF/PEI woven fabric composites. In accordance to the results presented here, Hou et al. reported an increase in the value of the critical strain energy release rate at crack propagation with an increase in void content. However they found this increase in the energy release rate to originate in an enlarged crack tip region rather than in ply-

splitting. Due to the fiber architecture, no ply splits were reported to appear in the woven composites.

#### *ENF tests*

For both types of laminates the crack growth was unstable when loaded in pure mode II. In the ENF tests, presence of voids was found to have a slightly deleterious effect on the critical strain energy release rate.  $G_{IIC}$  at crack growth initiation was 8% lower for the laminate containing voids compared to the void-free one. To assure that the resin pocket created at the starter film tip did not affect the measured energy release rate, tests of four pre-cracked ENF specimens were performed. The specimens were pre-cracked in mode I until the starter crack length exceeded 37 mm. These tests confirmed the results, and hence any effect of the resin pocket was excluded. However, in these additional tests it was found that stable crack growth can be achieved as the initial crack length exceeds 37 mm. According to the analysis by Reeder and Crews [6] stable crack growth is expected for a crack length larger than 35 mm. Observations of the crack tip indicated that the crack propagated in one plane, only. As a consequence, no crack bridging was detected. This is coherent with observations reported for mode II tests on CF/PEI woven composites by Hou et al. [12].

#### *MMB tests*

Stable crack propagation was achieved in both laminates. In mixed mode loading the presence of voids was found to decrease the critical strain energy release rate at crack growth initiation by 20%. However, as the crack propagated the critical strain energy release rate increased and a R-curve behavior was recorded for the void containing specimens. Due to this R-curve behavior the recorded maximum strain energy release rate at propagation was at the same level for the two laminates. As in the DCB test results, the scatter in data, at propagation, for the laminate containing voids is larger than for the void-free laminate, see Table I. Crack bridging was not observed in either of the two laminates. As the crack propagated in the  $0^\circ/5^\circ$  interface only, the recorded R-curve behavior of the laminate containing voids is explained by multiple crack planes at the crack tip. Multiple crack planes were observed on the edge of the specimens at crack propagation and in post-mortem optical microscopy.

The mode mixture in the MMB test deviated from the expected  $G_{II}/G=0.5$ . The achieved mode mixture was found to be 0.54 for the laminate containing voids as well as for the void-free laminate. These deviations from the expected mode mixture are due to the evaluation method used. Based on linear elasticity, methods based on load and load-displacement measurements should give the expected mode mixity of 0.5 [6]. In fact, load based methods give a mode mixture of 0.5. However, a previous investigation [7] revealed non-linear load-compliance relationships and indicated methods based on load-displacement measurements to be more accurate than methods based on load measurements only. For this reason, results based on load and displacement measurements only are reported here.

#### *Dependency of delamination toughness on mode mixture*

In Fig. 5 the critical strain energy release rates at crack growth initiation are presented as a function of mode mixture. To show trends, data points for void-free laminate and the laminate containing voids, marked voided laminate, have been curve fitted by interpolation.

The graph shows that presence of voids reduced the critical strain energy release rate at crack growth initiation in pure mode II and mixed mode ( $G_{II}/G \approx 0.5$ ). In pure mode I, however,  $G_C$  was unaffected by the present voids. In contrast, at crack propagation, presence of voids most strongly affected the critical strain energy release rate in pure mode I.

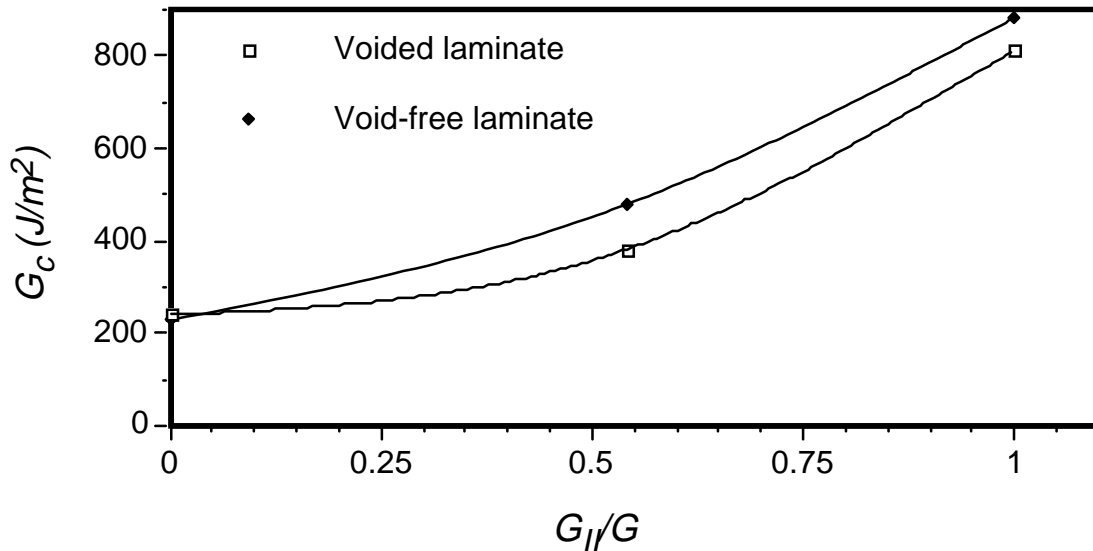


Fig. 5: Critical strain energy release rate at crack growth initiation as a function of mode mixture. Interpolations between data points are included to show trends for the two laminates.

## CONCLUSIONS

The influence of voids on the interlaminar delamination toughness of a carbon fiber/epoxy composite in pure modes I and II as well as mixed mode has been investigated. Voids were found to have a deleterious or no effect on the critical strain energy release rate at crack growth initiation. However, at propagation in pure mode I and mixed mode load-cases presence of voids was found increase  $G_C$ . This increase, which was found to be very strong in mode I and moderate in mixed mode, is inherent to changes in failure mechanisms. In pure mode I, ply splits were observed to bridge the crack as the crack locally leaped between plies at propagation. In mixed mode ( $G_{II}/G \approx 0.5$ ), the crack propagated in one interface. However, multiple cracks observed at the crack tip and in front of the crack, resulted in an increased  $G_C$  at crack propagation in mixed mode loading. From the observed R-curve behavior it is concluded that pores and voids do not impair the delamination toughness of the HTA/6376C composite in static loading.

## REFERENCES

1. Judd, N.C.W. and Wright, W.W., "Voids and their effects on the mechanical properties of composites- An appraisal", *SAMPE Journal*, **14**, 1978, pp. 10-14.
2. Cantwell, W.J. and Morton, J., "The significance of damage and defects and their detection in composite materials: A review", *J. strain analysis*, **27**, 1992, pp. 29-42.
3. Bowles, K.J. and Frimpong, S., "Void effects on the interlaminar shear strength of unidirectional graphite-fiber-reinforced composites", *J. Comp. Mat.*, **26**, 1992, pp. 1487-1509.
4. Wisnom, M.R., Reynolds, T. and Gwilliam, N., "Reduction in interlaminar shear strength by discrete and distributed voids", *Comp. Sci. Techn.*, **56**, 1996, pp. 93-101.
5. Ghiorse, S.R., "Effect of void content on the mechanical properties of carbon/epoxy laminates", *SAMPE Quart.*, 1993, pp. 54-59.
6. Reeder, J.R. and Crews, Jr, J.H., "Mixed-mode bending method for delamination testing", *AIAA Journal*, **28**, 1990, pp. 1270-1276.
7. Asp, L.E., "Moisture and temperature effects on the interlaminar delamination toughness of a carbon/epoxy composite", *FFA TN 1996-52*, The Aeronautical Research Institute of Sweden, 1996.
8. Olsson, R., Thesken, J.C., Brandt, F., Jönsson, N. and Nilsson, S., "Investigations of delamination criticality and the transferability of growth criteria", *FFA TN 1996-31*, The Aeronautical Research Institute of Sweden, 1996.
9. Hashemi, S., Kinloch, A.J. and Williams, J.G., "Corrections needed in double cantilever beam tests for assessing the interlaminar failure of fibre composites", *J. Mat. Sci. Lett.*, **8**, 1989, pp. 125-129.
10. Olsson, R., "A simplified improved beam analysis of the DCB specimen", *Comp. Sci. Techn.*, **43**, 1992, pp. 329-338.
11. Carlsson, L.A. and Gillespie, Jr., J.W., "Mode-II interlaminar fracture of composites", In *Application of fracture mechanics to composites*, K. Friedrich, Ed., Elsevier, Amsterdam, 1989, pp. 113-158.
12. Hou, M., Ye, L. and Mai, Y.-W., "Effect of moulding temperature on flexure, impact strength and interlaminar fracture toughness of CF/PEI composite", *J. Reinf. Plast. Compos.*, **15**, 1996, pp. 1117-1130.

# A STATISTICAL MODEL FOR CRACK GROWTH IN COMPOSITE MATERIALS

**Biao Wang, Jin Dai and Shanyi Du**

*Research Center for Composite Materials, Harbin Institute of Technology, Harbin, China*

**SUMMARY:** In this paper, the crack propagation problem in composite with random microstructures was considered in detail. Along the crack path, the material is assumed to contain randomly distributed crack-arresting points which have stochastic fracture strength. The model can be used to describe a large variety of composite materials, such as continuous fiber composites and short-fiber composites, etc. The aim of this study is to calculate the probability of fracture for a given material, crack length and external load. As an example, the unidirectional fiber reinforced composite was considered in detail. The fiber strength was assumed to be a random variable with the Weibull distribution, and both the strong and weak interface between the fiber and matrix were considered. It was found the fracture strength was sensitive to the interface behavior.

**KEYWORDS:** heterogeneous materials, micro-mechanics, statistical model, crack growth

## INTRODUCTION

The fracture toughness of heterogeneous materials, such as composites is quite different from the fracture toughness of their constituents. For example, composite materials can be obtained with much higher fracture toughness than the matrix materials. It is a well-known fact that such enhancements of fracture strength are due to the matrix, the reinforcement and the interface interaction with each other. Whereas, it is a extreme difficult task to predict the overall toughness and the probability of fracture from data on the microstructure.

Many theories have been proposed to understand the fracture mechanism of heterogeneous solids, such as fiber-reinforced composite [6,7]. The most significant works are those on fiber reinforced ceramic and the other brittle matrix composites, for example Ref.[1-5]. When the tensile load which is much lower than the utmost load of the material is applied on fiber-reinforced brittle matrix composite, closely spaced matrix cracks are induced perpendicular with the direction of the tensile load, and each crack almost completely traverses the material, but the applied load continues to be supported by unbroken fibers that bridge each matrix crack between its faces. In this paper, different fracture mechanism was considered. Along the crack path, the material is assumed to contain randomly distributed crack-arresting points which have stochastic fracture strength. For the crack to propagate over a distance  $\Delta x$ , it must cut off all the obstacles, such as fibers, in this area. The model can be used to describe a large variety of composite materials, such as continuous fiber composites and short-fiber composites, etc. Through the microstructural analysis, the hyperbolic differential equation was derived for determining the probability density function of crack length for given external load, the average fracture toughness of the material was also obtained. As an example, the unidirectional fiber reinforced composite was considered in detail. The fiber strength was

assumed to be a random variable following the Weibull distribution, and both the strong and weak interface between the fiber and matrix were considered. It is found that the fracture strength is sensitive to the interface behavior.

### THE STATISTICAL MODEL FOR CRACK GROWTH IN COMPOSITES

Consider a general heterogeneous materials containing a straight crack as shown in Fig.1.

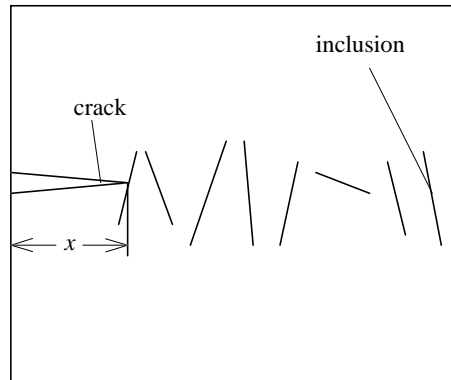


Fig. 1: Heterogeneous material containing a crack

When the applied load increases, the crack should propagate forward. Along the crack path, the inclusions, such as fiber, play the role of arresting point for the crack propagation. Since the inclusion usually has a stochastic strength value, and is distributed randomly in space, the following assumption are introduced in this model.

1. The occurrence probability of a crack arresting-point in region  $(x, x + \Delta x)$  is given by  $\lambda(x)\Delta x$  ;
2. The probability for no crack arresting-point in region  $(x, x + \Delta x)$  is given as  $1 - \lambda(x)\Delta x$  ;
3. The occurrence probability for two and more crack arresting-points in this region is the higher-order smaller quantity as  $o(\Delta x)$  .

If the strength distribution of the crack arresting-point is given by  $F$ ,  $\lambda(x)\Delta x$  can be derived as following

$$\begin{aligned} \lambda(x)\Delta x &= \text{Prob}[\text{there is an inclusion in the region } (x, x + \Delta x)] \\ &\quad \bullet \text{Prob}[\text{the inclusion will not break at the tip of the} \\ &\quad \text{crack under the action of external load}] \\ &= n\Delta x[1 - F] \end{aligned} \tag{1}$$

where  $n$  is the average number of the inclusions in unit length. In deriving Eqn (1), We assumed that distribution of the inclusions in space is statistically uniform.

If  $P_0(x)$  is denoted as the probability that there is no crack arresting-point in region  $(x_0, x)$ , one can obtain

$$P_0(x + \Delta x) = P_0(x)[1 - \lambda(x)\Delta x] = P_0(x) - \lambda(x)P_0(x)\Delta x \tag{2}$$

Therefore, one can derive

$$\frac{dP_0(x)}{dx} = -\lambda(x)P_0(x) \quad (3)$$

The solution of equation (3) is given by

$$P_0(x) = \exp\left\{-\int_{x_0}^x \lambda(x)dx\right\} \quad (4)$$

If the crack starts to propagate from  $x_0$  under the action of the external load, the probability for it to be arrested in the region  $(z, z + \Delta z)$  is given by

$$\langle z|x_0 \rangle > \Delta z = \exp\left\{-\int_{x_0}^z \lambda(x)dx\right\} \lambda(z)\Delta z \quad (5)$$

therefore the probability density function of arresting the crack at  $z$  is given by

$$\langle z|x_0 \rangle = \lambda(z) \exp\left\{-\int_{x_0}^z \lambda(x)dx\right\} \quad (6)$$

Once the crack starts to propagate at  $x_0$ , the probability for it to be arrested without increasing the load is given by

$$P_s = \int_{x_0}^{\infty} \langle z|x_0 \rangle dz = 1 - \exp\left\{-\int_{x_0}^{\infty} \lambda(z)dz\right\} \quad (7)$$

Therefore, once the crack starts to propagate at  $x_0$ , the probability that it will propagate to infinity and induces the material to fracture is given by

$$P_f = 1 - P_s = \exp\left\{-\int_{x_0}^{\infty} \lambda(z)dz\right\} \quad (8)$$

As defined in Kunin[6], a load-specimen configuration is stable if  $P_f = 0$ , i.e., the crack will be arrested with probability 1, otherwise it is unstable.

The mean crack arrest length for cracks initiated at  $x_0$  is

$$m_1(x_0) = \int_{x_0}^{\infty} \langle z|x_0 \rangle dz = x_0 + \int_{x_0}^{\infty} \exp\left\{-\int_{x_0}^z \lambda(x)dx\right\} dz \quad (9)$$



The above analysis is suitable for crack propagation spontaneously in a single excursion without increasing the load. In what following, we try to incorporate the effect of increasing load to derive the differential equation for determining the crack length distribution  $p(x, \sigma)$ .

Let us consider a loaded solid described in Fig.1. Denote by  $\xi(\sigma)$  the random position of the crack tip at an external load  $\sigma$ , and by  $P(x, \sigma)\Delta x$  the probability of finding the crack tip at a length  $x$  at the external load  $\sigma$ , assuming that at  $\sigma = 0$  the tip was at  $x_0$

$$p(x, \sigma)\Delta x = \text{Pr ob}[x \leq \xi(\sigma) \leq x + \Delta x | \xi(0) = x_0] \quad (10)$$

To relate  $p(x, \sigma + \Delta\sigma)$  to the distribution  $p(\bullet, \sigma)$  of crack locations at  $\sigma$ , notice first that the crack tip ends up at the length  $x$  at the load  $\sigma + \Delta\sigma$  in one of the following mutually exclusion ways: during  $\Delta\sigma$ , it either propagated to  $x$  from one of the length  $z$  between the notch tip and  $x$ ,  $x_0 \leq z < x$ , or it was at  $x$  at the load  $\sigma$  and remained there. By the formula of total probability, one obtains

$$\begin{aligned} p(x, \sigma + \Delta\sigma)\Delta x &= \int_{x_0}^x \langle x|z \rangle dx \cdot \frac{dF}{d\sigma} \cdot P(z, \sigma)\Delta z\Delta\sigma \\ &+ (1 - \frac{dF}{d\sigma} \cdot \Delta\sigma) p(x, \sigma)\Delta x \\ &= \int_{x_0}^x \langle x|z \rangle p(z, \sigma) f(z, \sigma) dz \Delta x \Delta\sigma \\ &+ [1 - f(x, \sigma)\Delta\sigma] p(x, \sigma)\Delta x \end{aligned} \quad (11)$$

where  $f(z, \sigma) (= \frac{dF}{d\sigma})$  is the probability density function of strength for a crack arresting-point.

Rearranging equation (11), one can derive

$$\frac{\partial p(x, \sigma)}{\partial \sigma} = \int_{x_0}^x \langle x|z \rangle p(z, \sigma) f(z, \sigma) dz - f(x, \sigma) p(x, \sigma) \quad (12)$$

From equation (6), one obtains

$$\langle x|z \rangle = \lambda(z) \cdot \frac{\langle x|x_0 \rangle}{\langle z|x_0 \rangle} \quad (13)$$

Substitution of equation (13) into equation (12) yields

$$\frac{\partial p(x, \sigma)}{\partial \sigma} = \langle x|x_0 \rangle \int_{x_0}^x \lambda(z) p(z, \sigma) f(z, \sigma) / \langle z|x_0 \rangle dz - f(x, \sigma) p(x, \sigma) \quad (14)$$

Divide equation (14) by  $\langle x|x_0 \rangle$  and denote

$$q(x, \sigma) = \frac{p(x, \sigma)}{\langle x|x_0 \rangle} \quad (15)$$

Then equation (14) becomes

$$\frac{\partial q(x, \sigma)}{\partial \sigma} = \int_{x_0}^x \lambda(x) f(z, \sigma) q(z, \sigma) dz - f(x, \sigma) q(x, \sigma) \quad (16)$$

Differentiating equation (16) in  $x$ , one obtains the following equation for  $q$ :

$$\frac{\partial^2 q(x, \sigma)}{\partial x \partial \sigma} = \lambda(x) f(x, \sigma) q(x, \sigma) - \frac{\partial f(x, \sigma)}{\partial x} q(x, \sigma) - f(x, \sigma) \frac{\partial q(x, \sigma)}{\partial x} \quad (17)$$

Substitution of equation (15) into equation (17) yields

$$\begin{aligned} & \frac{\partial^2 p}{\partial x \partial \sigma} + \frac{\partial p}{\partial x} \left[ f(x, \sigma) - \frac{1}{\langle x|x_0 \rangle} \frac{\partial \langle x|x_0 \rangle}{\partial \sigma} \right] - \frac{\partial p}{\partial \sigma} \cdot \frac{1}{\langle x|x_0 \rangle} \cdot \frac{\partial \langle x|x_0 \rangle}{\partial x} \\ & + p(x, \sigma) \left[ \frac{\partial f}{\partial x} - \lambda(x) f(x, \sigma) - \frac{1}{\langle x|x_0 \rangle} f(x, \sigma) \frac{\partial \langle x|x_0 \rangle}{\partial x} \right. \\ & \left. + \frac{2}{\langle x|x_0 \rangle^2} \cdot \frac{\partial \langle x|x_0 \rangle}{\partial x} \cdot \frac{\partial \langle x|x_0 \rangle}{\partial \sigma} - \frac{1}{\langle x|x_0 \rangle} \cdot \frac{\partial^2 \langle x|x_0 \rangle}{\partial x \partial \sigma} \right] = 0 \end{aligned} \quad (18)$$

Equation (18) can be expressed in the form as

$$\frac{\partial^2 p}{\partial x \partial \sigma} + a(x, \sigma) \frac{\partial p}{\partial x} + b(x, \sigma) \frac{\partial p}{\partial \sigma} + c(x, \sigma) p = 0 \quad (18')$$

where

$$\begin{aligned} a(x, \sigma) &= f(x, \sigma) - \frac{1}{\langle x|x_0 \rangle} \cdot \frac{\partial \langle x|x_0 \rangle}{\partial \sigma} \\ b(x, \sigma) &= -\frac{1}{\langle x|x_0 \rangle} \cdot \frac{\partial \langle x|x_0 \rangle}{\partial x} \\ c(x, \sigma) &= \frac{\partial f}{\partial x} - \lambda(x) f(x, \sigma) - \frac{1}{\langle x|x_0 \rangle} f(x, \sigma) \cdot \frac{\partial \langle x|x_0 \rangle}{\partial x} \\ &+ \frac{2}{\langle x|x_0 \rangle^2} \cdot \frac{\partial \langle x|x_0 \rangle}{\partial \sigma} \cdot \frac{\partial \langle x|x_0 \rangle}{\partial x} - \frac{1}{\langle x|x_0 \rangle} \cdot \frac{\partial^2 \langle x|x_0 \rangle}{\partial x \partial \sigma} \end{aligned} \quad (19)$$

From equation (6), one finds that if we know the microstructural characteristics of the material, represented by the average number of inclusions in unit length  $n$ , the strength distribution  $F(\sigma)$  of the crack arresting-points and the applied load, the parameters  $a(x, \sigma), b(x, \sigma), c(x, \sigma)$  can be determined easily. If the initial crack tip is at  $x_0$  when  $\sigma = 0$ , the probability density function  $p(x, \sigma)$  of the crack tip location at  $\sigma$  can be determined by equation (18') and the initial condition

$$\begin{aligned} p(x, \sigma) &= \delta(x - x_0) \\ p(x, \sigma) &= 0, x < x_0, \sigma \geq 0 \end{aligned} \tag{20}$$

The derivation of equation (18) is quite similar with the work of Kunin[6], whereas in Kunin's work, the mode of crack growth was modeled by a Markovian stochastic pattern of a microscopic random jump, followed by a random waiting time, a random jump, and so on. In our model, the applied load plays the role of the time  $t$ . In the following part, as an example, the unidirectional fiber reinforced composite was considered in detail.

### CRACK GROWTH IN UNIDIRECTIONAL FIBER COMPOSITES

In most composites of current interest, the extensional stiffness of the fibers is much greater than that of the matrix. As a result, the fibers support most of the load in case of uniaxial tensile loading. Considering a  $90^\circ$ -slit notch in a unidirectional composite (Fig.2), for it to extend in an unstable manner at an applied load, it is necessary that the intact fiber at the root of the notch breaks. This requires that the stress in this fiber exceeds its strength. Generally speaking, the fiber strength can be reasonably assumed to follow the Weibull distribution, therefore

$$F(\sigma) = 1 - \exp \left\{ - \left( \frac{k_x \sigma}{\sigma_0} \right)^\beta \right\} \tag{21}$$

where  $k_x$  is the stress concentration factor for the intact fiber at the tip  $x$  of the notch.

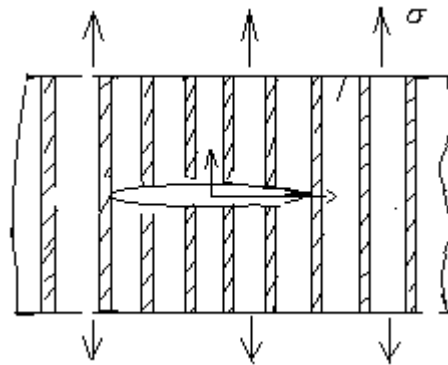


*Fig.2: A  $90^\circ$ -Slit notch in unidirectional composite*

To calculate the stress concentration factor for the intact fiber, following Zweben[1], the modified shear-lag model was used as shown in Fig.3.

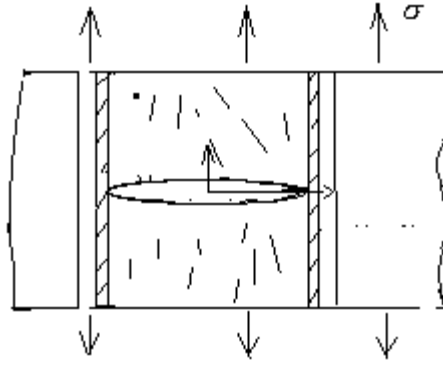


Fig.3: Model for the analysis of stress concentrations including nonelastic matrix effect

It consists of a central core of  $n$  broken fibers separated from two adjacent intact fibers by a matrix region whose effective width is  $d$ . The intact fibers are representative of regions of fibers which are subjected to a stress concentration resulting from the notch. The intact fibers, in turn, are flanked by regions of matrix of width  $d$ , beyond which lies material which is assumed to have the behavior of overall composites, so as the part of central core.

Because of the large elastic shear stress concentration in the matrix at the root of the notch and the relatively weak interfacial strength and strength of most composite materials, it can be anticipated that there will be nonelastic effects such as debonding and plasticity in the matrix between the core and intact fibers at the root of the notch. We therefore include in the model a region of matrix in which the behavior is nonelastic, such as the interfacial slip. The axial dimension of this region is  $2a$ . In this nonelastic region, the shear stress is assumed to be constant and equal to the interfacial failure stress.

The boundary conditions at  $x=0$  are zero stress in the core and zero displacement in the intact fibers. Because of the mixed boundary conditions, we choose as unknowns the axial displacements of the core and intact fibers,  $U_0$  and  $U_1$ , respectively. By using the nondimensional quantities, the equation of equilibrium are

$$\begin{aligned} n \frac{d^2 u_0}{d\xi^2} - 2\bar{\tau}_m &= 0 & 0 \leq \xi \leq \alpha & \quad (22) \\ \frac{d^2 u_1}{d\xi^2} - u_1 + \frac{E_f}{E_c} \xi + \bar{\tau}_m &= 0 \end{aligned}$$

$$\begin{aligned} n \frac{d^2 u_0}{d\xi^2} - 2(u_1 - u_0) &= 0 & \xi \geq \alpha & \quad (23) \\ \frac{d^2 u_1}{d\xi^2} + 2u_1 - u_0 - \frac{E_f}{E_c} \xi &= 0 \end{aligned}$$

where

$$u_i = \frac{1}{\sigma} \left( \frac{A_f d}{E_f G_m h} \right)^{-1/2} U_i, \quad \bar{\tau}_m = \left( \frac{G_m A_f}{E_f d h} \right)^{-1/2} \frac{1}{\sigma} \tau_m$$

$$\xi = \left( \frac{E_f A_f d}{G_m h} \right)^{-1/2} x, \quad \alpha = \left( \frac{E_f A_f d}{G_m h} \right)^{-1/2} a \quad (24)$$

and

- $A_f$  = fiber cross-sectional area
- $E_f$  = fiber extensional modulus
- $E_c$  = composite extensional modulus
- $G_m$  = matrix shear modulus
- $\alpha$  = nondimensional length
- $d$  = fiber spacing
- $h$  = material thickness
- $u$  = nondimensional axial displacement
- $\xi$  = nondimensional axial coordinate
- $\tau_m$  = matrix shear stress
- $\bar{\tau}_m$  = nondimensional shear stress
- $\sigma$  = applied stress at infinity

The boundary conditions are

$$\frac{du_0(0)}{d\xi} = 0, \quad u_1(0) = 0,$$

$$\frac{du_0}{d\xi} = \frac{du_1}{d\xi} = 1 \quad \xi \rightarrow \infty \quad (25)$$

In addition, the displacements and forces should be continuous at  $\xi = \alpha$ , and also

$$u_1(\alpha) - u_0(\alpha) = -\bar{\tau}_m \quad (26)$$

By solving equations (22) and (23) under the given boundary condition, the stress concentration factor for the intact fiber at the tip of the notch which contains  $n$  broken fibers is given by

$$k_x(0) = \left. \frac{du_1(\xi)}{d\xi} \right|_{\xi=0} \quad (27)$$

The material constants are:

$$E_f = 360 \text{GN} / \text{m}^2, \nu_f = 0.4, \beta = 6.98, \sigma_0 = 355 \text{Mpa}, d = 8 \times 10^{-6} \text{m}, L = 25.4 \times 10^{-3} \text{m}$$

The results are shown in Fig.4

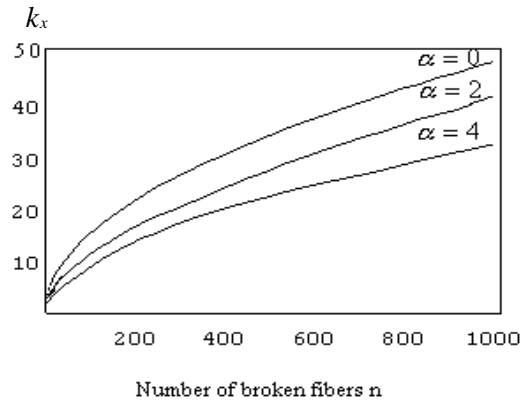


Fig. 4 The stress concentration factor for the intact fiber

Substituting the stress concentration factor into equation (21), then into equation(8), we obtain the failure probability of the specimen under the given applied load and the notch size. The results are shown in Fig.5 as the function of the interfacial strength  $\tau_m$  between the fiber and matrix.

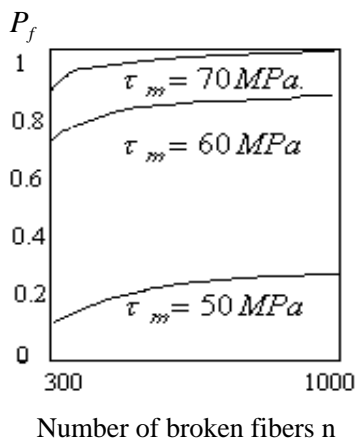


Fig.5 The failure probability of unidirectional composites with a notch

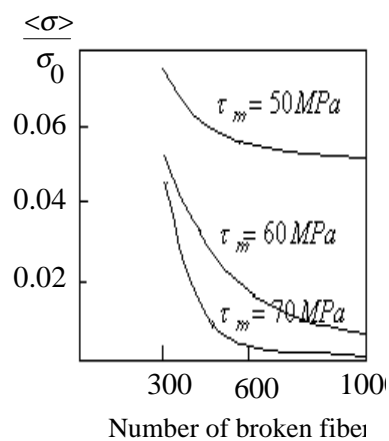


Fig.6. The average fracture stress of the notched specimen

To calculate the average fracture strength of the unidirectional composite with a notch, one can write,

$$\langle \sigma \rangle = \int_0^{\sigma_{\max}} \sigma \frac{dp_f}{d\sigma} \cdot d\sigma = \sigma_{\max} - \int_0^{\sigma_{\max}} p_f d\sigma \quad (28)$$

where  $\sigma_{\max}$  is the utmost strength for all the specimens of the material, the result given by equation (28) is shown in Fig.6.

## CONCLUDING REMARKS

In this paper, a statistical model for crack growth in general heterogeneous solid was proposed based on the material microstructure and the strength distribution of the inclusion. As an example, the unidirectional fiber composite with a  $90^{\circ}$ -slit notch was considered in detail. We believe that the effect of the interfacial strength on the fracture stress was magnified due to the assumption that the fiber will break at the point with the maximum stress. In fact, the breaking point along the intact fiber should be widely dispersed due to the stochastic nature of the fiber strength.

## REFERENCES

1. Zweben, C., An Approximate Method of Analysis for Notched Unidirectional Composites, *Engineering Fracture Mechanics*, Vol.6, No.1,1974
2. Cox, B.N., Marshall, D.B. and Thouless, M.D., Influence of Statistical Fiber Strength Distribution on Matrix Cracking in Fiber Composite, *Acta Metall*, Vol.37, p1933, 1988.
3. Rubinstein, A.A. and Kang Xu, Micromechanical of Crack Growth in Fiber-reinforced Ceramics *J.Mech.Phys.Solids*,V.40, p105, 1992.
4. Gao, Y.C.,Mai, Y.W. and Cotterall, B., Fracture of Fiber-Reinforced Materials, *Journal of Applied Mathematics and Physics (ZAMP)*, V.39,p.550, 1988
5. Chang, Y.C.,Wang, A.S.D. and Chou, T.W., On matrix Cracking in Fiber Reinforced Ceramics, *J.Mech.Phys.Solids*, V.41, p.1137, 1993.
6. Kunin, B.I., A Stochastic Model For Slow Crack Growth in Brittle Materials, *ASME Appl.Mech.Rev.*, V.47,No1,173, 1994.
7. Jeulin, D., Fracture Statistics Models and Crack Propagation in Random Media, *ASME Appl.Mech.Rev*,V.47, No.1,p.141, 1994.

# MODELLING PROBLEMS OF DAMAGE AND FRACTURE OF NOTCHED FIBRE COMPOSITES

R. A. Dimant, H. R. Shercliff and P. W. R. Beaumont

*Cambridge University Engineering Department  
Trumpington Street, Cambridge CB2 1PZ, England*

**SUMMARY:** The Kortschot, Spearing, Beaumont model of notch-tip damage in carbon fibre/epoxy laminates has had some success at predicting the early stages of damage growth in glass fibre/epoxy laminates under monotonic and cyclic loading. However, the model is not universally applicable in its present form to the propagation of damage in glass/epoxy, particularly in high cycle fatigue. This deficiency in the model can be attributed to the effects of the transverse (90°) ply crack on the breakage of glass fibre within the 0° ply neighbour. Although the K-S-B model takes into account the effect of transverse ply cracking on changes in laminate compliance, it does not consider the stress concentration effect of the transverse ply crack on the localised tensile stress in the fibres of the adjacent 0° ply.

**KEYWORDS:** modelling, damage, fracture, cracks, carbon fibre, glass fibre, epoxy

## INTRODUCTION

An important difference between carbon/epoxy and glass/epoxy is in the degree of anisotropy. Whilst the ratio of longitudinal modulus to transverse modulus of a unidirectional carbon/epoxy laminate is between 15 and 20, that of glass/epoxy is closer to 3 or 4. This means for a cross-ply glass/epoxy laminate, the 90° ply carries a greater share of the applied tensile load than would carbon fibre. Thus, the relative magnitude of the stress increment transferred into a longitudinal 0° ply adjacent to a transverse ply crack (tpc) in the 90° ply neighbour is greater for the glass/epoxy.

The Kortschot, Spearing and Beaumont model is of damage accumulation in the vicinity of a notch-tip. This physical model is based on the identification by direct observation of matrix-dominated cracking processes in cross-ply and multi-directional carbon/epoxy laminates under monotonic [1,2] and cyclic loading [3,4]. This paper assesses the applicability of the K-S-B model to a wider range of composite material systems, notably glass/epoxy laminates, in terms of:

- (1) monotonic and cyclic tensile loading
- (2) damage, applied stress, and load cycles
- (3) transverse ply thickness
- (4) terminal damage-state, fracture stress, and post-fatigue strength.



## **K-S-B MODEL**

The K-S-B model is based on the direct observation and assessment of matrix-dominated cracking in the vicinity of a notch-tip: a split in the 0° ply; a delamination at the 0°/90° interface, roughly triangular in shape; and a crack in the transverse or 90° ply, (see Kortschot and Beaumont [1,2] and Spearing and Beaumont [3,4]). Under monotonic or cyclic loading, the damage zone doesn't change its shape, it simply grows in size. The extent of damage can be characterised by a straightforward measurement of split length and angle at the tip of the split and delamination crack which forms the triangle, known as the delamination angle. This is physically sound for cross-ply carbon/epoxy laminates.

The fracture stress of the damaged laminate depends on competition between these mechanisms which, on the one hand, reduce the stress concentration of the notch by notch-tip blunting, and on the other by reducing the tensile strength of the load bearing 0° ply close to the notch-tip. In carbon/epoxy, the notch-tip blunting mechanisms dominate and the post-fatigue strength of the laminate actually goes up. This may not be the case in other fibre-matrix systems.

## **COMPOSITE SYSTEMS, SPECIMEN DESIGN**

### **Composite Materials**

Glass/epoxy laminates (913G-E) were prepared by Polymeric Composites, Bristol (UK) and carbon/epoxy laminates (924C-T300) were made by Ciba-Geigy, Duxford (UK). The laminates were moulded into sheets measuring 600mm by 750mm and cured in accordance with the manufacturers specifications. Tensile tests in monotonic and cyclic loading were performed on (0/90/0), (0/90)<sub>s</sub>, (0/90<sub>2</sub>)<sub>s</sub> and (0/90<sub>4</sub>)<sub>s</sub> laminate configurations.

### **Specimen Geometry**

Parallel-sided tensile specimens were cut to a width of 20mm and a gauge length of 160mm using a guillotine. Two 2mm diameter holes, centres spaced 6mm apart, were drilled at the mid-section of the specimen. These holes were connected by an 8mm long central notch, cut with a diamond-coated hacksaw blade. The notch/specimen width ratio ( $2a/w = 0.4$ ), is similar to that used by Kortschot and Beaumont [1,2] and Spearing and Beaumont [3,4]. For comparative purposes, some tests were carried out on unnotched samples.

## **EXPERIMENTAL PROCEDURE**

### **Quasi-static Tensile Strength and Fatigue Strength**

Five duplicate tensile tests were performed to determine the quasi-static fracture strength. A computer-controlled Instron 6025 screw-driven mechanical testing machine was used for this purpose at a displacement-rate of 1mm/min. Similar notched specimens were cyclically-loaded in tension using an Instron 1271 servo-hydraulic mechanical testing machine in load control with a cyclic stress ratio  $R = 0.1$  at a frequency of 5Hz. Each specimen was fatigued at 80% of its quasi-static fracture strength.

## Damage Observation and Assessment

Damage growth in carbon/epoxy laminates was observed using a zinc iodide penetrant dye solution and X-ray radiography. The optical properties of glass/epoxy laminates allow the direct observation of damage growth. Split length in glass/epoxy was determined by placing a micrometer against the actual surface of the specimen and from measurements taken from photographs of cracks at regular intervals. Where possible to do so, the delamination angle was calculated by assuming a triangular-shaped delamination crack, after K-S-B.

## QUASI-STATIC FRACTURE STRESS MEASUREMENTS

### Components of Damage

In notched glass/epoxy laminates, as with carbon/epoxy, the mechanisms of cracking are:

- (1) splitting within the  $0^\circ$  ply
- (2) transverse ply ( $90^\circ$ ) matrix cracking
- (3) delamination of the  $0^\circ/90^\circ$  interface
- (4) fibre fracture within the  $0^\circ$  ply.

### Damage Growth

Damage growth in glass/epoxy with increasing load and ply thickness is shown in Fig. 1.

#### *(0/90/0) glass/epoxy*

A split initiates at the notch-tip and propagates under increasing load. A fine dispersion of closely-spaced transverse ply cracks also develops in the vicinity of the notch-tip. At stresses approaching the fracture stress of the laminate, fibres in the longitudinal  $0^\circ$  ply snap sequentially at the notch-tip. By these processes, the notch-tip damage zone grows by a series of localised fibre breaks until the laminate finally separates into two pieces.

#### *(0/90)<sub>s</sub> glass/epoxy*

The appearance and development of damage are similar to that observed of the (0/90/0) laminate. Having either a single or double transverse ply within the laminate, fibre fracture is not dominant but part of the overall failure process. The relationship between applied tensile stress and normalised split length ( $l/a$ ) is one where split length scales with the square of applied stress, as found and modelled by Korschot and Beaumont for carbon/epoxy.

#### *(0/90<sub>2</sub>)<sub>s</sub> glass/epoxy*

A split initiates at an applied stress close to the fracture stress. Transverse cracks in the quadruple-layered  $90^\circ$  ply are prominent and widely-spaced. At final fracture, damage propagates from the tip of the notch to the edge of the specimen in a series of sub-failures with fibres snapping in the  $0^\circ$  ply. This effectively increases stably the length of the notch. A new split initiates in the  $0^\circ$  ply at the edges of the notch-tip crack. The notch extends by stable crack growth until the laminate fractures completely. Figure 1 indicates that fibre breaks in

the 0° ply are coincident with the plane of transverse ply cracks in the vicinity of the notch-tip. Delamination at the 0°/90° interface is apparent.

*(0/90<sub>4</sub>)<sub>s</sub> glass/epoxy*

In this 8-layer transverse ply laminate, failure is characterised by the growth at the notch-tip of a single transverse crack only. Under increasing stress, the tpc extends towards the edge of the specimen. Close to specimen fracture, fibre breakage in the 0° ply adjacent to the notch-tip is apparent along the line of the tpc. Ultimate failure of the laminate is accompanied by delamination of the 0°/90° interface which initiates at the single transverse ply crack.

We observe that damage which develops in the (0/90<sub>2</sub>)<sub>s</sub> laminate is a combination of the two modes of failure. The transverse ply thickness of the (0/90<sub>2</sub>)<sub>s</sub> laminate represents a transition between dominating failure mechanisms.

### Fracture Stress and Transverse Ply Thickness

The effect of transverse ply thickness on laminate fracture stress, where fracture stress is expressed as the average failure stress carried by the longitudinal 0° plies, is shown in Fig. 2.

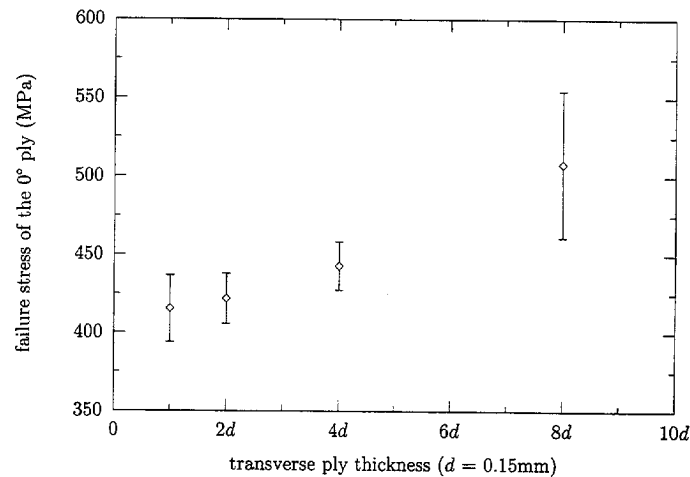


*Fig. 2: The effect of transverse ply thickness on notched glass/epoxy fracture stress, where fracture stress is expressed as the average stress carried by the longitudinal 0° plies*

## FATIGUE DAMAGE AND POST-FATIGUE STRENGTH

### Components of Fatigue Damage in Glass/Epoxy

The components of damage are similar to but more extensive than observed in monotonic loading. Even in the early stages of fatigue damage, it is possible to identify and determine the delamination angle (Table 1).

*Table 1: Approximate delamination angle*

<i>laminate</i>	$\alpha$
(0/90/0)	4°
(0/90) <sub>s</sub>	6°
(0/90 <sub>2</sub> ) <sub>s</sub>	12°
(0/90 <sub>4</sub> ) <sub>s</sub>	40°

### Fatigue Damage Growth

The extent of fatigue damage in glass/epoxy with load cycling at 80% of laminate strength depends on ply thickness (Fig. 3). The stress indicated for each specimen is based on the stress carried by the 0° plies of the laminate.

#### *(0/90/0) glass/epoxy*

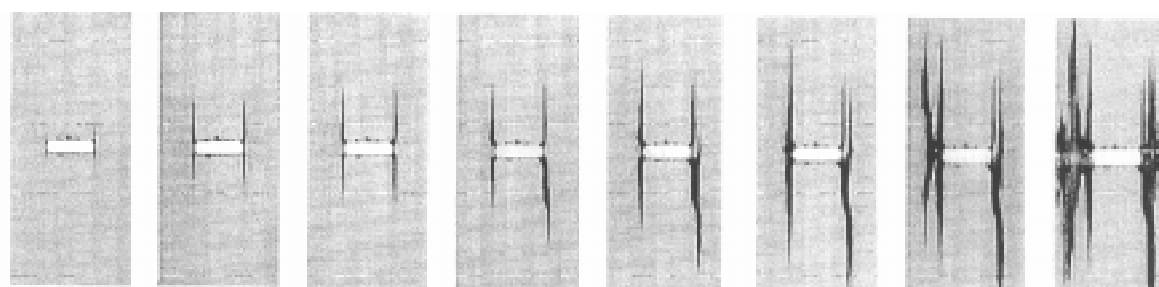
Initially, fatigue damage accumulates with the characteristic pattern identified by Kortschot, Spearing and Beaumont (Fig. 3). Furthermore, an additional damage mode develops between 10K and 20K load cycles: fibres in the 0° ply at the tip of a split fracture through the thickness of that ply. This creates effectively a secondary notch at the tip of the split from which a second series of splits form. As the cross-sectional area reduces, the stress in the remaining ligament increases, which subsequently affects the split growth-rate. With additional fatigue, further splitting occurs at broken fibre bundles. In this way, random damage develops in the composite. Damage progresses from the notch-tip towards the edge of the specimen, as it does so reducing the load-carrying capacity of the laminate. At 70K load cycles, the damage has spread throughout the laminate. In one ligament of specimen, four or more groups of splits can be seen. Damage continues to propagate until catastrophic failure, in this example, at 71.3K load cycles. The development of a non-geometrical damage zone occurred between 10K and 20K load cycles.

#### *(0/90)<sub>s</sub> glass/epoxy*

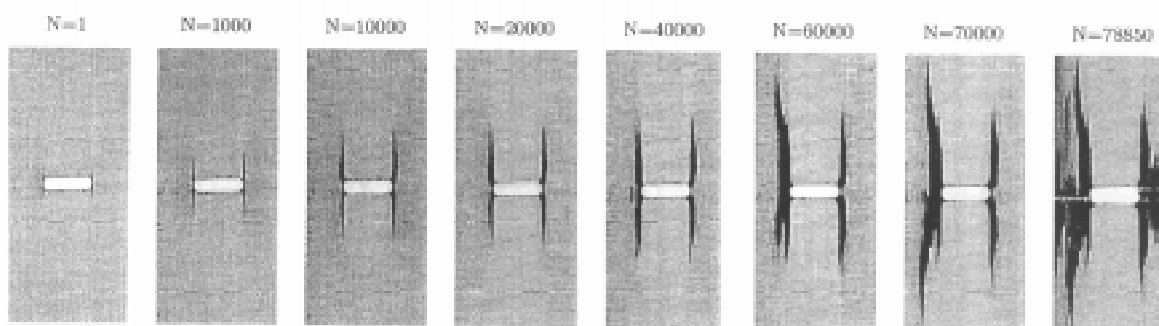
Initially, a similar pattern of damage to that reported by Kortschot, Spearing and Beaumont is observed in specimens fatigued at 340 MPa (Fig. 3). However, by 10K cycles, it is apparent that each split is made up of a multiple array of closely spaced cracks. While these cracks initiated from or near to the notch-tip, the behaviour of the specimen resembles essentially single crack growth as observed in isotropic materials. At 40K load cycles, a new split has nucleated at the tip of a bundle of fractured fibres lying in the plane of the notch. At 60K load cycles, secondary damage has grown beyond the original splits resulting in additional fibre fracture. This process continues until the weakened specimen is no longer able to support the applied load. It fails at 78.8K load cycles. Most fatigue failures occurred at approximately



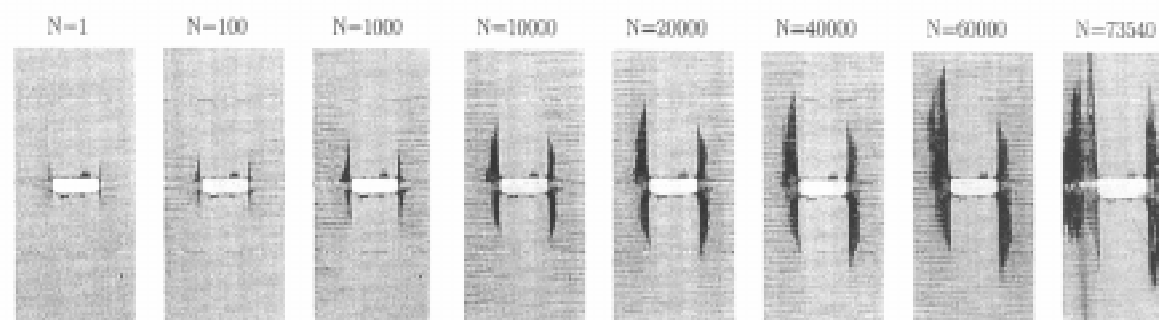
Fig. 1: Sequence of X-ray pictures showing the effects of load and transverse ply thickness on damage growth in glass/epoxy



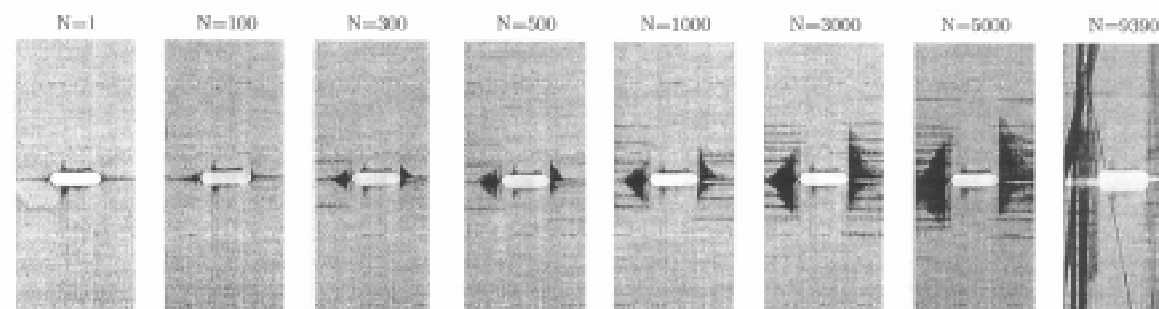
(0/90/0) glass/epoxy laminate fatigued at 330MPa.



(0/90) glass/epoxy laminate fatigued at 340MPa.



(0/90)<sub>2</sub> glass/epoxy laminate fatigued at 360MPa.



(0/90)<sub>4</sub> glass/epoxy laminate fatigued at 405MPa.

*Fig. 3: Sequence of X-ray pictures showing the effects of load cycling and transverse ply thickness on damage growth in glass/epoxy*

120K load cycles. In this material, damage could no longer be described in simple geometrical terms by 20 or 30K load cycles.

*(0/90<sub>2</sub>)<sub>s</sub> glass/epoxy*

Overall, damage is different to that observed in laminates having fewer transverse plies (Fig. 3). It is dominated by the development of splits and delaminations, rather than by fibre fracture. At 40K load cycles, some damage has extended across the specimen by fibre fracture but the extent of this damage is considerably less than in laminates having only one or two transverse plies. The form of damage remains predominantly one of splitting and delamination. Finally, the material fractured at 73.5K load cycles.

*(0/90<sub>4</sub>)<sub>s</sub> glass/epoxy*

The most significant feature of this damage is the absence of fibre fracture in the 0° ply prior to fatigue failure (Fig. 3). Damage develops simply as splitting at the notch-tip with delamination at the 0°/90° interface. Interaction between the delamination and transverse ply cracking plays an important part in the damage process. Failure of the specimen occurs at 9.4K load cycles and is characterised by large delaminated regions extending across the width of the specimen.

### **UNNOTCHED POST-FATIGUE STRENGTH**

Aluminium end-tabs were bonded to 140mm wide by 300mm length plates of glass/epoxy and carbon/epoxy laminates with a heat-curing resin. Each plate was cyclically-loaded in a 20-tonne Losenhauserwerk servo-hydraulic mechanical test machine.

Glass/epoxy laminates were cyclically-loaded to 50% of their ultimate strength of 600MPa. Laminates were fatigued in load control up to 10K load cycles at 5Hz and a stress ratio  $R = 0.2$ . To begin with, the carbon/epoxy laminates were also fatigued at 50% of their fracture strength but due to a large number of laminate failures below 10K cycles, the maximum cyclic stress was reduced to 720MPa or 35% of ultimate.

Parallel-sided specimens for determining post-fatigue tensile strength were cut and ground from these fatigue-damaged plates to a size of roughly 6mm wide by 100mm length. To ensure failure within the gauge length, these specimens were further waisted to a width of 2mm at the mid-plane using a 125mm diameter grinding wheel. Thirty specimens were prepared for each fatigue loading history and laminate. The post-fatigue tensile tests were performed using an Instron 6025 screw-driven mechanical testing machine, as described in section 4.1.

#### **Unnotched Post-Fatigue Tensile Strength**

For comparative purposes, the post-fatigue strength was calculated by assuming the applied load is carried essentially by the longitudinal plies only. This method of normalisation is based on the premise that the laminate close to failure has a multiple array of matrix cracks in the transverse ply. Thus, the applied load is carried principally by the 0° ply.

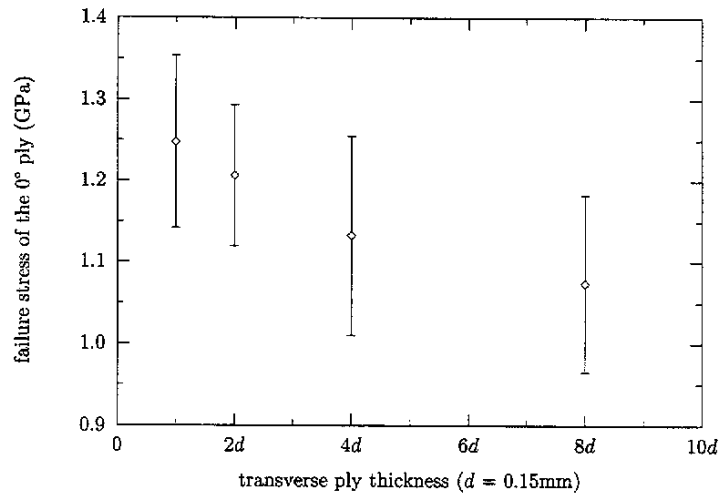


Fig. 4 Unnotched monotonic tensile strength of glass/epoxy with transverse ply thickness

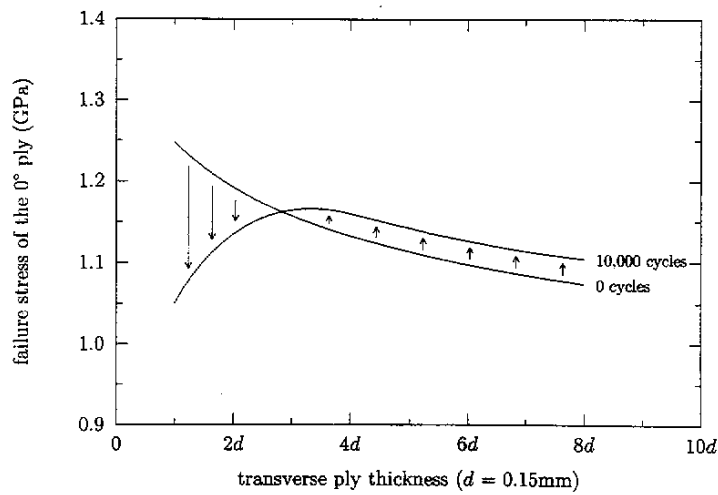


Fig. 5 Unnotched tensile strength of glass/epoxy with transverse ply thickness before and after 10K cycles

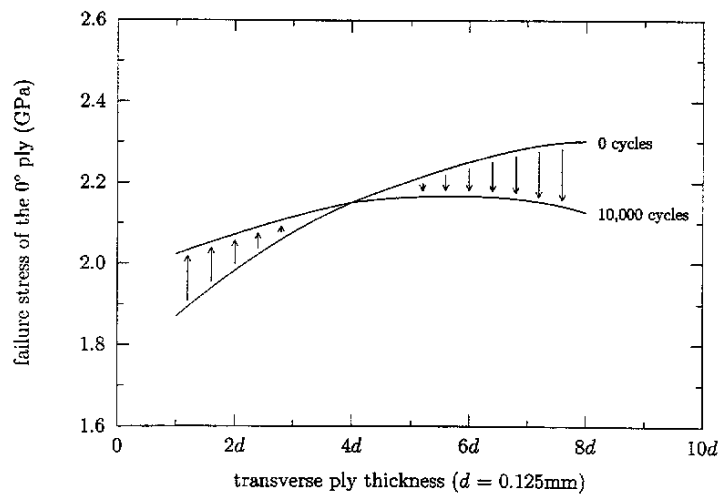


Fig. 6 Unnotched tensile strength of carbon/epoxy with transverse ply thickness before and after 10K cycles



### *Glass/Epoxy laminates*

The monotonic tensile strength of the longitudinal ply decreases continuously as the thickness of the transverse ply increases (Fig. 4). The error bars correspond to one standard deviation. The fracture stress of the (0/90/0) laminate is approximately 20% greater than that of the (0/90<sub>4</sub>)<sub>s</sub> laminate. This variation in strength is sensitive to the density or spacing of the transverse ply crack which in turn depends on thickness of the 90° layer. By 10K cycles, fatigue has little effect on the residual strength of (0/90<sub>2</sub>)<sub>s</sub> and (0/90<sub>4</sub>)<sub>s</sub> laminates, while the residual strength of (0/90/0) and of (0/90)<sub>s</sub> laminates has decreased by 18% and 8%, respectively, (Fig. 5). The implication is that for laminates containing a single or double transverse ply, fatigue results in rapid degradation of the laminate strength. The transition occurs for laminates having three transverse plies, or a thickness of 0.45mm .

Recall that in the notched laminate having a single or double central 90° ply, fatigue loading resulted in massive, progressive fibre-fracture prior to ultimate failure. In monotonic loading, fibre breakage was evident only at loads close to ultimate failure. In laminates containing four and eight central transverse plies, the dominant mode of failure was by delamination. It is the absence of delamination and notch-tip blunting at the 0°/90° interface of the single or double transverse ply which is responsible for the strength degradation.

### *Carbon/Epoxy laminates*

The effect of transverse ply thickness on the monotonic tensile strength of carbon/epoxy is the opposite to that observed for glass/epoxy, where the fracture stress of (0/90<sub>4</sub>)<sub>s</sub> is approximately 20% greater than the (0/90/0) laminate. The general effect of load cycling is shown in Fig. 6. This is the mirror-image of the pattern observed for glass/epoxy. Cracks form in the transverse ply. Fatigue damage results in an increase in laminate compliance as the density of transverse cracks increases. The post-fatigue strength of the carbon/epoxy is relatively unaffected since the strength of the longitudinal ply is essentially retained.

## **FINAL REMARKS**

The most significant difference between the carbon/epoxy and glass/epoxy laminate containing a notch is that the latter fails in fatigue whereas the post-fatigue strength of the former actually goes up. In fatigue of unnotched glass/epoxy, there are significant reductions in the residual strength of the laminate containing a single or double transverse ply. Delamination at the 0°/90° interface of the 4 and 8-transverse ply laminate, however, results in crack-tip blunting effects. The result is that strength of the thicker laminate becomes independent of transverse ply thickness because of these blunting effects. The relation between unnotched post-fatigue strength and transverse ply thickness of carbon/epoxy is the mirror-image due to the difference in the degree of anisotropy.

The Kortschot, Spearing, Beaumont model which has considerable success with carbon/epoxy has limited application to glass/epoxy due to the development of complex damage modes in the vicinity of a notch. The evidence presented here indicates that the breakage of glass fibre which results from transverse ply cracking is not confined to the interlaminar region but develops through the thickness of the ply. This substantially compromises the load-carrying capability of the laminate. Emphasis must shift, therefore, from modelling the geometry of

the damage zone to include in the model a component for the strength degradation of the 0° ply and by taking into account the thickness of the transverse ply, also.

### **ACKNOWLEDGEMENTS**

RAD acknowledges the financial support of the EPSRC in the form of a CASE Studentship. We acknowledge the valuable discussions with Professor M. T. Kortschot, Professor S. M. Spearing, Dr P. A. Smith and Professor M. F. Ashby throughout this and earlier work.

### **REFERENCES**

1. Kortschot, M.T., Beaumont, P.W.R., "Damage Mechanics of Composite Materials - Parts 1-4", *Composites Science and Technology* 39 (1990) 289-301; 303-32; 40 (1991) 147-165; 167-179.
2. Kortschot, M.T., Beaumont, P.W.R., "Damage-Based Notched Strength Modelling", *ASTM STP 1110 Composite Materials: Fatigue and Fracture (3rd Volume)* Editor: O'Brien, pp 596-616 (1991).
3. Spearing, S.M., Beaumont, P.W.R., Ashby, M.F., "Fatigue Damage Mechanics of Notched Graphite-Epoxy Laminates", *ibid* pp 617-637 (1991).
4. Spearing, S.M., Beaumont, P.W.R., "Fatigue Damage Mechanics of Composite Materials - Parts 1-4", *Composites Science and Technology* 44 (1992) 159-168; 169-177; 299-307; 309-317.

# IMPROVED FRACTURE MECHANICS PREDICTIONS FOR DELAMINATION OF COMPOSITES ACCOUNTING FOR YIELD ZONES

Z. Petrossian and Michael R. Wisnom

*Department of Aerospace Engineering, University of Bristol, Bristol, BS8 1TR, U.K.*

**SUMMARY:** Analysis was carried out on a composite specimen containing discontinuous plies, previously tested in three-point bending. The locations of delaminations from the block of discontinuous plies were determined using the strain energy release rates from a finite element analysis. A mixed-mode failure criterion, based on the strain energy release rate, grossly overestimated the failure loads of the specimen under two different ratios of bending to out-of-plane shear loading. An improved approach, also based on the mixed-mode failure criterion but which took account of yielding in the resin at the onset of delamination, was able to predict the failure loads to within 3% of the experimental values.

**KEYWORDS:** delamination, fracture mechanics, strain energy release rate, finite element analysis, discontinuous plies, through thickness stress, plastic zone, initial defect

## INTRODUCTION

Fibre-reinforced composite materials have lower transverse and interlaminar strengths compared to fibre-direction strengths. This means interlaminar failure can occur when the interlaminar stresses are much lower than the in-plane stresses. Significant interlaminar stresses can arise, for instance, at the ends of discontinuous plies. Such discontinuities are found in composite structures when plies are dropped off within a laminate to taper the thickness. Interlaminar shear stresses can arise when out-of-plane loading is applied to laminates. Helicopter rotor blades, aircraft wing boxes and floor beams are examples of structures susceptible to both out-of-plane loading and bending moments, which contain dropped plies. Bending moments cause local interlaminar stresses at discontinuous plies, and out-of-plane loading causes overall shear stresses. The combination of these two stress distributions can lead to cracks initiating at the ends of the discontinuous plies and propagating along the resin rich layers between the continuous and discontinuous plies. These cracks or delaminations can greatly reduce the strength and stiffness of the laminate, which in turn can lead to catastrophic failure of the whole structure. It is therefore very desirable to be able to predict the loading conditions at which delamination occurs.

Delamination is often predicted using the strain energy release rate,  $G$ . This approach was used to predict delamination from the free edges of laminates in [1]. Furthermore,  $G$  is usually calculated from finite element analysis via the virtual crack closure technique. This was done to investigate delamination from the ends of discontinuous plies in [2,3]. In [2] the laminates were in four-point bending and in [3] pure axial tension was applied. In [4] a stress based criterion was used to predict the initiation and location of damage in a composite specimen in

pure bending. Fracture mechanics was then used to predict the growth of delamination from the initial damage. Finally, in [5] fracture process zones at the free edge of laminates were taken into account. This enabled the initiation and growth of delamination to be predicted without any assumed initial defect.

In this paper, delamination from the ends of discontinuous plies is predicted with fracture mechanics taking into account the material yielding which occurs before crack propagation. The results of this improved approach are then compared to predictions which do not take account of the yielding, and to experimental data.

In [6] an account is given of the testing of straight unidirectional laminates in three-point bending, shown schematically in Fig. 1. The laminates consisted of 32 plies of E glass/ epoxy 913 and were nominally 10mm wide. Four of the plies near the tension surface were cut across the complete width. The bending moment caused local interlaminar stresses to arise around the cut. The shear force caused overall interlaminar shear stresses to arise in the section of the specimen between the loading rollers. The combination of these two stress distributions caused cracks to initiate at the cut and propagate along the interfaces of the continuous and cut plies, as seen in Fig. 1. Thus, specimen failure was due to delamination at the top left and bottom right of the cut. The ratio between the overall and local stresses was varied by changing the axial distance,  $d$ , between the cut and the central loading roller. The test results indicated a strong interaction between the two types of stress distributions. It was thought that this might be because the overall interlaminar shear stresses enlarged the zones of yielding in the resin rich layers between plies where the delaminations initiated.

When yielding occurs in the resin, the plies on either side are able to move relative to each other. Hence, strain energy can be released even when no physical crack is present. Thus, the larger the yield zone, the longer the effective crack length [7]. This is similar to the Irwin approach where the crack length is assumed to equal its physical length plus the length of the yield zone ahead of the crack tip. The yield zone length is estimated assuming linear-elastic material behaviour. His approach was developed for predicting crack propagation in metal plates with an initial crack. In this paper it is adapted for predicting delamination in composite laminates with no initial delamination.

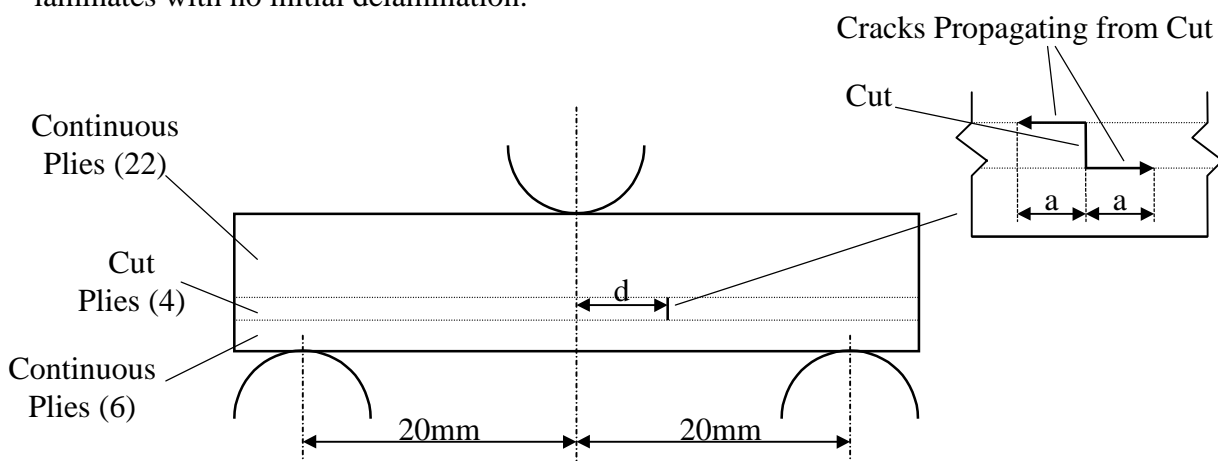


Fig. 1: Schematic diagram of specimen with cut plies in three-point bending

The specimens described above are analysed. Two positions of the cut are studied;  $d = 5\text{mm}$  and  $d = 15\text{mm}$ . A finite element model is created and the strain energy release rates of various

positions and combinations of cracks is evaluated. From the curves of  $G$  with respect to crack length, the locations of the cracks are predicted. The failure load is then predicted both with and without taking the yield zones into account. Both predictions are then compared to the experimental results.

### FINITE ELEMENT MODEL

A two-dimensional finite element model was created using CPS4 elements in ABAQUS [8]. These are four-noded plane-stress elements. A plot of the mesh can be seen in Fig. 2, together with the boundary conditions corresponding to  $d = 5\text{mm}$ . For  $d = 15\text{mm}$  the same model was used but the boundary conditions were moved left along the mesh by  $10\text{mm}$ . Hence, the central loading point was slightly to the right of the centre of the model when  $d = 5\text{mm}$ , and slightly to the left when  $d = 15\text{mm}$ . This is exactly what was done during the tests. Since there were stress singularities present at the top and bottom of the cut a fine mesh was created around these two points. The mesh at the cut can be seen more clearly in Fig. 3. The cut is shown by the bold vertical line and four possible delamination paths are indicated with dashed horizontal lines. At the cut the elements are one ply thick and about  $0.031\text{mm}$  long, and the length gradually increases moving away from the cut. There are dual coincident nodes along the possible crack interfaces and ends of the block of cut plies. During the testing of the specimens [6], the resin between the ends of the cut plies was seen to crack well before delamination occurred. Thus, the nodes on either side of the cut are not held together. Each pair of nodes along the crack interfaces is initially held together by one stiff spring acting in the horizontal direction and another acting in the vertical direction. This is to enable the virtual crack closure technique to be used. There are also gap elements along the interfaces to stop the two surfaces from crossing once the springs are removed.

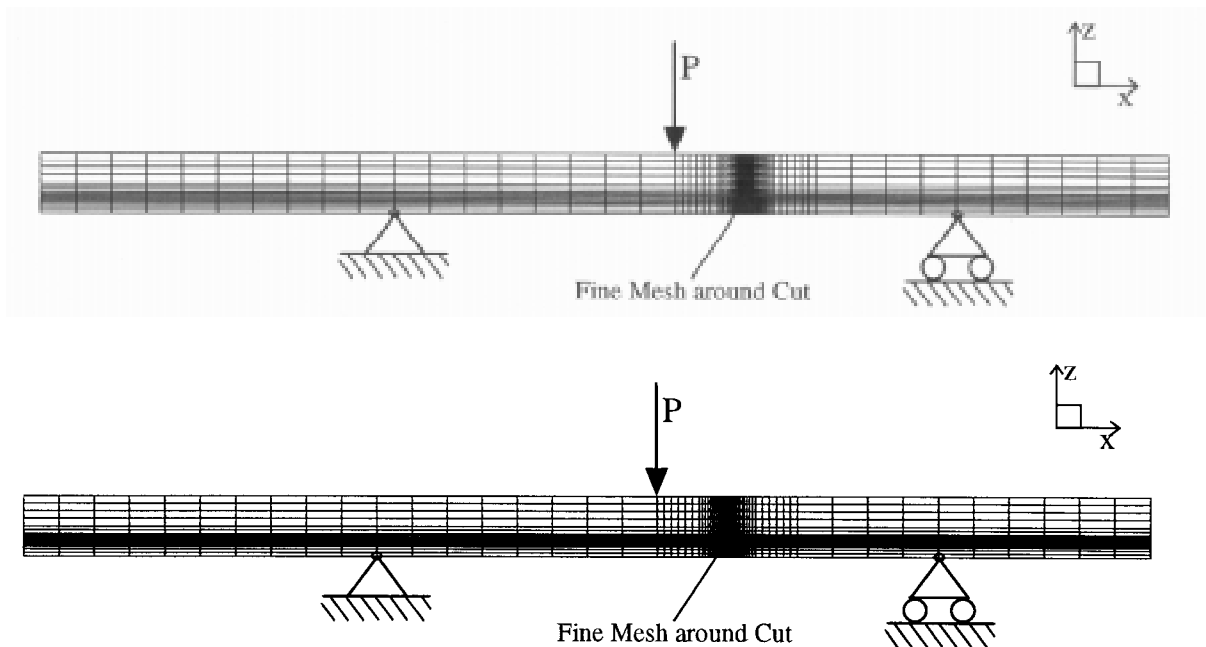


Fig. 2: Finite Element Model with Boundary Conditions Corresponding to  $d = 5\text{mm}$

A downward vertical concentrated load per unit width,  $P$ , is applied to the node at the point of contact of the central roller. The node at the point of contact of the left-hand roller is constrained to have zero  $x$  and  $z$  translation. The node at the point of contact of the roller on the right is constrained to have zero  $z$  translation.  $P$  is equal to the average experimental failure load per unit width. The value of  $P$  is 432.4 N/mm for  $d = 15$ mm, and 284.0 N/mm for  $d = 5$ mm. Refer to Table 1 for the material properties and dimensions of the model. The nominal value of the specimen thickness was initially assumed in the finite element analysis. From the corresponding results, the crack locations were determined. For the failure load predictions, it was deemed more accurate to use the average measured thickness of the specimens and to correct the axial Young's modulus for the lower fibre volume fraction. However, the change in the values of  $G$  were small enough not to affect the predicted crack locations.

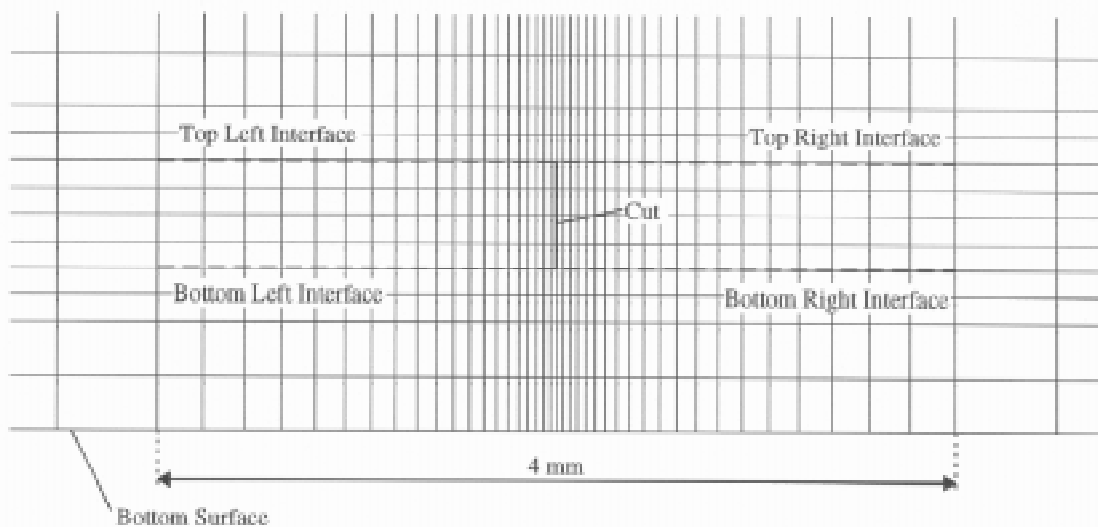
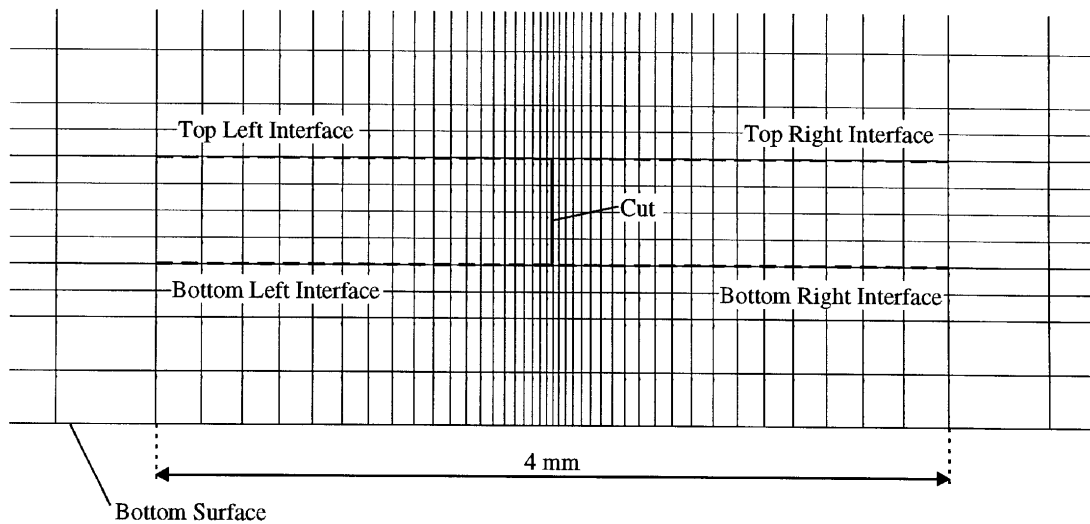


Fig. 3: Close-Up of Mesh showing Cut and Possible Locations of Delaminations

*Table 1: Material Properties and Dimensions.*

Axial Young's Modulus, $E_x$ , for Nominal Thickness	43.9 GPa
Axial Young's Modulus, $E_x$ , for Measured Thickness	41.2 GPa
Through-Thickness Young's Modulus, $E_z$	15.4 GPa
Shear Modulus, $G_{xz}$	4.34 GPa
Poisson's Ratio, $\nu_{xz}$	0.3
Length of Specimen	80 mm
Nominal Thickness	4 mm
Measured Thickness	4.33 mm
Width	10 mm
Distance between Outer Rollers	40 mm

### **DETERMINATION OF CRACK LOCATIONS BY TOTAL ENERGY APPROACH**

The total strain energy release rate,  $G_T$ , was firstly found for individual cracks at each of the four possible crack locations, seen in Fig. 3.  $G_T$  was then found for cracks propagating simultaneously along all four crack paths, and finally for cracks propagating simultaneously along the top left and bottom right interfaces.

$G_T$  was calculated from the change in total strain energy in the model as the crack was allowed to propagate by gradually removing the horizontal and vertical springs along the interfaces. This was done at each increment of crack length,  $a$ . The schematic definition of  $a$  is given in Fig. 1.

Graphs of  $G_T$  against  $a$  were plotted for all the cases and are given together in Fig. 4 for  $d = 15\text{mm}$ , and Fig. 5 for  $d = 5\text{mm}$ . It can be seen that in every case the value of  $G_T$  decreases with crack length until it reaches a minimum value,  $G_{\min}$ . After this, the value of  $G_T$  generally grows with crack length. This means, as the load is increased, the cracks will propagate in a stable manner up to a short crack length (corresponding to the minimum value of  $G_{\min}$ ) and then crack propagation will be unstable. This behaviour was observed in the tests in [6]. Therefore, catastrophic failure occurs when  $G_{\min}$  reaches the critical value,  $G_c$ .

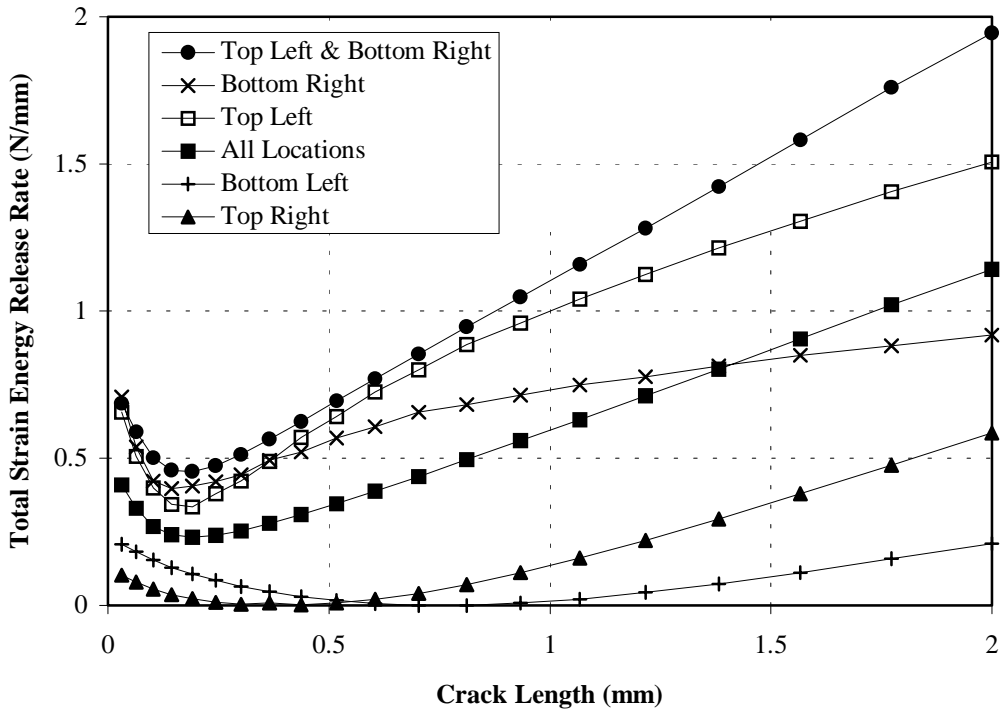


Fig. 4: Strain Energy Release Rate with Respect to Crack Length for Different Positions and Combinations of Cracks (Cut 15mm from Central Roller)

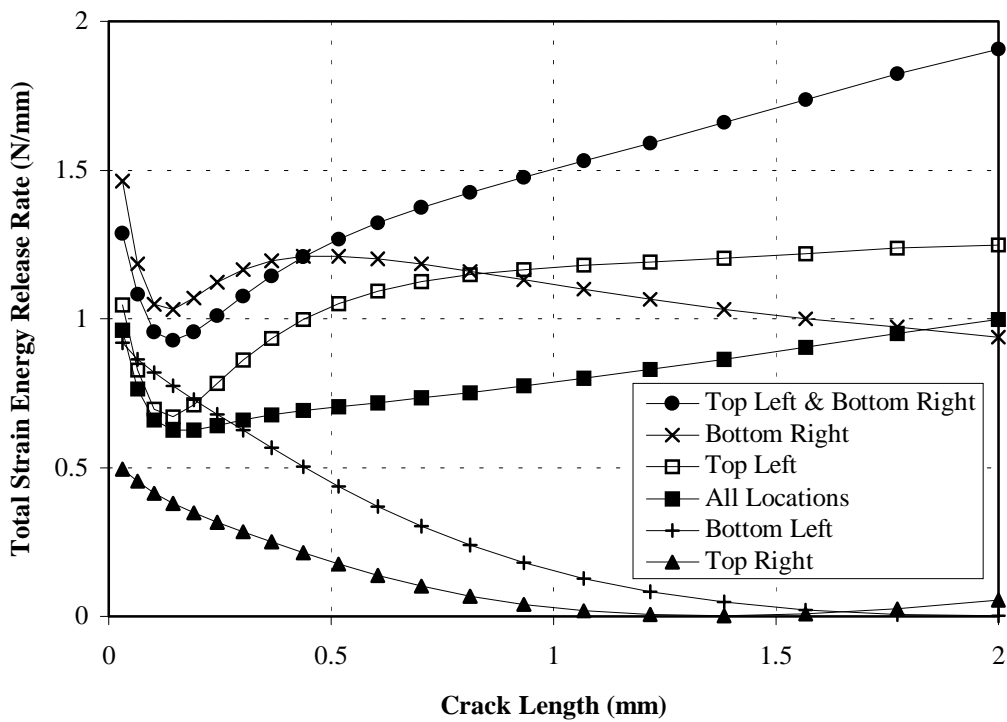


Fig. 5: Strain Energy Release Rate with Respect to Crack Length for Different Positions and Combinations of Cracks (Cut 5mm from Central Roller)



Since catastrophic failure depends on the value of  $G_{min}$ , the locations of the delaminations at failure can be determined by comparing the values of  $G_{min}$  corresponding to the different cases studied. The values of  $G_{min}$  are given in Table 2. Referring to the table, it is clear that for  $d = 15\text{mm}$  the most likely type of failure is by delaminations propagating simultaneously from the top left and bottom right of the cut, since the value of  $G_{min}$  is the highest for this situation. For the  $d = 5\text{mm}$  case,  $G_{min}$  is highest when a crack propagates from the bottom right corner only. However, cracks from both the bottom right and top left of the cut were observed in the tests.

Although cracking is primarily mode II due to the type of loading, a small amount of mode I is generally present. Furthermore, the difference between the values of  $G_{min}$  for cracking at the bottom right only, and simultaneous cracking at the bottom right and top left is not very great. Thus, the fact that cracking occurred simultaneously at the bottom right and top left, even when the value of  $G_T$  was lower in the  $d = 5\text{mm}$  case, can be explained by more mode I being present. It was therefore concluded that the mode ratio would have to be taken into account for accurately predicting the failure loads.

Table 2: Minimum Values of  $G_T$  for Various Cracks (From Figures 4 and 5)

	<b>d = 15mm</b>	<b>d = 5mm</b>
Crack at Top Left Only	0.34 N/mm	0.67 N/mm
Crack at Top Right Only	0.00 N/mm	0.00 N/mm
Crack at Bottom Right Only	0.39 N/mm	1.03 N/mm
Crack at Bottom Left Only	0.00 N/mm	0.00 N/mm
Cracks at All Locations	0.23 N/mm	0.63 N/mm
Cracks at Bottom Right & Top Left	0.45 N/mm	0.93 N/mm

### **FAILURE LOAD PREDICTION USING STANDARD MIXED MODE APPROACH**

Cracks were assumed to propagate simultaneously (and at the same rate) along the top left and bottom right interfaces, for both cut positions. The following mixed-mode criterion was used to predict the failure loads:

$$G_I / G_{Ic} + G_{II} / G_{IIc} = 1 \tag{1}$$

where  $G_I$  and  $G_{II}$  are the mode I and mode II components of the strain energy release rate, respectively, and  $G_{Ic}$  and  $G_{IIc}$  are their critical values. For E glass/ epoxy 913,  $G_{Ic} = 0.25$  N/mm and  $G_{IIc} = 1.08$  N/mm, [9].

$G_I$  and  $G_{II}$ , were found with respect to the crack length,  $a$ , using the virtual crack closure technique. This assumes the strain energy released when a crack propagates is equal to the energy required to close the crack.  $G_I$  was calculated from the spring forces and relative nodal displacements in the vertical ( $z$ ) direction, and  $G_{II}$  was calculated from the spring forces and relative nodal displacements in the horizontal ( $x$ ) direction.  $G_I$  and  $G_{II}$  were then each normalised by their corresponding critical values.

The graphs of normalised  $G$  against  $a$  for the two cut positions ( $d = 15\text{mm}$  and  $d = 5\text{mm}$ ) can be seen in Figures 6 and 7. One can see the sum of the normalised strain energy release rates,  $(G_I/G_{Ic} + G_{II}/G_{IIc})$ , decreases to a minimum value as the cracks start propagating. Then, after a crack length between  $0.2\text{mm}$  to  $0.3\text{mm}$ , the value starts to increase again. As explained in the previous section, this means the load at catastrophic failure is governed by the minimum value of  $(G_I/G_{Ic} + G_{II}/G_{IIc})$ . At the average experimental failure loads, the minimum values of  $(G_I/G_{Ic} + G_{II}/G_{IIc})$  are  $0.61$  for the  $d = 15\text{mm}$  case, and  $0.83$  for the  $d = 5\text{mm}$  case. Thus, according to Eqn 1, both the predicted failure loads are higher than the experimental failure loads. The strain energy release rate is proportional to the square of the applied load, so the predicted failure loads per unit width are:

$$P = 553 \text{ N/mm} \quad \text{for } d = 15\text{mm}$$

and

$$P = 312 \text{ N/mm} \quad \text{for } d = 5\text{mm}.$$

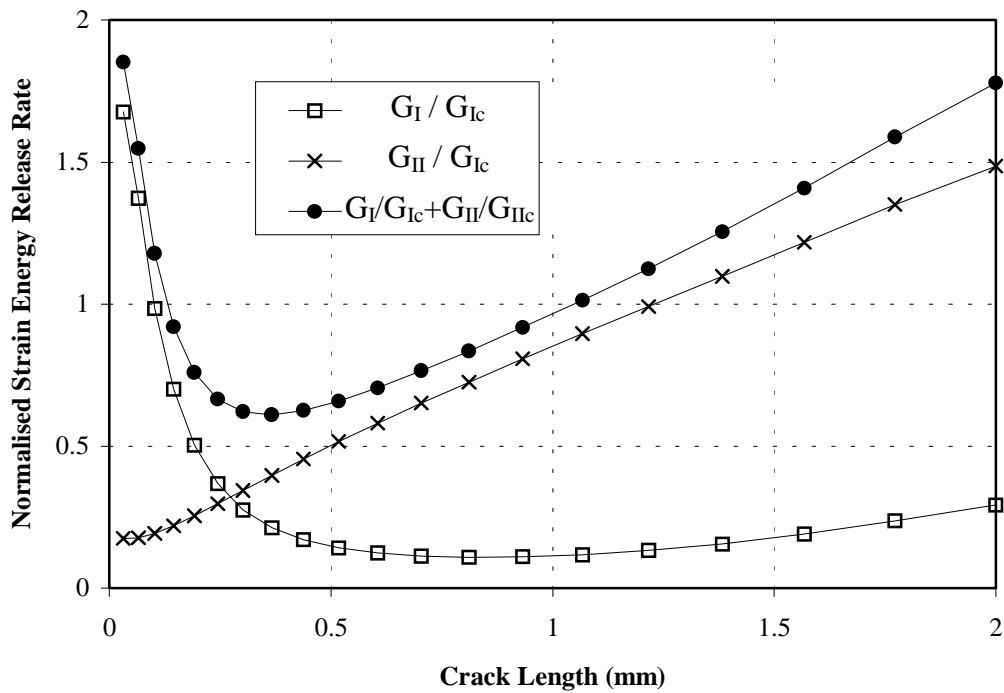


Fig. 6: Normalised Strain Energy Release Rate at Experimental Failure Load (Cut 15mm from Central Roller)

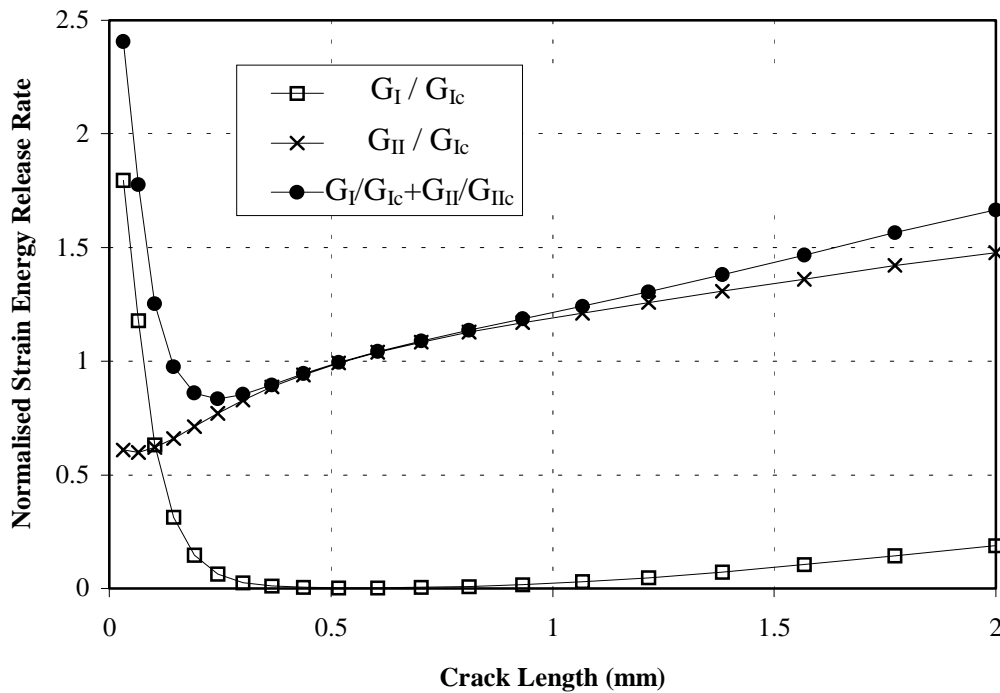


Fig. 7: Normalised Strain Energy Release Rate at Experimental Failure Load (Cut 5mm from Central Roller)

### IMPROVED FAILURE LOAD PREDICTION

The axial distance from the cut to which the zones of yielding material extended was estimated from the finite element analysis. This was done at the top left and bottom right of the cut. The resin along the interfaces of the cut and continuous plies was assumed to yield when the interlaminar shear stress exceeded 70 MPa. This value was estimated from the measured in-plane shear stress-strain response of glass/ epoxy  $\pm 45^\circ$  specimens in tension [10], and assuming transverse isotropy. The yield zone length at the top left was averaged with the length at the bottom right. This was the effective initial crack length. The corresponding value of  $(G_I/G_{Ic} + G_{II}/G_{IIc})$  was found by interpolation. If the value of  $(G_I/G_{Ic} + G_{II}/G_{IIc})$  was less than one at the effective initial crack length, it meant the predicted failure load was higher than the experimental failure load, and vice versa. If this was the case, the value of  $(G_I/G_{Ic} + G_{II}/G_{IIc})$  and the yield zone lengths were recalculated at higher (or lower) values of  $P$ . No further finite element calculations were necessary since the shear stress was proportional to  $P$ , and the value of  $(G_I/G_{Ic} + G_{II}/G_{IIc})$  was proportional to  $P^2$ . After a small number of iterations, the predicted failure load converged. The values for  $d = 5\text{mm}$  and  $d = 15\text{mm}$  are given in Table 3, alongside the previous predictions and the average experimental values. The values of the yield zone lengths in the  $d = 5\text{mm}$  case were 0.70 mm at the top left and 0.48 mm at the bottom right of the cut. The values for  $d = 15\text{mm}$  were 1.57 mm at the top left and 0.38 mm at the bottom right. Although there was a big difference between the latter values, averaging them together was considered to be the best solution for the purposes of keeping the approach manageable.

Note that both the strain energy release rate and the yield zone lengths were calculated assuming linear-elastic material properties. The estimated yield zone lengths would be longer if non-linear stress-strain behaviour was taken into account. However, the strain energy release rate would be lower since yielding limits the stresses at the crack tip. Thus, to some degree these two effects cancel each other out. Also, to accurately predict the yield zone length and corresponding strain energy release rate, the resin along the interfaces would have to be modelled using non-linear material properties. This would require much more computational time, and for the purpose of engineering design, the approach used above is thought to be reasonable.

*Table 3: Failure loads (per unit width)*

	d = 15mm	d = 5mm
Experimental Average	432.4 N/mm	284.0 N/mm
Prediction (Standard Mixed-Mode)	553 N/mm	312 N/mm
Prediction (Including Yield Zones)	444 N/mm	280 N/mm

## DISCUSSION

The analysis showed that when no account is taken of yielding, linear-elastic fracture mechanics is not able to accurately predict delamination in laminates with significant overall interlaminar shear stresses. Referring to Table 3, it can be seen that the failure loads predicted without accounting for yielding at the onset of delamination are both very unconservative. The prediction for the  $d = 15\text{mm}$  case is 28% higher than the experimental value, and the prediction for the  $d = 5\text{mm}$  case is 10% higher. The prediction corresponding to the  $d = 15\text{mm}$  case is worse because the ratio between the shear force and the bending moment is higher when the cut is further from the central roller. Hence, the relative importance of the overall interlaminar shear stress is greater, and the yield zones are generally longer when  $d = 15\text{mm}$ . When the improved approach is applied to the two cases, the predictions are within 3% of the experimental results. Therefore, the improved approach was able to accurately predict the failure loads of laminates with two different levels of yielding.

Previously it was found that a linear interaction equation between the effects of overall interlaminar shear stresses and local stresses at the cut gave a good prediction of failure [6]. The results presented here explain the interaction in terms of the increased effective crack length as the overall interlaminar shear stresses become high compared with the yield stress.

## CONCLUSIONS

A composite specimen containing cut plies under three-point bending was analysed. The ratio between the bending moment and the shear force at the cut was varied by changing the position of the cut relative to the applied loads. The strain energy release rate was calculated for delaminations spreading from the cut using finite element analysis. A mixed-mode failure criterion, based on the strain energy release rate, grossly overestimated the failure loads for both cut positions. An improved approach, also based on the mixed-mode failure criterion but which took account of yielding in the resin at the onset of delamination, was able to predict

the failure loads to within 3% of the experimental values. This shows the importance of considering the yielding that occurs before crack formation when predicting delamination in laminates under high overall interlaminar shear stresses.

### **ACKNOWLEDGEMENTS**

The support of Westland Helicopters and the UK Engineering and Physical Sciences Research Council is gratefully acknowledged.

### **REFERENCES**

1. O'Brien, T. K., "Characterization of Delamination Onset and Growth in a Composite Laminate", *Damage in Composite Materials*, ASTM STP 775, K. L. Reifsnider, Ed., American Society for Testing and Materials, 1982, pp. 140 - 167.
2. Wisnom, M. R. and Jones, M. I., "Delamination of Unidirectional Glass Fibre-Epoxy with Cut Plies Loaded in Four Point Bending", *Journal of Reinforced Plastics and Composites*, Vol. 14, 1995, pp. 45 - 59.
3. Harbert, S. J. and Hogan, H. A., "An Analysis of Curvature and Layup Effects on Delamination in Notched Composite Beams", *Journal of Reinforced Plastics and Composites*, Vol. 11, 1992, pp. 443 - 457.
4. Minguet, P. J. and O'Brien, T. K., "Analysis of Composite Skin/Stringer Bond Failure Using a Strain Energy Release Rate Approach", *Proc. Of ICCM-10*, Whistler, B.C., Canada, August, 1995, pp. 245 - 252.
5. Amrutharaj, G. S., Lam, K. Y. and Cotterell, B., "Delaminations at the Free Edge of a Composite Laminate", *Composites*, 27B, 1996, pp. 475 - 483.
6. Wisnom, M. R. and Jones, M. I., "Delamination due to Interaction between Overall Interlaminar Shear and Stresses at Terminating Plies", *Composite Structures*, Vol. 31, 1995, pp. 39 - 47.
7. Wisnom, M. R., "Shear Fracture of Unidirectional Composites without Initial Cracks", *Composites Science and Technology*, Vol. 52, 1994, pp. 9 - 17.
8. ABAQUS, Hibbitt, Karlsson and Sorensen Inc., 100 Medway Street, Providence, R.I., U.S.A.
9. Partridge, I., Cranfield University. Private communication.
10. Wisnom, M. R., "The Effect of Fibre Rotation in  $\pm 45^\circ$  Tension Tests on Measured Shear Properties", *Composites*, Vol. 26, No. 1, 1995, pp. 25 - 32.

# DAMAGE MECHANICS OF REINFORCEMENT CRACKING IN PARTICLE OR SHORT-FIBER REINFORCED COMPOSITES

Keiichiro Tohgo, Young-Tae Cho and Hitoshi Ishii

*Department of Mechanical Engineering,  
Shizuoka University, 3-5-1, Johoku, Hamamatsu 432, Japan*

**SUMMARY:** In particle or short-fiber reinforced composites, cracking of the reinforcements is a significant damage mode because the broken reinforcements lose load carrying capacity. This paper deals with the load carrying capacity of intact and broken ellipsoidal inhomogeneities embedded in an infinite body and a damage theory of particle or short-fiber reinforced composites. The average stress in the inhomogeneity represents its load carrying capacity, and the difference between the average stresses of the intact and broken inhomogeneities indicates the loss of load carrying capacity due to cracking damage. The load carrying capacity of the broken inhomogeneity is expressed in terms of the average stress of the intact inhomogeneity and some coefficients. The composite in damage process contains intact and broken reinforcements in a matrix. An incremental constitutive relation of particle or short-fiber reinforced composites including the progressive cracking damage of the reinforcements have been developed based on the Eshelby's equivalent inclusion method and Mori and Tanaka's mean field concept. Influence of the cracking damage on the stress-strain response of the composites is demonstrated.

**KEYWORDS:** damage mechanics, reinforcement cracking, particle or short-fiber reinforced composites, broken ellipsoidal inhomogeneity, load carrying capacity, equivalent inclusion method, mean field theory, micromechanics

## INTRODUCTION

Composites which contain particles or short-fibers in a ductile matrix have already used or have the potential as engineering material because of their good formability and machinability as well as improved mechanical properties. In the composites, a variety of damage modes such as fracture of reinforcements, interfacial debonding between reinforcements and matrix, and cracking in matrix develop from early stage of deformation under monotonic or cyclic loads [1-4]. The observed damage modes depend on the combination of the mechanical properties of the constituents and the in-situ interfacial strength between them. In the particle or short-fiber reinforced composites, for example, both the fracture of reinforcements and interfacial debonding may be main damage modes. These damage modes affect the mechanical performance of the composites, and the micromechanism of damage process seems to be responsible for the low ductility and low fracture toughness of the composites. In order to extend the application of the composites and to develop a new composite system, an

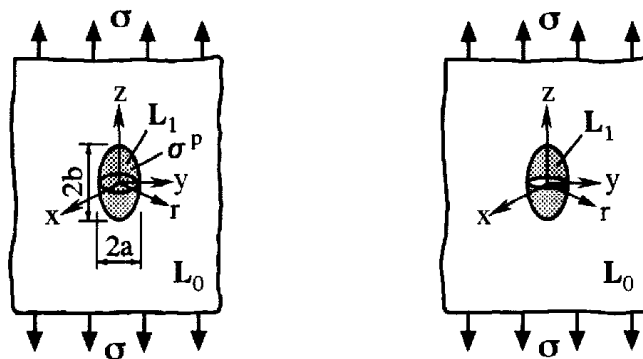
understanding of the micromechanism of damage process in the composites is essential.

For the debonding damage of the particle-reinforced composites, Tohgo and Chou [5] and Tohgo and Weng [6] developed an incremental damage theory based on the Eshelby's equivalent inclusion method [7] and Mori and Tanaka's mean field concept [8], and showed that the influence of the debonding damage on the stress-strain response of the composite is very drastic. On the other hand, the theory for the cracking damage in the composites is also necessary, since the cracking of the reinforcement is well observed in the actual composite, particularly, short-fiber reinforced composites. Many theories [5, 6, 9-11] for particle or short-fiber reinforced composites were established based on the Eshelby's solution [7] for an ellipsoidal inhomogeneity in an infinite body. However, the corresponding solution for a broken ellipsoidal inhomogeneity has not been reported. Therefore, it is impossible to construct the theory of the composite containing cracking damage in the same scheme.

This paper deals with the load carrying capacity of intact and broken ellipsoidal inhomogeneities in an infinite body and a damage theory of particle or short-fiber reinforced composites. The load carrying capacity of the broken inhomogeneity is expressed in terms of the average stress of the intact inhomogeneity and some coefficients. Based on the finite element analyses of the intact and broken ellipsoidal inhomogeneities, the coefficients are given as functions of an aspect ratio for a variety of combinations of the elastic moduli of inhomogeneity and matrix. An incremental constitutive relation of particle or short-fiber reinforced composites including the progressive cracking damage of the reinforcements have been developed based on the Eshelby's equivalent inclusion method and Mori and Tanaka's mean field concept. Influence of the cracking damage on the stress-strain response of the composites is demonstrated.

### LOAD CARRYING CAPACITY OF AN ELLIPSOIDAL INHOMOGENEITY

Load carrying capacity of an ellipsoidal inhomogeneity embedded in an infinite body can be defined as an average stress in the inhomogeneity. The load carrying capacity depends on the elastic moduli of the inhomogeneity and matrix. High average stress comparing with the remote applied stress means high load carrying capacity of the inhomogeneity. On the other hand, when the average stress is reduced by the debonding or cracking damage of the inhomogeneity, the load carrying capacity is also reduced, and the stress free in a void means that the load carrying capacity of the void is equal to zero. In this section, the load carrying capacity of intact and broken inhomogeneities in an infinite body subjected to the remote applied stress as shown in Fig. 1 is discussed.



(a) Intact ellipsoidal inhomogeneity (b) Broken ellipsoidal inhomogeneity

Fig.1 Intact and broken ellipsoidal inhomogeneities in an infinite body subjected to applied stress.

### Intact Ellipsoidal Inhomogeneity

Figure 1(a) shows an intact ellipsoidal inhomogeneity embedded in an infinite body under applied stress  $\sigma$ . The elastic stiffness tensors of the infinite body (matrix) and the inhomogeneity are denoted by  $L_0$  and  $L_1$ , respectively. The stress of the ellipsoidal inhomogeneity  $\sigma^P$  is uniform and is given by the Eshelby's equivalent inclusion method as well known [7].

$$\sigma^P = L_0 (S - I) [(L_1 - L_0) S + L_0]^{-1} L_1 (S - I)^{-1} L_0^{-1} \sigma \quad (1)$$

where  $S$  is Eshelby's tensor which is expressed as a function of shape of the inhomogeneity and Poisson's ratio of the matrix.

### Broken Ellipsoidal Inhomogeneity

For an ellipsoidal inhomogeneity cracked on the cross section of  $xy$ -plane as shown in Fig. 1(b), the stress distribution in the inhomogeneity seems to be complex and its solution has not been reported as far as the authors traced references. Figure 2 shows the principle of superposition for a broken ellipsoidal inhomogeneity in an infinite body. The stress state in the broken inhomogeneity  $\sigma^{\mathcal{P}}$  is given by the sum of the stresses  $\sigma^P$  and  $\sigma^{\mathcal{P}*}$ , where  $\sigma^P$  is the stress in the intact inhomogeneity under the applied stress  $\sigma$  and  $\sigma^{\mathcal{P}*}$  is the stress in the broken inhomogeneity subjected to internal stress  $-\sigma^P$  on the crack surface. Therefore, the average stress of the broken inhomogeneity is expressed by

$$\bar{\sigma}^{\mathcal{P}} = \sigma^P + \bar{\sigma}^{\mathcal{P}*} \quad (2)$$

Since  $\bar{\sigma}^{\mathcal{P}*}$  is taken as a function of the stress of the intact inhomogeneity  $\sigma^P$ , Eqn (2) can be written as

$$\begin{aligned} \bar{\sigma}^{\mathcal{P}} &= \sigma^P + h \sigma^P \\ &= (I + h) \sigma^P = k \sigma^P \end{aligned} \quad (3)$$

where  $h$  is a coefficient expressing the reduction of average stress due to the cracking damage of an ellipsoidal inhomogeneity,  $k$  is the ratio of the average stresses of the broken and intact inhomogeneities and  $I$  is unit tensor. The components of the average stresses are given by

$$\sigma^P = [\sigma_x^P, \sigma_y^P, \sigma_z^P, \tau_{yz}^P, \tau_{zx}^P, \tau_{xy}^P] \quad (4)$$

$$\bar{\sigma}^{\mathcal{P}} = [\bar{\sigma}_x^{\mathcal{P}}, \bar{\sigma}_y^{\mathcal{P}}, \bar{\sigma}_z^{\mathcal{P}}, \bar{\tau}_{yz}^{\mathcal{P}}, \bar{\tau}_{zx}^{\mathcal{P}}, \bar{\tau}_{xy}^{\mathcal{P}}] \quad (5)$$

$$\bar{\sigma}^{\mathcal{P}*} = [\bar{\sigma}_x^{\mathcal{P}*}, \bar{\sigma}_y^{\mathcal{P}*}, \bar{\sigma}_z^{\mathcal{P}*}, \bar{\tau}_{yz}^{\mathcal{P}*}, \bar{\tau}_{zx}^{\mathcal{P}*}, \bar{\tau}_{xy}^{\mathcal{P}*}] \quad (6)$$

The average stress components in the broken inhomogeneity shown in Fig. 2(c) are  $\bar{\sigma}_z^{\mathcal{P}*}$ ,  $\bar{\sigma}_x^{\mathcal{P}*}$  and  $\bar{\sigma}_y^{\mathcal{P}*}$  due to internal stress  $-\sigma_z^P$  on the crack surface,  $\bar{\tau}_{yz}^{\mathcal{P}*}$  due to  $-\tau_{yz}^P$ , and  $\bar{\tau}_{zx}^{\mathcal{P}*}$  due to  $-\tau_{zx}^P$ . Therefore, we have

$$k = \begin{bmatrix} 1 & 0 & h_{13} & 0 & 0 & 0 \\ 0 & 1 & h_{23} & 0 & 0 & 0 \\ 0 & 0 & 1+h_{33} & 0 & 0 & 0 \\ 0 & 0 & 0 & 1+h_{44} & 0 & 0 \\ 0 & 0 & 0 & 0 & 1+h_{55} & 0 \\ 0 & 0 & 0 & 0 & 0 & 1 \end{bmatrix} \quad (7)$$



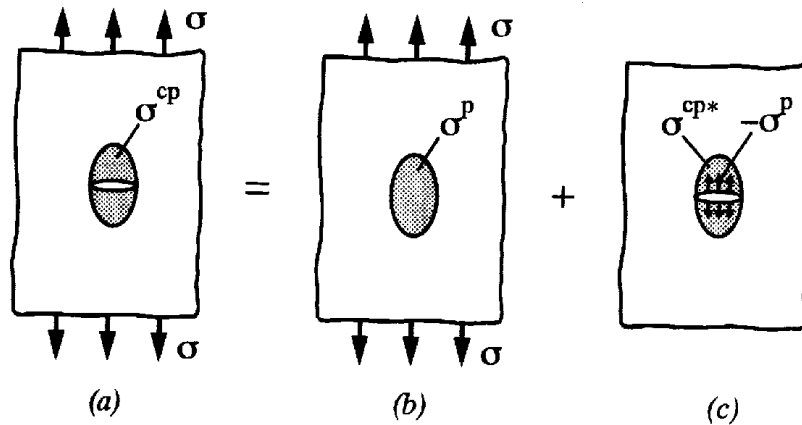


Fig.2 Principle of superposition for a broken ellipsoidal inhomogeneity in an infinite body.

in the matrix form. Furthermore, in the case of the axisymmetric ellipsoidal inhomogeneity, the next relations are obtained.

$$h_{13} = h_{23}, \quad h_{44} = h_{55} \quad (8)$$

As a result, once the three components  $h_{33}$ ,  $h_{13}$  and  $h_{44}$  are obtained, the average stress, i.e. the load carrying capacity, of the broken ellipsoidal inhomogeneity can be evaluated by the average stress of the intact inhomogeneity which is already obtained by the Eshelby's equivalent inclusion method. Out of the three components,  $h_{33}$  and  $h_{13}$  are determined by the analysis under uniaxial tension, and  $h_{44}$  is by the analysis under pure shear.

### Load Carrying Capacity Ratio

Based on the axisymmetric and three dimensional finite element analyses of the intact and broken ellipsoidal inhomogeneities under uniaxial tension and under pure shear, three components  $h_{33}$ ,  $h_{13}$  and  $h_{44}$  have been obtained as functions of the aspect ratio ( $b/a$ ) and the combination of the elastic moduli as shown in Figs. 3, 4 and 5. When Fig. 3 is observed for a scale of the right hand side, it exhibits a ratio of the load carrying capacity on tensile stress  $\bar{\sigma}_z^p / \sigma_z^p$ . Figure 5 also exhibits a ratio of the load carrying capacity on shear stress  $\bar{\tau}_{yz}^p / \tau_{yz}^p$  for a scale of the right hand side. As shown in Fig. 3, the load carrying capacity ratio on tensile stress is always smaller than one, i.e. the inhomogeneity reduces its load carrying capacity by the cracking damage. It is found that the load carrying capacity ratio increases with increasing the aspect ratio and depends on the combination of the elastic moduli. The load carrying capacity ratio is equal to zero for a penny shape inhomogeneity ( $b/a=0$ ), while it approaches to one for a continuous long fiber ( $b/a=\infty$ ). This means that a penny shape inhomogeneity loses completely the load carrying capacity by the cracking damage while the infinitely long fiber in an infinite body never loses it. The characteristics of the load carrying capacity ratio on shear stress in Fig. 5 are almost the same as those mentioned above for Fig. 3.

## INCREMENTAL THEORY FOR PROGRESSIVE CRACKING DAMAGE

Figure 6 schematically illustrates the microstructure of the aligned particle or short-fiber reinforced composite with the cracking damage. In the composite, the microscopic stresses and strains in the reinforcements and matrix are created due to the material heterogeneity, in

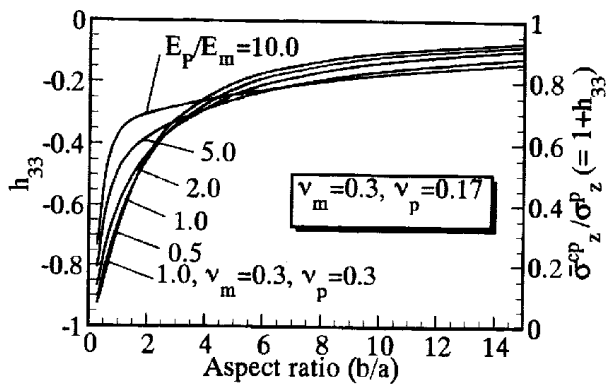


Fig.3 Coefficient ( $h_{33}$ ) and load carrying capacity ratio on tensile stress as a function of an aspect ratio.

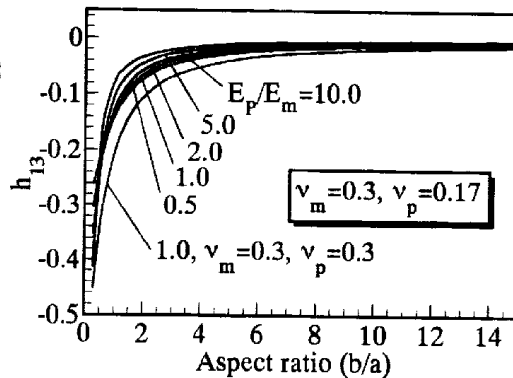


Fig.4 Coefficient ( $h_{13}$ ) as a function of an aspect ratio.

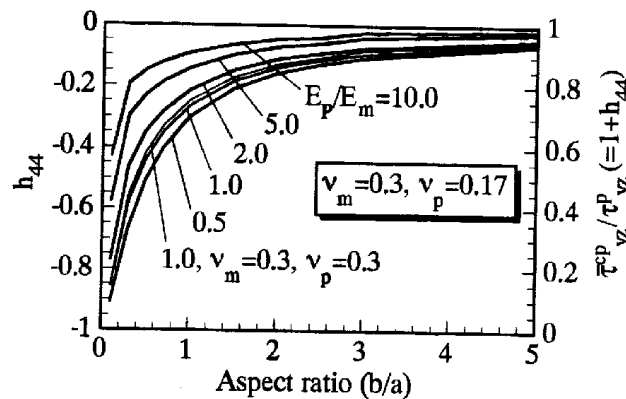


Fig.5 Coefficient ( $h_{44}$ ) and load carrying capacity ratio on shear stress as a function of an aspect ratio.

addition to the applied macroscopic stress and strain. Furthermore, the cracking of reinforcement leads to the stress release and the reduction of load carrying capacity. In this section, an incremental damage theory to describe the progressive cracking damage of the reinforcements is developed based on Eshelby's equivalent inclusion method [7], Mori-Tanaka's mean field concept [8] and the load carrying capacity of broken ellipsoidal inhomogeneity, under the following assumptions.

- (1) The cracking damage of reinforcements is controlled by the stress of the reinforcements and the statistical behavior of the strength of reinforcements.
- (2) During cracking, the stress of the cracked reinforcement is released and its load carrying capacity is described by the average stress of the broken inhomogeneity.
- (3) The progressive damage of the composite is described by a decrease in an intact reinforcement content and an increase in a cracked reinforcement content. The composite undergoing the damage process contains the intact and cracked reinforcements, and the reinforcements in the cracking process in the matrix.

In the composite system the stress and strain of the intact and damaged reinforcements and matrix are represented with the superscripts  $p$ ,  $d$  and  $\theta$ , respectively, and those of the composite are shown by symbols without superscript.

### Formulation

Figure 6 illustrates the states before and after incremental deformation of the composite in

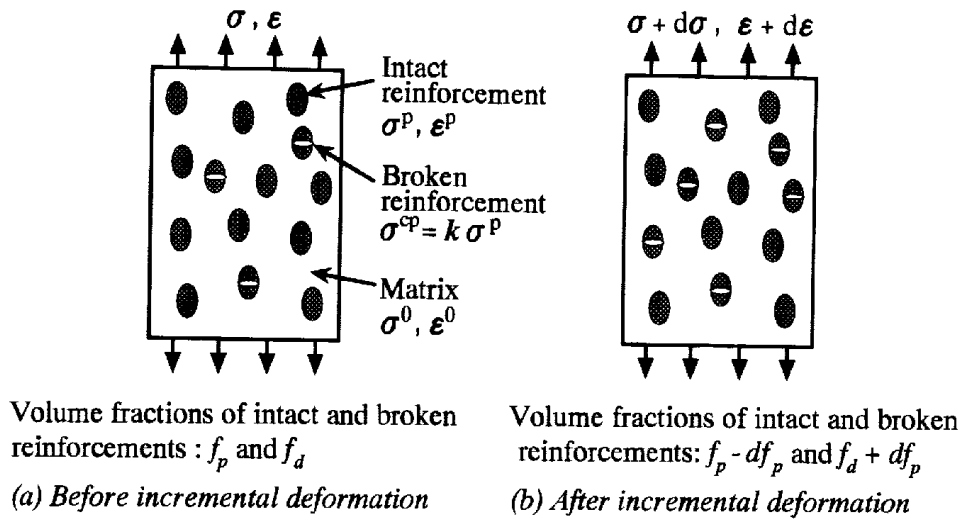


Fig.6 The states of composite undergoing damage process before and after incremental deformation.

the damage process. The state before deformation shown in Fig. 6(a) is described in terms of the volume fractions of the intact and damaged reinforcements  $f_p$  and  $f_d$ . If the volume fraction of the reinforcements cracked during the incremental deformation is denoted by  $df_p$ , the state after deformation shown in Fig. 6(b) is described in terms of the volume fractions of the intact and damaged reinforcements  $f_p - df_p$  and  $f_d + df_p$ . In order to describe the deformation and damage of the composite in this incremental process, Eshelby's equivalent inclusion method [7] and Mori and Tanaka's mean field theory [8] are used for the heterogeneous body containing the intact and damaged reinforcements and the reinforcements to be cracked.

Following Eshelby's equivalence principle combined with Mori and Tanaka's mean field concept [9-11], the incremental stress in the reinforcements  $d\sigma^p$  is given by

$$\begin{aligned} d\sigma^p &= d\sigma + d\tilde{\sigma} + d\sigma_1^{pt} \\ &= L_1 (d\epsilon_0 + d\tilde{\epsilon} + d\epsilon_1^{pt}) = L_0 (d\epsilon_0 + d\tilde{\epsilon} + d\epsilon_1^{pt} - d\epsilon_1^*) . \end{aligned} \quad (9)$$

Since the average stress of the cracked reinforcements is given by Eqn (3), Eshelby's equivalence principle for the cracked reinforcements can be written in the form of

$$\begin{aligned} k d\sigma^p &= d\sigma + d\tilde{\sigma} + d\sigma_2^{pt} \\ &= k L_1 (d\epsilon_0 + d\tilde{\epsilon} + d\epsilon_1^{pt}) = L_0 (d\epsilon_0 + d\tilde{\epsilon} + d\epsilon_2^{pt} - d\epsilon_2^*) . \end{aligned} \quad (10)$$

Furthermore, for the reinforcements in the cracking process, since the current reinforcement stress should be released up to  $k\sigma^p$  in the next incremental deformation, the next equation is obtained:

$$-(I - k) \sigma^p = d\sigma + d\tilde{\sigma} + \sigma_3^{pt} = L_0 (d\epsilon_0 + d\tilde{\epsilon} + \epsilon_3^{pt} - \epsilon_3^*) . \quad (11)$$

Neglecting high-order terms of increments, the above relation becomes

$$-(I - k) \sigma^p = \sigma_3^{pt} = L_0 (\epsilon_3^{pt} - \epsilon_3^*) . \quad (12)$$

In the above equations,  $L_1$  and  $L_0$  are tangential modulus tensors for the reinforcements and

matrix, respectively.  $d\sigma$  and  $d\tilde{\sigma}$  are the incremental applied stress and the incremental average stress based on Mori and Tanaka's mean field concept, and they are related to  $d\epsilon_0$  and  $d\tilde{\epsilon}$  by

$$d\sigma = L_0 d\epsilon_0, \quad d\tilde{\sigma} = L_0 d\tilde{\epsilon}. \quad (13)$$

$d\sigma_1^{pt}$ ,  $d\sigma_2^{pt}$ ,  $\sigma_3^{pt}$  and  $d\epsilon_1^{pt}$ ,  $d\epsilon_2^{pt}$ ,  $\epsilon_3^{pt}$  represent the perturbed parts of the stress and strain in the intact and damaged reinforcements and the reinforcements to be cracked, respectively.  $d\epsilon_1^*$ ,  $d\epsilon_2^*$  and  $\epsilon_3^*$  are Eshelby's equivalent transformation strains. The perturbed strains are related to the transformation strains:

$$d\epsilon_1^{pt} = S d\epsilon_1^*, \quad d\epsilon_2^{pt} = S d\epsilon_2^*, \quad \epsilon_3^{pt} = S \epsilon_3^*. \quad (14)$$

$S$  is Eshelby's tensor for a ellipsoidal inclusion.  $d\sigma_1^{pt}$ ,  $d\sigma_2^{pt}$  and  $\sigma_3^{pt}$  are described by

$$d\sigma_1^{pt} = L_0 (S - I) d\epsilon_1^*, \quad d\sigma_2^{pt} = L_0 (S - I) d\epsilon_2^*, \quad \sigma_3^{pt} = L_0 (S - I) \epsilon_3^*, \quad (15)$$

where  $I$  is the fourth-rank identity tensor. Since the incremental applied (macroscopic) stress  $d\sigma$  is represented by

$$d\sigma = (f_p - df_p) d\sigma^p + f_d k d\sigma^p - df_p (I - k) \sigma^p + (1 - f_p - f_d) (d\sigma + d\tilde{\sigma}), \quad (16)$$

neglecting the high-order terms of increments, the incremental average stress  $d\tilde{\sigma}$  is given by

$$d\tilde{\sigma} = -f_p d\sigma_1^{pt} - f_d d\sigma_2^{pt} - df_p \sigma_3^{pt} \quad (17)$$

Substituting Eqns (13) and (15) into the above equation, one obtains the next equation for the incremental average strain:

$$d\tilde{\epsilon} = - (S - I) (f_p d\epsilon_1^* + f_d d\epsilon_2^* + df_p \epsilon_3^*). \quad (18)$$

The incremental macroscopic strain  $d\epsilon$  of the composite is expressed as

$$d\epsilon = (f_p - df_p) (d\epsilon_0 + d\tilde{\epsilon} + d\epsilon_1^{pt}) + f_d (d\epsilon_0 + d\tilde{\epsilon} + d\epsilon_2^{pt}) + df_p (d\epsilon_0 + d\tilde{\epsilon} + \epsilon_3^{pt}) + (1 - f_p - f_d) (d\epsilon_0 + d\tilde{\epsilon}). \quad (19)$$

Considering Eqns (14) and (18) and neglecting high-order terms of increments, the above equation becomes

$$d\epsilon = d\epsilon_0 + f_p d\epsilon_1^* + f_d d\epsilon_2^* + df_p \epsilon_3^*. \quad (20)$$

By solving the above equations, Eshelby's equivalent transformation strains  $d\epsilon_1^*$ ,  $d\epsilon_2^*$  and  $\epsilon_3^*$  can be described as a function of incremental applied stress  $d\sigma$  and  $df_p$ . Finally, the incremental strain  $d\epsilon$  - stress  $d\sigma$  relation of the composite is obtained as

$$d\epsilon = \left( I + f_p A_1^{-1} B_1 + f_d A_2^{-1} B_2 \right) L_0^{-1} d\sigma + \left[ (I - S)^{-1} + f_p A_1^{-1} B_1 + f_d A_2^{-1} B_2 \right] L_0^{-1} (I - k) \sigma^p df_p, \quad (21)$$

where

$$A_1 = (L_1 - L_0)^{-1} [L_0 + (L_1 - L_0) S + (L_1 - L_0) (I - S) f_p] - f_d [L_0 + (kL_1 - L_0) f_d]^{-1} [kL_1 S + (kL_1 - L_0) (I - S) f_p] , \quad (22)$$

$$B_1 = f_d [L_0 + (kL_1 - L_0) f_d]^{-1} (kL_1 - L_0) - I , \quad (23)$$

$$A_2 = [L_0 + (L_1 - L_0) S + (L_1 - L_0) (I - S) f_p]^{-1} (L_1 - L_0) (I - S) f_d - [kL_1 S + (kL_1 - L_0) (I - S) f_p]^{-1} [L_0 + (kL_1 - L_0) f_d] (I - S) , \quad (24)$$

$$B_2 = [kL_1 S + (kL_1 - L_0) (I - S) f_p]^{-1} (kL_1 - L_0) - [L_0 + (L_1 - L_0) S + (L_1 - L_0) (I - S) f_p]^{-1} (L_1 - L_0) . \quad (25)$$

As shown in Eqn (21), the composite strain increment is given by the sum of the strain increment due to the stress increment and the strain increment due to the cracking damage. The incremental average stresses of the matrix and the intact and damaged reinforcements,  $d\sigma^0$ ,  $d\sigma^p$  and  $d\sigma^d$ , are given by

$$d\sigma^0 = L_0 (I - S) [(I - S)^{-1} + f_p A_1^{-1} B_1 + f_d A_2^{-1} B_2] L_0^{-1} [d\sigma + (I - k) \sigma^p df_p] , \quad (26)$$

$$d\sigma^p = L_0 (I - S) [(I - S)^{-1} - (1 - f_p) A_1^{-1} B_1 + f_d A_2^{-1} B_2] L_0^{-1} [d\sigma + (I - k) \sigma^p df_p] , \quad (27)$$

and

$$d\sigma^d = k d\sigma^p . \quad (28)$$

### Cumulative Probability of Damaged Reinforcements

The following Weibull distribution is adopted for the cumulative probability of the fracture of reinforcements:

$$P_v(\sigma_{max}^p) = 1 - \exp\left[-\left(\frac{\sigma_{max}^p}{S_0}\right)^m\right] , \quad (29)$$

where,  $\sigma_{max}^p$  is the maximum tensile stress of the reinforcements and  $S_0$  and  $m$  are the scale and shape parameters, respectively. The average strength of the reinforcements is given by

$$\bar{\sigma}_{max}^p = S_0 \Gamma\left(1 + \frac{1}{m}\right) \quad (30)$$

where  $\Gamma(\cdot)$  is Gamma function. If an initial reinforcement volume fraction is denoted by  $f_{p0}$ , as a cumulative volume fraction of the damaged reinforcements is represented by  $f_{p0} P_v$ , the volume fraction  $df_p$  of the reinforcements to be cracked in the incremental deformation is given by

$$df_p = f_{p0} \frac{dP_v}{d\sigma_{max}^p} d\sigma_{max}^p . \quad (31)$$

## NUMERICAL RESULTS AND DISCUSSION

The stress-strain response under uniaxial tension has been calculated on particle or short fiber reinforced composites taking account of progressive cracking damage of the reinforcements.

The constituent materials are isotropic elastic. Young's modulus and Poisson's ratio are

$$E_1 = 2500 \sigma_0, \quad \nu_1 = 0.17 \quad (32)$$

for the reinforcements, and

$$E_0 = 500 \sigma_0, \quad \nu_0 = 0.30 \quad (33)$$

for the matrix, where  $\sigma_0$  is the reference stress. For the cracking damage of the reinforcements, Weibull distribution Eqn (29) with  $m=5.0$  and  $\bar{\sigma}_{max}^p=3.0 \sigma_0$  is adopted. Initial volume fraction of the reinforcements contained in the composites is 20%.

The variations of macroscopic stress (composite stress,  $\sigma_z$ ), microscopic stresses of the reinforcements and matrix ( $\sigma_z^p$  and  $\sigma_z^0$ ), volume fractions of intact and damaged reinforcements ( $f_p$  and  $f_d$ ) are shown as a function of the macroscopic composite strain  $\epsilon_z$  in Fig. 7. Furthermore, the variations of the stresses for the composite without cracking damage are shown by dashed lines. On the perfect composite, linear stress-strain relations are obtained, and the microscopic stresses are higher in the reinforcements and lower in the matrix than the macroscopic stress. On the composite with progressive damage, the stress-strain relations deviate from linear relations for the perfect composite with increasing cracking damage of the reinforcements. After all reinforcements encounter the cracking damage, the stress-strain relations become linear again. Fig. 8 shows the influence of the aspect ratio of the reinforcements on the

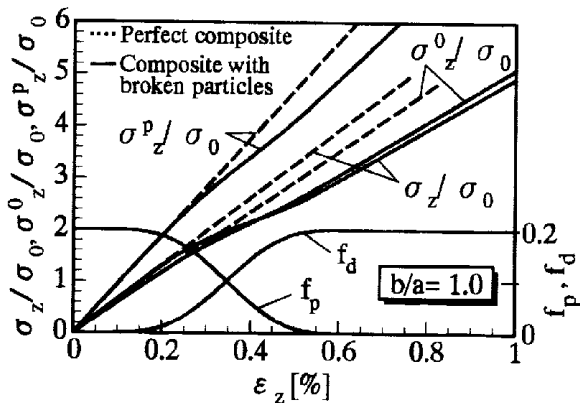


Fig.7 Stress-strain relations of perfect composite and composite with progressive cracking damage.

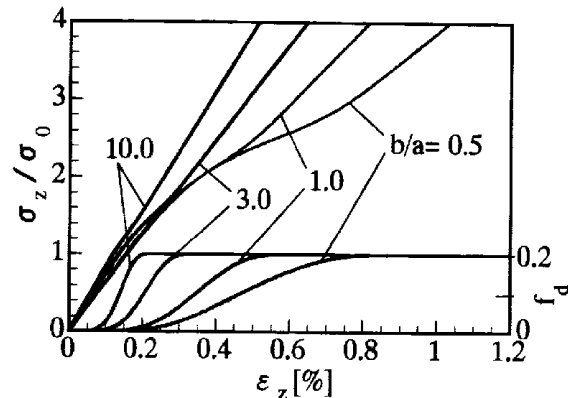


Fig.8 Influence of an aspect ratio of reinforcements on the stress-strain relations.

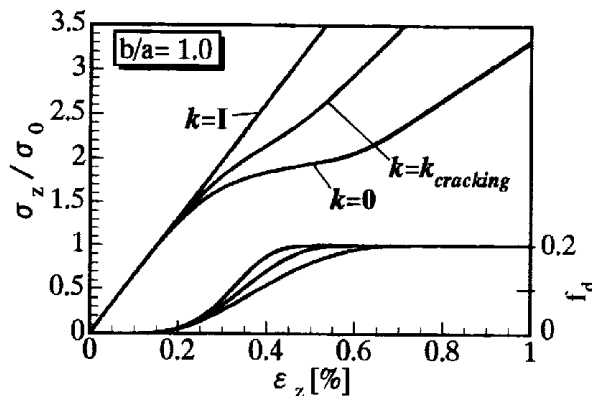


Fig.9 Influence of k-matrix on the stress-strain relations.

stress-strain relations of the composites with progressive damage. When the aspect ratio of the reinforcements is lower, the influence of the cracking damage of the reinforcements is more drastic because the reinforcements lose the larger amount of load carrying capacity. The present theory can describe a variety of damage patterns of the reinforcements such as the cracking damage and the debonding damage by modifying the  $k$ -matrix. Fig. 9 shows the influence of the  $k$ -matrix on the stress-strain relations of the particle reinforced composites. When  $k$  is unit matrix, the present theory describes the perfect composite because of no loss of load carrying capacity. On the other hand, since the condition of null matrix for  $k$  means the complete loss of load carrying capacity of the reinforcement, the present theory describes the interfacial debonding between the reinforcement and matrix, and corresponds to the previous incremental damage theory for particle reinforced composite with debonding damage [5, 6]. It is noted from Fig. 9 that the debonding damage corresponding to  $k=0$  gives the lower limit of the stress-strain relation with the reinforcement damage.

### REFERENCES

1. Loretto, M.H. and Konitzer, D.G., "The Effect of Matrix Reinforcement Reaction on Fracture in Ti-6Al-4V-Base Composites", *Metall. Trans. A*, Vol. 21A, 1990, pp. 1579-1587.
2. Llorca, J., Martin, A., Ruiz, J. and Elices, M., "Particulate Fracture during Deformation of a Spray Formed Metal-Matrix Composite", *Metall. Trans. A*, Vol. 24A, 1993, pp. 1575-1588.
3. Whitehouse, A.F. and Clyne, T.W., "Cavity Formation during Tensile Straining of Particulate and Short Fibre Metal Matrix Composites", *Acta Metall. Mater.*, Vol. 41, 1993, pp. 1701-1711.
4. Tohgo, K., Mochizuki, K., Takahashi, H. and Ishii, H., "Application of Incremental Damage Theory to Glass Particle Reinforced Nylon 66 Composites", *Localized Damage IV, Computer-Aided Assessment and Control*, Computational Mechanics Publications, 1996, pp. 351-358.
5. Tohgo, K. and Chou, T.-W., "Incremental Theory of Particulate-Reinforced Composites Including Debonding Damage", *JSME Int. J.*, Vol. 39, 1996, pp. 389-397.
6. Tohgo, K. and Weng, G.J., "A Progressive Damage Mechanics in Particle-Reinforced Metal-Matrix Composites under High Triaxial Tension", *Trans. ASME, J. Eng. Mater. Technol.*, Vol. 116, 1994, pp. 414-420.
7. Eshelby, J. D., "The Determination of the Elastic Field of an Ellipsoidal Inclusion, and Related Problems", *Proceedings of the Royal Society*, London, Vol. A241, 1957, pp. 376-396.
8. Mori, T. and Tanaka, K., "Average Stress in Matrix and Average Elastic Energy of Materials with Misfitting Inclusions", *Acta Metall.*, Vol. 21, 1973, pp. 571-574.
9. Mura, T., *Micromechanics of Defects in Solids*, Martinus Nijhoff, The Hague, 1982.
10. Arsenault, R.J. and Taya, M., "Thermal Residual Stress in Metal Matrix Composite", *Acta Metall.*, Vol. 35, 1987, pp. 651-659.
11. Tandon, G.P. and Weng, G.J., "A Theory of Particle-Reinforced Plasticity", *Trans. ASME, J. Appl. Mech.*, Vol. 55, 1988, pp. 126-135.

# PARALLEL COMPUTING AND DAMAGE IN COMPOSITE STRUCTURES

F. Devries, F. Léné, G. L'Hostis, D. Soulat

*Laboratoire de Modélisation et Mécanique des Structures, UPMC / ENSAM / ENS Cachan - U.R.A. 1776 C.N.R.S., Université Pierre et Marie Curie - Tour 66, 5eme étage, 4, place Jussieu - 75252 Paris cedex 05, France*

**SUMMARY:** A model for the damage's evolution in composite materials is here proposed. It consists in a microscopic/macroscopic approach requiring the solution of two uncoupled steps. The first one consists in the computation of the composite's homogeneous equivalent behaviors, damaged by defects postulated at the microscopic composite's level. The second, consists then in solving a nonlinear, time-dependent, macroscopic problem.

These steps require unfortunately a lot of computations whose numerical costs may be prohibitive. It is here proposed to reduce them, thanks to the development of a strategy allowing to take benefit from the parallel computers performances.

Starting from two three-dimensional, industrially-realistic examples, one shows that this methodology may be fruitful if one knows how to choose a subdomain decomposition, taking in account the damages and the heterogeneities of the composite's representative volume element.

**KEYWORDS:** damage, thermoelasticity, homogenization, subdomain decomposition techniques, parallelism

## INTRODUCTION

This paper deals with the simulation of damage's propagation in composite structures. To this way we use an homogenization technique which leads to a microscopic/macroscopic approach. To this purpose we first postulate damage criteria in the composite representative volume element. These criteria introduce parameters which are chosen as microscopic damage parameters. The use of the homogenization technique, allows then to construct a damaged macroscopic medium model, based on a microscopic approach of a body weakened by microdefects. The damage's evolution may be then modelled and computed inside an adjusted thermodynamic framework.

Unfortunately this methodology requires a lot of computations, required for the construction of composite homogenized behaviors connected to each of its microscopic damaged configuration. In addition to the three-dimensional geometry, a good description of the damage process needs the choice of a lot of microscopic damage parameters and a lot of values for these parameters. Thus, this methodology requires large computer CPU times and large memory spaces, and comes up against the limitations prescribed by the actual computers technology.



A way to get round these overcosts consists in using multiprocessor computers. We propose thus in this communication to show how one can use homogenization techniques and substructuring techniques to take advantage of the parallel computers performances.

In order to assess the benefit of this methodology, we consider two kinds of three-dimensional composites, used at the industrial level as covering materials for aeronautical engines. The first one is made up of glass microballoons coated in a resin (syntactic foams). The observed damage process of this composite consists of the implosion of the balloons. The second example concerns sewed layers of unidirectional composites. Due to the different expansion coefficients of these materials, when the structure undergoes a high temperature increase, damage occurs under the form of delaminations between constituents.

### **A MODEL FOR DAMAGE'S EVOLUTION SIMULATION IN COMPOSITE STRUCTURES**

In order to simulate the damage's evolution in composite structures, we use hereafter a microscopic/macroscopic approach of a macroscopic medium weakened by microdefects. To this purpose we classically consider two scales: the microscopic scale is attached to the representative volume element of the composite and is thus representative of microscopic effects such damages; its basis is denoted by  $(0, y_1, y_2, y_3)$ ; at the macroscopic level any point of the structure is marked with respect of a system of axis denoted by  $(0, x_1, x_2, x_3)$ .

This approach consists first in postulating damages at the microscopic level. The connected damaged homogeneous behavior laws are then computed thanks to the homogenization principle. In order to simulate the damage's evolution in the composite structures under consideration, it remains lastly to solve, at the macroscopic level, a nonlinear, time-dependent problem .

#### **Computation of Homogenized Damaged Behaviors**

We consider in what follows that the composite under consideration admits a geometric and mechanic periodicity, such that this material may be defined by the knowledge of its period or basic cell, denoted by  $Y$ . In order to describe the damage's evolution in this material, let us consider its basic cell as a real structure containing defects, as for example stress-free holes (denoted by  $C$ ). Let us associate to these defects, parameters, denoted in vectorial notations by  $D$ . Thanks to the homogenization process for periodic media [1], [2], one can associate to this microscopic description of the damaged composite material a homogeneous equivalent behavior. To this way and when a thermo-elastic behavior for the constituents is chosen, we have to find the microscopic deviation in temperature  $\tau$  and the microscopic displacement field  $u$ , solutions in the elastic part of  $Y$  (denoted by  $Y^*$ ) to the following problems, also known as cellular problems [3], [4]:

Elasticity cellular problem:

$$(1) \quad \begin{cases} \operatorname{div}_y \boldsymbol{\sigma} = 0, \quad \boldsymbol{\sigma} = \mathbf{a} [ \mathbf{e}(\mathbf{u}) - \boldsymbol{\alpha} (T - T_0) ] & \text{in } Y^* \\ \mathbf{u} - \mathbf{E} \mathbf{y} \text{ Y-periodic, } \boldsymbol{\sigma}(\mathbf{n}) \text{ Y-antiperiodic} \\ \boldsymbol{\sigma}(\mathbf{n}) = 0 \text{ on } \partial C, \quad \langle\langle \mathbf{e}(\mathbf{u}) \rangle\rangle_Y = \mathbf{E} \end{cases}$$

Thermal conduction cellular problem:

$$(2) \quad \begin{cases} \operatorname{div}_y \mathbf{q} = 0, \quad \mathbf{q} = -\boldsymbol{\lambda} \nabla_y \tau & \text{in } Y^* \\ \tau - \mathbf{F} \mathbf{y} \text{ Y-periodic, } \mathbf{q} \cdot \mathbf{n} \text{ Y-antiperiodic} \\ \mathbf{q} \cdot \mathbf{n} = 0 \text{ on } \partial C, \quad \langle\langle \nabla_y \tau \rangle\rangle_Y = \mathbf{F} \cdot \end{cases}$$

In these problems  $\operatorname{div}_y$  and  $\nabla_y$  respectively denote the divergence and gradient operators with respect to the microscopic coordinates  $y$ . We have also used the following notations:

$$(3) \quad \begin{cases} \mathbf{e}(\mathbf{u}) = \frac{1}{2} (\nabla_y \mathbf{u} + {}^t\nabla_y \mathbf{u}), \quad \langle\langle \nabla_y f \rangle\rangle_Y = \frac{1}{|Y|} \int_{\partial Y} f \mathbf{n} \, dS \\ \phi \text{ Y-periodic} \Leftrightarrow \phi \text{ admits the same value at points belonging to opposite faces of } Y \end{cases}$$

and respectively denoted by  $\lambda$ ,  $\mathbf{a}$ ,  $\boldsymbol{\alpha}$ ,  $\rho$ ,  $c$  the conduction, stiffness, expansion tensors, the mass density and the specific heat, and introduced the fields  $\mathbf{E}$ ,  $\mathbf{F}$ ,  $T$  which represent the macroscopic strain tensor, the macroscopic temperature gradient tensor and the macroscopic temperature ( $T_0$  is the reference macroscopic temperature).

Once these problems have been solved, one may then construct the damaged homogenized behavior sought, through the computation of the stiffness, conduction and expansion homogenized tensors  $\mathbf{Q}^h(\mathbf{D})$ ,  $\boldsymbol{\lambda}^h(\mathbf{D})$ ,  $\boldsymbol{\alpha}^h(\mathbf{D})$  which connect the microscopic fields to the macroscopic ones by the relations:

$$(4) \quad \begin{cases} \langle \boldsymbol{\sigma} \rangle_Y = \boldsymbol{\Sigma} = \mathbf{Q}^h(\mathbf{D}) \mathbf{E} - \mathbf{Q}^h(\mathbf{D}) \boldsymbol{\alpha}^h(\mathbf{D}) (T - T_0) \\ \langle \mathbf{q} \rangle_Y = \mathbf{S} = -\boldsymbol{\lambda}^h(\mathbf{D}) \mathbf{F} \end{cases}$$

$$\text{with } \langle f \rangle_Y = \frac{1}{|Y|} \int_{Y^*} f(y) \, dy$$

and the homogenized specific heat denoted by  $C^h(\mathbf{D})$ .

Let us lastly specify that thanks to the linearity of these problems with respect to the macroscopic data (strain  $\mathbf{E}$ , temperature deviation  $(T-T_0)$ , temperature gradient  $\mathbf{F}$ ) the solutions to problems (1) and (2) are usefully splitted in the following forms:

$$(5) \quad \begin{cases} \mathbf{u} = \mathbf{u}^{kh} E_{kh} + \mathbf{w} (T - T_0) & (k, h \in \{1, 2, 3\}) \quad (\text{with } \mathbf{u}^{kh} = \mathbf{u}^{hk} \text{ thanks to } E_{kh} = E_{hk}) \\ \tau = \tau^k F_k & (k \in \{1, 2, 3\}) \end{cases}$$

allowing to solve once and for all these problems, undependently from the macroscopic fields which have to be now computed.

### Damage's Evolution

Once previous step has been carried out, one knows each of the homogenized equivalent behaviors of the composite material under consideration, corresponding to given values of the damage parameters considered at the microscopic level.

For a given thermo-mechanical loading prescribed to the composite structure (which occupies the volume  $\Omega$ ), the damage's evolution is then modelled by introducing the macroscopic free energy density defined by:

$$(6) \quad \langle \rho \rangle_Y \psi(\mathbf{E}, T, \mathbf{D}) = \frac{1}{2} \mathbf{E} \mathbf{Q}^h(\mathbf{D}) \mathbf{E} - \mathbf{Q}^h(\mathbf{D}) \boldsymbol{\alpha}^h(\mathbf{D}) \mathbf{E} (T - T_0) - \frac{1}{2} \frac{\langle \rho \rangle_Y C^h(\mathbf{D})}{T_0} (T - T_0)^2$$

where the vector  $\mathbf{D}$  ( $n$  entries assumed) is constituted by the damage parameters.

The volume dissipation  $\Delta$  is then given by:

$$(7) \quad \Delta = \sum_{i=1}^n F_i \frac{dD_i}{dt} - \frac{\mathbf{S}}{T} \nabla_x T$$

where we have denoted by  $F_i$  the thermodynamical damage force associated to the damage parameter  $D_i$ , defined by:

$$(8) \quad F_i = - \frac{\partial \{ \langle \rho \rangle_Y \psi(\mathbf{E}, T, \mathbf{D}) \}}{\partial D_i} \quad (i = 1, 2, \dots, n)$$

A useful means for satisfying the positivity of the dissipation (7) consists in using the thermodynamic framework of standard generalized materials [5]. Assuming the classical decoupling between the mechanical and thermal dissipations and starting from the existence of pseudo potentials of dissipation denoted by  $\phi^{th}(\nabla_x T)$  and  $\phi^{mec}(F_1, \dots, F_n)$  which are chosen as positive or zero functions, convex and zero in 0, this framework allows one to obtain the complementary laws under the forms:

$$(9) \quad \frac{\mathbf{S}}{T} = - \frac{\partial \phi^{th}(\nabla_x T)}{\partial (\nabla_x T)}, \quad \frac{dD_i}{dt} = \frac{\partial \phi^{mec}(F_1, \dots, F_n)}{\partial F_i} \quad (i = 1, \dots, n)$$

The choice of these potentials has to be *a posteriori* justified by collation of results with experimental data. In what follows we choose the thermal potential in order to obtain the

classical Fourier's law for the temperature. Concerning the mechanic potential, it may be for instance chosen as follows:

$$(10) \quad \phi^{mec}(F_1, \dots, F_n) = \sum_{i=1}^n \frac{\alpha_i}{1 + \beta_i} |F_i|^{1 + \beta_i} \quad (\alpha_i > 0, \beta_i > 0 \quad \forall i \in \{1, \dots, n\})$$

This particular choice leads to a damage's evolution law of Norton's kind [6].

Once these choices have been made the evolution of damages will be obtained by the solution of the following macroscopic problem:

$$(11) \quad \left\{ \begin{array}{ll} \operatorname{div}_x \Sigma = 0 & \text{in } \Omega \\ \Sigma = Q^h(\mathbf{D}) \mathbf{E} - Q^h(\mathbf{D}) \alpha^h(\mathbf{D}) (T - T_0) & \text{in } \Omega \\ 2 \mathbf{E} = \nabla_x \mathbf{u} + {}^t \nabla_x \mathbf{u} & \\ \langle \rho \rangle_Y C^h(\mathbf{D}) \frac{T}{T_0} \frac{dT}{dt} + \operatorname{div}_x \mathbf{S} = \sum_{i=1}^n (F_i - T \frac{\partial F_i}{\partial T}) \frac{dD_i}{dt} - Q^h(\mathbf{D}) \alpha^h(\mathbf{D}) T \frac{d\mathbf{E}}{dt} & \text{in } \Omega \\ \mathbf{S} = -\lambda^h(\mathbf{D}) \nabla_x T & \text{in } \Omega \\ \frac{dD_i}{dt} = \frac{\partial \phi^{mec}}{\partial F_i} & (i = 1, \dots, n) \quad \text{in } \Omega \end{array} \right.$$

for which it is required to specify boundary and initial conditions.

The damage's evolution may be thus computed in the two steps given above which consists in:

1. constructing the homogeneous equivalent damaged behaviors connected to chosen values of microscopic defects;
2. solving the macroscopic time-dependent problem describing the damages evolution.

### THE SCHUR COMPLEMENT METHOD FOR THE SOLUTION OF CELLULAR PROBLEMS

The method explained above for the computation of damage's evolution in composite structures has been already successfully used for the study of damage by fibers breaks in unidirectional composites [7]. It requires however the solution of the cellular problems (1), (2) for each set of values of the damage parameters postulated at the composite's microscopic level. These computations may induce very large CPU times in the case where, like here, the geometry is three-dimensional. This is the reason why we have developed a parallel way for these solutions; it consists in using a subdomain decomposition technique (Schur complement method) and allows to take benefit from the parallel computers performances.

In order to present the application of this technique to the solution of cellular problems, let us consider the thermal cellular problems (2). Thanks to the decomposition (5) it may be easily shown that the fields  $\tau^k$  are the solutions to the following problems:

$$(12) \quad \begin{cases} \operatorname{div}_y \mathbf{q}^k = 0, \quad q_j^k = -\lambda_{jk} - \lambda_{ji} \frac{\partial \tau^k}{\partial y_i} & \text{in } Y^* \\ \mathbf{q}^k \cdot \mathbf{n} \text{ Y-antiperiodic}, \quad \tau^k \text{ Y-periodic} \\ \mathbf{q}^k \cdot \mathbf{n} = 0 & \text{on } \partial C \end{cases}$$

Let us then introduce a subdomain decomposition of  $Y$  into 2 subdomains (for reader's convenience), denoted by  $(1)Y$  and  $(2)Y$ . We denote by  $\Gamma$  the common boundaries of these subdomains and the external boundary of  $Y$  (on which periodicity conditions for  $\tau^k$  are prescribed).

Let us next introduce the fields  $(i)\tau^k, (i)q^k$  solutions in the subdomain  $(i)Y$  to the following problem:

$$(13) \quad \begin{cases} \operatorname{div}_y (i)\mathbf{q}^k = 0, \quad (i)q_j^k = -\lambda_{jk} - \lambda_{ji} \frac{\partial (i)\tau^k}{\partial y_i} & \text{in } (i)Y^* \\ (i)\tau^k = \mu & \text{on } \Gamma \cap \partial(i)Y \\ (i)\mathbf{q}^k \cdot (i)\mathbf{n} = 0 & \text{on } \partial C \end{cases}$$

where we have denoted by  $(i)\mathbf{n}$  the unit outward normal to  $\partial(i)Y$  and introduce the (not yet known) temperature field  $\mu$  which has to be characterized.

These fields will coincide with the restrictions of  $\tau^k$  and  $q^k$  in  $(i)Y$  if and only if they satisfy the continuity of normal heat flux on  $\Gamma$ :

$$(14) \quad (1)\mathbf{q} \cdot (1)\mathbf{n} = (2)\mathbf{q} \cdot (2)\mathbf{n} \quad \text{on } \Gamma$$

In order to deduce the problem whose solution is  $\mu$ , let us use the linearity of problem (13) and thus split its solution as follows:

$$(15) \quad (i)\tau^k = (i)\theta^k + (i)\omega^k, \quad (i)q^k = (i)\Theta^k + (i)\Omega^k$$

where  $(i)\theta^k$  and  $(i)\omega^k$  are the solutions to:

$$(16) \quad \begin{cases} \operatorname{div}_y (i)\Theta^k = 0, (i)\Theta_j^k = -\lambda_{jk} - \lambda_{ji} \frac{\partial (i)\theta^k}{\partial y_i} & \text{in } (i)Y^* \\ (i)\theta^k = 0 & \text{on } \Gamma \cap \partial(i)Y \\ (i)\Theta^k \cdot (i)\mathbf{n} = 0 & \text{on } \partial C \end{cases}$$

$$(17) \quad \begin{cases} \operatorname{div}_y (i)\Omega^k = 0, (i)\Omega_j^k = -\lambda_{ji} \frac{\partial (i)\omega^k}{\partial y_i} & \text{in } (i)Y^* \\ (i)\omega^k = \mu & \text{on } \Gamma \cap \partial(i)Y \\ (i)\Omega^k \cdot (i)\mathbf{n} = 0 & \text{on } \partial C \end{cases}$$

Problem (16) may be solved once for all. Let us associate to its solution the normal heat flux on  $\Gamma$ , defined by:  $(i)b^k = (i)\Theta^k \cdot (i)\mathbf{n}$ .

Next, let us introduce the linear operator  $(i)S$ , defined on the subdomain  $(i)Y$ , which associates to the prescribed (but unknown) temperature  $\mu$  of problem (17) its connected normal heat flux on  $\Gamma$ :

$$(18) \quad (i)S : \mu|_{\Gamma} \rightarrow (i)S(\mu) = [(i)\Omega^k \cdot (i)\mathbf{n}]|_{\Gamma}$$

Thanks to these quantities the normal heat flux connected to the solution of problem (13) satisfies:

$$(19) \quad [(i)\mathbf{q}^k \cdot (i)\mathbf{n}]|_{\Gamma} = (i)S(\mu) + (i)b^k$$

The continuity condition (14) leads then to the interface problem to be solved on  $\Gamma$  which writes:

$$(20) \quad \text{Find } \mu \text{ such that: } (1)S(\mu) + (2)S(\mu) = -(1)b^k + (2)b^k$$

The symmetric, definite positive operator  $S = (1)S + (2)S$  is called the Schur complement operator [8]. It determines the problem to be solved at the interface  $\Gamma$  between the subdomains. This problem is classically solved by use of the iterative preconditioned conjugate gradient algorithm, whereas the problems to be solved in each subdomain (problems 16 and 17) are fruitfully solved by a direct method, such the Cholesky method.

As mentioned above the use of this method for the "in parallel" solution of the cellular problems requires the choice of a subdomain decomposition for the composite's basic cell. Many subdomain decomposition procedures are available [9], [10]. However, in order to obtain an efficient speed-up, this choice has to almost satisfy some principles, such the minimization of the interface problem size and the load-balancing of the tasks on each of the processors used. We shall see hereafter that mechanical phenomena complicate this choice.

## APPLICATION OF PARALLELISM

In order to illustrate the means given above for the parallel simulation of damage's propagation in composite structures, we consider two kinds of three-dimensional composites, used at the industrial level as covering materials for aeronautical engines. These materials and the damages which are experimentally observed are now briefly presented.

### Syntactic Foam

The first material we consider is a syntactic foam. It consists of an isotropic resin into which nine glass balloons are arranged in a cubic centered network (see fig. 1). Their internal boundaries are assumed to be stress free.

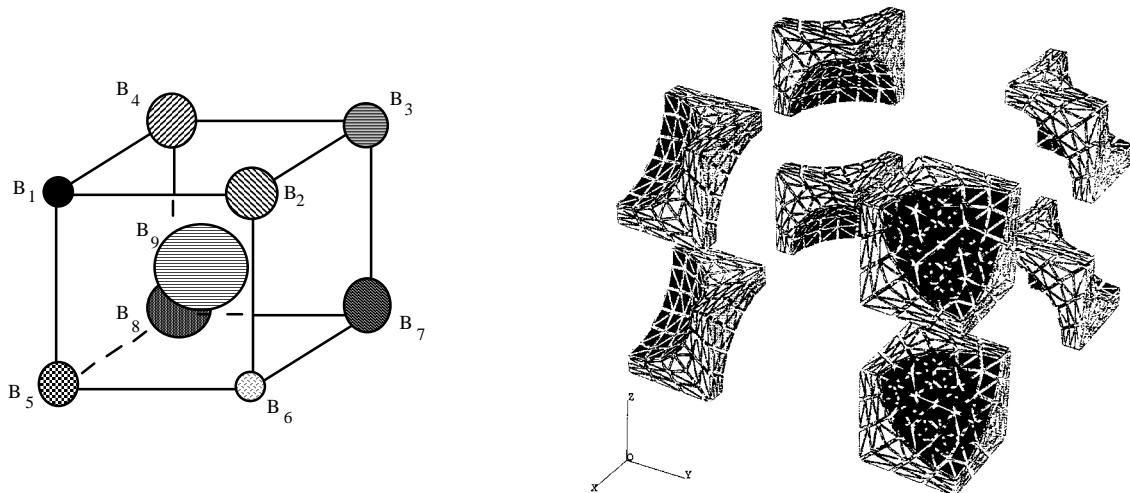


*Fig. 1: Geometric arrangement of the syntactic foam and subdomain decomposition*

The experimentally-observed damage process in this composite consists of the implosion of the microballoons, and thus their disappearances. In order to simulate this kind of damage we attach to each (say  $B_i$ ) of these balloons a scalar denoted by  $D_i$  which take the value 1 or 0 depending on whether the balloon is broken or not.

The parallel solution of the cellular problems has been carried out thanks to a decomposition in 8 subdomains shown in figure 1. This choice has been directly induced by the geometry of the basic cell. Indeed, it insures the load-balancing of tasks on each of the 8 processors which are allocated to each of the 8 subdomains, and minimize the size of the interface problem to be solved.

The characteristics of this decomposition are presented in figure 2, which points out the number of degrees of freedom (Finite Element Method) for the global and interface problems corresponding to each of the damaged configurations of the composite's basic cell, in the case of the elasticity cellular problems (1).

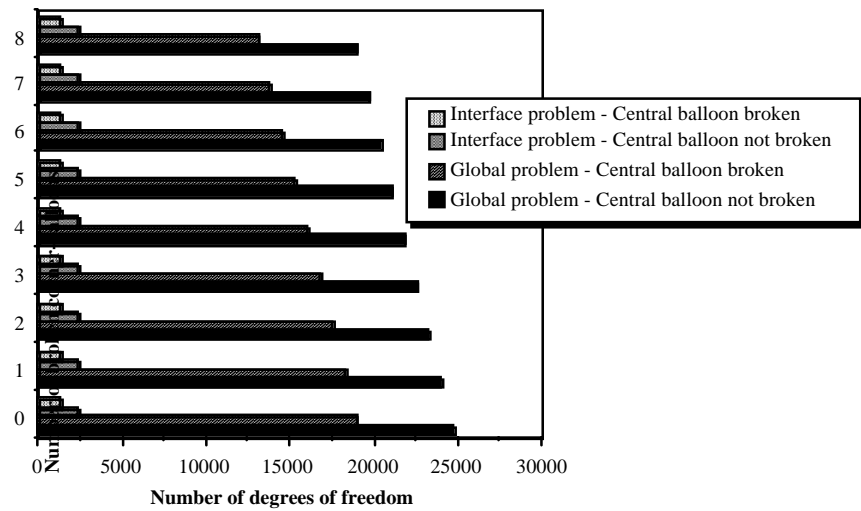


Fig. 2: Size of the damaged elastic problems

Thanks to this decomposition, the parallel solution of problems (1) on a MIMD machine (KSR1), leads to times savings which appear very good, as figure 3 attests (the C.P.U. times given in this figure correspond to the solution of one cellular problem (1)) .

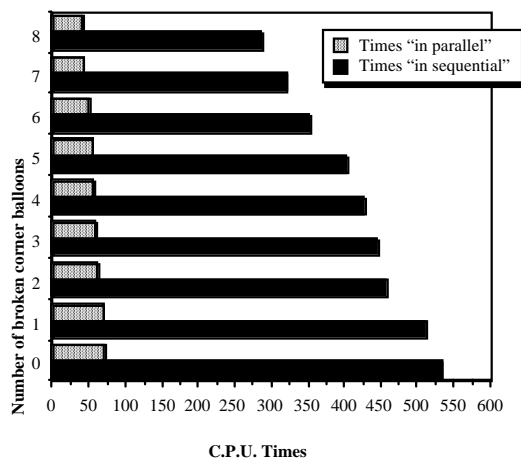


Fig. 3: C.P.U. times for the solutions of one elastic cellular problem

Indeed, from these results, it appears that the times speed-up is around 7 and thus very close to the optimal and maximal one which is equal to 8.

### Sewed Layers of Unidirectional Composites

The second composite we have considered, consists in two layers of unidirectional composites, whose orientations are respectively equal to 0 and 90 degrees, held in contact (one hopes so) by a third constituent, perpendicular to them, called in the sequel the "picot".

Due to the different expansion coefficients of the materials of this basic cell, when the structure undergoes a thermo-elastic loading, the damage occurs under the form of debondings between the constituents. We postulate thus three kinds of defects which are modelled by cavities (denoted by  $C_i$  in figure 4) with zero thickness and whose lengths are denoted by  $L_i$  . These cavities respectively model the debondings appearing at the interface between the layers and the picot and between the layers themselves.



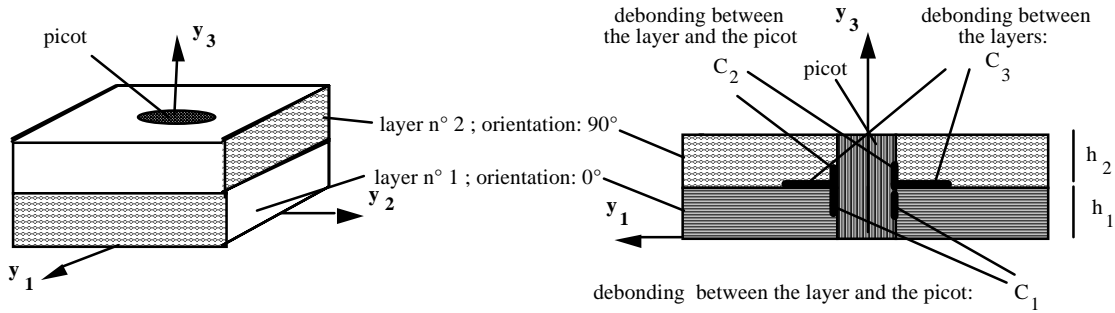


Fig. 4: Basic cell of the sewed composite - Location and geometric modelization of damages

We associate to these defects three damage parameters defined as follows:

$$(21) \quad D_1 = \frac{L_1}{h_1} \quad D_2 = \frac{L_2}{h_2} \quad D_3 = \frac{L_3}{R}$$

where  $h_1$ ,  $h_2$  and  $R$  respectively denote the thicknesses of the layer number 1, number 2 and the radius of the picot.

Unlike the syntactic foam considered before, the choice of a subdomain decomposition for the basic cell of this composite is not straightforward, because of its geometry and the presence of damages. This is the reason why we have considered two subdomain decompositions. The first one consists of 20 subdomains whose boundaries coincide with the debondings between the composite's constituents (the degrees of freedom located at the debondings belong thus to the problem to be solved at the interface  $\Gamma$ ). The second one consists of 8 subdomains whose boundaries, a priori, do not coincide with the damages localizations. The main disadvantage of the first decomposition stems from the bad load-balancing it induces, whereas the second insures a good load-balancing. Let us lastly note that both decompositions lead to some "floating" subdomains (the local problems such (17) do not admit a unique solution); this fact requires the use of a particular preconditioner technique. We used to this purpose the "Coarse Neumann" [11] and "Neumann-Neumann" preconditioners [12].

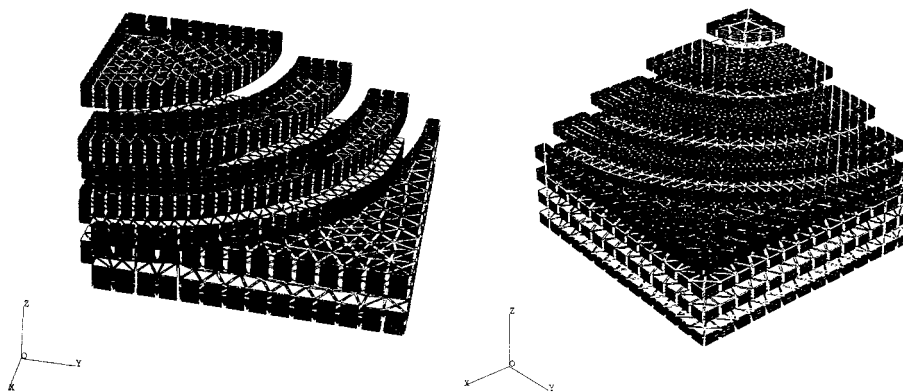


Fig. 5: Decompositions in 8 and 20 subdomains

The characteristics of both decompositions are presented on the following figure, for two particular states of damage of the composite's basic cell:

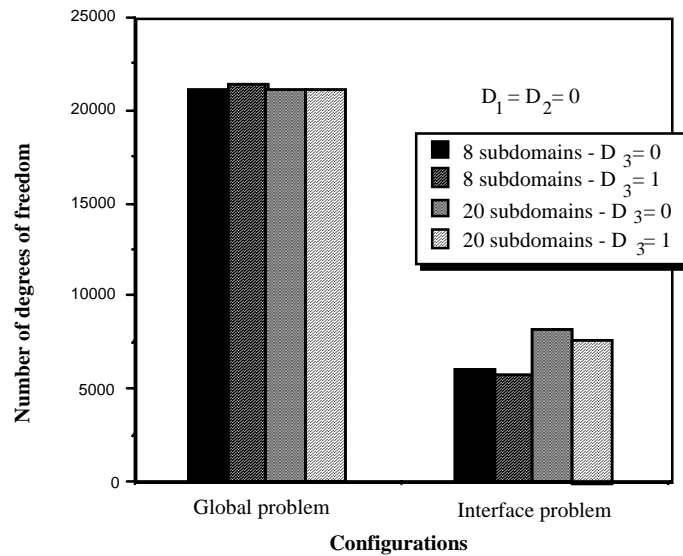


Fig. 6: Size of the elastic problems

We report in figure 7 the C.P.U. times consumed for the solution of one elastic cellular problem by use of these two decompositions and the two preconditioning techniques.

Starting from these results it first appear that, from the point of view of parallelism, the "Coarse Neumann" preconditioner lead to better times savings than the "Neumann-Neumann".

From the times savings point of view, the decomposition in 8 subdomains leads to a speed-up around 6, whereas the decomposition in 20 conducts to a speed-up which is only around 4 (the best are respectively 8 and 20). These results clearly assert that load-balancing is an essential "pre-requisite" for the obtention of good times-savings in parallel, even if it is very difficult to realize this task in case of heterogenous and damaged structures.

Once this choice has been made, the results presented in the case of these two applications, clearly show that parallelism and the methodology used, are powerful.

## CONCLUSION

Thanks to the use of the homogenization technique and a subdomain decomposition technique, a computational strategy and a parallel numerical tool have been made available for the simulation of damage's propagation in composite materials. They enable to obtain appreciate times-savings in most cases. However, the results presented in this paper, clearly show that the problem of the choice of a well-suited subdomain decomposition for the composite's representative volume element, remains to be solved, even if the times-savings we have obtained are very encouraging.

In order to allow for the proposed modelization of damage's evolution in composite materials, to fully reveal its potentialities, the work, which has began consists in developing a parallel strategy for the solution of the nonlinear, time-dependent, macroscopic problem.

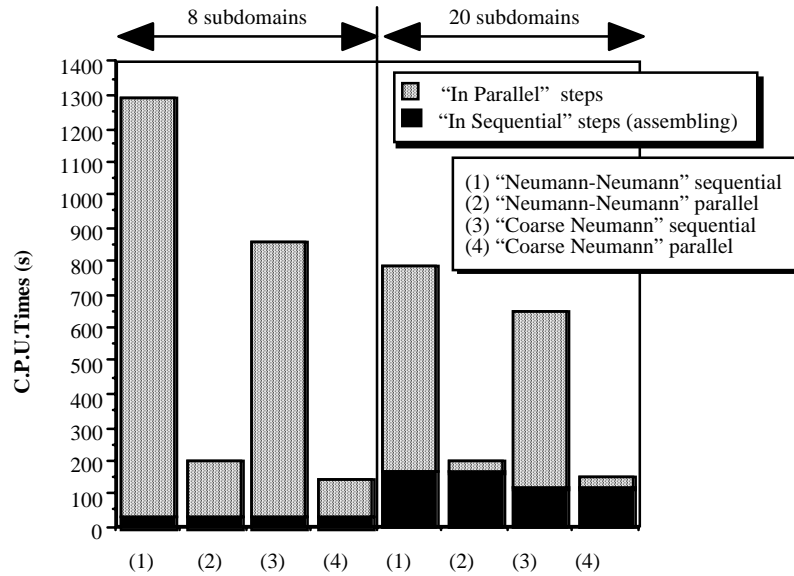


Fig. 7: C.P.U. times for the solutions of one elastic cellular problem versus subdomain decomposition and preconditioning technique

### ACKNOWLEDGMENTS

This work has been made available thanks to the collaboration of the I.N.R.I.A. and more particularly the Modulef department, which has given us the opportunity to use the KSR1 parallel machine.

### REFERENCES

1. Duvaut G. "Analyse Fonctionnelle et mécanique des milieux continus. Application à l'étude des matériaux composites élastiques à structure périodique - Homogénéisation", *Theoretical and Applied Mechanics*, WT. Koiter editor, North-Holland, 1976, pp.119-132.
2. Sanchez E. "Non homogeneous media and vibration theory", *Lecture Notes in Physics*, 127, Springer Verlag, Berlin, 1980.
3. Francfort G. "Homogenization and linear thermoelasticity", *SIAM Journal of Mathematical Analysis*, Vol. 14, 1983, pp. 696-708.
4. Hashin Z. "Thermoelastic properties of fiber composites with imperfect interface", *Mechanics of Materials*, Vol. 8, 1990, pp. 333-348.
5. Halphen B., Nguyen Quoc Son. "Sur les matériaux standards généralisés", *Journal de Mécanique*, Vol. 14, 1985, pp. 39-63.
6. Friaa A. "Le matériau de Norton-Hoff généralisé et ses applications en analyse limite", *Comptes Rendus de l'Académie des Sciences I*, Vol. 286, 1978, pp. 953-956.

7. Devries F.. "A fatigue damage model by fibres breaks in unidirectional composites", *Proceedings of the Fourteenth annual Energy-Sources Technology, ASME, Composites Materials Techonoly*, Houston, USA, 1991, pp. 137-144.
8. Bjordstad P., Wildlund O. "Iterative method for the resolution of elliptic problems on regions partitioned into substructures", *SIAM Journal of Numerical Analysis*, Vol. 23, 1986, pp. 1097-1120.
9. Farhat C. "A simple and efficient automatic F.E.M domain decomposer", *Computers and Structures*, Vol. 28, 1988, pp. 579-602.
10. Malone JG. Automated mesh decomposition and concurrent finite element analysis for hypercube multiprocessor computer. *Computational Methods Applied Mechanical in Engineering*, Vol. 70, 1988, pp. 27-58.
11. Mandel J. "Balancing domain decomposition", *Numerical Methods in Engineering*, Vol. 19, 1993, pp. 233-241.
12. Agoshkov V.I. Poincare's-Stecklov operators and domain decomposition methods. *Proceedings of the Fourth International Symposium on Domain Decomposition Methods for Partial Equations*, Glowinski, Golub, Meurant, Periaux eds., SIAM, Philadelphie, USA, 1987, pp. 73-112.

# A PROPER TREATMENT OF INTERFACIAL CRACKS IN THE PRESENCE OF FRICTION

C. T. Sun and W. Qian

*School of Aeronautics and Astronautics, Purdue University,  
West Lafayette, Indiana 47907-1282, USA*

**SUMMARY:** Frictional sliding on interface crack surfaces results in weak crack tip stress singularity and zero strain energy release rate. A new fracture criterion based on finite extension strain energy release rate is proposed to capture the intrinsic fracture toughness. The finite extension strain energy release rate is shown to represent the magnitude of the singular stress field. Numerical simulation of a center crack in a bimaterial infinite media under remote shear as well as fiber pull-out and push-out are presented to illustrate the frictional effect in both small and large scale contacts near the crack tip.

**KEYWORDS:** friction, fracture, interfacial crack, crack tip stress singularity, strain energy release rate, toughness, fiber pull-out and push-out

## INTRODUCTION

The development of classical fracture mechanics is based on the open crack assumption, i.e., the crack surfaces are not in contact. That assumption leads to, in linear elastic solids, stress singularity of inverse square root that enables one to employ either strain energy release rate or stress intensity factor to characterize fracture toughness and predict crack movement.

When crack surfaces are under combined compression and shear, the effect of sliding frictional stresses on the crack surfaces cannot always be ignored. Only in the case in which the neartip contact zone is extremely small, the K-dominated field basically agrees with that of the open crack solution. This was discussed in detail by Sun and Qian [1] for bimaterial interfacial cracks under "Mode I" loading. On the other hand, if the contact zone is finite, frictional contact of the crack surfaces can no longer be neglected. Most importantly, the frictional contact alters the stress singularity to weak singularities [2]. Consequently, the strain energy release rate as conventionally defined vanishes [3] and cannot be used as a fracture parameter.

Many researchers have attempted to extend the fracture mechanics approach to treat various engineering problems involving interfacial cracks with frictional contact. Fiber pull-out and push-out problems have attracted the most attention (e.g., [4-7]). Delamination in thin film/substrate micro-electronics systems [8] and composite laminates [9] also have been investigated. Various methods were proposed by these authors to derive the strain energy release rate or to employ different parameters for characterizing the interfacial crack toughness. Many of these approaches suffer deficiencies mainly due to the weak singularity and the energy dissipation associated with the frictional sliding of crack surfaces.

In this study, the concept of strain energy release rate for interfacial cracks in the presence of friction is reexamined. A finite element based numerical procedure is introduced to calculate the strain energy release rate and energy dissipation due to friction for a finite crack extension. An explicit relation between the generalized stress intensity factor and the finite extension strain energy release rate is derived based on the neartip field. Thus, the finite extension strain energy release rate with a fixed crack extension can be used to represent the magnitude of the singular stress field and, therefore, to quantitatively characterize the intrinsic fracture toughness. For numerical examples, a center crack in a plane strain infinite bimaterial medium under shear loading (see Fig. 1) and fiber pull-out and push-out tests (see Fig. 2) are simulated.

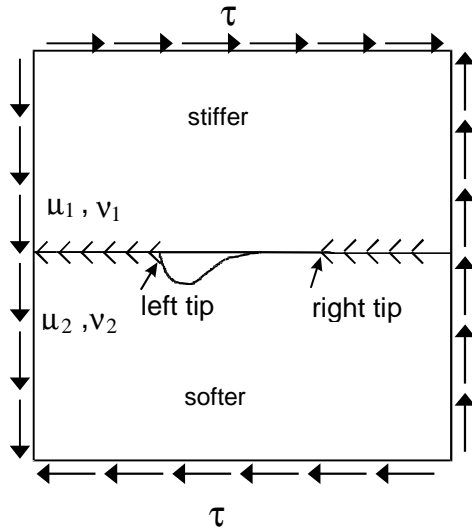


Fig. 1 A bimaterial centered crack panel, 20m x 20m, under remote loading  $\tau = .12\text{MPa}$

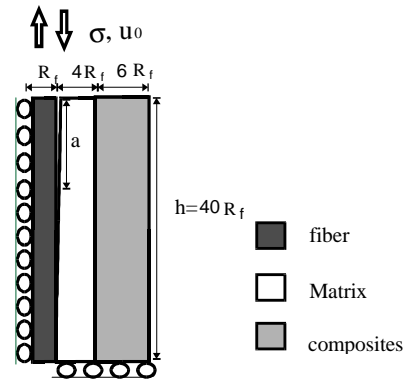


Fig. 2 Geometry and boundary condition of fiber pullout and pushout specimen.  $R_f = 0.64, E_f = 100, E_m = 1, \nu_f = \nu_m = 0.3,$  35 % fiber in composites.

### NEAR TIP FIELD AND STRAIN ENERGY RELEASE RATE

For a crack in homogenous media with friction or an interface crack without friction, there is always square root singularity associated with the neartip field. However, it was originally shown by Comninou [2] for an interface crack between two dissimilar isotropic media with friction and later confirmed and extended by Deng [3] for an interface crack between two dissimilar anisotropic media that the stress singularity  $r^{-\lambda}$  is always weak ( $\lambda < 0.5$ ) for a static crack under monotonic loading. The singularity index  $\lambda$  is related to one of Dundurs parameters  $\beta$  and coefficient of friction  $\mu$  as

$$\cot \lambda\pi = \mu\beta \tag{1}$$

It is easy to see that  $\lambda$  is 0.5 if  $\beta$  or  $\mu$  is zero which corresponds to homogenous media or frictionless condition, respectively. The neartip stress field ahead of the crack tip along the bimaterial interface and the relative crack surface sliding displacement in plane strain condition are

$$\begin{aligned}
 \sigma_{xy}(r,0) &= K_{II} (2\pi r)^{-\lambda} \\
 \sigma_{xy}(r,\pm\pi) &= K_{II} \cos\lambda\pi (2\pi r)^{-\lambda} \\
 \sigma_{yy}(r,\pm\pi) &= -K_{II}\beta \sin\lambda\pi (2\pi r)^{-\lambda} \\
 \Delta u_x(r) &= u_x(r,\pi) - u_x(r,-\pi) = \left[ K_{II}\gamma \sin\lambda\pi / 2(1-\lambda)(2\pi)^\lambda \right] r^{1-\lambda}
 \end{aligned}
 \tag{2}$$

where the generalized stress intensity factor  $K_{II}$  is defined as

$$K_{II} = \lim_{r \rightarrow 0} (2\pi r)^\lambda \sigma_{xy}(r,0) \tag{3}$$

$$\gamma = \left[ \frac{((3-4\nu_1)(1-\beta) + (1+\beta))}{2\mu_1} \right] + \left[ \frac{((3-4\nu_2)(1+\beta) + (1-\beta))}{2\mu_2} \right] \tag{4}$$

In Eqn (4),  $\mu_i$  and  $\nu_i$  are the shear modulus and Poisson's ratio, respectively, for material  $i$  ( $i = 1,2$ ).

It has been pointed out by Dundurs and Comninou [10] that the problem of interface crack with friction is a linear process in the context of monotonic loading. In this context, relation of the strain energy release rate and stress intensity factor can be obtained through a finite crack extension  $\Delta a$  as

$$\begin{aligned}
 \hat{G}(\Delta a) &= \frac{1}{2\Delta a} \int_0^{\Delta a} \left[ \sigma_{xy}(r,0) - \sigma_{xy}(\Delta a - r, \pi) \right] \Delta u_x(\Delta a - r) dr \\
 &= \frac{K_{II}^2 \gamma \sin\lambda\pi}{4(1-\lambda)(2\pi)^{2\lambda}} \Delta a^{1-2\lambda} \left[ \frac{\Gamma(2-\lambda)\Gamma(1-\lambda)}{\Gamma(3-2\lambda)} - \frac{\cos\lambda\pi}{2(1-\lambda)} \right]
 \end{aligned}
 \tag{5}$$

In Eqn (5),  $\Gamma$  is the gamma function.

The conventional strain energy release rate is defined as  $G = \lim_{\Delta a \rightarrow 0} \hat{G}(\Delta a)$ . It is seen from Eqn (5) that strain energy release rate  $G$  vanishes as  $\Delta a \rightarrow 0$  due to the fact that  $\lambda < 0.5$  in the presence of friction.

### FINITE ELEMENT PROCEDURE FOR ENERGY CALCULATION

The finite element method is used to perform the energy calculation during crack extension. A two-step release technique is recommended so that self-similar mesh along the entire crack surface is not needed in calculating strain energy release rate as well as dissipation energy rate during crack extension. In calculating the strain energy release rate at the crack tip of finite contact, special care should be taken to separate the elastic nodal force from the frictional nodal force due to crack surface frictional traction near the crack tip.

In view of the foregoing, a procedure to calculate the strain energy release rate and dissipation energy rate based on crack tip nodal forces and displacements is presented. A two-step crack release method is used to allow non-self-similar mesh along the crack surface. Contact element is used behind and ahead of crack tip. For four-noded elements, the strain energy

release rate  $\hat{G}(\Delta a)$  and dissipation energy rate  $G_d(\Delta a)$  can be calculated as

$$\hat{G}(\Delta a) = \frac{1}{2\Delta a} \left( F_x^a - \mu F_y^a \right) \left( \Delta u_x^{(2)} - \Delta u_x^{(1)} \right)$$

$$G_d(\Delta a) = G_d^N(\Delta a) + G_d^e(\Delta a) \quad (6)$$

$$G_d^N(\Delta a) = \frac{1}{2\Delta a} \mu F_y^a \left( \Delta u_x^{(2)} - \Delta u_x^{(1)} \right)$$

where  $G_d^e(\Delta a)$  is the portion of the dissipation energy rate from existing crack surface, and  $G_d^N(\Delta a)$  is the portion of the dissipation energy rate from the new crack surface.  $F_x^a$  and  $F_y^a$  are the nodal forces at crack tip node “a” (see Fig. 3). Superscripts 1 and 2 in Eqn (6) stand for the states before and after crack release, respectively.

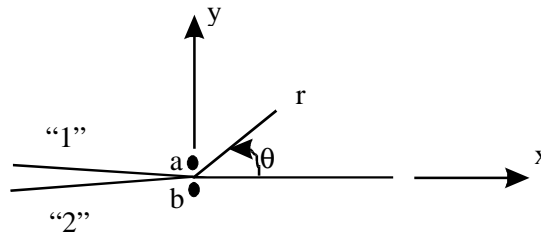


Fig. 3: Bimaterial crack and its coordinate system

A center crack lying between two dissimilar infinite isotropic media under remote shear loading (see Fig. 1) is used to illustrate the validity of the aforementioned technique. The commercial code ABAQUS is used to perform the analysis. The size of the panel is  $20\text{m} \times 20\text{m}$  with a finite crack of  $2\text{m}$ . The Dundurs parameters  $\beta$  and coefficient of friction  $\mu$  are chosen to be  $0.5$ . A similar problem of infinite plate was also investigated by Dundurs and Comninou [10] using elastic dislocation approach. The stress intensity factor obtained by calculating the strain energy release rate and using the relation in Eqn (5) for closed crack tip (right tip in Fig. 1) is given together with those from Dundurs and Comninou [10] in Table 1. There is excellent agreement between these two methods, and the difference is believed to be due to the finite size effect of the panel in the present study compared with the infinite medium in Dundurs and Comninou’s study.

Table 1: Comparison of stress intensity factor  $K_{II}$  from present analysis and  $K_{II}^d$  obtained by Comninou, et al. [10],  $\bar{K}_{II} = (1 + \mu^2 \beta^2) K_{II} / \tau(2a)^\lambda$ ,  $\mu = 0.5$ ,  $\beta = 0.5$

$\Delta a / a$	$\bar{K}_{II}$ (present)	$\left  (K_{II} - K_{II}^d) / K_{II}^d \right  \times 100\%$
$3.18 \cdot 10^{-2}$	0.9723	1.28
$1.59 \cdot 10^{-2}$	0.9720	1.25
$7.96 \cdot 10^{-3}$	0.9724	1.29
$3.98 \cdot 10^{-3}$	0.9737	1.42



### A FRACTURE CRITERION

For the center cracked problem as discussed in the previous section, it is recognized that there is always a sizable contact zone at one crack tip (denoted as closed crack tip), and an extremely small contact zone at the other tip (which can be virtually regarded as open crack tip) under pure shear loading. This problem is studied using the finite element procedure to understand the frictional effect on the interfacial crack under small scale as well as large scale contacts. In the finite element analysis, the applied shear stress  $\tau$  is assumed to be 0.12 MPa,  $\mu_1 = 35$  MPa,  $\mu_2 = 0.35$  MPa, and  $\nu_1 = \nu_2 = 0.0$ . These material properties yield  $\beta = 0.49$ .

The strain energy release rate  $\hat{G}(\Delta a)$ , dissipation energy rate  $G_d(\Delta a)$  as well as total energy release rate  $\hat{G}(\Delta a) + G_d(\Delta a)$  for the problem of Fig. 1 with  $\beta = 0.49$  and  $\mu = 0.5$  corresponding to various crack extensions are shown in Fig. 4 and Fig. 5 for open and closed crack tips, respectively.

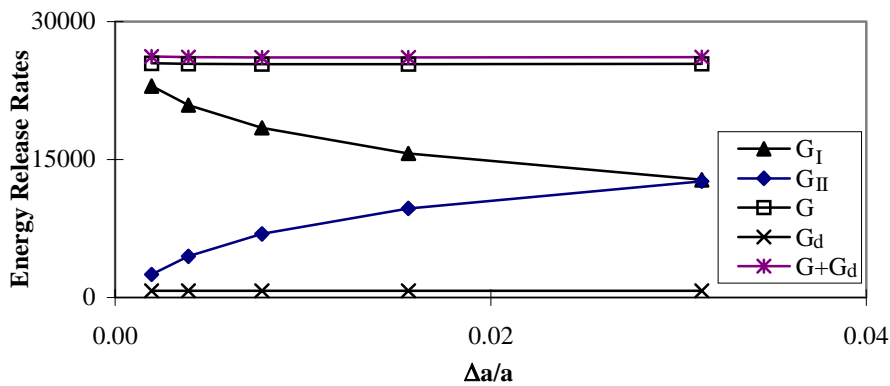


Fig. 4: Finite energy release rates at the open crack tip for the panel shown in Fig. 1

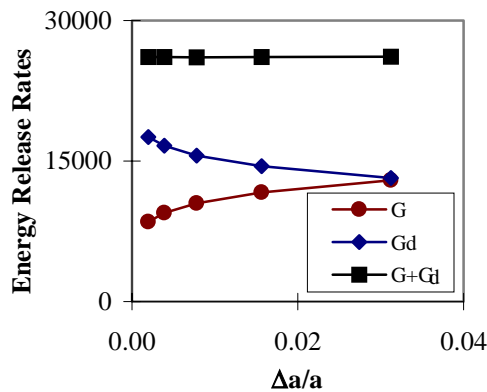


Fig. 5: Finite extension energy release rates at the closed crack tip for the panel shown in Fig. 1

At the open crack tip, the contact zone  $r_c / a$  is usually around  $10^{-5}$  to  $10^{-7}$  and can be virtually treated as an open crack tip. The modified crack closure technique can therefore be applied to calculate the strain energy release rates. It is seen in Fig. 4 that individual finite extension strain energy release rates are  $\Delta a$  dependent, while the total strain energy release rate as well as the dissipation energy rate remain constant for different crack extensions. It is

noted that dissipation energy rates are fairly small compared with strain energy release rate. This indicates that the frictional effect on the open crack tip is fairly small. It can also be shown that the stress distribution ahead of the open crack tip is very close to those of the oscillatory solution obtained based on traction free crack surface condition. It is concluded that frictional effect at the open crack tip is negligible. All existing approaches for the calculation of fracture parameters for bimaterial interfacial cracks are thus applicable (e.g., see Ref. 1).

As for the fracture behavior at the closed crack tip, it is clearly seen in Fig. 5 that the finite extension strain energy release rate decreases, and dissipation energy rate increases, while total energy release rate remains constant when crack extension  $\Delta a$  decreases. Recall the relationship between strain energy release rate and crack extension  $\Delta a$  in Eqn (5) that strain energy release rate indeed decreases and eventually vanishes when  $\Delta a$  approaches zero due to the weak stress singularity. The strain energy release rate is therefore  $\Delta a$ -dependent, while the increase of dissipation energy rate make up the decrease of strain energy release rate for total energy balance when  $\Delta a$  decreases. The implication of decreasing strain energy release rate is that the classical strain energy release rate concept is no longer valid because of its zero value. Consequently, a new finite extension strain energy release rate associated with a finite crack extension is needed to quantify the weak singular stress field ahead of the crack tip.

The decreasing behavior of strain energy release rate was also noticed by Stringfellow and Freund [8] who computed the J-integral for the frictional sliding fracture in a thin film on a substrate. It was pointed out later by Deng [3] that the path independence of J-integral no longer exists due to the crack surface traction resulting from friction, and the J-integral for a vanishingly small contour becomes zero indicating strain energy release rate also vanishes.

In view of the foregoing, a fracture criterion using the strain energy release rate  $\hat{G}$  of a critical finite crack extension  $\Delta a_0$  as a fracture toughness parameter is proposed, i.e.,

$$\hat{G}(\Delta a_0) = \frac{\Delta W_e}{\Delta a} - G_d(\Delta a_0) - \frac{\Delta U}{\Delta a} = \hat{G}_c(\Delta a_0) \quad (7)$$

where  $\Delta W_e$ ,  $\Delta U$  and  $G_d(\Delta a_0)$  are the external work done, strain energy change and the dissipation energy rate for a crack extension of  $\Delta a_0$ , respectively. From Eqn (5), it is seen that, for a fixed  $\Delta a_0$ , the finite extension strain energy release rate  $\hat{G}$  has a unique relation with the generalized stress intensity factor  $K_{II}$ . The fracture criterion given by Eqn (7) states that the interfacial crack would grow if the neartip stress field reaches a certain critical state.

Note that the simple relations below

$$\frac{dU}{da} = \frac{1}{2} \frac{dW_e}{da}, \quad G = \frac{dU}{da} \quad (8)$$

between strain energy release rate, strain energy and work done in linear elastic fracture mechanics are no longer valid in the presence of friction. Table 2 shows the result obtained from the finite element analysis for the center crack problem (Fig. 1) with  $\beta = 0.49$  and different coefficients of friction. It is evident that the above relations are no more valid in the presence of friction.

Table 2: Energy ratios for  $\beta = 0.49$  and different coefficients of friction  $\mu$

$\mu$	$\Delta U / \Delta W_e$	$(\Delta W_d + \hat{G}(\Delta a) \cdot \Delta a) / \Delta W_e$
0.02	0.4917	0.5084
0.2	0.4883	0.5117
0.5	0.4705	0.5295

### FIBER PULL-OUT AND FIBER PUSH-OUT

The mechanical properties of the fiber/matrix interface are important in determining the mechanical behavior of fibrous composites. The local response of the fiber-matrix interface during fracture has pronounced effects on the mechanical performance and structural integrity of the composite. Fiber pull-out as well as fiber push-out are the two major methods to determine the fiber/matrix interfacial properties as well as to understand the toughening effect of fiber composites due to frictional sliding after debonding.

There have been numerous theoretical models based on fracture mechanics to analyze the fiber-matrix interface toughness and toughening effect due to fiber sliding. In these studies, classical strain energy release rate was the key fracture parameter in determining the debonding initiation and debonding progression. However, most researchers did not account for the effect of the weak interfacial stress singularity due to friction. Some researchers used approximate interfacial shear stress distributions to calculate the “strain energy release rate” assuming  $G = dU / da$  (e.g. [4,6]). Consequently, none of these models can accurately characterize the intrinsic interfacial toughness. In this section we investigate the debonding process in the fiber pull-out and fiber push-out problem using the new finite extension strain energy release rate  $\hat{G}(\Delta a)$ .

It is noted that fiber pull-out and fiber push-out models adopted here are axisymmetric. However, It can be shown that the neartip stress field ahead of the crack tip and the characteristic equation for determining the singularity  $\lambda$  are exactly same as the plane strain problem. These features were noticed by Atkinson [11] who compared the elastic equilibrium equations for both axisymmetric and plane strain conditions near the crack tip. Therefore, the result of 2D plane problem is valid for fiber pull-out and push-out problem.

An axisymmetric section of the fiber-matrix-composite specimen shown in Fig. 2 is used for the present study. The fiber, matrix and the composite regions are assumed to be isotropic. The elastic moduli of the composite region are obtained using the rule of mixtures with fiber volume fraction of 35%. The Young’s moduli for the fiber and matrix are 100 units and 1 unit, respectively, and the Poisson’s ratios are assumed to be 0.3 for both. The characteristic crack extension length  $\Delta a_0$  is taken to be 0.01 throughout the debonding process. Two types of loading are used for various debonding lengths; one is constant load for both fiber pull-out and push-out, the other is constant displacement loading for fiber push-out only.

An open debonding crack tip is associated with the fiber pull-out under constant load  $\sigma$  (see Fig. 6). The total strain energy release rate increases at initial debonding stage and become steady state after debonding length reaches two times the fiber diameter. For the open crack,

the critical strain energy release rate  $G_c$  with a mode mixity must be determined.

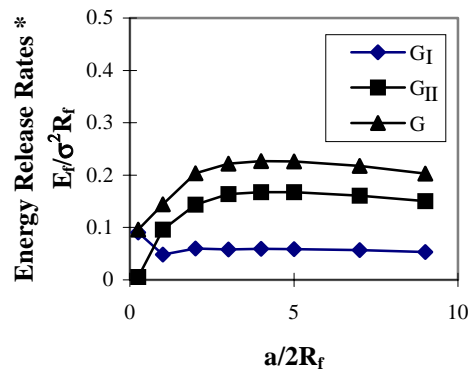


Fig. 6: Finite extension energy release rates for fiber pull-out under constant load  $\sigma$

During fiber push-out under constant load  $\sigma$ , the debonding crack surface is completely closed and the frictional effect is significant. Figure 7 shows the finite extension strain energy release rate, dissipation energy rate and total energy rate for various debonding lengths. It is seen that  $\hat{G}$  and  $G_d$  increase until debonding reaches two times the fiber diameter. There is a slight decrease for both energy rate afterwards. Figure 8 gives the ratios of strain energy change in the elastic body and total external work done during crack release for two different coefficient of friction  $\mu$ . It is seen that those ratios are no longer 0.5 as these in the frictionless case, especially at initial and final debonding stages. However, Eqn (8) may still be a good approximate when  $\mu$  is very small.

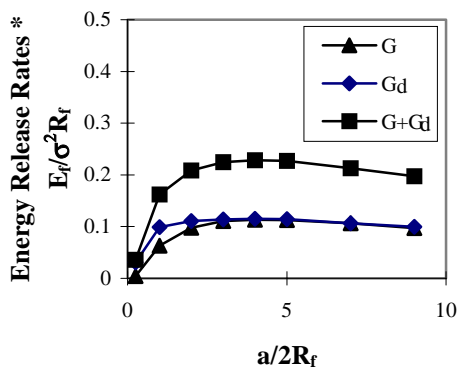


Fig. 7: Finite extension energy release rates for fiber change and push-out under constant load  $\sigma$

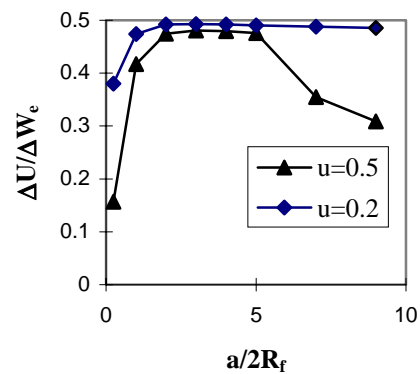


Fig. 8: Ratio of strain energy external work done during crack growth in fiber push-out for  $\mu = 0.5$  and  $0.2$ .

Results for fiber push-out under constant displacement loading  $u_0 = 0.2$  are shown in Fig. 9 and Fig. 10 for two coefficient of friction. It can be easily seen that the initial crack growth is unstable. Stable crack growth prevails after debonding reaches two times the fiber diameter. Besides, It is seen that there are virtually no change in total energy rate  $\hat{G} + G_d$  and external applied force for different friction coefficient. However, value of  $\hat{G}$  for  $\mu = 0.5$  is much smaller than that for  $\mu = 0.2$ . This indicates that a larger applied force is needed for larger

coefficients of friction to raise  $\hat{G}$  to the level of the critical intrinsic fracture toughness  $\hat{G}_c$ .

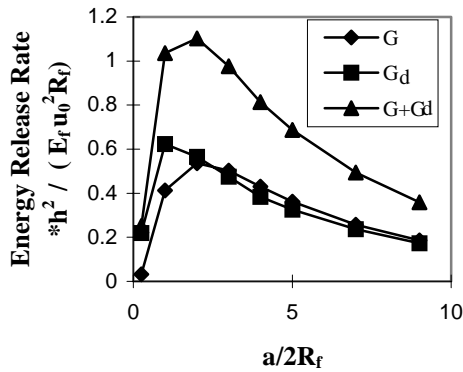


Fig. 9: Finite extension energy release rates for fiber push-out under constant displacement  $u_0 = 0.2$  with  $\mu = 0.5$ .

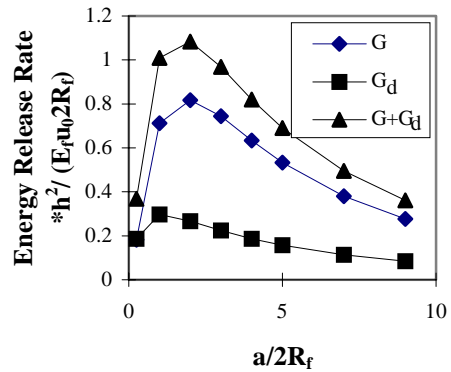


Fig. 10: Finite extension energy release rates for fiber push-out under constant displacement  $u_0 = 0.2$  with  $\mu = 0.2$ .

### EFFECT OF COMPRESSIVE LOADING

An open crack may be forced to close if compressive loads normal to the crack surfaces are applied in addition to the shear load. This condition may exist in fiber composite due to the mismatch of coefficients of thermal expansion between the fiber and matrix. For such a closed interfacial crack, the near tip stress field has a stronger singularity, i.e.,  $\lambda > 0.5$  [12], and the classical strain energy release rate becomes unbounded. Consequently, the intrinsic interfacial fracture toughness must be measured in terms of the finite extension strain energy release rate for a critical distance  $a_0$ . However, the toughnesses of the two closed cracks with stronger and weaker singularities, respectively, should not be interchanged.

### CONCLUSIONS

The presence of friction on interfacial cracks lying between two dissimilar media may cause the crack surfaces to close and crack tip stress singularity to become less singular than the inverse square root singularity. Depending on the loading direction, the contact size may be extremely small or finite. For the case of small contact zones, the crack tip can be treated effectively as an open crack and the fracture criterion in terms of total strain energy release rate and mode mixity can be employed. For the case of finite contact zones, the classical strain energy release rate vanishes and thus cannot be used as a fracture parameter as in linear fracture mechanics. A strain energy release rate based on a finite crack extension is shown to be uniquely related to the near tip stress field and is capable of capturing the intrinsic fracture toughness of the interfacial crack.

### ACKNOWLEDGMENT

This work was supported by Office of Naval Research grant No. N00014-90-J-1666 to Purdue University. Dr. Y.D.S. Rajapakse was the grant monitor.

## REFERENCES

1. Sun, C.T. and Qian, W., "The Use of Finite Extension Strain Energy Release Rates for Fracture in Interface Cracks," to appear in *International Journal of Solids and Structures*.
2. Comninou, M., "Interface Crack with Friction in the Contact Zone," *Journal of Applied Mechanics*, Vol. 44, 1977, pp. 780-781.
3. Deng, X., "An Asymptotic Analysis of Stationary and Moving Cracks with Frictional Contact along Bimaterial Interfaces and in Homogeneous Solids," *International Journal of Solids and Structures*, Vol. 31, No. 17, 1994, pp. 2407-2429.
4. Gao, Y. C, Mai, Y.W. and Cotterell, B., "Fracture of Fiber Reinforced Materials", *Journal of Applied Mathematics and Physics. (ZAMP)*, Vol. 39, 1988, pp. 550-572.
5. Sigl, L.S. and Evans, A.G., "Effects of Residual Stress and Frictional Sliding on Cracking and Pullout in Brittle Matrix Composites," *Mechanics of Materials*, Vol. 8, 1989, pp.1-12.
6. Kerans, R.J. and Parthasarathy, T.A., "Theoretical Analysis of the Fiber Pullout and Pushout Tests," *Journal of the American Ceramics Society*, Vol. 74, 1991, pp. 1585-1596.
7. Hutchinson, J.W. and Jensen, H.M., "Models of Fiber Debonding and Pullout in Brittle Composites with Friction," *Mechanics of Materials*, Vol. 9, 1990, pp. 139-163.
8. Stringfellow, R.G. and Freund, L.B., "The Effect of Interfacial Friction on the Buckle-Driven Spontaneous Delamination of a Compressed Thin Film, ," *International Journal of Solids and Structures*, Vol. 30, No. 10, 1993, pp. 1379-1395.
9. Buchholz, F.G., Wang, H., Ding, S. and Rikards, R., "Delamination Analysis For Cross-Ply Laminates under Bending with Consideration of Crack Face Contact and Friction," *Proceedings of the 10th International Conference on Composite Materials (ICCM-10)*, Vol. 1, Whistler, BC, Canada, August 14-18, 1995, pp. 141-148.
10. Comninou, M. and Dundurs, J., "Effect of Friction on the Interface Crack Loaded in Shear," *Journal of Elasticity*, Vol. 10, No. 2, 1980, pp. 203-212.
11. Atkinson, C., Avila, J., Betz, E. and Smelser, R.E., "The Rod Pull Out Problem, Theory and Experiment," *Journal of Mechanical and Physical Solids*, Vol. 30, No. 3, 1982, pp. 97-120.
12. Qian, W. and Sun, C.T., "Frictional Interfacial Fracture under Combined Compressive and Shear Loading," to be published.

# AN EFFECTIVE METHOD FOR MODELING THE TENSION FRACTURE OF COMPOSITE STRUCTURES

Khanh Trinh<sup>1</sup>, Fu-Kuo Chang<sup>2</sup>

<sup>1</sup>*Structural & Thermalmechanical Modeling Department, Sandia National Laboratories  
PO Box 969, Livermore, California 94551, USA*

<sup>2</sup>*Department of Aeronautics and Astronautics, Stanford University  
Stanford, California 94305-4035, USA*

**SUMMARY:** A modeling method that uses finite element analyses together with a progressive damage model was developed to predict the fracture strength of composite shells with cut-outs subjected to in-plane tensile loads. The use of a progressive damage model for composites involves degrading elastic stiffnesses when material failures are detected. This material degradation can cause severe non-convergence difficulties in the solution process of the finite element analyses. This problem can prematurely terminate the finite element analyses and prevent accurate fracture strength predictions, especially for larger panels. In the developed modeling method, artificial viscosity was added to an existing material damage model to overcome the convergence problems. Fracture strength predictions using this modeling method compared well with experimental data for both small and large notched panels. Furthermore, the developed method was able to overcome convergence problems using the quasi-static solution procedure. This characteristic makes the developed modeling method much more computationally effective than modeling methods that require dynamic solution procedures, which are often used to partially treat the non-convergence problems.

**KEYWORDS:** damage tolerance, composite progressive failure, finite element modeling, artificial viscosity.

## INTRODUCTION

Predicting notch strengths of composite laminates with cut-outs is an important and difficult modeling problem that has been studied extensively. This type of modeling is required to study the damage tolerance of composite structures such as airplane fuselages and other composite pressure vessels. Numerous analytical techniques ranging from semi-empirical fracture models to comprehensive numerical methods have been proposed [1]. Most existing modeling methods work well for small coupons, but are not effective for larger panels [2]. Large panels here indicate panels that are wider than ten inches. Comprehensive numerical methods are required to study the damage tolerance of structures with multiple failure modes. For example, there are three failure modes in a damage tolerance study of an airplane fuselage: skin fracture, stiffener failures, and skin/stiffener joint failures.

In this study, a modeling method that uses finite element analyses together with a progressive failure model was developed to simulate failures of large composite panels with cut-outs. Figure 1 shows the type of geometry and loads to be studied using this modeling method. In

this paper, notch strength predictions for flat notched panels under uniaxial tension are presented. The materials under consideration here are continuous fiber reinforced composite systems such as graphite/epoxy.

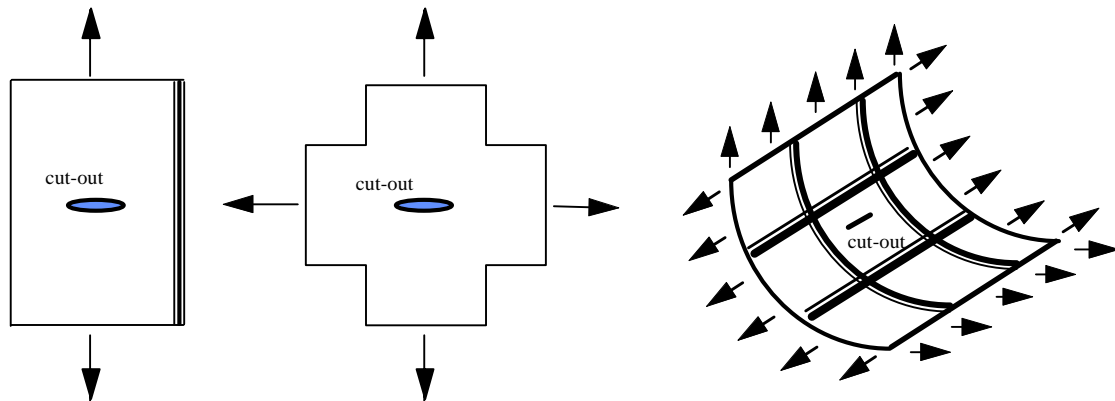


Figure 1: Geometry and loads to be studied

Modeling failures in composites is difficult for at least two reasons. First, the failure mechanism is complex. It involves many failure modes including fiber breakage, matrix cracking, and shear failures. These different failure modes cause different types of material degradation. In addition, these failure modes interact. To accurately predict notch strengths, the material model must capture the relevant and important failure modes and the corresponding material degradations. Second, the finite element analyses must overcome numerical problems caused by the material degradations. This material nonlinearity in composites is severe because the fibers, the main load carrying constituent, fail in a brittle manner. The brittle fiber failure introduces a singularity in the constitutive relations. This singularity can cause serious convergence problems in the nonlinear solution process of the finite element analyses. Furthermore, brittle failure is a form of strain softening, which may cause the results to be mesh sensitive [3].

The first problem, the failure mechanism, has been extensively studied and many composite progressive failure models have been proposed. In this study, a composite failure model recently developed by Shahid and Chang [4] was adopted. The focus of this study was on the second problem, for which there is very little reported work. The goal was to overcome numerical problems caused by the brittle fiber failure, so that accurate notch strength predictions could be made.

Although not studied extensively, the non-convergence problem is important to the notch strength modeling problem, especially for large panels. In small coupons, accumulated damage including fiber failure is normally confined to a small area at the notch before final failure occurs. However, for large panels, experiments have shown that damage can accumulate to a substantially larger area before final failure occurs [5]. The extensive damage could significantly reduce material properties in this area which could potentially cause the convergence problems. In the small coupon analyses, even if numerical problems prematurely terminated analyses, notch strength predictions based on maximum analysis loads can often be made without great loss of accuracy. This practice will often underpredict notch strengths of larger panels. For larger panels, numerical problems due to brittle fiber failures must be overcome to obtain accurate notch strength predictions.



## NUMERICAL PROBLEMS

The numerical problems that prematurely terminated the finite element analyses include the non-convergence problem in the Newton-Raphson nonlinear solution scheme in most cases and floating point problems in a few other cases. Floating point problems can be cured by simply degrading stiffnesses to small, but non-zero numbers. However, the non-convergence problem is not trivial. A non-convergence problem is the condition where the solver can not find an equilibrium solution after several Newton-Raphson iterations inside a load increment, even after the load increment had been cut back several times. Note that Arc-length methods are not solutions to these problems. All analyses in this study were displacement controlled, and the displacement boundary condition was defined a-priori to increase monotonically.

The brittle material degradation caused by fiber failures in composite is the main cause of the convergence problem. Figure 2 shows this troublesome characteristic in the on-axis stress and strain behavior of a unidirectional ply subjected to a uniaxial tension load. This abrupt and total stiffness degradation is a singularity in the constitutive relations. The brittle degradation often causes two conditions that can lead to the non-convergence problem: shocks in the displacement field, and an ill-conditioned consistent tangent stiffness.

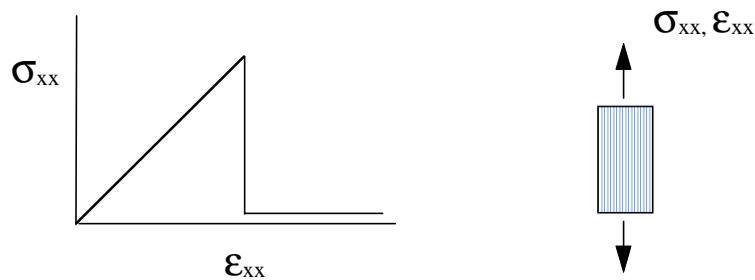


*Figure 2: Abrupt stiffness degradation caused by fiber failure*

A displacement field shock is a large and sudden jump in the structure deformation. This occurs when the loaded composite laminate adjusts itself to the directional stiffness loss. This directional stiffness loss is unique to brittle failures in laminate composites. For a “strain driven” finite element analysis, large deformation moves the solution (equilibrium displacement field) far away from the current displacement field, making it difficult for the nonlinear solution scheme to converge.

The consistent tangent stiffness is the coefficient matrix in the linear matrix equation used to advance the solution in the nonlinear solution scheme [6]. When this matrix becomes ill-conditioned, the solution scheme has more difficulty converging.

In the developed modeling method, an existing composite progressive damage model was adopted to model the failure response of composite structures, and artificial viscosity was added to this damage model to overcome the convergence problem. The following sections describe the modeling method, a brief description of the composite failure model, and the artificial viscosity material model. Notch strength comparisons between experimental data and model predictions are presented, together with the effects of the artificial viscosity on fracture strength predictions.

## MODELING METHOD

The commercial finite element code ABAQUS/Standard [7], together with a user defined material model was used to predict notch strengths of notched composite panels. ABAQUS reduced integration layered shell elements S4R and S8R were used. The loads were uniaxial tension and were perpendicular to the cut-outs (first problem in figure 1). The load was applied quasi-statically by fixing the panel's bottom side and prescribing a displacement boundary condition to the top side (displacement control analyses). The full Newton-Raphson method (not modified Newton) was used in the nonlinear solution process. Finite deformation theory was used since large deformations were anticipated at the notch.

The quasi-static solution procedure makes this modeling method very effective computationally compares to modeling methods that require dynamic solution procedures. Although, the notch strength problem is a static problem, dynamic solution procedures are often used because it can partially improve the convergence characteristic of the analyses.

The composite progressive failure model used in this study was based on a model recently developed by Shahid and Chang [4], which describes the failure criteria, and degradation rules. This material model is a nonlinear elastic model (elastic with damage). Four failure modes are considered: fiber breakage, fiber compression failure, matrix cracking and shear failure. Modified Hashin's failure criteria were used to predict the failure modes [8]. Failures and damages are tracked in each ply, and ply stiffnesses are reduced based on the cumulative damage state of the ply. The constitutive relations are as follows:

$$\begin{bmatrix} \sigma_{xx} \\ \sigma_{yy} \\ \sigma_{xy} \end{bmatrix} = \begin{bmatrix} Q_{xx}(d) & Q_{xy}(d) & 0 \\ Q_{yx}(d) & Q_{yy}(d) & 0 \\ 0 & 0 & Q_{ss}(d) \end{bmatrix} \begin{bmatrix} \epsilon_{xx} \\ \epsilon_{yy} \\ \gamma_{xy} \end{bmatrix} \quad (1)$$

where  $d$  is the material damage state, and  $Q_{ij}$  are stiffnesses.

The important degradation characteristic is that stiffness degradations are gradual and small for matrix cracking and shear failure modes, and the degradation is abrupt and total for the fiber failure modes (see figure 2). The degradations due to matrix cracking and shear failures cause no convergence problem in the analyses. However, the brittle degradation due to fiber failure can cause severe convergence problem.

To overcome the convergence problem caused by the fiber failure mode, artificial viscosity was added to the material model. The added artificial viscosity acts as a shock absorber and damps out displacement jumps and discontinuities in the stress and strain fields. The viscosity term also adds viscous stiffness to the material, which helps to keep the consistent tangent matrix from becoming ill-conditioned. The added viscosity will also help to reduce the mesh sensitivity problem [3].

The constitutive relations of the progressive damage model with the added artificial viscosity is as follow:

$$\begin{bmatrix} \sigma_{xx} \\ \sigma_{yy} \\ \sigma_{xy} \end{bmatrix} = \begin{bmatrix} Q_{xx}(d) & Q_{xy}(d) & 0 \\ Q_{yx}(d) & Q_{yy}(d) & 0 \\ 0 & 0 & Q_{ss}(d) \end{bmatrix} \begin{bmatrix} \epsilon_{xx} \\ \epsilon_{yy} \\ \gamma_{xy} \end{bmatrix} + \begin{bmatrix} b(d)E_{xx}\dot{\epsilon}_{xx} \\ b(d)E_{yy}\dot{\epsilon}_{yy} \\ b(d)G_{xy}\dot{\gamma}_{xy} \end{bmatrix} \quad (2)$$

$$\begin{aligned}
 b(d) &= 0 & t_f > t > (t_f+t_0) \\
 b(d) &= b_0[1-\frac{(t-t_f)}{t_0}] & t_f < t < (t_f+t_0)
 \end{aligned}
 \tag{3}$$

where  $\dot{\epsilon}_j$  are the strain rates,  $b_0$  is the artificial viscosity parameter,  $t_f$  is the fiber failure time, and  $t_0$  is the viscosity ramp down period.  $b_0$  and  $t_0$  are parameters required for the viscous model. However, a constant  $t_0$  was used in this study so that the viscous model is essentially a simple one parameter model. Since the artificial viscosity may add undesirable effects to the analysis result, this viscosity should be added only when it is needed. In the current model, the artificial viscosity is added after the fiber failure mode is detected. The viscosity is also removed slowly over a predetermined period after this fiber failure occurs.

For quasi-static analyses, time in the strain rate equation is directly related to the “load” progression in the analysis. For example, if the total displacement boundary condition is applied at time 1.0, then half of this displacement boundary condition is applied at time 0.5. Figure 3 shows the effect of the artificial viscosity to the material degradation of a unidirectional ply subjected to uniaxial load.

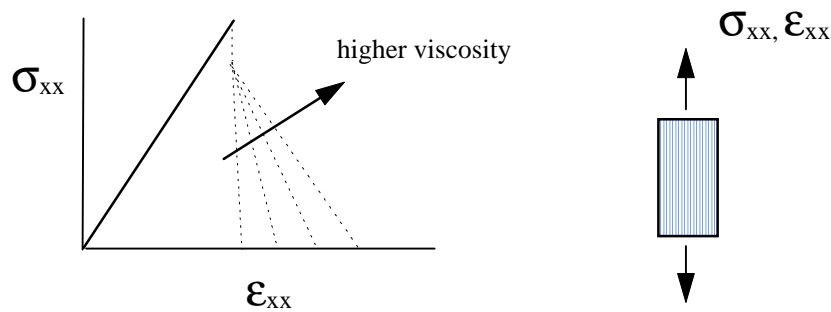


Figure 3: Effects of artificial viscosity on the fiber failure mode

The artificial viscosity can change the results of an analysis; too much viscosity will increase a structure’s stiffness, and erroneously increase the notch strength prediction. Thus, it is important to use enough viscosity to overcome convergence problem, but not too much. For this modeling method to work, the problem must have a “proper range” of artificial viscosity. When using an artificial value in the proper range, assuming it exists, the artificial viscosity will be enough to overcome convergence problems, and will not cause error to the strength prediction. Figure 4 shows the idea of the “proper viscosity range” in an ideal problem.

The proper range of artificial viscosity is problem dependent, since the susceptibility of an analysis to convergence problems and the notch strength prediction depends on the loading, the geometry, the material, the discretizations, and the solution path. This means there is no a priori knowledge of the proper amount of viscosity, and analysis iterations may be required to obtain a valid notch strength prediction. Limiting the viscous model to one parameter ( $b_0$ ) will simplify any required parametric studies.

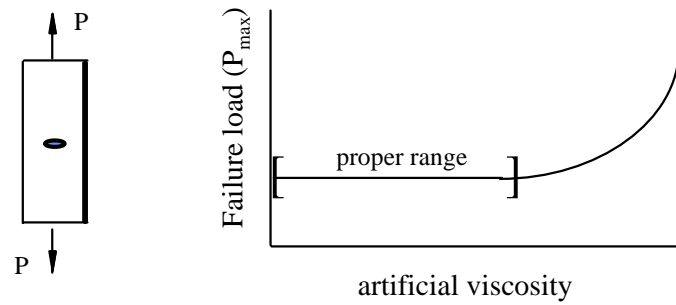
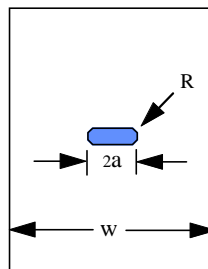


Figure 4: Proper range of artificial viscosity in an ideal problem

### MODEL VERIFICATION

Finite element analyses were performed to validate the developed modeling method for 11 test cases where notch strength experimental data was available. These test cases included 7 small coupons and 4 large panels. The small coupon test data was obtained from Sandia National Laboratories [9]. The large panel test data was obtained from the Boeing Company [5]. The load in all test cases was uniaxial tension. Table 1 shows the geometry, material, and lay-up for the test cases.

Table 1. Geometry, material and lay-up of test cases.



Case	w (mm)	a (mm)	R (mm)	Material	Lay-up
70B	38.1	6.35	6.35	T800/3900-2	$[(45/90/-45/0)_2]_s$
54B	38.1	6.35	6.35	T800/3900-2	$[-45/0/45/90_2/-45/90_2/45/0]_s$
76B	38.1	6.35	6.35	T800/3900-2	$[45/90/-45/0/\pm 45/90/\pm 45/0/\pm 45]_s$
70C	38.1	6.35	1.59	T800/3900-2	$[(45/90/-45/0)_2]_s$
70E	25.4	9.5	1.59	T800/3900-2	$[(45/90/-45/0)_2]_s$
54E	25.4	9.5	1.59	T800/3900-2	$[-45/0/45/90_2/-45/90_2/45/0]_s$
76E	25.4	9.5	1.59	T800/3900-2	$[45/90/-45/0/\pm 45/90/\pm 45/0/\pm 45]_s$
P8	914.	102..	0.89	AS4/938	$[\pm 45/90/0/\pm 60/90]_s$
P9	914	114.	0.89	AS4/938	$[\pm 45/0/90/\pm 30/0]_s$
P12	1524.	152.	0.89	AS4/938	$[\pm 45/0/90/\pm 30/0]_s$
P12 B	1524.	152.	0.89	AS4/938	$[\pm 45/90/0/\pm 60/15/90/\pm 60/0/90/\pm 45]$

For comparison, the same analyses were performed using the progressive damage model without the added artificial viscosity. Material properties and parameters required for the composite progressive damage model can be found in reference 4.

Table 2 summarizes notch strength results. These results show that analyses with and without artificial viscosity predicted the notch strength of small coupons well. Analyses without the viscosity severely underpredicted the notch strength of the large panels. Notch strength prediction for large panels using analyses with the viscosity compared well with experimental data.

*Table 2: Failure load comparison*

Test	Experimental data (N)	Model with viscosity (N)	Model w/o viscosity (N)
70B	45,400	47,200	47,200
54B	31,200	45,000	45,000
76B	50,300	57,000	57,000
70C	44,100	47,200	46,700
70E	16,900	21,500	21,400
54E	13,800	16,500	15,600
76E	25,800	27,100	25,400
P8	347,000	356,000	191,000
P9	316,000	312,000	169,000
P12	601,000	650,000	312,000
P12B	668,000	601,000	245,000

Table 3 shows the effects of artificial viscosity on failure load predictions for seven of the cases shown above. These results show that a low level of viscosity was required to overcome the non-convergence problem, and that failure load predictions were not very sensitive to the viscosity level.

*Table 3: Effects of artificial viscosity on failure load prediction*

Case	analysis 1		analysis 2		analysis 3	
	$b_0$	Failure load (N)	$b_0$	Failure load (N)	$b_0$	Failure load (N)
70B	1.E-5	47,200	1.E-4	47,200	1.E-3	50,700
54B	1.E-6	45,000	1.E-5	45,000	1.E-4	45,000
70C	1.E-5	47,200	1.E-4	48,000	1.E-3	51,200
70E	1.E-6	21,500	1.E-5	21,500	1.E-4	21,500
76E	1.E-6	27,100	1.E-5	27,100	1.E-4	32,000
P8	1.E-4	356,000	1.E-3	356,000	3.E-3	401,000
P9	1.E-4	312,000	1.E-3	334,000	3.E-3	343,000

## CONCLUSION

It has been demonstrated that artificial viscosity can be used to overcome non-convergence problems caused by brittle fiber failures when modeling composites. A simple artificial viscosity model along with a modeling method on using this viscous model to predict notch strengths of composites has been presented. Together with the progressive damage model developed by Shahid and Chang [4], the developed artificial viscosity modeling method was successfully used to predict the notch strength of both small and large composites panels subjected to uniaxial tension load. The artificial viscosity modeling method allowed accurate notch strength predictions for large panels, which could not be effectively done previously.

## ACKNOWLEDGEMENTS

This work was supported by the U.S. Department of Energy under Contract #DE-AC04-94AL85000.

## REFERENCES

1. J. Awerbuch, and M. S. Madhukar, "Notched Strength of Composite Laminates: Predictions and Experiments-- A review", *Journal of Reinforced Plastics and Composites*, Vol. 4, pp. 1-159, 1985.
2. L. B. Ilcewicz, et. al., "Tension Fracture of Laminates for Transport Fuselage Part 4: Damage Tolerance Analysis", *Fourth NASA/DoD Advanced Technology Conference*, NASA CP3229, pp. 254-298, 1993.
3. A. Needleman, "Material rate dependence and mesh sensitivity in localization problems", *Compu. Methods Appl. Mech. Eng.*, 67, 68-85, 1987.
4. I. Shahid, and F.K. Chang, "An Accumulative Damage Model for Tensile and Shear Failures of Laminated Composite Plates", *Journal of Composite Materials*, Vol. 29, pp. 926-981, 1995.
5. T.H. Walker, et. al., "Tension Fracture of Laminates for Transport Fuselage - Part 2: Large Notches", *Third NASA Advanced Technology Conference NASA CP 3178*, pp. 727-758, 1992.
6. T.J.R. Hughes, *Nonlinear Finite Element Methods*, Stanford University custom course materials, Stanford Bookstore, 1996.
7. ABAQUS is a commercial general purpose finite element code, Hibbit, Karlsson & Sorensen Inc., Pawtucket, Rhode Island, USA, 1994.
8. Z. Hashin, "Failure Criteria for Unidirectional Fiber Composites", *Journal of Applied Mechanics*, 47, pp. 329-334, 1980.
9. W. Lu, and K. Trinh, "An Experimental and Computational Study of Progressive Failure of Laminated Composites with Cut-outs", *10th International Conference on Composite Materials*, Whistler, British Columbia, Canada, August 14-18, 1995.

# EFFECT OF STRAIN RATE ON TENSILE FRACTURE BEHAVIOUR OF FIBRE REINFORCED POLYAMIDE COMPOSITES

M. Todo<sup>1</sup>, K. Takahashi<sup>1</sup>, Ph. Béguelin<sup>2</sup> and H.H. Kausch<sup>2</sup>

<sup>1</sup>Research Institute for Applied Mechanics, Kyushu University, Kasuga, Fukuoka 816, Japan

<sup>2</sup>Polymer Laboratory, Swiss Federal Institute of Technology, CH-1015 Lausanne, Switzerland

**SUMMARY:** Tensile testing of four different woven fabric polyamide composites was performed at various loading rates ranging from  $1 \times 10^{-3}$  to 3m/s using a servohydraulic testing apparatus. Two kinds of reinforcements, carbon fibre (CF) and glass fibre (GF), and two kinds of matrices, polyamide-6 (PA6) and modified polyamide-6 (mPA6), were the components of the four composites. The results showed that both tensile strength and failure strain of these composites tend to increase with increase of strain rate except for GF/mPA6 whose tensile strength and failure strain were stabilized at high rates ( $>1 \times 10^0$  1/s). Fracture regions of the tested specimens were also observed to study micromechanisms of tensile failure using a polarized optical microscope. The results showed that in the composites with mPA6 matrix, extensive microcracking occurred in the matrix regions prior to the final failure. Rate effects on the tensile fracture behaviour of the polyamide composites are discussed on the basis of these experimental results.

**KEYWORDS:** polyamide composites, tensile behaviour, strain rate dependence, high speed testing

## INTRODUCTION

Dynamic tensile testing of continuous fibre reinforced polymer composites has been performed to characterize the tensile mechanical behaviour of the composites [1-6]. Dynamic mechanical properties such as elastic modulus, tensile strength and failure strain were obtained in these studies by using specific high speed tensile testing systems such as a one bar method [1], split-Hopkinson pressure bar techniques [2-5] and a falling weight impact tester [6]. Dynamic testing results are sometimes compared with static data obtained by different tests to study rate effects on the mechanical properties. On the other hand, as one attempt to extend static test to a higher rate test, Béguelin and Kausch have developed a high speed testing system using a modified servohydraulic testing machine and an optical extensometer [7]. They have applied this system to study rate effects on the tensile mechanical behaviour of polymers in a wide range of loading rates.

In the above studies, most of the attention were paid to thermoset matrix composites. With increasing interests in thermoplastics as matrices for polymer composites, many works have been carried out to characterize the mechanical behaviour of thermoplastic matrix composites; however, few attempts have been made to study the dynamic tensile behaviour of the composites. In the present study, dynamic tensile testing of continuous fibre reinforced

polyamide composites was carried out by means of the high speed testing system developed by Béguelin and Kausch, and effects of strain rate on the tensile fracture properties were investigated. In this paper, the experimental results are presented, and the tensile failure mechanisms of this type of thermoplastic matrix composites are discussed.

## EXPERIMENTAL PROCEDURE

### Material and Specimen

Four different polyamide composites were studied in this work. Plain woven fibre cloth made of carbon fibre (CF) or E-glass fibre (GF) was used as the reinforcement in these composites. The matrix was polyamide-6 (PA6) or modified polyamide-6 (mPA6). It is known that mPA6 has higher stiffness and strength than PA6. The four composites are denoted hereafter by CF/PA6, CF/mPA6, GF/PA6 and GF/mPA6. Thin laminates of 1mm thickness containing six plies of reinforcements were fabricated for each material. The fibre volume fractions were 56% for CF/PA6 and CF/mPA6, 51% for GF/PA6 and 54 % for GF/mPA6. Tensile specimens were cut from the laminates, and the direction of the warp threads corresponded with the tensile loading direction. Specimen geometry is shown in Fig.1.

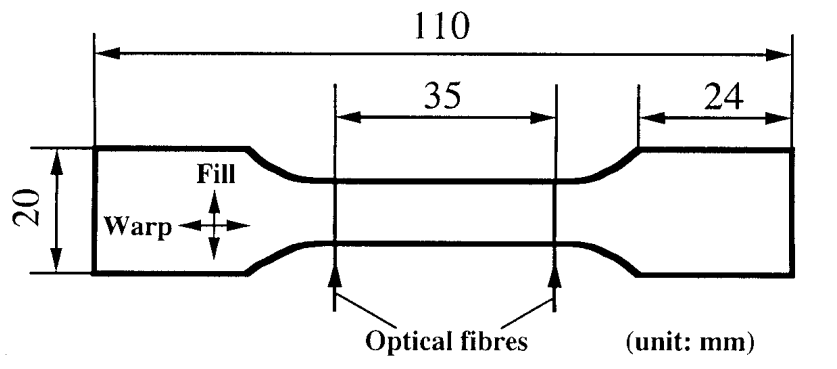


Fig.1: Tensile specimen geometry (the thickness of the specimen is 1mm).

### Testing Apparatus

Tensile testing of the four composites was carried out in a range of loading rate from  $1 \times 10^{-3}$  to 3 m/s using a servohydraulic testing machine. This apparatus has been modified so as to reduce dynamic effects at high rates of loading by using a viscoelastic damper in the loading unit [8]. A piezoelectric load cell was used for the measurement of load in high sensitivity. Strain was measured by means of an optical extensometer that was designed for the purpose of dynamic testing [8]. Two optical fibres were placed on specimen surface at an interval of 35 mm as shown in Fig.1, and the tensile deformation of the specimen was evaluated from the positions of two light points emitted through the optical fibres.

### Microscopic Observation

Polarized optical microscopy (POM) was carried out to investigate fracture micromechanisms of the composites. Longitudinal cross sectional area near failure region was examined by



POM. For each of the four composites, a thin sample (about 100  $\mu\text{m}$  thickness) was prepared from the failure region of a tested specimen by using cutting and polishing technique. The prepared samples were observed on a polarized optical microscope under transmitted and/or reflected light.

## RESULTS AND DISCUSSION

### Tensile Testing

Stress-strain relations of four different polyamide composites obtained at the lowest loading rate ( $1 \times 10^{-3}$  m/s) are shown in Fig.2. A knee phenomenon was observed for all four composites. It has been postulated that the nonlinearity in woven fabric composites is caused by micromechanical deformations such as shear deformation of the longitudinal threads, extensional deformation of the matrix regions and transverse cracking of the transverse threads [9,10]. It is clearly seen from Fig.2 that the nonlinear stress-strain behaviour after the knee

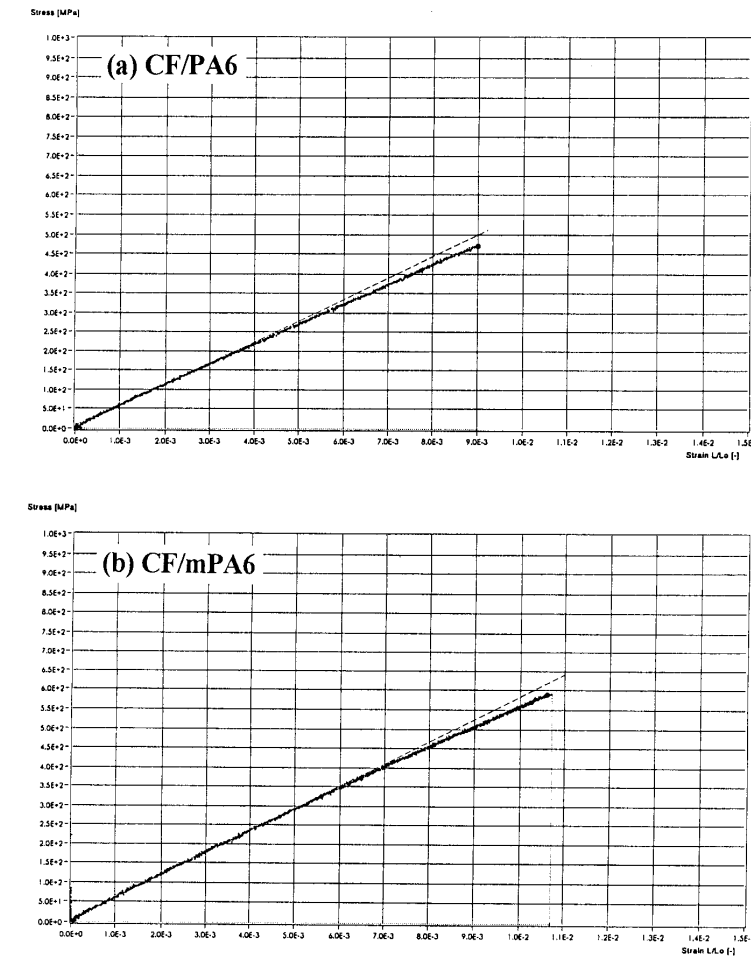


Fig.2: Stress-strain relations of four polyamide composites: (a) CF/PA6, (b) CF/mPA6, (c) GF/PA6 and (d) GF/mPA6.

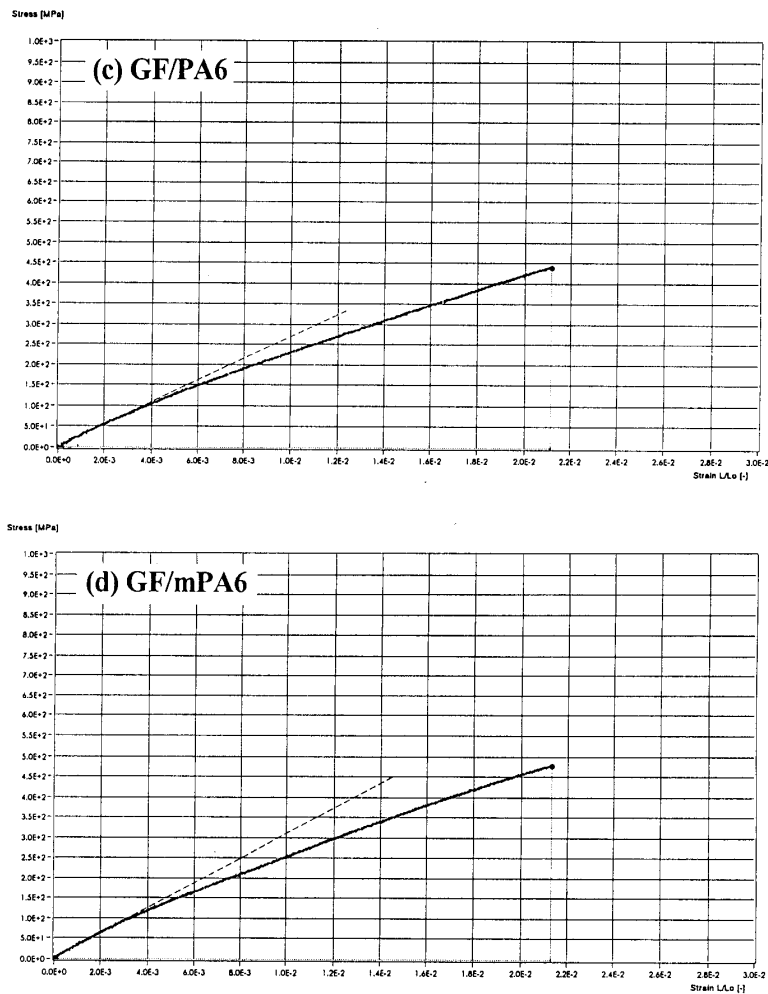


Fig.2 (continued)

point was much larger in the glass fibre composites than that in the carbon fibre composites. Dependence of the initial tensile modulus on strain rate is shown in Fig.3. The tensile moduli of CF/PA6, CF/mPA6 and GF/PA6 tended to slightly increase as strain rate increased, while the modulus of GF/mPA6 appeared to be insensitive to strain rate.

Dependence of the tensile strength on strain rate is shown in Fig.4. The tensile strength of the carbon fibre composites increased with increase of strain rate. CF/mPA6 exhibited the highest tensile strength of all four composites at all strain rates as a result of the combination of high strength carbon fibre and mPA6 matrix. Thus, the better tensile properties of mPA6 than PA6 was well transferred to this type of composite system. The tensile strength of GF/PA6 also increased with increase of strain rate. The increase was 54% at the highest rate ( $4 \times 10^1$  1/s), while that of CF/PA6 was 28%. It should be noted that the tensile strength of GF/PA6 at the highest rate was almost equivalent to that of CF/mPA6, which possessed the highest strength at all rates. On the other hand, the tensile strength of GF/mPA6 increased as strain rate increased up to  $1 \times 10^0$  1/s and then slightly decreased with increase of strain rate.

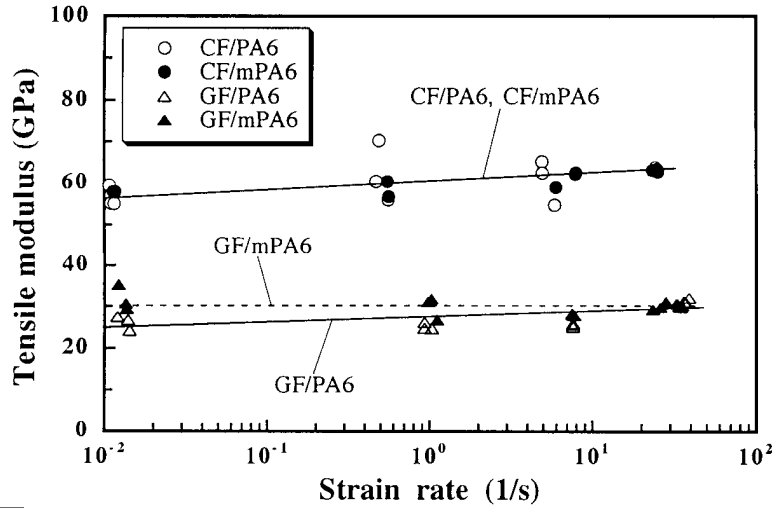


Fig.3: Dependence of the tensile modulus on strain rate for four polyamide composites.

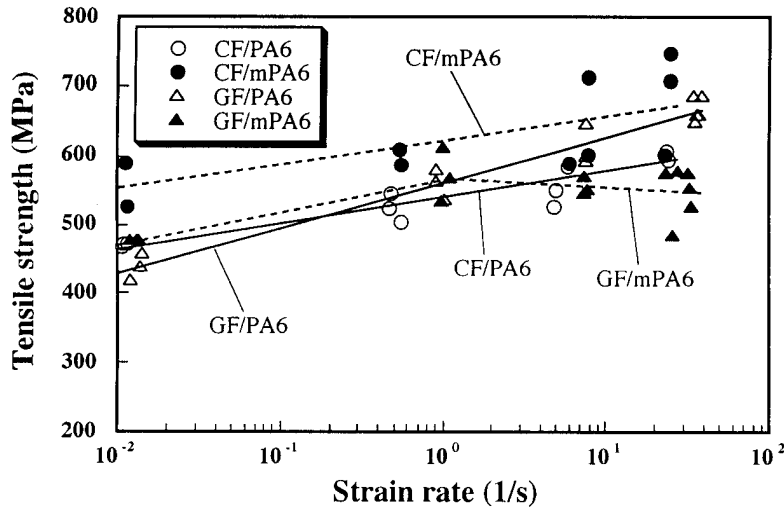


Fig.4: Dependence of the tensile strength on strain rate for four polyamide composites.

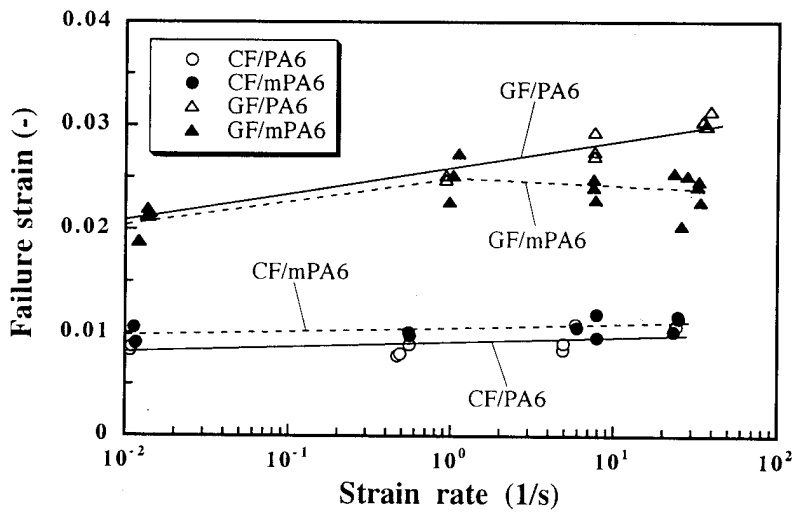


Fig.5: Dependence of the failure strain on strain rate for four polyamide composites.

As a result, the strength of GF/mPA6 was equivalent to that of CF/PA6 and higher than that of GF/PA6 at the lowest rate ( $1 \times 10^{-2}$  1/s) but the least of all four composites at the highest rate ( $3 \times 10^1$  1/s).

Dependence of the failure strain on strain rate is shown in Fig.5. The failure strain of the glass fibre composites was larger than that of the carbon fibre composites as expected because glass fibre generally shows larger elongation than carbon fibre. The failure strain of the carbon fibre composites slightly increased with increase of strain rate. The failure strain of GF/PA6, on the other hand, increased as strain rate increased, whereas the failure strain of GF/mPA6 increased up to  $1 \times 10^0$  1/s and then slightly decreased at higher rates. These strange odd rate dependencies on the tensile strength and the failure strain of GF/mPA6 appear to be related to the tensile failure mechanism of this composite discussed later.

Strain-rate dependence of the absorbed fracture energy is shown in Fig.6. The absorbed energy was directly estimated by numerical integration of the stress-strain curves. The absorbed energy for the glass fibre composites was higher than that of the carbon fibre composites at all strain rates tested, which is ascribed to the larger failure strain of the glass fibre composites as seen in Fig.5. Values of the absorbed energy for the carbon fibre composites and GF/PA6 tended to increase with increase of strain rate. However, the rate dependence for GF/mPA6 was very similar to those of the tensile strength (Fig.4) and the failure strain (Fig.5). Thus, it appears that the modified polyamide resin mPA6 fulfills its superior tensile performance as a matrix for carbon fibre composite at all strain rates tested. On the other hand, mPA6 loses its good function as a matrix for glass fibre composite under high strain rates ( $>1 \times 10^0$  1/s).

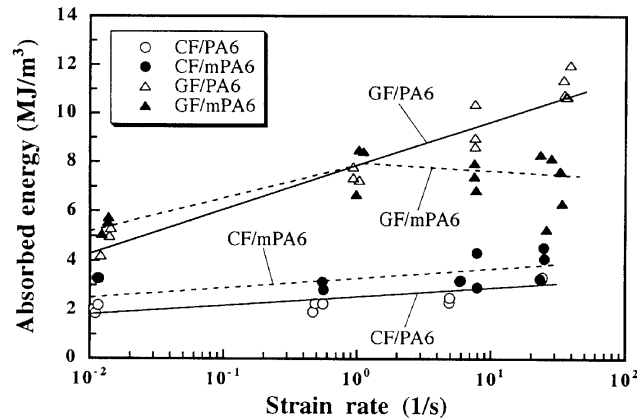
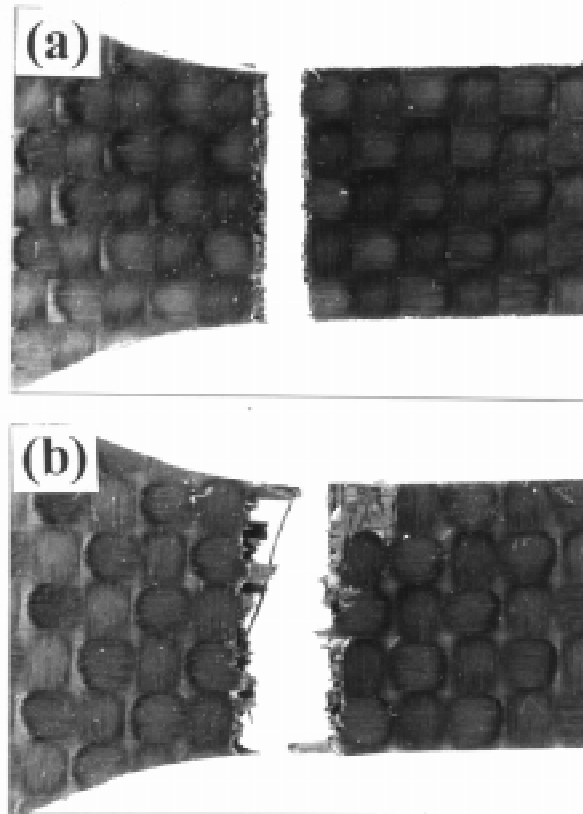


Fig.6: Dependence of the absorbed fracture energy on strain rate for four polyamide composites.

## Fracture Mechanism

Failure regions of the carbon fibre composites at the highest loading rate (3 m/s) are shown in Fig. 7. For CF/PA6, a relatively straight fracture line perpendicular to the tensile direction was observed, whereas pull-outs of fibre bundles were significant in CF/mPA6. This tendency was seen at all the testing rates. Failure regions of the glass fibre composites at the highest loading rate (3 m/s) observed under transmitted light are shown in Fig.8. Dark regions in these photographs are thought to correspond to the damages such as matrix cracking, debonding, interfacial failure and delamination. More extensive damage zone was clearly observed in



*Fig. 7:* Failure regions of carbon fibre polyamide composites at a high loading rate (3 m/s):  
(a) CF/PA6 and (b) CF/mPA6.

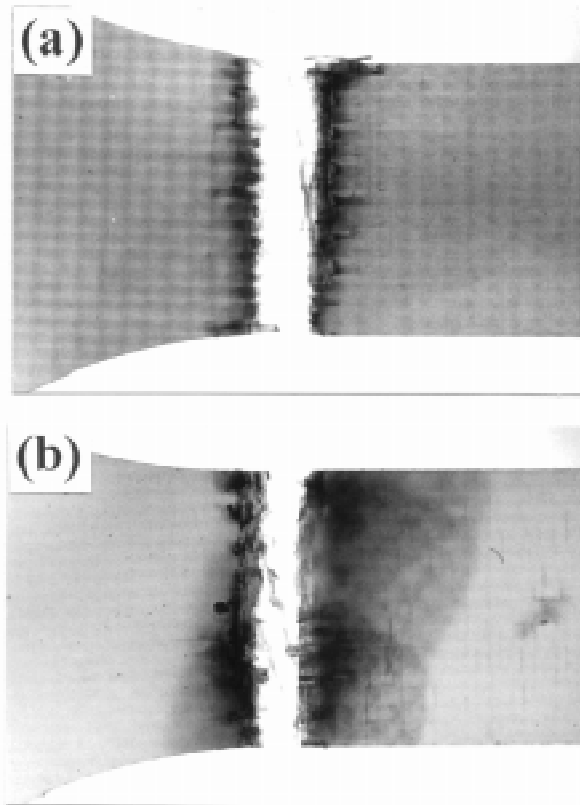


*Fig. 8:* Failure regions of glass fibre polyamide composites at a high loading rate (3 m/s):  
(a) GF/PA6 and (b) GF/mPA6.

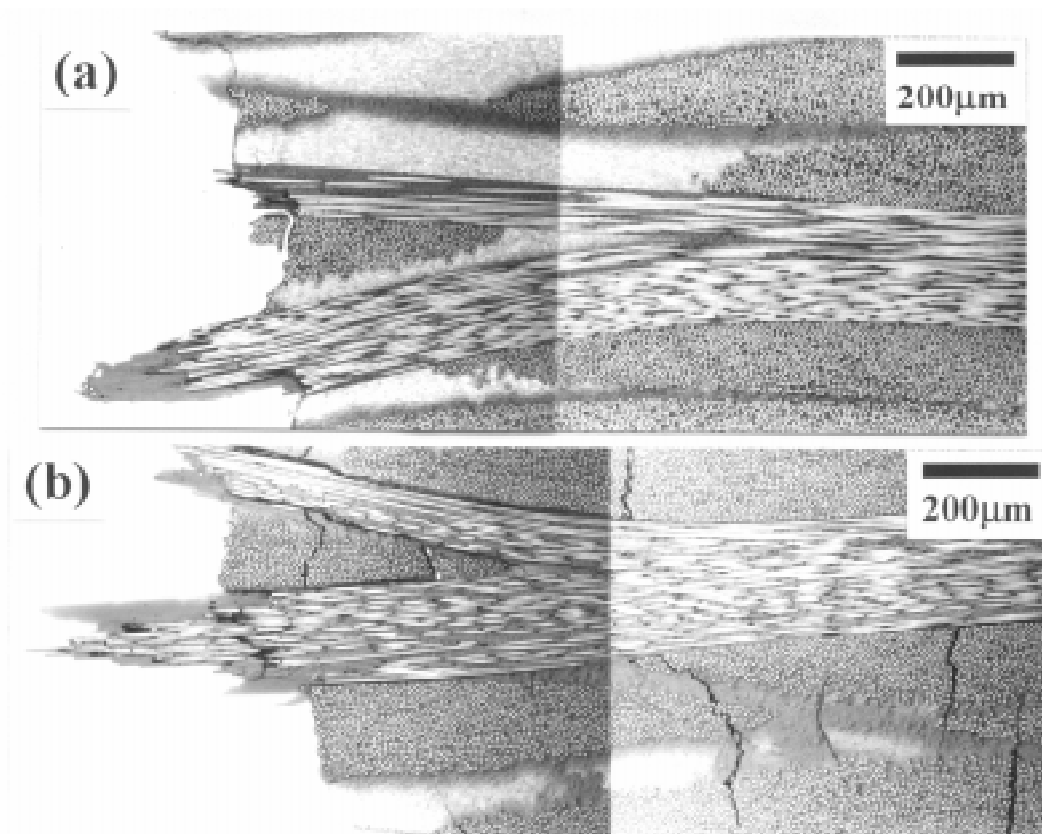


Fig.9: POM photographs of the failure regions for carbon fibre polyamide composites at a high loading rate (3 m/s): (a) CF/PA6 and (b) CF/mPA6.

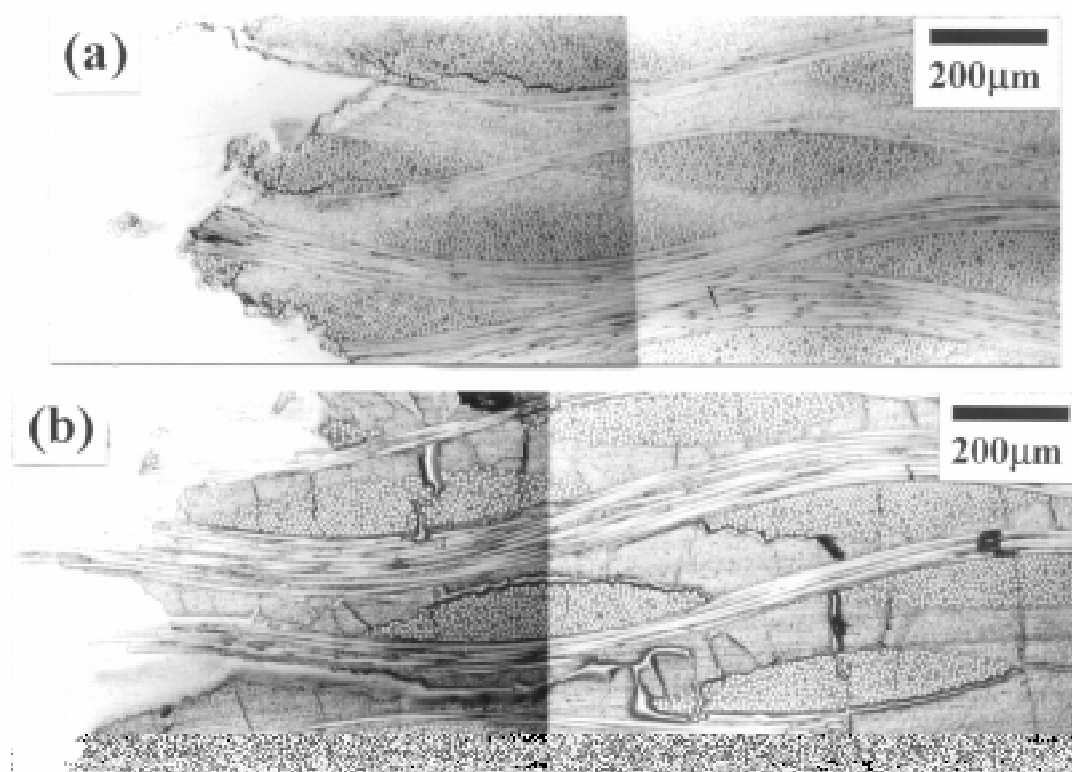


Fig.10: POM photographs of the failure regions for glass fibre polyamide composites at a high loading rate (3 m/s): (a) GF/PA6 and (b) GF/mPA6.

GF/mPA6 than that in GF/PA6. The damage development prior to the final tensile failure of GF/mPA6 was larger than that of GF/PA6 at all testing rates.

POM photographs of the failure regions of the carbon fibre composites at the highest loading rate (3 m/s) are shown in Fig.9. For CF/mPA6, microcracks were formed perpendicular to the tensile direction and they were observed in the matrix regions and the transverse threads. It is also seen that these cracks propagated toward the interface between the longitudinal threads and the transverse threads. As a result, interfacial debonding must be generated. On the other hand, such kinds of failure modes were not observed in CF/PA6. POM photographs of the failure regions of the glass fibre composites generated at the highest loading rate (3 m/s) are shown in Fig.10. For GF/mPA6, extensive microcracks were observed in both the matrix regions and the transverse threads. Interfacial debonding and delamination were also seen in GF/mPA6. For GF/PA6, only a few cracks were initiated at the fracture point. At all the loading rates, microdamage formation was observed in both the carbon and the glass fibre composites with mPA6 matrix. Thus, the modified polyamide composites tended to generate microcracking in the matrix regions and also in the transverse threads under tensile loading condition. This may be related to the brittleness of mPA6. As seen in Figs.4, 5 and 6, the tensile failure properties of the carbon fibre composites could be improved by using mPA6 as a matrix at any testing rates. It is therefore considered that the microdamages observed in CF/mPA6 (Fig.9 (b)) did not affect the tensile fracture properties. On the other hand, in the case of GF/mPA6 (Fig.10 (b)), extensive microcracking occurred prior to the final failure and it prevented the increase of the tensile strength under high strain rates ( $>1 \times 10^0$  1/s), although GF/mPA6 showed better tensile performance at low loading rates ( $<1 \times 10^0$  1/s).

## CONCLUSIONS

Tensile fracture properties of four different polyamide composites were studied at loading rates from  $1 \times 10^{-3}$  to 3 m/s using a high speed tensile testing apparatus. Carbon fibre composite with modified polyamide-6 matrix showed better tensile performance at all testing rates than carbon fibre composite with polyamide-6 matrix. Tensile mechanical properties such as tensile strength, failure strain and absorbed failure energy for both the carbon fibre composites tended to increase with increase of strain rate. Glass fibre composite with polyamide-6 matrix showed superior tensile performance especially at higher strain rates. The tensile mechanical properties of this composite dramatically increased as strain rate increased. On the other hand, the tensile mechanical properties of glass fibre composite with modified polyamide-6 matrix increased as strain rate increased up to  $1 \times 10^0$  1/s and then slightly decreased at higher strain rates ( $>1 \times 10^0$  1/s). As a result, the mechanical properties of the modified composite were higher than those of the unmodified composite at low rates ( $<1 \times 10^0$  1/s). However, the relation was reversed at higher rates ( $>1 \times 10^0$  1/s). Extensive microdamage formation observed in the modified composite was related to this kind of rate dependence.

## ACKNOWLEDGEMENTS

This work was supported by Grant-in-Aid for International Scientific Research (Joint Research No. 07044160) sponsored by Monbusho. The authors also wish to thank Nittobo Co. for providing the polyamide composites.

## REFERENCES

1. K.Kawata, S. Hashimoto and N. Takeda, In 'Proc. 4th Int. Conf. on Composite Materials', ICCM IV, Eds T. Hayashi et al., Tokyo, 1982, 829-836.
2. J. Harding and L.M. Welsh, *J. Mater. Sci.*, 18, 1983, 1810-1826.
3. C.A. Ross, W.H. Cook and L.L. Wilson, *Exp. Tech.*, 8, 1984, 30-33.
4. Z.G. Liu and C.Y. Chiem, *ibid*, 12, 1988, 20-21.
5. G.H. Staab and A. Gilat, *J. Comp. Mater.*, 29, 1995, 1308-1320.
6. S. Barre, T. Chotard and M.L. Benzeggagh, *Composites, Part A*, 27A, 1996, 1169-1181.
7. Ph. Béguelin, M. Barbezat and H.H. Kausch, *J. Phys. III France*, 1, 1991, 1867-1880.
8. Ph. Béguelin, PhD Thesis No1572, EPFL CH Lausanne, 1996.
9. T. Ishikawa and T.-W. Chou, *J. Mater. Sci.*, 17, 1982, 3211-3220.
10. T. Ishikawa and T.-W. Chou, *J. Comp. Mater.*, 17, 1983, 399-413.



# FIBRE ORIENTATION EFFECTS ON INTERLAMINAR FRACTURE TOUGHNESS OF MARINE COMPOSITES

P. Compston<sup>1</sup>, P.-Y. Jar<sup>1</sup> and P. Davies<sup>2</sup>

<sup>1</sup> *Department of Engineering, The Australian National University,  
Canberra, ACT 0220, Australia*

<sup>2</sup> *Marine Materials Laboratory, IFREMER,  
Centre de Brest BP 70 - 29280, Plouzané, France*

**SUMMARY:** This paper discusses the characterisation of the delamination resistance of marine composites, i.e. low fibre volume fraction woven glass fibre reinforced polyester and vinylester materials, manufactured by hand lay-up and resin transfer moulding (RTM). These materials are very different to the carbon fibre aerospace composites, for which fracture toughness testing standards are currently being developed, and there has been little study of their interlaminar fracture behaviour. Three aspects are considered in the paper: the stability of the matrix resins with time, the applicability of current mode I and mode II test standards, and the influence of fibre angle on measured toughness values. Composites with woven reinforcements and central plies at different fibre angles ( $0^\circ$ ,  $+/+30^\circ$ ,  $+/-30^\circ$ ) were employed to examine how fibre angle affects crack initiation and propagation.

**KEYWORDS:** delamination, woven glass fibres, fibre orientation, marine, thermoset, toughness,

## INTRODUCTION

The most vulnerable zone in fibre composites is the interlaminar resin-rich region where cracks often develop. The presence of such cracks can lead to a drastic reduction in structural integrity, and even catastrophic failure. Consequently, material scientists have long been searching for methods to characterise interlaminar fracture toughness of composites, both for material selection and in order to design damage tolerant structures. International collaboration from the late 1980's to early 1990's between ESIS (European Structural Integrity Society), ASTM (American Society for Testing and Materials) and JIS (Japanese Industrial Standards) groups has led to a joint proposal to ISO (International Standards Organisation) for a mode I test [1], and a joint round robin exercise under the auspices of VAMAS (Versailles Agreement for Materials and Standards) to compare

mode II test procedures [2]. Although these methods differ slightly in sample preparation and initial crack generation, they all recommend the test coupons to have unidirectional fibres along the coupon length. This is justified to some extent by published results which indicate that mode I initiation values in non-woven carbon fibre composites based on prepreg are lowest in the fibre direction [3-5]. The use of unidirectional specimens greatly simplifies the materials selection process by excluding fibre orientation as a factor in performance variation. However, this simplification may make the standard test results unsuitable for use in design, particularly outside the aerospace industry, because the composites used are then frequently based on woven glass fibres and initial defects may not be aligned in the fibre direction. It is therefore important to provide information that bridges the gap between the standard test results and the performance of non-aerospace composite structures.

The most common matrix resins for marine composites are thermosetting polyesters. Such materials are inexpensive and can be easily manufactured by hand lay-up, but they are not usually post-cured and their properties tend to evolve with time. Cross-linking is not complete when the composite leaves the boatyard and the glass transition temperature may increase over several months. This creates a problem for their characterisation. The simple solution is to post-cure the specimens before testing to stabilise them, but this results in materials whose behaviour is no longer representative of that to be expected in practice. Alternatively, great care must be taken to compare only materials which have been manufactured and tested at the same time. A second option is to use composites which are more stable after manufacture, such as vinyl esters. In the present work both materials have been tested. A second problem to be addressed is the scatter in properties due to the fabrication process, as there may be considerable variations in panel thickness and higher defect levels (porosity, incomplete impregnation) than would be found in aerospace composites.

Three sets of results will be presented here. First, the influence of the resin state on mode I and mode II properties will be illustrated, using results from tests on as-moulded and post-cured quasi-unidirectional glass reinforced polyester composites. Then results from mode I tests on polyester composites in which central fibres were oriented at angles up to  $45^{\circ}$  will be shown. These first two series are intended to indicate the problems associated with testing marine composites. Finally, mode I and mode II tests on vinyl ester composites produced by RTM will be described, to demonstrate the influence of fibre angle for materials which are both more stable with time and produced by a process aimed at reducing scatter in properties. It should be emphasised that the determination of the influence of fibre orientation is not trivial. Davidson et al. have recently discussed the problems inherent to tests on multi-directional laminates [6,7]. These include residual thermal stresses, large deflections (if real laminates are used rather than modified unidirectional laminates), and significant three dimensional effects. The latter may be due to either bending-stretching and bending-twisting of sub-laminates or finite width effects. These effects may invalidate the data analysis. It is believed that in the present case the adoption of a modified unidirectional laminate to examine orientation effects should minimise these effects, by maintaining a small value of critical bending rigidity ratio  $D_c$  ( $D_{12}^2/(D_{11}D_{22})$ ).

## MATERIALS AND EXPERIMENTAL METHODS

### Composite Laminates

The materials tested in this study were all reinforced with E glass fibres. Their compositions are shown in Table 1. Polypropylene (PP) insert film 8 microns thick was used to introduce a starting defect at mid-thickness.

Table 1: Composites tested

Test Series	Reinforcement	Matrix	Manuf./Mass Frac.
1 (mode I)	0/90° outer, UD 300 g/m <sup>2</sup>	Isophthalic polyester	Hand lay-up, 50%
1 (mode II)	800 g/m <sup>2</sup> , woven quasi-UD		
2	0/90° outer, UD 300 g/m <sup>2</sup>	Isophthalic polyester	Hand lay-up, 50%
3	12 plies 800 g/m <sup>2</sup> , woven quasi-UD	vinyl ester	RTM, 58%

### Test Coupons

Specimens 20 mm wide were cut from the laminates using a water-cooled diamond-embedded slitting wheel. The water on the specimens was soon wiped out after the cutting. The specimens were then left in a vacuum oven overnight to ensure that the residual water introduced by the cutting was completely removed from the specimens.

For mode I tests, double cantilever beam (DCB) specimens were tested, rectangular loading blocks were attached to the specimen end containing the starter film. The specimen was loaded in a crack opening mode through the blocks. For mode II tests, ENF (end notched flexure) specimens were loaded in a 3-point bend fixture with a span length of 120 mm and a starter defect length of 30 mm, measured from the tip of the defect to the closest support. Unless otherwise specified cracks were grown directly from the PP film insert.

### Delamination Tests and Data Analysis

Mode I delamination tests were conducted with a testing speed of 1 mm/minute. Crack length increment was measured on the side of specimen. The crack length was marked on the load-displacement curve for every 1 mm of crack growth in the first 5 mm and then for every 5 mm of stable crack growth. Two methods were used for calculation of  $G_{Ic}$ , as suggested in the ESIS protocol [8]. The first method was corrected beam theory (cbt) in which:

$$G_{Ic} = \frac{3P\delta}{2B(a - \Delta)} \quad (1)$$

where  $P$  is load,  $\delta$  is displacement,  $B$  is specimen width and  $a$  is the measured crack length from the edge of the specimens.  $\Delta$  is a correction factor that is obtained from the negative x-axis intercept on a plot of  $a$  versus  $C^{1/3}$  where  $C$  is the compliance, defined as  $\delta/P$ . The second method for  $G_{Ic}$  calculation was experimental compliance method (ecm) in which:

$$G_{Ic} = \frac{nP\delta}{2Ba} \quad (2)$$

where  $n$  is the slope of the log-log plot of compliance versus the measured crack length. Flexural modulus ( $E_f$ ) was determined using the following equation:

$$E_f = \frac{8(a - \Delta)^3}{CBh^3} \quad (3)$$

where  $h$  is thickness of one arm of the specimen, that is, half of the specimen thickness.

Mode II delamination tests were conducted at a cross head speed of 1 mm/min, and load-displacement curves were recorded for analysis. The equation used for calculation of  $G_{IIc}$  (critical strain energy release rate in mode II) was based on direct beam theory [9]:

$$G_{IIc} = \frac{9a^2P^2}{16EB^2h^3} \quad (4)$$

where the symbols have the same meaning as those used in equation (1) & (2). Shear corrections were also applied [9], as RTM specimens were quite thick. Corrections up to 6% were required for those tests.

## RESULTS AND DISCUSSION

### Influence of delay after fabrication

The effect of time between manufacture and testing on the state of the matrix in a polyester composite is complex, as internal stresses may relax, cross-links may develop and generally glass transition temperature ( $T_g$ ) will increase. In terms of composite properties an idea of the extent to which fracture properties can evolve is given by Fig. 1 for two polyester systems. For the first, the mode I toughness at crack initiation ( $G_{Ic-imit}$ , calculated from the non-linear point on the load-displacement plot, which indicates first damage) is seen to decrease from 300 to 220 J/m<sup>2</sup> between  $N$  months and  $N + 6$  months after fabrication. For the second, mode II toughness is seen to change over the period from 1 week to 10 weeks after fabrication,  $G_{IIc-imit}$  increasing but maximum load values (onset of unstable propagation),  $G_{IIc-max}$ , decreasing. These results underline the importance of knowing both the initial chemistry and the aging history of such composites.

### Influence of fibre angle, polyester composites

In a preliminary study [10] fracture tests were run on polyester composites with different starter film inserts to confirm that the minimum film thickness (less than 13 microns)

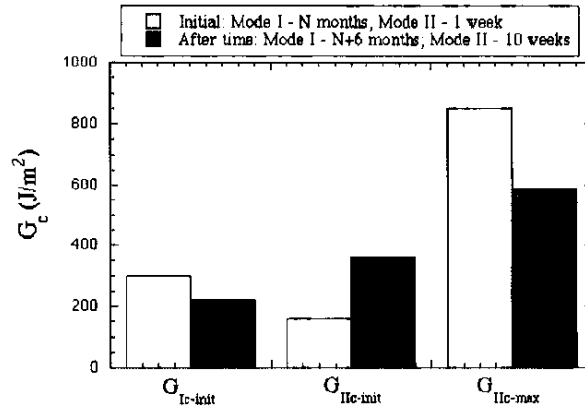


Figure 1: Evolution of fracture properties of polyester composites tested at different times after fabrication.

specified for aerospace materials [8] was appropriate for these materials. This proved to be the case, and a series of mode I tests was then performed on composites in which the majority of the plies were aligned along the specimen axis, and only the two central plies above and below the starter film were oriented. The results from this study are shown in Fig. 2. They are in contradiction with published results for aerospace composites, which suggest that the lower mode I values are obtained for unidirectional composites. That conclusion was also reached in some recent work on polyester composites [11]. Here the  $G_{Ic}$  initiation values decrease with angle. However, the term "polyester composites" en-globes a wide range of resin and fibre combinations with different behaviours, so care should be taken in comparing results. Fig. 2 also shows that scatter may be significant in these hand-made materials and in the final part of the paper results will be shown for materials made by RTM in an effort to reduce this scatter.

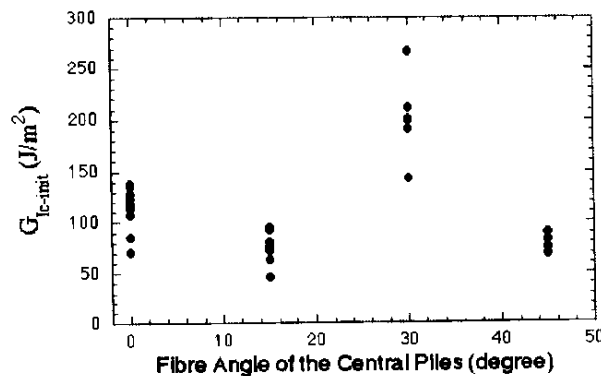


Figure 2:  $G_{Ic-init}$  v. fibre angle for glass-fibre/polyester composites.

### Influence of fibre orientation, vinyl ester composites

In order to improve reproducibility and minimise the effect of resin evolutions a series of panels was produced by RTM with vinyl ester resin. These were about 9 mm thick, with 5 of the 6 plies in each arm unidirectional ( $0^\circ$ ), and the two central plies either  $0^\circ$ ,  $+/+30^\circ$  or  $+/-30^\circ$ . The off angle composites are dominated by the  $0^\circ$  plies and still show a low  $D_c$  value of around 0.06 [7].

#### Mode I

Results from mode I interlaminar fracture toughness are summarised in Fig. 3. The results suggest that  $G_{Ic-init}$  for  $+/+30^\circ$  and  $+/-30^\circ$  GF/VE is larger than that for  $0^\circ$  GF/VE; although the order for modulus is reversed. Difference in the modulus was caused by fibre orientation in the central layer. Since the modulus was calculated from bending stiffness of one arm of the specimen, in which the central layers became the outer layers, variation of fibre orientation in these layers caused significant difference in the measured stiffness.

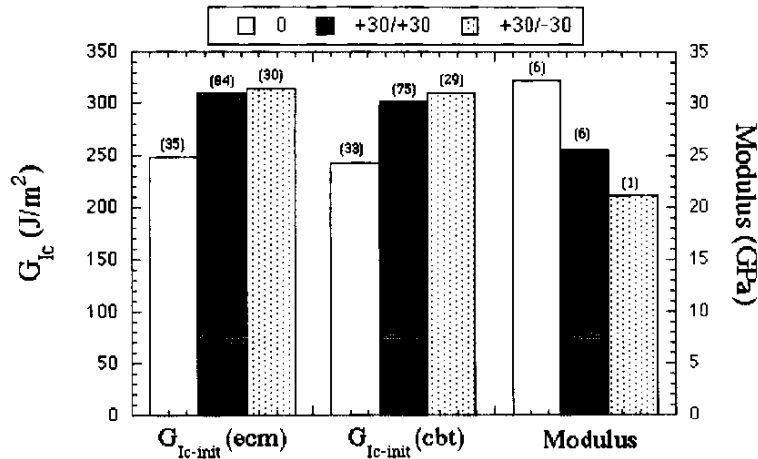
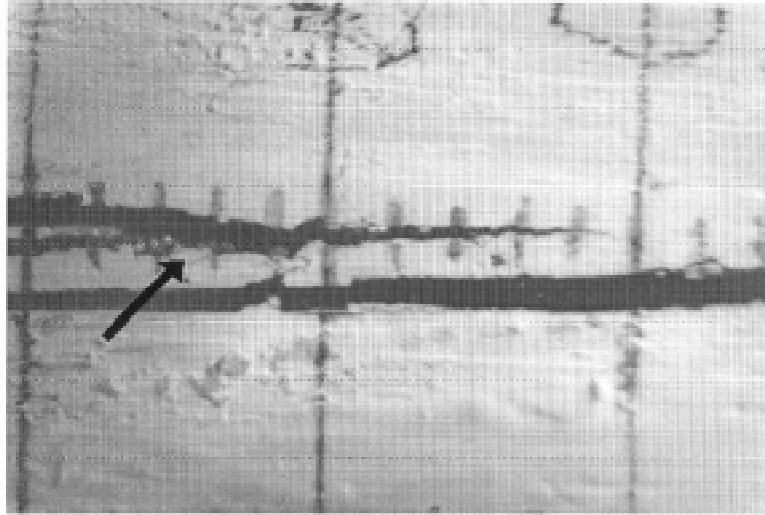


Figure 3: Results for  $G_{Ic-init}$ , using ecm and cbt, and modulus for  $0^\circ$ ,  $+/+30^\circ$  and  $+/-30^\circ$  GF/VE. Numbers in the parentheses are standard deviation of the values.

The values of  $G_{Ic-init}$  in Fig. 3 suggest that interlaminar fracture toughness in a direction not parallel to the fibre is higher than that in the fibre direction. The same trend was also observed for the  $G_{Ic-prop}$  ( $G_{Ic}$  measured during stable crack growth). However, crack growth initiated in the  $+/+30^\circ$  and  $+/-30^\circ$  interface often deviated from the interlaminar region between the 6th and 7th layers, as shown in Fig. 4. When this occurs, a layer of lamina that bridges the two crack surfaces can be formed, greatly increasing the measured  $G_{Ic-prop}$  value. Therefore, great caution should be taken in direct comparison of the  $G_{Ic-prop}$  from  $+/+30^\circ$  and  $+/-30^\circ$  GF/VE with that from  $0^\circ$  GF/VE. Nevertheless, the limited number of  $G_{Ic-prop}$  values that were measured from  $+/+30^\circ$  GF/VE in the beginning of crack growth, that is, before the formation of bridging lamina, are indeed

larger than those from  $0^\circ$  GF/VE.



*Figure 4: Depiction of the lamina bridging (indicated by the arrow) in  $+/+30^\circ$  GF/VE*

Earlier work has shown that the interlaminar crack growth tends to occur near the fibre/matrix interface, especially when the interface is weaker than the matrix [12]. This is believed to be due to easy debonding of the fibre from the matrix, causing the crack progress along the interface faster than that in the matrix. In  $0^\circ$  GF/VE, the fast crack progress at the interface introduced stress concentrations in the surrounding matrix, accelerating the crack development in the matrix. This effect is aggravated when the crack growth is along the fibre direction. In the other directions, the crack advancement is slowed, increasing the measured fracture toughness value.

#### *Mode II*

In order to analyse the results from mode II tests a value of modulus is required. Flexural tests were first performed on un-cracked specimens at different span length to thickness ratios (from 10 to 20) to obtain these values. The moduli obtained were 28.5, 27 and 26 GPa, for  $0^\circ$ ,  $+/+30^\circ$  and  $+/-30^\circ$  specimens respectively.

The results from mode II tests are shown in Table 2 and are less clear-cut than those in mode I. It is apparent that values of  $G_{IIc}$  measured from the starter film are consistently lower for the interfaces between plies at  $+/+30^\circ$  and  $+/-30^\circ$  than those at  $0^\circ$ . This result is very important as it suggests that the  $0^\circ$  values are not conservative in mode II. Values are similar for the  $+/+30^\circ$  and the  $+/-30^\circ$  interfaces and both are about 20 to 25% lower than those in the  $0^\circ$  direction. In addition both types of  $30^\circ$  interface specimens showed a clear R-curve behaviour, with stable crack growth and continuously increasing load, whereas the  $0^\circ$  direction specimens showed an unstable load drop after some subcritical propagation. The transparent nature of the specimens made it easy to

follow crack advance and no indications of crack front curvature were noted. One possible explanation for the difference in behaviour is the flatness of the starter film insert, as an undulating film will give initiation in different crack planes. Films were examined and although the woven nature of the reinforcement makes it impossible to introduce a perfectly flat film there were no obvious differences in roughness for the three fibre orientations. Once the test had been interrupted and the specimen unloaded the new crack tip was marked, the specimen was re-located with a 30 mm crack length, and a second test was performed from the mode II precrack. In this case the values from all three specimen types were similar but all were higher than values from inserts. Given the different propagation modes from the insert the validity of these tests from mode II precracks must be questionable, as the damage associated with an unstable jump ( $0^\circ$  case) is probably different from that preceding a stable crack propagation ( $30^\circ$  interfaces).

*Table 2: Results from mode II ENF tests on glass/vinyl ester composites, mean (standard deviation) of five specimens for each condition.*

Defect type	$0^\circ$	$+/+30^\circ$	$+/-30^\circ$
Film insert	559 (40)	449 (39)	422 (89)
Mode II precrack	811 (214)	835 (146)	833 (55)

## CONCLUSIONS

This paper has highlighted some of the difficulties in measuring useful values of delamination resistance on low fibre fraction, hand lay-up marine composites. When specimens are manufactured by RTM, in order to reduce scatter, mode I delamination resistance was found to be lowest for  $0^\circ$  fibre orientation, but under mode II loading this was not the case. Values for  $G_{IIc}$  measured between  $+/+30^\circ$  and  $+/-30^\circ$  interfaces were up to 25% lower than those for cracks running in the  $0^\circ$  direction. This result indicates that the adoption of specimens with unidirectional fibres in the specimen long axis may not always be conservative and further tests are urgently required to investigate this behaviour.

## References

- [1] ISO project CD 15024, "Determination of the mode I delamination resistance of unidirectional fiber reinforced polymer laminates using the double cantilever beam (DCB) specimen", 1996.
- [2] Davies P, Ducept F, Brunner AJ, Blackman BRK, de Morais AB, "Development of a standard mode II shear fracture test procedure", *Proc. ECCM7-CTS3*, London May 1996, vol 2, pp9-15.
- [3] Nicholls DJ, Gallagher JP, "Determination of  $G_{Ic}$  in angle ply composites using a cantilever beam test method", *J. Reinf. Plastics*, 2, 1983, pp2-17



- [4] Johnson WS, Mangalgi PD, "Investigation of fiber bridging in double cantilever beam specimens", *Comp. Tech. Review*, 1987, p10-13.
- [5] Russell, A. J. and Street, K. N., "Factors Affecting the Interlaminar Fracture Energy of Graphite/Epoxy Laminates", *ICCM-IV*, Tokyo, 1982, pp. 279-86.
- [6] Davidson BD, "An analytical investigation of delamination front curvature in double cantilever beam specimens", *J. Comp. Materials*, 24, 1990, pp1124-1137.
- [7] Davidson BD, Kruger R, Konig M, "Three dimensional analysis and resulting design recommendations for unidirectional and multidirectional end notched flexure tests", *J. Comp. Materials*, 29, 16, 1995, pp2108-2133.
- [8] BSIS protocols for interlaminar fracture testing, (available from P. Davies, Ifremer).
- [9] Carlsson LA, Gillespie JW Jr, "Mode II interlaminar fracture testing", Ch 4 in *Application of fracture mechanics to composite materials*, ed Friedrich K, Elsevier 1989, p113.
- [10] Davies P, "Fracture of marine composites", in *Fracture of composites*, ed Armanios E, Transtec publications 1996, pp583-596.
- [11] Carlsson LA, Florida Atlantic University, private communication.
- [12] Compston et al., to complete.

# IMPROVING OF THE FRACTURE TOUGHNESS OF MG-ALLOY COMPOSITES PRODUCED BY POWDER METALLURGICAL TECHNIQUE

P. Abachi, B. L. Mordike and K. U. Kainer

*Institute of Werkstoffkunde and Werkstofftechnik  
T.U.Clausthal, Agricolastr.6, 38678 Clausthal-Z., Germany*

**SUMMARY:** Metal matrix composites of QE22 magnesium alloy reinforced with SiC particles of different shapes were produced using powder metallurgical technique. Particle content of up to 25 volume per cent was chosen. The fracture toughness tests were carried out at room temperature and at 125°C in the as extruded as well as in the T6 heat treated condition. The reinforcement decreases in general the fracture toughness of the alloy QE22. Sharp irregular SiC particles reduce the fracture toughness of composites more than that of the blocky type. This was observed for composites tested under all experimental conditions.

**KEYWORDS:** fracture toughness, magnesium alloy, SiC particles, powder metallurgical technique

## INTRODUCTION

Light metal matrix composites offer higher specific strength, higher elastic moduli, wider temperature range for application and lower thermal expansion than conventional light metals and alloys. These can be exploited by designers seeking high temperature strength, dimensional stability and light weight. Although aluminium and its alloys have been frequently used as the light metal for the matrix of MMCs, magnesium alloys with a much lower density have recently been considered as an alternative to Al for the matrix [1-3]. Incorporation of ceramic reinforcements into a light metals matrix enhances markedly the physical and mechanical properties of these metals, but the composites exhibit low fracture-related properties, which limit their widespread application [4-6]. Therefore, the fracture toughness behaviour of metal matrix composites has been the subject of the recent studies [7,8]. The examination of the effect of the particles shape and content on the fracture toughness of a magnesium alloy, QE22, which is a heat treatable and relatively temperature resistant magnesium alloy was the main objective of the present work.

## TEST PROCEDURE

Powder metallurgical technique was used to produce metal matrix composites. For the matrix QE22 magnesium alloy powder of 39 µm average diameter was prepared by gas atomizing. The alloy powder was mixed with SiC particles of 9 µm average diameter. The consolidation of the cold prepressed alloy powder-particle mixture was carried out by extrusion. Two types of particle shapes, blocky and sharp, were used to examine the effect of the particle shape on the mechanical properties of composites. The content of SiC particles

reinforcement was in all cases 25 volume per cent. Unreinforced QE22 magnesium alloy powder was consolidated under the same conditions for use as a reference material to compare the mechanical properties. Examination of the unreinforced alloy and composites were carried out on samples in the as extruded as well as in the T6 condition. For the T6 heat treatment the specimens were solution treated at 530°C for 6 h followed by air cooling and ageing for 8h at 204°C. The microstructures of alloy and composites were examined by light microscopy. Fracture toughness tests were carried out at room and elevated temperature using the short rod specimen method of measuring fracture toughness [ 8-10 ]. The fracture surfaces of the tested specimens were examined in the scanning electron microscope.

## RESULTS AND DISCUSSION

The micrographs of the figures 1 and 2 show the microstructures of the materials tested. Figure 1 shows the particle distribution for composites of 20 volume per cent of blocky and sharp particles respectively. The SiC particles are aligned in the extrusion direction. The microstructure of the matrix alloy of the composite contains much finer precipitates than the unreinforced QE22, ( Fig. 2a ). A comparison of the microstructure of the composite in the extruded and in the T6 condition indicates that the particles facilitated the precipitation of the second phase, which may be  $Mg_{12}Nd$  or  $Mg_{12}Nd_2Ag$ , ( Fig. 2b ) [ 11-14].

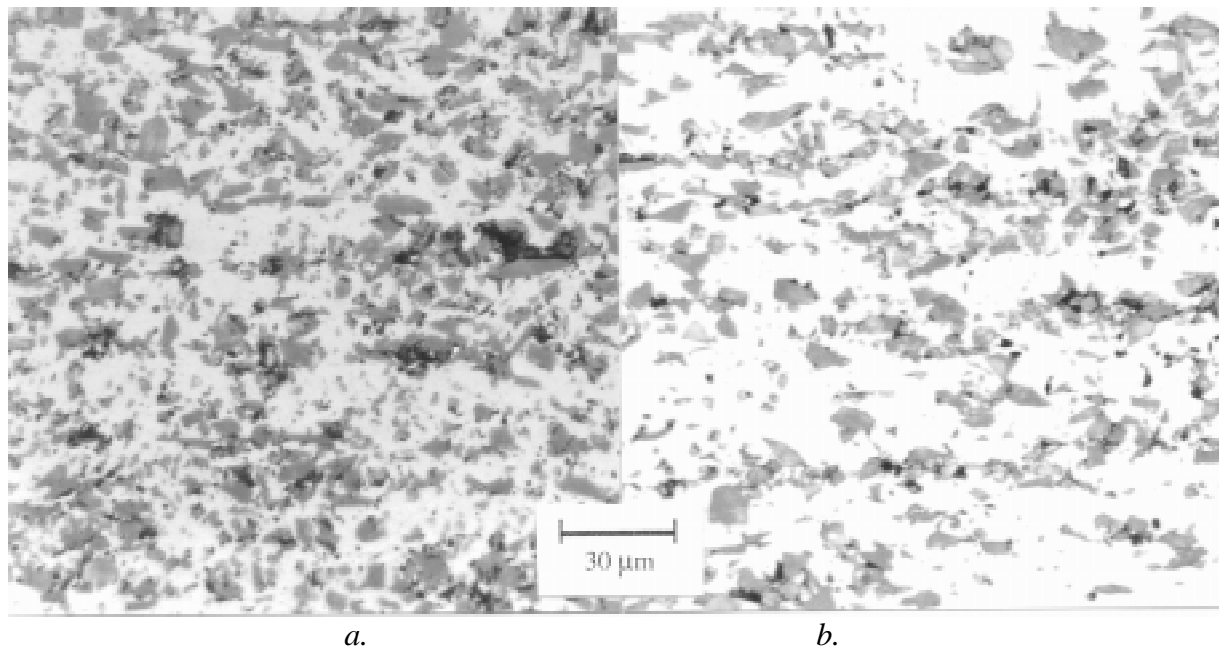


*Fig. 1: Microstructure of extruded QE22 + 20 vol. % SiC composites.  
a) Blocky shape particles, b) Sharp shape particles.*

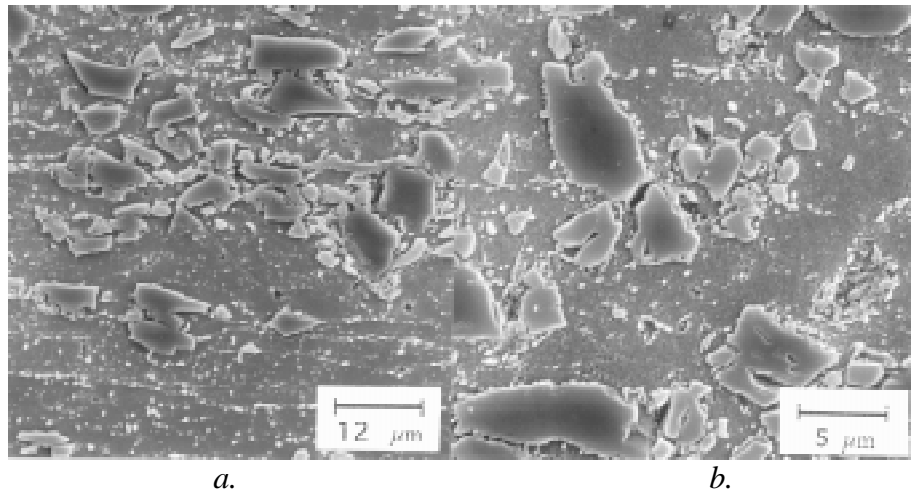


Fig. 2: Microstructure of QE22 + 20 vol. % SiC composites  
a) as extruded, b) as T6 heat treated condition.

The fracture toughness tests of materials in extruded condition were carried out at room temperature and at 125°C, as well as in the T6 heat treated condition. Figure 3 shows the results of fracture toughness of unreinforced and composites reinforced by SiC particles of blocky type. The fracture toughness values of composites decrease with increasing content of the reinforcement independently of test conditions. However, the T6 heat treated composites reveal lower fracture toughness compared with those extruded. The results of fracture toughness values of specimens carried out at 125°C were higher than those tested at room temperature.

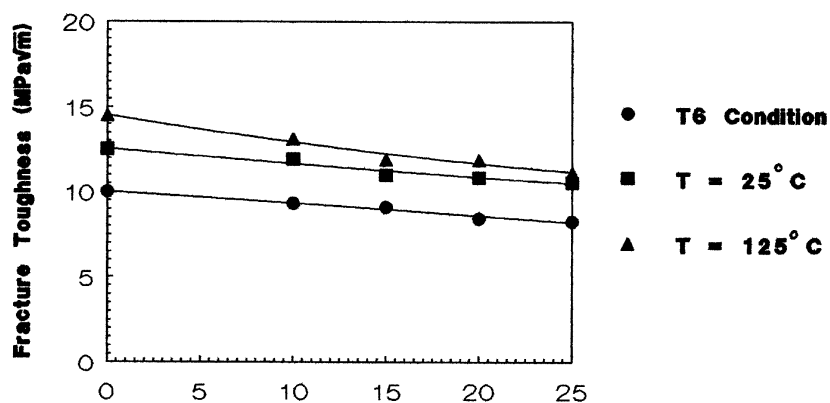


Fig. 3: Showing the results of fracture toughness tests on QE22 alloy and composites with blocky type SiC particles

Figure 4 shows the results of fracture toughness of composites reinforced by SiC particles of the sharp type. The fracture toughness values of composites were lower compared with the unreinforced alloy. The fracture toughness values of composites reinforced by the SiC particles of the sharp type show little change with increasing content of particles. These unexpected results may be due to proper distribution of the particles in the matrix alloy and the production procedure as a whole. The differences between the fracture toughness values of these composites in the as extruded as well as T6 condition were not as much observed as by

composites with SiC particles of blocky type. Nevertheless, composites with SiC Particles of the blocky type show higher fracture toughnesses over the whole particle content range than those of sharp type, ( Fig. 5 ).

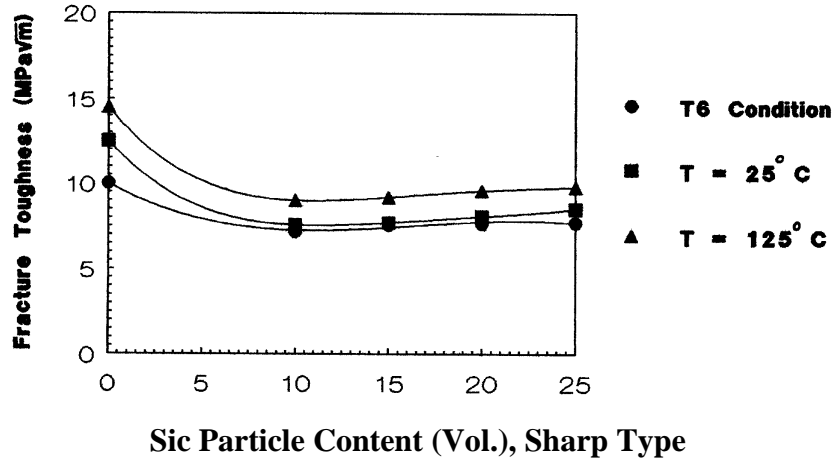


Fig. 4: Showing the results of fracture toughness tests on QE22 alloy and composites with sharp type SiC particles

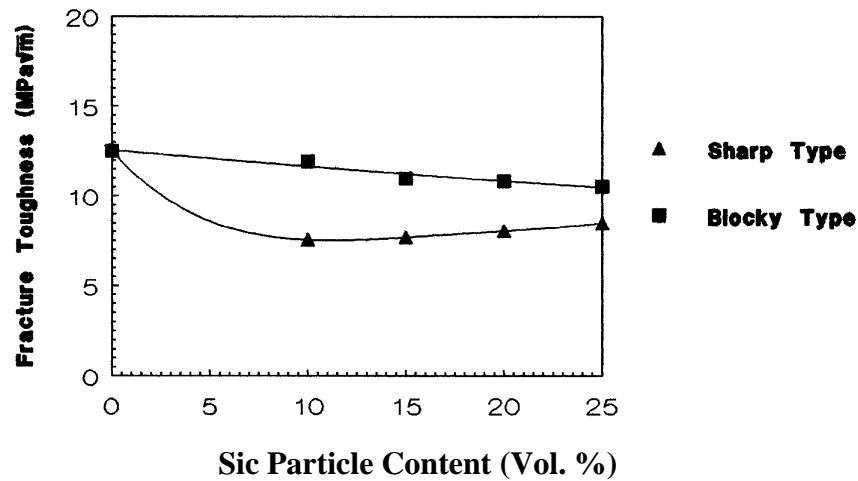
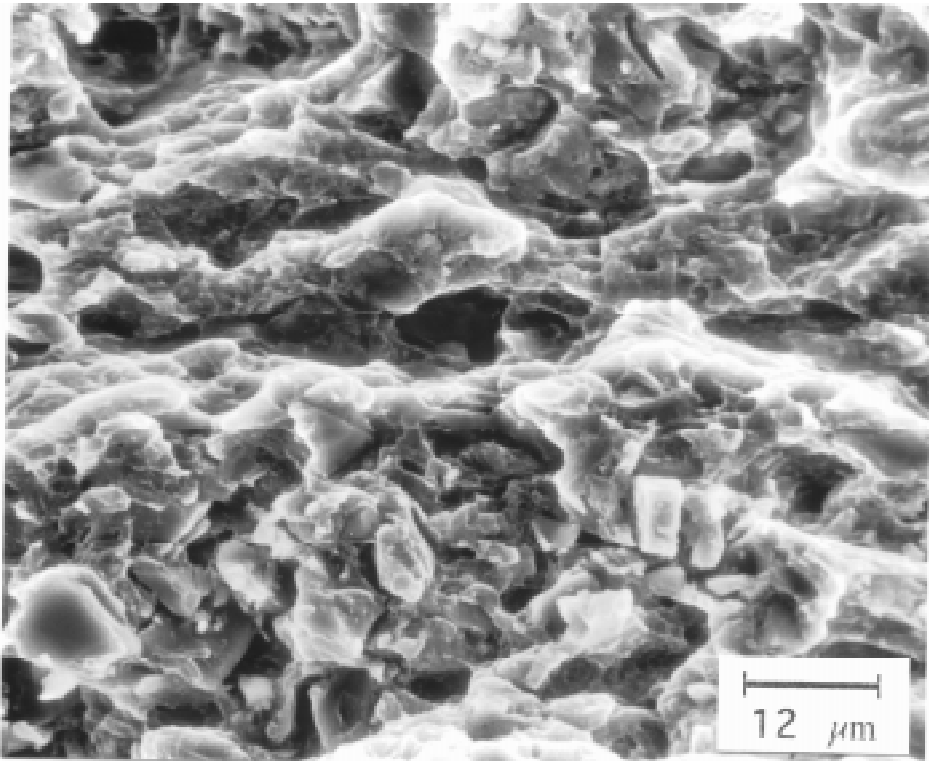
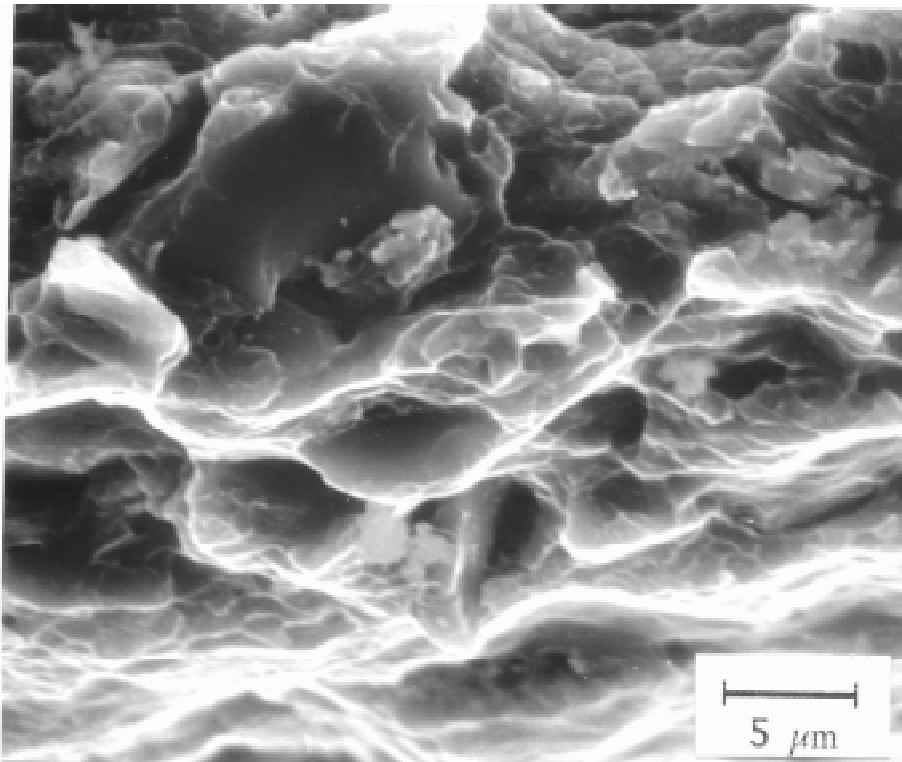


Fig.5: The effect of particle shape on fracture toughness values of composites at RT.

The fractograph of the fracture surfaces of composites showed a preferentially oriented fracture plane in the extrusion direction ( Fig. 6 ). In addition the fracture surface of composites revealed mainly a brittle fracture appearance. Occasionally some dimples like ductile fracture around the particles and frequently in the form of the elongated dimples in the extrusion direction on the plane perpendicular to the fracture surface were observed ( Figs. 7, 8 ). The micrographs of figure 1 indicate on proper distribution of the reinforcement but sometimes clustering of the particles due to poor mixture of alloy powder and particles was observed ( Fig. 8 ). This may be one reason for the scatter of the results.



*Fig. 6: A fractograph of the short rod specimen of the composites with 20 vol. % SiC particles ( blocky type )*



*Fig. 7: Showing the fracture surface of a composite tested with some elongated dimples*

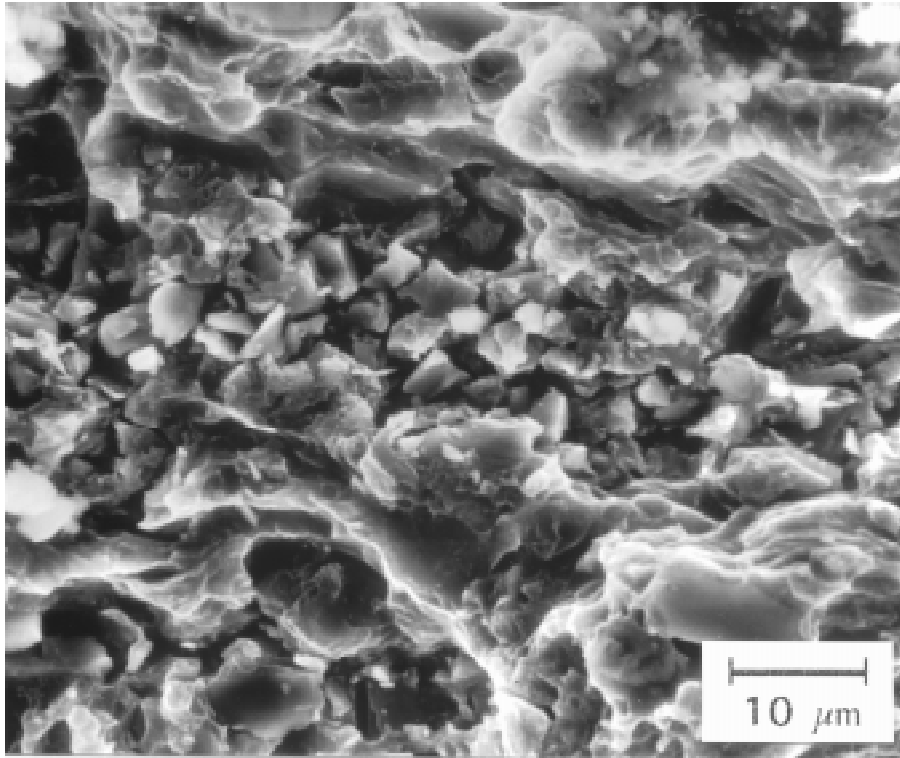


*Fig. 8: Showing an example of SiC particles clustering and dimple like fracture around some particles*

### **CONCLUSION**

1. The QE22 magnesium alloy may be reinforced using powder metallurgical technique by SiC particles of blocky and sharp shapes.
2. As a result of production route the composites show directionally oriented microstructures in the extrusion direction.
3. The SiC particles are responsible for the fine microstructure in composites and facilitate the precipitation of the second phase on T6 heat treatment.
4. The fracture toughness of the QE22 alloy decreases with the SiC particle reinforcement. However, the decrease in fracture toughness depends on the particle shape and content. The fracture toughness of the composites as improved more in the case of blocky type particles as reinforcement than for the sharp particles.
5. T6 heat treatment of the composites causes additional embrittlement of the composites.
6. The particles facilitate crack formation on loading. This may be confirmed by the effect of particle shape on fracture toughness of tested composites.

## REFERENCES

1. Rack H.J., "Light - weight, High - Performance Metal Matrix Composites", in Processing and Properties for PM Composites, Kumar P. and Ritter A., Eds, The Met. Soc., AIME, Feb. 1988, pp.155-168.
2. Arsenault R.J., "The Strengthening of Aluminium Alloy 6061 Fiber and Platelet Silicon Carbide", Mat. Sci. Eng., 64, 1984, pp. 171-181.
3. Kainer K.U. and Mordike B.L., "Herstellung und Eigenschaften von kurzfaserverstärkten Magnesiumlegierung", Metall, 44, 1990, pp.438-443.
4. Divecha A.P., Fishmann S.G. and Karmarker S.D., "Silicon Carbide Reinforced Aluminium-a Formable Composite", J. of Metals 33, Sept. 1981, pp. 12-17.
5. Logsdon W.A. and Liaw P.K., "Tensile, Fracture Toughness and Fatigue Crack Growth Rate Properties of SiC Whisker and Particulate Reinforced Al-Metal Matrix Composites", 83 -ID3- NODEM - PI (Westinghouse Scientific Paper), December 1983.
6. Crowe C.R., Gray R.A. and Hasson D.F., "Microstructural controlled Fracture Toughness of SiC / Al Metal Matrix Composites", in Proc. ICCM-V, Harrigan W.C. , Jr., Strife J. and Dhingra A.K., Eds, The Metallurgical Society Inc., Warrendale, P.A., USA, 1985, pp. 843- 866.
7. Evans J.T., "Fracture and Subcritical Crack Growth in Alumina Fiber - Magnesium Composites", Acta Metall. 34, No.10, 1986, pp. 2075 - 2083.
8. Purazrang K., Abachi P. and Kainer K.U , "Mechanical Behaviour of Magnesium Alloy MMCs Produced by Squeeze Casting and Powder Metallurgy Techniques", Composites Eng., 3, 1993, pp. 489 - 505.
9. Barker L.M., "A Simplified Method for Measuring Plane Strain Fracture Toughness", Eng. Fracture Mech., 9, 1977, pp. 361 - 369.
10. Standard Test Method for Plane - Strain ( Chevron - Notch ) Fracture Toughness of Metallic Materials, in Annual Book of ASTM Standard, E1304-89, Vol. 03.01, 1990, pp. 927-937.
11. Evdokimenko V.I. and Kripyakevich P.I., "The Crystal Structures of Magnesium Rich Compounds in the Systems La-Mg, Ce-Mg and Nd-Mg", Soviet Physics-Crystallography, 8, 1963, pp.135-141.
12. Payne R.J.M. and Bailey N., "Improvement of the Age Hardening Properties of Magnesium-Rare Earth Alloys by Addition of Silver", J. of the Inst. of Met., 88, 1960, pp. 417-427.
13. Lorimer G.W., "Structure-Property Relationship in Cast Magnesium Alloys", Magnesium Technology, The Institute of Metals, 1987, pp.47-53.
14. Borradaile J.B., Threadgill P.L. and Mordike B.L., "The Structure of Complex Mg-Ag-RE-Th Alloys", in Proc.4th Int. Conf. on Strength of Metals and Alloys, Laboratoire de Physique de Solide, E.N.S.M.I.M. I.N.P.L., Nancy, 1976, pp.1385-1388.



# STUDY ON THE MODE I INTERLAMINAR FRACTURE TOUGHNESS OF MULTI-DIRECTIONAL LAMINATES

Li Yong, Li Shunling, Xiao Jun, Tao Jie

*Department of Material Science and Engineering, Nanjing University of Aeronautics and Astronautics, 29 Yu Dao Street, 210016, Nanjing P.R. China*

**SUMMARY:** Based on the conventional compliance and area methods, a high precision method named angle method is present in this work, the interlaminar fracture toughness is determined by measurement of the load and the bend angle at the loading point without measurement of the crack length. And the improvement of the conventional compliance method is made, which is more precise and can be used to general DCB specimen with unequal flexural stiffness of the cantilevers.

The interlaminar fracture toughness in  $0/\theta$  ( $\theta=0^\circ, 30^\circ, 60^\circ, 90^\circ$ ) interface of two epoxy composites, one is carbon fibre reinforced brittle matrix T300/4211, the other is carbon fibre reinforced tough matrix T300/3261, is measured by both compliance and angle methods, and the relationship between fracture toughness and the ply angle  $\theta$  is obtained. It's found that interlaminar fracture toughness is correlated with the type of matrix and the ply angle local the crack front.

**KEYWORDS:** laminate, delamination, crack, fracture toughness

## INTRODUCTION

There are many fracture modes in fibre reinforced composite materials, such as interface debonding, matrix cracked, fibre broken and delamination. Delamination is one of the most common failure modes in composite materials, delamination growth redistributes the stresses in the plies of a laminate and can greatly reduce stiffness and fatigue life. The resistance to crack propagation is usually characterized by fracture toughness, i.e. the energy dissipated on creation of new surfaces. Interlaminar fracture toughness of reinforced composites depends on several factors, such as the toughness of matrix, matrix thickness in the space between neighboring fibres and fibre content.

Analysis and evaluation of delamination toughness in laminated composites become the important research on the delamination failure, especially to evaluation, for fracture toughness is a property of composite materials. Recently, much more work were about evaluation of mode I and mode II fracture toughness, in which the fracture toughness of unidirectional laminates has been found early and the research on each mode toughness of them was also widely. However, much more multi-directional laminates are used in structure, interlaminar fracture toughness of unidirectional laminates is sufficient to compare different materials, but to predict the delamination of multi-directional laminates with fracture mechanics, the fracture toughness of multi-directional layers must be considered. To multi-directional laminates,

more works were about the mixed-mode delamination[1,2]. But, a few works on single mode delamination were reported[3].

The single mode fracture toughness is basic data of the research on mixed-mode delamination, so evaluation of it is very important. So far, the research on the fracture toughness of multi-directional laminates is only confined to its test methods and mixed-mode fracture toughness, nobody has studied the law of single mode fracture toughness of  $0/\theta$  interface of multi-directional laminates against the ply angle  $\theta$ . Since mode I interlaminar fracture is the weakest mode of the three modes, systematic study on the mode I fracture toughness of  $0/\theta$  interface has theoretical and practical significance. The properties of matrix are varied, some show brittle, and some show tough. Delamination crack usually grows along the matrix. There is a lot of research on the property of matrix effecting on the fracture toughness of unidirectional laminates, and a little on that of multi-directional laminates, and not on that of  $0/\theta$  interfaces at all. This study is mainly on the law of fracture toughness of fibre reinforced two different type epoxy composite against the ply angle  $\theta$ . In order to obtain the law completely, the interval of  $\theta$  must be small, the angle  $\theta$  used in this study is  $0^\circ, 30^\circ, 60^\circ, \text{ and } 90^\circ$ .

Recently, the double cantilever beams(DCB) test has been widely used for measurement of mode I interlaminar fracture toughness  $G_{IC}$  in fibre reinforced composite. In conventional DCB test, the fracture toughness was determined by compliance and area methods. S.L. Bazhancy [4] proposed a new method named angle method. In this study, the fracture toughness is determined by compliance and angle method.

## EXPERIMENTAL

### MATERIAL AND SPECIMEN FABRICATION

The materials used in this study is unidirectional fibre reinforced plastic which is fabricated by autoclave. The reinforcement is carbon fibre T300 and the matrix is epoxy which included brittle system 4211 and tough system 3261 (rubber modified epoxy). Mechanical properties of the CFRP are shown in table 1, where L is a subscript fibre longitude direction, and T is a transverse one.

Table 1. Mechanical properties of CFRP.

	T300/4211	T300/3261
$E_L$ (GPa)	126	127
$E_T$ (GPa)	8.0	8.4
$E_T$ (GPa)	3.7	4.3
$\nu$	0.33	0.30

Each volume fraction of fibre is 34.0%(T300/4211) and 34.4%(T300/3261).

The geometry of DCB specimen is shown in fig.1.

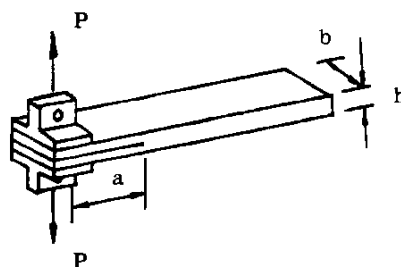


Fig.1. The geometry of DCB specimen.

A precrack is introduced by a 20µm thick film of Teflon which is inserted into a midplane of CFRP at its fabrication.

### STACKING SEQUENCES

In design of lay-up, three factors must be considered, the first is to eliminate the bending-twisting coupling, the second is to decrease the difference of stiffness between the two cantilevers, and the third is to reduce the thermal residual stress. The first and the second factors are used to ensure pure mode I delamination, the third is used for eliminating energy release rate caused by thermal load.

According to the above factors, the concrete basis for lay-up is given:

1. The laminates must be composed of 0/θ interface and this interface is in the midplane.
2. In order to eliminate mode III energy release rate caused by bending-twisting coupling, the lay-up must be attached a -θ ply to form a θ/-θ sequence.
3. To decrease the energy release caused by thermal residual stress, the number of ±θ plies must be very small. So the lay-up used in this study is [0<sub>10</sub>/θ/-θ/0<sub>8</sub>] (θ=0°,30°,60°,90° means precrack of delamination), for 0/90 interface, the lay-up is [0<sub>10</sub>/90/0<sub>9</sub>]. The total number of layers is 20.

The bending-twisting coupling has been eliminated for the above lay-ups, i.e. eliminate mode III energy release. But due to difference of stiffness between two cantilevers, there is mode II energy release rate caused by partial shear stress. The finite element was used to calculate mode I and mode II energy release rate of the DCB test of T300/4211 when the load P<sub>1</sub>=P<sub>2</sub>=1.0N, each of lay-up are shown in table2, where the total energy release rate G<sub>T</sub>=G<sub>I</sub>+G<sub>II</sub>.

Table 2. The energy release rate of each lay-up of the DCB test of T300/4211 when the load P<sub>1</sub>=P<sub>2</sub>=1.0N.

lay-up	G <sub>I</sub> (J/m <sup>2</sup> )	G <sub>II</sub> (J/m <sup>2</sup> )	G <sub>T</sub> (J/m <sup>2</sup> )	G <sub>II</sub> /G <sub>T</sub>
[0 <sub>10</sub> /0 <sub>10</sub> ]	0.256	0	0.256	0
[0 <sub>10</sub> /30/-30/0 <sub>8</sub> ]	0.314	2.76×10 <sup>-2</sup>	0.342	0.0808
[0 <sub>10</sub> /60/-60/0 <sub>8</sub> ]	0.120	1.26×10 <sup>-2</sup>	0.133	0.0950
[0 <sub>10</sub> /90/0 <sub>9</sub> ]	0.290	7.4×10 <sup>-3</sup>	0.297	0.0249

According to the table 2, mode II energy release rate is much smaller than the total, so the fracture toughness of the DCB specimen of such lay-up is belong to mode I by the large.

### MODE I INTERLAMINAR FRACTURE TOUGHNESS TEST

Test is performed with 3 mm/min of cross-head speed without unloading. In reference[5], G<sub>IC</sub> values with and without unloading were compared, it was found that there was no significant difference between these two test conditions. To angle method, fracture toughness is determined by measurement of the load and bend angle of the cantilever beams at the loading point. But to compliance method, it is determined by measurement of the load and the crack length and the displacement at the loading point conventionally, however, the direct measurement of crack length is generally difficult and inaccurate, especially for no-straight crack fronts. The conventional compliance method can be improved by measurement of the flexural stiffness of subbeams in a separate test without crack length, and the crack length can

be calculated. Thus the compliance and angle methods can be used at the same time. The displacement can be determined with percentile gauge. The angle and the gauge reading are recorded by use of a camera during the testing and subsequent development of a film, and measurement of angles on the negatives (or on the photographs). Fig.2 shows a photograph of recording of the angle with growing crack and the gauge reading.

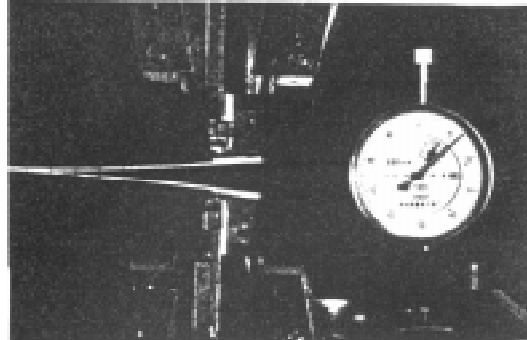


Fig.2. Photograph of recording of the angle and the gauge reading.

### DATE REDUCTION

#### COMPLIANCE METHOD

When the stiffness of the two cantilevers is difference, the displacement at the loading point is given by:

$$\delta = \frac{P a^3}{3} \left( \frac{1}{(EI)_1} + \frac{1}{(EI)_2} \right) \quad (1)$$

where subscripts 1 and 2 correspond to the first and second cantilevers, and a is crack length. The compliance (ratios of displacement  $\delta$  to load P) for DCB is given by:

$$C = \frac{a^3}{3} \left( \frac{1}{(EI)_1} + \frac{1}{(EI)_2} \right) = \frac{a^3}{3} k \quad (2)$$

where  $k=1/(EI)_1+1/(EI)_2$ , The fracture toughness is given by :

$$G_{IC} = \frac{P_c^2}{2b} \frac{dC}{da} = \frac{P_c^2 a^2}{2} k \quad (3)$$

where  $P_c$  is the crack extension force, b is width of the crack. The stiffness of both cantilevers can be determined after testing, the crack length a can be calculated from the load and the deflection:

$$a = \sqrt[3]{\frac{3\delta}{Pk}} \quad (4)$$

Combining equation(3) and (4), the following equation is obtained:

$$G_{IC} = \sqrt[3]{\frac{9k \delta^2 P_c^4}{8b^3}} \quad (5)$$

This method needn't determine the crack length a.

#### ANGLE METHOD

According to elasticity theory, the fracture toughness is equal to the derivative of strain energy Q over crack surface area at a fixed applied force P:

$$G_{IC} = - \left. \frac{\partial Q}{b \partial a} \right|_{P=const} \quad (6)$$

Considering the strain energy of both cantilevers, the following equation is obtained:

$$G_{IC} = \frac{M_c^2}{2b(EI)_1} + \frac{M_c^2}{2b(EI)_2} \quad (7)$$

where  $M_c$  is the critical bend moment in the crack tip. Bending effects during the DCB testing are considered theoretically by William's[6], the fracture toughness  $G_{IC}$  is given by:

$$G_{IC} = \frac{P_c}{b} (\sin \alpha_1 + \sin \alpha_2) \quad (8)$$

where  $P_c$  is the crack extension force,  $\alpha_1$  and  $\alpha_2$  are the bend angle of the first and second cantilevers respectively.

## RESULTS AND DISCUSSION

In the fracture test, no fibre bridging appears in the DCB specimen of  $[0_{10}/0_{10}]$  and  $[0_{10}/90/0_9]$ , its R-curves(fracture toughness plotted against crack extension  $\Delta a$ ) are nearly horizontal. But to the specimen of  $[0_{10}/30/-30/0_8]$  and  $[0_{10}/60/-60/0_8]$ , fibre bridging and crack jumps are taking place, especially to  $[0_{10}/60/-60/0_8]$  specimen, the fracture toughness is varied against the crack extension  $\Delta a$ . Fig.3 shows the typical R-curve of the specimen of  $[0_{10}/30/-30/0_8]$  of T300/3261 composite.

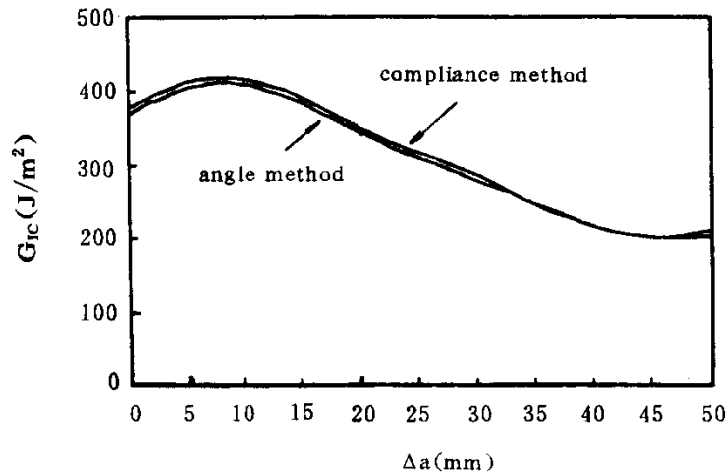


Fig.3. The R-curve of specimen of  $[0_{10}/30/-30/0_8]$  of T300/3261 composite.

The fracture toughness of 0/30 and 0/60 interfaces is taken from the R-curves depending on the feature of its macro-crack surface, and that of 0/0 and 0/90 interfaces is the average value of the R-curves.

Fig.4 shows the relationship between the fracture toughness  $G_{IC}$  and the 0/θ interfaces of both composites with the compliance and angle methods, from which we can find some laws about the fracture toughness. The fracture toughness of 0/90 interfaces of both composites is 2 times the value of 0/0 interfaces, and the value of 0/30 and 0/60 interfaces is higher than that of 0/0 and 0/90 interfaces. However, the value of 0/30 interface is difference between the two composites, the value of 0/30 interface of brittle epoxy composite is slightly higher than that of 0/90 interface (Fig.4a), but the value of 0/30 interface of toughened epoxy composite, is approximately 2 times higher than that of 0/90 interface(Fig.4b). In a word, the fracture toughness of multi-directional interlamina is higher than that of unidirectional interlamina, and the fracture toughness of noncross-ply interlamina is higher than that of cross-ply interlamina.

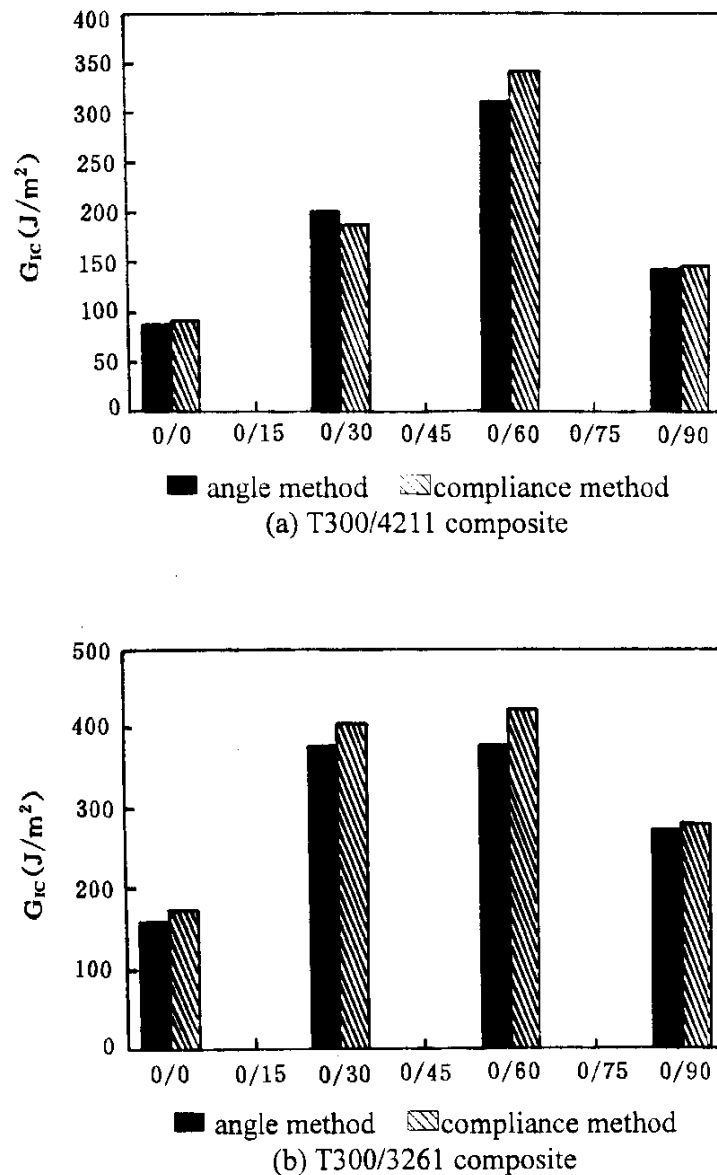


Fig.4. The relation between  $G_{IC}$  and the  $0/\theta$  interfaces of both composites.

### CONCLUSIONS

1. The result of angle method is very close to that of the compliance method.
2. In this study, the improved compliance method avoids the inaccuracy of direct measurement of crack length  $a$ , whose precision is higher than that of conventional method, and can be used to evaluate the fracture toughness of DCB specimen with unequal flexural stiffness of the two cantilevers like angle method.
3. Interlaminar fracture toughness is correlated to the type of the matrix and the ply angle local the crack front. The fracture toughness of 0/90 interface is nearly 2 times the value of

0/0 interface, and the value of 0/30 and 0/60 interfaces is higher than that of 0/0 and 0/90 interfaces.

#### REFERENCES

1. O'Brien, T.K. ASTM STP775 (1982).
2. O'Brien, T.K. ASTM STP837 (1987).
3. Xiao Jun, Li Shunling, Study on the mode II interlaminar fracture toughness of multi-directional laminates. *Journal of Aeronautics*, 11(1990),267.
4. Bazhenov, S.L., Interlaminar fracture modes in 0/90 cross-ply glass/epoxy laminate. *Composite*, 26(1995),125.
5. Masaki Hojo\*, Kazuro Kageyama, Kiyoshi Tanaka, Prestandardization study on mode I interlaminar fracture toughness for CFRP in Japan. *Composite*, 26 (1995),243~255.
6. Williams, J.G., Large displacement and end block effects in the DCB interlaminar test in mode I and II. *J. Composite Mater.*, 21(1987),330~347.

# EXPERIMENTAL DELAMINATION BEHAVIOR OF ANISOTROPIC LAYERED PLATES WITH DIFFERENT INTERNAL ARTIFICIAL DELAMINATIONS UNDER COMPRESSION LOADING

M. Sczepanik-Weinmann, U. Stoll, F.J. Arendts

*Institute for Aircraft Design,  
University of Stuttgart, Pfaffenwaldring 31, D-70550 Stuttgart, Germany*

**SUMMARY:** The experimental investigation studies the influence on the load carrying capability of CFRP specimen with artificial delaminations. Every tested specimen had one circular delamination of 15, 17 or 19 mm diameter embedded between the first and second, the second and third or the third and fourth layer. All the specimens were subjected to a compression load. Global buckling of the total specimen had been prevented by an anti buckling guide. Only in a smaller inspection window could buckling occur. To measure the out of plane displacements of the specimens in the inspection window the laser Moiré interferometry was used. The resulting behavior of the different specimens can be described as follows: the larger and deeper the delamination size was, the lower the failure load was. Even if no local delamination buckling occurred the delamination size has a strong influence on the ultimate failure load. If the delamination was located closer to the surface delamination buckling occurs in a stable manner. Deeper delaminations tended to exhibit more unstable delamination growth.

**KEYWORDS:** delamination, buckling, local, global, compression loading, Moiré, interferometry, artificial inserts

## INTRODUCTION

In aerospace structures composite parts are more and more common. One of the major lacks of these structural components is their low impact resistance and such an impact is often followed by delaminations caused by the impact. Therefore it is of interest how different shaped delaminations at different depths influence the load carrying capability of the structure. This had been done to get experimental reference values for a comparison with simulation results. If the simulated results fit well with the experimental results a better valuation of a real damage is possible. If the simulation can describe the failure behavior the design rules for composite components could be less restrictive. This would make it possible to take greater advantage of the material properties.

## EXPERIMENTAL SETUP

In a experimental investigation it is necessary to have reproducible experimental conditions. For that reason different artificial delaminations made of a thin (12  $\mu\text{m}$ ) Teflon film were used to get a defined failure inside the specimen. The used laminate had the



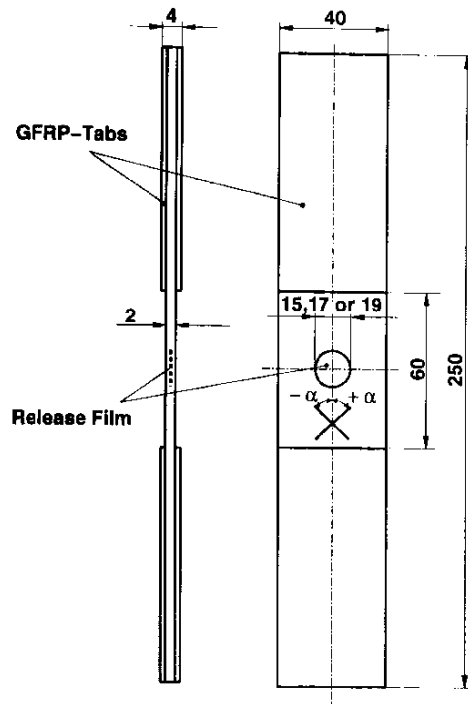


Figure 1: The used specimen with internal delamination (dimensions are in mm).

stacking sequence  $[\pm 45^\circ, 0_2^\circ, 90^\circ, 0_3^\circ]_s$ , containing different types of circular delaminations between different layers.

The experiments should give some answers regarding the dependence of delamination growth on size and depth of the delamination. Three delamination sizes (15 mm, 17 mm and 19 mm) between three different layers had been investigated. All three delamination sizes had been applied between first and second, second and third or third and fourth layer. From each type 6 specimens were tested. The material used is the carbon fiber reinforced epoxy C914/T300 produced by Ciba Geigy.

The used specimen for the delamination tests are sketched in Fig.1 and is similar to the experimental environment in [2]. The global buckling of the whole specimen was prevented

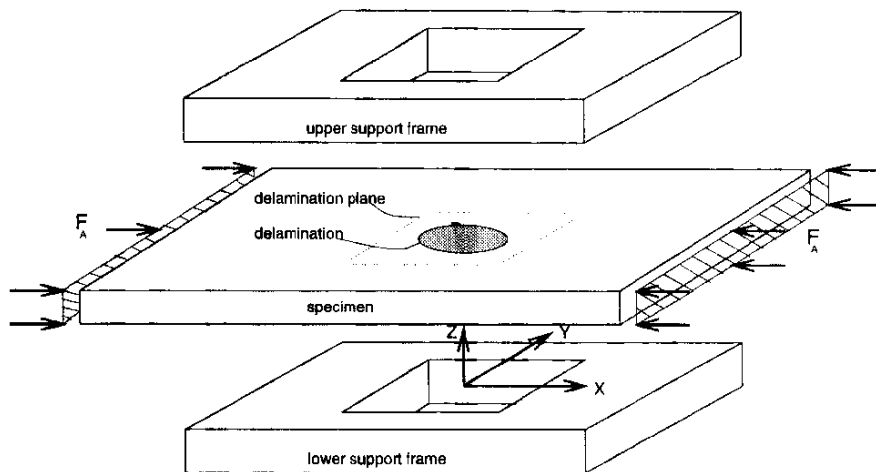


Figure 2: Specimen setup

by an anti buckling guide according to Fig.2.

Laser Moiré interferometry was the measuring method to inspect the delamination buckling behavior. The experiments were performed as static compression loading in steps of 10 N to record the delamination growth step by step if it appeared in a stable manner. After each load step a laser scan had been taken to get the Moiré pictures. The method was used to get the out-of-plane displacement in the inspection window. The Moiré setup is depicted in Fig.3. A detailed description can be found in [1]. The method leads to a two dimensional grey level picture stored in a 8 bit matrix (512x512 pixel) for the out-of-plane displacements of the specimen in the investigated window. The 512x512 pixel image was captured with a CCD camera. The resulting out-of-plane displacements are the basis to extract the delamination contours for the different load levels. A computer algorithm had to be designed which could filter the contours out of the two dimensional pixel matrix.

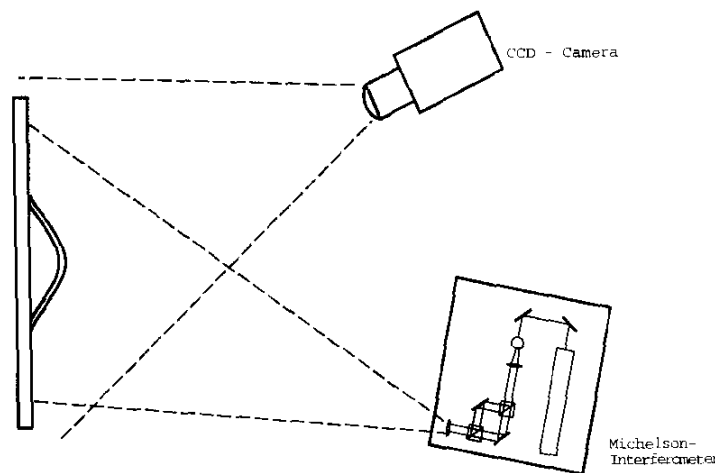


Figure 3: Moiré setup

### DATA SELECTION

As already mentioned in the previous section the Moiré method results were two dimensional matrices with an 8 bit resolution per matrix point. Because of the noise on the measurement signal and local minima it was difficult to detect the contour line of the delamination, especially with a computer. For that reason the signal had to be filtered in different ways without changing the geometrical location of the delamination contour. Low path and Median filter had been investigated. A one dimensional column filtering had been performed. Most of the times a Median filter had been preferred to take away the nonlinear noise.

To find the delamination contour a specially designed local gradient filter yielded good results. That could be tested by visualizing the computed results in a diagram which represented a one dimensional cut. The human eye can find the relevant minimum right away. An example can be seen in Fig.4 and 5. Also, it can be seen that the filter parameters have a big influence on the results. The data after a filtering can be destroyed totally if the wrong filter parameters are used. For that reason the filtering has to be done very carefully.

### EXPERIMENTAL RESULTS

The first result which had been gained during the experiments was the failure load for

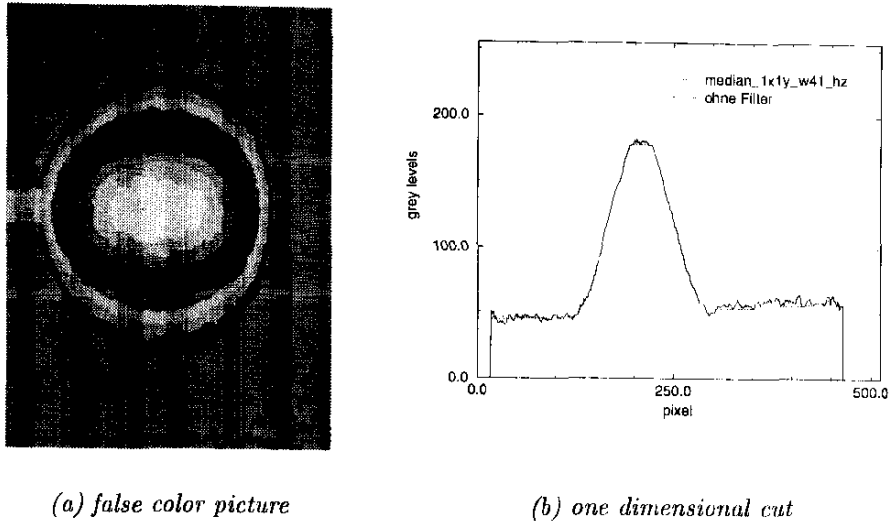


Figure 4: Two dimensional local buckling picture and a one dimensional cut trough the middle of the specimen.

each specimen. These failure loads are listed in Table 1 which show a significant influence of the delamination size and depth.

size mm]	layer	failure load [MPa]	start local buckling [MPa]	failure type
15	1//2	513	233	local $\Rightarrow$ global
15	2//3	465	305	local $\Rightarrow$ global
15	3//4	467		only global
17	1//2	487	225	local $\Rightarrow$ global
17	2//3	462	370	local $\Rightarrow$ global
17	3//4	454		only global
19	1//2	477	231	local $\Rightarrow$ global
19	2//3	412	320	local $\Rightarrow$ global
19	3//4	397		only global

Table 1: Failure loads of the used specimens.

The following dependences can be found according to Table 1:

- The failure load decreases as the start delamination size increases. With delaminations between the first and second layer it changed from 513 MPa for the 15 mm delamination to 477 MPa for the 19 mm delamination.
- For deeper delaminations the behavior is similar but with a lower start level. That means that the deeper and wider the delaminations are the lower the failure load is.
- During the testing of the specimen with the delamination between the third and fourth layer no local buckling or delamination growth could be detected until final failure. On the other hand these specimens failure load had been the lowest of all tested specimen. Even if no local buckling could be detected the delamination size and depth determine the failure load.

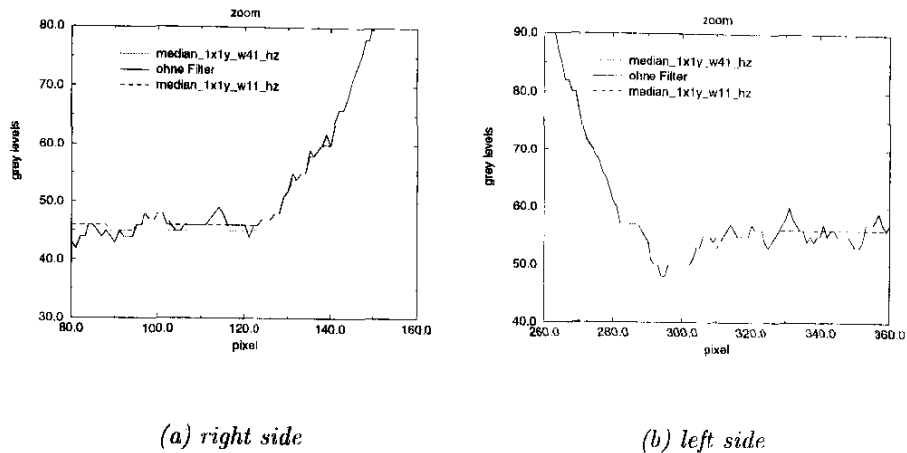
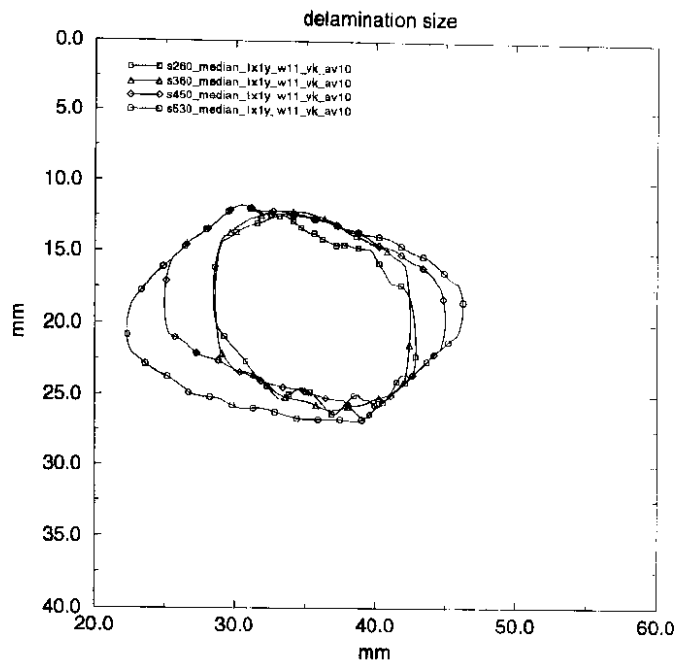


Figure 5: Relevant delamination areas zoomed from Fig.4 with different filter parameters.

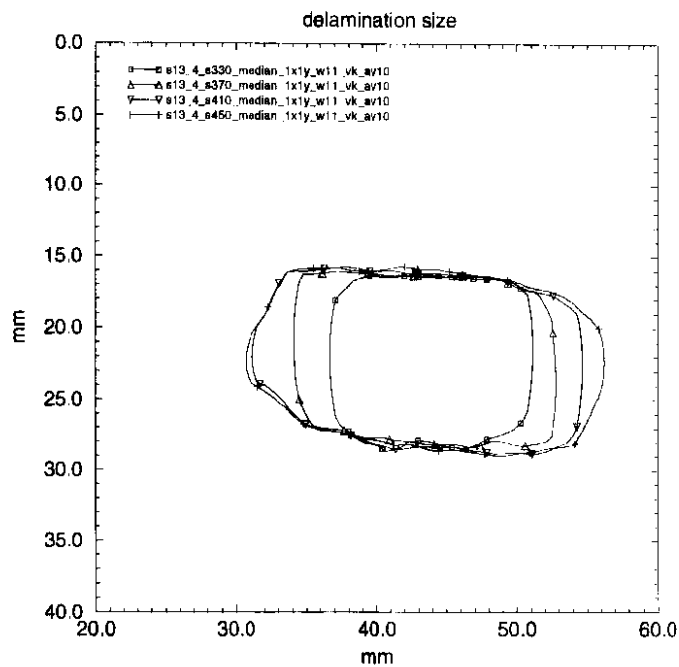
- The beginning of local buckling changed from a lower load to a higher load the deeper the delamination is inserted. There is only little size influence.

These results could be found only by looking at the failure loads of the different specimens. The resulting delamination contours for the different specimen are shown in Fig.6, 7 and 8. They yield more information about the delamination behavior. According to these graphs following can be considered:

- The delamination area never became smaller than the start area, but later delamination closing could occur.
- Delamination growth between the first and second layer had been mostly stable, between the second and third mostly unstable.
- Delaminations between the two  $\pm 45^\circ$ -layers started to align their shape in orthotropic axes direction according to Fig.6.
- In loading direction there were only little delamination growth compared to the horizontal direction as shown in Fig.6. Only if the delamination already reached the fixture, the delamination started growing in load direction.

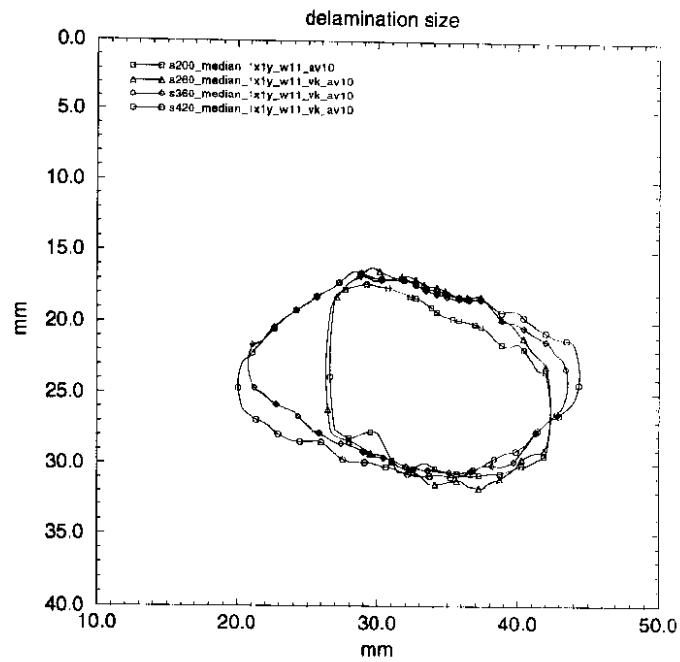


(a) 15mm 1//2

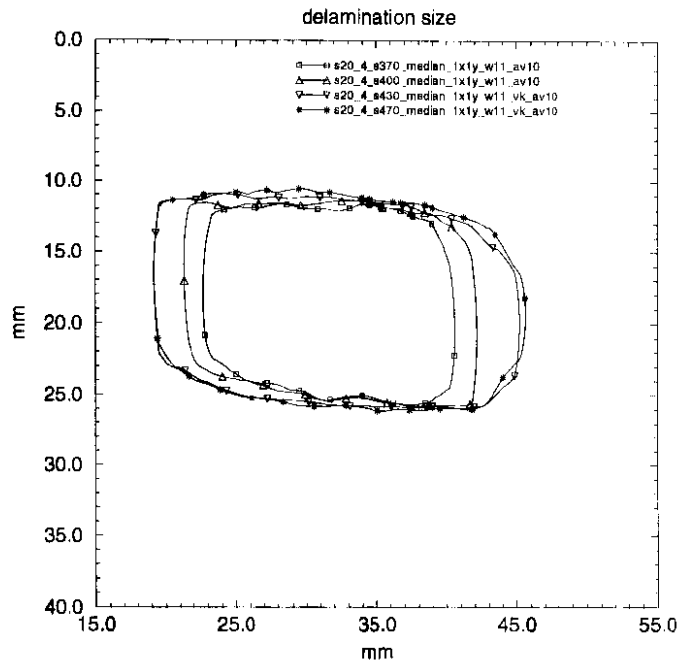


(b) 15mm 2//3

Figure 6: Delamination growth for specimens with 15 mm delamination.

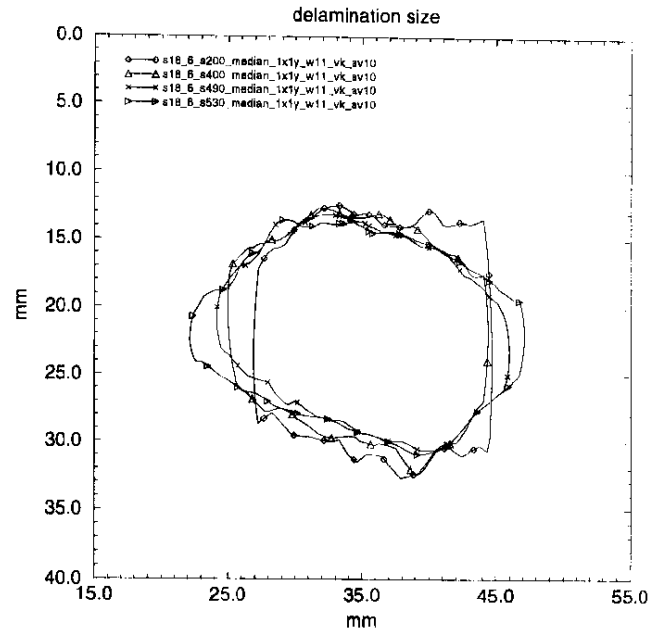


(a) 17mm 1//2

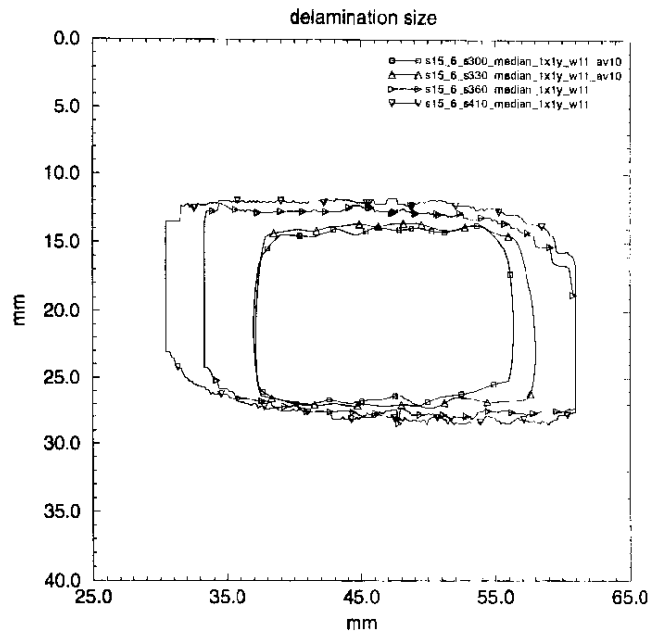


(b) 17mm 2//3

Figure 7: Delamination growth for different specimens with 17 mm delamination.



(a) 19mm 1//2



(b) 19mm 2//3

Figure 8: Delamination growth for different specimens with 19 mm delamination.

## CONCLUSIONS

Different types of specimens with internal delaminations had been tested. As a simple rule it could be derived that the deeper and larger the initial delamination was the lower was the ultimate failure load of the specimen. Local buckling occurred only if the delamination was close to the surface, that means between the first and the second or the second and third layer. With deeper delaminations delamination buckling could not be observed. The deeper the delaminations are located the greater is the tendency to unstable delamination growth. Only for delaminations between the first and second 45°-layer stable delamination growth could always be observed. Also the angle of the adjacent layer influenced the delamination direction.

It seems as if the non-visible inner delaminations are the most dangerous ones and also, they are not easy to detect.

## ACKNOWLEDGEMENTS

The financial support of the "Deutsche Forschungsgemeinschaft" (DFG) through the grant no. Ar 146/11-2 is great-fully acknowledged.

## References

- [1] Hänsel, C.; Eberle, K.: "Measuring Propagation of Delaminations in CFRP-Laminates by Moiré Technique" In: Hogg, P.J.; Sims, G.D.; Matthews, F.L.; Bunsell, A.R.; Massiah, A. (ed.): *Composites Testing and Standardization* (European Conference on Composites Testing and Standardization, Amsterdam, 8.-10. September 1992), European Association for Composite Materials, pp 417-424
- [2] Bergmann, H.W. et al.: "*Mechanical Properties and Damage Mechanisms of Carbonfiber-Reinforced Composites - Compression Loading*", Deutsche Forschungs- und Versuchsanstalt für Luft- und Raumfahrt, Institut für Strukturmechanik, Braunschweig, DFVLR-FB 88-41



# EFFECT OF FABRIC ORIENTATION ON FRACTURE TOUGHNESS OF GLASS FABRIC/PC COMPOSITE

J.B. Wang<sup>1</sup>, Y.Q. Sun<sup>1</sup>, S.R. Zheng<sup>2</sup> and X.T. Jing<sup>3</sup>

<sup>1</sup> *Mechanical Engineering Department, Northwest Institute of Textile Science and Technology, Xi'an, 710048, China.*

<sup>2</sup> *Chemical Engineering Department, Northwestern Polytechnical University, Xi'an, 710072, China*

<sup>3</sup> *Material College, Xian University of Science and Technology, Xi'an, 710048, China*

**SUMMARY:** Mode I interlaminar fracture toughness tests were conducted by using DCB specimens of glass woven fabric/PC composites. The panels were laid up with different fabric orientation ( $0^\circ/0^\circ$ ,  $0^\circ/90^\circ$ ). Test results shown: Mode I interlaminar fracture toughness  $G_{IC}$  of the  $0^\circ/90^\circ$  specimen was higher than that of the  $0^\circ/0^\circ$  specimen. This is caused by the difference in crack propagation resistance provided by their intrinsic structures. The weft or warp perpendicular to the crack growing direction has higher resistance to the crack propagation than the parallel. The amount of resin collected in a crack tip damage zone is another factor leading to the increase of fracture toughness. The tough PC resin rich zone provides a larger resistance path for the interlaminar crack. The scanning electron microscopic observation indicated that the crack met with more perpendicular yarns in the  $0^\circ/90^\circ$  specimen than that in the  $0^\circ/0^\circ$  sample before it propagated. Also, there was more resin and plastic deformation occurred in the crack tip of the  $0^\circ/90^\circ$  specimen than that of the  $0^\circ/0^\circ$  sample.

**KEYWORDS:** woven fabric composite, fabric orientation, fracture toughness, glass fabric, polycarbonate

## INTRODUCTION

Woven fabric composite materials have advantages over their unidirectional prepreg tape counterparts, such as the favourable mechanical properties, ease of handling, low manufacturing cost, etc. Therefore, they have been widely used in technical practice, especially in the field of aerospace, marine and sports technology, and have attracted more and more interests of investigators<sup>[1~4]</sup> in the composites community.

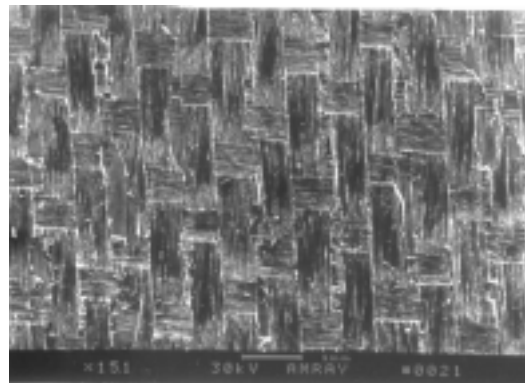
Interlaminar fracture behavior is one of the most important characteristics related to the overall performance of composite systems. In comparison with the composites made of unidirectional prepreg tape, the mechanisms of the fracture failure of woven fabric reinforced composites are more complicated. In addition to the influences of variables which include the fiber and resin type, and yarn type, the failure mechanisms involve their intrinsic weaving structure; the weaving density between weft and warp yarn<sup>[5,6,7]</sup>, the laying-up orientation and so on. The composites with different intrinsic structures differ greatly in interlaminar fracture toughness values. Therefore, It is important to have a better understanding of effects of various parameters affecting the fracture properties.

The objective of present investigation was to explore the influence of fabric orientation on the fracture toughness of glass fabric reinforced polycarbonate (PC) composite through the Mode I fracture tests and scanning electron microscope observation of fractured sample surfaces.

## EXPERIMENTAL PROCEDURES

### Material

The material chosen for this investigation was glass fabric reinforced polycarbonate. The reinforcement is E-glass fabric Ew160. The fabric is a four-harness satin weave, as shown in Figure 1. The matrix resin was polycarbonate film CH8301. The specifications of the fabric and the matrix resin were given in Table 1.



### Specimen Preparation

The 0° orientation and the 90° orientation of plain glass woven fabric were fabricated on alternate plies by hand laying-up technique and hot pressed (The fabric warp direction parallel to sample longitudinal direction is called "

0° orientation" for short. The fabric weft direction parallel to sample longitudinal direction is called "90° orientation" for short. ). In order to explore the effect of the fabric orientation on fracture toughness of the glass fabric reinforced polycarbonate, the panels were laid up with different fabric orientation (90°/0°-90°/0° and 90°/0°-0°/90°) in the midplane. They are called the 0°/90° specimen and the 0°/0° specimen for short respectively. A per-crack of 50mm was introduced by a 25µm thick film of polytetrafluoroethylene (PTFE) which was inserted into the midplane of the composite during fabrication. The midplane of the 0°/90° specimen is between 0° and 90° laminate and the midplane of the 0°/0° specimen is between 0° and 0° laminate. The volume fraction of glass fabric is about 50% in the specimen.

Table 1: Specifications of the fabric and matrix resin

material type	thickness (mm)	area density (g/m <sup>2</sup> )	warp (yarn/dm)	weft (yarn/dm)
PC	0.07	87.139		
E-glass fabric	0.14	171.429	182	146

The double cantilever beam (DCB) specimens were used to measure the fracture toughness. Specimens were cut from the laminate using a diamond embedded slitting wheel, with water being as a coolant during the cutting. The specimens were then dried in an oven. The dimension of DCB specimens were 250 × 25 × 4.8mm.

### Fracture Toughness Tests

Mode-I delamination tests were conducted in a Instron universal testing machine (Model 1253) at a loading rate of 0.5mm/min. Crack length increment was marked on the load-displacement curve. Interlaminar fracture toughness  $G_{IC}$  was calculated by the following equation:

$$G_{IC} = 3PY / (2B \cdot a) \tag{1}$$

where the P is the load, the Y is the displacement, the B is the specimen width and the a is the crack length.

### SEM Observation of the Fracture Surfaces

The fracture surface of specimens were coated with carbon and observed under a scanning electron microscope (SEM).

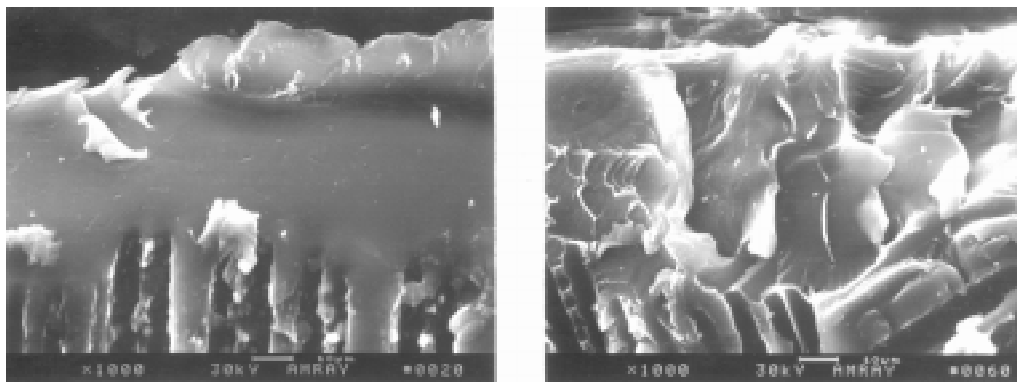
## RESULTS AND DISCUSSION

The results of tests are shown in table 2. From the table, it can be seen the fracture toughness  $G_{IC}$  of the  $0^\circ/90^\circ$  specimen has higher values than the  $0^\circ/0^\circ$  specimen. It shows that the orientation of laying up has a significant influence on the fracture property of fabric reinforced composites.

*Table 2: Test results of fracture toughness*

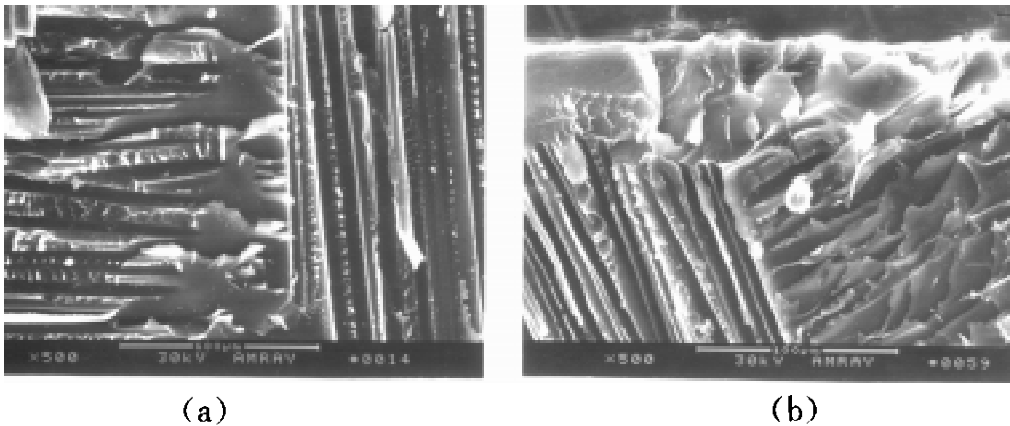
type	fracture toughness $G_{IC}$ (J/m <sup>2</sup> )
$0^\circ/0^\circ$	708.79
$0^\circ/90^\circ$	1088.66

Figure 2 shows SEM micrographs of the precrack tip zone of the fracture surface. On Figure 2(a), the fracture surface of precrack zone of  $0^\circ/0^\circ$  specimen is smooth. The imprints of plastic deformation are much shallower. It means that the little fracture energy was dissipated. Figure 2(b) shows that the surface of the  $0^\circ/90^\circ$  specimen is much rougher, and the crack tip damage zone is larger than that of the  $0^\circ/0^\circ$  specimen. It also shows that a precrack tip of the  $0^\circ/90^\circ$  specimen is in a resin rich zone, where larger deformation occurred, and much more deformation energy is dissipated. Therefore, the  $0^\circ/90^\circ$  specimen has higher resistance to crack propagation than the  $0^\circ/0^\circ$  specimen. The difference in fracture toughness between the  $0^\circ/0^\circ$  and the  $0^\circ/90^\circ$  specimen is caused by the different content of resin collected in woven structure. There is obvious space between the yarns. Different laying orientations form the difference in space and resin contents. The tough PC resin rich zone provides a larger resistance path for the interlaminar crack. The  $0^\circ/90^\circ$  specimens have more resin collected in a crack tip damage zone.



(a) (b)  
 Fig. 2: SEM photographs of the precrack zone,  
 (a).  $0^\circ/0^\circ$  specimen, (b).  $0^\circ/90^\circ$  specimen

SEM photographs in Figure 3 show that the weft or warp perpendicular to the crack growing direction has higher resistance to the crack propagation than the parallel. In Figure 3(a), the transverse imprints is weft. In Figure 3 (b), the right side is warp imprints. They are perpendicular to crack propagation orientation, and had experienced more plastic deformation than those parallel to the crack propagation orientation. It shows that the weft or warp perpendicular to crack propagation orientation has higher resistance to crack propagation. SEM observation indicated that the  $0^\circ/90^\circ$  specimens have more yarns perpendicular to the crack growing direction. It means that the crack met with more perpendicular yarns in the  $0^\circ/90^\circ$  specimen than that in the  $0^\circ/0^\circ$  specimen before it propagated.



*Fig. 3: SEM photographs of the delamination fracture surface, (a).  $0^\circ/0^\circ$  specimen, (b).  $0^\circ/90^\circ$  specimen*

## CONCLUSIONS

1. The  $0^\circ/90^\circ$  specimens of plain glass fabric reinforced polycarbonate composite has higher Mode I interlaminar toughness  $G_{IC}$  than the  $0^\circ/0^\circ$  specimens. This is caused by the different fabric orientation which resulted in the difference in the intrinsic structures.
2. The tough resin rich zone provides a larger resistance path for the interlaminar crack.
3. The weft or warp perpendicular to crack propagation direction has higher resistance to crack propagation than the parallel.

## ACKNOWLEDGMENT

The financial support of the National Natural Science Foundation of China, and the Laboratory for Nonlinear Mechanics of Continuous Media, Institute

of Mechanics, Chinese Academy of Science, is gratefully acknowledged.

### REFERENCES

1. Vandeurzen, P. , Ivens, J. and Verpoest, I. , " Structure — performance Analysis of Two — dimensional Woven Fabric Composites" , Proc. of ICCM — 10, 1995 , Vol. IV , pp261 — 268
2. Naik, N. K. and Ganesh, V. K. , " Failure Behavior of Plain Weave Fabric Laminates Under In — plane Shear Loading" , J. Comp. Tech. Res. , 1994, Vol. 16, pp3 — 20
3. Karagaka, M. and Kurath, P. , " Deformation and Failure Behavior of Woven Composite Laminates" , J. Engg. Mater. Tech. , Trans. ASME 116, 1994, pp222 — 232
4. Kumar Rajesh S. and Naik, N. K. , " Prediction of Compressive Strength of Plain Weave Fabric Composites" , Proc. of ICCM — 10, 1995, Vol. IV, pp333 — 340
5. Sun, F. , IWAMOTO, M. , JINEN, E. and SWZUKI, M. , " Fracture Mechanisms of Plain Woven Fabric Laminated Composites" , Material (Japan), 1989, Vol. 38(427), pp360 — 366
6. HAMADA, H. , KOTAKI, M. and HIRAI, Y. , " Effect of Surface Treatment and Weave Structure on Mode I Interlaminar Fracture Behavior of Glass Woven Fabric Composites" , Proc. of ICCM — 10, 1995, Vol. VI, pp643 — 650
7. Wang, Y. J. and Zhao, D. M. , " Characterization of Interlaminar Fracture Behaviour of Woven Fabric Reinforced Polymeric Composites" , Composites, 1995, Vol. 26, pp115 — 124

# INTERFACE MODELLING IN LAMINATE COMPOSITES FOR FREE-EDGE EFFECTS ANALYSIS

Mohamed Haboussi, H el ene Dumontet, Jean Louis Bill ot

*Laboratoire de Mod elisation et de M ecanique des Structures (URA CNRS 1776)  
ENSAM/UPMC/ENS Cachan, 151 Bd. de l'H opital 75013 Paris*

**SUMMARY:** Two interface models based on physical considerations are suggested and used to analyse the free-edge effects in unidirectional multi-layered composites. These models question the pertinence of the classical perfect interface model to represent the interface physical reality. The first model is transition spatial evolution behavior law defined for an interlayer according to the laying direction. It is based on a microscopic analysis of the fiber distribution in the interface vicinity between two layers. The numerical simulation of this model gives exact stress tensor in all the laminate, especially the values of the interlaminar stresses which verify exactly the free-edge conditions. The second model is an interface law defined on material surface, resulting from the resolution of a problem to the limits on the interlayer, simulating a very thin flexible layer. This model also gives no singular free-edge interlaminar stresses.

**KEYWORDS:** unidirectional laminates, free-edge effects, transition behavior law, wall effect, asymptotic expansion method, material surface law, singular interlaminar stresses

## INTRODUCTION

The idea that the quality of a composite does not depend only on the nature and properties of its constituents but also of their binding region is now known [1]. Many samples exist where the interface modelling wake has been considered responsible for real or supposed miscalculations [2,3]. Enhancing the interfacial region analysis is not a simple task, as this zone does not exist itself, it is formed during the material manufacture [4]. Thus, some unidirectional thermosettable laminate processes like RTM, induce microscopic scale changes, that manifest by resin focusing at the interface. This focusing is due notably to specific fiber distribution at the interface vicinity, generated by "the wall effect", introduced by Bill ot for laminate composites [5], Fig. 1.

The aim of this work is to investigate the influence of a refined interfacial regional description on free edge effect and to compare this approach with classical methods of analysis.

Usually, at the free-edge vicinity of a laminate plate, a complex 3D state stresses is observed, presenting an important concentration effect, able to provoke delamination failures. The classical theories or the piece wise approach do not reveal this state of stresses, many structural free-edge effect developments have been then proposed these last years, [6]. In these models, the interlaminar interface is commonly assimilated to a perfect surface, or sometimes to a very thin layer of an adhesive material, [7]. These approaches, after simulation, generate singular free-edge interlaminar stresses. These singularities create

difficulties in the application of onset delamination criteria, as they overestimate the physical interlaminar stresses, [8].

In this work, we start by setting a transition behavior model for the interface region or the interlayer. This model constitutes the essence of our approach. The evolutive law has therefore been served in a 3D finite element tensile test simulation of a  $(0^\circ, 90^\circ)_s$  laminate. Comparisons with classical results show that our approach allows the best perception of the stresses in the totality of the composite laminate, especially at the free edge.

This approach presents the inconvenient of being numerically expensive and badly adapted to the study of any multi-layer containing several interfaces. We have therefore decided to develop an interface law defined on a material surface, translating the evolutive continue behavior of the interface region to render our approach more profitable. In order to achieve this, we have used the asymptotic expansion method where the interface thickness constitutes the small parameter of the problem.

We obtain a first interface law, asymptotically equivalent, to transmission conditions through a thin interlayer, relating by stiffness the stresses interface vector to the displacement jumps. Note that, we have mathematically obtained the supposed imperfect interface model proposed in [3].

Several basic numerical tests have permitted the theoretical validation of the interface law. The interlayer was successively discretized for different values of its thickness. The numerical stiffnesses values converge when the thickness decreases towards the theoretical values given by the interface law.

Furthermore, the interface law is implemented in the industrial finite element software ABAQUS. Different tests validate the interface card implementation and show its capacity to restore the stress and the displacement vector at the interface correctly. Finally, this law has been used to analyse the free-edge effects in  $(0^\circ/90^\circ)_s$  laminate in extension, presenting a very thin flexible interface, representing an adhesive material.

## **INTERLAYER TRANSITION NOTION**

The classical piecewise approach that averages the behavior in the thickness of each layer and assimilates the interfacial region as a perfect adherence surface is only an approximation of the reality. Indeed, the interface, which is the area separating two layers, is a layer of very weak thickness, Fig. 1.

This layer is constituted in part of resin in the case of organic matrix laminates, with a specific fiber distribution.

So, to describe more clearly the interlaminar unidirectional laminate interface, we propose a model that takes into account the three dimensional and heterogeneous nature of the interface. This model is based on the wall effect notion, a classical notion in granular mechanics [10].



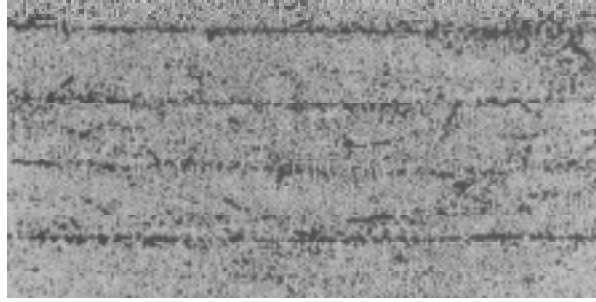


Fig.1: Laminate micrographic section (S. I. Anderson and K. Nielsen, ECCM 5 1992)

**Wall Effect Comments**

The wall effect allows us to demonstrate the fiber specific spatial distribution in the vicinity of a contact surface. In the case of a laminate, the contact surface can be a layer whose reinforcements are oriented differently to the studied layer or the composite fabric mould wall.

Let  $\Omega'$  be a longitudinal surface of a layer, parallel to the wall  $\Omega$ , Fig. 2. In full mass, by unit area of this surface  $\Omega'$ , the fiber section area  $S_f$  and the resin one  $S_r$  are in the same proportion as the volume rates ( $S_f + S_r = V_f + V_r = 1$ ).

If  $\Omega'$  and  $\Omega$  are too close in comparison with the fiber diameter, the surface fiber fraction  $S_f$  becomes insignificant compared to the resin fraction  $S_r$  ( $S_f \ll S_r$ ).

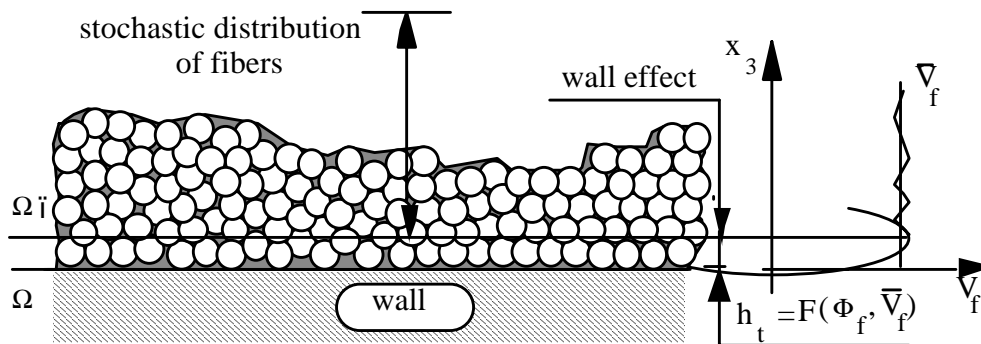


Fig. 2: Definition of the wall effect and the transition area

In contact with the wall, by a geometrical effect, the layer enriches in resin and sufficiently far from the wall by a distance equal to the fiber diameter  $\Phi_f$ , we find the full mass composition, the fiber rate is then equal to its average value  $\bar{V}_f$ . This description explains for example the external appearance of the moulding manufactured composite.

**Transition Behavior Law**

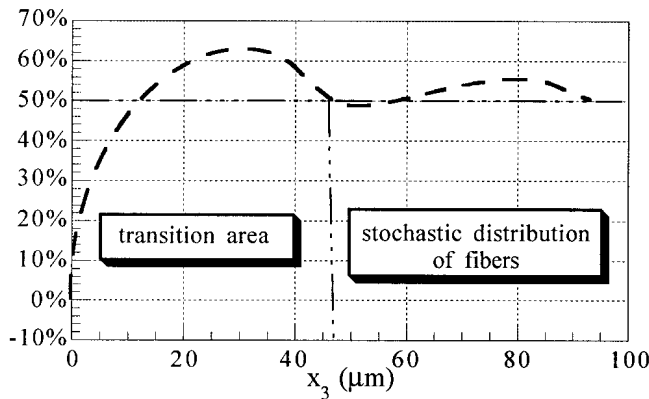


Fig. 3: Fiber rate distribution along the thickness  
 ( $\bar{V}_f = 50\%$ ,  $\Phi_f = 20 \mu m$ )

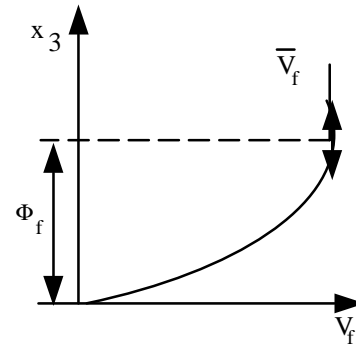


Fig. 4: Theoretical evolution of  $V_f$

The study of volume fraction of the resin is based on the definition of a representative volume (or slice) of a periodic fiber arrangement whose width corresponds to the periodicity.

Therefore, we quantify the volume fraction of the fibers in the region situated between the plan  $\Omega'$  and the wall  $\Omega$ . We show that the distribution according to  $x_3$  depends, for a given arrangement, on the diameter and the average volume rate of the fibers in the layer.

The curve, Fig. 3, represents this distribution in the case of an hexagonal fiber arrangement. In numerical simulations, we have retained an evolutive fiber distribution in a reduced zone whose thickness is equal to the fiber diameter, Fig. 4.

The elasticity tensor of the transition region,  $C_{ijkl}$ , is then obtained by a classical homogenisation technique [9]. It appears as a function of  $x_3$  due to the  $x_3$  evolution fiber rate, linking up with the behaviors of the adjacent layers, Fig. 5.

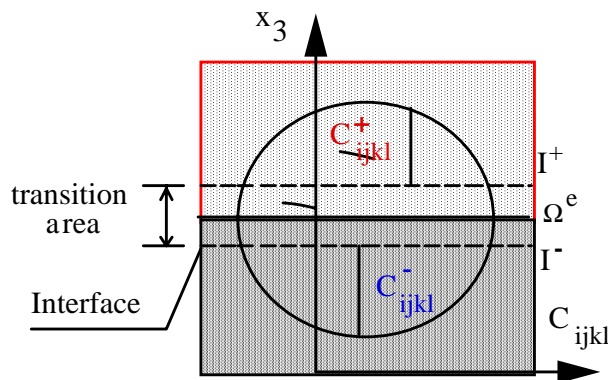


Fig. 5: Evolutive behavior law

## NUMERICAL STUDY

The laminate studied is made of 4 elementary unidirectional layers,  $(0^\circ, 90^\circ)_s$ , with the same thickness,  $h$ , Fig. 6. The layers are transversely isotropic with the following characteristics :

$$E_{11} = 38250 \text{ MPa} ; E_{22} = E_{33} = 9200 \text{ MPa}$$

$$G_{23} = 3135 \text{ MPa} ; G_{13} = G_{12} = 3770 \text{ MPa} ; \nu_{12} = \nu_{13} = 0.325$$

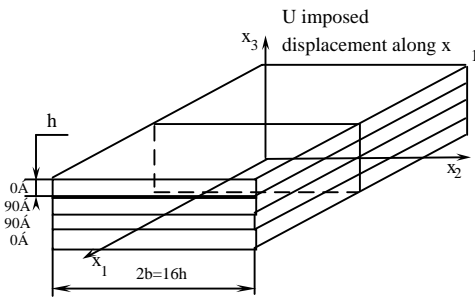


Fig.6 a: Laminate plate  $(0^\circ, 90^\circ)_s$

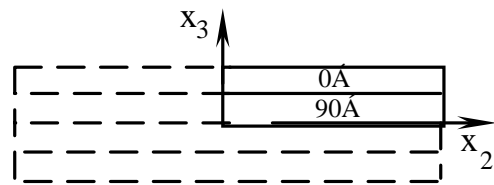


Fig. 6 b: F. E. modeled part

A refined meshing of the plate has been implemented, Fig. 7, using quadratic 20 nodes solid finite elements listed C3D20 on the industrial software ABAQUS.

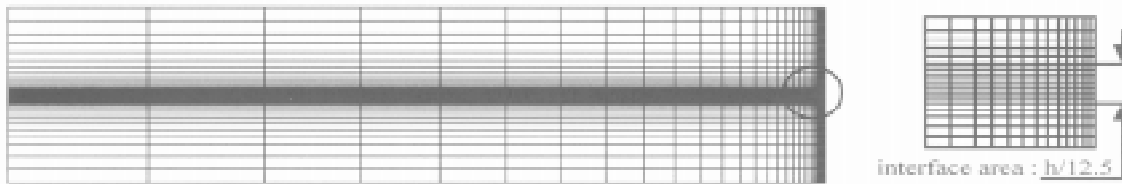


Fig. 7: F. E. meshing

It contains 1200 elements and 26259 degrees of freedom. This specific element permits the introduction of an evolutive law on the thickness.

Two numerical simulation types have been carried out :

- the first corresponds to the classical perfect piecewise approach of the interface, without a transition law, referenced "SLT".
- the second corresponds to the proposed model and takes into account the evolutive transition law identified previously, referenced "LTE".

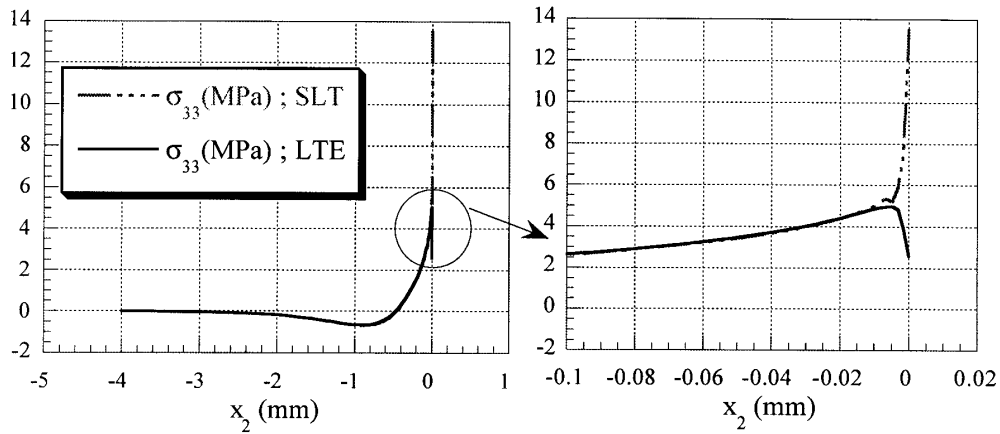


Fig. 8:  $\sigma_{33}$  along the interface with an expansion at the vicinity of the free edge

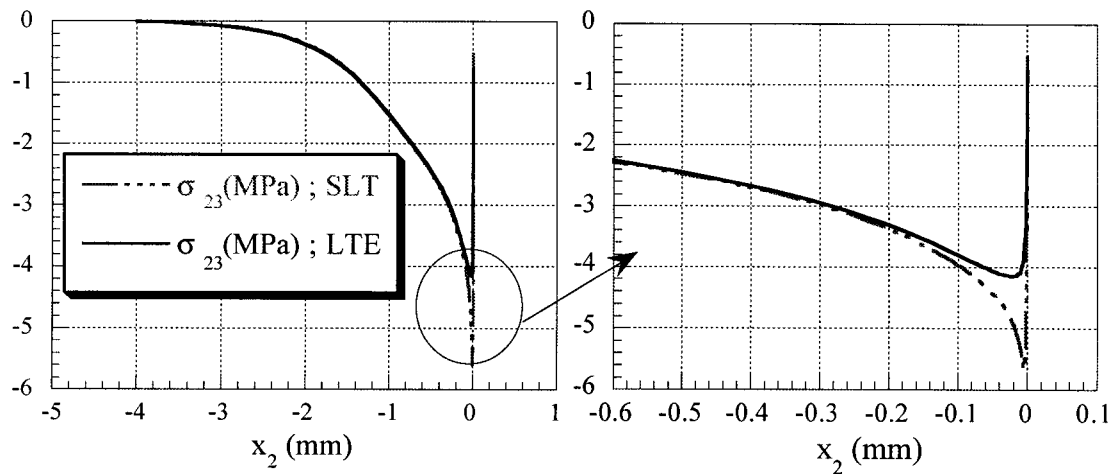


Fig. 9:  $\sigma_{23}$  along the interface with an expansion at the vicinity of the free edge

The results in figures 8, 9, 10 and the expansions associated, show the concentration effect expected of the stresses at the intersection of the free edge and the interface. On the other hand, successive meshing refinements at the interface and the free edge vicinity show the non singular and singular character of the free-edge interlaminar stresses respectively, when using a continuous evolutive behavior interface law and conditions of a classical perfect interface.

So, the taking into account of the fiber specific distribution in the vicinity of the interface leads to more physical stresses [12], which are more appropriate for delamination onset criteria applications.

In addition, this approach allows us to consider a resin interlayer met in some injection manufacturing processes (RTM). Similarly, the existence of transition film at the composite periphery during their manufacturing with kit under pressure can be simulated.

These numerical calculations, undertaken in ABAQUS, have needed a very thin discretization of the interface region. Nevertheless, it is necessary to note that the cost of this approach render it badly adapted to the study of any industrial multilayer; this is why, we have decided to develop a simplified transition element, so as to integrate them in a more industrial meshing, making the approach numerically profitable.

Thus, a first interface model based on asymptotic calculations is established. It permits us to substitute this interlayer discretization for an interfacial law defined on a material surface without thickness. Its numerical implementation in an industrial software code resulted to a representative interface card of a transition layer composed by an adhesive material.

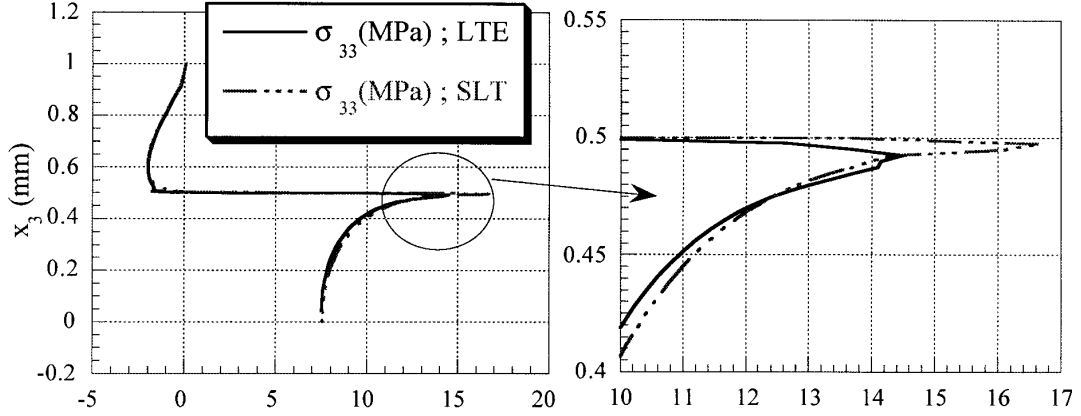


Fig. 10:  $\sigma_{33}$  along the free edge ( $x_2=0$ )

### ASYMPTOTIC INTERFACE LAWS

Using asymptotic development, we seek to replace the very thin interlayer behavior law given in Fig. 5. To make matters simpler, we assume, that it concerns a linear elastic behavior per part that connects with the adjacent layers behavior :

$$C_{ijkl}^e(x_3) = \begin{cases} C_{ijkl}^r + \frac{2x_3}{el} (C_{ijkl}^+ - C_{ijkl}^r) & 0 \leq x_3 \leq +\frac{el}{2} \\ C_{ijkl}^r - \frac{2x_3}{el} (C_{ijkl}^- - C_{ijkl}^r) & -\frac{el}{2} \leq x_3 \leq 0 \end{cases} \quad (1)$$

$C_{ijkl}^r$  represents the elasticity tensor of the resin.  $e$  is a dimensionless number less than 1.  $l$  is a length equal thereafter to  $l$ , which will not affect the general character of the statement. More flexible than the adjacent layers, the interfacial region behavior and particularly the resin one is a function of its dimensionless thickness :

$$C_{ijkl}^r = e \tilde{C}_{ijkl}^r \quad (2)$$

$\tilde{C}_{ijkl}^r$  being a finite entity of the same order as  $C_{ijkl}^+$  and  $C_{ijkl}^-$ .

So, the tensor  $C_{ijkl}^e(x_3)$  becomes for example :

$$C_{ijkl}(y_3) = e \left( 1 - \frac{2y_3}{l} \right) \tilde{C}_{ijkl}^r + \frac{2y_3}{l} C_{ijkl}^+ \quad 0 \leq y_3 = \frac{x_3}{e} \leq \frac{l}{2} \quad (3)$$

and appears as the sum of three different behavior representative terms :

$$C_{ijkl}(y_3) = \tilde{C}_{ijkl}(y_3) e^m \quad (4)$$

where  $m$  successively takes the values  $m=1$ ,  $m=0$ .

The typical studied tensor is then an orthotropic rigidity tensor, function of the expanded variable  $y_3 = x_3 / e$ , the reduced thickness  $e$  and a real power value  $m$ .

We use the asymptotic expansion that consists to research displacements and stresses in the interlayer function of the small parameter  $e$  under the form :

$$\begin{aligned} {}^e U(x_1, x_2, x_3) &= U^0(x_1, x_2, y_3) + e U^1(x_1, x_2, y_3) + \alpha(e^2) \\ {}^e \sigma(x_1, x_2, x_3) &= e^{n_0} \sigma^{n_0}(x_1, x_2, y_3) + e^{n_0+1} \sigma^{n_0+1}(x_1, x_2, y_3) + \alpha(e^{n_0+2}) \end{aligned} \quad (5)$$

$n_0$  depending on  $m$  value.

Displacement and stresses  $({}^e U, {}^e \sigma)$  are solutions of a classical problem with perfect adhesion conditions on the interfaces I+ et I- between the interlayer and the adjacent layers. To this problem, we add a "non-interpenetrability" physical condition :

$${}^e U(x_3 - \xi e) - {}^e U(x_3) = 0 \quad -\frac{e}{2l} \leq x_3 \leq 0 \quad 0 \leq \xi \leq 1 \quad (6)$$

By replacing (4) in these equations, we obtain succession balance equations corresponding to the development orders. At the first order, the resolution of the problem provides the following interface law asymptotically equivalent to transmission conditions through a very thin layer, whose behavior is given by (3).

$$\left\{ \begin{array}{l} \text{if } m \geq 1 \\ \quad [\sigma_{i3}^0] = 0 \\ \quad \sigma_{i3}^0 = k_i [U_i^0] \quad k_i = \frac{1}{\langle \frac{1}{\tilde{C}_{i3i3}} \rangle} \\ \text{if } m < 1 \\ \quad [\sigma_{i3}^0] = 0 \\ \quad [U_i^0] = 0 \end{array} \right. \quad i = 1, 2, 3 \quad (7)$$

$$\sigma_{33}^0 < 0 \Rightarrow [U_3^0] = 0 \quad (8)$$

In these relations  $i$  is not an added sign, the symbols  $\langle \rangle$  and  $[ ]$  respectively designate the thickness averaging  $\langle f \rangle = \int_{-1/2}^{+1/2} f dy_3$  and the jump

$$[f] = f\left(y_3 = +\frac{1}{2}\right) - f\left(y_3 = -\frac{1}{2}\right) = f^+ - f^- \text{ operators.}$$

### Mechanical interpretation of the interface law :

When  $m < 1$ , a case corresponding either to quite flexible or rigid layer, we find perfect transmission conditions.

When  $m < 1$ , a case corresponding to a flexible or a very flexible layer, we obtain interface conditions that permit sliding and decohesion, the stiffnesses  $(k_1, k_2, k_3)$  being respectively the coefficients of elastic sliding and decohesion.

- when these coefficients take infinite values, we find again the transmission law of perfect interface,  $m < 1$ .
- when they take zero values, the interface does not ensure its binding function (stresses transmission at the interface,  $\sigma^0 = 0, m > 1$ ).
- when  $k_1, k_2$  and  $k_3$  take intermediate values, the interface is elastic.
- when the normal stress  $\sigma_{33}$  is negative (crushing), the relation (8) imposes the normal displacement continuity, according to the laying direction.

The interface region plays a role in the global composite system resistance through stiffnesses  $k_1, k_2$  and  $k_3$ , which control the transfer level of stresses.

### NUMERICAL LAW INTERFACE TREATMENT

In this paragraph, we are going to show that previously established interface conditions can be implemented in an industrial software ABAQUS.

- Elementary tests are first undertaken to validate both the interface law on the theoretical aspect and its implementation.
- The interface card has then been used to analyse the influence of a thin flexible interlayer on laminate free-edge effects.

#### Plane strain elementary tensile test :

The test structure is an isotropic plate with an isotropic flexible behavior interlayer, ( $m=1$ ), submitting to a tension displacement loading, Fig. 11.

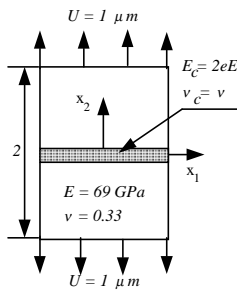


Fig. 11: Elementary test

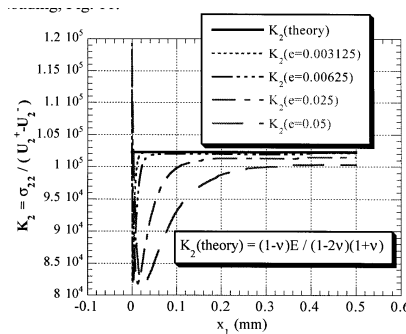


Fig. 12: Normal stiffness (MPa/mm)

A first interface law validation can be made by comparison between explicit stiffnesses obtained analytically by formula (7) to stiffnesses obtained numerically equal to the ratio between the interlayer stresses and the jump displacements, for different decreasing small thickness values. We note that for sufficiently thin thickness, the numerical normal stiffness converges towards the explicit one, Fig. 12. For this simple tensile test sample, it is not possible to obtain numerically the tangential stiffness by discretizing the interlayer, because the sliding and the shear stress vanish in this case.

To see if the interface law correctly restore the stresses and displacements at the interlayer, we have replaced the interlayer by a material surface where we have traduced the interface law using an interface card, elaborating by associating two finite elements in ABAQUS ; a spring finite element, and a contact finite element insuring the "non-interpenetrability" condition and authorising the weak sliding.

We can thus verify in figures 13 and 14, for example, that the interface card, whose results are referenced as "CI", restore the interlayer lateral displacement and the shear stress well that naturally tends to zero in this case.

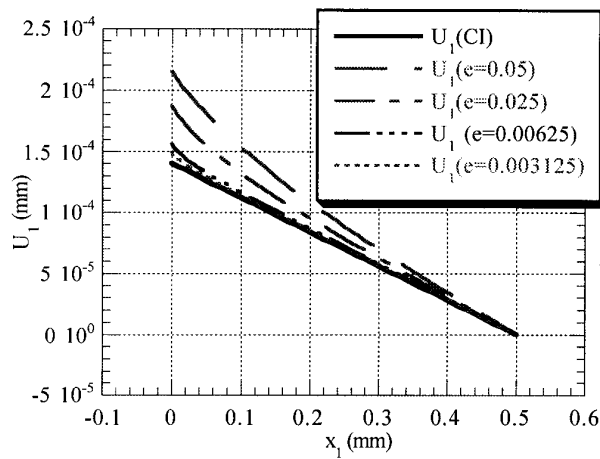


Fig. 13: Interlayer lateral displacement

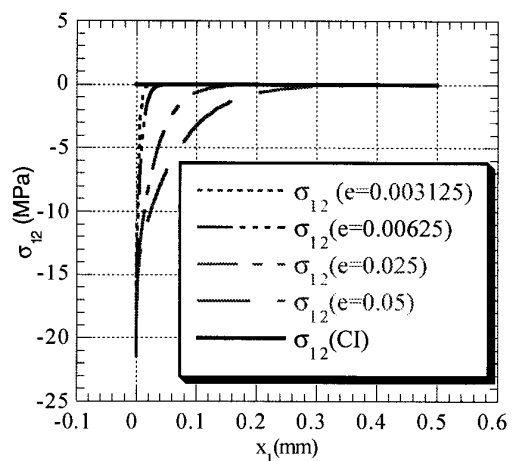


Fig. 14: Interlayer shear stress

Since the law and its implementation are validated, we have then used it to simulate the free-edge effects in a laminate, presenting a thin flexible interlayer.

### Tensile test of a $(0^\circ/90^\circ)_s$ laminate composite

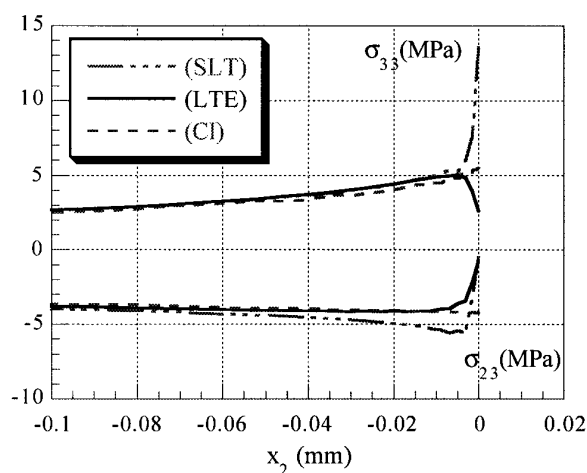


Fig. 15: Interlaminar stresses at the free-edge Vicinity

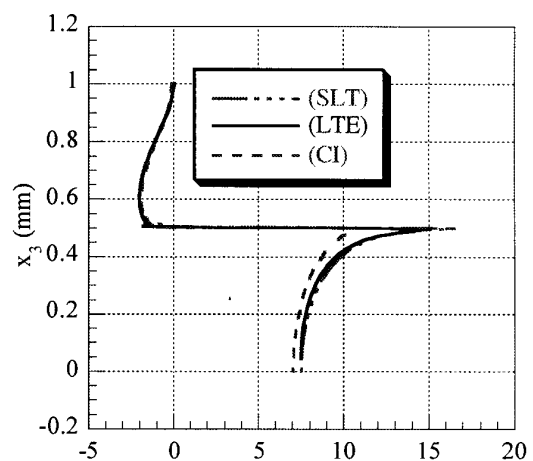


Fig. 16:  $\sigma_{33}$  distribution along the free edge

For this study, we use the same geometrical and mechanical characteristics of the  $(0^\circ,90^\circ)_s$  laminate used previously.



The first important test result undertaken in this part of the work shows that the stresses obtained by the interface card, with a certain degree of approximation representative of a flexible thin layer, are not singular, Fig. 15. These stresses have the same magnitude as the stresses obtained before using a transition evolutive behavior law.

Nevertheless, in Fig. 16, a loss of the free-edge stress gradient intensity can be seen. This can be explained by the flexible character of the interface, whose stiffnesses here correspond to those of pure resin. This is not the case for the evolutive behavior.

In conclusion, the established interface law is representative of a very thin flexible layer. It is defined on material surface and allows us to undertake numerical simulations of thin and flexible layer cheaply. Now, we are working on the global evolutive behavior tensor to establish a representative surface material interface law.

### REFERENCES

1. J. K. Kim and Y. W. Mai, Interfaces in Composites, *Materials Science and Technology*, Volume 13, 1993.
2. F. Erdogan and G. D. Gupta, "Layered Composites with an Interface Flaw", *Int. J. Solids Structures*, 1971, Vol. 7, pp. 1089 - 1107.
3. J. D. Achenbach, H. Zhu, " Effect of Interfacial Zone on Mechanical Behavior and Failure of Fiber Reinforced Composites", *Journal of the Mech. and Phy. of Solids*, vol. 37, 1989, pp. 381-393.
4. N. L. Hancox, "High Performance Composites with Resin Matrices", *Handbook of Composites*, Volume Editors : A. Kelly and S. T. Mileiko, North-Holland, 1983
5. J. L. Billöet, T. Ben Zineb, B. Ben Lazreg, "Surface Transition Effect And Analysis of Free Edge Stresses for Laminated Composite Plates", *Journées Nationales des Composites 9*, France 1994.
6. N. J. Pagano, S. R. Soni, "Models of Studying Free-Edge Effects", *Composite Materials Series, Interlaminar Response of Composite Materials*, Volume 5, Elsevier, 1989.
7. S. S. Wang, "Elasticity Solutions for a Class of Composite Laminate Problems with Stress Singularities", in *Herakovich Hashin Mechanics of composite materials recent advances*, 1983.
8. R. Y. Kim, S. R. Soni, "Experimental and Analytical Studies on the Onset of Delamination in Laminated Composites", *Journal of Composite Materials*, Vol. 18, January 1984.
9. J. Sanchez-Hubert, E. Sanchez-Palencia, "Introduction aux méthodes asymptotiques et à l'homogénéisation", Masson Editeur, 1992.
10. M. Mooney, "The viscosity of Concentrated Suspension of Spherical Particles", *Journal of Colloids and Interface Science*, Vol. 6, p.162, 1950.
11. Z. Hashin, B. W. Rosen, "The Elastic Moduli of Fiber Reinforced Materials", *Journal of Applied Mechanics*. June 1964 - Vol 31 - pp. 223-232..
12. D. W. Oplinger, B. S. Parker, F. P. Chiang, "Edge-Effect Studies in Fiber-Reinforced Laminates", *Experimental Mechanics*, September 1974.

# BEHAVIOR OF GRADIENT DESIGNED COMPOSITE UNDER BALLISTIC IMPACT

Frank K. Ko<sup>1</sup>, Amotz J. Geshury<sup>1</sup>, and John W. Song<sup>2</sup>

<sup>1</sup>*Fibrous Materials Research Center, Department of Materials Engineering  
Drexel University, Philadelphia, PA 19104, USA*

<sup>2</sup>*US Army Natick Research, Development and Engineering Center  
Natick, MA 01760, USA*

**SUMMARY:** A ceramic plate is often added to the surface of the polymer composite backing in order to create a mechanism to destroy the projectile and spread the impact energy. In order to lessen the weight of the hard ceramic face plate and introduce additional energy dissipation and defeating mechanisms, a Gradient Design Composite (GDC) was developed; Ceramic spheres are embedded in a matrix to form a face component while the backing plate is composed of Spectra Shield® composite.

The ceramic spheres have the capability of defeating the projectile similar to ceramic plate. The ballistic limit of a GDC composite is a function of sphere size. The bigger the sphere, the bigger the penetration hole, thus improve the ballistic performance by having more backing materials to participate in absorbing the kinetic energy. Visual examination of the experimental panel shows that the backing material have gone through severe delamination and out-of-plane deformation.

**KEYWORDS:** composite armor, gradient design concept, small arms body armor

## INTRODUCTION

Composite materials have been used successfully as a light weight material for many protective applications under low and high velocity impacts. By proper selection of material systems and design of fiber architecture, it has been shown that a high level of damage containment can be achieved as demonstrated in a compression after impact test [1]. As the velocity of impact and the nature of the impactor changes, as in the case of a very high velocity projectile (~ 3000 ft/s.), a ceramic plate is often added to the surface of the polymer composite backing in order to create a mechanism to destroy the projectile and spread the impact energy over a wide area on the backing plate. Current small arms protective body armor systems used in the U.S. Army frequently consist of a ceramic face backed by fiber reinforced composite. These body armors is used to protect effectively against threats such as .30 caliber type bullets which have a higher and more concentrated energy impact than fragments. In order to lessen the weight of the hard ceramic face plate and introduce additional energy dissipation and defeating mechanisms against the projectile, a Gradient Design Composite (GDC) was developed by a combination of material and geometric hybrid [2].

The Gradient Design Composite - GDC (Fig. 1) is a design concept wherein the material system consists of a harden component, an energy dissipation component and a damage containment component which are organized according to a gradient of varying functions. Ceramic spheres of various sizes are embedded in a matrix of appropriate rigidity to form a face component. The backing plate is composed of fiber reinforced composite with various levels of structural integration.

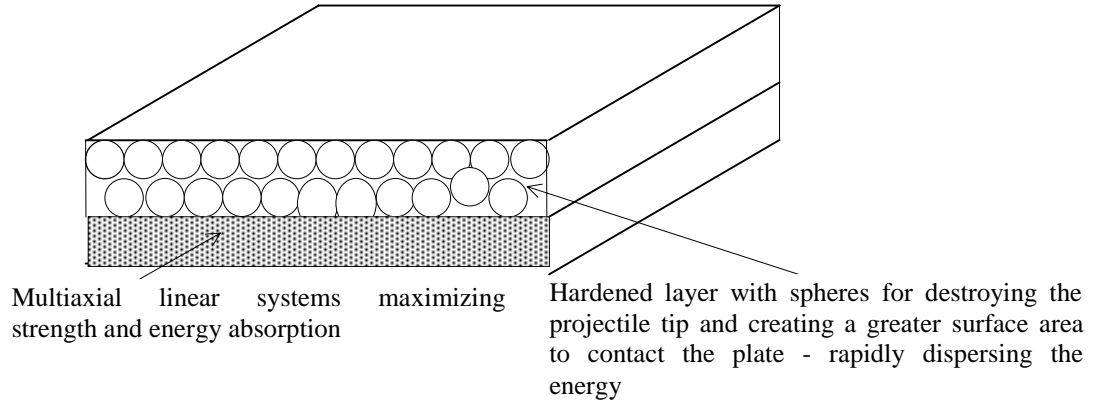


Fig. 1: Gradient design concept for multifunctional ballistic composites

The goal of a recent study [3] was to verify the ballistic protection of Gradient Design Composite (GDC) consist of aluminum oxide ceramic spheres as a hard/facing layer and Spectra Shield® as a backing layer. The target zone for armor protection was: areal density between 6.0 to 10.0 lb/ft<sup>2</sup> and Ballistic protection based on “Military Standard V50 Ballistic Test for Armor, MIL-STD-662E” of 3000-4000 ft/s.

## EXPERIMENTAL WORK

### *Experimental Design*

The experimental design of the research program was aimed to verify the ballistic protection performance of the GDC with areal density between 6.0 to 10.0 lb/ft<sup>2</sup>. A two layer composite armor of a ceramic sphere layer bonded by epoxy and a Spectra Shield backing could be designed with various sphere sizes and thickness of ceramic layer and backing plate offering a range of protection levels. An analytical model developed by Florence [4], was modified and employed for predicting ballistic limit velocities in the experimental design stage.

$$V_{50} = [\sigma_o \epsilon H_b \pi R^2 (1 + \psi) / 0.91 m_p]^{1/2}$$

where, the values used in the computations were the following

$V_{50}$ : the ballistic limit of the armor

$\sigma_o$ : the ultimate tensile strength of the backing plate, 3.0 x 10<sup>9</sup> Pa (Spectra® 1000 fiber tensile strength was used in calculation for estimation of an ultimate strength of Spectra Shield® backing plate.)

$\epsilon$ : the rupture strain of the backing plate, 3.4% (Spectra® 1000 fiber breaking elongation was used in the calculation)

$H_c, H_b$ : the thickness of the ceramic tile and back-up plate, respectively.

$\rho_c, \rho_b$ : densities of ceramics and backing composite materials, respectively; 2610 kg/m<sup>3</sup> for aluminum oxide sphere layer, 3400 kg/m<sup>3</sup> for ceramic tile and 1000 kg/m<sup>3</sup> for Spectra backing layer

$m_p$ : the projectile mass.

$m_t$ : the mass of the target involved in the penetration, varies depending on the thickness of the two layers process,  $m_t = \pi R^2 (\rho_c H_c + \rho_b H_b)$

$\Psi$ : the ratio of  $m_t/m_p$

$R$ : the radius of the zone of the target affected by the impact

$r$ : the projectile radius, 3.81 mm.

A constant impact target zone of  $R=17.5$  mm was used for all the experimental panels. This value is based on previous test information [2]. Fig. 1 shows predicted V50 as function of the weight of the experimental panels. The panels with areal density below 6.0 lb/ft<sup>2</sup> were added to evaluate the backing (Spectra Shield®) only. The experimental panels with areal density above 10.0 lb/ft<sup>2</sup> were added to allow investigation of 3 layer sphere structures. Table 1 provides detailed description and predicted performance of the experimental panels. Spectra Shield® layers varied from 105 to 145. One, two, and three layers of ceramic spheres were used while two sizes of spheres: 7/32" or 1/2". The V50 performance of the panels were predicted to be from around 3000 to 4000 ft/s based on Florence's model [4] in which the value of  $R$ , the radius of the target zone affected by the projectile, used was 17.5 mm for all the experimental panels.

### Materials and Panel Fabrication

Spectra Shield® was provided in roll form [0/90], 54" wide, weighing 3.8 oz/yd<sup>2</sup> or 0.027 lb/ft<sup>2</sup> per ply. The Spectra Shield® prepregs were prepared with Kraton thermoplastic resin, which is a copolymer of styrene and butadiene produced by Shell.

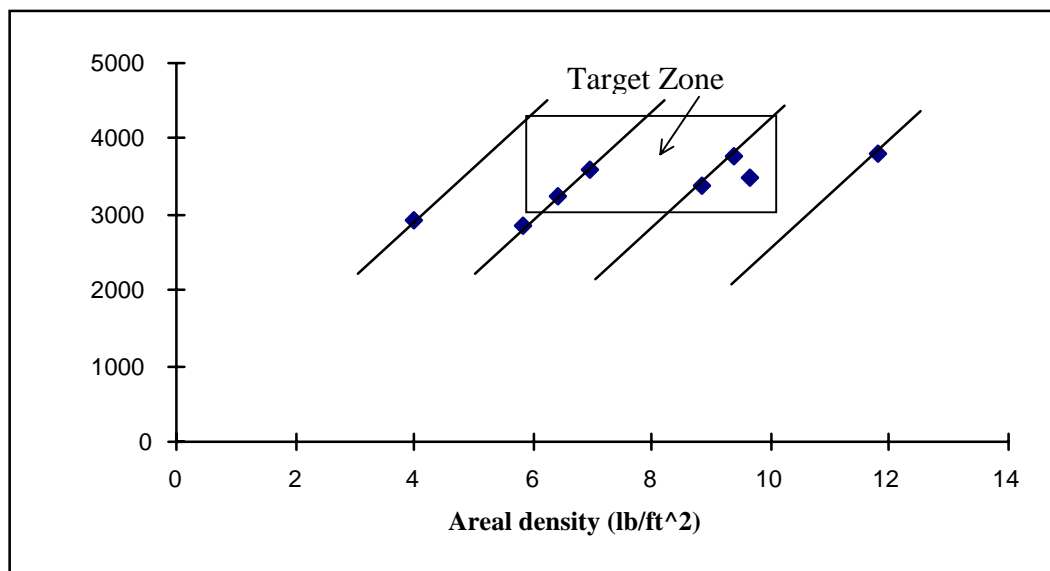


Fig. 2: Experimental panels - predicted V50 vs. areal density

Table 1: Experimental panels - predicted performance

Panel No.	No. of Spectra Shield	Layers Spheres (7/32")	Predicted Areal Density (lb/ft <sup>2</sup> )	Performance V50 (ft/s)
1-3	145	0	3.991	2923
4-6	105	1	5.855	2859
7-9	125	1	6.405	3229
10	145	1	6.956	3593
13	105	2	8.82	3367
16-17	125	2	9.37	3768
22-23	105	1 (1/2")	9.667	3499
27	105	3	11.785	3808

A specially designed steel mold was used to make 12"x12" ballistic testing samples. Dake Hot Press was used for hot pressing the prepregs. Thermocouples were used to monitor the temperature of the upper and lower platens and Frekote 700-NC releasing agent by The Dexter Corporation was used for mold release.

The Spectra Shield® prepregs were stacked to desired number of layers/total areal density using the following empirical equations

$$\text{Thickness of the panel(in)} = N (\# \text{ of plies}) \times 0.0053 \text{ (in, thickness/ply)} \quad (2)$$

$$\text{Areal Density (lb/ft}^2\text{)} = 4.9 \times \text{thickness of the panel (in)} \quad (3)$$

The layers were placed into the hot mold (125°C ) for 20 minutes under constant press of 125 Psi, and observe the temperature of the filled mold maintained at 120°C. Then the panel was let to cool down to 100°C under pressure and removed from the mold.

### Processing of the Sphere/Hard Facing Layer

As mentioned before, in order to see the effect of aluminum oxide spheres size as hard facing plate, two sizes were selected: 7/32" and 1/2", these spheres were fabricated into 1,2 or 3 layers. Fig 3. shows the arrangement of 7/32" ceramic spheres. In the case of 1/2" spheres (panel No. 22 and 23), in order to fill the gaps between the spheres a smaller size (1/8") spheres were added as filler as seen in Fig. 4. The spheres were bonded to each other as well as to the backing material by epoxy (Shell Epon Resin 828 and Shell Epi-Cure 3282). The spheres and epoxy were placed on the bottom of the mold, and then the spheres were evenly arranged and distributed to maximize the packaging density inside the mold. At this stage, a Spectra Shield Panel made by hot press was placed into the mold on top of the sphere mixture. Then the mold was closed, and placed on the press for curing under pressure of 500 Psi. To get the desired mechanical properties, all the assembled armors were post cured under 100°C for 2 hours.

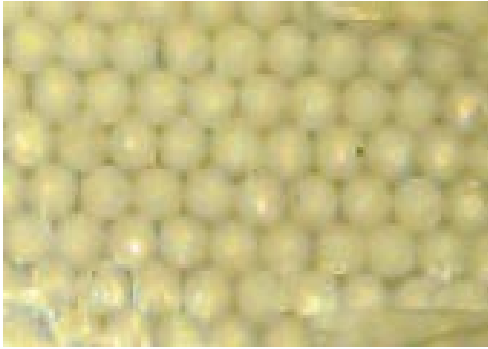


Fig. 3: Arrangement of 7/32" ceramic spheres



Fig. 4: 1/2" spheres and 1/8" spheres as filler

### Panel Properties

Table 2 list the structure and physical properties of the experimental samples that were made for the study.

Table 2: Experimental panels - structure and physical properties

Panel No.	Spectra Layer	Spheres layer/size	Spectra Thickness (in)	Spheres Thickness (in)	Total Thickness (in)	Spectra Weight (lb)	Spheres Weight (lb)	Total Weight (lb)
1	145	0	0.833	-	0.833	3.950	-	3.950
4	105	1/ 7/32"	0.602	0.228	0.831	2.838	3.084	5.92
7	125	1/ 7/32"	0.722	0.227	0.949	3.418	3.088	6.51
10	145	1/ 7/32"	0.838	0.226	1.064	3.975	3.125	7.10
13	105	2/ 7/32"	0.603	0.439	1.042	2.860	5.556	8.416
16	125	2/ 7/32"	0.720	0.452	1.171	3.419	5.446	8.87
23	105	1/ 1/2"	0.607	0.541	1.147	2.885	7.085	9.97
27	105	3/ 7/32"	0.603	0.755	1.358	2.877	8.509	11.386

## RESULTS AND DISCUSSIONS

### Ballistic Testing

Ballistic testing were carried out at H. P. White Laboratory, Inc. in accordance with the "Military Standard V50 Ballistic Test for Armor, MIL-STD-662E". The projectile used for the testing was 7.62 mm M60 Ball type with a lead core encased in a brass jacket. The projectile weighs about 7 to 9 grams. The exact type and weight of the projectile are proprietary information.

A machine gun was used for the firing. The samples were rigidly mounted by heavy duty clamps with the area of impact normal to the line of fire. A witness plate made of 0.002" thick aluminum sheet was located 6 inch behind and parallel to the test sample. Four electronic counter type chronograph measuring devices were used to measure the velocity of the projectile.

One to four shots were fired on each sample. The location of the next shot was selected upon inspecting the target after the previous shot. The normal up-and-down firing procedure was

used. In this study, the ballistic limit V50 is defined as the average of the highest partial penetration velocity and the lowest complete penetration velocity. Table 3 shows the results obtained in the ballistic testing.

In the case of Panel No. 10, and 27, the V50 values were incalculated due to a missing data: either partial penetration or complete penetration information was unavailable. In these cases the high partial or the low complete projectile velocity were chosen to represent the ballistic performance of the experimental panel. Fig. 5 shows the ballistic performance of the GDC panels.

Table 3: Summary of ballistic testing results

Panel No.	Spectra Layer	Spheres layer/size	Average Thickness (in)	Average Weight (lb)	Number of Shots	V50	High Partial	Low Complete
1,2,3	145	0	0.839	3.95	6	2456	2372	2551
4,5,6	105	1/ 7/32"	0.835	5.91	4	2943	2900	3000
7,8,9	125	1/ 7/32"	0.952	6.51	2	3493	3428	3557
10	145	1/ 7/32"	1.070	7.10	2	Incalculable	NA	3560
13	105	2/ 7/32"	1.036	8.40	2	3527	3472	3582
16,17	125	2/ 7/32"	1.176	8.85	2	3583	3549	3617
22,23	105	1/ 1/2"	1.156	9.97	2	3703	3674	3732
27	105	3/ 7/32"	1.302	11.37	2	Incalculable	3794	NA

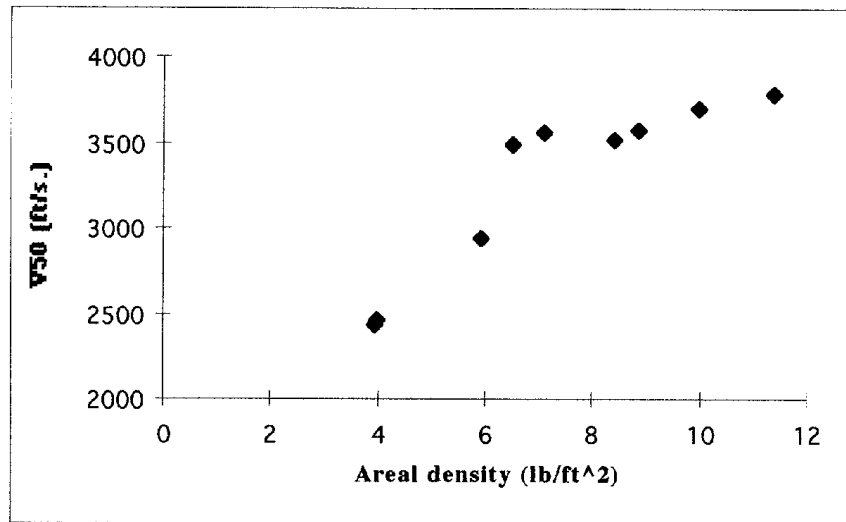
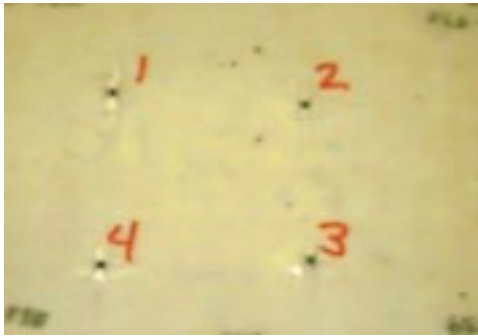


Fig 5: V50 results of the experimental panels

Figures 6-A,B,C,D, and E shows the penetration hole created on the facing (sphere) layer.





*Fig. 6A: Penetration hole panel No. 1 (no spheres)*



*Fig. 6B: Penetration hole panel No. 5 (1 layer)*

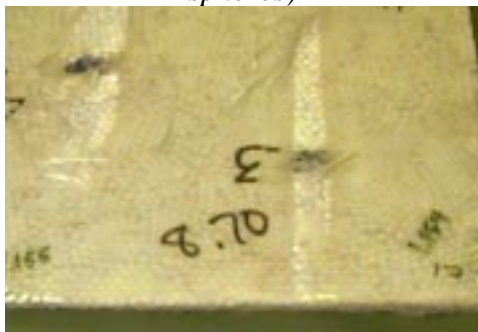


*Fig. 6C: Penetration hole panel No. 17 (2 sphere layers)*

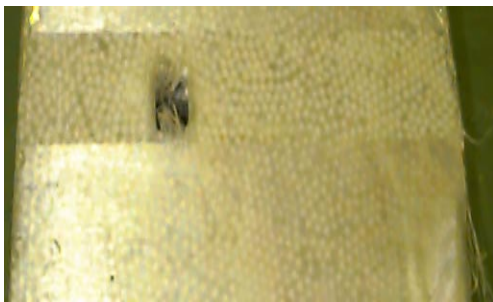


*Fig. 6D: Penetration hole panel No. 27 (3 layers)*



*Fig. 6E: Penetration hole panel No. 23 (1/2'')*

Table 4 contains information regarding the size (diameter) of the penetration hole from the front and the thickness of the Spectra Shield<sup>®</sup> layers that did not showed evidence of delamination (pre-delamination thickness). These results shows the direct relationship between the sphere size and sphere layers on the front penetration hole. Fig. 6 illustrated the relation between the number of sphere layers and the size of the penetration hole. There are no evidence that the Spectra Shield<sup>®</sup> layer - the backing layer influence the size of the penetration hole.

Fig. 7 - A and B shows typical delamination and Out-of plane deformation of the Spectra Shield<sup>®</sup> layer as observed from the back side of the experimental panels after the ballistic testing. Taking into the consideration the difficulties in measuring and averaging the intact layer (as reported in Table 5) it is clearly evident that the bigger the penetration hole size, the delimitation region start earlier due to decrease in the projectile velocity.



Table 4 Penetration hole and pre-delamination thickness

Panel No.	Spectra Shield®	Spehers layer/size	Penetration Hole Diameter Size (mm)	Pre-Delamination Thickness inch/number of layers
1,2,3	145	0	4.66	0.551/104
4,5,6	105	1/ 7/32"	15.58	0.353/67
7,8,9	125	1/ 7/32"	14.99	0.384/72
10	145	1/ 7/32"	14.36	0.532/100
13	105	2/ 7/32"	23.14	0.260/49
16,17	125	2/ 7/32"	20.92	0.369/70
22,23	105	1/ 1/2"	35.18	0.230/43
27	105	3/ 7/32"	27.71	0.468/88



Fig.7: Typical Delamination and Out-of plane deformation of the Spectra Shield®  
 A - Panel No. 2 and B - Panel No. 16

### COMPARISON OF RESULTS WITH PREDICTION

Experimental V50 as well as the predicted V50 based on Florence's model of the experimental panels are listed in Table 5. Only the experimental panels with both facing/sphere layer and backing/Spectra Shield® layer are listed. The last column in Table 5 shows the difference between the experimental V50 and the predicted V50 (% Difference = (V50 Experimental - V50 Predicted)/V50 Experimental). It is clear that the modified Florence model with several simplifying assumptions provide a good prediction regarding the ballistic velocities at the experimental design stage. However, when measuring R - the radius of the zone of the target affected by the impact and recalculate V50 values based on the penetration hole size as listed in Table 5 a totally different values for V50 are obtained. Table 6, lists the predicted V50 from Florence's model based on:

- cone radius from previous study (R=17.5mm)
- actual measured value of the cone radius.

Table 5: V50 -Experimental vs. Prediction

Panel No.	Spectra Layer	Spheres layer/size	V50 Experimental	V50 Predicted	% Difference
4,5,6	105	1/ 7/32"	2943	2859	+2.8
7,8,9	125	1/ 7/32"	3493	3229	+7.6
10	145	1/ 7/32"	Incalculable <3560	3593	-0.9
13	105	2/ 7/32"	3527	3367	+4.5
16,17	125	2/ 7/32"	3583	3768	-5.2
22,23	105	1/ 1/2"	3703	3499	+5.5
27	105	3/ 7/32"	Incalculable >3794	3808	-0.3

In order to overcome the above limitation, it is suggested to try and introduce a geometric factor into Florence's model. The geometric factor could provide a link between the material and geometric parameters of the ceramic spheres and the ballistic limits. more experimental results are needed to explore the values of this suggested factor and relay them with the spheres size, shape and packaging.

Table 6: V50 - 2 Predictions

Panel No.	Spectra Layer	Spheres layer/size	V50 Predicted R=17.5 mm	Actual R	V50 Predicted R=actual
4,5,6	105	1/ 7/32"	2859	7.79	792
7,8,9	125	1/ 7/32"	3229	7.50	834
10	145	1/ 7/32"	3593	7.18	862
13	105	2/ 7/32"	3367	11.57	1632
16,17	125	2/ 7/32"	3768	10.46	1539
22,23	105	1/ 1/2"	3499	17.59	3536
27	105	3/ 7/32"	3808	13.86	2494

## CONCLUSIONS

The ceramic spheres have the capability of defeating the projectile similar to ceramic tiles as evident by the flattening of the projectile. The fracture cone radius varied according to the sphere radius and energy dissipation was through the breaking up of the ceramic spheres and failure of the backing composite by shearing, fiber cutting and extensive delamination. The ballistic limit of a GDC composite is a function of sphere size. The bigger the sphere, the bigger the penetration hole, thus improve the ballistic performance by having more backing materials to participate in absorbing the kinetic energy. Visual examination of the experimental panel after the ballistic testing shows that the backing material (Spectra Shield® composite) have gone through severe delamination and out-of-plane deformation.

## ACKNOWLEDGMENTS

The authors thank US Army Soldier systems Command, Natick RD & E Center for sponsoring the study.

## REFERENCES

1. Ko, F. K., Three dimensional Fabrics for Composites, in Textile Structural Composites, edited by Chou, T.W. and Ko, F.K., pp. 129-171, Elsevier Science Publishers B.V., Amsterdam 1989.
2. Ko, F.K., Yu, J.Z., and Song, J.W., Characterization of Multifunctional Composite Armor, Proceedings of the American Society for Composites, Atlanta, GA. October 8, 1996.
3. Ko, F.K., Geshury, A., and Song, J.W., Multifunctional Composite Armor - Phase II, Final Report to be submitted to U.S. Army Natick.
4. Florence, A.L., Interaction of Projectile and Composite Armor, Part II, Stanford Research Institute Report, AMMRG-CR-69-15, 1969.

# HYPERVELOCITY IMPACT DAMAGE TO COMPOSITE MATERIALS

R. C. Tennyson and G. D. Shortliffe

*University of Toronto Institute for Aerospace Studies  
4925 Dufferin Street, North York, Ontario, Canada, M3H 5T6*

**SUMMARY:** This paper describes an experimental program undertaken to study the impact damage of laminated graphite/PEEK plates and cylinders subjected to particle impacts at velocities ranging from 3 to 7 km/s. This velocity range corresponds to that found in space due to impacting micrometeoroids and space debris (MOD). To assess this problem, impact tests were conducted at three facilities in the U.S., with most of the tests undertaken at the NASA Johnson Space Center in Houston, using their two-stage light gas guns. Aluminum spheres were fired at composite material targets using various diameters and velocities to determine the damage correlation with energy, laminate thickness and material properties. Flat plate targets were first investigated to establish damage thresholds, followed by tests on laminated cylinders characteristic of the robot arm structures being designed for the Space Station. This paper presents the results of these studies showing the correlations found in terms of impact crater size, front face total damage, rear face spallation damage and secondary damage resulting from the ejecta plume impacting the rear wall of the cylinder.

**KEYWORDS:** hypervelocity impact damage, composite materials, orbital debris, design.

## INTRODUCTION

Spacecraft in low Earth orbit (LEO) are vulnerable to impact damage resulting from collisions with micrometeoroids and orbital debris (MOD). Micrometeoroids originate naturally from planetary or asteroidal collisions and cometary ejecta. Although there is no particular direction in which micrometeoroids approach the Earth, spacecraft experience a bias in the direction of travel (known as the RAM direction). This can readily be seen from the impact distributions measured on the NASA Long Duration Exposure Facility (LDEF) which spent almost six years in space. Figure 1 presents this data for impacts arising from the MOD environment and it is quite apparent that the RAM direction recorded significantly more impacts, although it is noteworthy that even the back surface was hit as well. Artificial space debris consists of everything from spent satellites and rockets to aluminum oxide fuel particles, paint chips and fragmentation objects from collisions of these bodies in orbit. A plot of the MOD environment as a function of altitude and particle size is shown in Fig. 2. Although micrometeoroids have been a design issue since the 1960's, concern about the rowing amount of orbital debris did not receive serious attention until the mid-1980's. The problem has grown to such an extent that the probability of impact by space debris exceeds that due to micrometeoroids in some cases. There is currently an astounding  $2.5 \times 10^6$  kg of debris in LEO. Since first entering space in 1957, almost 20,000 objects have been launched with approximately 7,000 still in orbit.

Polymer matrix composites are used extensively in spacecraft structures and components, such as antenna struts, panels and low distortion frames. The largest composite structure in space is the Canadian robot arm on all of the Space Shuttles. A much more complex robot system consisting of graphite/PEEK tubes is currently being assembled for the Space Station Remote Manipulator System. Although these materials provide significant advantages in terms of high specific stiffness and strength, as well as low thermal expansion properties, the problem of MOD impact damage needs to be addressed.

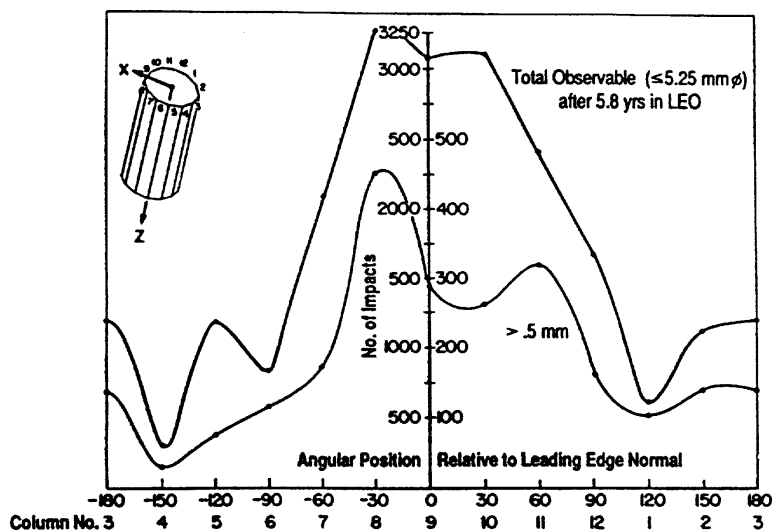


Fig. 1: Circumferential distribution of micrometeoroid/debris impacts on LDEF (NASA M&D/SIG Rept; Aug. 1990).

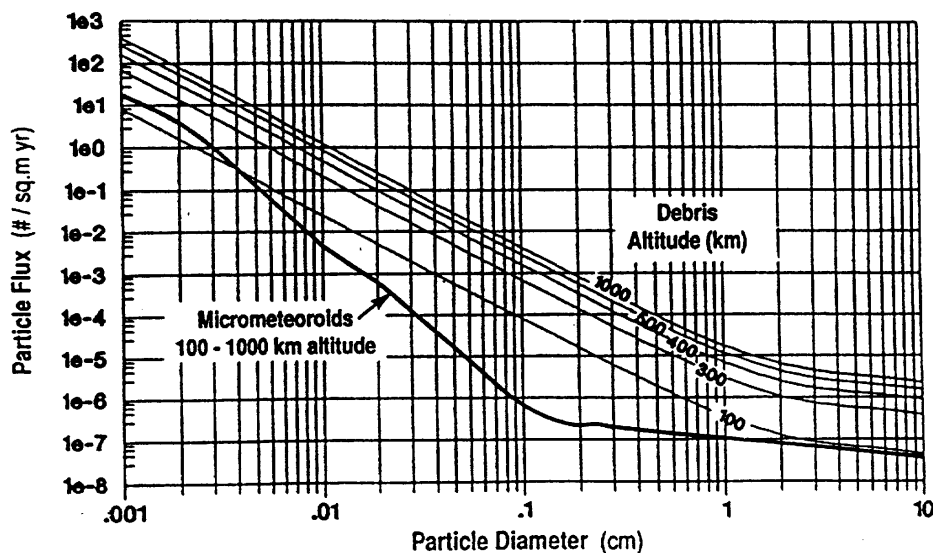


Fig. 2: Micrometeoroid and orbital debris flux vs. particle size as a function of altitude (NASA CR#BB000883A, Jan. 1991).

Very few studies have been conducted on MOD hypervelocity impact (HVI) damage to polymer matrix composites. Some of the earlier work on graphite/epoxy plates includes that done by Yew et al [1] (identified in graphs as “Austin” data) at the NASA Johnson Space Center in 1986 using two of their light gas guns to achieve hypervelocity impact conditions. A wide range of plate thicknesses was investigated using quasi-isotropic lay-ups.

A more detailed series of tests was reported by Christiansen in 1988 [2] (identified in graphs as “Eagle” data) in which both low and high modulus graphite/epoxy plates and tubes were studied. Again, various target thicknesses were used and different impact angles were employed. It was observed that fiber modulus has a greater effect than lay-up. Christiansen developed two impact damage models based on this data for energies above and below 150 J. Lower energy impact data on both graphite/epoxy and PEEK plates were reported in [3] (identified as “Auburn” data) but the range of test parameters was very restricted.

The following report presents the results of a series of tests on PEEK/IM7 and PEEK/AS-4 flat plate and cylinder laminates of varying thickness and lay-ups conducted at the NASA Johnson Space Center (JSC” data), the Southwest Research Institute (“SwRI” data), and the NASA Marshall Space Flight Center (“MSFC” data) using their two-stage light gas guns.

## EXPERIMENTS

### Test Set-Up

A series of flat plates (primary target) were tested in these facilities with a second plate (secondary target) located about 33 cm behind the primary impact plate. The purpose of the second plate was to determine the ejecta damage emanating from the first wall impact and assess the extent of rear wall penetration and overall structural degradation (i.e., loss in stiffness and strength). All tests were conducted with aluminum impactor spheres of varying diameter and at different velocities. Energies ranging from 2 to 2000 J were investigated. In the following graphs, results from other test programs are also included for comparison purposes. A summary of our test data is presented below in Table 1.

*Table 1: HVI shot matrix performed on graphite/PEEK composite*

Shot Id	Configuraton	Primary Target		Secondary Target		Projectile		
		Thickness [mm]	Layup	Thickness [mm]	Layup	Diameter [mm]	Velocity [m/s]	Energy [J]
JSC #1	PEEK & Al proj. (0 deg.)	2.7	(+/-43)s	0.5	(0,90)s	1.5	6.05	90.6
JSC #2	PEEK & Al proj. (0 deg.)	2.0	(0,+/-45,90)s	1.9	(0,+/-45,90)s	2	6.75	267.2
JSC #3	PEEK & Al proj. (0 deg.)	1.8	(0,+/-45,90)s	2.0	(0,+/-45,90)s	3	6	712.5
JSC #4	PEEK & Al proj. (0 deg.)	0.5	(0,90)s	0.5	(0,90)s	1.5	7	121.2
JSC #5	PEEK & Al proj. (0 deg.)	2.9	(0,+/-45,90)s	2.9	(0,+/-45,90)s	2.5	6.98	558.0
JSC #6	PEEK & Al proj. (0 deg.)	2.7	(+/-43)s	2.0	(0,+/-45,90)s	2	7.2	304.0
JSC #7	PEEK & Al proj. (0 deg.)	2.7	(+/-43)s	1.9	(0,+/-45,90)s	2.5	6.85	537.4
JSC #8	PEEK & Al proj. (0 deg.)	2.9	(0,+/-45,90)s	1.9	(0,+/-45,90)s	2.5	6.21	441.7
JSC #9	PEEK & Al proj. (0 deg.)	1.0	(0,+/-45,90)s	0.9	(0,+/-45,90)s	2	5	146.6
SwRI #1	PEEK & Al proj. (0 deg.)	0.5	(0,90)s	0.5	(0,90)s	1	6.82	20.9
SwRI #2	PEEK & Al proj. (0 deg.)	0.9	(0,+/-45,90)s	1.0	(0,+/-45,90)s	1	7.27	23.8
SwRI #3	PEEK & Al proj. (0 deg.)	2.9	(0,+/-45,90)s	2.9	(0,+/-45,90)s	1	7.18	23.2
SwRI #4	PEEK & Al proj. (0 deg.)	0.4	(0,90)s	0.5	(0,90)s	0.4	6.26	2.0
SwRI #5	PEEK & Al proj. (0 deg.)	1.9	(0,+/-45,90)s	1.9	(0,+/-45,90)s	1	7.18	25.8
SwRI #6	PEEK & Al proj. (0 deg.)	1.9	(0,+/-45,90)s	1.9	(0,+/-45,90)s	0.4	7.3	2.7
SwRI #7	PEEK & Al proj. (0 deg.)	1.0	(0,+/-45,90)s	1.0	(0,+/-45,90)s	0.4	7.07	2.5
MSFC #1	PEEK & Al proj. (0 deg.)	0.9	(0,+/-45,90)s	0.9	(0,+/-45,90)s	4.0	6.57	1978

A subsequent series of tests on composite cylinders were performed using the 0.50 Cal two-stage light gas gun at the Johnson Space Center. The gun is equipped with a Cordin high-speed camera system, capable of snapping 2.25 million frames per second of the projectile impact and the debris cloud formation processes. The cylinder targets were 30 cm long, 33 cm in diameter and 2.7 mm thick. Aluminum spherical projectiles, 3.18 mm to 9.13 mm in diameter, travelling at velocities ranging from 6.4 km/s to 6.91 km/s, were used in all of the experiments. Only normal impacts were performed. The test results for this series are summarized below in Table 2.

Table 2: HVI database for the composite cylinder targets.

Target Shot Id	Projectile			Damage
	$D_p$ [mm]	$V$ [km/s]	$E$ [J]	$D_c^*$ [mm]
#1	3.18	6.4	961	8.5
#2	5.16	6.8	4646	13.2
#3	5.95	6.91	7396	14.3
#4	9.13	6.56	24007	18.3
#5	9.13	6.56	24009	18.4
#6	9.13	6.55	23937	18.2

\*The equivalent circular diameter ( $D_c$ ) represents the diameter of a circle which encompasses the same area as the irregularly-shaped crater hole or damage area.

## HYPERVELOCITY IMPACT (HVI) TEST RESULTS

### Entry Crater Damage

The entry crater model derived from the HVI data is presented in Fig. 3. It is based on a functional relationship between the observed entry crater diameter,  $D_c^*$  (mm), and an energy

parameter  $\sqrt[3]{E \frac{t}{D_p}}$ , where  $E$  is the projectile's kinetic energy (Joules),  $t$  is the target thickness (mm), and  $D_p$  is the projectile diameter (mm). This parameter was first introduced by Christiansen [2] for use with composites, and is reused in this report with similar success.

Although other test data for graphite/epoxy materials are included, the model is fitted with a regression line, forced to pass through zero, which only considers those data points involving PEEK matrix targets, impacted with aluminum or glass spherical projectiles.

Each entry in the legend of the graph provides four distinct pieces of information. A legend entry consists of a data point marker, the test series alias, the type of target material (carbon fibre/PEEK or GRE), and the type of projectile material (aluminum, glass, or nylon). For example, a legend entry such as : "■ JSC PEEK (Al)" implies that solid squares on the graph represent data points for the "JSC" test series using PEEK based composite targets. The projectiles used in the experiments are aluminium spheres.

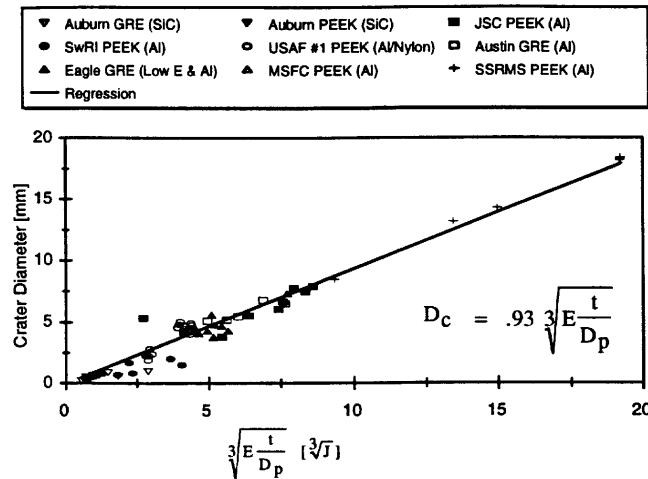


Fig. 3: Entry crater model.

The functional relationship is given by,

$$D_c = .93 \sqrt[3]{E \frac{t}{D_p}} \quad (1)$$

The model is generally applicable to PEEK and epoxy matrix based composites. The carbon fibres used all have a modulus in between 135 and 235 GPa. Applicable laminate thicknesses range from 0.5 mm up to 6.7 mm. The model is independent of laminate lay-up. It is consistent for a broad range of projectile diameters, extending from 0.4 mm to 9.13 mm, travelling at velocities ranging from 4 to 7.5 km/s. Aluminum, glass, and nylon projectiles are compatible with the model.

### Total Entry Damage

From a design point of view, the entry damage on the front face is more critical since it includes the crater hole and associated damage to the laminate. Entry damage, as defined by the equivalent diameter method, is plotted in Fig. 4 as a function of the same energy parameter. Included in this plot is the regression curve based on C-scan measurements of the sub-surface damage zones. It can be seen that even though the delamination lies below the surface, the enhanced area is only about 20% greater than the surface area. The entry damage area can be estimated from measuring the crater area, based on the equivalent diameter method, using the formula:  $Entry\ Area = 20 \times Crater\ Area$ .



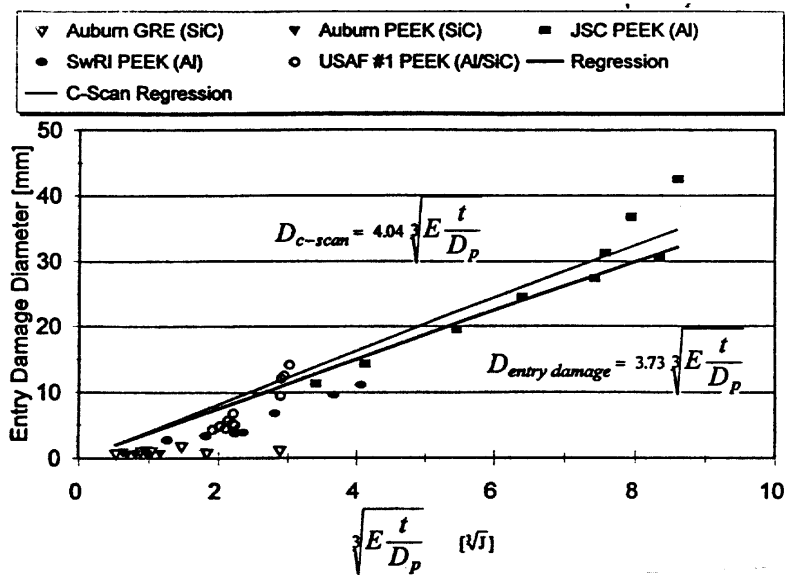


Fig. 4: Entry damage diameter vs.  $\sqrt[3]{E \frac{t}{D_p}}$ .

Rear face spallation damage on the primary impact plate was also measured, the results of which are plotted in Fig. 5. The regression analysis indicates that the damage area is comparable to that observed on the front face for a given energy parameter.

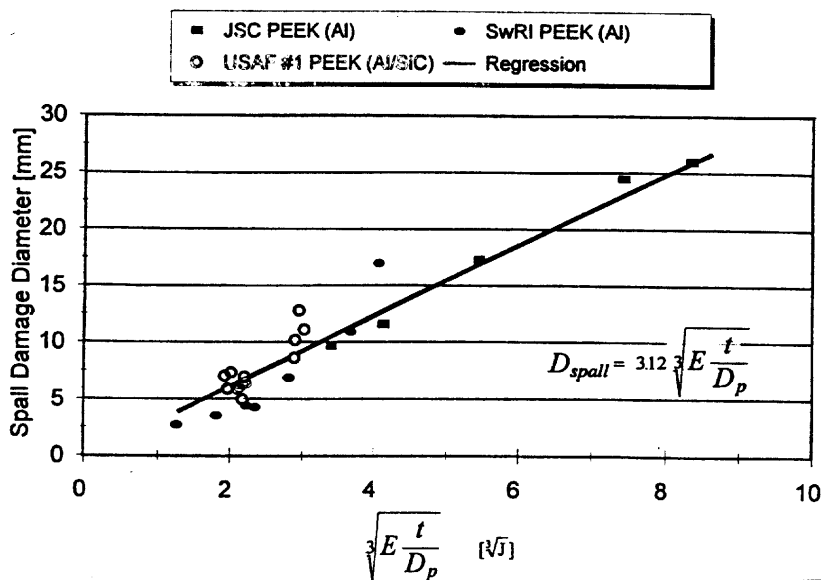


Fig. 5: Spall damage diameter vs.  $\sqrt[3]{E \frac{t}{D_p}}$ .

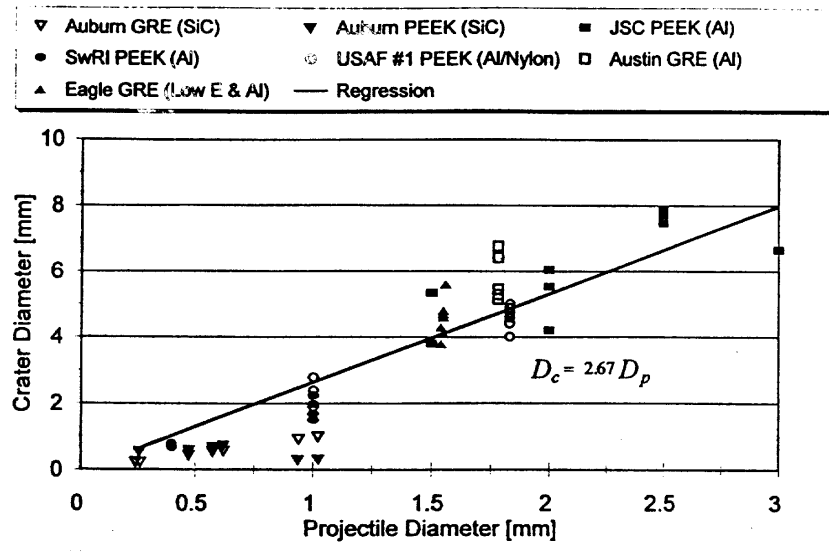


Fig. 6: Crater vs. projectile diameter.

A plot of the crater diameter as a function of the projectile diameter is shown in Fig. 6. The regression curve was constructed only through the PEEK data, excluding the nylon cylinder results. There appears to be no energy dependence for the range of parameters studied. Interestingly, one can see that the nylon results correlate with the curve quite well, although the sub-millimeter SiC particle impact data do not agree at all. Generally, one can assume that for hypervelocity impacts for particles greater than 1 mm in diameter, the crater hole size produced will be about 2.7 x the projectile diameter. Below this threshold, it would appear that the hole diameter can be taken as equal to the particle diameter.

## SECONDARY DEBRIS PLUME DAMAGE

Considerable effort was made to investigate the debris plume size and corresponding damage to the rear plate. The debris plume is composed of impactor fracture particles and delaminated spallation particles. Based on detailed mapping of the debris impact sites (see Fig. 7), the primary debris plume cone angle was measured for flat plates. These results are plotted in Fig. 8 and demonstrate a consistent angle of about 11.6°.

The next series of experiments using the composite cylinders produced some valuable insight into the debris and ejecta cloud processes. The Cordin high-speed camera is capable of snapping approximately 80 frames of the target over the entire impact process, for an elapsed time of about 100  $\mu$ s.

They depict the progression of the intact projectile, the initial impact, the formation of the debris cloud, and finally, the rejection of ejecta out the front surface of the cylinder. An excerpt of the footage produced in the #4 experiment is shown in Fig. 9. In the first frame, the incoming projectile can be seen just prior to impacting the surface of the cylinder. In the subsequent frames, the formation of the secondary debris and ejecta clouds is clearly apparent. Analysis of the debris cloud velocity reveals that the cloud tip travels at approximately the same velocity as the projectile.

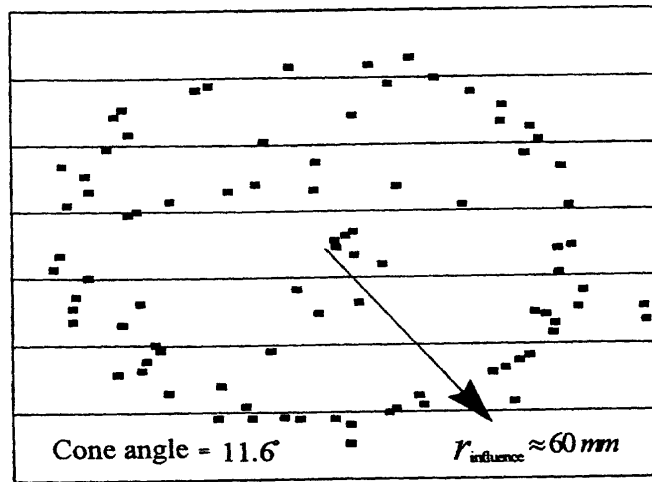


Fig. 7: 87 distinct craters catalogued.

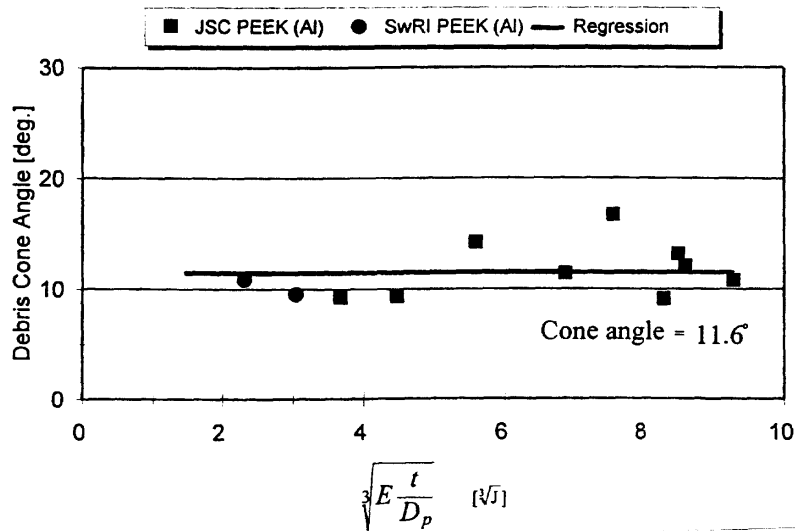


Fig. 8: Debris cone angle vs.  $\sqrt[3]{\frac{E \cdot t}{D_p}}$ .

The energetic debris clouds generated in shots #4 and #6 completely destroyed the rear wall of the cylinder, as can be seen in Fig. 10. The photographic analysis, combined with post impact visual observations of the cylinders, yields a debris cloud cone angle of,

$$\theta_{dc} \approx 17^\circ \tag{2}$$

where  $\theta_{dc}$  represents the 100 mm cutout radius of holes from the debris cloud. For the cylinders tested, the damage zone was about 200 mm in diameter. This is more than the 11.6°

previously found during the flat plate tests. The vastly higher impact energies involved may contribute to the wider debris cloud spread.

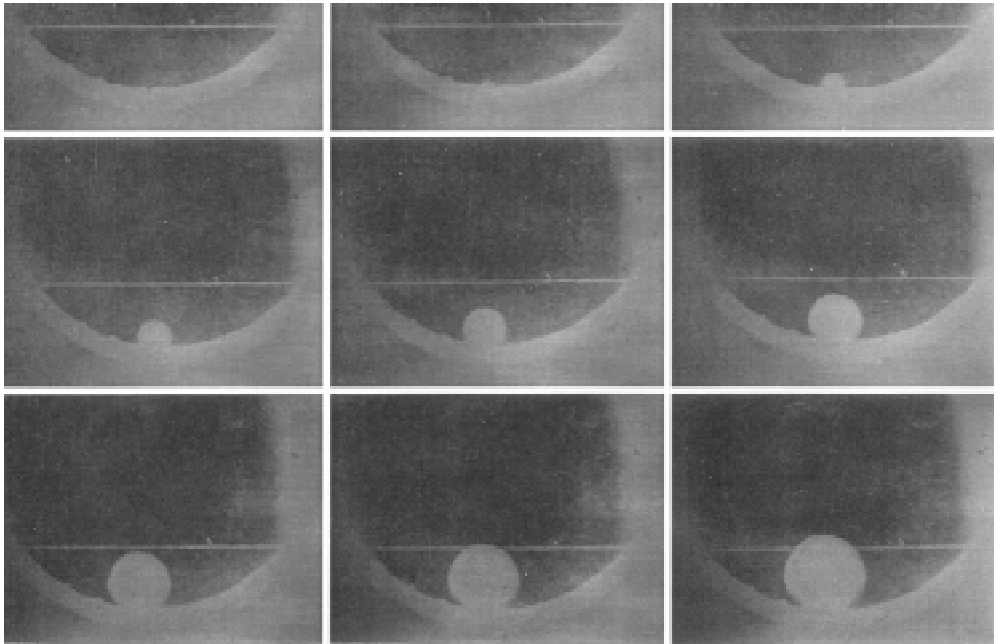


*Fig. 9: High-speed photography of the impact process in model #4.*

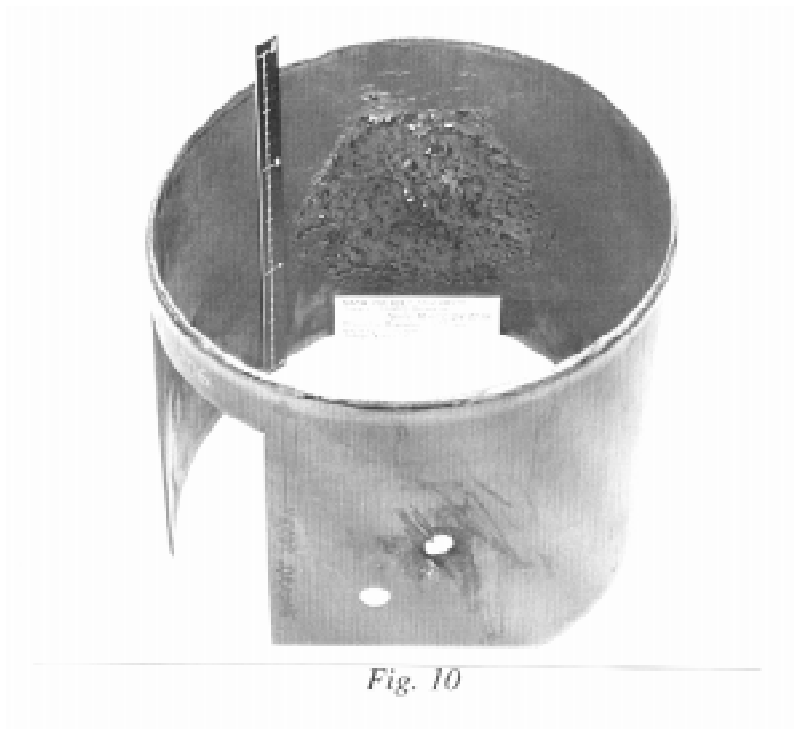


*Fig. 10*

### **STRUCTURAL FAILURE ASSESSMENT**

In the design of a composite structure for spacecraft applications, there are two apparent failure modes which must be considered:

1. An energetic MOD fragment creates a large crater and surrounding damage area, causing structural failure.
2. An energetic secondary debris cloud destroys a larger area of the rear wall of an enclosed composite structure (such as a cylinder).

The first scenario, structural failure of the cylinders due to a large entry crater, is highly unlikely, due to the improbability of encountering a large enough MOD particle. However, the fracture damage from the debris plume is sufficiently large in area to cause a major reduction in structural stiffness and buckling strength. For example, the effect of a 200 mm diameter 'cutout' on the buckling strength of a cylinder is shown in Fig. 11. Strength reductions of the order of 52% and 61% were found for compression ( $F_x$ ), torsion ( $M_x$ ) and bending ( $M_y$ ) loading, respectively.

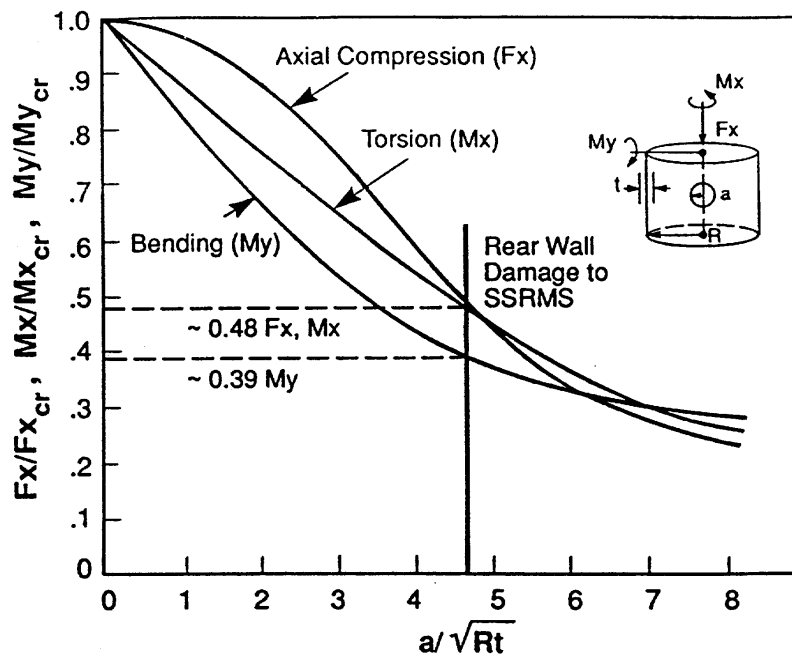


Fig. 11: Effect of cutouts on reduction of buckling strengths.

## CONCLUSIONS

As part of this study, two dozen HVI experiments were conducted using flat plate and cylindrical sections of PEEK matrix based composites. Many parallel studies were uncovered which had investigated HVI response in similar composites. All of these experiments were amalgamated to form an extensive HVI database specific to carbon fibre PEEK and epoxy based composites.

From the database, an entry crater damage model was produced. The entry crater diameter was found to be functionally dependent on a defined energy parameter,  $\sqrt[3]{E \frac{t}{D_p}}$ , over a wide range of target thickness, lay-up, fibre and matrix material, as well as projectile diameter,

velocity, energy, geometry, and composition. In general, the crater diameter can be modelled by the relationship  $D_c = .93 \sqrt[3]{E \frac{t}{D_p}}$ .

The initial projectile impact produces a secondary debris cloud of high energy projectile and target fragments. The debris cloud cone angle, which spans the radius of influence attributable to debris cloud damage, was estimated to be 17°, as observed during tests on the cylinders. The secondary debris cloud is capable of producing severe damage to any spacecraft composite component lying in its path.

### **ACKNOWLEDGMENTS**

The authors wish to acknowledge the financial support of the Institute for Space and Terrestrial Science, an Ontario Centre of Excellence, the Canadian Space Agency, and Spar Aerospace Ltd., for their in-kind support of this project. Special thanks to J. L. Crews, E. Christiansen, J. Kerr of NASA JSC, and A. Nolan of NASA MSFC for their assistance and use of their hypervelocity impact test facilities. Without their willing assistance, this project would not have been possible.

### **REFERENCES**

1. Yew, C. H., Yang, C. Y., and Crews, J., "A Phenomenological Study of the Effect of Hypervelocity Impacts on Graphite-Epoxy Plates," Engineering Mechanics, University of Texas at Austin and NASA JSC, 1986.
2. Christiansen, E. L., "Investigation of Hypervelocity Impact Damage to Space Station Truss Tubes," *Journal of Impact Engineering*, Vol. 10, 1990.
3. Tennyson, R. C., "Debris and Micrometeoroid Impact Damage on Spacecraft Materials and Structures," Final Report, Canadian Space Agency, Contract No. 9F011-3-1372/01-XSD, March 1994.

# RESULTS FROM TESTING OF THE HELICOPTER TAIL ROTOR BLADE MADE OF COMPOSITE LAMINATED MATERIALS AFTER BALLISTIC DAMAGES

**Boško Rašuo**

*Aeronautical Department, Faculty of Mechanical Engineering,  
University of Belgrade, 27 Marta 80, 11000 Belgrade, Yugoslavia*

**SUMMARY:** This paper presents the analysis of the dynamic behavior of a heavy transport helicopter tail rotor blade made of composite laminated materials after ballistic damage made by the bullet of 7.9 mm caliber shoulder weapons. Penetrating damages made in the root part of the tail rotor blade spar have been analyzed. The blades have been made of composite laminated materials.

The test program for the tail rotor helicopter blades has included dynamic testing non-damaged and damaged blades in full-scale. Based on the results of vibratory testing and fatigue testing an assessment is made about the vulnerability and the survivability of the heavy transport helicopter tail rotor blade made of composite laminated materials after ballistic damage made by the bullet of shoulder weapons.

**KEYWORDS:** vibratory and fatigue characteristics, ballistic damages, survivability

## INTRODUCTION

Survivability is one of the essential technical properties of the state-of-art aircraft materials. The aircraft ability to survive even after being exposed to severe damages on vital and load-carrying parts of the aircraft constructions is an imperative for combat but civil aircraft as well.

Helicopters are given special attention in this analysis as they are rather specific, highly vulnerable and greatly exposed to threats due to their vertical take-off and landing, low speed and flight altitudes etc.

In respect to survivability, composite laminated materials show the best behavior and results if compared to the other materials that are nowadays used in aviation. [1-3].

This paper presents the analysis of the dynamic behavior of a heavy transport multipurpose helicopter tail rotor blade (Figs. 1 and 2) before and after ballistic damages caused by 7.9 mm caliber shoulder weapons that may occur as a consequence of combat as well as terrorist actions.

First of all a non-damaged tail rotor blade behavior was analyzed by exposing the blade to static and dynamic loads in extreme flight conditions; after that the blade was exposed to the long-lasting dynamic loads with an aim to define fatigue characteristics; and finally, following the same testing program, the blade behavior was analyzed but after penetrating damages on its most vital load-carrying part i.e. at the root of the spar (Figs. 3 and 4). For

each of these tests identical special blades made in technologically the same way, in the same two-parts metal die were used [4].

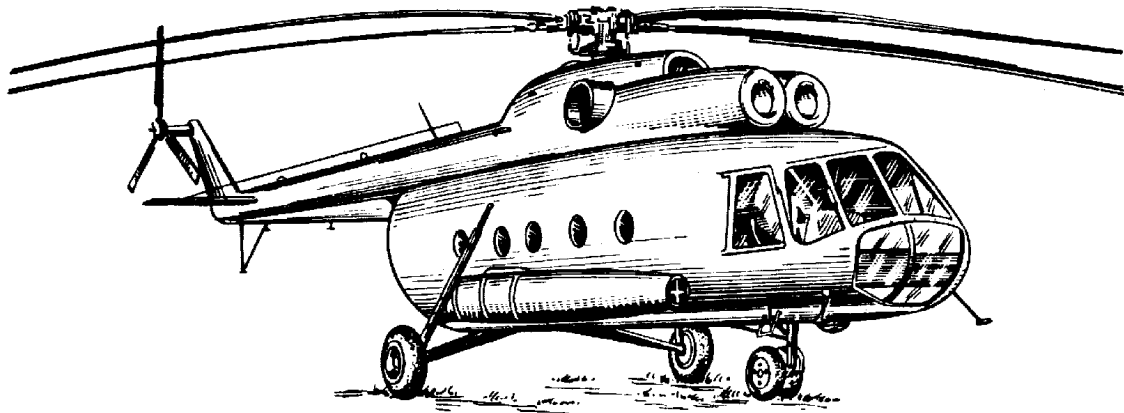
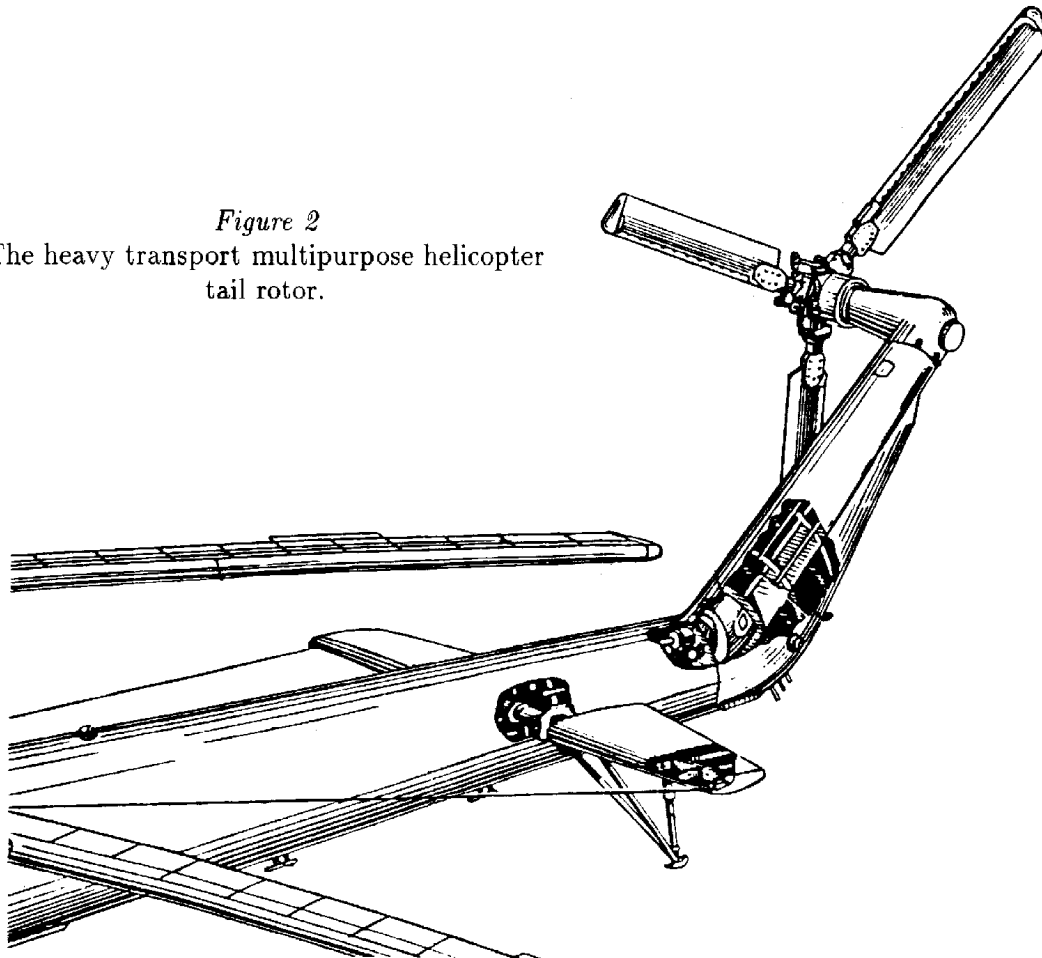


*Figure 1* The heavy transport multipurpose helicopter.

*Figure 2*  
The heavy transport multipurpose helicopter  
tail rotor.



In the tail rotor blade manufacturing procedure the conventional composite materials with epoxy resin matrix, fiberglass filament spar and 18-section laminated fabrics skin of fiberglass filament, some carbon filament embedded along the trailing edge, a foam core,



leading edge protection strips polyurethane, etc. were used [4]. All the used materials are standard products fabricated at Ciba-Geigy Interglas-Textil GmbH, Torayca and others.

The vibratory test program included experimental determination of the natural oscillation modes and the tail blade natural frequency as well as its structural damping. On the other hand the fatigue test program included: interlaminar separation (delamination) testing and geometric deformation of the blade cross-sections following the fatigue tests program during which real tail rotor blade loads were simulated - the same loads to which blade is exposed under extreme flight conditions, before and after ballistic damages of the blade [5,6].

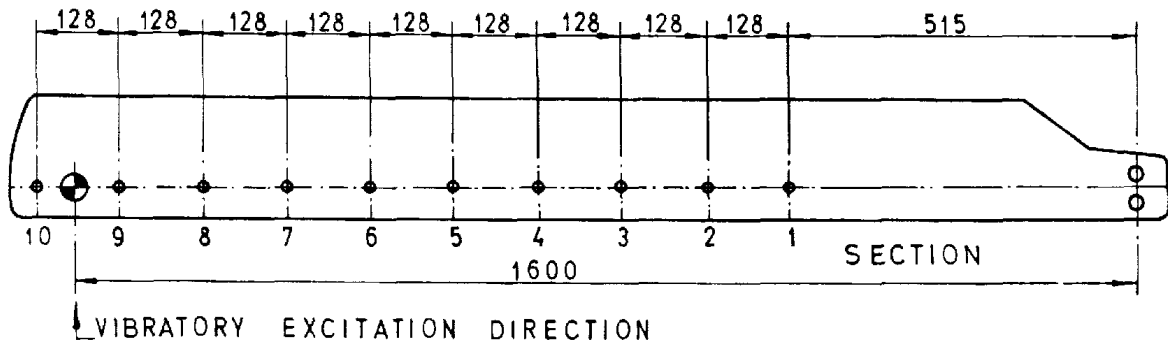


Figure 3 Measurement points in vibratory testing.

All the tests on the helicopter tail rotor blade were performed at the Belgrade University, Faculty of Mechanical Engineering, Aeronautical Department Laboratory.

### EXPERIMENTAL PROCEDURE AND RESULTS

The main objective of the testing that was to be done on non-damaged and damaged helicopter tail rotor blade was to verify experimentally the level of the blade survivability which is defined through degradation degree of its vital mechanical characteristics after ballistic damage. Bearing in mind the stochastic nature of damages and their respective influence on total blade load carrying ability, on this occasion only one particular case was analyzed: damages on the most vital load carrying part of the blade, i.e. on the root of the spar (Figure 4). The resulting damage together with its in-going and out-going penetration presents a vital structural damage on the load carrying part in the area usually exposed to heaviest loads.

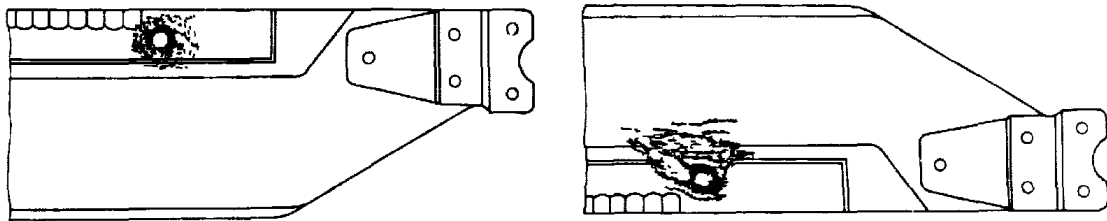


Figure 4 The Helicopter tail rotor blade made of composite laminated materials after ballistic damage made by the bullet of 7.9 mm caliber shoulder weapons, in-going (left) and out-going (right) penetration.

The program and the way in which these investigations were carried out on both tail rotor blades represents a standard practice followed by majority of scientific and research aeronautical institutions [5-7].

### Vibratory testing

The aim of the tail rotor blade vibratory testing was to define the basic aeroelastic properties of the blade. This testing included determination of the natural oscillation modes and natural frequency of the structure in oscillations, as well as defining of the blade structural damping.

In the course of the tail rotor blade attachment vibratory testing program, a very robust facility frame made of steel *U* and *L*-profiles tied together with screws was used (Figure 5). Several control measurements were performed with an aim to check the rigidity of the frame and its eventual interference in the course of the experiment itself. At the beginning the model frame frequency characteristics were measured, and then a new load of about 500 kg was added to the frame and new measurements were carried out. The results in both measurements coincided which meant that the rigidity of the frame was absolutely satisfactory, proving that its influence on the measurement could be neglected.

All the elements used in these testing are shown in the flow-chart diagram, Figure 5. There it can be clearly seen that all the elements were divided into two functional sections. The first one was composed of excitation apparatus while the second one was made of response-detection equipment. Measuring points were placed along the elastic axes of the blade in the same order as shown in Figure 3.

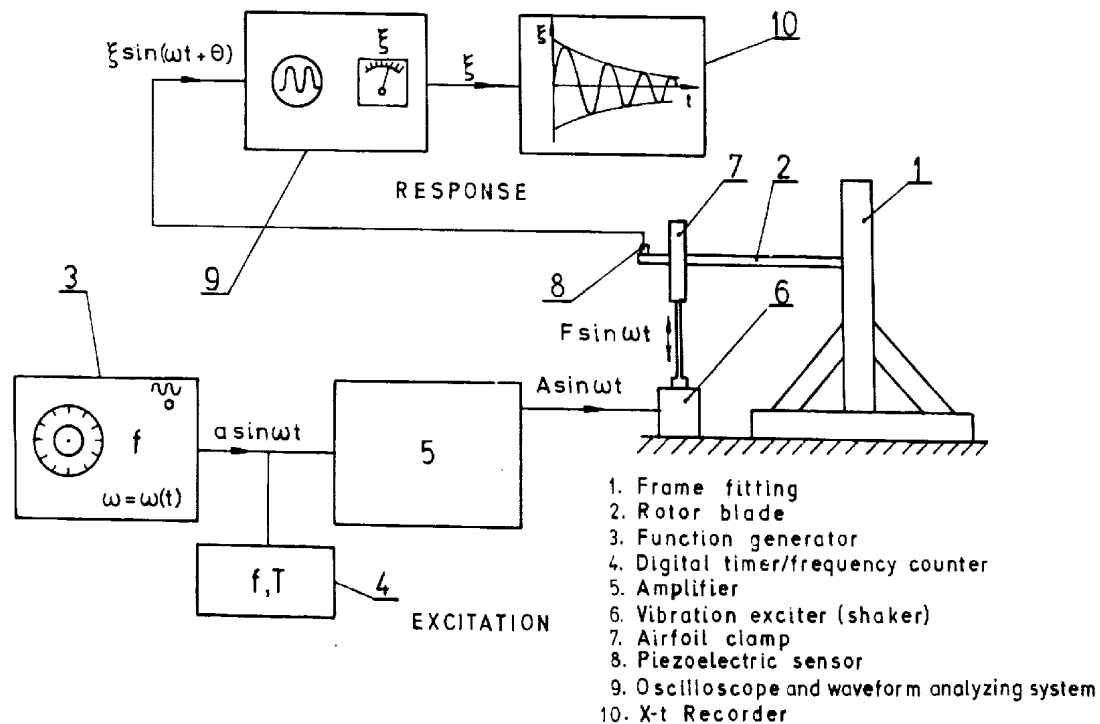


Figure 5 Employed equipment in vibratory testing.

The excitation apparatus consisted of a pulse generator, a signal amplifier, a digital timer/frequency counter, a vibration exciter (shaker) and an airfoil clamp; while the response detection group was made of: piezoelectric accelerometers, oscilloscope with voltmeters and a multichannel X-t recorder. This equipment was made by *Robotron* and *Philips*.

A pulse generator with a sinusoidal excitation function and with a precise adjusting of frequency set-point value in a range from 0.01-10 000 Hz was used in this experiment. A digital frequency counter was used for precise read-out of excitation frequency. The vibration

exciter was an electrodynamic one which is also considered to be the most suitable for harmonic analysis and this type of experiment. The link between the vibration exciter and the rotor blade was formed of a rigidly tied aluminum alloy pipe with adjustable length and by use of a panel airfoil clamp which was shaped so as to fit the rotor blade cross-section at the location of application of excitation. For displacement measurement in these investigations the piezoelectric accelerometers (pick-ups) were used and they measured displacements at selected points on the blade as shown in Figure 3. A special kind of cement was used to provide a close link between the pick-up and the blade in the course of measurement.

As a first step within these investigations a harmonic analysis for both tail rotor blade types was performed. Having determined the frequencies for the first-four harmonic's natural (resonant) modes of oscillations, displacement vectors for the first-four basic oscillation modes were measured. Some measurement results are shown in Figures 6 and 7. Figure 6 shows the harmonic analysis results of the first-four oscillation harmonics for the non-damaged tail rotor blade, while Figure 7 gives us a comparative presentation of the second oscillation mode for both non-damaged and damaged tail rotor blade.

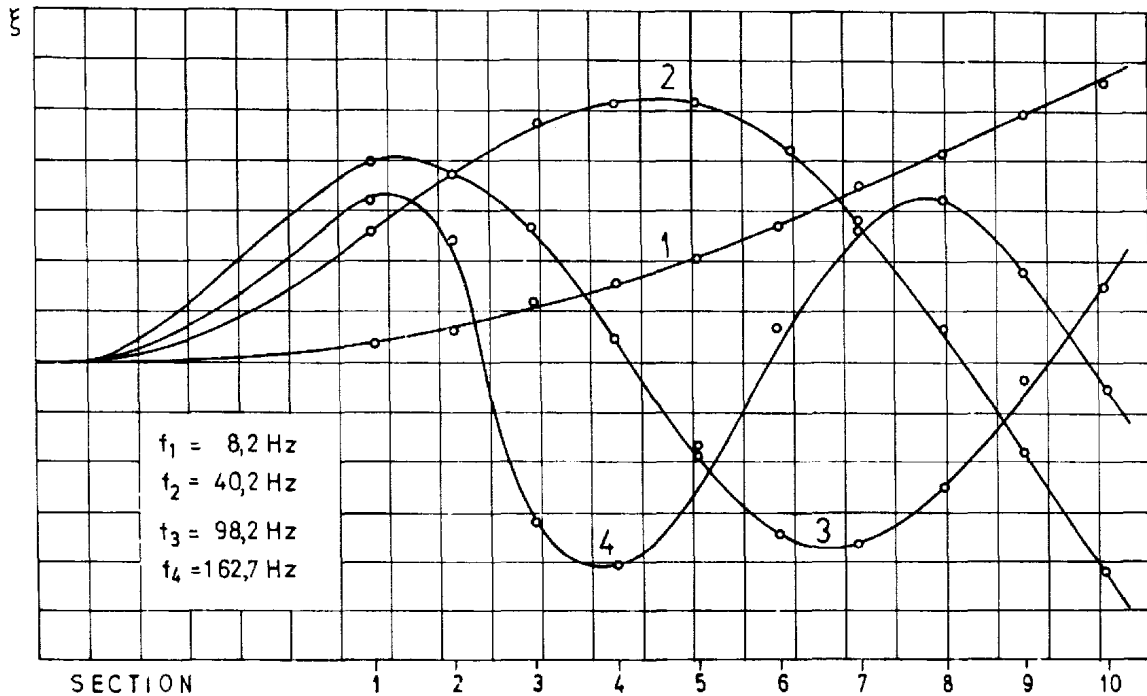


Figure 6 Natural modes of oscillation for the non-damaged tail rotor blade.

Tail rotor blades' structural damping was determined from amplitude reduction of free vibrations. At first the blades were excited to vibrate with the first basic (resonant) oscillation mode with gradually decreasing amplitude due to the damping effects of the structure. The original records obtained from these tests for non-damaged and damaged tail rotor blade at the measured cross-section 10 with time base 1 s/cm are shown in Figure 8.

The logarithmic decrement of the free vibrations was utilized to characterize the structural damping diagram (Figure 8). Its value is determined as:

$$\delta = \frac{1}{n} \ln \frac{x_k}{x_{k+n}} \tag{1}$$

where  $n = 10$  is the number of observed oscillations,  $x_k$  is observed initial amplitude in the

time interval, whereas the correspondent average value of amplitude is:

$$x_n = \frac{1}{2}(x_k + x_{k+n}) \quad (2)$$

$Q$ -factor is also usually used to define the structural damping and it gives relative energy ( $E$ ) reduction in successive oscillations.  $Q$ -factor is defined as

$$Q = \frac{E_1}{E_1 - E_2} \approx \frac{1}{2\delta} \quad (3)$$

The structural damping results for the non-damaged tail rotor blade expressed by the logarithmic decrement and  $Q$ -factor are given in Figure 9.

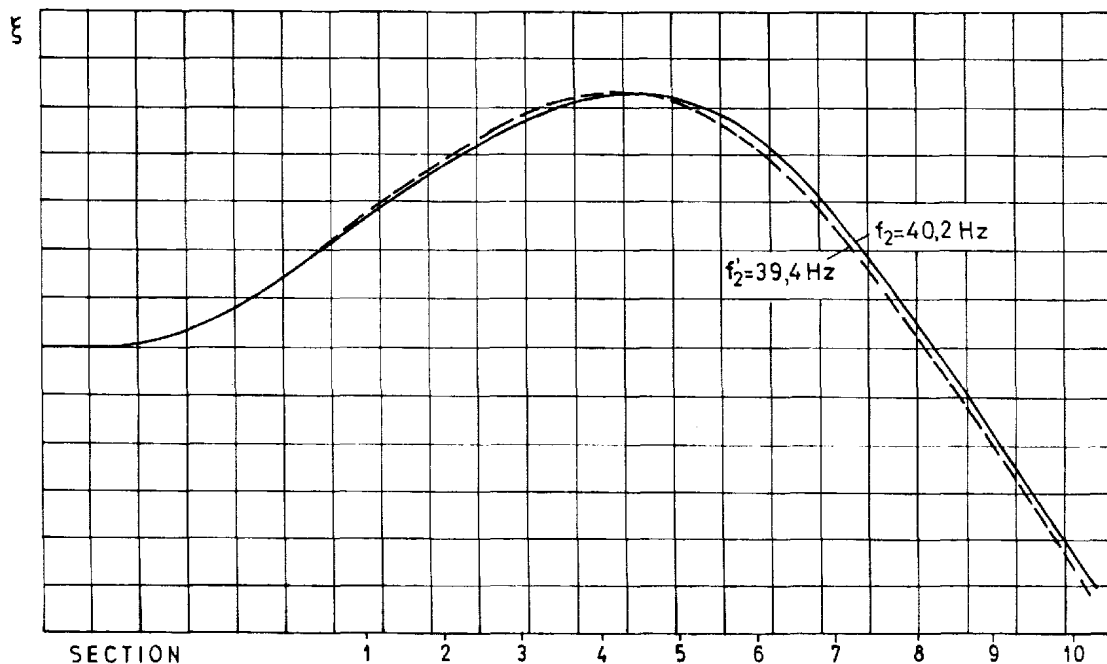


Figure 7 The second oscillation mode for both non-damaged ( $f_2 = 40.2 \text{ Hz}$ ) and damaged ( $f'_2 = 39.4 \text{ Hz}$ ) tail rotor blade.

### Fatigue testing

Fatigue testing of the root part of the blade spar is one of the most important investigations of the helicopter blades made of composite laminated materials in respect to their load carrying ability and survivability check-ups. These tests are carried out with an aim to define eventual delamination of the composite laminated structure, changes of shape of the root part of the blade and the loss of its load carrying ability after having been exposed to a certain cycle of alternating variable loads which, on their part, are a consequence of the inflight combined load influence. The applied test loads include simulated steady centrifugal, vibratory chordwise bending, vibratory flapwise bending, and vibratory torsional pitch motion.

The simulated forces' values were: the centrifugal force  $11\,350 \text{ daN}$ , while resulting excitation alternating variable load that was vertical to the rotation plane and originated from vibratory chordwise bending, vibratory flapwise bending and vibratory torsional pitch motion had the value of  $500 \text{ daN}$  at the  $6.5 \text{ Hz}$  ( $390 \text{ rpm}$ ) frequency and at the angle of attack

of 18°. A special facility frame (Figure 10) was constructed to simulate these combined and heavy loads.

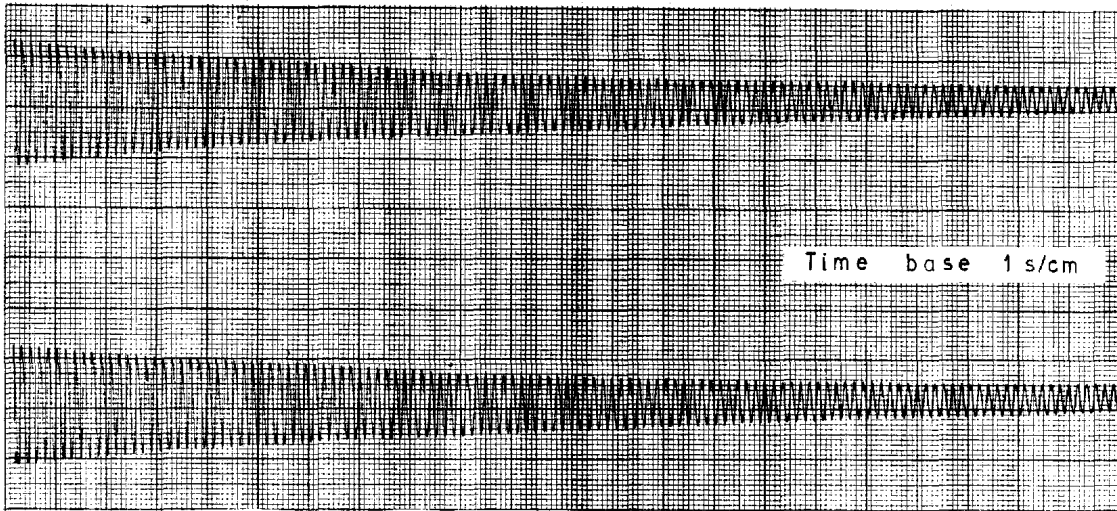


Figure 8 Structural damping for both non-damaged (above) and damaged (below) tail rotor blade.

Facility test frame used in the helicopter tail rotor blade fatigue testing was constructed as a very robust three-dimensional frame made of steel *U* and *L*-profiles and was composed of several basic modules: facility to which tail rotor blade was attached and fixed, the excitation group and modules for centrifugal force simulations (Figure 10).

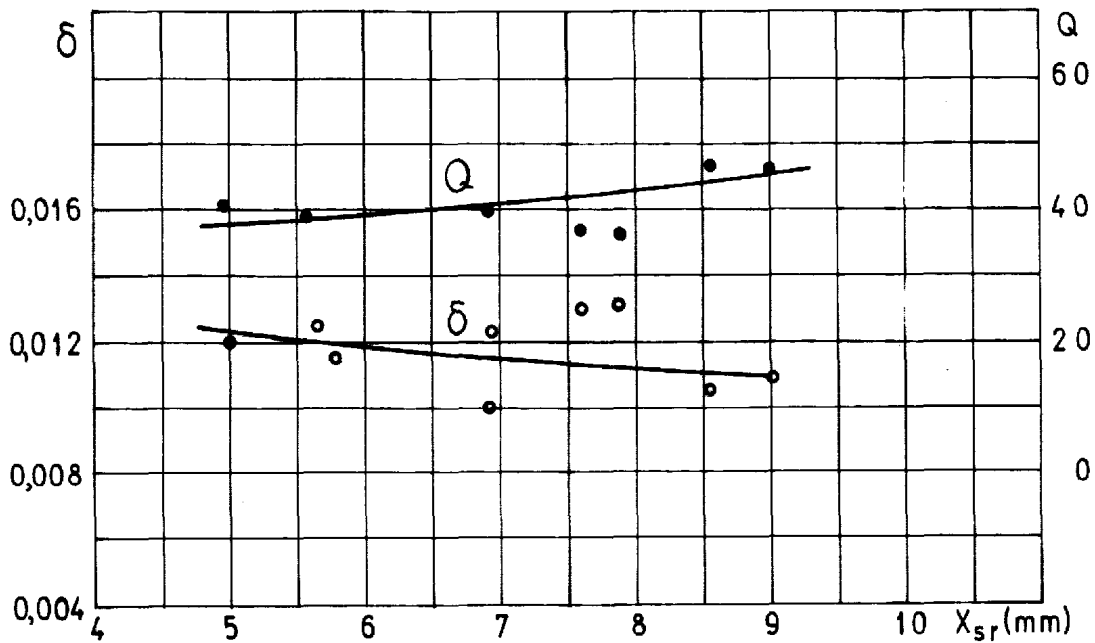


Figure 9 Logarithmic decrement and *Q*-factor of non-damaged tail rotor blade.

The blade attachment module enabled the tail rotor blade to be fixed into the facility frame and provided an attachment link between the tail rotor blade and the facility frame thus enabling blade adjustments according to the angle of attack. The link was formed by two plates and a double tapered spindle. The front plate had the angle of attack graduation

and the front nut enabled the blade to be securely fixed. The back plate and the nut completely secured the link from being unscrewed. Additional means used to prevent any eventual loosening was a slotted bar with the inverted slider-crank mechanism placed at the area of attachment.

The excitation group consisted of an electric motor with a rating of 2.2 kW and rotation speed of 1 420 rpm, a belt drive with transmission ratio of 1:3, variable speed drive (variable reduction gear), with a transmission ratio 1-3.25, eccentric mechanism with an adjustable eccentricity of 0-25 mm and an eccentric crank arm with bonded strain gages for excitation for selection. The variable transmission ratio enabled the desired excitation force frequency to be adjusted. A stroboscope was used for an accurate detection of excitation force frequency whereas the changeable eccentricity of the eccentric arm allowed adjustment of the excitation force intensity.

The module for the centrifugal force simulation included a section for generation of the static load i.e. the centrifugal force, the section that transmitted the force to the blade root section and the blade root attachment fitting at which at one end centrifugal force was applied and at the same time the excitation force at the other end. A hydraulic servo-controlled actuator composed of a hydraulic cylinder, distribution system with oil lines and a pump with a servo motor and control manometer was used as the centrifugal force generator. Its maximum force was 40 000 daN. Thanks to this system the basic functioning of the facility frame became automatic.

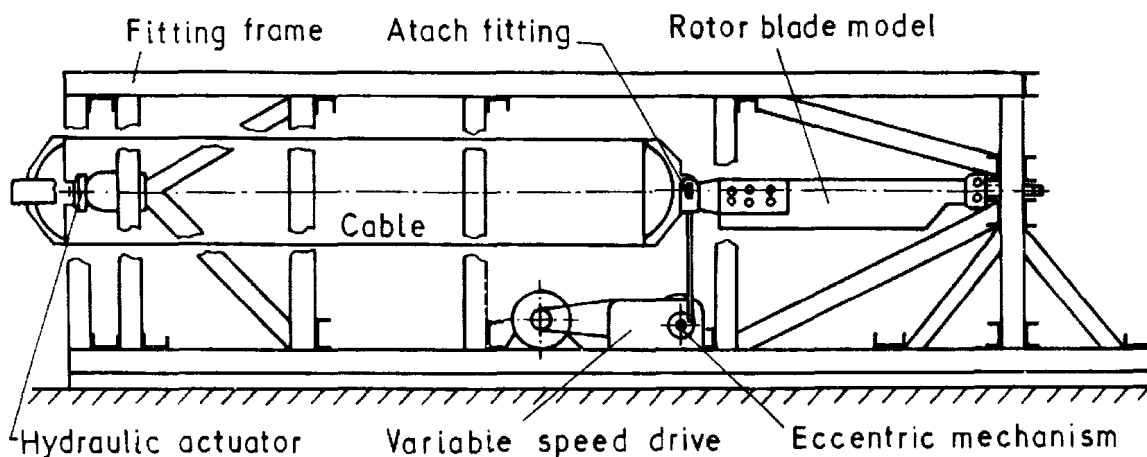


Figure 10 Tail rotor blade fatigue test facility.

The fatigue testing program of the root part of the tail rotor blade, aimed at the assessment of its load-carrying ability and survivability, included - in accordance with the standards - time fatigue tests together with the simulated centrifugal force-relaxing loading program for both damaged and non-damaged blades [2-8]. The blades were tested for the time fatigue by applying the excitation force at the 6.5 Hz frequency with simultaneous application of full-magnitude centrifugal force in a duration corresponding to  $1.5 \times 10^6$  cycles. After every  $3 \times 10^5$  cycles the blade root relaxation was performed by gradually increasing and decreasing the intensity of the centrifugal force in a 0-11 350-0 daN.

In the course of those investigations the behavior of the blade, particularly of the damaged parts of the damaged one, was permanently and closely followed. No further damages or delamination of the structures, i.e. no further changes were observed at the damaged areas in the course of the testing itself. When the fatigue testing program was finished on both non-damaged and damaged blades, further detailed check-ups and controls in respect to the deformation and degradation of geometrical shape of the blades and delaminations were

carried out. On that occasion no changes were observed on either type of the blade. Also no delamination was observed and the damaged areas of the blades were not expanded in any way.

## DISCUSSION

The achieved vibratory testing results astonishingly coincided for non-damaged and damaged heavy transport helicopter tail rotor blades (Figures 1 and 2). The obtained differences in frequencies and displacement vectors for some basic types of oscillation were within the range 2-5%. The structural damping results coincided to even higher degree and the differences in the logarithmic decrement and  $Q$ -factor were less than 2% (Figure 8). These minor differences in basic dynamic characteristics of non-damaged and damaged helicopter tail rotor blade made of composite laminated materials cannot significantly change or endanger the helicopter flight security.

The results of the damaged tail rotor blade fatigue testing have proved that even thus severely damaged blade is capable of performing all its vital functions on the helicopter even after 65 working hours in extremely difficult flight conditions. Very interesting and extremely important conclusion is that the damaged blade survived the whole testing program with all and full loads relevant for the non-damaged blade and that certainly proves the superiority of the composite laminated materials in production of aircraft vital and load-carrying parts.

## CONCLUSION

The degradation level of the vital mechanical characteristics after penetrating/ballistic damage (Figure 4) is within such limits that the mission of this heavy transport helicopter (Figure 1) can quite safely be continued and extended much longer than the minimum 30 minutes flight prescribed by standards to reach the emergency landing site. Taking in consideration the results achieved in vibratory testing as well as in fatigue investigations on non-damaged and damaged tail rotor blade made of composite laminated materials (Figures 7-9), the obtained level of blade survivability is of such a nature that the aircraft could and would survive even considerably worse damages both in the root as well as in the other parts of the blade.

Stochastic nature of the impact that ballistic damages produce on the helicopter tail rotor blade prevent us from going into more precise and detailed quantitative analysis of the survivability level, and thus we are only left with the possibility to estimate it. Very low level of differences in the results obtained through the investigation of vibratory characteristics, structural damping and fatigue characteristics (less than 5%) - all point to low level vulnerability of composite laminated materials to damages. That is why those materials give constructions with exceptionally high level of survivability so important in both military and civil aviation.

## REFERENCES

- [1] R. E. Ball, "THE FUNDAMENTALS OF AIRCRAFT COMBAT SURVIVABILITY ANALYSIS AND DESIGN", *AIAA Education Series*, AIAA Inc., New York, 1985.
- [2] B. C. Hoskin and A. A. Baker, "COMPOSITE MATERIALS FOR AIRCRAFT STRUCTURES", *AIAA Education Series*, AIAA Inc., New York, 1986.
- [3] P.R. Guyett and A.W. Cardrick, "THE CERTIFICATION OF COMPOSITE AIRFRAME STRUCTURES", Symposium on large scale composite structures, *Aeronautical Journal*, July 1980.

- [4] B. Rašuo, "TEHNOLOGIJA PROIZVODNJE LETELICA" (*Aircraft Production Technology*), Mašinski fakultet, Beograd, 1995, (in serbian).
- [5] T. Dragović and B. Rašuo, "STATIC, VIBRATORY AND FATIGUE TEST RESULTS FOR THE HELICOPTER MAIN ROTOR BLADE OF COMPOSITE LAMINATED MATERIALS", *Proceedings First Australasian Congress on Applied Mechanics*, Melbourne, Australia, 21-23 Februar 1996.
- [6] "HOMOLOGTION DES FABRICATIONS PREVISION DES ESSAIS JUSTIFICATIFS", Paris, France, 1979.
- [7] D.O. Adams and H.L. Kearney, "FULL-SCALE FATIGUE TESTING OF ADVANCED FIBER COMPOSITE COMPONENTS", *Journal of the American Helicopter Society*, Vol. 31, April 1986.
- [8] P.T. Curtis, "THE FATIGUE BEHAVIOR OF FIBROUS COMPOSITE MATERIALS", *The Journal of Strain Analysis for Engineering Design*, Vol. 24 No. 4. 1989.



# LOW VELOCITY IMPACT FAILURE ANALYSIS OF SANDWICH BEAM

Ya-Jung Lee, Yau Shyu

*Department of Naval Architecture and Ocean Engineering, National Taiwan University, 73  
Chou-shan Street, Taipei, Taiwan, R.O.C.*

**SUMMARY:** As concluded experimentally on low-velocity impact behavior of sandwich beam subjected to the cylindrical impactor, the core material and face sheets dominate the failure modes. The main failure pattern of sandwich beam with lower density core material is shear cracks in foam (Mode I), whereas crushed in core and damage in the top face sheets right underneath the impactor (Mode II) when core material density is higher. Finite element software ABAQUS is used, and maximum stress failure criterion and a modified stiffness degradation method are adopted to investigate the initiation of failure, the failure modes and post-failure behavior of sandwich beam. The numerical results are in good agreement with experimental results. Parametric studies, including stiffness ratio of face sheets to core and ratio of impactor diameter to simple support span, are also conducted

**KEYWORDS:** Impact, sandwich beam, post-failure behavior, stiffness degradation, maximum stress failure criterion.

## INTRODUCTION

Owing to the advantages of lightweight and high bending strength, the composite sandwich materials play an important role in today's industry. In marine engineering, more and more ships of small sizes such as fishing boats, and yachts, use sandwich panels in ship hull construction. However, inadvertent collision during the fabrication process, wave impact during sailing, and so on, may induce damage of sandwich structures and cause significant reduction of the stiffness and strength of materials. Thus, further understanding of impact loading, impact response and impact damage of composite sandwich is necessary for the sake of safety.

Much work has been done on impact resistance and impact tolerance of composite sandwich panels as in Ref. [1]-[3]. However, because of the complication of contact behavior between the projectile and sandwich panels, it is very difficult to predict the impact behavior by establishing mathematical model. An well-known approach, proposed by Tan and Sun in Ref. [4], considered for determining the impact response is, firstly, to measure the local contact behavior of the panel by static indentation test; secondly, to use this experimental results in conjunction with an impact analytical model. This approach, however, can not be regarded as true prediction since it requires the fabrication of the entire sandwich and indentation tests to be made for various impactors and structures under consideration. The true prediction should possess the ability to predict the impact response from a knowledge of the behavior of the individual components of the sandwich panels as in Ref. [3]. Therefore, many of researches use finite element method to analyze the impact responses and predict the fracture initiation of

materials, however, simulation on post-failure behavior by FEM is rarely seen.. The objectives of this study is to develop a failure analysis procedure by FEM, which can investigate the failure modes and post-failure behavior of sandwich beam subjected to the cylindrical impactor. Maximum stress failure criterion and a modified stiffness degradation method are adopted to analyze the failure responses, and compared with the experimental results. After verification of this failure analysis procedure, parametric studies, including the stiffness ratio of face sheets to core and ratio of impactor diameter to simply-supported span are conducted as well.

### **LOW VELOCITY IMPACT TESTS**

Sandwich panels made of laminated face sheets MAM (M : REM 300-65 glass mat; A : T-900 Aramid) and two DIVINYCELL core material with different density 0.1, 0.2 g/cm<sup>3</sup> are taken into consideration. These sandwich panels are fabricated by IHI craft in Japan. The dimension of specimens is 9cm4.5cm and specimen are simply-supported at two edges with a span of 6 cm. The detailed description of test system and test procedure can be referred to Ref. [5]. As stated before by authors in Ref. [5], the main failure pattern of sandwich beam with foam core density of 0.1 is shear cracks in core material, located at some distance away from the impact point and with an inclined direction of 40~50 degrees. As the impact energy increases, the cracks will extend to the face-core interface, and then induce the delamination. The characteristic of impact force history when shear cracks occur is an sharp load drop. In contrast, when foam core density changed to 0.2, no shear cracks are found in core material, but crush in core and damage in top face sheets beneath the impact point are found, however, no abrupt load drop is shown in the impact force history. As mentioned above, it is evident that the core material has a great influence on failure modes, and for the sake of simplicity, the failure modes of sandwich beams with core density of 0.1 and 0.2 are named as Mode I and Mode II, respectively.

### **NUMERICAL SIMULATION AND DISCUSSION**

The commercial finite element software ABAQUS and user-defined subroutine UMAT are used to simulate the failure behavior of sandwich beams. Because of the line load condition, the sandwich panels subjected to a cylindrical impactor can be modeled as 2-D plain strain problem. Since the core material dominates the failure behavior, an precise understanding of the response of core material to stress is required, especially the yielding or failure behavior. In Ref. [6], Shaw and Sata suggest that failure of foam is governed by the maximum principal stress, independent of the minor principal stress and that statement is strongly supported by Patel and Finnie in Ref. [7] and Zaslavsky in Ref. [8]. The micro-structure of foam considered in this study is similar to those used by Ref. [6]-[8], and due to the foam behavior which yields plastically under compression, but cracks under tension, the maximum principal stress failure criterion is chosen to predict the onset of cracks and yielding in foam core. The failure prediction and the algorithm as well as an illustration to modify the stiffness when core is degraded due to cracks or yielding are as follows;

When  $\sigma_1 > X_t$ , cracks occur, then  $E_1, G_{12}, \nu_{12}$  are reduced to zero

When  $\sigma_2 > X_c$ , yielding occur, then  $E_2, G_{12}$  are modified depending on  
the plastic behavior of foam material

where,  $X_t$  and  $X_c$  are the tensile and compressive stresses of foam core, respectively.

As for the face sheets, because the delamination and matrix crackings on laminated face sheets have little effects on failure mechanism, it can be reasonably ignored and only fibers damage is considered. When fibers damage occurs in tension or in compression, a degradation factor of 0.14 is used to modify the  $E_1$  as suggested by Ref. [9].

### STATIC TESTS SIMULATION

According to the phenomenon that the damage patterns of sandwich beams under dynamic condition are similar to those produced under static condition, thus, for saving the computing time, the check on performance of numerical failure analysis is conducted under static case.

#### Mode I

The typical static tests curve of sandwich beams indented by a cylindrical impactor is shown in Fig. 1. For convenience, several checkpoints are marked along the curve. Initially, the specimen is loaded up from checkpoint O to A, without any observable damage. Over the checkpoint A, minor matrix crackings on top face sheets and yielding of the core in the region underneath the indenter result in the reduction of bending stiffness of specimen. When the load path reaches B, the loading immediately drops from B to C due to the onset of shear cracks in core and the extension of cracks along the face-core interfaces. During the path CD, the specimen continuously deforms without further extreme failure. The comparison between numerical and experimental F-d curves is shown in Fig.2. It can be seen that those curves fit each other well. On the numerical F-d curve, there is a slight drop resulted from fibers breakage right over the level of A. This discrepancy is owing to the drawbacks of that method which simulates the fibers damage by multiplying a degradation factor right after the failed elements detected.

The progressive illustrations of simulation for shear cracks and yielding in core are shown in Fig.3, Fig.4, respectively. It can be concluded from Fig.3 that the progressive crack failure pattern is in consistence with the one observed during experiments.

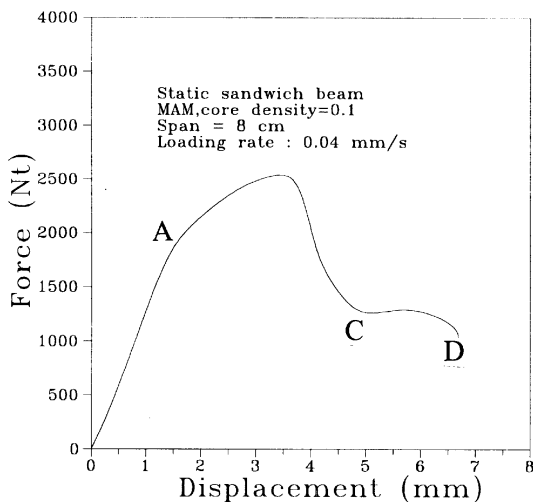


Fig.1: The basic pattern of static indentation of sandwich beam with core density 0.1

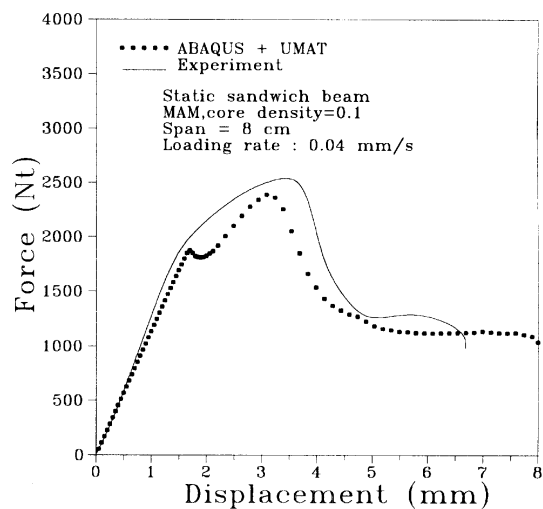
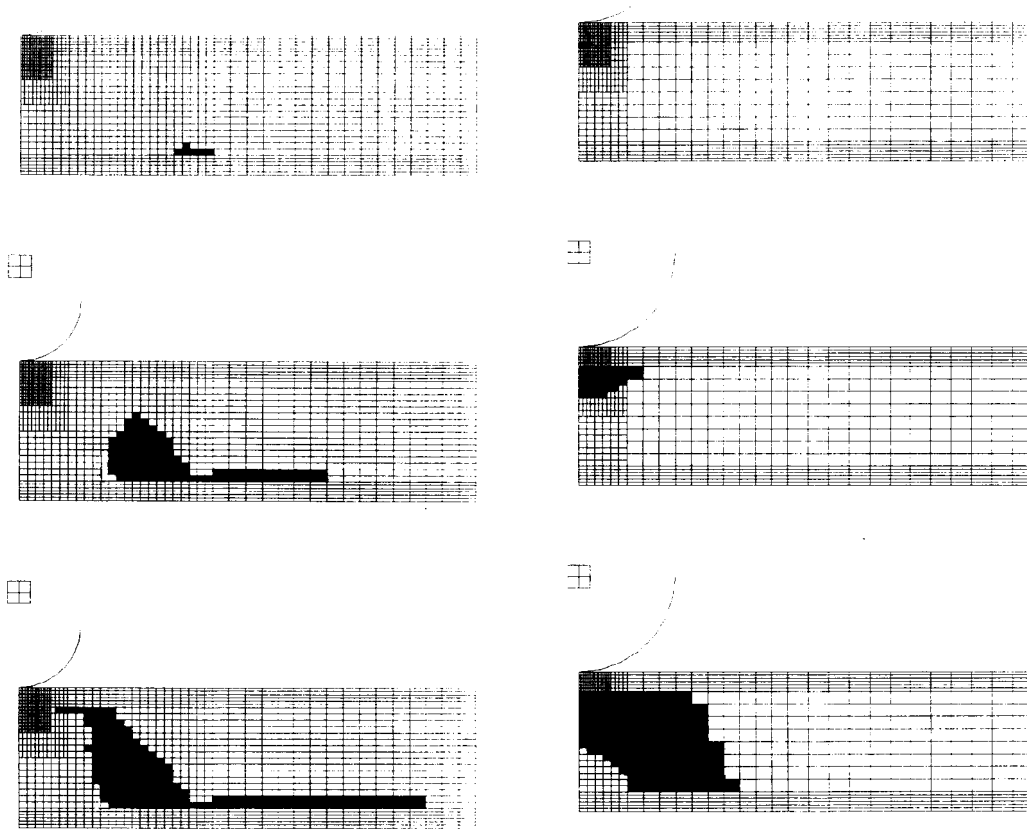


Fig.2: The comparison on numerical and experimental results



*Fig. 3: The progressive shear crack failure    Fig 4. The progressive yielding in core*

## Mode II

When the core density is changed to 0.2, under the same configuration and loading condition, the failure patterns of sandwich beams are different from those of Mode I. From Fig. 5, the specimen is loaded from O to A without any failure, however, over the level of A, the core exhibits plastic behavior and face sheets are damaged in the region right under the indenter. As going further along the path AB, the degree of plasticity in core and damage in face sheets grows continuously. When checkpoint B is reached, fibers of top face sheets beneath the indenter are almost broken totally and a vertical crack located in the center line of the core is found. As the loading path moves, the crack propagates downward and the loading-carrying capacity of specimen loses gradually as seen in path BC. The comparison on computational and experimental F-d curves is shown in Fig.6. Although these curves are generally in consistent with each other, however, as mentioned before, the modeling on fibers damage needs to be further improved.

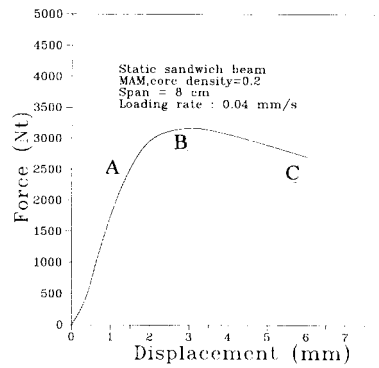


Fig. 6: The basic pattern of static indentation of sandwich beam with core density=0.2

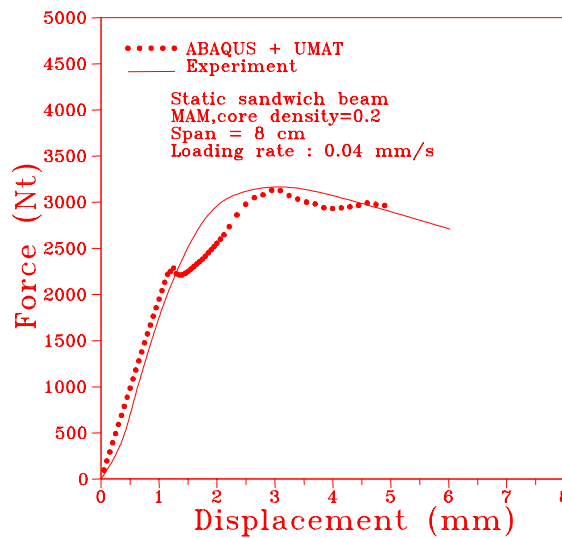


Fig. 7: The comparison of numerical and experimental results

### Dynamic impact analysis

After verification on static failure analysis of sandwich beam, the same failure analysis procedure is applied to the impact study. Due to the low velocity impact, effect of strain rate is not considered here. The mass of the impactor is 1.52Kg and the incident impact velocity is 2.174 m/s, making the impact energy 3.59 Joules. As expected, the failure patterns of sandwich beams with core density 0.1 and 0.2 are almost the same to those produced in static tests. Fig.7 shows the comparison on numerical and experimental impact force histories of sandwich beam with core density 0.1. It is evident that they fit each other very well.

### COMPARISON ON STATIC AND DYNAMIC BEHAVIOR

As concluded above, under the low impact velocity considered in this study, the failure modes and failure patterns of dynamic cases can seem to be simulated from static cases. This conclusion can be further supported from the viewpoints of energy. In static case, the work done to specimens by the indenter can be obtained from integrating the force-displacement curve of the indenter. The amount of this work can also be regarded as the energy absorbed by specimens under the assumption of no energy loss. In dynamic case, there are two ways to calculate the energy absorption of specimens. (a) computing the loss of kinetic energy of the

projectile during impact (b) calculating the work done by the projectile in use of integrating the dynamic force-displacement curve of the projectile. These methods to evaluate the energy absorbed by sandwich beam are compared in Fig. 8. From Fig. 8, it is surprisingly shown that three curves fit each other very well. Further, at the same energy level, the energy absorbed curves are shown to be quite the same under various combinations; large mass impactor with low velocity and small mass one with high velocity. From the discussion above, it can be reasonably concluded that the dynamic behavior can be approximately simulated from the static one. For example, if the energy needed to move along the loading path from O to B as shown in Fig.2 is known, then the estimation whether the specimen will fail or not, for given impact velocity and mass of the impactor, can be done by comparing the static energy value with that of  $1/2 mv^2$ .

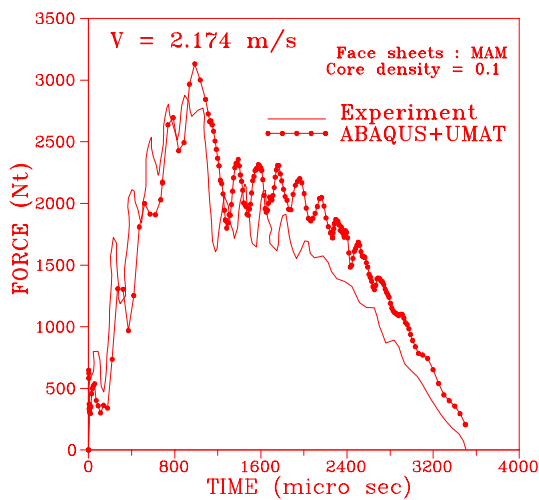


Fig. 7: The comparison on impact force histories

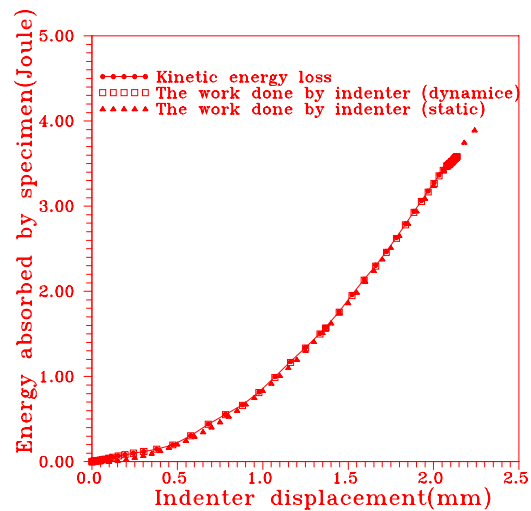


Fig. 8: The comparison on energy absorbed curves

### PARAMETRIC STUDY

#### Core Material

Under the same face sheets MAM and geometric configuration, several sandwich beam with different core material densities are investigated. Core densities of 0.08, 0.1, 0.13, 0.16, 0.2 are taken into account and denoted by H80, H100, H130, H160, and H200, respectively. The elastic properties, yielding strength, and failure strength of each are listed in Table 1. The effective in-plane elastic property of face sheets is about 14.25 Gpa. The results of parametric study are tabulated as shown in Table2.

Table 1: Material properties of DIVINYCELL foam core

Core	E (MPa)	yielding strength (MPa)	failure strength (MPa)
H80	80	1.2	2.2
H100	115	2.0	2.75
H130	140	2.5	4.2
H160	170	3.4	5.1
H200	230	3.8	5.8

Table 2: Parametric study on core materials

Core	failure strength of sandwich(N)	energy needed to fail	failure mode
H80	1454	4.79	Mode I
H100	1874	4.51	Mode I
H130	1888	8.18	Mode II
H160	2066	6.86	Mode II
H200	2287	6.03	Mode II

From Table 2, it can be seen that the failure modes of sandwich beams with core H80, H100 are Mode I, the others are Mode II. Typically, no matter failure modes, the higher the core density is, the higher the failure strength of sandwich beam is. However, for the corresponding failure modes, the higher the core density is, the smaller the energy needed to fail is. These results show that sandwich with core material of higher density has better static fracture resistance, however, worse impact resistance from the viewpoint of energy.

### Ratio of indenter diameter to span

The diameter (R) of the indenter is fixed to 1.2 cm, and the span (S) of simple support boundary condition are changed to 2 cm, 3 cm, 4 cm and 5 cm, thus, the corresponding ratio of R/S is 0.12, 0.15, 0.2 and 0.3. The results of parametric study are shown in Table 3. Under the ratio of R/S considered, failure modes of all the sandwich beams are Mode I. As the ratio of R/S increases, the failure strength of specimen also increases, however, the opposite tendency is obtained from the energy viewpoint. Therefore, as the increase of ratio of R/S, sandwich beams have better static fracture resistance, but worse impact resistance.

## CONCLUSION

To simulate the failure mechanism of sandwich beams subjected to a cylindrical impactor, the maximum principal stress criterion and a stiffness degradation method are coded into the user-defined subroutine UMAT provided by finite element software ABAQUS. This failure analysis procedure can precisely model two of different failure modes; Mode I: shear cracks in core and Mode II: yielding in core and damage in top face sheets right under the indenter. In the range of impact velocity considered in this study, it can be concluded that the dynamic behavior can be simulated from static results. The parametric studies on core density, and ratio of R/S are also conducted. The failure modes of sandwich beams with lower core density trend toward Mode I, whereas toward Mode II with higher core density, however, all the failure modes of sandwich beams are Mode I in the range of ratio of R/S considered in this study.

Table 3: Parametric study on ratio of R/S

R/S	failure strength of sandwich(N)	energy needed to fail	failure mode
.12	2219	6.048	Mode I
0.15	2389	4.51	Mode I
0.2	2639	4.173	Mode I
0.3	3222	4.085	Mode I

## REFERENCES

1. Michael L. Bernard and Paul A. Lagace, "Impact Resistance of Composite Sandwich Plates", *J. Reinforced Plastics and Composites*, Vol. 8, 1989, pp.432-445
2. W. K. Shin and B. Z. Jang, "Instrumented Impact Testing of Composite Sandwich Panels", *J. Reinforced Plastics and Composites*, Vol. 8, 1989, pp.270-289
3. J. A. Nemes and K. E. Simmonds, "Low-Velocity Impact Response of Foam core Sandwich Composites", *J Com. Mat.*, Vol. 26, No. 4, 1992, pp. 500-519
4. T. M. Tan and C. T. Sun, "Use of Statical Indentation laws in the Impact Analysis of Laminated Composites Plates", *J. App. Mat.*, Vol. 52, 1985, pp. 6-12
5. Y. J. Lee, Y. Shyu, "Low Velocity Impact Behavior of Composite Sandwich Used in Ship Structures", *Proceedings Tenth International Conference of Composite Materials*, 1995
6. M. C. Shaw and t. Sata, *Int. J. Mech. Sci.* 8, 1996, pp. 496
7. M. R. Patel and I. Finnie, *Lawrence Livermore Laboratory Report UCRL-13420*, 1969
8. M. Zaslowsky, *Exper. Mech.* No. 2 February, 1973, pp.70
9. Youngchan Kim, Julio F. Davalos and Ever J. Barbero, "Progressive Failure Analysis of Laminated Composite Beam", *J. Composite Materials*, Vol. 30, No. 5, 1996



# INFLUENCE OF WATER ABSORPTION ON DELAMINATION INDUCED BY LOW-VELOCITY IMPACT AND CAI STRENGTH OF FRPS

Kenjiro Komai, Kohji Minoshima and Kazuto Tanaka

*Department of Mechanical Engineering, Kyoto University  
Yoshida-Honmachi, Sakyo-ku, Kyoto 606-01, Japan*

**SUMMARY:** An investigation of water absorption effects on the impact fracture mechanism and compression after impact (CAI) behavior was conducted using carbon fiber reinforced thermoplastic matrix composite (AS-4/PEEK) and aramid fiber reinforced epoxy matrix composite (K-49/828), which have a quasi-isotropic stacking sequence of  $[0^\circ/45^\circ/90^\circ]_{2S}$ . The impact tests were carried out using a falling weight tester. Impact-induced internal damage was observed with a scanning acoustic microscope (SAM). The delamination area of AS-4/PEEK was much smaller than that of a CF/epoxy composite (MM-1/982X), and no influence of water absorption was observed. In contrast, that of K-49/828 was the largest, and the impact-load-induced delamination area was increased by water absorption. In the case of AS-4/PEEK, the compressive strength of the impacted specimen at 3J was the same as that of a virgin specimen, and no influence of water absorption was observed. Impact energy affected the CAI strength of K-49/828 as much as that of MM-1/982X. The fracture surface was closely examined using a scanning electron microscope, and the fracture mechanisms were discussed.

**KEYWORDS:** delamination, CF/PEEK composite, aramid fiber reinforced epoxy matrix composite, impact loading, compression after impact, water absorption, nondestructive inspection, scanning acoustic microscope

## INTRODUCTION

Advanced fiber-reinforced polymer matrix composites (FRP) that have high strength and high stiffness-to-weight ratios are now widely used in high technology engineering applications. When these are used in a service condition, impact events, such as tool drops, occur, and environmental exposure also affects the mechanical properties of FRPs. Hence, influences of impact and environment on mechanical properties of FRPs must be clarified. It is well known that carbon/epoxy laminates are susceptible to low velocity impact [1,2]. To improve impact resistance, ductile matrix such as PEEK [3] and aramid fibers [4-6] are reported to be alternative candidate materials. In this study, effects of water absorption on impact fracture and compression after impact (CAI) behavior were investigated using carbon fiber reinforced thermoplastic matrix composite (AS-4/PEEK) and aramid fiber (Kevlar 49) reinforced epoxy matrix composite (K-49/828), having a quasi-isotropic stacking sequence of  $[0^\circ/45^\circ/90^\circ]_{2S}$ . We compared the results with those of carbon fiber reinforced epoxy matrix composite (MM-1/982X) [1].

## EXPERIMENTAL PROCEDURES

The composites used in this study were carbon fiber reinforced thermoplastic matrix (PEEK) composite (AS-4/PEEK) and aramid fiber (Kevlar 49) reinforced epoxy matrix composite (K-49/828), having a quasi-isotropic stacking sequence of  $[0^\circ/45^\circ/90^\circ]_{2S}$ . Average thickness, fiber-volume fraction, tensile strength and initial elastic modulus are listed in Table 1. The data for MM-1/982X [1] is also listed. Rectangular specimens of 200mm in length and 40mm in width were used.

Specimens were immersed in distilled water at  $80^\circ\text{C}$  for 2 months. The weight gain of the specimens in time is shown in Fig.1, with the data of angle-ply AS-4/PEEK ( $[45^\circ]_{3S}$ ) and unidirectionally reinforced AS-4/PEEK ( $[0^\circ]_{14}$ )[7]. In the case of AS-4/PEEK, the quasi-isotropic laminates absorbed more water than angle-ply and unidirectionally reinforced laminates. The angle-ply and the unidirectionally reinforced laminates were well fabricated, and no void was observed. However, the quasi-isotropic laminates contained many voids. Figure 2 shows the surface and the side surface of the quasi-isotropic laminate of AS-4/PEEK.

*Table 1: Materials used in this study*

Name	AS-4/PEEK	K-49/828	MM-1/982X
Construction of laminate	$[0^\circ/45^\circ/90^\circ]_{2S}$		
Average thickness mm	2.0	2.4	2.5
Fiber volume fraction %	61	66	59
Tensile strength MPa	720	500	840
Initial modulus GPa	48	31	63

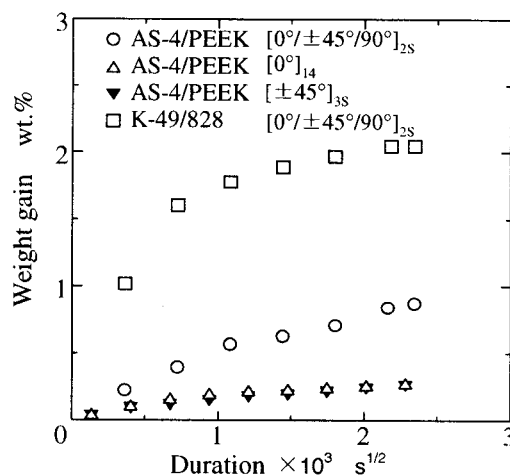


*Fig. 1: Relationship between weight gain and (immersional duration)<sup>1/2</sup>*

This is the reason why the quasi-isotropic laminate of AS-4/PEEK absorbed more water than other laminates ( $[45^\circ]_{3S}$  and  $[0^\circ]_{14}$ ). The weight gain of K-49/828 leveled off at 2.0%. The weight gain of MM-1/982X was about 1.0% [1]. Specimens immersed in water will be referred to as “wet” specimens, while the specimens held in room air referred to as “dry” specimens.

The impact tests were carried out by a falling weight tester. The steel ball (1/2 inch in diameter) was attached to the falling weight. By this steel ball, the center of specimen whose both ends (75mm) were fixed was impacted. Compression tests after impact (CAI) were performed on impacted dry and wet specimens, as well as non-impacted dry and wet specimens as a reference. Aluminum tabs were glued to both ends of a specimen, giving a gage length of 63mm. Compression tests were carried out at a constant crosshead speed of 1mm/min, using a electro-hydraulic servo controlled fatigue testing machine (Shimadzu, EHF-FB20, Load Capacity: 200kN).

The internal damage after impact was observed using a scanning acoustic microscope (SAM, Olympus Optical Co., UH3) with a pulse wave of 50MHz for 1600ns gate time. The fracture surfaces of the specimens were observed using a scanning electron microscope (SEM, JEOL, JSM-5400LV).

## EXPERIMENTAL RESULTS AND DISCUSSION

### Impact Test

Figures 3 and 4 respectively show the front and rear surfaces of impacted dry specimens of AS-4/PEEK and K-49/828. Front surface of AS-4/PEEK has a crease and rear surface has cracks. For K-49/828, there is no crease and crack. This means that the visible surface damage of K-49/828 is less than that of AS-4/PEEK.

Figures 5(a) and (b) show SAM photographs of a AS-4/PEEK specimen before and after impact test. In the case of AS-4/PEEK, even a virgin specimen had internal defects introduced by insufficient matrix infiltration. Therefore, the subtraction of SAM images between virgin and impacted specimens was adopted to evaluate impact-induced delamination. The result is shown in Fig. 5(c). We use the same method for K-49/828, which had no internal defect such as observed in AS-4/PEEK.

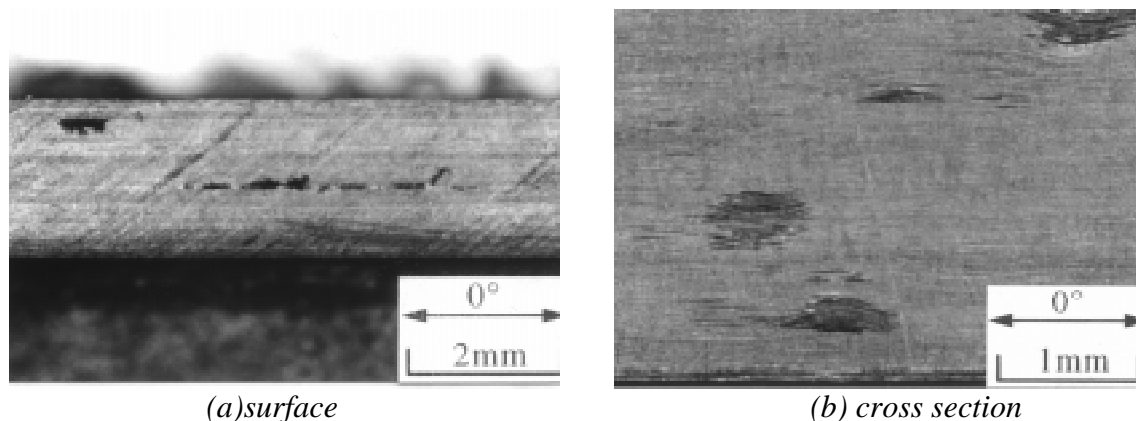


*Fig.2: Virgin specimen (AS-4/PEEK)*

Figure 6 shows the impact-induced delamination area as a function of impact energy. Delamination area of AS-4/PEEK was smaller than that of MM-1/982X, and no influence of water absorption was observed. For K-49/828, impact induced-delamination area was the largest, and it was increased by water absorption. The threshold impact energy below which no-delamination occurred was 3J for both dry and wet AS-4/PEEK specimens. For K-49/828, it was assumed to be almost 0J.

On the fracture surfaces of an impacted AS-4/PEEK specimen, many defects introduced during manufacturing could be observed (Fig.7). Those defects were imaged by SAM as white areas, shown in Figure 5(a). Figure 8 shows a cross section of an impacted point. A crack is initiated at a defect. Improved manufacturing process will further increase the impact resistance of the composite.

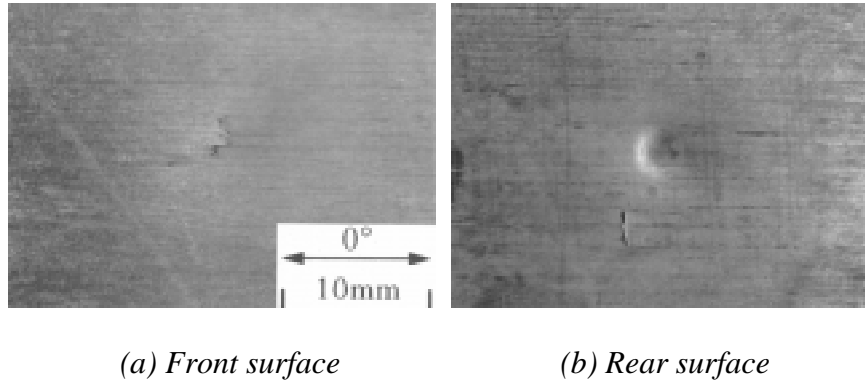


Fig. 3: Impacted specimen (AS-4/PEEK)

The characteristic fracture feature of AS-4/PEEK is that the fiber surface was covered by matrix material, irrespective of water absorption (Fig.9). This indicates that the composite had superior fiber/matrix interfacial strength. There is little difference in fracture morphology between dry and wet specimen. For K-49/828, the fracture was caused by interfacial debonding (Fig.10), indicating low fiber/matrix interfacial strength of the composite. Figure 11 shows the magnified fiber surface in K-49/828. Although water absorption was reported to promote fiber splitting [8-10], the number of fiber splitting of the wet specimens were less than that of dry ones. This means that water absorption degraded the fiber/matrix interfacial strength, thereby promoting the impact-induced delamination by water absorption.

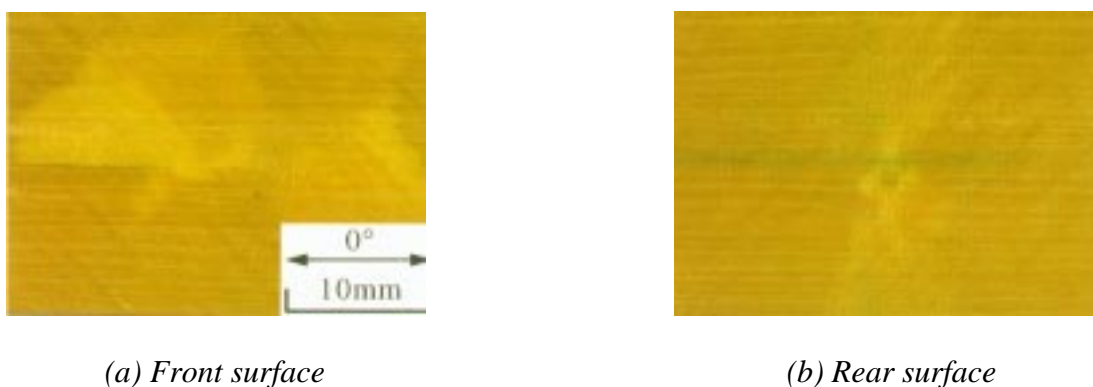
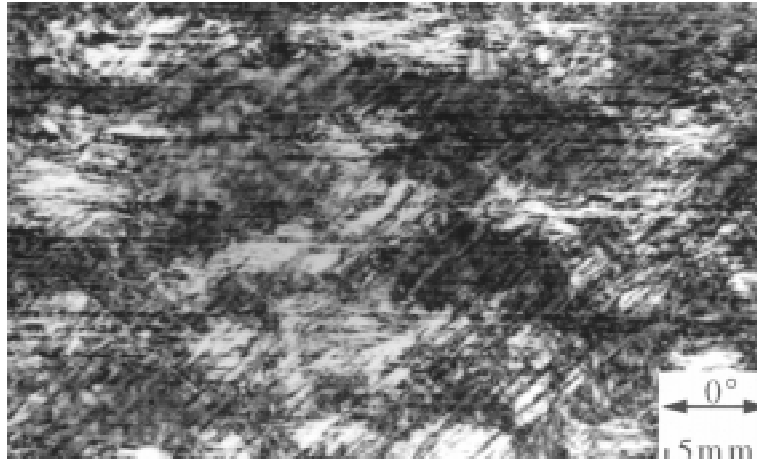
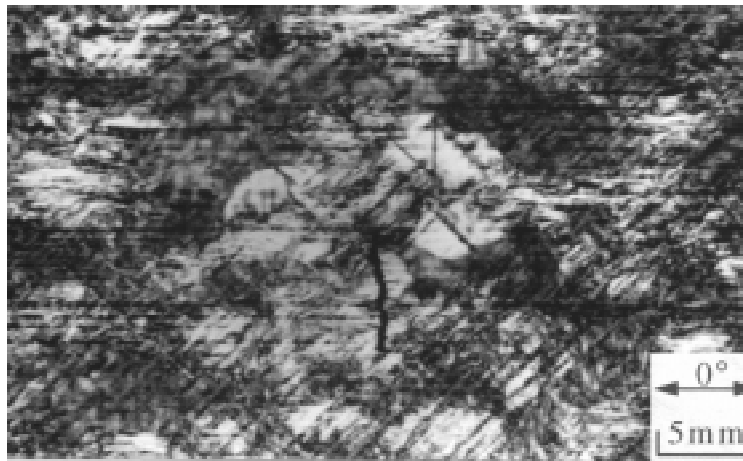


Fig. 4: Impacted specimens (K-49/828)



*Fig. 5 (a): SAM photograph of virgin specimen (AS-4/PEEK)*



*Fig. 5 (b): SAM photograph of impacted specimen (AS-4/PEEK)*

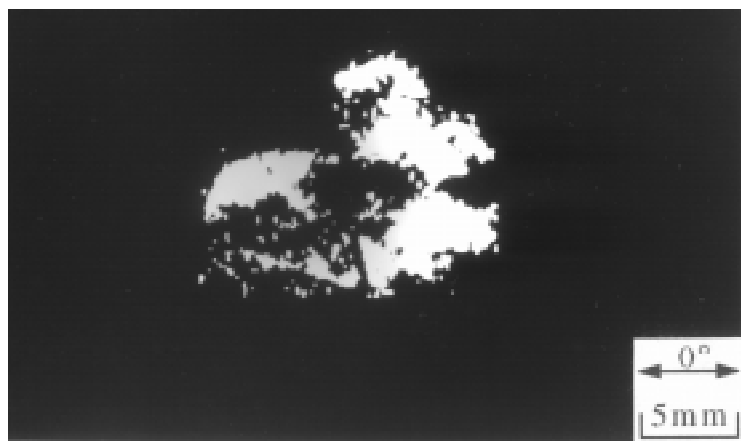


*Fig. 5 (c): Extracted delamination (AS-4/PEEK)*

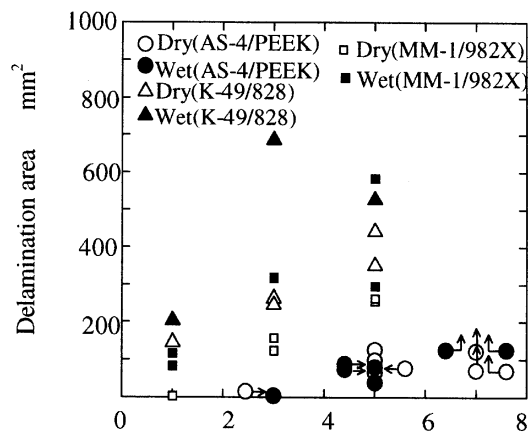


Fig. 6: Relationship between impact energy and delamination area

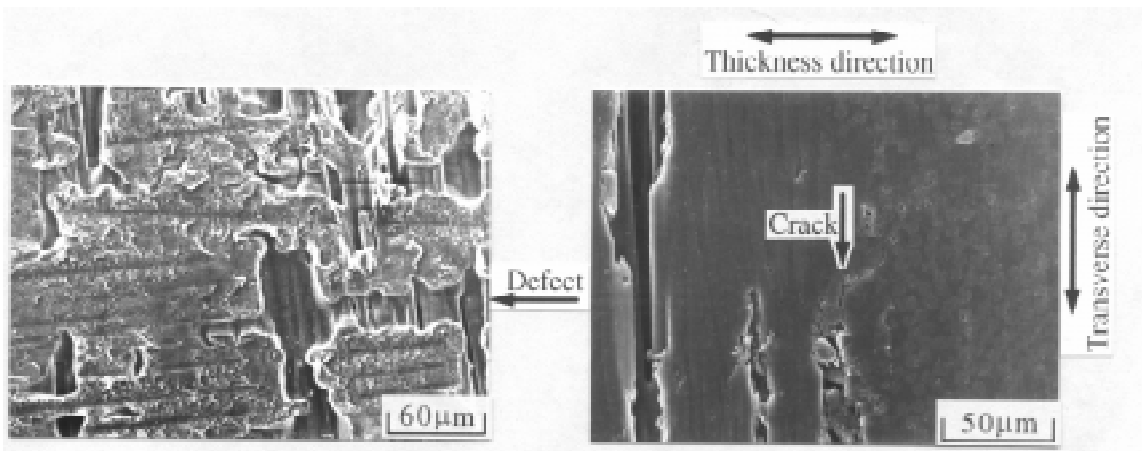
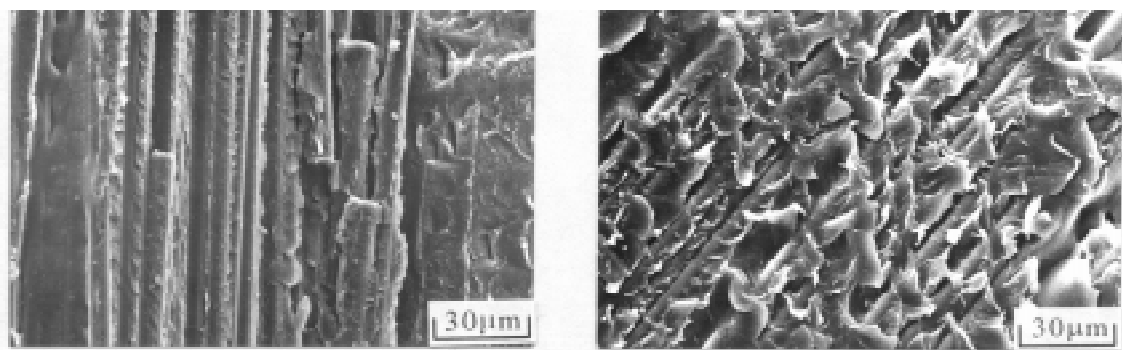


Fig. 7: Fracture surface (AS-4/PEEK, Dry specimen, Impact energy: 5J)

Fig. 8 Cross section of an impacted point (AS-4/PEEK), Dry specimen, Impact energy: 5J)



(a) Dry specimen

(b) Wet specimen

Fig. 9 Fracture surface of AS-4/PEEK (Impact energy: 5J)

### CAI Test

The relationship between impact energy and residual compressive strength after impact is illustrated in Fig. 12. In the case of AS-4/PEEK, the compressive strength of the impacted

specimen at 3J was the same as that of a virgin specimen, because no impact-induced delamination occurred. Above 3J, however, residual compressive strength decreased with an increase in impact energy. Also we must note that no influence of water absorption was observed. The compressive strength of K-49/828 was the lowest in all FRPs tested, as the aramid fiber has low compressive strength [11].

To examine the ratio of the residual compressive strength to the compressive strength of non-impacted specimens, the relationship between impact energy and normalized residual compressive strength was analyzed (Fig.13). The normalized strength was defined by residual compressive strength divided by compressive strength of non-impacted specimen in a respective environment. The normalized strength of AS-4/PEEK was the highest, indicating superior resistance against impact. For K-49/828, it was almost the same as that of MM-1/982X.

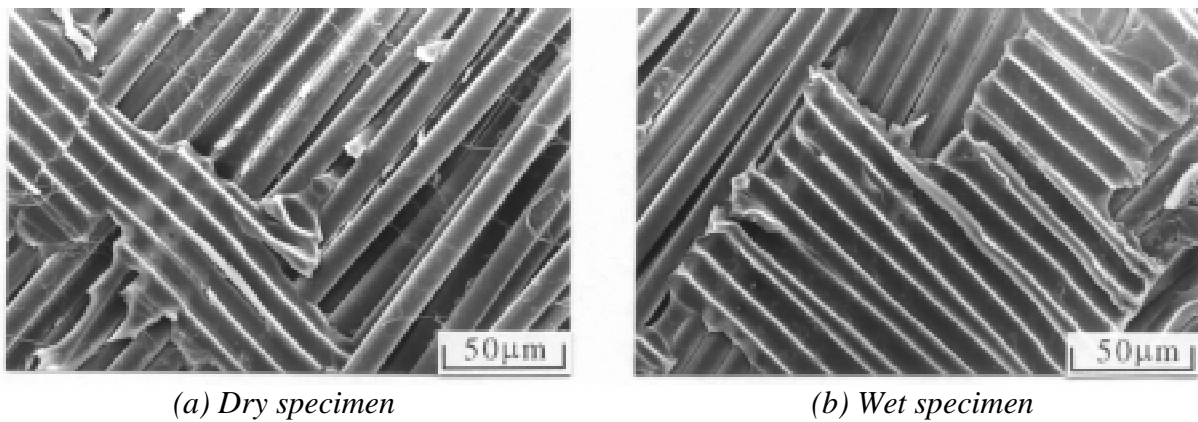


Fig. 10: Fracture surface of K-49/828  
(Impact energy: 5J)

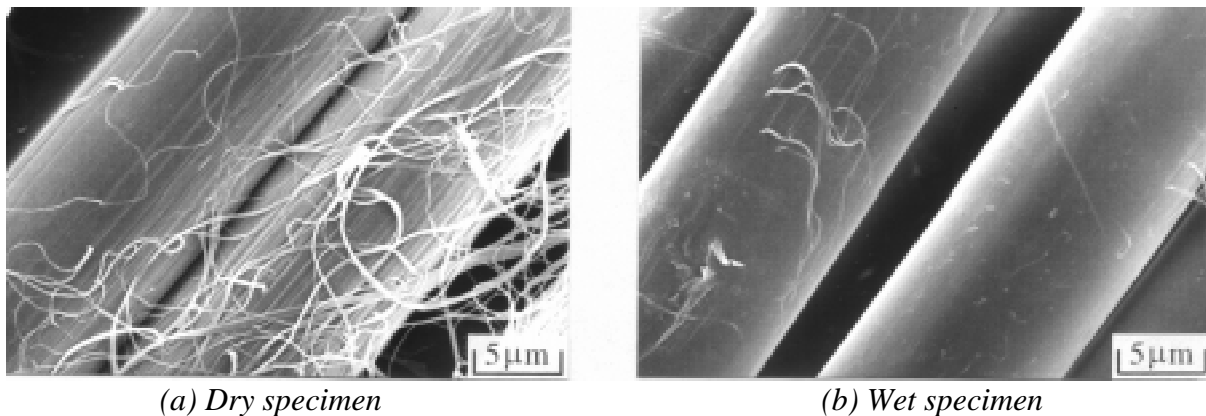


Fig.11: Magnified fiber surface  
(K-49/828, Impact energy:5J)

The relationship between impact-induced delamination area and normalized residual compressive strength is illustrated in Fig. 14. At a certain delamination area, the normalized residual compressive strength of K-49/828 was higher than that of MM-1/982X. However, impact-induced delamination area of K-49/828 was larger than that of MM-1/982X (Fig.6).

Therefore, as is shown in Fig. 13, the normalized residual compressive strength of K-49/828 and MM-1/982X was similar when compared at a certain impact energy.

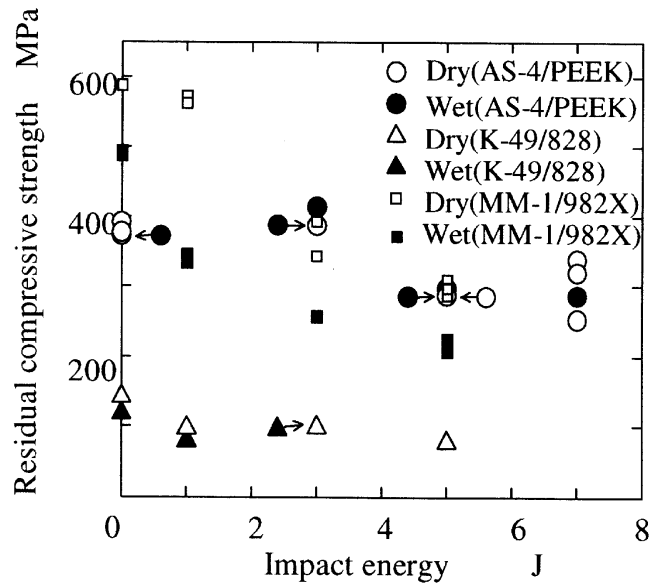


Fig. 12 Relationship between impact energy and residual compressive strength

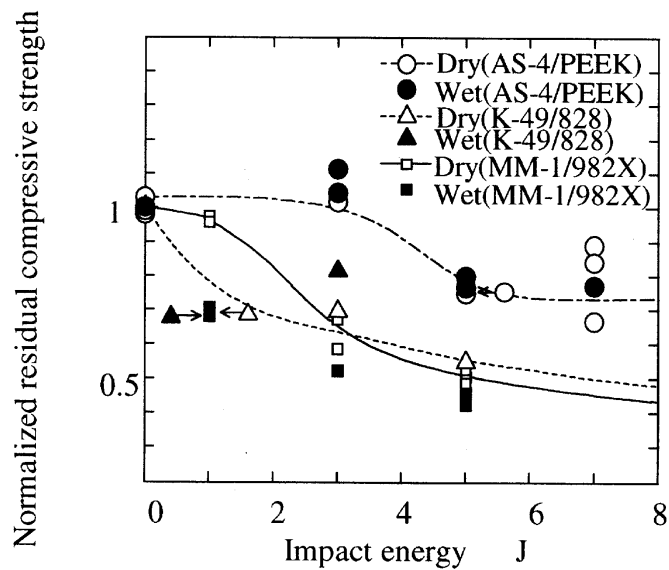
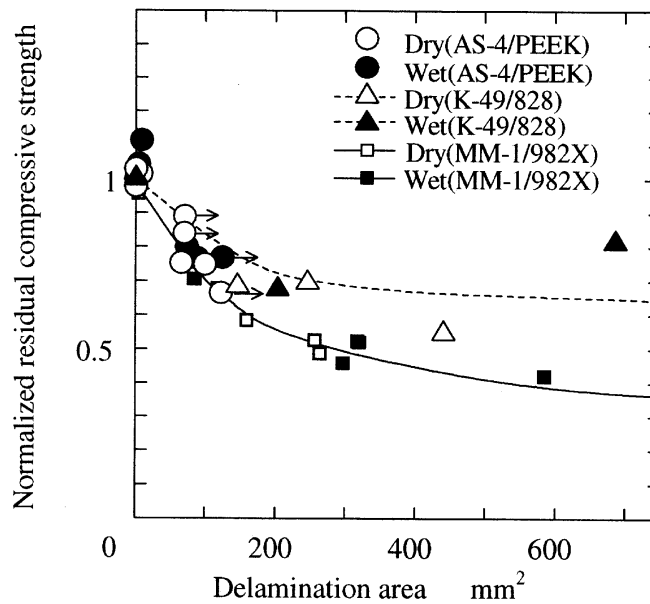


Fig. 13 Relationship between impact energy and normalized residual compressive strength



## CONCLUSIONS

1. Even though composites have initial defects introduced by a defective manufacturing process, the delamination area can be accurately evaluated by the subtraction of SAM images between virgin and impacted specimens.
2. The surface damage tolerance of K-49/828 is superior to that of AS-4/PEEK.
3. Delamination area of AS-4/PEEK was the smallest, and no influence of water absorption was observed. For K-49/828, impact induced-delamination was the largest, and it was increased by water absorption. The impact-induced delamination tolerance of PEEK matrix composite is superior to that of epoxy matrix composite.
4. The compressive strength of K-49/828 was the lowest in all FRPs tested. However, the normalized residual compressive strength of K-49/828 was the same as that of MM-1/982X. In the case of AS-4/PEEK, the normalized CAI strength was the highest, indicating superior resistance against impact. Also there is no influence of water absorption in AS-4/PEEK, showing superior resistance against water absorption.
5. At a certain delamination area, the normalized residual compressive strength of K-49/828 was higher than that of MM-1/982X. However, the delamination area of K-49/828 was larger than that of MM-1/982X. Therefore, the normalized residual compressive strength of K-49/828 became almost the same as that of MM-1/982X, when compared at a certain impact energy.
6. The fracture surface examined indicates that AS-4/PEEK has superior fiber/matrix interfacial strength. However, K-49/828 has low fiber/matrix interfacial strength. In the case of K-49/828, the number of fiber splitting of the wet specimens were less than that of dry ones, because water absorption degraded the fiber/matrix interfacial strength.



*Fig.14 Relationship between delamination area and normalized residual compressive strength*

## REFERENCES

1. Komai, K., Minoshima, K. and Yamasaki, H. "Evaluation of Low-Velocity Impact Induced Delamination by Scanning Acoustic Microscope and Influence of Water Absorption on Delamination and Compression after Impact of CFRP", *Proceedings of the First International Conference on Mechanics of Time Dependent Materials*, Emri, I. and Knauss, W.G. Eds., 1995, pp. 287-292.
2. Morita, H. and Matsumoto, H., "Characterization on Impact Damage Resistance of CFRP Laminates under Falling Weight Test", *Transactions of The Japan Society of Mechanical Engineers*, Vol.61, No.581-A, 1995, pp.127-132(in Japanese).
3. Morton, J. and Godwin, E. W., "Impact Response of Tough Carbon Fiber Composites", *Composite Structures*, Vol.13, 1989, pp.1-19.
4. Dorey, G., Sidey, G. R. and Hutchings, "Impact properties of carbon fiber/Kevlar 49 fiber hybrid composites", *Journal of Composites*, January, 1978, pp.25-32.
5. Sakai, H. and Kuhino, S., "Aramid Fiber "Kevlar" as reinforcing Material of Plastics", *Reinforced Plastics*, Vol.31, No.12, 1985, pp.591-596(in Japanese).
6. Kamiyoshi, M., "Aramid Fiber", *Reinforced Plastics*, Vol.33, No.1, 1987, pp.28-32(in Japanese).
7. Komai, K., Minoshima, K. and Nitta, Y., "Influence of Water Environment on Fracture and Fatigue Strength of CF/PEEK Composite", *Proceeding of the 1994 Annual Meeting of JSME/MMD*, No.940-37, Vol.B, 1994, pp.382-383(in Japanese).
8. Allred, R.E. and Roylance, D. K., "Transverse moisture sensitivity of aramid/epoxy composites", *Journal of Materials Science*, Vol.18, 1983, pp.652-656.
9. Komai, K. and Shiroshita, S., "The Influence of Water and Test Frequency on the Fatigue Strength of Aramid/Epoxy Composites", *Proceeding of the Thirty-fifth Japan Congress on Materials Research*, 1992, pp.153-159.
10. Komai, K., Minoshima, K. and Turu, K., "The effect of Environment on the Tensile Fracture Behavior of Aramid Fibers", *Proceeding of the 72nd JSME Spring Annual Meeting*, Vol., 1995, pp.196-197(in Japanese).
11. Kato, S., "Aramid Fiber", *Journal of the Japan Society for Composites Materials*, Vol.17, No.51991pp.198-204(in Japanese)

# LOW VELOCITY IMPACT DAMAGE OF ORGANIC FOAM CORE SANDWICH COMPOSITES

**William J. Craft, Derke R. Hughes, and Ajit D. Kelkar**

*Department of Mechanical Engineering, North Carolina A&T State University,  
Greensboro, NC 27411, USA*

**SUMMARY:** The purpose of this study was to determine the amount of damage resulting in a sandwich shell composite due to impact by a mass with different impact energies. In addition, information on the failure characteristics versus the energy of the impact was desired. While there has been substantial work on impact damage of a number of laminated composites, little work exists on sandwich composites. The authors intended to investigate low velocity impact of sandwich panels using a drop weight system. The dynamic response of sandwich shells to low velocity impact is complex, and our ability to detect threshold damage is important, and the influence of core density on impact dynamics has not been investigated. We just concluded tests on 23 sandwich panels of three core densities at the Wright Patterson Flight Dynamics Laboratory Dynatup drop weight facility. Impact energies ranged from 0.28 to 36.9 Newton Meters.

While the number of samples is low, we have been able to determine the threshold energy producing incipient front-face damage as well as the energy producing maximum impact force after which catastrophic front face failure results. In addition, we have compared our results with those of laminated composite panels with a comparable number of plies. Sandwich panels are surprisingly robust, particularly resisting lower energy damage, and the density of the core has minimal affect on the panel stiffness. However, core density has a dramatic affect on the contact forces at impact. In addition, peak forces during impact are equivalent to peak forces achieved in quasi-static tests indicating that the inertia of a sandwich system is of no significant influence.

**KEYWORDS:** low velocity impact, sandwich plates, damage, damage tolerance

## INTRODUCTION

Low velocity impact is important in sandwich shell composites for a number of reasons. Perhaps most importantly, low-velocity impact can lead to damage which is frequently not detected by visual means. Secondly, it can lead to damage which substantially reduces the ability of the structure to survive the loads it was designed to resist. Since modern aircraft and aerospace vehicles are designed to minimize added weight, there is less margin of safety than with fixed structures making an accurate knowledge of failure more important.

Since composite materials are typically strong and stiff, they are prime candidates for aircraft structures, and since many applications are stiffness rather than strength driven, sandwich shell composites are ideal candidates for efficient aerospace structures. Some properties shared by many fiber-reinforced composites laminates include a low ultimate strain and

strength through the thickness [1]. Sandwich shell composite core materials also have a low shear and compression strength in comparison to the face sheets. By comparison to laminates, sandwich shell structures exhibit excellent stiffness and strength in bending and a low specific weight.

While this sounds like an ideal structural material for aeronautical and aerospace applications, impact resistance restricts the use of such structures where public safety is an issue. Low velocity impact testing, where velocities are under 12.2 m/s, is particularly important because 1) it can weaken the material without producing visible damage, 2) there are so many phenomena including improper manufacturing and assembly of sandwich shell components which can lead to this damage, and 3) the need to create more cost-effective, stiff, light-weight structures is forcing the industry to reconsider sandwich shells. Other factors limiting the usefulness of such materials include their tendency to absorb moisture. In fact foam cores made of polymethacrylimide (PMI) absorb high amounts of water as compared to honeycomb cores [2]. The objectives of the research were to investigate the low velocity impact damage at different energies, to determine the characteristics three different core densities contribute to the impact resistance of sandwich composites, and to compare the nature of damage inflicted by static and dynamic events.

### **PREPARATION OF PANELS**

Only sandwich plates formed into layered flat plates of dimension 178 mm by 254 mm are used for this study. The thickness of the plates is standardized at 19 mm although a planned extended study will include other core thicknesses. The external (face) sheets are made of nine laminae made of single plain weave carbon graphite fibers with an epoxy resin (Diaminodiphenyl Sulfone). This produces a final sheet of from 1.65 to 1.73 mm in thickness. The resulting plane weave laminate is similar to the [0/90] orientation in unidirectional laminates. The [0/90] stacking sequence is a common one which parallels that of the Cristescu [3] study. The McQuillen & Gause study, where a stacking sequence of  $[\pm 45/0_2/\pm 45]_s$  was used, gave very similar results for low velocity impact damage [4].

The external sheets of graphite epoxy laminates were fabricated and tested in the Center for Composite Materials Research (CCMR) within the Department of Mechanical Engineering at North Carolina A&T State University. The outer and inner face sheets were laminated in a hydraulic press. The Hydraulic Press was initially heated to 121°C and allowed to reach a pressure 689.5 kPa and temperature of 177°C. throughout all layers of

The coefficient of expansion for the resin and fibers are substantially different, and they can cause parasitic internal stresses unless processing is done carefully and consistently. After the laminate has been maintained at the prescribed temperature and pressure, the laminate was allowed to cool at 2 degrees per minute. This rate allows enough time for an annealing action reducing the parasitic stresses due to the thermal expansion mismatch. Material Property tests were conducted on the face sheets via an MTS-810 machine; the in-plane properties along the fiber directions are: 68.2 GPa (tensile modulus), 633 MPa (tensile strength), and 412 MPa (compressive strength). The external sheets strength properties were taken from a nine ply laminate specimens cut from sheets originally of dimension 0.42 Meter by 0.51 Meter. The tensile tests followed the American Standard for Test and Materials (ASTM) D 638-94b. Compression tests followed ASTM D 1621-94.

Rohacell is a polymethacrylimide (PMI) foam. The core material for our sandwich panels was fabricated from one layer of Rohacell. The construction was chosen to approximate an efficient structure maintaining both high stiffness and strength, in resisting bending loads. Rohacell foam can be acquired in a variety of densities and shear and compressive strengths. One important consideration in using it for this work is that we could experiment with combinations of core properties to obtain an optimized structure.

The Rohacell core is easily machinable and the cost is less than standard honeycomb (Nomex); however, it is hygroscopic and it has both a low shear strength and stiffness. Mass densities of 32, 52, and 75 Kg/M<sup>3</sup> have been selected for the core since they represent a range of properties of sandwich cores, and the effect of core density on impact damage is an important part of the study. They are referred to as R-31, R-51, and R-71. The Table below indicates some important stiffness and strength parameters for Rohacell.

*Table 1: Rohacell stiffness and strength properties*

Density (Kg/M <sup>3</sup> )	Young's Modulus (N/mm <sup>2</sup> )	Shear Modulus (N/mm <sup>2</sup> )	Tensile Strength N/mm <sup>2</sup>	Compressive Strength N/mm <sup>2</sup>	Shear Strength N/mm <sup>2</sup>	Flexural Strength N/mm <sup>2</sup>
32	36	13	1.0	0.4	0.4	0.8
52	70	19	1.9	0.9	0.8	1.6
75	92	29	2.8	1.5	1.3	2.5

Once the face sheet is formed, the internal sheet is bonded to each of the external sheet in an oven with AF-163 film adhesive. A prescribed heating and cooling rate as part of the curing process helps to control parasitic stresses. Once the sandwich shell laminated composites structures are assembled, they are checked for warping and dimension. They are edge cut to their final shape required for low velocity impact tests, measured for dimensional tolerances, and weighed.

There was concern that conventional cutting equipment could cause delamination at the face-core interfaces, and an Ingersoll-Rand HS-3000 water jet system was used to final cut all specimens. The closed cell geometry is destroyed near machining cuts, and since a water jet was used, each specimen absorbed some water and had to be dried. To do this, specimens were placed into an autoclave for 6 hours at 71.1°C. After cooling, Dow Corning RTV # 737 100% silicone rubber was applied to specimens for water proofing and left intact there through C-SCAN evaluations.

All impact studies were performed at the Wright-Patterson Flight Dynamic Laboratory Dynatup machine drop weight system. In our configuration, the system employs a free-falling drop weight and precision recording system. The drop weight mass was 3.37 Kilograms, and contact with the specimen was made through a 12.7 mm radius indentor normal to the specimen centers. The Boeing test fixture simulating simple support was used. The fixture is important since it controls fixity; fixity affects specimen compliance which changes the force-time impact curve.

## EXPERIMENTAL RESULTS

All impact specimens were identical except for the density of the Rohacell foam core. The specimens of Table 2. are sorted by density and drop height. A total of twenty-three specimens were tested in the Dynatup machine. For completeness, specimen ID, impact velocity (m/s), maximum contact force (Newtons), and impact duration (msec.) are displayed. The drop height was measured using a precision gage block set. The quantities including impact velocity, impact force, and impact event duration were all determined experimentally through drop-weight accelerometers which had an output sampling rate of 40 samples per millisecond. All other data in this study can be derived from these values.

*Table 2: Tested impact specimens sorted by core density and drop weight height*

Specimen ID	Drop Height mm	Density designation	Impact vel. (m/s)	Contact force (N)	Impact duration (msec.)
1	25.40	R-31	0.7071	1458.90	10.97
2	39.42	R-31	0.8778	1569.30	11.65
3	51.77	R-31	0.9997	1721.40	12.15
4	75.74	R-31	1.2009	1887.70	12.90
5	101.60	R-31	1.3929	2176.90	12.57
6	127.00	R-31	1.5575	2264.00	13.25
7	139.70	R-31	1.6368	2303.60	13.43
8	25.67	R-51	0.7102	1672.90	9.05
9	39.22	R-51	0.8717	1949.10	9.70
10	51.36	R-51	0.9967	2216.00	9.88
11	75.77	R-51	1.2009	2393.50	10.55
12	101.50	R-51	1.3929	2471.80	11.23
13	127.00	R-51	1.5575	2698.20	10.95
14	139.70	R-51	1.6368	2537.60	11.75
15	25.40	R-71	0.6706	1790.30	8.02
16	38.86	R-71	0.8656	2162.20	7.93
17	51.13	R-71	0.9967	2471.30	8.43
18	75.44	R-71	1.1979	2985.10	8.25
19	101.20	R-71	1.3868	2852.90	9.72
20	101.60	R-71	1.3929	2890.30	9.40
21	127.00	R-71	1.5606	3253.70	8.85
22	127.00	R-71	1.5636	2944.60	9.60
23	138.90	R-71	1.6368	3047.30	9.92

Before dynamic tests were conducted, a static test was conducted on a sample of each density. Static tests were run on a universal testing machine with the same indenter and Boeing fixture which would be used in all drop weight impact tests. All static tests was conducted at

crosshead velocities of 0.02 millimeters per second. Samples required 5 to 10 minutes for the maximum contact force to occur. In each case, the time force curve was smooth until it was reached. Afterwards, the force decreased somewhat erratically and was accompanied by popping noises indicating the integration of additional damage.

An initial drop height for each density was selected by trial-and-error. The initial heights were chosen so that a contact force of about 50% of the static test maximum contact force would be developed. From this initial setting, the drop weight height was increased until additional drop heights produced no higher contact force maximum. After this, the drop weight heights were decreased until a height was reached which produced no detectable impact damage.

Two techniques were used to determine the force producing incipient damage in these sandwich plates. Incipient damage was determined by: 1) decreasing the drop weight height until there was no visible asymmetry in the force-time curves and 2) noting at what level the impact force-time plot first deviated from a smooth curve. This point was characterized by substantial "ringing" in the accelerometer output. As it turns out, both methods produced results which were very similar. This is to be expected if the inertia of the plates is negligible in the impact event and if there are no significant time-dependent mechanics at work. A post-impact study of foam core structures has been reported by Caprino and Teti [5]; new theories of non-linear behavior mechanics have been proposed by Kuhhorn and Schoop [6], but our study did not extend past the energy producing maximum contact force since this constitutes failure of the outer face sheet.

The force-time histories for all twenty-three specimens of all three density core sandwich panels were numerically smoothed and displayed in an overlay as Figure 1. All impact tests on all twenty-three sandwich panels are included. These graphs are separated into three sections as a function of core densities and drop heights. For comparison, one overlaid graph of force-time histories for R-51 for the lowest, mid-level, and highest impact energies is also reproduced in *as recorded* format, Fig. 2.

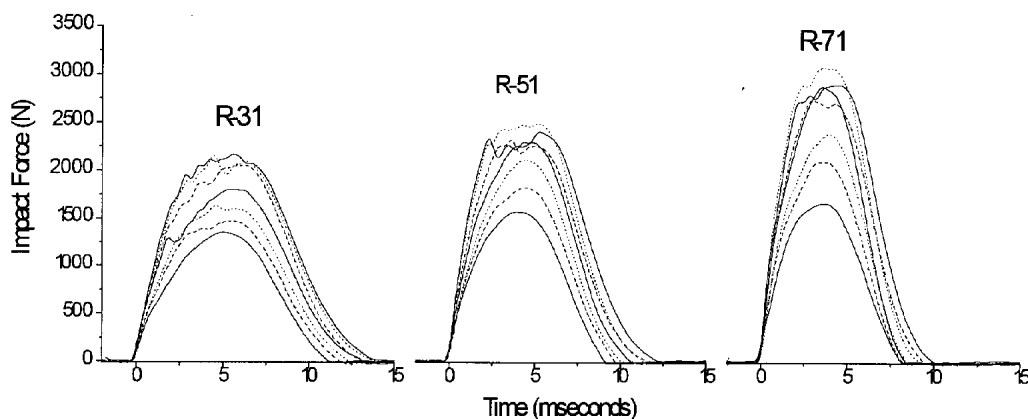


Fig. 1: Force-time histories of impacted sandwich panels (smoothed data)

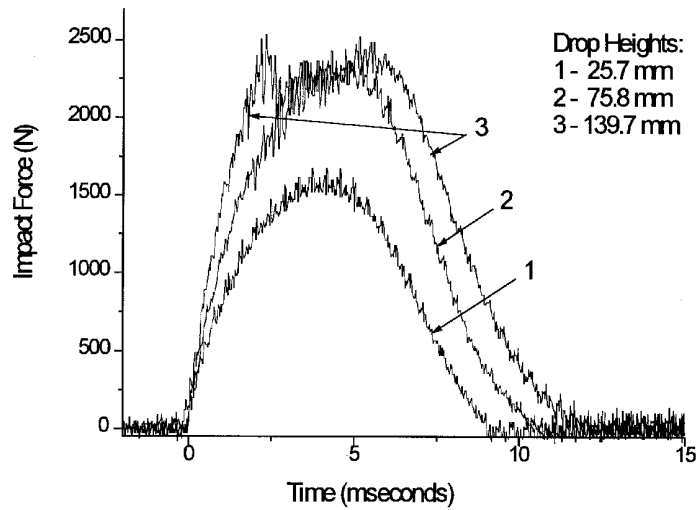


Fig. 2: Unsmoothed force-time histories for R-51 core panels

The fact that higher impact forces are developed in stiffer panels for a given drop height is easily seen in Fig. 3 where three specimens (numbers 4, 11, and 18) were subjected to [almost identical] drop heights of about 75 millimeters. The force change due to the foam cores is substantial even though all face sheets are identical. Note also the increased contact time and the equal impulse to all three specimens. The largest impact force developed in the R-71 highest density core panel specimen is 58% more than the force developed during impact with the R-31 specimen.

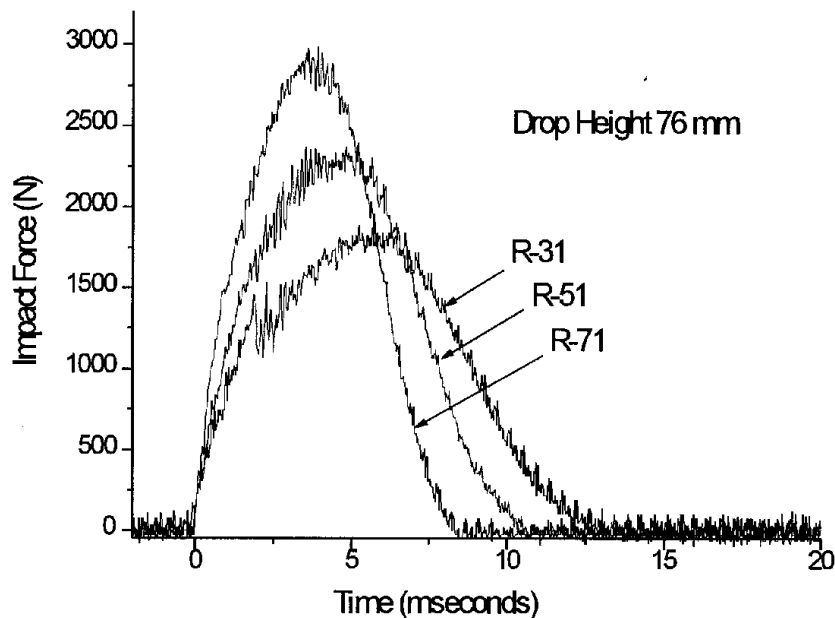


Fig. 3: The effect of stiffness on force-time history for a given drop height



Figs. 4 and 5 are overlays of tests on all twenty-three specimens. The maximum impact force is shown both as a function of drop height and core density. Least square generated curves are generated for the portion of the curves indicating a leveling-off at the high drop heights as a result of the inability of the specimen to sustain additional impact load.

For low drop heights, the R-51 and R-71 curves in Fig. 4 are linear as indicated by the dark lines. The R-31 curve is less linear in this range indicating the potential that some damage has already occurred. Impact duration in milliseconds is plotted vs. drop height for each of the three core density specimens. Fig. 5 shows data and a linear curve fit for each density foam. Even though there is scatter, the figure demonstrates that lower density cores contribute dramatically to the ability of the panels to decelerate the drop weight more slowly, thereby extending the drop height at which catastrophic failure occurs. As a practical measure, we attempted to compare the performance of sandwich panels to that of laminated panels of equivalent numbers of layers, panel dimensions, and fixture.

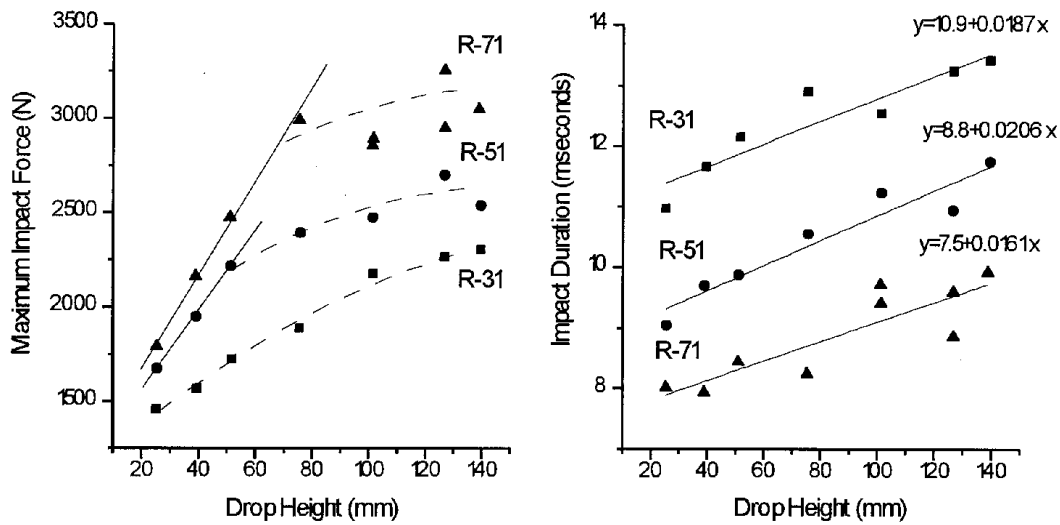


Fig. 4: Maximum impact force vs. drop height      Fig. 5: Impact duration vs. drop height

Prior impact tests were conducted by the authors on 16, 32, and 48 ply laminated panels [7]. While these panels were made of quasi-isotropic layers of uniaxial laminates, the results attained on 16 ply panels parallels closely the current study. Fig. 6 shows a comparison of the threshold damage energy levels in panels in each study. Note that the energy required to produce incipient damage in the R-31 sandwich and the 16 ply laminates are virtually identical. What is remarkable is the energy required to produce threshold damage in sandwich panels. R-51 and R-71 density core sandwich composites with 9 ply plain weave graphite laminate face sheets are about as resistant to incipient damage as are laminated panels of 32 ply and 48 ply, respectively.

While sandwich panels are robust in absorbing energy without suffering incipient damage, they lack resistance to damage at higher energies. This is clearly shown in Fig. 7. In this case, the energy producing maximum force and damage of the front face sheet is plotted for each of the three density foam sandwich panels. Beside these data are plotted the equivalent energies producing backface spalling in 16, 32, and 48 ply laminated panels. Here there is substantial improvement in the laminated thicker panels.

Calculations were also made comparing the coefficients of  $D$  [bending stiffness] Matrix for the sandwich specimens with those of the laminated specimens of [7]. While bending stiffness coefficients for the laminated panels varied greatly, those of the sandwich panels were almost identical no matter which density core is used; they varied by less than 1%. In ongoing studies, deflection measurements were made on sandwich beams made of the same panels of this study. Such materials deflected up to four times the amount predicted by bending theory. This indicated that there is substantial shear deformation in low-density sandwich panels. This may also help explain the resistance of these panels to low energy impact.

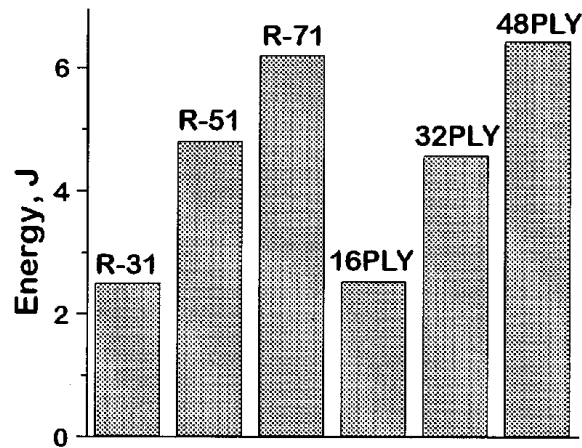


Fig. 6: Energy required to produce incipient damage in both sandwich and laminated panels

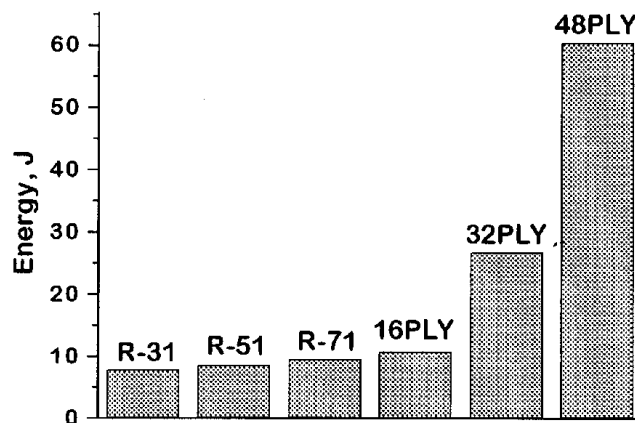


Fig. 7: Damage tolerance of sandwich and laminated panels at peak energies

## CONCLUSIONS

This work shows that damage in sandwich shells and laminated composite structural panels is substantially different. A major difference is the localization of damage in sandwich panels. In this case, the face sheets become more loaded in membrane rather than in bending. Another difference is the compliance of the core in sandwich panels as a factor in their damage resistance. While we did not present extended data about NDE techniques, we C-

SCANNED all tested panels. That information is currently being analyzed, however it has been difficult to determine the nature and degree of damage to sandwich panels through C-SCAN techniques.

Another interesting result is the substantial effect of core density on impact force. Higher impact forces were developed at a given drop height in panels made of stiffer cores even the classical laminate theory bending stiffness coefficients hardly changed. However, impact forces developed only until the material strength limit was reached no matter how much the impact energy was increased. At threshold damage levels, there was little difference in contact forces developed.

There was also no indication that the inertial of sandwich panels had an affect on the maximum force sustained at peak energy impact. Perhaps the most interesting finding was the ability of sandwich panels to perform exceedingly well in resisting initial damage. In fact, the higher density sandwich panels performed better than laminated panels of over 2.5 times their specific weight. On the other hand, if failure of a sandwich panel is defined as failure of the outer skin, then thin laminated panels perform about the same as sandwich panels while thick laminated panels perform substantially better.

### **ACKNOWLEDGEMENTS**

In closing, we wish to thank the NASA Center for Research Excellence for the support of Mr. Derke Hughes and for assisting with materials and travel expenses. We also wish to thank the Center for Composite Materials Research for the use of fabrication facilities and Wright Patterson Air Force Base for the use of structural testing and NDE facilities.

### **REFERENCES**

1. Kelkar, A., "Analysis of Composite Laminates Subjected to Low Velocity Impact Loading", Wright-Patterson Air Force Base, AFB 45433-6553, June 1992, pp. 4-5.
2. Granville, D. M., "Moisture Effects of Polymethacrylimide Foam and Honeycomb Comb Core in Sandwich / Skin Structures", 43<sup>rd</sup> Annual National Forum and Technology Display of the Helicopter Society, St. Louis, MO, May 1987.
3. Cristescu, N., Malvern, L. E., and Sierakowski, R. L., "Failure Mechanisms in Composites Plates Impacted by Blunt-Ended Penetrators", Foreign Object Impact Damage to Composites, ASTM STP 568, *American Society for Test and Materials*, 1975, pp. 159-172.
4. McQuillen, E. J. and Gause, L. W., "Low Velocity Transverse Normal Impact of Graphite Epoxy Composite laminates," *Journal of Composite Materials*, Vol. 10, January, 1976.
5. Caprino, G., and Teti, R., "Impact and post-impact behavior of foam core sandwich structures", *Composite Structures*, 1994, pp. 47-55.
6. Kuhhorn, A., and Schoop, H., "A nonlinear theory for sandwich shells including the wrinkling phenomenon," *Archives of Applied Mechanics*, 1992, pp. 413-427.
7. Kelkar, A. D., Craft, W. J., and Sandhu, R. S. "Study of Progressive Damage in Thin and Thick Composite Laminates Subjected to Low Velocity Impact Loading." PVP-Vol. 13, *Recent Advances in Structural Mechanics*, ASME 1993.

# PERFORATION CHARACTERISTICS PREDICTION OF MULTI-LAYERED COMPOSITE PLATES SUBJECTED TO HIGH VELOCITY IMPACT

**Hideaki Kasano and Kenichi Abe**

*Department of Mechanical Systems Engineering, Takushoku University  
815-1 Tate-machi, Hachioji City, Tokyo 193, Japan*

**SUMMARY:** The purpose of this work is to present a new analytical model for predicting the perforation characteristics of unbonded multi-layered composite plates. Two models are introduced to predict the perforation characteristics of a single-layered plate, which are based on the conservation laws of momentum and/or energy. These models are extended to a model for a  $n$ -layered plate to predict the residual velocity of a projectile after perforation as well as the ballistic limit velocity. The effects of the stacking sequences of the constituting layers on these characteristics are also investigated.

**KEYWORDS:** high velocity impact, impact perforation, composite layered plate analytical modeling, residual velocity, ballistic limit velocity, conservation laws

## INTRODUCTION

Since the perforation characteristics is a critical factor in the design of protective structures, the problems of a projectile perforating a target plate made of concrete and/or metal have been extensively investigated in the field of nuclear power plants and body armours. Recently, with an expected use of composite materials in structural applications threatened by high velocity impact, the attention is also being attracted to the fiber reinforced plastic plates such as CFRP, GFRP and AFRP [1]- [5]. Most of these investigations deal with single-layered plates and only a few considered multi-layered plates [6]-[8]. In general, the multi-layered plates are expected to be more effective in the protective structures compared to the single-layered plates. Meanwhile, three approaches have traditionally been used in these investigations, i.e., empirical formulation, analytical modeling, and computer simulation[9]. Among them, the analytical modeling often provides simple expressions for predicting the perforation characteristics without resorting to an extensive database or a time-consuming calculation. Therefore, in the present investigation, the method of analytical modeling is employed together with the conservation laws of momentum and/or energy. Two models are

first introduced for predicting the perforation characteristics of a single-layered plate. High velocity impact tests are performed to verify the models and to characterize the residual velocity and the ballistic limit velocity for two kinds of CFRP plates as well as aluminum plates. These models are then extended to a model for unbonded  $n$ -layered plates. By using the new model, the corresponding characteristics of some layered-plates is predicted.

## PERFORATION MECHANICS OF A SINGLE-LAYERED PLATE

### General Expressions for Residual Velocity and Ballistic Limit Velocity

Consider a projectile impinging on a target plate as shown in Fig.1 and passing through it.

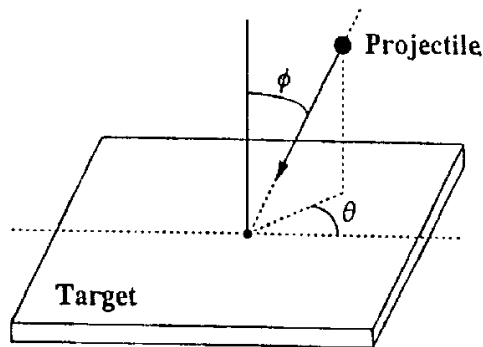


Fig. 1: A single-layered plate impacted by a steel ball

In this problem, the perforation characteristics is expressed in terms of a residual velocity of the projectile after perforating the target plate and a ballistic limit velocity which indicates the preventability of perforation. In general, these characteristics are functions of many factors associated with a projectile, a target plate and impact conditions. A general form of the residual velocity  $V_R$  may be expressed with

$$V_R = F(a_1, a_2; V_i, \Psi) \quad (1)$$

in which,  $a_1$ : material properties of a projectile and a target plate,  $a_2$ : initial geometry of a projectile and a target plate,  $V_i$ : impact velocity of a projectile and  $\Psi$ : obliquity =  $(\phi, \theta)$ . The ballistic limit velocity  $V_b$  is defined as the velocity beyond which a specified projectile perforates a specified target plate and below which it will not. So it is given by,

$$V_b = \max \{V_i: V_R=0\} = \inf \{V_i: V_R>0\} \quad (2)$$

Then, by using Eqs.(1) and (2), we have

$$0 = F(a_1, a_2; V_b, \Psi)$$

and, from this equation, the ballistic limit velocity  $V_b$  is expressed in the form of

$$V_b = G(a_1, a_2; \Psi) \quad (3)$$

The ballistic limit velocity given by Eq.(3) being regarded as one parameter affecting the residual velocity , the expression (1) may also be rewritten in the form of :

$$V_R = \bar{F}(a_1, a_2, V_b; V_i, \Psi) \quad (4)$$

### Governing Equations

Consider a normal impact ( $\phi=0$ ) of a steel ball projectile on a single-layered target plate. The projectile will go through the plate accompanying a plug as shown in Fig.2, in which  $V_i$  : impact velocity of a projectile,  $V_R$  : residual velocity of a projectile and also a plug,  $M$  : mass of a projectile and  $m$  : mass of a plug removed from the plate due to impact.

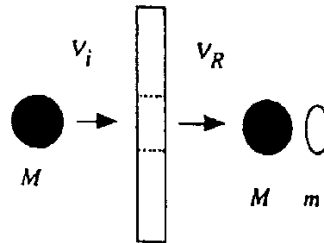


Fig.2: Perforation process of a projectile running through a single-layered plate

The equations governing this process is described by the two conservation laws, that is, the conservation of momentum:

$$MV_i = MV_R + mV_R + I \quad (5)$$

and the conservation of energy:

$$\frac{1}{2}MV_i^2 = \frac{1}{2}MV_R^2 + \frac{1}{2}mV_R^2 + E_p \quad (6)$$

in which  $I$  : impulse transmitted to the plate and  $E_p : = E_p(V_i)$  total energy lost during the perforation process.

### Analytical Modeling

Two analytical models are introduced to predict the residual velocity and the ballistic limit velocity for a single-layered plate.

#### Model A

By using Eqs.(2) and (6), we have

$$\frac{1}{2}MV_b^2 = E_p(V_b) \tag{7}$$

Assuming here that, for the impact velocity greater than the ballistic limit velocity, the perforation energy does not depend on the impact velocity and it is constant, then, it follows from Eq.(7) that

$$E_p(V_i) = \frac{1}{2}MV_b^2 \tag{8}$$

Substituting Eq(8) into Eq(6), we get

$$\frac{1}{2}MV_i^2 = \frac{1}{2}(M+m)V_R^2 + \frac{1}{2}MV_b^2 \tag{9}$$

for  $V_i \geq V_b$ , from which the expressions for  $V_b$  and  $V_R$  are derived as follows:

$$V_b = \sqrt{V_i^2 - \left(\frac{M+m}{M}\right)V_R^2} \quad V_R = \left(\frac{M}{M+m}\right)^{1/2} \sqrt{V_i^2 - V_b^2} \tag{10}$$

**Model B**

This model was proposed by Recht and Ipson [10]. In the modeling, we first consider the inelastic impact of a projectile and a plug which is assumed to be unconstrained by the plate. Then, from Eqs.(5) with  $l=0$  and (6) with  $E_p = E_{Pf}$ , we get

$$E_{Pf} = \frac{1}{2} \frac{Mm}{(M+m)} V_i^2 \tag{11}$$

in which  $E_{Pf}$  is elastoplastic deformation energy associated with free impact of the projectile and the plug. Next we consider the inelastic impact of a projectile and a target plate. We assume that the plug with mass of  $m$  is removed from the plate during the perforation process and that it flies at the same velocity as the projectile. By dividing the total energy  $E_p$  in Eq.(6) into two parts of  $E_{Pf}$  and  $E_{Ps}$ , we have

$$\frac{1}{2}MV_i^2 = \frac{1}{2}(M+m)V_R^2 + E_{Pf} + E_{Ps} \tag{12}$$

where  $E_{Ps}$  is elastoplastic deformation energy due to the plug being constrained by the plate. By substituting Eq.(11) into Eq.(12), we have the expression for  $E_{Ps}$  as follows:

$$E_{Ps} = \frac{1}{2} \frac{M^2}{(M+m)} V_i^2 - \frac{1}{2}(M+m)V_R^2 \tag{13}$$

Assuming that, for the impact velocity greater than the ballistic limit velocity, the elastoplastic deformation energy  $E_{Ps}$  is not dependent on the impact velocity and it is constant,

then, by putting  $V_i = V_b$  and  $V_R = 0$  in Eq.(13), we get

$$E_{fb}(V_i) = \frac{1}{2} \frac{M^2}{(M+m)} V_b^2 \quad (14)$$

Finally, substitution of Eqs. (14) into Eq.(13) leads to the following expressions for the ballistic limit velocity and the residual velocity:

$$V_b = \sqrt{V_i^2 - \left(\frac{M+m}{M}\right)^2 V_R^2} \quad V_R = \frac{M}{M+m} \sqrt{V_i^2 - V_b^2} \quad (15)$$

Accordingly, Eqs.(10) and (15) are expressed in the same form of

$$V_b = \sqrt{V_i^2 - V_R^2 / \alpha^2} \quad (16)$$

$$V_R = \alpha \sqrt{V_i^2 - V_b^2} \quad (17)$$

in which the mass coefficient  $\alpha$  is given by

$$\alpha = \left(\frac{M}{M+m}\right)^{1/2}, \quad \alpha = \frac{M}{M+m} \quad (18)$$

for *Model A* and *Model B*, respectively.

For a pair of  $V_i$  and  $V_R$  along with  $\alpha$  obtained from an impact test, the corresponding  $V_b$  is calculated from Eq.(16). An average of these calculated  $V_b$ 's for some different pairs of  $V_i$  and  $V_R$  is regarded as the ballistic limit velocity, which is a constant value. The ballistic limit velocity being thus determined, the residual velocity of the projectile for a given impact velocity is predicted from Eq.(17).

## DETERMIATION OF PERFORATION CHARACTERISTICS

In order to verify the analytical models and to determine the perforation characteristics for some single-layered plates, high velocity impact tests were performed. A steel ball is used as a projectile, which is 5mm in diameter and 0.51g by weight. The testing machine is capable of firing a projectile at a maximum velocity of 330m/s. Orthotropic and quasi-isotropic CFRP plates and A5052 aluminium plates are chosen as the target plates. The preliminary tests showed that *Model A* is applicable to CFRP plates and *Model B* to aluminium plates. Figure 3 shows the residual velocity as a function of impact velocity, where the open symbols represent the experimental results. In this figure, no perforation occurred at the impact velocity represented by the filled symbols. Figure 4 shows the ballistic limit velocity as a function of plate thickness. From these figures, the ballistic limit velocity and the residual velocity are determined and predicted by

$$V_{bt} = \beta t \quad (19)$$



$$V_{RT} = \alpha \sqrt{V_i^2 - V_{bT}^2} = \alpha \sqrt{V_i^2 - \beta^2 t^2} \quad (20)$$

with  $\alpha = 0.915$  and  $\beta = 70(\text{m/s/mm})$  for the orthotropic, and  $\alpha = 0.907$  and  $\beta = 63$  for the quasi-isotropic CFRP plates. On the other hand, for aluminium plates, although we have  $\alpha = 0.933$ , the ballistic limit velocity is given by,

$$V_{bT} = \beta_1 t \quad (0 \leq t \leq 1.5) \text{ and } \beta_1 t + \beta_2 (t - 1.5)^2 \quad (1.5 \leq t \leq 2.0) \quad (21)$$

with  $\beta_1 = 188.6$  and  $\beta_2 = -424.3$ .

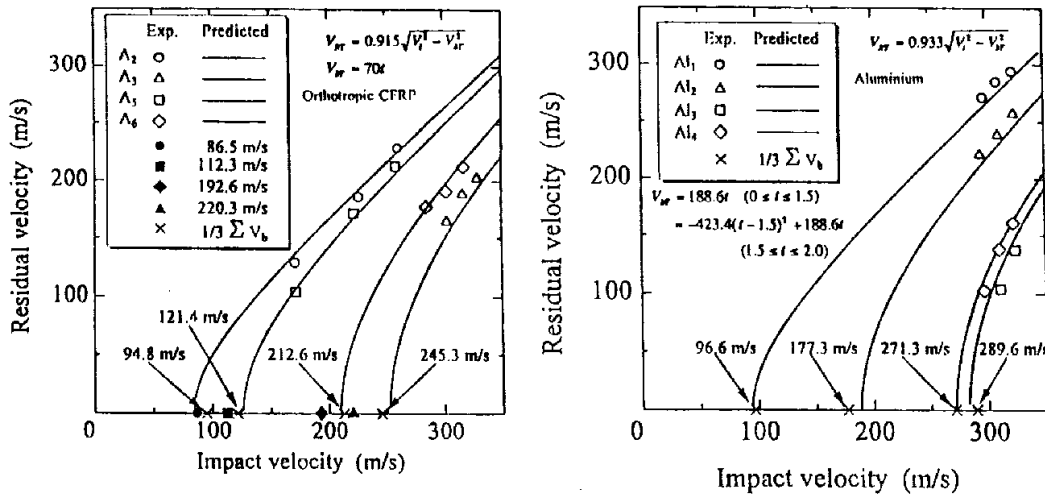


Fig.3 : Residual velocity as a function of impact velocity

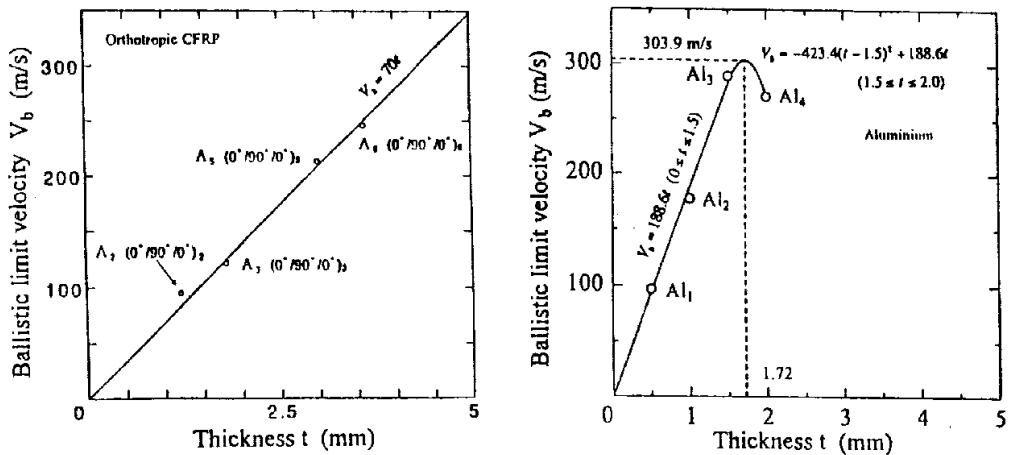


Fig.4 : Ballistic limit velocity as a function of plate thickness

### PERFORATION MECHANICS OF A MULTI-LAYERED PLATE

#### N-layered Plate Model and Assumptions

Suppose that a multi-layered plate is composed of  $n$  single-layered plates as shown in Fig. 5 and that the perforation characteristics of each single plate is given, then the final residual

velocity of a steel ball projectile after perforating the last layer and the ballistic limit velocity of the  $n$ -layered plate are predicted using a new analytical model proposed in the following.

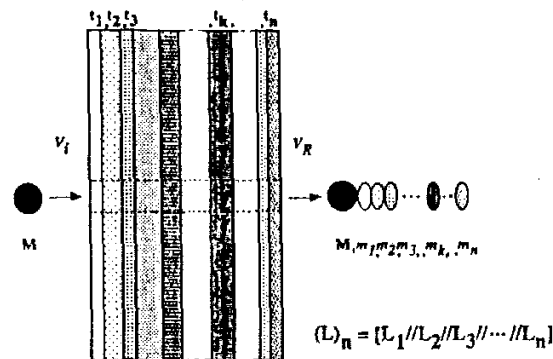


Fig.5 : A projectile perforating an unbonded  $n$ -layerd plate accompanying plugs

For simplifying the problem, we make the following assumptions in the analysis :

- adjacent layers in the plate are in contact without bonding
- interaction of the perforation process with the overall structural response is neglected
- mass of a projectile when it impacts the  $n$ th layer is sum of the initial mass of the projectile and the total plug mass removed from the  $n-1$  layers
- impact velocity of a projectile when it impinges on the  $n$ th layer is equal to the residual velocity after it perforated the  $n-1$ th layer

### Analytical Modeling

By using an expression for a residual velocity of a single-layered plate, the residual velocity  $V_{R1}$ , after the steel ball projectile impinging on the 1st layer at the initial impact velocity  $V_{i1}$  and perforating it, is given by

$$V_{R1} = \alpha_1 \sqrt{V_{i1}^2 - V_{b1}^2} \tag{22}$$

Continuously, the projectile impinges on the 2nd layer at the velocity of  $V_{i2}$  and perforates it. The residual velocity  $V_{R2}$  is then given in the same form:

$$V_{R2} = \alpha_2 \sqrt{V_{i2}^2 - V_{b2}^2} \tag{23}$$

If we put here  $V_{i2} = V_{R1}$  from the assumptions, it follows:

$$V_{R2} = \alpha_2 \sqrt{\alpha_1^2 (V_{i1}^2 - V_{b1}^2) - V_{b2}^2} = \alpha_1 \alpha_2 \sqrt{V_{i1}^2 - (V_{b1}^2 + \frac{V_{b2}^2}{\alpha_1^2})} \tag{24}$$

In addition, if we use this expression as the impact velocity at which the projectile impinges on the 3rd layer, the residual velocity for the 3rd layer perforation is obtained as follows:

$$V_{R3} = \alpha_1 \alpha_2 \alpha_3 \sqrt{V_{i1}^2 - \left\{ V_{b1}^2 + \frac{V_{b2}^2}{\alpha_1^2} + \frac{V_{b3}^2}{(\alpha_1 \alpha_2)^2} \right\}} \quad (25)$$

In a like manner, we can deduce the residual velocity after the  $n$ th layer is perforated. Then the final residual velocity after the steel ball projectile completely goes through the  $n$ -layered plate is expressed with the following form:

$$V_R = \alpha^* \sqrt{V_i^2 - V_B^2} \quad (\alpha^* = \alpha_1 \alpha_2 \cdots \alpha_k \cdots \alpha_n) \quad (26)$$

The ballistic limit velocity  $V_B$  for the  $n$ -layered plate is also given by

$$V_B = \sqrt{\sum_{k=1}^n \frac{V_{bk}^2}{(\alpha_1 \alpha_2 \cdots \alpha_{k-1})^2}} \quad (27)$$

where  $V_{bk}$  is a ballistic limit velocity for the  $k$ th layer and the mass coefficient is

$$\alpha_k = \sqrt{\frac{M + m_1 + m_2 + \cdots + m_{k-1}}{M + m_1 + m_2 + \cdots + m_{k-1} + m_k}} \cdots (k = 1, 2, \cdots, n) \quad (28)$$

for the  $k$ th layer with the *Model A* applied. Meanwhile, when the *Model B* is applied

$$\alpha_k = \frac{M + m_1 + m_2 + \cdots + m_{k-1}}{M + m_1 + m_2 + \cdots + m_{k-1} + m_k} \cdots (k = 1, 2, \cdots, n) \quad (29)$$

In these expressions,  $m_0=0$  and  $\alpha_0=1$  are presumed.

### THEORETICAL PREDICTIONS FOR SOME LAYERED PLATES

#### Constituting Layers with Ballistic Limit Velocity Propotional to Thickness

Consider a  $n$ -layered plate with the  $k$ th layer having a ballistic limit velocity of  $V_{bk} = \beta_k t_k$ , in which  $t_k$  is thickness of the  $k$ th layer. We represent the layer by  $L_k = L(\alpha_k, \beta_k t_k)$  and the layered plate by  $(L)_n = [L_1 // L_2 // \cdots // L_n]$ . Then, Eq.(27) yields as follows:

$$V_B = \sqrt{\sum_{k=1}^n \frac{\beta_k^2 t_k^2}{(\alpha_1 \alpha_2 \cdots \alpha_{k-1})^2}} \quad (30)$$

If each layer has the same perforation characteristics ( $\alpha, \beta$ ) and thickness  $t$ , then Eqs.(26) and (30) become:

$$V_R = \alpha^n \sqrt{V_i^2 - V_B^2} \quad (31)$$

$$V_B = \sqrt{\sum_{k=1}^n \frac{\beta^2 t^2}{\alpha^{2(k-1)}}} = \frac{1}{\alpha^{n-1}} \sqrt{\frac{1 - \alpha^{2n}}{1 - \alpha^2}} \beta t \quad (32)$$

Table 1 shows one example of the predicted and the measured residual velocities for the 2, 3,

and 4-layered aluminium plates, where  $\alpha=0.933$ ,  $\beta=188.6$ , and  $t=0.5$ . A fairly good agreement is found between them.

Table 1: Comparison of predicted and measured residual velocity for  $(Al)_n$

Specimen	$V_i$ (m/s)	$V_R$ (m/s)	$V_{RT}$ (m/s)
(Al)2	319.8	252.1	239.5
	321.9	252.1	241.5
	318.1	241.9	237.9
(Al)3	321.2	220.6	218.4
	322.9	222.2	220.1
	319.1	222.2	216.4
(Al)4	318.8	179.6	181.4
	319.8	184.0	182.4
	318.5	185.2	181.1

### Stacking Sequences and Perforation Characteristics

The expressions for the predicted residual and ballistic limit velocities of a  $n$ -layered plate obtained in the previous section suggest that these characteristics depends on the stacking sequences of the constituting layers. So it is interesting to investigate the effects of the stacking sequences on the residual and the ballistic limit velocities. Here we consider only two examples of two-layered plates as shown in Figure 6.

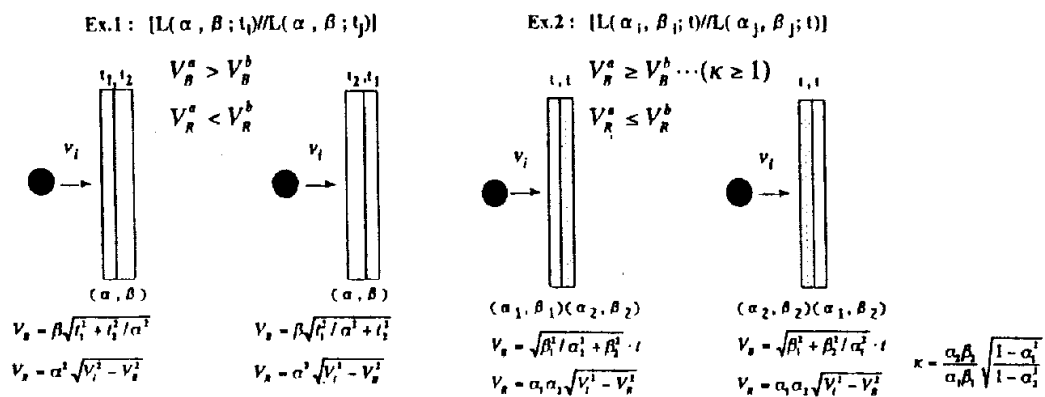


Fig.6: Two-layered plates of different stacking sequences

If the two layers have the same perforation characteristics  $(\alpha, \beta)$  and the different thickness  $t_1, t_2$  ( $t_1 < t_2$ ), the ballistic limit velocity of the plate with a thicker layer placed on the back side is greater than otherwise. The situation is reversed for the residual velocity. On the other hand, if the two layers have the different perforation characteristics  $(\alpha_1, \beta_1), (\alpha_2, \beta_2)$  and the same thickness  $t$ , the preventability of perforation depends on the characteristics ratio  $\kappa$  which is a function of the perforation characteristics of the constituting layers.

## CONCLUSION

A new analytical model for predicting the residual velocity of a steel ball projectile after perforating an unbonded multi-layered plate and the ballistic limit velocity of the plate was proposed. This is a direct extension of the predictive model for a single-layered plate. The residual velocity predicted from the model fairly agreed with the available experimental results for aluminium layered plates. The effects of the stacking sequences of the constituting layers on the perforation characteristics was also investigated for some examples. In order to verify this new model, more experimental results may be required.

## ACKNOWLEDGEMENTS

One of the authors (H.K.) wishes to acknowledge the support of the Iketani Science and Technology Foundation in the improvement of the impact testing machine.

## REFERENCES

1. Cantwell, W.J. and Morton, J., "Impact Perforation of Carbon Fiber Reinforced Plastic", *Composites Science and Technology*, Vol. 38, 1990, pp. 119-141.
2. Zhu, G., Goldsmith, W. and Dharan, C.K.H., "Penetration of Laminated Kevlar by Projectile: II. Analytical Model", *Int. J. Solids & Struct.*, 29-4, 1992, pp.421-436.
3. Lee, S.W.R. and Sun, C.T., "Dynamic Penetration of Graphite/Epoxy Laminates Impacted by A Blunt-ended Projectile", *Composites Science and Technology*, Vol. 49, 1993, pp. 369-380.
4. Goldsmith, W., Dharan, C.K.H. and Chang, H., "Quasi-static and Ballistic Perforation of Carbon Fiber Laminates", *Int. J. Solids & Struct.*, 32-1, 1995, pp. 89-103.
5. Sun, C.T. and Potti, S.V., "A Simple Model to Predict Residual Velocities of Thick Composite Laminates Subjected to High Velocity Impact", *Int. J. Impact Engng.*, 18-3, 1996, pp. 339-353.
6. Maron, I. and Bodner, S.R., "Projectile Perforation of Multi-layered Beams", *Int. J. Mech. Sci.*, Vol. 21, 1979, pp. 489-504.
7. Radin, J. and Goldsmith, W., "Normal Projectile Penetration and Perforation of Laminated Targets", *Int. J. Impact Engng.*, 7-2, 1988, pp. 229-259.
8. Hetherington, J.G., "The Optimization of Two Component Composite Armours", *Int. J. Impact Engng.*, 12-3, 1992, pp. 409-414.
9. Zukas, J.A., *High Velocity Impact Dynamics*, John Wiley & Sons, Inc., New York, 1990.
10. Recht, R.F. and Ipson, T.W., "Ballistic Perforation Dynamics", *J. Appl. Mech.*, Vol. 30, 1963, pp. 384-390.

# FINITE ELEMENT ANALYSIS OF THE BALLISTIC IMPACT RESPONSE OF COMPOSITE HELMET MATERIALS

J. van Hoof<sup>1</sup>, M.J. Worswick<sup>1</sup>, P.V. Straznicky<sup>1</sup>, M. Bolduc<sup>2</sup>, S. Tylko<sup>3</sup>

<sup>1</sup> *Department of Mechanical and Aerospace Engineering, Carleton University,  
1125 Colonel By Drive, Ottawa, Ontario, K1S 5B6, Canada*

<sup>2</sup> *Defence Research Establishment Valcartier, 2459 Pie XI Blvd. North,  
PO Box 8800, Courcellette, Quebec, G0A 1R0, Canada*

<sup>3</sup> *Biokinetics and Associates Ltd., 2470 Don Reid Drive,  
Ottawa, Ontario, K1H 8P5, Canada*

**SUMMARY:** The response of aramid fibre-reinforced composites to ballistic impact is investigated using the finite element method. A user material routine incorporating fibre breakage, delamination, and matrix crushing has been developed and implemented within the LS-DYNA3D code. Post failure response has been implemented for the various failure modes using the MLT approach. Penetration and backplane delamination due to a *1.1g* fragment simulating projectile (FSP) have been predicted for flat plates. The effect of post failure modelling on the extent of damage and on the backplane response is shown to be significant.

**KEYWORDS:** ballistic impact, post failure, delamination, fibre breakage

## INTRODUCTION

Fibre-reinforced laminate composite materials offer a variety of desirable characteristics for ballistic helmet applications such as light-weight, high strength, good damage tolerance, and tailorability. However, a major disadvantage of composite materials is the existence of the so-called backplane deformation. This deformation mode occurs through delamination of the composite after partial penetration by the projectile. In such cases, complete penetration of the helmet may be prevented, but the motion of the delaminated backplane can be sufficient to cause serious head injury to the helmet wearer. In order to support further optimisation of the ballistic performance of composite materials, a more thorough understanding of the mechanisms causing backplane deformation is required. This paper presents a numerical study into the parameters determining the extent of backplane deformation.

For a given impact velocity, the extent of penetration and backplane deformation will be determined by the amount of energy transferred from the projectile to the composite material. Langlie and Cheng [1] indicated that punching of the material, fibre breakage, and delamination are the major mechanisms of energy absorption in ballistic composite materials. While a variety of models exist for the prediction of failure initiation in composite materials, recent work [2,3,4] has shown that post failure models can significantly improve damage predictions and reduce mesh sensitivity in models of low velocity transverse impacts on graphite fibre-toughened epoxy resin systems. In the current research, the effects of post

failure behaviour on the predicted delamination and backplane response under ballistic impact conditions are studied.

The impact of a fragment simulating projectile on woven Kevlar laminates is simulated using the LS-DYNA3D [5] finite element code modified to incorporate user material subroutines developed as part of this research. Models of 9 mm thick plates were considered under impact velocities of 500 m/s.

## CONSTITUTIVE MODEL

### Failure Criteria

Failure criteria for fibre breakage and matrix fracture or crushing were based on a modified version of the Chang and Chang model [6,7] implemented within a user material subroutine written for this work. Delamination was modelled outside of this constitutive routine as described below.

Since the current research considers woven composite materials, the mechanical properties are assumed equal in both in-plane directions. Therefore, fibre breakage can be caused by tensile and shear stresses acting in the in-plane directions, leading to the following failure criteria

$$f_i = \sum_{j=1}^3 \left( \frac{\sigma_{ij}}{S_{ij}} \right)^2 - r_i \geq 0 : \text{failure} \quad (1)$$

$$< 0 : \text{safe}$$

where  $i=1,2$ ,  $S_{ij}$  are the in-plane strength values (either tensile or shear), and  $r_i$  are the failure thresholds which are equal to 1. When fibre breakage occurs in the  $i$ -direction,  $\sigma_{ij}$  are set to zero.

During impact, the composite material in the impacted area will be compressed by the FSP. This will lead to high compressive stresses in the impacted area and high shear stresses in the surrounding area. When these stresses exceed their related strength values, the composite will fail and the FSP will punch a hole in the material. This penetration failure mechanism was modelled using the following criterion

$$f_3 = \sum_{j=1}^3 \left( \frac{\sigma_{3j}}{S_{3j}} \right)^2 - r_3 \geq 0 : \text{failure} \quad (2)$$

$$< 0 : \text{safe}$$

where  $S_{3j}$  are the through-thickness strength values (either compressive or shear), and  $r_3$  is the failure threshold and is equal to 1. When penetration failure occurs, all stresses are set to zero.

## Post-Failure Model

The post-failure model used in this study, known as the MLT model, was developed by Matzenmiller et al. [8] and is summarised below. This constitutive model was specifically developed to describe anisotropic damage in elastic-brittle fibre-reinforced composites. The elastic-brittle behaviour of these materials is characterised by the formation and evolution of microcracks (surface discontinuities) and cavities (volume discontinuities). These defects are considered irreversible and cause primarily stiffness degradation. A set of damage variables,  $w_i$ , were introduced to indicate the state of anisotropic damage and to reduce the stiffness in the damage related directions. The model assumes linear elasticity if the damage state (state of defects) does not change. This implies linear elastic unloading and reloading until the previous damage state is reached again. All non-linear effects of the constitutive behaviour are attributed to damage. Further, the orthotropic nature of the material is maintained throughout the damaging process. The stress-strain response according to the MLT-model, indicating the stiffness reduction due to damage, is depicted in Fig. 1.

Following Matzenmiller, et al. [8], the stiffness reducing damage variables  $w_i$  are introduced in the compliance matrix  $\mathbf{C}$

$$[\mathbf{C}] = \begin{bmatrix} \frac{1}{(1-w_{11})E_1} & \frac{-\nu_{21}}{E_2} & \frac{-\nu_{31}}{E_3} & 0 & 0 & 0 \\ \frac{-\nu_{12}}{E_1} & \frac{1}{(1-w_{22})E_2} & \frac{-\nu_{32}}{E_3} & 0 & 0 & 0 \\ \frac{-\nu_{13}}{E_1} & \frac{-\nu_{23}}{E_2} & \frac{1}{(1-w_{33})E_3} & 0 & 0 & 0 \\ 0 & 0 & 0 & \frac{1}{(1-w_{12})G_{12}} & 0 & 0 \\ 0 & 0 & 0 & 0 & \frac{1}{(1-w_{23})G_{23}} & 0 \\ 0 & 0 & 0 & 0 & 0 & \frac{1}{(1-w_{13})G_{31}} \end{bmatrix} \quad (3)$$

and the stiffness matrix is obtained by inverting the compliance matrix:  $\mathbf{S} = \mathbf{C}^{-1}$

The MLT model is based on classical continuum damage mechanics which assumes that only the undamaged part of the cross-section (net-area) carries loading, i.e. transmits stresses [9]. Consequently, the failure criteria should be defined in terms of the effective stresses, referred to the net area. In the MLT damage model, the effective stresses  $\hat{\sigma}$  and the nominal (true) stresses  $\sigma$  are related by

$$\{\hat{\sigma}\} = [\mathbf{M}] \{\sigma\} \quad (4)$$

where,



$$[M] = \begin{bmatrix} \frac{1}{1-w_{11}} & 0 & 0 & 0 & 0 & 0 \\ 0 & \frac{1}{1-w_{22}} & 0 & 0 & 0 & 0 \\ 0 & 0 & \frac{1}{1-w_{33}} & 0 & 0 & 0 \\ 0 & 0 & 0 & \frac{1}{1-w_{12}} & 0 & 0 \\ 0 & 0 & 0 & 0 & \frac{1}{1-w_{23}} & 0 \\ 0 & 0 & 0 & 0 & 0 & \frac{1}{1-w_{13}} \end{bmatrix}$$

If we substitute Eqn. 4 into the previously defined failure criteria and write the resulting criteria in terms of strains, we find the following failure criteria for the MLT-model for example for longitudinal tensile fibre failure:

$$g_1 = \left( \frac{c_{11}\varepsilon_{11} + c_{12}\varepsilon_{22} + c_{13}\varepsilon_{33}}{(1-w_{11})S_{11}} \right)^2 + \left( \frac{c_{44}\varepsilon_{12}}{(1-w_{12})S_{12}} \right)^2 + \left( \frac{c_{66}\varepsilon_{13}}{(1-w_{13})S_{13}} \right)^2 - r_1 \quad (5)$$

The symbol  $g_i$  is used to indicate that the failure criteria are expressed in terms of strains instead of stresses. The damage variables are represented by Weibull distribution functions, e.g., for longitudinal tension

$$w_{11} = 1 - e^{-\frac{-1}{me} \left( \frac{\varepsilon_{11}}{\varepsilon_{f1}} \right)^m} \quad (8)$$

with,

$$\varepsilon_{f1} = \frac{X_t}{E_1} \quad (9)$$

which is the “nominal” failure strain for a linear elastic material (in the absence of damage growth). Similar relations hold for the other damage parameters. The exponent  $m$  in Eqn. 8 determines the shape of the Weibull function. Fig. 2 shows the effect  $m$  has on the post-failure strength. High values of  $m$  approach instantaneous failure.

The damage thresholds  $r_i$  indicate the boundary of the elastic range. The material behaves linear elastically within these boundaries. The role of the damage threshold is equal to that of the yield stress in plasticity. The damage thresholds are initially set to 1, but will monotonically increase with increasing damage once failure has occurred. When at a certain time the strain state exceeds the boundary of the elastic range, the damage thresholds and damage variables need to be updated. Matzenmiller et al. [8] derived a method to accommodate coupling of growth for the individual damage variables in the various damage modes. For reasons of simplicity, damage growth coupling was not implemented in these preliminary calculations and the damage variables only grew when the corresponding strains increased.

The above model was implemented as a user material subroutine for brick elements in LS-DYNA3D. A numerical advantage of the MLT-model is that the damage level and, therefore, the failure mechanism, is based on the strain state. Thus, the duration of unloading after failure directly depends on the strain rate, which is significant in high velocity impacts. The elements that failed in penetration are deleted when  $w_{33}$  is equal to 0.999.

### Delamination Failure

Delamination is implemented in the current model by meshing the bottom layer of the composite separately and connecting this layer to the rest of the plate with so-called tiebreak

interfaces (slide line type 9 in LS-DYNA3D). The tiebreak interface rigidly connects the nodes of the slave segment to those of the master segment until the failure criterion is exceeded. The tiebreak failure criterion is given by

$$F_{delam} = \left(\frac{\sigma_n}{S_n}\right)^2 + \left(\frac{\sigma_s}{S_s}\right)^2 \tag{10}$$

where  $\sigma_n$  and  $\sigma_s$  are the normal and shear interface stresses, respectively, and  $S_n$  and  $S_s$  are the corresponding strengths. Delamination occurs when  $F_{delam} > 1$ . At this point, the interface is allowed to separate, simulating inter-ply cracking. A similar approach was undertaken by Hung et al. [9], who also modelled delamination in LS-DYNA3D with tiebreak interfaces and their numerical results were in good agreement with experimental data.

## MATERIALS

Elastic properties used for the woven aramid material studied are listed in Table 1. The strength values for the composite are given in Table 2. The 4340 steel FSP material was modelled using a yield strength of 1,034 MPa and a hardening modulus of 685 MPa. Young's Modulus was taken as 207 GPa and Poisson's Ratio was 0.3.

Table 1: Elastic properties for woven aramid from [1]

Young's Moduli (MPa)		Poisson's Ratio		Shear Moduli (MPa)		Density (g/cm <sup>2</sup> )
$E_{11}$	$E_{33}$	$\nu_{21}$	$\nu_{31}$	$G_{12}$	$G_{31}$	$\rho$
28,269	5,516	0.05	0.07	2,579	2,579	1.439

Table 2: Strength properties for woven aramid, partly from [1]

Tensile Strength (MPa)			Compressive Strength (MPa)	Shear Strength (MPa)			
$S_{11}$	$S_{22}$	$S_n$	$S_{33}$	$S_{12}$	$S_{23}$	$S_{31}$	$S_s$
482.6	482.6	100.0	350	34.5	350	350	100

The strength values in Table 2 were obtained from [1], except for  $S_n$ ,  $S_s$ ,  $S_{33}$ ,  $S_{23}$ , and  $S_{31}$  which were chosen to give reasonable results. These values are physically unrealistic, but planned impact tests on plates and helmets will provide more realistic values for these strengths.

## MODEL

A finite element model of a woven aramid composite plate was built using I-DEAS Masters Series, Version 2.1. The planar dimensions of the plate were *100 mm* by *100 mm* and the thickness was *9 mm*. The plate was impacted by a .22 calibre chisel-nose Fragment Simulating Projectile (FSP, MIL-P46593). The FSP was made of 4340 steel and weighed *1.1* grams. The impact speed of the FSP was *500 m/s*.

A typical mesh of the flat plate model with the FSP is shown in Fig. 3. Both the plate and the FSP were modelled with 8-node brick elements. To reduce the computational time, only one-half of the problem was modelled through symmetry. Fig. 4 shows a close-up of the impact site and FSP.

An automatic eroding contact algorithm was used to simulate contact and penetration between the FSP and the impacted area of the plate. This algorithm uses a penalty function approach to prevent penetration of contacting elements. In the event of failure of the composite through the erosion criterion given by equation Eqn. 3, the failed elements are deleted and the contact surfaces are automatically updated to consider the next layer of material. A delamination plane (tiebreak interface) was inserted adjacent to the inner-most layer of elements.

## RESULTS

Figure 5 compares the effects of post failure modelling on the FSP velocity time histories. In the instantaneous failure model, the stresses are immediately set to zero once the material fails in a certain mode. As already shown in Fig. 2, the stiffness degradation in the MLT model strongly depends on the value of  $m$ . Figure 5 shows that a higher amount of post failure strength leads to a higher energy transfer from the FSP to the composite material, which results in greater deceleration of the FSP. When the energy absorption is sufficient, complete penetration of the composite is avoided and backplane deformation occurs. This is the case for  $m=2$ , where the FSP is completely stopped by the backplane and rebounds. In all other cases the backplane is completely penetrated by the FSP. The predicted final velocity of the FSP after complete penetration depends heavily upon the post failure treatment. Figure 5 also shows that the MLT predictions approach those using instantaneous failure for high values of  $m$ .

The backplane displacement time histories for a node located at the centre of the delaminating backplane are shown Fig. 6 as function of the post failure exponent  $m$ . The only case for which the backplane was not penetrated by the FSP was for  $m=2$ . In all other post failure cases the backplane was initially pushed down by the FSP, but eventually failed in crushing. Therefore, the nodal displacements for these cases are not representative for the total backplane displacement. The instantaneous failure case was omitted because the backplane area under the FSP was completely eroded.

Figure 7 shows a series of deformed mesh plots for  $m=2$ . Penetration of the upper layers occurs through crushing and transverse shear failure as seen in Figs 7 (a) and (b). The nature of the eroding contact algorithm can be observed as a progressive removal of elements ahead of the penetrator. As the FSP nears the backplane its velocity decreases, resulting in lower normal compressive strain rates and through-thickness shear strain rates. This enables the in-plane stresses to build up before the element is eroded. Therefore, the dominant failure mode will gradually change from crushing to fibre breakage. When the FSP reaches the backplane its velocity will be so low that crushing of the underlying composite material will no longer occur and the composite will fail in fibre breakage and delamination. This agrees with Langlie and Cheng's findings [1], who observed that the failure process in a composite plate under ballistic impact can be visualised by three subsequent layers dominated by through-thickness failure, in-plane tensile failure, and delamination failure, respectively. Figure 8 shows the case for  $m=10$ , where the backplane is initially pushed down, but eventually fails in crushing.

## DISCUSSION AND CONCLUSIONS

The foregoing shows that the damage exponent  $m$  has a considerable effect on the impact response of the composite material. Unfortunately,  $m$  has no physical meaning and cannot be directly determined from experiments. Williams and Vaziri [4] suggested that  $m$  can be numerically calibrated to give the best representation for a certain impact test. Impact tests on flat plates and helmets are underway and these tests will hopefully yield a reasonable estimate for  $m$ . In addition to  $m$ , the numerical damage predictions are also strongly affected by the strength values. Material testing on the woven composite material and the aforementioned impact tests will yield better estimates for these strength parameters.

Despite its limitations, the implemented post failure model yields more realistic results than could have been obtained with the instantaneous failure models currently implemented in LS-DYNA3D. The MLT model is a promising and versatile numerical tool for simulating progressive damage in fibre reinforced composite materials.

In future, mesh refinement and delamination layers between each ply layer or between groups of plies at regular intervals through thickness will further improve the current model. Post failure modelling in the delamination criterion and linking the constitutive model with the tie-break interface model will also yield a more realistic response.

## ACKNOWLEDGEMENTS

Financial support for this research was provided by the Defence Research Establishment Valcartier and the Natural Sciences and Engineering Research Council of Canada.

## REFERENCES

1. Langlie, S. and Cheng, W., "A High Velocity Impact Penetration Model for Thick Fiber-Reinforced Composites", *ASME, Pressure Vessels and Piping Division* (Publication), 174, New York, 1989, pp. 151-158.

2. Majeed, O., Worswick, M.J., Straznicky, P.V., Poon, C., “Numerical modelling of Transverse Impact on Composite Coupons”, *Canadian Aeronautics and Space Journal*, Vol. 40, No. 3, 1994, pp. 99-106.
3. Straznicky, P.V., Poon, C., Worswick, M.J., Fuoss, E., Majeed, O., Vietinghoff, H., “Damage Resistance in Composite Materials”, *Proceedings of ICCM-10*, Whistler, British Columbia, Canada, August 14-18, Vol. V: Structures, pp. 607-614.
4. Williams, K. and Vaziri, R., “Finite Element Analysis of the Impact Response of CFRP Composite Plates”, *Proceedings of ICCM-10*, Whistler, British Columbia, Canada, August 14-18, Vol. V: Structures, pp. 647-654.
5. Hallquist, J.O., “LS-DYNA3D User’s Manual (Nonlinear Dynamic Analysis of Structures in Three Dimensions), Version 936”, Livermore Software Technology Corporation, Livermore, CA, May 1995.
6. Chang, F.K. and Chang, K.Y., “Post-Failure analysis of Bolted Composite Joints in Tension or Shear-Out Mode Failure”, *Journal of Composite Materials*, Vol. 21, 1987, pp. 809-833.
7. Chang, F.K. and Chang, K.Y., “A Progressive Damage Model for Laminated Composites Containing Stress Concentration”, *Journal of Composite Materials*, Vol. 21, 1987, pp. 834-855.
8. Matzenmiller, A., Lubliner, J. and Taylor, R.L., “A Constitutive Model for Anisotropic Damage in Fiber-Composites”, *Mechanics of Materials*, Vol. 20, 1995, pp. 125-152.
9. Kachanov, L.M., *Introduction to Continuum Damage Mechanics*, Martinus Nijhoff, Dordrecht, 1986
10. Hung, K.-S., Nilsson, L. and Zhong, Z.-H., “Numerical Studies on the Delamination Mechanism in Laminated Composites under Impact Loading”, *Proceedings of ICCM-10*, Whistler, British Columbia, Canada, August 14-18, Vol. V: Structures, pp. 623-6

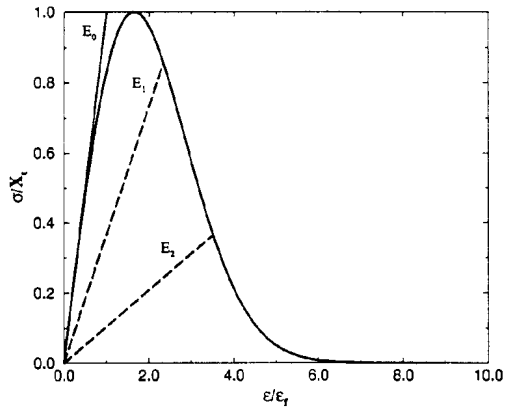


Fig. 1: Stress-strain relation for MLT-model

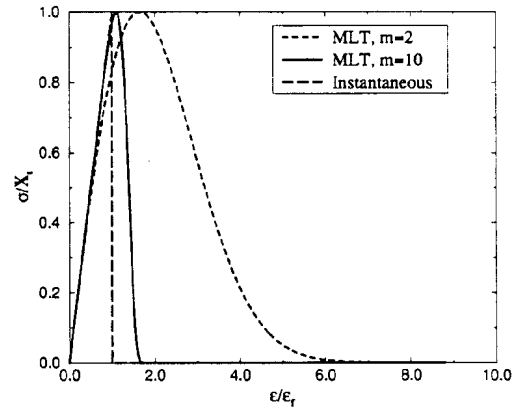


Fig. 2: Effect of failure exponent  $m$  on post-failure strength

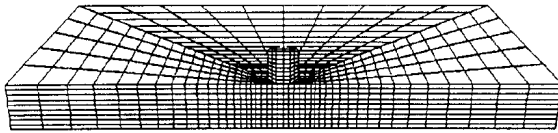


Fig. 3: Flat plate model

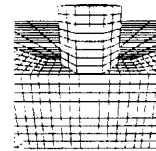


Fig. 4: Close-up of impact area

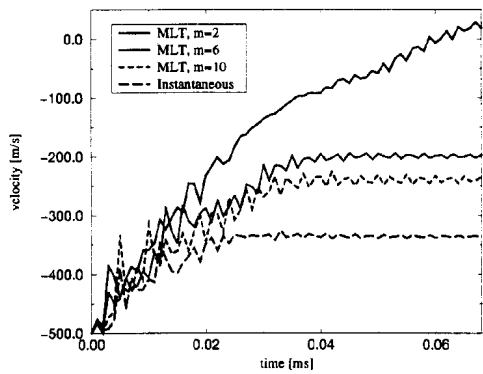


Fig. 5: FSP velocity time history as function of post-failure treatment

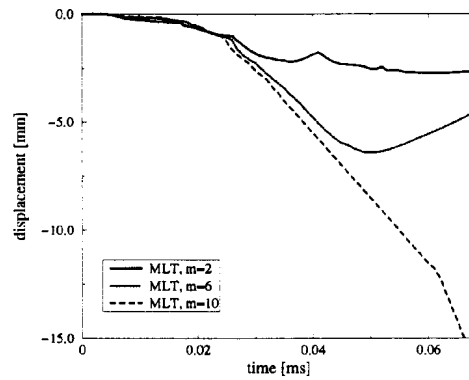
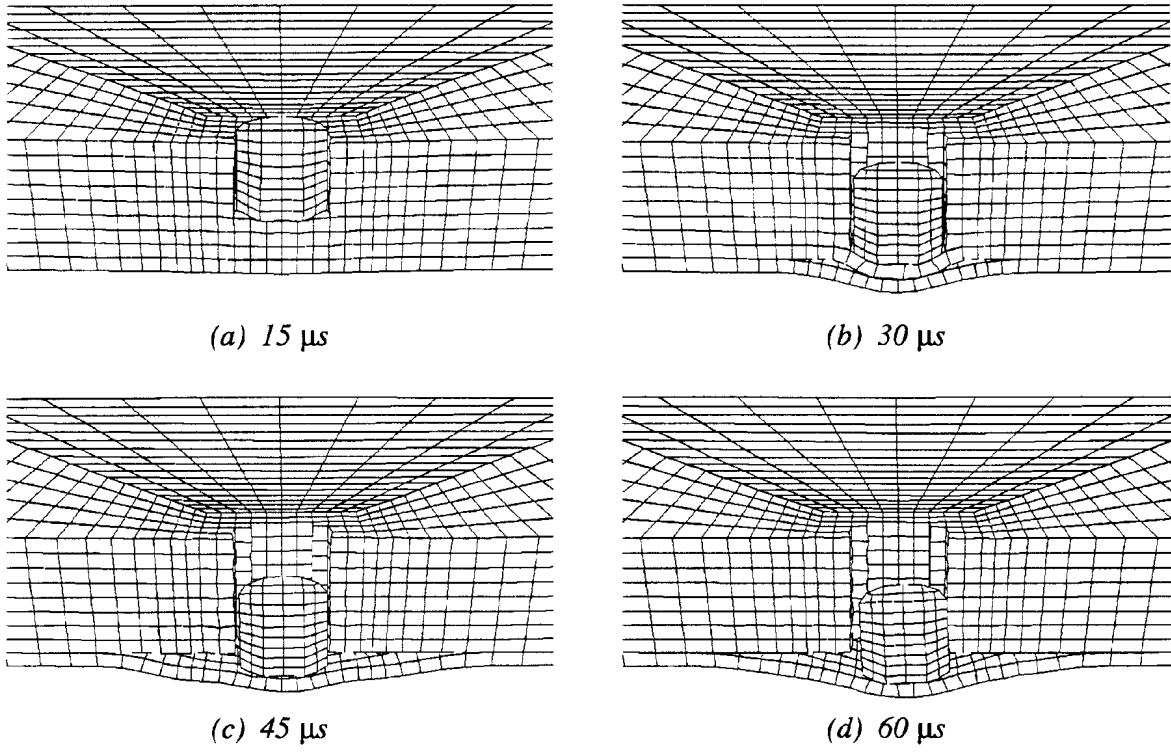
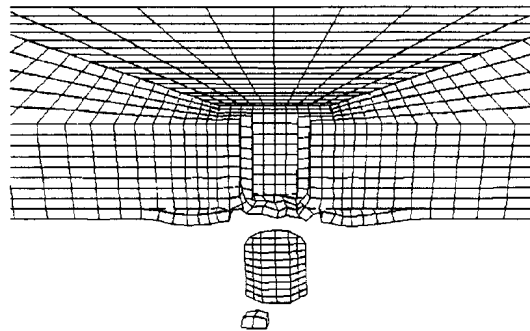


Fig. 6: Backplane displacement history as function of post-failure treatment



*Fig. 7: Sequence of penetration of plate by projectile and delamination of backplane*



*Fig. 8: Complete penetration of plate at  $t=60\mu$ s ( $m=10$ )*

# PERFORATION CHARACTERISTICS OF FABRICS MADE OF HIGH STRENGTH PE FIBERS

**K. Takahashi and H. Komatsu**

*Research Institute for Applied Mechanics, Kyushu University, Kasuga, Fukuoka 816, Japan*

**SUMMARY:** Perforation study was performed for textile fabrics made of high strength PE fibers to study effects of textile structure, strand twisting and fiber surface treatment on perforation energy, i.e., fabrics resistance at perforation. An air gun facility was used to accelerate a steel bullet in a velocity range 50-200 m/s. High speed photography was performed to observe high speed deformation of specimen cloth until breakage. The results shows that two kinds of perforation modes exist depending on the textile structure, and the perforation energy depends on the bullet velocity.

**KEYWORDS:** polyethylene, fabrics, ballistic impact, perforation

## INTRODUCTION

Textile fabrics made of high strength fibers have been widely used for industrial and leisure purposes. As the textile fabrics are regarded as high impact materials, they have been utilized to protect mankind under the conditions in which people may be injured by projectiles. For example, specially designed clothes such as space suits and bulletproof jackets are made from high impact textile fabrics. Therefore, it is important to understand the impact resistance of fabrics to know the limit of such clothes and to improve their properties. Also, fabric composites have been developed by impregnating fabrics into resins. Therefore, it is useful to characterize the impact properties of fabrics to know the impact resistance of the composites.

Aramid fibers such as Kevlar 29 and 49 have been widely used for high impact clothes, while high strength polyethylene (PE) fibers have been also developed. Since some of PE fibers have lower density and higher strength than the aramid fibers, the PE fibers may have an advantage over the aramid fibers as fabrics for high impact clothes.

A few attempts have been made to study impact performance of textile fabrics. Montgomery studied the effects of the shape of projectiles on impact energy absorbed by fabrics [1,2]. Wilde et al. studied impact performance of fabrics based on high speed photography [3,4]. Recently, Morrison et al. investigated the perforation phenomena of aramid laminates [5]. On the other hand, Leech et al. studied impact behavior of cloths and nets by projectile theoretically, and proposed a model to explain the behavior [6].

In the above studies, the velocities of the projectiles were in the range of several hundred meter per second. On the other hand, in the present study, impact testing was performed at relatively low bullet velocities (<200 m/s). Dependence of the bullet velocity on the perforation energy absorbed by PE cloths was mainly investigated.



## **EXPERIMENTAL**

### **Material**

High strength polyethylene cloths tested in the present study are shown in Table 1. In Table 1, surface treatment means that the oil used during the process of fiber forming is removed. Photographs of typical cloth surfaces and schematic drawings of the corresponding textile structures are shown in Fig.1. The mechanical properties of the row fiber which is used for the fabrication of cloth, are as follows:

density: 0.98 g/cm<sup>2</sup>, tensile strength: 2.92 GPa, tensile modulus: 137 GPa.

### **Air Gun**

A multipurpose air gun was used for the impact testing and the testing facility is shown in Fig.2. The air gun consists of a high pressure vessel, a launcher barrel and a low pressure vessel in which cloth specimen is held. The length of the whole apparatus is 4,000 mm. High pressurized air of 5 liter up to 150 atm can be filled up in the high pressure vessel using air compressor or high pressure gas cylinder. The inner diameter and the length of the launcher barrel are 25 mm and 2,000 mm, respectively. The diameter and the length of the low pressure vessel are 600 mm and 1,100 mm, respectively, and the inside pressure is reduced to about 10<sup>-2</sup> torr. This vessel has two pairs of window for observation. The projectile (sabot) used for the present study is made of polyethylene, and the geometry is shown in Fig.3.

### **Measurement of Bullet Velocity and High Speed Photography**

The whole system for the measurement of bullet velocity and high speed photography is shown in Fig.4. A chrome steel bullet (9.5 mm diameter and 3.55 g mass) is placed in the front of the polyethylene sabot, and the accelerated sabot stops at the sabot stopper placed at the end of the launcher barrel. As a result, only the steel bullet flies and collides against cloth specimen. The bullet velocity  $V_i$  before the collision is measured from the time difference when the bullet crosses over the two laser lights as shown in Fig.4. The deformation process of the cloth specimen after the collision and the bullet velocity  $V_o$  after the perforation are obtained using multiplex photography with transmitted light pulse emanated from the multi-flash.

### **Absorbed Perforation Energy**

If a steel bullet collides against cloth specimen at velocity  $V_i$  and the velocity reduces to  $V_o$  after perforation, then the perforation energy absorbed by the cloth can be estimated from the difference of the kinetic energy of the bullet before and after the perforation, i.e.

$$E_i - E_o = \frac{1}{2} m (V_i^2 - V_o^2) \quad (1)$$

where  $E_i$  and  $E_o$  are the kinetic energies before and after the perforation, respectively, and  $m$  the mass of the steel bullet.

## Fixation of Cloth Specimen

Cloth specimen is fixed perpendicular to the direction of bullet flight and the bullet collides at the center of the cloth. Detail of the specimen fixture is shown in Fig.5 (1). An example of cloth specimen after impact test is also shown in Fig.5 (2). Figs.5(3) and (4) show the two-dimensional distribution of elongation for unperforated cloth A obtained at  $V_i = 59.9$  m/s, and Fig.5(5) show the side view of the same specimen just after the impact. The side view of perforated cloth A obtained at  $V_i = 76.8$  m/s is shown in Fig.5 (6).

## RESULTS AND DISCUSSION

### High Speed Photography

Typical examples of high speed photography are shown in Fig.6(a) for cloth A and Fig.6(b) for cloth B. In the caption of Fig.6, *PI* expresses the interval of light pulses. For both cloth A and B, the figure (1) shows an unperforated result photographed at a velocity very close to the critical velocity at which perforation occurs. The figures (2), (3) and (4) show perforated results obtained at higher impact velocities. It is clearly seen from Fig.6 that for cloth A, the yarns are cut off completely and there is no pull-out of yarn after the perforation; on the other hand, the steel bullet perforates through the cloth B pulling out several yarns. It is also noted that for cloth B, different pull-out modes can be observed depending on the velocity  $V_i$ . In the present study, cloths A, A' and D show the same tendency of perforation with cutting of yarns as shown in Fig.6(a). On the other hand, for cloths B, B', C and E, steel bullet perforates through each cloth accompanied with pull-out of yarns as shown in Fig.6(b).

### Critical Perforation Velocity and Critical Perforation Energy

When a steel bullet collides a cloth specimen, the bullet cannot perforate through the cloth at the velocities lower than a critical value of impact velocity. The bullet perforates through the cloth when the impact velocity reaches a higher value than the critical velocity. This critical velocity is called the critical perforation velocity  $V_{ic}$  and the corresponding energy absorbed by cloth is called the critical perforation energy  $E_c$ . For each cloth,  $V_{ic}$  and  $E_c$  are shown in Fig.7 and Fig.8, respectively. The results shown in Fig.7 and 8 are very useful to estimate the perforation resistance of each cloth. However, these results may not present enough information to compare the perforation energies absorbed by the cloths which have different conditions such as the size of yarn, strand twisting, textile structure and raw material. In this study, the specific perforation energy is defined by

$$E_R = E_c / W_R \quad (2)$$

where  $W_R$  is the areal weight density, which is the weight of cloth per  $1 \text{ m}^2$ . For each cloth,  $E_R$  value is shown in Fig.9. Although  $E_R$  does not reflect the effect of each of the above conditions on the perforation energy, it is a convenient method to evaluate the perforation energy from comprehensive point of view.

The followings are obtained from the data for the specific perforation energy  $E_R$ .

(1) Effect of surface treatment

Treated cloth absorbs larger energy than untreated one even if the yarn size, the number of twists, the textile structure and the areal weight density are the same in both cloths. It appears that this is mainly because the frictional force between yarns in the treated cloth becomes larger than in the untreated one owing to the removal of oil used during fiber forming process.

(2) Relation between the areal weight density and perforation energy

Regarding plain woven untreated polyethylene fiber cloth, the specific perforation energy absorbed by cloth A is much lower than those of cloths C, D and E as shown in Fig.9. The difference of the mean values is approximately  $10 \text{ J/kg/m}^2$ . The critical perforation energy  $E_C$  is shown as a function of the areal weight density  $W_R$  in Fig.10. A linear relation between  $E_C$  and  $W_R$  is observed in Fig.10. It is also observed that  $E_C$  of cloth A is lower than that of cloth D, although both cloths have the almost same  $W_R$  value. It may be understood that this is due to the effect of the number of twists considering that the other conditions are the same in both cloths. Thus, it is expected that the number of twists, 160 times/m, for cloth D gives higher  $E_C$  value than 80 times/m for cloth A.

On the other hand, the  $E_C$  value of basket woven untreated polyethylene cloth B is lower by 20 % than the extrapolated value of the plain woven untreated cloths. It is expected that a group of basket woven cloths also has a linear relation between  $E_C$  and  $W_R$ , and a straight line situated at a lower position than the line for the plain woven cloths may be drawn in Fig.10. This is further discussed in the following.

(3) Relation between the difference of textile structure and perforation energy

As described above, the perforation energy absorbed by plain woven cloth is larger than that absorbed by basket woven cloth. This relation may originate in the difference of textile structure. By comparing plain woven and basket woven cloths, in which the size of yarn and the yarn density are the same, it can be said that the frictional force between yarns in plain woven cloth is larger than in basket woven cloth, because the number of the crossing points of warp and fill for plain woven cloth are four times that for basket woven cloth. This results in the larger perforation energy absorbed by plain woven cloth.

### Dependence of Perforation Energy on $V_i$

It is interesting to know the  $V_i$ -dependence of the perforation energy absorbed by cloth when steel bullet collides the cloth at relatively low velocities ( $\leq 200 \text{ m/s}$ ) exceeding the critical perforation velocity. Dependence of the perforation energy,  $E_i - E_o$ , on  $V_i$  is shown in Fig.11. Fig.11 (a) shows the classification of marks used in the figures (b)-(h). The figures (b), (c) and (g) show the examples of the case in which steel bullet cuts off the yarns. On the other hand, the figures (d), (e), (f) and (h) show the examples of the case in which steel bullet perforates through the cloth accompanied with the pull-out of yarns. From these experimental results, the following can be shown with respect to  $V_i$ -dependence of perforation energy.

(1) Relation between the difference of pull-out modes and perforation energy

Perforation energy absorbed by cloth depends on the pull-out mode, i.e. the number of yarns pulled out. In general, larger number of pull-out results in larger absorbed perforation energy.

(2)  $V_i$ -dependence of perforation energy

Perforation energy of polyethylene cloth tends to increase with increase of  $V_i$  in a certain range of velocity greater than the critical velocity and decrease at higher velocities. However, for cloth B (Fig.11(d)) and cloth E (Fig.11(h)), wide scatters are observed in the data because the perforation energy varies with the pull-out mode. In general, the perforation energy tends to increase with increasing  $V_i$ . In Figs.11(d) and (h),  $V_i$ -dependence of the perforation energy is not clear for the velocities greater than 200 m/s. Considering the  $V_i$ -dependency of the other cloths, it is expected that for cloth B and E, the perforation energy also decreases with increase of  $V_i$  for  $V_i > 200$  m/s, and then reaches a constant value. This  $V_i$ -dependency appears to depend on the shape and size of projectiles and the range of the impact velocity [2].

Generally, absorbed perforation energy by cloth due to the collision of steel bullet depends on the way of the specimen fixation and the mechanical properties of the row fibers. It is also considered that the pull-out resistance of yarn, the change of textile density generated by the collision and the microdamage morphology of yarn and filament including heat effects have influence on the perforation energy. A further study is needed for understanding the detailed mechanisms.

## CONCLUSIONS

Perforation study of high strength polyethylene fiber cloths was performed in a velocity range 50-200 m/s using an air gun facility. The followings have been shown by the study.

1. The perforation energy initially increases linearly with increase of the bullet velocity. However, it tends to decrease over a limit which is around at 150 m/s.
2. The critical perforation energy, which is defined as the minimum energy required to cause perforation, can be shown as a linear function of areal weight density of fabrics.
3. Two kinds of perforation modes, that is, cutting of yarns and pull-out of yarns are observed depending on the textile structure.
4. Effects of fiber surface treatment as well as of strand twisting are shown to exist.

## REFERENCES

1. T.G. Montgomery, PhD Thesis, 1980, North Carolina State University.
2. T.G. Montgomery, P.L. Grady and C. Tomasino, Textile Research Journal, 52 (1982), 442.
3. A.F. Wilde, Textile Res. J., 44 (1974) 772.
4. A.F. Wilde, J.J. Ricca, J.M. Rogers and L.M. Cole, Polym. Eng. Sci., 12 (1972) 41.
5. C.E. Morrison and W. H. Bowyer, Proc. ICCM 2, (1980) 233.
6. C. Leech, J.W.S. Hearle and J. Mansell, J. Text. Inst., 70 (1979) 469.

Table 1: Characteristics of cloth specimens

Specimen	Yarn		WD* <sup>1</sup> (per inch)	Twisting* <sup>2</sup> (times/m)	Textile structure	AWD* <sup>3</sup> (kg/m <sup>2</sup> )	Surface treatment	Thickness (mm)
	Denier	Filament						
A	300	300	50	160	plain weave	0.146	untreated	0.27
A'	300	300	50	160	plain weave	0.146	treated	0.27
B	1160	960	35	80(W) 0(F)	2x2 basket	0.411	untreated	0.71
B'	1160	960	35	80(W) 0(F)	2x2 basket	0.411	treated	0.75
C	800	795	36	70(W)90(F)	plain weave	0.280	untreated	0.50
D	300	280	50	80	plain weave	0.144	untreated	0.29
E	600		34	45	plain weave	0.215	untreated	0.39

\*<sup>1</sup> WD is the weave density.

\*<sup>2</sup> W and F are the warp and fill, respectively.

\*<sup>3</sup> AWD is the areal weight density.

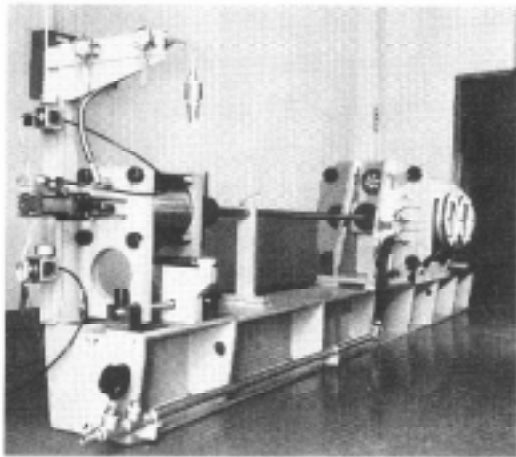


Fig.1: Multipurpose air gun facility

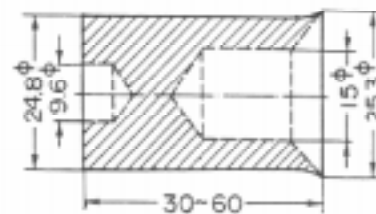


Fig.2: Geometry of projectile (sabot)

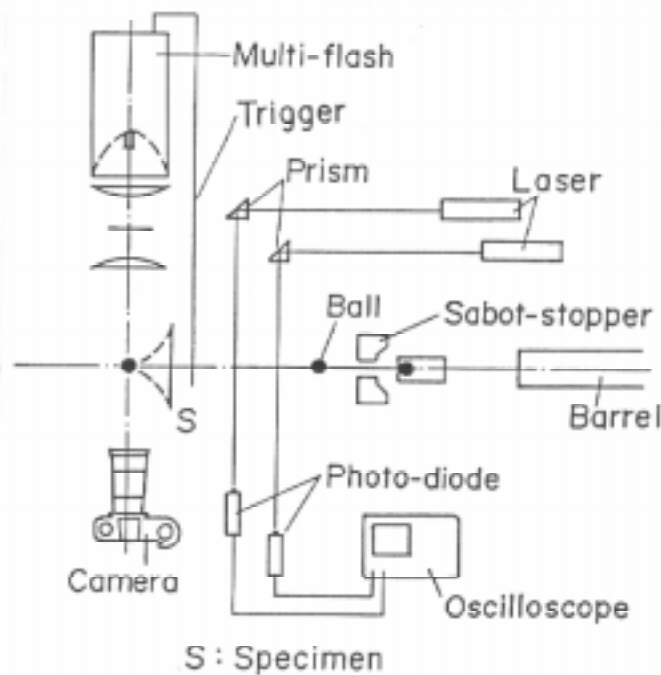


Fig.3: System for the measurement of bullet velocity and high speed photography

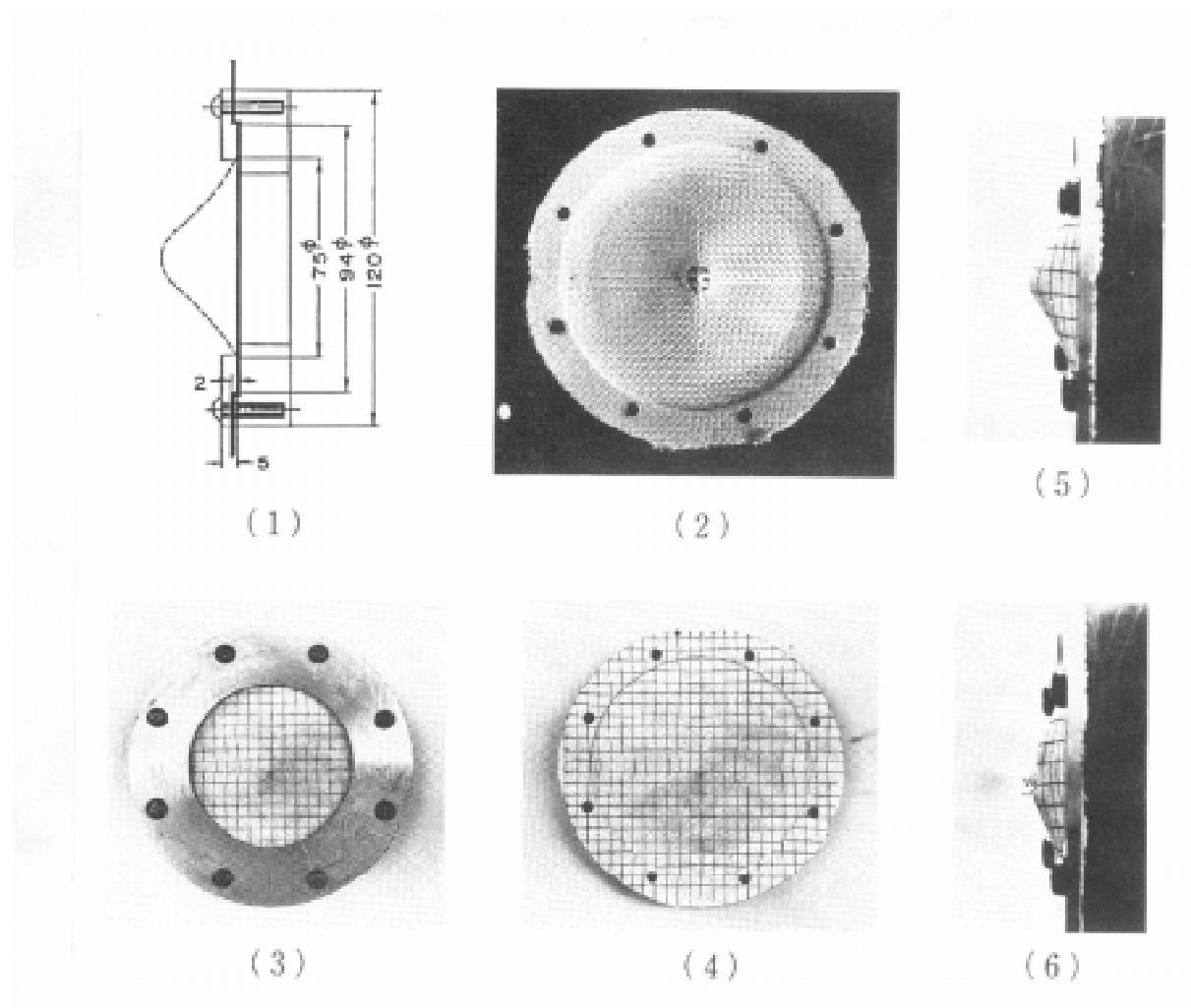


Fig.4: (1) specimen fixture, (2) cloth specimen after impact, (3, 4, 5) deformation of unperforated cloth specimen for  $V_i=59.9$  m/s and (6) perforated specimen for  $V_i=76.8$  m/s

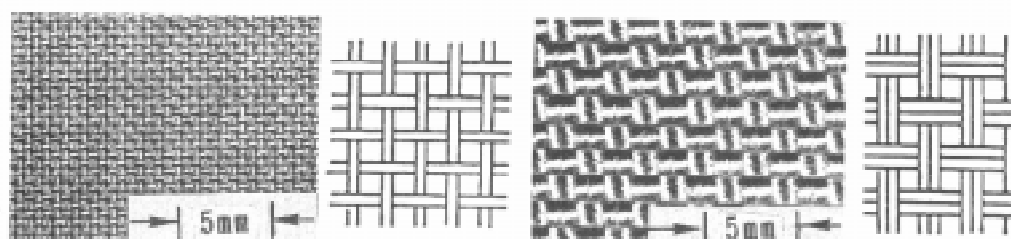
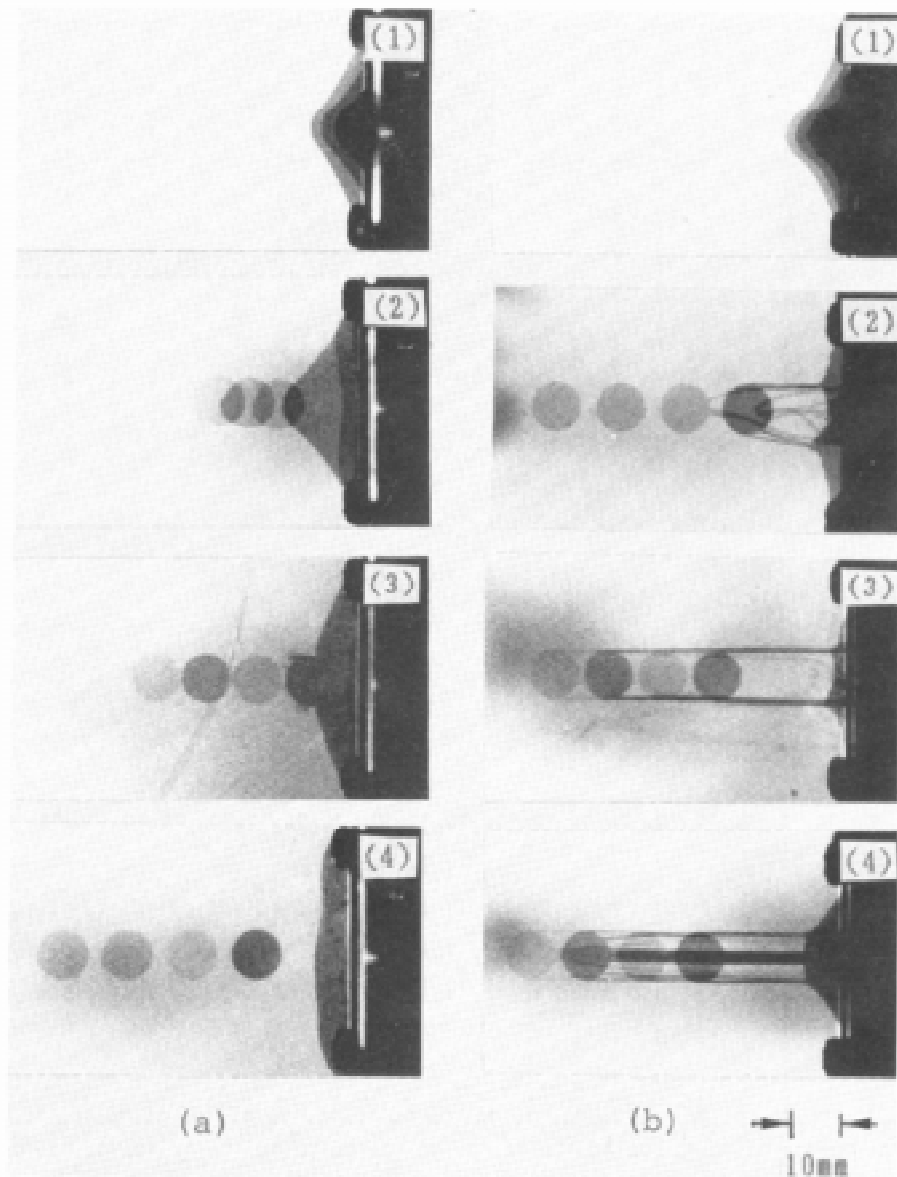


Fig.5: Textile structures of typical cloth specimens



*Fig. 6:* (a) deformation and perforation mode of cloth A ((1)  $V_i=59.9$  m/s,  $PI=150$   $\mu$ s, (2)  $V_i=90.7$  m/s,  $V_o=37.7$  m/s,  $PI=150$   $\mu$ s, (3)  $V_i=136.5$  m/s,  $V_o=100.3$  m/s,  $PI=100$   $\mu$ s and (4)  $V_i=147.5$  m/s,  $V_o=122.7$  m/s,  $PI=100$   $\mu$ s ) and (b) deformation and perforation mode of cloth B ((1)  $V_i=105.1$  m/s,  $PI=150$   $\mu$ s, (2)  $V_i=134.3$  m/s,  $V_o=82.7$  m/s,  $PI=150$   $\mu$ s, (3)  $V_i=160.0$  m/s,  $V_o=107.6$  m/s,  $PI=100$   $\mu$ s and (4)  $V_i=172.8$  m/s,  $V_o=112.3$  m/s,  $PI=100$   $\mu$ s )

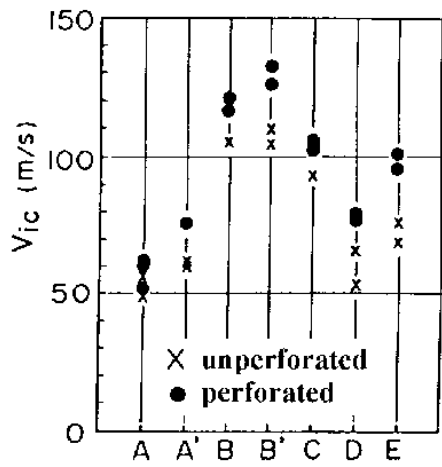


Fig.7: Critical perforation velocity of cloth specimen

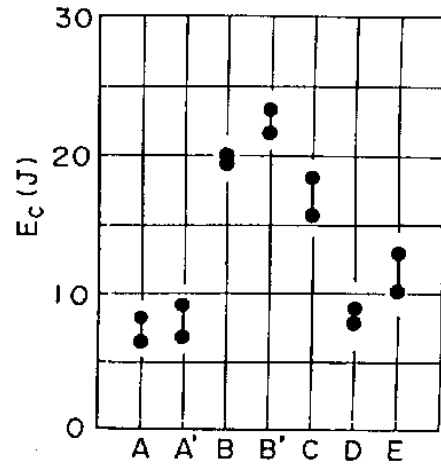


Fig.8: Critical perforation energy of cloth specimen

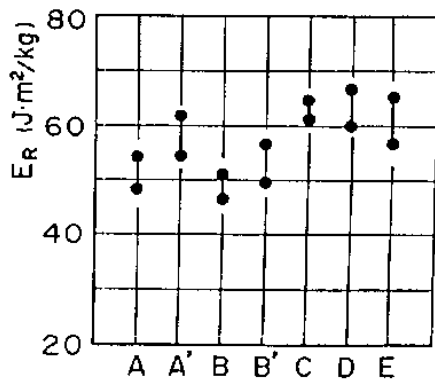


Fig.9: Specific perforation energy of cloth specimen

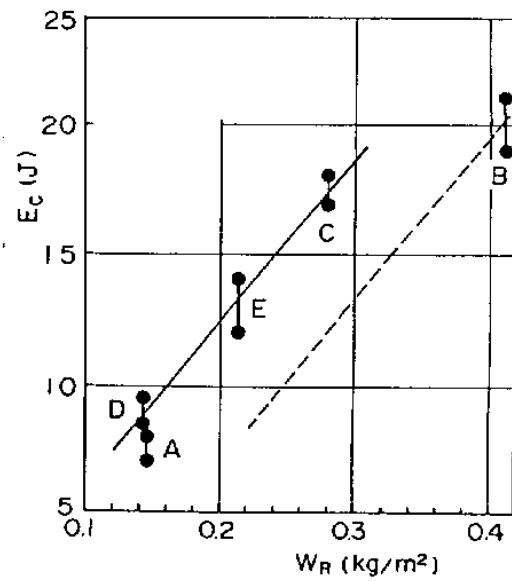
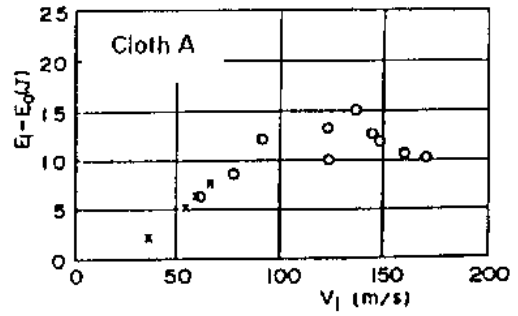


Fig.10:  $W_R$ - $E_c$  relation of cloth specimen

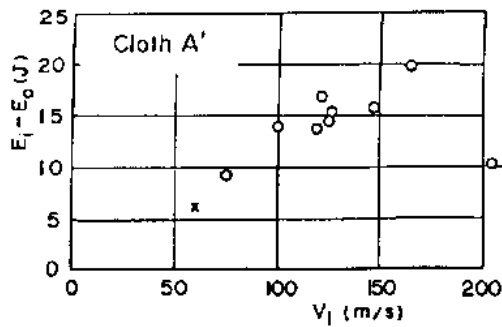


	Mark	Perforation mode
Unperforated	X	
Perforated	○	○ ○ ○ ○
	●	○ ○ ○ ○
	●	○ ○ ○ ○
	⊙	○ ○ ○ ○

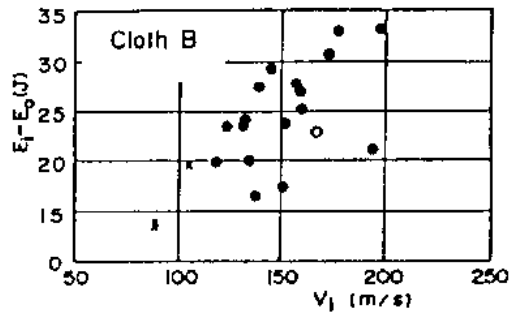
(a)



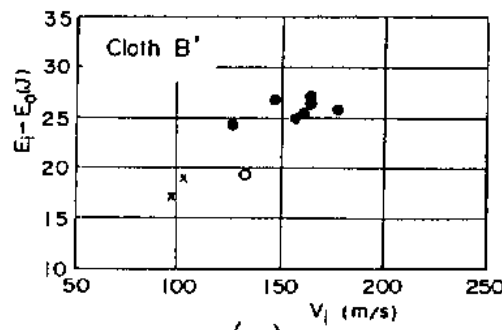
(b)



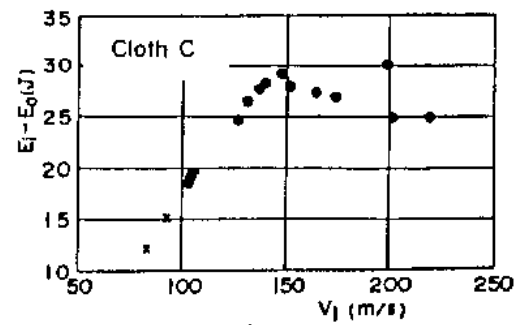
(c)



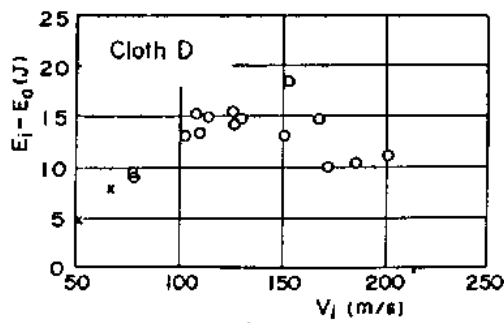
(d)



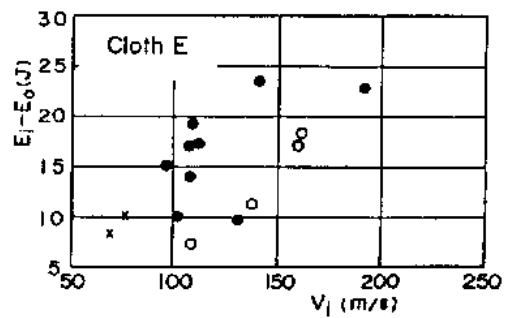
(e)



(f)



(g)



(h)

Fig. 11: Dependence of perforation energy on  $V_i$

# USING A HOMOGENIZATION PROCEDURE FOR PREDICTION OF MATERIAL PROPERTIES AND THE IMPACT RESPONSE OF UNIDIRECTIONAL COMPOSITE

A. D. Resnyansky<sup>1</sup> and E. I. Romensky<sup>2</sup>

<sup>1</sup> *School of Mechanical and Manufacturing Engineering, UNSW, Sydney 2052, Australia*

<sup>2</sup> *Sobolev Institute of Mathematics Siberian Division of Russian Academy of Sciences, Novosibirsk 630090, Russia*

**SUMMARY:** The aim of the work is to design hierarchical model for description of the dynamic behaviour of unidirectional composite. On the basis of the Maxwell-type viscoelastic model [1] a procedure of derivation of dynamic equations for the composites is proposed. The space arrangement of constituents in the direction transversally to the symmetry axis is out of consideration. In the present paper the bonding between the constituents is assumed to be perfect. Comparing data of the known theories and experiments with the results obtained, the effective elastic characteristics are in good agreement for fibrous composites, and are coincident with the known theory [2] for laminated composites. Assuming finite elastic deformations, the procedure gives the equations containing the well-known plastic spin. The model obtained is applied to the problem of the shock-wave propagation in an obliquely loaded laminated composite. The shock-wave splitting is observed that is in agreement with the experiment [3]. The phenomenon is explained by analysis of peculiarities of the load-deformation curve. The cause is seen in the variation of the strength properties of the composite due to the reinforcement rotation during the loading.

**KEYWORDS:** hierarchical model, homogenization approach, shock-wave propagation, off-axis loading, laminated composite

## INTRODUCTION

Practical needs in the consideration of composite as a homogeneous anisotropic medium gave a rise in popularity of homogenization procedures. This consideration provides quite correct general description of the process of loading. Simple homogenization rules work quite well in numerous applications and they are very convenient for the finite-element computations of structures containing composite members. However, in some cases the micromechanical peculiarities are of interest and description of residual stresses and internal microstresses is required.

Micromechanical approaches give a useful information but they are restricted to the consideration of individual fibre [2, 4-6]. Therefore, the homogenization approach is best suited for an analysis the composite as a whole. Most of the known procedures aim to derive

elastic moduli of composite in order to use the anisotropic theory of elasticity in finite element computations.

Our objective is to design a procedure for derivation of evolution equations. In doing so the effective elastic characteristics are a by-product. Three-level hierarchy is established during the application of the procedure. The low level is associated with the microstructural process in the composite's constituents (irreversible processes in the lattice caused by dislocations and microdefects). In the paper this level is realized by the description of the constituents by the Maxwell-type viscoelastic model [1]. The second level is associated with the micromechanics of the composite and results from the description of the fibre-matrix interaction. Finally, the upper level is presented by the description of the composite as a whole (the phenomenological description) within the framework of the conservation laws and constitutive equations; these latter are derived from the basic model (the low level) and the homogenization procedure (the second level).

The resultant equations can also be used in the finite element computations. An application of the model to the three-point bending problem is presented in the proceedings [7]. The Onzager principle, expressing the symmetry of inelastic reactions to the load, is valid for the model. This principle is of fundamental significance for the design of finite-element algorithm because it enables one to derive the symmetrical stiffness matrix.

### **THE HOMOGENIZATION APPROACH: BRIEF DESCRIPTION**

Homogenization procedure has to take into consideration a great number of factors. The composite is a very complex structure and the interaction between components is hard to analyse. Therefore, a certain degree of idealisation is necessary to describe both the composite as a whole and at least the main features of the constituents' interaction.

The main problem in the design of the phenomenological theories is to take into consideration as many factors as possible and to make the derivation as simple and utilitarian as possible. As a basis, we take quite complex model for the description of the constituents. This gives us some reserve in manipulation by assumptions of the second level. Because the utility of derivation and thermodynamical correctness of the model are among our aims, we select a simple set of assumptions for the description of the constituents' interaction.

Due to the presupposed perfect bonding of components the equality of velocities in the fibres and matrix is the case. The load transfer between the components is quite complex and depends on the length and quality of fibres. Distribution of radial and circumferential stresses around fibre and the interaction of the stress fields among individual fibres and matrix are also nontrivial issues in the micromechanics of composites. Taking as an example the fibrous unidirectional composite, we consider that the following assumptions are absolutely necessary: i) the difference between the constituents' stresses in direction of the fibre line can not be neglected; ii) this difference induces internal microstresses acting in the longitudinal direction. For simplifying assumptions we take: i) stresses in the transversal direction are distributed uniformly in both composite's components; ii) the mixture rule for stresses in the longitudinal direction is valid. Mathematical representation of the assumptions stated above is:

$$\sigma_{ij}^{(1)} = \sigma_{ij}^{(2)} = \sigma_{ij}, \quad (i, j) \neq (1,1) \quad (1)$$

Here the  $x_1$  - direction is assumed to be coincident with the fibre direction, the stresses inside fibres are  $\sigma_{ij}^{(1)}$ , inside matrix -  $\sigma_{ij}^{(2)}$ , 'averaged' stresses of the composite as a whole -  $\sigma_{ij}$ . Hereafter, the upper indices in parentheses are associated with the number of a composite's constituent ("1" - fibre, "2" - matrix). It is assumed that only the difference between  $\sigma_{11}^{(1)}$  and  $\sigma_{11}^{(2)}$  can not be neglected. This difference generates internal microstresses determined by variable  $\Delta_{11}$  that presents the difference between elastic microstrains  $\varepsilon_{11}^{(1)}$  and  $\varepsilon_{11}^{(2)}$ :

$$\Delta_{11} = \varepsilon_{11}^{(1)} - \varepsilon_{11}^{(2)}. \quad (2)$$

Connection with the internal microstresses is obvious because microstresses  $\sigma_{ij}^{(k)}$  are related to elastic microstrains  $\varepsilon_{ij}^{(k)}$  by the Hooke's law. An interesting peculiarity of this structural parameter is that it is irreducible at elastic deformations of the composite as a whole including the stress release. Therefore,  $\Delta_{11}$  is connected directly with the residual stresses in the composite.

On the microlevel the longitudinal stress  $\sigma_{11}$  is a sum of the longitudinal microstresses  $\sigma_{ij}^{(k)}$  proportionally to the fibre volume fraction  $c$ :

$$\sigma_{11} = c\sigma_{11}^{(1)} + (1-c)\sigma_{11}^{(2)} \quad (3)$$

Thus, this procedure avoids the fibre arrangement, the component's bonding and local distributions of the transverse stresses but enables the longitudinal microstresses to be taken into account. Additional hypotheses for elastic microstrains and thermophysical variables (temperature  $T$  and specific entropy  $s$ ) are:

$$T = T^{(1)} = T^{(2)}, \quad s = cs^{(1)} + (1-c)s^{(2)}, \quad (4)$$

$$\varepsilon_{11} = \varepsilon_{11}^{(1)} - \bar{\varepsilon}_{11}^{(1)}, \quad (5)$$

$$\varepsilon_{ij} = c(\varepsilon_{ij}^{(1)} - \bar{\varepsilon}_{ij}^{(1)}) + (1-c)(\varepsilon_{ij}^{(2)} - \bar{\varepsilon}_{ij}^{(2)}), \quad (i, j) \neq (1,1), \quad (6)$$

here  $\bar{\varepsilon}_{ij}^{(k)}$  - microstrains induced in the constituents by the irreversible processes after the stress release has occurred.

The origin of the least obvious hypothesis (5) results from the micromechanical consideration of the loading-unloading cycle of unidirectional composite in the longitudinal direction. A detailed analysis and derivation of (5) have been carried out in [8]. Absolutely similar hypotheses are constructed for the unidirectional laminated composite.

Introduction of the assumptions for microstrains and temperature gives an opportunity to connect all microstresses, microstrains and corresponding thermophysical characteristics to the macrovariables. If the equations of dynamic behaviour for each the composite's components are given, then, using the hypotheses stated above, we can obtain: i) relationships between stresses and strains (including the temperature and entropy); ii) equations of the dynamics of composite.

Detailed derivation for the case of small elastic deformations is stated for the unidirectional fibrous and laminated composites in [8,9]. Generalisation for the case of finite elastic deformations is based on the use of a transformation of a rectangular system associated with fibre into the Cartesian coordinate system. In fact, the transformation is a matrix of the fibre rotation and it determines fibre location in the stress release state.

The transformation of the tensor variables (strains, stresses, the structural parameter  $\Delta$ ) results in the appearance of the plastic spin in the right-hand sides, which are responsible for the inelastic behaviour of composite. In general form the system of equations of the model is:

$$\begin{aligned} \frac{da_{ij}}{dt} + a_{ik} \frac{\partial u_k}{\partial x_j} &= -a_{ik} \psi_{kj}, & \frac{db_{ij}}{dt} &= \theta_{ik} b_{kj}, \\ \frac{d\Delta_{ij}}{dt} &= -\lambda_{ij} + \theta_{ik} \Delta_{kj} - \Delta_{ik} \theta_{kj}, \end{aligned} \quad (7)$$

where

$$\begin{aligned} \tilde{\psi}_{11} &= \alpha_{11} \tilde{\sigma}_{11} + \alpha_{12} \tilde{\sigma}_{22} + \alpha_{12} \tilde{\sigma}_{33} + \beta_1 \tilde{q}, \\ \tilde{\psi}_{22} &= \alpha_{12} \tilde{\sigma}_{11} + \alpha_{22} \tilde{\sigma}_{22} + \alpha_{23} \tilde{\sigma}_{33} + \beta_2 \tilde{q}, \\ \tilde{\psi}_{33} &= \alpha_{12} \tilde{\sigma}_{11} + \alpha_{23} \tilde{\sigma}_{22} + \alpha_{22} \tilde{\sigma}_{33} + \beta_2 \tilde{q}, \\ \tilde{\psi}_{ij} &= \alpha_{66} \tilde{\sigma}_{ij}, \quad \tilde{\lambda}_{11} = \beta_1 \tilde{\sigma}_{11} + \beta_2 \tilde{\sigma}_{22} + \beta_2 \tilde{\sigma}_{33} + \gamma \tilde{q}, \quad i \neq j \end{aligned} \quad (8)$$

here  $\alpha_{ij}, \beta, \gamma$  - the coefficients derived by use of the homogenization procedure from the functions of the Maxwell-type model for the composite's components [9], they depend on the relaxation functions and the stress state in the constituents. The symmetry of coefficients in (8) expresses the fundamental fact - the Onsager symmetry principle. In the system (7)  $\theta_{ij}$  are components of a tensor which is responsible for irreversible change in the fibre orientation, it is a given function when the functions  $\tilde{\psi}_{ij}$  are given. The tensor with components  $b_{ij}$  is a tensor of irreversible rotation for fibre,  $\tilde{q} = E_{\tilde{\Delta}}$ , a tilde-variable  $\tilde{f}_{ij}$  is a tensor in the rectangular system associated with either the fibre or the normal to lamina, it is expressed through that in the Cartesian system by the standard transformation rule:  $f_{ij} = b_{ik} \tilde{f}_{km} b_{mj}$ . The system (7) is completed by the conservation laws for energy and momentum, and a given dependence of the internal energy  $E$  on the strain tensor, structural parameter and entropy.

## EFFECTIVE ELASTIC CHARACTERISTICS

To illustrate the influence of the fibre content on elastic moduli, the characteristics in this section will be analysed for the case of isothermal deformation. Invoking the procedure of homogenization, the Hooke's laws for constituents yield the stress-strain relations which are typical for the transversely isotropic material:

$$\begin{aligned}
 \sigma_{11} &= C_{11}\varepsilon_{11} + C_{12}\varepsilon_{22} + C_{12}\varepsilon_{33}, \\
 \sigma_{22} &= C_{12}\varepsilon_{11} + C_{22}\varepsilon_{22} + C_{23}\varepsilon_{33}, \\
 \sigma_{33} &= C_{12}\varepsilon_{11} + C_{23}\varepsilon_{22} + C_{22}\varepsilon_{33}, \quad \sigma_{ij} = 2C_{66}\varepsilon_{ij}, \quad i \neq j
 \end{aligned} \tag{9}$$

where

$$\begin{aligned}
 C_{11} &= \langle \lambda + 2\mu \rangle + \left\langle \frac{\lambda}{\lambda + \mu} \right\rangle^2 \left\langle \frac{1}{\lambda + \mu} \right\rangle^{-1} - \left\langle \frac{\lambda^2}{\lambda + \mu} \right\rangle, \quad C_{12} = \left\langle \frac{\lambda}{\lambda + \mu} \right\rangle \left\langle \frac{1}{\lambda + \mu} \right\rangle^{-1}, \\
 C_{22} &= \left\langle \frac{1}{\lambda + \mu} \right\rangle^{-1} + \left\langle \frac{1}{\mu} \right\rangle^{-1}, \quad C_{23} = \left\langle \frac{1}{\lambda + \mu} \right\rangle^{-1} - \left\langle \frac{1}{\mu} \right\rangle^{-1}, \\
 C_{66} &= \frac{1}{2}(C_{22} - C_{23}) = \left\langle \frac{1}{\mu} \right\rangle^{-1},
 \end{aligned} \tag{10}$$

here  $\lambda, \mu$  are the Lamé coefficients. Expressions in the angle parentheses present the mixture rule  $\langle K \rangle = cK_2 + (1-c)K_1$ .  $\langle K \rangle = cK_2 + (1-c)K_1$ . The longitudinal and transverse Young's moduli  $E_1, E_2$ , the shear modulus  $G_2$  and the longitudinal and transverse Poisson's coefficients  $\nu_1, \nu_2$  can be easily linked with  $C_{ij}$ :

$$\begin{aligned}
 E_1 &= \frac{2C_{12}^2}{C_{22} + C_{23}}, \quad E_2 = \frac{(C_{22} - C_{23})[C_{11}(C_{22} + C_{23}) - 2C_{12}^2]}{(C_{11}C_{22} - C_{12}^2)}, \\
 G_2 &= C_{66}, \quad \nu_1 = \frac{C_{12}}{C_{22} + C_{23}}, \quad \nu_2 = \frac{C_{11}C_{23} - C_{12}^2}{C_{11}C_{22} - C_{12}^2}.
 \end{aligned} \tag{11}$$

It is interesting to note that the procedure applied to the laminated structure gives the elastic moduli which coincide identically with those stated in the popular monography by Christensen [2]. Therefore, we shall analyse the dependencies of the elastic constants on the fibre content only for the fibrous composite.

The well-known estimates for an effective modulus of the composite  $K_c$  ( $K_f$  - the respective elastic modulus of fibres,  $K_m$  - the elastic modulus of matrix) are the Voigt estimate (the mixture rule) and the Reuss estimate, respectively:

$$K_c = cK_f + (1-c)K_m, \quad 1/K_c = c/K_f + (1-c)/K_m,$$

where  $c$  - the fibre volume concentration.

The longitudinal Young's modulus  $E_1$  for the composite in most of theories is in very good agreement with the Voigt estimate (the rule of mixture), experiments are in agreement with this rule, too. Our formulas are not an exclusion and they are practically coincident with the linear dependence of the mixture rule.

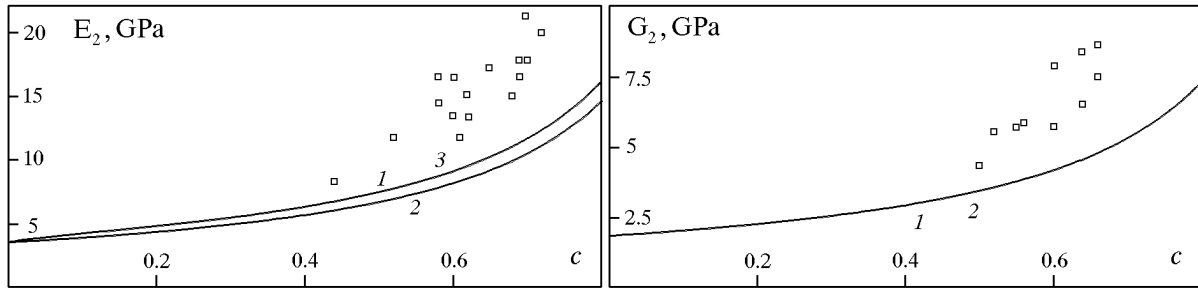


Fig. 1: The transversal Young's modulus (a) and the rigidity modulus (b) for the glass/epoxy fibrous composite

Theoretical and experimental dependencies are not so simple for the transversal Young's modulus  $E_2$  and the rigidity modulus  $G_2$ . The well-known approximation for the moduli is the Reuss estimate. It is interesting to note that our dependence for the rigidity modulus is exactly the Reuss estimate. Experiments stated in [4] give the moduli (points in Fig. 1) for the glass/epoxy composite (elastic constants for fibre and matrix are  $E_f = 731 \text{ GPa}$ ,  $G_f = 302 \text{ GPa}$ ,  $\nu_f = 0.22$ ,  $E_m = 3.45 \text{ GPa}$ ,  $G_m = 1.8 \text{ GPa}$ ,  $\nu_m = 0.35$ ). Our results (curves 1 according to equations (10), (11)) are compared in Fig. 1 with the theory of [4] and the Reuss estimate of the effective moduli. It is seen that the discrepancy between all the theories and experiment is of the same order.

Experimental data for the graphite/epoxy-resin composite by Goggin [10] are stated by points in Fig. 2. Elastic data for the constituents are: the type 1 fibre  $E_f = 395 \text{ GPa}$ ,  $\nu_f = 0.28$ ; the type 2 fibre  $E_f = 230 \text{ GPa}$ ,  $\nu_f = 0.28$ ; the fibre in the transversal direction:  $E_f = 276 \text{ GPa}$ ,  $\nu_f = 0.28$ ; the epoxy resin system:  $E_m = 3.9 \text{ GPa}$ ,  $\nu_m = 0.33$ . Fig. 2, (a) corresponds to the transversal Young's modulus  $E_1$ , Fig. 2, (b) - the rigidity modulus  $G_2$ , Fig. 2, (c,d) - the longitudinal and transversal Poisson's ratios  $\nu_1$  and  $\nu_2$ , respectively. Curves 1, 2, 3 in Fig. 2, (a) correspond to the three types of fibres mentioned above according to the formulas (10), (11), curve 1 in Fig. 2, (b-d) - to the fibre type 1 calculated by the same formula.

The data by Goggin have quite large scatter, especially for the Poisson's ratio. The Young's modulus of the fibre type 2 is less than that of the fibre type 1. However, the transverse Young's modulus of the composite with the fibre type 2 is higher than that with the fibre type 1 (Fig. 2, (2)). Apparently, this feature is associated with the strong anisotropic properties of fibres. Our model of the constituents is an isotropic material. Therefore, we calculated curve 3 in Fig. 2 (a) for a fibre with the Young's modulus corresponding to the experimental transversal Young's modulus of the graphite fibre.

Among theoretical data the well-known formulae are those by R. Hill stated in [5]. For the constants from (10) they take the form:

$$C_{11} = \langle \lambda + 2\mu \rangle - c(1-c) \frac{(\lambda_1 - \lambda_2)^2}{\hat{\lambda} + \hat{\mu} + M}, \quad C_{12} = \langle \lambda \rangle - c(1-c) \frac{(\lambda_1 - \lambda_2)(\lambda_1 + \mu_1 - \lambda_2 - \mu_2)}{\hat{\lambda} + \hat{\mu} + M},$$

$$C_{66} = \frac{1}{2}(C_{22} - C_{23}) = \langle \mu \rangle - c(1-c) \frac{(\mu_1 - \mu_2)^2}{\hat{\mu} + M}, \quad (12)$$

$$\frac{1}{2}(C_{22} + C_{23}) = \langle \lambda + \mu \rangle - c(1-c) \frac{(\lambda_1 + \mu_1 - \lambda_2 - \mu_2)^2}{\hat{\lambda} + \hat{\mu} + M},$$

here  $\hat{f} = (1-c)f_1 + cf_2$ . It is easy to check that at  $M=0$  these formulæ reduce to dependencies (10). Because  $M$  has the meaning of the shear modulus we take as an example  $M = \langle \mu \rangle$ . Calculations according to (12) give the curve 4 in Fig.2, (a) and curves 3 in Fig. 2, (c-d). The semi-empirical dependencies by C.Chamis stated in [6] are the curve 5 in Fig. 2, (a) and curves 2 in Fig. 2, (b-d). Our formulæ describe experiments on the Poisson's ratio in the best way among theoretical data mentioned above. For the transversal Young's modulus and the rigidity modulus the discrepancy between all the theories and experiment is again of the same order.

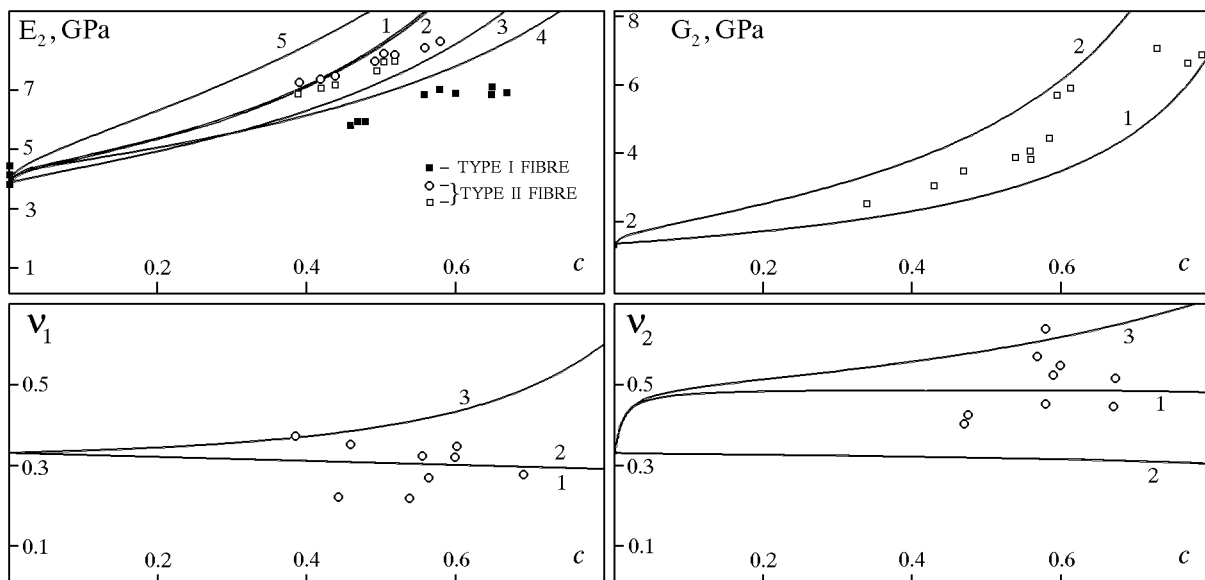


Fig. 2: The effective elastic characteristics for the graphite/epoxy composite. The transversal Young's modulus (a) (points are the experiments [10]); the rigidity modulus (b); the longitudinal Poisson's ratio (c); the transversal Poisson's ratio (d)

The comparison gives us a confidence in use of the homogenization approach for the derivation of dynamic equations.

### THE SHOCK WAVE RESPONSE OF COMPOSITE

To illustrate the potential of the model a computation of the shock wave propagation in obliquely oriented laminated composite has been conducted. The method of calculation of the system (7) is the finite-difference Godunov scheme. The composite structure has been chosen in accordance with an experimental sample by Sve and Okubo [3], where the Al/Lexan composite has been oriented symmetrically (Fig. 3,a) and obliquely (Fig. 3, b) to the shock wave.



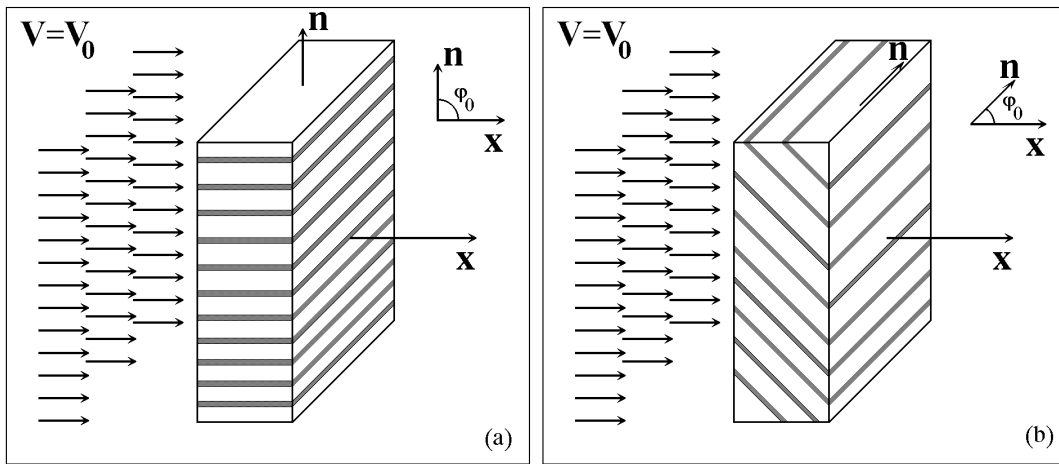


Fig. 3: Sketches for the straightward and oblique shock-wave loading of the laminated composite

In order to understand the process of the off-axis loading let us consider the loading of the representative volume of the composite by uniaxial stress. The sketch of the process is drawn in Fig. 4. The corresponding load-deformation curve computed by the model shows that in certain range of orientations the stress response is complex due to rearrangement of the composite structure during the loading. At the symmetrical loadings (the cases 1 and 3) the composite strengths correspond to those of the fibre or matrix. For the off-axis loading (the case 2) the composite strength changes during the deformation, depending on the reinforcement direction.

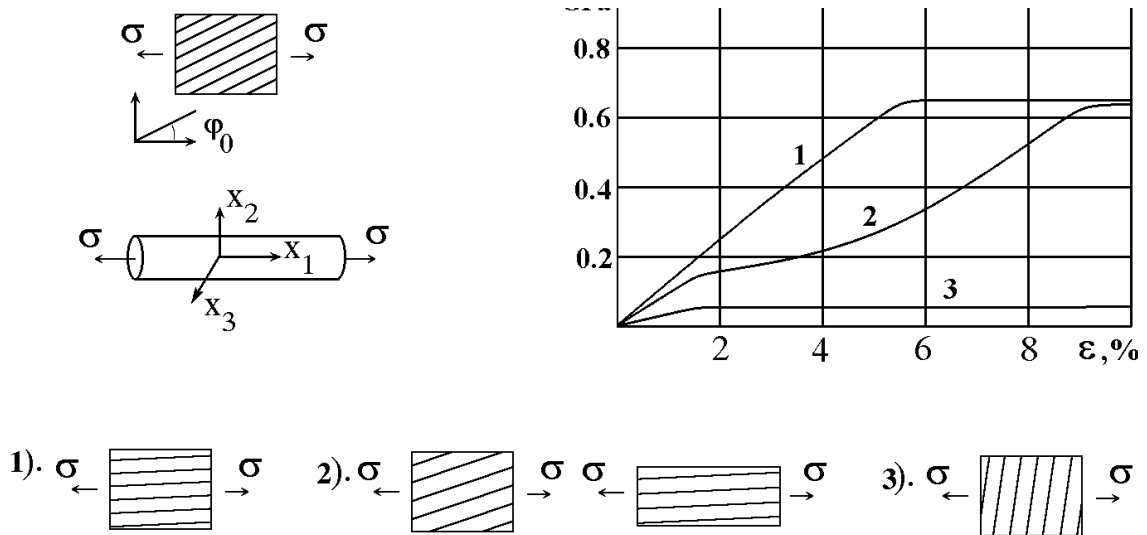


Fig. 4: Schemes of the off-axis loading and calculation of the load-deformation curve for the case of rotation of the reinforcement

Coefficients  $\alpha, \beta, \gamma$  of the functions  $\psi_{ij}$  in (8) which are responsible for the inelastic behaviour of the constituents are constructed from experimental dependencies of the yield limit on the strain rate. The method for the construction of the functions can be found in [11].

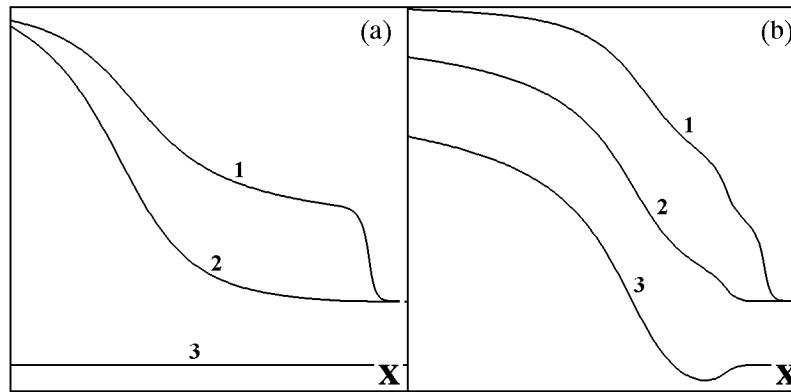


Fig. 5: Calculation of the shock-wave response of the symmetry-oriented and obliquely oriented laminated composite; 1 - the velocity profile, 2 - the microstress profile, 3 - the change in the fibre orientation

The shock-wave propagation calculated for the samples in Fig. 3 has a number of peculiarities. At symmetrical loading (velocity versus coordinate in the sample at a moment of time - the curve 1, Fig. 5, a), the fibre orientation does not change during the process (curve 3),  $\tilde{\Delta}$  (curve 2) associated with the internal microstress (the difference in elastic strains between the constituents) changes only after the elastic wave has passed and the plastic wave has induced the microstress in the sample.

However, in the case of off-axis loading (the orientation angle  $\varphi_0 = 47^\circ$ ) the fibre orientation becomes an essential factor due to the rearrangement stated in Fig. 4. Initially, the elastic wave acts as in the preceding case (velocity - curve 1 in Fig. 5, b), then the successive load changes the layer orientation and modifies the strength properties of the sample. It is seen from Fig. 5, (b) that in the second wave the angle orientation has been changed (curve 3), a rise in  $\tilde{\Delta}$  (curve 2) indicates that the composite in these points is out of elastic range and the change is associated with the structural rearrangement. The third wave performs the final loading up to the limit determined by the striker.

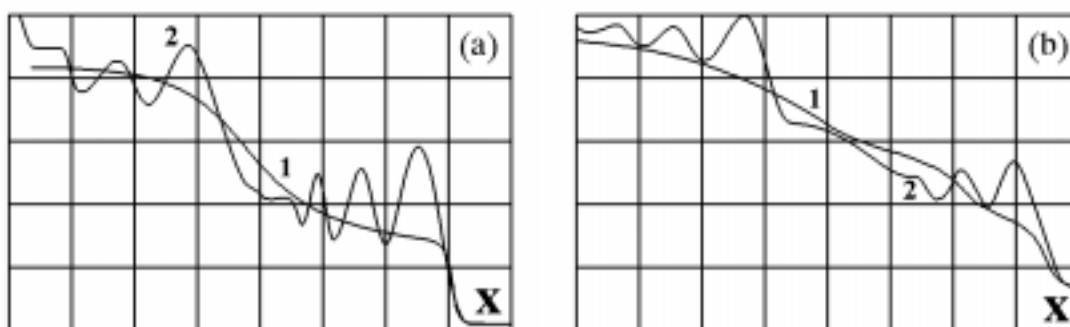


Fig. 6: Comparison between the calculated (curve 1) and the experimental [3] (curve 2) velocity profiles

The comparison of the calculation with the experiments [3] shows good agreement between the velocity profiles (Fig. 6).

## CONCLUSION

A homogenization procedure for unidirectional composite is proposed in the paper. The aim of the approach is to design a three-level hierarchical model for description of the dynamic behaviour of the composite materials. Effective elastic characteristics obtained by the procedure for the fibrous and laminated composite are within the range of the well-known theoretical and experimental data. The model is suitable for description of the shock-wave data for composites. The calculation of the obliquely loaded composite is in good agreement with the known experiment [3].

## REFERENCES

1. Godunov, S.K. and Romensky, E.I., "Nonstationary Equations of Theory of Nonlinear Elasticity in the Eulerian Coordinates", *Prikl. Mekh. i Tekh. Fiz. [Engl. transl. Appl. Mech. Techn. Phys.]*, Vol. 13, No. 6, 1972, pp. 124-144.
2. Christensen, R.M., *Mechanics of Composite Materials*, John Wiley, New York, 1979.
3. Sve, C. and Okubo S., "Experiments on Pulse Propagation in an Obliquely Laminated Composite", *Journal of Applied Mechanics*, Vol. 39, 1974, pp. 1052-1056.
4. Tsai, S.W. and Hahn, H.T., *Introduction to composite materials*, Technomic Pub., Westport, 1980.
5. Tewary, V.K., *Mechanics of Fibre Composites*, John Wiley, New York, 1978.
6. Chawla, K.K., *Composite Materials*, Springer-Verlag, New York, 1987.
7. Resnyansky, A.D., Simulation of Flexure in Off-axis Three-Point Bending Test by a Finite-Element Code, *The Present Proceedings*.
8. Resnyansky, A.D. and Romensky, E.I., "Model of Viscoelastic Unidirectional Composite with Coupled Thermal and Elastic processes", *Proceedings 19th International Symposium on Shock Waves*, Marseille, France, July 26-30, 1993, Vol. III: Shock Waves in Condensed Matter and Heterogeneous Media, Brun, R., Dumitrescu, L.Z., Eds, pp. 273-278.
9. Resnyansky, A.D. and Romensky, E.I., "Model of Dynamic Deformation of a Laminated Thermoviscoelastic Composite", *Combustion, Explosion, and Shock Waves (Fizika Gorenia i Vzryva)*, Vol. 29, No. 4, 1993, pp. 535-541
10. Goggin, P.R., The Elastic Constants of Carbon-Fibre Composites, *Journal of Materials Science*, Vol. 8, 1973, pp. 233-244.
11. Resnyansky, A.D. and Merzhievsky, L.A. "On Determination of Parametres of Dependence of The Shear-Stress-Relaxation Time", [In Russian], *Fizika Gorenia i Vzryva*, Vol. 28, No. 3, 1992, pp. 123-124.

# IMPACT DAMAGE AND FAILURE MECHANISMS IN STRUCTURE RELEVANT COMPOSITE SPECIMENS

J. F. M. Wiggeraad and L. C. Ubels

*National Aerospace Laboratory NLR, P.O. Box 153, 8300 AD Emmeloord, The Netherlands*

**SUMMARY:** Impact damage and failure mechanisms, representative of stiffened composite wing panels, were studied using small but structure relevant (SR) specimens. It was investigated how laminate stacking sequence influences the location within a laminate of the major delaminations that are generated by impact. Impact damages for six different lay-ups showed major delaminations predominantly at the ply interfaces where they were expected. Subsequently, the residual strength of the SR specimens was determined in compression. The major impact induced delaminations were also the delaminations that propagated under loading, driven by bending or buckling of the 0-degree plies. However, with increased loading, transverse shear of the delaminated sublaminates became the ultimate failure mechanism. Thus it was concluded that the residual strength of the SR specimens depends primarily on the reduced global stability of the damaged laminate, and less on the individual stability of the delaminated sublaminates. A failure criterion is needed, based on longitudinal compressive strain and transverse shear strain in 0-degree dominated ply stacks.

**KEYWORDS:** design, impact, damage tolerance, modelling, testing

## INTRODUCTION

The development of structural concepts for compression loaded, damage tolerant, stiffened composite wing panels requires an experimental investigation of the failure mechanisms that may occur. Insight into these mechanisms will lead to design guidelines for the structural configuration considered, and can be incorporated in design optimization procedures. One of the most critical states of damage to consider is the presence of one or more delaminations between the plies of a laminate, caused by low velocity impacts. Such delaminations tend to spread when the panel is loaded in compression, reducing the overall stability of the panel until ultimate failure occurs. (Delamination "spread" is defined as the quasi-static or dynamic propagation of a delamination under increased static loading, as opposed to delamination "growth" under fatigue loading).

The fabrication and testing of full scale stiffened panels is an expensive procedure, so for economic reasons most experiments are commonly performed on relatively simple specimens: plain laminates with corresponding material properties. When testing a laminate in the form of a small specimen supported by a frame, the damage resulting from the impact event as well as the residual compression strength may deviate considerably from the experimental values that are obtained when the laminate forms part of a larger structural configuration. Structural properties, such as the different dynamic response during impact and the presence of multiple load paths in a larger structure are thought to be responsible for the often superior damage tolerance observed when testing structures instead of small specimens.

At ICCM-9, a small Structure Relevant (SR) specimen was described [1], which is less expensive to make and test than a full scale panel. When combined with a support to simulate the stiffener [1-2], it maintains the essential design features of the panel configuration that is being investigated, see Fig. 1. The SR specimen was shown to be useful in providing insight in delamination spread mechanisms. In this study, delaminations were provoked by the insertion of circular bronze foils. However, a proper evaluation of the damage tolerance of different design concepts requires that genuine damage is induced in the SR specimens by impact. This impact damage must correspond to the damage resulting from impacts on the stiffened panels that are represented by the SR specimens. At ICCM-10 a method was presented to apply structure relevant impact damage to SR specimens [3]. It was shown that the flexibility present in a larger structure can be approximated by selecting the proper support conditions for the SR specimen. It appeared that if the support conditions are such that the maximum deflection measured during impact at the impact site is approximately the same for stiffened panel and SR specimen, this will result in similar damage.

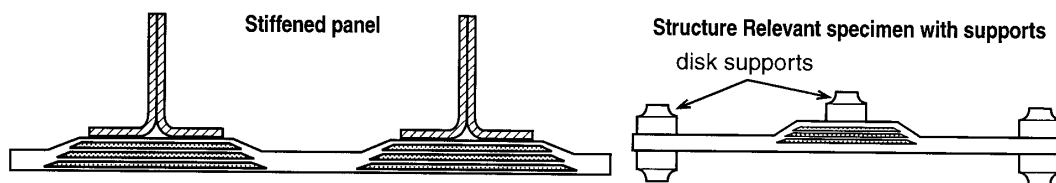


Fig. 1 Concept of Structure Relevant specimen

Fig. 1: Concept of structure relevant specimen

Based on the previous studies [1-3] it was believed that the failure mechanism related to the damage configuration considered, consists of the spread of a few preferred delaminations out of the multitude of delaminations and matrix cracks present in the impacted area, followed by sequential buckling of the delaminated sublaminates. When the overall stability of the panel reaches a critical value, ultimate failure occurs. As delamination spread occurs mainly in the lateral direction (perpendicular to the stiffeners) it is expected to start from delaminations with the widest span. The findings reported in [1-3] also revealed that the major impact induced delaminations are formed along certain preferred ply interfaces. Hence, it was postulated in [3] that by a deliberate positioning of these preferred interfaces deeper inside the laminate, thicker sublaminates will be formed by the impact. As thicker sublaminates have a higher resistance against buckling, delamination spread and ultimate failure are expected to be delayed when the specimen is loaded by increased compression.

In the present study the results are presented of a test programme, in which SR specimens with six different lay-ups were provided with impact damage and subsequently loaded in compression up to failure. The objectives of this programme were to investigate whether the major impact induced delaminations occur at the interfaces where they are expected, and to evaluate the validity of the postulated failure mechanism.

## PANEL DESIGN AND SR SPECIMEN CONFIGURATION

The configuration of the SR specimens was based on a damage tolerant stiffened carbon/epoxy panel concept developed by Boeing [4], now applied in the V-22 Osprey wing. This concept comprises a soft (low axial stiffness) skin, doublers (extra plies added locally to the skin underneath the stiffeners) and discrete (pre-cured) stiffeners, see Fig. 2. A panel design with I-stiffeners was determined for an ultimate load level of 2000 N/mm, using the PANOPT optimization code for stiffened panels [5], see Fig. 3. One of the six SR specimen lay-ups was identical to the skin/doubler configuration of the panel design, while the other lay-ups were variations thereof. The lay-ups of the six different SR configurations are listed in table 1 and are shown in Fig. 4. In the present paper, results are discussed for five specimens of each lay-up.

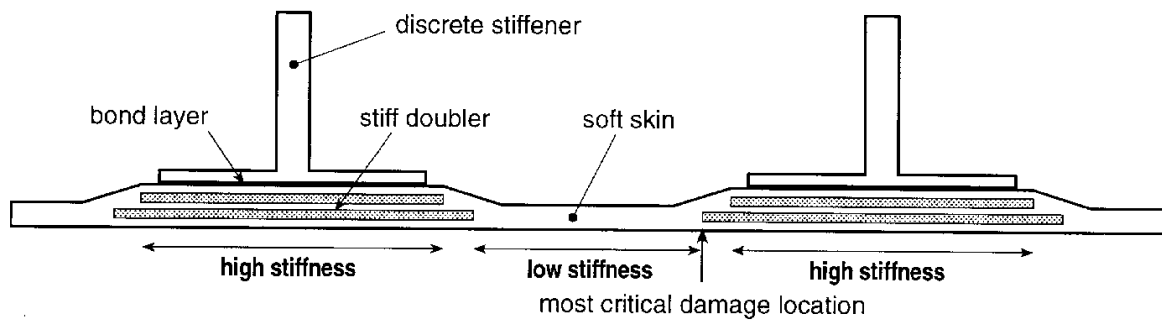


Fig. 2: Boeing's damage tolerant panel concept with soft skin, doublers and discrete stiffeners

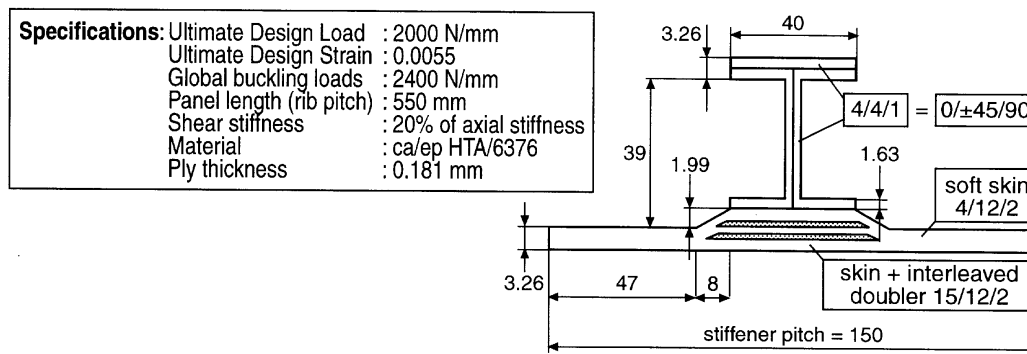


Fig. 3: Design specifications, geometry and lay-up (dimensions in mm)

Table 1: Laminate configurations

Configuration	Laminate stacking sequence (starting at flat side)
1	$(\pm 45)_2/0/[0_6]/90/(\pm 45)/0/[0_5]/0/(\pm 45)/90/0/(\pm 45)_2$
2	$(\pm 45)_2/0/90/(\pm 45)/0/[0_6]/0/(\pm 45)/90/0/[0_5]/(\pm 45)_2$
3	$(\pm 45)_2/0/[0_6]/90/(\pm 45)/0_2/(\pm 45)/90/0/[0_5]/(\pm 45)_2$
4	$(\pm 45)/0/(\pm 45)/[0_6]/90/0/(\pm 45)/(\pm 45)/0/[0_5]/90/(\pm 45)/0/(\pm 45)$
5	$(\pm 45)/0/(\pm 45)/90/0/(\pm 45)/(\pm 45)/0/90/(\pm 45)/0/(\pm 45)/[(\pm 45)/0_3/90/0_3/(\pm 45)]$
6	$(\pm 45)_2/0/[0_6]/B/90/(\pm 45)/0/[0_5]/0/(\pm 45)/B/90/0/(\pm 45)_2$

note: B = bond film; plies between [ ] are doubler plies

### EXPERIMENTAL PROCEDURE

Low velocity impact damage was applied to the first three specimens of each lay-up with an instrumented impactor, at the flat skin opposite to the edge of the doubler as shown in Fig. 4. The impactor used had a mass of 2.312 kg and a semi-spherical tup with a diameter of 1.0 inch (25.4 mm). The impact energy was 35J for the first specimen and 50J for the second and third specimens of each lay-up. The fourth specimen of each lay-up was statically indented up to the same deflection as the maximum deflection measured during the 35J impacts. The fifth specimen of each lay-up was left undamaged. All damaged specimens were C-scanned, and the first specimen of each lay-up was dissected for a post-mortem investigation of the impact damage.

After impact damage was induced, the specimens were loaded in static uni-axial compression up to failure (or up to a compressive strain of 0.0070 in case of several of the undamaged specimens), mounted in the anti-buckling guide shown in Fig. 5. Displacements were measured with LVDT's, and strains with strain gauges at locations also shown in Fig. 5. The failure mode was established with post-mortem fractography for specimens '3' of each lay-up.

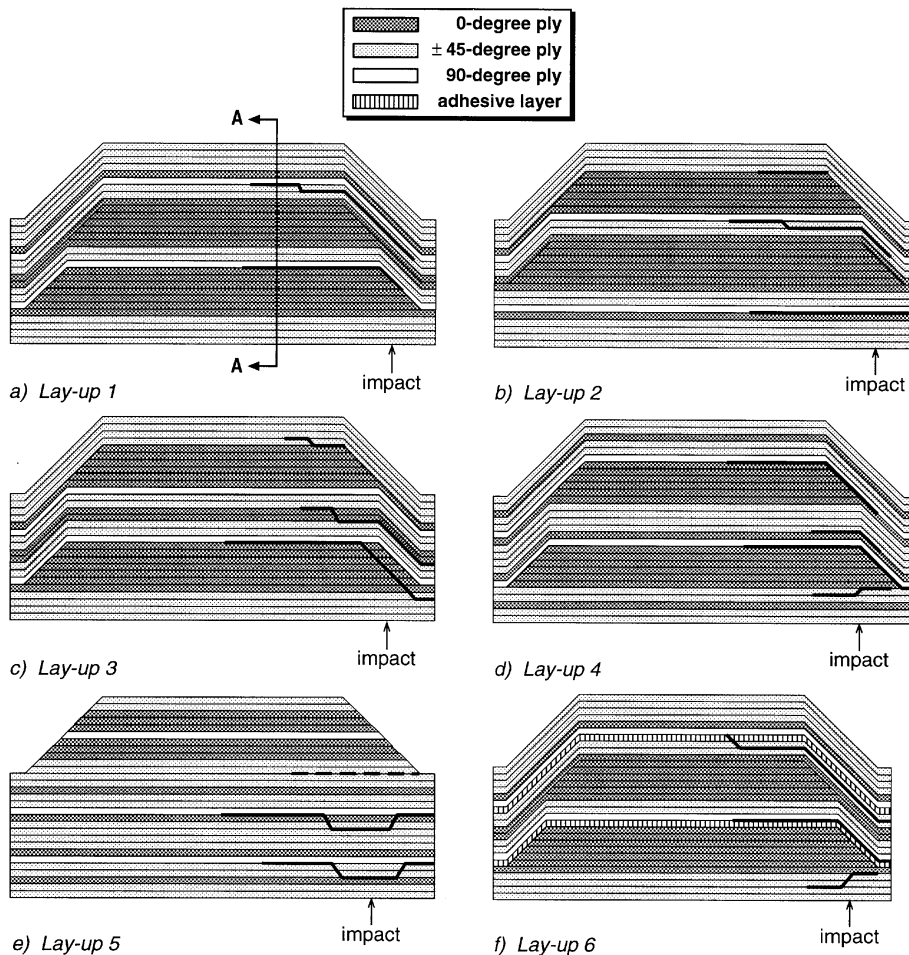


Fig. 4: Lay-ups of six SR-specimens with major impact induced delaminations (cross-section A – A refers to figure 8)



## RESULTS AND DISCUSSION

### Impact Damage

Impact parameters are not discussed, except to indicate that the static and dynamic (35J) responses of the SR specimens were very close, as shown in Fig. 6 for Lay-up 1. This similarity may warrant the approach to design for "static" rather than dynamic impacts, an observation which may simplify optimization procedures in the future, as static responses are easier to compute. The first specimen of each lay-up was dissected, and the major delaminations were made visible with uv-light, illuminating a penetrating fluid (Fig. 7). The cross sections shown are located at a distance of approximately 20 mm from the impact site to eliminate the smaller delaminations. The location of the major delaminations relative to the stacking sequence are indicated in Fig. 4 for all six lay-ups.

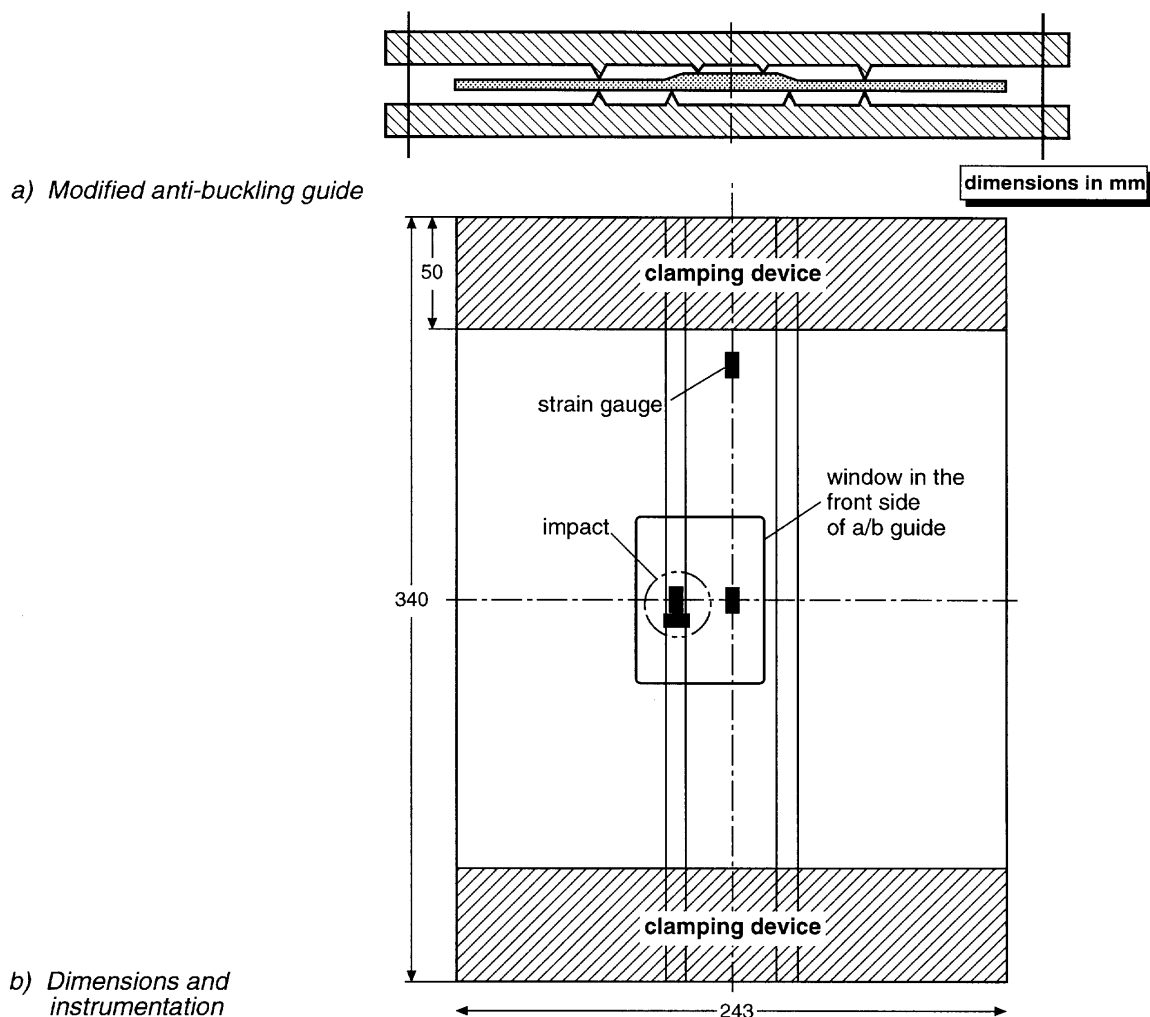


*Fig 5: Test configuration of SR-specimens*

In the following discussion the damage is described with reference to the impact direction: the front is the flat, impacted side of the laminate. Most lay-ups contained two 0-degree ply stacks and all lay-ups contained two 90-degree skin plies. The major impact induced delaminations were expected to occur behind the 0-degree ply stacks and along the 90-degree plies when these were nearby. Lay-up 1 shows two major delaminations behind the two 0-degree ply stacks, and



along or close to the 90-degree plies which are located behind these ply stacks, as expected. Lay-up 2 shows three major delaminations: two behind the 0-degree ply stacks, very deep inside the laminate, but also one in front of the first ply stack, very close to the free surface. This undesirable delamination is caused by the presence of a 0/90 degree ply interface in front of the first ply stack. Lay-up 3 also shows two major delaminations behind the 0-degree ply stacks. However, another large delamination is found in the wide space between the two thick 0-degree ply stacks, behind a thinner stack of two 0-degree skin plies that pass through this space. Lay-up 4 shows two large delaminations behind the two doubler ply stacks, as well as two smaller delaminations in front of each doubler ply stack. The two continuous 0-degree skin plies passing in front of the two doubler ply stacks are apparently responsible for these smaller delaminations. Lay-up 5 has a discrete doubler ply stack located on top of an uninterrupted flat skin. The damage, very different in character compared to the damage of the other lay-ups, resembles damage in a quasi-isotropic flat laminate, where the many ply angle changes (stiffness jumps) result in a larger number of smaller delaminations. The widest ones are located along the two 90-degree plies. Lay-up 6 is identical with Lay-up 1, except for two bond films added immediately in front of the two 90-degree plies. Just as for Lay-up 1, the major delaminations are located behind the doubler ply stacks. The bond layers apparently had no benevolent effect on the size of the impact damage.

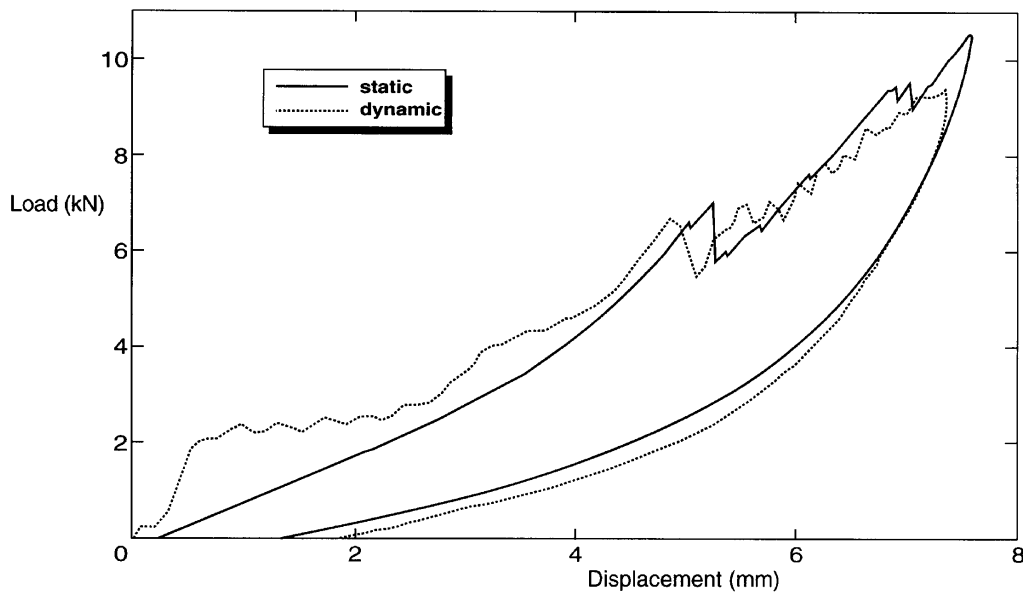


Fig. 6: Dynamic response (35J) versus static response for lay-up 1

Ranking the six lay-ups for expected "damage tolerance", based on the location and size of the major impact induced delaminations, and in correspondence with the postulated failure mechanism of buckling sublaminates, the following order (from best to worst) was tentatively established: Lay-ups 1, 6, 3, 2, 4 and 5. Apparently, to "place" delaminations deep inside a laminate, and to avoid the formation of additional undesirable delaminations at other locations, the number of ply angle changes should be limited. This can best be achieved by stacking the 0-degree doubler stacks adjacent to the 0-degree plies of the skin, by positioning the 90-degree plies immediately behind the 0-degree ply stacks where they will certainly provoke the formation of the major delaminations, and by surrounding these "planks" with uninterrupted  $\pm 45$  ply stacks.

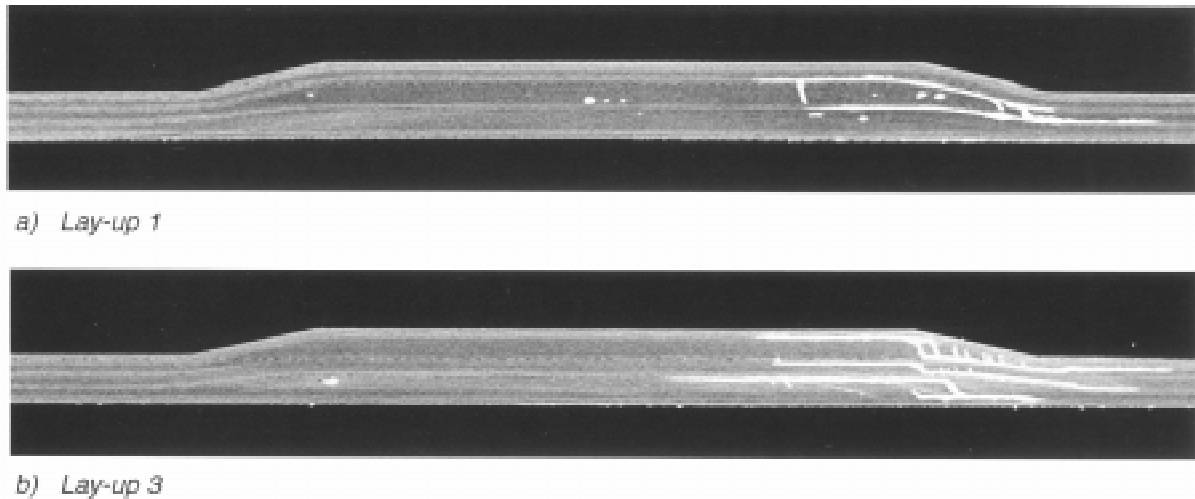


Fig. 7: Major delaminations in SR specimens

### Failure Mechanisms

Specimens 2-5 of each lay-up were loaded in compression up to failure, or up to a compressive strain of 0.0070 for some of the undamaged specimens (to prevent damage to the test instrumentation). The maximum loads achieved are shown in table 2. The size of the total C-scan damage area is also presented for these specimens. Most configurations had C-scan areas of approximately 1800 mm<sup>2</sup>. The C-scan areas for Lay-up 4 are somewhat smaller at 1500 mm<sup>2</sup>, and the C-scan areas of Lay-up 5 (with a discrete doubler on top) are showing a much larger scatter, from 1450 mm<sup>2</sup> to 2450 mm<sup>2</sup>. This scatter is related to the large delamination occurring between doubler and skin, which is less consistent than the "enclosed" delaminations of the other configurations.

It appears from table 2 that the maximum loads of the undamaged specimens (specimens 5 of each lay-up) are much higher than those of the damaged specimens, all corresponding to axial compressive strains in excess of 0.0070. It should be noted that the axial stiffness of Lay-up 5 is less than the stiffness of the other lay-ups, because its discrete doubler stack on top of the skin is "softer" than  $O_{11}$  (to limit the stiffness difference between soft skin and stiff doubler). The failure loads of indented specimens 4 are, like the damage areas, of the same order of magnitude as those of the impacted specimens 2-3. For five of the six lay-ups the failure loads of the damaged specimens were very close. For Lay-up 4 the difference between specimens 2 and 3 was much larger (20%). This difference is due to the different failure modes observed for these two specimens: bending of the damaged area toward the window in the anti-buckling frame support (Fig. 5), or bending backward against the support. It must be concluded that the SR specimens do not provide residual strength values representative of the stiffened panel configuration. Unlike for the thicker (and stiffer) SR specimens described in [1-2], the absence of the stiffener can not be fully compensated by the influence of the support, which can push but not pull. Hence, the final failure mode of most specimens was by buckling in the direction away from the support into the window. Two of the higher failure values were observed for specimens which bent in the opposite direction, toward the support (specimens 2 of Lay-up 3 and Lay-up 4).

Table 2: Damage areas and failure loads

Config-uration	Specimen number	C-scan area (mm <sup>2</sup> )	Failure load (kN)	Config-uration	Specimen number	C-scan area (mm <sup>2</sup> )	Failure load (kN)
1	1	1610	-	4	1	1450	-
	2	1810	236		2	1558	275
	3	1877	229		3	1665	219
	4	1638	255		4	1346	238
	5	-	362		5	-	294*
2	1	1530	-	5	1	1570	-
	2	1874	229		2	1445	203
	3	1699	230		3	1916	222
	4	1867	234		4	2451	232
	5	-	372		5	-	270*
3	1	1600	-	6	1	1650	-
	2	1764	249		2	1827	266
	3	1963	259		3	1634	266
	4	1698	246		4	1700	264
	5	-	295*		5	-	306*

\* (test stopped at a compressive strain of 0.0070)

However, to validate the postulated failure mechanism, of major delaminations growing and sublaminates buckling, post-mortem cross sections (as indicated by A-A in Fig. 4a) were made of specimens 3 of each lay-up, all of which had failed in the same mode: buckling away from the support (opposite to the impact direction). Photographs of these sections are shown in Fig. 8 of the skin/doubler zone, in which the 0-degree plies are visible as the lighter layers. The failure loads of these specimens were 259/266J for Lay-ups 3 and 6, 229/230 J for Lay-ups 1 and 2, and 219/222 J for Lay-ups 4 and 5. Comparing this order of "damage tolerance" to the order concluded above on the basis of the impact induced delaminations, there is not much difference: Lay-up 3 was better than expected and changed positions with Lay-up 1, most likely because it is an almost symmetric laminate and remained straight up to higher loads. Lay-up 6, thought to be equivalent to Lay-up 1 because it has the same stacking sequence, while the added bond layers had not limited the size of the damage, was actually better than Lay-up 1. The superior residual strength of Lay-up 6 may be caused by a higher resistance against delamination spread or by the improved stability due to the added thickness of the bond layers.

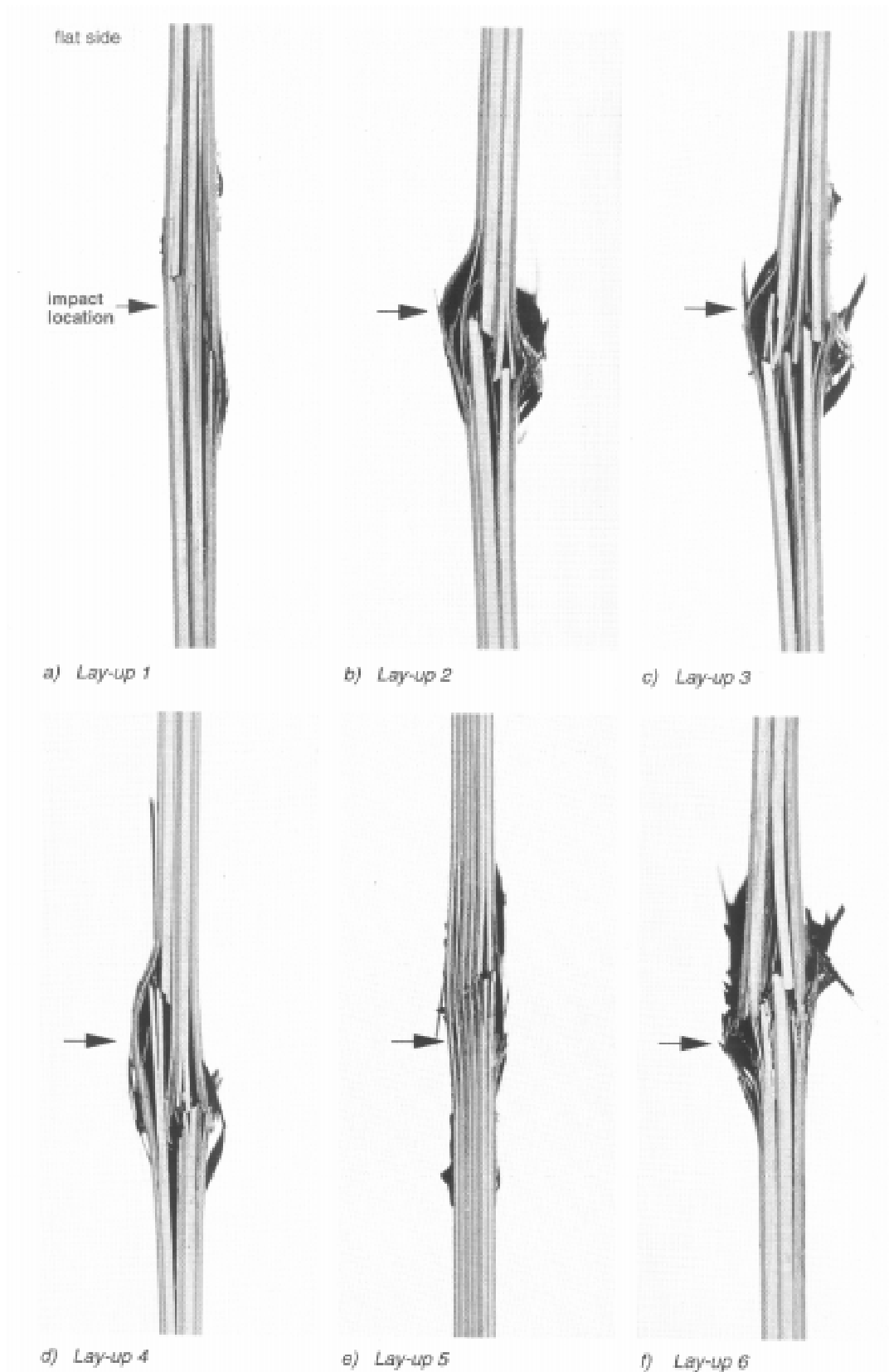


Fig 8: Post-mortem cross-sections of SR specimens '3' in figure 4A (A-A)

Based on the most-mortem results it is concluded that the postulated failure mechanism is correct in the sense that the major impact induced delaminations located behind the 0-degree doubler plies are the delaminations that grow, driven by the buckling or bending of these ply stacks.

However, the differences between the failure loads of the different lay-ups are smaller than expected, indicating that buckling of the delaminated sublaminates is not the only acting failure mechanism. From the photographs in Fig. 8 it is clear that ultimate failure occurs by transverse shear of the unsupported 0-degree ply stacks. This failure mechanism does not seem to depend much on the location of the 0-degree ply stacks, but rather on the amount of transverse shear deformation that occurred. Increasing the global stability of the laminate, by maintaining symmetry even in the doubler area (Lay-up 3) or by increasing the laminate thickness with bond layers (Lay-up 6) apparently resulted in a higher damage tolerance. The global stability of an impacted laminate is also increased by the presence of a stiffener. In fact, stiffened panels, made according to the same design as shown in Fig. 2, and tested in compression with similar impact damage [3], failed at much higher strains of 0.0062 and 0.0070 than the 0.0050-0.0055 observed for the damaged SR specimens. The failure modes of the panels were not even related to these damages, which illustrates the effect of the support of stiffeners in particular, and the damage tolerance of Boeing's design concept in general.

### **CONCLUDING REMARKS**

Impact damage and failure mechanisms were studied using small (unstiffened) structure relevant (SR) specimens. By varying the stacking sequence of the skin/doubler laminate it was tried to influence the location of the major impact induced delaminations within the laminate. It was believed that delaminations located deeper inside a laminate would lead to improved damage tolerance. Results for six different lay-ups were compared, and the major delaminations were found at the ply interfaces where they were expected. In some cases, additional "undesirable" delaminations were found also.

Subsequently, damaged and undamaged specimens for each lay-up were loaded in compression while supported in an anti-buckling frame; the damage reduced the residual strength as expected. For five of the six lay-ups the failure loads of the damaged specimens were very close. The failure loads for the damaged specimens of the sixth lay-up were 20% apart due to the occurrence of different failure modes. Specimens which were damaged by slow indentation showed similar damage and similar residual strength as impact damaged specimens. This may have important implications for design optimization procedures, as static responses are easier to compute than dynamic responses.

A postulated failure mechanism was confirmed to a certain extent, in the sense that the major impact induced delaminations were indeed the delaminations that propagated, driven by the bending or buckling of the doubler ply stacks. However, transverse shear of the increasingly unsupported 0-degree ply stacks became the ultimate failure mechanism. As a result of these observations, it will be undertaken to develop a failure criterion based upon the interaction of longitudinal compressive strain  $\epsilon_x$  and transverse shear strain  $\gamma_{xz}$  for 0-degree dominated ply stacks.

## **ACKNOWLEDGEMENTS**

The work on damage tolerance of composite structures described in this paper is part of a wider research programme carried out at NLR. This particular task was carried out for the Netherlands Agency for Aerospace Programs (NIVR).

## **REFERENCES**

1. Labonté, S. and Wiggenraad, J.F.M., "Development of a Structure Relevant Specimen for Damage Tolerance Studies", presented at the 9th International Conference on Composite Materials (ICCM-9), Madrid, Spain, 12-16 July 1993.
2. Labonté, S. and Wiggenraad, J.F.M., "A Damage Tolerance Study Conducted with Structure Relevant Specimens", NLR TP 93067 U, 1993.
3. Ubels, L.C. and Wiggenraad, J.F.M., "A Method to Apply Structure Relevant Impact Damage to Small Structure Relevant Specimens for Damage Tolerance Studies", presented at the 10th International Conference on Composite Materials (ICCM-10), Whistler, Canada, 14-18 August, 1995.
4. McCarty, J.E. and Roeseler, W.G., "Durability and Damage Tolerance of Large Composite Primary Aircraft Structure", NASA CR-003767, 1984.
5. Arendsen, P., Thuis, H.G.S.J. and Wiggenraad, J.F.M., "Optimization of Composite Stiffened Panels with Postbuckling Constraints", 4th CADCOMP, Southampton, UK, 1994.

# IMPACT DAMAGE GROWTH AND FAILURE OF CARBON-FIBRE REINFORCED PLASTIC SKIN-STRINGER PANELS

Emile Greenhalgh, Sunil Singh, Donald Roberts

*Structural Materials Centre, DRA, Farnborough, Hants, UK, GU14 6TD*

**SUMMARY:** This paper describes an investigation into low velocity impact damage in skin-stringer panels. The effect of panel geometry and impact site on the damage growth and compressive strength was investigated. Impact damage beneath a stringer was less detrimental to strength than damage in the bay. In five of the six panels, failure was precipitated by a combination of bay buckling and skin/stringer detachment, except in one panel where massive lateral delamination growth led to a large reduction in strength. For impact damage in a bay, a wide-bay/thick-skin design was the most damage tolerant whilst for impact damage beneath a stringer, a high buckling strain design was the most tolerant. The results suggest that, at current in-service strain levels, impact damage may be tolerated in some cases.

**KEYWORDS:** structures, impact, fractography, delamination, skin-stringer, buckling

## INTRODUCTION

The specific in-plane properties of carbon-fibre composites make them invaluable for use in aircraft structures. However, they are limited by their inherent susceptibility to impact and other out-of-plane loadings. In coupons a low velocity impact can reduce the compressive properties by up to 50% [1]. However, damage in coupons is more severe than that in structures since, in the latter, much of the incident energy is absorbed through elastic structural response [2]. Only through tests on structural elements (skin-stringer panels) can the damage processes and failure of impacted composite structures be understood.

There has only been limited work conducted on the effect of impact damage on skin-stringer panels. Madan showed that the greatest strength reduction was from bay impacts [3]. However, most studies have investigated 'softer' skinned panels; *i.e.* containing few 0° plies [4,5]. In these structures, impact over the stringers led to the greatest reductions in strength.

This paper describes the second part of an investigation into impact damage in skin-stringer panels. In the first part of the work panels of different geometries were impacted at 15J at various sites [2]. For impacts over the panel bay, the energy was mainly absorbed through the formation of delaminations and matrix cracking. However, as the impact site approached the stringer, or the bay aspect ratio increased, more energy was absorbed through elastic response, leading to less severe damage states. Generally, the damage distribution through the thickness was conical. In the bays, it was roughly circular in area whilst over the stringer feet it was elliptical, with the major axis parallel to the stringers. The damage from impact over the stringer centreline was negligible.

In this part of the investigation identical panels were impacted either over the bay or the stringer foot, and then tested to failure in quasi-static compression. The effect of panel geometry and impact location were addressed, and compared with results from similar panel tests with embedded defects [6].

## EXPERIMENTAL DETAILS

The stiffened carbon-fibre reinforced panels (Figure 1), each made up of a quasi-isotropic skin ( $[+45^\circ/-45^\circ/0^\circ/90^\circ]_{nS}$ ) and three I-section stringers, were manufactured. Seven panels, of three different geometries were studied. The first (Type 1) was designed to buckle at a compressive strain of  $6000\mu\epsilon$  whilst the second and third panels were designed to buckle at  $3700\mu\epsilon$ . In the second case (Type 2) this was achieved by increasing the stringer spacing and in the third case (Type 3) by decreasing the skin-thickness. One panel of each type was compressively tested with impact damage either in the bay or in the stringer foot regions. Further details of the manufacture and preparation of the panels are given elsewhere [2].

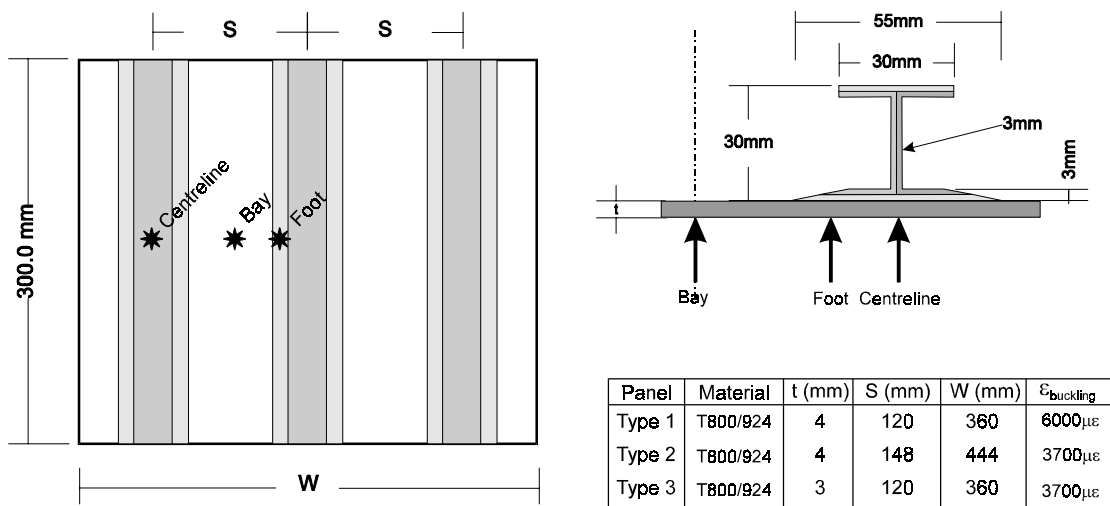


Figure 1: Geometries and impact sites in the skin-stringer panels

The panels were impacted using instrumented drop-weight equipment at an incident energy of 15J; all the impacts were applied to the skin on the outer (non-stringer) face. The panels were impacted at the mid-length, 150mm from the panel ends, either in the left bay, or over the tapered section of the central stringer foot. The seventh panel was subjected to a 30J impact at the mid-length over the centreline of the left-hand stringer foot. The panel was of the Type 1 design and had originally been used to study the effect of artificial defects on the performance of skin-stringer panels [6], but did not fail during testing.

After impacting, the dent depth and damage area (ultrasonic attenuation of 6dB or more compared with best material) were measured. The panels were then compressively tested at a rate of 0.005mm/s and the strains, displacements and loads recorded. Displacement transducers and Moiré interferometry were used to monitor out-of-plane deformations of the damaged regions and the stringer deflections. Following testing to failure, the panels were photographed, and examined to determine the damage growth and failure processes [7].



## EXPERIMENTAL RESULTS

When compared to the previous studies [2], the impact forces, deflections and damage areas were found to be repeatable, particularly for impacts over the stringer feet. For identical impacts, the damage was generally similar in shape and distribution through the thickness. However, for impacts over the bay, the damage areas differed by as much as 26%.

*Table 1: Results from the compressive tests on the skin-stringer panels*

Panel Type	Type 1			Type 2		Type 3	
Impact Location	Bay	Foot	Centreline	Bay	Foot	Bay	Foot
<b>Damage Area (mm<sup>2</sup>)</b>	2141	778	50	675	824	534	1071
<b>Buckling Strain (μϵ)</b>	-	-5803	-7100	-4400	-4500	-3530	-4600
<b>Failure Strain (μϵ)</b>	-3662	-5803	-7464	-4543	-4964	-3597	-4697
<b>Failure Load (kN)</b>	-529	-803	-995	-734	-840	-460	-554

The results of the compressive testing of the skin-stringer panels are shown in Table 1. In general, damage in the bay was more critical than damage beneath the stringer foot, particularly for the Type 1 panel. Impact damage beneath the stringer centreline had a negligible effect on the panel strength and did not initiate failure of the structure.

Figure 2 shows the typical damage development from an impact in the bay.

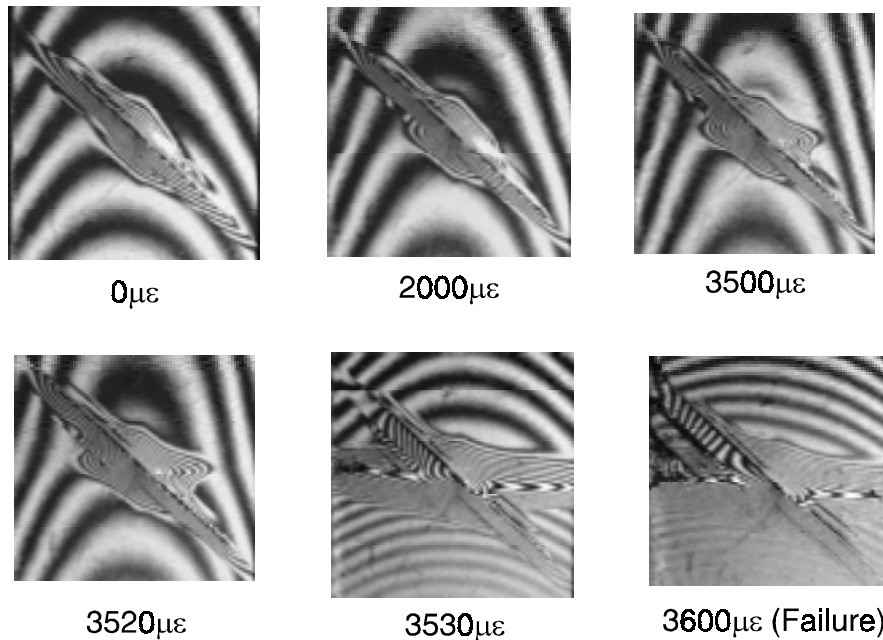


*Figure 2: Development of the damage in a Type 3 panel with a bay impact*

The image width is equivalent to the bay width and each Moiré fringe is equivalent to an out-of-plane deflection change of 0.2mm. The applied strain is shown below each image.

For the panels with impacts in the bay the early damage development was similar for all three types. Upon loading the impacted region formed a blister and the bay displaced outwards, away from the stringers. The blister was elliptical, with the major axis perpendicular to the applied load, and was highest in the Type 3 panel. However, the blister was smaller than the damage observed from the non-destructive analysis. The damage grew laterally in a stable manner from the impact site across the bay width. In the panels with 120mm bay widths, at an applied strain of about  $-3500\mu\epsilon$  the growth became more rapid, extending towards and beneath the stringers. However, in the panel with a 148mm wide bay, the damage growth was limited, and the damage front did not reach the stringers before panel buckling.

The Type 1 panel failed at a strain well below the design strain ( $-3662\mu\epsilon$ ). The Type 2 and 3 panels failed at and beyond buckling, at strains of  $-4543\mu\epsilon$  and  $-3597\mu\epsilon$  respectively. The Type 2 panel exhibited significant post-buckling performance and the buckling strain was only slightly depressed. However, the Type 3 panel exhibited a significant fall in buckling strain, and failed during panel buckling.

The performance of the panels containing impact damage beneath the stringer foot were very different to those containing damage in the bays. As the load was applied the damaged region started to displace outwards, with the largest displacement in the bay adjacent to the impact site. There was little damage growth observed although there was some lifting of the stringer foot from the skin. The Type 1 panel failed as it buckled at a strain of  $-5803\mu\epsilon$  whilst the Type 2 and 3 panels both buckled at values greater than their design strains. The Type 3 panel failed soon after buckling ( $-4697\mu\epsilon$ ) and the Type 2 panel had significant post-buckling performance, failing at a strain of  $-4964\mu\epsilon$ .

Failure analysis (fractography) showed that five out of the six panels which had failed due to impact damage, had failed in a similar manner. After the initial growth stages, the combination of damage beneath the stringer foot and bay buckling precipitated detachment of the stringer from the skin. This led to skin crippling and catastrophic panel failure. In the Type 1 panel with damage in the bay, massive unstable delamination spread across the panel width, leading to catastrophic failure of the skin.

## **DISCUSSION**

### **Damage Growth and Failure Mechanisms**

Before discussing the effect of various parameters, the mechanisms for damage growth and structural failure should be considered. The overriding factor in controlling these mechanisms was the location of the impact site; the failure processes of the panels with impact damage in the bay was very different to that of the panels with damage beneath the stringer feet. An impact over the stringer centreline had a negligible effect on the panel failure.

The failure processes for a panel containing impact damage in the bay is shown in Figure 3. As the load was introduced the impacted bay deflected outwards, away from the stringer face (Figure 3a). The damaged region also started to deflect, but inwards, towards the stringer face (Figure 3b) and the damage started to grow from the impact site (Figure 3c). The damage growth was predominantly transverse, growing towards the stringers. Initially the growth was stable, but there reached a point where it became unstable and rapidly spreading across the bay and beneath the stringers.

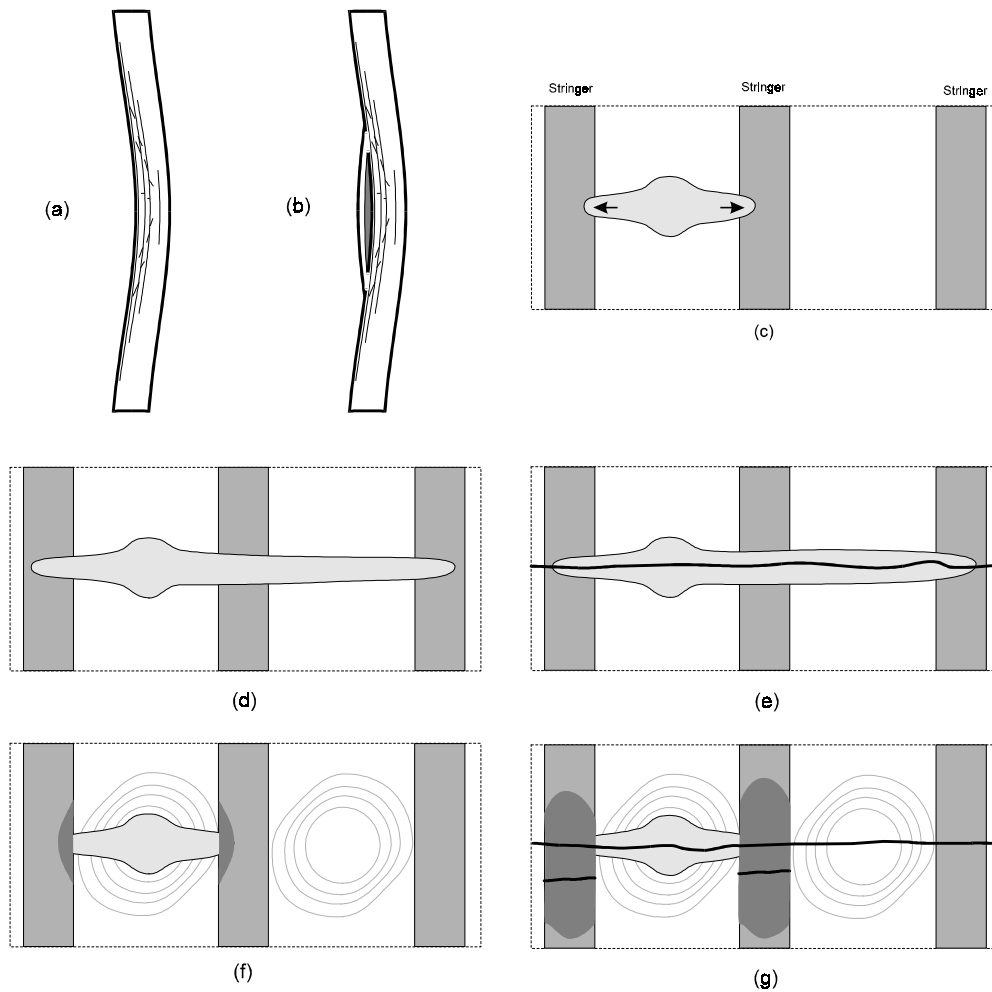


Figure 3: Failure mechanisms for panels with an impacted bay

The later stages of damage growth were dependant on the panel type. In the panel designed to the higher buckling strain (Type 1) the damage continued to spread across the panel width (Figure 3d), rapidly developing into the undamaged bay and beneath all the stringers. Once the damage had spread over 80% of the panel width, compressive failure of the remaining skin initiated in the impacted bay and spread across the entire panel width (Figure 3e).

In the panels designed to the lower buckling strain (Types 2 and 3), the failure mechanism was different. As the damage grew towards the stringers, the bays started to buckle. As in the panels containing single plane defects in the bay [6] the presence of the damage reduced the panel buckling strain. As the bays buckled, opening forces were promoted beneath the stringers, leading to local detachment of the stringers from the skin (Figure 3f). This loss of local support led to skin instability (cripling) and compressive failure (initiating at the impact site), and finally the stringers detached and failed in flexure (Figure 3g).

All three panels which were impacted over the stringer foot failed by the same damage process (Figure 4). Although the early stages of damage growth were different to those observed in the panels containing impacts in the bay, the later stages of growth and failure were similar to those observed in the Type 2 and 3 panels. Firstly, as the load was introduced, the bay adjacent to the impacted stringer started to deflect outwards (Figure 4a), eventually

leading to lifting of the stringer foot. There was no transverse damage growth, but damage spread longitudinally, along the stringer foot (Figure 4b). The rate of damage growth was much less than that observed in the panels containing damage in the bay, leading to higher strains to failure. Eventually, the panels buckled which promoted partial stringer detachment (Figure 4c). As with the impacts in the bay, this led to skin crippling, compressive failure (initiating from the impact site) and failure of the central stringer (Figure 4d).

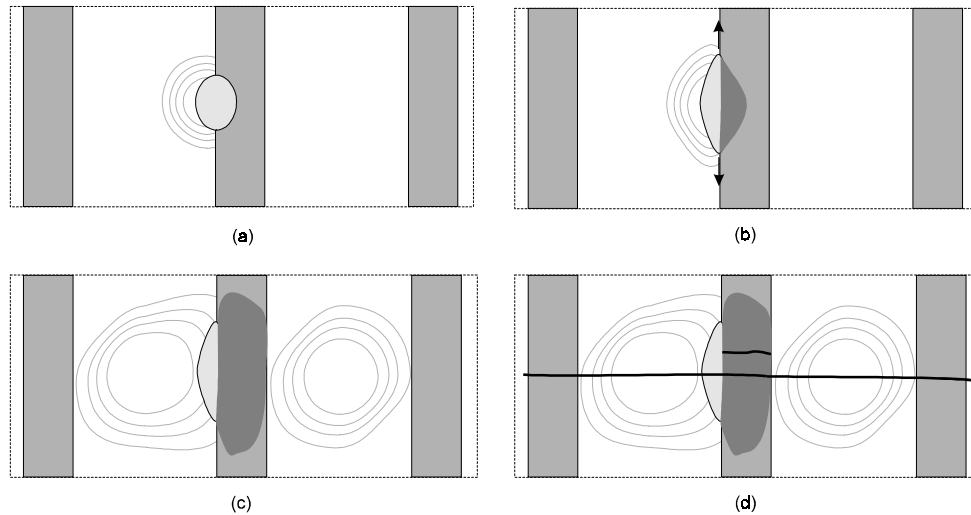


Figure 4: Failure mechanism for panels with an impacted stringer foot

The failure of the panel containing the impact damage on the stringer centreline was not attributed to the impact damage. The failure initiated as massive lateral delamination growth across most of the panel width, initiating from the artificial defect. This was followed by stringer detachment and compressive failure of the skin.

### Effect of Impact Location

As shown in Figure 5, the impact location had the largest effect on the panel performance.

Firstly, consider the Type 1 design of which there were three panels tested. Since the failure of the panel containing the damage beneath the stringer centreline was not due to the impact, this can be treated as a lower bound on the undamaged strength of this design. Considering this, a 15J impact over the stringer foot led to a 12% drop in strength whilst a similar impact in the bay led to a 51% drop in strength, the latter representing a significant drop in strength.

For the other two panel types the undamaged strengths were not known. However, there was less reduction in strength between the stringer feet and bay impacts (9% and 23% for the Type 2 and 3 panels respectively) than was observed in the Type 1 panel (37%). The reduction in the Type 3 panels was attributed to the bay damage reducing the buckling strain which promoted stringer detachment. In the Type 2 panels, the failure mechanisms due to damage in the bay and stringer foot were very similar, leading to the negligible drop in strength.

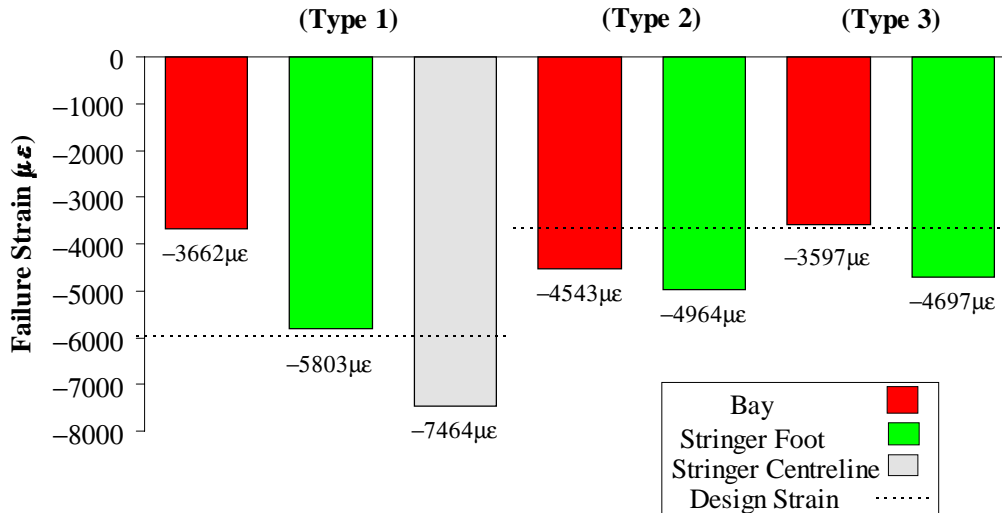


Figure 5: Failure strains for skin-stringer panels containing impact damage

### Effect of Panel Geometry

For impact to the bay, there was a clear effect of panel type on the failure process. The Type 1 panel did not buckle and failed due to massive delamination growth. The Type 2 panel exhibited little damage growth and failed by a combination of bay buckling and stringer detachment. In the Type 3 panel, the failure was attributed to stringer detachment which was promoted by the reduced buckling performance of the damaged bay. The higher failure strain in the Type 2 panel was due to the slower development of the damage. This was attributed to the impact damage being distant from the stringer feet and the out-of-plane deflection of the damaged region being less than that in the other panel types. This subsequently led to two factors which improved the damage tolerance for this design. Firstly, the reduced growth led to the damage having less of an influence on buckling. Secondly, the damage had less effect on the stringers, not promoting stringer detachment to the same extent in the Type 3 design.

For the damage beneath the stringer feet, there was less effect of panel geometry. Firstly, the damage had little effect on buckling, therefore not promoting failure to the same extent as from bay damage. The largest effect of geometry was observed in the Type 3 panels, again due to the sensitivity of this design to stringer debonding.

### Comparison with Embedded Defects

In earlier work [6], Type 1 panels containing Teflon discs between the plies were tested. These defects were located at either of two different ply interfaces and were either in the bay or beneath the stringer foot. The results were compared to the current work to gauge the validity of modelling impact as single plane defects. There were some similarities between the growth processes for the two types of damage. In both instances the damaged bay firstly deflected outwards and the initial growth was transverse to the loading direction, leading to the damage extending towards the stringer feet. However, at a given applied strain, the height and width of the impact damage were much less than those of the artificial damage. This was attributed to the impact damage consisting of small, deep defects which could not deflect outward to the same extent that the relatively large, shallow single-plane defects could.

As the damage front approached the stringer feet, the growth processes were accelerated. In the panel containing impact damage in the bay this led to catastrophic compressive failure. However, in the panels containing artificial defects, the growth promoted stringer detachment only after panel buckling. For similar damage areas, the impacted panel had 60% of the strength of the panel containing an artificial defect. In the panels containing artificial defects, the growth was dominated by blistering of the surface plies and was subsequently dominated by stable mode I growth [8,9]. In the impacted panel the damage was mainly deeper and mode II dominated, so stable damage growth was limited. Furthermore, the local bending of the damaged region subsequently led to unstable mode II growth from the impact site. When the damage was beneath the stringers, the out-of-plane constraint on the skin inhibited mode I dominated growth, as from the artificial damage, but would have had little effect on mode II dominated growth, as from the impact damage. For both impact damage and artificial defects beneath the stringer, the strength reduction was less than that from those in the bay.

### **IMPLICATIONS IN-SERVICE AND FOR DESIGN**

The current results allow some prediction of the severity of the damage and suggest that in many cases an impact over the stringer can be tolerated. Furthermore, damage beneath the stringer had little effect on panel buckling and only for designs sensitive to skin/stringer debonding did damage beneath the stringer become significant. When impact damage was present in the bays, rapid unstable growth, sometimes leading directly to failure, occurred at strains above  $-3500\mu\epsilon$  (below most aircraft limit loads).

Based on studies from material testing, the current philosophy is to gauge the severity of an impact by the damage area; the larger the damage area, the lower the failure strain, and this relationship did hold for stringer foot impacts. However, for impacts to the bay, large damage areas did not necessarily correspond to low failure strains since the panel geometry had a significant effect on the failure processes.

Understanding of the damage growth and failure processes can be utilised to produce impact tolerance in new structural designs. The driving force for impact damage growth was a combination of mode II forces generated by bending of the damaged region, and mode I forces from the blistering of the surface plies. However, unlike embedded defects, relatively little stable damage growth was observed prior to panel buckling. The wide-bay/thick-skin design exhibited the slowest damage development before failure and consequently had the highest strength.

A measure with which to rank the damage tolerance is the load intensity/unit areal weight [6] as shown in Figure 6.

All these panel designs were less tolerant of damage within the bay than beneath the stringer foot, particularly for the high buckling strain structures (Type 1). Impacts over the stringer foot did not pose a significant threat whilst those over the stringer centreline had no observed effect on strength. It should be noted that all these designs had relatively 'hard' skins; a significant proportion of the load was carried by the skin. In 'soft' skin designs (most of the load is carried by the stringers) impact damage beneath the stringers may be more critical.

For the low buckling strain designs, the wide-bay/thick-skin approach (Type 2) was clearly the more damage tolerant, particularly for impacts to the bay. Comparing all three panel types,

for bay impacts this design (Type 2) also out-performed the high strain buckling design (Type 1). However, for stringer foot impacts, where the panel buckling precipitated failure in all panel types, the high buckling strain design was the most damage tolerant.

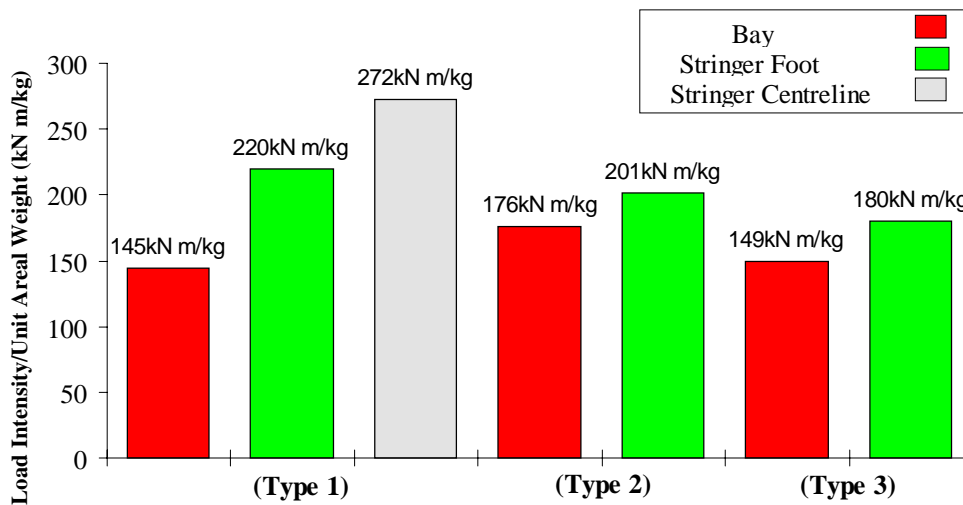


Figure 6: Load intensity/unit areal weight for skin-stringer panels

### CONCLUSIONS

The following conclusions have been drawn from investigations of the damage, growth and structural failure in damaged skin-stringer panels under compressive loading:

1. Generally, the forces, displacements and damage areas were reproducible, except that the damage areas from impacts over the bay which exhibited a large degree of scatter.
2. There was no direct relationship between impact damage area and failure strain.
3. In panels containing impact damage in the bays, the damage firstly spread laterally towards the stringers, which in some cases significantly reduced the panel buckling strain. During buckling, this led to stringer detachment, skin crippling and catastrophic failure. In the high buckling strain design, massive unstable delamination growth occurred, promoting failure.
4. In panels containing impact damage beneath the stringer foot, the local substructure constrained and limited damage growth. Failure eventually occurred when the panel buckled; the combination of the out-of-plane deflection of the bay and the presence of damage beneath the stringer led to stringer detachment and catastrophic failure.
5. Panels containing impact damage in the bay exhibited a strength reduction of up to 37% with respect to panels containing impact damage beneath the stringer foot. Impact damage directly beneath the stringer centreline had a negligible effect on panel strength.
6. For the low buckling strain designs, a wide-bay/thick-skin was the most damage tolerant. Of all the panels tested, this design was the most tolerant to impacts in the bay whilst the high buckling strain design was the most tolerant of impact damage beneath the stringer foot.
7. Panels containing single plane embedded delaminations were 60% stronger than panels containing impact damage of the same dimensions.
8. At current in-service strain levels, impact damage may be tolerated in some cases. Certainly for low buckling strain designs, there was no significant reduction in strength. At current design strains for primary structures, damage may be tolerated in many cases.



## ACKNOWLEDGEMENTS

The authors acknowledge the support of DTI CARAD and the MOD Corporate Research Programme.

The contributions of Mr S Lahiff, for designing the panels, Mrs A Dewar for panel manufacture, Miss S Minshull and Mr R Thompson for assistance in panel testing and Non-Destructive Evaluation Section are also acknowledged. Dr Sarah Bishop (MoD), Mr R Sharp (BAe) and Prof G Davies (Imperial College) are also acknowledged for their general advice.

## REFERENCES

1. Gadke M. *et al.*, "GARTEUR Damage Mechanics for Composite Materials; Analytical/Experimental Research on Delaminations", Proceedings of the 74th AGARD Structures and Materials Panel, Patras, Greece, 1992
2. Greenhalgh, E.S., Bishop, S.M., Bray, D., Hughes, D., Lahiff, S. and Millson, B., "Characterisation of Impact Damage in Skin-Stringer Composite Structures", Composite Structures, To be Published, 1997.
3. Madan, R., "Influence of Low Velocity Impact on Composite Structures". In "Composite Materials; Fatigue and Fracture", Edited by K O'Brien, ASTM STP 1110, 1991.
4. Avery, J., Allen, M., Sawdy, D. and Avery, S., "Survivability Characteristics of Composite Compression Structure". Proceedings of the 8th DOD/NASA/FAA Conference, "Fibrous Composites in Structural Design", Edited by Lenoe *et al*, Part 2, 1989.
5. Ishikawa, T., Matsushima, M., Hayashi, Y. and Noguchi, T. "Compression After Impact Properties of CF/PEEK(APC2) and Conventional CF/EPOXY Composite Structures", Proceedings of the 8th International Conference on Composite Materials, Honolulu, Hawaii, 1991, pp28S1-28S10.
6. Wiggendaad, J., Aoki, R., Gadke, M., Greenhalgh, E., Hachenberg, D., Wolf, K. And Bubl, R., "Damage Propagation in Composite Structural Elements - Analysis and Experiments on Structures", Composite Structures, To be Published, 1997.
7. Greenhalgh, E. and Cox, P., "A Method to Determine Propagation Direction of Compressive Fracture in Carbon-Fibre Composites", Composite Structures, Vol 21, 1992, pp1-7.
8. Greenhalgh, E., "Characterisation of Mixed-Mode Delamination Growth in Carbon-Fibre Composites", PhD Thesis, Imperial College of Science, Technology and Medicine, London (to be published), 1997.
9. Singh, S. and Greenhalgh, E., "Micromechanisms of Interlaminar Fracture in Carbon-Fibre Composites at Multidirectional Ply Interfaces", Proceedings of the 4th International Conference on Deformation and Fracture of Composites, Manchester, UK, 24-26 March 1997.



# **SIMULATION OF IMPACT DEFORMATION, DAMAGE & FRACTURE IN COMPOSITE LAMINATES**

**Da-Zhi Jiang<sup>1</sup>, Wei Shen<sup>2</sup> and Xing-Ye Wang<sup>1</sup>**

<sup>1</sup> *Department of Material Engineering & Applied Chemistry, National University of Defense Technology, Changsha, Hunan, 410073, P.R. China*

<sup>2</sup> *Department of Mechanics, Huazhong University of Science and Technology, Wuhan, Hubei, 430074, P. R. China*

**SUMMARY:** Numerical analyses to study the characteristics of deformation, damage and fracture for orthotropic composite laminates impacted by a projectile were reported in this paper. According to continuum damage mechanics, a damage constitutive equation in incremental form was derived. The stress and strain distributions of the target were obtained at each increment ( $\Delta t$ ) by solving the central differential equations. The stiffness degradation of materials reflects the meso-damage which included in constitutive equations. Macro-damage includes matrix cracking, interlaminar delamination and fiber breaking, which were simulated by nodal division. Eight-node and six-node iso-parameter elements were used to delimit the elements of the projectile and target, respectively. The characteristics of the deformation, contact force, damage and failure of glass fiber reinforced epoxy matrix (GFRP) laminates under spherical steel projectile impact were consistent well with experimental data or references.

**KEYWORDS:** impact damage, finite element method, composite laminates

## **INTRODUCTION**

Fiber reinforced composite laminates are widely used in the aerospace, ship, automobile industries and military armor systems, etc. This class of materials exhibits many superior properties including high specific strength and stiffness, good formability, corrosion resistance. However, one well known problem of the fiber composite materials is their susceptibility to damage which may lead to premature structural failure under either low or high velocity impact<sup>[1]</sup>. Impact can produce extensive internal damage, including matrix cracking, delamination and fiber breakage. Their combination constitutes a complex damage pattern and failure process.

Impact damage is influenced by many factors including: (i) projectile (shape, mass, stiffness and its velocity before impact); (ii) target (ply moduli, stacking sequence, ply orientation, conventional strength and fracture toughness); (iii) behavior of fiber/matrix interface, and (iv) damage behavior (damage threshold, damage-strain relation) etc.

There is a great need to analyze, understand and quantitatively characterize the complex impact damage mechanisms and damage-failure process of composite laminated structures under projectile impact.

A theoretical analysis and 3-dimensional numerical simulation for damage-failure process of anisotropic composite laminates subject to projectile impact were carried out and reported in this paper.

## NUMERICAL SIMULATION OF IMPACT PROCESS

### Theoretical Analysis

The theoretical assumption made in this work include: impact process was considered to be a combination of both kinematics contact of the projectile-target system and target's material damage that is dependent on both time and space; material damage was divided into both micro-damage and macro-damage; the physical equation is based on anisotropic damage constitutive relation which reflects material micro-damage, and the large displacement in the impact process is characterized by using the updated Lagrangian description; the collision contact process of projectile-target system satisfies momentum conservation; the initiation and propagation of macro-damage may be treated by the nodal division technique of FEM; the contact surface between projectile and target is modelled by kinematics constraint.

#### *Damage Constitutive Relations*

The stress-strain relationships of damaged element, both the material and the damage are considered to be anisotropic can be expressed as follows:

$$\sigma_{ij} = \tilde{E}_{ijmn} \varepsilon_{mn} \quad (1)$$

where  $\tilde{E}$  is the effective elastic moduli tensor that is dependent of the damage.  $\sigma$  is the Cauchy stress tensor and  $\underline{\varepsilon}$  is the Green strain tensor.

Damage variable is assumed to be a 2-order tensor form and called the continuity tensor  $\underline{\psi}$  which reflects micro-scope damage of material, and it can be expressed in terms of a strain tensor  $\underline{\varepsilon}$  as:

$$\tilde{\varepsilon}_{ij} = \frac{1}{2} (\psi_{im} \delta_{nj} + \psi_{nj} \delta_{im}) \varepsilon_{mn} \quad (2)$$

where  $\delta$  is Kronecker tensor, and  $\tilde{\varepsilon}$  and  $\underline{\varepsilon}$  are effective strain tensor and true strain tensor

respectively.

Based on the conjugate relation, the damage growth force  $\underline{R}$  which is also a 2-order tensor is

$$R_{ij} = \frac{\partial \Phi}{\partial \psi_{ij}} \quad (3)$$

where  $\Phi$  is the Helmholtz free energy density function with internal state variable  $\underline{\psi}$ .

It is assumed that the damage evolution equation, where the continuity rate relates to the strain rate has usually the following form:

$$\dot{\psi}_{ij} = -\lambda_{ijmn} \dot{\varepsilon}_{mn} \quad (4)$$

where  $\underline{\lambda}$  is a 4-order tensor, and called as damage evolution coefficient.

The incremental form of elastic-brittle damage constitutive relation can be then derived as follows:

$$d\sigma_{ij} = E_{ijmn}^T d\varepsilon_{mn} \quad (5)$$

in which

$$E_{ijmn}^T = \tilde{E}_{ijmn} - K_{ijkl} \lambda_{klmn} \quad (6)$$

where  $\tilde{E}$  is the effective moduli tensor of material element, and

$$K_{ijmn} = \frac{\partial R_{ij}}{\partial \varepsilon_{mn}} \quad (7)$$

The constitutive relation for a finite element of the target has been performed with update Lagrangian description where the coordinate frame may be taken to trace the displacement of large deformation problems. If large deformation was taken into account, the above Eqn 5 should be changed as

$$dS_{ij} = E_{ijmn}^* d\varepsilon_{mn} \quad (8)$$

where  $dS$  is the increment of second Piola-Kirchhoff stress tensor, and  $\underline{E}^*$ , the tangential moduli tensor of the finite element, that has considered both the material damage and the structural large deformation, can be expressed by <sup>[2]</sup>

$$E_{ijmn}^* = \frac{\rho'}{\rho^{t+dt}} B_{ik} B_{jl} E_{klmn}^T \quad (9)$$

where  $\rho^t$  and  $\rho^{t+dt}$  are the material density at moments  $t$  and  $t+dt$  respectively, and  $\underline{B}$  is the tensor components transferring the Cauchy stress  $\underline{\sigma}$  into the second Piola-Kirchhoff stress  $\underline{S}$ , i.e.

$$B_{ij} = (\delta_{ij} - du_{i,j})^{-1} \quad (10)$$

### *Equilibrium Equation in Motion*

Based on the virtual work principle, the increment of equilibrium equation in motion which is the governing equation for a finite element can be written by

$$\int_{V^t} S_{ij}^{t+dt} \delta \varepsilon_{ij}^{t+dt} dV = F_k^t \delta (u^e)_k^{t+dt} - \int_{V^t} \rho^{t+dt} \ddot{u}_k \delta u_k^{t+dt} dV \quad (11)$$

where,  $\delta \underline{u}$  and  $\delta \underline{\varepsilon}$  are the variation of displacement and strain, respectively;  $\ddot{\underline{u}}$  is the acceleration vector;  $\underline{F}$  and  $\delta \underline{u}^e$  are the nodal force and the variation of nodal displacement, respectively. The integral is over the volume  $V$  of element at moment  $t$ .

### *Initial and Boundary Conditions*

The target is fixed along its edges and initially at rest. It is taken that the initial velocity  $\underline{v} = \underline{v}_0$  for projectile at moment  $t=0$  when it starts to contact with the target.

### *Kinematics Contact-Surface Treatment*

The contact particle system can be considered to consist of nodes which include the projectile slave nodes and the corresponding nodes of master element of target which directly collide with the slave node and which were included in the 'influence area'<sup>[2]</sup>.

In the collision process, the total momentum of contact particle system is conserved step by step, i.e.

$$\sum (M^m \underline{v}^m + M^s \underline{v}^s)_{t+dt} - \sum (M^m \underline{v}^m + M^s \underline{v}^s)_t = \sum F_k^t dt \quad (12)$$

where  $\underline{M}$  and  $\underline{v}$  are the mass and the velocity, respectively.  $\underline{F}$  is the reacting force of constraint induced from out of the contact particle system. (m) and (s) express belonging to the master element of target or to slave node of projectile.

### *Failure Criterion and Nodal Division*

The failure criterion based on maximum strain component is used to predict matrix cracking, fiber breakage and delamination. The critical conditions in the formation of damage can be defined as: matrix cracking when one (normal or shear) strain component reaches the failure threshold of matrix material; fiber fracture when one normal strain component along fiber-

direction reaches the longitudinal tensile failure strain of unidirectional lamina, and delamination cracking when any component of interlaminar strain reaches the failure threshold of the matrix material.

The criteria presented can be used to describe initiation and propagation of cracks combining with the modified technique of nodal division in FEM. For a given node, when a component of strain related to  $x_i$ -direction reaches its critical value, the node may be divided into two nodes along the  $x_i$ -direction and forms a new crack surface on which the traction is free. In this case, set the relative components of stress to zero for two nodes divided, i.e.

$$\sigma_{ij} = 0 \quad (j = 1,2,3) \quad (13)$$

and the strain components will be determined by Eqn 8.

#### *Solution for the Governing Equations*

The equilibrium equation (11) in motion can be written in terms of finite element terminology as

$$[M]\{d\ddot{u}^e\} = \{F^t\} - [M]\{\ddot{u}^e\} - \int_{V'} [B]\{\underline{\sigma}^t\}dV - [K]\{du^e\} \quad (14)$$

where  $[M]$  and  $[K]$  are the mass and the stiffness matrices of element given, respectively.  $\{F\}$  is the nodal force for the element,  $[B]$  is the strain matrix,  $\underline{\sigma}$  is the Cauchy stress tensor in Voigt's notation. In order to solve the finite element equations, the central difference method is employed<sup>[2]</sup>.

#### *Measurement Principle for Impact Damage Variable*

The damage variable (continuity) is often defined by the effective elastic moduli of the damaged material from the continuum damage mechanics. Besides, according to the anisotropic elastic wave theory, the transmitting speed of elastic wave is only dependent of the material properties including both mass density and elastic modulus. Therefore, the damage and its variance can be estimated if the variations in wave speed have been measured by using the strain response in a given element of the target<sup>[3]</sup>.

#### **Numerical Simulation**

A three-dimensional computer simulation method and its corresponding software<sup>[2]</sup> was developed to quantitatively characterize complex damage mechanisms and damage-failure process of composite laminates under impact.

In order to verify the method developed by authors, it was applied on a reference [4]. The contact force history obtained by our method (shown in Fig. 1) was consistent well with the experimental data listed in the reference<sup>[4]</sup>.

A true impact process was simulated. The target was made of GFRP laminated structure with  $126.0 \times 126.0 \times 2.0$  (in mm), and the spherical projectile was made of steel, with 14.5 mm in diameter. The target plate fixed along the edges is a undamaged laminate before impact. Each ply is a unidirectional composite which can be modeled as an orthotropic elastic continuum with axis of symmetry about the fiber orientation. Perfect bonding is assumed between plies. The spherical projectile that is isotropic elastic solid with given motion velocity ( $v_0=49.16\text{m/s}$ ) collides at the top surface of the target which is considered to be initially at rest. The elastic properties of the target and projectile are listed in Table 1.

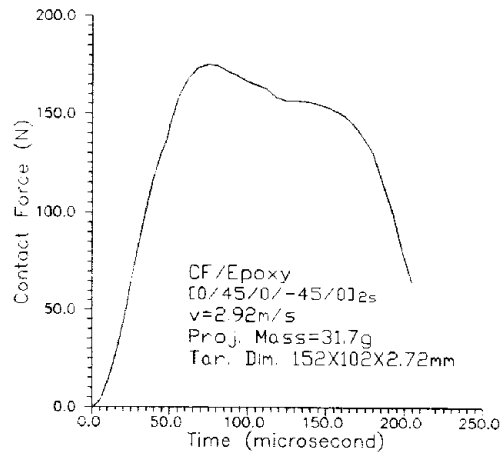


Fig 1: Contact force-time history

Table 1 : The elastic properties of the target and projectile

	Longitudinal Young's Modulus (GPa)	Transverse Young's Modulus (GPa)	In-plane Shear Modulus (GPa)	Main Poisson's Ratio	Mass Density (Kg/m <sup>3</sup> )
Target	18.6	9.0	3.6	0.22	1,700.0
Projectile	210.0	210.0	84.0	0.25	7,800.0

The damage and failure parameters in strains of the GFRP target are listed in Table 2.

Table 2: The damage and failure parameters in strains of GFRP

damage	damage threshold $\epsilon^{th}$		damage envolu -tion coefficient $\lambda$	
	tension	compression	$\lambda=f(\epsilon - \epsilon^{th})$	
	$2.4 \times 10^{-3}$	$-1.2 \times 10^{-3}$		
failure	unidirectional laminate		epoxy matrix	
	tension	compression	tension	compression
	$27.5 \times 10^{-3}$	$-15.8 \times 10^{-3}$	$20.6 \times 10^{-3}$	$-20.6 \times 10^{-3}$

Some important results and conclusions have been obtained from this computer simulation:

*Contact Force*

The contact forces for undamaged and damaged target of GFRP [0/90]<sub>2s</sub> laminated structure

are shown in Fig.2(a) and Fig.2(b), respectively.

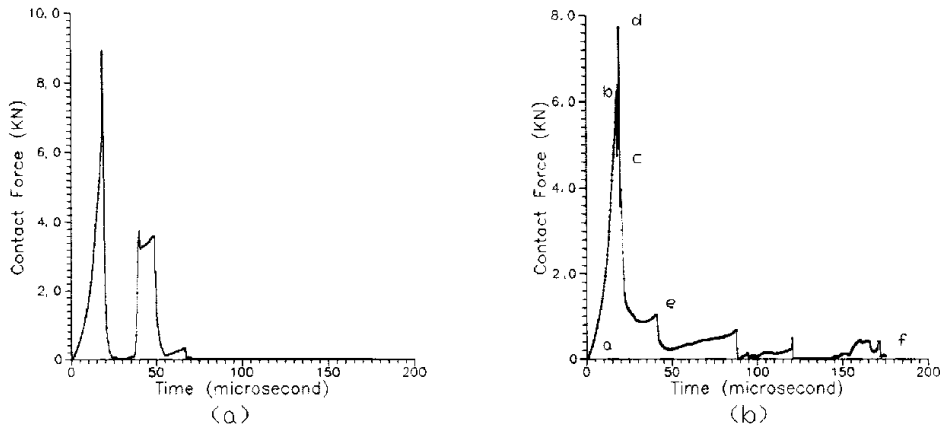


Fig.2: Contact force-time history of  $[0/90]_{2s}$  GFRP laminate impacted by spherical steel projectile with  $v_0=49.16\text{m/s}$ . (a)- undamaged laminate. (b)- damaged laminate

It was found from Fig.2(a) that there was a second contact loading curve for the undamaged target, this phenomenon was consistent with elastic wave theory, but the phenomenon disappeared for damaged target (Fig.2(b)). In Fig.2(b), a local unloading curve (b-c segment) which reflects delaminated failure mode was shown. d-e and e-f segments indicated that the resistance of projectile moving through the target. The areas of the curve of d-e-f segments with the horizontal axis in Fig.2(b) were equate to the dissipated energy of damage.

For the same contact conditions, the contact force history and contact force via displacement for  $[0/45/90/-45]_s$  laminated target were shown in Fig.3. We defined the ratio of  $U_e$  and  $U_d$  in Fig.3 as impact toughness (IT), it is expressed as:

$$IT = \frac{U_d}{U_e} \tag{15}$$

The impact toughness for  $[0/90]_{2s}$  and  $[0/45/90/-45]_s$  laminates was listed in Table 3. It was found that the IT was larger for  $[0/45/90/-45]_s$  than  $[0/90]_{2s}$ . That is to say the  $[0/45/90/-45]_s$  laminates have a better ability to resist the damage than that the  $[0/90]_{2s}$  laminates. These results are consistent with experimental data<sup>[2]</sup>.

Table 3: Impact toughness of  $[0/90]_{2s}$  and  $[0/45/90/-45]_s$  laminates

	$U_e$ (J)	$U_d$ (J)	IT
$[0/90]_{2s}$	1.26	4.16	3.30
$[0/45/90/-45]_s$	0.64	5.44	8.50

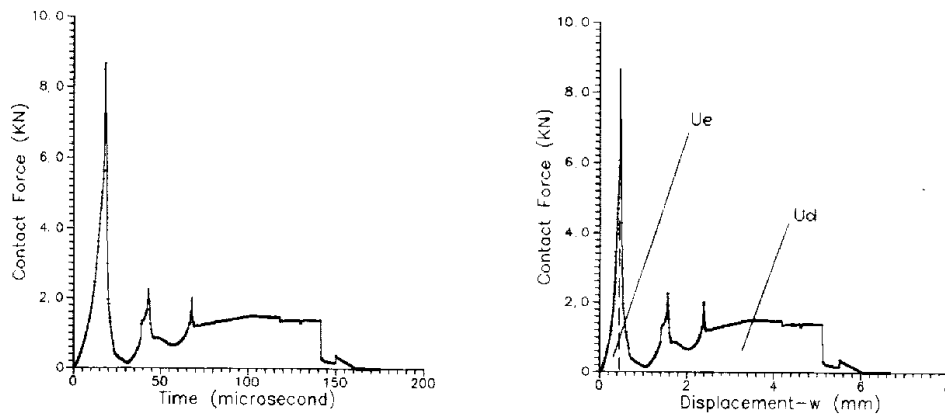


Fig.3: Contact force history of  $[0/45/90/-45]_2$  GFRP laminate impacted by spherical steel projectile with  $v_0=49.16\text{m/s}$ .

#### *Damage and Failure Process*

The degree of damage was obtained in every element of target from Eqn 2, then an iso-damage degree line in whole target was treated and shown in Fig.4. A nodal will be divided when any strain (or damage degree) components of the nodal reaches the criteria value, and marked with different symbol which represented different failure modes (including matrix cracking, delaminating and fiber breaking). The Failure modes and its distributions are shown in Fig.5. The areas of delamination in Fig.5 are consistent with the experimental results<sup>[2]</sup>.

#### *Deformation of the Target*

The through thickness deformation processes of the  $[0/90]_{2s}$  laminated target (in plane of  $x=63.0\text{mm}$ ) are shown in Fig.6.

## CONCLUSIONS

The projectile-target contact algorithm which consists of the basic equations and FEM were reviewed in this paper. The entire process of damage-failure which consists of three major macro-damage mechanisms, was successively simulated by using the modified method of node-division based on the failure criterion of maximum strain component. A map of collision contact force history has reflected the impact damage characteristics from some parameters, such as the energy dissipation and impact toughness etc. The damage variable field history was quantitatively estimated, and some mechanical and material parameter (such as strain, stress, strain, wave speed, etc.) field history can also be obtained from this simulating methods.



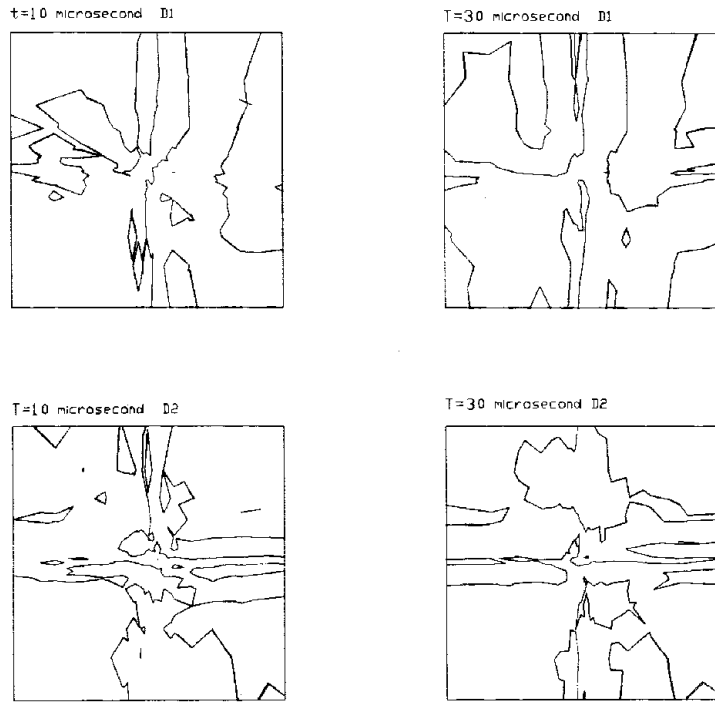


Fig.4 Iso-damage line of  $[0/90]_{2s}$  laminate  
 $D = \delta - \psi$ , and  $D_1$  and  $D_2$  equate to 0.50 and 0.75, respectively

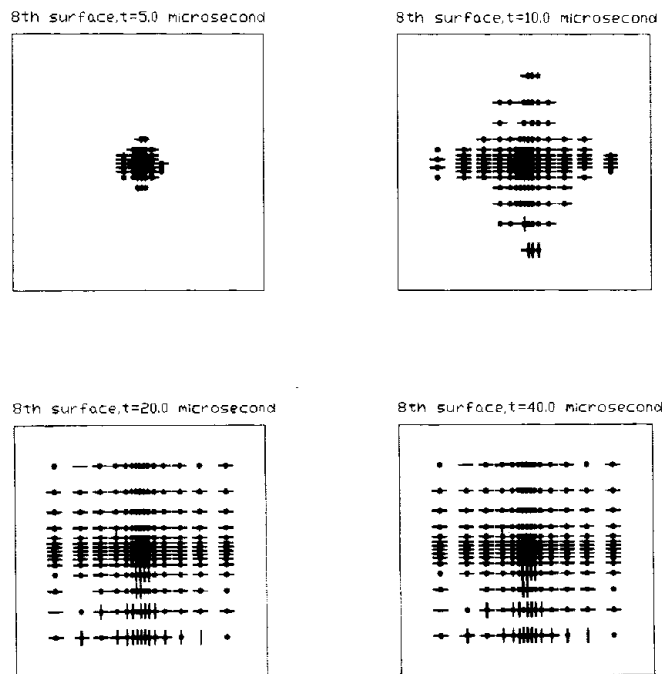


Fig.5 The Failure modes and its distribution in  $[0/90]_{2s}$  laminate  
 • – delamination, – – transverse matrix cracking, | – longitudinal matrix (or fiber) breaking

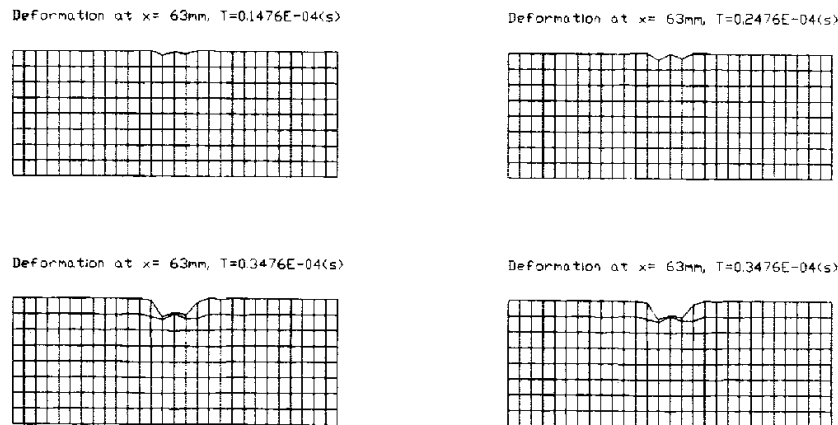


Fig.6 The deformation processes of  $[0/90]_{2s}$  laminated target in  $x=63.0\text{mm}$  cross section plane

### ACKNOWLEDGMENTS

This project was financial supported by the Natural Science Foundation of China through the grant 19372018. We would like to thank Prof. Y.-M. Xia of the Department of Mechanics, Chinese University of Science and Technology, for his useful suggestion. We also wish to thank Dr. Jiayu Xiao, Professor of Department of Material Engineering and Applied Chemistry , NUDT, for his support.

### REFERENCES

1. Abrate.S Impact on Laminated Composite Materials, *Applied Mechanics Review*, Vol.44, No.4, 1991, pp.155-190.
2. Jiang, Da-zhi, *Damage Characteristics and Failure Process of Composite Laminated Structures under Projectile Impact and its Numerical Simulation*, Ph.D. Thesis, Department of Mechanics, Huazhong University of Science and Technology, Wuhan, China, October, 1996. (in Chinese)
3. Jiang, D. Z., Shen, W., and Wang, X. Y., Huang, Y. Y., Impact Damage of Composite Laminates Measured by Variance of Wave Speed, *Journal of National University of Defense Technology*, Vol.19, No.1, 1997, pp.25-28.
4. Tan,T.N.,Sun,C.T.,Use of Static Indentation Laws in the Impact Analysis of Laminated Composite Plates, *Journal of Applied Mechanics*, Vol.52, 1985, pp.6-12.

# FABRICATION AND MECHANICAL PROPERTIES OF GLASS MATRIX COMPOSITES WITH DIFFERENT FIBRE ARCHITECTURES

Heinrich Kern, Volker Winkler and Aldo R. Boccaccini

*Fachgebiet Wekstofftechnik, Technische Universität Ilmenau, PF 100565  
D-98684 Ilmenau, Germany*

**SUMMARY:** Processing routes have been developed for the fabrication of glass matrix composites with 2-dimensional woven fibre mats as reinforcement. Carbon and metallic (stainless steel 316L) fibre mats were investigated. In order to achieve infiltration of the matrix material into the fibres tows and an adequate adhesion between matrix and fibres, an electrophoretic deposition (EPD) technique was used. The infiltration capability using both a glass powder suspension and a silica colloidal solution was investigated and compared. Thus, the processing routes involve three steps: 1) the infiltration of the fibre mats using electrophoretic deposition, 2) the preparation of composite green bodies by stacking of infiltrated prepregs and 3) the consolidation of the composites by a high-temperature densification process involving pressureless sintering or hot-pressing. A high-level of matrix infiltration in the intra-tow regions was achieved when a silica colloidal solution was used. These samples could be densified by pressureless sintering. On the other hand, when a glass powder suspension was used, there was not complete infiltration of the fibre mats. Porosity in these samples could not be eliminated even after a hot-pressing stage.

**KEYWORDS:** glass matrix composites, woven fibre reinforcement, electrophoresis, composites processing, metallic fibre reinforcement, hot-pressing, sintering

## INTRODUCTION

The brittle nature, and therefore, high susceptibility to catastrophic failure of glass and glass-ceramic materials limits their use in structural applications. One approach to the improvement of the thermomechanical properties of these materials is to produce a composite. In this way, the low-modulus, low-strength, brittle matrix is reinforced by a high-modulus, high-strength and/or high-ductility second constituent in the form of continuous or chopped fibres, whiskers, platelets or particulates [1].

The best results in terms of increasing the fracture tolerance and imparting a pseudo-ductile fracture behaviour to brittle matrices is achieved with continuous fibre reinforcement [1,2]. The vast majority of work concerned with fibre reinforcement of glasses and glass-ceramics has focused on using ceramic fibres, especially in unidirectional and cross-ply fibre alignments [2-7]. The reinforcement of glass matrices by 2-dimensional fibre architectures, including ductile (metallic) fibre preforms, has been much less investigated [8], despite the advantages that these architectures may have over their unidirectional counterparts. These are related to the more isotropic mechanical properties obtained with 2-dimensional reinforcing elements over unidirectional fibre reinforcement [9].

The use of metallic reinforcement may have still further advantages, including an improved resistance to fibre damage during composite processing due to the intrinsic ductility of metallic fibres and the possibility of exploiting their plastic deformation for composite toughness enhancement [10]. However, the authors are only aware of the work of Russian workers on the use of 2-dimensional metallic fibre mats to reinforce glasses [8].

When using fibre mats as reinforcement, it is normally extremely difficult to achieve complete infiltration of the matrix material into the fibre tows, where the openings are of the order of  $\leq 100$  nm. Electrophoretic deposition (EPD) of colloidal ceramic sols has been shown recently to be a simple and inexpensive method for achieving complete infiltration of tightly woven fibre preforms [9, 11,12].

The technique has been employed for infiltrating silica and alumina sols into ceramic fibre preforms, such as SiC (Nicalon) [9,11] and alumina woven mats [12], showing that EPD provides a more efficient infiltration and stronger adhesion between fibre and matrix than a simple slurry dipping technique.

In the present study processing routes to fabricate two types of glass matrix composites with 2-dimensional woven fibre mats as reinforcement are developed. Carbon and metallic (stainless steel 316L) fibre mats were investigated. EPD was used to deposit matrix material onto the fibre preforms. For the metallic fibre mat reinforced composites, which were consolidated by pressureless sintering of the glass matrix, a silica sol was used first to infiltrate the metallic fibre mats.

It was anticipated that the silica infiltration would not only contribute to reduce the intra-tow porosity but also, acting as coating for the metallic fibres, would minimise possible reactions of the metal with the glass matrix during high-temperature densification and would provide an adequate interface in order to improve the composite fracture behaviour. A borosilicate glass powder suspension was used to fabricate the carbon fibre mats reinforced composites.

The results of the EPD technique for both the colloidal silica and the glass powder suspension were compared in terms of their ability to infiltrate woven fibre mats.

## **EXPERIMENTAL PROCEDURES**

Figure 1 shows the processing routes employed in this study to fabricate glass matrix composite materials. The details are given below.

### **Materials**

#### *Woven carbon fibre reinforced composites*

Commercially available (Tenax, Akzo AG) woven carbon fibre mats were used, with a fibre diameter of  $\approx 10\mu\text{m}$ . The glass matrix employed was a borosilicate glass (DURAN, Schott Glaswerke, Mainz, Germany). The glass powder was milled and sieved so that all particles were  $< 40\mu\text{m}$ . The density of this glass is  $2.2\text{ g/cm}^3$  and its thermal expansion coefficient is  $3.3 \times 10^{-6}\text{ 1/}^\circ\text{C}$  [13]. DURAN glass was chosen because it is a well-known matrix material for the fabrication of glass matrix composites [3] and because its viscous flow and sintering behaviour are known [13]. For the EPD experiments a powder aqueous suspension containing

≈40vol% solid and ≈0.1 wt% PVA was prepared. The suspension exhibited a strong tendency to sedimentation.

***Woven metal fibre reinforced composites***

From the variety of metal fabrics commercially available [14], a woven satin 100% 316L stainless steel fabric (Bekitherm FA, Bekaert SA, Zwevegem, Belgium) was chosen, on the basis of its suitability to be infiltrated by sol particles using electrophoretic deposition. There are other fibre mats available also, made from alloys such as Inconel 601, which have better high temperature properties than 316L, but for this study, the more cost-effective 316L stainless steel was considered adequate to demonstrate the use of this particular processing technology. The individual fibres have an average diameter of 14 μm and the weaves have a nominal thickness of 0.4 mm [14]. The maximum using temperature of the 316L fibres in an oxidising atmosphere is 900°C and the thermal expansion coefficient (20-700°C) is  $16.8 \times 10^{-6} \text{ 1/}^\circ\text{C}$  [15,16].

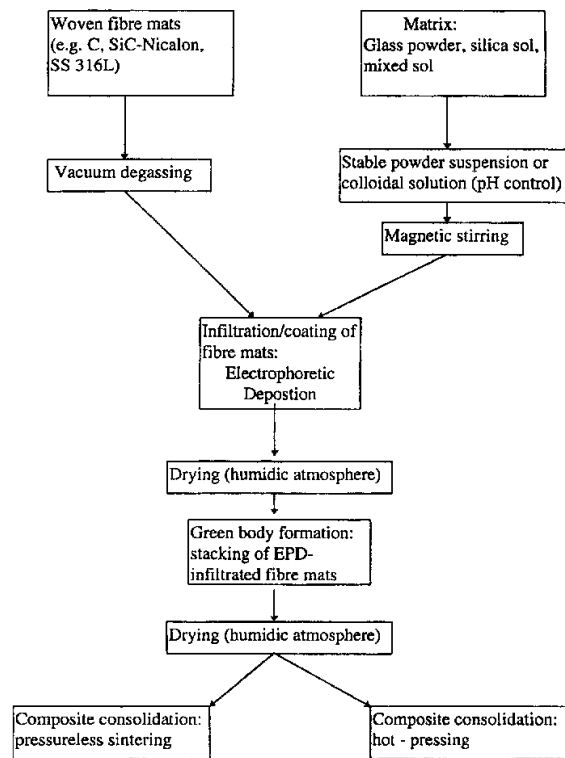


*Figure 1: Processing route for the fabrication of 2-dimensional woven fibre mat reinforced glass matrix composites*

Due to this relatively low thermal capability and limited oxidation resistance of the metallic fibre used, a glass with low sintering temperature was chosen for the matrix. The glass selected was a soda-lime glass, with a composition corresponding to that used in the German flat glass production [17]. The density of the glass is  $2.51 \text{ g/cm}^3$  and it was available as a powder with an average particle size of  $\approx 80 \text{ }\mu\text{m}$ . Its sintering and pressureless densification behaviour have been investigated previously and an optimised sintering temperature of  $670^\circ\text{C}$  was determined [17]. The thermal expansion coefficient of this glass is  $9.8 \times 10^{-6} \text{ 1/}^\circ\text{C}$ . A commercially available silica sol (Nyacol 2040 NH4, Akzo-PQ Silica, Amersfoort, The Netherlands) was used for the electrophoretic infiltration of the metallic fibre mats. This sol is

stable at pH 9, has a solid content of 40vol% and the sol particles are spherical with an average particle diameter of 20 nm. For the EPD experiments the sol was used as-received.

### **Infiltration of Fibre Mats by Electrophoretic Deposition (EPD)**

The EPD process relies on the presence of small charged particles within a liquid suspension, which, on the application of an electric field, will migrate toward and deposit on an electrode [18]. Movement of the particle occurs because the particle surface is charged with respect to the suspending medium. If the deposition electrode is replaced with a conducting fibre preform, the suspended particles are attracted to the fibre preform and then deposited on and within it. The movement of the ceramic particles in an aqueous suspension under an external applied electric field will be governed mainly by factors such as the field strength, the pH of the solution and the ionic strength of the solution [18]. In the present experiments, both the glass powder particles and the silica particles were negatively charged, as they migrated to the positive electrode.

Thus, the fibre mats were placed as the anode. A stainless steel plate served as the negative electrode. For the DURAN glass powder suspension a voltage of 30 V was applied to the electrodes that were 30mm separated. For the silica sol a much lower voltage (4 V) for the same electrodes separation was found to be adequate to obtain a reasonable deposition rate, in agreement with previous studies using SiC fibre mats [9,11]. The deposition time was varied to find the optimum time for the complete infiltration of the sol into the intra-tow regions, and for obtaining the desired thickness of the deposited layer in the case of the glass powder.

Controlled drying of the infiltrated/coated fibre mats is critical to the production of prepregs of sufficient quality, minimising the generation of cracks. The powder coated fibre mats were dried in normal atmosphere as no significant microcracking was expected due to the large powder particle sizes. The sol infiltrated fibre mats were dried both in normal air and in a humid atmosphere to investigate the effect of drying conditions on microcracking development. The dried fibre mats were impregnated with a vacuum resin and polished to a 1  $\mu\text{m}$  finish for scanning electron microscopy (SEM) examination. For the silica sol infiltrated mats, SEM energy dispersive X-ray analysis (EDX) was employed to differentiate between resin and silica in the intra-tow regions.

### **Forming of Green Bodies, Composite Consolidation, and Mechanical Tests**

#### *Woven carbon fibre reinforced composites*

A hot-pressing densification stage was chosen for the consolidation of these composites, as it was found (see Results below) that the EPD process did not yield complete infiltration of the woven carbon fibre mats. Typically, ten coated fibre mats were stapled, introduced in a graphite die and hot-pressed in vacuum at 900°C under an applied pressure of 10 MPa. The holding time was 30 minutes. In this way cylindrical samples (50 mm diameter,  $\approx$ 5.4 mm height) were obtained. From these samples test bars (5 x 4 x 40 mm) were prepared by cutting and polishing. These bars were tested in three-point bending (30 mm span). The load-displacement diagram was recorded and SEM was used to observe fracture surfaces.

### *Woven metal fibre reinforced composites*

The silica sol-infiltrated metallic fibre mats were used to prepare a glass matrix composite by a simple uniaxial cold-pressing and sintering route. Typically, two fibre mats were sandwiched between layers of the soda-lime glass matrix powder in a die (24 mm diameter) to form the green bodies. Similar laminated composites, but containing woven fabrics of Si-Ti-C-O fibres sandwiched between thin mullite layers have been reported in the literature [19]. Uniaxial pressures of 90 MPa were employed to obtain samples of sufficient strength to be handled. The specimens were heated at a rate of 10°C/min up to the sintering temperature of 670°C and the dwell time at temperature was 1 hour before a subsequent furnace cooling stage.

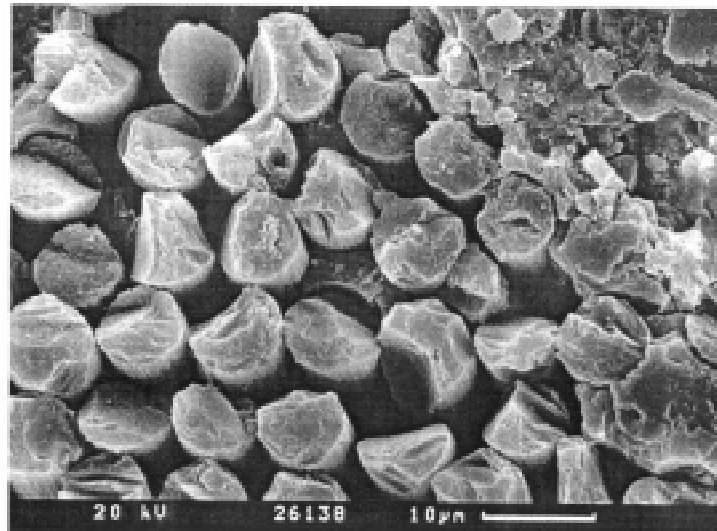
The samples were fabricated solely to investigate the possibility of composite consolidation by this simple, pressureless densification route, and to assess the presence of any reaction at the silica/metal fibre and silica/ glass matrix interfaces. Selected sintered samples were cut, polished and observed using SEM. In addition, several rectangular bars (20mm x 2mm x 3mm) were cut from the cylinders and used to investigate, in a qualitative manner, the fracture behaviour of the composites in three-point flexion (span: 16 mm). Fracture surfaces were observed using SEM.

## **RESULTS AND DISCUSSION**

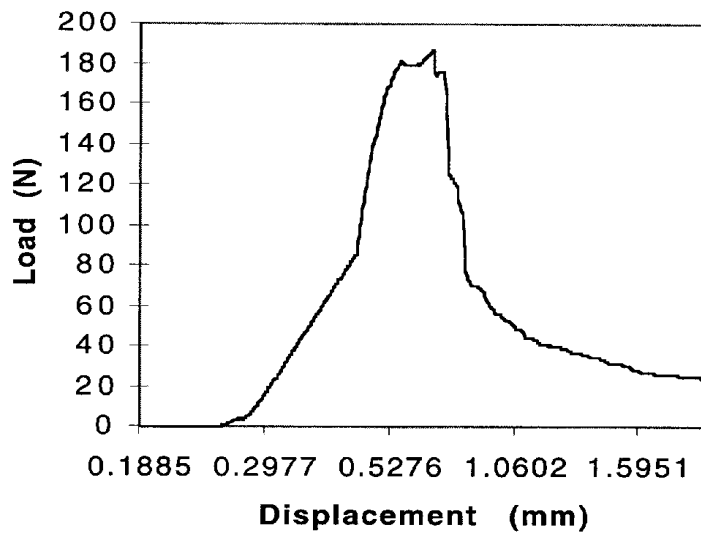
### **Woven Carbon Fibre Reinforced Composites**

Figure 2 is a SEM micrograph showing the microstructure of a woven carbon fibre reinforced DURAN glass matrix composite after hot-pressing at 900 °C. A poor infiltration of glass matrix in the spaces between the fibres is observed. This means that the combination of EPD and hot-pressing, as employed in this study, was unsuitable for obtaining pore-free materials. Indeed, using a suspension of  $\mu\text{m}$ -sized glass particles in the EPD cell was the reason why the fibre mats could not be infiltrated fully, and the glass particles were only (firmly) adhered to the surfaces of the fibre mat. Moreover, the viscosity of the glass at the hot-pressing temperature (900 °C) was not sufficiently low to allow an efficient infiltration. This effect may be enhanced by a poor wettability of the carbon fibres by the viscous glass. Figure 3 shows the load-displacement diagramme of a sample during the three-point bending test.

Composite behaviour, i.e. non-catastrophic fracture, is observed. However, due to the considerable porosity present, the absolute values of the mechanical properties achieved are rather low. The optimization of the hot-pressing parameters should result in a reduction of the intra- and inter-tow porosity in these samples and the attainment of better mechanical properties. These properties should be comparable to those measured in commercially available unidirectional carbon fibre reinforced DURAN glass matrix composites (ultimate fracture strength = 800-1200 MPa, Young's modulus = 120 GPa [3]), with the advantage, however, of being isotropic in 2 dimensions due to the particular fibre architecture used. It is suggested, however, that an increase of the hot-pressing pressure will not necessarily lead to better results in terms of glass infiltration, since this would tend to close the intra-and inter-tow spaces, making more difficult the flow and intra-tow penetration of the glass. Probably a pre-treatment of the carbon fibres surfaces to improve their wettability by the viscous glass would be an effective approach.



*Fig. 2: SEM micrograph showing the microstructure of a carbon fibre mat reinforced DURAN glass matrix composite. Poor infiltration of the matrix in the spaces between the fibres is observed*



*Fig. 3: Load-displacement diagramme for a carbon fibre mat reinforced glass matrix composite during a three-point bending test*



*Woven metal fibre reinforced composites*

Figures 4a and 4b show SEM micrographs of a metallic fibre mat infiltrated with silica sol, at low and high magnification, respectively. The SEM images demonstrate that the EPD technique was capable of producing a high level of sol infiltration into the electrically conducting fibre tows. It is suggested that the infiltration process is enhanced by the opening up of the spaces in the fibre tow through the mutual repulsion of the charged fibres. Owing to the small particle size of the silica sol used (20 nm), the particles are able to infiltrate the spaces between the fibre tows efficiently. In addition, the use of a relatively low EPD voltage minimised the electrolyte decomposition and subsequent hydrogen and oxygen gas evolution found to occur in previous work on EPD of silica sols [9].

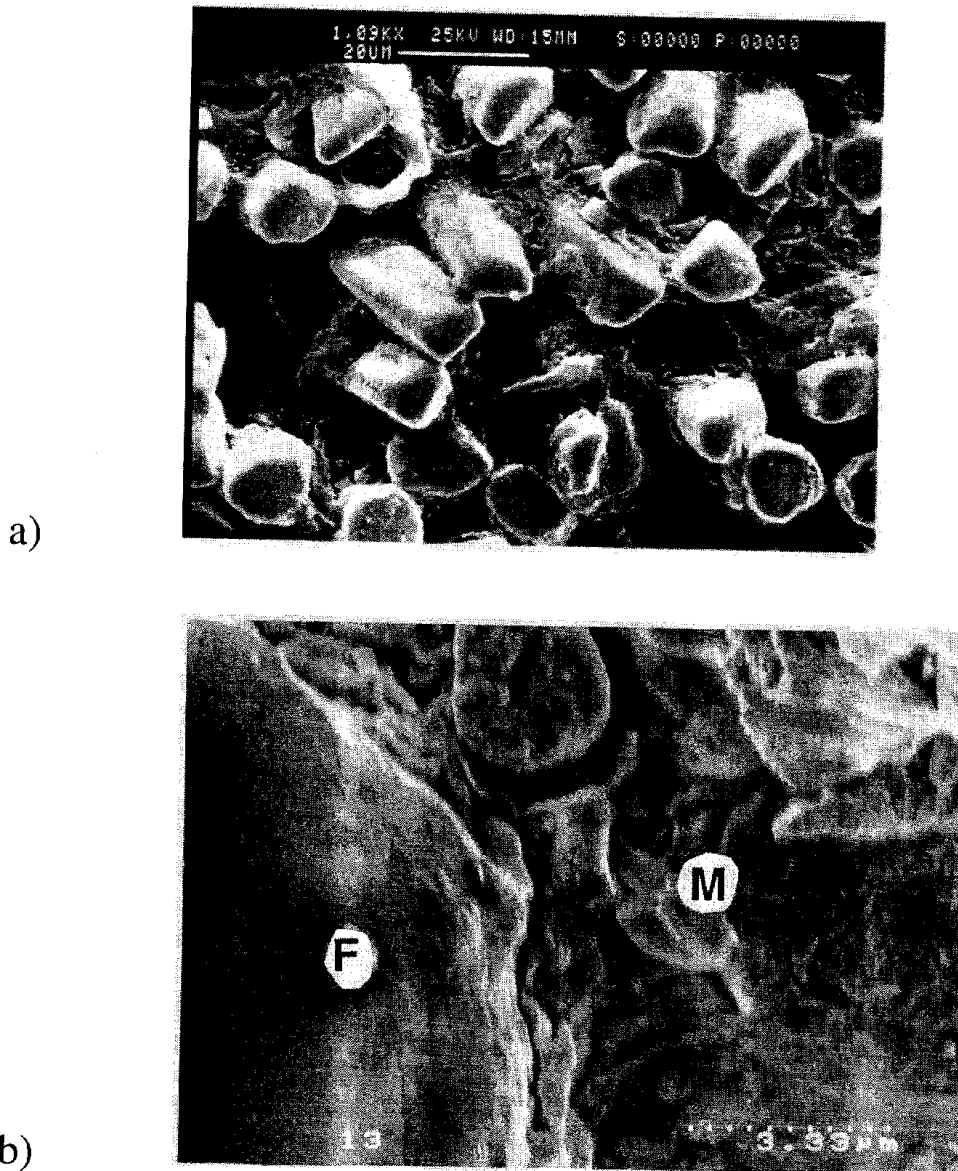


*Fig. 4: SEM micrographs of an impregnated metallic fibre mat, showing that during EPD the silica particles have infiltrated fully the intra-tow regions, a) low and b) high magnification (F: Fibre, M: electrophoretically deposited silica).*

As in all sol-gel preparation methods, control of the drying stage is important to reduce the likelihood of drying cracks being generated. The presence of such microcracks is apparent in

Figure 4 and they occur due to the differential shrinkage of the gel network, which generates tensile stresses at the surface and leads to the growth of microscopic flaws [20]. As mentioned before, no cracks were generated in the carbon fibre mats that were coated with the glass powder. Thus, when a sol is used, the selection of the appropriate drying method and the thickness of the deposited layer are critical factors in the preparation of high-quality prepregs for composite fabrication. A deposition time of 1 min was found here to be sufficient for the complete infiltration of the sol into the intra- and inter-tow regions, and for obtaining the desired thickness of the deposited layer. It was found also, that the deposition time has no effect on the quality of the intra-tow impregnation, in agreement with previous studies on SiC woven fibre mats [9,11]. Fibre mats that were impregnated using EPD times of 1 minute contained small cracks after drying in a normal atmosphere, whereas, the prepregs prepared by slow drying in a humid atmosphere (80% humidity) exhibited no crack formation in between the fibres. The cracks formed during air drying were, however, very narrow because the deposited film was extremely thin.

A more detailed investigation of the densification behaviour and microstructural characteristics of the woven metal fibre reinforced glass composites has been given elsewhere [21]. Although with the present samples the mechanical properties could not be evaluated quantitatively, observation of the fracture surfaces of the bars broken in flexion supplies some information on the fracture behaviour of the material. Figure 5 shows a typical fracture surface. The sample failed in a "graceful", i.e. non-catastrophic, manner and pull-out of the fibres was observed. This mechanism is compatible with the presence of a weak interface. However, the pull-out lengths are short, and some deformation of the fibres can be seen also in the micrograph. Thus, this preliminary result seems to indicate that in the present composites, both plastic deformation of the reinforcement and frictional sliding between the fibres and the glass matrix can be utilised for toughness improvement. It has been shown in the literature [22], that an optimum interfacial bonding strength is essential to exploit both the aforementioned toughening mechanisms. The presence of the porous silica coating in the present composites would seem to be responsible for this behaviour. It is suggested that the silica particles provide i) sufficient interfacial strength for load transfer between the matrix and the fibres due to the fact that they are adhered to the metallic fibre by the EPD process, and ii) the weaker interfacial bonding necessary for the fibre pull-out behaviour. This last requirement is achieved due to the partial densification of the silica coating and the presence of drying-induced microcracks, which cannot be closed during the pressureless densification process. These suggestions, however, need to be verified by a proper characterisation of the interfaces and by a detailed study of the fracture behaviour of the composites, which is the focus of current research.

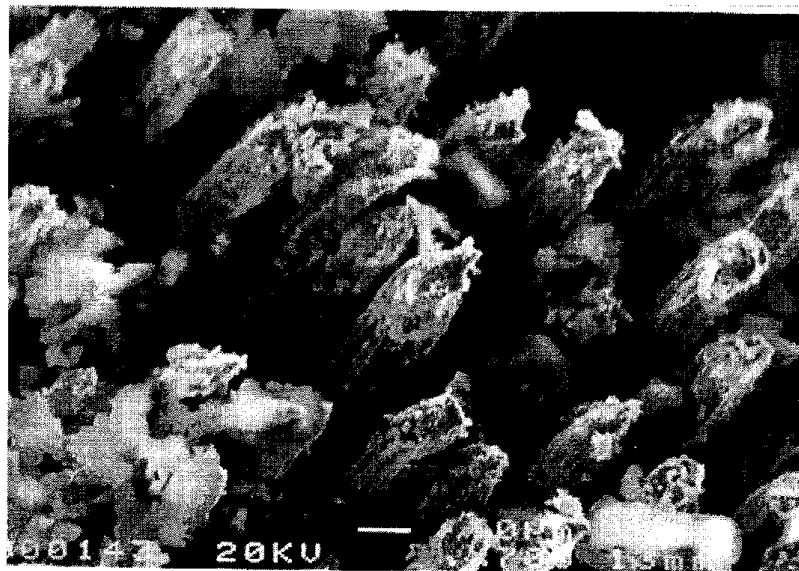


*Fig. 5: SEM micrograph of the fracture surface of a metallic fibre reinforced glass matrix composite fractured in flexion. Pull-out of the fibres can be seen, as well as some deformation at the fibre ends.*

## CONCLUSIONS

Processing routes have been presented for the fabrication of glass matrix composites containing 2-dimensional fibre reinforcement. Both woven carbon and metallic (316L SS) fibre mats were used. The composite fabrication involves the use of electrophoretic deposition to infiltrate and coat the fibre mats. The infiltration capability using both a glass powder suspension and a silica colloidal solution was investigated and compared. A high-level of infiltration in the intra-tow regions was achieved when a silica colloidal solution was used. These samples could be densified by pressureless sintering. Although the mechanical properties of these samples were not determined, the observation of fracture surfaces revealed that both fibre pull-out and fibre deformation occur, which should lead to a significant toughness enhancement. For the carbon fibre mat containing composites, the glass powder suspension used for EPD did not yield complete infiltration of the fibre mats. To reduce porosity, these samples had to be densified by hot-pressing. The hot-pressing parameters need to be optimised, however, as residual porosity was still present in the samples. The poor wettability of the carbon fibres by the viscous glass at the working temperature may enhance the lack of penetration of the glass into the intra- and inter-tow spaces.

## Acknowledgements

The authors acknowledge the experimental support of Dr. P. A. Trusty (IRC in Materials University of Birmingham). Dr. R. de Bruyne, NV Bekaert S. A. (Belgium), is acknowledged for supplying the metallic fibre mats.

## REFERENCES

1. Hyde, A. R., Ceramic Matrix Composites, "A New Generation of Materials for Mechanical and Electrical Applications", *GEC J. Res.*, Vol. 7, 1989, pp. 65-71.
2. Philips, D. C., Sambell, R. J. A., Bowen, D. J., "The Mechanical Properties of Carbon Fibre Reinforced Pyrex Glass", *J. Mat. Sci.*, Vol. 7, 1972, pp. 1454-1464.
3. Brückner, R., "Glass Composites", *Proc. XVI International Congress on Glass*, Madrid (Spain) 1992. Vol.1, p. 97-118.
4. Prewo, K. M., Brennan, J. J. and Layden, G. K., "Fiber Reinforced Glasses and Glass-Ceramics for High Performance Applications", *Am. Ceram. Soc. Bull.*, Vol. 65, 1986, pp. 305-322.
5. Briggs, A. and Davidge, R. W., "Borosilicate Glass Reinforced with Continuous Silicon Carbide Fibres: a New Engineering Ceramic", *Mat. Sci. Eng.*, Vol. A109, 1989, pp. 363-372.
6. Rawlings, R. D., "Glass-Ceramic Matrix Composites", *Composites*, Vol. 25, 1994, pp. 372-379.
7. Vaidya, R. U., Fernando, J., Chawla, K. K. and Ferber, M. K., "Effect of Fiber Coating on the Mechanical Properties of a Nextel-480-Fiber-Reinforced Glass Matrix Composite", *Mat. Sci. Eng.*, Vol. A150, 1992, pp. 161-169.
8. Rutkovskij, A. E., Sarkisov, P. D., Ivashin, A. A. and Budov, V. V., "Glass Ceramic-Based Composites", *Ceramic- and Carbon-matrix Composites*, Trefilov, V. I., Ed., Chapman and Hall, London, 1994, pp. 255-285.
9. Illston, T. J., Ponton, C. B., Marquis, P. M. and Butler, E. G., "The Manufacture of Woven Fibre Ceramic Matrix Composites Using Electrophoretic Deposition", *Third Euroceramics* Vol. 1, Duran, P. and Fernandez, J. F., Eds., Faenza Editrice Iberica, Madrid, 1993, pp.419-424.
10. Donald, I. W., Metcalfe, B. L. and Bye, A. D., "Preparation of a Novel Unidirectionally Aligned Microwire-Reinforced Glass Matrix Composite", *J. Mat. Sci. Lett.*, Vol. 7, 1988, pp. 964-966.
11. Boccaccini, A. R. and Ponton, C. B., "Processing Ceramic-Matrix Composites Using Electrophoretic Deposition", *JOM*, Vol. 47, No.10, 1995, pp. 34-37.
12. Trusty, P. A., Boccaccini, A. R., Butler, E. G. and Ponton, C. B., "Novel Techniques for Manufacturing Woven Fiber Reinforced Ceramic Matrix Composites. I. Preform Fabrication", *Mat. and Manuf. Processes*, Vol. 10, 1995, pp. 1215-1226.
13. Boccaccini, A. R., PhD Thesis, Aachen University of Technology, Aachen, 1994.

14. *Bekitherm, Heat Resistant Separation Materials*, N.V. Bekaert S.A., Zwevegem, Belgium, Produkt Information.
15. *Metals Handbook*, Taylor Lyman, (Ed.), The American Society for Metals, (1948).
16. Pernot, F. and Rogier, R., "Mechanical Properties of Phosphate Glass-Ceramic-316L Stainless-Steel Composites", *J. Mat. Sci.*, Vol. 28, 1993, pp. 6676-6682.
17. Boccaccini, A. R. and Kramer, R., "Experimental Verification of a Stereology-Based Equation for the Shrinkage of Glass Powder Compacts During Sintering", *Glass Technol.*, Vol. 36, 1995, pp. 95-97.
18. Andrews, J. M., Collins, A. H., Cornish, D. C. and Dracass, J., "The Forming of Ceramic Bodies by Electrophoretic Deposition", *Proc. Br. Ceram. Soc.*, Vol. 12, 1969, pp. 211- 229.
19. Hirata, Y., Matsuda, M., Takeshima, K., Yamashita, R., Shibuya, M., Schmücker, M. and Schneider, H., "Processing and Mechanical Properties of Laminated Composites of Mullite/Woven Fabrics of Si-Ti-C-O Fibres", *J. Europ. Ceram. Soc.* , Vol. 16, 1996, pp. 315-320.
20. Brinker, C. J. and Scherer, G. W., *Sol-Gel Science*, Academic Press, New York, 1990.
21. Boccaccini, A. R., Ovenstone, J. and Trusty, P. A., "Fabrication of Woven Metal Fibre Reinforced Glass Matrix Composites", *Appl. Comp. Mat.*, 1997, in press.
22. Lee, T. K. and Subramanian, K. N., "Optimisation of Interfacial Bonding to Enhance Fracture Toughness of Ceramic Matrix Reinforced with Metallic Ribbon", *J. Mat. Sci.*, Vol. 30, 1995, pp. 2401-2405.

# THERMOELECTRIC PROPERTIES OF B<sub>4</sub>C-BASED COMPOSITE CERAMICS PREPARED BY ARC-MELTING

Takashi Goto, Jianhui Li and Toshio Hirai

*Institute for Materials Research, Tohoku University  
2-1-1 Katahira Aoba Sendai 980-77, Japan*

**SUMMARY:** B-C system solid solutions and B<sub>4</sub>C-based composites (B<sub>4</sub>C-SiC system and B<sub>4</sub>C-TiB<sub>2</sub> system) were prepared by arc-melting in an argon atmosphere. The microstructure and thermoelectric properties were studied. The solid solutions of the B-C system ranged between 10 and 25 at% C, and the dimension-less thermoelectric figure-of-merit (ZT) was the greatest at the composition of 25 at% C (B<sub>4</sub>C). Both the B<sub>4</sub>C-SiC and B<sub>4</sub>C-TiB<sub>2</sub> systems were quasi-binary, and typical lamellar structures were observed indicating eutectic reactions. In the SiC-B<sub>4</sub>C system, the eutectic composition was 45 mol% SiC, and the ZT value was the highest at 40 mol% SiC. In the B<sub>4</sub>C-TiB<sub>2</sub> system, 25 mol% TiB<sub>2</sub> was the eutectic composition, and the ZT showed the maximum values at 6 mol% TiB<sub>2</sub>. The greatest ZT value of 0.55 at 1100K was obtained in the B<sub>4</sub>C-TiB<sub>2</sub> system at 6 mol% TiB<sub>2</sub>.

**KEYWORDS:** B-C system solid solution, B<sub>4</sub>C-SiC composite, B<sub>4</sub>C-TiB<sub>2</sub> composite, boron-rich boride, eutectic reaction, arc-melting, thermoelectric property

## INTRODUCTION

Boron carbide (B<sub>4</sub>C) could be a candidate as a high-temperature thermoelectric material because of its high Seebeck coefficient, low thermal conductivity and moderate electrical conductivity [1]. So far several methods including melting [2], hot-pressing [3] and chemical vapor deposition (CVD) [4] have been applied to prepare boron carbides; however, the thermoelectric properties are scattered depending on preparing methods. The reason may be partly caused by its non-stoichiometry. In the present work, wide-ranged non-stoichiometric boron carbides were prepared by arc-melting.

The performance of boron carbides, however, is not enough to be used in practical applications. In order to improve the thermoelectric property of boron carbides, one has tried to make composites, e.g., B<sub>4</sub>C-SiC composites sintered body [5]. Since boron carbide and silicon carbide are hardly sintered due to high-melting points and the covalent nature, it is more difficult to obtain dense B<sub>4</sub>C-based composites by sintering [5]. On the other hand, an arc-melting method has an advantage to prepare fully dense materials. We have been fabricating B-C system solid solutions and several composites including B<sub>4</sub>C-SiC and B<sub>4</sub>C-TiB<sub>2</sub> systems by arc-melting. In this paper, we describe the microstructure of the B-C system solid solutions and the B<sub>4</sub>C-based composites, and report their thermoelectric properties.

## EXPERIMENTS

The starting materials were  $B_4C$ , SiC,  $TiB_2$ , Si, C and B powders. After drying these powders, specified amounts were weighed and mixed with a small amount of acetone in an agate mortar. The mixed powder was pelletized in a size of 15 mm in dia. by 5 mm thick. The pellets were arc-melted in an argon atmosphere using a tungsten electrode, and solidified button specimens were obtained. The densities of the specimens were measured in toluene by an Archimedean method. The specimens were mounted in resins, and polished metallurgically with diamond paste ( $0.7 \mu m$ ). The microstructure was studied with scanning electron microscopy (SEM), transmission electron microscopy (TEM) and electron probe microanalysis (EPMA). The crystal structure was investigated with X-ray diffraction (XRD). Impurities were analyzed with an induction coupled plasma method.

The button specimens were cut into sheets (10 mm by 4 mm by 0.1 to 2 mm) for electrical measurements. Seebeck coefficient ( $\alpha$ ) was measured with an AC method under a small temperature gradient (0.3 to 0.8K) [6]. We confirmed that the results by the AC method agreed with those of the steady state (DC) method [6]. A four-probe method was used to measure electrical conductivity ( $\sigma$ ). Disk-shaped specimens (10 mm in dia. by 2 mm thick) were cut from the button specimens, then thermal conductivity ( $\kappa$ ) was measured with a laser-flash method. The measurements were conducted in a vacuum in the temperature range between room temperature and 1100K. The thermoelectric figure-of-merit ( $Z$ ,  $Z = \alpha^2 \sigma / \kappa$ ) and the dimension-less figure-of-merit ( $ZT$ ) were calculated.

## RESULTS AND DISCUSSION

### B-C system solid solutions

Fig.1 shows the relationship between lattice parameters ( $a$  and  $c$  in a hexagonal unit) and carbon content. The lattice parameters changed gradually in the range between 8 and 20 at%C. A small amount of free-boron was observed by XRD in specimens of 8 to 10 at%C, and free-carbon in specimens of 25 at%C. The specimens obtained by arc-melting are not always in an equilibrium state due to rapid cooling; then the lattice parameters still changed even a second phase appeared. There have been many reports on the region of solid solution for boron carbides, e.g., 12.5 to 20.0 at%C by Allen [7], 8.8 to 20.0 at%C by Bouchacout and Thevenot [8]. The reported lattice parameters ranged between  $a=0.560$  and  $0.567$  nm, and  $c=1.207$  and  $1.219$  nm [9,10]. Our results of the solid solution range and their lattice parameters are almost in agreement with those previous reports.

Fig.2 represents the temperature dependence of Seebeck coefficient ( $\alpha$ ) of the B-C system specimens. The  $\alpha$  values increased or decreased with increasing temperature depending on the compositions. In literatures, the  $\alpha$  increased or decreased with carbon content, or

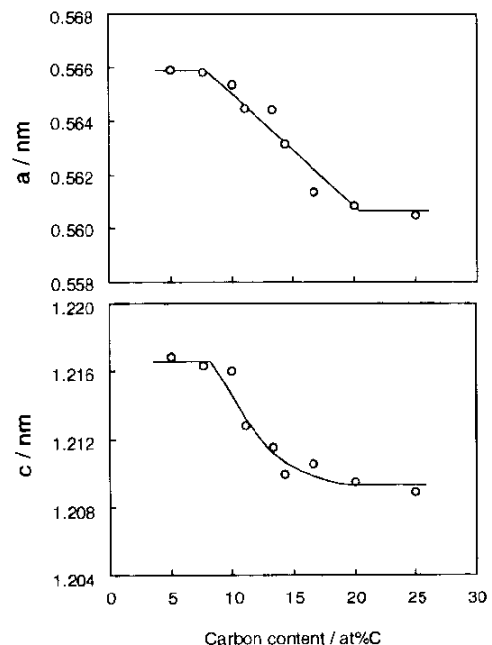


Fig. 1: Relationship between lattice parameters (hexagonal  $a$  and  $c$ ) and carbon content.

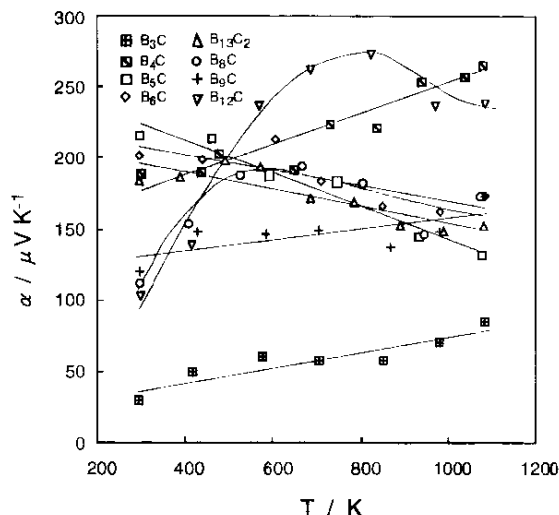


Fig.2: Temperature dependence of Seebeck coefficient ( $\alpha$ ) of boron carbides.

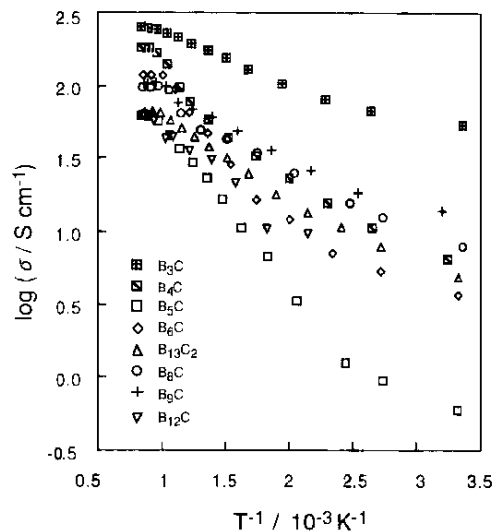


Fig.3: Temperature dependence of electrical conductivity ( $\sigma$ ) of boron carbides.

showed the maximum values at 13.3 at% C ( $B_{13}C_2$ ) [8]. In the present work, the  $\alpha$  showed the maximum values at 20 at% C ( $B_4C$ ) in the solid solution range. The specimens of 8 at% C also have great  $\alpha$  values which are almost the same as those of  $B_4C$ . It is known that  $\beta$ -boron (100 at%B) also shows high  $\alpha$  values. Further study should be necessary for the specimens of high boron content regions.

Fig.3 shows the temperature dependence of electrical conductivity ( $\sigma$ ) of the B-C system specimens. The  $\sigma$  values were almost the same as literature values. In the past, the  $\sigma$  increased with increasing carbon content, or showed the maximum values at 13.3 at% C ( $B_{13}C_2$ ) [3]. In the present study, the  $\sigma$  showed the minimum values at 17 at% C ( $B_5C$ ).

The temperature dependence of thermal conductivity ( $\kappa$ ) of the B-C system specimens is shown in Fig.4. The specimens of 25 at% C ( $B_3C$ ) had high  $\kappa$  values which decreased with increasing temperature. In the range between 8 and 20 at% C, the  $\kappa$  values were relatively small (5 to 12 W/m K) which were almost independent of temperature. This trend is similar to many amorphous materials. It is known that boron atoms in  $B_{12}$  clusters are partially substituted by carbon atoms, and carbon atoms in C-C-C bonds are partially substituted by boron atoms in the crystal structure of boron carbides [11]. Therefore, the distribution of boron and carbon atoms tends to be irregular in  $B_4C$ . This will cause the amorphous-like behavior of thermal conductivity of  $B_4C$ . The  $\kappa$  values increased with increasing carbon content. This trend is similar to that of literatures [11].

Fig.5 demonstrates the temperature dependence of dimension-less figure-of-merit (ZT) of the B-C system specimens. The ZT values increased exponentially with increasing temperature. This trend is similar

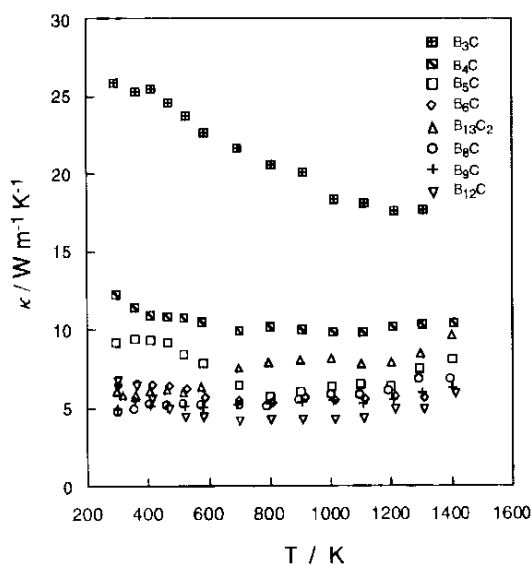


Fig.4: Temperature dependence of thermal conductivity ( $\kappa$ ) of boron carbides.

to many boron-rich borides [10]. The maximum ZT values were observed at 20 at% C ( $B_4C$ ). The greatest ZT value of the B-C system specimens at 1100K was 0.15.

#### $B_4C$ -SiC system composites

The composition of B, C and Si after arc-melting was the same as those of starting compositions. The structures of  $B_4C$  and SiC in the button specimens were also the same as the starting powders, i.e., rhombohedral  $B_4C$  and cubic ( $\beta$ -type) SiC. A few mass% of tungsten was contained in the specimens as an impurity from tungsten electrodes. The effect of impurity tungsten on the thermoelectric properties was negligibly small when the tungsten content was an order of a few mass% [12].

Fig. 6 represents a phase diagram of B-C-Si system at 2173K [13] and the composition of the specimens prepared in the present work. The specimens were two-phase mixtures of  $B_4C$  and SiC when the compositions were on the  $B_4C$ -SiC tie-line. Free-carbon and free-silicon were observed when the compositions were at carbon-rich sides and silicon-rich sides of the  $B_4C$ -SiC tie-line, respectively. The specimens on the  $B_4C$ -SiC tie-line showed better thermoelectric performance than those which are not on the tie-line. Therefore, we focus on the properties of the  $B_4C$ -SiC composites (i.e., the compositions on the  $B_4C$ -SiC tie-line).

Fig.7 shows the microstructure of the  $B_4C$ -SiC composites. The dark parts are  $B_4C$  phases and the bright parts are SiC phases according to EPMA measurements. Typical lamella textures were observed in the specimens at 45 to 50 mass%SiC, indicating the eutectic reaction.

The temperature dependence of Seebeck coefficient ( $\alpha$ ) of the  $B_4C$ -SiC composites is shown in Fig.8. The  $\alpha$  is positive (p-type) which means that the charge carrier is hole. The  $\alpha$  values increased with increasing temperature. The  $\alpha$  showed the maximum values at near the eutectic composition (40 mol%SiC). The  $\alpha$  values of boron-rich borides have been always positive (i.e., p-type) in literatures [1]. The polarity of  $\alpha$  for SiC depends on impurity, and boron is a p-type impurity. Therefore, the SiC phase in the  $B_4C$ -SiC composites could be p-type because impurity boron should be saturated in the SiC phase. Koumoto et al. [15] reported that the  $\alpha$  values of their p-type SiC increased from 200 to 400  $\mu$  V/K with increasing temperature from room temperature to 1300K. In the present study, the  $\alpha$  values at 65 mol%SiC, in which the SiC phase formed the matrix, were almost in agreement with those of the p-type SiC. In TEM observation, we found many twin boundaries in the  $B_4C$  phase in the  $B_4C$ -SiC composites. It is said that the structural defects such as twin boundaries result in the high  $\alpha$

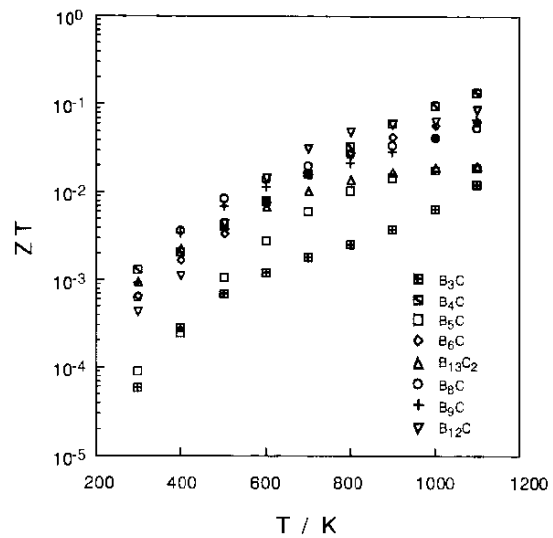


Fig.5: Temperature dependence of dimension-less figure-of-merit (ZT) of boron carbides.

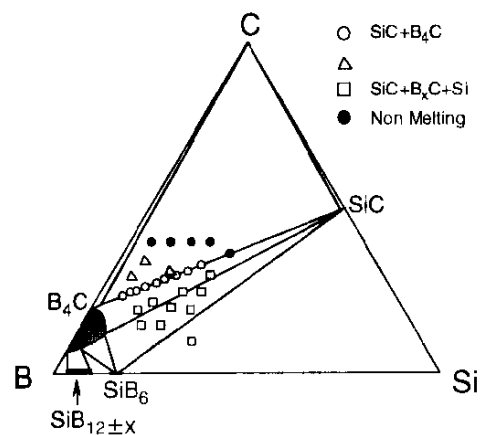


Fig.6: Experimental compositions and a B-C-Si system phase diagram at 2173K.



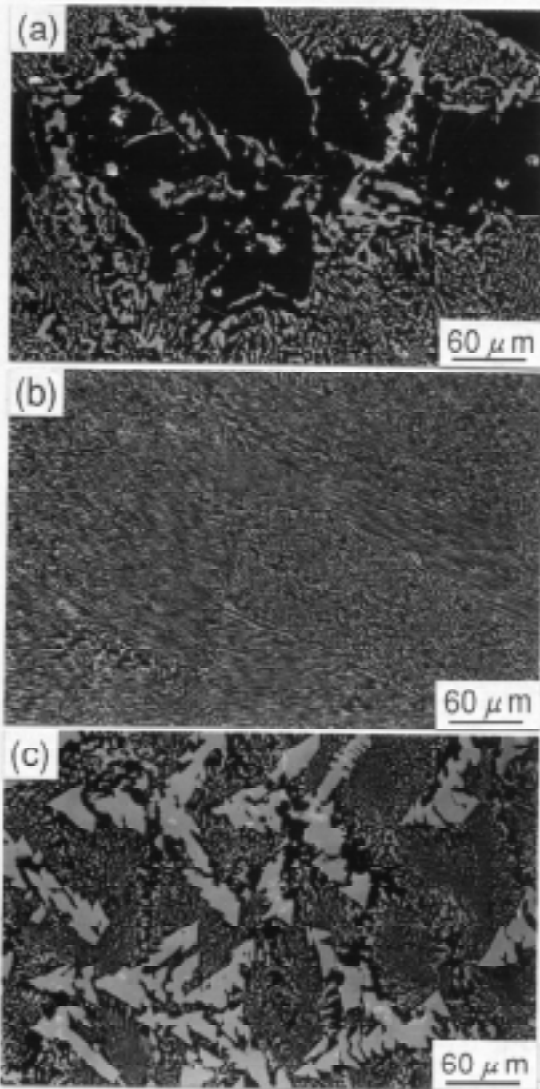


Fig.7: Microstructures of  $B_4C$ -SiC composites. (a):SiC35mol%, (b):SiC50mol%, (c):SiC65mol%

values of  $B_4C$  [2]. The twin boundaries in the  $B_4C$ -SiC composites might also cause the increase of  $\alpha$  values particularly near the eutectic compositions (see Fig. 8).

Fig.9 shows the temperature dependence of electrical conductivity ( $\sigma$ ) of the  $B_4C$ -SiC composites. The  $\sigma$  values increased with increasing temperature. The activation energy for the electrical conduction ranged from 0.19 to 0.27 eV, which is between that of  $B_4C$  (0.12 to 0.14 eV [14]) and p-type SiC (0.71 eV) [15]. The  $\sigma$  also showed the maximum values at 40 mol%SiC. This may be also associated with the structural defects, i.e., twin boundaries, relating to the hopping conduction of boron carbides [1].

Fig.10 depicts the temperature dependence of thermal conductivity ( $\kappa$ ) of the  $B_4C$ -SiC composites. The  $\kappa$  values decreased with increasing temperature. Since the  $\kappa$  values of SiC [15] are greater than those of  $B_4C$  [16], the  $\kappa$  values of  $B_4C$ -SiC composites increased with increasing SiC content. The  $\kappa$  values at 35 to 50 mol%SiC could be slightly smaller

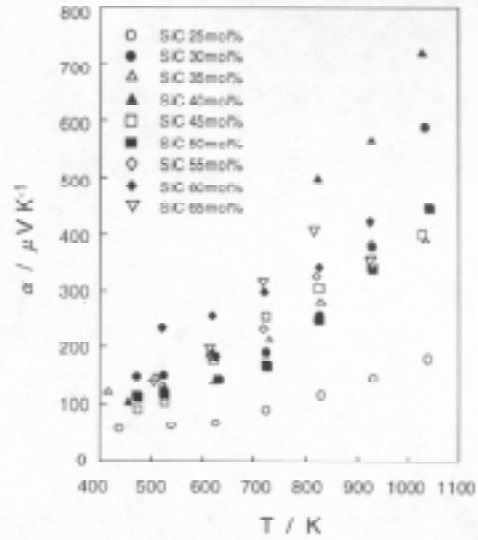


Fig.8: Temperature dependence of Seebeck coefficient ( $\alpha$ ) of  $B_4C$ -SiC composites.

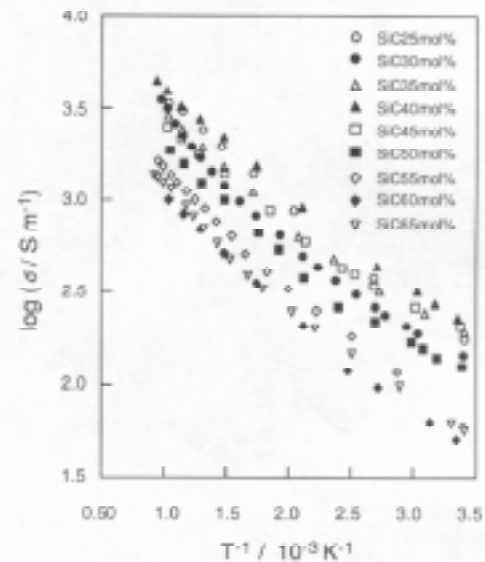


Fig.9: Temperature dependence of electrical conductivity ( $\sigma$ ) of  $B_4C$ -SiC composites.

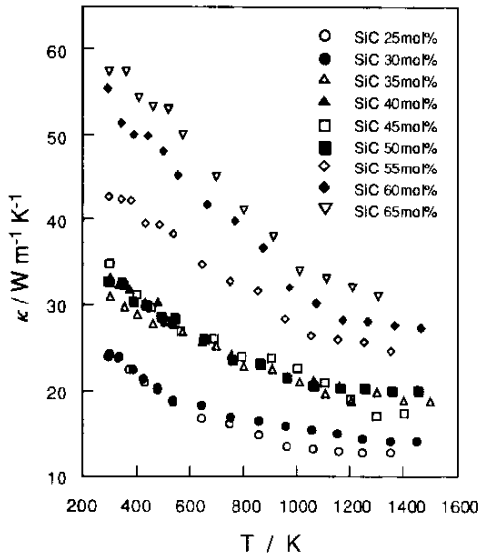


Fig. 10: Temperature dependence of thermal conductivity ( $\kappa$ ) of  $B_4C$ -SiC composites.

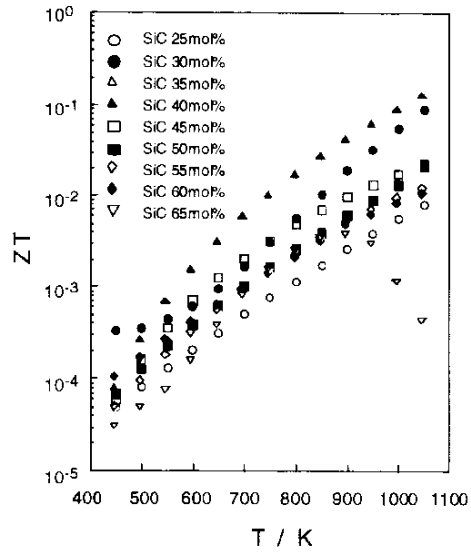


Fig. 11: Temperature dependence of dimensionless figure-of-merit (ZT) for  $B_4C$ -SiC composites.

than those calculated from a simple mixture rule. This might be caused from the scattering of phonons at the twin boundaries or  $B_4C$ /SiC interfaces.

Fig. 11 represents the temperature dependence of the dimensionless figure-of-merit (ZT) of the  $B_4C$ -SiC composites. The ZT values increased exponentially with increasing temperatures in the range between 25 and 60 mol%SiC. The ZT showed maximum values at 40 mol%SiC. The greatest ZT value at 1100K was 0.2.

**$B_4C$ -TiB<sub>2</sub> system composites**

Fig. 12 represents a B-C-Ti ternary phase diagram at 1773K, and a  $B_4C$ -TiB<sub>2</sub> quasi-binary phase diagram [13]. We obtained two-phase mixtures of  $B_4C$  and TiB<sub>2</sub> ( $B_4C$ -TiB<sub>2</sub> composites) on the  $B_4C$ -TiB<sub>2</sub> tie-line. We also prepared carbon and boron excess specimens. Since free-carbon and free-boron contained specimens had less thermoelectric performance, we describe only about  $B_4C$ -TiB<sub>2</sub> composites.

Fig. 13 shows the microstructure of the  $B_4C$ -TiB<sub>2</sub> composites. The bright parts are TiB<sub>2</sub>, and dark parts are  $B_4C$ . Large  $B_4C$  primary phases and  $B_4C$ -TiB<sub>2</sub> eutectic texture were observed at 13 mol%TiB<sub>2</sub> (Fig. 13(a)). A typical eutectic texture can be seen at 25 mol%TiB<sub>2</sub> (Fig. 13 (b)). The TiB<sub>2</sub>

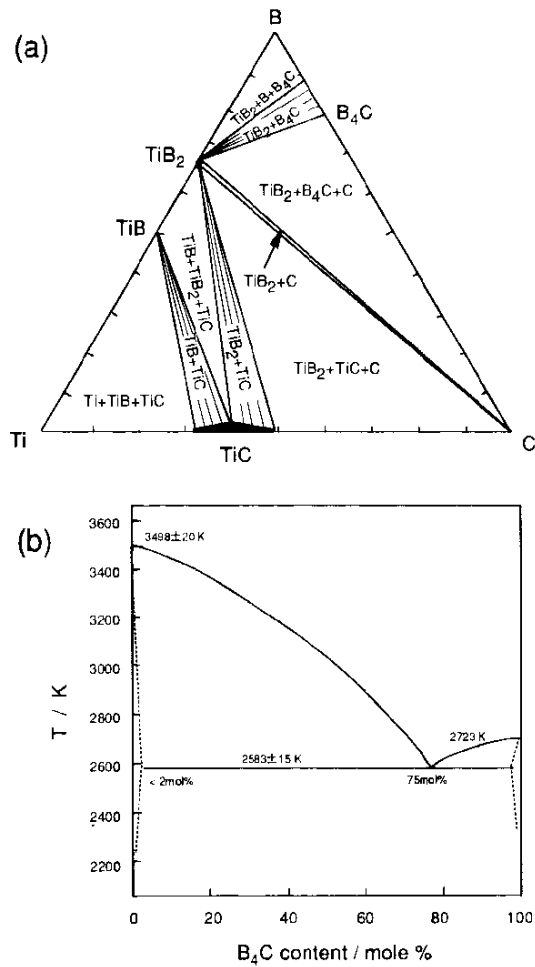


Fig. 12: A B-C-Ti ternary phase diagram at 1773K (a) and a  $B_4C$ -TiB<sub>2</sub> quasi-binary phase diagram (b).

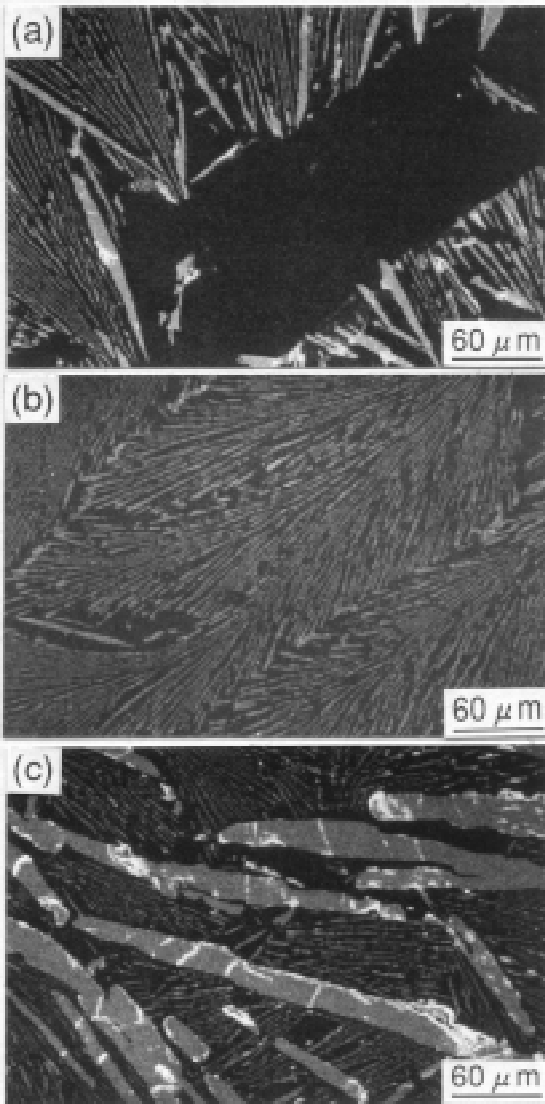


Fig.13: Microstructures of  $B_4C-TiB_2$  composites. (a): 13mol% $TiB_2$ , (b): 25mol% $TiB_2$  (c): 45mol% $TiB_2$ .

phase in the eutectic texture was 0.3 to 0.8  $\mu m$  in width and several to 100  $\mu m$  in length. Rod-shaped  $TiB_2$  phases precipitated at  $TiB_2$  rich compositions (Fig.13(c)).

Fig.14 depicts the temperature dependence of Seebeck coefficient ( $\alpha$ ) of the  $B_4C-TiB_2$  composites. The  $\alpha$  values increased with increasing temperature showing the maximum values at 2 to 6 mol% $TiB_2$ . The greatest  $\alpha$  value at 1100K was 354  $\mu V/K$  at 6 mol% $TiB_2$ . Since  $TiB_2$  is a metallic conductor, the increase of the Seebeck coefficients cannot be explained by a simple mixture rule of  $B_4C$  and  $TiB_2$ . As described previously, the significant increase of  $\alpha$  was observed in the  $B_4C-SiC$  composites in which many twin boundaries have been frequently observed. The structural defects like twin boundaries might also affect the increase of the  $\alpha$  values in the  $B_4C-TiB_2$  composites.

The temperature dependence of electrical conductivity ( $\sigma$ ) of the  $B_4C-TiB_2$  composites is shown in Fig.15. The  $\sigma$  values of 2 mol% $TiB_2$  were about 10 times greater than those of

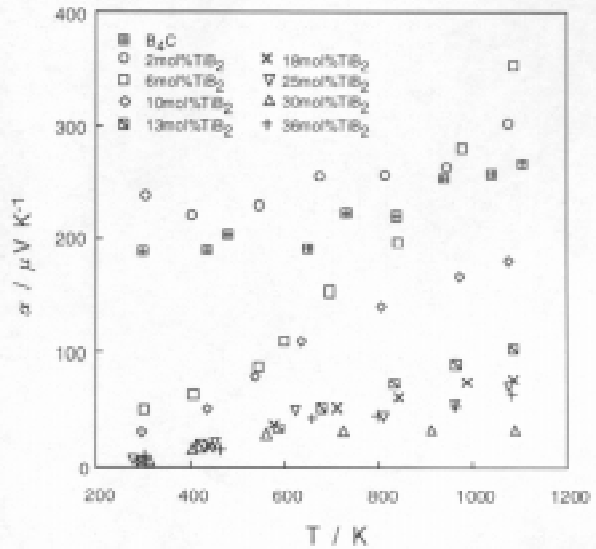


Fig.14: Temperature dependence of Seebeck coefficient ( $\alpha$ ) of  $B_4C-TiB_2$  composites.

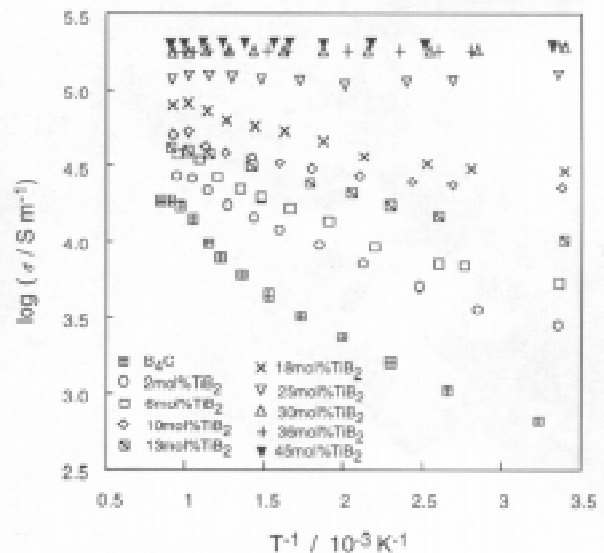


Fig.15: Temperature dependence of electrical conductivity ( $\sigma$ ) of  $B_4C-TiB_2$  composites.

$B_4C$  at room temperature. Since  $TiB_2$  phases are highly conductive, locally connecting  $TiB_2$  phases might contribute the increase of  $\sigma$  values. The structural defects (i.e., twin boundaries) may otherwise increase the  $\sigma$  as well as the case of  $B_4C$ -SiC composites. The temperature dependence of  $\sigma$  became almost independent of temperature at more than 20 mol% $TiB_2$  (near the eutectic composition).

Fig.16 shows the temperature dependence of thermal conductivity ( $\kappa$ ) of the  $B_4C$ - $TiB_2$  composites. In the  $TiB_2$  content range up to 6 mol% $TiB_2$ , the  $\kappa$  values are slightly smaller than those of  $B_4C$ . Since the  $\kappa$  value of  $TiB_2$  is 24 W/m K at room temperature [18], which is several times greater than that of  $B_4C$ , the decrease of  $\kappa$  is not explained by a simple mixture rule. The reason may be the scattering of phonons at the twin boundaries or  $B_4C$ / $TiB_2$  interfaces. At more than 6 mol% $TiB_2$ , the  $\kappa$  values increased with increasing  $TiB_2$  content. The temperature dependence of  $\kappa$  was significantly small like many amorphous materials.

Fig.17 represents the temperature dependence of the dimension-less figure-of-merit (ZT) of the  $B_4C$ - $TiB_2$  composites. The ZT values increased exponentially with increasing temperature. The specimens of 2 mol% $TiB_2$  and those of 6 mol% $TiB_2$  showed the greatest ZT values at less than 900K and at more than 1000K, respectively. The greatest ZT value obtained in the  $B_4C$ - $TiB_2$  composites at 1100K was 0.55. Fig.18 compares the ZT values of several boron-rich borides in literatures and present study. It can be understood that the  $B_4C$ - $TiB_2$  composites (6 mol% $TiB_2$ ) had almost the greatest values among the previously reported boron-rich borides [10].

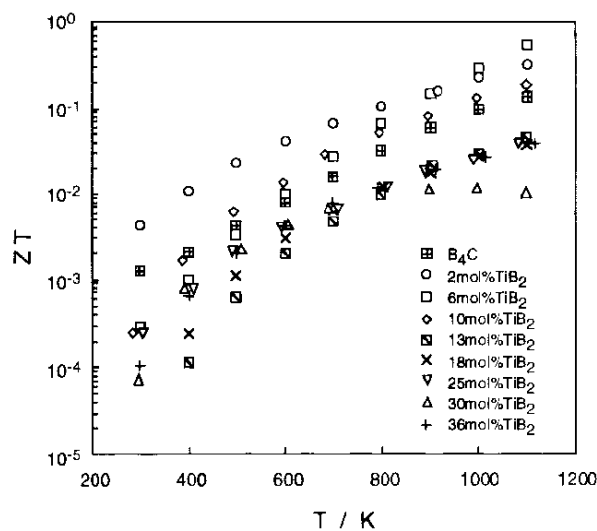


Fig.17: Temperature dependence of dimension-less figure-of-merit (ZT) of  $B_4C$ - $TiB_2$  composites.

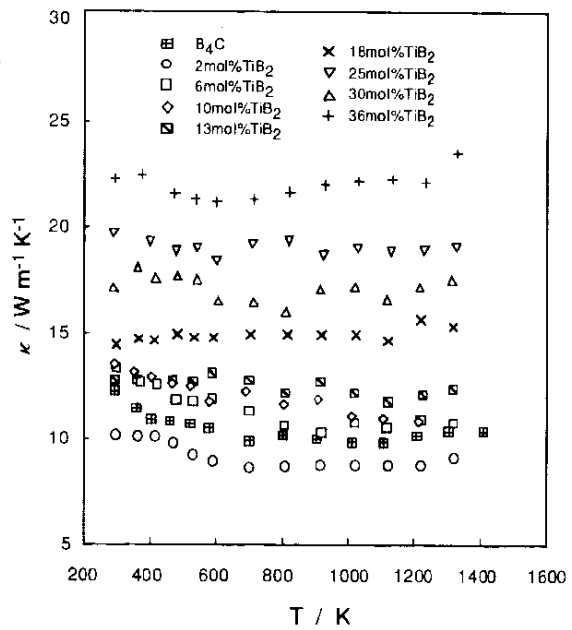


Fig.16: Temperature dependence of thermal conductivity ( $\kappa$ ) of  $B_4C$ - $TiB_2$  composites.

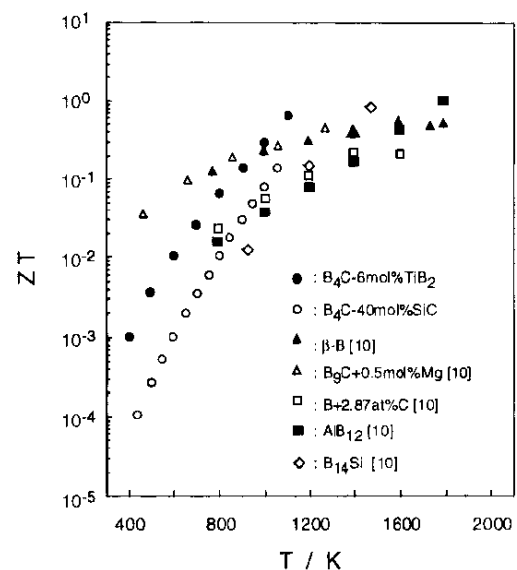


Fig.18: Comparison of dimension-less figure of merit (ZT) among several boron-rich borides.

## CONCLUSION

A wide ranged B-C system solid solutions and B<sub>4</sub>C-based composites were prepared by arc-melting. The B<sub>4</sub>C-SiC and B<sub>4</sub>C-TiB<sub>2</sub> systems were quasi-binary eutectic. The thermoelectric properties for these specimens were evaluated.

(1) The solid solutions of the B-C system ranged between 10 and 25 at%C. The Seebeck coefficient ( $\alpha$ ) and electrical conductivity ( $\sigma$ ) showed the maximum values at 20 at%C (B<sub>4</sub>C) and 17 at%C (B<sub>5</sub>C), respectively. The thermal conductivity ( $\kappa$ ) increased with increasing carbon content. The dimension-less figure-of-merit (ZT) showed the maximum values at 20 at%C; the greatest ZT value at 1100K was 0.15.

(2) The eutectic composition of the B<sub>4</sub>C-SiC system was 45 mol%SiC. The  $\alpha$  and  $\sigma$  of the B<sub>4</sub>C-SiC composites showed the maximum values at 40 mol%SiC (near the eutectic composition). The  $\kappa$  increased with increasing SiC content. The greatest ZT value at 1100K was 0.2 at 40 mol%SiC.

(3) The eutectic composition of the B<sub>4</sub>C-TiB<sub>2</sub> system was 25 mol%TiB<sub>2</sub>. The  $\alpha$  showed the maximum values at 2 to 6 mol%TiB<sub>2</sub>, and the  $\sigma$  and  $\kappa$  increased with increasing TiB<sub>2</sub> content at more than 6 mol%TiB<sub>2</sub>. The ZT showed the maximum values at 6 mol%TiB<sub>2</sub>. The greatest ZT value at 1100K was 0.55.

## ACKNOWLEDGMENTS

This research was supported in part by the Grant-in-Aid for Scientific Research from the Ministry of Education, Science and Culture under contact No. 06453081, also supported by the Special Coordination Funds for Promoting Science and Technology from the Science and Technology Agency of Japan.

## REFERENCES

1. Emin, D., "Electronic Transport in Boron Carbides", *Boron-rich Solids, AIP Conference Proceedings 140*, Emin, D., Aselage, T. L., Beckel, C. L., Howard, I. A. and Wood, C., Eds., American Institute of Physics, New York, 1985, pp. 189-205.
2. Aselage, T. L., Emin, D., Wood, C. and Mackinnon, I., "Anomalous Seebeck Coefficient in Boron Carbides", *Novel Refractory Semiconductors, Materials Research Society \ Symposium Proceedings, Vol. 97*, Emin, D., Aselage, T. L. and Wood, C., Eds., Materials Research Society, Pittsburgh, 1987, pp. 27-38.
3. Bouchacourt, M. and Thevenot, F., "The Correlation between the Thermoelectric Properties and Stoichiometry in the Boron Carbide Phase B<sub>4</sub>C-B<sub>10.5</sub>C", *J. Mater. Sci.*, Vol. 20, 1985, pp. 1237-1247.
4. Koumoto, K., Seki, T., Pai, C-H. and Yanagida, H., "CVD Synthesis and Thermoelectric Properties of Boron Carbide", *J. Ceram. Soc. Jpn.*, Vol. 100, No. 6, 1992, pp. 853-857.
5. Okamoto, Y., Aruga, A., Shioi, K., Morimoto, J., Miyakawa, T. and Fujimoto, S., "Thermoelectric Properties of B<sub>4</sub>C doped SiC", *Proceedings 12th International Conference on Thermoelectrics*, Matsuura, K., Ed., Institute Electrical Engineers Japan, Tokyo, 1994, pp.184-187.

6. Goto, T., Li, J., Hirai, T., Maeda, Y., Kato, R. and Maesono, A., "Seebeck Coefficient Measurements by AC Method for Thermoelectric Materials", *Proceedings fourth Asian Thermophysical Properties Conference, (ATPC'95)*, Nagashima, A., Ed., Tokyo, 1995, pp. 405-408.
7. Allen, R. D., "The Solid Solution Series, Boron-Boron Carbide", *J. Amer. Chem. Soc.*, Vol. 75, No. 7, 1953, pp. 3582-3583.
8. Bouchacourt, M. and Thevenot, F., "The Properties and Structure of the Boron Carbide Phase", *J. Less-Common. Met.*, Vol. 82, 1981, pp. 227-235.
9. Glaser, F. W., Moskowitz, D. and Post, B., "An Investigation of Boron Carbide", *J. Appl. Phys.*, Vol. 24, No. 6, 1953, pp. 731-733.
10. Wood, C., "Refractory Semiconductors for High Temperature Thermoelectric Energy Conversion", in Ref. 2, pp. 335-346.
11. Emin, D., "Icosahedral Boron-rich Solids as Refractory Semiconductors", in Ref. 2, pp. 3-25.
12. Goto, T., Li, J. and Hirai, T., "Preparation of W-B-C System Composites by Arc Melting and their Thermoelectric Properties", *J. Jpn. Soc. Powder and Powder Metallurgy*, Vol. 42, No. 12, 1995, pp. 1406-1410.
13. Schouler, M. C., Ducarroir, M. and Bernard, C., "Mise au Point sur la Topographie et les Proprietes des Systemes Metal-Carbone-Azote (M-C-N) et Metal-Carbone-Bore (M-C-B)", *Rev. Int. Hautes Temper. Refract. Fr.*, Vol. 20, 1983, pp. 261-311.
14. Vodakov, Yu. A. and Mokhov, E. N., "Diffusion and Solubility of Impurities in Silicon Carbide", *Silicon Carbide-1973*, Marshall, R. C., Faust, Jr., J. W. and Ryan, C. E., Eds., University of South Carolina Press, Columbia, 1974, pp. 508-519.
15. Koumoto, K., Shimohigoshi, M., Takeda, S. and Yanagida, H., "Microstructure and Thermoelectric Energy Conversion in Porous SiC Ceramics", *Silicon Carbide '87, Ceramic Transactions Vol. 2*, Cawley, J. D. and Semler, C. E., Eds., American Ceramic Society, Westerville, 1989, pp. 501-510.
16. Moss, M., "Thermal Conductivity of Boron Carbides", in Ref. 2, pp. 77-82.
17. MacLeod, A. D., Haggerty, J. S. and Sadoway, D. R., "Electrical Resistivities of Monocrystalline and Polycrystalline  $TiB_2$ ", *J. Amer. Ceram. Soc.*, Vol. 67, No. 11, 1984, pp. 705-708.
18. Pierson, H. O. and Randrich, E., "The Coating of Metals with Titanium Diboride by Chemical Vapor Deposition", *Proceedings sixth International Conference Chemical Vapor Deposition*, Donaghey, L. F., Rai-Choudhury, P., Tauber, R. N., Eds., Electrochemical Society, Princeton, 1977, pp. 304-317.

# FORMATION AND CHARACTERISATION OF FIBRE-MATRIX INTERFACES IN CONTINUOUS FIBRE REINFORCED SILICON CARBIDE

Pamela M. Farries and Jean-Bernard Veyret

*European Commission, Joint Research Centre, Institute for Advanced Materials,  
PO Box 2, 1755 ZG Petten, The Netherlands.*

**SUMMARY:** The effect of processing conditions on interface formation in a fibre reinforced silicon carbide composite was investigated through infiltration of a uni-directional lay-up of pitch-based carbon fibres with an aqueous ceramic powder suspension and subsequent consolidation at high temperature. Interface formation by a conventional method - the attempted preservation of a pyrolytic carbon coating applied to the fibres by CVD - is contrasted to an *in-situ* method, involving the exploitation of the migration of yttria (included with the SiC powder along with alumina as sintering aids) to the fibre-matrix interface by hot-pressing at temperatures of 1750 and 1800°C in an ambient argon atmosphere and sintering without mechanical pressure at 1850°C in an argon atmosphere. Basic indications of mechanical properties determined from 4-point bending tests at room temperature are included. Early indications are that fibre degradation is inhibited in hot-pressing producing an interface which can debond.

**KEYWORDS:** silicon carbide, interfaces, fibres, liquid phase sintering, hot-pressing, YAG (yttrium aluminium garnet)

## INTRODUCTION

Commissioning of long fibre reinforced ceramics into industrial service is becoming an achievable goal as properties are improved to meet target requirements, but this success simultaneously shifts emphasis for improvement towards the cost of producing a composite of consistent high quality. Consolidation methods without applied mechanical pressure are being investigated, however, process development is still constrained by the need to create or preserve a pre-designed fibre-matrix interface architecture, often generated by complex and expensive fibre coatings, during the very high temperature consolidation cycle. These two constraints are inextricably linked and serious process developments can be made only by considering the implications to interface structure and chemistry throughout production and service.

Carbon and boron nitride are the most common choices of material which satisfy the required criteria for debonding and controlled sliding at the fibre/matrix interface of silicon carbide based CMC's, so imparting a degree of toughness to a material comprising two brittle components. Both C and BN are susceptible to oxidation and in systems using SiC fibres, the gap left by the removal of the interphase is filled by a silicate layer produced from the oxidation of the fibre which does not satisfy the debonding and sliding requirements [1]. This is unfortunate when the layer was produced *in-situ* during composite production, such as in

the case of Nicalon reinforced lithium aluminium silicate (LAS) glass, but is a much more serious concern when the interface was deliberately deposited. The move towards oxide-oxide composite systems has prompted investigation of porous oxide and refractory metal coatings [2]. Sputter deposited yttria coatings have been utilised in metal matrix composites to protect SiC monofilaments from reaction with an Mg-Li alloy[3]. Combining the metal matrix and oxide-oxide composite experience with the observations that alumina and yttria sintering aids in silicon carbide have a propensity to migrate to free surfaces at high temperatures [4-7] and alumina is observed to evaporate at high processing temperatures [4,6] presents the possibility of a novel mechanism for the production of a compatible oxide interface during the processing and use of a SiC/SiC composite which may be investigated in tandem with existing methods [8].

## EXPERIMENTAL PROCEDURE

The conditions necessary for production of a silicon carbide matrix composite, reinforced with pitch-based carbon fibre by infiltration of a uni-directional lay-up with an aqueous ceramic powder suspension containing silicon carbide and the liquid phase forming additives alumina and yttria, and consolidation by hot-pressing are investigated, with the eventual aim of including Hi-Nicalon silicon carbide fibre. The interfaces produced when composite samples are densified with and without the application of mechanical pressure are compared through EDX analysis and a first indication of mechanical properties obtained from four point bending. Background to the chemical and physical development of the interface during processing is provided from the results of an extensive study into the effects of varying alumina and yttria additive concentration, sintering temperature, hold time and sintering environment on the density, microstructure and chemical composition of free sintered silicon carbide [8]. The effect of these sintering variables on free sintered tows of un-coated and pyrolytic carbon coated carbon fibres are also detailed.

### Sample Preparation

Monolithic silicon carbide samples were prepared from  $\alpha$ -SiC powder with a mean particle diameter of 0.6 $\mu$ m - UF-15 from H.C. Starck - by pressure filtration of an aqueous powder suspension (optimised at 47vol% powder using information obtained with Matec™ Applied Sciences, Electrokinetic Sonic Analysis System) dispersed using an ultrasonic probe. Alumina (Baco RA 207LS Grade) and yttria (H.C. Starck Fine Grade) were added in the 3:5 (alumina:yttria) YAG molar ratio and their combined mass was either 3 or 9wt% of the total powder, Table 1. Amoco P25 pitch based carbon fibre was dipped as tows into the slurries used for monolith production and wound as 1D lay ups for composite casting from a slurry of composition B containing a reduced volume of solids (40%) and a small amount of wetting agent to allow complete infiltration.

*Table 1: Sample compositions and theoretical densities (TD)*

Composition	Sintering aid content (Al <sub>2</sub> O <sub>3</sub> +Y <sub>2</sub> O <sub>3</sub> ) wt%	Molar % Y <sub>2</sub> O <sub>3</sub> in mix	Theoretical Density g/cm <sup>3</sup> (rule of mixtures)
A	9	62.5	3.30
B	3	62.5	3.24



## Densification

Composite samples were hot-pressed at 1750 and 1800°C in an ambient argon atmosphere. Mechanical pressure of 27MPa was applied incrementally beginning when the temperature reached 1500°C and reaching its maximum at the peak sintering temperature. Thereafter both temperature and pressure were maintained at maximum for 60 minutes. Heating and cooling temperature ramps were set at 10°/min.

Pressureless sintering was carried out in a graphite resistance furnace at temperatures between 1750 and 1900°C under 10bar argon pressure for hold times of up to 120 minutes in a closed graphite crucible. Sample-crucible contact was prevented by the use of the minimum amount of coarse SiC powder required, except in the case where and sinter bed containing 1.33wt% alumina (indicated in Table 2) was used.

Table 2: Pressureless densification conditions

Temperature (°C) Hold Time (mins)	1750	1800	1850	1900
30			A, B, fibre+B	
60			A, B, Composite	
120	A, B	A, B, fibre+A	A, B, fibre+A, fibre+B, coated fibre+B	A, B, fibre+A, fibre+B, coated fibre+B
120 alumina bed			A, B	

## Analysis

Monolithic samples were subjected to phase analysis by X-ray diffraction (XRD), aluminium and yttrium content analysis by atomic absorption spectroscopy and density measurement by mercury immersion. Linear shrinkage and mass loss during sintering were also determined for these samples. All samples were examined by scanning electron microscopy (SEM) and the composite hot-pressed at the lower temperature tested in 4-point bending.

## RESULTS AND DISCUSSION

### Monolithic Silicon Carbide Densification

The peak density achieved when sintering without a sinter bed was 2.97g/cm<sup>3</sup> or 90% of the theoretical density (TD) for samples of composition A sintered at 1900°C. The samples sintered for 120 minutes all showed a markedly improved final density figure when sintered at temperatures above 1850°C, when shrinkage values were correspondingly greater, as too were mass loss figures. Atomic absorption spectroscopy revealed, however, that up to half of the

aluminium originally added was being lost from the samples of composition A sintered at 1900°C along with approximately 20% of the yttrium [8], this observation being backed up by the detection of an yttria rich phase in XRD ( $2Y_2O_3:Al_2O_3$  as opposed to the expected YAG phase  $3Y_2O_3:5Al_2O_3$ ) indicating that a shift in the composition of the liquid phase had occurred. The holding time at peak temperature was reduced in an attempt to minimise alumina volatilisation and mass loss, Fig. 1.

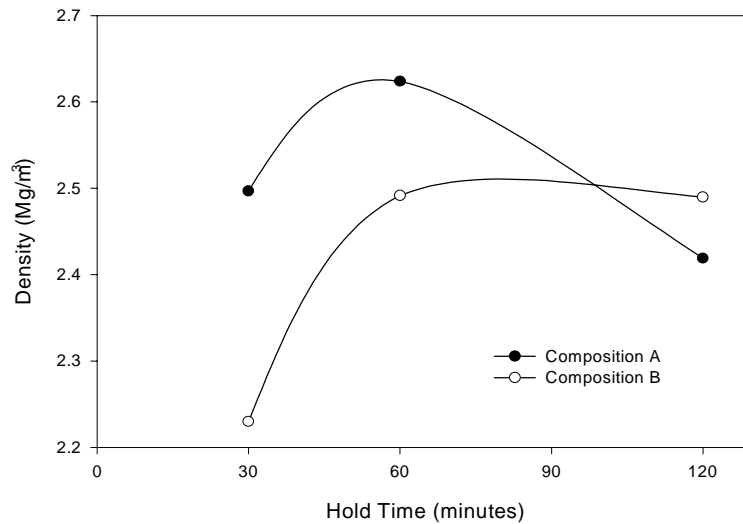


Figure 1: Density variation of monolithic SiC with hold time at 1850°C

Trends projected from sintering carried out at 1850°C for 30, 60 and 120 minutes, suggested that the maximum density for composition A would be achieved at this temperature from a high temperature hold of 45 to 60 minutes in length, while for composition B the optimum soak time is around 90 minutes. Prolonged holds are damaging for both compositions. The increased density drop for the samples containing larger amounts of alumina (and hence having the capacity to lose a larger proportion of their mass) held for 120 minutes at high temperature proves the influence of time on alumina volatilisation. Mass losses are reduced significantly with a sintering hold time of 30 minutes but densification is no longer satisfactory.

Addition of 1.33wt% alumina to a sinter bed of coarse silicon carbide resulted in the highest density figure achieved - 92.4% TD for a sample of composition A for a two hour hold at 1850°C. Calculating the density increase as a percentage of the original green density of the sample provides a convenient method for monitoring densification efficiency under different conditions, while neutralising the effect of any variation in green density, Fig. 2.

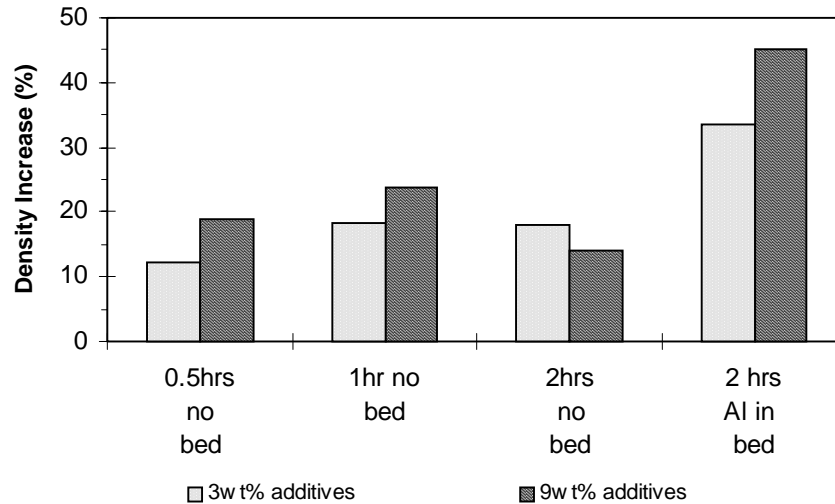


Figure 2: Effect of alumina on densification efficiency at a sintering temperature of 1850°C

As also demonstrated in Fig. 1, a hold time of 60 minutes at temperature produces a greater density increase than a 120 minute hold, Fig. 2, the effect being especially noticeable for samples containing 9wt% which under these circumstances achieve a smaller density increase than samples containing 3wt% additives, again demonstrating the volatility of the sintering additions. This order is reversed when a sinter bed containing alumina surrounds the samples, presumably preventing the evaporation of alumina and emission of carbon dioxide produced on its reaction with SiC [5], and allowing the full benefit of an increased volume of liquid phase to be realised.

## Microstructural Observations

### *Monolithic Silicon Carbide*

Silicon carbide was seen to densify leaving only isolated porosity at temperatures of 1850°C and above where the hold time was at least 60 minutes. Samples of composition B sintered for a shorter time or at lower temperature were dense only in a region extending 0.5mm from the surface (overall dimensions, 15 x 15 x 5 mm) seeming to indicate densification occurring from outside inward. When viewed in back scattered mode, the 1850 and 1900°C samples sintered for 120 minutes show an unusual distribution of light contrast areas, Fig 3(a), shown to be rich in yttrium through Energy Dispersive X-ray analysis (EDX), the contrast effect being associated with yttrium's high atomic number. The central zone at the top of the micrograph contains a few widely spaced areas of the yttrium rich material up to 100µm in length. The outer zone contains a more even dispersion of small areas rich in yttrium. The effect was not seen for any composition A samples sintered at temperatures lower than 1850°C, for a hold time shorter than 120 minutes or for any of the composition B samples. Combination of these observations suggest that densification occurs from the surface to the centre and when the hold time is long enough and temperature high enough, the excess of a high yttrium content second phase begins to segregate out, possibly to flaws and grain boundaries.

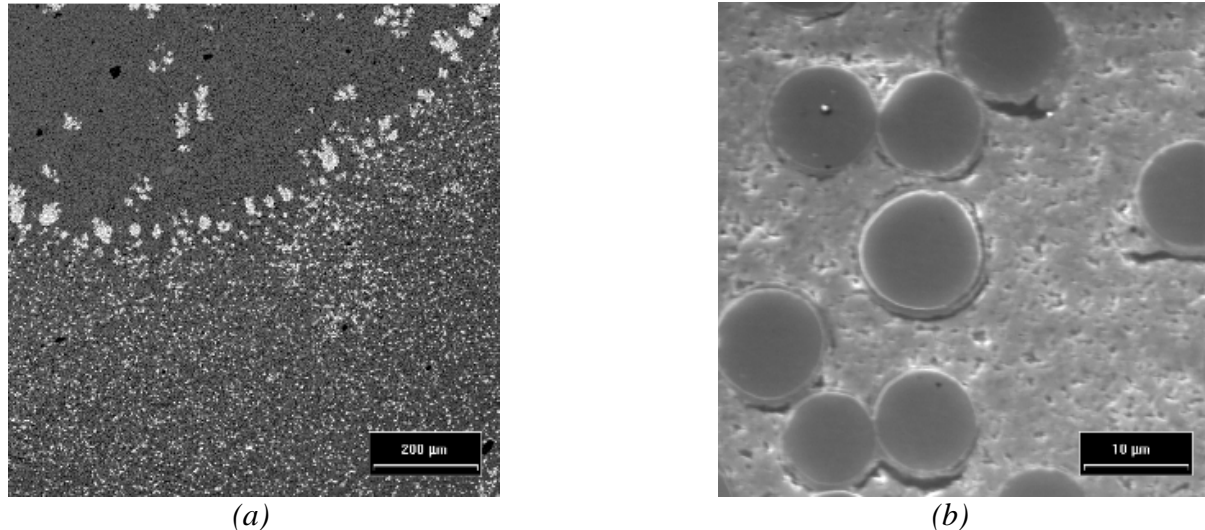


Figure 3: (a) SiC monolith containing 9wt% alumina and yttria in the YAG ratio sintered for 120 minutes at 1850°C (b) Carbon coated fibre and SiC+3wt% YAG sintered for 120 minutes at 1850°C

Examination of samples sintered in an alumina containing bed at 1850°C showed microstructures similar to those sintered without bedding powder at 1950°C but without the light contrast areas of yttria rich material.

#### *Fibre Tows*

Of the fibre tows sintered alongside the monolithic samples, the carbon coated fibre showed the most interesting behaviour. Tows dipped in slurry of composition B and sintered for 120 minutes at 1850°C did not appear to be badly damaged and the area previously occupied by the pyrolytic carbon coating is now filled with an yttrium rich phase, Fig. 3(b). Uncoated fibres sintered under the same conditions were slightly degraded by the matrix Carbon coated fibre dipped in slurry containing 9wt% additives showed yttrium ingress well into the body of the fibre [8]. Fig. 3(b) appears to illustrate that at lower temperatures and with less oxide additives the pyrolytic carbon layer is consumed sacrificially and the an yttrium rich interphase subsequently forms.

#### **Composite Properties**

Composite green bodies were manufactured with a fibre volume fraction designed to rise to 35% on densification of the matrix. Initial hot-pressing at 1750°C, judged to be the lower temperature limit for feasible densification of the matrix and coinciding with the lowest temperature applied in the pressureless sintering study, produced a composite with only 80% TD and a correspondingly low volume fraction of fibres - 27vol%. This was reflected in the mechanical properties of the material, the failure stress reaching a maximum of 200MPa in 4-point bending. Sonic resonance measurements however indicated a Young's modulus of around 170GPa, not significantly lower than the value predicted by the rule of mixtures. Hot-pressing at 1800°C produced a composite of 98% TD which has yet to be analysed.

Examination of the fracture surfaces of the bend tested material hot-pressed at 1750°C and cross-sections of this and a similarly prepared green body sintered with out pressure

application at 1850°C in a 10 bar argon atmosphere, give reason for optimism regarding interface formation, even with this uncoated fibre.

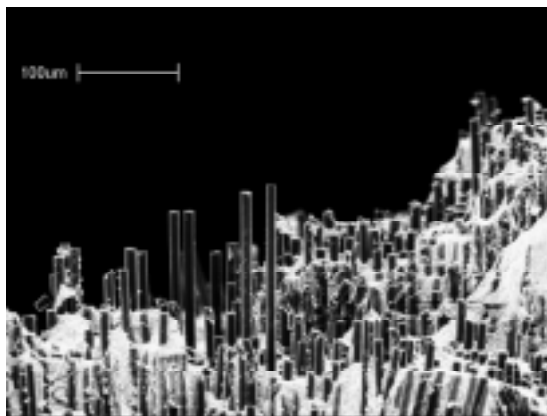


*Figure 4: Fibre pull-out on 4-point bend specimen - un-coated P25 fibre, hot-pressed at 1750°C, 3wt% sintering additives*

Clean fibre surfaces pulled up to 150µm out of the fibre surface are shown in figure 4 indicating surprisingly little fibre damage. Cross sections prepared to allow analysis of the fibre matrix interface confirm the assertion.

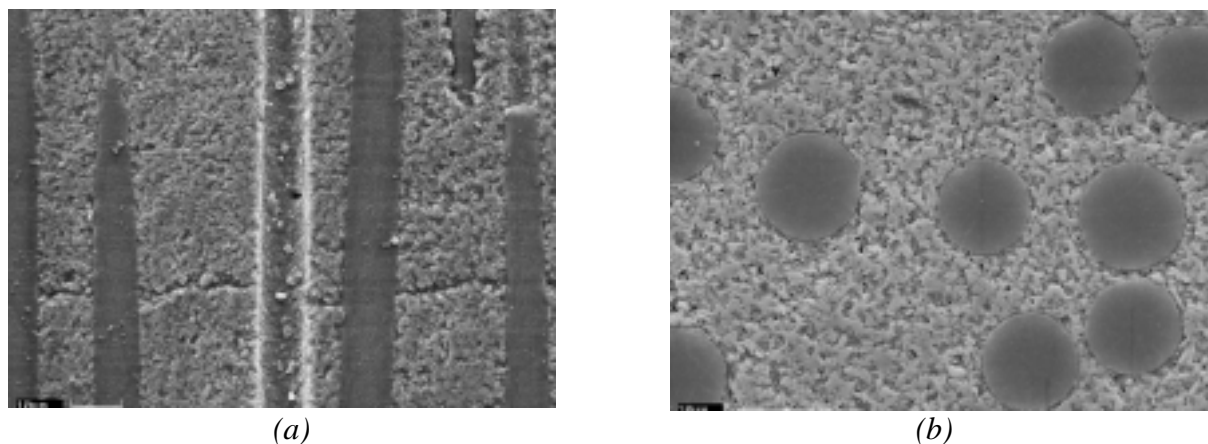


*Figure 5: (a) Longitudinal section of material hot-pressed at 1750°C (b) Cross section of composite free sintered at 1850°C, both reinforced with un-coated fibre*

EDX spot analysis on the cross section shown in Fig 5(a) showed no significant trace of silicon in the fibre centre, indicating that the fibres are being protected from reaction with the oxide additives by the high pressure exerted during hot-pressing. No significant concentrations of alumina or yttria were observed in the sample. The matrix of the free sintered sample (Fig. 5(b)) is much more porous than that of the hot-pressed sample, but the fibres still retain complete integrity of form even at the very high processing temperature and without the benefit of applied mechanical pressure to inhibit reactions. A stronger silicon signal is detected in these fibres but the presence of a significant carbon peak indicates that the phase is far from SiC in composition. When carbon and silicon are present in equal quantities the strong silicon signal swamps the peak due to carbon. The darker amorphous annulus visible around these fibres is found to be rich in yttrium and to contain some aluminium.

## CONCLUSIONS

Pressureless liquid phase sintering of silicon carbide with additions of  $\text{Al}_2\text{O}_3$  and  $\text{Y}_2\text{O}_3$  was carried out successfully at temperatures at and above  $1850^\circ\text{C}$ . Placing samples in an alumina containing silicon carbide sinter bed further improved densification and inhibited the loss of alumina from the sample and migration of the liquid phase.

The application of mechanical pressure did not lower the temperature required for SiC densification as far as expected, but processing at  $1750^\circ\text{C}$  did produce a composite with a fibre matrix interface capable of debonding.

Yttria rich material is seen at the fibre matrix interface in composites densified by pressureless means, but this migration appears to be hindered by the application of mechanical pressure in hot-pressing.

## ACKNOWLEDGEMENTS

This work was carried out under the Fourth Framework Programme of the European Commission and the principal author is grateful to The European Commission for the provision of a fellowship under the Human Capital and Mobility Programme.

## REFERENCES

1. Thouless, M.D., Sbaizero, O. and Evans, A.G., "Effect of Interface Mechanical Properties on Pullout in a SiC-Fiber-Reinforced Lithium Aluminium Silicate Glass-Ceramic", *Journal of the American Ceramic Society*, Vol. 72, No. 4, 1989, pp.525-32.
2. Davis, J.B., Löfvander, J.P.A. and Evans, A.G., "Fiber Coating Concepts for Brittle-Matrix Composites", *Journal of the American Ceramic Society*, Vol. 76, No. 5, 1995, pp.1249-57.
3. Kieschke, R.R., Warwick, C.M. and Clyne, T.W., "Sputter Deposited Barrier Coatings on SiC Monofilaments for use in Reactive Metal Matrices - III. Microstructural Stability in Composites Based on Magnesium and Titanium", *Acta. metallurgica et materialia*, Vol. 39, No. 4, 1991, pp.445-452.
4. Kerber, A. and Velken, S.V., "Liquid Phase Sintered Silicon Carbide: Production Properties and Possible Applications", *Proceedings of the Fourth European Ceramic Society Conference*, Riccione, Italy, October 2-6, 1995, Vol. 2: Developments in Processing of Advanced Ceramics - II, Galassi, C., Ed, pp.177-184.
5. Mulla, M.A. and Krstic V.D., "Low-Temperature Pressureless Sintering of  $\beta$ -Silicon Carbide with Aluminium Oxide and Yttrium Oxide Additions", *Ceramic Bulletin*, Vol. 70, No. 3, 1991, pp.439-442.
6. Kahlman, L., Rundgren, K., Lidén, E., Nyberg, B. and Calström. E., "Processing of Liquid Phase Sintered SiC - Mechanical and Wear Properties", *Proceedings of the Third European Ceramic Society Conference*, Madrid, Spain, September 12-17, 1993, Vol. 3: Engineering Ceramics, Duran, P. and Fernandez, J.F., Eds., pp.477-482.
7. Kostic, E., "Sintering of Silicon Carbide in the Presence of Oxide Additives" *Powder Metallurgy International*, Vol. 20, No. 6, 1988, pp.28-29.
8. Farries, P.M., Veyret, J-B. and Rawlings, R.D., "Fibre Reinforced Silicon Carbide: Effect of Densification Method and Parameters", *Key Engineering Materials*, Vols. 127-131, 1997, pp.295-302.

# STRUCTURAL ANALYSIS OF CERAMIC-MATRIX COMPOSITES

Alain Burr<sup>1</sup>, Francois Hild<sup>1</sup>, Frederick A. Leckie<sup>2</sup>

<sup>1</sup>*Laboratoire de Mécanique et Technologie, E.N.S. de Cachan, C.N.R.S. , Université Paris 6*

<sup>2</sup>*Department of Mechanical and Environmental Engineering  
College of Engineering, University of California, Santa Barbara, CA 93106*

**SUMMARY:** A constitutive law is proposed for Ceramic–Matrix Composites which models matrix–cracking, sliding, fiber–breakage, and fiber pull–out. These different mechanisms induce loss of stiffness, inelastic strains, hysteresis loops, and crack closure. The features are analyzed within the framework of Continuum Damage Mechanics by the introduction of physical internal variables identified previously in material science investigations. The procedure is applied to a SiC/SiC [0/90] laminate. The description is applied to some structural problems including a plate in tension penetrated by a hole and subjected to tension and the Iosipesco specimen subjected to shear. It is observed that the SiC/SiC has the ability to redistribute stress so that the presence of stress concentrations does not compromise the performance of the component.

**KEYWORDS:** ceramic-matrix composite, matrix cracking, stress redistribution

## INTRODUCTION

Composites consisting of a ceramic matrix reinforced by continuous ceramic fibers (CMC) are candidates for application in components which operate at temperatures in excess of those which are normal for metallic structures. In spite of the fact that the constituents of the CMC are both brittle it has been demonstrated by Aveston et al. [1971] that following matrix–cracking, sliding occurs at the fiber–matrix interface which causes inelastic deformations. The presence of matrix cracks and inelastic deformations may impart to the material the ability to redistribute stresses. The ability to redistribute stress is an important property since design studies indicate that working stresses for CMC components are sufficiently high for matrix–cracking to be unavoidable in regions of stress concentration occurring at the junctions and penetrations which are a feature of engineering components.

The intention then of the present study is to develop a continuum description of the damage processes which is mechanism–based and which may be used to describe the behavior of Ceramic–Matrix Composites (CMCs) under the conditions of multiaxial stress occurring in practice. Since crack spacing at saturation is small [Beyerley et al., 1992] in most CMCs, Continuum Damage Mechanics is an appropriate means of describing degradation since changes in elastic moduli measured on a macroscopic level provide a simpler and more robust means of measuring damage than does microscopic measurement of crack density, which requires the average of many readings before reliable values are established [Jansson & Leckie, 1993].

By combining Continuum Damage Mechanics (CDM) [Lemaitre, 1992] with micromechanical studies which are mechanism-based constitutive equations are developed which lend themselves to the finite element procedures commonly used in practice. The CDM formulation applied to reinforced composites is written within the framework of the Thermodynamics of Irreversible Processes [Coleman & Gurtin, 1967; Rice, 1971; Germain et al., 1983]. The first step in establishing such a model is to identify the internal variables which define the state of the material. The second is to determine the expression of the state potential in terms of the state variables and the third one to define the evolution laws of the internal variables.

The model is integrated into a finite element system (ABAQUS) and is used to estimate the behavior of a beam subjected to four point bending and a plate subjected to tensile stress which has been penetrated by a hole. The calculations have been performed using data for a SiC/SiC.

### THE TENSILE STRESS–STRAIN RELATIONSHIP FOR UNIDIRECTIONAL CMCS

The results of loading / partial unloading tensile tests on SiC/SiC composites have the form shown in Fig 1. Compared to the initial elastic modulus the unloading modulus is substantially less. Plastic straining is also observed but the magnitude is usually quite modest. Post-mortem analyses of broken specimens indicate the presence of arrays of microcracks in the matrix which are accompanied by debonding and friction at the fiber–matrix interface. Matrix–cracking is responsible for the decrease of stiffness observed in experiments on CMCS and release of residual stresses due to processing, and sliding at the fiber–matrix interface is the source of irreversible deformation.

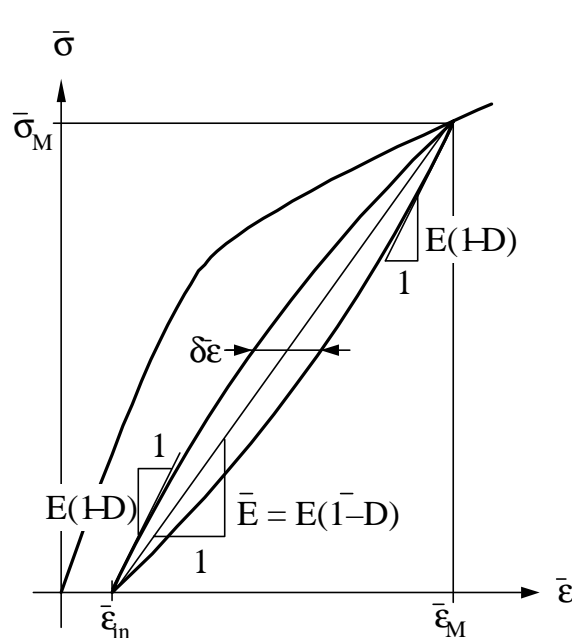


Fig 1 Typical Stress/Strain

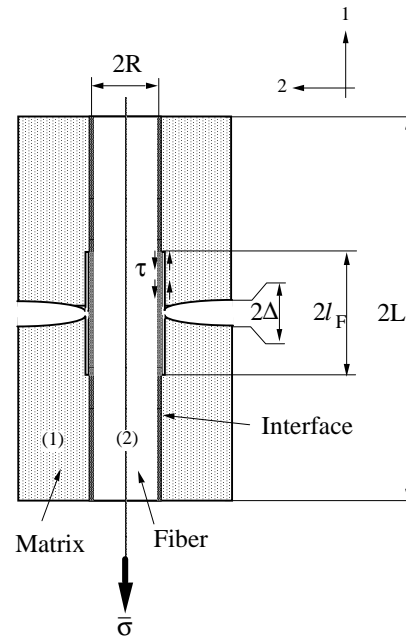


Fig 2 Unit Cell

The cell model illustrated in Fig. 2 was first proposed by Aveston and Kelly (1971). In the unit cell shown in Fig. 2 the elastic moduli of the fiber and matrix are  $E_f$  and  $E_m$ , respectively, the volume fraction of the fiber is  $f$  and  $R_f$  is the fiber radius. The elastic modulus of the



undamaged composite is  $E = f E_f + (1-f) E_m$  and average distance between cracks is denoted by  $2L$ . The debond length at the fiber/matrix interface is  $2l_d$ , and the interface is assumed to have a constant shear strength  $\tau$  whose value is unknown at this stage. Residual stresses are introduced during processing so that the residual stresses  $\rho$  in the matrix is an additional unknown.

If the initial behavior of the elementary cell is isotropic and elastic, and Young's modulus is  $E$ , it can be shown that the stiffness loss depends on the crack density defined as  $\pi a^2 / 4LW$  where  $W$  is the width of the element. By assuming plane stress conditions, and that the crack interactions can be neglected, a first approximation for the reduced elastic modulus  $\tilde{E}$  can be written as

$$\frac{\tilde{E}}{E} = \frac{1}{1 + 2 \frac{\pi a^2}{4LW}}$$

This relationship can be recast in the framework of CDM as

$$\frac{\tilde{E}}{E} = 1 - D$$

where

$$(1) \quad D = \frac{2 \frac{\pi a^2}{4LW}}{1 + 2 \frac{\pi a^2}{4LW}}$$

is the damage variable associated with the crack density. When  $D$  is small, a first order solution to Eq. (1) is given by

$$D \approx 2 \frac{\pi a^2}{4LW}$$

so that the damage variable is proportional to the crack density.

The internal elastic energy density in the unit cell [Hild et al., 1996] can be found by using the two step approach introduced by Volterra [1907]. The first step is to calculate the contribution of debonding and sliding at the interface using the 'cut and paste' approach in which the unbroken part (2) is moved with respect to the broken part (1) by an amount  $\Delta_s$  over a length  $l_F$  (Fig3). Because of interfacial sliding, this displacement  $\Delta_s$  gives rise to a self-balanced linear stress field along a length  $l_F$  in parts (1) and (2) when the interfacial behavior is assumed to be characterized by a constant shear strength. By integration over  $l_F$  and then averaging over the total length  $L$ , the elastic energy density associated with this process is given by

$$\psi^s = \frac{2}{3} \frac{fE_1(1-f)E_2}{E} \left\{ \frac{\Delta_s}{l_F} \right\}^2 \frac{l_F}{L}$$

The crack opening displacement  $\Delta_s$  due to slip induces an irreversible or inelastic strain  $\alpha$  expressed as

$$\alpha = \frac{fE_1}{E} \frac{\Delta_s}{L}$$

The second step consists of an elastic loading of the damaged system so that the elastic energy density is given by

$$(2) \quad \psi^e = \frac{1}{2} E (1-D) (\bar{\epsilon} - \alpha)^2$$

where the current elastic modulus is  $E (1-D)$ .

The total elastic energy density is then the sum of the two elements of the energy densities so that

$$(3) \quad \psi = \frac{1}{2} E (1-D) (\bar{\epsilon} - \alpha)^2 + \frac{2}{3} \frac{fE_1(1-f)E_2}{E} \left\{ \frac{\Delta_s}{l_F} \right\}^2 \frac{l_F}{L}$$

For convenience the energy density can be expressed in a more compact form by using state variables which are the total strain  $\bar{\epsilon}$ , the damage variable  $D$  modeling the loss of stiffness due to the cracking mechanism, the inelastic strain  $\alpha$  derived previously, and the damage variable  $d = 3fE_1 l_F/4(1-f)E_2$  which defines the size of the slip zone related to the average crack spacing. The elastic energy density in terms of the new internal variables is [Hild et al., 1996]

$$(3) \quad \psi = \frac{1}{2} E (1-D) (\bar{\epsilon} - \alpha)^2 + \frac{1}{2} E \left( \frac{\alpha^2}{d} \right)$$

The forces associated with the state variables  $(\bar{\epsilon}, D, d, \alpha)$  are respectively given by

$$(4.1) \quad \bar{\sigma} = \frac{\partial \psi}{\partial \bar{\epsilon}} = E (1-D) (\bar{\epsilon} - \alpha)$$

$$(4.2) \quad Y = -\frac{\partial \psi}{\partial D} = \frac{E}{2} (\bar{\epsilon} - \alpha)^2$$

$$(4.3) \quad y = -\frac{\partial \psi}{\partial d} = \frac{E}{2} \left( \frac{\alpha}{d} \right)^2$$

$$(4.4) \quad X = \frac{\partial \psi}{\partial \alpha} = -\bar{\sigma} + E \frac{\alpha}{d}$$

The associated forces are used to define the relevant forces driving each mechanism. Matrix cracking is assumed to be driven by  $Y$ , which plays an identical role as the energy release rate  $G$  in the framework of Linear Elastic Fracture Mechanics. From a micromechanical analysis [Hild et al., 1996], it can be shown that the back-stress is dependent on the applied stress  $\bar{\sigma}$ . therefore the driving force of the inelastic strains can be taken as the stresses acting in the same direction. The same assumption can be made when the evolution of the damage variable  $d$  related to sliding is analyzed, i.e. the driving force of  $d$  can be chosen to be its associated force  $y$ , or the applied stress  $\bar{\sigma}$ .

In the present approach the growth laws of the internal variables ( $D, d, \alpha$ ) are established from macroscopic quantities measured in the course of unloading and reloading sequences. To this end use is made of the solution of the response of the unit cell (Fig. 2) when subjected to an unloading/reloading sequence during which the magnitude of the shear stress remains constant.

The expressions obtained from the analysis for the residual stress  $\rho_1$  and the internal variables  $D, d, \alpha$  in terms of the macroscopic quantities shown in Fig. 1 are given respectively by [Hild et al., 1996]

$$(5.1) \quad \frac{-\rho_1}{E} = \left( \sqrt{\frac{\bar{\epsilon}_{in} + 2\delta\bar{\epsilon}}{4\delta\bar{\epsilon}}} - 1 \right) (\bar{\epsilon}_M - \bar{\epsilon}_{in} - 2\delta\bar{\epsilon})$$

$$(5.2) \quad D = \frac{\bar{\epsilon}_M \bar{D} - \bar{\epsilon}_{in} \bar{D} - 2\delta\bar{\epsilon}}{\bar{\epsilon}_M - \bar{\epsilon}_{in} - 2\delta\bar{\epsilon}}$$

$$(5.3) \quad \frac{d}{4} = \frac{\sqrt{(\bar{\epsilon}_{in} + 2\delta\bar{\epsilon})\delta\bar{\epsilon}}}{\bar{\epsilon}_M - \bar{\epsilon}_{in} - 2\delta\bar{\epsilon}}$$

$$(5.4) \quad \alpha = \frac{d}{2} \frac{\bar{\sigma}_M - \rho_1(1-D)}{E(1-D)}$$

where  $-\rho_1 E_1 / E$  is the residual stress in the broken layer (1). Equations (5) are only valid when a constant shear strength characterizes the interfacial behavior, and lastly Eqn. (5.4) is only valid for monotonic loading conditions.

By performing a series of unloading/reloading sequences the internal variables can be determined from experiment using Eqns (5). The residual stress  $\rho_1$  is calculated from Eqn. (5.1) and it is a test of the effectiveness of the model that the same value of the residual stress is obtained for each loading sequence. The values of  $D$  and  $d$  are given by applying Eqns (5.2) and (5.3) respectively. The information is now available to complete the calculation for Eqn. (5.4). The corresponding associated forces are obtained by the expressions given in Eqns. (4). The relationship between the internal variables and the associated forces can then be

investigated by knowing the driving forces of each state variable. It is this method which is proposed to model the behavior of CMC laminates.

### CMCS WITH MULTIDIRECTIONAL FIBER SYSTEMS

The one-dimensional investigation can be extended to a [0/90] laminate composite and to a [0/90] woven composite subjected to multiaxial plane stress states by establishing first the properties of each layer and then using laminate analysis.

The components of each layer consist of the matrix, the fiber and the interface, with  $f$  being the fiber volume fraction. The fiber direction defines the 1–2 axes. The axes  $x$ – $y$  correspond to the principal axes of the strains in the ceramic matrix. The definition of the axes used at the constituent, layer and composite levels are shown in Fig. 4. For the case of a 0/90 symmetric layup Burr et al (1996) have established that the free energy has the expression

$$(6) \quad \psi = \frac{1}{2} (\underline{\underline{\epsilon}} - \underline{\underline{\alpha}}) : \underline{\underline{E}}(D_{my}^{00}, D_{my}^{90}, D_{fl}^{00}, D_{fl}^{90}) : (\underline{\underline{\epsilon}} - \underline{\underline{\alpha}}) + \psi^S(\underline{\underline{\alpha}}, \underline{\underline{d}})$$

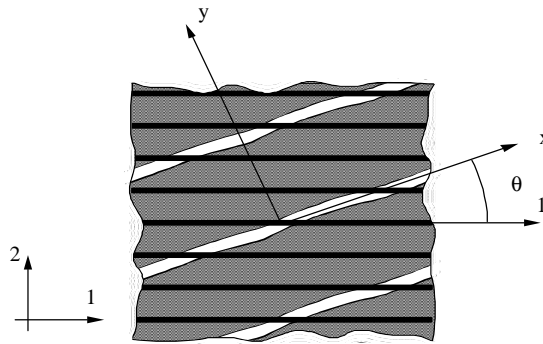


*Fig 4 Orientation of axes*

where  $D_{my}^{00}, D_{my}^{90}$  are the matrix damage parameters and  $D_f = \{D_{fl}^{00}; D_{fl}^{90}\}$  is the set of damage variables modeling fiber-breakage in the 0 and 90 plies respectively. The interface slip parameters are  $\underline{\underline{d}} = \{d_{11}; d_{22}; d_{12}\}$

### Finite Element Analysis

The resulting constitutive equations have been introduced into a UMAT routine of the finite element code ABAQUS (Hibbitt et al 1993). Early calculations of beams in four-point bending, proved to be simple to run, and indicated the ability of the CMC to redistribute stress and agreed with experimental observation that elastic calculations are very conservative. Components which were more challenging were the Iosipescu specimen (Fig 5) and a plate, penetrated by a hole, subjected to a tensile stress parallel to the fiber directions.

When the availability of materials is restricted to planar form shear data data is to subject the Iosipescu to shear loads specimen [Iosipescu, 1967]. The shear properties of the material are obtained by plotting the average stress at the minimum section against the shear strain measured by strain gauges placed at the center of the specimen.

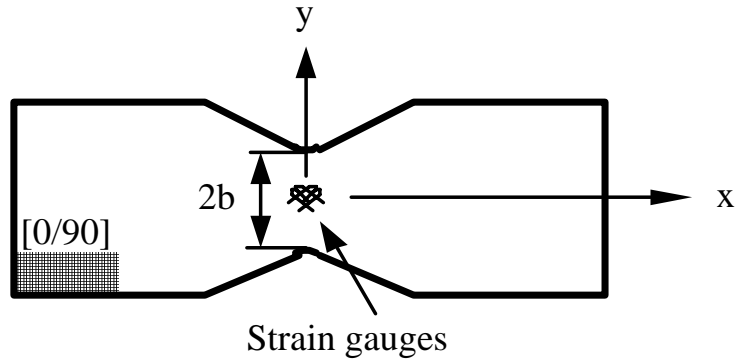


Fig 5: The Iosipescu specimen

It is known that the shear stress at the minimum section of this specimen is sensibly constant when the material is elastic and isotropic, but it is not known if the constant shear stress assumption is valid when cracking occurs. In addition to verifying the suitability of the Iosipescu specimen for obtaining the properties of materials which crack as illustrated in Fig, the tests provide an opportunity to measure the ability of the constitutive equations to predict the behavior of a component in which the stress state is different from those used in the identification procedure.

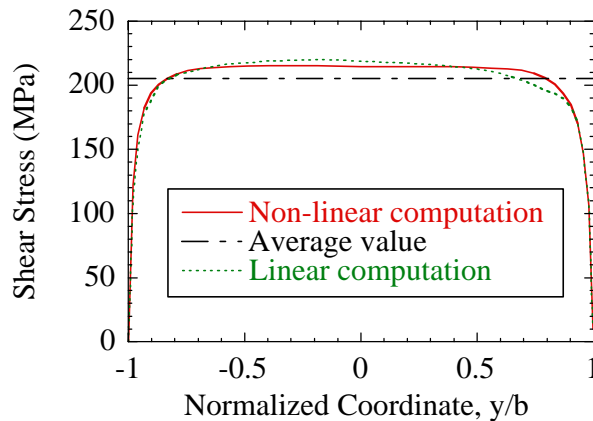


Fig 6: Stress distribution at minimum section

The prediction of the average stress against strain at the center of the specimen is agrees with the experimental observations to within 5%. The results of the finite element analysis shown in Fig. 6 indicate that the shear stress at the minimum section is essentially constant therefore justifying the use of the Iosipescu specimen as a means of obtaining shear data. Experiments on plates in tension which are penetrated by holes suggest that strength is dictated by the nett cross section and that the effect of the initial elastic stress concentration is minimised by the stress redistribution due to matrix cracking. The calculations indicate because of stress redistribution that almost half of the ligament stress carries the same stress. The elastic stress concentration factor is 4.1 which following the effects of stress redistribution reduces to 2.4. The large effect of matrix cracking is evident.

## CONCLUSIONS

A CDM model is proposed for CMCs which is mechanisms-based. The laws which relate the growth of the internal state variables to their associated forces have been derived from the unloading-reloading paths during tensile experiments for two different directions. The ability of the model to predict the response to another state of stress suggests the advantage of a mechanism-based approach.

When applied to SiC/SiC [0/90] lay-ups, the present model has 10 internal variables, viz. three inelastic strains modeling sliding, three damage variables describing the amount of debonding and four damage variables accounting for matrix-cracking and fiber-breakage in the two plies. It is shown that only two different experiments in tension are needed to identify the growth laws of the ten internal variables. The model has the potential to be applied to other material configurations (e.g., SiC/CAS, SiC/C, C/C, and presumably SiC/Al<sub>2</sub>O<sub>3</sub>) and architectures (e.g., woven configurations). Furthermore, the general framework presented herein has been applied to room temperature configurations and monotonic loading conditions. However extensions to cyclic load histories as well as high temperature applications can be included with minimal change to the state potential formulations. Evolution laws will have to be modified slightly.

The reliability of the Iosipescu test is confirmed as a means of average stress-strain shear data, and the constitutive equations are able to predict the shear properties correctly. However, it is shown that the average shear properties may be slightly different from the actual stress-strain shear data in the center of the ligament. Therefore the identification of the shear properties based upon the measurements on an Iosipescu test are, strictly speaking, only an approximation of the actual response in pure shear.

The ability of stress redistribution due to the non-linearity of the stress/strain curve has been shown in the case of the Iosipescu experiment. Stress redistribution important for structural applications has been demonstrated for beam bending and tensile plate penetrated by holes.

## REFERENCES

1. Aveston, J., Cooper, G. A., Kelly, A., 1971, Single and Multiple Fracture, National Physical Laboratory: Properties of Fiber Composites, IPC Science and Technology Press, Surrey (UK), 15-26.
2. Beyerley, D., Spearing, S. M., Zok, F. W., Evans, A. G., 1992, Damage, Degradation and Failure in a Unidirectional Ceramic-Matrix Composite, *J. Am. Ceram. Soc.*, 75, n° 10, 2719-2725.
3. Burr, A., Hild, F., Leckie, F. A., 1995, Micro-Mechanics and Continuum Damage Mechanics, *Arch. Appl. Mech.*, 65, n° 7, 437-456.
4. Coleman, D. B., Gurtin, M. E., 1967, Thermodynamics with Internal Variables, *J. Chem. Phys.*, 47, 597-613.
5. Germain, P., Nguyen, Q. S., Suquet, P., 1983, Continuum Thermodynamics, *J. Appl. Mech.*, 50, 1010-1020.

6. Hibbitt, H. D., Karlsson, B. I., Sorensen, P., 1993, Abaqus, version 5.3.
7. Hild, F., Burr, A., Leckie, F. A., 1996, Matrix Cracking and Debonding in Ceramic-Matrix Composites, *Int. J. Solids Struct.*, 33, n° 8, 1209-1220.
8. Iosipescu, N., 1967, New Accurate Procedure for Single Shear Testing of Metals, *J. Mater.*, 2, 537-566.
9. Jansson, S., Leckie, F. A., 1993, The Mechanics of Failure of Silicon Carbide Fiber-Reinforced Glass-Matrix Composites, *Acta Metall. Mat.*, 40, n° 11, 2967-2978.
10. Lemaitre, J., 1992, A Course on Damage Mechanics, Springer-Verlag, Berlin (Germany).
11. Rice, J. R., 1971, Inelastic Constitutive Relations for Solids: An Internal Variable Theory and its Application to Metal Plasticity, *J. Mech. Phys. Solids*, 19, 433-455.
12. Volterra, V., 1907, Sur l'équilibre des corps élastiques multiplement connexes, *Annales Scientifiques de l'Ecole Normale Supérieure, Paris*, 24, n° 3, 401-518.

# FAILURE MECHANISM OF A MULTI-LAYER COATING FOR THE OXIDATION PROTECTION OF C/C COMPOSITES

Laifei Cheng, Litong Zhang, Yongdong Xu

*State Key Laboratory of Solidification Processing,  
Northwestern Polytechnical University, Xi'an Shaanxi 710072, P. R. China*

**SUMMARY:** A multi-layer coating for carbon-carbon composites (C/C) with a Si-W outer layer, a SiC barrier layer and a SiC transition layer was prepared by the combination of Siliconization, CVD and Liquid Reaction method. The oxidation experiments at from 1600°C to 1700°C were conducted. The coated C/C always gained in weight at beginning. When it started to loss in weight, deep holes could be observed on the coating surface. At this time, the thickness of the oxide film on the coating surface at different temperature was found to vary little. Thermochemical analysis shows that the gas pressure at the interface of the coating and its oxide film could be higher than the ambient pressure, and gas bubbles would be formed in the oxidation process. The nucleation, growth, bursting and self-sealing processes of the bubbles were studied.

**KEY WORDS:** C/C composites, coating, oxide film, failure mechanism

## INTRODUCTION

Carbon-carbon composites (C/C) exhibit excellent structural properties above 1650°C, and are considered as the most promising candidate materials for the high thrust-weight ratio turbine engines. As a key technology for the high-temperature structural applications of C/C, oxidation protection is paid more and more attention recently. A number of studies have been conducted on the short-time oxidation protection, including various oxidation inhibitors, protection coating and sealants. For the long-time coating, not much progress has been made, in spite of years of intense effort. The study of failure mechanism is very important to the prolongation of protection life for a high-temperature coating and the development of a long-time protection coating system of C/C aimed at the components of advanced aircraft engines [1].

At above limiting use temperature, the coating will be destroyed entirely in a short time because of chemical compatibility of interfaces. At below cracking temperature, failure will take place at the coating-substrate interface because of oxygen diffusion through the cracking. At between intrinsic protection range temperature, failure is mainly influenced by the oxygen diffusion through the coating [2, 3]. Can we think simply the time obtained by dividing the coating thickness with the diffusion rate constant of oxygen at some temperature as the protection life at this temperature? In this paper, we will answer this question.



## EXPERIMENTAL PROCEDURE

The substrate material used in experiments, cut off from aircraft brakes, is a 2D-C/C with a density of  $1.7\text{g/cm}^3$ . The substrates are of cubed shape with a size of  $5\text{mm}\times 5\text{mm}\times 25\text{mm}$ . The multi-layer coating consists of three layers. The SiC transition layer was prepared by Siliconazition on the surface of the substrates to decrease the interfacial mismatch and increase the adhesive strength. The SiC barrier layer was prepared on the transition layer by CVD to prevent carbon outward diffusion and out layer inward penetration[4]. The Si-W sealant layer was prepared by Liquid Reaction to provide an effective barrier to inward diffusion of oxygen. The purity of the Si and W powder used to prepare the transition and sealant layer is above 99.5%, and that of the MTS used in CVD is above 98%. The Si-W layer was prepared in a vacuum furnace in which the spreading out of the Si-W layer can be observed timely[5]. The work temperature and the vacuum of this furnace is respectively  $1600^\circ\text{C}$  and  $0.0133\text{Pa}$ . Oxidation tests of long-time in dry air at  $1600^\circ\text{C}$ ,  $1650^\circ\text{C}$  and  $1700^\circ\text{C}$  were conducted in a furnace heated with  $\text{MoSi}_2$  rods. The thickness of the oxide film on the coating surface was identified with EMPA and SEM.

## RESULTS AND DISCUSSIONS

Because the coated C/C firstly gains and then losses in weight in the oxidation, the time the weight change is equal to zero can be defined as the protection life  $t_c$ , which can be called the critical protection life or effective protection time also.

The measured protection life at different temperature is listed in Table 1. It is shown that the relation curve of the protection life with temperature fits Arrhenius's law

$$\lg t_c = \frac{44104}{T} - 25.311 \quad (1)$$

*Table1: Effect of temperature on the oxidation protection life*

Temperature ( $^\circ\text{C}$ )	1600	1650	1700
Oxidation protection life (h)	168	30	4

When the oxidation time is beyond the critical protection life, the coated C/C losses in weight rapidly. This tells us that catastrophic oxidation has taken place. The catastrophic oxidation always starts from one or two points which appear to be black at high temperature. Deep holes will be formed at the black points which become the diffusion channel of oxygen. Fig.1 is the SEM micrograph of a deep hole on the coating surface.

It is not difficult to find that the deep holes are produced by escape of gas bubbles from their shape. The thermochemical diagram (Fig.2) shows that the gas pressure  $P_i$  at the interface of the coating and its oxide film can be higher than the ambient pressure, and gas bubbles will be formed in the oxidation process[6]. The gas products at the interface are mainly SiO. Partial pressure of the oxides of W is negligible. They dissolve in the oxide film, and then diffuse

towards the surface, and run away at last (Fig.3). The W dissolved in the liquid Si increases the interfacial gas pressure greatly.

The high-valence W ion is a glass former. It will get into the molecule net of the silica and make the oxide film become silica glass in the oxidation process (Fig.4 and Fig.5). From Raman spectrum of the oxide film, we know that the silica glass is highly stable in more than one hundred hours (Table 2). Formation of silica glass layer is very important to the long-term coating. Of course, glass layer will drop its using temperature.

Because the oxide film is thinner and resists to the nucleation and bursting of the gas bubbles less at the beginning of oxidation, more bubbles will be formed. The holes leaved on the oxide film by bursting of gas bubbles is smaller and less shallow. They will be sealed fastly by the viscous flow of glass. The longer of the oxidation time, the thicker the oxide film and the larger the resistance, then the more difficult for the bubbles to nucleate. Consequently, The bubbles formed are fewer, and greater and deeper when they burst. At some temperature, the viscous flow is limited. When the bubbles are large enough so that they can not be sealed in time, holes appear on the oxide film. At the same time, new oxide film is formed at the holes. Obviously, bubbles will prior necleate, grow and burst at the holes in further oxidation as the new film formed is very thin. As a result, the holes get deeper and deeper. When they penetrate through the coating at last, failure takes place. The failure precess is summarizd in Fig.6.

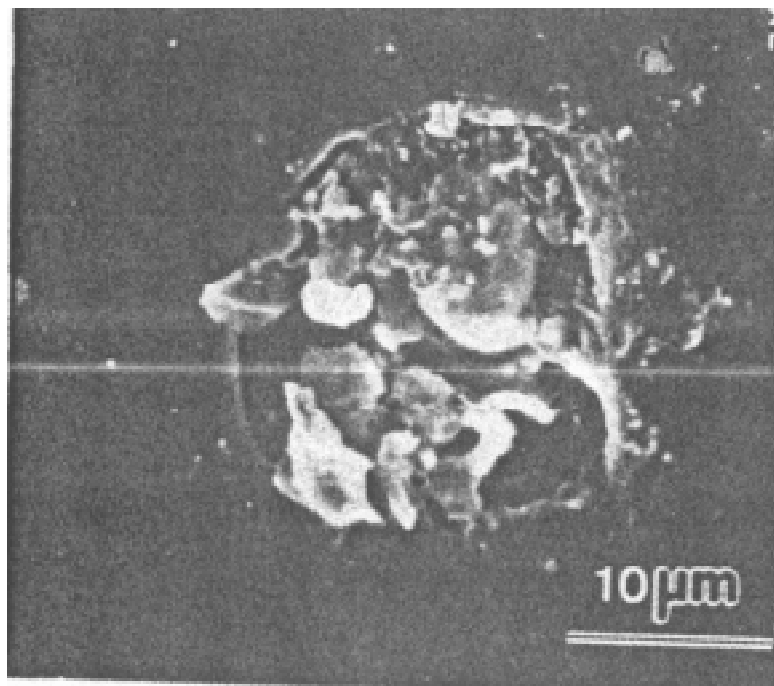


*Fig.1: SEM micrograph of a deep hole on the coating surface*

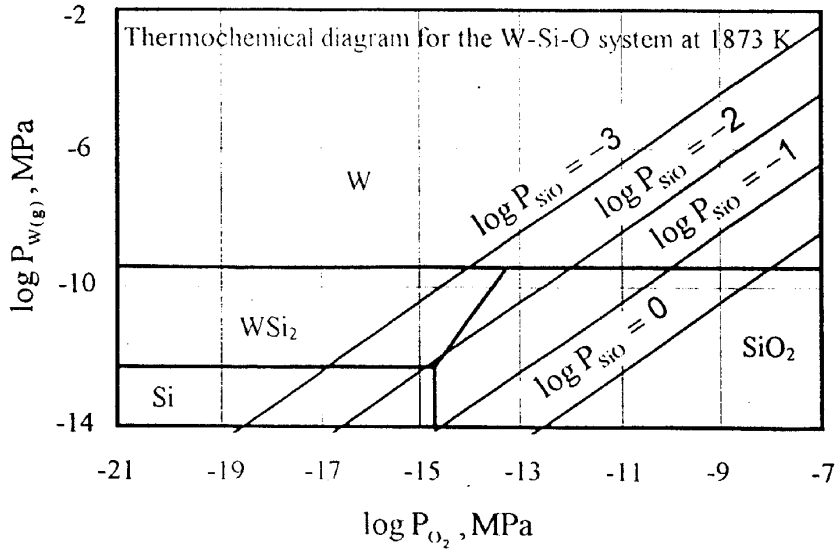


Fig.2 Thermochemical diagram for the W-Si-O system at 1873 K

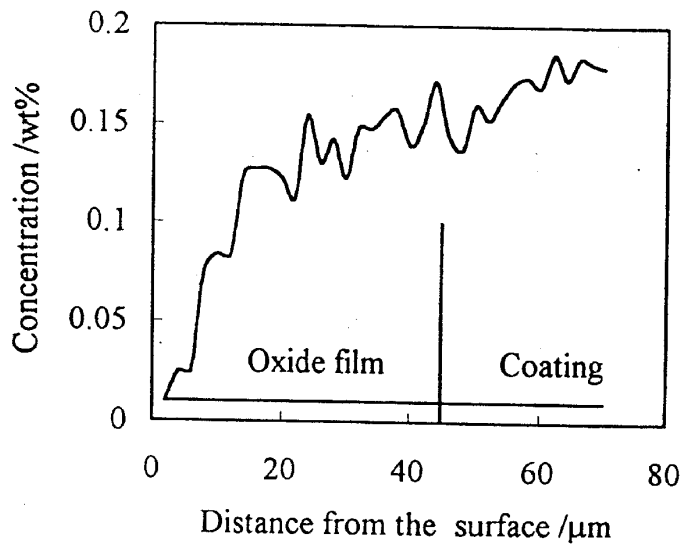


Fig.3 Distribution of W ion on the coating after oxidation for 168 h at 1600 °C

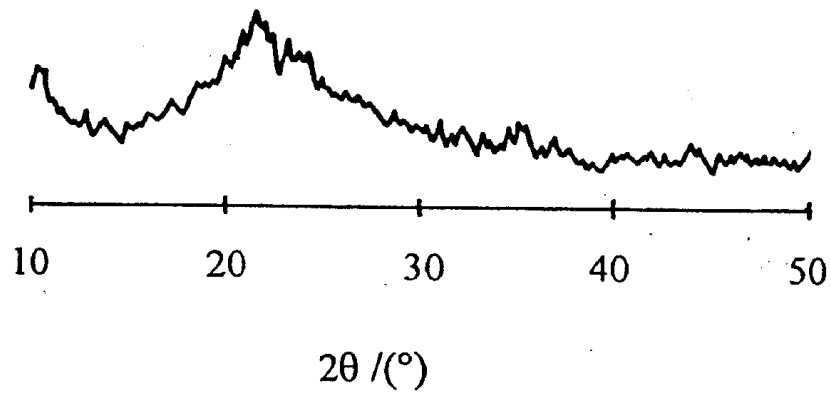


Fig.4: X-ray diffraction pattern of the coating after oxidation

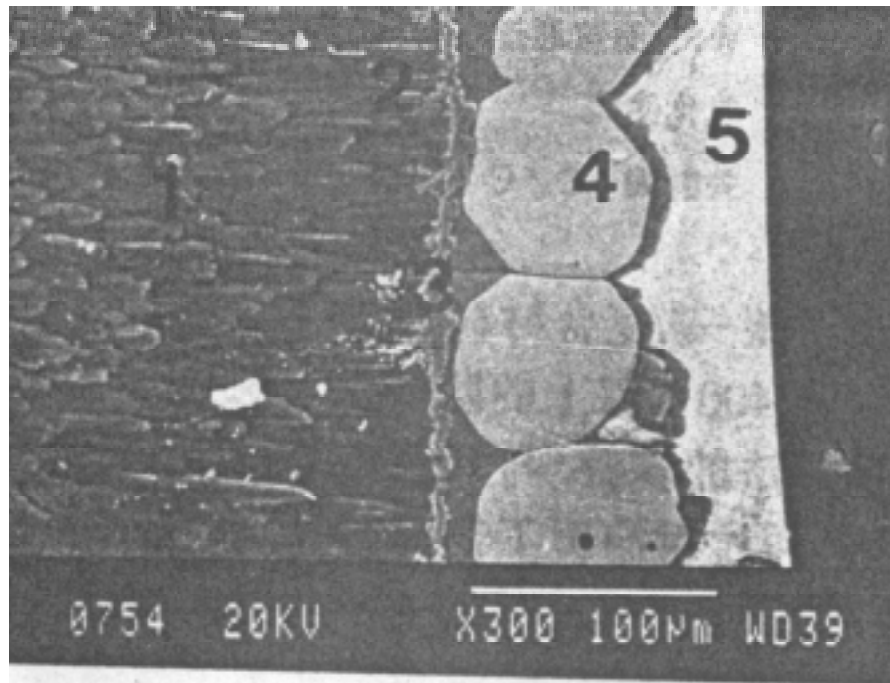


Fig.5: SEM micrograph of the coating after oxidation

1. C/C; 2. Transition layer; 3. Barrier layer; 4. Si-W layer; 5. Silica layer

Table 2: The effect of oxidation time on the network structure of the silica glass formed on the coating surface after oxidation at 1600°C

Oxidation time /h	Composition of the molecule network structure /%				Broken bonds /%
	Dimer	Sheet	Network	Pure network	
Before oxidation	22	0	34	44	18.5
45	21	0	69	10	19.9
168	16	11	30	43	16.6

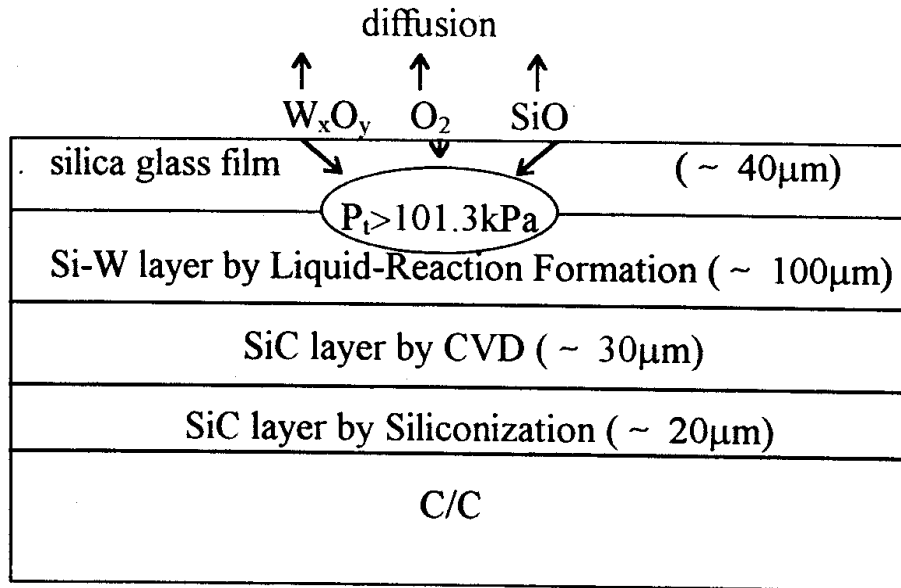


Fig.6: The failure process of the coating in oxidation

If the analysis about the failure process is correct, there certainly is a critical oxide thickness  $X(t_c)$ , corresponding to the critical life. That is to say, the oxide thickness when the coating fails depends on the diffusion rate constant and has nothing to do with temperature. Relation of the critical thickness with the critical life fits a parabolic law [7,8].

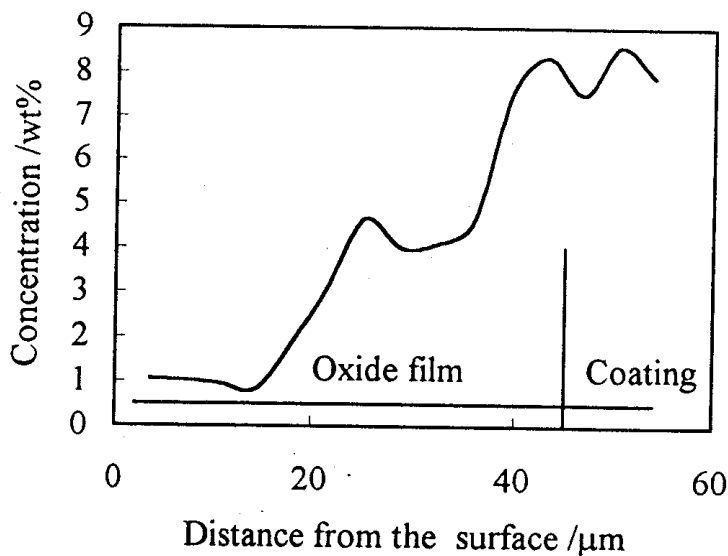


Fig 7: Distribution of oxygen ion on the coating after oxidation for 168h at 1600 °C

$$X(t_c) = \sqrt{Bt_c} \tag{2}$$

For this coating, the critical thickness of the oxide film is founded to be always 40  $\mu\text{m}$  less or more at different oxidation temperature (Fig.7). On the basis of critical thickness, we can obtain a relation of the critical life with temperature as following

$$\lg t_C = \frac{44104}{T} - 25.340 \quad (3)$$

This relation calculated is identical with the that put forward derrectly from the oxidation tests. This demonstrates clearly the failure mechanism presented.

It is meant by  $X(t)_C$  that a coating would fail because some defects are formed when the thickness of the film reaches its critical value.  $X(t)_C$  is a constant which is only influenced by the coating materials, coating structure, coating method and coating process, but not related to the oxidation temperature. The properties of the coating materials determine the characteristics of the oxide film and the interfacial gas pressure. The critical thickness of the film increases with increasing the interfacial gas pressure, decreasing the diffusion rate of oxygen and increasing the diffusion rate of gas species. In the presence of a barrier layer in the coating, the diffusion of oxygen along the deep holes would be blocked, and the critical thickness of the film would be increased. Deep holes could be considered to be formed at the sites where there are some original defects. Obviously, the defects are conditioned by the non-homogeneity of the coating preparation. Consequently, improving homogeneity of the coating is a very effective way to increase the critical thickness and prolong the protection life. After the coating materials are selected, the critical thickness depends upon the quality of the multi-layer coating. Only proper methods are selected or developed to prepare every layer of the multi-layer coating, the quality could be ensured. Although the interfacial gas pressure varies with temperature, the limited step of the interfacial gas reaction is the diffusion rate but not the reaction rate. Clearly, it is the diffusion rate constant but not the critical thickness that is influenced by temperature. Generally, the viscosity of the oxide film drops when temperature rises. The viscosity drop, on the one hand, makes the holes easy to be sealed and is favorable to increasing the critical thickness. On the other hand, it promotes the nucleation and growth of bubbles, and unfavorable to increasing the critical thickness. It can be argued that viscosity has not influence on the critical thickness in a certain range of temperature.

## CONCLUSIONS

1. The gases produced by the interfacial reaction between the outer layer and its oxide film are responsible for the coating failure. When the gas pressure is higher than the ambient, bubbles are formed at the interface.
2. The oxide film is a silica glass. When the bubbles are large enough that holes caused by their bursting can not be sealed in time, non-homogeneous nucleation, growth and bursting of the gas bubbles take place at the holes in further oxidation. As a result, deep holes are formed, which will become the channel of oxygen diffusion.
3. It is the critical thickness of the oxide film but not the coating thickness that affects the oxidation protection life. The relation of the protection life obtained from experiments is highly identical with that calculated based on the critical thickness.

## ACKNOWLEDGMENTS

The author gratefully acknowledges the support of K. C. Wong Education Foundation, Hong Kong.

## REFERENCES

1. Deborah, D. L., *Carbon Fiber Composites*, Butterworth-Heinemann, London, 1993
2. Strife, J. R., Sheehan, J. E., "Ceramic Coating for Carbon-Carbon Composites", *Ceramic Bulletin*, Vol.67, No.2, 1988, pp. 369-374
3. Luthra, K. L., "Oxidation of Carbon-Carbon Composites—A Theoretical Analysis", *Carbon* Vol.26, No.2, 1988, pp. 217-224
4. Yongdong, Xu, Litong, ZHANG and Laifei, CHENG, "Three Dimensional Carbon Fiber Reinforced Silicon Carbide Composites Prepared By Chemical Vapor Infiltration", *J. Chinese Ceramic Society*, Vol.24, No.5, 1996, pp. 485-489
5. Litong, ZHANG, Laifei, CHENG, "Measurements for the Wetting Angel Between Ceramics and Metals", *Yuhang Cailiao Gongyi*, No.99, 1988, pp. 49£55
6. Knacke, O., Kubaschewski, O. and Hwsselmann, K., *Thermochemical Properties of Inorganic Substance*, Heidelberg, Berlin, 1991
7. Deal, B, E., "General Relationship for the Thermal Oxidation of Silicon", *J. Appl. Phys.*, Vol.36 ,No.12, 1965, pp. 3770£78
8. Schiroky, G. H., "Oxidation Behavior of Chemically Vapor-Deposited Silicon Carbide", *Advanced Ceramic Materials*, Vol. 2, No.2, 1987, pp. 137£141

# **SUBSURFACE DAMAGE MEASUREMENT ON CARBON CARBON COMPOSITE MATERIALS IN BRAKING APPLICATIONS**

**Yves Remond and Christiane Wagner**

*Groupe de Modélisation et Simulation en Plasturgie et Mécanique – ECPM  
UP22 CNRS - Université Louis Pasteur 4, rue Boussingault, 67000 Strasbourg FRANCE*

**SUMMARY :** This paper deals with the measurement of subsurface damage of composite materials after braking solicitations. Several carbon carbon composites materials are studied. They have been tested under industrial braking conditions. Different damage methods are also used to estimate the braking effects on the mechanical behavior of these materials. In particular, a meso-hardness test is adapted to the heterogeneity of carbon carbon composite and to their porosity. Depending on the type of material, the results show the evolution of the meso-harness as a function of the distance to the braking surface. In the case of the quasi transverse isotropic behavior, we obtain a measurement of a damaged subsurface. An other original compression-bending test is also used, which confirms this damaged subsurface effect before wear occurs.

**KEYWORDS:** carbon-carbon, braking, wear, subsurface, damage, hardness, compression

## **INTRODUCTION**

Carbon carbon materials present a good mechanical behavior under specific conditions as high temperature. Besides, their low density is a main quality used for manufacturing brake discs of heavy vehicles as planes or trains. In this case, the braking system is made of several carbon carbon discs which are rubbing one against another - rotor against stator. Three different carbon carbon composites have been tested under industrial conditions as braking to a stop, and with neutral, wet or usual environment. Recalling the main results of thermal and wear behavior, we develop here experiments on CC composite materials after series of braking tests in order to measure the braking effects on the composite subsurface. For homogeneous materials, several authors show the deterioration of the material, with plasticity or microcraks, in proximity of the damaged surface [1], [2], [3]. Then we develop specific tests to quantify a possible damage during and after wear (braking) solicitations.

## **CARBON CARBON COMPOSITE MATERIALS AND BRAKING**

### **Description**

Three carbon carbon composites materials are compared here [4].

Material A : Carbon carbon laminates with thick woven layers in different directions in the disc plane. This material presents a quasi isotropic behavior in this plane.



Material B : Carbon carbon laminates with long fibers in a random distribution in the disc plane. As material A, this one presents a similar isotropic behavior in this plane.

Material C : Tridirectional carbon carbon composite material with needle bonding normal to the disc and presenting an orthotropic behavior.

**Thermal and Wear Behavior**

During the braking tests, Jeanne [5] measures the disc temperature and the wear rate. The main test characteristics are: a normal pressure of 1.3 MPa and angular velocity of  $365 \text{ rad.s}^{-1}$ . With these parameters, the surface energy density reaches  $300 \text{ J/cm}^2$ . An example of temperature evolution is given in Fig. 1 (material B). The measurements are realized at distance of 1 mm, 3.5 mm and 6 mm to the friction surface. The highest temperature varies with the type of environment up to  $1000^\circ\text{C}$  with the experimental conditions. In the same way, the thermal gradient varies too and presents a low variation under wet environment.

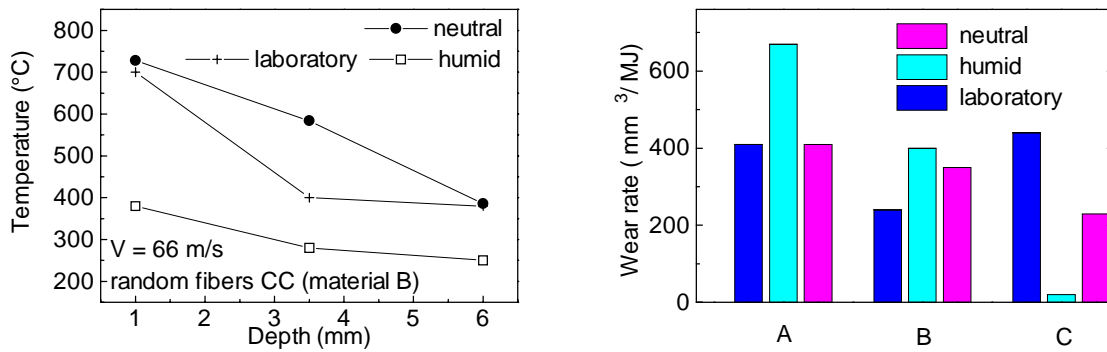


Fig. 1: Temperature evolution (material B) and wear rate of carbon carbon composites (A, B and C) during braking

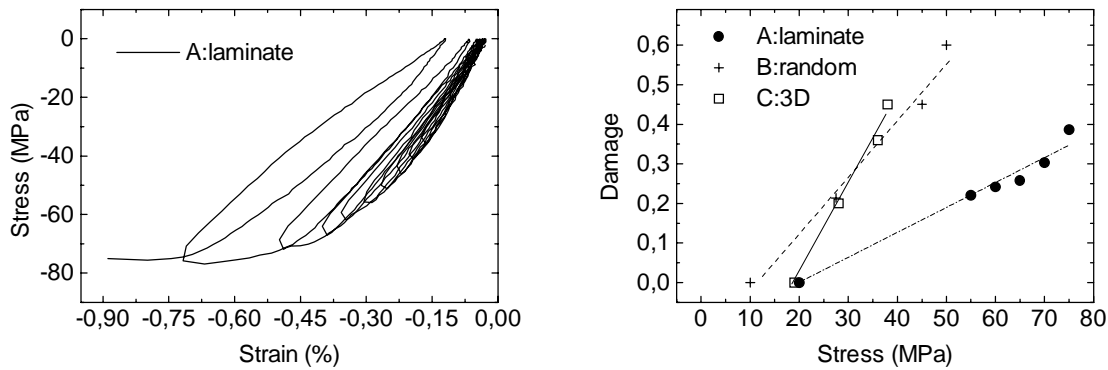


Fig. 2: Mechanical behavior (material A) and damage in compression test

The whole wear rate after different braking tests are presented below. For each material, this higher wear rate does not occur for the same environment. That shows the great complexity of the phenomena associated with thermal, chemical and mechanical processes [7], [8], [9], [10].

### Modeling of the Mechanical Behavior

The three carbon carbon composite materials present a similar macroscopical behavior. Fig. 2 shows a characteristic compression behavior (material A) in the disc plane with cyclic loading and unloading to free stress. They present an elasto plastic behavior with a linear damage evolution.

As we can see in Fig. 3, the Young modulus normal to the disc plan is very small. The in plane elastic behavior is determined by :

$$\epsilon_{ii}^e = \sigma_{ii} / E_{ii}^0(1 - d_i)$$

with  $i=1,2$  and  $d_i=1-E_i/E_i^0$

The damage evolution is described by :

$$d = f(\sigma^s) = (\sigma^s - \sigma^e) / b \quad \text{with : } \sigma^s = \text{Sup}_{\tau \leq t} |\sigma|$$

Beside a typical non linear modeling is obtained by the equations :

$$\dot{\epsilon}_p = \dot{\lambda} \frac{\partial g}{\partial \sigma} \quad \text{and} \quad \dot{p} = -\dot{\lambda} \frac{\partial g}{\partial L}$$

where  $g$  is the coupled plastic criterion :  $g(\tilde{\sigma}) = \tilde{\sigma}_{II} - L(p)$  with :  $\tilde{\sigma} = s/(1-D)$  and  $L$  the hardening function which must be identified for each material.

	$E_1=E_2$ (GPa)	$E_3$ (GPa)	$\sigma_e$ (MPa)	$b$ (MPa)	$d_{critique}$	$\epsilon_{rupture}$ (%)	$\epsilon_{pl.rupt.}$ (%)	$\sigma_{rupture}$ (MPa)
Material A	30	1	20	137,5	0,7	0,9	0,15	75
Material B	32	0,7	10	66,7	0,6	0,52	0,075	50
Material C	18	1,25	20	44,5	0,45	1,18	0,1	40

Fig. 3: Mechanical characteristics of CC

### MESO-HARDNESS

A specific meso-hardness test is developed here taking into account the particular geometry of the three carbon carbon materials. A spherical indenter is chosen and optimized. Its diameter must be proportional to the surface elementary cell size in order to measure the meso-hardness corresponding to the homogeneous behavior and not the meso-hardness of the constituents. The carbon carbon samples are then machined with a succession of steps whose thickness is 0.05 mm. For each step we measure twelve meso-hardness under progressive loading. The mass used in the test are 0.3 kg, 1 kg and 15 kg. The optimal diameter of the spherical tip is 6.35 mm. Each test lasts about one minute.

During the meso-hardness test, the indenter penetrates the sample in a very small thickness, much smaller than the thickness of a fiber layer. In that case, it is possible to obtain the evolution of the meso-hardness in the material, due to the braking solicitations.

The results are analyzed with two classical concepts of harness : HB is the Brinell hardness taking into account the permanent or plastic deformation of the material under loading :  $h_p$ . HR is the Rockwell hardness taking into account the total deformation, id est the elasto-plastic deformation of the material under the indenter :  $h_{ep}$ .

With F, the load, D, the diameter of spherical tip and d the diameter of the indentation area, we have :

$$HB = \frac{F}{\pi D h_p} , \quad HR = \frac{F}{\pi D h_{ep}} , \quad h_{ep} = [D - (D^2 - d^2)^{1/2}] / 2$$

The measure of  $h_p$  is obtained during the test with unloading to free stress.

Results are presented in Fig. 4a, 4b and 4c.

Material A : The meso-hardness from the braking surface to the middle of the sample describes a periodical evolution where the periodic distance is equal to the thickness of the fiber woven layers. It is difficult to observe a particular evolution of the hardness near the braking surface.

Material C : The hardness evolution does not present a characteristic variation between the surface and the middle of the sample. We note that the accuracy of the results is not good. That is an indicator of the heterogeneity of this material coming from the needle bonding normal to the disc plane.

Material B : The results are presented here in term of damage, with D a scalar parameter equal to the ratio of the meso-hardness in the middle of the sample and the local meso-hardness [6], [4].

$$D = 1 - \frac{H}{H^*}$$

Lemaître [6] showed a similar evolution of the damage measure by classical tests as tension test  $D=1-E/E_0$  and hardness test  $D=1-H/H^*$  for isotropic material. If  $E_0$  represents the initial Young's modulus, the meso-hardness  $H^*$  is more complex to obtain. In the case of an elastoplastic behavior with hardening, the damage must appear at the same time as hardening.

So, if H represents the hardness of the material after loading, and  $H_0$  the hardness before loading, we should obtain :

$$H > H_0 \text{ with } H_0 = k \sigma_p , \quad H = k (R + \sigma_p) (1 - D) ,$$

R is the hardening variable and  $\sigma_p$  the plastic low threshold stress.

The measure of damage must be so :

$D = 1 - \frac{H}{H^*}$  with  $H^* = k(R + \sigma_p)$  hardness of the material with hardening but without damage, obtained by calculus. For the carbon carbon composite material B under braking solicitation, we observe a hardness  $H$  at the surface smaller than  $H_0$  in the middle of the sample,  $H < H_0$ . That means that damage appears without hardening, this phenomenon is similar to the damage evolution in elastic fatigue test for isotropic metals. Consequently, we propose the hypothesis that under braking solicitations, appears a damage evolution mainly due to thermal and physicochemical phenomena, and without hardening.

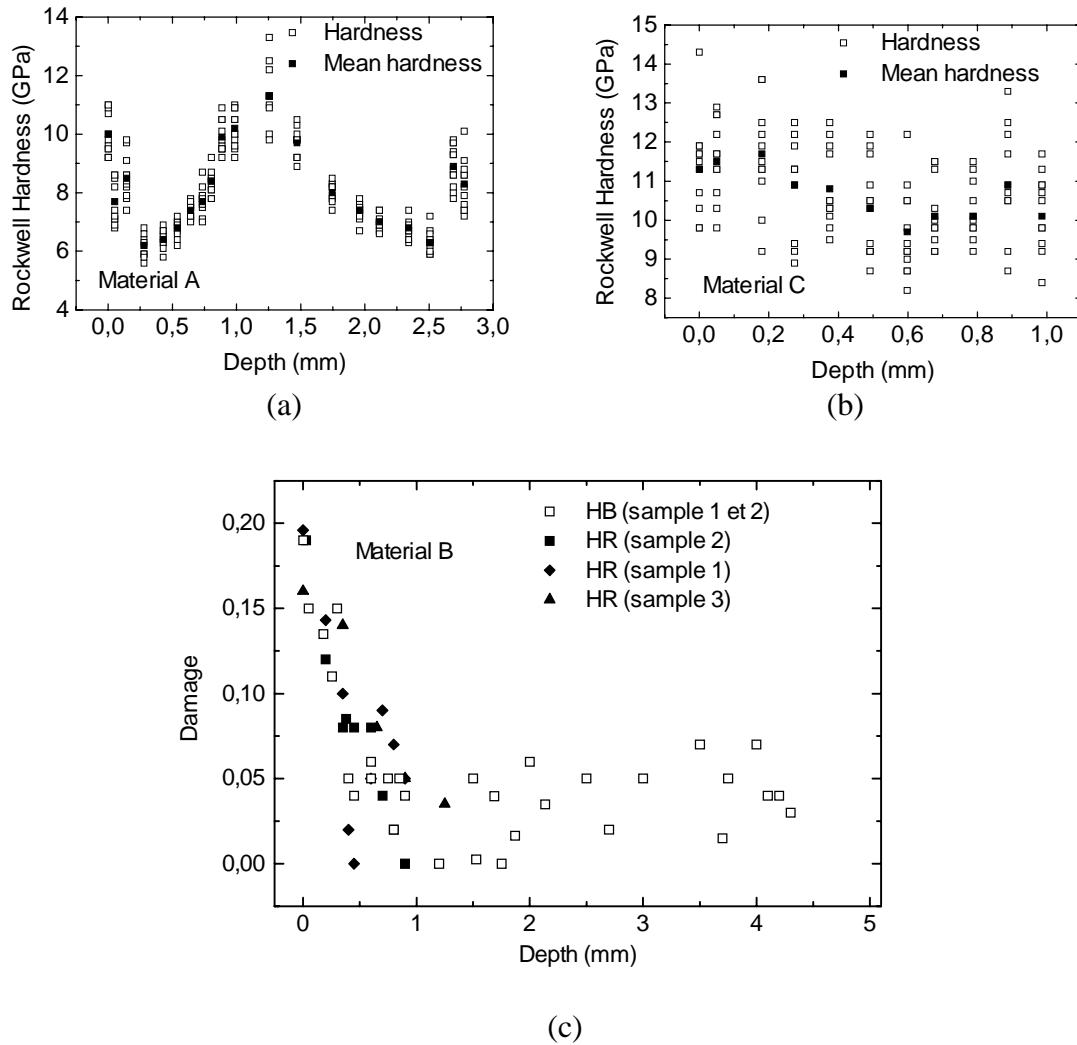


Fig. 4: Meso hardness ((a) and (b)) and damage (c)

The model of damage measurement is then :

$$D = 1 - \frac{H}{H^*}$$

with  $H^* = k \sigma_p$  and  $H = k \sigma_p (1 - D)$

The damage evolution shows a decreasing from the surface of the material.

In the middle of the disc, the variation of measurement  $\Delta H$  corresponds to the heterogeneity of the carbon carbon with a relative ratio :  $\Delta H/\Delta H^* = 7.5\%$ .

Near the surface, the ratio  $\Delta H/\Delta H^*$  measured reaches 20%. Between 7.5% and 20%, it is possible to consider this ratio as a measurement of damage in a subsurface of this carbon carbon composite material. The depth of this subsurface is  $a=0.4 \pm 0.1$  mm. The thickness of this damaged subsurface will probably vary as a function of the nature of the braking solicitation (frequency, energy level...). In case of very dissipate braking, the damaged subsurface will disappear in wear.

### COMPRESSION BENDING TEST

The brake discs in material B are damaged only in a small thickness near the surface. We tried to define a macroscopical test sensitive to a variation on rigidity in the subsurface. The principle of this test is shown in Fig. 6a and 6b. Parallelepipedic samples are taken out of the brake discs after braking test.

If a sample is not damaged, its rigidity center and its geometrical center match each other in a cross section. If not, appears a distance between these two points, that generates a bending couple when the sample is loaded in compression. Using strain gauges in all the lateral surfaces of the sample, it is possible to measure the bending effect due to the damaged subsurface. A specific experimental setup (Fig. 6b) is then constructed in order to apply the compression load with a good accuracy (0.01 mm) exactly in the center of the cross-section. A steel ball permits the free rotation of the head sample.

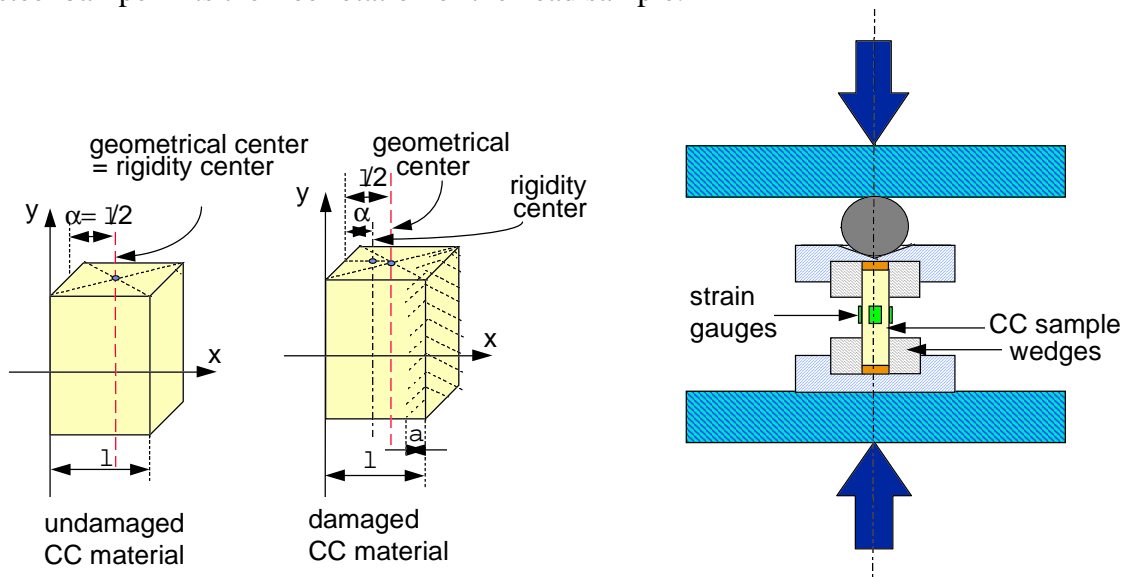


Fig. 6: Samples and compression-bending setup

This experimental setup has been tested on model materials for which a subsurface with a different rigidity was prepared and then well known. Its accuracy permits to detect a damaged subsurface with the following characteristics :  $a.d = 0.02$  mm with  $a$  : the thickness of the damaged zone and  $d$  : the mean damage in this subsurface.

With  $E_i$ , the Young modulus of the CC sample in the compression direction, and  $l/2-\alpha$  the distance between the center of rigidity and the center of the cross section, we can write :

$$\int_s E_i(x - \alpha) dS = 0 \tag{1}$$

Suppose that the damage evolution is linear, as shown with the meso-hardness results, we obtain :

$$E_i(x) = E_i^0(1-d(x)) \quad \text{for } x \in [1-a, 1]$$

$$\text{and } E_i(x) = E_i^0 \quad \text{for } x \in [0, 1-a].$$

Assume too that :

$$E_i(x) = E_i^0 [1 + d_c[(1-x)/a - 1]]$$

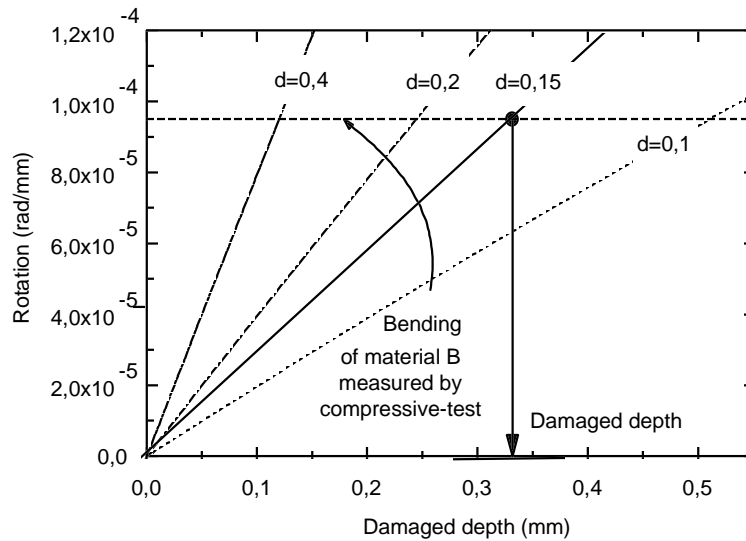


Fig. 7: Identification of the damaged depth

It means that the critical damage is obtained at the braking surface, so previous relation (1), could be written :

$$2\alpha = (d_m a(a-2l) + l^2) / (1 - d_m a)$$

Note that this scalar equation permits only to obtain one scalar unknown, the measure of  $\alpha$  by the rotation of the head sample permits to find the thickness of the damaged subsurface. The results of this compression bending test are shown in Fig. 7.

All specimens in material B present a bending effect corresponding to the values of  $a$  and  $d$  :  $a \cdot d_m = 0.05$  mm

Then if we consider a linear evolution of the damage in the subsurface, with a critical damage  $d_c=0.2$  measured with the meso-hardness results, we obtain a thickness of this subsurface equal to  $a=0.35$ mm.

## DISCUSSION AND CONCLUSION

Note that the measure of the bending effect must be absolutely realized in the beginning of the rotation. If not, a complementary bending couple appears due to the progressive lateral displacement of the setup induced by the bending strains.

The both results of meso-hardness and compression bending test developed here are in good agreement. They show that, for the carbon carbon composite materials B, it can exist a damaged subsurface induced by specific braking solicitations. Naturally, this subsurface is progressively turning into wear particles, during a braking test. However, it seems to be necessary to take into account the real damaged behavior of materials in order to have a better understanding of their surface deterioration. The main difficulties which limit these approach are the heterogeneity of carbon carbon composites and their porosity, which stop us developing others methods to measure this subsurface.

## REFERENCES

1. A.T. Alpas, J.D. Embury, "The role of subsurface deformation and strain localization on the sliding wear behaviour of laminated composites", *Wear*, 146, 1991, pp. 285-300
2. J.D. Chen, J.H. Chern Lin, C.P. Ju, " Effect of load on tribological behaviour of carbon-carbon composites ", *Journal of Materials Sciences* 31 (1996), pp. 1221-1229
3. M. Cirino, R.B. Pipes, K. Friedrich, "The wear behavior of continuous fiber polymer composite", *ICCM 6th, Vol 5*, London 1987, pp. 311-323
4. C. Wagner, "Matériaux composites carbone carbone et freinage : étude de l'endommagement au voisinage d'une surface de contact", *Thèse de doctorat de l'Université Louis Pasteur*, Strasbourg, France, 1996
5. J.F. Jeanne, " Etude de l'endommagement surfacique de matériaux composites type Carbone/Carbone sous sollicitations tribologiques ", *Thèse de Doctorat, Ecole Centrale de Nantes*, 1994
6. J. Lemaitre, J. Dufailly, R. Billardon, *C. R. Acad. Sc. Paris*, "Evaluation de l'endommagement par mesures de microdureté ", *t.304, Série II, N°12*, 1987,
7. F. Durand, D. Rouby, G. Fantozzi, "Characterization of the high-temperature mechanical behaviour of carbon materials ", *Carbon vol 32, No 5*, pp.857-865, 1994
8. J. Xiaoyu, " Frictionnal contact analysis of composite materials, " *Composite science and technology* 54, 1995, pp. 341-348
9. F.M. Kustas, R.R. Hanson, J.L. Summer, " Tribological performance of 3D carbon-carbon composite, Part I : Ambient Environment ", *Lubrication Engineering, Vol.51, 7* (1995), pp. 599-604
10. C. Ahearn, B. Rand, " Modification of the fibre-matrix bonding in a brittle carbon-carbon composite by controlled oxidation ", *Carbon, Vol 34, N°2*, 1996, pp. 239-249.

# MICROSTRUCTURAL CHARACTERISATION OF 3-D WOVEN SiC/SiC-BASED COMPOSITES AFTER TENSILE TESTING AT ROOM AND ELEVATED TEMPERATURE IN DIFFERENT ATMOSPHERES

Ian J. Davies<sup>1</sup>, Takashi Ishikawa<sup>1</sup>, Masaki Shibuya<sup>2</sup>, and Tetsuro Hirokawa<sup>3</sup>

<sup>1</sup>*Airframe Division, National Aerospace Laboratory,  
6-13-1 Ohsawa, Mitaka-Shi, Tokyo 181, Japan*

<sup>2</sup>*Corporate Research and Development, Ube Industries Ltd.,  
1978-10 Kogushi, Ube-Shi, Yamaguchi 755, Japan*

<sup>3</sup>*Research and Development Department, Industrial Textile Division, Shikibo Ltd.,  
1500-5 Shibahara-Minami, Yokaichi-Shi, Shiga 527, Japan*

**SUMMARY:** 3-D woven SiC/SiC-based composite consisting of surface-modified Si-Ti-C-O fibres and polymer conversion-derived matrix was tested in tension in vacuum (1200-1380°C) and air (1000-1200°C). In addition, several specimens were surface-sealed using a proprietary technique prior to mechanical testing. Resultant tensile property/strain curves are discussed together with fracture surface characteristics such as main failure mode and fibre pull-out length distribution. The effect of test condition on intra-fibre bundle spatial distribution of fibre fracture characteristics is also mentioned. Composite properties at room and elevated temperature in vacuum (unsealed) and air (surface-sealed) were generally consistent with a stable fibre/matrix interface. Unsealed specimens tested at elevated temperature in air exhibited properties consistent with extensive fibre/matrix interface oxidation.

**KEYWORDS:** microstructural characterisation, SiC/SiC, tensile test, stress/strain, fibre pull-out, fracture mirror

## INTRODUCTION

Ceramic matrix composites (CMCs) which have shown potential for use in high temperature structural applications include those based on the SiC/SiC system. These composites contain fibres with either Si-C-O or Si-Ti-C-O structures comprising of  $\beta$ -SiC nanoparticles partially surrounded by aromatic carbon layers in an amorphous  $\text{SiO}_x\text{C}_y$  matrix for the Si-C-O fibre and  $\text{SiO}_x\text{C}_y\text{Ti}_z$  matrix for the Si-Ti-C-O fibre. Matrix densification is generally achieved using either chemical vapour infiltration (CVI) or polymer conversion (PC) techniques.

Significant research has been conducted into optimisation of the fibre/matrix interface which is known to significantly influence high temperature mechanical properties (particularly for oxidising atmospheres). The problem of high temperature fibre/matrix interface stability has also been addressed through coating or sealing the composite surface with an oxidation-resistant glass layer.



The present work is concerned mainly with mechanical and microstructural characterisation of a 3-D woven SiC/SiC-based composite (without an oxidation-resistant glass layer) after tensile testing in vacuum and air from room temperature (RT) up to 1380 °C. In addition, exploratory tests were also carried out on a limited number of specimens after the surface had been sealed with an oxidation-resistant glass compound.

### **EXPERIMENTAL PROCEDURE**

The composite examined in this work utilised continuous Si-Ti-C-O fibres woven into an orthogonal 3-D configuration with fibre ratios in the x, y, and z directions being 1, 1, and 0.13, respectively and a fibre volume fraction estimated to be 40 %. The Si-Ti-C-O fibres (Tyranno LoxM) had been surface-modified to produce an outer 10 nm SiO<sub>x</sub>-rich layer surrounding an inner 40 nm carbon-rich layer whilst matrix densification used the PC method and a precursor similar to polytitanocarboasilane (PTCS). After machining to a geometry suitable for tensile testing, a limited number of specimens were surface-sealed using a proprietary technique (Kawasaki Heavy Industries, Kakamigahara City, Japan).

Mechanical testing of unsealed specimens was carried out with the loading direction parallel to the specimen y-axis (experimental details being given elsewhere) at RT and also at elevated temperature in vacuum (1-3 Pa)(1200-1380 °C) and in air (1000-1200 °C). Surface-sealed specimens were tested in a similar configuration up to 1200 °C in air. It should be noted that tensile strain could not be accurately measured beyond 1300 °C in vacuum (limitation of the specimen grip) and also for unsealed specimens at elevated temperature in air.

Experimental stress/strain curves were characterised by computer fitting of a high-order polynomial curve after which the instantaneous tensile modulus, E, and cumulative damage energy could be derived. Cumulative damage energy (CDE) indicates the energy absorbed by the composite during failure and so may be used to qualitatively measure the “toughness” of the composite, with:

$$\text{Cumulative damage energy} = \frac{1}{b \cdot h \cdot L_o} \int_0^S F dA \quad (1)$$

where b is the mean initial test specimen width (m), h is the mean initial test specimen thickness (m), L<sub>o</sub> is the specimen gauge length (m), F is the tensile force acting on the specimen (N), S is the composite failure strain, and A is the longitudinal elongation (m). The majority of energy absorbed during failure is known to result from fibre pull-out so that CDE may also provide information concerning fibre pull-out properties and hence the status of the fibre/matrix interface.

Microstructural observations to evaluate the general nature of the fracture surface were initially carried out using a zoom lens optical microscope (OM) (Olympus SZH) at low magnification (≤20). Additional investigation concerning the fracture surface in the composite zy-plane was carried out at higher magnification (~50) (Olympus STM5-BD). Fibre pull-out length distributions were determined using this technique through measuring the projection of fibre pull-out length in the zy-plane. Obscuration of fibres with small pull-out lengths behind those with larger pull-out lengths was minimised through considering only fibres which had

pulled-out nearest to the microscope lens. Fibre pull-out length distributions will also be examined using scanning electron microscopy (SEM) at a later date.

Preliminary examination of individual fibre fracture surfaces was carried out for selected specimens using SEM (JEOL JSM-6300F). In order to determine any spatial dependence of fibre fracture properties within fibre bundles, fibres were examined at the end and centre of the fibre bundle major axis for each specimen. In both cases the fibre bundle was scanned from edge to edge along its minor axis with all fibres within an approximate 100  $\mu\text{m}$  “corridor” being analysed. A minimum of 100 fibres were analysed in each area with the relative position, fibre diameter, surface character, and fracture mirror size (if applicable) being measured for each fibre. Only initial results are presented here with a more complete analysis being given elsewhere.

## **RESULTS AND DISCUSSION**

### **Mechanical Properties**

Representative tensile property/strain curves for composites examined in this paper have been presented in Fig. 1. The unsealed composite exhibited excellent mechanical properties at RT with a tensile strength of 389 (+/-48) MPa (Fig. 2) and tensile strain to failure of 1.14 (+/-0.04) % (Fig. 3(a)). Such values, combined with a CDE of 2634(+/-340)  $\text{kJm}^{-3}$  (Fig. 3(b)) compare extremely favourably with those obtained for previous SiC/SiC-based composites and suggest the fibre/matrix interface to possess near-optimal properties. Tensile strength,  $\sigma$ , and modulus,  $E$ , values obtained from Fig. 1 were broadly similar to those predicted by modified Rule of Mixtures equations:

$$E = \eta_f E_f V_f + E_m V_m \quad (2a)$$

and

$$\sigma = \eta_f \sigma_f V_f + \sigma_m V_m \quad (2b)$$

where  $V$  is the volume fraction of the respective phase,  $\eta_f$  is the fibre orientation factor, and the subscripts  $f$  and  $m$  refer to fibre and matrix properties respectively, with the following assumptions:

The decrease in tensile modulus with increasing strain at small strain levels ( $\leq 0.2$  %) was attributed to a reduced contribution from the matrix component (due to microcracking). The matrix in SiC/SiC-based composites is known to have a substantially lower tensile strain to failure ( $\approx 0.1$  %) compared to that of the fibres ( $\approx 1$  %).

Mechanical properties from  $\epsilon \approx 0.4$  % until just prior to failure were due almost entirely to fibre and fibre/matrix interface properties.

Following on from the previous assumption, the composite failed at a tensile strain similar to that of the fibres. However, the tensile strength of the composite was only 50 % of that predicted from Eqn. 2b (with  $\sigma_m V_m \approx 0$ ). A large proportion of this difference may be attributed to fibre strength reduction upon inclusion in the composite whilst another factor in

the present case may be the non-alignment of fibres along the loading axis (due to the weaving procedure).

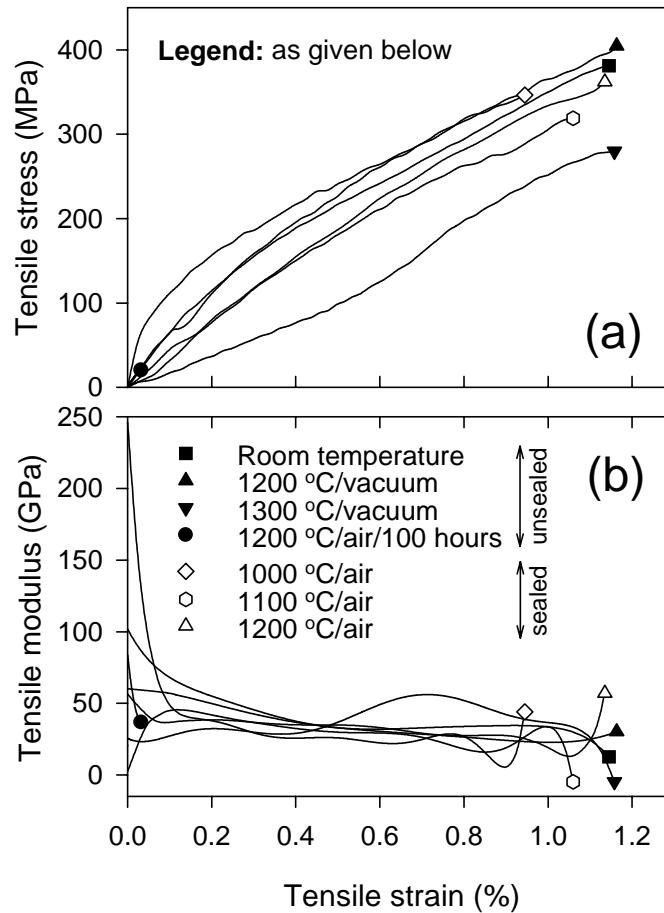


Fig. 1: Tensile property curves for unsealed and surface-sealed SiC/SiC-based composite: (a) stress/strain, and (b) modulus/strain

It should also be noted that the composite initial tensile modulus was determined by significant contributions from both fibre and matrix. This situation is different from the case of SiC/SiC-based composites with CVI-derived matrices where the majority of the initial tensile modulus contribution is due to the matrix.

Tensile properties were almost identical for unsealed composite at 1200 °C in vacuum as for the RT case (Figs. 1-3) apart from a slight reduction in initial tensile modulus (attributed to matrix degradation) indicating the fibre/matrix interface to be stable at 1200 °C in vacuum.

Further increases in test temperature for unsealed specimens in vacuum resulted in a 50 % decrease in tensile strength by 1380 °C (compared to RT and 1200 °C). A decrease in mechanical properties under these conditions would be expected as Si-Ti-C-O fibres are known to degrade at elevated temperature, even in vacuum. Thus, a decrease in composite mechanical properties under such conditions does not necessarily imply a degradation of the fibre/matrix interface.

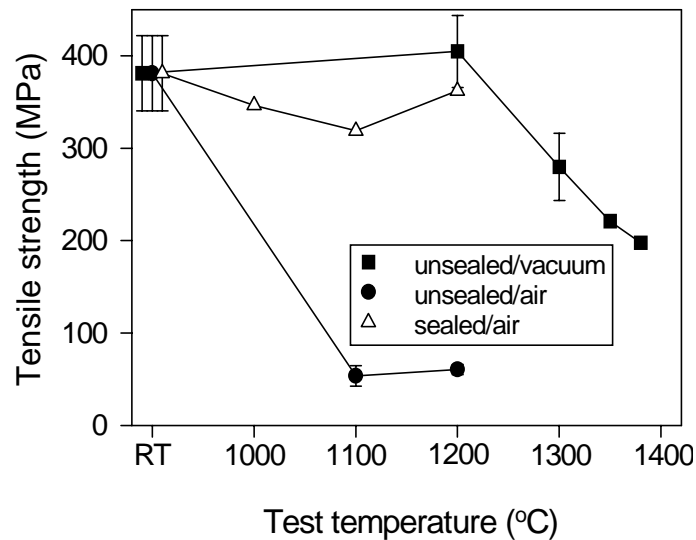


Fig. 2: Tensile strength vs test condition for unsealed and surface-sealed SiC/SiC-based composite. Note non-linear temperature scale

Although strain measurement was not possible for unsealed composite at elevated temperature in air, qualitative observations indicated the tensile stress/strain curve to be approximately linear with a strain to failure of <0.1 % and, as such, is consistent with mechanical property/strain data presented in Fig. 1 for unsealed composite tested at RT after ageing in air (1200 °C/100 hours). The implication is that mechanical properties of unsealed composite are significantly reduced by exposure to oxygen at elevated temperature and this is borne out by tensile strength data presented in Fig. 2. The exact mechanism for the reduction in mechanical properties under these conditions has not been established for the composite under investigation but would be consistent with oxidation of the fibre/matrix interface producing a substantial increase in interface sliding stress and transformation to notch-sensitive behaviour observed by previous authors. The fibre/matrix interface in the present composite is known to consist essentially of a carbon-rich layer which makes such a scenario likely.

Tensile property/strain curves for surface-sealed composite tested at elevated temperature in air have also been included in Fig. 1. Although it should be stressed that such data is preliminary, the curves appear similar to those of unsealed composite at elevated temperature in vacuum. Such a conclusion may also be inferred from comparison of respective tensile strength (Fig. 2), strain to failure (Fig. 3(a)), and CDE (Fig. 3(b)) data. It is suggested that surface-sealing of the specimen is effective in severely retarding oxidation of the fibre/matrix interface, at least for short-term exposure (in the order of several minutes). These results are also consistent with preliminary creep investigations (1100 °C in air) of surface-sealed composite which have shown typical lifetimes of  $6 \times 10^4$  s at 200 MPa and may indicate that long-term exposure at elevated temperature in air is feasible for these materials.

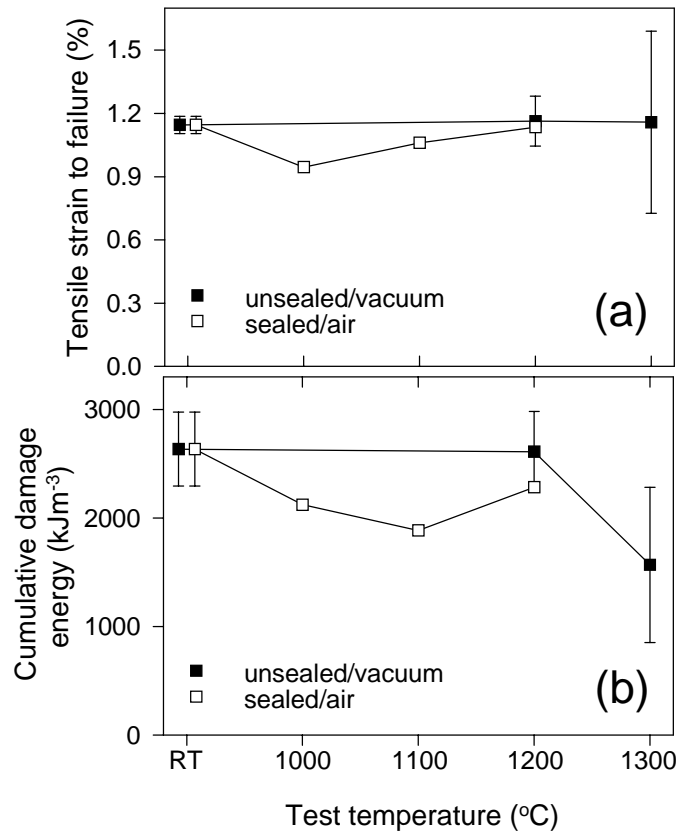
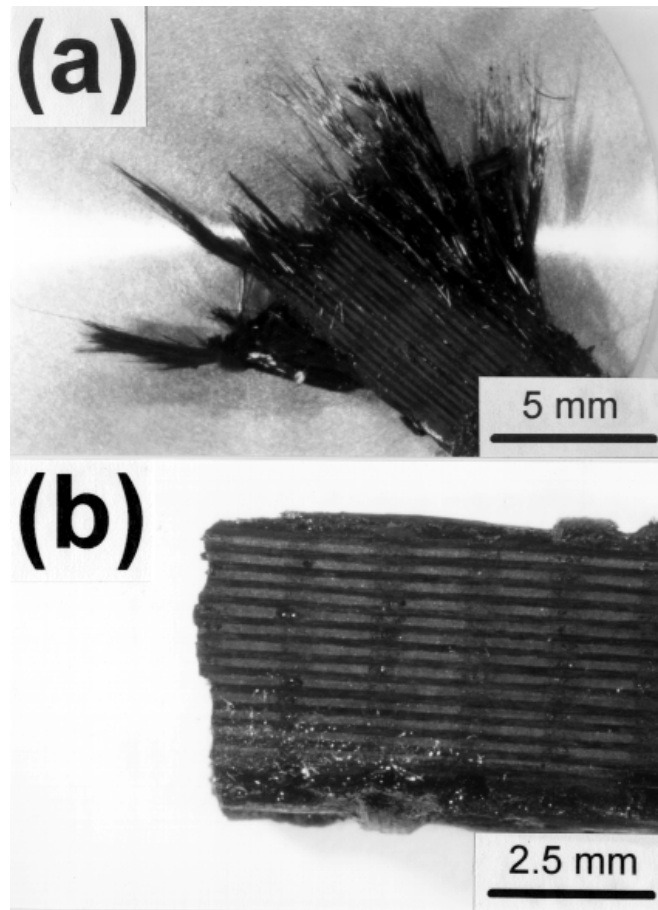


Fig. 3: Parameters determined from tensile stress/strain curves of unsealed and surface-sealed SiC/SiC-based composite: (a) tensile strain to failure, and (b) cumulative damage energy. Note non-linear temperature scale

### Microstructural Investigation

The composite tensile tested at RT exhibited a “brush-like” fracture surface (Fig. 4(a)) with extensive fibre pull-out characteristic of “tough” CMCs and reflected in the relatively high CDE values achieved (Fig. 3(b)). The primary crack path in the composite tested at RT followed the inter-fibre bundle porosity perpendicular to the loading axis, indicating such pores to be a preferred route for crack propagation under these conditions. A similar fracture mode was also observed in unsealed specimens tested at elevated temperature in vacuum and also for surface-sealed specimens tested at elevated temperature in air, indicating crack initiation and propagation to be similar for these cases.

In contrast to this, unsealed composite tested at elevated temperature in air possessed a relatively smooth fracture surface (Fig. 4(b)) with little evidence of fibre pull-out, indicating brittle failure to have occurred. As stated earlier, such a failure mode was attributed to oxidation of the fibre/matrix interface. The primary crack path in this case showed no preference for the inter-fibre bundle porosity and was consistent with crack initiation within a fibre bundle followed by catastrophic crack propagation.



*Fig. 4: Optical micrographs illustrating fracture surfaces for unsealed SiC/SiC-based composite after tensile testing: (a) room temperature, and (b) 1200 °C in air*

Fig. 5(a) illustrates the effect of test temperature on fibre pull-out length distribution for unsealed composite tensile tested in vacuum with the distributions being similar for the RT, 1200 °C, and 1350 °C cases. The shift in fibre pull-out length to smaller values at 1300 °C was attributed to a transient deterioration in vacuum condition during testing. Previous researchers found that exposure to oxygen at elevated temperature may increase the fibre/matrix interface sliding stress by an order of magnitude compared to that at RT and thus even a minor decrease in vacuum quality may have a noticeable effect on fibre/matrix interface-dependent properties. A bimodal fibre pull-out length distribution was noted for the composite when tested at 1380 °C with a transition point of approximately 370  $\mu\text{m}$ . Although not fully understood at present, such a change in behaviour at 1380 °C would be consistent with changes in the Si-Ti-C-O fibre (and fibre/matrix interface) at this temperature.

Preliminary fibre pull-out length distributions for surface-sealed specimens tested in air (Fig. 5(b)) show the pull-out length range to be similar to that of the unsealed composite tested at RT and elevated temperature in vacuum (Fig. 5(a)). The general form of the distributions in Fig. 5(b) is uncertain but at least one specimen (1200 °C) bears a resemblance to those seen in Fig. 5(a). From mechanical property data presented earlier it would be reasonable to expect fibre pull-out distributions for surface-sealed specimens at elevated temperature in air to be similar to those of unsealed specimens in vacuum at the respective test temperature. Thus, the fibre pull-out length data appears to add weight to the unsealed specimen fibre/matrix interface being stable at elevated temperature in vacuum (at least up to 1350 °C) with similar behaviour probable for surface-sealed specimens at elevated temperature in air.

Preliminary fibre fracture surface characteristics of unsealed composite tested in air at RT, 1100 °C, and 1200 °C were examined using SEM. Fibre fracture surfaces could be characterised into two main groups (“rough fracture surface” (RFS) and “smooth fracture surface” (SFS)) with the RFS fibres being further sub-divided into three categories, i.e.,

- (i) rough fracture surface with a fracture mirror origin at the fibre surface (RFS-S),
- (ii) rough fracture surface with a fracture mirror origin within the fibre body (RFS-B),
- (iii) rough fracture surface with no obvious fracture mirror (RFS-N), and
- (iv) smooth fracture surface (SFS).

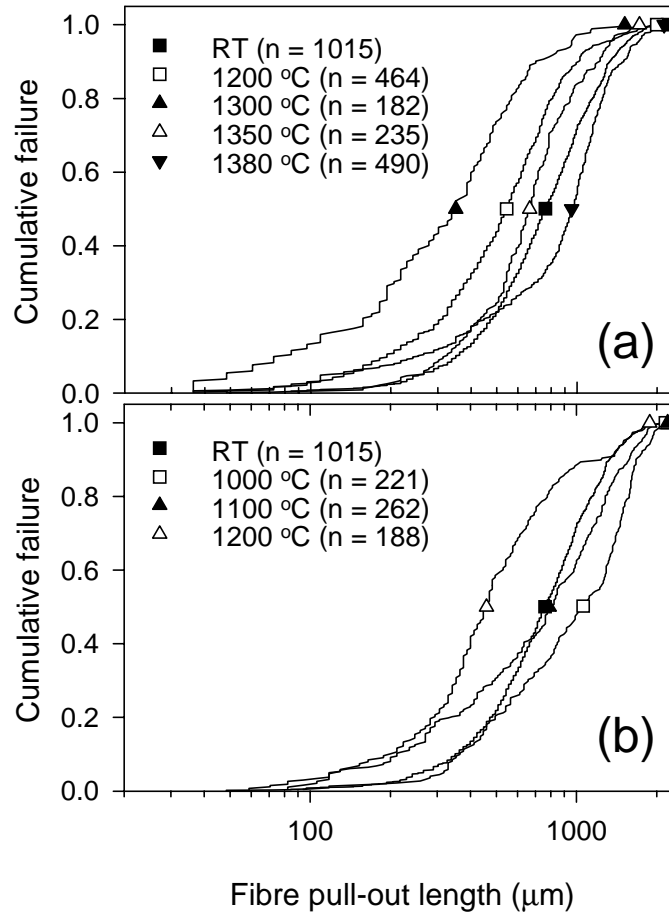


Fig. 5: Cumulative failure vs fibre pull-out length for SiC/SiC-based composite: (a) unsealed tested in vacuum, and (b) surface-sealed tested in air

Fig. 6 illustrates the fraction of fibres with different fracture surface characteristics as a function of test temperature and position with the fibre bundle for unsealed composite tested in air. Although not included in Fig. 6, the fraction of RFS-B fibres in all cases was almost insignificant compared to that of RFS-S fibres ( $\leq 2\%$  for the RT specimen) and is consistent with results of previous researchers. It may also be observed that the percentage of SFS fibres was substantially larger at 1100 °C and 1200 °C compared to at RT. One explanation for the presence of SFS fibres is that they represent fibres with such low fracture strength that a fracture mirror boundary was not formed. However, the more likely scenario in the present case is of the fibre and matrix being so strongly bonded following exposure to oxygen at elevated temperature that the propagating crack passed from matrix to fibre with little or no

change in velocity or direction. Further evidence for such a scenario is that all SFS fibers possessed negligible fibre pull-out.

It was also noted that SFS fibres were preferentially positioned around the perimeter of the fibre bundle, i.e., not in the centre. This can be more clearly observed in Fig. 7(b) with SFS fibres being preferentially positioned towards lower and higher values of the fibre bundle minor axis (which corresponds to the outer edge of the fibre bundle). In contrast to this, RFS-S fibres appear mainly limited to the central portion of Figure 7(b) parallel to the major axis (which corresponds to the central region of the fibre bundle). If the SFS fibres were indeed due to oxidation of the fibre/matrix interface, as seems likely, then it would suggest oxygen to have infiltrating the fibre bundle from the outer surface. Such a proposition is in contrast to previous researchers who concluded that oxygen attacks the fibre/matrix interface along the length of individual fibres. One explanation for this difference may be that the narrow (40 nm) carbon-rich layer at the interface in the present composite allows rapid SiO<sub>2</sub> formation and so limits oxidation to the composite surface, i.e., self-healing behaviour .

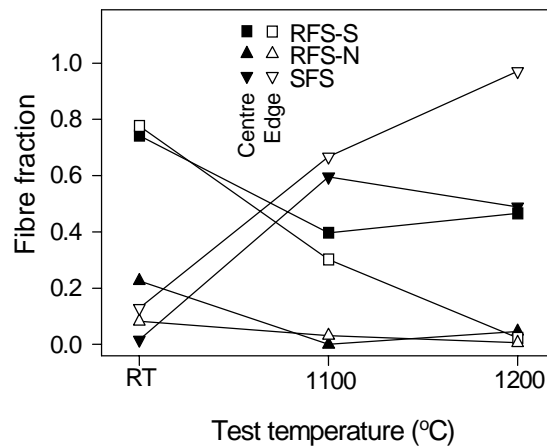


Fig. 6: Fibre fracture characteristics at the centre and edge of a fibre bundle for unsealed SiC/SiC-based composite tensile tested in air. Note non-linear temperature scale

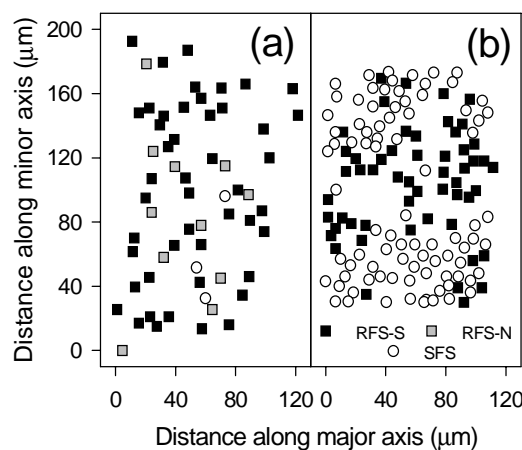


Fig. 7: Fibre fracture surface characteristics at the centre of a fibre bundle after tensile testing: (a) room temperature, and (b) 1100 °C in air



## CONCLUSIONS

- (i) The main characteristics of tensile property/strain curves were found to be consistent with predictions obtained from the modified Rule of Mixtures equation together with several assumptions.
- (ii) At room temperature the composite exhibited extensive fibre pull-out with the main crack path following the inter-fibre bundle porosity. This was accompanied by excellent mechanical properties including a tensile strength of 389 (+/-48) MPa and strain to failure of 1.14 (+/-0.04) % and suggested the fibre/matrix interface to have near-optimal properties.
- (iii) Unsealed composite tested at 1200 °C in vacuum possessed similar mechanical properties (except initial tensile modulus) and fracture surface characteristics as for the room temperature case. Increasing the test temperature further resulted in similar fibre pull-out properties but decreased tensile strength (50 % at 1380 °C) compared to at room temperature. It was proposed that the fibre/matrix interface was stable up to at least 1350°C in vacuum.
- (iv) Unsealed composite tested in air at 1100 °C and 1200 °C had a relatively flat featureless fracture surface with little evidence of fibre pull-out. This was reflected in poor mechanical properties and attributed to oxidation of the fibre/matrix interface under such conditions.
- (v) Surface-sealed composite tested in air up to 1200 °C had similar mechanical, fracture surface, and (possibly) fibre pull-out properties as for the unsealed composite in vacuum. This indicated that the surface-sealant utilised was successful in dramatically reducing oxygen diffusion into the composite under these conditions.
- (vi) Most fibres in the composite tested at room temperature possessed “rough” fracture surfaces with well-defined fracture mirrors originating at the fibre surface (RFS-S). However, for the unsealed specimen tested in air at elevated temperature the majority of fibre fracture surfaces were “smooth” with no evidence of a fracture “mirror” (SFS) whilst RFS-S fibres were mainly limited to the central portion of the fibre bundle. These results suggested oxidation to have proceeded from the outer surface of the fibre bundle (as opposed to along the fibre/matrix interface of individual fibres).

## ACKNOWLEDGEMENTS

This work was supported by funding from the Science and Technology Agency of Japan whilst one of the authors (IJD) was supported as a Science and Technology Agency Fellow. The authors gratefully acknowledge Y. Nomura and N. Suzuki for help with mechanical testing.

## REFERENCES

1. Bodet, R., Bourrat, X., Lamon, J., and Naslain, R., "Tensile creep behaviour of a silicon carbide-based fibre with low oxygen content", *Journal of Materials Science*, Vol. 30, 1995, pp. 661-677.
2. Bunsell, A. R., Berger, M. H., and Hochet, N., "Structural and mechanical characterisation of some alumina and SiC based fibres", *High-temperature ceramic-matrix composites II (A. G. Evans and R. Naslain, Ed.)*, *Ceramic Transactions*, volume 58, American Ceramic Society, Westerville, 1995, pp. 85-94.
3. Droillard, C., Voisard, P., Heibst, C., and Lamon, J., "Determination of fracture toughness in 2-D woven SiC matrix composites made by chemical vapor infiltration", *Journal of the American Ceramics Society*, Vol. 78, No. 5, 1995, pp. 1201-1211.
4. Ishikawa, T., Shibuya, M., Hirokawa, T., and Watanabe, N., "Mechanical properties of 3-D fabric ceramic composites using new PC type matrix for improved oxidation resistance", *Proceedings of the 37th JSASS/JSME structures conference, July 12th-14th, Fukuoka, Japan*, Japan Society of Aeronautical and Space Sciences, Tokyo, 1995, pp. 29-32 (in Japanese)
5. Naslain, R., "Challenging ceramic matrix composites for applications in severe environments", *Advanced Composite Materials*, Vol. 5, No. 1, 1995, pp. 35-44.
6. Masaki, S., Moriya, K., Yamamura, T., Shibuya, M., and Ohnabe, H., "Development of Si-Ti-C-O fiber reinforced SiC composites by chemical vapor infiltration and polymer impregnation and pyrolysis", *High-Temperature Ceramic-Matrix Composites II (A. G. Evans and R. Naslain, Ed.)*, *Ceramic Transactions volume 58*, American Ceramic Society, Westerville, OH, 1995, pp. 187-192
7. Ishikawa, T., Yamamura, T., Hirokawa, T., Hayashi, Y., Noguchi, Y., and Matsushima, M., "Strength and fracture toughness properties of oxidation resistant high-temperature ceramic matrix composites", *Proceedings of the 9th International Conference on Composite Materials: Volume II (A. Miravette, Ed.)*, Woodhead Publishing Co., Madrid, 1993, pp. 137-144.
8. Davies, I. J., Ishikawa, T., Shibuya, M., and Hirokawa, T., "Stress/strain behavior of 3-D woven SiC/SiC-based composites", submitted to *Journal of the American Ceramic Society*, 1996
9. "Advanced technical ceramics - Mechanical properties of ceramic composites at room temperature. Part 1: Determination of tensile strength", Report no. DD ENV 658-1, British Standards, Manchester, U.K., March 1993
10. A. G. Evans, "Perspective on the development of high toughness ceramics", *Journal of the American Ceramic Society*, Vol. 73, 1990, pp. 187-206
11. Davies, I. J., Ishikawa, T., Shibuya, M., Hirokawa, T., "Optical microscopy of 3-D woven SiC/SiC-based composites", submitted to *Composites Science and Technology*, 1996

12. Davies, I. J., Ishikawa, T., Shibuya, M., and Hirokawa, T., "Fibre properties in 3-D woven SiC/SiC-based composites after tensile testing at room and elevated temperature", *in preparation*
13. Droillard, C. and Lamon, J., "Fracture toughness of 2-D woven SiC/SiC CVI-composites with multilayered interphases", *Journal of the American Ceramic Society*, Vol. 79, No. 4, 1996, pp. 849-858
14. Prewo, K., "Tension and flexure strength of silicon carbide fibre-reinforced glass-ceramics", *Journal of Materials Science*, Vol. 21, 1986, pp. 3590
15. Emig, G. and Wirth, R., "Tensile strength of silicon carbide fibre bundles at elevated temperatures", *Journal of Materials Science*, Vol. 30, 1995, pp. 5813-5818
16. Thouless, M. D., Sbaizero, O., Sigl, L. S., and Evans, A. G., "Effect of interface mechanical properties on pullout in a SiC-fiber-reinforced lithium aluminium silicate glass-ceramic", *Journal of the American Ceramic Society*, Vol. 72, No. 4, 1989, pp. 525-532
17. Davies, I. J., Ishikawa, T., Shibuya, M., and Hirokawa, T., "Damage characterisation of 3-D woven SiC/SiC-based composites", *Proceedings of the 21st Symposium on Composite Materials (Oct. 31st-Nov. 1st 1996, Toyama, Japan)*, Japan Society for Composite Materials, Tokyo, 1996, pp. 103-104
18. Eckel, A. J., and Bradt, R. C., "Strength distribution of reinforcing fibres in a Nicalon fiber/chemically vapor infiltrated silicon carbide matrix composite", *Journal of the American Ceramic Society*, Vol. 72, No. 3, 1989, pp. 455-458
19. Naslain, R., "The concept of layered interphases in SiC/SiC", *High-Temperature Ceramic-Matrix Composites II (A. G. Evans and R. Naslain, Ed.)*, *Ceramic Transactions volume 58*, American Ceramic Society, Westerville, OH, 1995, pp. 23-39

# THE MECHANICAL PROPERTIES OF 3D WOVEN CARBON FIBERS REINFORCED CERAMIC MATRIX COMPOSITES

Wenwei Zheng, Xingye Wang, Jiayu Xiao, Fengrong Liu, Dazhi Jiang, Zhaohui Chen

*Department of Materials Engineering and Applied Chemistry, National University of Defense Technology, NUDT, Changsha, Hunan 410073, P.R. China*

**SUMMARY:** The paper reported the preparation and mechanical properties of different 3D woven carbon fiber reinforced silicon carbide (SiC) matrix composites via repeated infiltration-curing-pyrolysis of Polycarbosilane(PCS)/Divinylbenzene(DVB). By applying SEM to the fracture surfaces, the toughening and failure mechanisms were investigated to involve matrix cracking, fiber pull-out, and fiber breakage.

**KEYWORDS:** ceramic matrix composites, 3D woven structure, mechanical properties, carbon fiber, precursor pyrolysis

## INTRODUCTION

The incorporation of continuous and/or discontinuous fibers into ceramics can enhance strength, improve fracture toughness, thermal-shock and impact resistance[1]. Therefore, much attention has been paid on the researches about Continuous Fiber Reinforced Ceramic Matrix Composites (CFRCMC). Since recent years, certain key techniques about manufacturing CFRCMC have been solved[2]. For instance , several acceptable processing methods such as Chemical Vapor Infiltration(CVI)[3], precursor pyrolysis, sol-gel[4], etc., have been developed. Among these methods, precursor pyrolysis is considered as an effective and advanced processing to produce CFRCMC, especially in the case of complex reinforcements (e.g., 3D woven fiber preform) [5,6], because of the advantages that the processing is simple and the pyrolysis temperature is lower.

Recently, some outstanding progresses have been made in improving toughness and enhancing mechanical properties. In Table 1, there list some data of advanced CMCs' mechanical properties.

In this paper, 3D-Orth, 3D-Braided woven carbon fiber reinforced Ceramic Matrix Composites via repeated infiltration-curing-pyrolysis of PCS/DVB were successfully prepared, and their the mechanical properties and the influences of different woven structures on the mechanical properties of the composites were also studied.

Table 1: Mechanical properties of advanced CMC

	SiC <sub>w</sub> /Si <sub>3</sub> N <sub>4</sub>	SiC <sub>w</sub> /Al <sub>2</sub> O <sub>3</sub>	SiC <sub>f</sub> /Al <sub>2</sub> O <sub>3</sub>	SiC/Si <sub>3</sub> N <sub>4</sub>
Strength(MPa)	900	800	450	700
Toughness(MPam <sup>1/2</sup> )	20	8.7	18-23	/
	SiC <sub>f</sub> /AlN	SiC <sub>f</sub> /SiC	C <sub>f</sub> /Si <sub>3</sub> N <sub>4</sub>	C <sub>f</sub> /SiC
Strength(MPa)	440	300	481	500
Toughness(MPam <sup>1/2</sup> )	14-20	33	29	10

**EXPERIMENTAL PROCEDURE**

**Raw Materials**

Three different PAN-based carbon fibers (Jilin Chemical Inc., China) are used as reinforcing materials. The 3D woven carbon fiber preforms used in the present paper are the three dimensional orth and braided textile structures, which were fabricated by Tianjing Institute of Textile Technology (China). The principal properties of 3D woven carbon fiber preforms are shown in Table 2.

Table 2: The principal properties of 3D woven carbon fiber preforms

Woven Preforms	3D-O	3D-B4	3D-B6
Fiber Strength (MPa)	2700	4000	4200
Fiber Volume Fraction (%)	45.0	45.9	54.0
Ratio *	1:1:1	4:1:1	6:1:1

\* the fiber volume fraction ratio in the three principle marerial directions (v<sub>f</sub>)<sub>x</sub>: (v<sub>f</sub>)<sub>y</sub>: (v<sub>f</sub>)<sub>z</sub>.

The polymer PCS[7] is synthesized by the Department of Materials Engineering and Applied Chemistry at NUDT. Its molecular weight is 1200-1300, and soft point is 165-175<sup>o</sup>C, A mixture of PCS and DVB was used as precursor in the present paper.

**Production of the Composites**

The route of processing of 3D woven carbon fiber reinforced CMC by infiltration-curing-pyrolysis of PCS/DVB is shown in Fig.1.

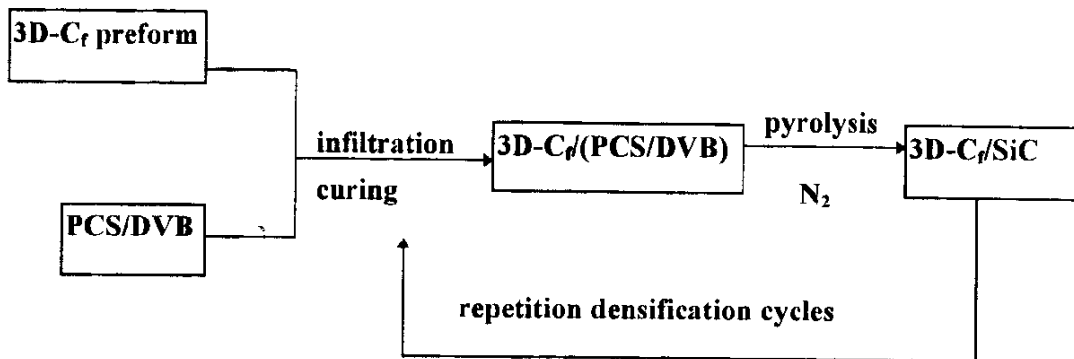


Fig.1: The sketch of processing by infiltration-curing-pyrolysis of PCS/DVB

The tailored and treated 3D woven carbon fiber preforms are infiltrated with PCS/DVB solution. After curing the solution to three dimensional network structures, 3D woven carbon fiber preforms reinforced PCS/DVB were pyrolyzed under N<sub>2</sub> atmosphere protection and controlled heating rate. In order to improve the mechanical properties, the repeated infiltration-curing-pyrolysis are needed to densify the composites.

### Measurement of the Composites

In this study, three point flexural strengths[8] were measured using CSS-1101 electronic omnipotent experimental machine (made in Changchun, China), with 12-15 ratio of span to height and 0.2mm/min crosshead speed. Fracture toughness  $K_{IC}$  were measured with the single edge notched beam technique (S.E.N.B) with  $a/w=0.48$  ( $a$ : initial crack length;  $w$ : thickness of the specimen). The calculation of  $K_{IC}$  is based on the assumption of a linear-elastic behavior.

## RESULTS AND DISCUSSION

### Densification of the Composites

Dense composites were obtained by repeated infiltration-curing-pyrolysis of PCS/DVB. The composites densification can be illustrated by Table 3 and Fig.2.

From Table 3 and Fig.2 , the density of 3D-Orth (1:1:1) and 3D-Braided (4:1:1) woven carbon fiber composites are lower than that of 3D-Braided (6:1:1) woven carbon fiber composites during densification of the early stage, which is due to the difference of fiber volume fraction of 3D woven preforms, and show that the density increasing is mainly controlled by fiber volume fraction during the early stage. During the later period, the density curves of 3D woven carbon fiber composites are reaching unanimity. The results show that the differences of 3D woven structure don't influence the densification of the composites when the processing condition is unanimous.

Table 3: Experimental density and porosity ratio data of the composites

materials	3D-O		3D-B4		3D-B6	
	density (g/cm <sup>3</sup> )	porosity ratio (%)	density (g/cm <sup>3</sup> )	porosity ratio (%)	density (g/cm <sup>3</sup> )	porosity ratio (%)
0	0.79	55.1	0.81	54.0	0.95	46.0
1	0.97	47.9	1.03	45.2	1.13	38.8
2	1.19	39.1	1.20	38.4	1.26	33.6
3	1.34	33.1	1.32	33.6	1.37	29.2
4	1.46	28.3	1.43	29.2	1.44	26.4
5	1.53	25.5	1.52	25.6	1.50	24.0
6	1.59	23.1	1.60	22.4	1.56	21.6
7	1.63	21.5	1.65	20.4	1.62	19.2
8	1.66	20.3			1.66	17.6

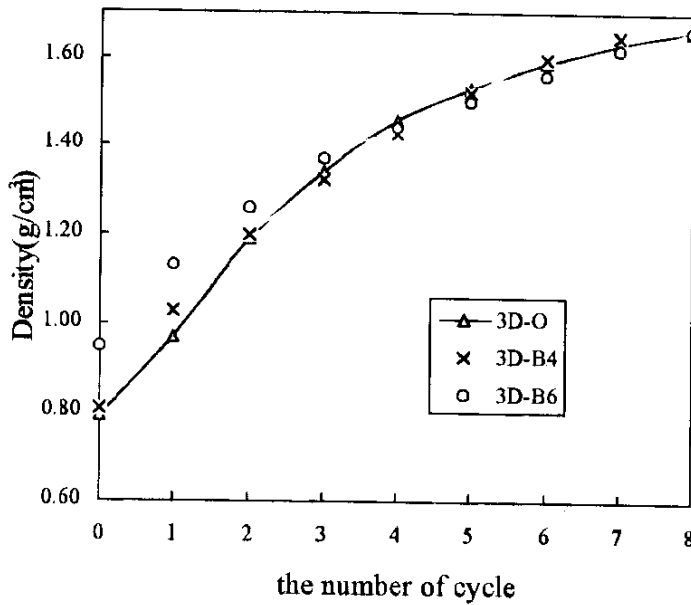


Fig. 2: The density of the composites versus the number of cycles

**The Mechanical Properties of the Composites**

High strength, high stiffness carbon fibers in CMC undertake most loads, block cracks spreading, make cracks breakage and fiber pull out to prevent material from disastrous destroy. Therefore, the goal of 3D woven carbon fiber reinforced silicon carbide matrix composites is to enhanced strength and improve fracture toughness. The results of mechanical properties of 3D woven C<sub>f</sub>/SiC CMC are shown in Table 4.

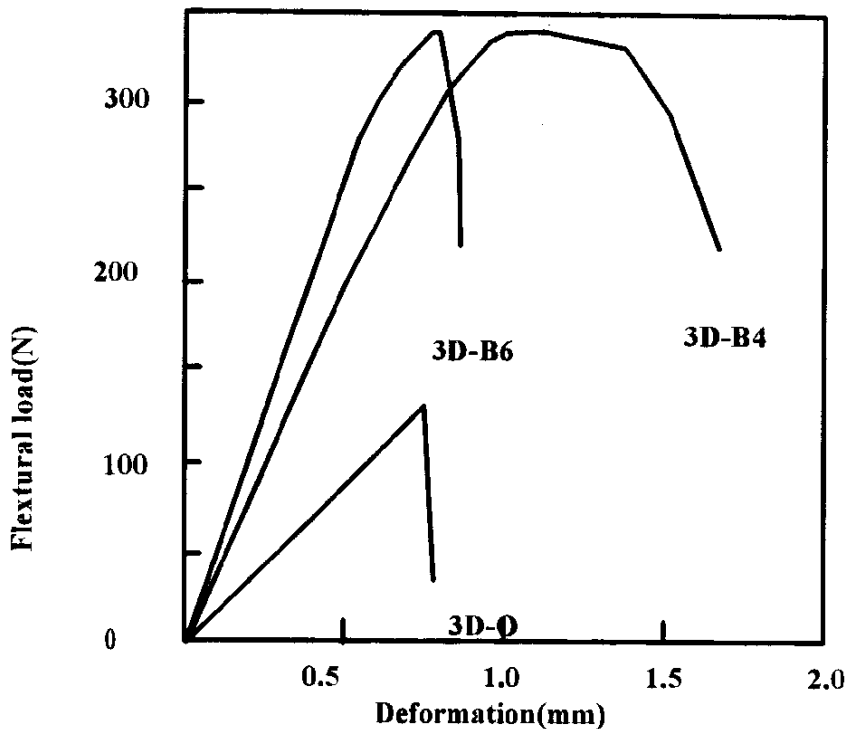


Fig.3: The flexural load versus deformation curves obtained in three-point bending.

Table 4: The mechanical properties of 3D woven C/SiC CMC.

	3D-O	3D-B4	3D-B6
cycles	8	7	8
density(g/cm <sup>3</sup> )	1.66	1.65	1.66
fiber volume fraction(%)	45.0	45.9	54.0
porosity ratio(%)	20.3	20.4	17.6
flexural strength(MPa)	140	330	390
toughness(MPam <sup>1/2</sup> )	5.4	13.7	8.4

The difference of mechanical properties of 3D woven carbon fiber reinforced CMC is from the influences of different 3D woven structures. The fiber in 3D-Orth woven preform (the fiber volume fraction is 45%) is continuous in x direction, but uncontinuous in y, z directions, the fiber strength only has 2700MPa, and its fiber volume fraction proportion in the three principle marerial directions  $(v_f)_x: (v_f)_y: (v_f)_z$  is equal to 1:1:1, the fiber volume fraction in x direction only has 15%. Therefore, the capability of high strength, high stiffness carbon fiber to undertake load in CMC is bad, its mechanical properties are not good. But the fibers in 3D-Braided woven preforms are all continuous in x, y, z directions, the fiber strength has more 4000MPa, and because their fiber volume fraction proportions in the three principle marerial directions  $(v_f)_x: (v_f)_y: (v_f)_z$  are equal to 4:1:1 and 6:1:1, respectively. The fiber volume fractions in x direction are higher than those of 3D-Orth woven preform, and the fibers in 3D-Braided woven preforms have small cross angle with x direction, entirety is good. Therefore, the mechanical properties of 3D-Braided woven carbon fiber reinforced CMC (flexural strength: 330MPa and 390Mpa, fracture toughness: 13.7Mpa<sup>1/2</sup> and 8.4Mpa<sup>1/2</sup>) are better than those of 3D-Orth (1:1:1) woven carbon fiber reinforced CMC (flexural strength: 140MPa, fracture toughness: 5.4MPa<sup>1/2</sup>).

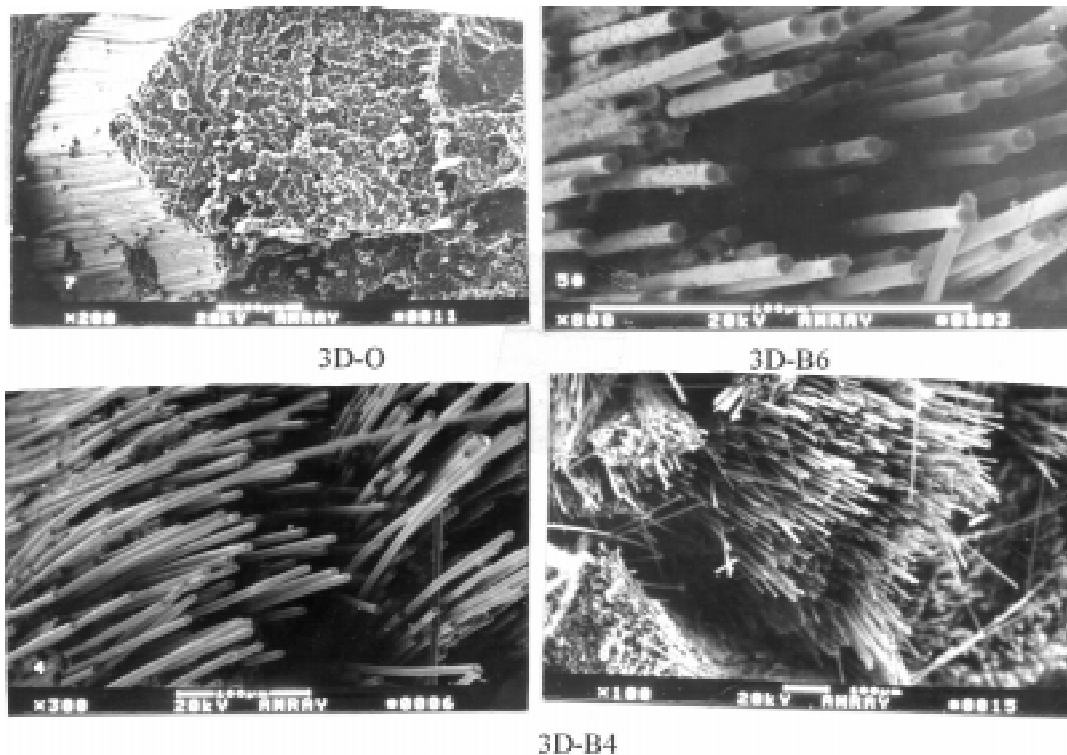


Fig. 4: SEM micrographs of fracture surfaces



The curves of flexural load versus deformation obtained in three-point bending test for 3D-Braided (4:1:1) and 3D-Braided (6:1:1) woven carbon fiber reinforced CMC (figure 3) show an evident tough mechanical behavior, which is due to the 3D-Braided woven structure, and show also that the fiber/matrix interface is weak and several energy dissipate mechanisms occurred during crack propagation (e.g.: crack breakage, deviation and division, interface debonding, fiber pull-out...) and lead to the increase in the crack propagation resistance.

From Fig. 4, 3D-Braided (4:1:1) woven C<sub>f</sub>/SiC fracture surfaces have a lot of pull out of long fibers, its fracture toughness is high (13.7MPam<sup>1/2</sup>), show that the interface strength is weak, by contrast, 3D-Braided (6:1:1) woven C<sub>f</sub>/SiC have few fibers pull out, its fracture toughness is not high (8.4MPam<sup>1/2</sup>), show that the interface strength is strong.

### CONCLUSION

- (1) Polymer precursor pyrolysis is an effective and advanced method to manufacture 3D woven carbon fiber reinforced ceramic matrix composites.
- (2) The mechanical properties of 3D-Braided structure C<sub>f</sub>/SiC CMC are significantly better than those of 3D-Orth structure C<sub>f</sub>/SiC CMC.
- (3) 3D-Braided woven carbon fiber reinforced SiC composites have excellent mechanical properties: the 3D-Braided (4:1:1) C<sub>f</sub>/SiC composites has a density of 1.65g/cm<sup>3</sup>, a flexural strength of 330MPa and a fracture toughness of 13.7MPam<sup>1/2</sup> after 7 times of infiltration-curing-pyrolysis, and 3D-Braided (6:1:1) C<sub>f</sub>/SiC composites has a density of 1.66g/cm<sup>3</sup>, a flexural strength of 390MPa and a fracture toughness of 8.4MPam<sup>1/2</sup> after 8 times of infiltration-curing-pyrolysis of PCS/DVB.

### REFERENCES

1. Salvatore, R. and Mary, K.M., "3-D Ceramic Matrix Composites Development", *Journal of Advanced Material*, vol.1, 1994, pp.22-28.
2. Laurel, M.S., "Progress in Composites Processing", *American Ceramic Bulletin*, vol.69, No.4, 1990, pp.
3. Caputo, A.J. and Lackey, W.J., "Fabrication of Fiber-Reinforced Ceramic Composites by Chemical Vapor Infiltration", *Ceramic Engineering Science Proceedings*, vol.5, No.7-8, 1984, pp. 654-667.
4. Sumio, S., "Sol-gel Synthesis of Glasses: Present and Future", *American Ceramic Society Bulletin*, vol.64, No.11, 1985, pp.1463-66.
5. Frank, K.K., "Preform Fiber Architecture for Ceramic-Matrix Composites", *American Ceramic Bulletin*, vol.68, No.2, 1989, pp.401-414.
6. Cecil, O.H.Jr and Gary L.F., "Development of Generalized 3-D Braiding Machines for Composite Preforms", *Composites Engineering*, vol.3, No.3, 1993, pp.209-218.

7. Delverdier, O., Monthieux, M., Mocaer, D., and Paillet, R., "Thermal Behavior of Polymer-derived Ceramics. I. Si-C and Si-C-O Systems from both Commercial and New Polycarbosilane (PCS) Precursors", *Journal of European Ceramic Society*, vol.12, 1993, pp. 27-41.

8. Hiroshi, A., "Mechanical Properties of Engineering Ceramics", *American Ceramic Society Bulletin*, vol.64, No.12, 1985, pp.1594-96.

# EFFECTS OF TEMPERATURE AND LAYUP ON THE MIXED-MODE DELAMINATION TOUGHNESS OF A CERAMIC MATRIX COMPOSITE MATERIAL

Jonathan J. Polaha, Tor W. Sherwood and Barry D. Davidson

*Department of Mechanical, Aerospace and Manufacturing Engineering,  
Syracuse University, Syracuse, NY 13244*

**SUMMARY:** The mixed-mode toughness of a Nicalon/MAS-5 ceramic matrix composite material was evaluated as a function of temperature and layup. Delamination toughness tests were performed at 21°C and at 500°C on unidirectional and crossply specimens. The fracture toughness,  $G_c$ , was evaluated at the mode mix  $G_{II}/G \approx 0.4$  using the single leg bending test; here,  $G_{II}$  is the mode II energy release rate and  $G$  is the total energy release rate. Specimens were tested with a mode I precrack, and then tested again after the crack advanced under the mixed-mode condition. All data was reduced by a compliance calibration method. In all tests, the onset of crack advance was ascertained with the aid of a laser interferometer, used to monitor the near-tip opening displacements during the tests, and an advanced ultrasonic inspection system. Ultrasonic inspections were performed whenever nonlinearities were observed in either the global load versus center-point deflection or the local load versus near-tip opening displacement results. The results from this study show that the crossply layup is approximately 30% tougher than the unidirectional layup and that, in both layups, a significant amount of toughening occurs with increasing crack advance. Mechanisms for this effect are described. No effect of temperature was observed.

**KEYWORDS:** delamination, fracture, single leg bending, mixed mode, crack tip element

## INTRODUCTION

Continuous fiber ceramic matrix composite (CMC) materials are increasingly being proposed for high temperature structural applications. However, as a result of their lack of through-the-thickness reinforcement and their relatively brittle matrix, these materials are susceptible to failure by delamination. Thus, the determination of the delamination toughness of a given material, commonly expressed through the critical energy release rate,  $G_c$ , is important for purposes of design as well as for quantitative comparisons of various material systems.

Previous investigations into the toughness of CMC materials have shown that  $G_c$  is a function of mode ratio, layup and temperature [e.g., 1,2]. Typically, the double cantilever beam (DCB) test is used to determine the mode I toughness [2] and the end-notched flexure (ENF) test is used to determine the mode II toughness [1]. The cracked four-point bend specimen [2,3] is perhaps the most common method for determining the mixed-mode toughness of CMCs. However, there are difficulties involved in introducing a well-defined delamination in this test, and one must make certain assumptions about material properties and the applicability of beam theory to reduce the test data to obtain  $G_c$ ; these and other issues concerning the failure mode of these specimens [2,4] may affect the validity of the results.

In this work, results are presented for the mixed-mode toughness of a Nicalon/MAS-5 CMC material. Unidirectional  $[0]_{16}$  and crossply  $[(90/0)_4]_5$  specimens were tested to evaluate the effects of layup. Both of these plates were manufactured by Corning Glass Works, and consist of a magnesium aluminosilicate matrix doped with 5% borosilicate glass reinforced with silicon carbide fibers produced by Nippon Carbon [5]. Delamination toughness tests were performed at room temperature (21°C) and at 500°C. The elevated temperature was chosen to be somewhat below that temperature where oxidation of the fibers has been observed (@650°C). The delamination toughness was evaluated at the mode mix  $G_{II}/G \approx 0.4$  using the single leg bending (SLB) test [6]; here,  $G_{II}$  is the mode II energy release rate and  $G$  is the total energy release rate. The advantage of the SLB test over other test methods is that a compliance calibration method of data reduction may be used to obtain highly accurate results.

## TEST METHOD AND DATA REDUCTION

A drawing of a typical SLB test is presented in Fig. 1. All tests were performed in a three-point bend fixture which was fabricated from silicon-carbide to provide the high temperature capability. In order to keep the upper surface of the specimen horizontal, the cut portions of the specimens (from the lower cracked region) were used as spacers beneath the right side support. The fixture had a half-span length,  $L$ , equal to 20 mm, and the support rollers had a diameter of 3.175 mm. Fig. 2 shows a schematic of the high temperature test configuration. The loading fixture resides within a furnace with large ports for optical viewing and making various measurements (described subsequently). A nickel-based super-alloy bracket is used to attach the fixture to the load frame actuator. Cooling attachments to the load frame are utilized at both the actuator and load cell connections.

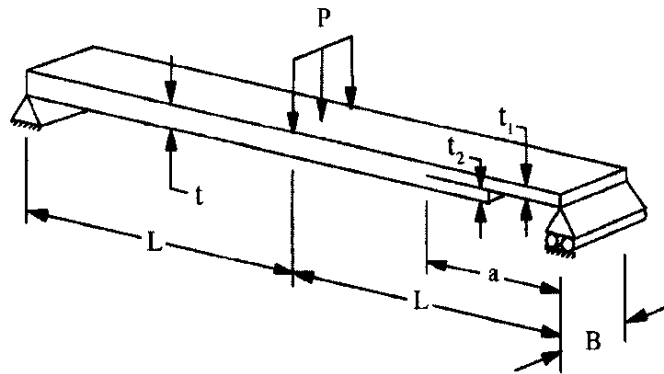


Fig. 1: SLB Specimen and Test Geometry

Data reduction for all tests was performed by compliance calibration. To this end, a compliance versus crack length curve was developed for each specimen tested. Each specimen was loaded to approximately 50% of its predicted fracture load at five different crack lengths. These predictions were based on preliminary tests that were performed to obtain an estimate of  $G_c$  at this mode mix. The crack length where the compliance tests were performed included the crack length at which the fracture test was to be run,  $a_c$ ,  $a_c \pm \delta a$ , and  $a_c \pm 2\delta a$ . To facilitate this process, the specimens were prepared with cracked and uncracked regions that were longer than required, and the crack length was adjusted by placing the specimen appropriately into the testing fixture. During the test, the displacements at the center of the specimen, beneath the loading point, were measured using a high sensitivity linear variable displacement transducer (LVDT). Three compliance tests were performed at each of the five crack lengths and the compliance at a given crack length,  $a$ , was obtained from the slope of a linear least-squares curve fit of the deflection versus load data. At each crack length, the compliance used for data reduction was taken to be the average value obtained from the three tests. A compliance versus crack length curve was obtained, for each specimen, by fitting a polynomial of the form

$$C = C_0 + C_1 a + C_3 a^3 \quad (1)$$

to the compliance versus crack length data. Once the compliance versus crack length relations were obtained for each specimen, all specimens were loaded to fracture.  $G_c$  for each specimen was obtained by substituting the appropriate compliance calibration curve, Eqn (1), into the expression [7]

$$G = \frac{P^2}{2B} \frac{\partial C}{\partial a} \quad (2)$$

and evaluating this result at the critical load,  $P_c$ , and critical crack length,  $a_c$ . In the above,  $B$  is the specimen width and  $C$  is compliance.

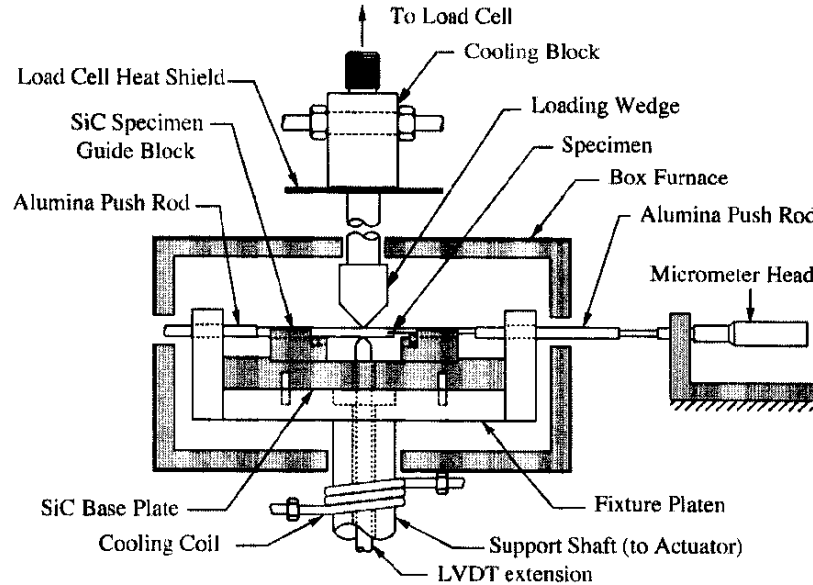


Fig. 2: High Temperature Test Configuration

### SPECIMEN PREPARATION

One 155 mm x 155 mm plate was supplied in a  $[0]_{16}$  layup, and one was supplied in a  $[(90/0)_4]_8$  layup. The plates were first cut into strips that were 6.35 mm wide, using a 0.38 mm thick diamond blade and a standard cut-off saw, such that delamination growth would proceed in the  $0^\circ$  direction. The specimen preparation procedures for the two specimen types were slightly different and are therefore described separately below.

For the unidirectional specimens, the strips were scored with crack growth "guides" along their centerlines along the two cut sides. These cuts were approximately 0.13 mm deep and were made using a 0.18 mm thick diamond blade. Following this, a notch, approximately 2 mm long, was introduced at one end of the specimen at its midplane. This was also performed using the 0.18 mm thick diamond blade. Next, the specimens were placed in the "precracking fixture" shown in Fig. 3. The fixture holds the specimen by clamping it in (what will remain) the uncracked region. A metal dowel pin is bonded onto one-half of the clamping fixture to arrest crack advance at the desired location. A micrometer head is used to slowly drive a razor blade into the specimen and drive the precrack by a prescribed amount. Precracks were driven until they (1) reached a length of approximately 17 mm, or (2) deviated significantly from the midplane. When this latter case occurred, defined by us as when  $|(t/t_2) - 1| > 0.17$  (cf. Fig. 1), the specimen was trimmed off beyond the end of the precrack, the precracked portion was discarded, a new notch was introduced, and the process was repeated. When the former case occurred, the specimen was trimmed to a total length of approximately 56 mm, and then the lower cracked region was cut off at a distance of 2.5 mm from the crack tip. The crack length at which the fracture test was performed,  $a_c$ , was 11.4 mm, and the compliance calibration increment,  $\delta a$ , was equal to 1.9 mm. The average uncracked thickness,  $t$ , of these specimens was 3.0 mm. This specimen and test geometry were such that, when all compliance calibration tests were performed, the right side loading fixture roller would only contact the precracked surface. This was necessary due to the large finite thickness of the notch. In addition, the value of  $a_{min}/t_1$  is sufficiently large that

the specimen always behaves like a short beam and allows Eqn (1) to reasonably fit the compliance versus crack length data. Also,  $(L - a_c)/t$  was sufficiently large so that transverse compression stresses in the vicinity of the center loading wedge should not affect the toughness. We point out that the specimen width,  $B$ , used in data reduction in Eqn (2) corresponded to the actual width less the depth of the two crack growth guiding grooves.

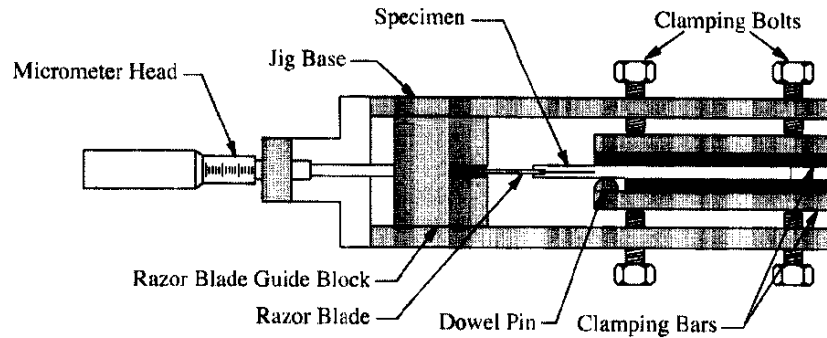


Fig. 3: Precracking Fixture

For the crossply layup, we were not able to precrack the specimens in a manner that would cause the crack to remain in the center 0/0 interface. Rather, the crack routinely would leave this interface, propagate into the adjacent 90° ply, and then either (1) remain within this ply (the 7<sup>th</sup> ply from the top of the specimen), but nearer to the upper 90/0 interface, or (2) continue to "jump" interfaces, causing the delamination to become further removed from the centerline. This behavior occurred whether or not the sides of the specimens were scored. After several different trial methods had been evaluated, we began introducing the notch within the 90° ply that was seven plies from the top of the specimen. The precrack was propagated from this point, for approximately 17 mm, and the specimen was not scored. For those cases where the delamination remained primarily within the 90° ply and the crack tip wholly within the 90° ply, the specimen was trimmed to a total length of 56 mm. For these specimens,  $a_c = 9.6$  mm and  $\delta a = 1.9$  mm were used for testing. This gave nearly the same  $a_{min}/t_1$  as the unidirectional specimens, and a slightly larger  $(L - a_c)/t$ . The average uncracked thickness of these specimens was 3.3 mm. The lower cracked region was cut off at a distance of 2.5 mm from the crack tip and, similar to the case of the unidirectional specimens, these resulting geometries were such that all compliance calibration tests could be performed with the loading fixture contacting only the precracked surface. For those specimens where the precrack reached almost 17 mm and the delamination moved out of the 90° ply, the specimen was trimmed off beyond the end of the precrack, a new notch was introduced, and the process repeated.

The above descriptions qualitatively agree with observations. However, other complex behaviors also occurred. Most notably, if one were to observe the specimen from one side, call it side 1, the precrack would not be perfectly planar. This "length planarity", is important if compliance calibration is to accurately simulate crack advance and therefore for the data reduction method to give accurate values of  $G_c$ . In addition, if at any given length location, one were to compare the location of the crack on side 1 versus side 2, exactly the same results would not be obtained. This "width planarity" is important, as the ratio of  $t_1/t_2$  determines the mode mix (this is discussed in the following section). Thus, specimens that lack width planarity will have nonuniform mode mixities (and likely energy release rates) along the delamination front, and the results of a test on such a specimen would be of little practical utility. The above geometric features were quantified in an effort to develop test specimens where these effects would be minimized. To this end, thickness measurements of the regions above and below the crack were taken at 5 locations on each side of each specimen. As described previously, the "length planarity" of all unidirectional specimens was less than 0.17; the width planarity of all unidirectional specimens, defined as  $|(t_{iL}/t_{iR}) - 1|$ , where  $i = 1, 2$ , and  $L, R$  stand for left, right, was also less than 0.17. For the crossply

specimens, width planarity was defined similarly and was less than 0.12 for all specimens. The length planarity for these specimens was defined, for each side, as  $|[(t_1/t_2)_{max}/(t_1/t_2)_{min}] - 1|$ , where the "max" and "min" denote the maximum and minimum ratios, respectively, of all the measurements made on that side. In all cases, the length planarity was less than 0.24. All of these upper limits were chosen simply because they were the lowest values we could enforce and still retain enough specimens to have a statistically significant pool.

### MODE MIX ANALYSIS

For both specimen types, it was assumed that the individual plies can be modelled as an equivalent homogeneous orthotropic material. The Young's moduli in the fiber and matrix directions for a unidirectional ply of the Nicalon/MAS-5 material are essentially the same, and were taken equal to 130 GPa. The Poisson's ratio,  $\nu_{xy}$ , was taken to be 0.22. These values came from micromechanical analyses and agreed with test results supplied by Corning. The mode mix of any test, defined here as  $G_{II}/G$ , was obtained by a crack tip element analysis [8]. This approach has the advantage of being in closed form, and as described below, allows mode mixities to rapidly be determined for each and every specimen based upon its individual geometry.

Due to the fact that the Young's moduli for this material are essentially the same in the fiber and matrix directions, the mode mix for both specimen types loaded in the SLB configuration depends primarily on the thickness ratio at the crack tip (there is also a weak dependence on  $a/t$  that is not reflected in the crack tip element results [6]). For these calculations, the thickness ratio at the crack tip was taken as the average of the values measured at this location on the two sides of the specimen, and the mode mix parameter was evaluated using the expression given in Ref. 8. Table 1 presents the specimens used in this study, broken up into the room temperature (RT) unidirectional, high temperature (HT) unidirectional, RT crossply and HT crossply. The first column of the table gives the specimen number, the second gives the thickness ratio,  $t_1/t_2$ , at the crack tip (taken as the average of those values measured at the two edges), and the third column gives the mode ratio. Note that, due to the fact that the delaminations in the crossply specimens were not at the midplane, the average mode mixity of these specimens is not exactly equal to that of the unidirectional specimens. However, as will be shown subsequently, the values are sufficiently close to draw some conclusions from a comparison of the test results.

Table 1: Specimen Mode Mixities

RT Unidirectional			HT Unidirectional			RT Crossply			HT Crossply		
Spec.	$t_1/t_2$	$G_{II}/G$	Spec.	$t_1/t_2$	$G_{II}/G$	Spec.	$t_1/t_2$	$G_{II}/G$	Spec.	$t_1/t_2$	$G_{II}/G$
10B	1.02	0.430	19B	1.05	0.431	18A	0.654	0.392	12A	0.605	0.359
19C	1.02	0.430	7B	0.99	0.430	11B	0.659	0.400	13A	0.612	0.362
20B	1.03	0.431	1A	0.97	0.431	22A	0.661	0.397	11A	0.642	0.382
13B	1.11	0.435	13C	1.10	0.434	7A	0.629	0.377	9B	0.630	0.375
9A	1.05	0.432	20C	1.12	0.435	13B	0.623	0.374	10B	0.643	0.389
AVG.	1.05	0.432	AVG.	1.04	0.432	AVG.	0.645	0.388	AVG.	0.632	0.373

### TEST PROCEDURE

#### Room Temperature Tests

All specimens were ultrasonically inspected (c-scanned) after precracking and prior to testing using a 25 MHz transducer and a system with a 200 MHz transient waveform digitizer. These results provided "baseline" delamination front profiles to which subsequent scans could be compared to assess whether delamination growth occurred. They were also used to

accurately determine the location of the delamination front with respect to the tip of the notch. Following this, all compliance tests were performed following the procedure previously defined, and then the fracture tests were performed. All compliance and fracture tests were performed in displacement control at a rate of 0.00127 mm/s.

To assist in determining the exact point of crack initiation, a laser interferometric displacement gage (LIDG), developed by Hartman and Nicholas [9], was used to monitor the real-time near-tip *opening* displacements during the fracture tests. In this technique, a laser is used to illuminate two reflective indentations on the specimen, and the fringe pattern produced by the interference of the reflected light from the two indents is resolved into a relative displacement. This is accomplished using linear array photo detectors which, in the present study, were positioned to receive the fringe patterns produced in the vertical (opening) plane. Because the CMC material used in this study was non-reflective, platinum foil tabs, measuring 2.5 mm x 1.5 mm, were bonded to each of the cracked regions of the specimen as shown in Fig. 4. Indentations were made using a micro-hardness indenter with a sapphire tip that produced a tetrahedral indent. As shown in Fig. 4, the tabs were bent to right angles, and then the portions of the tabs on the upper and lower surfaces were bonded with instant adhesive. For the HT specimens, a second coat of ceramic adhesive was applied on top of this region and cured according to the manufacturer's specifications. The indent-to-indent spacing, denoted as "x" in Fig. 4, was 100-200  $\mu\text{m}$ , and the indents themselves were approximately 1.3 mm behind the crack tip.

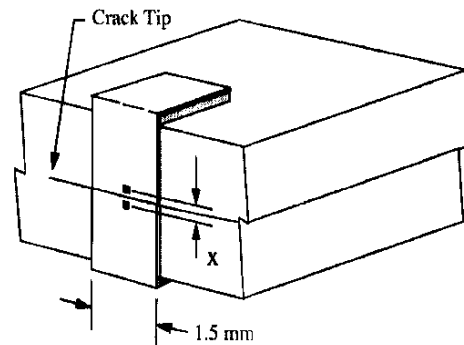


Fig. 4: LIDG Tab Geometry

During the fracture test, the load versus LVDT displacement and the load versus LIDG displacement curves were monitored in real-time. When nonlinearities in either of these plots were observed, the test was stopped to assess whether crack advance occurred. This was accomplished by removing the specimen from the fixture and ultrasonically inspecting the region containing the delamination front. The limit of sensitivity of this system was approximately  $\pm 0.25$  mm; typically, there would be greater than approximately 0.75 mm of advance over all or some of the delamination front for us to be certain that delamination growth occurred. For those cases where the test was stopped and no discernible advance was evident from the ultrasonic images, the specimen was returned to the fixture and the test repeated in the same manner. It is interesting to note that delamination advance was always observed some time *after* the first nonlinearities in the load versus LIDG displacements and load vs. LVDT displacements occurred. No quantitative evidence was observed that would correlate the onset of nonlinearity in these plots to delamination advance. It is possible that these nonlinearities corresponded to near-tip microcracking, or it may be that the rotations of the specimens, superposed onto the opening displacement, was the cause.

When delamination advance occurred as discussed above, the critical load was used with Eqns (1) and (2) to obtain  $G_c$ . Subsequently, this value of  $G_c$  will be referred to as  $G_c^{MI}$  to denote it is from a mode I precrack. Next, if the entire delamination front had not advanced, the specimen was returned to the fixture and re-loaded until delamination growth occurred over the entire front. The specimen was then scanned again to ascertain the new crack length and another fracture test was performed. This was done in the same manner as that described above. Subsequently, the critical energy release rate from any of these latter tests will be referred to as  $G_c^{MM}$  to denote it is from a mixed-mode precrack.

### Elevated Temperature Tests

The elevated temperature tests were performed identically to those at room temperature, with the exception that they were run in a furnace with large ports for optical viewing and to accommodate the laser light paths. Prior to any of the high temperature tests (compliance calibration or fracture), the specimen and fixture were allowed to "soak" in the furnace for a



period of time sufficient for the system to reach uniform temperature conditions. For the high temperature compliance calibration tests, the position of the specimen was adjusted using alumina push rods (cf. Fig. 2). To account for thermal expansions, careful measurements of the fixture and specimen at 21°C and at 500°C were obtained using an optical microscope with a digital displacement readout. This allowed the room temperature c-scans to be used to accurately position the specimen when it was in the furnace, i.e., to obtain the desired crack length for the compliance or fracture test.

## RESULTS

Fig. 5 shows typical results from the compliance calibration tests on the unidirectional and crossply specimens. The figure shows the individual results for each test at each crack length, as well as the curve-fit given by Eqn (1). Recall that, for the  $[(90/0)_4]_S$  layup, the total thickness,  $t$ , is greater than for the unidirectional specimens, but the cracked leg thickness,  $t_c$ , is less. This accounts for the lower compliance at short crack lengths and the larger compliance at long crack lengths of the crossply layup. Eqn (1) is observed to do a reasonable job of fitting the data in each case.

The  $G_c$  values obtained for all specimens are presented in Table 2. The fourth column in the table presents the change in crack length from the test with a mode I precrack to the test with a mixed-mode precrack, and the fifth column gives the increase in toughness for the mixed-mode precrack test. The last row in the table gives the normal standard deviations for each column. Referring first to the  $G_c^{MI}$  values, it is observed that there is no effect of temperature, and that the  $[(90/0)_4]_S$  layup is the tougher of the two. For the unidirectional tests from the mixed-mode precracks, it is observed that the amount of toughening is roughly scaled by the amount of crack advance. There is once again no significant effect of temperature, and the higher  $\Delta G_c$  values obtained in the HT tests are primarily a result of the larger  $\Delta a$  values that occurred. Interestingly, the proportional increase in the average  $\Delta a$  from the RT to the HT tests, roughly 1.5 times, essentially matches the proportional increase in the average  $\Delta G_c$ . For the crossply specimens tested with the mixed-mode precracks, a similar toughening that is roughly scaled by  $\Delta a$  is observed. Here, the proportional difference in  $\Delta a$  for the RT as compared to the HT tests, approximately 2 times, essentially matches the proportional difference in  $\Delta G_c$  between the two test groups. Finally, since toughness generally increases with increasing  $G_{II} / G$  [1], the greater toughness evidenced by the crossply specimens cannot be attributed to their different mode mix.

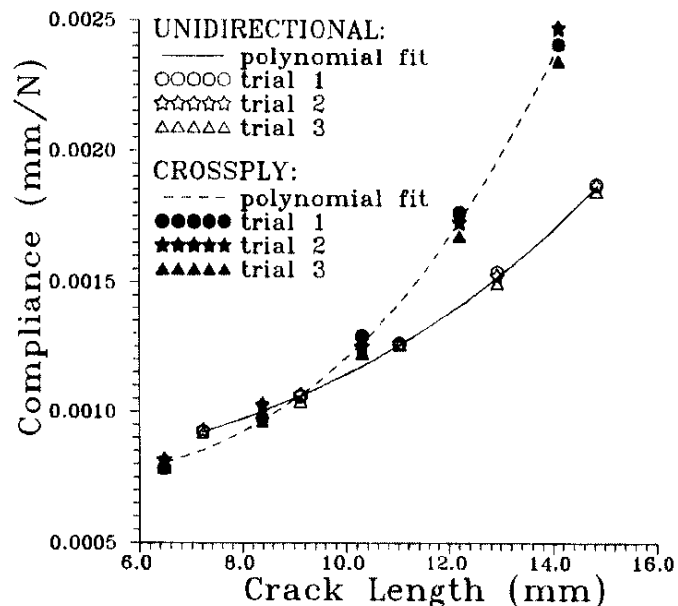


Fig. 5: Typical Compliance Calibration Results

Following the tests, the delaminated surfaces of many of the specimens were propped open and the specimens were examined from their edges to look for fiber bridging. Next, many of the specimens were split along their entire length and the delaminated surfaces examined. Both of these were done with an optical microscope at various magnifications and viewing angles. The unidirectional specimens showed fiber bridging in both the region of the mode I precrack and in the region of crack growth during the test. An examination of the fractured

surfaces showed relatively few broken fibers in the region of the mode I precrack. Thus, the bridged fibers in this region, which were at a relatively shallow angle, were presumed to have nestled back into the precracked surface. In contrast, there was a dramatic increase in surface roughness starting at the location where the first fracture test was conducted that was characterized by large numbers of broken fibers. The majority of these fibers were pulled up from the plane of the crack at a relatively steep angle and their broken ends were pointing in the direction of crack advance. This was accompanied, macroscopically, by a general trend of decreasing  $t_i$  with increasing  $\Delta a$ . By the end of the test from the mixed-mode precrack, the crack had generally moved sufficiently to be just out of the scored crack growth guides. Thus, further R-curve characterization of these specimens was not possible. There was no significant difference in these observations between the RT and HT specimens, with the exception that slightly greater reductions in  $t_i$  were observed for the HT specimens. This is consistent with their larger  $\Delta a$  and  $\Delta G_c$  values (cf. Table 2).

Table 2: Fracture Test Results

Unidirectional RT					Unidirectional HT				
Spec.	$G_c^{MI}$ ( $J/m^2$ )	$G_c^{MM}$ ( $J/m^2$ )	$\Delta a$ (mm)	$\Delta G_c$ ( $J/m^2$ )	Spec.	$G_c^{MI}$ ( $J/m^2$ )	$G_c^{MM}$ ( $J/m^2$ )	$\Delta a$ (mm)	$\Delta G_c$ ( $J/m^2$ )
10B	59.8	69.1	0.76	9.3	19B	50.7	69.7	1.52	19.0
19C	42.5	51.7	0.30	9.2	7B	58.5	78.1	1.14	19.6
20B	47.4	55.7	1.22	8.3	1A	78.3	128.3	2.67	50.0
13B	50.2	55.7	0.15	5.5	13C	38.6	59.7	1.22	21.1
9A	47.5	95.6	2.44	48.1	20C	39.5	61.3	0.99	21.8
AVG.	49.5	65.6	0.97	16.1	AVG.	53.1	79.4	1.51	26.3
S.D.	6.4	18.0	0.92	18.0	S.D.	16.3	28.3	0.68	13.3

Crossply RT					Crossply HT				
8A	112.0	137.5	3.12	25.5	12A	74.3	95.3	0.76	21.0
11B	34.7	101.4	2.51	66.7	13A	67.9	82.0	0.99	14.1
22A	69.9	107.0	0.76	37.1	11A	66.0	116.2	0.76	50.2
7A	72.3	137.5	1.60	65.2	9B	58.7	66.9	1.07	8.2
13B	59.2	85.5	1.91	26.3	10B	62.0	84.3	1.22	22.3
AVG.	69.6	113.8	1.98	44.2	AVG.	65.8	88.9	0.96	23.2
S.D.	28.0	23.0	0.90	20.4	S.D.	5.9	18.3	0.20	16.1

For the crossply specimens, fiber bridging was also observed. In many specimens, this was in both the region of the precrack and of the test. Upon examination of the fractured surfaces, it was found that the delaminated region in the center of the specimen had often moved into the  $0^\circ$  ply by the end of the mode I precrack, although it was still within the  $90^\circ$  ply at the specimen's edges. For those specimens or those regions of various specimens where delamination growth remained within the  $90^\circ$  ply, crack branching generally occurred, with the crack advancing at two or three different planes within the ply. When the primary delamination left the  $90^\circ$  ply, it always did so into the upper  $0^\circ$  ply. In these cases, bridged fibers from the mode I precracked region and from the test region generally stayed intact until the end of the test from the mixed-mode precrack. The fractured surfaces showed many broken fibers. In contrast to the unidirectional specimens, however, the debonded fiber lengths were relatively long, and the angles at which the fibers protruded from the fractured surface were very shallow. Thus, it appears that the two primary toughening mechanisms in the crossply layup are crack branching within the  $90^\circ$  ply and the extensive length and number of bridged fibers when the primary crack enters a  $0^\circ$  ply. Toughening in the unidirectional layup is also due to fiber bridging, but the length and number of fibers bridging the crack at any one time is less. In both layups, the numbers of bridged fibers are likely greater than would be observed in a mode I test; this is primarily due to the crack

rapidly changing planes as it grows under the mixed-mode conditions. Similar to the unidirectional layup, the crossply specimens showed a general trend of decreasing  $t_1$  with increasing  $\Delta a$ . By the end of the test from the mixed-mode precrack, the delamination had moved a sufficient amount from its original plane that the data reduction procedure was deemed to no longer be accurate, and further R-curve behavior could therefore not be examined.

## CONCLUSIONS

This study illustrated toughening behaviors that may occur in mixed-mode delamination growth in other CMC materials. For design purposes, the roughly 30% difference in toughness between the  $[0]_{16}$  and  $[(90/0)_4]_8$  layups indicates that it may be overly conservative to use toughness values as obtained from unidirectional specimens. For a given layup, it may be most appropriate to use that value of toughness obtained from a mode I precrack for prediction of delamination initiation, as this will give the most conservative result. However, any observed R-curve effects may be used to investigate the propensity for the delamination to continue to grow, provided that the R-curve is obtained during the test without the delamination moving a significant amount from its original plane. When this latter event occurs, as was observed herein, the accuracy of the compliance calibration (or any other) method of data reduction becomes questionable. Finally, this study demonstrated the utility of the SLB test to investigate mixed-mode behaviors. This test, used in conjunction with the DCB and ENF tests, will likely provide a sufficient amount of information on the variation in  $G_c$  with mode mix for practical design applications.

## ACKNOWLEDGEMENTS

This work was primarily supported through the NASA/Syracuse University Center for Hypersonics, NASA Headquarters Grant NAGW-3713, Isaiah Blankson, monitor. Additional support was provided by the Materials Behavior Branch of Wright Laboratory (WL), where the majority of this work was performed. The authors gratefully acknowledge the help of a great number of the personnel at WL and at the University of Dayton Research Institute, and in particular Dr. Theodore Nicholas for his assistance on all phases of this project, Dr. Andrew Rosenberger for assistance in developing the experimental set-up, and Mr. Larry Zawada for providing the materials used.

## REFERENCES

1. Mall, S. and Hoobler, M.A., "Fracture Toughness of a Fiber-Reinforced Ceramic Composite Under Mode I and Mode II Loadings," *Achievement in Composites in Japan and the United States, Proceedings of the Japan-U.S. CCM-V*, A. Kobayahi, Ed., 1990, pp. 211-218.
2. Shercliff, H.R., Vekins, G. and Beaumont, P.W.R., "Direct Observation of the Fracture of CAS-Glass/SiC Composites; Part I - Delamination," *Journal of Materials Science*, Vol. 29, 1994, pp. 3643-3652.
3. Charalambides, P.G., Lund, J., Evans, A.G. and McMeeking, R.M., "A Test Specimen for Determining the Fracture Resistance of Bimaterial Interfaces," *Journal of Applied Mechanics*, Vol. 56, 1989, pp. 77-82.
4. Davidson, B.D., Altonen, C.S. and Polaha, J.J., "Effect of Stacking Sequence on Delamination Toughness and Delamination Growth Behavior in Composite End-Notched Flexure Specimens," *Composite Materials: Testing and Design (Twelfth Volume)*, ASTM STP 1274, C.R. Saff and R.B. Deo, Eds., American Society for Testing and Materials, 1996, pp. 393-413.
5. Larson, D.C., "Thermally Durable Glass-Ceramic Matrix Composites," *Corning Incorporated R&D Status Report No. 11 for May 1 - June 30, 1992*, Contract F33615-90-C-5909, 1992.

6. Davidson, B.D. and Sundararaman, V., "A Single Leg Bending Test for Interfacial Fracture Toughness Determination," *International Journal of Fracture*, Vol. 78, No. 2, 1996, pp. 193-210.
7. Broek, D., "Elementary Engineering Fracture Mechanics," *Martinus Nijhoff*, 1982.
8. Davidson, B.D., Hu, H. and Schapery, R.A., "An Analytical Crack Tip Element for Layered Elastic Structures," *Journal of Applied Mechanics*, Vol. 62, No. 6, 1995, pp. 294-305.
9. Hartman, G. and Nicholas, T., "An Enhanced Laser Interferometer for Precise Displacement Measurements," *Experimental Mechanics*, 1992, pp. 234-239.

# TOUGHENING OF SILICON NITRIDE MATRIX COMPOSITES BY THE ADDITION OF SI-C-N NANOMETER PARTICLES

Xingui Zhou, Changrui Zhang, Zhaohui Chen, Kai Xie and Anchen Zhou

*Department of Materials Engineering and Applied Chemistry,  
Changsha Institute of Technology, 410073, Changsha, Hunan, P.R.China*

**SUMMARY:** In this paper,  $\text{Si}_3\text{N}_4$  matrix composites reinforced by Si-C-N nanometer particles or SiC whiskers were fabricated using the hot-pressing technique. The mechanical properties of the composites containing various amounts of these Si-C-N nanometer particles were investigated. The maximum fracture toughness of these composites was  $11.96 \text{ MPam}^{1/2}$  and the flexural strength was 878.50 MPa after addition of 20 wt% of Si-C-N nanometer particles. It showed that the Si-C-N nanometer particles can remarkably improve the properties of  $\text{Si}_3\text{N}_4$  matrix. Fracture surface and the micrographs of local intend areas were examined by SEM, the results revealed that the reinforcing mechanisms acting in these nanocomposites were crack deflection and crack branching by Si-C-N particles.

**KEYWORDS:** toughening, si-c-n nanometer particles, silicon nitride, fracture toughness, ceramic matrix composites

## INTRODUCTION

$\text{Si}_3\text{N}_4$  and SiC ceramic are well known for their high strength, hardness and thermal stability, as well as the extreme brittleness that prevents their application in many critical components. The mechanical properties of these ceramics have been improved by the microstructure development, however, it seems to be difficult to expect the further improvement of mechanical properties by this technique. The need for further improvement in the mechanical properties has led to the development of high-strength and high-toughness ceramics, such as fiber-, whisker- and particulate- reinforced ceramic matrix composites[1,2]. SiC was used as a reinforcing material for  $\text{Si}_3\text{N}_4$  more than 20 years ago[3], for the attempt to take advantage of the characteristics of both materials. Owing to process problems and the cost of SiC whiskers and fibers, the attention was being devoted to particulate composites. However, the use of SiC as uniform particles cannot improve noticeably the properties of the  $\text{Si}_3\text{N}_4$  matrix.

Recently, researchers have found that the properties of ceramic can be dominantly improved by reducing particle sizes to nanometer levels, Niihara and his colleagues have been investigating the  $\text{Si}_3\text{N}_4$  based nanocomposites, in which the nano-size SiC particles are dispersed mainly with the matrix grain[4-6], the flexural strength reaches 1550 MPa, the fracture toughness reaches  $7.5 \text{ MPam}^{1/2}$ . The materials are referred to as “nanocomposites” and the approach is generally indicated as a “new design concept” in the structure ceramic field. Research on nanometer particles toughening ceramic matrix composites becomes a new “hot point”.

In this paper, nanometer Si-C-N particle reinforced  $\text{Si}_3\text{N}_4$  composites were made, the mechanical properties were measured, the phase structure was studied by XRD, the main goal was to improve the properties of  $\text{Si}_3\text{N}_4$  matrix and to understand the reinforcing mechanisms of these nano-size SiC dispersed composites.

## EXPERIMENTAL PROCEDURE

### Fabrication of Composites

Si-C-N nanometer particles used as the reinforcing materials were made in our laboratory, through a Chemical Vapor Condensation (CVC) method, the average particle sizes were 70 nm, the total carbon in the particles was 24.08wt%, and the total nitrogen was 18.06wt%, Fig.1 showed the shape. As another reinforcing materials SiC whiskers with an average diameter of 0.6  $\mu\text{m}$  were used, starting powders for the matrix material were  $\text{Si}_3\text{N}_4$  (average particle size 1.0  $\mu\text{m}$ ), and  $\text{La}_2\text{O}_3$  (average particle sizes 2.0  $\mu\text{m}$ ),  $\text{Y}_2\text{O}_3$  (average particle size 0.5  $\mu\text{m}$ ).

As the Si-C-N nanometer particles contained many agglomerates which obstructed the densification of the composite, the particles must be through dispersion. This dispersion was executed by ultrasonication and stirring in alcohol. The SiC whiskers were pretreated using 50vol%HF + 50vol%HNO<sub>3</sub> for 30 minutes, then washed with deionized water. After the treatment, the Si-C-N nanometer particles and SiC whiskers were dried and used for the reinforcing materials.

The Si-C-N nanometer particles (or SiC whiskers) were mixed with the  $\text{Si}_3\text{N}_4$  matrix powders which had been obtained by mixing of  $\text{Si}_3\text{N}_4$  powder and sintering-aid powders in advance. The contents of the sintering-aid powders were 10wt%  $\text{La}_2\text{O}_3$  and 10wt%  $\text{Y}_2\text{O}_3$  with respect to the weight of the matrix powders. The powders were wet milled in alcohol for 24h,  $\text{Si}_3\text{N}_4$  grinding media were used in all milling step. After drying, the obtained powders were sieved to under 100 mesh and were molded in a BN-coated graphite die for sintering. Hot-pressing was carried out at 1800 for 1h in a flowing nitrogen atmosphere under a pressure of 27.5 MPa for all composites. As comparison, monolithic  $\text{Si}_3\text{N}_4$  with the same sintering-aid was also fabricated under the same conditions. Table 1 showed the contents of the composites.

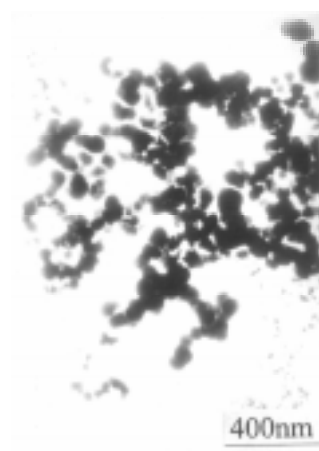


*Fig.1: The shape of Si-C-N nanometer particles*

Table 1: The contents of the composites (wt%)

Sample	Si-C-N	SiC whiskers	Si <sub>3</sub> N <sub>4</sub>	La <sub>2</sub> O <sub>3</sub>	Y <sub>2</sub> O <sub>3</sub>
S1	---	---	80	10	10
S2	10	---	70	10	10
S3	20	---	60	10	10
S4	---	20	60	10	10

### Measurements of Composite Properties

Hot-pressed plate samples were cut into bars and polished for measuring the mechanical properties of the composites. Flexural strength were measured by three-point bending test, the sample size was 3mm x 4mm x 35mm, the span was 30mm. Fracture toughness was measured by a Single-End Straight-notch Beam (SENB) method, the sample size was 2.5mm x 2.5mm x 30mm, the notches were machined using a diamond blade 0.15mm wide deeply cut in the center.

Fracture toughness was also measured by an indentation fracture (IF) method. A surface flaw was made in the Well-polished specimens plane perpendicular to the hot-pressing axis by a standard diamond Vickers' indenter using a 19.6 KN load with a loading time of 20 seconds,  $K_{IC}$  values were calculated using the following equation:.

$$K_{IC}=0.142(c/a)^{-1.56}(E\Phi/H)^{2.5}Ha^{1/2}/\Phi \quad (1)$$

Where  $c$  is the radius of crack length,  $a$  is the impression radius,  $H$  is the hardness value calculated from the diagonal length,  $E$  is the Young's modulus of the composites, and  $\Phi$  is the constraint factor ( $\approx 3$ ). An average elastic modulus of 310GPa was assumed for the composites.

Density of the composites was measured by the Archimede's method using deionized water as the immersion medium, and their relative densities were evaluated using the theoretical densities calculated from simple mixing theory.

### Results and Discussion

The Density and hardness of the composites reinforced with Si-C-N nanometer particles and SiC whiskers are listed in Table 2. All of the composites had densities higher than 3.2 g/cm<sup>3</sup>, indicating that the composites were densified using Y<sub>2</sub>O<sub>3</sub>-La<sub>2</sub>O<sub>3</sub> sintering additives. The differences in relative density among these composites may be attributed to the presence of the Si-C-N nanometer particles, the results showed that the obstacle role of Si-C-N nanometer particles to the sintering of Si<sub>3</sub>N<sub>4</sub> was more than that of SiC whiskers, and the sintering condition of Si-C-N nanometer particle reinforced Si<sub>3</sub>N<sub>4</sub> composite wasn't very suitable, which should be studied further. The density and content of the composites will affect the hardness, with the density increasing, the hardness increases; with the SiC adding in, the hardness increases, it was confirmed by the values of hardness in Table 2.

Table 2: The Density of the composites

Sample	Measured density (kg/cm <sup>3</sup> )	Calculated density (kg/cm <sup>3</sup> )	Relative density (%)	Hardness (GPa)
S1	3.53	3.49	100	14.20
S2	3.41	3.43	99.42	14.17
S3	3.29	3.39	97.05	13.26
S4	3.42	3.39	100	15.57

The room-temperature flexural strength of the composites measured by three-point bending are listed in Table 3, varied from 689.9~878.5MPa, the fracture toughness values measured by both the SENB method and indentation fracture method are also listed in Table 3, the fracture toughness measured using SENB method varied from 8.27~11.24MPam<sup>1/2</sup>. The result values of the indentation technique were lower than those of the SENB values, but the rules were the same. The fracture toughness showed strong dependence on the amount of the Si-C-N particles, the 10 wt% Si-C-N particles had no significant effect on the fracture toughness. In contrast, the 20wt% Si-C-N powder addition significantly improved toughness.

It is well known that the porosity of the composites will significantly affect the mechanical properties of Si<sub>3</sub>N<sub>4</sub> matrix, it was very interesting that the density of S3 (reinforced with 20wt% Si-C-N nanometer particles) was the lowest, the relative density was only 97.05%, and the hardness was also the lowest, but the flexural strength and the fracture toughness values were the highest, even more than S4 (reinforced by 20wt% SiC whiskers). In Ref.7, the fracture toughness of SiC particle reinforced Si<sub>3</sub>N<sub>4</sub> was improved significantly by the addition of SiC particles, but the flexural strength of the composite was decreased by introducing SiC particles. In this paper with the nano size Si-C-N adding, both of the toughness and the flexural strength were increased. It showed that the presence of Si-C-N nanometer particles make remarkable improvement of Si<sub>3</sub>N<sub>4</sub> matrix, it revealed a bright prospect of nanocomposites.

Table 3: The mechanical properties of the composites

Sample	Item	Flexural strength (MPa)	Fracture toughness (MPam <sup>1/2</sup> )	
			SENB	IF
S1		689.9	8.36	7.87
S2		785.4	8.27	7.72
S3		878.5	11.96	8.85
S4		804.8	11.24	8.78



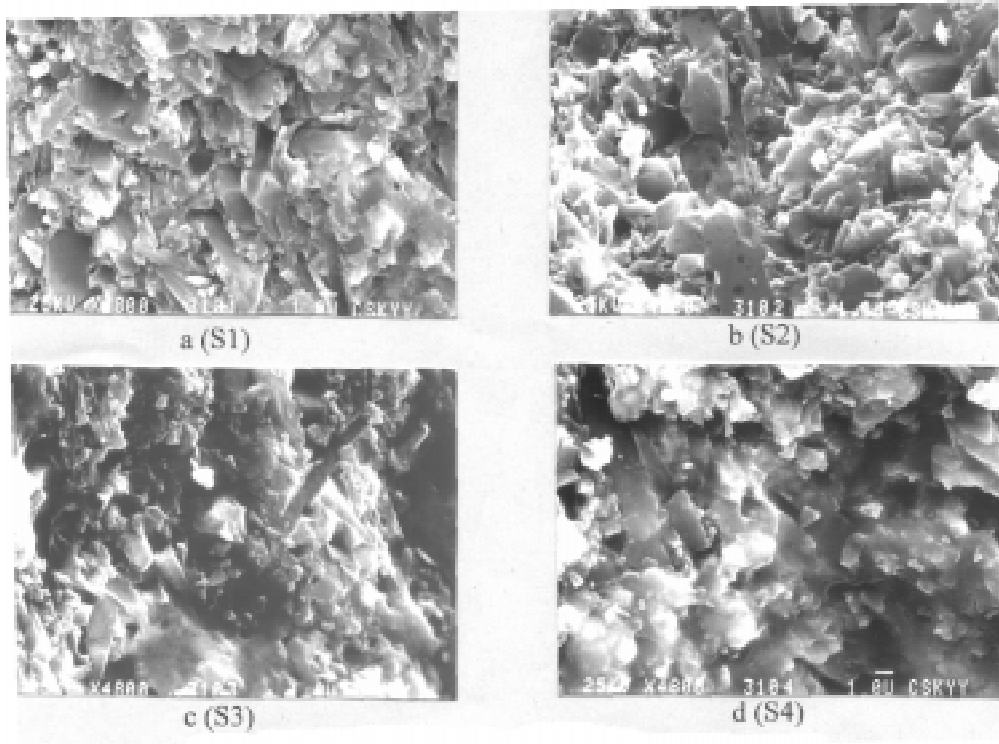


*Fig.2: The fracture surfaces of the composites (SEM)*

The fracture surfaces of the composite examined by SEM are shown in Fig.2, It showed that intergranular fracture and “rough” fracture surfaces developed in all cases. The photos indicated that the morphology of  $\text{Si}_3\text{N}_4$  grains in the nanocomposites was strongly influenced by the Si-C-N dispersions, the growth of of elongated  $\text{Si}_3\text{N}_4$  grains was accelerated by the SiC dispersion, as compared with monolithic  $\text{Si}_3\text{N}_4$ , the nanocomposites were composed of more uniform and homogeneous elongated  $\text{Si}_3\text{N}_4$  grains. SiC whisker “pull-out” was observed in Fig.2d and elongated  $\beta\text{-Si}_3\text{N}_4$  grain “pull-out” in other photos in Fig.2.

The micrographs of local intend areas examined by SEM are shown in Fig.3, it can be seen that the crack length of S3 and S4 was shorter than that of S1 and S2, this showed more evidence of why the fracture toughness of S3 and S4 were higher than that of S1 and S2.

The X-ray diffraction analyses of the composites revealed that the major phases were  $\beta\text{-Si}_3\text{N}_4$  and  $\beta\text{-SiC}$ , Fig.4 shows the XRD parttern. Work is in process to characterize further the effect of phase structure of Si-C-N nanometer particles reinforced  $\text{Si}_3\text{N}_4$  composites on their mechanical properties.

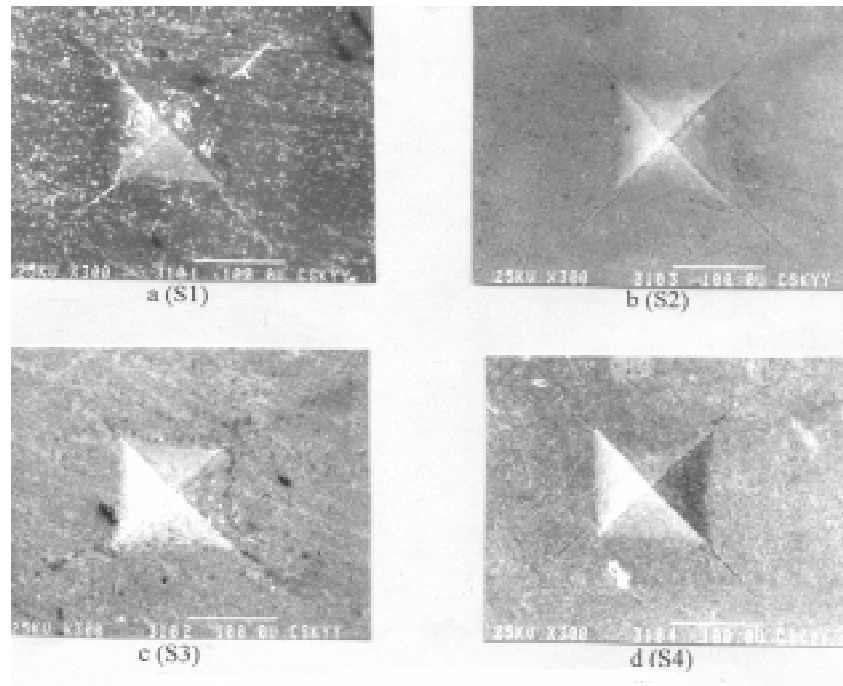


*Fig.3: The micrographs of local interfacial areas (SEM)*

### **CONCLUSIONS**

1. Si-C-N nanometer particles has noticeable reinforcement to  $\text{Si}_3\text{N}_4$  matrix, it can improve both of the fracture toughness and flexural strength.
2. The obstacle role of Si-C-N nanometer particles to the sintering of  $\text{Si}_3\text{N}_4$  was more than that of SiC whiskers.
3. The fracture toughness showed strong dependence on the amount of the Si-C-N nanometer particles.
4. The reinforcing mechanisms acting in the Si-C-N nanometer particle reinforced  $\text{Si}_3\text{N}_4$  composites were crack deflection and crack branching by Si-C-N particles.

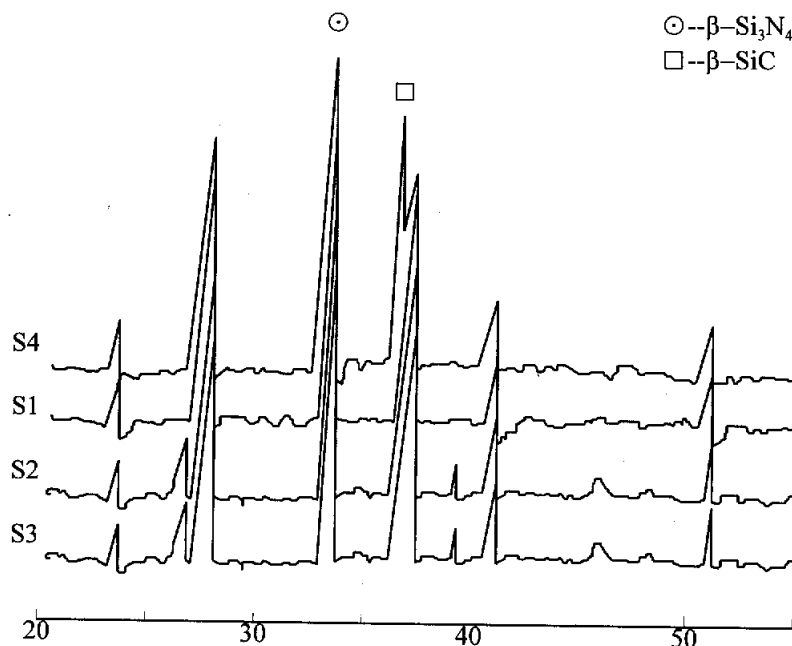


Fig.4: The XRD of the composites

### REFERENCES

1. Buljan, S.T. and Zilberstein, G., *Advanced Structure Ceramics*, edited by Becher, P.F., Suain, M.V. and Somiya, S., (MRS, Pittsburgh, PA), 1987, pp.273-281.
2. Wei, G.C. and Becher, P.F., "Development in SiC-Whisker-Reinforced Ceramics", *Am. Ceram. Soc. Bull.*, Vol.64, No.2, 1985, pp.298-304.
3. Lange, F.F., "Effect of Microstructure on Strength of  $\text{Si}_3\text{N}_4$ -SiC Composite System," *J. Am. Ceram. Soc.*, Vol.56, No.9, 1973, pp.445-490.
4. Niihara, K., "New Design Concept of Structural Ceramics: Ceramic Nanocomposites", *J. Ceram. Soc. Jpn.*, Vol.99, No.10, 1991, pp.974-982.
5. Niihara, K., Suganuma, K., Nakahira, A. and Izaki, K., "Interfaces in  $\text{Si}_3\text{N}_4$ -SiC Nano-composite", *J. Mater. Sci. Lett.*, Vol.9, No.10, 1990, pp.598-599.
6. Niihara, K., Izaki, K. and Nakahira, A., "The Silicon Nitride-Silicon Carbide Nanocomposites with High Strength at Elevated Temperatures", *J. Jpn. Soc. Powder Metall.*, Vol.37, No.2, 1990, pp.352-356.
7. Hironori, K, Takaaaki, S., Hiroshi, S. and Tadahiko, M., "Toughening of Silicon Nitride Matrix Composites by the Addition of Both Silicon Carbide Whiskers and Silicon Carbide Particles", *J. Am. Ceram. Soc.*, Vol.73, No.3, 1990, pp.678-683.

# NON LINEAR BEHAVIOR OF TWO WOVEN CERAMIC MATRIX COMPOSITES UNDER CYCLIC LOADING

Jean-Marie Morvan and Stéphane Baste

*Université Bordeaux I, C.N.R.S. URA 867, Laboratoire de Mécanique Physique,  
351, Cours de la Libération, 33405 TALENCE Cedex, France.*

**SUMMARY:** The non-linear mechanical behavior of both a 2D SiC-SiC and a 2D C-SiC woven ceramic matrix composites is investigated under cyclic loading by means of a metrology coupling an ultrasonic method and classical strain measurements. It appears that the loss of stiffness during monotonous loading is mainly due to transverse microcracks density and that the changes in elasticity during cyclic loading are the result of the opening/closure of these cracks. In order to take this effect into account, an internal variable that represents the damage accumulated along the loading is introduced. The non linear behavior of both materials is predicted under both monotonous and cyclic loading. The constitutive laws of the crack density and opening/closure variable describe the three-dimensional changes in elasticity under cyclic loading as well as the inelastic strains along the whole test.

**KEYWORDS:** microcracking, anisotropic damage, ceramic matrix composites, cyclic loading, inelastic strains

## INTRODUCTION

The non-linear behavior of ceramic matrix composites (CMC) has been extensively studied under monotonous loading [1]. Concerning cyclic loading, the knowledge is mostly concentrated on cyclic fatigue and frictional sliding determination. It is now commonly recognize that the macroscopic behavior of these materials under tensile loading is the result of the combination of three main damage mechanisms [2]: the matrix microcracking normal to the tensile axis, the deflection of these cracks at the fiber-matrix interface if the interface is weak enough and the fibers fracture. The matrix microcracking induces a loss of stiffness. The Mode II cracking prevents the composite from failing too early. The fiber-matrix debonding leads to a fiber-matrix sliding with friction depending on the nature of the interface. The interfacial shear stress is thus of first importance in the global behavior. The combination of these mechanisms leads to a highly non linear behavior.

The stress-strain curves of these materials clearly show that the global strain is the sum of an elastic and an inelastic strain. The inelastic strain comes from both the opening of the transverse cracks and the interfacial fiber-matrix sliding [3]. Nevertheless this sliding is subordinate to the direction of the load. Assuming the damage is the relative variation of the stiffness tensor [4], it appears that the damage does not increase, or slightly, during the cycles. The value of damage reached during monotonous loading is the upper limit of

damage during the cycles. When a cyclic loading is performed, as the stress decreases during unloading, a sliding opposite to the one created by an increase in stress can occur. The transverse cracks that have been created during the monotonous loading are then prone to close (Fig. 1). They are still present anyway but their closure simulates an increase of stiffness as if the material could recover its mechanical properties. The cracks that remain open represent the active part of the microcracking. The sample exhibits an apparent state of damage while the damage accumulated is greater.

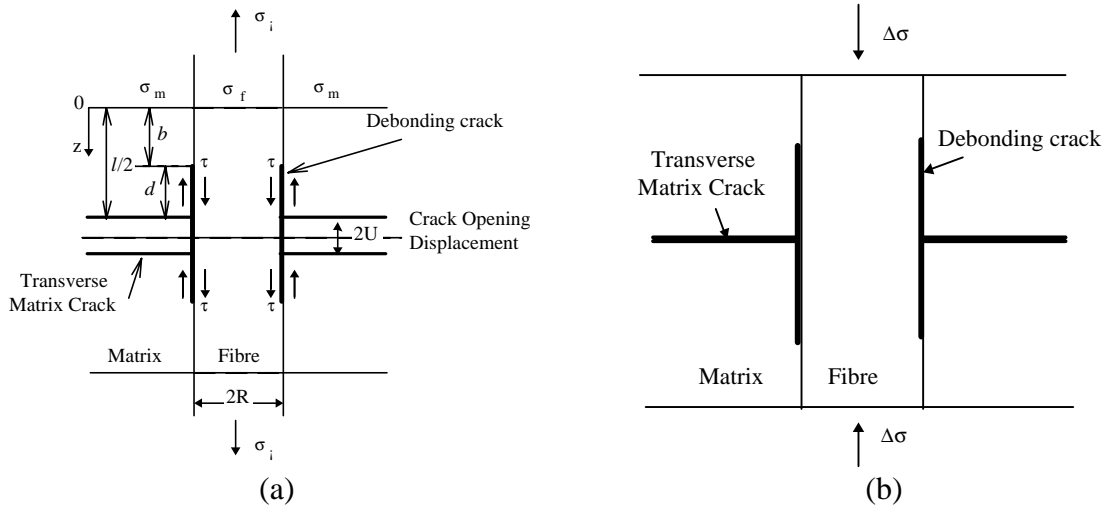


Fig. 1: States of the transverse cracks: (a) Open crack, (b) Close crack

In order to separate and to identify accurately the effects of the initiation and growth of matrix microcracks under tensile loading as well as the effect of these cracks under cyclic loading on both the stiffness and the inelastic strains, it is necessary to perform a strain partition under load.

### FORMULATION OF THE MODEL

With the cracked media replaced by an effective equivalent medium, it is possible to deduce the variations of the elastic properties of the cracked material. By modeling the cracks as elliptic cylinders;  $x_1^2/a^2 + x_2^2/b^2 = 1, |x_3| < \infty$ , the effective elastic properties of a fibrous composite containing cracks are [5]:

$$S = S_0 + \frac{\pi}{4} \beta \Lambda \tag{1}$$

where S is the compliances tensor of the material,  $S_0$  is the compliances tensor of the uncracked material,  $\Lambda$  is a fourth order tensor which terms depend upon both the cracks whose aspect ratio  $\delta=b/a$  tends to zero and the mechanical properties of the medium that surrounds them and  $\beta$  is the crack density. Cracks thickness  $2b$  in Direction 3 is considered as negligible. Length  $2c$  in Direction 2 is higher than depth  $2a$  in Direction 1.

Thus, the damage due to a single damage orientation can be described with one parameter only: the crack density. This formulation was written for a single crack system. Actually the degradation process exhibits several specific orientations. It is very common to observe three

orthogonal crack systems in CMC; a transverse one due to matrix cracking, a longitudinal one due to fiber-matrix debonding as well as an interlaminar one when delamination occurs [6]. It is also important to keep in mind that these systems might interact. For the transverse crack system, normal to the tensile axis, only three components of  $\Lambda$  are different from zero [7]:  $\Lambda_{33}^T$ ,  $\Lambda_{44}^T$  and  $\Lambda_{55}^T$ . As the cracks are deviated in mode II in the fiber-matrix interphase, a longitudinal crack system with crack density  $\beta_L$  must be taken into account. For this longitudinal crack system, parallel to the tensile axis, the non zero components of the crack tensor  $\Lambda^L$  are obtained by a simple index transformation:  $\Lambda_{22}^L$ ,  $\Lambda_{44}^L$  and  $\Lambda_{66}^L$ . When delamination occurs, the interstacks cracks that appear are modeled by a family of slit cracks parallel to Plane (2, 3) and normal to Axis 1. The crack density is  $\beta_L$ . We then have for the crack tensor  $\Lambda^I$ :  $\Lambda_{11}^I$ ,  $\Lambda_{55}^I$  and  $\Lambda_{66}^I$ .

As a proportion of the transverse cracks can close during unloading, it is necessary to differentiate an apparent state of cracking and the number of cracks that have been created effectively [8]. The closing effect induces a damage deactivation leading to unilateral behavior [9]. Obviously, the crack density parameter is very sensitive to the effect of the opening/closure of the cracks. Just as the active cracks were defined, we can define an active crack density:

$$\beta = F \cdot \beta^* \quad (2)$$

where  $F$  is the proportion of active cracks and  $\beta^*$  is the density of cracks that have been accumulated.  $F$  represents the proportion of cracks that remains open during unloading.

Taking into account the phenomenon of opening-closure of the cracks, assuming that the effects of the various cracks systems are additive and adding a corrective term that takes into account their interaction, the compliance tensor of the cracked material becomes:

$$S = S_0 + \frac{\pi}{4} F_T \cdot \beta_T^* \Lambda^T + \frac{\pi}{4} F_L \cdot \beta_L^* \Lambda^L + \frac{\pi}{4} F_I \cdot \beta_I^* \Lambda^I + S^{interaction} \quad (3)$$

Thus, the global behavior depends upon six functions:  $\beta_i^*$  and  $F_i$  ( $i=T,L,I$ ). The compliances variations are then simply a function of the various cracks systems that appear through the variations of the crack densities and of the mechanical properties of both the uncracked and damaged material. When cyclic loading is performed, the opening/closure functions  $F_i$  modulate the compliances variations.

The inelastic strains represent a large part of the total strains in CMC. It is now commonly recognized that they mainly come from the crack opening displacements, in other words, the cracks thicknesses. In an extensometer length  $L$ , if there are  $n$  cracks,  $2a$  deep and  $2b$  thick, the distance between them is  $2a/\beta_T^*$ . So:

$$n = L \beta_T^* / 2a, \quad (4)$$

and then:

$$\varepsilon^{inelastic} = \Delta L^{inelastic} / L = n U / L = n 2b / L = \delta \beta_T^* \text{ where } \delta = 2b / 2a \quad (5)$$

During unloading, the effect of closure of the cracks must be taken into account. It is clear as well that some cracks will not close completely, some have a residual thickness. This thickness is most probably due to the roughness of the cracks edges coming from both wear debris at the sliding interfaces and wedging of the cracks by grain bridging. That is why another aspect ratio  $\delta'$  that takes this new thickness into account is introduced. Finally, the variations of inelastic strains during the whole test can be described by:

$$\epsilon^{inelastic} = \beta_T^* (F(\delta - \delta') + \delta') \quad (6)$$

The inelastic strains are thus a function of the transverse crack density and of the aspect ratio of the cracks whether they are completely open or not. As for the compliances, the opening/closure function modulates the inelastic strains variations during cyclic loading.

The opening of the cracks is strongly correlated to the sliding stress that takes place at the fiber/matrix interface. The measurement of the inelastic strains and the identification of the transverse crack density had lead us, with the help of a modified shear lag model [10], to establish a new formulation to identify the interfacial sliding stress  $\tau$ :

$$\tau = RE_f \left( \left( \alpha / \beta_T \right) \epsilon^{anelastic} - \epsilon^{elastic} \left( \left( l/8 \right) - \left( b^2 / 2l \right) \right) \right) \left( (l/2)^2 - b^2 \right)^{-1} \quad (7)$$

Eqn (7) simply relates  $\tau$  to the radius of the fibers  $R$ , their Young modulus,  $E_f$ , the distance between the cracks,  $l$  and the length along which the interface remains bonded,  $b$  (Fig. 1 (a)).

### EXPERIMENTAL RESULTS

In order to study accurately the damage evolution in composites, an experimental device that couples an ultrasonic immersion tank associated to a tensile machine and an extensometer has been developed. It allows to study the loss of stiffness of the material under tensile stress because it makes it possible to perform under load the angular investigation necessary to identify the elastic tensor variation. As it gives access to the complete stiffness tensor, it becomes possible to know which coefficients are affected during the damage [11]. It also allows to know precisely which proportion of the global strain is either elastic or inelastic [12].

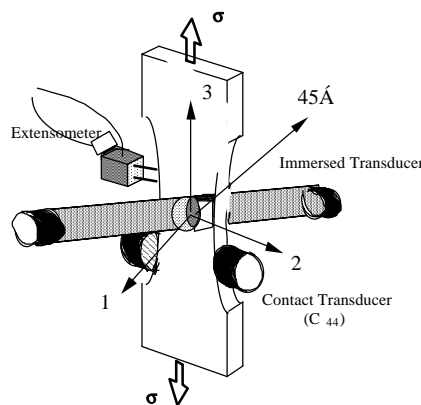


Fig. 2: Under load strain partition equipped sample

The characterization of anisotropic materials using an ultrasonic method gives access to the purely elastic part of their behavior. The main principles of ultrasonic evaluation have been given by Roux [13] for the elastic coefficients evaluation of homogeneous anisotropic materials. The nine elastic constants  $C_{ij}$  which fully describe the elastic behavior of an orthotropic material are identified by the wave propagation velocities in three data planes: Plane (1, 2), Plane (1, 3) and Plane (1,  $45^\circ$ ) described by the bisectrix of axis 2 and 3 (Fig. 2) [14].

The two composites studied, a 2D SiC-SiC and a 2D C-SiC, are of woven type. They are manufactured from preforms built up from multiple layers of respectively Silicon Carbide and Carbon cloth by S.E.P. (Société Européenne de Propulsion, France). The SiC matrix was in both cases added by chemical vapor infiltration. Under tensile stress, they exhibit rapidly a non linear behavior mainly due to the matrix microcracking. Because of the woven nature of the samples, Directions 2 et 3 are initially symmetrically equivalent. Both specimens are thin plate shaped, 3 mm in thickness and  $2.7 \text{ g.cm}^{-3}$  in density. They were submitted to tensile stress in Direction 3 parallel to one of the bundle direction.

The stress-strain curves of the samples are shown on Fig. 3 and 4. Although the strain to failure is about 0.8 per cent for the two composites studied, they reach this value in a different manner. The 2D C-SiC exhibits quite immediately a non linear behavior whereas the 2D SiC-SiC remains elastic until about 80 MPa as the linear variation of the strain testifies. About the cycles performed, the lack of hysteresis in the 2D C-SiC curve is relevant of the fact that the sliding occurs with little or no friction in the fiber-matrix interface whereas the large loops with many changes in slopes that appear in the curve of the 2D SiC-SiC are relevant of the interfacial debonding extent and emphasize the presence of sliding with friction that needs a threshold of stress to occur. But in both cases, the permanent strains are far from negligible. It is noteworthy that, until 120 MPa, the stress-strain curve of the 2D SiC-SiC shows that the strain increases during the steps necessary for the ultrasonic evaluation while the loading device is constant stress controlled.

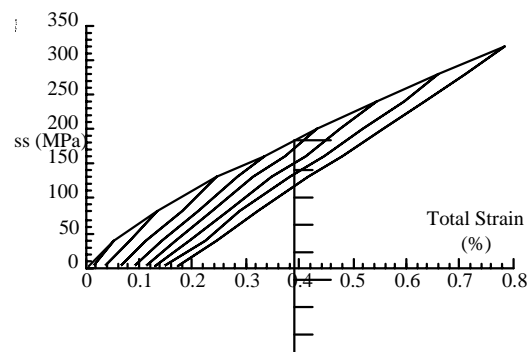
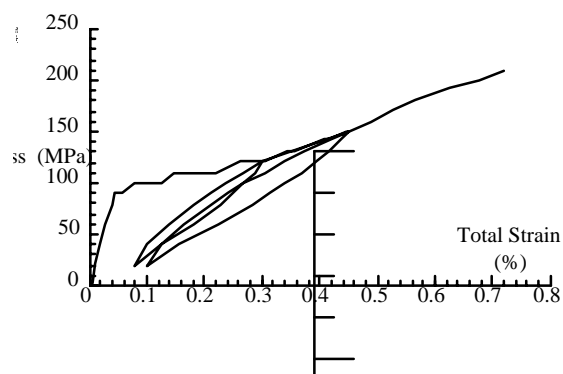


Fig. 3: Stress-Strain Curve of a 2D SiC-SiC

Fig. 4: Stress-Strain Curve of a 2D C-SiC

The accuracy and the reliability of the complete determination of the stiffness tensor together with its variation during the test allow, by inverting this tensor, to get the tensor of elastic compliances and its own variation. The variation of all the components of the compliance tensor of the 2D SiC-SiC with their confidence interval is shown in Fig. 5. The compliances variations exhibit three domains. Until 70 MPa, damage threshold of this composite, the various compliances remain the same. From then, the matrix microcracking begins. The compliances increase along the tensile axis is very large;  $S_{33}$  increases more than 300%. This represents the increase in compliance due to the inter-bundles matrix cracks until saturation at



about 120 MPa. Then, this variation becomes slighter as the matrix microcracking spreads inside the bundles. The shear moduli related to the planes that include the tensile axis,  $S_{44}$  and  $S_{55}$ , also increase a lot. The microcracking affects more slightly the elastic coefficients in Plane (1, 2) normal to the cloth plane.

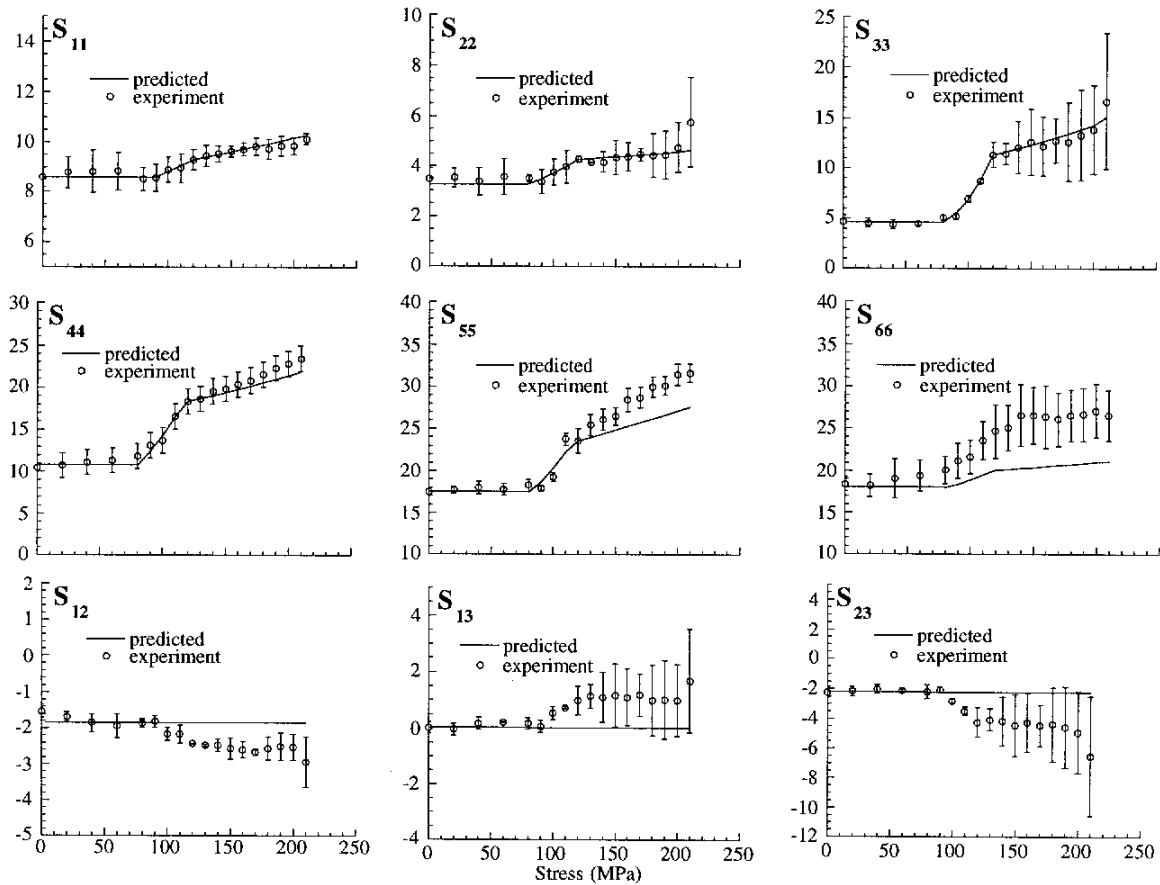


Fig. 5: Comparison between experimental data and predicted evolution of the compliances  $((1000.GPa)^{-1})$  of a 2D SiC-SiC.

Fig. 6 shows the variations during the cycles of the compliances of the 2D C-SiC that were the most influenced by the damage with their relative confidence intervals. The cycles are shifted for clarity.  $S_{33}$ ,  $S_{44}$  and  $S_{55}$  relative to the transverse cracks system are the only compliances to exhibit a variation during the cycles.  $S_{11}$  does not vary at all during the whole test and nor  $S_{66}$  nor the off diagonal compliances,  $S_{12}$ ,  $S_{13}$  and  $S_{23}$ .  $S_{22}$  varies during the monotonous loading but do not change along the cycles. The progressive variation of  $S_{33}$ ,  $S_{44}$  and  $S_{55}$  during the cycles points out a progressive closure of the cracks. As the cracks close, they are active no more and they lose the effect they had on the stiffness constants. When the sample is reloaded, the cracks re-open, become active again and every compliance reaches the value it has before unloading.

The elastic strains are obtained with the generalized Hooke's law:

$$\varepsilon_i^{elastic} = (C_{ij})^{-1} \sigma_j = S_{ij} \sigma_j \quad (8)$$

Therefore the elastic strain along the tensile axis is simply  $S_{33}$  times the applied stress. As an extensometer indicates the total strain, the inelastic strain is then obtained simply:

$$\epsilon^{inelastic} = \epsilon^{total} - \epsilon^{elastic} \quad (9)$$

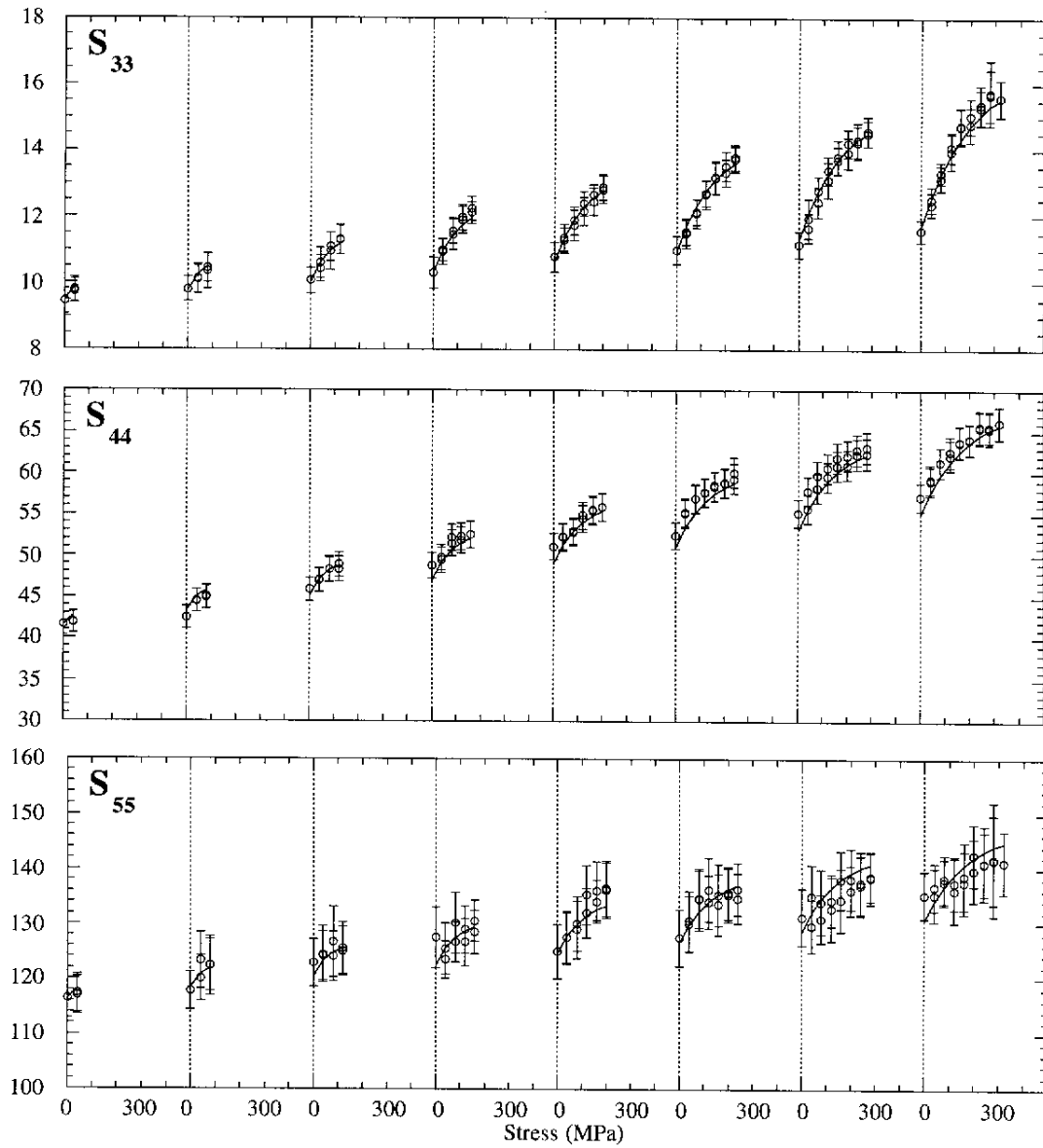


Fig. 6: Comparison between experimental data (o) and predicted evolution (—) of the most influenced compliances ( $(1000.GPa)^{-1}$ ) of a 2D C-SiC.

Fig. 7 and 8 show respectively the relative part of the elastic and inelastic strains on the total strain during the monotonous loading of the 2D SiC-SiC and of the 2D C-SiC. Fig. 8 also shows what happen during the cycles in the 2D C-SiC. In both cases, the inelastic strains are far from negligible. Unlike the 2D C-SiC, the strain partition of the 2D SiC-SiC exhibits three zones during monotonous loading. If for the 2D SiC-SiC, the inelastic strains do not appear until the beginning of the inter-bundles matrix microcracking, it is clear that they are present from the very beginning of the test in the case of the 2D C-SiC. There is no damage threshold for the 2D C-SiC whereas the behavior remains linear elastic until about 80 MPa for the 2D SiC-SiC.

The inelastic strains of the 2D SiC-SiC exhibit two very different increases that correspond to the scale at which they occur; an increment of strain at constant stress  $\Delta\epsilon_{bs}$  which starts around 80 MPa and stops at about 140 MPa due to inter bundles microcracking and a strain  $\epsilon_{fs}$  which needs an increase in stress and which begins at 120 MPa when the cracking starts to occur at the fibers scale inside the bundles. The strain partition on the cycles of the 2D C-SiC indicates that the linear variation observed is the sum of the non linear variation of both the elastic strain and inelastic strains. As it could have been awaited for, the elastic strain comes back to zero when no stress is applied whereas the inelastic strains are still present in the form of residual strains.

This emphasizes that the strain measured when the sample is fully unloaded represents only the residual part of the inelastic strain because the reversible sliding has closed some of the cracks. It is noteworthy that the residual strain value at the unloading point is far smaller than the under load inelastic strain. This establishes the partly reversible nature of the inelastic strain and therefore the necessity of doing the strain partition under load.

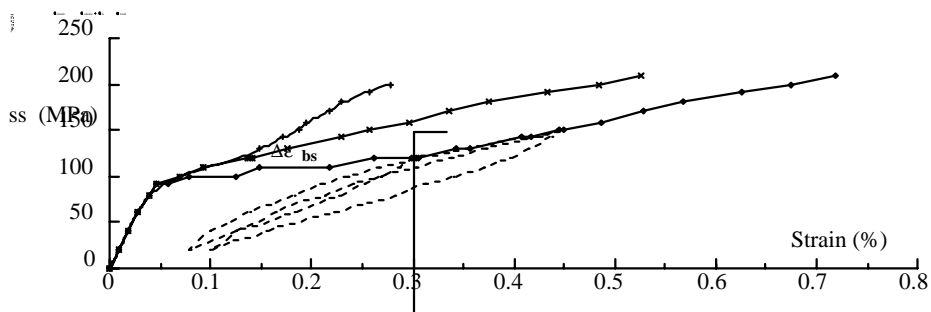


Fig. 7: Under load strain partition of a 2D SiC-SiC

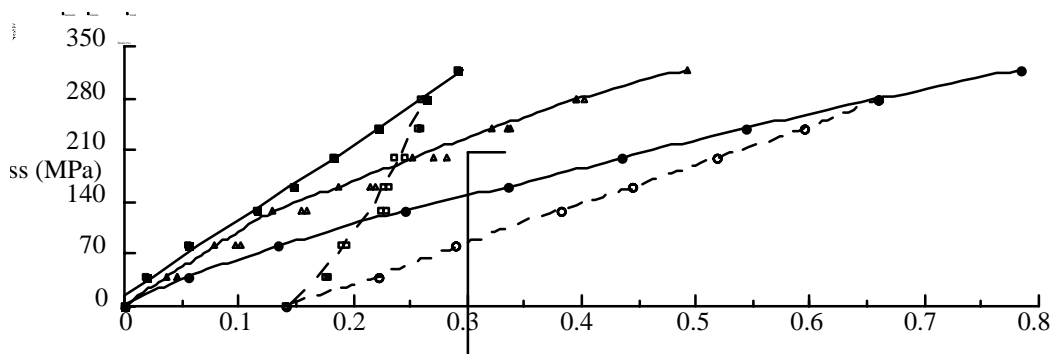


Fig. 8: Under load strain partition of the 2D C-SiC with a cyclic loading at 280 MPa

## IDENTIFICATION OF THE MODEL

The experimental variations of the elastic constants and Eqn (1) give access to the constitutive laws of the cracks density, Fig. 9 and 10. Only the monotonous loading is necessary to identify the crack densities. From the variations of the compliances of both samples, it results that every cracks density variation exhibits a linear behavior, the transverse variation having the greatest slope whatever the material and the scale considered. The interlaminar crack density  $\beta_I$  of the 2D C-SiC does not vary during the test meaning that no or very small delamination occur between the stacks for this sample. The fact that the two longitudinal cracks systems display a more stochastic behavior indicates that these damage mechanisms may be more influenced by local variations of the composite microstructure. About the 2D SiC-SiC, up to 80 MPa, as the damage has not begun, the crack densities are equal to zero. Then, at the inter-bundle scale, a 10 MPa delay necessary for the mode II cracking to start is highlighted.

During monotonous loading, all the transverse cracks are open. So the opening/closure function  $F$  is equal to 1. Eqn (2) reduces to:

$$\beta_T = \beta_T^* \quad (10)$$

The comparison between the experimental data and the predicted variations are depicted in Fig. 5 and 6. For the 2D SiC-SiC, a good correlation is obtained for the first three diagonal compliances,  $S_{11}$ ,  $S_{22}$  and  $S_{33}$ . The three remaining ones,  $S_{44}$ ,  $S_{55}$  and  $S_{66}$ , exhibit a more or less large deviation between the predictions and the experimental results. Anyway, concerning the inter-bundle part of the cracking, up to about 120 MPa, the predictions for  $S_{44}$  and  $S_{55}$  are good. For  $S_{66}$ , the deviation probably indicates that the transverse cracks thickness must be taken into account in the model. In the intra-bundle part of the prediction of the shear moduli, the deviations might be explained this way: first, as the crack systems are not independent, they might interact and second, one of the hypothesis of the model is that the cracks are elliptic, but, actually, at the intra-bundle scale they are more likely to be circular because their extent is limited by the fibers arrangement. This is emphasized by the similar variation of  $S_{44}$  and  $S_{55}$  in the intra-bundle part. Finally, concerning the off-diagonal compliances, the remark about taking into account the transverse cracks thickness is also valid to improve the prediction. For the 2D C-SiC, the comparison between the experimental data and the predicted variations shows a good correlation for the monotonous loading represented by the top of the cycles.

Clearly, during loading-unloading cycles, only the mechanism of the opening/closure of the transverse microcracks will take place. The state of the longitudinal and interstacks cracks does not, or slightly, vary. Thus the model of compliance variation can be simplified:

$$F_L = 1 \quad \beta_L^* = \beta_L \quad \text{and} \quad F_I = 1 \quad \beta_I^* = \beta_I. \quad (11)$$

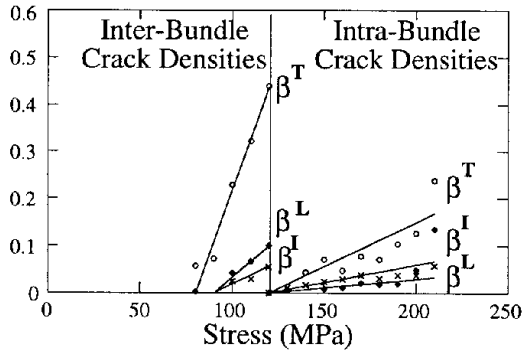


Fig. 9: Cracks densities of a 2D SiC-SiC under tensile loading.

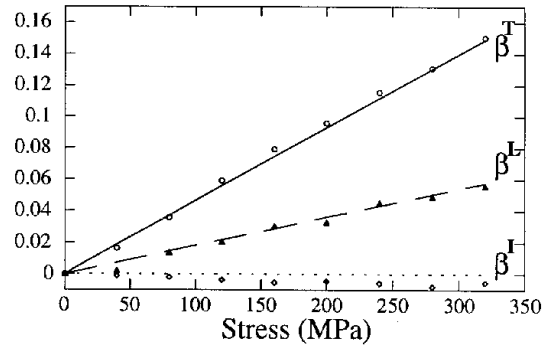


Fig. 10: Cracks densities of a 2D C-SiC under tensile loading.

At the top stress of a cycle,  $\sigma_{max}$ , all the cracks are open. We get the maximum of active cracks and thus,  $F=1$ . At zero stress, there is still a non zero proportion of open cracks leading to residual strains.  $F$  is minimum but different from zero as all the cracks do not close.

On Fig. 11 is represented the opening/closure variable  $F$  of the 2D SiC-SiC. This step function is representative of the existence of the threshold of stress needed to begin the fiber/matrix sliding at the interface. Fig. 12 shows the evolution of  $F$  during the various cycles of the 2D C-SiC. The proportion of open cracks can be described by a unique scalar function describing the progressive opening /closure of the transverse cracks:

$$F = 1 - ((1 - r)/(1 + r))^m \quad \text{where} \quad r = (Y_0 + Y)/(Y_0 + 1) \quad \text{and} \quad Y = \sigma/\sigma_{max} \quad (12)$$

where  $Y_0 = -0.25$  is the threshold where all the cracks close and  $m = 1.2$  a constant.

So, for this material, the behavior during the cycles is fully described by four functions:  $\beta^*_T$ ,  $\beta^*_L$ ,  $\beta^*_I$  and  $F$  that can predict the compliances variations (Fig. 6).

The inelastic strains prediction (Fig. 13) during both monotonous and cyclic loading is rather good as well once the residual opening of the cracks of the 2D C-SiC has been taken into account ( Eqn (6)). Fig. 14 describes the evolution of the inelastic strains for the 2D SiC-SiC at the various scales of its behavior as a function of the two transverse cracks densities and the aspect ratio using Eqn (5). A 10 MPa delay for the sliding to begin can clearly be seen. However, there is a gap between the experimental data and the prediction at the end of the inter-bundles phenomenon because the two slidings coexist in a 40 MPa range.

About the 2D C-SiC, micrographs have indicated that the material contains a lot of porosities and that many transverse cracks are situated in the SiC mantel around the bundles. The opening/closure of these cracks certainly occurs without any friction because the opening takes place on the pore side. This can explain the lack of hysteresis during the cycles. The interfacial shear stress of the 2D SiC-SiC has been identified to be about 27 MPa using Eqn (7) at the inter bundle scale and much higher at the fibers scale. This is in line with the assumption of a strong cohesive zone inside the bundles.

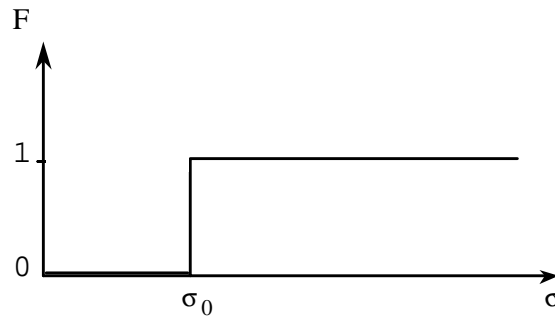


Fig. 11: Opening-closure variable for transverse microcracks of a 2D SiC-SiC

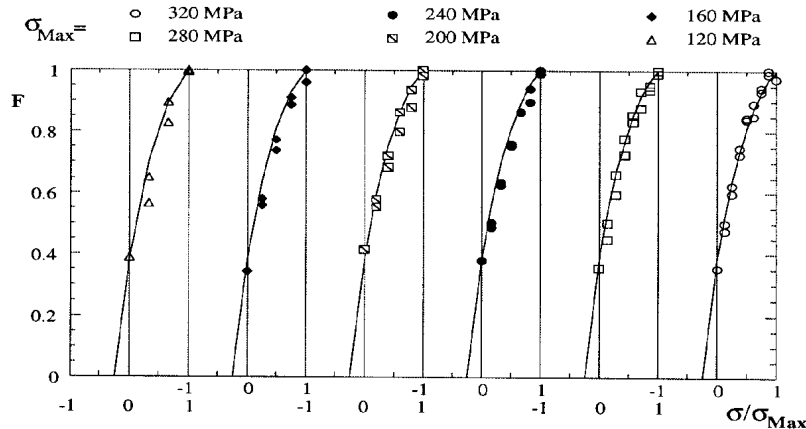


Fig. 12: Opening-closure variable for transverse microcracks of a 2D C-SiC.

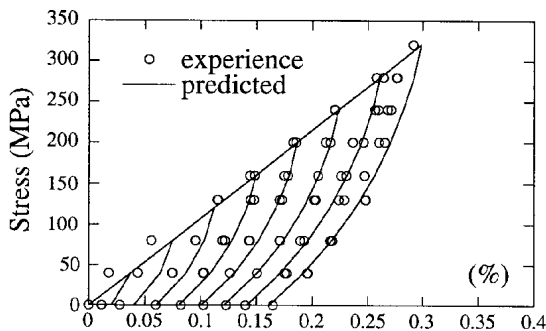


Fig. 13: Evolution of the inelastic strains during cyclic loading of a 2D C-SiC.

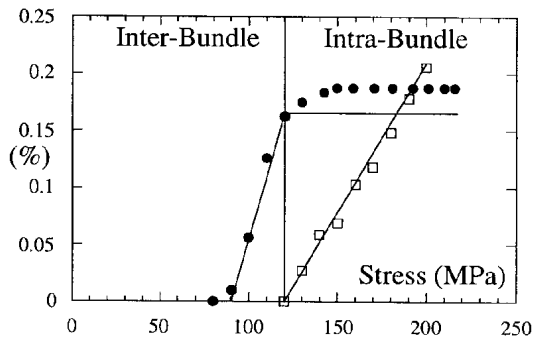


Fig. 14: Evolution of the inelastic strains of a 2D SiC-SiC.

### CONCLUSION

The behavior of ceramic matrix composites is strongly influenced by matrix microcracking. The ultrasonic characterization through the complete determination of the stiffness tensor along the whole test can detect all the damage mechanisms of CMC: the transverse matrix microcracking as well as the presence of longitudinal cracks at the fiber-matrix interface. Thus this technique is of great help in measuring the anisotropic damage and it also allows to perform the strain partition under load which is the only way to separate the various damage mechanisms. This technique gives a correct estimation of both the inelastic strains and the elastic modulus drop. The problem of the three-dimensional description of the non linear behavior of ceramic matrix composites can be solved by the measurement of the cracks

density parameters and the closing-opening variable. Their knowledge can fully predict the loss of stiffness due to matrix microcracking responsible for the non linear behavior of CMC. These parameters, representative of the initiation and growth of the cracks, describe the elastic part of the behavior. Furthermore, with the estimation of the cracks aspect ratio, the inelastic strains can be predicted accurately.

## REFERENCES

1. Evans A. G. and Zok F. W., "The physics and mechanics of fiber-reinforced brittle matrix composites", *J. Mat. Sci.*, Vol. 29, 1994, pp. 3857-3896.
2. Marshall D. B. and Evans A. G., "Failure mechanisms in ceramic-fiber/ceramic-matrix composites", *J. Am. Ceram. Soc.*, Vol. 68, No. 5, 1985, pp. 225-231.
3. He M. Y., Wu B.-X., Evans A. G. and Hutchinson J. W., "Inelastic strains due to matrix cracking in unidirectional fiber-reinforced composites", *Mech. Mater.*, Vol. 18, 1994, pp. 213-229.
4. Baste S. and Audoin B., "On internal variables in anisotropic damage", *Eur. J. Mech., A/Solids*, Vol. 10, No. 6, 1991, pp. 587-606.
5. Laws N., Dvorak G.J. and Hejazi M., "Stiffness changes in unidirectional composites caused by crack systems", *Mech. Mater.*, Vol. 2, 1983, pp. 123-137.
6. Camus G., Guillaumat L. and Baste S., "Evolution of Damage in a 2D Woven C/SiC Composite under Mechanical Loading. Part I: Mechanical Characterization", *C. Sci. and Tech.*, to be published.
7. Laws N., "A note on interaction energies associated with cracks in anisotropic solids", *Phil. Mag.*, Vol. 36, 1977, pp. 367-372.
8. Baste S., El Guerjouma R. and Audoin B., "Effect of Microcracking on the Macroscopic Behavior of Ceramic Matrix Composites, Ultrasonic Evaluation of Anisotropic Damage", *Mech. Mater.*, Vol. 14, 1992, pp. 15-31.
9. Chaboche J.-L., "A Continuum Damage Theory with Anisotropic and Unilateral Damage", *La Recherche Aéronautique*, Vol. 2, 1995, pp. 139-147.
10. Danchaivijit S. and Shetty D. K., "Matrix cracking in ceramic matrix composites", *J. Am. Ceram. Soc.*, Vol. 76, No. 10, 1993, pp. 2497-2504.
11. Audoin B. and Baste S., "Ultrasonic Evaluation of Stiffness Tensor Changes and Associated Anisotropic Damage in a Ceramic Matrix Composite", *J. Appl. Mech.*, Vol. 61, 1994, pp. 309-316.
12. Baste S. and Morvan J.-M., "Under Load Strain Partition of a Ceramic Matrix Composite Using an Ultrasonic Method", *Experimental Mechanics*, Vol. 36, No. 2, 1996, pp. 428-434.
13. Roux J., "Elastic wave propagation in anisotropic materials", *Proceedings IEEE 1990 Ultrasonics Symposium*, Honolulu, Dec. 1990, pp. 1065-1073.
14. Baste S. and Hosten B., "Évaluation de la matrice d'élasticité des composites orthotropes par propagation ultrasonore en dehors des plans principaux de symétrie", *Rev. Phys. Appl.*, Vol. 25, 1989, pp. 161-168.

# FRACTURE IN OFF-AXIS AND ANGLE-PLY FIBER REINFORCED CERAMICS

Alex S. Selvarathinam & Y.J. Weitsman

*Department of Mechanical & Aerospace engineering & Engineering Science  
307 Perkins Hall, University of Tennessee, Knoxville, Tennessee-37996-2030*

**SUMMARY** : An analytical/computational fracture mechanics scheme, combined with finite element computations, is presented to explain observed fracture patterns in off-axis and angle-ply fiber-reinforced ceramic composite laminates. Unlike polymeric composites, where microcracks are channelled parallel to the fiber directions, cracks in ceramic composites initiate normal to the load axis. The results provide rational explanations for the experimental observations and confirm the advantages bestowed by multi-directional reinforcements. Such reinforcements would still allow the development of multitudes of matrix cracks, bridged by intact fibers, that lead to the desirable gradual and "graceful" failure of the composite. On the other hand, multi-directional reinforcement prevents premature failures by constraining the laminate against interfacial fiber/matrix debondings, which may grow rapidly along those weak interfaces.

**KEYWORDS:** ceramic composites, fracture, oblique reinforcement

## INTRODUCTION

Fiber-reinforcement enhances the ductility of the otherwise brittle ceramic matrix materials by about one order of magnitude. However, since the above enhancement occurs in the fiber direction only, it is necessary to employ multi-directional lay-ups in structural applications.

Most of the experimental and analytical investigations to date concerned uni-directional and cross-ply laminates. A limited number of experimental works concerned the behavior of uni-directional off-axis plies and of angle ply laminates [1],[2] and [3]. It was observed that, in both cases, fiber-bridged matrix cracks tended to form perpendicularly to the load direction as shown in Figs. 1(a) and 2.

This is in contrast with polymeric composites where matrix cracks were channeled parallel to the fiber directions. Upon increasing the load levels on the off-axis ceramic composites,



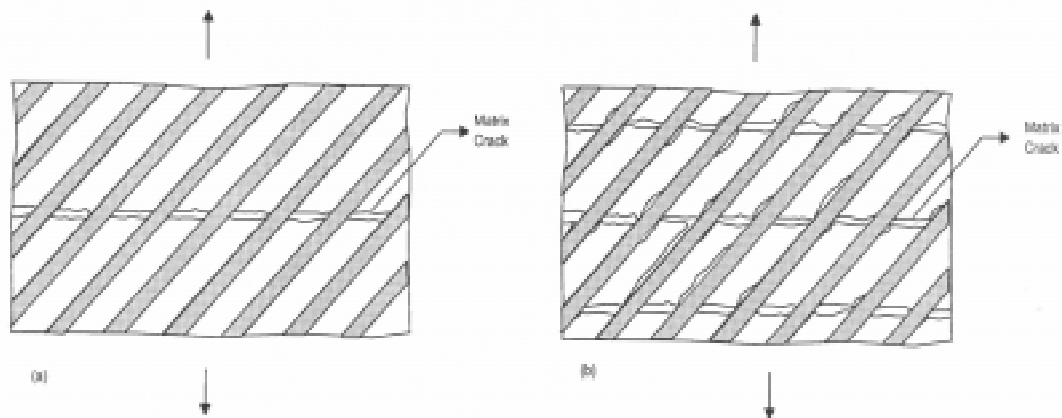
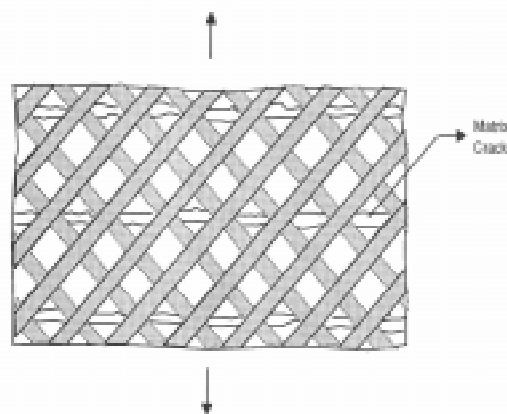


Figure 1: *Failure in Off-Axis Uniaxially Reinforced Ceramic Composites (a) A Single Crack Bridged by Oblique Fibers. (b) Observed Pattern of Matrix Cracks Branching into Interfacial Debonds When the Applied Stress Exceeds a Saturation Level  $\sigma_s$ .*

the fiber-bridged matrix cracks tended to branch into the fiber/matrix interfaces as shown in Fig. 1(b).



The purpose of this article is to provide an analytical explanation for the observations sketched in Figs. 1 and 2. The analysis employs linear elastic fracture mechanics and displacement based finite element methods (FEM) to determine the stresses near the tip of a crack that impinges upon an inclined bi-material interface. The eigen function approach is utilized to determine the stress singularities and finite element computations are performed to determine the stress intensities. The foregoing analysis is then blended with FEM results to evaluate the remote field.

### THE NEAR FIELD SOLUTION

This solution consists of the singular part and the leading non-singular term. The solution is established by combining the eigen function analysis with finite element computations. To focus ideas consider first the case of off-axis laminates.

Let  $r$  and  $\theta$  denote polar coordinates and consider two isotropic half planes bonded along the inclined interface  $\theta=\phi$ ,  $\theta=\phi+\pi$ ,  $0 \leq r \leq \infty$ , with a semi-infinite crack along  $\theta = \pi$ ,  $0 \leq r \leq \infty$  terminating at the inclined interface as shown in Fig. 3.

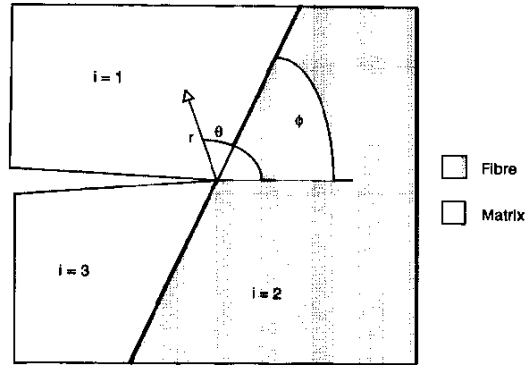


Figure 3: *Geometry of the Problem as Discussed in the Eigen Function Analysis*

Refer to the three extended regions shown in Fig.3 by subscripts  $i=1,2,3$ . The asymptotic stress and displacement field around the crack tip is obtained by means of the eigen function expansion method of Fenner [4]. The stress and displacement fields around the crack tip can be expressed as

$$\begin{aligned}
 \sigma_{irr} &= r^{\lambda-1} [F_i'' + (\lambda + 1)F_i] \\
 \sigma_{i\theta\theta} &= r^{\lambda-1} [\lambda(\lambda + 1)F_i] \\
 \sigma_{ir\theta} &= r^{\lambda-1} [-\lambda F_i'] \\
 u_{ir} &= \frac{r^\lambda}{2G_i} [- (\lambda + 1)F_i + (\lambda\omega_i)^{-1} \{F_i'' + (\lambda + 1)^2 F_i\}] \\
 u_{i\theta} &= \frac{r^\lambda}{2G_i} [-F_i' - (\lambda(\lambda - 1)\omega_i)^{-1} \{F_i''' + (\lambda + 1)^2 F_i'\}]
 \end{aligned} \tag{1}$$

where  $i = 1, 2, 3$  correspond to the material regions shown in Fig. 3.

In the above equations primes denote differentiation with respect to  $\theta$ ,  $G_i$  is the shear modulus and  $\omega_i$  is given in terms of Poisson's ratio  $\nu_i$ , namely,  $\omega_i = (1 + \nu_i)$  for generalized plane stress and  $\omega_i = 1/(1 - \nu_i)$  for plane strain.

The functions  $F_i$  are defined as

$$F_i(\theta, \lambda) = a_i \sin(\lambda + 1)\theta + b_i \cos(\lambda + 1)\theta + c_i \sin(\lambda - 1)\theta + d_i \cos(\lambda - 1)\theta \tag{2}$$

where  $a_i, b_i, c_i, d_i$  ( $i=1,2,3$ ) and  $\lambda$  are undetermined constants, thirteen in all. It should be noted that  $\lambda$  can be real or complex. However, the complex case is not considered in the present study since, in view of the material properties of fibrous ceramic composites, it does not seem to occur in these circumstances.

The field Eqns 1 are accompanied by 12 boundary conditions and continuity conditions that are omitted here for the sake of brevity. A complete listing is given in [4] and [5]. The foregoing conditions yield 12 homogeneous equations in  $a_i, b_i, c_i, d_i$  ( $i=1,2,3$ ), expressible as follows:

$$[A]\{X\} = 0 \tag{3}$$

The requirement that  $\det [A]=0$  results in a characteristic equation involving the eigen value  $\lambda$ , namely

$$f(\lambda, \alpha, \beta, \phi) = 0. \tag{4}$$

Note that only roots with  $0 < \text{Re}(\lambda) < 1$  yield bounded displacements with unbounded stresses as  $r \rightarrow 0$ . In Eqn 4  $\alpha$  and  $\beta$  are related to the material properties of regions 1 and 2 through their Dundurs parameters [4],[5].

Turning to the leading non-singular term in the near field solution, it can be shown [5],[6] that stresses and displacements are expressible in terms of functions  $F_i$  ( $i=1,2,3$ ) as follows

$$\begin{aligned} \sigma_{irr} &= F_i'' + 2F_i \\ \sigma_{i\theta\theta} &= 2F_i \\ \sigma_{ir\theta} &= -F_i' \\ u_{ir} &= \frac{r}{2G_i} \left[ -2F_i + (\omega_i)^{-1} \{ F_i'' + (\lambda + 1)^2 F_i \} \right] \\ u_{i\theta} &= -\frac{rF_i'}{2G_i} + rH_i - \frac{4C_i}{E_i(1-\nu_i^2)} r \ln r \end{aligned} \tag{5}$$

In (13)  $rH_i$  represents rigid body rotation and  $E_i$  is the stiffness, where

$$F_i(\theta) = A_i \sin(2\theta) + B_i \cos(2\theta) + D_i \tag{6}$$

The complete near field solution, which combines expressions (1) through (6), can be shown to read

$$\begin{aligned} \sigma_{irr} &= \frac{Q_1}{r^{1-\lambda_1}} f_{1rr}(\lambda_1, \theta) + \frac{Q_2}{r^{1-\lambda_2}} f_{2rr}(\lambda_2, \theta) + Q_3 f_{3rr}(1, \theta) \\ \sigma_{i\theta\theta} &= \frac{Q_1}{r^{\lambda_1-1}} f_{1\theta\theta}(\lambda_1, \theta) + \frac{Q_2}{r^{1-\lambda_2}} f_{2\theta\theta}(\lambda_2, \theta) + Q_3 f_{3\theta\theta}(1, \theta) \\ \sigma_{ir\theta} &= \frac{Q_1}{r^{1-\lambda_1}} f_{1r\theta}(\lambda_1, \theta) + \frac{Q_2}{r^{1-\lambda_2}} f_{2r\theta}(\lambda_2, \theta) + Q_3 f_{3r\theta}(1, \theta) \\ u_{ir} &= \frac{Q_1 r^{\lambda_1}}{2G_i} g_{1r}(\lambda_1, \theta) + \frac{Q_2 r^{\lambda_2}}{2G_i} g_{2r}(\lambda_2, \theta) \\ u_{i\theta} &= \frac{Q_1 r^{\lambda_1}}{2G_i} g_{1\theta}(\lambda_1, \theta) + \frac{Q_2 r^{\lambda_2}}{2G_i} g_{2\theta}(\lambda_2, \theta) \end{aligned} \tag{7}$$

where

$$\begin{aligned}
 f_{jrr} &= [F''_{ij} + (\lambda_j + 1)F_{ij}] \\
 f_{j\theta\theta} &= [\lambda_j(\lambda_j + 1)F_{ij}] \\
 f_{jr\theta} &= [-\lambda_j F'_{ij}] \\
 f_{3rr} &= F''_{i3} + F_{i3} \\
 f_{3\theta\theta} &= 2F_{i3} \\
 f_{3r\theta} &= -2F'_{i3} \\
 g_{jr} &= [-(\lambda_j + 1)F_i + (\lambda_j \omega_i)^{-1} \{F''_{ij} + (\lambda_j + 1)^2 F_{ij}\}] \\
 g_{j\theta} &= [-F'_{ij} - (\lambda_j(\lambda_j - 1)\omega_i)^{-1} \{F'''_{ij} + (\lambda_j + 1)^2 F'_{ij}\}]
 \end{aligned} \tag{8}$$

with

$$\begin{aligned}
 F_{ij} &= a_{ij} \sin(\lambda_j + 1)\theta + b_{ij} \cos(\lambda_j + 1)\theta + c_{ij} \sin(\lambda_j - 1)\theta + d_{ij} \cos(\lambda_j - 1)\theta \\
 F_{i3} &= A_i \sin(2\theta) + B_i \cos(2\theta) + D_i
 \end{aligned} \tag{9}$$

In Eqns 7-9  $i=1,2,3$  corresponding to the regions shown in Fig.3 and  $j=1,2$  corresponding to two distinct eigen values  $\lambda_1$  and  $\lambda_2$ , ordered such that  $\lambda_1 < \lambda_2$ . Furthermore,  $Q_1$ ,  $Q_2$  and  $Q_3$  are three scaling parameters determined in terms of the boundary conditions and geometrical features of the problem.

In the present analysis we chose to prescribe remote displacements as boundary conditions and thereby determined  $Q_1$  and  $Q_2$  from the displacement field. However, since the displacement terms associated with  $Q_3$  were comparatively negligible, it was expedient to evaluate  $Q_3$  using any one of the three stress expressions in (7). For this reason  $Q_3$  was not included in the displacement therein.

The scaling parameters  $Q_1$  and  $Q_2$  were evaluated by the FEM method based upon eight node, plane strain, continuum quadrilateral elements except near the crack tip, where six node triangular elements were employed. The scheme to evaluate  $Q_1$  and  $Q_2$  resembles analogous techniques [6],[7],[8],[9],[10] and [11], whereby the position of the mid side node along the triangular element was allowed to slide along the element's boundary and displacements were determined corresponding to the dominant singularity  $\lambda_1$ . Values of  $Q_1$  and  $Q_2$  were determined so as to minimize the residuals of  $u_r$ ,  $u_\theta$  and a combination thereof along rays at 33 distinct angles  $\theta$  emanating from the crack tip [5].

## THE COMPLETE SOLUTION FOR FRACTURED OFF-AXIS REINFORCED LAMINATES

Consider the off-axis fibrous configuration consisting of nine cracks as shown in Fig. 4. Computations for the circumstance of adjacently positioned three horizontal cracks and three diagonally directed cracks [5] indicated the central crack "C" in the nine crack geometry sketched Fig.4 provides an adequate representation for an extended periodic array of cracks in off-axis laminates.

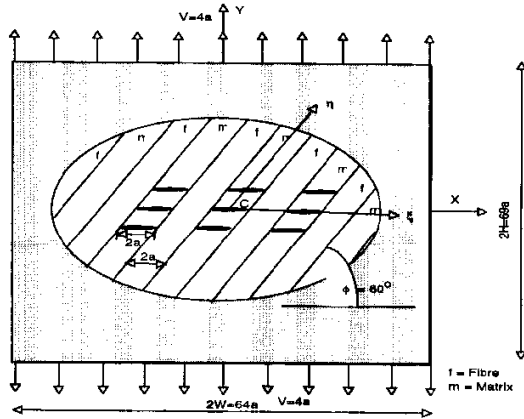


Figure 4: A System of Nine Cracks with the Representative Central Crack C

The outer dimensions of the off-axis laminate were  $2H=69a$  and  $2W=64a$  where  $a=0.25$  with its units being consistent with other length dimensions of the geometry. In addition, we selected the ratio of the fiber and matrix moduli to be  $E_f/E_m=1.78$  with Poisson's ratios of  $\nu_f=0.2$  and  $\nu_m=0.35$ . The volume fractions were  $V_f=V_m=0.5$ . Substituting into Eqn 4 yielded two real roots  $\lambda_1=0.509$  and  $\lambda_2=0.569$ , which do not depend on the specifics of the geometry. The remote displacements were specified by  $V=\pm 4a$  along  $Y=\pm H$ . Subsequently it was possible to evaluate  $Q_1, Q_2$  and  $Q_3$ .

Results for the normal tractions  $\sigma_{\theta\theta}$  along the fiber/matrix interfaces emanating from the tips  $\eta = 0, \xi = \pm a$  are shown in Fig. 5. The tractions  $\tau_{r\theta}$ , given in [5], are omitted for the sake of brevity.

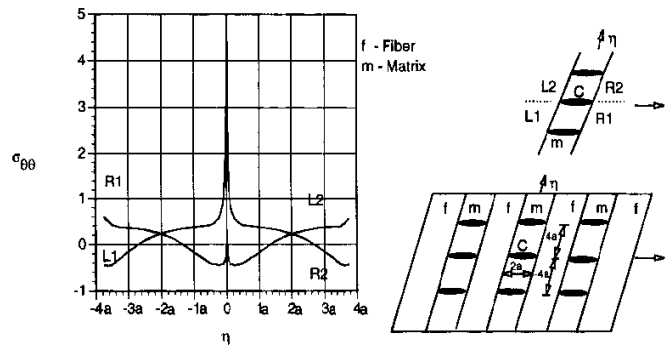


Figure 5: Variation of the Normalized Interfacial Normal Stress ( $\sigma_{\theta\theta}$ ) Emanating from the Tip of the Central Crack, as a Function of  $\eta$  ( $\xi=\pm a$ ) for the Nine Crack Geometry. Off-Axis Laminate

It is interesting to note that  $\sigma_{\theta\theta}$  undergoes a sharp stress reversal as the crack tip is approached along the interface R1 as detailed by curve "O" in Fig.6.

ANGLE PLY LAMINATES

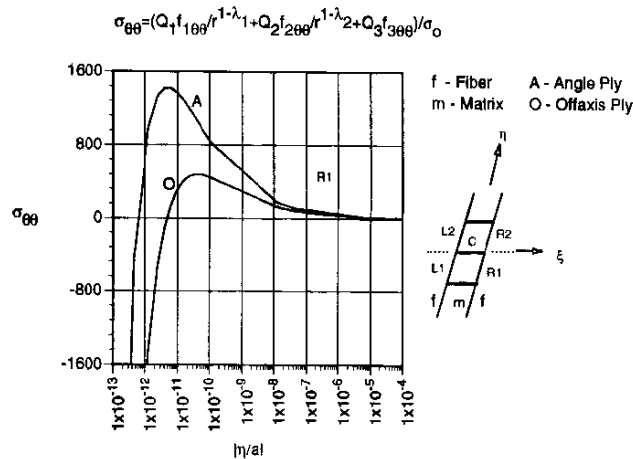


Figure 6: Variation of the Normalized Asymptotic Near Crack-Tip Interfacial Normal Stress ( $\sigma_{\theta\theta}$ ) Emanating from the Tip of the Central Crack, as a Function of  $\eta$  ( $\xi = \pm a$ ) for the Nine Crack Geometry Sketched in Fig.5

Consider an extended  $[\pm\psi]$  ceramic composite lay-up with matrix cracks bridged by fibers oriented at the  $+\psi$  and  $-\psi$  directions. Since  $\psi$  is measured from the Y axis we have  $\psi = 90 - \phi$  and  $-\psi = 180 - \phi$ . The laminate is subjected to a remote uniform displacement  $V$  as before.

Due to laminate-level interactions the deformation of the plies at angle  $+\psi$  is constrained by the presence of the  $-\psi$  plies. A straightforward utilization of laminate analysis [12] yields that the traction boundary conditions that prevail along the edges  $X = \pm W = \pm 32a$  may be replaced by normal and shear tractions equivalent to the effects of a uniform strain  $\epsilon_x^0$ , or a constant displacement  $U = \pm 32a\epsilon_x^0$  along the aforementioned edges. Upon considering the same material properties and nine crack geometry as before we obtain  $U = \pm 1.09a$ .

While essential feature of the near field analysis remain unchanged the complete solution, which depends on the remote boundary conditions, differs from that for off-axis laminates. Results for the  $+\psi$  ply are shown in Fig. 7. These results are plotted in the same format of Fig. 5. As before, the normal interfacial traction  $\sigma_{\theta\theta}$  undergoes a sharp, though somewhat severe, stress reversal upon approaching the crack tip along the interface  $R1$ . This is shown in more detail by curve "A" in Fig.6.

The differences between curves "O" and "A" in Fig.6 is due to the disparate values of the scaling parameters  $Q_1$  and  $Q_2$  that corresponds to the distinct lay-ups. On the other hand, the far field results shown in Figs. 5 and 7 respectively, are closer to each other.

The solution for the  $-\psi$  ply (i.e. fibers oriented at  $180^\circ - \psi$  about the x axis) is obtainable by reflecting the results plotted in Fig. 7. This is indicated in Fig. 8 where symbols "+" and "-" refer to the  $+\psi$  and  $-\psi$  plies respectively. Accordingly, the tractions along interfaces  $R2^+$ ,  $R1^+$ ,  $L2^+$  and  $L1^+$  are the same as those along  $L1^-$ ,  $L2^-$ ,  $R1^-$  and  $R2^-$  respectively. (As noted earlier  $R1^+$  is equivalent to  $L2^+$  and  $R2^+$  is equivalent to  $L1^+$ ).

### DISCUSSION OF RESULTS

The results shown in Figs. 5,6 and 7 indicate that in the vicinities of the crack tips, the interfaces R2 and L1 are dominated by tension, while compression prevails along R1 and L2. In the case of off-axis laminates (Fig. 5) this suggests that debondings would tend to develop along R2 and L1, which give rise to the observed patterns sketched in Fig. 1b.

The above circumstances differ from those in angle-ply laminates. Although tensile tractions in both  $+\psi$  and  $-\psi$  plies prevail along the rays oriented in directions  $R2^+$ ,  $R2^-$ ,  $L1^+$  and  $L1^-$ , debondings along the corresponding interfaces are nevertheless resisted by the fact that they must cut across fibers in either the  $+\psi$  or the  $-\psi$  ply. This explains the observed patterns of fracture in angle-ply laminates, which consists of matrix cracks perpendicularly to the load direction with few, if any, interfacial debonding. The above cracks are bridged by the  $\pm\psi$  fibers.

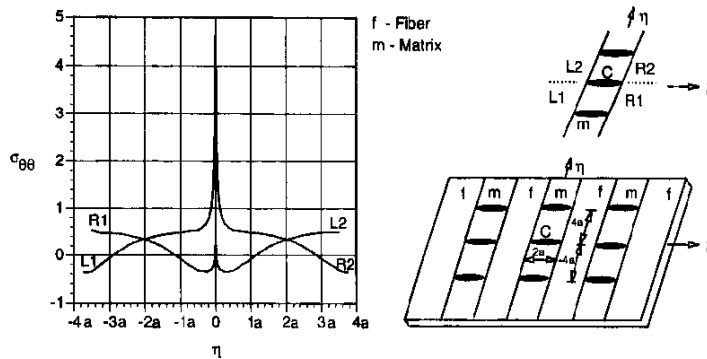


Figure 7: Variation of the Normalized Interfacial Normal Stress ( $\sigma_{\theta\theta}$ ) Emanating from the Tip of the Central Crack, as a Function of  $\eta$  ( $\xi = \pm a$ ) for the Nine Crack Geometry in  $\phi = 60^\circ$  ply. Angle-Ply Laminate.

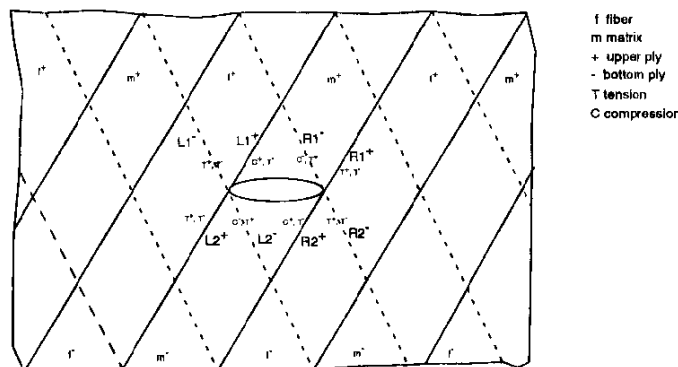


Figure 8: Correlation Between the Interfacial Stresses in the  $+\psi$  and  $-\psi$  plies indicated by "+" and "-" symbols, for the Nine Crack Configuration (Only the Central Crack is Shown for Clarity). C and T Indicate Compressive and Tensile Tractions Respectively

## ACKNOWLEDGMENTS

The authors thanks Professor P.J. Joseph of Clemson University for the helpful suggestions he made upon reading a preliminary version of this article. The support of AFOSR through Grant No. AF F49620-94-1-0344 (Dr. W. Jones, Program Manager, Y.J. Weitsman, Principal Investigator) is gratefully acknowledged.

## REFERENCES

1. Cady, C., Heredia, F.E., and Evans, A.G., "In-Plane Mechanical Properties of Several Ceramic Matrix Composites", *Journal of American Ceramic Society*, Vol. 78, 1995, pp. 2065-2078.
2. Bhatt, R.T. and Phillip, R.E., "Laminate Behavior for SiC Fiber-Reinforced Reaction-Bonded Silicon Nitride Matrix Composites", *NASA technical Memorandum 101350*
3. Nardone, V.C. and Prewo, K.M., "Tensile Performance of Carbon-Fiber-Reinforced Glass", *Journal of Materials Science* Vol.23, 1988, pp. 168-180.
4. Fenner, D.N., "Stress Singularities in Composite Materials with an Arbitrarily Oriented Crack Meeting an Interface", *International Journal of Fracture*, Vol. 12, pp. 705-721, (1976).
5. Selvarathinam, A.S., *Fracture in Unidirectional Off-axis Ceramic Matrix Composite*, Report MAE S96-4.0-CM, University of Tennessee, Knoxville, September 1996.
6. Munz, D., Fett, T. and Yang, Y.Y., "The Regular Stress Term in Bonded Dissimilar Materials After a Change in Temperature", *Engineering Fracture Mechanics*, Vol. 44, 1993, pp. 185-194.
7. Lim, W.K. and Lee, C.S., "Evaluation of Stress Intensity Factors for a Crack Normal to Bimaterial Interface Using Isoparametric Finite Elements", *Engineering Fracture Mechanics*, Vol. 52, 1995, pp. 65-70.
8. Raju, I.S. and Crews Jr., J.H., "Interlaminar Stress Singularities at a Straight Free Edge in Composite Laminates", *Computers and Structures*, Vol. 14, 1981, pp. 21-28.
9. Yang, Y.Y. and Munz, D., "Stress Distribution in a Dissimilar Materials Joint for Complex Singular Eigenvalues Under Thermal Loading", *Journal of Thermal Stresses*, Vol. 18, 1995, pp. 407-419.
10. Munz, D. and Yang, Y.Y., "Stress Singularities at the Interface in Bonded Dissimilar Materials Under Mechanical and Thermal Loading", *Journal of Applied Mechanics*, Vol. 59, 1992, pp. 857-861.
11. Munz, D. and Yang, Y.Y., "Stresses Near the Edge of Bonded Dissimilar Materials Described by Two Stress Intensity Factors", *International Journal of Fracture Mechanics*, Vol. 60, 1993, pp. 169-177.
12. Agarwal, B.D. and Broutman, L.J., *Analysis and Performance of Fiber Composites*, 2nd Edition, John Wiley and Sons.



# THE RESEARCH OF SELF-REINFORCED HP SILICON NITRIDE

Li Fengmei

*Institute of Aeronautical Materials, Beijing 100095, China*

**SUMMARY:** For the self reinforced HP  $\text{Si}_3\text{N}_4$  ceramics the effects of  $(\text{Y}_2\text{O}_3 + \text{La}_2\text{O}_3)$  wt% and the ratio between  $\text{Y}_2\text{O}_3$  and  $\text{La}_2\text{O}_3$  on the mechanical properties and microstructure were studied. While  $\text{Y}_2\text{O}_3 : \text{La}_2\text{O}_3 = 1 : 1$  (wt%) the flexure strengths and fracture toughness reach to a maximum at same time and the content of  $(\text{Y}_2\text{O}_3 + \text{La}_2\text{O}_3)$  approaches 20 wt% the flexure strength goes through a maximum 715 MPa (at 1350 °C), the content of  $(\text{Y}_2\text{O}_3 + \text{La}_2\text{O}_3)$  approaches 16 wt%, the fracture toughness goes through a maximum, 7.8  $\text{MPaM}^{1/2}$  (at room temperature). Analysis of toughening processes indicated that both crack deflection and  $\beta$   $\text{Si}_3\text{N}_4$  bridging or pullout mechanisms can contribute to the fracture toughness of HPSi<sub>3</sub>N<sub>4</sub> ceramics.

**KEYWORDS:** self reinforce, silicon nitride, mechanical properties, microstructure

## INTRODUCTION

Silicon nitride has the potential to become the material of choice for advanced application because of a combination of excellent mechanical and thermal properties. In general, fibers or whiskers are introduced to overcome the brittleness of unique ceramics, but there are several processing problems eliminating its application. For example, the component of different shape is difficult to well distributed. Selfreinforced silicon nitride or in situ toughened  $\text{Si}_3\text{N}_4$  is based upon microstructural engineering through the controlled nucleation and growth of the  $\beta\text{Si}_3\text{N}_4$  grains. During sintering,  $\beta\text{Si}_3\text{N}_4$  grains with high aspect ratios were formed, therefore, the results are obtain similar to the  $\text{Si}_3\text{N}_4$  toughened by fibers or whisker. Silicon nitride is a highly covalent material that requires the use of sintering additives to reach full densification. During sintering silica on the silicon nitride surface react with sintering additives to a glass. At high temperatures, the  $\alpha\text{Si}_3\text{N}_4$  dissolves into the glass and precipitates in the form of  $\beta$   $\text{Si}_3\text{N}_4$ . The morphology of the  $\beta\text{Si}_3\text{N}_4$  can vary from equiaxied to highly elongated grains depending on the characteristics of the oxynitrid glass as well as other factors such as  $\text{Si}_3\text{N}_4$  powder, sintering additives, and processing condition. In this paper, the effects of  $\text{Y}_2\text{O}_3$  and  $\text{La}_2\text{O}_3$  sintering additives on the mechanical properties and microstructure of Selfreinforced HP silicon nitride are reviewed.

## EXPERIMENTAL PROCEDURE

The characteristics of used  $\text{Si}_3\text{N}_4$  powder are shown in Table 1. Sintering additives are  $\text{Y}_2\text{O}_3$  and  $\text{La}_2\text{O}_3$ , its pureness is 99.9%. The preparation process of  $\text{Si}_3\text{N}_4$  ceramic parts are shown in Figure 1. The trial compositions ( $\text{Si}_3\text{N}_4$ ,  $\text{Y}_2\text{O}_3$  and  $\text{La}_2\text{O}_3$ ) were mixed. Mixing time was 24 h

in the polyethylene bottle with HPSN milling medium and pure ethanol as mixing fluid. After mixing, the ethanol was evaporated from the powder slurries. The powders were dried further in a air oven at 110 °C and then sieved through a 100 mesh stainless steel screen . Composite bars were obtained by hot pressing the mixture in a graphite die at 1780 °C, 25 MPa applied pressure in a nitrogen atmosphere, in 1 h. The initial experimental work of this study involved the determination of the content and ratio of sintering additives. For this, ten trial compositions were chosen Table 2. The composite blocks were loaded in three point bend at 1350 °C and room temperature at a constant displacement rate of 0.5 mm/min in air.

Table 1: Characteristics of  $\text{Si}_3\text{N}_4$  raw power

$\alpha/(\alpha+\beta)$ %	Diameter $\mu\text{m}$	BET $\text{m}^2/\text{g}$	Impurity wt%			
			Fe	Al	Si	W
90	0.3	20	0.16	0.07	0.6	0.11

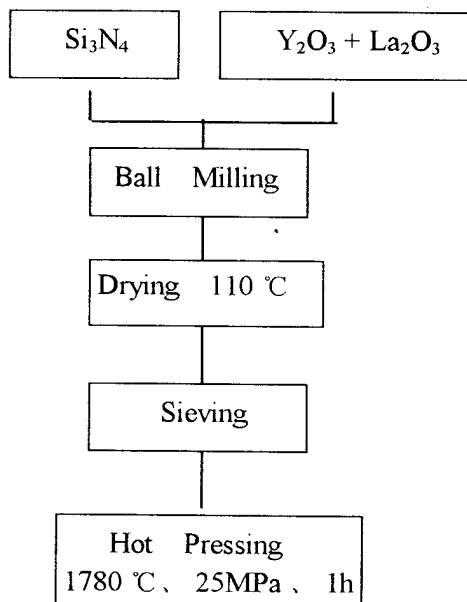


Fig. 1 Preparation process of  $\text{Si}_3\text{N}_4$  ceramic parts

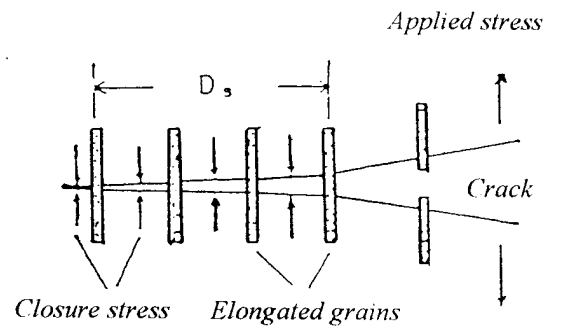


Fig. 2 Grain bridging or pull - out

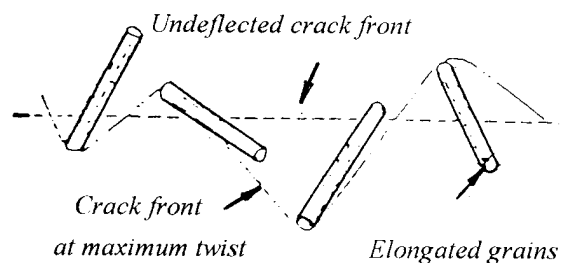


Fig. 3 Crack deflecting

## RESULTS AND DISCUSSION

Two toughening mechanisms are shown in Fig. 2, Fig. 3, grain bridging or pullout and crack deflecting. As this bridge zone develops, a closure stress is placed on the propagating crack that effectively increased the fracture resistance of the material. This increased fracture resistance is a result of crack bridging and pullout (Fig. 2). As the propagating crack collides with elongated grains, the crack would be deflected (Fig. 3). The extremely high fracture toughness is produced by an interaction between the propagating crack and the elongated grains in the material. Many investigators have demonstrated that the fracture toughness of  $\text{Si}_3\text{N}_4$  is strongly dependent upon grains morphology. In materials containing elongated grains with high aspect ratios and large diameters, fracture toughness can reach higher values. Mitomo et al<sup>[1]</sup> and Matsuhiro et al<sup>[2]</sup> have shown that the fracture toughness of  $\text{Si}_3\text{N}_4$  depends on the size and fraction of these elongated grains. Figure 4 summarizes the relationship

between fracture toughness and grain size for  $Y_2O_3 - Al_2O_3 - Si_3N_4$  and  $Y_2O_3 - MgO - Si_3N_4$  systems processed at different temperature. Figure 5 summarizes the relationship between the relative fracture toughness and the percentage of elongated grains.

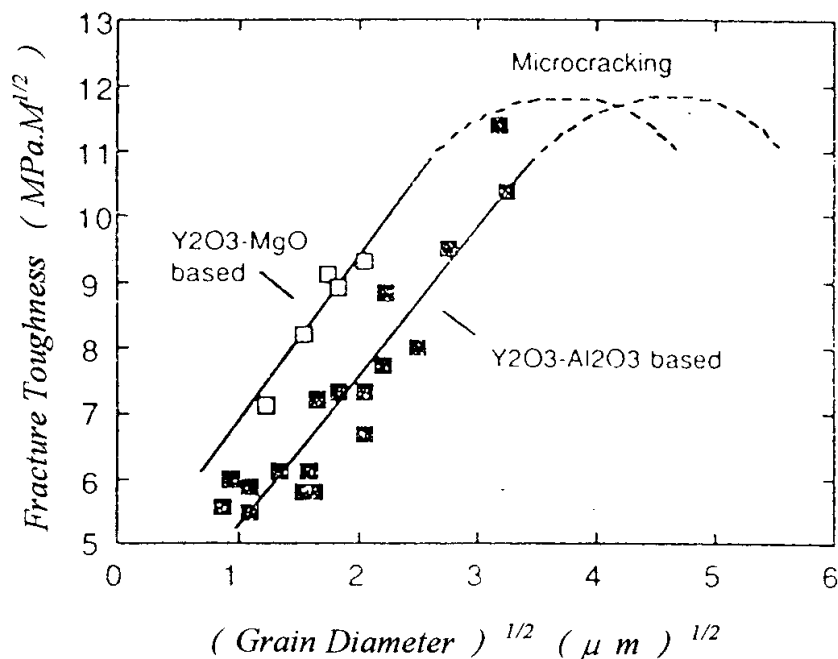


Fig. 4: The relationship between fracture toughness and the diameter of elongated  $Si_3N_4$  grain

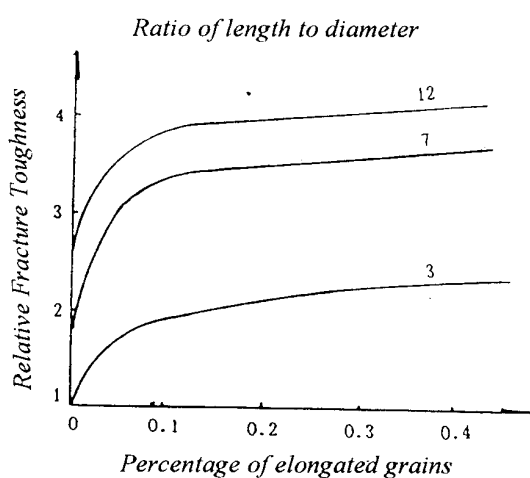


Fig. 5: The relationship between the relative fracture toughness and the percentage of elongated  $Si_3N_4$  grains

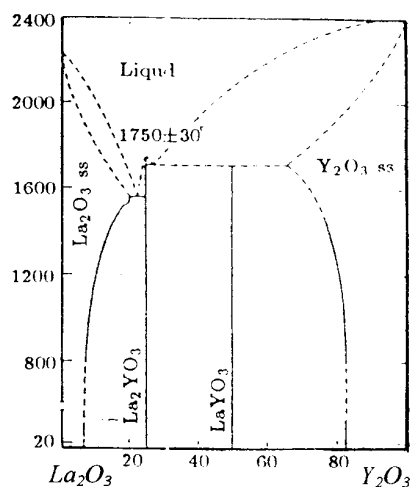


Fig. 6:  $Y_2O_3 - La_2O_3$  binary diagram

The selection of sintering additives not only is a density criterion, but also is a key parameter in controlling the morphology of silicon nitride grains. The chemical composition of the glass determines the temperature and the rate of the  $\alpha$  to  $\beta$  transformation. The glass composition also determines the rate of mass transport, which is directly related to the kinetics of grain growth. The effects of the ratio between  $Y_2O_3$  and  $La_2O_3$  on the HP  $Si_3N_4$  mechanical properties are shown in Fig. 7, while  $Y_2O_3 : La_2O_3 = 1 : 1$  (wt%), the flexure strengths and fracture toughness reach to a maximum at same time, flexure strength approaches 676 MPa (at 1350 °C), fracture toughness is 6.13  $MPa.M^{1/2}$  (at room temperature). From  $Y_2O_3$  and  $La_2O_3$  binary diagram (Fig. 6), we know, while  $Y_2O_3 : La_2O_3$  is close to 1 : 1, compound

(LaYO<sub>3</sub>) was forming easy, sintering additives were at grain boundary in the compounds, not in glass, therefore, raising the softening temperature of glass and improving the Si<sub>3</sub>N<sub>4</sub> mechanical properties.

Table 2: Effects of the content of (Y<sub>2</sub>O<sub>3</sub> + La<sub>2</sub>O<sub>3</sub>) wt% and the ratio between Y<sub>2</sub>O<sub>3</sub> and La<sub>2</sub>O<sub>3</sub> on the HP Si<sub>3</sub>N<sub>4</sub> mechanical properties

Composition (wt %)			Y <sub>2</sub> O <sub>3</sub> :La <sub>2</sub> O <sub>3</sub>	$\sigma_f^{RT}$ (MPa)	$\sigma_f^{1350}$ (MPa)	$K_{Ic}^{RT}$ (MPa.M <sup>1/2</sup> )
Si <sub>3</sub> N <sub>4</sub>	Y <sub>2</sub> O <sub>3</sub>	La <sub>2</sub> O <sub>3</sub>				
87	0	13	0 : 13	586.8	447.3	5.78
87	4	9	4 : 9	773.0	669.4	5.49
87	6.5	6.5	1 : 1	581.1	676.6	6.13
87	9	4	9 : 4	365.7	589.4	5.82
87	13	0	13 : 0	703.0	128.0	5.05
95	2.5	2.5	1 : 1	413.5	212.0	4.60
90	5	5	1 : 1	660.0	380.4	5.67
84	8	8	1 : 1	880.9	686.1	7.78
80	10	10	1 : 1	890.7	715.6	7.68
75	12.5	12.5	1 : 1	801.4	595.04	7.93

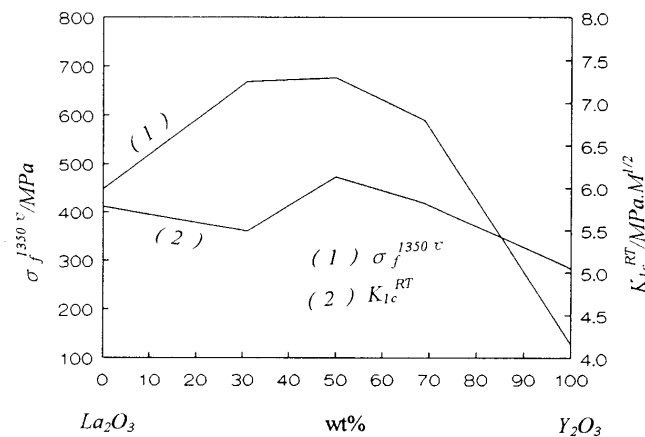


Fig. 7: The relationship between the ratio of sintering additives ( Y<sub>2</sub>O<sub>3</sub> : La<sub>2</sub>O<sub>3</sub> ) and Si<sub>3</sub>N<sub>4</sub> mechanical properties

The effects of the content of sintering additives (Y<sub>2</sub>O<sub>3</sub> + La<sub>2</sub>O<sub>3</sub>) wt% on the HP Si<sub>3</sub>N<sub>4</sub> mechanical properties and microstructure are shown in Fig. 8 and Fig. 9. While the content of sintering additives (Y<sub>2</sub>O<sub>3</sub> + La<sub>2</sub>O<sub>3</sub>) approaches 16 wt%, the fracture toughness goes through a maximum, 7.8 MPa.M<sup>1/2</sup> (at room temperature). While the content of sintering additives (Y<sub>2</sub>O<sub>3</sub> + La<sub>2</sub>O<sub>3</sub>) approaches 20 wt%, the flexure strength goes through a maximum, 715 MPa (at 1350 °C). Fig. 9 is scanning electron micrographs of a self-reinforce Si<sub>3</sub>N<sub>4</sub>. Fig. 9 illustrates how the microstructure can be varied by the content of sintering additives when materials are made from the same starting powder and processed under identical conditions. In these materials, the grains with highest aspect ratios have been produced in the material containing 16-20 wt% (Y<sub>2</sub>O<sub>3</sub> + La<sub>2</sub>O<sub>3</sub>) sintering additives. The materials made with 5 or 25 wt% sintering additives (Y<sub>2</sub>O<sub>3</sub> + La<sub>2</sub>O<sub>3</sub>) contained mainly a large number of fine grains. These results clearly show that the grain morphology is strongly influenced by the content of sintering additives. The main benefit of controlling the formation of elongated grains is a dramatic improvement in the mechanical properties of silicon nitride. The improved fracture resistance and mechanical performance is the result of a reinforcing phenomenon from the whiskerlike grains, similar to the behavior observed in whisker-reinforced ceramics<sup>[3]</sup>.

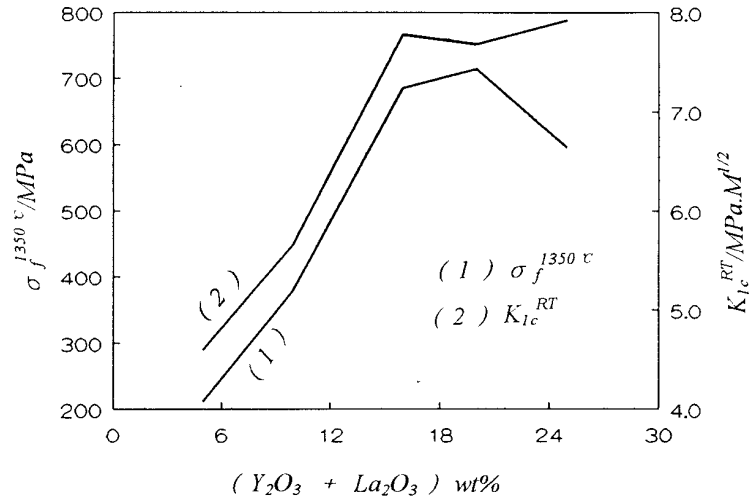


Fig. 8: The relationship between the content of sintering additives ( $Y_2O_3 + La_2O_3$ ) and HP  $Si_3N_4$  mechanical properties

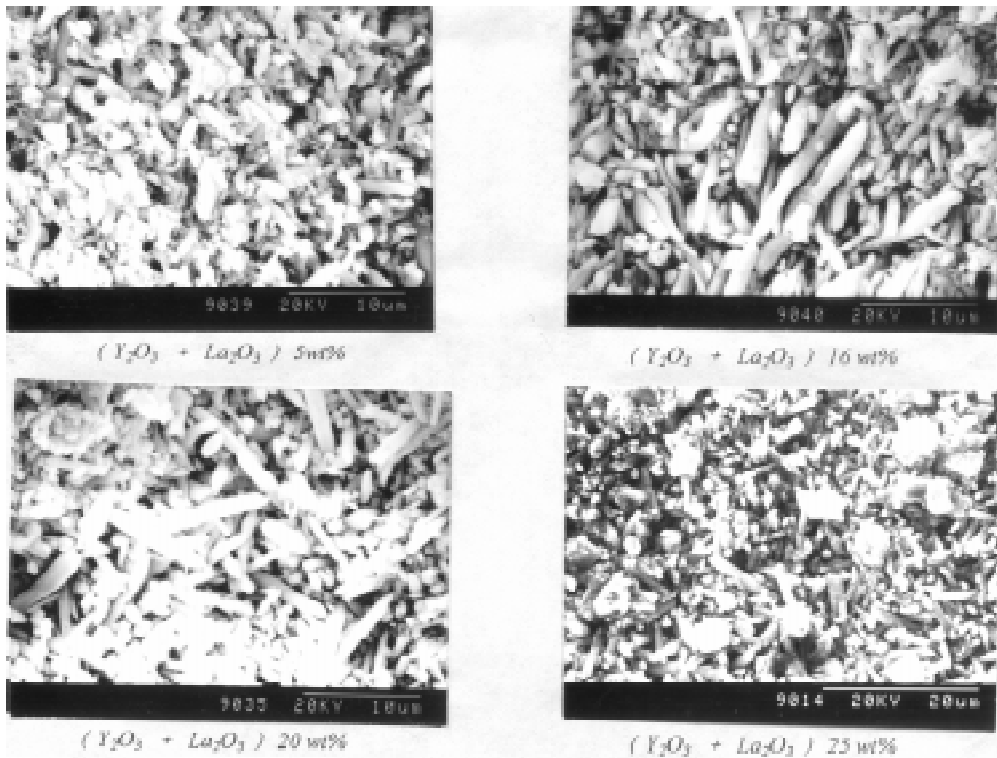


Fig. 9: SEM morphology of fracture surface of different content of sintering additives ( $Y_2O_3 + La_2O_3$ ) for HP  $Si_3N_4$

### CONCLUSIONS

Toughening mechanisms of self-reinforced  $Si_3N_4$  are crack bridging, grain pullout and crack deflecting. In materials containing elongated grains with high aspect ratios and large diameters, fracture toughness can reach higher values.

While  $Y_2O_3 : La_2O_3$  close to 1 : 1, the compound ( $LaYO_3$ ) was forming easy, therefore, the mechanical properties were improved. While  $Y_2O_3 : La_2O_3 = 1 : 1$ , the flexure strength of the

material made with 20 wt% ( $Y_2O_3 + La_2O_3$ ) sintering additives goes through a maximum, 715 MPa (at 1350 °C), the fracture toughness of the material made with 16 wt% ( $Y_2O_3 + La_2O_3$ ) reaches a maximum, 7.8 MPa.M<sup>1/2</sup> (at room temperature).

### REFERENCES

1. Mitomo M, Uenosono S. *J. Am. Ceram. Soc.* 1992, 751038
2. Matsuhiro K, Takashashi T. *Ceram. Eng. Sci. Proc.* 1989, 1080716
3. Becher P F. *J. Am. Ceram. Soc.* 1991, 74225569

# MICROSTRUCTURAL STUDY OF THE SINTERED COMPOSITE COMPOSED OF TIN AND NI

Shujie Li<sup>1,2,3</sup>, Yuping Li<sup>3,4</sup>, J. H. Maas<sup>3</sup>, J. Boeijma<sup>3</sup> and B. H. Kolster<sup>2,5</sup>

<sup>1</sup>Currently: Beijing University of Aeronautics and Astronautics, Department of Materials Science and Engineering, Beijing 100083, P.R.China

<sup>2</sup>Former Foundation for Advanced Metals Science, The Netherlands

<sup>3</sup>University of Twente, P.O. Box 217, 7500 AE Enschede, The Netherlands

<sup>4</sup>Currently: College of Traditional Chinese Medicine and Pharmacology, Division of Analytical Chemistry, Beijing 100013, P.R.China

<sup>5</sup>Currently: PIM-Tech b.v., P.O. Box 192, 7360 AD Beekbergen, The Netherlands

**SUMMARY:** Pure TiN powder was mixed with pure Ni powder at a volume ratio of 1:1. Then, the mixed powder was cold compacted. The compacts were pressureless sintered at 1150, 1250 and 1350 °C respectively for 1 hour in vacuum. X-ray diffraction analysis and microstructural analysis by SEM and EDX were carried out with the sintered samples. It is shown that the lattice constant of Ni increases with increasing sintering temperature, but the crystal structure of TiN is stable under the experimental conditions. The Ti content of the Ni solid solution determined from the lattice constant value is very close to the one obtained by EDX quantitative analysis. The experimental results indicate that interdiffusion takes place at the TiN/Ni interface during sintering.

**KEYWORDS:** ceramic matrix composite, cermet, interface

## INTRODUCTION

Various kinds of cermets are widely employed in industry due to their favorable properties which are different from those of ceramics and metals. As one of their representatives, the cermet composed of WC and Co has been used as a wear-resistant material for several decades. However, this cermet is expensive because both tungsten and cobalt are not abundant materials. Furthermore, the high specific gravity of this material makes the parts too heavy to use in some cases especially for aeronautical and astronautical applications. Hence, during the last 30 years many attempts have been made to find alternatives with low specific gravity and relatively comparable mechanical properties coupled with favorable cost [1-9]. Although much significant progress has been reported [1-9], the cermet composed of WC and Co has not been replaced in industry so far. Nevertheless, the effort to look for the alternatives has not stopped.

As reported in Ref. 10-12, in order to achieve this goal, Al<sub>2</sub>O<sub>3</sub> and Ni were selected as the starting materials due to their favorable properties and easy availability. However, the problem associated with these two components is the poor wettability between solid Al<sub>2</sub>O<sub>3</sub> and liquid Ni [13], which hinders the manufacturing of this cermet by liquid phase sintering. In order to improve the sintering ability of this material, attention was focused on introducing interlayers which could adhere strongly to both the ceramic phase and the metallic phase. It is

reported that TiN was found to be the best suited to achieve this goal. The TiN interlayer was introduced by coating the Al<sub>2</sub>O<sub>3</sub> powder with a layer of TiN using CVD process. Then, Al<sub>2</sub>O<sub>3</sub> powder coated with TiN (denoted by Al<sub>2</sub>O<sub>3</sub>-TiN) was mixed with Ni powder. The mixture was hot-pressed to manufacture the composite, which is expressed by Al<sub>2</sub>O<sub>3</sub>-TiN+Ni [10-12].

In order to investigate the mechanism that TiN interlayer remarkably enhances the sintering ability and mechanical properties of the material, it is essential to study the two interfaces (TiN/Ni and Al<sub>2</sub>O<sub>3</sub>/TiN) involved in this system. This paper deals with the TiN/Ni interface.

## **EXPERIMENTAL PROCEDURES**

Pure TiN powder (particle size: 5-25 $\mu$ m, purity: 99.9 Wt%) was mixed with pure Ni powder (particle size: 1-3 $\mu$ m, purity: 99.9 Wt%) at a volume ratio of 1:1 for 45 minutes using a powder mill. The powder was loaded in a plastic cylindrical vessel containing TiN balls 10 mm in diameter for mixing. The mixed powder, 1 gram for each sample, was cold compacted at 750 MPa for 60 seconds. Neither lubricant nor binder was used during compacting. The compacts were pressureless sintered at 1150, 1250 and 1350 °C respectively for 1 hour in vacuum of  $7 \times 10^{-3}$  Pa ( $5 \times 10^{-5}$  Torr). After sintering for the required duration, the samples were left in the furnace in vacuum to cool gradually to room temperature.

The sintered billets were ground lightly with 1000 mesh sand paper to remove the surface layer. Then, they were washed in alcohol using an ultrasonic bath. After drying, X-ray diffraction was carried out on all these samples. The polished sections were observed by SEM and the composition of the various phases at the sections was analyzed qualitatively and quantitatively by EDX (Energy Dispersive X-ray Microanalysis System).

## **RESULTS AND DISCUSSION**

Fig. 1 shows the X-ray diffraction patterns of the samples sintered at the various temperatures. For comparison, the X-ray diffraction pattern of the compact with the same composition is also included in the figure. This figure indicates that with increasing sintering temperature every diffraction peak of Ni shifts to the left side of the figure (low angle), whereas, the diffraction peaks of TiN do not shift. So, according to Bragg's law, the lattice constant  $a$  of Ni increases with increasing sintering temperature. Its value as a function of sintering temperature is presented in Fig. 2.



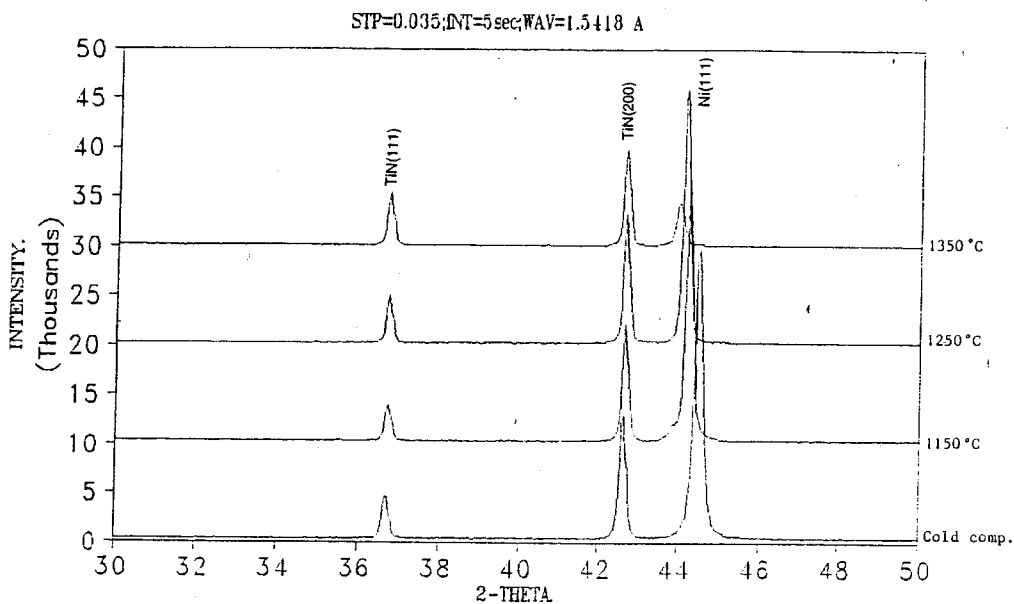


Fig. 1: X-ray diffraction patterns of the cermet composed of 50 Vol% TiN + 50 Vol% Ni before and after pressureless sintering at various temperatures in vacuum for 1 hour

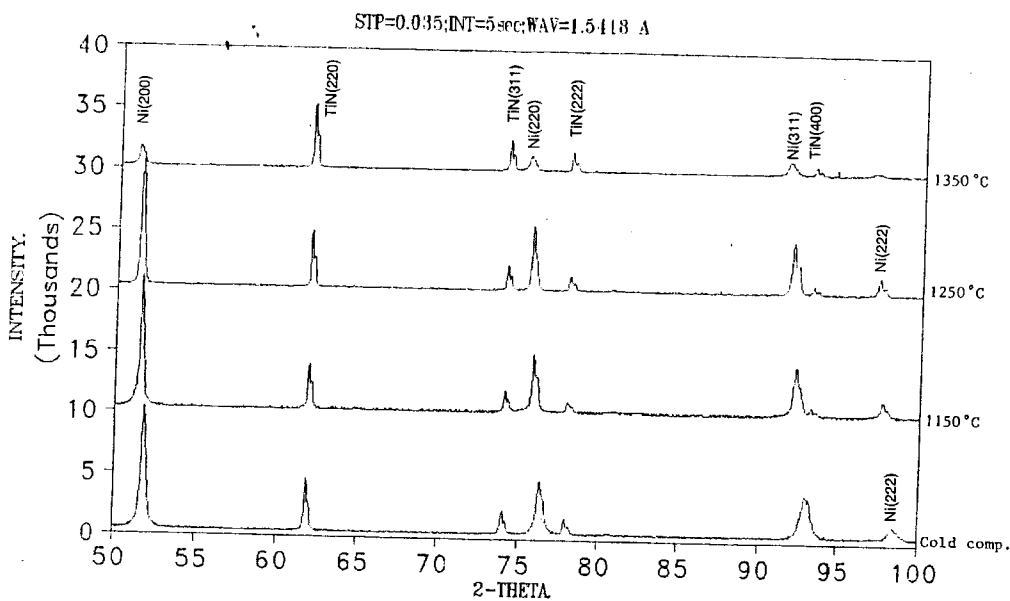


Fig. 1: Continuing

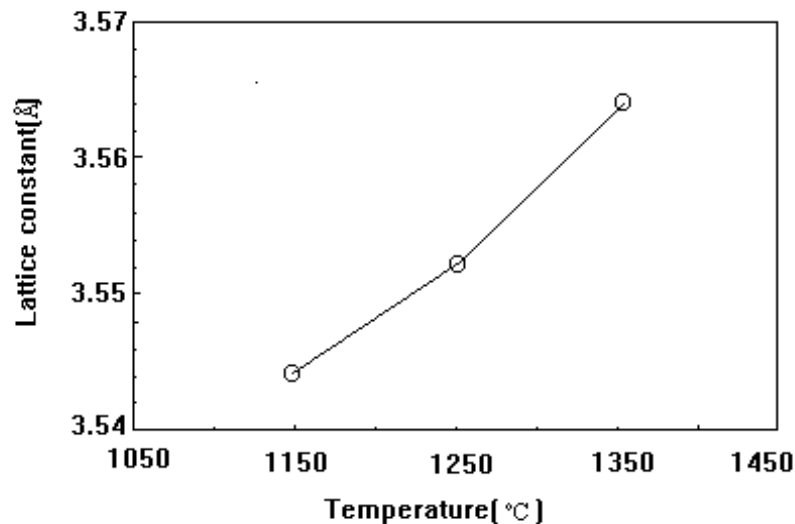


Fig. 2: Lattice constant  $a$  of the Ni solid solution as a function of sintering temperature (For pure Ni:  $a=3.5238\text{Å}$ )

A conceivable explanation for the expansion is that dissociation of TiN takes place during sintering [14] resulting in the formation of Ti atoms (or Ti ions), then the Ti atoms diffuse into Ni lattices leading to the expansion, as the atomic radius of Ti ( $2.00\text{ Å}$ ) is larger than that of Ni ( $1.62\text{ Å}$ ). The higher the sintering temperature, the more Ti atoms diffuse into Ni lattices, consequently, the larger the lattice constant value will be. Fig. 1 also shows that there is no diffraction peak broadening meaning that the Ni solid solution is homogeneous, which is not surprising for the high temperatures and long duration of sintering applied and the small particle size of Ni.

The quantitative relationship between the lattice constant of Ni solid solution and its Ti content is given in Fig. 3 [15]. Using this figure the Ti content of the Ni solid solutions can be obtained as illustrated in Fig. 4, which shows the Ti content as a function of sintering temperature acquired from the data presented in Fig. 2. From Fig. 4, one can see that the amount of Ti diffused into Ni lattices is significant.

Fig. 5 shows the scanning electron micrographs of the cermet pressureless sintered at  $1350\text{ °C}$  for 1 hour. Two phases are visible in the micrographs. Various areas from each phase were analyzed by EDX. A representative EDX spectrum for the metallic phase corresponding to the area indicated by the arrow in Fig. 5A is presented in Fig. 6. This figure confirms that the metallic phase consists of Ni and Ti. The quantitative EDX analysis gives the Ti content as  $11.1 \pm 0.1\text{ At\%}$  (The uncertain range is standard deviation). This value is very close to the one given in Fig. 4. A representative EDX spectrum for the ceramic phase corresponding to the area indicated by the arrow in Fig. 5B is presented in Fig. 7. This figure indicates that the ceramic phase consists of Ti, N and a small amount of Ni as well. Quantitative EDX analysis shows that the Ni content is below  $6\text{ At\%}$ .

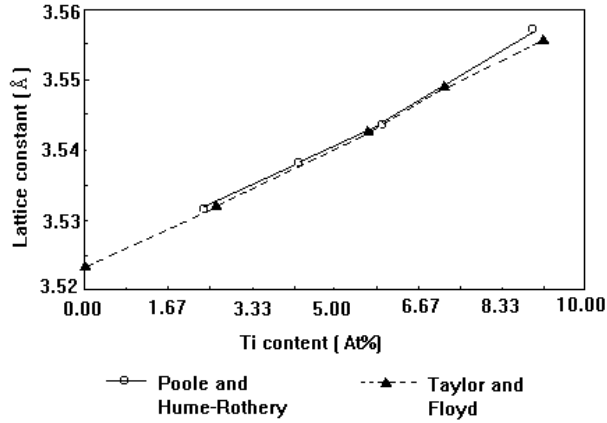


Fig. 3: Lattice constant  $a$  of the Ni solid solution as a function of Ti content

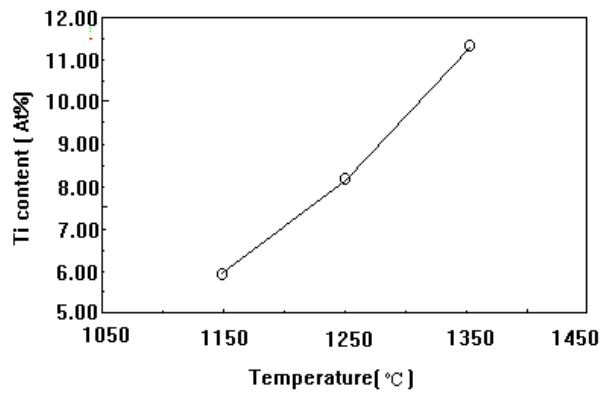


Fig. 4: Ti content of the Ni solid solution as a function of sintering temperature

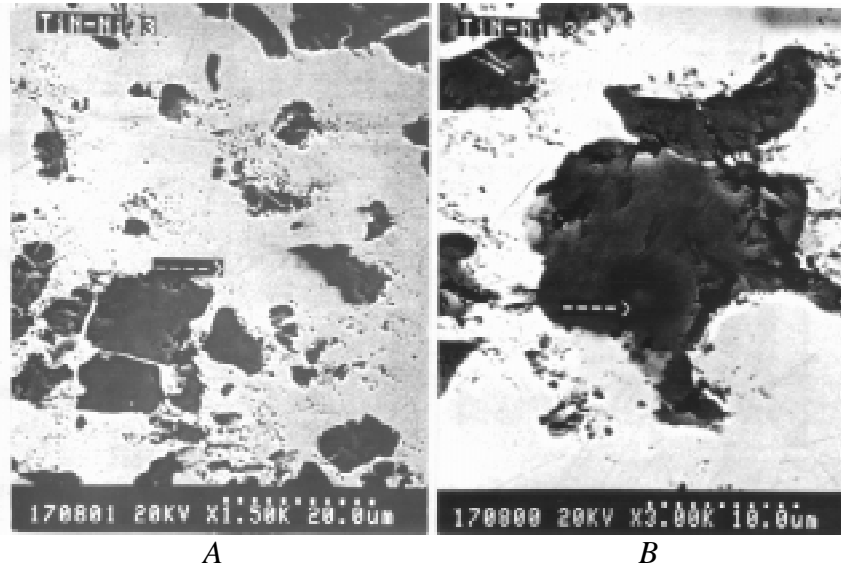


Fig. 5: Scanning electron micrographs of the cermet composed of 50 Vol% TiN + 50 Vol% Ni pressureless sintered at 1350 °C in vacuum for 1 hour. The metallic phase (A) and the ceramic phase (B) were analyzed by EDX

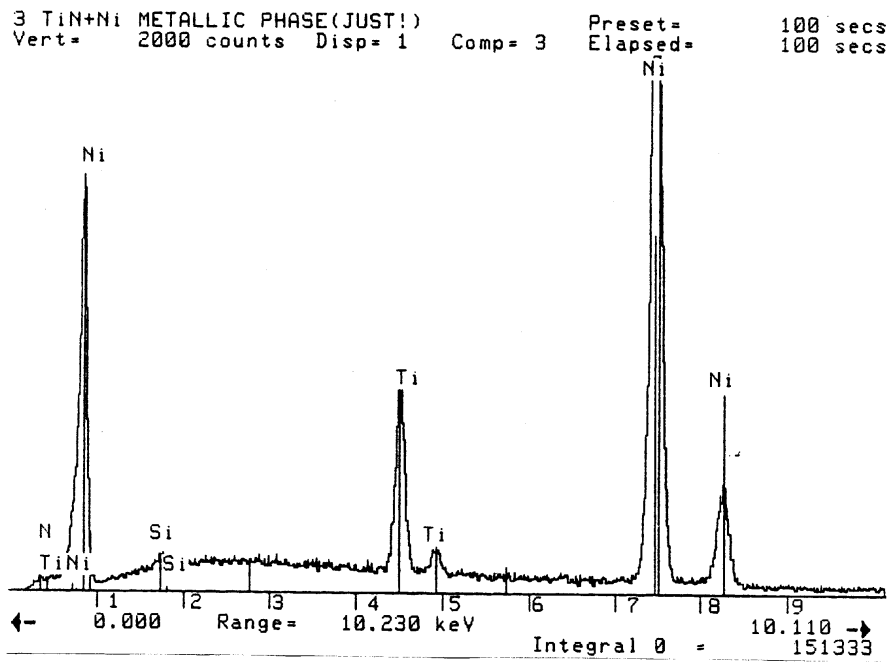


Fig. 6: EDX spectrum analyzed at the metallic phase as indicated by the arrow in Fig. 5A

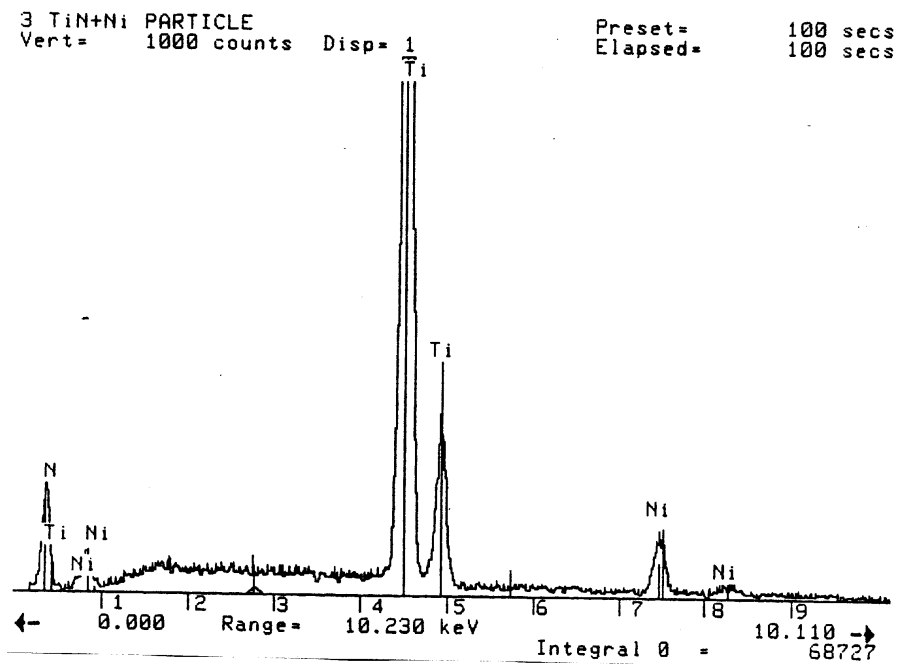


Fig. 7: EDX spectrum analyzed at the ceramic phase as indicated by the arrow in Fig. 5B

## CONCLUSIONS

Based on the aforementioned experimental results, it can be concluded that during sintering of the compacts composed of 50 Vol% TiN + 50 Vol% Ni at 1150-1350 °C in vacuum for 1 hour, Ti atoms diffuse into Ni lattices forming homogeneous solid solution. This leads to the expansion of the lattice constant. The higher the sintering temperature, the more Ti atoms dissolve, and the more obvious expansion occurs. Only a small amount of Ni diffuses into TiN and dissolves in it. The amount of the Ni is so small that the X-ray diffraction patterns show a stable crystal structure of TiN within the temperature range tested.

It is believed that this interdiffusion also takes place at the TiN/Ni interface involved in the Al<sub>2</sub>O<sub>3</sub>-TiN+Ni system. For the hot-pressed cermet Al<sub>2</sub>O<sub>3</sub>-TiN+Ni, this interdiffusion is beneficial to the adhesion at the TiN/Ni interface. Therefore, it can be an explanation of the mechanism that TiN interlayer remarkably enhances the sintering ability and mechanical properties of the Al<sub>2</sub>O<sub>3</sub>-TiN+Ni system.

## ACKNOWLEDGEMENTS

The authors gratefully acknowledge that this project is financially supported by former Foundation for Advanced Metals Science, the Netherlands, University of Twente, the Netherlands, and National Natural Science Foundation of China.

## REFERENCES

1. McHugh, C. O., Whalen, T. J. and Humenik, M., "Dispersion-strengthened Aluminum Oxide", *Journal of American Ceramic Society*, Vol. 49, No. 9, 1966, pp. 486-491.
2. Gazza, G. E., Barfield, J. R. and Preas, D. L., "Reactive Hot-pressing of Alumina with Additives", *American Ceramic Society Bulletin*, Vol. 48, No. 6, 1969, pp. 606-610.
3. Rankin, D. T., Stiglich, J. J., Petrak, D. R. and Ruh, R., "Hot-pressing and Mechanical Properties of Al<sub>2</sub>O<sub>3</sub> with a Mo-dispersed Phase", *Journal of American Ceramic Society*, Vol. 54, No. 6, 1971, pp. 277-281.
4. Whitney, E. D., "New Advances in Ceramic Tooling in the USA", *Powder Metallurgy International*, Vol. 10, No. 1, 1978, pp. 16-21.
5. Naerheim, Y., "Strength, Toughness and Thermal shock Resistance of Al<sub>2</sub>O<sub>3</sub>-Ti Cermets", *Powder Metallurgy International*, Vol. 18, No. 3, 1986, pp. 158-162.
6. Brook, R. J., "Additives and the sintering of Ceramics", *High Tech Ceramics*, Vincenzini, P., Ed., Elsevier Science Publishers BV, Amsterdam, 1987, pp. 757-761.
7. Trabelsi, R., Treheux, D., Goeuriot-Launay, D., Goeuriot, P., Thevenot, F., Orange, G. and Fantozzi, G., "Friction, Wear Resistance and Mechanical Properties of an alumina-g Aluminum Oxynitride Composite (Aluminalon)", *High Tech Ceramics*, Vincenzini, P., Ed., Elsevier Science Publishers BV, Amsterdam, 1987, pp. 2683-2695.

8. Lee, M. and Borom, M. P., "Rapid Rate Sintering of  $\text{Al}_2\text{O}_3$ -TiC Composites for Cutting-Tool Applications", *Advanced Ceramic Materials*, Vol. 3, No. 1, 1988, pp. 38-44.
9. Goeriot, P., Goeriot-Launay, D. and Thevenot, F., "Oxidation of an  $\text{Al}_2\text{O}_3$ -g AlON Ceramic Composite", *Journal of Material Science*, Vol. 25, 1990, pp. 654-660.
10. Li, Shujie, *Investigation of Powder Metallurgical Route for Manufacturing  $\text{Al}_2\text{O}_3$ /Ni Cermets with Interlayers*, Quick Service drukkerijen Nederland B. V., Enschede, The Netherlands, 1992, ISBN 90-9005531-2.
11. Li, Shujie, Khosrovabadi, P. B. and Kolster, B. H., "Effect of a Titanium Nitride Interlayer on the Densification, Properties and Microstructure of Cermets Based on Alumina and Nickel;"Part 1: Densification and Properties", *International Journal of Refractory Metals and Hard Materials*, Vol. 11, No. 3, 1992, pp. 181-192.
12. Li, Shujie, Khosrovabadi, P. B. and Kolster, B. H., "Effect of a Titanium Nitride Interlayer on the Densification, Properties and Microstructure of Cermets Based on Alumina and Nickel;"Part 2: Microstructure", *International Journal of Refractory Metals and Hard Materials*, Vol. 11, No. 3, 1992, pp. 193-200.
13. Feidorlqink, U. M., *Principles of Powder Metallurgy*, The Publishing House for Metallurgical Industry, Beijing, 1974, (Chinese translation from Russian), p. 329.
14. Mnatsakanyan, E. D., Vil'k, Yu. N., Paputskii, Yu. N., Kozlovskii, L. V. and Ordan'yan, S. S., "Interfacial Reaction and Mass Transport of the Components in The  $\text{Al}_2\text{O}_3$ -TiN System During Sintering", *Sov. Powder Metall. Met. Ceram.* (English Translation), Vol. 24, No. 11, 1985, pp. 812-817.
15. Pearson, W. B., *A Handbook of Lattice Spacings and Structures of Metals and Alloys*, Pergamon Press Ltd, Oxford, London, Edinburgh, New York, Paris, Frankfurt, Reprinted with corrections 1964, p. 779 and p. 791.

# STRUCTURAL EVOLUTION OF C/C-SiC COMPOSITES THROUGH THE MAIN PRODUCTION STEPS ON THE LIQUID SILICON INFILTRATION (LSI) ROUTE

Herbert Mucha<sup>1</sup>, Akira Kamiya<sup>2</sup>, Bernhard Wielage<sup>1</sup>

<sup>1</sup>*Technical University Chemnitz-Zwickau, Institute of Composites and Surface Technology, D-09107 Chemnitz, Germany*

<sup>2</sup>*National Industrial Research Institute Nagoya, 1-1 Hirate-cho, Kita-ku, Nagoya, 462, Japan*

**SUMMARY:** Carbon fiber reinforced carbon- and SiC-matrix composites can be made by different production methods and are displaying characteristic microstructures. This paper focuses on the analysis of structural aspects induced by the fabrication process of C/C-SiC composites fabricated by the Liquid Silicon Infiltration (LSI) method which was developed by DLR (German Aerospace Research Establishment).

The LSI method consists in three main production steps (CFRP, C/C and C/C-SiC state) and the evolution of the composite's morphology and structure is traced through these production steps from the carbon fiber reinforced plastics (CFRP) state to the finally processed C/C-SiC composite. Conventional optical microscopy, EPMA, REM and TEM serve as tools to disclose the microstructural organization and elemental informations in order to understand their origins and the implications on the finally processed composite materials.

## INTRODUCTION

Several methods are well suited to produce carbon fiber reinforced SiC-matrix composites. Examples are the chemical vapour infiltration (CVI), various Si-polymer pyrolysis routes with/without filler and the Liquid Silicon Infiltration (LSI) method [1] which is developed at DLR (German Aerospace Research Establishment). It is based on a C-polymer pyrolysis and subsequently followed by an infiltration of liquid silicon. Each of these methods offers merits for particular economical or technological requirements. The LSI-method as a one shot-near net shape fabrication process is a quick and economical alternative to the other processes for many technical applications in near future [2]. The upscaling from the laboratory to a technical scale proved feasible. A large number of high performance real parts as e.g. an intake ramp for hypersonic propulsion systems or brakes are produced by this way and confirm the high level of technological development of the LSI-method [3,4,5].

Starting from the raw components the material has to undergo several transformations before the product reaches the final C/C-SiC condition. The following discussion puts emphasis on the elucidation of structural changes which take place accompanied with the three main processing steps which are Carbon Fiber Reinforced Plastic (CFRP), Carbon/Carbon (C/C) and C-fiber reinforced ceramic state (C/C-SiC).

For tracing the structural changes a specialized sample preparation is applied adequate to handle the strong heterogeneity of the composites. Through all the material states this is a basic requirement for the optical microscopy, REM (Raster Electron Microscope), EPMA (Electron Probe Micro Analyser) and TEM (Transmission Electron Microscope) investigations. The sample's architecture is shown clearly by the optical microscopy. EPMA serves informations about elemental distributions within the C/C-SiC samples, whereas REM and imaging TEM disclose further details of the microstructural organization. This way the fiber/matrix interfaces, the reaction zones or even C-fiber damages are depicted.

### **THE LIQUID INFILTRATION METHOD**

The LSI method [1,2,3] is a relatively fast fabrication process that consists of three processing steps, which are passed through just one time during the whole fabrication cycle (Fig. 1). Starting materials are stacks of 2D carbon fiber cloth (plain weave) and high carbon yield polymeric C-precursors which have to fulfill particular requirements induced by the processing.

#### 1. CFRP forming (5-20bar, Polymerization, 200°C, inert atmosphere):

The first step of composite fabrication applies the Resin Transfer Moulding to inject the polymer into the stack of carbon fiber cloth. The subsequent polymerization is performed in a furnace applying a well defined time-temperature profile. It is accompanied with development of little matrix porosity but significant matrix shrinkage which causes a periodic primary segmentation within the fiber bundles.

#### 2. C/C forming (Pyrolysis, 1 bar, N<sub>2</sub>, 900°C):

The CRFP composite undergoes a thermolysis with well controlled time-temperature profile during the next fabrication step. A great matrix volume shrinkage is accompanied by substantial structural changes. A multiply connected translaminar channel system and a second segmentation of fiber bundles is formed. The characteristic micro crack pattern depends essentially on the fiber matrix binding strength.

#### 3. C/C-SiC forming ( Liquid Silicon infiltration, vacuum, 1550°C):

Capillary forces are the driving forces of the infiltration of liquid elemental Si into the C/C channel system under vacuum conditions, after preheating the C/C composite. The accompanied diffusion controlled reaction between carbon and silicon is strongly dependent on the pore size distribution of the infiltrated C/C-composite but also on the particular modification of carbon being present within the reaction zone. The time-temperature profile is very essential for tailoring the desired product properties. Fig. 1 schematically displays such a profile ("Brennkurve") [3].



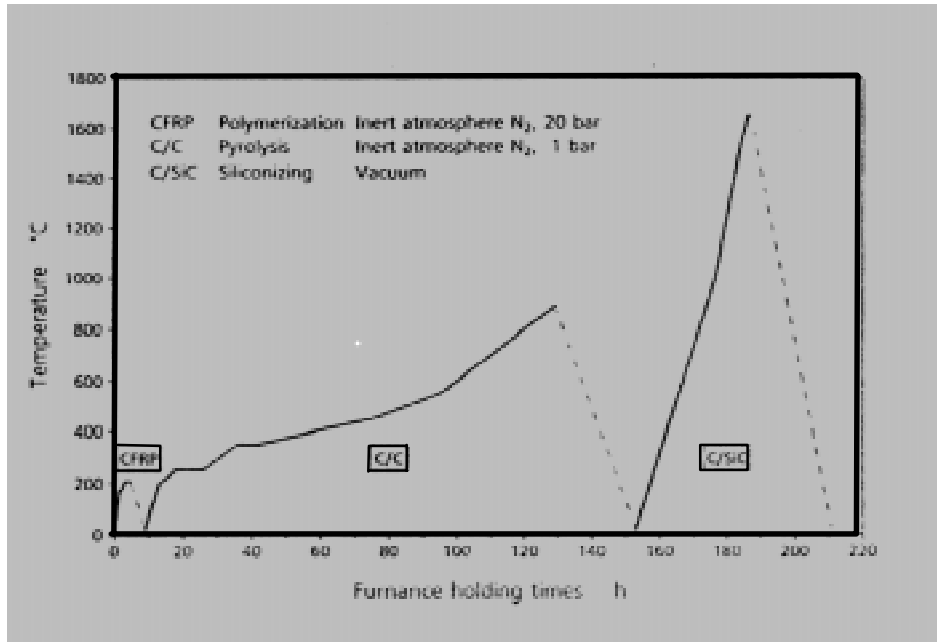


Fig. 1: Schematic Time-Temperature Profile (‘Brennkurve’) of the LSI process [3]

## EXPERIMENTAL

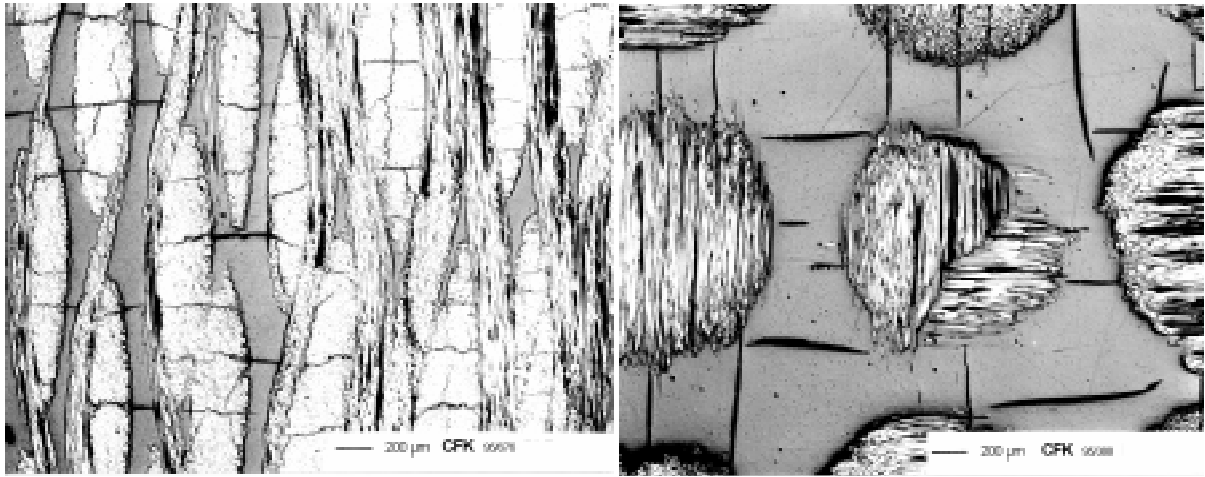
All samples independently whether CFRP, C/C or C/C-SiC state are cut from plate like composites using a diamond saw under well defined angles with the laminate layers. The ceramographical preparation makes use of supporting rings inserted into the conductive embedding material. Grinding applies various SiC papers down to 14  $\mu\text{m}$  grain size. Polishing on cotton cloth using OP-S suspensions (0,25  $\mu\text{m}$  grain size) follows subsequently. To prevent electron induced matrix degradation of CFRP samples a gold coating is applied and REM is operated in such cases at low voltages (<5kV). The TEM preparation additionally required dimple grinding (diamond paste of 3  $\mu\text{m}$ ) and subsequent conventional ion milling (PIPS).

## RESULTS

### CFRP State

The CFRP real structure (Fig. 2a,b) results from the matrix shrinkage and superimposed shrinkage impediment along the C-fiber axes. An almost periodic division of the fiber bundles in small segments is seen. Preparation of samples parallel to the laminate layers discloses the existence of two perpendicular crack systems which are almost independent of each other (Fig. 2b). The polymerisation and degassing conditions (one parameter e.g. is the pressure) as well as the type of raw materials exercise a strong influence on the development of open and closed porosity within matrix rich areas and inside the fiber bundles.

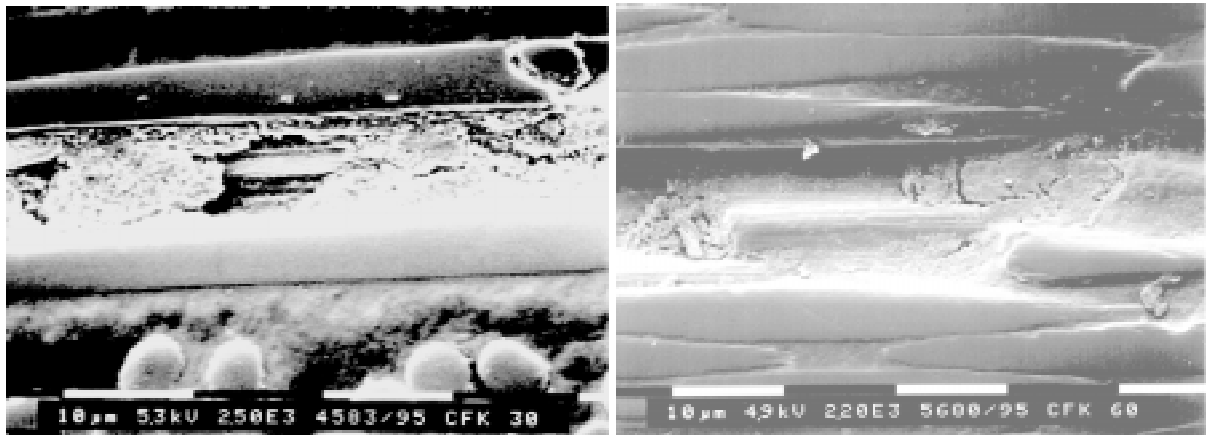
The matrix rich areas usually display a homogeneously dispersed closed porosity. A careful mechanical sample preparation partially retains an additional foamy phase located at crack sites (Fig. 3a) or independent of cracks (Fig. 3b).



(a)

(b)

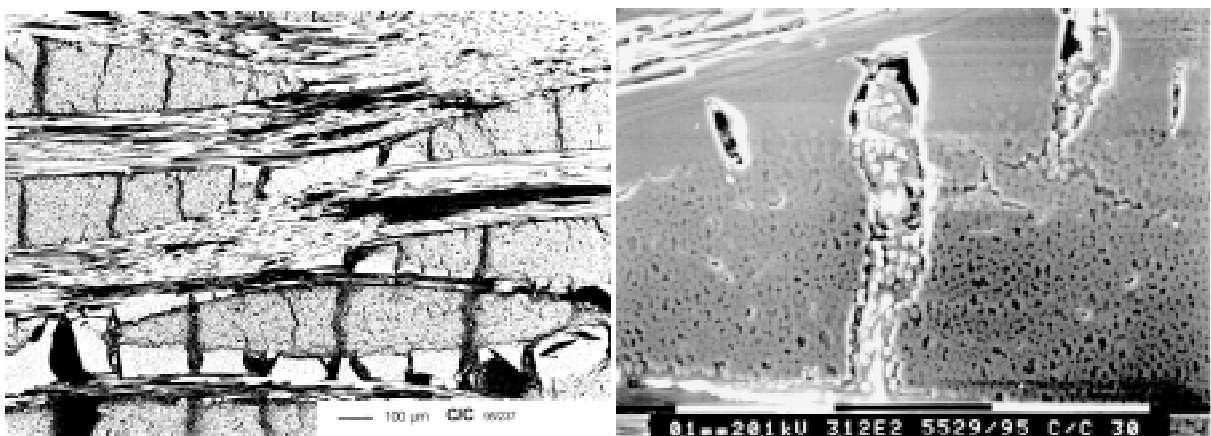
Fig. 2: Optical micrograph of CFRP composite: a) perpendicular b) parallel to laminate layer



(a)

(b)

Fig. 3: REM micrograph of foamy matrix (CFRP) a) adjacent to crack b) independent of crack



(a)

(b)

Fig.4: C/C state sample (a) overview (b) foamy matrix component

## **C/C State**

The applied pyrolysis induces very severe structural changes to the CFRP-composite caused by the mass loss (60% carbon yield) during pyrolysis (Fig. 4a). A multiply connected open channel system develops and the closed porosity in bulk matrix areas grows significantly.

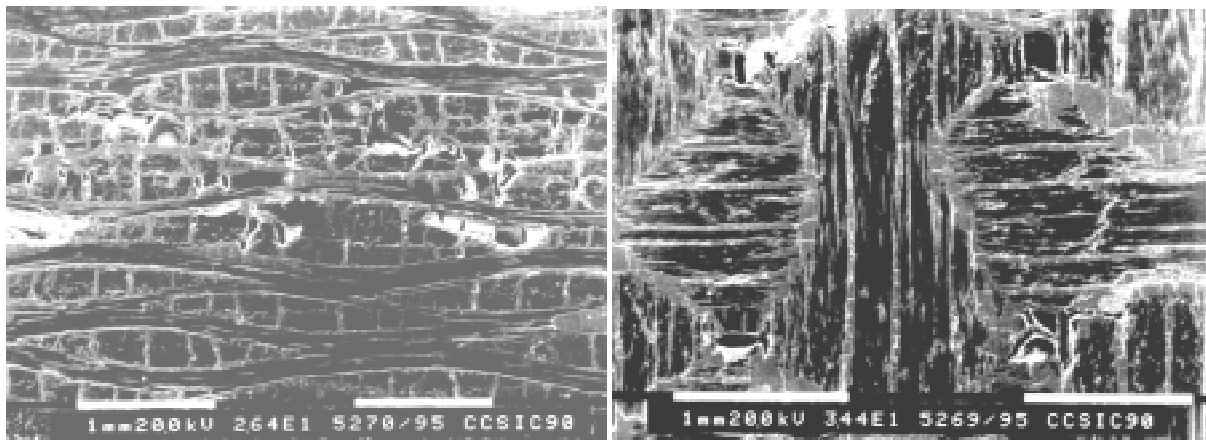
The increased crack width in matrix rich areas is evident as well as the periodical occurrence of regions within the fiber bundles where the average distance between neighbouring fibers increased (zone of reduced fiber density). This periodicity corresponds to that of the primary segmentation as observed in the CFRP-state. To some extent a fiber rearrangement takes place (larger fiber distance) in areas of primary segmentation but also a displacement of a foamy matrix component into the bulk matrix cracks is observed (Fig. 4b). The foamy matrix component usually is separated from bulky matrix or fibers by very fine cracks (Fig.4a). Additionally a second segmentation takes place within the C-fiber bundles but these cracks are not filled by any foamy matrix component. Polarized light microscopy which is performed additionally gives indications that stress induced graphite is formed locally within the fiber bundles even at processing temperature as low as 900°C.

## **C/C-SiC State**

A characteristic of C/C-SiC is the segmented wall structure which develops from the open channel system of the C/C state by the infiltration of liquid silicon (Fig. 5a). This channel system extends over large distances and is shown most clearly if the cut section is in parallel to the laminate layers (Fig. 5b). The infiltration and the accompanied chemical reaction shows a locally different behaviour (Fig. 6a) which is dependent not only of the width of the pores but also correlated to the carbon modifications reacting with Si and their lateral distribution within the reaction zone. C-matrix modifications of different appearance were detected in the C/C state. After the infiltration the former crack areas still can be identified in large scale by optical microscopy. Their structure reflects the former course of reaction between Silicon and Carbon. The REM investigations of C/C-SiC materials require a gold coating in order to prevent charging but clearly reveal topographical inequalities at higher magnifications. They originate in the different hardness of the substrate's surface and become effective during the mechanical sample preparation (Fig.6b). The reaction zones mostly display a cloud like shape and consist of a brittle material (Fig. 7a) which is retained only under dedicated sample preparation. The reaction between silicon and carbon involves both fiber and matrix. Even submicrometric pores are efficiently infiltrated.

A typical crack area which generated from a zone of reduced fiber density by Si infiltration (Fig. 6b) shows sharp topographical steps in central areas and a less sharp and brittle type adjacent to the carbon fiber bundles or to bulky matrix areas as displayed in Fig. 7a under higher magnification. The gold coating, and the limited accuracy of conventional EDS (Energy Dispersive X-ray Spectroscopy) equipment for the detection of light elements, as carbon, give a preference to WDS (Wavelength Dispersive X-ray Spectroscopy) EPMA investigations of the elemental distribution. Since no sample charging was observed, no gold coating had to be applied. The Si elemental maps (as Fig.7b) and topographical images show some general features as pure Si areas (white) embedded in Si-rich areas of large grain size (central grey), Si-supply channels (dark grey) and fine grained areas (grey) with concentration gradients. They are adjacent to the unreacted carbon zones (dark black). Transmission electron micrographs usually show that even narrow infiltrated pores consist in a core of coarse grained SiC at almost the same position as the former pore and a reaction zone consisting of

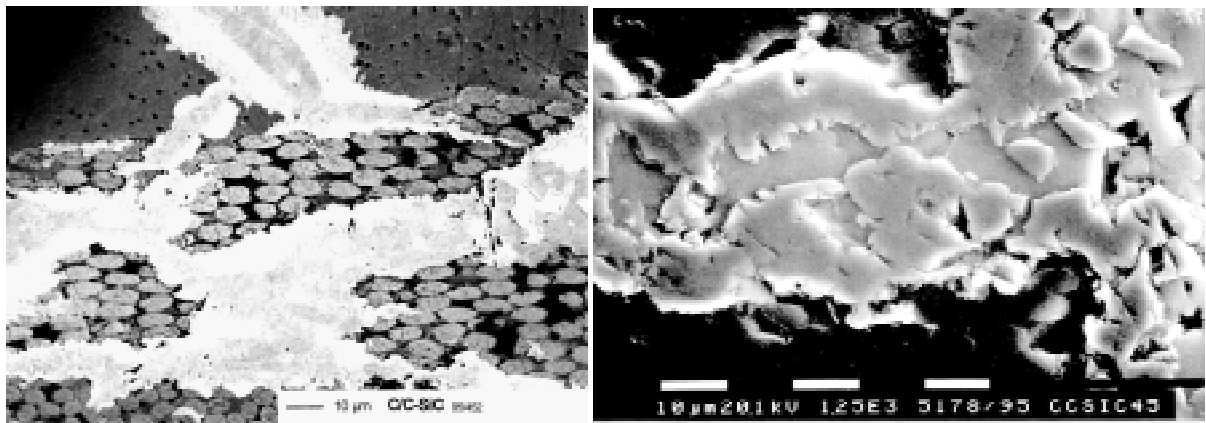
fine grained SiC surrounding it (Fig. 8a). Elemental Si also can be detected locally but preferentially within the wide “pores”. The fine grained SiC area occasionally displays microcracks ending at closed porosity. Closed porosity in the C/C state preferentially accumulates near fiber surfaces (Fig. 8b) and modifies the resulting fiber matrix binding strength. The closed C/C state porosity usually is retained during the silicon infiltration leading to voids in the C/C-SiC reaction zones. TEM imaging proves that even submicrometric cracks which are connected to the open channel system are infiltrated efficiently. Their reaction zones have the same characteristic appearance as the larger ones. Another interesting observation can be made in front of the reaction zones inside the carbon fibers. Analogous effects were found in the carbon matrix (Fig 8a), too. The fibers show indications of damages within a range of several hundred nanometers in front of the reaction zone in apparently unreacted areas of the fibers. Whereas the segregations in the fibers seem oriented along the fiber axis, the segregations in the matrix appear in a more spherical shape.



(a)

(b)

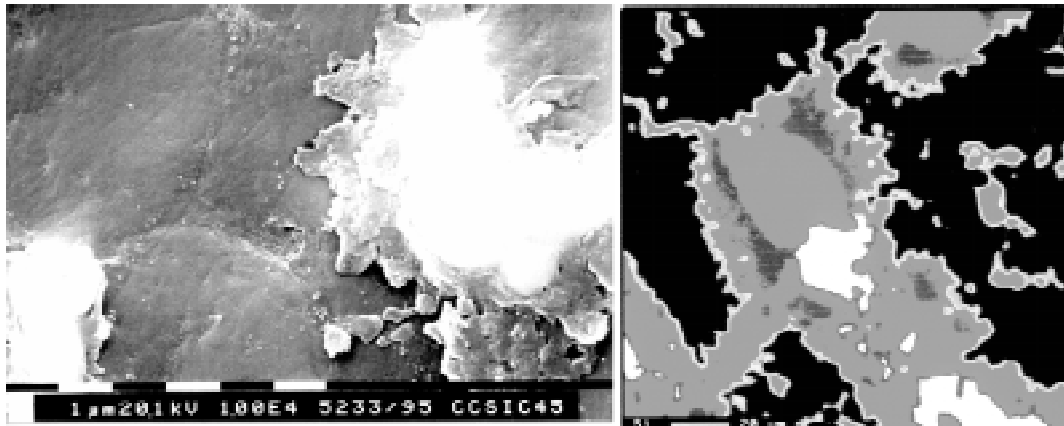
Fig. 5: Segmented wall structure of C/C-SiC a) perpendicular b) parallel to laminate layers



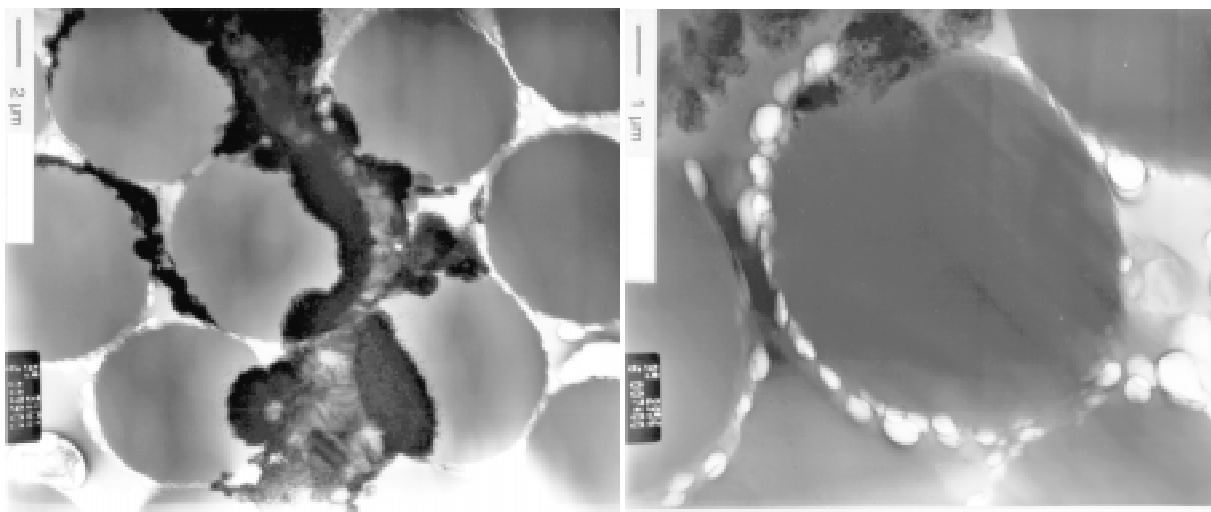
(a)

(b)

Fig. 6: C/C-SiC reaction zones (a) optical micrograph (b) REM micrograph



(a) (b)  
 Fig. 7: C/C-SiC (a) reaction zone (REM) (b) Si-elemental map (EPMA-WDS)



(a) (b)  
 Fig. 8: C/C-SiC (a) crack structure (TEM) (b) accumulated closed porosity (TEM)

## DISCUSSION

It is likely that the WDS Si-elemental map (Fig. 7b) is taken from an area which before the Si infiltration took place resembled that of Fig. 4b but showed additional open porosity. The narrow cracks separating the foamy matrix from the regular composite are assumed to be connected with the open porosity. Under this condition liquid silicon is supplied by the the open pores and distributed to the narrower cracks. The higher Si concentration compared to other crack areas can be explained by this argument. The foamy matrix in central parts of the zone of reduced fiber density serves as easily accessible carbon reservoir for the Si-C reaction. Due to the direct impregnation of the foamy matrix by liquid silicon the diffusion distances are short and the course of reaction is much more advanced compared to those regions where the reaction is based on the long distance diffusion of the reaction partners. Finally in such areas a recrystallization can take place and form large crystallites, as seen by TEM micrographs (Fig. 8a) or less pronounced in mass contrast or topo images. The hardest component is the coarse grained phase (SiC), whereas the weakest is elemental silicon. The correlated topographical steps can be detected on suitably prepared samples. Only pores

which are directly infiltrated can be filled up by this method; closed porosity will remain closed porosity, independent of whether the carbon of the surrounding reacts to SiC or not. As a hypothesis, the segregations within the fibers in front of the reaction zone may grow due to a Si gas phase infiltration inside the nanoporosity of the fiber.

A suitable segmentation and pore size distribution is essential for good infiltration results. The fiber-matrix binding strength is one of the controlling parameters of the segmentation width. Hardening during CFRP forming is accompanied with a matrix shrinkage and a first segmentation of the fiber bundles inside the 2D (0°-90°) CFRP composite. Subsequent pyrolysis causes further shrinkage and an additional segmentation. Wanner [6] created a model to describe the periodicity of this secondary segmentation based on the internal stress distribution of the composite.

The controlled release of gaseous reaction products has to take place in order to reduce the size of bubbles and not to accumulate too much closed porosity inside the composite. The corresponding time-temperature profiles ("Brennkurve") are tailored for each precursor and based on thermogravimetric and thermoanalytical investigations.

## CONCLUSIONS

Tracing the structure of the starting CFRP-material through the subsequent manufacturing steps (Pyrolysis and Si infiltration) the foamy matrix component leads to coarse grained SiC areas when infiltrated directly. If not infiltrated directly this porosity is conserved as an area of weak binding. The importance of an effective control of crack size and porosity during C/C-SiC fabrication is confirmed.

## ACKNOWLEDGEMENTS

The authors gratefully wish to acknowledge the support of the German Aerospace Research Establishment (DLR) which supplied the samples and made it possible to perform a part of this work in its laboratory for microstructure analysis.

## REFERENCES

1. Kochendörfer, R.; Liquid Silicon Infiltration - A fast and low cost CMC manufacturing process, ICCM 8, 1991, Honolulu
2. Krenkel, W.; Kochendörfer, R.; The LSI Process - A cost effective processing technique for ceramic matrix composites; Proc. of ICAM, Progress in Advanced Materials and Mechanics, Tagung 12.8.-15.8.1996, Peking
3. Krenkel, W.; CMC Design Consequences, AGARD Workshop Introduction of Ceramics into Aerospace Structural Composites, Antalya, 18-23 April 1993
4. R. Kochendörfer, W. Krenkel; CMC intake ramp for hypersonic propulsion systems; Proc. HT-CMC2, Santa Barbara, Ca, 21.8.-24.8.1995, S. 13-22
5. W. Krenkel; CMC Materials for high performance brakes; ISATA Conference on Supercars, Aachen, 31.10.-4.11.1996
6. A. Wanner; Gefüge und mechanische Eigenschaften des Kohlenstofffaser/Kohlenstoffmatrix-Verbundwerkstoffs CF222, Dissertation, Universität Stuttgart 1991

# THE FABRICATION OF TWO-DIMENSIONAL CARBON FIBER REINFORCED ALUMINA COMPOSITES BY PRESSURE INFILTRATION

Hsien-Kuang Liu and Bor-Horng Lin

*Department of Mechanical Engineering, Feng-Chia University  
100 Wenhwa Road, Taichung, Taiwan, R.O.C.*

**SUMMARY:** Using pressure infiltration can fabricate two-dimensional (2-D) textile ceramic matrix composites with uniform and dense microstructure. Based upon this processing technique, composites composed of silica sol, alumina particles, and 2-D satin weave carbon fibers were fabricated. The related processing parameters studied in this work include fiber surface treatment and fiber volume fraction. The woven carbon fabrics were treated by a liquid oxidation reaction method in order to study their surface conditions on mechanical properties of 2-D composites. Fiber volume fractions are varied by changing weave density of 2-D carbon woven fabrics. Material characterizations have been conducted by a three-point bending test and an indentation fracture toughness test. Therefore, the aim of this work is to optimize processing parameters for obtaining better mechanical properties of composites.

**KEYWORDS:** pressure infiltration, 2-D fabrics, liquid oxidation reaction

## INTRODUCTION

In practical applications, a structure component might be subjected to multidirectional loads, resulting in the need to arrange the reinforcing fibers in more than one direction. Textile composites using tailored preforms, such as woven, knitted, or braided fabrics, are versatile to accommodate a variety of requirements, such as stability (strength/stiffness) or extensibility in desired directions and relative ease of handling in fabrication [1]. The advantages have led to the current interest in fabricating ceramic matrix composites based on textile preforms. However, the microstructure of textile ceramic matrix composites (CMCs) is significantly influenced by the processing route. For example, textile CMCs fabricated by the chemical vapor infiltration (CVI) technique normally contain high porosity which results in the stiffness reduction of the composite [2].

Several processing routes for CMCs have their respective advantages. SiC matrix ceramic composites fabricated by CVI [3] have improved mechanical properties. The advantage of CVI is that chemical vapors can react and produce pure ceramic matrix at low temperature around 1200°C. 2-D Nicalon/BN/SiC composites processed by the isothermal chemical vapor infiltration (ICVI) method [4] have better load transfer efficiency under aggressive environment than typical SiC/C/SiC composites. 2-D woven fabric SiC/SiC composites with multilayered interphases fabricated by CVI method [5,6] have both high strength and toughness due to strong interphases and large amounts of matrix cracks at saturation,

respectively. 2-D woven fabric SiC/SiC composites can be produced by a slurry infiltration method [7] associated with multiple impregnation at a lower temperature. 3-D C/SiC and C/Si<sub>3</sub>N<sub>4</sub> composites made by polymer pyrolysis and repeated infiltration [8] gain their unique properties. A common advantage of these fabrication routes is that the processing temperature can be lowered to 1200°C. However, a common disadvantage of these fabrication routes is long processing time. Based on economical point of view, to cut down the processing time should be one of the important issues for fabrication of CMCs in the near future. To achieve the above goal, Liu and Parvizi-Majidi [9] tried to fabricate 3-D ceramic matrix composites with satisfactory density and uniformity in a single infiltration using the addition of solid particles to the sol during sol-gel processing of ceramic matrix composites.

Therefore, the purpose of this work is to introduce a pressure infiltration method which could fabricate 2-D woven carbon fabric reinforced alumina composites with dense microstructure. The woven carbon fabrics were treated by a liquid oxidation reaction method in order to evaluate the influence of their surface conditions on mechanical properties of 2-D woven fabric CMCs. To optimize processing parameters for obtaining better mechanical properties is the goal in this study.

## **MATERIAL PROCESSING**

### **Sol and Woven Fabric Preparation**

The silica sol was prepared using a modified recipe of Klein's work [10]. In this recipe, tetraethyl-orthosilicate (TEOS), ethanol, deionized water and 7 wt% of HNO<sub>3</sub> were mixed and stirred at a volume ratio of 1: 1: 1.6 : 0.06. All the reaction of the mixture was all at room temperature. 25 grams of the alumina powders ( $\alpha$  - Al<sub>2</sub>O<sub>3</sub>, Bayer process, average particle diameter of 0.45  $\mu$ m, purity of particle of 99.9%, and a density of 2.7g/cm<sup>3</sup>) were added to the sol to prepare the infiltrate. The infiltrate was further mixed both in ultrasonic bath and electromagnetic blender in turns until the powders in the infiltrate were dispersed uniformly and well wetted.

2-D plain carbon fabrics were used as preforms. The carbon fiber is Toho T-300 fiber with tensile strength of 3200 MPa. The first kind of fabric has fiber volume fraction ( $V_f$ ) of 33.7%. Each fiber yarn has 3000 fibers. Fiber has density of 1.78 g/cm<sup>3</sup> and diameter of 8  $\mu$ m. Weave density is warp 5 yarns/cm and weft 5 yarns/cm. Fabric weight is 194 g/m<sup>2</sup>. The second kind of fabric has fiber volume fraction of 21.5%. Weave density is warp 2 yarns/cm and weft 2 yarns/cm. Fabric weight is 87 g/m<sup>2</sup>. Each fabric was cut as a circle of 50 mm diameter. 12 layers of the woven fabrics were stacked together and stitched by a string as a preform with a thickness 3.67 mm (first kind) and 2.78 mm (second kind), respectively. The preform was further processed by pressure infiltration to obtain composites. The woven fabrics were either untreated (as-received) or treated by liquid oxidation reaction in order to compare the effect of fiber surface conditions on mechanical properties of the composites. The treated procedure is as follows. Carbon fabrics were dipped in 35wt% nitric acid solution at 70°C for 6 hours. Then the fabrics were washed by deionized water and dried at 150°C.



## Pressure Infiltration

The pressure infiltration apparatus was shown in Fig. 1, with an inner diameter of 50 mm in the cylinder, and a base cavity for collecting the liquid. The filter assembly consists of nitrate cellulose membrane filter paper with selected pore size, a wire cloth-stainless steel, and a perforated solid steel disk. The filter assembly was placed on the top of the base cavity. The wire cloth-stainless steel was used to keep the filter paper from rupture. Cylinder, filter assembly, and base were tightly sealed by thread and O-ring. Carbon fabrics were first put in the cylinder and attached to the filter assembly closely. A volume of 175 ml of infiltrate was then poured into the cylinder to infiltrate fabrics. An MTS testing machine set at constant crosshead speed mode was used to provide the infiltration pressure on the plunger. The use of a constant crosshead speed insured a gradual increase in pressure which consolidates powders inside the fabrics uniformly, and prevented filter paper from rupture. The maximum values of pressure were recorded: 46.7 MPa for the composite with untreated carbon fibers and 21.0 MPa for the composite with treated carbon fibers.

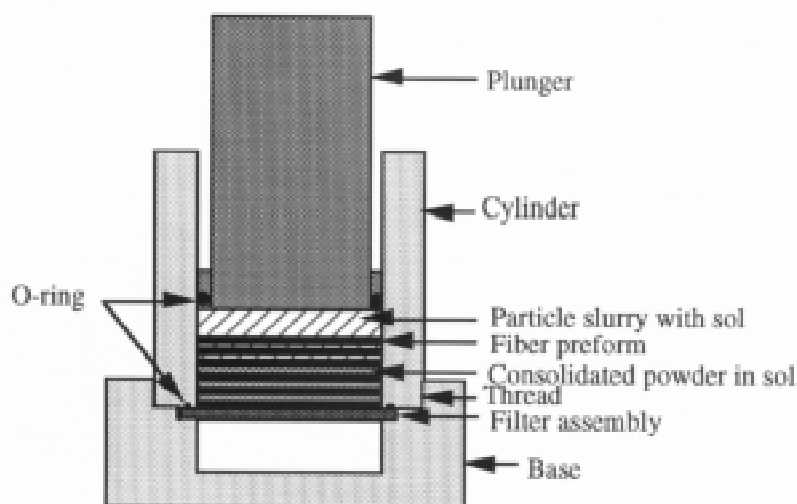


Fig. 1: Schematic diagram of pressure infiltration apparatus.

After first infiltration, the specimen was ejected and dried in an oven at 60°C for 24 hours. After the drying process, the composite was soaked in silica sol until saturation, and finally the composite green density was calculated from its dimensions and weight. Green composites were then hot pressed in a furnace (FCPHP-R-5, FRET-20, HIGH MULTI 5000, Multi-purpose High Temperature Furnace, Japan) under temperature 1600°C and pressure 25 MPa for one and half hours by first evacuated to  $10^{-5}$  torr, and then flowing nitrogen gas. After hot pressing, the percentage theoretical densities of composites were measured. In addition, microstructure and mechanical properties of composites were also evaluated.

## MATERIAL CHARACTERIZATION

The hot pressed composites were cut as specimen to evaluate mechanical properties and examine microstructure. Specimen cross sections were directly examined by a scanning electron microscope for bonding between fibers and matrix. Specimen before and after mechanical testing were embedded in urea, then polished with diamond paste and examined by an optical microscope. Specimen after mechanical testing were photographed by camera to observe their macroscopic failure.

The indentation fracture technique was adopted to determine the fracture toughness of composite materials. The Vickers diamond pyramid indenter was used to produce the crack patterns onto the well polished cross sections of specimen, which are on matrices between fiber layers. The indentation load is 5 kgw, which provides consistent indentation patterns with radial crack lengths substantially larger than the indentation diagonals. Thus, fracture toughness ( $K_{IC}$ ) can be calculated by measuring the lengths of diagonals and radial cracks by using the following equation

$$K_{IC} = \beta (E/H)^{1/2} (P/c^{3/2}) \quad (1)$$

where  $\beta$  is a constant around 0.016, E is modulus of composites, H is hardness of composites, P is indentation load, and c is half of the crack length.

A three point bending test was adopted to measure flexural strength and modulus of composites. An MTS testing machine was used to conduct the test. The span L, width w, and height h of the specimen were designed to be 40 mm, 9 mm, and 5 mm, respectively; detailed dimensions were measured for each specimen for further calculation of the strength and modulus. The width of the specimen is made larger compared to that of typical unidirectional ceramic composites to avoid scattering of the data. Crosshead speed was set at 0.008 mm/sec. The relationships of applied load (P) versus displacement ( $\delta$ ) were recorded during the test. The ultimate load ( $P_{max}$ ) were taken for the calculation of flexural strength ( $\sigma_{max}$ ) and modulus (E) according to the following equations

$$\sigma_{max} = 3P_{max}L/2wh^2 \quad (2)$$

$$E = P_{max}L^3/4wh^3\delta \quad (3)$$

## RESULTS AND DISCUSSION

### Effect of Liquid Oxidation Reaction

In order to enhance the bonding between carbon fabrics and alumina matrix as well as interlayer shear strength, liquid oxidation reaction was adopted to modify the surface condition of carbon fabrics. Nitric acid was used in the liquid oxidation reaction. The existence of shallow grooves on the surface of one-hour treated fibers was observed. After 6 hour treatment, the grooves become deeper; furthermore the outside layer have been etched as some fragments and then peeled off until the surfaces becomes rougher and rugged. This phenomena is beneficial for interfacial bonding due to more contacts between matrix particles and fibers. By liquid oxidation reaction, some active oxide functional groups are attached to the surface of carbon fabrics, such as hydroxyl group, ester group, carboxylic acid group, and carbonyl group. These functional groups were verified by IR spectrum for the surface of treated fibers [11]. After 300 minute treatment, the distribution of those functional groups is as follows: 80% for hydroxyl, 6% for carbonyl, 6% for carboxylic acid, and 8% for ester, respectively. Those active oxide groups may react with matrix particles and silica gels leading to chemical bonding between fibers and matrix. Treated carbon fabrics with active functional groups on their surfaces can have high affinity with silica in the matrix. Some of those groups have negative charge, such as hydroxyl. They attract hydrogen atoms with positive charge in silanol group on the surface of silica. Hence, during hot pressing, those

active functional groups can react with silanol via dehydration process and result in siloxane, then chemical bonds were formed [12]. Furthermore, silica may react with alumina and produce mullite with lower melting point resulting in better interfacial bonding. The evidences can be supported from several figures that discussed below.

Figs. 2(a) and 2(b) show cross sections of hot pressed composites with treated and untreated carbon fabrics, respectively. After cutting and polishing, the former shows better infiltration of matrix in the intrayarn pores inferring better bonding between fibers and matrix. While the latter shows worse infiltration corresponding to poor bonding at the interface. Fracture surfaces perpendicular to treated carbon fibers of 2-D carbon/alumina composites are flat indicating complete bonding between fibers and matrix (Fig. 3(a)). However, it seems that incomplete bonding between fibers and matrix occurs for composites with untreated carbon fibers because the surface of composites is likely in a molten state as shown in Fig. 3(b). The incomplete bonding may be due to the reaction of sizing on the carbon fabrics with silica gels. By our observation, it is found that the distribution of alumina matrix is inhomogeneous and sintering effect is nonuniform in two kinds of pore, interyarn pores and intrayarn pores. This may lead to the reduction of strength of composites. The content of matrix materials in intrayarn pores is less because they are much smaller compared to interyarn pores so that infiltration is more difficult. Furthermore, during hot pressing, fibers around intrayarn pores constrains matrix shrinkage more than fibers around interyarn pores. Both reasons result in poor bonding between fibers around intrayarn pores and matrix particles, but better bonding between fibers around interyarn pores and matrix particles as shown in Figs. 3 (a) and (b).

The influence of liquid oxidation reaction on fracture toughness of 2-D carbon/alumina composites is shown in Table 1. Composites with untreated fibers have higher fracture toughness than those of composites with treated fibers. It is because that the former have poor bonding at fiber/matrix interface so that propagation of cracks may go through interface. Its porosity is somewhat higher than that of the latter as can be compared by the final densities from Table 1. The above reasons explain why composites with untreated fibers obtain better fracture toughness. But, in Table 2, it is shown that composites with untreated fibers obtain both lower flexural strength and modulus of elasticity as compared to those of composites with treated fibers due to better bonding between fibers and matrix.

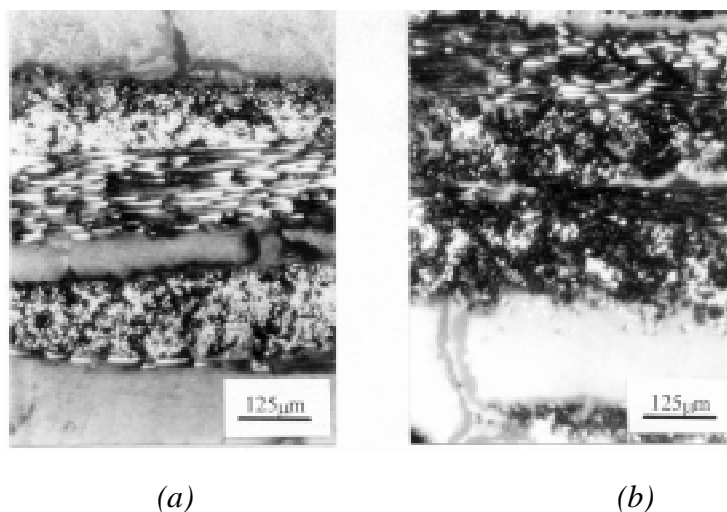


*Fig. 2: 2-D carbon/alumina composites with cross sections parallel to the hot pressing direction showing (a) better infiltration in the intrayarn pores among treated carbon fibers inferring better bonding between matrix and fibers in this region, (b) worse infiltration in the intrayarn pores among untreated carbon fibers*

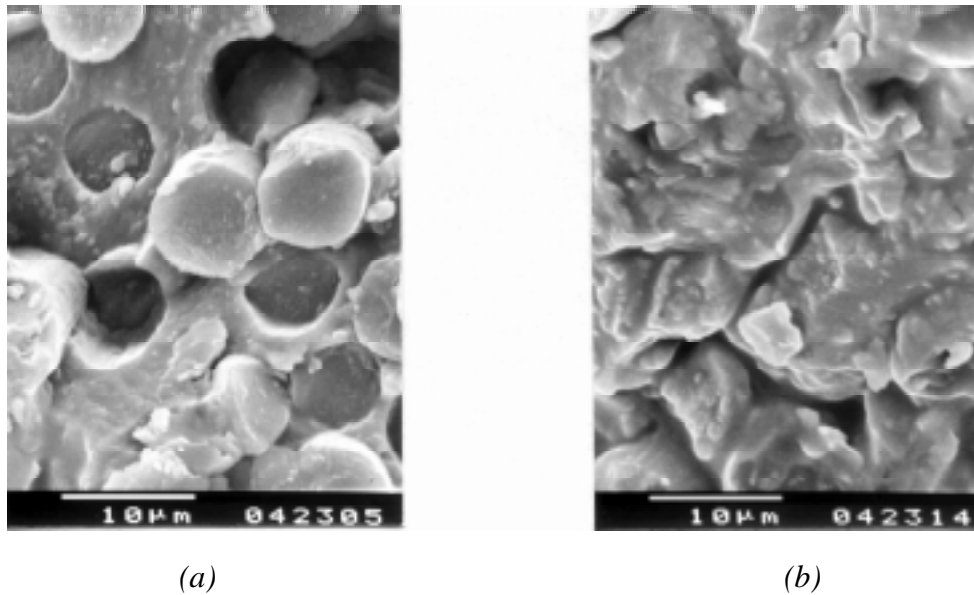


Fig. 3: Fracture surfaces of 2-D carbon/alumina composites perpendicular to the fibers showing (a) complete bonding between treated carbon fibers and matrix, (b) incomplete bonding between untreated carbon fibers and matrix

Table 1: Results of fracture toughness of 2-D carbon fabric/ $Al_2O_3$  ceramic matrix composites

Composite type	$K_{IC}$ ( $MPa \cdot m^{1/2}$ )	Hv (GPa)	Green density (% TD)	Final density (% TD)
fiber untreated ( $V_f = 33.7\%$ )	$7.0 \pm 0.2$	5.06	77.1	88.0
fiber treated ( $V_f = 33.7\%$ )	$6.5 \pm 0.1$	4.6	71.2	89.9
fiber treated ( $V_f = 21.5\%$ )	$2.0 \pm 0.2$	8.73	79.2	81.1

Table 2: Flexural strength and modulus of 2-D carbon fabric/ $Al_2O_3$  ceramic matrix composites

Composite type	Flexural strength (MPa)	Modulus of elasticity (MPa)
fiber untreated ( $V_f = 33.7\%$ )	$30.4 \pm 7.4$	$649.5 \pm 238.1$
fiber treated ( $V_f = 33.7\%$ )	$51.7 \pm 4.3$	$2081.4 \pm 494.8$
fiber treated ( $V_f = 21.5\%$ )	$76.7 \pm 31.3$	$608.5 \pm 212$

### Effect of Fiber Volume Fraction

The fracture toughness of composites increase with the increase of fiber volume fraction as shown in Table 1. It is known that fibers in ceramics can inhibit the propagation of cracks resulting in the increase of fracture toughness. The influence of volume fraction of fibers  $V_f$  on both flexural strength and modulus of elasticity is shown in Table 2. For lower fiber

volume fraction, less constraint of matrix shrinkage during sintering from fiber fabrics results in better densification and less porosity of matrix particles. This leads to higher strength. However, the sparse fiber yarns in the fabrics can distort during their preparation or infiltration of the composite resulting in its lower modulus of elasticity.

The failure procedure of 2-D carbon/alumina composites with untreated carbon fibers can be described by Fig. 4. Arabic numerals represent the sequence of the procedure. Cracks initiate at the matrix between fabric layer (1) and propagate at the interface between fiber layer and matrix. When cracks meet fiber yarns perpendicular to the paper plane (weft yarns), they propagate through intrayarn pores (2). Later, cracks would meet the fiber yarns parallel to the paper plane (warp yarns) and continue to propagate at the interface between fiber yarns and matrix (3). Eventually, as the energy of cracks is large enough, it breaks the fiber yarns parallel to the paper plane (4) and composites fail. According to the observation, most of cracks in the composite with untreated carbon fibers locate at interlayer matrix, between weft and warp yarns, inside weft yarns, and on warp yarns. The distribution of cracks is uniform. On the other hand, cracks in the composite with treated carbon fibers are located at interlayer matrix and inside weft yarns near matrix-fiber interface. The distribution of cracks is nonuniform and dense around large pores. An overview of failure of 2-D carbon/alumina composites can be seen in Fig. 5. Some transverse microcracks can be found in the photographs. Interlayer delamination is the major failure mode of composites with treated fibers (Fig. 5(a)) because interlaminar shear strength of 2-D ceramic composites is intrinsically weak and cracks may propagate through matrix between layers instead of stronger interface between fibers and matrix. But local kinking is the major failure mode of composites with untreated fibers (Fig. 5(b)) because cracks could propagate at weaker interface under large compressive stresses and then local fibers would bend or kink without the constraint of matrix.

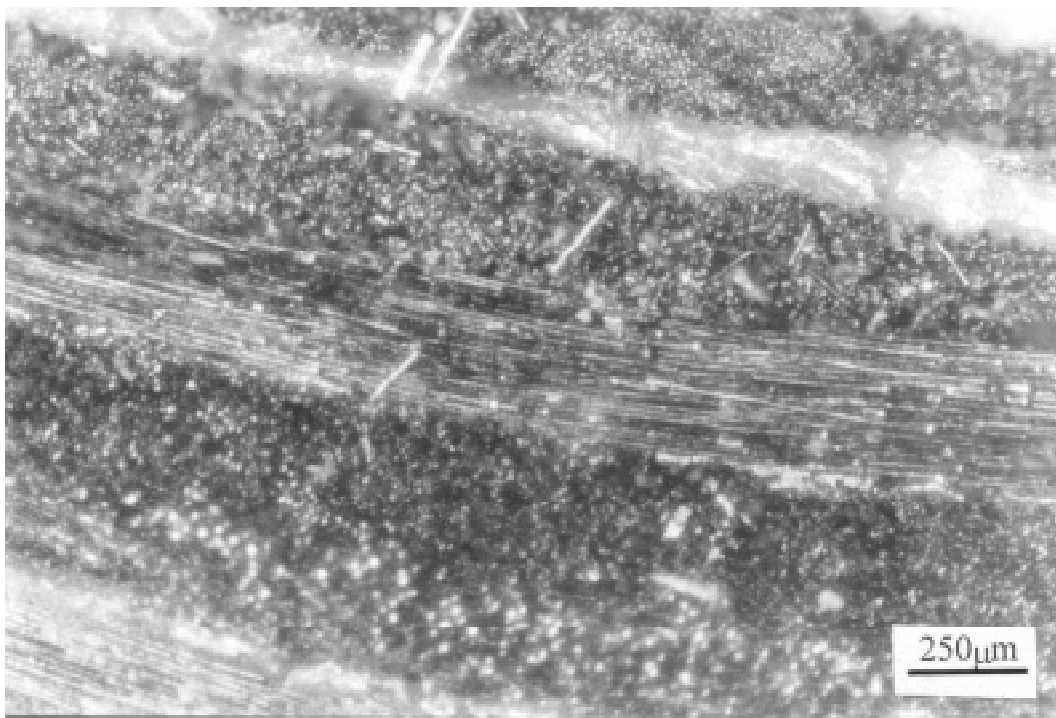


*Fig. 4: Failure procedure of 2-D carbon/alumina composites with untreated carbon fibers; Arabic numerals representing the sequence of the procedure*



*Fig. 5(a): Overview of failure of 2-D carbon/alumina composites showing first major failure mode delamination (fibers treated)*

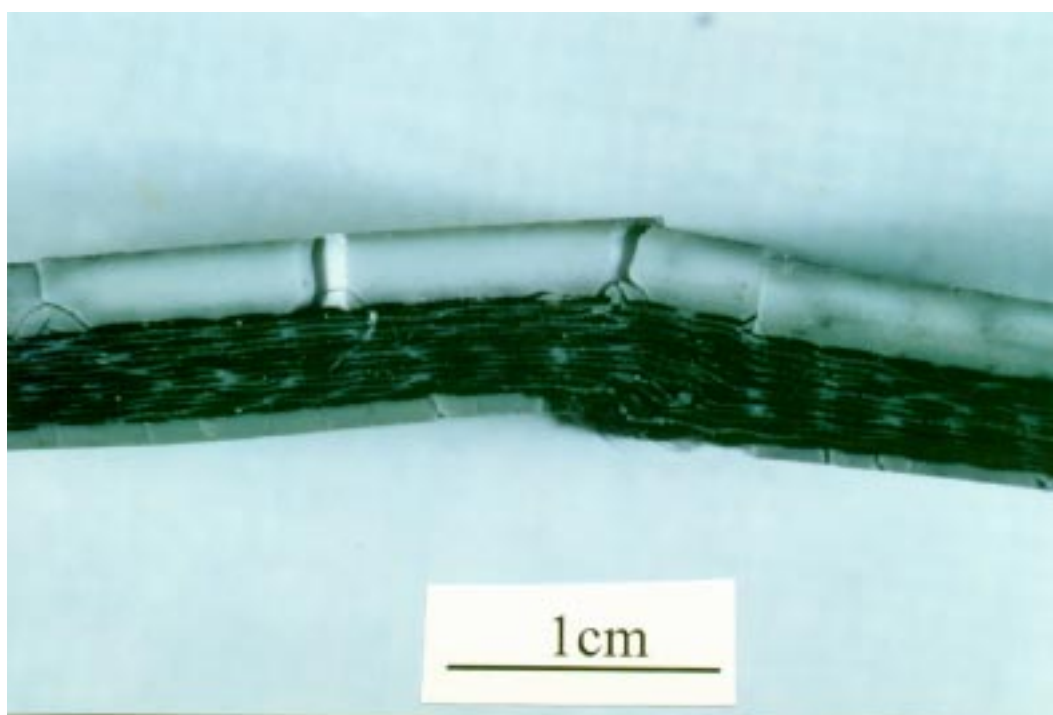


*Fig. 5(b): Overview of failure of 2-D carbon/alumina composites showing second major failure modes local kinking (fibers untreated)*

## CONCLUSIONS

2-D carbon/alumina composites were successfully fabricated by the pressure infiltration method. The fracture toughness increases but flexural strength decreases with increasing fiber volume fraction. Composites with untreated carbon fabrics have high fracture toughness of  $7.0 \text{ MPa}\cdot\text{m}^{1/2}$ , lower flexural strength of 30.4 MPa, and lower modulus of elasticity of 649.5 MPa. But composites with treated carbon fabrics by liquid oxidation reaction have lower fracture toughness of  $6.5 \text{ MPa}\cdot\text{m}^{1/2}$ , higher flexural strength of 51.7 MPa, and higher modulus of elasticity of 2081.4 MPa. Better bonding between treated fibers and matrix was found by scanning electron microscopic observation.

## ACKNOWLEDGMENTS

The authors are grateful to National Science Council, Taiwan R.O.C. for financial support under contracts : NSC 83-0405-E-035-017 and NSC 84-2216-E-035-027.

## REFERENCES

1. Chou, T. W. and Ko, F., *Textile Structure Composites*, Elsevier Science Publishers, New York, 1989.
2. Kuo, W. S. and Chou, T. W., "Elastic Response and Effect of Transverse Cracking in Woven Fabric Brittle Matrix Composites," *J. Am. Ceram. Soc.*, Vol. 78, No. 3, 1995, pp. 783-792.
3. Caputo, A. J., Stinton, D. P., Lowden, R. A. and Besmann, T. M., "Fiber Reinforced SiC Composites with Improved Mechanical Properties," *Am. Ceram. Soc. Bull.*, Vol. 66, No. 2, 1987, pp. 368-372.
4. Leparoux, M., Vandenbulcke, L., Goujard, S., Robin-Brosse, C. and Domergue, J. M., "Mechanical Behavior of 2D-SiC/BN/SiC Processed by ICVI," *Proceedings of The Tenth International Conference on Composite Materials*, Whistler, British Columbia, Canada, August 14-18, 1995, Vol. IV: Characterization and CMCs, Poursartip, A. and Street, K. N. Eds, pp. 633-640.
5. Droillard, C. and Lamon, J., "Fracture Toughness of 2-D Woven SiC/SiC CVI-Composites with Multilayered Interphases", *J. Am. Ceram. Soc.*, Vol. 79, No. 4, 1996, pp. 849-858.
6. Droillard, C., Voisard, P., Heibst, C. and Lamon, J., "Determination of Fracture Toughness in 2-D Woven SiC Matrix Composites Made by Chemical Vapor Infiltration", *J. Am. Ceram. Soc.*, Vol. 78, No. 5, 1995, pp. 1201-1211.
7. Shin, D. W. and Tanaka, H., "Low-Temperature Processing of Ceramic Woven Fabric/Ceramic Matrix Composites", *J. Am. Ceram. Soc.*, Vol. 77, No. 1, 1994, pp. 97-104 .

8. Nakano, K., Kamiya, A., Nishino, Y., Imura, T. and Chou, T. W., "Fabrication and Characterization of Three-Dimensional Carbon Fiber Reinforced Silicon Carbide and Silicon Nitride Composites," *J. Am. Ceram. Soc.*, Vol. 78, No. 10, 1995, pp. 2811-2814.
9. Liu, H. K. and Parvizi-Majidi, A., "The Effect of Solid Particles Addition in Sol-Gel Processing of Ceramic Matrix Composites," *Ceram. Eng. & Sci. Proc.*, Vol. 13, 1992, pp. 642-649 .
10. Klein, L. C., "Sol-Gel Processing of Silicates," *Ann. Rev. Mater. Sci.*, Vol. **15**, 1985, pp. 227-248 .
11. Chang, W. C., *Effects of Processing Parameters on the Properties of Carbon/Carbon Composites*, Ph.D. Dissertation, National Tsing-Hua University, Taiwan, 1995, pp. 5-6, 5-7.
12. Su, P. S., *The Material Technology of Nanometer Particles*, Fu-Han Publishing Inc., Taiwan, 1990.
13. Liu, H. K., Kuo, W. S. and Lin, B. H., "Pressure Infiltration of Sol-Gel Processed Short Fiber Ceramic Matrix Composites," in preparation , 1996.



# APPLICATION OF PRECERAMIC POLYMER FOR SHAPE FORMING OF MULTIPHASE SiC/Si<sub>3</sub>N<sub>4</sub> CERAMIC PARTS

Yongqing Li, Zhaohui Chen, Changrui Zhang, Haifeng Cheng, Ancheng Zhou and  
Xiaoheng Bao

*Department of Material Engineering and Applied Chemistry, National University of Defence  
Technology, Changsha, Hunan, PRC, 410073*

**SUMMARY:** The purpose of the present work is to fabricate shape-complex SiC/Si<sub>3</sub>N<sub>4</sub> multiphase ceramic parts (such as blade) using preceramic polymer (Polycarbosilane PCS) as shape-forming binders. SiC/Si<sub>3</sub>N<sub>4</sub> multiphase ceramics are formed by in-situ pyrolysis and sintering from PCS/Si<sub>3</sub>N<sub>4</sub> green body. Divinylbenzene(DVB) is used as active diluent agent to prepare slurry of PCS/DVB/Si<sub>3</sub>N<sub>4</sub> at room temperature, and as cross-linking agent to make solid green body of PCS/DVB/Si<sub>3</sub>N<sub>4</sub>. It is necessary to control precisely rate of pyrolysis temperature of 250-450 °C under 0.3 °C/min in order to obtain a pyrolysis with body of deformation-free and crack-free. Before sintering, decreasing the carbon-rich content in the pyrolysis body, the density of sintered body can be enhanced.

**KEYWORDS:** precursor, SiC/Si<sub>3</sub>N<sub>4</sub> ceramic, shaping, pyrolysis, sintering

## INTRODUCTION

SiC/Si<sub>3</sub>N<sub>4</sub> multiphase ceramic is one of the most promising candidate materials for high temperature structural components in heat engines for its attractive characteristics such as low density and excellent resistance to corrosion, wear, oxidation and heat-shocking at high temperature. Once it was used in heat engine, fuel would be saved, the working temperature, efficiency and power of the engine would be elevated. It may be the bottle-neck to prepare such engine parts as turbine blade and rotor to realize the practicability of a ceramic engine. The shaping technologies in common use in nowadays (e.g. injection and casting) are not much promising because of their shortcomings as high cost, long cycle, poor property of product and so on. The authors of this paper prepared ceramic blades using organosilicon precursor as shaping binder, and discussed the effects of processing parameters on the structure and performance of the pyrolyzed and sintered blades.

Preceramic polymer such as polycarbosilane (PCS) can be used as binder to fabricate ceramic part [1-5]. Unlike conventional binders (PE,PP etc.) that are totally burned out, during pyrolysis, the preceramic polymer binder can be chemically transformed into a continuous ceramic phase. For example, while PCS is used as a binder of Si<sub>3</sub>N<sub>4</sub> powder, PCS can be changed into nanophase SiC at over 1000 °C, and a multiphase ceramic can be in-situ formed in the final part.

## EXPERIMENTAL PROCEDURE

Polycarbosilane (PCS), as a preceramic polymer (dark black brittle melt point 125-135 °C) was dissolved into divinylbenzene (DVB) which acted as active dilute agent, to form viscous liquid for binder solution at room temperature.  $\alpha$ - $\text{Si}_3\text{N}_4$  powder and Sintering aids ( $\text{Al}_2\text{O}_3/\text{Y}_2\text{O}_3$ ) were incorporated into PCS/DVB solution by ultrasonic dispersion to form a slurry of PCS/DVB/ $\text{Si}_3\text{N}_4/\text{Al}_2\text{O}_3/\text{Y}_2\text{O}_3$ , then the slurry was cast into a mold. Heat treatment for curing of slurry was 130 °C, 7 hours at 1.6 MPa nitrogen pressure for preventing DVB from evaporation. First, Green body of ceramic parts was pyrolysed in nitrogen flow at 0.3~1 C/min from room temperature to 1000 °C, held for 1 hour at 1000 °C; Then, the pyrolysed body was cooled to room temperature in the furnace. Second, the pyrolyzed body was heated in nitrogen flow at 20 °C/min from room temperature to 1600 °C, held 1 hour at 1600 °C to crystalline amorphous SiC, and to react  $\text{Si}_3\text{N}_4$  with free carbon derived from pyrolysed PCS, and then sintered at 10 C/min from 1600 °C to 1930 °C, held for 120 minutes at 1930 °C and 1.0 MPa nitrogen pressure.

Density of specimens was determined by Archimedes immersion technique. Phase identification of sintered body was performed by X-ray diffraction using CuK $\alpha$ -radiation. Microstructure of pyrolysed body and sintered body was examined by scan electron microscopy (SEM). Fracture strength was evaluated using three-point bending over a 20 mm span. The ratio span to height specimens is 5.

## RESULT AND DISCUSSION

### Preparation of Slurry and Preforms

The slurry was composed of  $\text{Si}_3\text{N}_4$  powder, PCS, DVB, sintering aids and shaping aids (crosslinking initiator and coupling agent). The role of DVB in the slurry was: 1) a diluent to reduce the viscosity of the slurry, and 2) a solidifying agent to react with Si-H bonds in PCS (initiated by dicumylphene, pop above 120 °C) and self-crosslink due to the vinyl groups in its molecular. The effects of the concentration of DVB on the property of the crosslinked preform were listed in Table 1. According to these results, the ratio of PCS to DVB should be 1.5:1. Other experimental data proved that middle-molecular-weight PCS was appropriate and coupling agent (e.g. titanate serials) should added into the slurry before ball milling to improve the disconcentration of ceramic particles in precursor solution. For the same aim, further dispersing treatment by means of super sonic should be adopted.

*Table 1: Effects of PCS/DVB ratio on the facade of pyrolysed parts*

PCS/DVB	2:1	1.5:1	1:1
outward appearance of pyrolysed parts	metamorphosed obviously	without distortion no visible defects	cracked evidently

Different compositions of binder solution were used to prepare crosslinked preform and the crosslinking degrees of each sample were compared in Table 2. The data showed that middlemolecular-weight PCS was seemly and the incorporation of about 2wt.% of pop as initiator would promote the crosslinking reaction. IR analysis of the slurry, the crosslinked preform and the precursor saluted in xylene after extracting the preform revealed that most of

Si-H bonds did not crosslink as we expected. So, the microstructure of the crosslinked product was cured DVB net with PCS chains running through it.

Table 2: Crosslinking degrees of preforms with different binder compositions

	1	2	3	4	5
LPCS	100		100		
MPCS		100		100	
DVB	50	50	50	50	100
DCP		3		3	2
Crosslinking degree (%)	31.4	42.4	42.6	60.8	97

NOTE: All preforms were cured at 180 C in 1.0-2.0MPa N<sub>2</sub> for 8h. The crosslinking degrees were determined by measuring the maintained masses of the preforms after immersing them into xylene at room temperature for 24hrs and then drying them at 80 C in vacuum for 2hrs. MPCS=middle molecular weight PCS, LPCS=low molecular weight PCS

As discussed above, DCP was effective to initiate the self-polymerization of DVB and partial crosslinking of Si-H with vinyl group. TG analysis showed that DCP began decomposition at about 120 °C. Besides, the boiling point of DVB is 138 °C. So, the crosslinking reaction should be performed at 120-138 °C and nitrogen pressure (1.0-2.0 MPa) should be adopted to avoid the volatilisation of DVB and the oxidation of PCS.

### Pyrolyzation of the Preforms

TG analysis (10 °C/min, Ar) of shaped preforms revealed that most of the loss occurred below 550 °C, especially from 250 °C to 550 °C (see Figure 1). The said weight loss was due to the volatilisation of low-molecular-weight oligomer and pyrolyzation of the crosslinked precursor. it was important to control the heating rate this temperature scale to reduce the amount of the volatiled and pyrolysed gas and the possibility of deforming, cracking and bulging. Heating rates of 0.3, 0.5 and 1.0 °C/min were introduced to optimize the heating rate. Results in Table 3 showed that defect-free pyrolyzed parts could be obtained at a heating rate lower than 0.3°C/min.

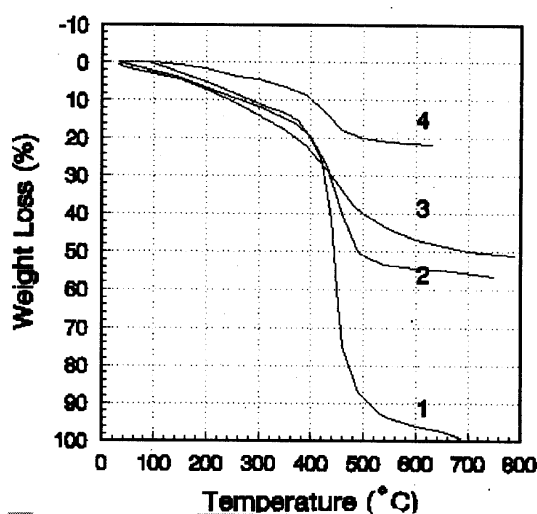


Fig 1: TG curves of crosslinked samples

Note: 1: DVB/DCP 2: LPCS/DVB/DCP 3: MPCS/DVB/DCP. 4. LPCS/DVB/DCP/Si<sub>3</sub>N<sub>4</sub>

Table 3: The property of ceramic parts pyrolysed at different heating rates

heating rate (°C/min)	property of pyrolyzed parts
1	heavily distorted and cracked
0.5	slightly distorted, cracked at large cross section
0.3	no deformation, crack-free

TG curves in Figure 1 also showed that the weight loss above 800 °C was negligible. This result implied that the inorganization of the precursor was almost complete before 800 °C. The pyrolyzed ceramic bars that were further treated up to 1500 °C (holding for 120 min) showed very slight shrinkage and weight loss (about 2 wt.%). Their bending strength ( $60 \pm 10$  MPa) were almost the same as that before the treatment. So it was necessary to elevate the sintering temperature to improve the strength of the parts.

As concluded above, the microstructure of the cured preceramic binder was a inter-joined 3dimensioned network with PCS chains running through crosslinked DVB moleculars, and in the network there was about 12-18 wt.% of uncured PCS that would melt at elevated temperature to cause distortion of the preform. This kind of deformation could be reduced by extracting 8-10 wt.% of the soluble PCS out of the preform with xylene as solvent, without distorting the preform during extraction. The extracted preforms were heated at a faster temperature rate, and defect-free pyrolyzed parts were obtained with highly reduced linear shrinkage. The reasons for such a improvement might be that absence of low molecular weight PCS decreased the volatilization during pyrolyzation and gangways for pyrolyzed gas were left after extraction.

### Sintering of Pyrolyzed Parts

Pyrolysed body has too low density, much more porosity and poor strength to use. It is desired to sinter for dense SiC/Si<sub>3</sub>N<sub>4</sub> ceramic parts. In the sintering process, free carbon derived from pyrolysis of PCS/DVB will react with sintering aids (Al<sub>2</sub>O<sub>3</sub>, Y<sub>2</sub>O<sub>3</sub>, La<sub>2</sub>O<sub>3</sub>, etc.) to decrease the amount of liquid phase for sintering, and react with SiO<sub>2</sub> on the surface of Si<sub>3</sub>N<sub>4</sub> powder to increase the content of SiC. Those are retarded to densely sinter. Thus decarbonation is important prior to sintering.

Table 4: Weight loss and density of Sintered body by deferent pretreatment

specimen	pretreatment	density of pyrolysis body (g/cm <sup>3</sup> )	weight loss of sintering (%)	density of sintered body (g/cm <sup>3</sup> )	relative density (%)	defect
pyrolysis body		2.25	21.1	3.236	92.2	no
extraction and pyrolysis body		1.79	13.5	3.274	93.6	no
pyrolysis body	oxidation	2.20	15.7	3.351	95.8	deform and crack
pyrolysis body	NH <sub>3</sub>	2.18	19.5	3.328	93.6	no
extraction and pyrolysis body	NH <sub>3</sub>	1.70	11.4	3.371	96.4	no

Table 4 shows weight loss and density of Sintered body by different pretreatment before sintering. The result indicates that deformation and crack had been found in the sintered specimen which the removal of carbon-rich by oxidating was at 700 °C for 120 minutes, but no defect had been found in the sintered specimens when oxidation condition changed to 500 °C for 180 minutes. That is because oxygen reacts not only with carbon-rich, but also with amorphous SiC derived from PCS. Large amount of SiO<sub>2</sub> formed on the surface of pore, in the sintering process, liquid-phase sintering aid was so heterogeneous distributing that nonhomogeneously shrinkage of sintering resulted deformation and crack. Otherwise, gradual change of carbon-rich content from the surface to the middle will influence the well distributed of composition and microstructure of sintering body. The improvement of relative density for sintered body which had been treated with NH<sub>3</sub> is not pronounced due to low efficient of removal of carbon-rich. Density of sintered body which had been treated by extraction of PCS and removal of carbon-rich in NH<sub>3</sub> atmosphere is high due to low content of SiC, carbon-rich derived from PCS/DVB. Thus the main factors which influenced densely sintering are the content of PCS/DVB in the green body, SiC and carbon-rich in as-fired body

Effect of sintering temperature on density of the sintered body is shown as Table 5. Increasing sintering temperature, density of sintered body can be enhanced. Increasing size of blade, density of sintered body decreased. A multiphase SiC/Si<sub>3</sub>N<sub>4</sub> dense ceramic part, with a relative density of 93 % and no defect (such as deform, crack etc.), is obtained at 1930 °C for 120 minute.

Table 5: Effect of sintering temperature on the density of sintered body

	1850 °C/120 min.		1870 °C/120 min.		1900 °C/120 min.	
	density (g/cm <sup>3</sup> )	relative density (%)	density (g/cm <sup>3</sup> )	relative density (%)	density (g/cm <sup>3</sup> )	relative density (%)
large blade	2.87	82	3.02	86	3.15	90
small blade	3.18	91	3.27	93.5	3.31	94.7

### Microstructure and Strength of Sintered Body

Figure 2 shows X-ray diffraction patterns of sintered specimen of PCS/DVB/Si<sub>3</sub>N<sub>4</sub>. This result indicates that β-SiC and β-Si<sub>3</sub>N<sub>4</sub> grain phase was in-situ formed in the final sample. β-SiC come from crystallization of amorphous silicon carbide derived from PCS. β-Si<sub>3</sub>N<sub>4</sub> come from transformation of α-Si<sub>3</sub>N<sub>4</sub>.



Fig. 3: Microstructure of the etched and fracture surface of sintered parts

The etched and fracture surface of  $\text{SiC}/\text{Si}_3\text{N}_4$  multiphase ceramic is shown as Figure 3. The fracture mode is predominantly intergranular debonding.  $\beta\text{-Si}_3\text{N}_4$  grain shape is pillar-like.  $\beta\text{-SiC}$  is aggregated submicron particle. Mechanical property of sintered body (Table 6) is not high. The research on the improvement of mechanical property is under process.

Table 6: Mechanical property of  $\text{SiC}/\text{Si}_3\text{N}_4$  multiphase ceramic derived from PCS/DVB/ $\text{Si}_3\text{N}_4$

density ( $\text{g}/\text{cm}^3$ )	relative density (%)	$\sigma_b$ (R.T.) (MPa)	$K_{IC}$ ( $\text{MPa} \cdot \text{m}^{1/2}$ )
3.20	91	403	7.530

## CONCLUSIONS

1. Low viscosity slurry could be obtained using MPCS as precursor, DVB as diluent and crosslinking agent and titanate as coupling agent.
2. The crosslinking reaction of PCS/DVB/DCP was performed at about  $120^\circ\text{C}$  in  $\text{N}_2$  (1.0-2.0Mpa) for 8 hours.
3. Defect-free pyrolyzed parts could be prepared as heating rate was lower than  $0.3^\circ\text{C}/\text{min}$ ; it was effective to improve the property of pyrolyzed parts by extracting low molecular weight PCS out of the green body prior to pyrolyzation.
4. Extraction before pyrolyzation and using  $\text{NH}_3$  as sintering atmosphere would decrease the content of free carbon in sintering product, and this would increase the density of the sintered parts.

## REFERENCES

1. Mutsuddy, Beebhas C. *Ceram. Int.* 1987, 13(1), 41-53
2. Seyferth, Dietmar; Schwark, Joanne M.; Yu, Yuan Fu, *PCT Int. Appl. Wo 8801260*, (1988)
3. Moehle, William E.; Rogers, John J.; Semen, John *U.S. US 4,942,145*, (1990)
4. Zhang, T.; Evans, J. R.G. *J.Eur.Ceram.Soc.* 1991, 7(6), 405-12
5. Semen, John; Loop, John G. *Ceram. Eng. Sci.Proc.* 1991, Pt. 2). 1967-80

# KEY COMPONENTS OF HIGH TEMPERATURE STABLE HIGH OXIDATION RESISTANT CERAMIC MATRIX COMPOSITES OF SiC/SiC TYPE WORKING OUT AND TECHNOLOGICAL WAYS OF THEIR MAKING

A. M. Tsirlin<sup>1</sup>, V. G. Gerlivanov<sup>1</sup>, N. A. Popova<sup>1</sup>, Yu E. Pronin<sup>1</sup>,  
E. K. Florina<sup>1</sup> and S. P. Gubin<sup>2</sup>

<sup>1</sup> *State Scientific Center of Russian Federation State Scientific-Research Institute of Chemistry and Technology Organoelement Compounds, 38 Shosse Entusiastov, 111123 Moscow, Russia.*

<sup>2</sup> *Institute General and Neorganic Chemistry of Russian Academy of Science, 31 Lenin Prospect, 117071 Moscow, Russia.*

**SUMMARY:** In a short form the grounding of the task priority is given. Necessity of complex key components of ceramic matrix composites (CMC): polymer precursors, fibers and interface coatings - working out is the important line in this area. Some positive new results in the chemistry and technology of high temperature stable high oxidation resistant CMC for civil aviation and automotive industry have been received. The easy production process of oxygenless polycarbosilane has been developed, high pressure and oxygenated initiators were not used. A new method to synthesise oxygenless polymetallo-carbosilanes (PMCS) to stabilize ceramic fine structure has been proposed and preliminary checked. New PMCS having metals in cluster form (nano-particles) without any oxygen links between metal and silicon atoms are called cluster polymetallo-carbosilanes (CIPMCS). They have improved structure and are cheaper in making also. Preliminary research stages in oxygenless polymer curing with unsaturated organosilicon compounds and complex interface molybdenum disilicide - silicon carbide coatings have been carrying out. They have made possible to get specimen fiber with - 0,3%O<sub>2</sub> and 0,1-5% of Ti or Zr and have shown some perspectives in more economical technology and better oxidation resistance.

**KEYWORDS:** oxygenless ceramic polymer precursors, cluster polymetallo-carbosilanes, unsaturated curing organosilicons, tetravinylsilane, molybdenum disilicide, interface coating

## INTRODUCTION

A high temperature stable high oxidation resistant CMC for a long work at 1500 – 1700°C in civil aviation and automotive engines is a subject of priority working out nowadays [1]. From working temperature 1100-1200 (now maximum) to 1500-1700°C transition make it possible to decrease fuel consumption and increase flight distant by 25% and to duplicate specific thrust. Cooling systems in some cases become unnecessary and in Diesel engine as well (adiabatic cycle) and so on [2,3]. One of good potential variants is CMC of SiC/SiC type with coreless SiC fiber. Unfortunately all components of this material now known: polymer

precursors, commercial (Nicalon and Tyranno) and pilot (radiation or unsaturated organic vapour curing) grade fibers, matrix compositions and structures, interface coatings - can not support work for a long time at temperatures more than 1100°C and too expensive. It is necessary to delete oxygen in all the components, to stabilize fine ceramic structure at high working temperatures, to work out very high oxidation resistant complex interface coating. It is very important to depreciate the production of components and the material on the whole. This aspects are the subjects of many publications and have been intensely discussed at the last international conferences (ICCM-9, ICCM-10, HT-CVC-1, HT-CMC-II, MICC-93) in 1993-96. There is a wide range of difficult problems to overcome. The authors think especially important to work out all key components of this material in the frame of one complex program as for example it is not possible to develop oxygen resistant interface coating or rational stabilizing methods without well finished oxygenless fiber. This is a base for their research program and this paper.

## MAIN LINES OF RESEARCH AND RESULTS

### Polymer Precursors

PCS was first synthesized on the 70-th [4] by pyrolysis and thermal rearranging of polydimethyl silane (PDMS) in autoclave in inert environment (10 MPa, 470°C). This method is too expensive for industrial production. A lot of attempts to avoid high pressure and PDMS using through the help of initiators and other organosilicon compounds have not given positive results as far as PCS quality is concerned. The oxygen is introduced with initiators and stoichiometry and structure composition of PCS is distorted (Fig.1).

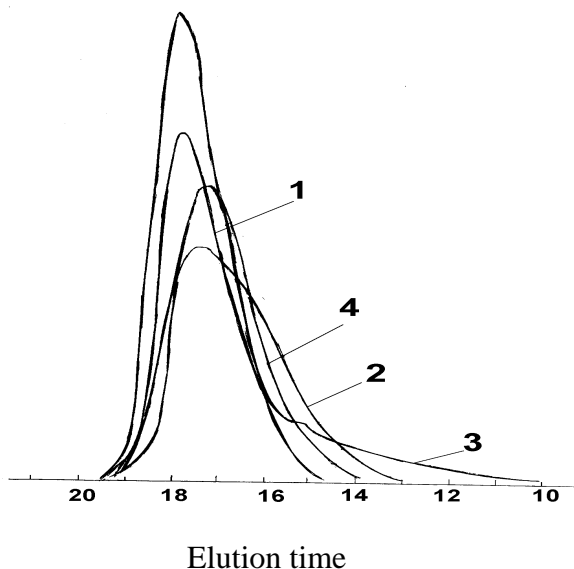


*Fig.1. MWD of synthesized PCS  
1-high pressure, 2-low pressure, boron  
initiated, 3- low pressure, titanium initiated,  
4- low pressure without initiators*

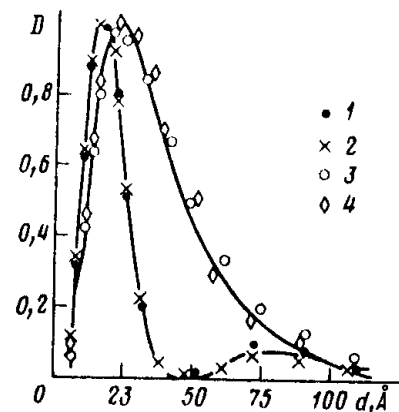


*Fig.2. Iron cluster particle distribution by  
size in high pressure polyethylene.  
Content of Fe,%mas. 1-0,7; 2-1,0;  
3-5,0;4-7,0 (model system)*

It is the studying of PDMS and PCS syntheses, chemical composition and molecular structure of initial and final products that have given the optimal regime in the temperature-pressure-



time-composition system. This regime makes it possible not to use oxygen containing initiators and any exotic initial products and to have as good PCS as autoclave one at handy temperature, pressure and process duration (Table 1). A considerable depreciation of PCS is reached which as is known becomes then 3- fold much in fibre and (4-5)- fold much in the composite production.

Table 1: Polymer precursors characteristics

Characteristics	[HSiC <sub>3</sub> ]/ [SiC <sub>4</sub> ]	Content, % mass.			MWD		
		O <sub>2</sub>	H at Si	Init.(metal)	M <sub>n</sub>	M <sub>w</sub>	M <sub>z</sub>
PCS autoclav.	0,9-0,95	0,3 - 0,8	0,65 - 0,75	–	830	1310	2290
PBCS	0,8-0,85	1,0 - 3,0	0,55 - 0,65	0,5 - 1,0	1050	3010	9100
PTiCS	0,2-0,3	4,0 - 6,0	0,30 - 0,60	≤ 5,0	890	7300	250000
PCS(without in.)	0,9-0,93	0,3 - 0,8	0,60 - 0,70	–	1060	2070	4830
CIPMCS	0,95-1,1	< 0,5	0,92 - 0,98	0,5 - 5,0	1220	1830	3580

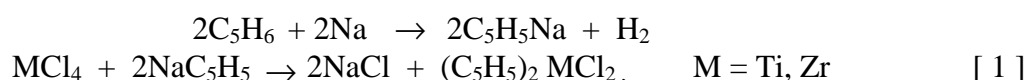
### Ceramic Phase Structure Stabilizers, Polymetallo-carbosilanes

As it is generally known effective stabilizers of fine ceramic structure are hetero-atoms of many elements oxygen and nitrogen as well. By-effects such as fusibility, thermal stability, sintering ability and so on changing are positive using high melting metals (Ti, Zr, Hf, B, Mo and some other). The problem is working out of a method to introduce the metal into the polymer providing with the homogeneous distribution just on the synthesis stage and disusing of oxygen. The first demand was only fulfilled in the practical method of metal-stabilizers introducing through tetraalkoxi-compounds of metals. The «Tyranno» - fiber of Ube Industries (Japan) was made with tetraalkoxititan. But ceramic phase in this fiber is of Si-C-O-Ti type as Si-O-Ti link (oxygen bridge) takes place. More over active Si-H - links valuable for curing are spent in this reaction. So it is necessary to work out essential new way of metal introducing in the PCS or new method of PMCS synthesis.

The last task is carrying out by the authors on the base of an experience of linear monophase metallo-polymers making: polyethylene, polypropylene, polytetrafluorethylene [5]. It is quite different from traditional methods to introduce metal particles of 5-100 μm in size into polymer to form homogenized and aggregatively stable but two-phase systems. Two-phase metallo-polymers do not have so high physical and mechanical properties as initial polymer because their ordering (crystallinity) become lower. They cannot be used for spinning fiber also.

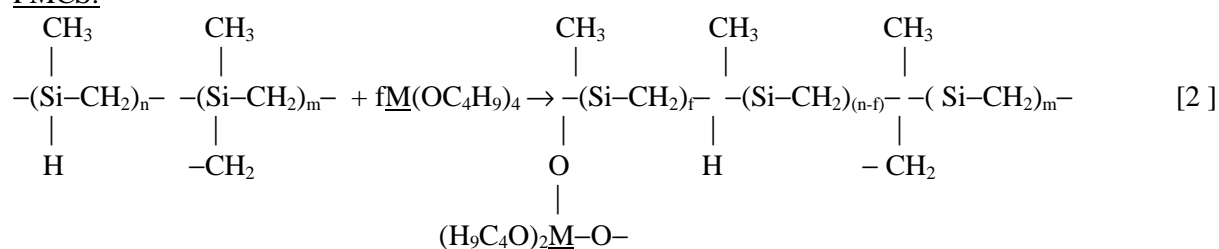
The new method introduce the metals in cluster form into micro voids which is natural in every polymer. These voids are connected with polymer molecules packing and located between crystalline and amorphous parts of micro volumes. Clusters (nano-particles) of metals are formed in situ as a result of high velocity thermodestruction of organometallic compound solutions during their input in polymer solutions or melts [6]. Carbonyls, acetates, phormiates and some other classes of metal compounds are applicable. Fig. 2 gives a notion of the method possibility. It shows Fe particles size distribution (small angle scattering of X-ray (XSAS)) in the high pressure polyethylene at different general metal concentrations. In the most interesting for ceramic stabilization 1-3% Fe particle sizes is in narrow interval 5-50 Å. Some testing methods have shown a separate metal phase is absent at these concentrations and active interaction of metal and polymer is observed.

As PMCS are vastly different from linear polymers in structure and thermal properties and high melting metals are used to stabilize them so it was necessary to use other initial compounds or synthesize them. Also the technological method of thermodestruction and the stage of synthesis of cluster PMCS (CIPMCS) to introduce organometallic compound solution is different for each of them. This compound should have full solubility in synthesis solvent and be fast and clearly decomposed to metal and volatile ligand. The introduction of metals on the intermediate stage of syntheses gives the most effective results because they take part in chemical processes of regrouping and polycondensation. The cyclopentadienyl complexes and carbonyls of metals seem the best to fulfil these demands in the case of CIPMCS. The Ti and Zr complexes syntheses were made as follows. On the first stage sodiumcyclopentadienyl was synthesized from sodium suspension and cyclopentadien in toluene. On the second stage it was transformed into dicyclopentadienylchlorides of Ti and Zr by reaction with metalochlorides in toluene or benzene (inert atmosphere):

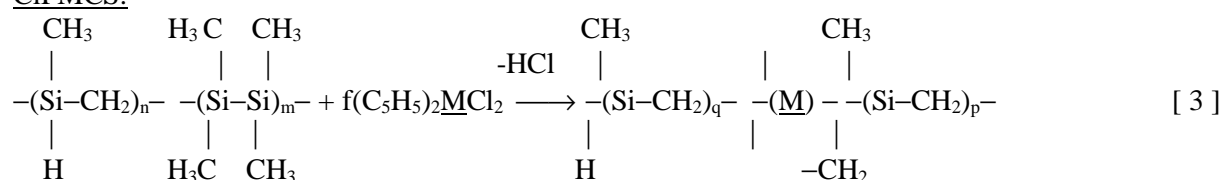


PMCS by the traditional method and CIPMCS through organometallic complexes syntheses can be illustrated by following general schemes:

PMCS:



CIPMCS:



CIPMCS syntheses were carried at 250-280 °C and higher dicyclopentadienylchlorides being introduced into fused oligocarbosilanes (dimetildichlorsilane pyrolysis products) mixture at the period when about 10% of Si yet stayed in a Si-Si- fragments. After metals introduction the process speeds up but without any negative by-effect. Si-Si-fragments fully disappear, no insoluble or high fusible products are formed, only high vacuum topping is necessary. To study CIPMCS by nuclear  $\gamma$ -resonance method the model FePMCS was synthesized via ferrumpentacarbonyl with the same method of synthesis.

The cluster polymers average molecular mass were 1200-2500 (gel-penetration chromatography), base skeleton (IR-spectroscopy) like the usual PCS formed by  $\equiv Si-C-Si \equiv$  (1050 and 1350  $cm^{-1}$ ) links with hydride  $\equiv SiH$  (2100  $cm^{-1}$ ) and methyl  $\equiv Si-CH_3$  (1250 and 1400  $cm^{-1}$ ) side substituents at Si-atoms. NMR ( $^{29}Si$ )-spectroscopy showed high regularity in CIPMCS structure: groups  $H\text{SiC}_3/\text{SiC}_4$  relationship ( $\delta = -16$  m.f. and 0 m.f.) is about unity, oxygen containing fragments such as  $[SiSi(C_2)O]$  and  $[OSi(C_2)O]$  ( $\delta = -6,5$  and  $-22$  m.f.) were not discovered. Metals are present in the polymers in the form of cluster particles not

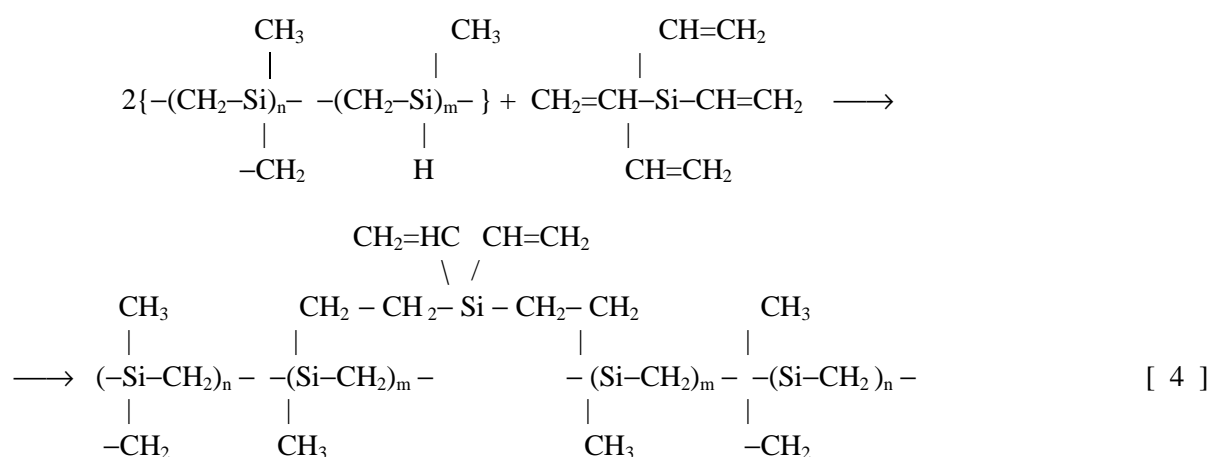
more than 10-50Å in size in the concentration of 0,1-10% (different initial loading) (XSAS, X-ray fluorescence). Preliminary data show that till concentration of 3% metal does not prevent stable spinning of fiber from fused polymer at 250-280 °C. Ceramic yield is up to 75%.

As it can be seen in Table 1 the new (cluster) method of PMCS synthesis provides the same metal introduction without using deficit Si-H - links and more regular polymer structure. It is possible to suppose the evenly dispersed through the polymer clusters act as active centre of polymer molecular embranchment without Si-H-links using. This differs from the method [7], according to which a treating of hidrydesilanes with a catalytic quantity of Ti and Zr complex compounds lead to crosslinking by Si-H links interaction. Certainly the mechanism of cluster (nano-particles) action in the polymer matrix of the PCS-type is a question of series studying.

### Oxygenless Curing of Polycarbosilanes

Several methods of this process implementation are known. The most practical now with λ- and e- rays treating [8, 9] are difficult (i.e. expensive ) in technology. It is necessary to use unique equipment, flame- and explosion-proof systems, cumbersome schemes for preparing and recovering organic containing gas mixtures. Technological difficulties are not small with the ammonia atmosphere using also [10]. The most valuable from the technological view point would be methods of curing in the atmosphere of pure nitrogen. These methods are based as a rule on unsaturated organic or organoelement compounds introducing into PCS. The heating to the temperature which is higher then the synthesis one cures PCS with this active unsaturated links help [11]. The difficulties are in provision of nearly ideal (molecular) dispersion of additives, their action in rather near temperature interval with high selectivity. Nevertheless this way maybe would be the most effective.

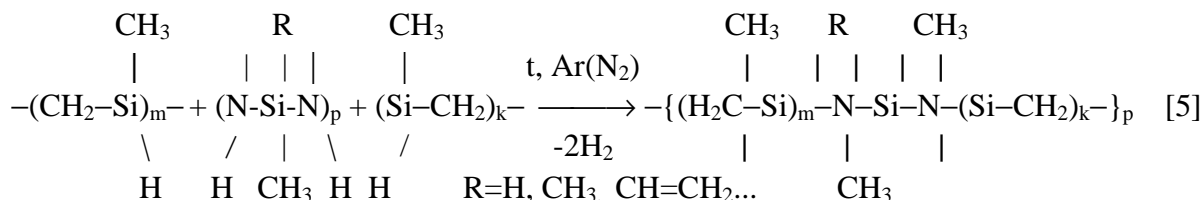
So as the first laboratory results showed that the using of monosilanes with vinyl and allyl substituents such as tetravinyl-, tetraallyl-, trivinylmetyl-, trivinylfenyl- and other monosilanes is very attractive. Advantage and peculiarity on the tetravinylsilane example can be seen from the following scheme:



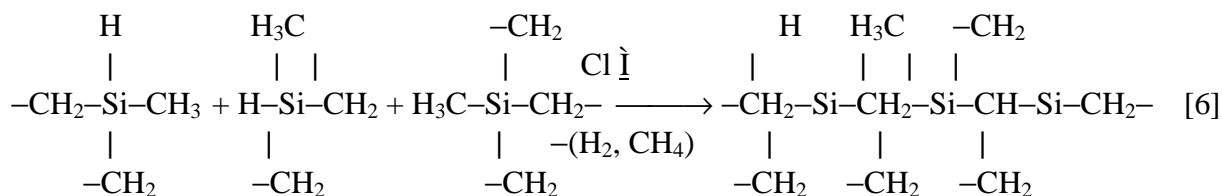
Unlike other methods there is no gas evolution in this one. It is very important to have dense and regular structure of the ceramic product. Then as reactivity of vinyl groups in the same molecule is different they can react with PCS for example in two stages which is useful for large items. It is handy to cure these items preliminary at not top temperature for some

strengthening in the forming equipment. Then it become possible to remove them into high temperature furnaces to finish the curing and carrying out the heat treating.

An analogous method uses an active amino groups by introducing into PCS some polysilazanes [11] but it is necessary to optimize a residual nitrogen:



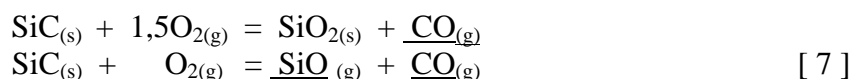
One more way of oxygenless curing is now in authors' working out. That is to use cluster (nano-particles) of metals not only for structure stabilizing but for curing as well. They possess a very great surface energy and are possible to tear not only Si-H, but Si-C and C-H links also and to initiate regroup and polycondensation processes at additional thermal treating:



A lot of complicated variants of chemical interaction arise of course, so very fine control of physical and chemical parameters is necessary.

### CMC Interface Coatings

This CMC component provides high strength and toughness and long time work at high temperatures in aggressive environment. Its polyfunctionality is illustrated on Fig.3. Massive SiC matrix in the air defends itself by a fine selfcuring film of SiO<sub>2</sub>. But it is not enough to defend CMC as a whole. On mechanical force influence microcracks arise in the matrix. They give way for the oxygen into the material right to fiber surface but thin fiber is not possible with the oxide film to defend. More over they move across the fibber and can cut them adhesion between fiber and matrix being strong enough. A fast and even catastrophic brittle destruction of material will follow at rather small load. So it is necessary to have as a minimum two layers on the fiber surface: dense high oxidation resistant (protective) and friable or weak adhesive contributing to local defoliation at crack front-fiber surface point («rheological»). The system fiber-coating-matrix components do not as a rule compatible in thermal expansion coefficients that demands to add in the coating one or more buffer (compensating) layers. The scheme of Fig. 3 shows that there is no protection from initial oxygen in the fiber. No good makes the initial oxygen in the matrix also as its interaction with SiC lead to gas evolution that is harmful for ceramic dense structure:



Attempts to use for high oxidation resistant CMC coatings C, BN, their combinations with TiC and SiC were not successful [12-14 et al.]. High thermostable oxides -  $\text{Al}_2\text{O}_3$ ,  $\text{Zr}_2\text{O}_3$ - do not hold stable dense structure for a long time at cycle load especially. Practically all of high temperature stable carbides, borides, nitrides, aluminides and silicides are not thermodynamically compatible with SiC and long time oxidation resistant enough. This is why the authors selected as a main research and technology way to use molybdenum disilicide ( $\text{MoSi}_2$ ) for protective layers and polymer precursor SiC - for friable «rheological» layers.

$\text{MoSi}_2$  characteristics are rather well known [15]. The highest oxidation resistance and thermodynamic and thermal expansion compatibility with SiC among refractory compounds, 2000 °C melting point, complementary positive results with W, Ge, Re et al. silicides alloying. Besides it is cheaper and more handy for machining than SiC and  $\text{Si}_3\text{N}_4$ . Its limitations are more density, lower creep characteristic, fast oxidation process at about 500 °C if pour and microcracks are present. These limitations are difficult to overcome in the matrix and not so difficult in the coating case of using the material. «Rheological» layer for CMC SiC/SiC of SiC or  $\text{Si}_3\text{N}_4$  is obviously reasonable. Polymer technology provides flexible process control with type and composition of polymer precursors, degree of dilution, number of treating cycles. This in no case excludes the CVD and CVI methods using at some technological stages.

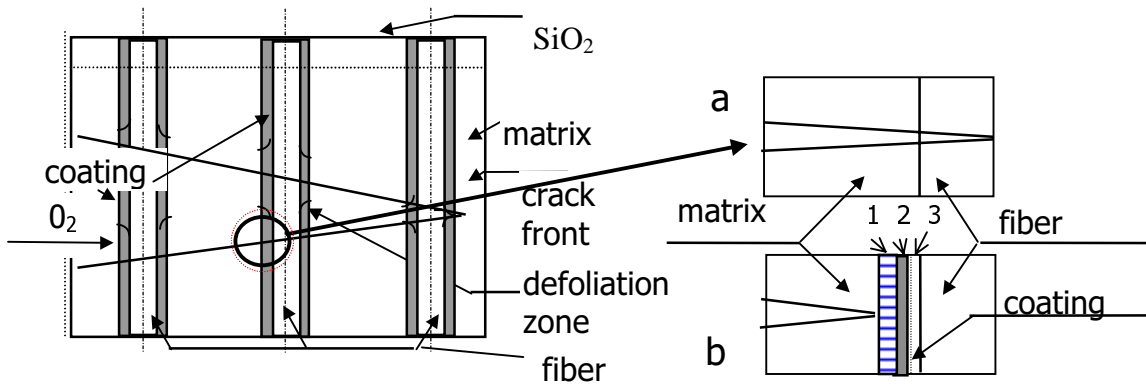


Fig. 3: CMC structure and cracks' spreading scheme  
«rheological» layer, 2- protective layer, 3- buffer layer

The experiments were carried out in two types furnaces: with the direct and indirect heating and with the cameras of cold and hot walls accordingly (Fig. 4). Metering and heating means provided 2500 and 1200 °C accordingly both from about  $1 \cdot 10^5$  to 1 Pa. Gas mixture preparing system gave possibility to have mixtures of organometallic compounds and metal chlorides with the hydrogen, nitrogen and inert gases of 0,01 - 30% in composition.

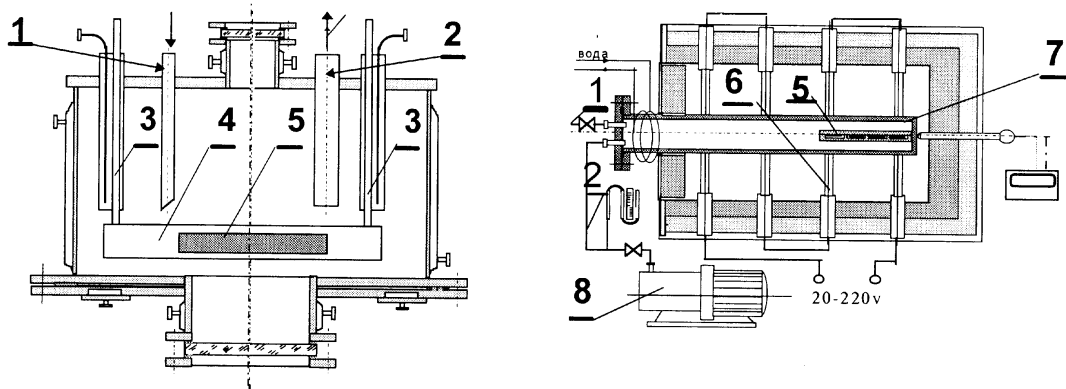


Fig. 4: Furnace scheme for interface coatings applying  
 1-gas inlet, 2-to vacuum pump outlet, 3- copper water-cooled electrodes, 4- graphite heater, 5- treated sample, 6- silicon carbide heater, 7- steel vessel, 8- vacuum pump

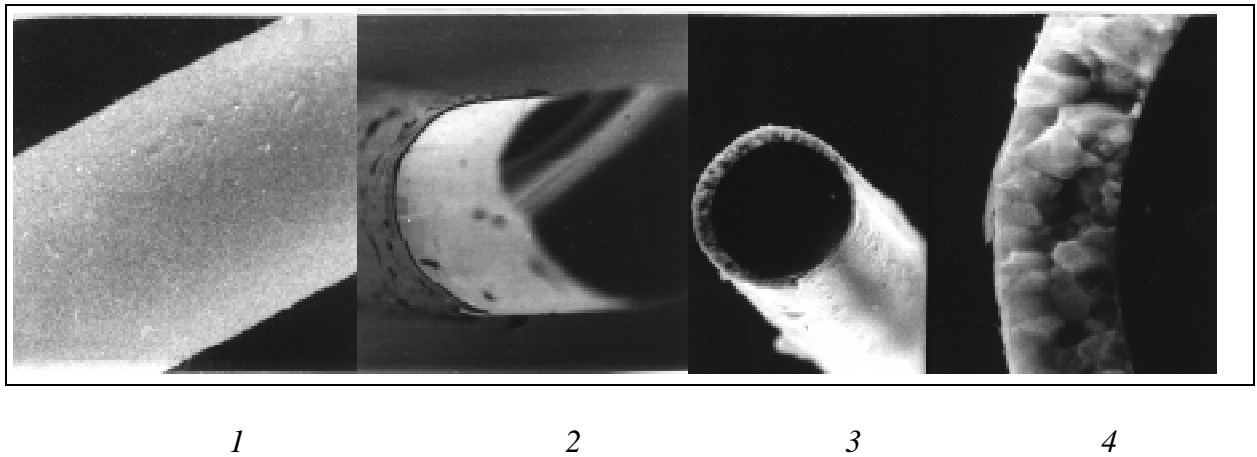


Fig.5: Coating on Nicalon fiber  
 1,2–molybdenum: end view ( $\times 2980$ ), side surface ( $\times 4000$ ), 3,4–friable SiC–layer (1% PCS solution, pyrolysis at  $1000^{\circ}\text{C}$  in inert atmosphere) – end view ( $\times 2200$ ,  $\times 17600$ )

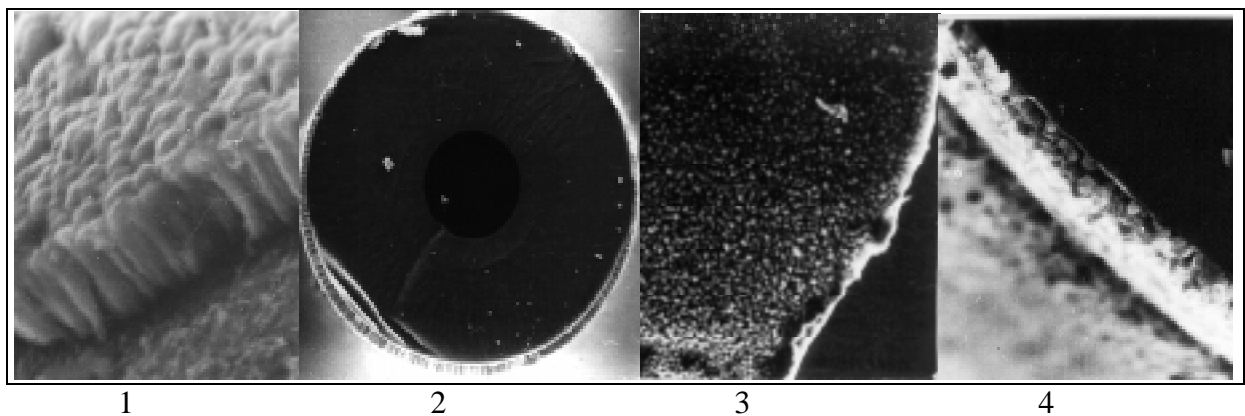


Fig.6. Coating on SiC/C fiber  
 1,2– molybdenum: surface and structure ( $\times 6750$ ), end view ( $\times 503$ ), 3,4– two-layer coating of silicon and molybdenum: side surface ( $\times 2020$ ), end view ( $\times 4020$ )

## CONCLUSIONS

The results support the authors' conception of complex program necessity in working out key components of high oxidation resistant for long time work CMC for civil technical products. New methods for production of oxygenless polymer precursors (PCS and CIPMCS) are an important step in this program. Next one must be the finishing of oxygenless technologically cheap curing methods that will give real possibility to have cheaper oxygenless fiber and to carry active work on interface coatings. This chief line does not exclude parallel experimental work on the all particular subjects of the program.

## ACKNOWLEDGMENTS

The authors are very grateful to State Scientific Center of Russian Federation GNIChTEOS, Moscow, for providing resources for this work and to International Science and Technology Center for support in presenting this paper.

## REFERENCES

1. Ho, C.Y. and El-Rahaiby, S.K., "Assessment of the Status of Ceramic Matrix Composites Technology in the United States and Abroad." *Ceramic Engineering & Science Proceedings*, vol.13, 1992, No 7-8, pp. 3-17.
2. Bulter, E.G., "Needs and Market Prospects for Ceramic Fibres in the Aero Engine Industry", *ECCM-6, Euro-Japanese Colloquium on Ceramic Fibres*, Bunsell, A.R. and Kimpara, I., Eds., Woodhead Publishing, Ltd., Abington Hall, England, 1993, pp. 81-108.
3. Tsirlin, A.I., "Nepriyvnye Neorganicheskie Volkna dlya Compozitsionnyh Materialov", *Ioskva, Iatallurgiya*, 1992, 237 s.
4. Yajima, S., "Silicon Carbide Fiber", *Handbook of Composite*, vol.1, Watt, W. and Perov, B.V., Eds. Elsevier Publishers, New York, 1985, pp. 201-237.
5. Gubin, S.P. i Kosobudskii, I.D., "Iatallicheskie Klasteri v Polimernyh Matritsah", *Zhurnal Uspehi Himii*, tom LII, vyp. 8, s. 1350-1364.
6. Kozinkin, A.V., Vlasenko, V.G., Gubin, S.P., Shuvaev, A.O. i Dubovtsev, I.A. "Klasteri v polimernyh matritse. 2. Issledovanie sostava i stroeniya zhelezosoderzhashih klasterov v polietilenovoi matritse", *Zhurnal Neorganicheskie Materialy*, 1996, tom 32, 14, s. 422-428.
7. Seyferth, D., Wood, T., Tracy, H. and Robiso J., "Near-Stoichiometric Silicon Carbide from an Economical Polysilane Precursor", *Journal American Ceramic Society*, Vvol.75, No 5, 1992, pp. 1300-1302.
8. Ichikawa, H., Okamura, R. and Seguchi, T., "Oxygen-Free Ceramic Fibers from Organosilicon Precursors and E-beam Curing", *High-Temperature Ceramic -Matrix Composites*, vol. II, pp. 65-74.

9. Hasegawa, Y., "New Curing Method for Polycarbosilane with Unsaturated Hydrocarbons and Application to Thermally Stable SiC Fibre", *Journal Composites Science and Technology*, No 51, 1994, pp. 161–166.
10. Patent, Japan, 03 40,814 (CI D 01 F 9/10), Seguchi, T., Nishii, M., Okamura, K., et al., 1991.
11. Patent, United States, 4 780 337 (CI B 32 B 9/00), Seyferth, D., 1988.
12. Nair, S.V., Wang, Yu-Lin, "Failure Behaviour of a 2-di Woven SiC Fiber/ SiC Matrix Composite at Ambient and Elevated Temperatures", *Ceramic Engineering & Science Proceedings*, vol.13, 1992, No 7–8, pp. 433–441.
13. V., Harkins, B., Beyermann, W., Keiser, J., et al., "Evolution of SiC/SiC composites for Heat Exchanger Applications", *Ceramic Engineering & Science Proceedings*, vol.13, 1992, No 7–8, pp. 503–519.
14. Yamamura, T., "Tyranno Fibers", *ECCM-6, Euro-Japanese Colloquium on Ceramic Fibres*, Bunsell, A.R. and Kimpara, I., Eds., Woodhead Publishing, Ltd., Abington Hall, England, 1993, pp. 187–202.
15. *Journal Material Science & Engineering*, vol. A 155, 1992, No 1–2, (Papers, Presented at First High Temperature Structural Silicides Workshop).



# MICROSTRUCTURE OF THE TZP PARTICULATE COMPOSITES

Marek Faryna<sup>1</sup>, Zbigniew Pedzich<sup>2</sup>, Lidia Litynska<sup>1</sup> and Krzysztof Haberk<sup>2</sup>

<sup>1</sup> *Institute of Metallurgy and Materials Science, Polish Academy of Sciences,  
30-059 Krakow, ul. Reymonta 25, Poland*

<sup>2</sup> *Department of Special Ceramics, Faculty of the Materials Science and Ceramics  
University of Mining and Metallurgy, 30-059 Krakow, al.Mickiewicza 30, Poland*

**SUMMARY:** The aim of this paper is to present results of the microstructure investigations in the tetragonal zirconia polycrystals (TZP) - tungsten carbide system. Microscopic observations compared with phase composition investigations confirmed that the reaction between composite components occurred. They also revealed close adhering of the matrix and carbide grains with no discontinuities. Crystallographic correlations between zirconia and carbides grains was shown.

**KEYWORDS:** tetragonal zirconia polycrystals, tungsten carbides, particulate composites,

## INTRODUCTION

Yttria stabilized tetragonal zirconia polycrystals (Y-TZP) are well known for their good mechanical properties. These are due to the tetragonal to monoclinic martensitic transformation at the crack tip advancing through the material. However, still better properties could be obtained by incorporation WC inclusions into the TZP-matrix. Our previous works [1,2] pointed out that hardness, fracture toughness, Young's modulus and, especially, wear resistance of the material can be improved. It is worth to notice that dense composite bodies (> 98 % theoretical density) were obtained by the pressureless sintering.

Thermodynamic calculations [3] show that under the potentially necessary sintering conditions reaction between ZrO<sub>2</sub> and WC could not result in the formation of any of the tungsten oxides. However, the reaction (1)



could proceed towards the right hand side if the CO partial pressure would be lower than indicated in the Table 1.

The samples were sintered in the carbon bed. So, the following reaction had also to be considered.



Table 1: Limiting CO partial pressure (in atms)

Temperature, °C	1400	1500	1600	1700
Reaction 1	0.95	5.20	23.8	93.0
Reaction 2	0.054	0.20	0.65	1.89

## EXPERIMENTAL PROCEDURE

### Composites processing

The 2.8 mole % of  $Y_2O_3$  - 97.2 mole %  $ZrO_2$  solid solution was selected as the matrix material. The starting powder was prepared by the coprecipitation - calcination technique [4]. The commercially available tungsten carbide powder (Baildon, Poland) was applied.

Homogenization of the oxide and carbide powders was performed by one hour attrition milling in ethyl alcohol using 2 mm Y-TZP balls as the grinding media. Volume of the carbide additives was 20 %. Dry powders with no lubricating additives were uniaxially pressed under 50 MPa and isostatically repressed under 350 MPa. By this procedure cylindrical samples of 23 mm diameter and 10 mm thickness were prepared. The samples were placed in a carbon bed and sintered in the argon atmosphere at temperature ranging from 1400 to 1700°C with the two hour soaking at each temperature. Sintering was performed in a furnace equipped with the tungsten heating elements.

### Experimental methods

X-ray diffraction was used to establish the phase composition of the bodies sintered at different temperatures. Scanning electron microscope PHILIP XL30 equipped with an energy dispersive spectrometer LINK ISIS was used to investigate morphology of the thermally etched surfaces as well as the chemical composition of the composites. Transmission electron microscope PHILIPS CM20 equipped with energy dispersive spectrometer LINK eXL was applied to determine crystalline structure and chemical composition from both TZP grains and WC inclusions. Thin foils were prepared by ion milling of the samples using the Duo Mill GATAN 600 equipment.

## RESULTS AND DISCUSSIONS

Figures 1 and 2 show X-ray patterns of the composites sintered at the whole range of temperature. In the *as received* surfaces of the bodies (Fig. 1.), ZrC is present even at the lowest sintering temperature.  $W_2C$  appears in samples sintered at 1700°C. This fact indicates that ZrC is formed due to reaction (2). The limiting CO partial pressure for the reaction (2) at 1400°C is 0.054 atm. Under such conditions reaction (1) should also proceed at 1400°C. This is not the case, plausibly because of the kinetic effect.

Fig. 2. Shows the X-ray diffraction patterns of the samples having thin near surface layer (~100 microns) removed. It is different from that taken from the *as received* surface (Fig. 1.). In the composite sintered at the 1400°C only  $ZrO_2$  and WC were detected. At higher sintering temperatures phases not introduced into the starting material, ZrC and  $W_2C$  appear. They

undoubtedly result from the reaction (1). In the composite achieved at the 1700°C W<sub>2</sub>C is the dominant carbide phase.

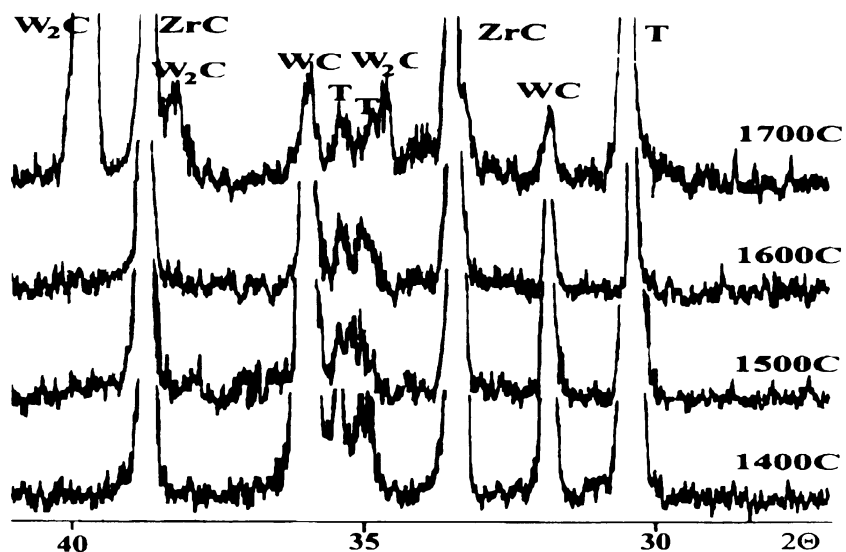


Fig. 1: X-ray diffraction patterns of the as received surfaces of the composites sintered at indicated temperatures. T - tetragonal zirconia phase

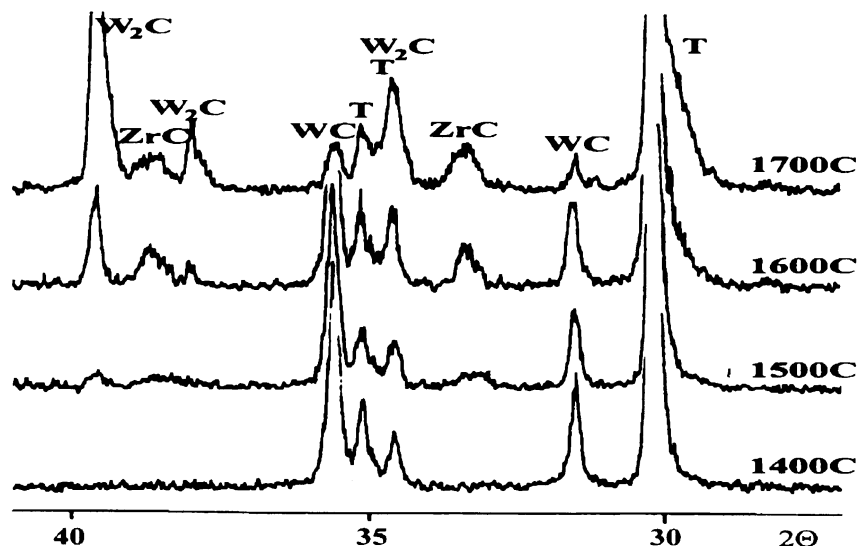
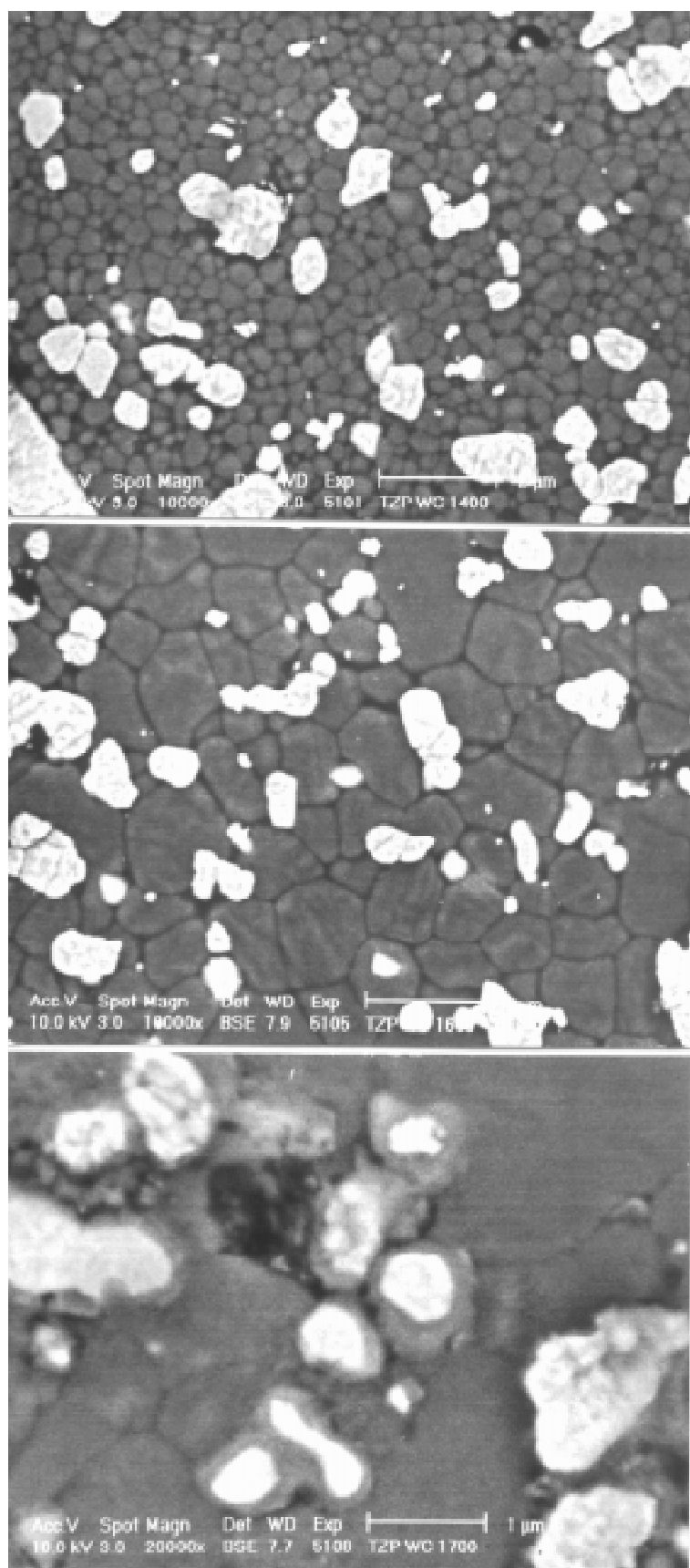


Fig. 2: X-ray diffraction patterns of the composites sintered at indicated temperatures. Surface layer of about 100 microns was removed by grinding and polishing

SEM micrographs of the composite microstructures are shown in Fig. 3. In the samples sintered both at 1400°C and 1600°C the boundaries between zirconia and carbide grains are distinct and well defined. The increase of the sintering temperature up to 1700°C results in the rims surrounding carbide inclusions. X-ray energy dispersion microanalysis shows that in these rims both zircon and tungsten are present.



*Fig. 3: SEM micrographs of the thermally etched composite surfaces. Sintering temperatures: 1400, 1600 and 1700°C (starting from top of the figure)*

TEM observations of the sample sintered at 1400°C revealed that not only WC (Fig. 4.) but also W<sub>2</sub>C are present (Fig. 5.). The identification of the phases is based on indexing of the electron diffraction patterns. Diffraction pattern taken from the border zone between ZrO<sub>2</sub> and WC grains (Fig. 4.D.) indicates the existence of the following crystallographic relationships:

$$\begin{aligned} [0001] \text{ WC} & \parallel [001] \text{ t-ZrO}_2 \\ [\bar{1}010] \text{ WC} & \parallel [010] \text{ t-ZrO}_2 \end{aligned}$$

The presence of the W<sub>2</sub>C grains in material achieved at 1400°C confirms that reaction (1) proceeds at this temperature.

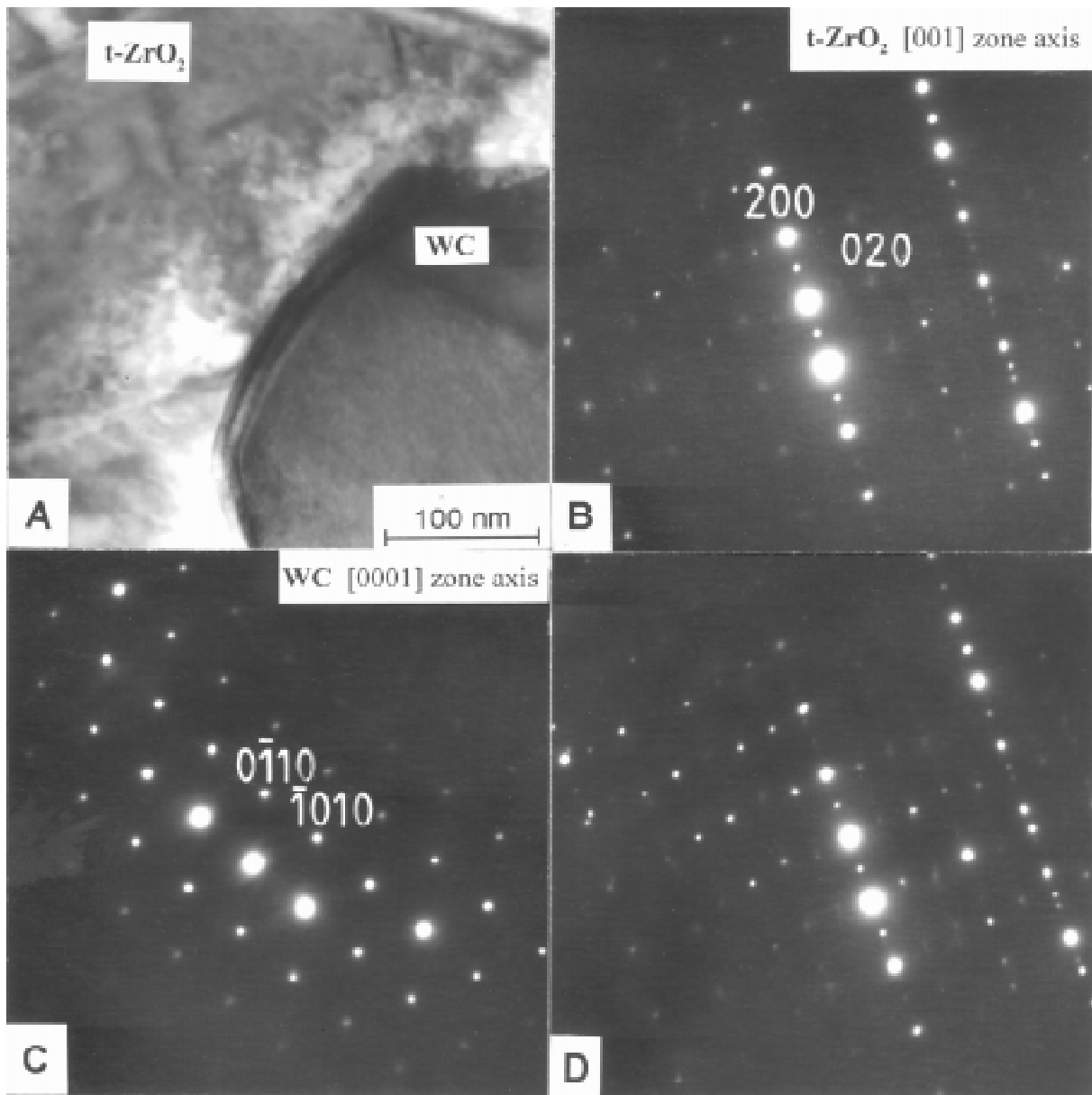


Fig. 4: A. Transmission electron micrograph the TZP-WC composite sintered at 1400°C, B. selected diffraction pattern (SADP) of tetragonal zirconia phase, C. SADP of hexagonal WC, D. SADP of boundary between ZrO<sub>2</sub> and WC grains

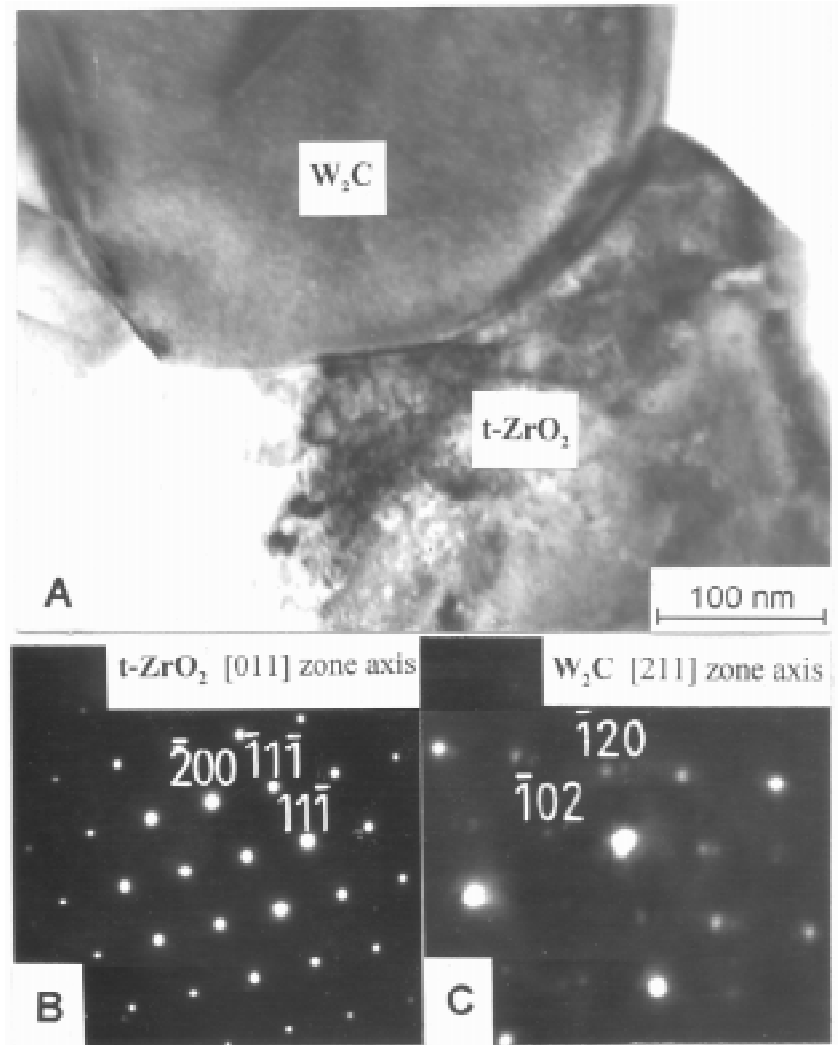


Fig.5: A. Transmission electron micrograph the TZP-WC composite sintered at 1400°C, B. selected diffraction pattern (SADP) of tetragonal zirconia phase, C. SADP of orthorhombic  $W_2C$

In the composite sintered at 1700°C  $W_2C$  is the dominating tungsten carbide phase. Fig. 6. shows the TEM micrograph in which the tetragonal (Fig. 6B.) and monoclinic (Fig. 6C.)  $ZrO_2$  as well as  $W_2C$  (Fig. 6D.) grains coexist. The presence of martensitic transformation and modulated structure characteristic for the tetragonal phase (the state just before transformation) suggests that tetragonal to monoclinic transformation takes place during the thin section preparation. This has been confirmed by the X-ray diffractometric measurements, where no monoclinic phase was observed in the as received surfaces. Crystallographic correlation observed between tetragonal and monoclinic  $ZrO_2$ :

$$\begin{aligned} [100] \text{ t-}ZrO_2 & \parallel [100] \text{ m-}ZrO_2 \\ [001] \text{ t-}ZrO_2 & \parallel [010] \text{ m-}ZrO_2 \end{aligned}$$

confirms Wen *et. al.* investigations of the 3Y-TZP system [5].

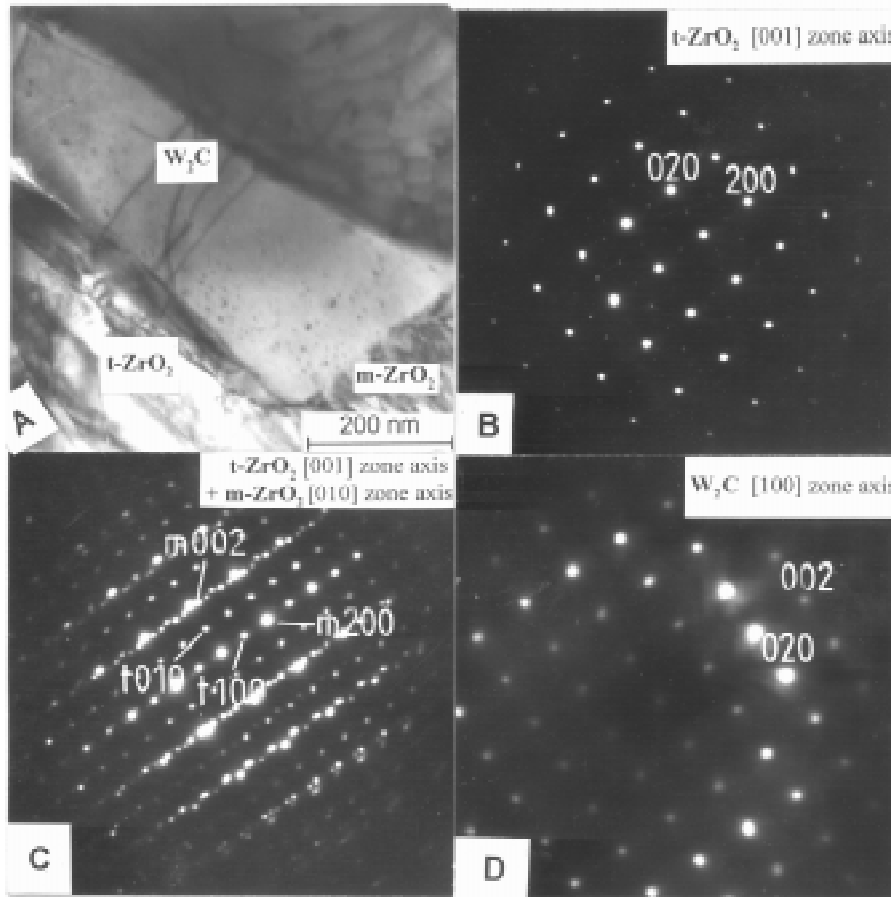


Fig. 6: A. Transmission electron micrograph the TZP-WC composite sintered at 1700°C, B. selected diffraction pattern (SADP) of tetragonal zirconia phase, C. SADP of monoclinic and tetragonal zirconia, D. SADP of orthorhombic  $W_2C$ .

The crystallographic correlations between tungsten carbide phases and the matrix has also been found:

$$\begin{aligned} [100] W_2C & \parallel [001] t\text{-}ZrO_2 \\ [010] W_2C & \parallel [010] t\text{-}ZrO_2 \end{aligned}$$

In all sintering temperatures applied in this work close adhering of the matrix and carbide grains with no discontinuities occurred. ZrC distinct in X-ray patterns was not identified by the electron diffraction. It is probably localized in the rims surrounding tungsten carbides grains.

## CONCLUSIONS

Reaction between composite components under applied sintering condition occurred. It results in the  $W_2C$  and ZrC formation inside the material. Reaction between the zirconia matrix and the carbon bed is limited only to the near surface layer (~100 microns).

It was revealed that by means of the TEM microscopy carbide/matrix contacts were tight. No microcracks were observed. A crystallographic correlations between  $ZrO_2$  and both WC and  $W_2C$  were observed. It indicates that under the applied sintering conditions components tend

to arrange in way that a minimum interface energy is achieved. This is substantiated by the crystallographic arranging of the composite phases.

### **ACKNOWLEDGEMENT**

This work was supported by the Polish State Committee for Scientific Research under the grant no. 7 T08A 052 10.

### **REFERENCES**

1. Haberko, K., Pêdzich, Z., Piekarczyk, J., Róg, G., "Zirconia - Tungsten Carbide Particulate Composites. Part I: Manufacturing and Physical Properties", in Fourth Euro-Ceramics, vol. 4, *Basic Science - Trends in Emerging Materials and Applications*, A. Bellosi (Eds.), Gruppo Editoriale Faenza Editrice S. p. A., 1995, pp. 29-36.
2. Pêdzich, Z., Haberko, K., Faryna, M., "Zirconia - Tungsten Carbide Particulate Composites. Part II: Microstructure and Wear Resistance", in Fourth Euro-Ceramics, vol. 3, *Basic Science - Optimization of Properties and Performance by Improved Design and Microstructural Control*, S. Meriani, V. Sergo (Eds.), Gruppo Editoriale Faenza Editrice S. p. A., 1995, pp. 433-438.
3. Haberko, K., Pêdzich, Z., Róg, G., Buæko, M. M., Faryna, M., "The TZP Matrix - WC Particulate Composites", *European Journal of the Solid State and Inorganic Chemistry*, Vol. 32, 1995, pp. 593-601.
4. Pêdzich, Z., Haberko, K., "Coprecipitation Conditions and Compaction Behaviour of Y-TZP Nanometric Powders", *Ceramics International*, Vol. 20, No. 2, 1994, pp. 85-89.
5. Wen, S., Ma, L., Guo, J., Yen, T., "Transmission Electron Microscopic Observations of the Martensitic Phase Transformation in Tetragonal ZrO<sub>2</sub>", *Journal of the American Ceramic Society*, Vol. 69, No. 7, 1986, pp. 570-572.



# FEM ANALYSIS OF MICRO-INDENTATION TEST FOR C/C COMPOSITES

H. Serizawa <sup>1</sup>, S. Sato <sup>2</sup>, H. Tsunakawa <sup>3</sup> and A. Kohyama <sup>4</sup>

<sup>1</sup> *Joining and Welding Research Institute, Osaka University,  
11-1, Mihogaoka, Ibaraki, Osaka 567, Japan*

<sup>2</sup> *Department of Mechanical Engineering, Fukushima National College of Technology,  
30 Nagao, Kamiarakawa, Taira, Iwaki-shi, Fukushima 970, Japan*

<sup>3</sup> *Engineering Research Institute, The University of Tokyo,  
Yayoi, Bunkyo-ku, Tokyo 113, Japan*

<sup>4</sup> *Institute of Advanced Energy, Kyoto University, Gokasho, Uji, Kyoto 611, Japan*

**SUMMARY:** To investigate the mechanism of energy loss in load - displacement of indenter curve (indentation curve) under fiber indentation test of unidirectionally reinforced C/C composites, the fiber indentation tests were performed and the indentation curve was analyzed by an axis symmetrical finite-element method (FEM) model including a newly designed fiber-matrix interfacial bonding. In this model, only elastic deformations were considered for both fiber and matrix, and the interfacial bonding was assumed to yield not to fracture. From this FEM analysis, a hysteresis loop was obtained in the indentation curve and the interfacial debonding was founded to start from the inside of specimen under the indentation test. And the indentation curve calculated by the FEM analysis was coincide with the experimental results, so compressive Young's modulus of carbon fiber in C/C composite was founded to be predictable from the FEM analysis.

**KEYWORDS:** C/C composite, carbon fiber, indentation test, interface, finite element method, Young's modulus, transmission electron microscopy, graphite

## INTRODUCTION

Mechanical properties of interface between fibers and matrices are known to be quite influential in determining properties of fiber reinforced composites. Some of the previous reports have indicated the effectiveness of controlling fiber-matrix interface on improving properties of composite materials [1]. So the effects of surface treatment or coating on fibers for several composites have been studied [2] and many experiments have been carried out to measure the interfacial mechanical properties by various methods, those were pull-out test [3], push-out test [4], protrusion test [5] and multiple fracture test [6]. And most of these studies have done by using simple model composites reinforced with single thick fiber. But practical carbon reinforced carbon (C/C) composites are reinforced with a large number of very thin fibers and have many pores and cracks in matrix [7]. Therefore, to measure the mechanical properties of practical C/C composites in the micro area is very difficult and the micro indentation test is considered to be one of the suitable test method.

There were some reports of the indentation tests about carbon materials [8], but in these reports maximum load and displacement of indenter were too large to indent only one fiber in

the practical C/C composites. So, to study mechanical properties of fiber, matrix and their interface in C/C composites, the authors have applied a newly developed ultra micro indentation test machine to fiber indentation tests in C/C composites [9-11]. Where, any indications of plastic deformation were not observed on specimen surfaces after indentation test by scanning electron microscopy (SEM), although load - displacement of indenter curve (indentation curve) showed large hysteresis loop, that indicated the existence of some energy loss under the test [10]. However this experimental result could not be understood by any models including the indentation tests of carbon materials as far as the authors knowledge. So, in this study, fiber indentation tests were performed and a new finite-element method (FEM) model was provided for analyzing the deformations of fiber, matrix and their interface.

## EXPERIMENTAL

### Material Used and Specimen

Material used was unidirectionally reinforced C/C composite, heat treated at 1873 K. Carbon fiber used was mesophase pitch-based fiber and its characteristics are shown in Table 1. Matrix precursor was a mixture of green coke and phenolic resin (80/20 in volumetric ratio). And a fiber volume fraction and a density of C/C composite were 45.0 % and 1.69 Mg/m<sup>3</sup>, respectively.

*Table 1: Characteristics of fibers used*

Diameter ( $\mu\text{m}$ )	9.8
Tensile Modulus (GPa)	542
Tensile Strength (Gpa)	2.92
Heat Treatment Temperature (K)	2473

Schematic flow of specimen preparation for fiber indentation test is shown in Fig. 1. C/C specimen, whose size was  $20^l \times 5^w \times 1^t$  mm, was fixed at the center of acrylic pipe by resin. And next, the fixed specimen was sliced perpendicular to the fiber direction with about 200  $\mu\text{m}$  thickness by low speed diamond saw. Then the thickness of sliced specimen was reduced 80  $\mu\text{m}$  by mechanical grinding and the pipe and resin were removed in acetone. Finally the size of specimen for fiber indentation test became  $5^l \times 1^w \times 0.08^t$  mm.

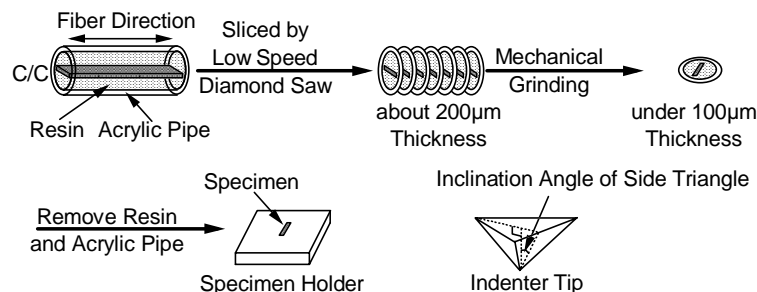


*Fig. 1: Schematic flow of specimen preparation and shape of indentation tip*

## Fiber Indentation Test

Fiber indentation tests were carried out by utilizing the dynamic ultra indentation test machine [8]. The specimen was placed on a specimen holder made of SUS and fibers in C/C composites were loaded by triangular diamond pyramid indenter tip, where maximum loads were 0.2 N. The shape of triangular diamond pyramid indenter tip is shown in Fig. 1. The inclination angle of side triangle was 68 degrees.

## Structural Inspections

Macroscopic structure, including fiber volume fraction, was determined by both optical microscopy and SEM. And microstructural inspections of interface were performed with high resolution transmission electron microscopy (TEM : JEOL-4000FX), where an acceleration voltage was 400 kV. Specimens for TEM observation were prepared by dimple grinding and Ar ion milling, and were observed parallel to the fiber direction.

## RESULTS OF FIBER INDENTATION TEST

Typical examples of indentation curves under fiber indentation tests are shown in Fig. 2. For all cases, the indentation curves showed large hysteresis loops and came back to the origin. Under indentation tests of glasslike carbon, same hysteresis loops were reported [8]. However maximum load and displacement of indenter were over 10 N and 100  $\mu\text{m}$  under the carbon indentation test, respectively. In addition to that, cracks were observed at the specimen surface after carbon indentation tests by SEM. But, after the fiber indentation tests, the interfacial debonding and the indentation mark could not be observed at the specimen surface. It indicates that the origin of the hysteresis loops under the fiber indentation tests was different from that under the carbon indentation tests, that is, the loops under the fiber indentation tests were not resulted from the essential property of carbon.

And micro steps can be detected in Fig. 2 and some of them are pointed out by arrows, those are considered to be indications of interfacial debonding. So, for the exact understanding of the indentation curves and the deformations of fiber, matrix and interface in C/C composites under fiber indentation test, a new FEM analysis including the interfacial debonding seems to be needed.

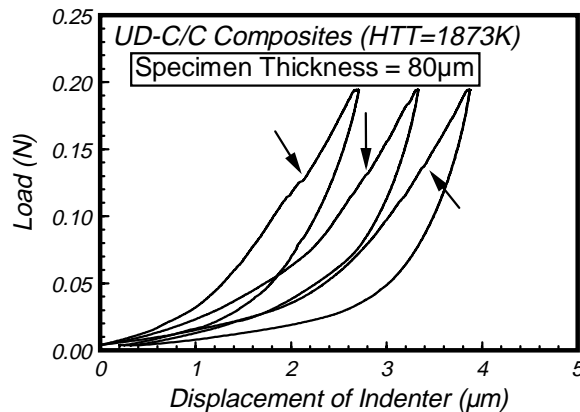


Fig. 2: Indentation curves under fiber indentation test in C/C composites

## FEM MODEL

### Shape of FEM Model

By using an axis symmetrical FEM model shown in Fig. 3, the deformations of fiber, matrix and interface in C/C composite under fiber indentation test were calculated. For the analysis of practical composites, the correlation between adjacent fibers must be taken into account, but in this study, two dimensional models were used for the first step of FEM examination including the interfacial debonding. So C/C composites reinforced with only single carbon fiber were used for this calculation, and the matrix phase was assumed to be carbon layer. The width of this layer was assumed to be 2  $\mu\text{m}$ , that reflects a fiber volume fraction of specimen for fiber indentation test correctly (Fig. 4).

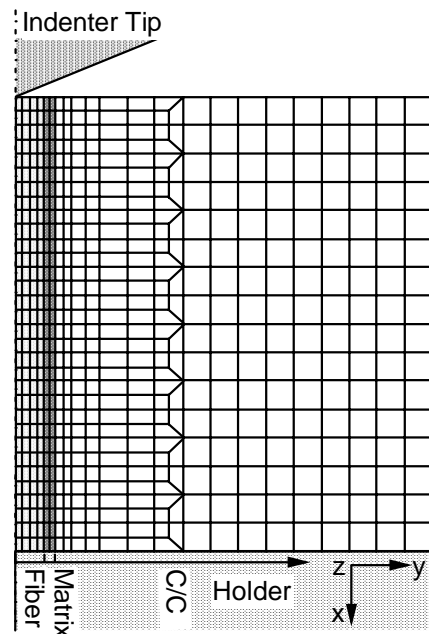


Fig. 3: FEM model of fiber indentation test

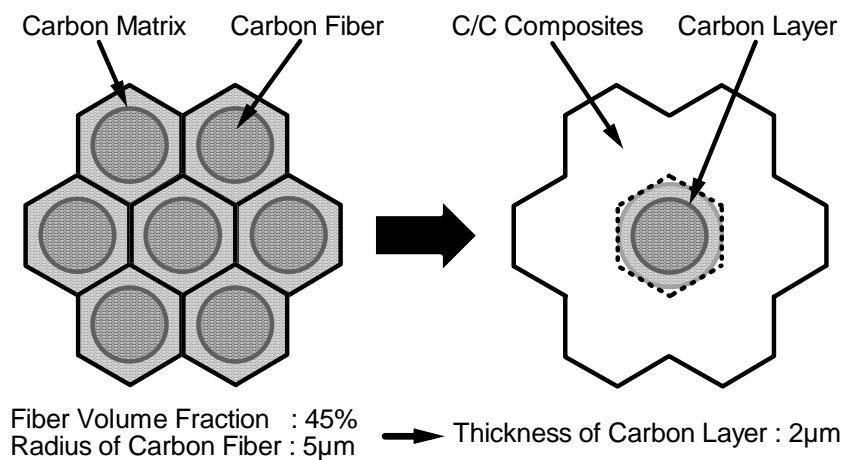


Fig. 4: Thickness of carbon layer around fiber

Under the indentation test, the effect of the area of contact between indenter tip and specimen on stress distribution was considered to be very large [10]. For this axis symmetrical FEM model, the shape of indenter tip was a cone not a triangular pyramid. Therefore, in this analysis, indenter tip was assumed to be a cone with 145.6 degrees of the apical angle so that the area of contact in case of the cone was as same as in case of the triangular pyramid at the same displacement of indenter, shown in Fig. 5.

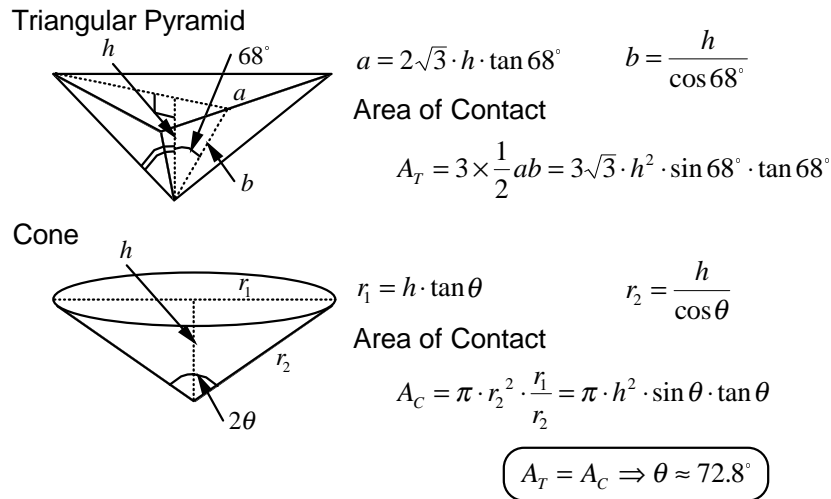


Fig. 5: Shape of indenter tip

### Interfacial Bonding Between Fiber and Matrix

Fig. 6 shows a typical example of TEM image at interface between fiber and matrix. A vertical direction of this figure is fiber direction. From this figure, the thickness of interface seems to be about 30 nm. And a structure of carbon at interface was observed to be graphite layers parallel to the fiber direction. That is, c-axis direction of this graphite was parallel to radial direction of the fiber. And, for graphite structure, bonding strength at c-axis direction is very weak because there are van der Waals' bonds between graphite layers [7]. So the debonding of fiber-matrix interface is considered to be as same as the debonding between the graphite layers.

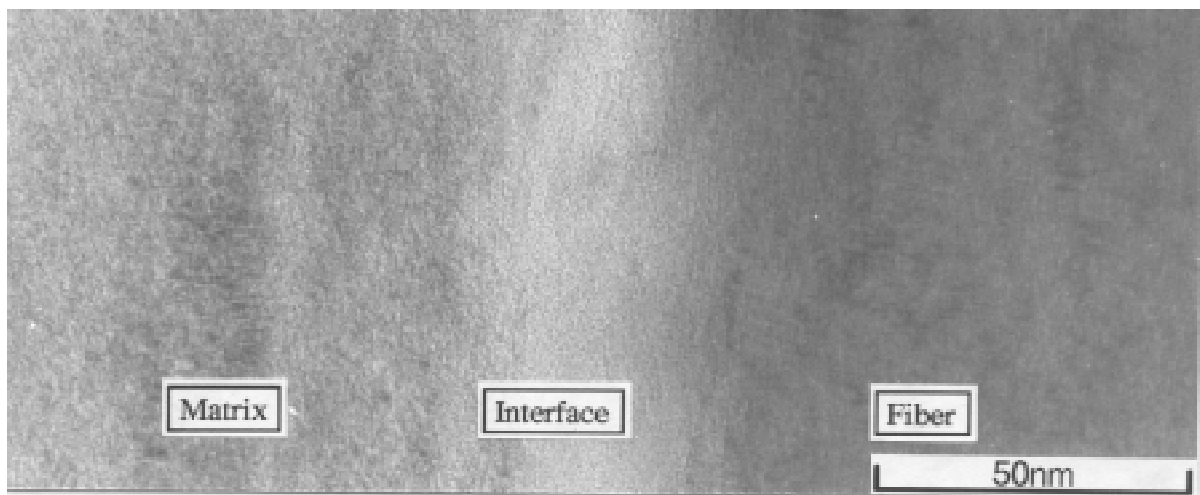
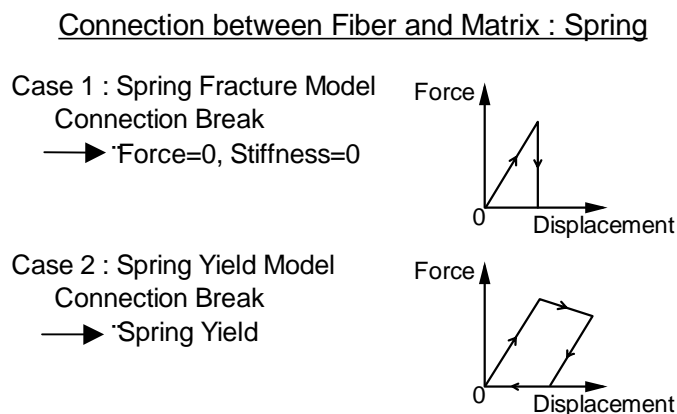


Fig. 6: TEM image at interface between fiber and matrix

In the most previous analysis of micro indentation test, an extra interphase, which was made from reaction of fiber and matrix, was set up independently [12]. For C/C composites, the extra interphase seems to be the graphite layer. Now, in this FEM analysis, the graphite layers were assumed to be springs between nodes of fiber and matrix element in the FEM model. And debonding was assumed to occur when a length of the spring, that was 30 nm in the beginning of the FEM analysis, changed to 45 nm, which indicates that the distances between each graphite layers expand to one and half times. Where stiffness of the spring parallel and transverse to the fiber direction were determined to 50 GPa and 20 GPa, respectively, from mechanical properties of graphite [13].

And two kinds of the stress-transmission method in the spring were assumed to be as shown in Fig. 7 after the debonding at fiber-matrix interface. In Fig. 7, the case 1 is a usual method of the interfacial debonding on FEM analysis under the fiber indentation test. Under the condition of case 1 on the axis symmetrical FEM model, a debonding at one point on fiber surface seems to be equivalent to a debonding on one circumference of fiber surface including the debonding point. But this phenomena is considered not to exactly express a three dimensional phenomena of the debonding at fiber-matrix interface, because under the three dimension the debonding at one point on fiber surface seems to be gradually spread on the circumference including the debonding point. So a newly designed interfacial bonding was constructed shown in case 2 of Fig. 7. Under the condition of case 2, the bonding force of the spring between fiber and matrix was assumed to linearly decrease after the beginning of the interfacial debonding, that is considered to indicate the gradual spread of the interfacial debonding. That is, the interfacial bonding was presumed to yield not to fracture. And the slope of the bonding force in an unloading under the fiber indentation test was assumed to be as same as that in loading, because the bonding between fiber and matrix was considered to be supported by the residual bonding interface that has the same stiffness in both loading and unloading.



*Fig. 7: Condition of debonding at fiber-matrix interface*

### Condition of FEM Model

After the fiber indentation test, the interfacial debonding and the indentation mark could not be observed at the specimen surface by SEM. So, in this FEM analysis, only the elastic deformations of fiber, matrix and C/C composites were considered. That is, the origin of the large hysteresis loop in Fig. 2 was assumed to be only an energy loss caused by the fiber-matrix interfacial debonding. The specimen holder and the indenter tip were presumed to be rigid. The condition of FEM analysis is as shown in Table 2. The Young's moduli of C/C

composite were determined from the measured values [14], except to the longitudinal Young's modulus of unidirectional C/C composites. The radial Young's modulus of fiber and the isotropic Young's modulus of matrix was assumed to be same as the transverse Young's modulus of unidirectional C/C composites. And the Poisson's Ratio and the shear modulus were determined from the previous researches [15] except for  $\nu_{xy}$  and  $\nu_{zx}$  of fiber, which was decided in reference of the Poisson's Ratio of composite and fiber.

On the other hand, the carbon fiber was considered to be mainly received the compressive stress at the fiber direction under the fiber indentation test, and the compressive Young's modulus of fiber has been reported to be the quarter of the tensile Young's modulus [16]. And the longitudinal Young's modulus of fiber are known to have the strain dependence. So the longitudinal Young's modulus of carbon fiber was assumed to be the quarter of the calculated value from the longitudinal Young's modulus of unidirectional C/C composites [14] according to the simple law of mixture, and the longitudinal Young's modulus of C/C composites was determined from this Young's modulus of fiber.

Table 2: Condition of FEM model

Analysis Model	Axis Symmetrical FEM Model
Specimen Size :	Radius 2500 $\mu\text{m}$ , Thickness 80 $\mu\text{m}$
Radius of Fiber :	5 $\mu\text{m}$
Indenter Tip :	Cone with 145.6° of the Apical Angle
Thickness of Carbon Layer	:2 $\mu\text{m}$ • (from Fiber Volume Fraction)
Elastic Properties of Each Element	
Fiber :	$E_{xx}$ : 80GPa $\nu_{xy}$ :0.16 $G_{xy}$ :10GPa $E_{yy}$ : 8.9GPa $\nu_{yz}$ :0.30 $G_{yz}$ :20GPa $E_{zz}$ : 8.9GPa $\nu_{zx}$ :0.16 $G_{zx}$ :10GPa Density 2.08 Mg/m <sup>3</sup>
Carbon Layer :	$E$ : 8.9GPa $\nu$ : 0.30 Density 1.70 Mg/m <sup>3</sup>
C/C :	$E_{xx}$ : 40GPa $\nu_{xy}$ :0.20 $G_{xy}$ :8.9GPa $E_{yy}$ : 8.9GPa $\nu_{yz}$ :0.30 $G_{yz}$ :15GPa $E_{zz}$ : 8.9GPa $\nu_{zx}$ :0.20 $G_{zx}$ :8.9GPa Density 1.68 Mg/m <sup>3</sup>

## RESULTS OF FEM ANALYSIS

In this FEM analysis, only a displacement of indenter can be controlled. So the FEM analyses with the two kinds of interfacial bonding, that were case 1 and 2, were done in loading from 0 to 2.5  $\mu\text{m}$  displacement of indenter and in unloading from 2.5 to 0  $\mu\text{m}$  displacement. The indentation curves calculated from FEM model with the interfacial bonding of case 1 and 2 are shown in Fig. 8 (a) and (b), respectively. In Fig. 8 (a), the load was largely decreased over 0.6  $\mu\text{m}$  displacement of indenter, and the interfacial debonding started after the 0.6  $\mu\text{m}$  displacement in the FEM model with the interfacial bonding of case 1. But the large decrease of load was not detected in the experimental results. On the other hand, for the FEM model with the interfacial bonding of case 2, the load was continuously increased in loading although the interfacial debonding began after the 0.6  $\mu\text{m}$  displacement. That is, the indentation curve of case 2 showed the hysteresis loop as same as the experimental results. So

the FEM model with the interfacial bonding of case 2 is considered to be suitable for the analysis of the fiber indentation test of C/C composites.

And, in this FEM analysis of case 2, the start point of the interfacial debonding was the inside not the surface of specimen. To put it in the concrete, the interfacial debonding started at the interface under 5  $\mu\text{m}$  depth from the upper side of specimen surface. And the area of interfacial debonding gradually expanded into the lower side of specimen surface with increasing the displacement of indenter, but the interfacial debonding at both the upper and lower sides of specimen surface did not occur at the 2.5  $\mu\text{m}$  displacement of indenter. This result from the FEM analysis was in good agreement with the result by the SEM observation of specimen surface after the fiber indentation test. Furthermore, in this FEM analysis of case 2, the maximum value of load at the 2.5  $\mu\text{m}$  displacement of indenter was close to the experimental results. Therefore the compressive Young's modulus of carbon fiber in C/C composite was founded to be predictable from the FEM analysis with a newly designed interfacial bonding.

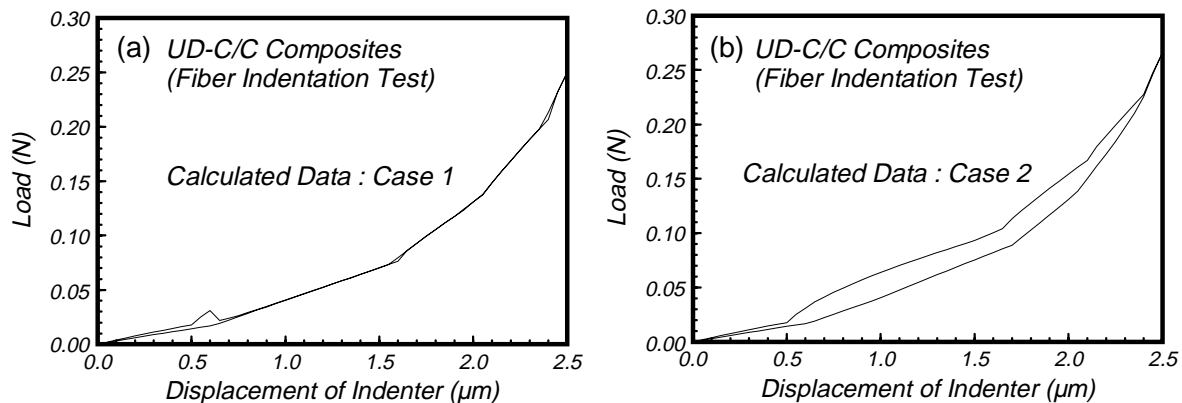


Fig. 8: Indentation curves calculated from FEM model with the interfacial bonding of case 1 (a) and case 2 (b)

## CONCLUSIONS

To investigate the mechanism of the energy loss in the indentation curve under the fiber indentation test of C/C composites, the fiber indentation tests were performed and the indentation curve was analyzed by an axis symmetrical FEM model including a newly designed fiber-matrix interfacial bonding. The conclusions could be summarized as follows.

- (1) From the FEM analysis, the hysteresis loop was obtained in the indentation curve and the interfacial debonding was founded to start from the inside of specimen under fiber indentation test.
- (2) The indentation curve calculated by this FEM analysis was coincide with the experimental results, so the compressive Young's modulus of carbon fiber in C/C composite was founded to be predictable from this FEM analysis.



## ACKNOWLEDGMENTS

The authors would like to express their sincere appreciations to Dr. E. Tsushima and Mr. J. Takayasu (TONEN Co.) for providing materials and to Mr. M. Fukunaga (Nippon MARC Co., Ltd.) for fruitful discussion.

## REFERENCES

1. Leparoux, M., Vandenbulcke, L., Goujard, S., Robin-Brosse, C. and Domergue, J.M., "Mechanical Behavior of 2D-SiC/BN/SiC Processed by ICVI", *Proceedings Tenth International Conference on Composite Materials*, Whistler, British Columbia, Canada, August 14-18, 1995, Vol. IV: Characterization and Ceramic Matrix Composites, Poursartip, A. and Street, K.N., Eds, pp. 633-640.
2. Grande, D.H., Mandell, J.F. and Hong, K.C.C., "Fiber-Matrix Bond Strength Studies of Glass, Ceramic, and Metal Matrix Composites", *Journal of Materials Science*, Vol. 23, 1988, pp.311-328.
3. Lawrence, P., "Some Theoretical Considerations of Fibre Pull-Out from an Elastic Matrix", *Journal of Materials Science*, Vol. 7, 1972, pp.1-6.
4. Marshall, D.B., "An Indentation Method for Measuring Matrix-Fiber Frictional Stresses in Ceramic Composites", *Journal of the American Ceramic Society*, Vol. 67, 1984, pp.C-259-C-260.
5. Kagawa, Y. and Honda, K., "A Protrusion Method for Measuring Fiber/Matrix Sliding Frictional Stresses in Ceramic Matrix Composites", *Ceramic Engineering and Science Proceedings*, Vol. 12, 1991, pp. 1127-1138.
6. Marshall, D.B. and Evans, A.G., "Failure Mechanisms in Ceramic-Fiber/Ceramic-Matrix Composites", *Journal of the American Ceramic Society*, Vol. 68, 1985, pp. 225-231.
7. Thomas, C.R., *Essentials of Carbon-Carbon Composites*, The Royal Society of Chemistry, 1993.
8. Sakai, M., Hanyu, H. and Inagaki, M., "Indentation-Induced Contact Deformation and Damage of Glasslike Carbon", *Journal of the American Ceramic Society*, Vol. 78, 1995, pp.1006-1012.
9. Hamada, K., Sato, S., Tsunakawa, H. and Kohyama, A., "Interfacial Microstructure and Mechanical Properties of C/C Composites", *Proceedings Tenth International Conference on Composite Materials*, Whistler, British Columbia, Canada, August 14-18, 1995, Vol. VI: Microstructure, Degradation, and Design, Poursartip, A. and Street, K.N., Eds, pp. 423-430.
10. Serizawa, H., Kohyama, A., Watanabe, K., Kishi, T. and Sato, S., "Elastic FEM Analysis of Fiber Push-Out Test for C/C Composites", *Materials Transactions, JIM*, Vol. 37, No. 3, 1996, pp. 409-413.

11. Watanabe, K., Kohyama, A., Sato, S., Serizawa, H., Tsunakawa, H., Hamada, K. and Kishi, T., "Evaluation of Interfacial Shear Strength of C/C Composites by means of Micro-Indentation Test", *Materials Transactions, JIM*, Vol. 37, No. 5, 1996, pp. 1161-1165.
12. Tsai, H.C., Arocho, A.M. and Gause, L.W., "Prediction of Fiber-Matrix Interphase Properties and their Influence on Interface Stress, Displacement and Fracture Toughness of Composite Material", *Materials Science and Engineering*, A126, 1990, pp. 295-304.
13. Kelly, B.T., *Physics of Graphite*, Applied Science Publishers, London and New Jersey, 1981.
14. Serizawa, H., Kohyama, A. and Sato, S., "Effect of Heat Treatment Temperature on Young's Modulus and Internal Friction of C/C Composites", *Proceedings of the Ninth International Conference on Composite Materials*, Madrid, Spain, July 12-16, 1993, Vol. 2, Miravete, A., Ed., pp. 524-531.
15. Goggin, P.R., "The Elastic Constants of Carbon-Fibre Composites", *Journal of Materials Science*, Vol. 8, 1973, pp. 233-244.
16. Shinohara, A.H., Sato, T., Saito, F., Tomioka, T. and Arai, Y., "A Novel Method for Measuring Direct Compressive Properties of Carbon Fibers Using A Micro-Mechanical Compression Tester", *Journal of Materials Science*, Vol. 28, 1993, pp. 6611-6616.

# PREPARATION AND PROPERTIES OF 3D-CARBON FIBER WOVEN PREFORM REINFORCED SiC AND $Al_2O_3$ HYBRID MATRIX COMPOSITES

Jiayu Xiao, Fengrong Liu, Wenwei Zheng, Xingye Wang, Dazhi Jiang, Zhaohui Chen

*Department of Materials Engineering and Applied Chemistry,  
National University of Defence Technology, NUDT, Changsha, Hunan, 410073, P.R. China*

**SUMMARY:** A three-dimensional carbon fiber woven preform reinforced SiC and  $Al_2O_3$  hybrid matrix composite was prepared by the following process:

The preform impregnated with a solution of polycarbosilane (PCS) and divinyl benzene (DVB) was heated to cure the solution, and then pyrolyzed under  $N_2$  atmosphere protection in order to transform the cured system into SiC matrix and to form a composite 3D-C/SiC. After certain densification cycles, the composite 3D-C/SiC was then impregnated with a sol prepared by aluminium isopropoxide, deionized water and hydrochloric acid. Under controlled conditions, the sol impregnating the composite was gelatinized and pyrolyzed into alpha- $Al_2O_3$  matrix. After several repetition cycles for densification, a three-dimensional carbon fiber woven preform reinforced SiC and  $Al_2O_3$  hybrid matrix composite (3D-C/SiC/ $Al_2O_3$ ) was prepared.

The 3D-C/SiC/ $Al_2O_3$  composite presents some properties that are different from those of its 3D-C/SiC counterpart. The former has a lower porosity and a higher density than the latter for the same volumetric fractions of fibers and SiC. The two composites are of an almost same three-point flexural strength at room temperature (about 400 MPa), however, the three-point flexural strength at an elevated temperature (1300°C) of the former (155 MPa) is much higher than that of the latter (100 MPa), although the measuring conditions for the former are much more severe than those for the latter.

**KEYWORDS:** carbon fiber, woven preform, SiC,  $Al_2O_3$ , hybrid matrix composite, precursor, sol-gel

## INTRODUCTION

Three dimensional (3D) fiber woven preform reinforced ceramic composites (3D-CMC) are of good resistance to impact, to fracture and to damage due to continuous fiber in the thickness direction which can strengthen the properties in the direction. Some of them, such as 3D preform reinforced carbon matrix (3D-C/C) or SiC matrix (3D-C/SiC), attract much attention during the last decade[1-4]. However, the oxidation of 3D-C/C at elevated temperature limits its structural application. Therefore, 3D-C/SiC, prepared with precursor pyrolysis, was studied in pursuit of obtaining a good resistance to oxidation. Unfortunately, the antioxidation of 3D-

C/SiC is not as good as desired because in this type of composite the SiC matrix prepared from polycarbosilane (PCS) pyrolysis contains some Si-O-C structures and some free carbon[1]. On the one hand, these impurities limit the improvement of the resistance to oxidation at elevated temperature; on the other hand, the porosity from PCS pyrolysis inside 3D-C/SiC facilitates the oxidation. So, it is also necessary to improve the behaviors at elevated temperature of this type of composite.

The aim of the present paper is to find a way to prevent the carbon fiber and the impure compositions in 3D-C/SiC from oxidation at elevated temperature. A 3D-C/SiC/Al<sub>2</sub>O<sub>3</sub> composite system was developed for this. The Al<sub>2</sub>O<sub>3</sub> matrix, prepared with sol-gel method and located on the outer layer of the 3D-C/SiC, can enhance the capacity to resist oxidation at high temperature of the composite. The precessing can be stated as follows.

A 3D woven preform impregnated with a mixture of PCS and divinyl benzene (DVB) was heated to cure the mixture solution, and then pyrolyzed under N<sub>2</sub> atmosphere protection in order to transform the cured system into SiC matrix and to forme a composite 3D-C/SiC. After certain densification cycles, the composite 3D-C/SiC was then impregnated with a sol prepared by aluminium isopropoxide, deionized water and hydrochloric acid. Under controlled conditions, the sol impregnating the composite was gelatinized and pyrolyzed into alpha-Al<sub>2</sub>O<sub>3</sub> matrix. After several repetition cycles for densification, a three-dimensional carbon fiber woven preform reinforced SiC and Al<sub>2</sub>O<sub>3</sub> hybrid matrix composite (3D-C/SiC/Al<sub>2</sub>O<sub>3</sub>) was prepared.

The 3D-C/SiC/Al<sub>2</sub>O<sub>3</sub> composite presents some properties that are different from those of its 3D-C/SiC counterpart. The former has a lower porosity and a higher density than the latter for the same fiber and SiC volume fraction and SiC. The two composites are of an almost same three-point flexural strength at room temperature (about 400 MPa), however, the three-point flexural strength at an elevated temperature (1300 °C) of the former (155 MPa) is much higher than that of the latter (100 MPa), although the measuring conditions for the former are much more severe than those for the latter.

## EXPERIMENT

### Raw materials

The woven preform used in the present paper is a type of three dimensional braid textile structure, of which the fiber volume fraction  $V_f$  ratio in the three principle material directions x, y and z, i.e.,  $(V_f)_x : (V_f)_y : (V_f)_z = 6:1:1$ , which was fabricated by Tianjing Institute of Textile Technology (China).

Two precursor solutions were used in the present paper. One is composed of a mixture of PCS and DVB. PCS is synthesized by the Department of Materials Engineering and Applied Chemistry at NUDT. DVB is provided by Zhuzhou Chemical & Industrial Factory. The composition of the mixture is 100 parts of PCS and 40 parts of DVB (by weight). The other precursor impregnating solution is an alumina sol which is prepared according to the method published in[5].

The principal raw materials used in the present paper are shown in Table 1.

Table 1: Raw materials for preparing the precursors

	Manufacturer	Properties
Carbon fiber	Jilin Carbon Factory	Diameter: 7-10 Density: 1.76g/cm <sup>3</sup> Tensile strength: 4220MPa
Polycarbonsilane	NUDT	Molecular weight: 1200 ~ 1300 Soft point: 165 ~ 175 °C

**Preparation of 3D-C/SiC and 3D-C/SiC/Al<sub>2</sub>O<sub>3</sub> composites**

*Preparation of 3D-C/SiC.* First, The 3D preform is tailored, in which the carbon fiber must be treated with certain ways. Second, the tailored and treated 3D preform is impregnated with the PCS/DVB solution previously prepared. Then, the system above mentioned can be heated from room temperature to 120 °C for two hours in order to cure the PCS/DVB system and to form the 3D preform, which can be considered as a green body. Finally, after the curing, the green body can be pyrolyzed from room temperature to 1100 °C under N<sub>2</sub> atmosphere protection and controlled heating program. In order to control the porosity, the impregnating-pyrolyzing repetition cycles can be effected for several times. So, a dense 3D-C/SiC composite can be prepared. The processing can be shown in Fig. 1.

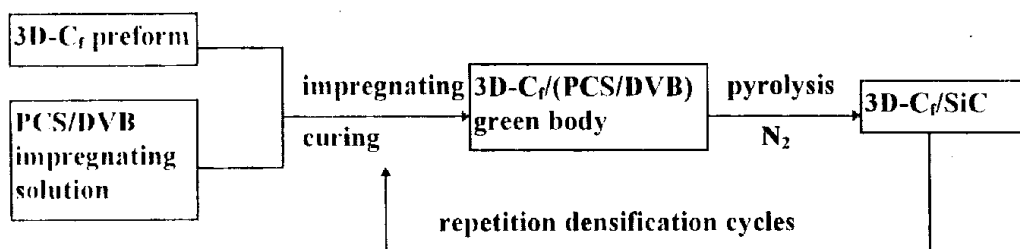


Fig. 1: Processing of 3D-C/SiC preparation

*Preparation of 3D-C/SiC/Al<sub>2</sub>O<sub>3</sub>.* The 3D-C/SiC composite above prepared can then be impregnated with a sol prepared by aluminium isopropoxide, deionized water and hydrochloric acid. Under controlled conditions, the sol impregnating the composite was gelatinized and

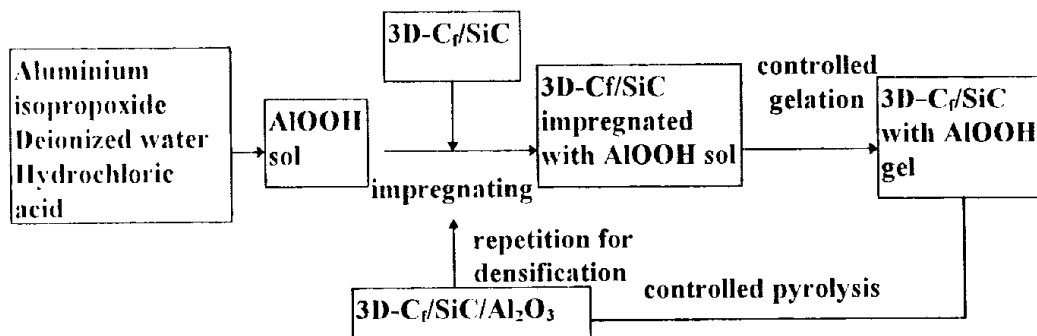


Fig. 2: Processing of 3D-C/SiC/Al<sub>2</sub>O<sub>3</sub> preparation

pyrolyzed into alpha- $\text{Al}_2\text{O}_3$  matrix under  $\text{N}_2$  atmosphere protection from room temperature to  $1260^\circ\text{C}$ . After several repetition cycles for densification, a three-dimensional carbon fiber woven preform reinforced SiC and  $\text{Al}_2\text{O}_3$  hybrid matrix composite (3D-C/SiC/ $\text{Al}_2\text{O}_3$ ) was prepared. The processing can be shown in Fig. 2.

*Measurement of the composite materials.* The composite material specimens are cut with a diamond tool, which have a width of 5-6 mm, a height of 3.2-3.5 mm. The ratio of the span to height for three point flexural test is 12-15. The three point flexural tests at room and elevated temperatures ( $1300^\circ\text{C}$ ) are effected in a New 810 MTS testing system. The tensile speed is about 0.2 mm/min. All of the data are acquired by a PC computer equipped with an acquirement program.

## RESULTS AND DISCUSSIONS

### Results

The essential parameters of the 3D-C/SiC and 3D-C/SiC/ $\text{Al}_2\text{O}_3$  composite materials are shown in Table 2. And the three point flexural test results are shown in Table 3.

Table 2: Essential parameters of the composite materials

code	composite type	$V_f(\%)$	$V_{\text{SiC}}(\%)$	$V_{\text{Al}_2\text{O}_3}(\%)$	$V_p(\%)$	$\rho$ (g/cm <sup>3</sup> )
CM I	3D-C/SiC	54.0	28.4	0	17.6	1.66
CM II	3D-C/SiC/ $\text{Al}_2\text{O}_3$	54.0	28.4	3.8	13.8	1.81

$V$  stands for the volume fraction;

Indices  $f$ , SiC,  $\text{Al}_2\text{O}_3$  and  $p$  stand for fiber, SiC,  $\text{Al}_2\text{O}_3$  and porosity, respectively;

$\rho$  means the density of the composite materials.

Table 3: Three point flexural ( $\sigma_{3b}$ ) test results

code	composite type	measuring conditions	$\sigma_{3b}$ (MPa)	$(\sigma_{3b})_{\text{RT}}/(\sigma_{3b})_{1300^\circ\text{C}}$ (%)
CM I	3D-C/SiC	Room temperature	386.0	100.0
		$1300^\circ\text{C}$ *	100.5	25.9
CM II	3D-C/SiC/ $\text{Al}_2\text{O}_3$	Room temperature	396.4	100.0
		$1300^\circ\text{C}$ **	155.3	39.1

\* Heating from room temperature to  $1300^\circ\text{C}$  during 25 minutes, and measuring the specimens in air immediately.

\*\* Heating from room temperature to  $1300^\circ\text{C}$  during 25 minutes, holding for 5 minutes at  $1300^\circ\text{C}$  and measuring the specimens in air immediately.

### Comparison of the strengths at room temperature between CMI and CMII

It can be seen from Table 3 that the three point flexural strength of CMII (396 MPa) is slightly higher than that of CMI (386 MPa). This means that the processing shown in Fig.2 does not cause a strength and other property degradation of the composite. A slight strength

improvement of the CMII is possibly due to its higher density.

### Comparison of the strengths at 1300°C between CMI and CMII

It can be also seen from Table 3 that the strength at 1300°C of the CMI (100.5MPa, 25.9% of  $\sigma_{3b}$  at room temperature) is much lower than that of CMII (155.3 MPa, 39.1% of  $\sigma_{3b}$  at room temperature). It can be observed after measuring at 1300°C that the two types of composites present an obvious ablative appearance. The type of CMI, seriously ablated, of which the weight loss is much greater than that of CMII, is fractured into two small pieces. On the contrary, the type of CMII, slightly ablated, of which the weight loss is much slighter than that of CMI, is not separated into two pieces. This is possibly due to  $Al_2O_3$  matrix existing on the outside of the composite, which can play a protecting role at higher temperature for the uncovered fibers and the impurities in the composites. According to the research work [6,7], as a coating on carbon fiber, it is clear that  $Al_2O_3$  can prevent carbon fiber from oxidation at 1300°C. However, this protecting role is limited, because many factors can cause a strength degradation at higher temperature: 1) structural changes of carbon fibers; 2) chemical reactions between the free carbon and the Si-O-C structures in SiC matrix (by PCS pyrolysis); 3) reactions between oxygen in air and carbon fiber throughout the interphases, porosity and uncovered fibers. It is obvious that the last factor is the main one. The shrinkage caused by crystal transformation during pyrolysis of  $Al_2O_3$  and SiC, and the thermal mismatch among  $Al_2O_3$ , carbon fibers and SiC can reduce the protecting effect. Therefore, the mechanism of strength increase at 1300°C for CMII compared to its counterpart needs to be further studied.

### CONCLUSIONS

With PCS pyrolysis and  $AlOOH$  sol-gel pyrolysis transformation methods, the 3D-C/SiC composite and 3D-C/SiC/ $Al_2O_3$  hybrid matrix composite can be prepared.

The 3D-C/SiC/ $Al_2O_3$  composite displays some properties that are different from those of its 3D-C/SiC counterpart. The former has a lower porosity and a higher density than the latter for the same volumetric fractions of fibers and SiC. The two composites are of an almost same three-point flexural strength at room temperature (about 400 MPa), however, the three-point flexural strength at an elevated temperature (1300°C) of the former (155 MPa) is much higher than that of the latter (100 MPa), although the measuring conditions for the former are much more severe than those for the latter. The mechanism of strength increase at 1300°C for the former compared to its counterpart (the latter) needs to be further studied.

### REFERENCES

1. Toshikatsu, I., "Recent Developments of the SiC Fiber Nicalon and its Composites, including Properties of the SiC Fiber Hi-Nicalon for Ultra-high Temperature", *Composites Science and Technology*, vol.51, 1994, pp.135-144.
2. Tanaka, T. et al., "Fabrication and Evaluation of 3D-dimensional Tyranno Fiber Reinforced SiC Composites by Repeated Infiltration of Polycarbosilane", *Journal of Ceramic Society of Japan*, vol.103, No.1, 1995, pp.1-5.

3. Itoh, K. et al., "Pulsed Chemical Vapour Infiltration of SiC to Three-dimensional Carbon Fiber Preform", *Journal of Material Science*, vol.27, 1992, pp.6022-6028.
4. Fengrong Liu, Jiayu Xiao, Xingye Wang et al., "Fabrication of Carbon Fiber Reinforced SiC Matrix Composite by Polycarbosilane Pyrolysis" (in Chinese), *Research report*, Department of Material Engineering and Applied Chemistry, NUDT, July 1995.
5. Yoldas, B. E., "Alumina Sol Preparation from Alkoxides", *American Ceramic Bulletin*, vol.54, No.3, 1975, pp.289-293.
6. Fengrong Liu, Qing Luo, Jiayu Xiao, et al., "The Effect of Serveral Carbon Fibers on the Behaviours of Carbon Fibers/SiC Matrix Composites" (in Chinese), *Proceedings of NCCM/9 of China*, vol.2, Aug 1996, pp.356-359.
7. Yong Meng, "Coating on Carbon Fiber Surfaces" (in Chinese), *Thesis of Bachelor Degree* (adviser: Professor Jiayu Xiao), Department of Material Engineering and Applied Chemistry, . NUDT, June 1995.



# CONTINUOUS FIBRE REINFORCED COMPOSITES WITH MULLITE MATRIX DERIVED FROM COLLOIDAL PRECURSORS

Jaili Wu, Frank R. Jones and Peter F. James

*Department of Engineering Materials, Sir Robert Hadfield Building, Mappin Street  
University of Sheffield, Sheffield S1 3JD England UK*

**SUMMARY:** In this paper, the preparation of carbon and SiC continuous fibre reinforced composites with mullite matrix derived from colloidal-size alumina powder and silica colloids is described. The prepregs was prepared by one infiltration of a fibre tow with high solids yield colloidal sols of 40 vol% containing an oxide composition corresponding stoichiometric mullite,  $3\text{Al}_2\text{O}_3 \cdot 2\text{SiO}_2$ . The composites were consolidated by hot-pressing at 1550 °C for 0.5 h at 15 MPa to form dense mullite matrix. The microstructures of the unidirectional composites were characterised by XRD and SEM. The structure of the interfaces was examined by TEM. The properties of the composites: flexural strength, modulus and work of fracture were measured by three point bending.

**KEYWORDS:** SiC, carbon, continuous fibre, colloidal, mullite, matrix, composites, unidirectional, mechanical properties, interface

## INTRODUCTION

Continuous fibre reinforced ceramic matrix composites have been extensively investigated for the improvement of the strength and toughness of ceramics, which can be used as structural materials at high temperatures. Densification of the ceramic matrix and control of the interface between fibre and matrix are vital in the production of composites with useful properties [1, 2]. Mullite combines excellent strength and creep resistance at high temperatures with good chemical and thermal stability and a low thermal expansion coefficient of  $4.5\text{-}5.6 \times 10^{-6} \text{ K}^{-1}$  [3]. Therefore, mullite-containing composites have a potential as a high performance material [4]. In previous work [5-7] it was shown that a sol containing 40% solids by volume, of the mullite composition,  $3\text{Al}_2\text{O}_3 \cdot 2\text{SiO}_2$ , could be prepared using  $\alpha$ -alumina powder and colloidal silica sol. This sol was transformed into a gel from which a mullite monolith was obtained by pressureless sintering at 1600°C for 2 h. A density of  $3.10 \times 10^3 \text{ kg / m}^3$  for the bulk sample was obtained, which corresponds to 98% of the theoretical density of  $3.17 \times 10^3 \text{ kg / m}^3$  for mullite. The microstructures of the bulk materials have been characterised and the densification mechanism analysed [6, 7]. It was demonstrated that a unidirectional carbon fibre reinforced crystalline mullite matrix composite could be fabricated by one infiltration with this sol and consolidated by hot-pressing [5].

In this paper, the fabrication of composites using colloidal precursors for a mullite matrix is described, in which either high strength carbon or Nicalon silicon carbide fibres were

employed as the reinforcement. The matrix was stoichiometric mullite,  $3\text{Al}_2\text{O}_3 \cdot 2\text{SiO}_2$ . The microstructures of the composites were characterised by X-ray diffraction (XRD) and scanning electron microscopy (SEM). The fibre-matrix interfacial characteristics were examined by TEM and related to the properties, fracture behaviour and processing conditions of the composites.

## **EXPERIMENTAL**

Prepregs of the unidirectional fibre reinforced mullite matrix composite samples were prepared by the single-stage infiltration of the fibre tows with a colloidal sol corresponding to an oxide composition of  $3\text{Al}_2\text{O}_3 \cdot 2\text{SiO}_2$ , which has been described elsewhere [5], using Ludox colloidal aqueous silica sol (Dupont AS40, 40 wt% of silica particles of 5-50 nm in diameter) and  $\alpha$ -alumina powder (Alcoa A1000 SG, with an average size of 0.5  $\mu\text{m}$ ) as starting materials. Briefly, the as-received  $\alpha$ -alumina powder was dispersed in Ludox colloidal silica sol to produce a homogenous sol. The viscosity of the sol was sufficiently low for the efficient impregnation of the fibre tow. The high solids concentration (alumina-silica mixture) of 40 vol% (68 wt%) enabled single-stage infiltration to be employed for the formation of a dense matrix.

Grafil LXA unsized high strength continuous carbon fibre tow has a diameter of 8  $\mu\text{m}$ , a strength of 4 GPa, an elastic modulus of 224 GPa, a ultimate strain of 1.78% and an average density of  $1.81 \times 10^3 \text{ kg / m}^3$ . The Nicalon-207 silicon carbide is a polyvinyl alcohol sized continuous fibre yarn which has a strength of 2.6 GPa, an elastic modulus of 189 GPa, a ultimate strain of 1.37%, an average density of  $2.55 \times 10^3 \text{ kg / m}^3$  and a diameter of 14  $\mu\text{m}$ . Nicalon-207 SiC polyvinyl alcohol sized fibre yarn was de-sized by passing through hot water at 90 °C, and then stored in vacuum ready for the preparation of the composites.

The composite prepregs were fabricated by infiltrating the continuous fibres using the above sols without additional binder in a single stage. The prepreg was dried in air at room temperature for 48 h and in an oven at 90°C for a further 48 h. By careful control of the solids concentration, composites with a fibre volume fraction in the range of 30-60% could be prepared. In the graphite die assembly, the composite stack of prepregs was sealed by two thick layers of graphite powder to ensure that a reducing atmosphere of CO existed during hot-pressing. The composite samples were consolidated by hot-pressing at 1550°C, for 0.5 h at 15 MPa for the formation of the mullite matrix. All hot-pressed composite samples were allowed to cool naturally to room temperature overnight within the furnace.

The densities of the composite samples,  $\rho_c$  were determined by mercury porosimetry using a Micromeritics Pore Size 9320 with a pressure range of ~174 MPa. The volume fraction of fibres in the composites and the crack spacing in the polished surface of the composites were determined by computer-controlled image analysis using an AMS OPTOMAX V. The maximum theoretical density of each composite (assuming no porosity),  $\rho_{0c}$  was calculated using the following equation:

$$\rho_{0c} = V_m \rho_m + V_f \rho_f \quad (1)$$

where  $\rho_m$  is the theoretical density of matrix;  $\rho_f$  is the theoretical density of fibre;  $V_f$  is the measured volume fraction of fibre in composite; and  $V_m$  is the measured volume fraction of matrix in composite. The phases present in the matrix of the composites were identified by XRD on a Philips 1710 X-ray Diffractometer with the scanning speed of  $2^\circ (2\theta)/\text{min}$ . SEM was performed on a JEOL JSM6400. TEM was performed on a Philips EM400T. Thin sections for TEM were prepared by ion beam milling a specimen which had been mechanically dimpled to less than  $30 \mu\text{m}$  in thickness using fine grinding paste.

The flexural strengths, flexural moduli, and work of the fracture of the composites at room temperature were determined in three point bend on a Mayes Universal Tester at a displacement rate of  $0.2 \text{ mm/min}$ . The span of the lower support pins was  $30 \text{ mm}$ , and a span to specimen thickness ratio greater than 20 was employed. Rectangular test specimens cut from hot-pressed cylindrical composite samples were ground and polished to the dimensions of  $37 \text{ mm}$  in length,  $2.0 \text{ mm}$  in width and  $1.5 \text{ mm}$  in thickness. The load-deflection curve for the composites was recorded to fracture. The mechanism of failure was identified by visual examination after the test and by SEM examination of the fracture surface of tested specimens.

The flexural strengths and moduli were determined according to British Standard Methods of Testing (10). The work of fracture was calculated from the area under the load-deflection curve. The ultimate failure strain,  $\epsilon$ , was calculated by an approximate eqn. (7).

## RESULTS

### Microstructures of Composites

Figure 1 shows the XRD pattern for the hot-pressed carbon fibre composites hot-pressed at  $1550^\circ\text{C}$ , for  $0.5 \text{ h}$  at  $15 \text{ MPa}$ . The composite matrix is predominantly crystalline mullite, although a trace of unreacted alumina is evident. For the SiC/M composite hot pressed under the same conditions as the C/M composite, XRD gave a similar result as in Fig. 1. Fig. 2 shows a polished section through the C/M composite approximately parallel to the fibre direction. A dense mullite matrix with a uniform distribution of carbon fibres ( $V_f=0.52$ ) was revealed. No large pores were observed, which was consistent with the measured density of 95% of the calculated theoretical density of  $2.46 \times 10^3 \text{ kg/m}^3$  for the composite. Mechanical polishing resulted in some degree of damage or "pluck-out" at the fibre-matrix interface (white areas indicated by arrows) suggesting that little or no chemical bonding had occurred. Some regularly spaced microcracks were observed in the matrix, which are perpendicular to the fibre direction in fig. 2, which are believed to be induced by thermal mismatch between the fibres and mullite matrix. Thermally induced cracks are produced by stresses resulting from a mismatch in the expansion coefficients of the carbon fibres and the mullite matrix on cooling from the high processing temperature to room temperature. The measured thermal expansion coefficient is  $4.83 \times 10^{-6} \text{ K}^{-1}$  for the bulk samples of mullite and that of the carbon fibres is about zero [8]. The thermally induced cracks and the interfacial pores are believed to be the main contributors to the 5% porosity within the C/M composite.

The thermal expansion coefficient for the SiC fibres at  $4.0\text{-}5.0 \times 10^{-6} \text{ K}^{-1}$  [8] is similar in magnitude to that of mullite. Thus, the potential for thermal mismatch cracking in the SiC/mullite composites is much lower as suggested by the observation of few cracks in a

random polished section through the SiC/M composite (not shown). A polished section perpendicular to the fibre direction (Fig. 3) shows that some fibres were in contact.

### **Fibre/matrix Interfaces in Composites**

The interfaces between the fibre and matrix in the composites were examined by TEM as shown in Fig. 4. A sharply defined interface was observed between the carbon fibre and the mullite matrix in the C/M composite (not shown). Some crevices appear to occur along the interface which would further weaken the interfacial bonding. The crevices are believed to be the consequence of the thermal expansion mismatch between fibre and matrix during cooling. No obvious chemical interaction between fibre and matrix was evident. Some mullite grains near the fibre surface were observed to have grown parallel to the fibre direction. Dislocations were also observed in the mullite grains or along grain boundaries. Evidence for a thin continuous interfacial layer between the SiC fibres and the mullite matrix in the SiC/M composite was revealed by TEM (Fig. 4). Energy dispersive spectroscopy (EDS) [7] indicated the layer mainly consisted of silica and carbon (amorphous or crystallised). It is possible that the SiC fibre degraded to form a silica layer at high temperatures.

### **Densification and Mullitisation of Composite Matrices**

Highly densified composites were produced including C/M, and SiC/M which have densities ranging from 95 to 98% of the theoretical density (Table 1). Glass viscous sintering is the main matrix densification mechanism as discussed previously (5-7). From XRD and TEM analysis, substantial mullitisation (approximately 90% or more by volume) could be achieved in the matrix. Complete mullitisation was not achieved at 1550 °C for 0.5 h because of the slowness of the interdiffusion processes [9].

During the three point bending test, most of the composites initially showed an elastic response with deflection increasing linearly with increase in load, followed by an extended non-elastic regime. Generally after the maximum value of load was reached, the degree of subsequent extension was strongly dependent on the nature of the interface between fibre and matrix. Figure 5 is representative examples of the stress vs. deflection curves for the carbon fibre mullite composite, C/M and SiC fibre mullite composite, SiC/M, compared with typical results for the matrix materials alone (dotted lines). A summary of hot-pressing parameters together with the properties of the composites is given in Table 1.  $V_f$  is the measured fibre volume fraction,  $\rho_c/\rho_{c0}$  the ratio of measured to theoretical density expressed as a percentage,  $\sigma$  the ultimate flexural strength,  $E$  the flexural modulus,  $W$  the work of fracture, and  $\varepsilon$  the ultimate failure strain.  $\sigma_c$  and  $E_c$  are the ultimate tensile strength and the modulus of the composites calculated theoretically according to theory [11]. In the flexural test, employed here, only the outside surface experiences a maximum stress. All failures were initiated on the tensile face of the specimen.

Referring to Table 1, the highest average flexural strength ( $737\pm 128$  MPa) was observed for the carbon fibre reinforced mullite matrix composite hot pressed at 1550 °C for 0.5 h at 15 MPa (C/M). This composite also exhibited the highest work of fracture,  $482\pm 122$  kJ/m<sup>2</sup>, and ultimate failure strain of  $0.37\pm 0.13\%$ . These values were considerably higher than those for unreinforced bulk mullite of 150 MPa for  $\sigma$ , 5.18 kJ/m<sup>2</sup> for work of fracture and 0.001% for  $\varepsilon$  [11]. Samples of bulk mullite were prepared by pressureless sintering of gels of  $\alpha$ -alumina and Ludox silica at 1600 °C for 2 h to  $3.1\times 10^3$  kg/m<sup>3</sup>, approximately 98% of the theoretical

density for mullite,  $3.17 \times 10^3 \text{ kg/m}^3$  [9]. The SiC fibre mullite matrix composite (SiC/M) hot pressed at  $1550 \text{ }^\circ\text{C}$  for 0.5 h also had a high strength,  $\sigma$  of  $630 \pm 98 \text{ MPa}$ ,  $W$  of  $293 \pm 111 \text{ kJ/m}^2$ , and  $\epsilon$  of  $0.30 \pm 0.1\%$ .

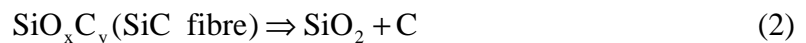
### Fracture Surfaces Observations

The nature of the fibre/matrix interface can be also revealed by examining the fracture surfaces of composite specimens after the three point test. Extensive fibre pull-out was observed in the fracture surfaces of both carbon fibre and SiC fibre reinforce mullite matrix composites. A typical fracture surface of SEM micrograph from SiC composite is shown in Fig. 6.

## DISCUSSION

### Strengths and Ultimate Failure Strains

In comparison with the bulk unreinforced matrix materials, all the composites demonstrated an enhanced flexural strength and a change in their fracture behaviour. The flexural strength of these materials correlate directly with the quality of the interfacial bond strength. As expected those materials with a weak interface exhibited tough behaviour (Table 1). However, there is a discrepancy between the experimental values and the theoretical predictions based on the mixture laws (Table 1). The experimental values of strength are lower than the theoretical predictions even assuming that there are no contributions from the matrices. Thus, other parameter needs to be considered. When exposed to high temperatures, carbon fibres oxidise, and the composition and structure of SiC fibres change. Consequently the retained strength of the fibres is affected and also the strength of the composite. Nicalon-SiC fibres generally show reaction even in a reducing atmosphere [12, 13] as follows:



The reduction in strength above  $1000 \text{ }^\circ\text{C}$  is caused by microcrystallisation of the fibre structure [12], although the degradation can be alleviated by employing reducing atmospheres [13]. Both a silica phase and the presence of carbon have been detected in the interfacial regions within the SiC/M composite using EDS [7], which are believed to be the products of the above reaction. A severe reduction in the strength of the SiC composites because of the high processing temperatures was also observed, however the longer processing time at  $1550 \text{ }^\circ\text{C}$  was not necessary to lead to a reduction in the SiC fibre strength according to the Raman spectroscopy analysis on the SiC fibre composite specimen [14].

### Interfaces, Fracture Behaviour and Fibre Pull-out

A glassy silica phase in the interfacial regions between the SiC fibres and matrices of the SiC/M was observed by TEM and defined by EDS. Silica is expected to form on the fibre surface as a product of reaction in equ. 2. A weak interface was observed for the SiC fibre/mullite composite, SiC/M hot-pressed for 0.5 h as shown by the extensive fibre pull-out after the bending test (Fig. 6). In this case the interfacial glass layer between the fibres and matrix in the composite may not be sufficiently thick to form a strong bond.

The influence of the porosity of the composites on the nature of the interface should also be considered. From SEM and TEM observations, some pores and crevices were detected along the interfacial region between the fibres and the mullite matrix within C/M. These pores may have resulted partly from incomplete densification and partly from the volume change during the mullitisation in the matrix, and the crevices may have formed as a result of a relative displacement between fibre and matrix on cooling from high temperature because of thermal expansion mismatch. These pores and crevices could contribute to the weak interfacial bonding, resulting in extensive fibre pull-out on failure (Fig. 5) with a substantial failure strain of  $0.37\pm 0.13\%$ .

## CONCLUSIONS

Carbon fibre and SiC fibre continuous reinforced mullite matrix composites were successfully fabricated by colloidal processing, using  $\alpha$ -alumina powder and colloidal silica sol as precursors by one stage infiltration followed by hot-pressing at 1550 °C. Highly densified composites were obtained.

The microstructures of the composites were examined by SEM and TEM. Parallel cracks were observed in the carbon fibre reinforced composites, resulting from thermal expansion mismatch. For the C/M composite a sharply defined interface with little sign of interaction was observed between carbon fibres and mullite matrix, and some crevices were also observed along the interface. A highly densified and nearly crack-free mullite matrix was observed in the SiC/mullite composite, SiC/M. For this composite a thin continuous interfacial silica layer was also observed by TEM and EDS, which may result from reaction at the SiC fibre surface at high temperatures.

Using the three point bending test, the properties of the composites were determined. The highest flexural strength of  $737\pm 128$  MPa, with the highest work of fracture,  $482\pm 122$  kJ/m<sup>2</sup>, and ultimate failure strain of  $0.37\pm 0.13\%$  were achieved for the C/M. The SiC/M also had a high  $\sigma$  of  $630\pm 98$  MPa,  $W$  of  $293\pm 111$  kJ/m<sup>2</sup>,  $\epsilon$  of  $0.30\pm 0.1\%$ . The fibre reinforcement to mullite is highly effective.

The amount of silica phase along the interface between SiC fibre and matrix is thought to be the main factor controlling the interfacial bonding strength in the SiC fibre composites. The thin silica layer at the interface as shown by TEM and EDS for the SiC/M composite may be account for the relatively weak interfacial bonding observed.

## REFERENCES

1. Sheppard, L.M. "Enhancing Performance of Ceramic Composites," *Am. Ceram. Soc. Bull.*, Vol. 71 1992, pp617.
2. Cornie, J.A., Chiang, Y.M., Uhlmann, D.R., Mortensen, A. and Collins, J.M., "Processing of Metal and Ceramic Matrix Composites," *Am. Ceram. Soc. Bull.*, Vol. 65 1986, pp293.
3. Hawkes, W.H., "The Production of Synthetic Mullite," *Trans. Brit. Ceram. Soc.*, Vol. 61 1962, pp689.
4. Sacks, M.D., Lee, H.W. and Pask, J.A., "A Review of Powder Preparation Methods and Densification Procedures For Fabricating High Density Mullite," *Ceram. Trans.* Vol. 6.

- Mullite and Mullite Matrix Composites, Edited by S. Somiya, R.F. Davis, J.A. Pask, 1990, pp167.
5. Wu, J., Jones, F.R. and James, P.F., "Mullite Matrix Continuous Fibre Reinforced Composites by Sol-gel Processing", *Ceram. Trans.*, Vol. 46: Advances in Ceramic Matrix Composites II, 1995, pp177.
  6. Wu, J., Chen, M., Jones, F.R. and James, P.F., "Characterisation of sol-gel derived alumina-silica matrices for continuous fibre reinforced composites", *J. Euro. Ceram. Soc.* Vol. 16 1996, pp619.
  7. Wu, J., PhD thesis, University of Sheffield 1995.
  8. Prewo, K., "Fiber-Reinforced Ceramics: New Opportunities for Composite Materials", *Am. Ceram. Soc. Bull.*, Vol. 68 1989, pp395.
  9. Pask, J.A., Zhang, X.M., Tomsia, A.P. and Yoldas, B.E., "Effect on Sol-Gel Mixing on Mullite Microstructure and Phase Equilibria in the  $\alpha$ -Al<sub>2</sub>O<sub>3</sub> – SiO<sub>2</sub> System", *J. Am. Ceram. Soc.*, Vol. 70 1987, pp704.
  10. British Standard Methods of Testing, "Method 1005, Determination of flexural properties--Three point method", (British Standards Institution) BS 2782: Part 10: Method 1005, EN63 1977.
  11. Kelly, A., *Strong Solids*, Clarendon Press, Oxford, 2nd Ed, 1973.
  12. Simon, G. and Bunsell, A.R., "Creep behaviour and structural characterisation at high temperatures of Nicalon SiC fibres", *J. Mater. Sci.*, Vol. 19, 1984, pp3658.
  13. Bender, B.A., Wallace, J.S. and Schrodt, D.J., "Effect of thermochemical treatments on the strength and microstructure of SiC fibres", *J. Mater. Sci.*, Vol. 26, 1991, pp970.
  14. Wu, J. and Colomban, Ph., "Raman spectroscopy study on continuous fibre reinforced ceramic matrix composites", in *J. Raman Spectrosc.* to be published..

Table 1: Summary of the hot-pressing conditions and properties of composites

Hot-pressing parameter	1550 °C 0.5 h 15 MPa	1550 °C 0.5 h 15 MPa
Fibre/Matrix	SiC/M	C/M
Number tested	6	6
$V_f$ ( $\pm 2\%$ )	60	52
$\rho_c/\rho_{c0}$ (%)	98	95
$\sigma$ (MPa)	630 $\pm$ 98	737 $\pm$ 128
$E$ (GPa)	208 $\pm$ 11	127 $\pm$ 64
$W$ (kJ / m <sup>2</sup> )	293 $\pm$ 111	482 $\pm$ 122
$\sigma_c$ (GPa)	1.6	2.2
$E_c$ (GPa)	149	160

$\pm$ : standard deviation

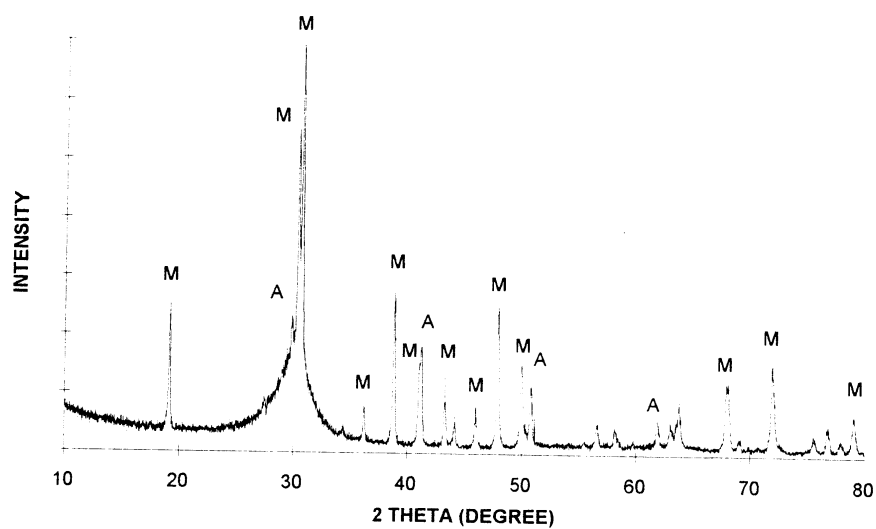


*Figure 1: XRD of mullite matrix carbon fibre reinforced composites of C/M hot-pressed at 1550 °C for 0.5 h at 15 MPa*

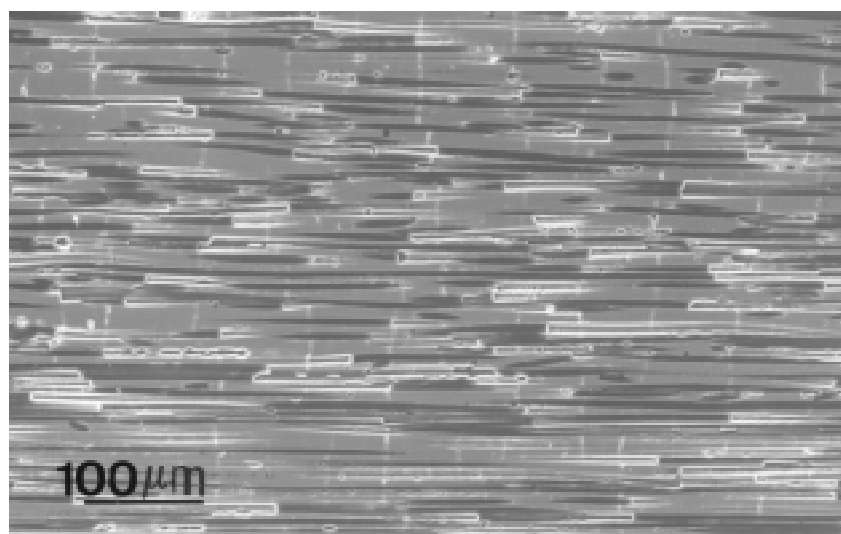


*Figure 2: SEM of polished section parallel to the fibre direction through the C/M composite hot-pressed at 1550 °C for 0.5 h at 15 MPa*



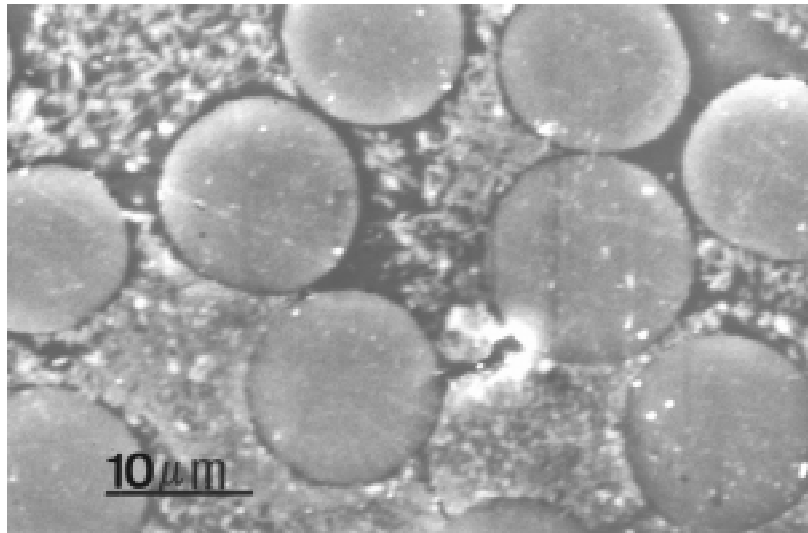


*Figure 3: SEM of polished cross section perpendicular to the fibre direction through the SiC/M composite hot-pressed at 1550 °C for 0.5 h at 15 MPa*

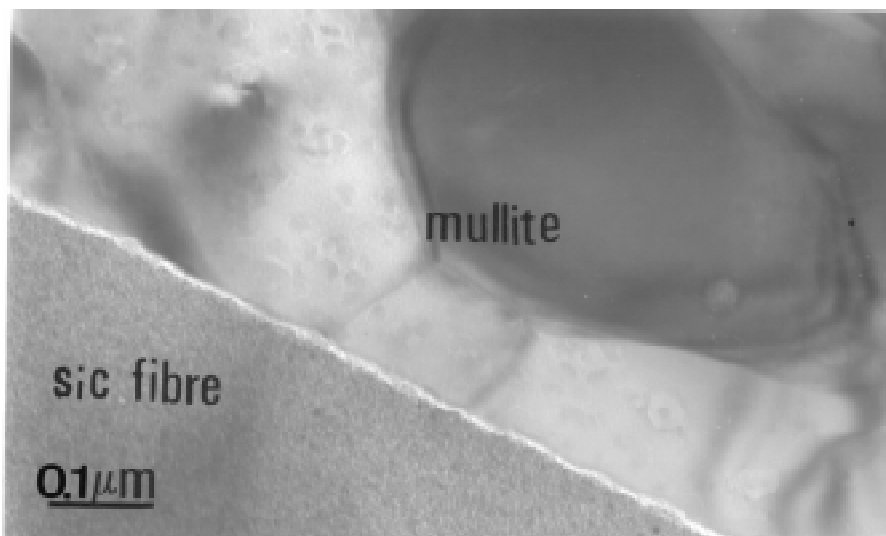


*Figure 4: TEM of the interfacial structure between fibre and matrix for the mullite matrix Nicalon-SiC fibre reinforced composite, SiC/M hot-pressed at 1550 °C for 0.5 h at 15 MPa*

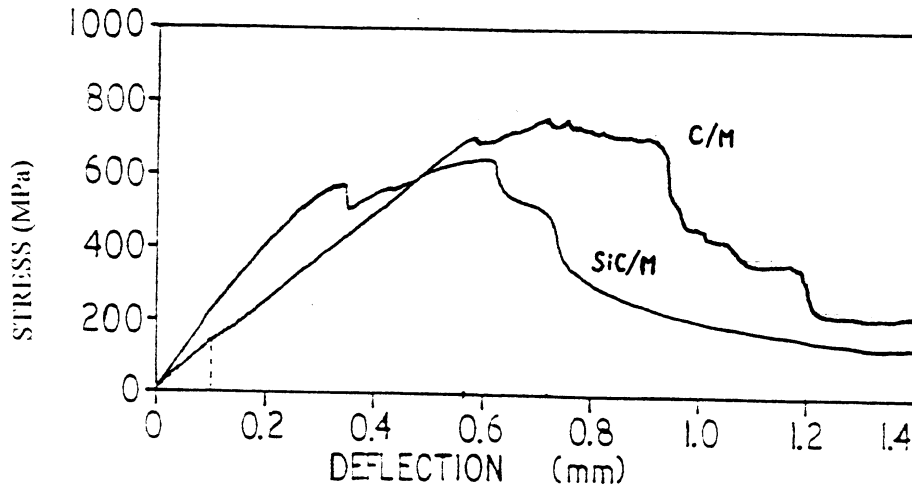


Figure 5: Typical load vs. deflection plots tested by three-point-bending; behaviour of matrix shown by dotted curves. C/M: Carbon fibre mullite composite C/M, SiC/M: Nicalon-SiC fibre mullite composite

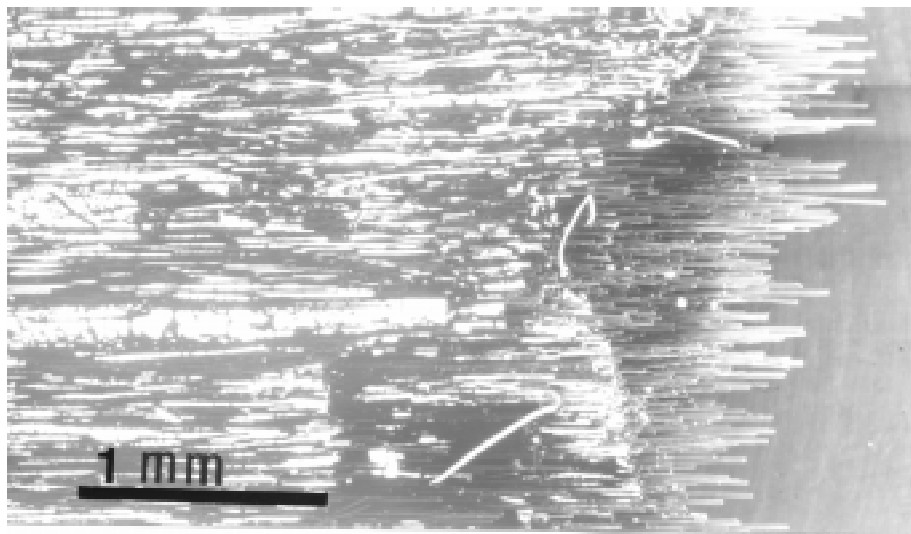


Figure 6: SEM of the fracture surface of SiC/M composite hot pressed at 1550 °C for 0.5 h at 15 MPa, parallel to the fibre direction

# MECHANICAL PROPERTIES OF SPIDER SILK

Sueo Kawabata<sup>1</sup>, Frank K. Ko<sup>2</sup>, Mari Inoue<sup>3</sup>, Masako Niwa<sup>3</sup> and John W. Song<sup>4</sup>

<sup>1</sup>*Department of Materials Sciences, University of Shiga Prefecture, Shiga, Japan*

<sup>2</sup>*Fibrous Materials Research Center, Department of Materials Engineering,  
Drexel University, Philadelphia, PA 19104, USA*

<sup>3</sup>*Nara Women University, Nara, Japan*

<sup>4</sup>*USArmy Natick Research and Development, Engineering Center, Natick, MA. USA*

**SUMMARY:** The mechanical properties of *Nephila clavipes* spider silk are presented to illustrate the unique combination of strength and toughness and the anisotropy of spider silk. The tensile properties of the silk of *Nephila clavipes* spider were characterized by simple elongation, transverse compression and torsion under various humidity conditions using an ultra-sensitive testing system. It was founded that, although the properties of the spider silks vary from species to species, they all have a high level of combined strength and toughness as well as shear resistance much greater than that of some of the toughest synthetic fibers such as the aramid fibers.

**KEYWORDS:** spider silk, tensile modulus, compressive modulus, shear modulus, micromasurement instrument, anisotropic properties, combined strength and toughness

## INTRODUCTION

Strength and toughness are usually considered mutually exclusive properties for materials. In spite of the progress made over the past century in polymeric fiber science and technologies, the search for a truly strong and tough fiber continues. It is of practical and scientific interest to explore the limit of strength and toughness of fibrous materials; and to examine the factors which contribute to the development of a combination of strength and toughness in materials. The answers to these questions may be found in nature.

In the world of natural fibers, spider silk has long been recognized as the wonder fiber for its unique combination of high strength and rupture elongation. An earlier study, as shown in Figure 1, indicated spider silk has strength as high as 1.75 GPa at a breaking elongation of over 26% [1]. With toughness more than three times that of aramid and industrial fibers, spider silk continues to attract the attention of fiber scientists and hobbyists alike.

Considering the remarkable mechano-chemical properties of spider silk and fueled by the recent progress in biotechnology, there is a revival of interest in using spider silk as a model for the engineering of high energy absorption fibers [2]. Because of the fineness of spider silk, on the order of 4 $\mu$ m, the characterization of the mechanical properties of spider silks are limited to tensile mode. Little is known about the response of spider silks to other modes of deformation in the transverse direction and in torsion. It is the objective of this paper to present, for the first time, the tensile, transverse compression and torsional stress-strain properties of the spider silk from *Nephila Clavipes* spiders. This was made possible by using

an ultra sensitive micromasurement fiber testing system developed by Kawabata [3]. From these experimental data, the engineering properties: tensile modulus, transverse compressive modulus, and shear modulus of the spider silk was determined.

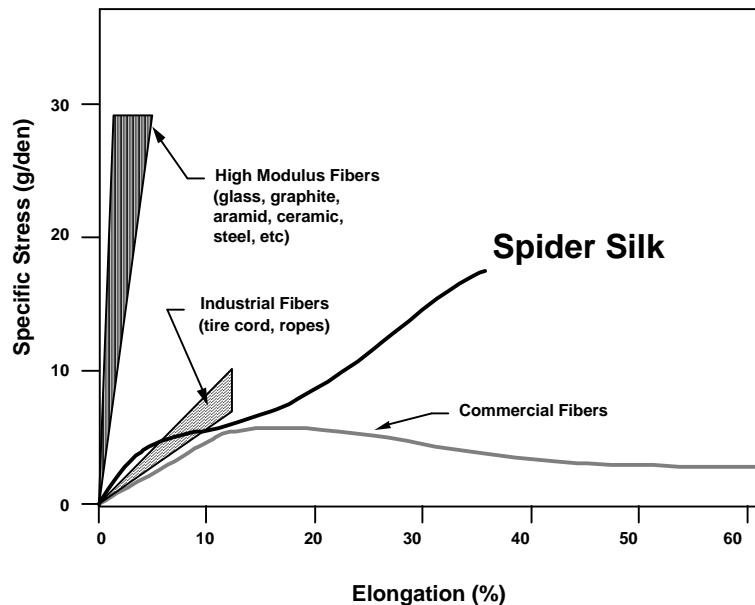


Figure 1: Tensile stress-strain behavior of *agiope aurentia* spider silk

### SPIDER SILK AND SPECIMEN PREPARATION

There are over one million species of spiders on earth. Less than one percent of the spiders are orb weavers or silk makers. Properties of spider silks vary by species and by functions. Depending upon the species an individual spider has more than five different silk glands where silks of different properties are produced before extrusion through three pairs of spinnerets. The drag line originates in the ampullate gland and is extruded through the anterior spinnerets. Spider drag line is the strongest and toughest of the silks a spider makes. Spider drag line is the structural framework of a spider web and the life line of a spider. Chemically spider silk is a fibroin composed of twenty-odd alpha amino acids connected by the amide linkage (-COHN-). Alanine, serine and proline account for eighty percent of the amino acids. Drag lines of *Nephila Clavipes* (golden silk spider) and *Argiope Aurentia* (black and yellow spider) are among the strongest spider silks that we know. The strength of the drag line of *Nephila Clavipes* obtained by forcible silking was reported to be about 8 grams/denier and the strength of the drag line of *Argiope Aurentia* was over 12 grams/denier. In fact the strength and toughness of the silk from *Nephila Clavipes* was recognized for a long time by the South Sea Islanders who use the silk to make various kinds of bags and fish nets.

The spider silks used in this study were forcible spun from *Nephila Clavipes* spiders. They were provided by the US Army Natick R&DEC. The diameter of the silk, averaging over 117 measurements using the scanning electron microscope, is  $3.67 \pm 0.47 \mu\text{m}$ . Figure 2 shows a SEM picture of the silk. To facilitate handling of this delicate silk fiber, each fiber was mounted carefully on a cardboard frame with an opening equal to the gage length of the specimen. Thirty eight (38) samples were prepared for tensile test. Fifty (50) samples were prepared for transverse compression test whereas a total of twenty nine (29) samples were

prepared for torsion test. In order to investigate the effect of water on the mechanical properties of the spider silk half of each group of fibers were tested in ambient condition (20°C, 65% RH) and the other half of the specimen were tested in wet condition. The diameter of each fiber was measured and recorded prior to testing. All the tests were performed with the micromasurement system developed by Kawabata, including a micro tensile tester, torsion tester, and single fiber transverse compression tester 3.

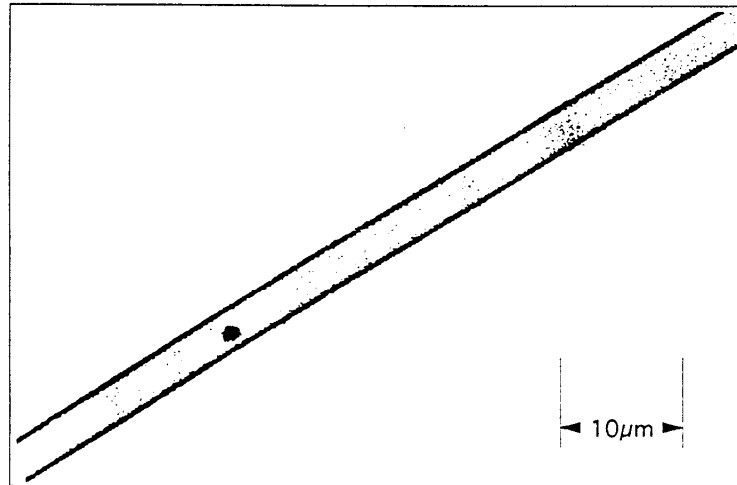


Figure 2: SEM picture of spider silk

### **TENSILE PROPERTIES**

The tensile properties of the spider silk were measured with the Kawabata micro tensile tester equipped with a special function "floating control". In order to minimize mechanical noise from the tester, a DC servo-motor system and simple transmission mechanism were used. The motor driving power is transmitted to the driving shaft through a helical rack-and-pinion mechanism similar to the driving mechanism of a microscope body tube. As shown in Figure 3, the control stroke of the driving chuck is 30 cm; however, in most of the fiber tensile testing, the dynamic stroke is measured in millimeters, requiring very precise measurement. Accordingly, the servo control system can be switched from the large stroke to the more precise small stroke zone at any portion of the large stroke travel. The control accuracy in the small stroke zone is 10 times more accurate, enabling a smoother control of fiber strain in the "floating zone". The maximum load capacity of this tester is 20 Kg and the maximum testing speed is 10 cm/sec. The position of the driving chuck can be controlled by an external servo-command signal (such as a sinusoidal signal) at any stage of the tensile testing process.

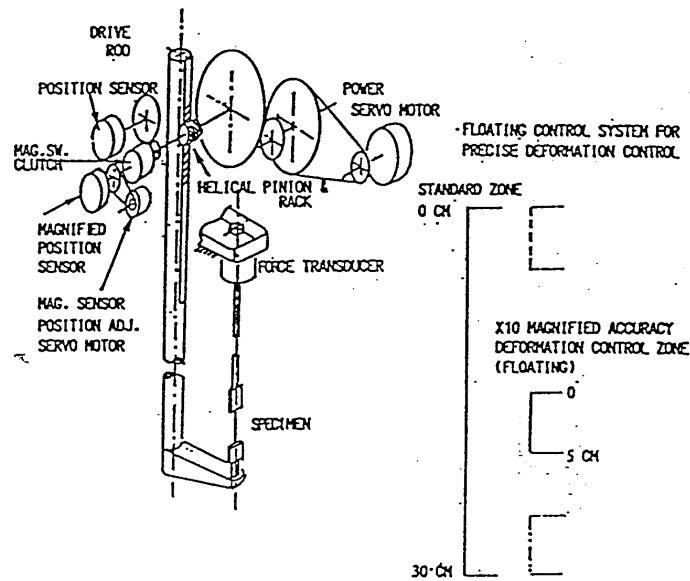


Figure 3: Floating-control tensile tester

The tensile testing were carried out under ambient and wet conditions with a cross head speed of 0.3 cm/min and a gage length of 2.53 cm. As shown in Figure 4, the stress-strain response of the spider silk tested under ambient condition assumed a sigmoidal shape with an initial modulus of 12.7 GPa. The breaking strength and elongation are 0.85 GPa and 20% respectively. When tested in water, there is no significant change in ultimate strength, however, a reduction of the initial modulus to 0.54 GPa and increased in ultimate elongation to 36% was observed. This phenomenon may be attributed to the rupturing of the secondary bonds which hold the helical molecular chains together resulting in greater elongation due to the uncoiling of the molecular chain.

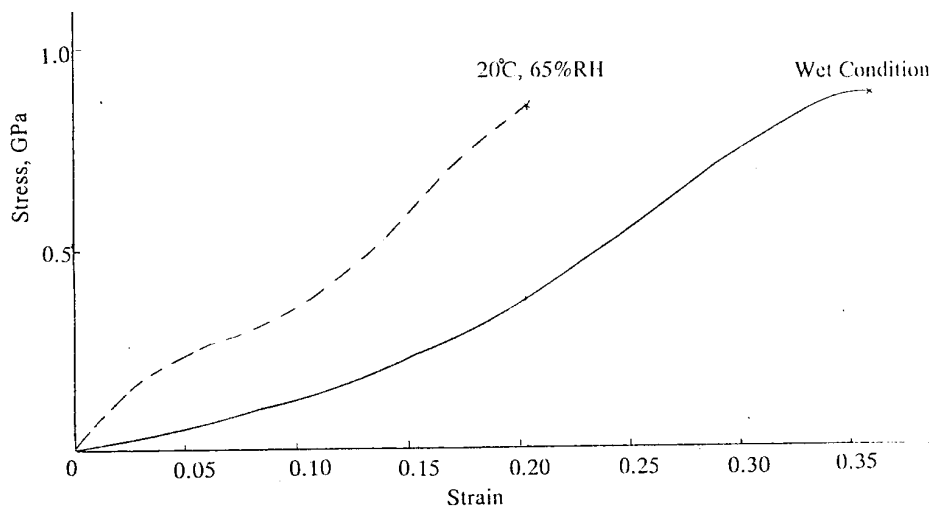


Figure 4: Tensile stress-strain properties of spider silk

### TRANSVERSE PROPERTIES

The compression tests in the transverse fiber diameter direction were carried out by placing a single fiber between a flat and mirror-finished steel plate and a mirror finished 0.2 mm square

compression plane. Because of the fineness of the spider fiber, a combination of sensitive instrumentation and mechanistic analysis are required in order to assure accurate measurement of the compressive stress-stain properties. For a compression force  $F$ , deforming the fiber cross-section as shown in Figure 5, its corresponding diameter change,  $U$ , can be calculated based on the following equations:

$$U = \frac{4F}{\pi} (S_{11} - \nu_{13}^2 S_{33}) \left( 0.19 + \sin h^{-1} \frac{R}{b} \right) \quad (1)$$

where

$$B^2 = \frac{4F}{\pi} (S_{11} - \nu_{13}^2 S_{33}) \quad (2)$$

- $R$  = fiber in undeformed state;
- $S_{11} = 1/E_T$
- $S_{22} = 1/E_L$
- $E_T$  = transverse modulus
- $E_L$  = longitudinal modulus
- $F$  = compression force/unit length of fiber

For polymers with highly oriented molecular-chain such as spider silk it is approximated that  $S_{33} \ll S_{11}$  and  $\nu_{13}$  is small; therefore, Equation (1) may be reduced to

$$U = \frac{4F}{\pi} \frac{1}{E_T} \left( 0.19 + \sin h^{-1} \frac{R}{b} \right) \quad (3)$$

$$B^2 = \frac{4F}{\pi E_T} \quad (4)$$

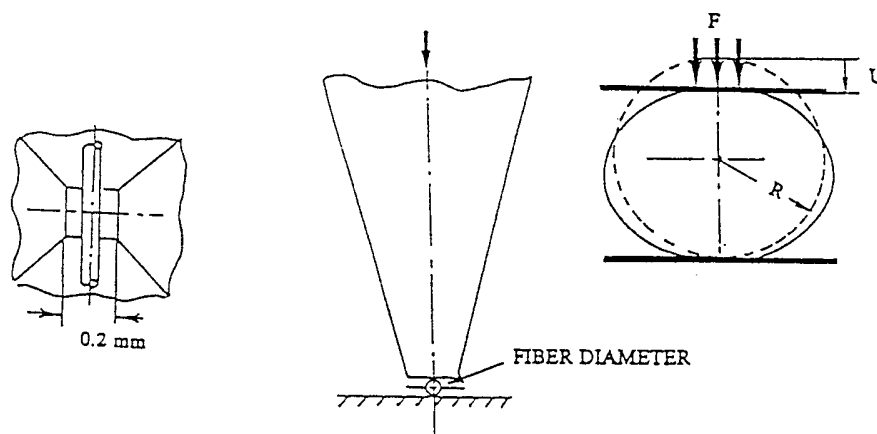


Figure 5: Diametrical compression of single fiber

The predictive accuracy of equation (3) have been verified using the Finite Element Method [3]. The FEM analysis also provides the stress distribution within the fiber cross-section. In the central area of the cross section, the maximum principal stress is:

$$\sigma_a = \frac{F}{2R} \quad (5)$$

and the maximum stress occurs in the area nearest the point of contact, approximated by

$$\sigma_m \approx 2\sigma_a \quad (6)$$

The compression force,  $F$ , is obtained by a moving electromagnetic coil acting against a strong fixed permanent magnet, which permits precise control of the compression rod.

The resolution of the displacement measurement is  $0.05 \mu\text{m}$ . The influence of the stiffness of the rod, etc. on the measured curve has been confirmed as negligible. Although  $U$  can be measured to a high degree of accuracy, the initial region of the  $F$ - $U$  curve has some uncertainty, which causes a degree of uncertainty in the measurement of  $U$  values. In order to eliminate the effect of this uncertainty on  $E_T$ , the use of the slope of the  $F$ - $U$  curve was applied as follows: From Equations 3 and 4,  $U$  is expressed only as a function of  $E_T$  for a fixed value  $F$ . For fixed  $F_1$  and  $F_2$ ,

$$U_1 = f(E_T)|_{F=F_1} \quad (7)$$

$$U_2 = f(E_T)|_{F=F_2} \quad (8)$$

where  $F_1$  and  $F_2$  are taken after passing the initial region to obtain the corresponding  $U_1$  and  $U_2$ , respectively, as well as the slope of the curve between  $F_1$  and  $F_2$ . The following relation may then be derived:

$$\Delta U = g(E_T) \quad (9)$$

or

$$E_T = g^{-1}(\Delta U) \quad (10)$$

where  $\Delta U = U_2 - U_1$  and  $g(E_T) = f(E_T)|_{F=F_2} - f(E_T)|_{F=F_1}$

The silk fibers were subjected to transverse cyclic loading at a compressive speed of  $0.3 \mu\text{m}/\text{sec}$ . under ambient and wet conditions, The compressive modulus of the fiber tested in ambient condition was  $0.58 \text{ GPa}$ . and the fiber experienced a high degree of permanent deformation ( $\sim 20\%$ ). As shown in Figure 6. similar to the tensile behavior, a drastic reduction in compressive modulus was also observed when the test was performed under wet testing conditions.



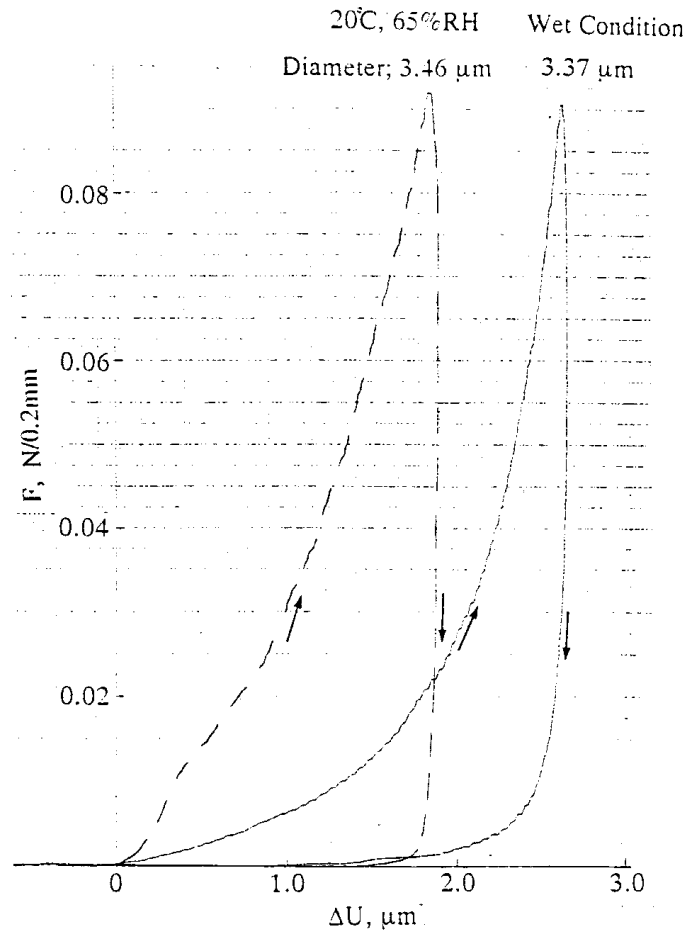


Figure 6: Compressive stress-strain behavior of spider silk

### TORSIONAL PROPERTIES

As shown in Figure 7, a single fiber having both ends reinforced by a paper backing using ceramic adhesives is hung on a top hook connected to a highly sensitive torque detector supported by two torque wires made of 0.2 mm piano wire. The bottom end is connected to a bar, and both ends of the bar are inserted into slits of a servo-driven cylindrical tube. The full scale of the torque meter is 0.0025 gf-cm/10 volt.

The specimens were tested in both ambient and wet conditions with a gage length of 1.33 mm at a torsion speed of  $0.3\pi$  rad/sec. Because of the low level of torsional load, great care must be taken to contain the mechanical noise. Figure 8 shows the smoothed out torsional stress-strain curves illustrating the effect of moisture on the shear rigidity of the fibers. In both cases, a significant hysteresis was observed. A shear modulus of 3.58 GPa was determined for the silk tested in ambient condition. On the other hand, under wet condition, the silk fiber has low resistance to deform after overcoming the frictional moment. This appears to be consistent with the tensile deformation mechanism of the helical molecular structure.

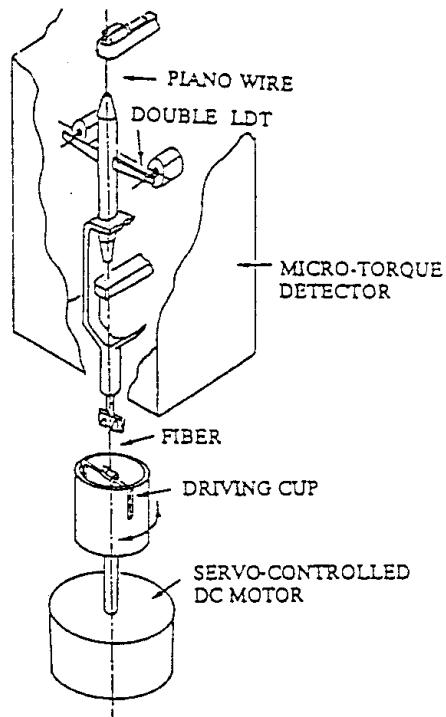


Figure 7: Torsion tester for single fiber

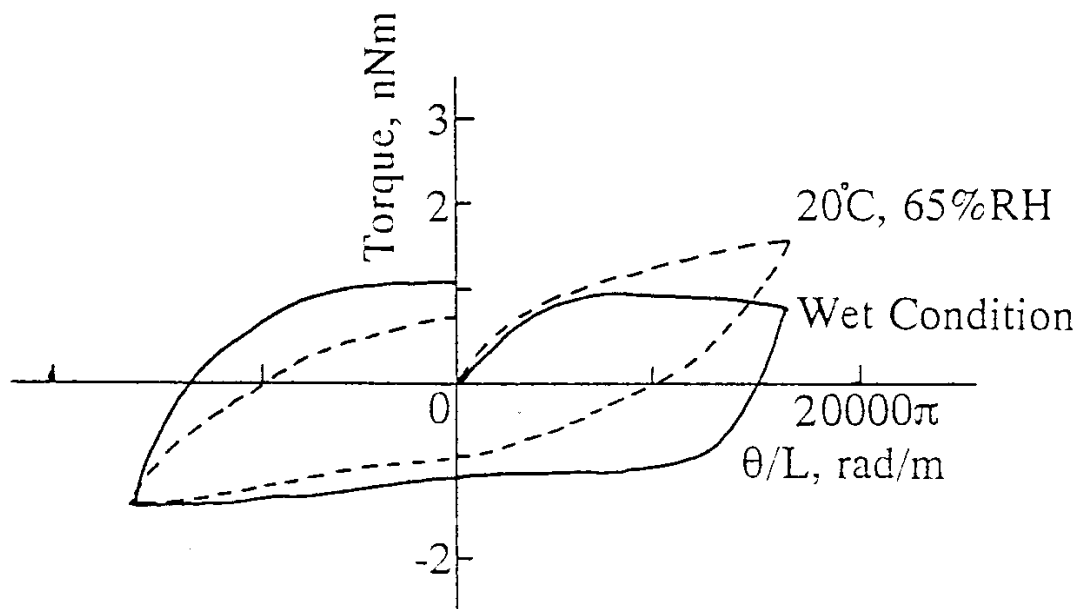


Figure 8: Torsional stress-strain behavior of spider silk

## CONCLUSIONS

Spider silk is an excellent model for the development of strong and tough materials. With a highly anisotropic mechanical behavior, the sensitivity of the initial modulus and elongation but not ultimate strength to moisture indicated an interesting molecular composite structure composed of well ordered fibrillar structures oriented in a primitive helical structure.

An ultra sensitive fiber testing system has been introduced and its capability demonstrated with the ultra-fine spider silk. This provides a useful tool in determining the engineering properties of single fibers as shown in Table 1.

*Table 1: Engineering properties of spider silk*

Tensile Modulus: $E_L$ (GPa)	Transverse Compressive Modulus: $E_T$ (GPa)	Shear Modulus $G$ (GPa)
12.71 (25.6%)*	0.579 (41.3%)*	3.58 (19.7%)*

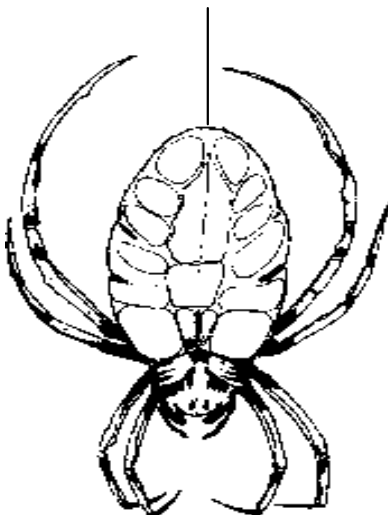
\* Coefficient of Variation

## ACKNOWLEDGEMENTS

This work was supported in part by the US Army Research Office through an ASSERT program to the second author for materials supply and training of graduate students.

## REFERENCES

1. Ko, Frank, Nonlinear Viscoelasticity of Aramid Fibers, Ph. D Thesis, Georgia Institute of Technology, Atlanta, Ga., 1977.
2. Kaplan, D., Adams, W. W., Farmer, B., and Viney, C., editors, Silk Polymers: Materials Science and Biotechnology, ACS Symposium Series 544, American Chemical Society, DC, 1994
3. Kawabata, S., Micromasurement of Mechanical Properties of Single Fibers, PP. 311-328, in Modern Textile Characterization Methods, Raheel, M., editor, Marcel Dekker, 1996



# NATURAL-FIBRE-MAT-REINFORCED THERMOPLASTIC COMPOSITES BASED ON FLAX FIBRES AND POLYPROPYLENE

S. Garkhail<sup>1</sup>, R. Heijenrath<sup>1</sup>, M. van den Oever<sup>2</sup>, H. Bos<sup>2</sup> and T. Peijs<sup>1</sup>

<sup>1</sup> *Centre for Polymer and Composites, Eindhoven University of Technology  
P.O. Box 513, 5600 MB Eindhoven, The Netherlands*

<sup>2</sup> *ATO-DLO, Agrotechnological Research Institute, Wageningen, The Netherlands*

**SUMMARY:** Natural-fibre-mat-reinforced thermoplastic (NMT) composites based on flax fibre mats and a Polypropylene (PP) matrix were manufactured using (i) a film-stacking method and (ii) a paper making process. The influence of fibre length and fibre content on stiffness and strength is reported and compared with data for glass-mat-reinforced thermoplastic (GMT) composites, including the influence of using maleic-anhydride grafted PP. The data is also compared with existing micromechanical models like Kelly-Tyson and Cox-Krenchel for strength and stiffness, respectively. A good agreement was found between theory and experiment in case of stiffness while in case of strength the experimental values fall well below the theoretical predictions. Results indicated that NMTs are of interest for low-cost engineering applications and can compete with commercial GMTs, especially when a high stiffness per unit weight is desirable. Results also indicated that the key area for future development lies not only in improved adhesion but mainly in improving the fibre strength.

**KEYWORDS:** natural fibre, thermoplastic, composites, mechanical properties, manufacturing

## INTRODUCTION

In the last decade, research activities in the area of thermoplastic composites have shifted towards the development of 'cost-performance' engineering materials. Especially, glass-mat-reinforced thermoplastic (GMT) materials [1], being stampable sheet products based on commodity resins such as polypropylene (PP) and moderate loadings of relatively long glass fibres in random array have proven to be very successful in high volume markets such as the automotive industry. Because of their excellent price-performance ratio, E-glass fibres are by far the most important fibres for these type of composites. However, these fibres do have some disadvantages regarding (thermal) recycling issues and abrasive wear of processing equipment. Moreover, glass fibres are non-renewable and can cause skin irritations during processing and assembly of fibre-reinforced parts.

Nowadays, ecological concern has resulted in a renewed interest in natural materials and issues such as recyclability and environmental safety are becoming increasingly important for the introduction of new materials and products. An interesting alternative for the use of glass fibres as reinforcement in engineering materials are natural fibres based on lignocellulose such as flax, sisal and jute [2]. These vegetable fibres are renewable, nonabrasive, can be thermally recycled, and show less concern with safety and health. In addition, they exhibit excellent mechanical properties, especially when their low density and price in comparison to

E-glass fibres is taken into account. Although these fibres are abundantly available, especially in developing countries such as Bangladesh and India, the applications are still rather conventional, i.e. ropes, matting, carpet backing and packaging materials. Moreover, in the last few decades the uses of natural fibres for these type of applications has been declined due to the introduction of synthetic fibres, such as nylon and polypropylene. Hence, also in the economic interests of developing countries, there is an urgent need for new application areas for these natural fibres.

The first natural-fibre-reinforced composites were based on thermoset matrices, such as unsaturated polyester or phenolic resins, together with sisal and jute [3,4]. More recently, developments shifted to thermoplastic matrix composites [5-7]. This research focuses on the development of natural-fibre-mat-reinforced thermoplastic (NMT) composites, being GMT-like materials based on natural fibres [8]. In this development study flax fibres are used as reinforcements, mainly because of their excellent mechanical properties when compared with other natural fibres and also because of availability in different forms in Western-Europe. PP is used for a number of reasons. First, it is easy to process and one of the cheapest polymers on the market. Secondly, it has a low processing temperature, which is essential because of the relatively low thermal stability of natural fibres (200-250°C). Finally, it has the perfect ability to protect the hydrophilic natural fibre because of its strong hydrophobic and apolar character. A clear disadvantage of this apolar character for composite applications is its limited wettability as well as poor interfacial bonding with reinforcing fibres. This disadvantage can, however, be overcome by functionalization of the polymer, which has proven to be very effective in enhancing fibre/matrix adhesion in composite systems based on polyolefins [9,10]. For the optimisation of the mechanical performance of the flax/PP composites it is expected that both flax content and the flax fibre length should be as high as possible. However, high fibre volume fractions and large fibre lengths will limit the processability of such composites. Therefore, a balance between mechanical performance and processability should be found.

In this research the influence of fibre length and volume fraction is investigated on random flax-mat-reinforced PP composites, which were manufactured using the film-stacking method and the suspension impregnation method, respectively. The latter method allows for a systematic variation of the fibre length, since no fibre break-up occurs during processing. The use of conventional melt-processing methods for the production of short fibre reinforced compounds such as extruders will degrade the fibre length and are therefore not suitable for such a systematic study. In addition, the influence of maleic-anhydride PP (MA-PP) on the mechanical performance of flax/PP composites was also studied. Flax fibres, as well as glass fibres, contain functional OH-groups that are able to interact chemically with the maleic anhydride grafted polypropylene. From this an improved interfacial bond strength between the flax fibre and the modified PP is expected. In order to get a better insight in the importance of all these different parameters, the experimental results were compared with model predictions using micromechanical models for random short-fibre-reinforced composites [11-15].

## EXPERIMENTAL

### Materials

In this study random flax fibre mats of Eco Fibre Products B.V. (The Netherlands) in combination with an isotactic-polypropylene (PP) matrix of Shell (XY6500T) with a melt flow index of 35 were used. In order to study the effect of improved fibre/matrix adhesion on composite performance, 5 wt.% of a maleic-anhydride-modified polypropylene (MA-PP) (Polybond® 3002, BP Chemicals Ltd.) was added to the homopolymer. NMT composite plates with different fibre contents were manufactured using the film-stacking method. In this film-stacking method, pre-dried flax fibre mats and PP film were stacked alternately. PP as well as films based on a blend of PP and MA-PP were made using film-blowing equipment. Impregnation was achieved by applying heat and pressure in a hot-press (200°C, 25 bar for 15 min.). The obtained composite plate was cut into tensile specimens according to ASTM-D 638 specifications. The Young's modulus of the PP matrix was approximately 1.6 GPa and the yield stress was about 32 MPa. Random MA-PP/flax composites were manufactured in a similar way. The modification of PP with a commercially available MA-PP (Polybond 3002, BP Chemicals Ltd.) was performed in a twin-screw extruder (Werner & Pfliederer ZSK25).

For the suspension impregnation process a dispersion of flax fibres and PP-fibres (Young's modulus = 1.6 GPa and yield stress = 29 MPa) was made in an ethanol/water (1:1) mixture. In separate production runs, three different flax fibre lengths were used (3, 6 and 25 mm). Significantly differing fibre lengths were removed before use. After drying of the materials at room temperature for 24 hours and at 60°C for one hour, this lofted mixture of flax fibres and PP fibres was consolidated in a hot-press. For the suspension impregnation process random flax/MA-PP composites were made by treating the fibres with MA-PP (Hostaprime® HC5, Hoechst). Degreasing of the flax fibres was executed via extraction of the flax fibres with an ethanol/toluene (2:1) mixture, refluxed for three hours. The extraction fluid was replaced by a new, fresh fluid after which it was refluxed for one hour. The fibres were subsequently washed for approximately 30 minutes with cold ethanol, followed by 6 litres of cold water over a büchner-funnel. The extracted fibres were dried at 60°C in an oven with circulating air for 24 hours. Afterwards they were immersed in a solution of MA-PP copolymer in hot toluene (100°C) for 10 minutes. The concentration of copolymer in solution was approximately 2 wt.% on the fibres. After treatment, the fibres were extracted with toluene for one and a half hour to remove all components not chemically bonded to the flax fibres. Finally, the fibres were dried at 60°C for 24 hours. These treated flax fibres were used in the suspension impregnation process, yielding a composite plate using the compression moulding method described above.

### Test methods

Uniaxial tensile tests on random flax mat composites were performed on a Frank tensile machine, type 81565, according to ASTM standards (D638M). The specimens were cut in a dog-bone shape with dimensions 200mm x 20mm x 1.8mm. An extensometer was used to monitor the elongation of the tested specimen. The uniaxial tests on random flax/PP composites, made by the paper making process, were performed on a Zwick tensile testing machine, type Z010. The specimens were rectangular cross-sections having dimensions of 100mm x 20mm x 2mm. Again, an extensometer was used to monitor the elongation of the tested specimen.

## RESULTS AND DISCUSSION

### Influence of fibre length

#### *Composite stiffness*

The results of the tensile tests on the manufactured flax-fibre-reinforced composites, with varying fibre lengths, are given in Figure 1 and 2. Figure 1 shows the Young's modulus for the systems based on PP and MA-PP together with the Cox-Krenchel model predictions. Cox [11] introduced a fibre length efficiency factor into the 'rule-of-mixtures' equation for the composite stiffness  $E_c$ , to account for the 'ineffective' loading of fibres over their stress transfer length. Since the fibre is only partly utilised in the case of a short fibre composite, these effects have to be taken into account when modelling the mechanical performance of such composites. The expression used by Cox yields:

$$E_c = \eta_{LE} V_f E_f + (1 - V_f) E_m \quad (1)$$

In the case of stiffness related problems Cox's 'shear lag' model is used for the calculation of the fibre efficiency factor  $\eta_{LE}$  [16-21] the assumption of elastic fibres in an elastic matrix, leading to:

$$\eta_{LE} = \left[ 1 - \frac{\tanh(\beta L / 2)}{\beta L / 2} \right] \quad (2)$$

$$\text{where } \beta = \frac{2}{D} \left[ \frac{2G_m}{E_f \ln(R/r)} \right]^{1/2} \quad (3)$$

The  $R/r$  factor can be related to the fibre volume fraction  $V_f$  by:

$$\ln(R/r) = \ln(\sqrt{\pi / \chi_i V_f}) \quad (4)$$

so that Equation 3 can be rewritten as

$$\beta = \frac{2}{D} \left[ \frac{2G_m}{E_f \ln(\sqrt{\pi / \chi_i V_f})} \right]^{1/2} \quad (5)$$

where  $c_i$  depends on the geometrical packing arrangement of the fibres,  $r$  is the fibre radius and  $R$  is related to the mean spacing of the fibres. In this study a square packed fibre arrangement is assumed, following Thomason *et. al* [20], where similar equations were used for the modelling of glass/PP composites. The inter-fibre spacing in the composite is  $2R$  and  $c_i$  equals 4. Besides the ineffective fibre length, another reason why the fibre can only be partially utilised is the fibre orientation. In order to take this into account, the theory of Cox was extended by Krenchel [12], who took fibre orientation into account by adding a fibre orientation factor  $\eta_o$  into the 'rule-of-mixtures' equation.

$$E_c = \eta_o \eta_{LE} V_f E_f + (1 - V_f) E_m \quad (6)$$

The Krenchel orientation factor  $\eta_o$  allows for the introduction of a fibre orientation distribution. If transverse deformations are neglected,  $\eta_o$  is given by:

$$\eta_o = \sum_n a_n \cos^4 \phi_n \quad (7)$$

where  $a_n$  is the fraction of fibres with orientation angle  $\phi_n$  with respect to the reference axis. For a two-dimensional (in-plane) random orientation of the fibres it can be shown that  $\eta_o = 3/8$ . In a three-dimensional random fibre orientation the fibre orientation factor yields the value of  $1/5$ . For thin section laminates with fibre lengths greater than the thickness of the sample, fibres are expected to be oriented mainly in two directions. However, deviations are expected to occur due to out-of-plane oriented fibres or bend fibres. In the model a modulus of 45 GPa for the flax fibre and a modulus of 1.6 GPa for the PP matrix is used. An effective fibre length of 25 mm for the random flax mat material, together with a distribution function for the fibre diameter is used. A rather good agreement is found between the model predictions and experimental data. No effect of improved adhesion on the modulus of flax/PP composites is observed indicating good wetting of the fibres. Only the data for a fibre length of 3 mm shows a somewhat increased composite stiffness with the use of MA-PP. Presumably, the higher interfacial bond strength in case of flax/MA-PP leads to a slight decrease of the critical fibre length (from  $\sim 3.5$  mm to  $\sim 2.5$  mm) and consequently a small improvement in composite stiffness might occur. At fibre lengths of 6 and 25 mm this improvement is not observed since in both cases the fibre length is well above the critical fibre length. No fibre length dependence is observed for the developed flax/MA-PP as the fibre lengths are higher than critical lengths thus showing the curve in the plateau zone.

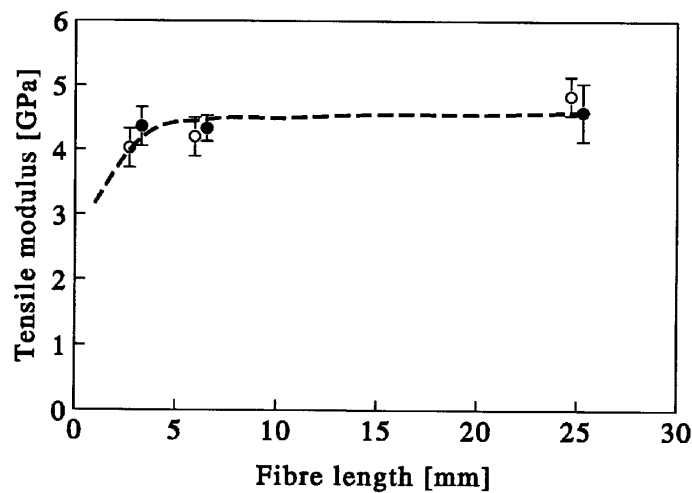


Fig. 1: Tensile modulus of the flax/PP composites (o) and the flax/MA-PP composites (●) as a function of the flax fibre length. The dashed line represents the Cox-Krenchel prediction

### Composite strength

In Figure 2 both the results of the tensile strength measurements as well as the model predictions for flax/PP and flax/MA-PP, as a function of the fibre length, are plotted. In the case of tensile strength modelling of discontinuous fibre composites, Kelly and Tyson [14] extended the 'rule-of-mixtures' equation for composite strength in a way similar to Cox's 'rule-of-mixtures' for composite stiffness:



$$\sigma_{uc} = \eta_o \eta_{LS} V_f \sigma_f + (1 - V_f) \sigma_m \quad (8)$$

where  $\eta_{LS}$  is the fibre length efficiency factor and  $\eta_o$  is the fibre orientation factor, similar to the Cox-Krenchel model, in order to take off-axis fibre orientation into account. For the fibre length efficiency factor, Kelly and Tyson used [14] :

$$\eta_{LS} = \frac{1}{V_f} \left( \sum_i \left[ \frac{L_i V_i}{2L_c} \right] + \sum_j \left[ V_j \left( 1 - \frac{L_c}{2L_j} \right) \right] \right) \quad (9)$$

The first summation term in Equation 9 accounts for the contribution of all fibres of sub-critical length ( $L < L_c$ ). The second summation term incorporates the strength contribution from fibres whose lengths are super-critical ( $L > L_c$ ). A combination of Equation 8 and 9 results in the Kelly-Tyson model [14,15] for the prediction of the strength ( $\sigma_{uc}$ ) of a polymer composite reinforced with short off-axis fibres:

$$\sigma_{uc} = \eta_o \left( \sum_i \left[ \frac{\tau L_i V_i}{D} \right] + \sum_j \left[ \sigma_j V_j \left( 1 - \frac{L_c}{2L_j} \right) \right] \right) + (1 - V_f) \sigma_m \quad (10)$$

In the case of stiffness, the related Cox-Krenchel model, including a theoretical orientation parameter for in-plane random fibre orientations ( $\eta_o = 3/8$ ), can be used quite effectively for the prediction of the stiffness of random fibre composites. However, previous studies have shown that the Kelly-Tyson model for strength yields far too high values for the strength of random fibre composites. In general this discrepancy is accounted for by adopting the fibre orientation efficiency parameter  $\eta_o$  and as a result no unambiguous value for  $\eta_o$  is found in the literature for the prediction of random composite strength. In this paper we used a value of 0.2 for the fibre orientation efficiency parameter  $\eta_o$  of our random flax/PP composites. This value, having no physical meaning, was reported by Thomason *et al.* [20] and was obtained by fitting  $\eta_o$  to the experimental strength data of a similar type of composite based on glass/PP. Moreover, a fibre strength of 750 MPa is used together with an interfacial bond strength ( $\tau$ ) of 10 MPa for flax/PP and 16 MPa for flax/MA-PP. The interfacial shear strength value of 16 MPa for the flax/MA-PP system is taken similar to the shear yield stress of the pure PP matrix as calculated from the Von Mises yield criterion (29/ $\sqrt{3}$  MPa), which means that for this composite system perfect adhesion, or a matrix dominated rather than interface dominated shear failure mode, is assumed. First of all, when looking at Figure 2, it becomes clear that the experimental results at high fibre lengths (6 and 25 mm) of the flax/PP as well as the flax/MA-PP composites are significantly lower than the Kelly-Tyson predictions for tensile strength. With respect to the effect of improved interfacial bonding the model predicts only a small increase in strength in the case of improved adhesion. Similar to the stiffness there appears to be no significant influence of the flax fibre length on the measured composite strength. Only the experimental results of the 3 mm flax/(MA-)PP composites are more or less comparable with the model prediction. Due to the easier way of mixing and consequently better impregnation, the composite with 3 mm long fibres is of a higher quality in comparison to the 6 and 25 mm ones. Moreover, during the chopping of the fibres into the desired length the weak internal interaction between the elementary fibres results in extensive fibrillation of the fibres and a decrease of the flax fibre diameter and consequently, an increase in fibre aspect ratio. As a result, the stress transfer becomes more effective, yielding a composite with relatively better properties.

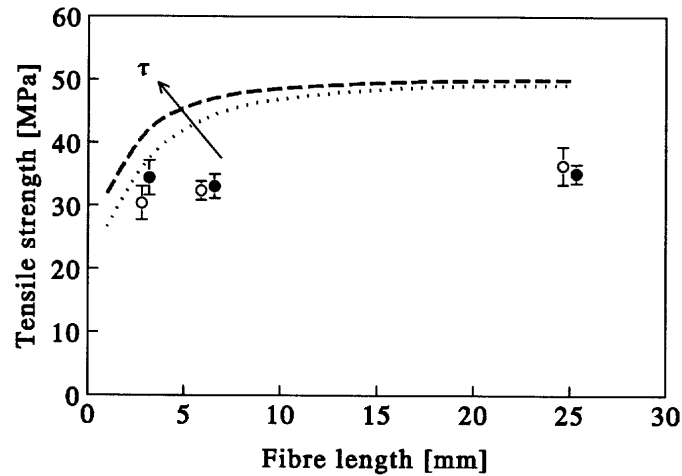


Fig. 2: Tensile strength of the flax/PP composites (o) and the flax/MA-PP composites (●) as a function of the flax fibre length. The dotted line and the dashed line represent the Kelly-Tyson prediction for the flax/PP and the flax/MA-PP composites, respectively

### Influence of fibre volume fraction

#### Composite stiffness

Figure 3 shows the tensile modulus of the flax/(MA-)PP composites together with the Cox-Krenchel prediction and the commercially known glass-mat-reinforced thermoplastic (GMT) materials, as a function of fibre volume fraction. Based on the data obtained, it can be concluded that the stiffness of flax-fibre-reinforced PP is comparable to E-glass fibre composites. Especially, when the relatively low density of the flax fibre is taken into account, the stiffness per unit weight approaches or even surpasses that of GMT materials. Moreover, as a result of the relatively low price of flax fibres compared to E-glass fibres these materials are particularly of interest from a cost-performance point of view. From this it can be concluded that flax/PP composites can compete with glass fibre based GMT materials in stiffness critical applications.

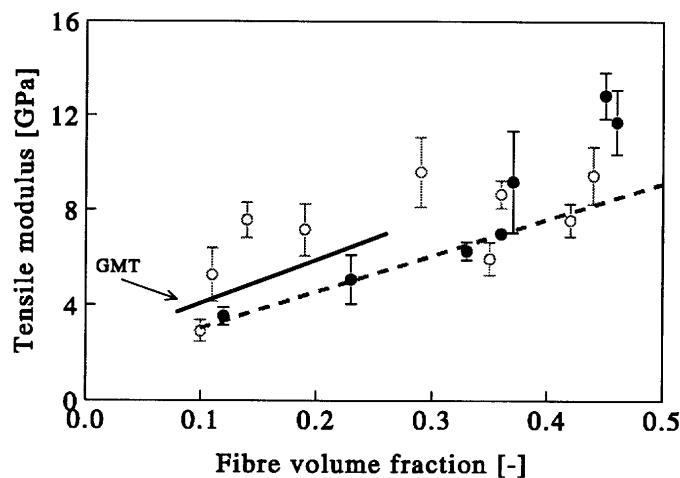


Fig. 3: Tensile modulus of the flax/PP composites (o) and the flax/MA-PP composites (●) as a function of  $V_f$ . The dashed line represents the Cox-Krenchel prediction

A rather good agreement is found between the experimental data and the predictions using the Cox-Krenchel model. In the model a modulus of 45 GPa for the flax fibre and a modulus of 1.6 GPa for the PP matrix is used, together with an effective fibre length of 25 mm for the random flax mat material and a distribution function for the fibre diameter.

### Composite tensile strength

Figure 4 shows the tensile strength of the manufactured flax/PP and flax/MA-PP composites, together with the Kelly-Tyson predictions for flax/PP and flax/MA-PP as well as the commercially glass fibre based GMT materials, as a function of the fibre volume fraction. In the model the same material parameters are used as in the Cox-Krenchel model for the prediction of composite stiffness. Again, a fibre strength of 750 MPa is used. These micromechanical calculations also indicate that the difference in interfacial bond strength in the case of flax/PP ( $\tau = 10$  MPa) and flax/MA-PP ( $\tau = 16$  MPa) has no significant influence on the predicted composite strength (see Figure 4).

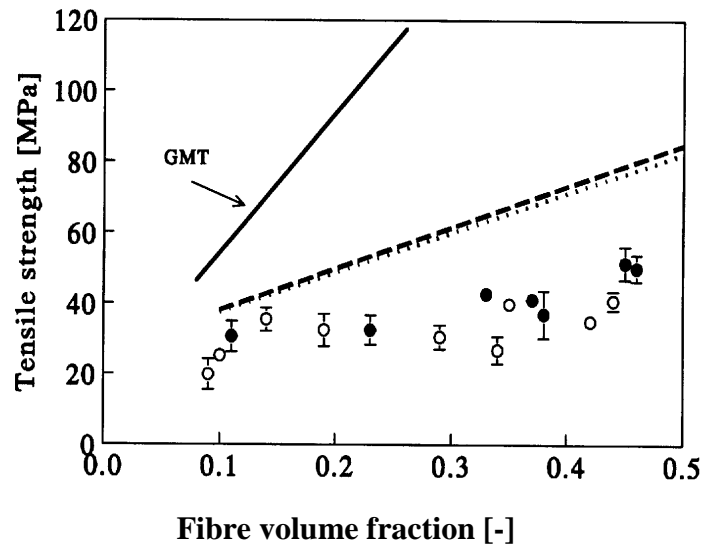


Fig. 4: Tensile strength of the flax/PP composites (o) and the flax/MA-PP composites (●) as a function of  $V_f$ . The dotted line and the dashed line represents the Kelly-Tyson predictions for flax/PP and flax/MA-PP composites, respectively. The solid line represents the commercially available GMT

Clearly, GMT materials show superior strengths compared to flax-fibre-reinforced PP composites for all volume fractions. With respect to the effect of improved interfacial bonding in the case of flax/MA-PP composites no significant difference in tensile strength was found. Moreover, based on micromechanical calculations no significant improvements can be expected since already an ‘upper limit’ matrix dominated shear strength value is used for the calculation of the theoretical strength of flax/MA-PP. Obviously, the strength of the flax based composites is intrinsically limited by the relatively low strength of the technical flax fibres (~750 MPa). Therefore the present study shows that the key area for the improvement of the tensile strength of the flax/PP composites lies not only in the interphase modifications for improved adhesion but mainly in fibre modifications for improved fibre strength.

## CONCLUSIONS

For the production of flax/PP random composites two production methods similar to the commercially known methods for glass/PP composites were used. First, the so-called film-stacking method based on flax non-woven fibre mats and secondly, a suspension impregnation process using chopped short flax fibres were used. Material parameters that were studied for the optimisation of the mechanical performance of such composites were (i) fibre volume fraction, (ii) fibre length and (iii) fibre matrix adhesion. In order to get a better insight in the importance of these different parameters for the optimisation of composites, the experimental results were compared with model predictions using micromechanical models for random short-fibre-reinforced composites. As expected, there is a significant effect of fibre volume fraction on mechanical properties, whereas, no real experimental evidence for the anticipated increase in mechanical performance with increasing fibre length was found.

Based on the experimental results it can be concluded that the tensile modulus of the flax-fibre-reinforced composites is comparable to E-glass-fibre-reinforced composites. Especially, when focusing on the specific properties as a result of the low density of flax, the stiffness per unit weight of flax-fibre-reinforced composites approaches that of glass-fibre-reinforced materials. Moreover, as a result of the relatively low price of flax fibre compared to E-glass fibres these materials might be of interest from a 'cost-performance' point of view. However, due to the relatively low tensile strength of flax fibres compared to E-glass fibres, the tensile strength of technical flax-fibre-reinforced composites is significantly lower than that of their glass fibre counterparts. In short, it can be concluded that thermoplastic NMT composites based on a PP matrix and flax fibres can compete with E-glass reinforced GMT materials in stiffness critical structures, whereas for strength critical applications these materials still need to be optimised.

## ACKNOWLEDGEMENT

The authors would like to acknowledge Dr. G. Pott of CERES Fibres BV for providing the flax fibre mats used in the present study.

## REFERENCES

1. Berglund, L.A. and Ericson, M.L. in: *Polypropylene: Structure, blends and composites*, Vol. 3, Ed. J. Karger-Kocsis, Chapman & Hall, London (1995) 202.
2. Morton, W.E. and Hearle, J.W.S., *Physical Properties of Textile Fibres*, 2nd ed., John Wiley & Sons, Inc., New York (1975).
3. Satyanarayana, K.G. et al. in: *Composite Structures*, Vol. 1, Ed. I.H. Marshall, Elsevier Appl. Sci., London (1981) 618.
4. Chawla, K.K. and Bastos, A.C. in: *Proc. 3rd. Int. Conf. Mech. Behaviour of Materials*, Vol. 3, Pergamon Press, Toronto (1979) 191.
5. Kuruvila, J., Thomas, S., Pavithran, C. and Brahmakumar, M., *J. Appl. Polymer Sci.*, 47, (1993) 1731.

6. Selzer, R., *Advanced Composite Letters*, 4(3), (1995) 87.
7. Sanadi, A.R., Caulfield, D.F., Jacobson, R.E. and Rowell, R.M., *Ind. Eng. Chem. Res.*, 34 (1995) 1889.
8. Heijenrath, R., Peijs, T., *Advanced Composite Letters*, 5 (3) 1996.
9. Rijdsdijk, H.A., Contant, M. and Peijs, A.A.J.M., *Composites Science & Technology*, 48, (1993) 161.
10. Felix, J., Ph.D Thesis, "Enhancing Interactions Between Cellulose Fibres and Synthetic Polymers", Chalmers University of Technology, Goteborg, Sweden 1993.
11. Cox, H.L., *Brit. J. Appl. Phys.*, 3 (1952) 72.
12. Krenchel, H. in: *Fibre reinforcement*, Akademisk Forlag, Copenhagen, 1964.
13. Folkes, M.J. in: *Short fibre reinforced thermoplastics*, Research Studies Press, Chichester, (1985) 16.
14. Kelly, A. and Tyson, W.R., *J. Mech. Phys. Solids*, 13 (1965) 329.
15. Kelly, A. and Macmillan, N.H. in: *Strong Solids*, Clarendon Press, Oxford (1986) 269.
16. Ericson, M. and Berglund, L., *Composite Science Technology*, 43 (1992) 269.
17. Ericson, M. and Berglund, L., *Composite Science and Technology*, 49 (1993) 121.
18. Thomason, J.L. and Vlug, M.A., *Composites, Part A*, 27A (1996) 477.
19. Rosenthal, J., *Polymer Composites*, 13 (1992) 462.
20. Thomason, J.L., Vlug, M.A., Schipper, G., Krikor, H.G.L.T, *Composites, Part A*, 27, (1996) 1075.
21. Pan, N., *Polymer Composites*, 14 (1993) 85.

# MECHANICAL PROPERTIES OF WOVEN FABRIC CARBON/MAGNESIUM-COMPOSITES

O.Öttinger, W.Schäff, C.Hausmann, T.Heyne and R.F.Singer

*Department of Materials Science  
University of Erlangen  
Martensstr.5, D-91058 Erlangen, Germany*

**SUMMARY:** The mechanical behaviour of a woven fabric carbon/magnesium-composite which is manufactured by a gas pressure infiltration technique is the subject of this research work. Apart from the investigation of the influence of the fibre volume content (50-70 vol.-%) on the bending strength, all other mechanical testing (bending, tensile and compression test) is carried out by using composites with a constant fibre volume fraction of about 60 vol.-%. The main points of the mechanical characterisations are the orientation and temperature dependence, as well as the thermal long term stability of the 0/90° woven fabric C/Mg-composites. The investigated two-dimensionally reinforced magnesium composites show a typical orthotropic mechanical behaviour. The 0/90° strength is temperature independent up to 300°C. Moreover, the outstanding mechanical properties stay unchanged even after a long thermal exposure (200°C; 1000h).

**KEYWORDS:** Woven fabric composite, carbon magnesium composite, MMC, mechanical properties, thermal stability, orientation influence, temperature influence.

## INTRODUCTION

Continuously reinforced metal matrix composites have received significant attention in the last few years. Compared to conventional engineering materials they offer high specific stiffness and strength, tailored thermal expansion and conductivity. Especially the low density (1.8 g/cm<sup>3</sup>), as well as the remarkable in-axis tensile, fatigue strength and stiffness make unidirectionally carbon fibre reinforced magnesium (C/Mg) extremely attractive for advanced aerospace and automotive applications [1-5]. However, C/Mg-composites have particularly poor off-axis properties [4,6]. Fibre coatings and adapted fibre/alloy systems are able to reduce the anisotropic behaviour of the composites slightly [6-8]. A much more effective way to surmount this specific weakness, which is pursued in the present paper, is to use two-dimensional (2D-) woven fabrics. The results reported in this paper are part of a more comprehensive study with different C/Mg-systems [9].

## EXPERIMENTAL

### Materials

The specific subject of this research work is the AM20/T300J-composite system, which is manufactured by a gas pressure melt infiltration technique [9, 10].

A magnesium matrix with 2 wt.-% aluminium (AM20: 2 wt.-% Al, 0.6 wt.-% Mn, balance Mg [11]) was chosen because of the comparatively moderate fibre/matrix-reaction ( $Al_4C_3$ ) resulting in an optimised interfacial strength [8, 12]. The commercial 2D satin 1/4 woven fabrics are made of the high-tenacity carbon fibre T300J produced by Toray. The woven fabric shows 7 filaments per cm in warp and fill direction and weigh 285 g/m<sup>2</sup>. The fibre preforms were manufactured without binder by stacking several woven fabric sheets (typically 180x80 mm<sup>2</sup>) in the infiltration form. Depending on the desired fibre volume fraction a certain amount of woven fabric layers, which can be calculated by Eqn.1, was used.

$$V_F = \frac{d^2 \pi N_L N_F x}{2h} 100\% \quad (1)$$

with:

$V_F$ :	Fibre volume fraction
$d$ :	Fibre diameter (here: $d=7.1\mu\text{m}$ )
$N_L$ :	Amount of woven fabric layers
$N_F$ :	Fibres per filament (here: $N_F=3000$ )
$x$ :	Filaments per cm
$h$ :	Thickness of the composite plate

### Mechanical testing

The mechanical characterisation including bending, tensile and compression tests was performed with an 100kN Instron 4505 machine.

The bending strength specimens had the dimensions of 100x10x2 mm<sup>3</sup> and were tested corresponding the German standard DIN 29971. According to this test method the influence of the following factors on the bending strength were examined:

- Fibre volume fraction
- Orientation of the fibres
- Temperature in the range of room temperature to 400°C
- Isothermal exposure at 200°C and a duration of 1h to 1000h

The composite 0/90° tensile strength was determined by using flat specimens with a total length of 175 mm. The gage length was 50 mm with a cross section of 8x2 mm<sup>2</sup>. The ±45° tensile samples had no gage length and a dimension of 100x10x2 mm<sup>3</sup>. All tensile tests were performed at a crosshead speed of 0.5 mm/min.

The compression strength was measured according to the German standard DIN 50106 for unreinforced metals. The cylindrical specimens had a diameter of 6 mm and height of 9 mm. For comparison the Celanese compression test method [13] with flat specimens of 112 mm in length and a cross section of 6.3x2 mm<sup>2</sup> were used. For both methods the crosshead speed was 0.5 mm/min.

## RESULTS AND DISCUSSION

### Influence of the fibre volume content on the bending strength of 2D-AM20/T300J

The influence of the fibre volume fraction on the bending strength and stiffness can be seen in Fig. 1.

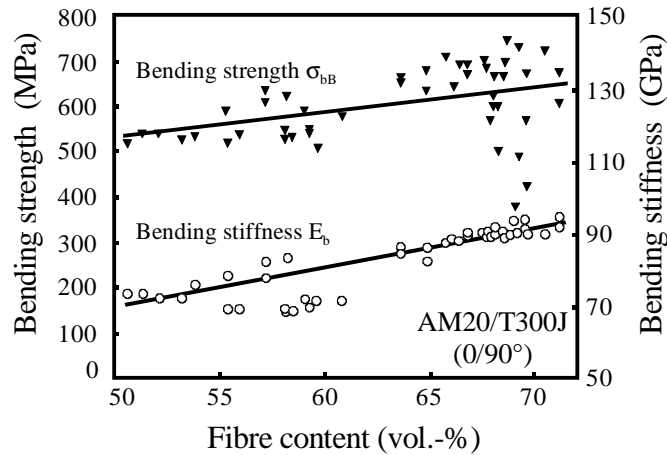


Figure 1: Influence of the fibre content on the 0/90°-bending strength and stiffness of 2D-AM20/T300J composites

According to the Rule of Mixture both the 0/90°-bending strength and stiffness show approximately a linear dependence of the fibre volume content in the range of 50-70 vol.-%. Large variations of the bending strength with about 70 vol.-% can be observed. However stable mechanical properties are obtained at volume fractions below 60 vol.-%. Therefore all further mechanical composite testing are carried out with a constant moderate fibre volume fraction of about 57 vol.-%.

### Orientation dependence on mechanical properties of 2D-woven fabric reinforced magnesium

As seen in Fig. 2, the two-dimensionally reinforced magnesium composites show a typical orthotropic mechanical behaviour which has been previously observed with other woven fabric composites [14]. Both the tensile and the bending strength reach the highest values in the 0° and 90°, respectively the fill and the warp direction. The total tensile strain at composite fracture does not exceed 1%. In contrast to the 0/90° response, the woven fabric reinforced composite show much lower strength in the  $\pm 45^\circ$  direction. Bending and tensile strength reach a minimum. The tensile strength is just slightly higher than the unreinforced matrix AM20. The total fracture strain of the  $\pm 45^\circ$  composite samples is about 5% and half as big as the unreinforced matrix. The  $\pm 45^\circ$  tensile test specimens show shear failure, i.e. the crack surface is parallel to fibre orientation. The 0/90° tensile specimens fail normal to the loading direction.

To analyse the orientation dependence of the compression strength of the 2D-AM20/T300J two types of fibre orientations are tested: Load direction perpendicular (Fig. 3a) and parallel (Fig. 3b) to the woven fabric layers.



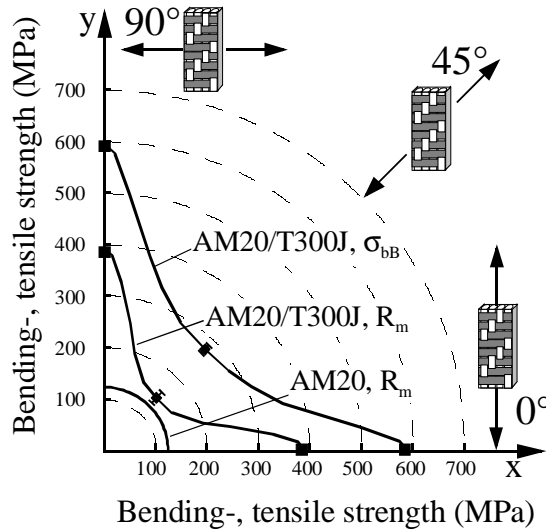


Figure 2: The orthotropic mechanical behaviour of 0/90°-reinforced AM20/T300J composites (57 vol.-% fibre content) in comparison to isotropic tensile behaviour of the unreinforced matrix AM20

Table 1: Influence of the fibre orientation on the compression strength of 2D-AM20/T300J (57 vol.-% fibre content)

Fibre orientation (related to the compression direction)	Compression strength [MPa]
0/90° parallel	505 ± 84
perpendicular	583 ± 48
unreinforced	225 [7]

As Table 1 indicates, the compression strength of the composite is more than twice as high as that of the unreinforced AM20, whereas the difference between loading the composite perpendicular and the parallel to the fibre orientation is rather small. However, both fracture modes can be clearly distinguished, as shown in Fig. 3.

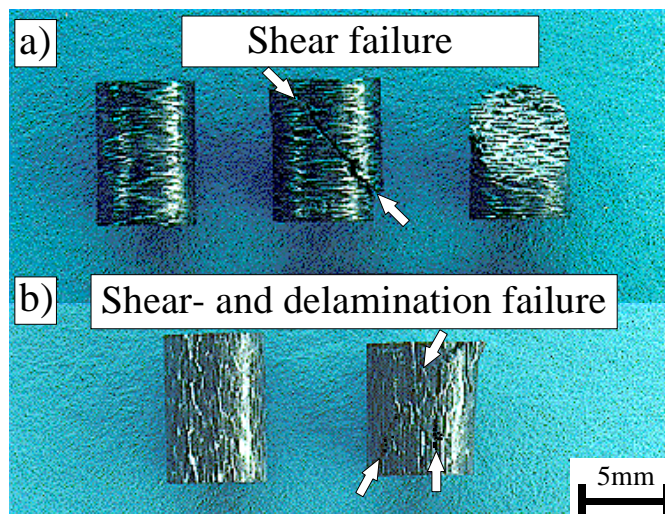


Figure 3: Influence of the fibre orientation on the fracture mode of the compression specimens. The white arrows are pointing out the shear and delamination cracks

With an orientation of the woven fabric laminates perpendicular to the compression direction only shear failure in the plane of the maximum shear stress can be seen (Fig. 3a). The compression specimen loaded parallel to the fibre direction demonstrates a different behaviour (Fig. 3b): Beside the shear-cracks additional delamination cracks parallel to the woven fabric layers occur. This is the reason why the attained compression strength is somewhat smaller. Compared to these results the Celanese compression test method of the 0/90°-bending strength parallel to the laminates showed without exception a slightly higher strength of about 580 MPa instead of 505 MPa.

### Mechanical properties at elevated temperatures and after thermal exposure

Fig. 4 illustrates the temperature influence on the mechanical behaviour of 0/90°-reinforced AM20/T300J in comparison to unreinforced AM20.

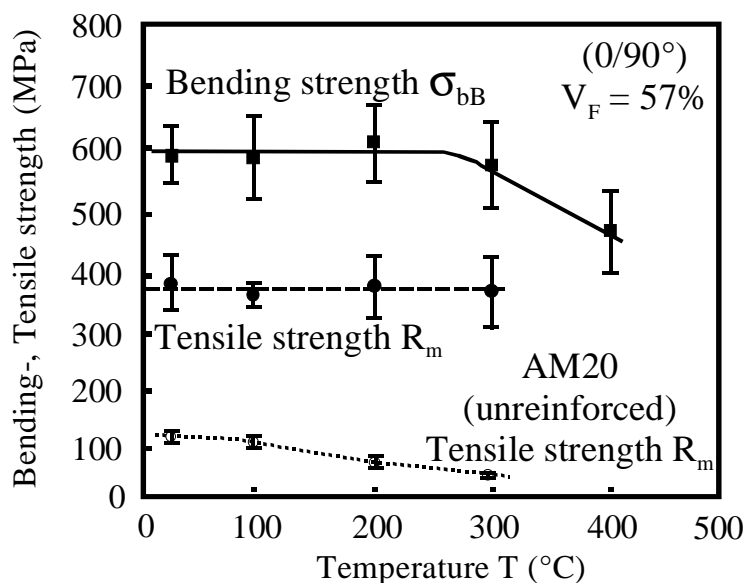


Figure 4: The influence of the temperature on the mechanical behaviour of 0/90°-reinforced AM20/T300J

Regarding the low fibre volume content of only half of 57 vol.-% in loading direction outstanding bending and tensile strength can be achieved even at elevated temperatures. In contrast to unreinforced AM20, which tensile strength decreases distinctly with increasing temperatures, the composite strength is constant up to 300°C. Only at higher temperatures (e.g. 400°C) the strength declines and the composite strength will not be longer determined by the fibre/matrix interface strength but by the very low matrix strength itself [9].

In contrast to many other magnesium matrix composites with e.g. alumina short-fibres [15] the excellent 2D-AM20/T300J-composite strength still exist even after long thermal exposure, as one can see in Fig 5.

Compared to the as-cast specimens neither the bending strength nor the bending stiffness is reduced. The main reason for this excellent thermal stability is that carbon and magnesium is thermodynamical inert (the Gibb's enthalpy values  $\Delta G^0$  for the formation of magnesium carbides  $MgC_2$  and  $Mg_2C_3$  are positive from casting to room temperature) [16] and that the

moderate reaction between the alloying element aluminium and the carbon fibre is completed during the composite processing.

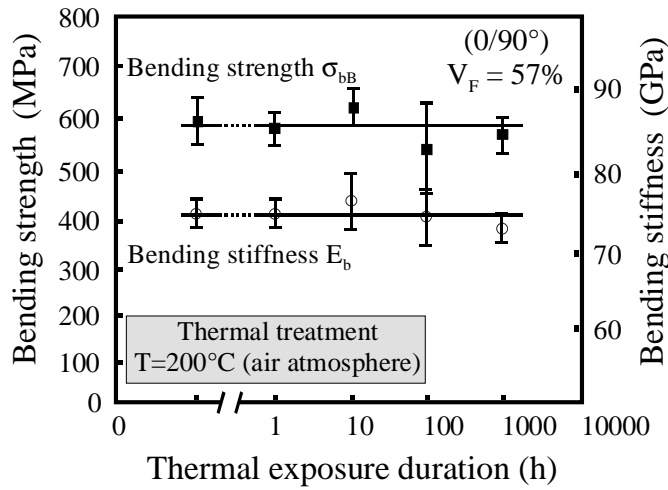


Figure 5: The influence of the thermal exposure duration at 200°C on the bending strength and stiffness of woven fabric reinforced AM20/T300J

**Comparison of the temperature influence on the composite strength of different woven fabric reinforced composite**

Fig. 6 gives a comparison of the temperature influence on the bending strength of different woven fabric reinforced composites. All composites are reinforced with woven fabric made of high tenacity carbon fibres with similar fibre strength. The fibre volume content of all composites is approximately 60 vol.-%.

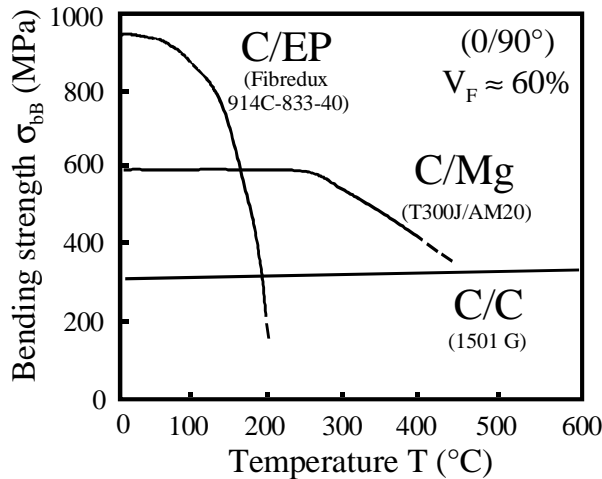
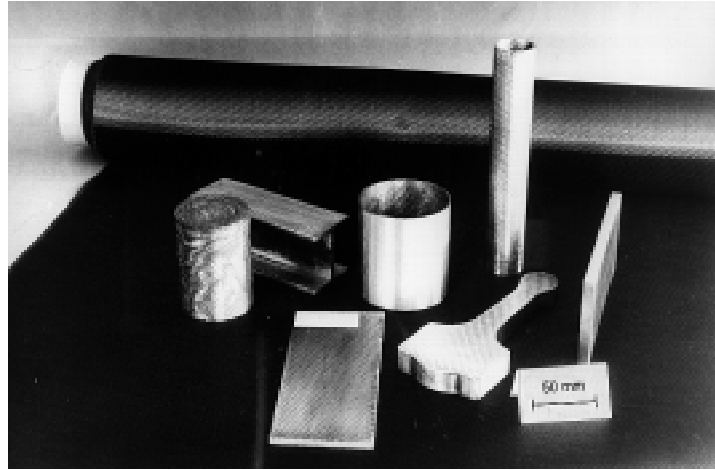


Figure 6: Comparison of the temperature influence on the bending strength of different woven fabric reinforced composites [17, 18]

At low temperatures (up to 100°C) the C/EP-system (carbon fibre reinforced epoxy) shows the highest bending strength whereas these properties get quickly lost at elevated temperatures [17]. In contrast, the strength of C/C composites (carbon fibre reinforced carbon) is relatively low at room temperature but increases slightly up to temperatures of 2000°C in an non-oxidising atmosphere [18]. However, the woven fabric reinforced AM20/T300J shows

medium strength at room temperature, but has superior properties in the temperature range of 180°C to 400°C. Therefore, the 2D-AM20/T300J-system is able to close the strength gap between C/EP and C/C-composites and makes C/Mg-composites extremely attractive for the internal combustion engine and other high temperature components. Some near-net-shape cast prototypes of woven fabric reinforced AM20/T300J are shown in Fig.7:



*Figure 7: Woven fabric reinforced AM20/T300J-prototypes manufactured at the university of Erlangen*

## CONCLUSIONS

The results of the present investigation lead to the following conclusions:

1. Strength and stiffness of 0/90° AM20/T300J increase linearly with the fibre volume fraction.
2. The 0/90°-reinforced AM20/T300J system shows an orthotropic mechanical behaviour. The 0/90°-tensile strength is more than three times higher than unreinforced AM20. The tensile strength with  $\pm 45^\circ$  fibre orientation is only slightly higher than the unreinforced matrix.
3. Bending and tensile strength of 0/90° reinforced AM20/T300J is constant up to 300°C. The composite system shows an excellent thermal stability even after long thermal exposure (200°C, 1000h).
4. Compared to other woven fabric reinforced composites (C/EP and C/C) the discussed C/Mg-system has superior strength in the temperature range of 180°C to 400°C. Therefore 2D-AM20/T300J-system is a very promising material for high temperature composites as required in internal combustion engines.

## REFERENCES

1. A.P.Diwanji, I.W.Hall: Effects of Surface Treatment and Elevated Temperature Testing on Mechanical Properties and Fibre/Matrix Interface of Gr/Mg Composites, Proc. of the 2<sup>nd</sup> Annual Joint Conference on the American Society for Composites, Metals Park, American Society for Composites, 1988, p.351-360

2. M.Rabinovitch, J.C.Daux, J.L.Raviart, R.Mevrel: Carbon-Reinforced Magnesium and Aluminium Composites Fabricated by Liquid Phase Hot Pressing, Proc. of 4<sup>th</sup> European Conf. on Composite Materials, Elsevier Applied Science, 1990, p.405-410
3. Y.Kagawa, E.Nakata: Some Mechanical Properties of Carbon Fibre-Reinforced Magnesium-Matrix Composite Fabricated by Squeeze Casting, Journal of Materials Science Letters 11 (1992), p.176-178
4. O.Öttinger, M.Gruber, C.Grau and R.F.Singer, Properties and Microstructures of Carbon Fiber Reinforced Magnesium Alloys, High Performance Composites: Commonalty of Phenomena, TMS, (1994), p.275-289
5. D.Wurm, O.Öttinger, R.F.Singer: The influence of Carbon Fibre Type and Stress-Ratio on the Fatigue Behaviour of Unidirectionally Reinforced C/Mg-Composites, in: Metal Matrix Composites, The Tenth International Conference on Composite Materials (ICCM10), Vol.1, 1995, p.537-544
6. M.Rabinovitch, M.H.Vidal Setif, J.C.Daux, J.L.Raviart, R.Mevrel, H.Abiven, J.F.Peltier: Proprietes Mecaniques de Composites Magnesium/Carbone Elabores Par Pressage Chaud sous Moyenne Pression, Proc. of Int. Symp. On Advanced Materials for Lighthouse Structures, Netherlands, Eur. Space Agency, ESA, 1992, p.135-139
7. M.Rabinovitch, M.H.Vidal Setif, J.C.Daux, J.L.Raviart, J.L.Gerard, R.Mevrel, M.Lancin, O.Perez: An Approach to Optimize Interfaces in Carbon/Aluminium and Carbon/Magnesium Metal Matrix Composites Elaborated by Hot Pressing, Proc. of the 9<sup>th</sup> Int. Conf. on Composite Materials, Vol. Metal Matrix Composites, 1993, p.683-690
8. O.Öttinger, C.Grau, R.Winter, R.F.Singer, A.Feldhoff, E.Pippel, J.Woltersdorf: The Effect of Aluminium Additions on the Interfacial Microstructur and Mechanical Properties of C/Mg-Composites, Proc. of the 10th Int. Conf. on Composite Materials, Vol. VI, 1995, p.447-454
9. O.Öttinger: Herstellung, Mikrostruktur und Eigenschaften von kohlenstofflangfaserverstärkten Magnesiumlegierungen, Fortschrittberichte VDI Reihe 5, Grund- und Werkstoffe Nr.450, 1996
10. O.Öttinger and R.F.Singer, An Advanced Melt Infiltration Process for the Net Shape Production of Metal Matrix Composites, Z. Metallkunde 84, (1993), p.827-831
11. Hydro Magnesium: Datasheet Magnesium, High Purity Casting Alloys, Stabbek ,Norway, 1994
12. A.Feldhoff, E.Pippel, J.Woltersdorf: Interface Reactions and Fracture Behaviour of Fibre-Reinforced Mg/Al Alloys, to be published in Journal of Microscopy, Vol.185, Part 2, 1997

13. ASTM Standards and Literature References for Composites Materials D 3410-85<sup>ε2</sup>, Standard Test Method for Compressive Properties of Unidirectional or Crossply Fiber-Resin Composites, Philadelphia, American Society for Testing and Materials, 1987, p.131-140
14. K.Schulte, Faserverbundwerkstoffe mit Polymermatrix - Aufbau und mechanische Eigenschaften, DLR-Forschungsbericht DLR-FB 92-28, Köln, Deutsche Forschungsanstalt für Luft und Raumfahrt, 1992
15. C.Köhler, K.U.Kainer: Thermal Exposure Effects on the Structure and Mechanical Properties of Short-Fibre Reinforced Magnesium Alloys, Proc. of the 9<sup>th</sup> Int. Conf. on Composite Materials, Vol. Metal Matrix Composites, 1993, p.347-354
16. I.Barin, O.Knacke: Thermochemical Properties of Inorganic Substances, Berlin, Springer, 1973
17. Ciba-Geigy: Datasheet Firedux 914, Cambridge, 1989
18. SGL Carbon Group: Datasheet Sigrabond, Meitingen, 1994

# MODELLING STRESS TRANSFER IN A WOOD COMPOSITE

**Rowan Paton**

*Department of Materials Engineering, Monash University, Clayton, Victoria, 3168, Australia*

**SUMMARY:** A model has been developed for the longitudinal elastic modulus of a new structural wood composite, Scrimber. The model has been developed using a micromechanics of composites approach, and is based on the Krenchel model. The morphology of Scrimber has been studied in order to estimate the effects of strand discontinuity, strand misorientation, strand damage during pressing, and wood densification during production of the composite. The prediction of the model was within 2% of the measured modulus for a single batch of Scrimber. Similar models should be very useful for other structural wood composites.

This paper concentrates on the effect of strand discontinuity on the modulus. The strand discontinuity factor was estimated using a measured strand aspect ratio distribution, modified by strand end shape criteria, and a form of the shear-lag theory of stress transfer.

**KEYWORDS:** wood composites, modelling, stress transfer, modulus

## INTRODUCTION

Wood composites are a class of materials which are formed by breaking down wood into smaller wood elements which are then bonded together again in a different form. A class of wood composites increasingly used for structural purposes are the "Artificial Lumber" or "Composite Lumber" materials such as Parallel Strand Lumber and Laminated Veneer Lumber, materials which have similar properties to wood itself. These have been developed to meet the demand for timber-like products at a time when the supply of large old-growth trees, which are the most suitable for sawn timber production, is steadily decreasing.

Despite the common use of the term wood composites to describe these materials, and the strong links with the polymer composites industry provided by groups like the US Forest Products Laboratory, the industry has tended to regard these materials as an exotic species of timber, rather than studying these materials as composites, an engineered material. Although a great deal of theory has developed to predict the properties of many composites, there appears to have been little serious use of such theory to predict the properties of wood composites.

A new form of "composite lumber", Scrimber, has been developed in Australia. Scrimber is produced from strands produced by passing juvenile Radiata Pine logs through a series of rolls. This splits the log in the grain direction, and produces batches of partially-connected strands called increments. The width and thickness of these strands typically varies from 1 to 10 mm, and their length typically varies from 10 to 200x the width or thickness. These are dried, coated with adhesive, and laid up into a preform. The preform is then consolidated before being compressed and cured in a radio frequency heated press. The principal direction

of the strands in the beam is close to parallel to the long direction of the Scrimber beam. Scrimber has an obvious “grain” and “grain direction”.

Scrimber is in many ways similar to a unidirectional fibre composite. The basic starting point for the prediction of the longitudinal modulus of such a composite is often the Rule of Mixtures:

$$E_c = E_f V_f + E_m V_m \quad (1)$$

where  $E$  is the modulus,  $V$  the volume fraction, and the subscripts "c", "f" and "m" refer to the composite, fibres and matrix respectively. In the derivation of this equation it is assumed that the fibres are continuous; that the fibres are perfectly aligned in the longitudinal direction; that there is perfect bonding between fibre and matrix; and that the constituents are linearly elastic for the stresses expected.

In Scrimber, as in many practical composites, the “fibres” are neither perfectly aligned nor continuous. Krenchel (Theory 1) [1] was one of the first to predict the modulus of such composites. He built on the Rule of Mixtures model, introducing two “fibre efficiency” factors. These factors (here referred to as  $\eta_o$ , for fibre orientation, and  $\eta_{st}$ , for stress transfer) allow for the effect of fibre orientation and fibre discontinuity on the composite modulus. His equation has been rewritten using the more usual terminology introduced above:

$$E_c = \eta_o \eta_{st} E_f V_f + E_m V_m \quad (2)$$

This approach is now a standard method for predicting the modulus of short fibre composites, and has been used in this work to model the modulus of Scrimber. Feedlog offcuts, an increment of strands, and two cured beams from a single batch of Scrimber were collected and tested in compression and shear, measured, and examined to provide data for the model. Predictions of the model were then compared with measured Scrimber modulus. This paper is primarily concerned with the estimation of the stress transfer factor  $\eta_{st}$  for the model.

## **PREVIOUS WORK**

Where the wood elements, (in Scrimber these are referred to as strands) are discontinuous, the stress and strain in these strands are not uniform, and it is necessary to characterise the stress transfer into the strands to determine how this affects the modulus of the wood composite. No useful work specifically concerning stress transfer between wood composite elements could be located. However a good model for the transfer of stress between fibres in a short-fibre composite, the “shear-lag” theory, which exists in many forms, was first presented by Cox [2]. His and other variants of the theory are reviewed in Holister and Thomas (Chapter 2) [3]. For this theory it is assumed that: the fibre and matrix are elastic and isotropic; a perfect bond exists between fibre and matrix; there is no load transfer through the ends of the fibre; and fibre shear strain is negligible compared to matrix shear strain.

Consider a tensile load is applied in the fibre longitudinal direction to an idealised composite consisting of aligned short cylindrical fibres, with length  $L$  and radius  $r$ , in an elastic matrix.



The tensile strain in the composite as a whole, and in the matrix, is considered uniform<sup>1</sup> and called  $\epsilon_c$ . The shear-lag theory holds that the shear stress on a fibre surface at a point near the end of the fibre varies along the length of the fibre, being directly related to the difference between the fibre tensile strain and the bulk composite tensile strain at each position along the fibre. Cox showed that the tensile stress in the fibre,  $\sigma_x$ , varies along the length of the fibre,  $L$ , as:

$$\sigma_x = E_f \epsilon_c \left[ 1 - \frac{\cosh \omega \left( \frac{L}{2} - x \right)}{\cosh \omega \left( \frac{L}{2} \right)} \right] \quad \omega = \sqrt{\frac{2\pi G_m}{E_f A_f \ln \left( \frac{s}{r} \right)}} \quad (3)$$

- $E_f$  = Fibre modulus in the x direction  
 $G_m$  = Matrix shear modulus  
 $A_f$  = Fibre cross-sectional area  
 $s$  = Mean separation of fibres normal to their length  
 $r$  = Fibre radius  
 $\epsilon_c$  = Matrix strain in the x direction

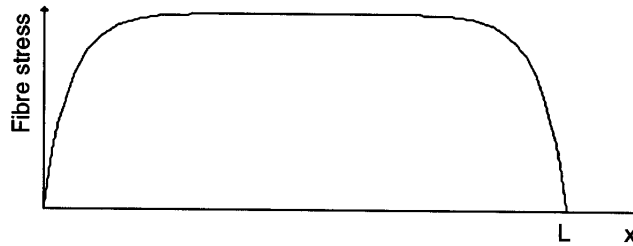


Fig. 1: Stress profile in a short fibre according to the Cox shear-lag theory

The form of this stress distribution is shown in Figure 1. Cox also showed that the average stress in a fibre is:

$$\sigma_{av} = E_f \epsilon_c \left[ 1 - \frac{\tanh \left( \frac{\omega L}{2} \right)}{\left( \frac{\omega L}{2} \right)} \right] \quad (4)$$

If the effective modulus of the fibres in the x (longitudinal) direction,  $E_{eff}$ , is defined as:

$$E_{eff} = \frac{\sigma_{av}}{\epsilon_c} \quad (5)$$

then the short fibre stress transfer efficiency factor,  $\eta_{st}$ , can be defined as:

$$\eta_{st} = \frac{E_{eff}}{E_f} = \frac{\sigma_{av}}{\sigma_{max}} = 1 - \frac{\tanh \left( \frac{\omega L}{2} \right)}{\left( \frac{\omega L}{2} \right)} \quad (6)$$

<sup>1</sup> A reasonable approximation where the fibre ends of adjacent fibres are evenly distributed along the length of the composite and the fibre cross-sectional area is small compared to the composite cross-sectional area.

Since  $\tanh \omega L/2 \approx 1$  where  $\omega L/2 > 3$ , it can be shown that  $\eta_{st}$  is dependent on  $\omega L$ . Space does not permit here, but it can be shown also that  $\omega L$  is related to the "fibre" aspect ratio,  $L/d$ , where  $d$  is the fibre diameter.

While the shape of the stress transfer profile shown in Figure 1 may well represent the situation in wood composite elements, these equations have been derived assuming a rigid, circular fibre, not a good description of wood composite elements. Another form of the shear-lag theory will now be examined.

For the purposes of investigating the stress transfer mechanism, a wood composite may be thought of as similar to a laminate (like plywood or laminated veneer lumber) made up from discontinuous bonded laminae. The geometry for stress transfer into a lamina in such a laminate is exactly analogous to that for a double lap bonded joint. The pioneering work in this area was done in 1938 by Volkerson, who presented a version of the shear-lag theory suitable for bonded lap-shear joints which is still considered accurate for double-lap joints where adherend bending is not a big factor. This arrangement of the original theory by Volkerson is from Adams and Peppiatt [4]. Figure 2 shows the geometry.

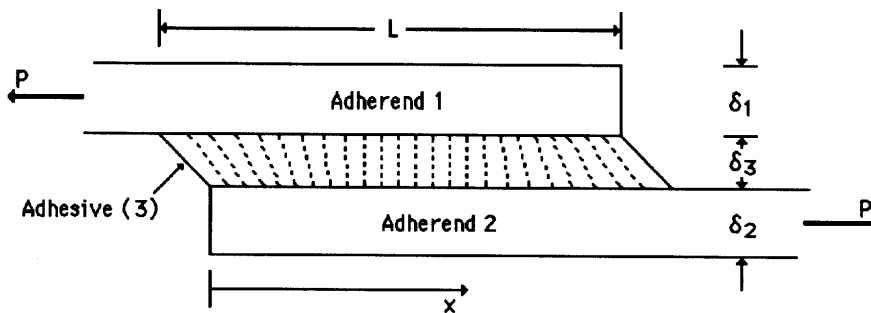


Fig. 2: Geometry of lap joint for Equation 2.10

$E$  and  $G$  are the elastic and shear moduli respectively,  $b$  is the lap joint width and  $P$  is the load on the joint; the subscripts 1, 2, 3 refer to adherend 1, adherend 2, and the adhesive. Volkerson showed that  $\sigma_{1x}$ , the tensile stress on adherend 1, is:

$$\sigma_{1x} = \frac{P}{b\delta_1} \left[ 1 - \psi (1 - \cosh \alpha x) - \frac{[1 - \psi (1 - \cosh \alpha L)] \sinh \alpha x}{\sinh \alpha L} \right] \quad (7)$$

where:

$$\alpha = \sqrt{\frac{G_3 (E_1 \delta_1 + E_2 \delta_2)}{E_1 E_2 \delta_1 \delta_2 \delta_3}} \quad \psi = \frac{E_2 \delta_2}{E_1 \delta_1 + E_2 \delta_2} \quad (8)$$

The form of the stress profile described by Equation 7 is shown below in Figure 3.

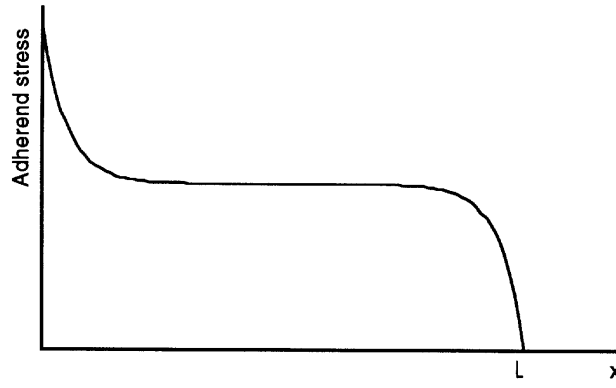


Fig. 3: Stress transfer profile in a lap joint

Volkerson's theory is based on the same assumptions as Cox's theory, although of course the assumptions are expressed in terms of the adherends and the adhesive, rather than the fibre and matrix. It can be demonstrated that the right-hand side of the two stress profiles is very similar. The rate of stress build up in a fibre or ply depends on the value of  $\omega$  or  $\alpha$  (in Equation 7 the value of  $\psi$  also has a very, very small effect), and for the conditions below Equations 3 and 7 give indistinguishable results to three significant figures. This shows that where stress transfer in a composite can be described by the Volkerson theory, the value of  $\alpha$  calculated using this theory could be substituted for  $\omega$  in Equation 6 to predict  $\eta_{st}$  for the composite.

$$L/2 \leq x \leq L \quad \alpha L > 25 \quad \alpha = \omega \quad \frac{P(1 - \psi)}{b\delta_1} = 2E_f\epsilon_c \quad (9)$$

Three of the assumptions behind the Volkerson theory, namely that the adherend and adhesive remain elastic, that a perfect bond exists between adherend and adhesive, and that there is no load transfer through the ends of the adherend, may be valid for wood composites at low strain. However the assumption that adherend shear strain is negligible compared to adhesive shear strain is clearly invalid, as the shear moduli of wood and adhesive are similar, and the wood element is normally much thicker than the adhesive. Adams and Peppiatt recognised that this is so for many practical lap joints, and presented a modification of the Volkerson theory which incorporates the effect of shear strains in the adherends. In their modified theory, Equation 8 is replaced by:

$$\alpha = \sqrt{\frac{2G_1G_2G_3(E_1\delta_1 + E_2\delta_2)}{E_1\delta_1E_2\delta_2(\delta_1G_2G_3 + \delta_2G_1G_3 + 2\delta_3G_1G_2)}} \quad (10)$$

This equation could be used to calculate the stress transfer profile for wood elements in a wood composite, and thus could be used to estimate  $\eta_{st}$  for a wood composite using Equation 6, rewritten here in terms of  $\alpha$  rather than  $\omega$ :

$$\eta_{st} = 1 - \frac{\tanh\left(\frac{\alpha L}{2}\right)}{\left(\frac{\alpha L}{2}\right)} \quad (11)$$

If Equations 10 and 11 are used to estimate  $\eta_{st}$  for a wood composite, it must be remembered that these equations assume no stress transfer through the ends or the sides of the adherends (wood elements). This assumption will be examined later.

### ASPECT RATIO OF SCRIMBER STRANDS

In most short fibre composites and many wood composites the fibre or wood element is an easily identifiable unit with a simple and consistent geometry. The Scrimber strand is a more complex entity, with a large variety of shapes and sizes. One of the first problems in describing Scrimber strands is to decide where one strand ends and the next begins; an increment can contain both independent strands and partially connected clumps. It has been assumed here that the wood in a clump is likely to lie together in the Scrimber, and to transfer stress as a unit. Therefore, for the purposes of stress transfer, a single strand was considered to be any part of the increment which was completely separate from the rest; clumps of partially connected pieces were considered to be a single strand. A representative strand is depicted in Figure 4.

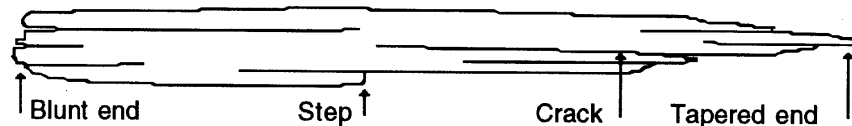


Fig. 4: Representative strand shape

The majority of strand ends were of the tapered type. Cracks were a feature of almost every strand, especially the clumps. Many of these cracks may be penetrated by adhesive and bonded during the pressing stage, but others are expected to persist in the cured composite. The presence of unbonded cracks within a strand is expected to lower the rate of stress transfer between strands, but no practical quantitative method of predicting the effect of this on Scrimber modulus could be conceived. Blunt steps were found on only a small minority of strands. Their effect would be the same as that of blunt-ended strands, discussed below, but on a much smaller scale; it was not possible to quantify it.

For stress transfer, it is considered that the most important feature of the strand is whether or not its end is bonded. When a strand end is unbonded, there is no stress transfer through the end, and shear-lag theory can be used to calculate  $\eta_{st}$  for that strand using the strand dimensions. When a strand end is bonded, most of the stress is expected to be transferred through the end. Adhesive bondlines in Scrimber are very thin, with a typical thickness of 0.1mm, and the adhesive modulus  $E_a$  is approximately half the strand modulus  $E_L$ . Therefore, where strand ends remain bonded, there is no significant variation in the fibre stress near the fibre end, and  $\eta_{st} \approx 1$ . Since Scrimber made up from end-bonded strands should have the same initial modulus as a hypothetical Scrimber made from continuous strands, for the purpose of calculating  $\eta_{st}$ , end-bonded strands can be considered to have an effectively infinite aspect ratio.

Whether or not a strand end in Scrimber is bonded appears to depend on its degree of taper. During the pressing stage, if the strand has a sufficiently fine taper, adjacent strands are able to deform around the strand end, and to remain in contact with it. This is depicted in Figure 5.

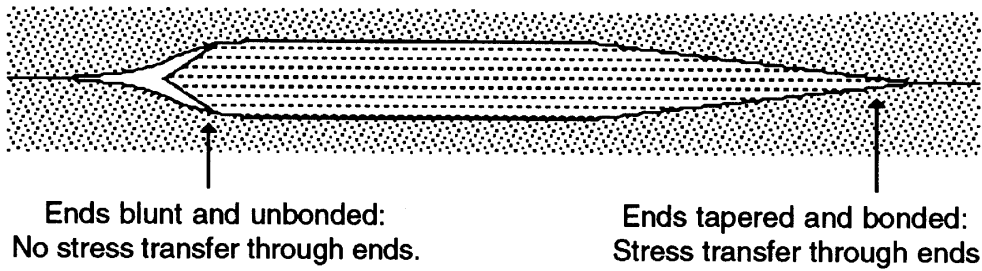


Fig. 5: Effect of strand end shape on end bonding and stress transfer.

Observation of the shapes of voids found at strand ends in Scrimber suggests that, for adjacent strands to be able to deform around the strand end and remain in contact with it, the strand end included angle needs to be less than approximately  $30^\circ$ .

On this basis, the strands in the sample increment were classified according to their end shapes and measured. The great majority of strands had at least one tapered end. Where the strand-end included angle was more than  $30^\circ$ , the end was considered to be blunt, and thus likely to be unbonded if incorporated into Scrimber. Approximately 25% of the strands by weight had two tapered ends. These were assigned an "infinite" aspect ratio, and their total weight fraction only was recorded. For strands with two blunt ends width, thickness, length and weight fraction were recorded. For strands with one blunt end only, the same dimensions were recorded; however in this case an effective length of twice the actual length was assigned and used to calculate an effective aspect ratio.

In total, three sets of data were recorded. In the first data set, as explained above, the actual strand length is recorded for strands with both ends blunt; the effective length for strands with one end blunt, and an "infinite" length for strands with two tapered ends.

A second set of aspect ratio data was recorded to investigate the effect on predicted Scrimber modulus of all strand ends being considered unbonded. In this set, the actual strand length was recorded for strands with one and both ends blunt. Since individual measurements had not been taken of strands with both ends tapered, these were excluded from this data set, which was recorded as a crude type of worst-case.

It was necessary to record a third aspect ratio data set because of a manufacturing practise at Scrimber International. The most common reason for strands having a blunt end was that this end was part of the original guillotined log end. These guillotined blunt ends were found close to the increment ends, which placed them on the surface of the cured beam. Since the average thickness of an increment after pressing was 5.5 mm, most of these blunt ends were found within that distance of the surface of the cured beam. It was regular Scrimber International practice to plane some material from all surfaces of the beam before use, and accordingly approximately 7mm was planed from the surface of beams 2270/4 and 2270/5 during production of the compression specimens. The compression specimens tested in this work therefore included few guillotined ends, and their modulus could be expected to reflect this.

For the third set of aspect ratio data, strands with the guillotined blunt end were re-evaluated, and considered to have a tapered end in its place, since those strands, after incorporation in the Scrimber beam, would have gained a tapered end during planing. Strand effective lengths

were modified accordingly. This third set of aspect ratio data is considered to be the most representative of the strands making up the compression specimens for Scrimber batch 2270.

### VERIFICATION OF THE SHEAR-LAG THEORY FOR WOOD COMPOSITES

To verify that the shear-lag theory as developed by Adams and Peppiatt [4] for non-rigid adherends adequately predicts stress transfer in wood composites, the predictions of that theory were tested against strain measurements near the end of a wood element in a simple wood composite. Laminated Veneer Lumber (LVL), was chosen as a suitable composite because it has a simple and consistent wood element geometry and similar glue-lines to Scrimber. Most importantly, the stress state within a loaded section of LVL was expected to be more predictable than in other wood composites, especially Scrimber, and the wood elements within LVL were large enough to easily apply bonded foil strain-gauges.

The LVL chosen was made up from 15 rotary-peeled 3mm plies of Radiata, from the same general area as the Scrimber feedlogs. The plies, each 1200 mm long, were bonded with phenol formaldehyde adhesive; the outer three plies on each face were scarf jointed, while the remainder were laid butt to butt with a small gap, typically 1 mm. The longitudinal direction of each ply coincided with the longitudinal direction of the specimen.

A 600mm long piece of LVL was cut as a test piece. The test specimen was 47mm thick (normal to the ply plane) and 10mm deep. A ply end near the centre of the test specimen, in an area generally free from other butt joints or grain irregularities, was chosen for measurement of the strain build-up. Foil strain gauges were bonded to the edge of the ply near its end. The gap between the two ply ends was 1mm; approximately 70% of the gap was filled with adhesive spew incorporating bubbles. Stress transfer in the LVL test specimen was expected to be similar to that in a double-lap-shear specimen. The geometry of the test specimen, considered as a double lap-shear specimen and using the notation of Adams and Peppiatt from Figure 2, is set out in Figure 6.

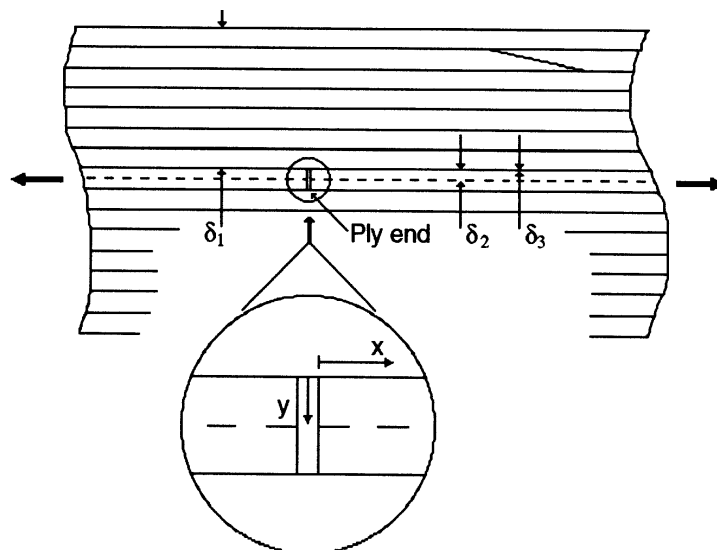


Figure 6. LVL considered as a double lap shear specimen.

The stress transfer Equation 7 from Adams and Peppiatt has been rewritten in terms of the notation in Figure 6. It predicts that for  $0 \leq x < L/2$ :

$$\sigma_{2x} = \frac{F}{2\delta_2 b} \left[ \psi (1 - \cosh \alpha x) + \frac{[1 - \psi (1 - \cosh \alpha L)] \sinh \alpha x}{\sinh \alpha L} \right] \quad (12)$$

where (Eqn 10):

$$\alpha = \sqrt{\frac{2G_1 G_2 G_3 (E_1 \delta_1 + E_2 \delta_2)}{E_1 \delta_1 E_2 \delta_2 (\delta_1 G_2 G_3 + \delta_2 G_1 G_3 + 2\delta_3 G_1 G_2)}}$$

A modification must be made to Equation 10 in order to predict a sensible value of  $\alpha$  for the LVL experimental configuration. Equation 10 is based on the assumption that both adherends are free to deform in shear. Since the gap between the ply ends is very small, adherend 1 is effectively rigid, and  $G_1 \gg G_2$ . In addition, because the adhesive is very thin,  $\delta_2 G_3 \gg 2\delta_3 G_2$ , and in this case  $E_1 = E_2$ . Therefore the equation can be simplified to:

$$\alpha = \sqrt{\frac{2G_2 (\delta_1 + \delta_2)}{E_1 \delta_1 \delta_2^2}} \quad (13)$$

Using Equation 13,  $\alpha$  was calculated for the LVL experimental configuration shown in Figure 6. The predicted value of  $\alpha$  for the LVL specimen was 0.26. The strain-gauged LVL specimen was loaded in tension to 20 kN, in 1 kN steps. At each step, individual gauge readings were recorded. All strain/load plots were linear for specimen loads up to 8 kN. For this initial linear section, Figure 7 shows the relative strain in the ply under each of the strain gauges plotted against the distance of the gauge from the ply end.

Extrapolation of the measured strain profile to the ply end indicates that the strain at the ply end was approximately 50% of the maximum ply strain; ie. roughly 50% of the load was transferred into the ply through its end. This load is thought to have been transferred by tensile stresses in the adhesive spew, which as noted previously filled approximately 70% of the inter-ply gap. In addition, the measured rate of strain transfer (controlled by the value of  $\alpha$  in the shear-lag model) for the ply is less than predicted, and therefore the predicted value of  $\alpha$  appears to have been too high. The rate of stress transfer into the ply could be expected to have been reduced by the peeling cracks observed in every ply. The presence of these cracks apparently lowers the ply shear stiffness  $G_2$  and consequently  $\alpha$  has been overestimated.

A shear lag profile can be shown to closely fit the measured strain transfer profile if  $\alpha = 0.15$  and  $\sigma = 0$  at  $x = -4.5$  mm (which corresponds to the strain at the ply end being 52% of the maximum strain), as demonstrated in Figure 7. This suggests that the chosen shear-lag theory can accurately predict the form of the stress transfer profile in a wood element if the amount of stress transferred through the end is known and the effect of wood element internal cracking on the effective shear modulus of the wood element can be estimated.

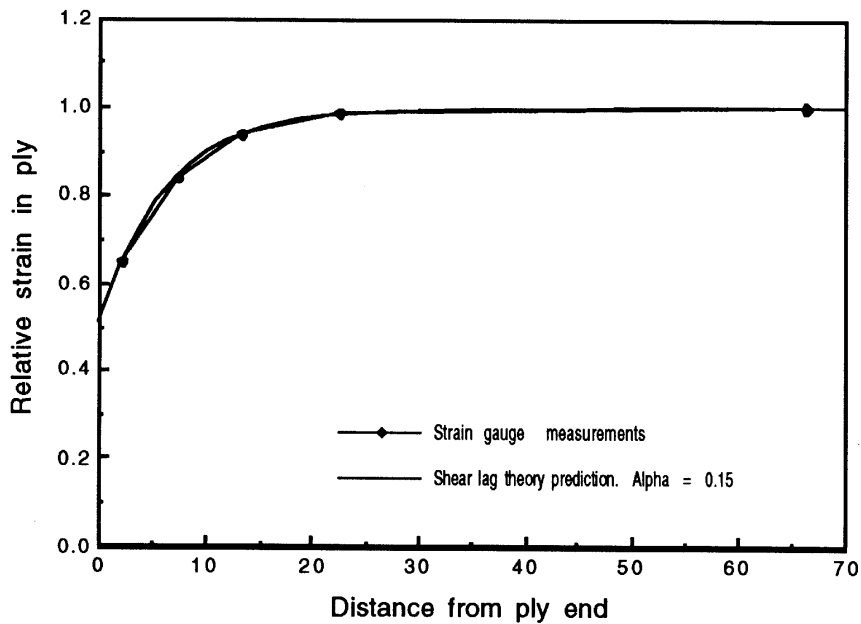


Figure 7. Fitting of the shear-lag prediction to the measured strain profile.

It must be emphasised that the stress transfer profile described above applied only where specimen load was less than 8kN. The strain gauge measurements also indicated partial failures of the ply end bond at 8kN and again at 15kN. The strain transfer profiles above these loads showed progressively less strain transfer through the end of the ply.

This experiment confirmed that the stress profile in a wood composite element fits the shear-lag form very well, and that the appropriate shear-lag theory can be used to predict  $\eta_{st}$  for wood composites. It also showed that estimates of  $\alpha$ , and therefore  $\eta_{st}$ , however, from wood element geometry and properties are likely to be too high if the wood element contains internal unbonded cracks. A porous spew fillet 1mm thick, bonding approximately 70% of the strand end surface, was apparently able to transfer 52% of maximum ply stress through a very blunt ply end. The result suggests that, in a lightly-loaded wood composite, for a wood element with a well-bonded end, almost all of the stress could be expected to be carried through the end. This justifies the proposal made earlier that end-bonded strands could be treated as effectively continuous for the estimation of  $\eta_{st}$ .

### ESTIMATION OF THE STRESS TRANSFER FACTOR FOR SCRIMBER

In detailed investigations of the microstructure of Scrimber it was found that the strand cross-section circumference was similar to that of a square of the same area, and that at least 40% of the strand surface was unbonded. Therefore for the purposes of predicting stress transfer between strands in Scrimber, the typical strand was assumed to be square in cross-section, and bonded on two opposite sides only. (The unbonded surface fraction was thus assumed to be 50%.) The strand was also assumed to be in the centre of the Scrimber compression specimen, as shown in Figure 8.



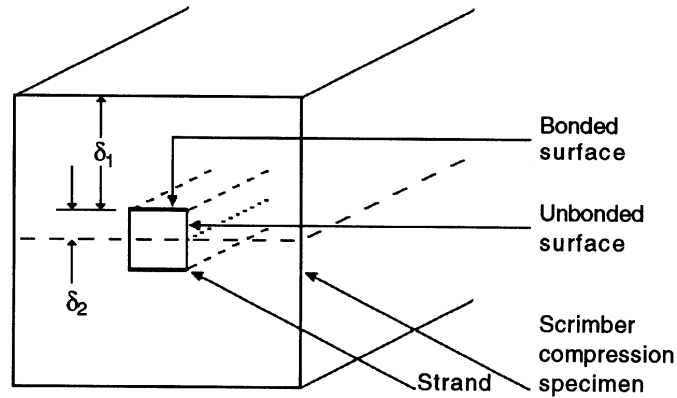


Figure 8. Geometry and notation for application of shear-lag theory to Scrimber.

The notation used is the same as for the LVL specimen in Figure 6. The strand cross-sectional dimensions were calculated as shown below, where  $A_s$  is the measured strand cross-section area and  $D_s$  is the batch 2270 densification factor:

$$2\delta_2 = \sqrt{\frac{A_s}{D_s}} \quad (14)$$

For each strand, the variable  $\alpha_{(i)}$  was calculated from Equation 13 and the stress transfer efficiency factor,  $\eta_{st(i)}$ , was then calculated from Equation 11.  $P_{(i)}$  was defined as the strand mass divided by the sample mass. For Scrimber batch 2270,  $\eta_{st}$  was calculated for each set of strand aspect ratio measurements using:

$$\eta_{st} = \sum_{i=0}^{i=n} \eta_{st(i)} P_{(i)} \quad (15)$$

For Set 3, believed to be the most representative set of aspect ratio measurements for the sample increment,  $\eta_{st}$  was calculated to be 0.98. For Set 1 (not corrected for the absence of guillotined ends in the Scrimber specimens)  $\eta_{st} = 0.96$ ; and for Set 2 (the crude worst case),  $\eta_{st} = 0.94$ .

The estimate of  $\eta_{st} = 0.98$  for batch 2270 reached above is probably too high, as it relies on the assumption that the Scrimber strands were internally intact. However investigations of Scrimber microstructure found that internal unbonded cracks were likely to be present in the majority of strands. No practical method of predicting the effect of these internal cracks could be conceived. The quantitative effect of these cracks can only be guessed, using the LVL stress transfer experiment as a guide. Given that relatively minor internal cracking lowered the effective value of  $\alpha$  in the LVL to 60% of the predicted value, it seems possible that the existence of cracks within the majority of Scrimber strands might reduce the effective value of  $\alpha$  for those strands to half or even a third of its predicted value, giving rise to an estimate for  $\eta_{st}$  as low as 0.95.

## MODEL PREDICTIONS AND CONCLUSIONS

The Krenchel-type model introduced in as Equation 2 was found to need modification as follows. The symbols are defined below.

$$E_s = \eta_d D_s E_w \quad (16)$$

This makes the full model:

$$E_B (\text{Scrimber}) = \eta_{st} \eta_o (\eta_d D_s E_w) V_s + E_a V_a \quad (17)$$

Values for all the variables in this relationship were found for Scrimber batch 2270. Using this proposed model, the average modulus of the Scrimber batch 2270 compression specimens was predicted to be 11.05 GPa at standard conditions. This compares well with the average measured modulus for those specimens of 10.8 GPa at standard conditions.

$\eta_{st}$ (stress transfer efficiency factor)	= 0.98.	$E_w$ (feedlog modulus)	= 12.9 GPa.
$\eta_o$ (orientation efficiency factor)	= 0.875.	$V_s$ (strand volume fraction)	= 0.875.
$\eta_d$ (strand damage factor)	= 0.88.	$E_a$ (adhesive modulus)	= 7.6 GPa.
$D_s$ (strand densification factor)	= 1.27.	$V_a$ (adhesive volume fraction)	= 0.03.

Although it was impractical to attempt to design an experiment to test the effect of strand aspect ratio, and therefore stress transfer, directly, the apparent accuracy of the whole model allows some confidence in the predicted value of the various factors.

Strand discontinuity was found to have only a small effect on Scrimber modulus. The high strand unbonded surface fraction of the batch studied also had little effect on modulus. Strand misorientation and damage were found to be the major factors reducing Scrimber modulus.

This method described here of estimating the effect of "fibre" discontinuity in wood composites is relatively simple and demonstrates the usefulness of applying standard composites theory, allied with a good grasp of the composite microstructure, to the modelling of wood composites. Procedures for estimating the efficiency factors could easily be modified for application to other wood composites.

## REFERENCES

1. Krenchel, H., *"Fibre Reinforcement"*, Akademisk Forlag, Copenhagen, 1964.
2. Cox, H.L., "The elasticity and strength of paper and other fibrous materials", *British Journal of Applied Physics*, Vol. 3, 1952, pp 72-79.
3. Holister, G.S., and Thomas, C., *"Fibre Reinforced Materials"*, Elsevier, London, 1966.
4. Adams, R.D., and Peppiatt, N.A., "Effects of Poisson's ratio strains in adherends on stresses of an idealised lap joint", *Journal of Strain Analysis*, Vol 8, 1973, pp 134-139.

# MICROCELLULAR GRAPHITIC FOAM PROCESSING

Kristen M. Kearns<sup>1</sup> and David P. Anderson<sup>2</sup>

<sup>1</sup> *Wright Laboratory Materials Directorate, US Air Force, 2941 P St. Ste. 1,  
Wright-Patterson Air Force Base, Ohio 45433-7750 USA*

<sup>2</sup> *University of Dayton Research Institute, 300 College Park Avenue,  
Dayton, Ohio 45469-0168 USA*

**SUMMARY:** This paper reviews the experimental work to develop processing conditions for pitch foams. The foams are produced by dissolving a gas into the pitch under pressure. After the appropriate amount of time has lapsed the pressure is released, the gas nucleates bubbles, and these bubbles grow, forming the pitch into the foam structure. The resultant foamed pitch is then stabilized in an oxygen environment. At this point a rigid structure exists with some mechanical integrity. The foam is then carbonized to 800°C followed by a graphitization to 2500°C. The shear action of the bubbles growing aligns the graphitic planes along the foam struts to provide the ideal structure for good mechanical properties. Variations of the blowing temperature, blowing pressure and saturation time results in foams of various open pore sizes. This study showed the final temperature and the duration of the hold time most effected the foam structure. A lower final temperature and a longer hold time produced a foam with a uniform porosity foam with a very small bubble size.

**KEYWORDS:** structural foams, graphitic foams, open-cell foams, processing

## INTRODUCTION

Structural composites are based on disconnected carbon fibers integrated in some type of matrix. The strength and stiffness of commercial carbon fibers are due to the graphitic morphology that originates from the melt spinning of the precursor pitch. If an interconnected network of struts could be produced which possessed a similar morphology to the carbon fiber, a new generation of composite reinforcement could emerge. Foams are an example of such materials with an open cell structure being the desired architecture. Microcellular, open cell foams can be produced from anisotropic pitch with graphitic planes aligned along the struts. The process sequence includes blowing, stabilizing, carbonizing, then graphitizing the foam, similar to the process for manufacturing pitch-based carbon fibers. A foam could be blown into a mold for net-shape composites or co-processed with fibers for anisotropic reinforcements. Model graphitic foams were predicted [1] to have a compression modulus of approximately 2 GPa with a density of about 0.1 gm/cm<sup>3</sup>. Not many other foams or core materials have a density and compression modulus near these values.

The original process for fabricating microcellular foams was developed by Suh *et al.* [2-3] They demonstrated microcellular foams could be produced from amorphous polymers by saturating the polymer with a gas then heating above the glass transition temperature. The sudden release of pressure resulted in a foam of uniformly distributed pores. Dutta, *et al.* [4] modified this process by saturating with nitrogen under pressure to get better solubility of nitrogen into pitch. In this process, the solubility of nitrogen into the pitch is critical to foam

fabrication. Therefore, they first melted the pitch in a steady flow of nitrogen. The pitch was then saturated with nitrogen gas and held for 10 minutes before dropping the pressure and temperature suddenly.

The current method of fabricating microcellular foams is a variation of both the Suh and Dutta work. It includes a slight initial pressurization before the pitch is heated. Thus, the pitch is under a slight pressure during heating and is further pressurized at the final temperature. For this process pressure, temperature and time are the controllable parameters and can be varied to produce foams with various magnitudes and types (closed or open) of porosity. Therefore, this study was done to determine the effect of these parameters on the final foam structure.

## **EXPERIMENTAL**

### **Materials**

Foams were processed from AR pitch manufactured by Mitsubishi Gas Chemical Co. The pitch is produced by the catalytic polymerization of naphthalene and supplied in a pellet form. Manufacturing data claims the softening temperature is 239°C and the material is 100 percent anisotropic. The glass transition temperature occurs over a temperature range of 230 to 260°C.

### **Processing**

The pitch pellet was jet-milled into particles of an average size of 1-3 microns. Approximately 10 grams of jet-milled pitch was pressed into a 5.7 cm diameter puck. The pitch puck was then placed in a Parr pressure reactor and heated (under a slight nitrogen pressure) at 3°C/min to the desired final temperature. When the puck reached the final temperature additional nitrogen was added to obtain the final desired pressure and the entire system was held at these conditions for a determined amount of time. The pressure was abruptly vented to the atmosphere. Figure 1 shows a process cycle, with a sample rate of one data point per 5 seconds. This processing created the foam structure to be further analyzed. Further processing was required to transform it from a pitch to a carbonaceous foam. After blowing, the foam was quickly removed from the reactor and placed in a 150 to 175°C oven. The foam was then cooled to room temperature and weight and dimensional measurements were taken. The foams were then oxygen stabilized in a forced air oven at 220°C until a weight gain of approximately 7 percent had been reached. Samples were then carbonized with a 60°C/hour heating rate to 850°C in a nitrogen environment.

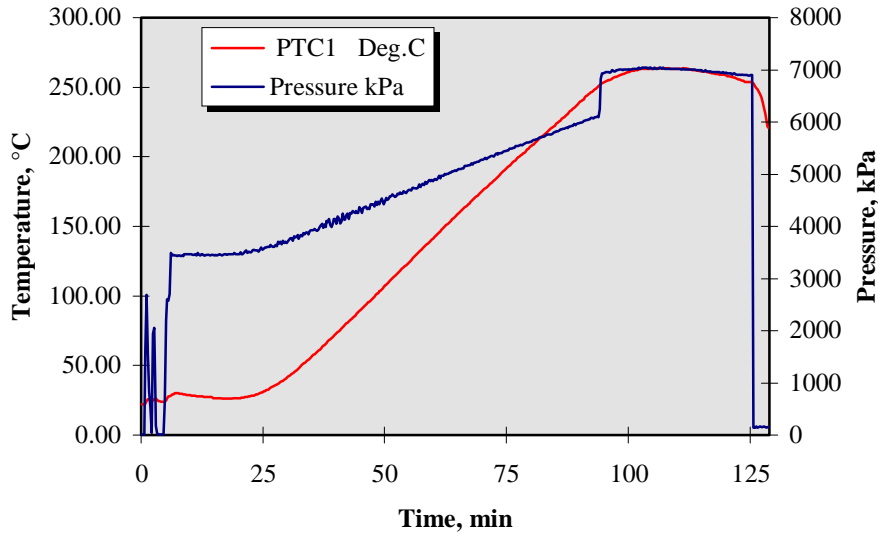


Figure 1: Foam Blowing Process Cycle

**Characterization**

Physical evaluations included weights and dimensional measurements. These measurements were taken after puck fabrication, after foaming, and after carbonization to give a non-destructive indication of any differences produced by the various processing conditions. The completely processed foams were examined under both optical and scanning electron microscopy (SEM) and measurements of the pore size, pore shape, and amount of open porosity were made. The relative pore size was measured using the SEM images. All samples were examined at the same magnification and pore sizes measured using arbitrary rulers in the imaging software program. Averages were calculated using 101 randomly chosen pores. The standard deviation of the pore size was also calculated and assumed to be a measure of the uniformity of the foam porosity.

Finally, compression tests were performed on samples from the experimental conditions that produced testable materials. The test configuration basically followed ASTM D695, however sample sizes were dictated by the size of the fabricated foam. From the tests both compression strength and modulus were calculated.

**Design of Experiment**

A 2<sup>4</sup> half factorial design of experiment was performed to look at the effect of four process parameters; the initial pressure, final temperature, final pressure, and the length of the hold time at the final conditions. Table 1 provides the experimental values for each parameter and Table 2 the conditions of each experimental run.

Table 1: Experimental Values

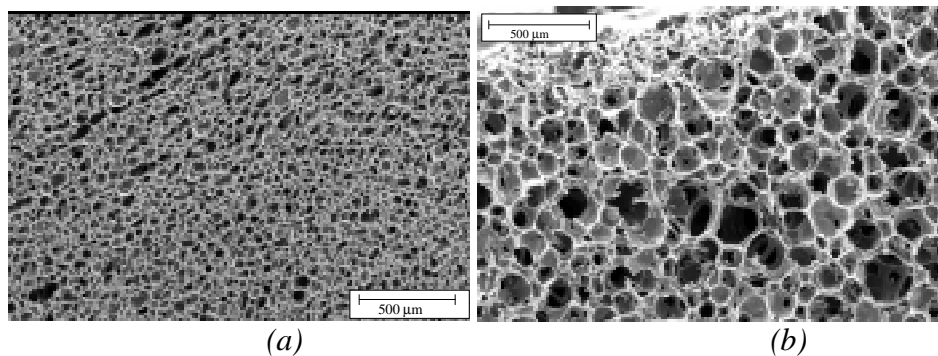
Initial Pressure (P <sub>i</sub> ):	1380 kPa (-)	3450 kPa (+)
Final Temperature(T <sub>f</sub> ):	250°C (-)	270°C (+)
Final Pressure (P <sub>f</sub> ):	6900 kPa (-)	10,350 kPa (+)
Hold Duration (t):	15 minute (-)	30 minute (+)

Table 2: Experimental Run Conditions

Sample #	P <sub>i</sub>	T <sub>f</sub>	P <sub>f</sub>	t
1	+	+	+	+
2	-	+	+	-
3	+	-	+	-
4	-	-	+	+
5	+	+	-	-
6	-	+	-	+
7	+	-	-	+
8	-	-	-	-

## RESULTS AND DISCUSSION

For all experiments, foams were created with varying microstructures and compression properties. Figure 2 shows SEM images of the extreme microstructures produced by varying the process parameters. The foam in Figure 2a was processed with higher initial pressure, the lower final temperature and final pressure, and the longer hold time. Figure 2b was processed with higher initial pressure and higher final temperature, lower final pressure, and the shorter hold time. The sample represented in Figure 2a had much more uniform porosity with a smaller bubble size than the non-uniform, large sized pores shown in Figure 2b. Figure 2a represented the more desired foam structure.



(a) *small, uniform porosity*, (b) *large, non-uniform pores*.

*Figure 2: SEM Images of foam samples,*

The volumetric change due to foaming was measured by comparing the pre-foamed puck volume to the foam volume before stabilization. Each process parameter was plotted versus the volumetric change to determine which had the most influence, Figure 3. As can be seen the only parameter that had any effect is the hold duration at the final temperature after the final pressure has been added. A shorter hold time resulted in a larger expansion in the foamed pitch. The longer time at the final conditions allowed the system to equilibrate and more nitrogen was able to diffuse into and uniformly disperse throughout the pitch. When the pressure was released the nitrogen nucleated and grew bubbles and quickly produced an open-cell structure. As the open cell structure formed, the nitrogen was able to diffuse out of the foam and bubble growth was terminated.

The final temperature had a minor secondary effect on the volumetric change. The foams produced with a lower final temperature did not expand as much as the ones made at the

higher temperature. At the lower temperature, the pitch had a higher viscosity and could keep more nitrogen trapped. When the pressure was released the nitrogen expanded and quickly created an open cell structure. The open cells allowed the nitrogen to vent to the atmosphere and minimized volume expansion. At the higher temperature, less nitrogen was available for bubble growth and an open structure was not produced until much later in the foaming process. Therefore, a larger expansion in volume occurred at the higher final temperature.

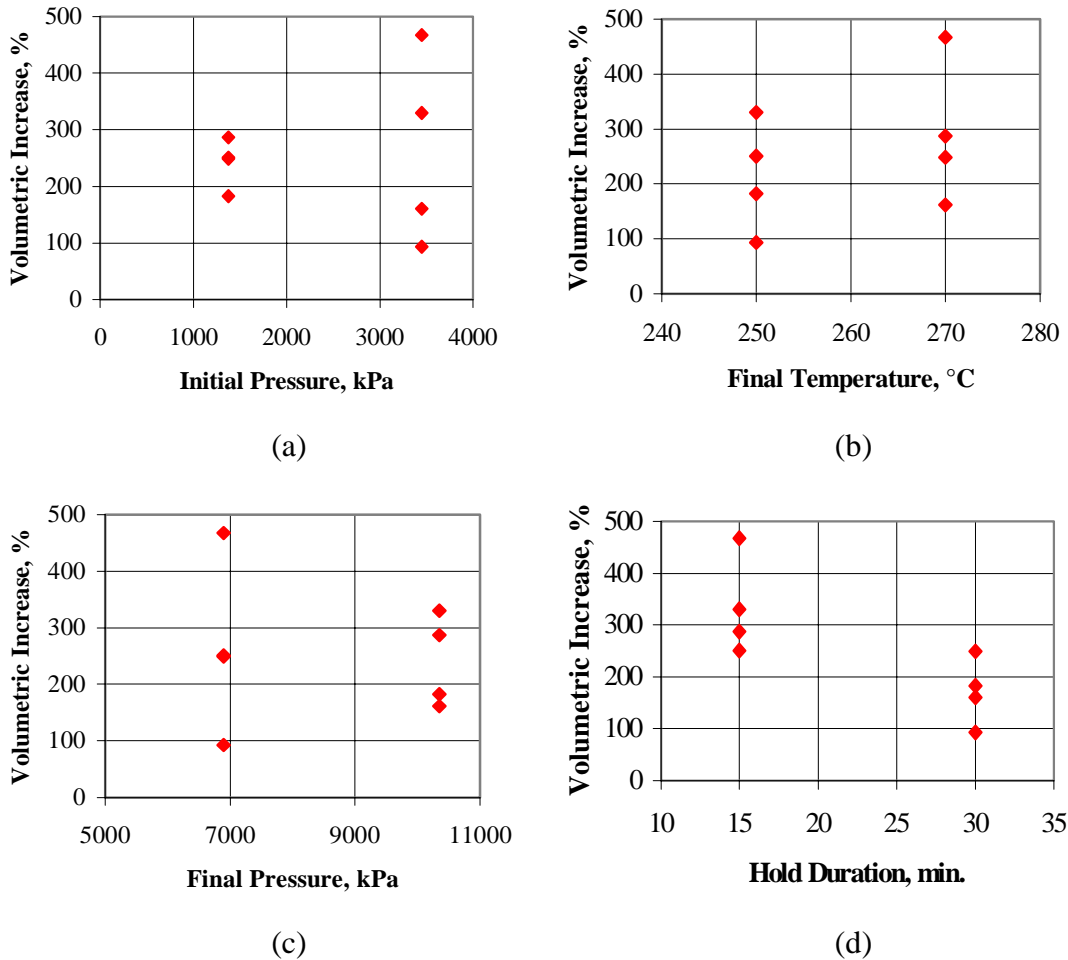


Figure 3: Volumetric Increase from puck to foam as a function of (a) initial pressure, (b) final temperature, (c) final pressure, and (d) hold duration.

The average pore size was plotted against each of the process parameters, Figure 4, to determine what were the effects of each parameter on the pore size. The results showed the final temperature had the largest influence on pore size. The higher final temperature produced foams with larger size pores than the lower final temperature. At the lower temperature the pitch has a much higher viscosity and thus a much greater ability to keep the nitrogen trapped. The greater amount of nitrogen trapped inside the pitch the more bubbles that could nucleate and/or the more nitrogen there is available to grow the bubbles. The viscosity of the pitch was high enough to restrict the bubble growth to keep the pores small.

When the results from the volume increase were compared to the relative pore size it was determined the smaller pore size also had the lower volume increase. Apparently the nitrogen nucleated bubbles and as they grew they formed an open-cell foam structure that allowed the

nitrogen to diffuse out before the bubbles grew to a larger size or coalesced to form larger pores. This would allow for a high density of very small bubbles.

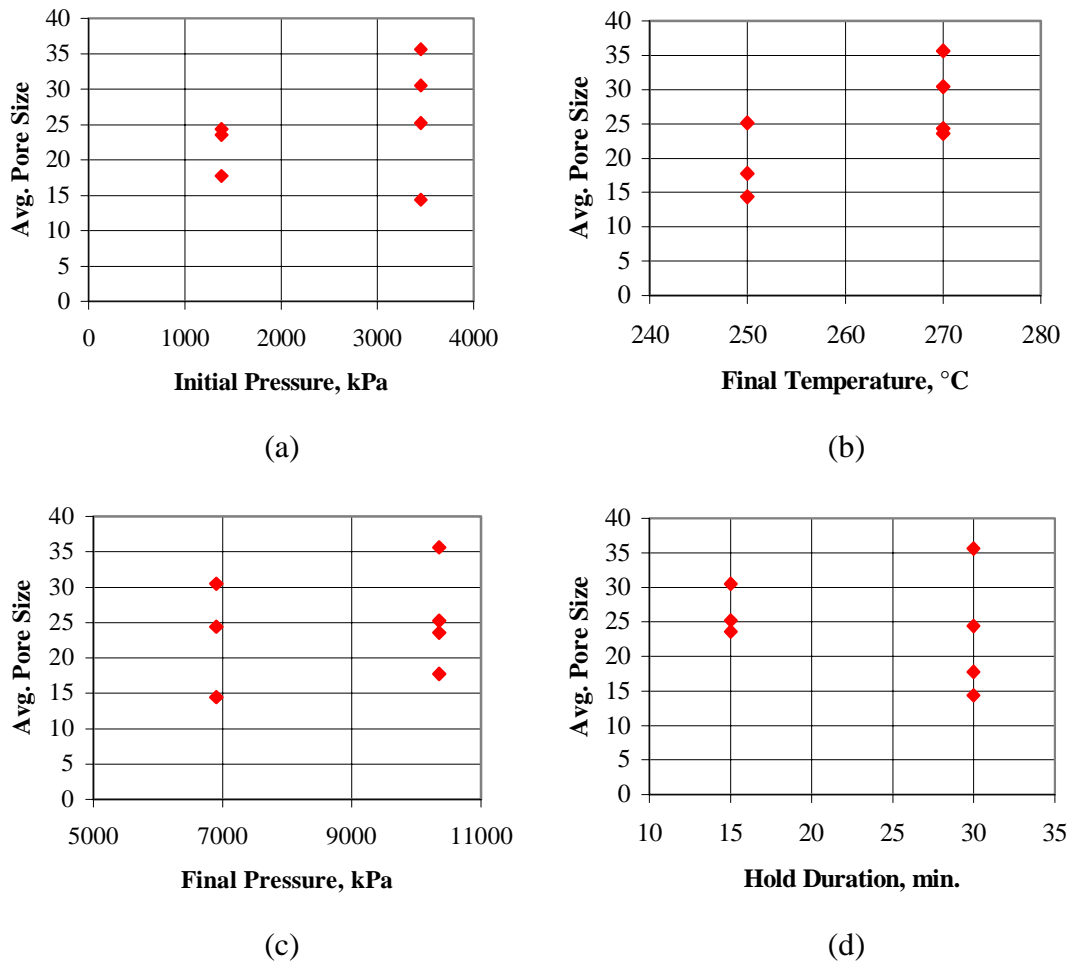


Figure 4: Average pore size as a function of (a) initial pressure, (b) final temperature, (c) final pressure, and (d) hold duration.

Compression tests were only done on material from experiments 3,4,5,7 in Table 1. These were the only experiments that produced samples large enough to make compression samples. The compression strength was plotted versus process parameters and shown in Figure 5. The higher final temperature produced lower strength foams than the lower final temperature. This trend could be correlated with the relative pore size. The larger pore size produced a foam with lower compression strength. This was due to the smaller strut size in the larger pore foam. As the bubble grows the strut becomes more elongated and thinner than the struts of the smaller pore foam. The pore size can be explained by the difference in the viscosity of the pitch at 250°C and 270°C. At 270°C the pitch molecules were more mobile and the nitrogen did not saturate the pitch as much as it did at 250°C.



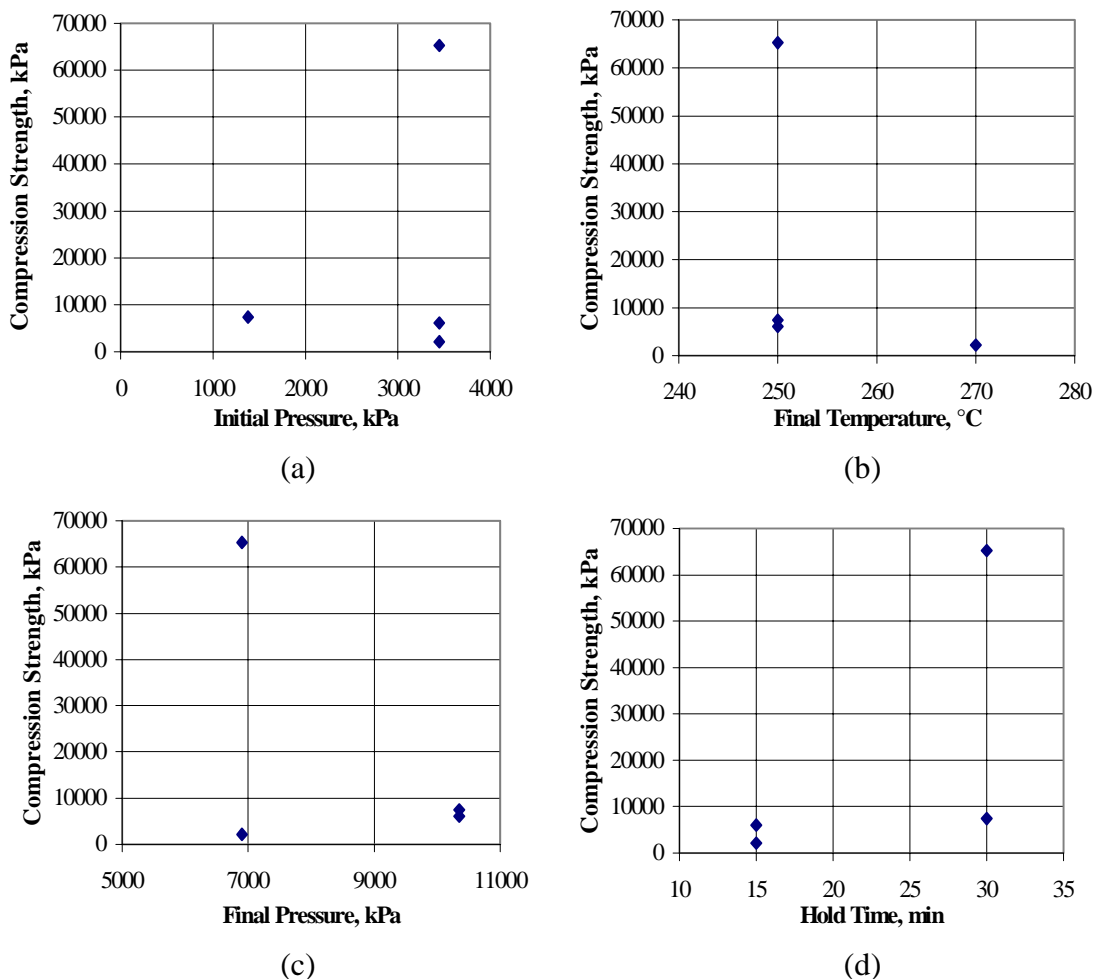


Figure 5: Compression strength as a function of (a) initial pressure, final temperature, (c) final pressure, and (d) hold duration.

## CONCLUSIONS

From the experiments the amount of pressure does not significantly contribute to the final foam structure. Foams processed at the high and low levels had the same structure. Therefore, the pressures that were studied were sufficient to diffuse nitrogen into the puck. Further studies need to be conducted to determine the lower limit on the amount of pressure required to produce a foam structure.

The final temperature did produce some variation in the foam materials. At the lower temperature the pitch is within the glass transition temperature range. In this range the material had more integrity and was able to restrict gas flow and bubble growth. When the foam was at 250°C and the pressure was released the pitch was viscous enough to restrict bubble growth and produce a small pore size foam. At 270°C the pitch viscosity was low enough so the nitrogen was able to diffuse in and out easily. When the pressure was released the nitrogen nucleated bubbles and the bubbles grew rapidly leaving a large cell foam behind.

The hold time produced variations in the different foam samples. A more uniform pore distribution was produced with the longer hold time. This could be attributed to the system having more time to reach an equilibrium at the final processing conditions. After the final

temperature is reached and the final pressure is applied, the 30 minute hold time allowed the pitch system to equilibrate and the nitrogen to further diffuse into the pitch. The more nitrogen in the pitch the more gas available to nucleate and grow bubbles. Experiments with additional hold times need to be conducted to determine the effect longer and shorter hold times have on the foam structure.

The most desirable foam structure was produced with a final temperature of 250°C and these conditions were maintained for 30 minutes before the 10350 kPa of pressure was suddenly released. These parameters allowed nitrogen to diffuse into the pitch, yet did not weaken the pitch's ability to restrict bubble growth to produce the small pores. This foam structure had the desired uniform, small pore size. The compression strength of this structure was the highest value achieved for all of the foam experiments.

### REFERENCES

1. Hall, R.B. and Hager, J.W., "Graphitic Foams as Potential Structural Materials", *21<sup>st</sup> Biennial Conference on Carbon Extended Abstracts*, 1993, pp. 100-101.
2. Colton, J.S. and Suh, N.P., "The Nucleation of Microcellular Thermoplastic Foam with Additives: Part I: Theoretical Consideration", *Polymer Engineering and Science*, Vol.27, No.7, 1987, pp.485-499.
3. Colton, J.S. and Suh, N.P., "Nucleation of Microcellular Foam: Theory and Practice", *Polymer Engineering and Science*, Vol.27, No.7, 1987, pp.500-503.
4. Dutta, D., Hill, C.S., and Anderson, D.P., "Processing, Structure, and Morphology of Graphitic Carbon Foams Produced from Anisotropic Pitch", *Novel Forms of Carbon II, MRS Symposium Proceedings*, Vol. 349, pp. 61-66.
5. Hager, J.W., Anderson, D.P., and Roy A.K., "Structure and Properties of Carbon Foams from Pitch and Phenolic Precursors", *22nd Biennial Conference on Carbon Extended Abstracts*, 1995, pp.106-107.
6. Hager, J.W., Anderson, D.P., and Roy, A.K., "Progress in Open-Celled Carbon Foams", *Proceedings of 40th International SAMPE Symposium (Closed Sessions)*, 1995, pg. 42-48.
7. Hager, J.W., and Anderson, D.P., "Idealized Ligament Formation and Geometry in Open-Celled Foams", *21st Biennial Conference on Carbon Extended Abstracts*, 1993, pp. 102-103.
8. Anderson, D.P., Gunnison, K.E., and Hager, J.W., "Ligament Structure of Open-Cell Carbon Foams and the Construction of Models Based on that Structure". *Novel Forms of Carbon, MRS Symposium Proceedings*, Vol. 270, 1992, pp.47-52.

# DEVELOPMENT AND CHARACTERISATION OF A NEW HIGH DAMPING COMPOSITE: $Mg_2Si/Mg$

Christine Mayencourt and Robert Schaller

*Institut de Génie Atomique, Ecole Polytechnique Fédérale de Lausanne,  
1015 Lausanne, Switzerland*

**SUMMARY:** A new, lightweight, high-damping material has been processed and characterised. It is a magnesium based composite with unidirectional  $Mg_2Si$  fibres. This natural composite has been produced by unidirectional solidification of a Mg-Si eutectic alloy (1.34 wt% Si) or near eutectic alloy (2 wt% Si). Mechanical strength was measured through tensile tests and the damping capacity was deduced from internal friction measurements in a low frequency torsion pendulum. The results show that these composites have a tensile strength comparable with industrial magnesium cast alloys such as AZ63 and a damping capacity which is 10 to 100 times higher. The mechanical properties and damping capacity are interpreted in terms of sample microstructure with emphasis on the effects of matrix and fibre orientation on the dislocation mobility.

**KEYWORDS:** damping capacity, mechanical strength, magnesium, unidirectional fibres, dislocations, microstructure

## INTRODUCTION

Modern technology tends to suppress mechanical vibrations for social and economic reasons. Mechanical vibrations produce undesirable noise and can affect the precision of a machine-tool or cause fatigue-induced rupture of devices. These mechanical vibrations can be reduced in many ways, for instance by using external dampers or by increasing the inertial masses. However, these solutions are not always applicable, particularly in transport systems, which require lightweight and small structures [1]. Thus, contemporary transport systems need low-density materials which exhibit simultaneously a high-damping capacity and a high mechanical-strength. These properties are often incompatible [2] because the microscopic mechanisms which are involved in strengthening and in damping are not independent [3]. It is therefore important to develop new materials such as two-phase composites in which each phase can play a specific role: strengthening or damping.

Pure magnesium is known to exhibit a very high damping capacity [4], but its mechanical strength is low [5]. This metal can be hardened by introducing second phase precipitates which are able to pin dislocations, in order to avoid plastic deformation and thereby to increase the yield stress. However, if the mechanical properties are better in magnesium alloys than in pure magnesium, the damping capacity is lost in most of them [5]. A pure magnesium matrix reinforced with high-strength fibres is hence a good candidate for a high-damping composite. Actually the damping capacity of magnesium is due to dislocation vibration [6]. In order to obtain a high damping, this implies that the dislocation loops, which

are defined between the pinning centres, must be relatively free to vibrate. Thus, the magnesium matrix has to be relatively pure. In other words, in order to keep the damping capacity high, attention must be paid to the choice of the alloying elements, whose solubility in magnesium has to be low enough.

In this context, Mg - Si alloys have been studied as a system of low solubility because silicon is almost insoluble in magnesium (solubility lower than 30 ppm) [7]. Using the eutectic composition properties, a Mg-Si eutectic alloy (1.34 wt% Si) or near eutectic alloy (2 wt% Si) is converted into a magnesium matrix composite with Mg<sub>2</sub>Si fibres by unidirectional solidification. The obtained natural composite is formed by a pure magnesium matrix reinforced with a low fraction of Mg<sub>2</sub>Si fibres. So the dislocation loops can be long enough to vibrate and dissipate energy while pinning by fibres avoids plastic deformation.

This paper presents Mg<sub>2</sub>Si / Mg composites which were processed by unidirectional solidification and characterised by optical and transmission electron microscopy, by tensile tests and by mechanical spectroscopy, i.e. measurements of the internal friction and of the elastic shear modulus as a function of temperature for different samples.

### **EXPERIMENTAL PROCEDURES**

Mg<sub>2</sub>Si / Mg composites were processed by unidirectional solidification of two different alloys. The grade A was an eutectic alloy (1.34 wt% Si) of low purity and the grade B was a near eutectic alloy (2 wt% Si) of medium purity, the mean impurity concentration is about 0.15%. Unidirectional solidification was performed using the same process as the Bridgman method for single crystal growth [8]. In a controlled atmosphere, a graphite crucible containing the alloy is moved in a vertical thermal gradient furnace. If the solidification surface is plane, the solid phase growth is regular and a two phase composite expands with vertical Mg<sub>2</sub>Si fibres in a pure magnesium matrix. This solidification mode can occur if the alloy concentration is the eutectic concentration or near eutectic concentration. The solidification rate ( $v$ ) and the distance between fibres ( $\lambda$ ) are related by [9]:

$$\lambda^2 v = \text{const.} \quad (1)$$

Plate shape specimens were cut from the solidified rods by spark machining, in such a way that the sample axis is parallel to the solidification direction, i.e. parallel to the fibres.

The mechanical properties have been studied by classical tensile tests which provide the 0.2% yield stress, the tensile strength and the rupture strain.

Damping properties were deduced from mechanical spectroscopy measurements [10]. When a material vibrates under low stress excitation (much lower than the elastic yield stress) anelastic deformation is responsible for energy dissipation.

In a free-decay inverted torsion pendulum, the internal friction (IF) at low frequency ( $\sim 2\text{Hz}$ ) and at a strain amplitude of about  $10^{-5}$  is given by:

$$\text{IF} = \frac{1}{n\pi} \ln \frac{A_0}{A_n} \quad (2)$$

where  $A_0$  and  $A_n$  are the amplitude of the first and the  $n^{\text{th}}$  oscillations. The shear modulus ( $G$ ) was determined by the following equation [11]:

$$G = \frac{8\pi\ell If^2}{a^4} \quad (3)$$

where  $a$  is the sample thickness,  $\ell$  its length,  $I$  the pendulum inertia momentum and  $f$  the vibration frequency.

A forced, inverted torsion pendulum, which allows one to vary the frequency in a wider range ( $10^{-3}$  to 10 Hz), was also used. In this case, the internal friction is given by:

$$IF = \tan(\delta) \quad (4)$$

where  $\delta$  is the phase lag between the strain and the applied stress.

## RESULTS

### Sample Microstructure

Unidirectional samples were processed from both alloys. Fig. 1 displays two pictures obtained by optical microscopy on an unidirectional sample solidified at 0.5 mm/min. One can see that the  $Mg_2Si$  fibres are parallel to the direction of solidification.

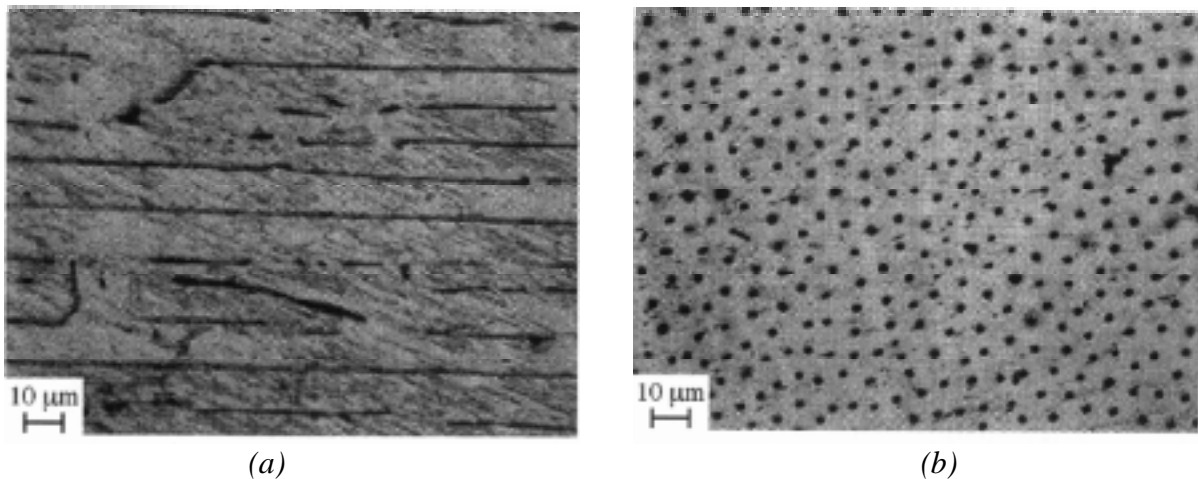


*Fig. 1: a) Lengthways image of an unidirectional sample. b) Transversal image of the same sample.  $Mg_2Si$  fibres are parallel to the solidification direction*

Depending on the solidification rate (or crucible speed in the furnace), thermal gradient and alloy purity, the sample structures can be rather different. If all the conditions are properly balanced, i.e. a high thermal gradient, a low solidification rate and a high alloy purity [8, 9], the  $Mg_2Si$  fibres are parallel to the direction of the thermal gradient (Fig. 1). Moreover, the distance between fibres depends on the solidification rate as predicted by Eqn 1, with a different constant for each alloy (Fig. 2).

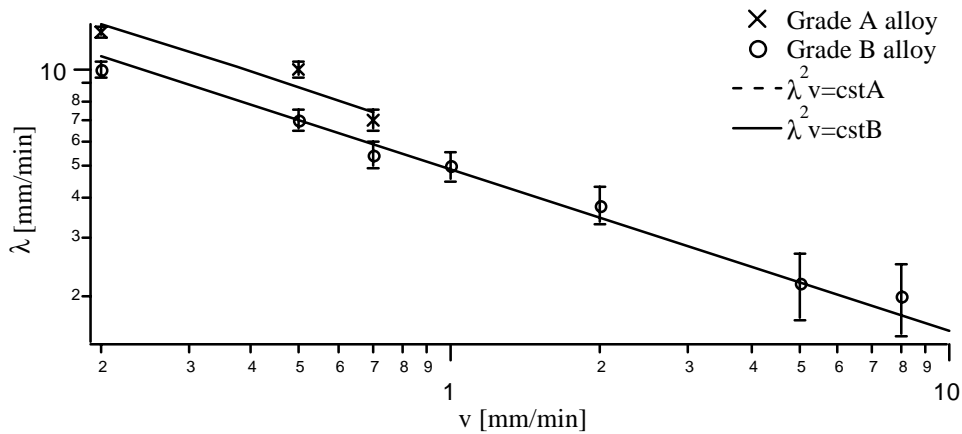


Fig. 2: Distance between fibres versus the solidification rate in a log-log graph. According with the error margins, the points follow the Eqn 1, with two different constants for both alloys, because of the different compositions

In addition, the matrix also exhibits a crystallographic orientation with the c-axis of the hexagonal structure parallel to the solidification direction. Fig. 3 is a Transmission Electron Microscopy (TEM) diffraction pattern associated with a magnesium grain, cut perpendicularly to the solidification direction. The hexagonal symmetry indicates that the matrix, which has an hexagonal structure, has its c-axis parallel to the specimen axis, i.e. the basal planes are perpendicular to the solidification direction.

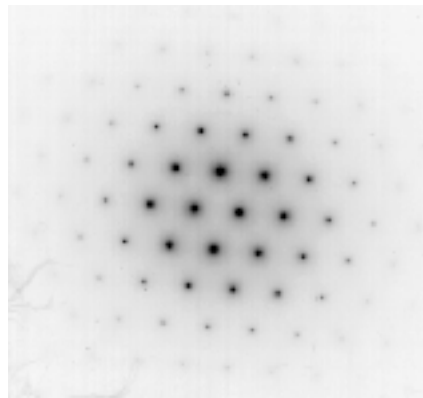


Fig. 3: MET diffraction pattern for a magnesium grain. The c-axis of the hexagonal structure is parallel to the solidification direction (photo by Christian Verdon)

Without good conditions, randomly oriented short fibres are obtained, but the matrix nonetheless exhibits an oriented c-axis. A disoriented matrix can be obtained by natural solidification. Unidirectional specimens were obtained from grade B alloy for all tested rates, i.e. from 0.2 to 8 mm/min. Unidirectional specimens were obtained from the grade A alloy only for low solidification rates, between 0.2 and 0.7 mm/min.

### Mechanical Properties

Tensile tests have been performed on these composites. Fig. 4 displays the mean ultimate tensile strength of different samples, in which the  $Mg_2Si$  fibres are parallel to the tensile

stress, as a function of the distance between fibres. One can see that the tensile strength is higher when the distance between fibres is lower, i.e. when the solidification rate is higher. For the shortest distances between fibres, the tensile strength is comparable with the industrial magnesium cast alloys such as AZ63 [5].

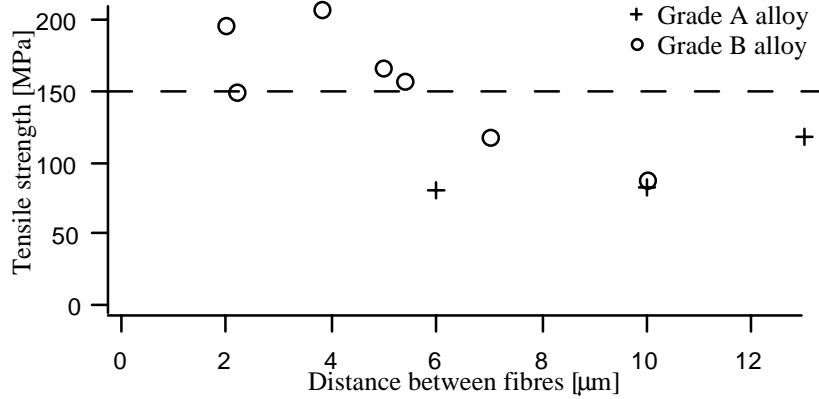


Fig. 4: Mean ultimate tensile strength of unidirectional samples versus distance between fibres. The tensile strength is higher when the distance between fibres is smaller. The dotted line corresponds to the level of the as cast AZ63 alloy

### Internal Friction Spectrum

The  $Mg_2Si / Mg$  natural composites are characterised by a high damping capacity. Fig. 5 displays the internal friction (IF) and the elastic shear modulus (G) as functions of the temperature, measured in a specimen annealed during 4 hours at 600 K. Curves were measured by means of a low frequency torsional pendulum on a sample of grade A alloy solidified at 0.5 mm/min, but the damping general features are similar in all studied samples and with all measurement methods.

The internal friction is high and rather constant. It exhibits a broad maximum at about 200 K and a smaller one at about 400 K. The shear modulus exhibits an unusual behaviour: although modulus usually increases with decreasing temperature, this material presents a decreasing modulus with decreasing temperature between 430 and 350 K. Both the damping and the shear modulus exhibit large hysteresis during thermal cycling: damping is higher and modulus lower during heating than cooling. When the temperature is kept constant after heating, the damping decreases continuously and the modulus increases until they reach the values of isothermal equilibrium.

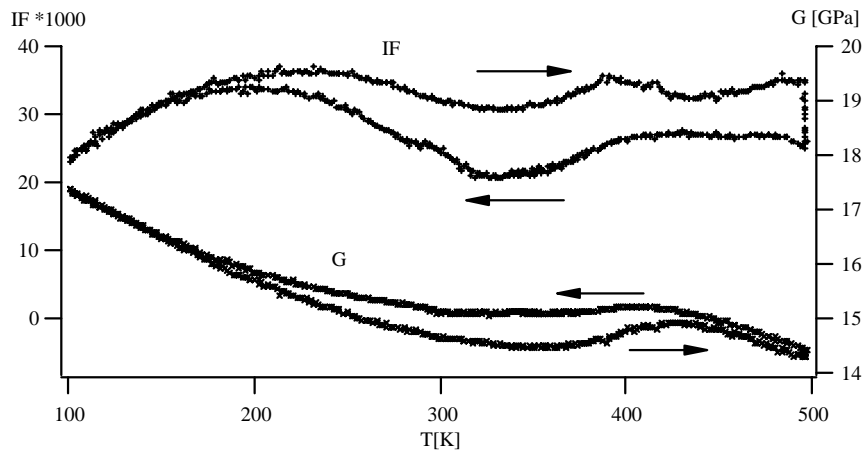


Fig. 5: Internal friction (IF) and shear modulus (G) versus temperature in a sample annealed 4 hours at 600K. IF is high and presents two maxima at 200 and 400K. G presents an unusual decrease between 430 and 350K. Both curves exhibit a large hysteresis

#### Effects of the Measurement Parameters on the Internal Friction

One way to understand the microscopic origin of the damping is to study the internal friction spectra, in particular the maxima of internal friction. Actually the microscopic phenomena, such as twinning or gliding of dislocations interacting with points defects, induce specific behaviour of the internal friction as functions of different parameters, as the strain amplitude or the frequency [10, 12]. The study of these dependencies generally allows one to determine some characteristic values of the phenomenon such as its activation energy and thus to deduce the involved phenomenon.

The study of the internal friction at different frequencies does not reveal a clear shift of the maxima, although a modification of the curve shape is observed. Fig. 6 displays the internal friction measured at room temperature (290K) as a function of the strain amplitude. The curve indicates a clear dependence on the amplitude. This reveals that the involved microscopic mechanism is complex.

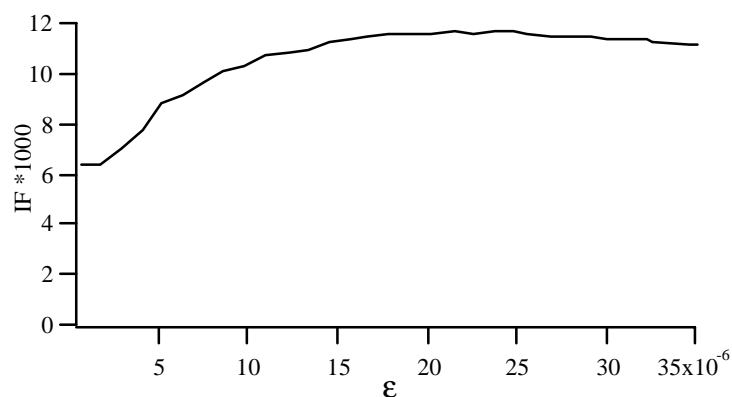


Fig. 6: Internal friction versus strain amplitude at 290K. The internal friction depends on the strain amplitude



Moreover, the internal friction also depends on the heating or cooling rate. Fig. 7a displays the internal friction and the shear modulus versus the temperature at different heating rate ( $\dot{T}$ ). One can observe that the internal friction is higher and the modulus lower when the heating rate is higher. Furthermore, Fig. 7b indicates that this dependence is complex. When  $\dot{T} \neq 0$ , the damping decreases linearly with  $\dot{T}$ , but the linear extrapolation for  $\dot{T}$  tending to zero (dotted line) is higher than the measured value for  $\dot{T} = 0$ . When heating is stopped, the stabilisation of the internal friction take a longer time than the stabilisation of the temperature. So it is possible to distinguish two effects: linear dependence with  $\dot{T}$  value (3) and time dependence at constant temperature (2). These two contributions are added to the intrinsic internal damping (1).

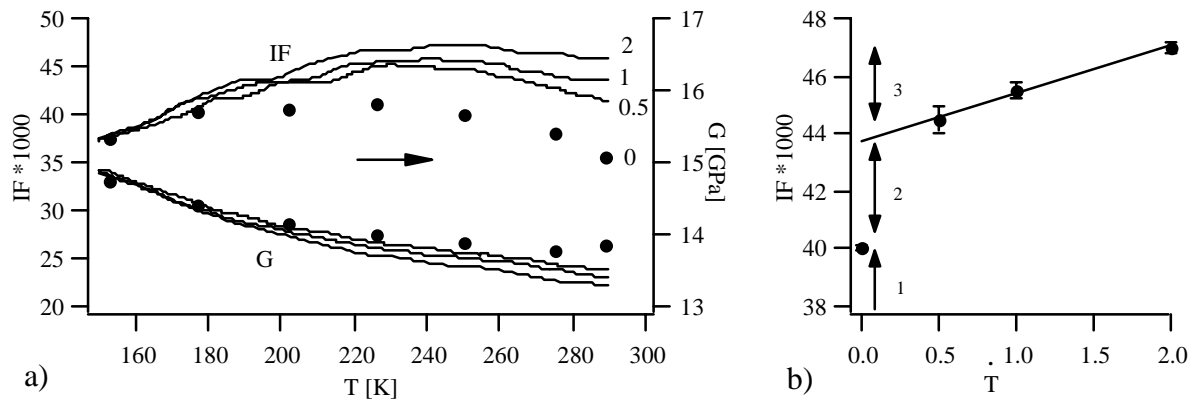


Fig. 7: (a) Internal friction (IF) and shear modulus (G) versus temperature at different heating rates: 0 K/min, 0.5 K/min, 1 K/min, 2K/min. The internal friction increases and the shear modulus decreases when the heating rate increases, (b) Internal friction (IF) versus heating rate ( $\dot{T}$ ) at 220K. The internal friction is composed of three parts. (1) Intrinsic damping, (2) time dependant damping and (3) heating rate dependant damping

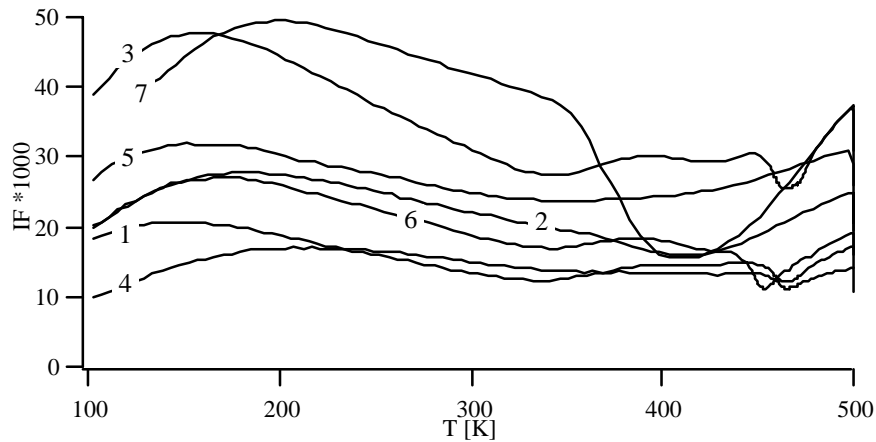
#### Effects of the microstructure on the internal friction

To enhance the composite properties, it is important to localise and to understand the mechanism of damping. Another way to obtain this information is to study the damping behaviour as a function of the sample structure.

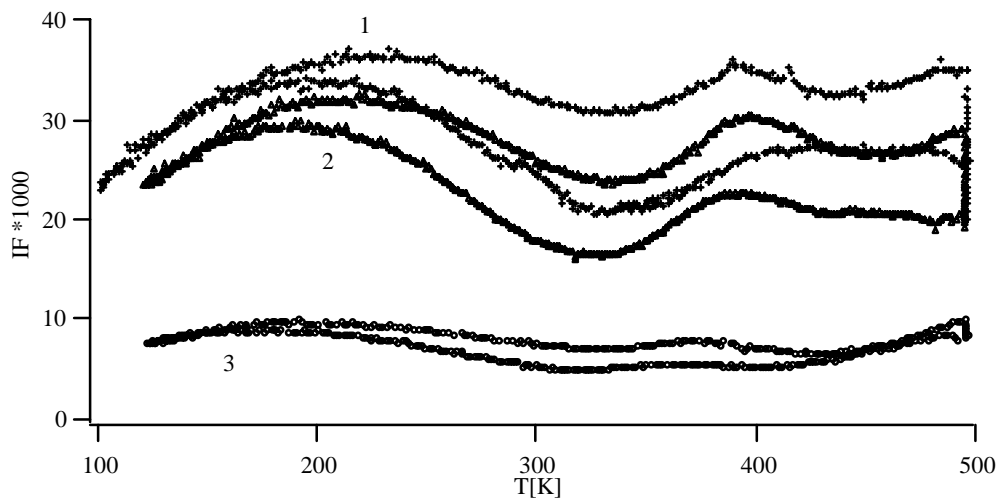
Fig. 8 displays the internal friction versus the temperature measured with the forced torsion pendulum in different samples, in which the c-axis of the hexagonal structure of the Mg matrix is parallel to the sample axis. One can see that the  $Mg_2Si$  fibre phase morphology has no obvious influence on the damping capacity.

Fig. 9 presents the internal friction spectra of three specimens: one specimen (1) where the Mg matrix c-axis and the  $Mg_2Si$  fibres are parallel to the specimen axis, a second one (2) where only the Mg matrix c-axis is aligned along the specimen axis, the  $Mg_2Si$  fibres exhibiting no preferential orientation, and a third one (3) in which neither the Mg matrix nor the  $Mg_2Si$  fibres show any orientation. In the two first cases, where the Mg matrix c-axis is oriented, the internal friction level is high. On the contrary, the internal friction is lower by a factor two or three in the sample which does not exhibit any structural orientation. One can deduce that neither the distance between fibres nor the fibre orientation modify significantly

the internal friction level. On the contrary, the orientation of the matrix has a great influence on damping.



*Fig. 8: Internal friction versus temperature in unidirectional samples of grade B alloy with different solidification rate: (1) 8 mm/min, (2) 5 mm/min, (3) 2 mm/min, (4) 1 mm/min, (5) 0.7 mm/min, (6) 0.5 mm/min, (7) 0.2 mm/min. The distance between fibres has no clear effect on the damping capacity*



*Fig. 9: Internal friction versus temperature in an unidirectional fibres/matrix sample (1), in an oriented c-axis matrix sample (2) and in a disoriented sample (3). Both the oriented c-axis matrix samples IF spectra have similar shape and height, but disoriented sample has much lower amplitude*

## DISCUSSION

### Sample Structure

Both alloys can be unidirectionally solidified, with  $Mg_2Si$  fibre structures in agreement with Eqn 1, but the rates which are required to solidify unidirectional composites and the constant

which appear in Eqn 1 are different. This means that the involved solidification mechanism is the same in both cases and correspond with the well known theory of unidirectional solidification [8, 9], but the involved parameters are merely different.

The mechanism of unidirectional solidification is based on the fact that both phases solidify together at the same time. The distance between fibres depends on the solidification rate as shown in Eqn 1, because it corresponds to an equilibrium between the needed energy to initiate a new phase and the energy to grow the existing phases. The major difference between the two alloys is the impurity concentration. In fact, the grade A alloy contains more impurities. All impurities are sites which might seed new phases, so the constant appearing in Eqn 1 depends on the alloy purity. Moreover, these impurities disturb the regular growth of the fibres, and the unidirectionality can be obtained only if the solidification rate is slow enough. A pure enough alloy is hence necessary to obtain a small distance between fibres. As the grade B alloy is purer than the eutectic alloy, finer structures can be obtain with this alloy.

### **Mechanical Properties**

The preliminary tensile tests are very promising. Although a large dispersion of the results, one can clearly see that the tensile strength is enhanced when the distance between fibres is small, i.e. when the solidification rate is high. These tests were performed on prismatic samples with a small cross section of 6 mm<sup>2</sup>. Some edge effects are certainly responsible for the dispersion of the results, because the stress accumulation at corners facilitate the formation of cracks. Furthermore, the presence of oxides induces some porosity during the solidification, which decreases the mechanical strength.

Future work will be to optimise the processing of this composite and to find the best sample configuration for tensile tests. But already, for the lowest distances between fibres, the tensile strength is comparable with the industrial magnesium cast alloys such as AZ63.

### **Internal Friction Spectrum**

#### *Modulus Anomaly*

Materials usually have a decreasing modulus as temperature increases. In these composites, on the contrary, the shear modulus increases between 350 and 430 K. This anomaly can be interpreted as follows: At the solidification temperature, the composite is at the equilibrium as it concerns the internal stresses, i.e. no internal stress appears between matrix and fibres. When the composite is subjected to an external stress such as torsion, the fibres are in extension. The high Young's modulus of the fibres acts as a restoring force, so the shear modulus of the composite is enhanced. During cooling, due to the thermal expansion coefficient mismatch, the internal stresses at the interface between fibres and matrix increase. These stresses can be first relaxed by dislocation creation and motion, but when the temperature decreases below a given temperature this relaxation is not sufficient, and the internal stresses compress the fibres. These compressed fibres are bent, they are no longer in extension under the external stresses and thus they can have no more effect on the shear modulus. So the shear modulus of the composite decreases to the modulus of the pure magnesium.

In other words, at high temperature the fibres participate in the modulus: the modulus is high and at low temperature the fibres do not participate in the modulus, hence, the modulus is low. This phenomenon occurs during each thermal cycle and explains the modulus anomaly.

### *Damping Behaviour*

The samples exhibit a high damping, as was desired. But, the internal friction level depends strongly on the sample microstructure (Fig. 8). In order to manage the internal friction level, it is thus important to localise and understand the mechanisms which lead to the high damping. Fig. 6 and 7 indicates that the involved phenomenon is complex, nevertheless some possible interpretations can be explored.

Fig. 8 and 9 show that only the matrix orientation significantly influences the internal friction, but neither the fibre orientation nor the distance between fibres does. Hence, the observed effects may be due to a microscopic phenomenon which occurs in the matrix, such as motion of dislocations, twinning or defect movement. It is well known [2, 4, 6] that internal friction in pure magnesium is due to dislocation motion in the basal planes. Therefore, the composites have a rather good damping capacity if the applied stress is in a preferred orientation to induce dislocation vibration and if the dislocations are free enough to vibrate. This explains the fact that the damping capacity is higher when the c-axis of the matrix is perpendicular to the stress, i.e. when the c-axis is aligned along the sample axis, as shown in Fig. 9.

In other words, if the matrix is c-axis oriented and if the magnesium matrix is pure, the damping must be high. As the matrix c-axis orientation is guaranteed when the fibres are unidirectional, mechanical properties of this composite can be optimised without care to the damping capacity. As presented in the introduction, the high-damping capacity and the high-mechanical strength can be reached in these composites, because the involved mechanisms are independent.

However, a large dispersion in the internal friction occurs between each measured sample (Fig. 8). Previous works [4, 6] have shown that the dislocation motion in the basal plane is controlled by their interaction with points defects, more precisely, the interaction consist in pinning and depinning of the dislocations from the points defects. Thus internal friction spectra are very sensitive to the impurity concentration. Fig. 6 confirms this interpretation, but the shape modification with the frequency indicates that the interaction between dislocations and point defects is not a pure pinning-depinning mechanism. The dependence of the internal friction on the frequency permits one to suppose a dragging of point defects of higher mobility.

### *Transient Internal Damping*

The internal friction depends on the heating or cooling rate ( $\dot{T}$ ). Such a dependence, called transient internal damping, has already been observed in some composites [13]. This is due to the thermal expansion coefficient mismatch between the matrix and the fibres. But, the dependence on  $\dot{T}$  value is more complex than effects commonly reported in literature. Usual dependence is linear, but here there are two different effects depending on the  $\dot{T}$  value. Fig. 7 shows that when  $\dot{T} \neq 0$  damping decreases linearly with  $\dot{T}$ , as studied in literature. The main characteristics of such an effect is a dependence with  $\dot{T}/(\sigma_0\omega)$  where  $\sigma_0$  is the applied stress amplitude and  $\omega$  is the circular frequency.

However, Fig. 7 displays also that the internal friction measured in isothermal conditions (at  $\dot{T}=0$ ) is lower than expected by extrapolation of the spectra measured for  $\dot{T}\neq 0$ . Moreover, when heating is stopped, the internal friction takes a longer time to stabilise than the temperature. Internal friction is then composed of three contributions: the intrinsic damping measured in isothermal conditions, a contribution which depends on the temperature stabilisation time and a contribution which depends on the heating or cooling rate  $\dot{T}$ .

### **CONCLUSION**

A new composite material has been developed and characterised. It is a natural composite formed by unidirectional solidification of a Mg-Si eutectic alloy (1.34 wt% Si) of low purity (grade A) or near eutectic alloy (2 wt% Si) of medium purity (grade B). Both the fibres and the matrix c-axes can be aligned in the direction of solidification. The distance between fibres depends on the solidification rate and on the alloy purity. The grade B alloy give access to the finest fibre structure, because of its higher purity. The unidirectional fibres enhance the mechanical strength up to some industrial magnesium cast alloys such as AZ63. The matrix orientation provides a very high damping capacity over a wide range of temperatures, without influence of the distance between fibres. These natural composites exhibit mechanical properties comparable with the ones of classical magnesium alloys with a damping capacity 100 time higher.

### **ACKNOWLEDGEMENTS**

The authors would like to thank Mr. Christian Verdon for his observations in Transmission Electron Microscopy. This work has been partially supported by the Swiss Priority Program for Materials.

### **REFERENCES**

1. R. Van Fleteren, Magnesium for automotive applications, *Advanced Materials & Processes* 5/96, 33
2. K. Sugimoto, Basic and Applied research on High-Damping Alloys for Application to Noise Control, *Mem. Inst. Sci. Res.*, vol.35, 31-44, 1978
3. R. Schaller and J. Van Humbeeck, High Damping Materials, *Materials Science Forum* Vol. 119-121, 803-808, Switzerland, 1993
4. S.M. Seyed Reihani, C. Esnouf, G. Fantozzi and G. Revel, Effect of impurities on the internal friction spectrum of magnesium after plastic deformation, *J. de physique* Tome 42, C5, 145-150, 1981
5. *Metal Handbook*, Vol.2, Ninth Edition, 1979

6. K. Sugimoto, K. Niiya, T. Okamoto and K. Kishitake, A study of Damping Capacity in Magnesium Alloys, Trans. JIM, Vol. 18, 277-288, 1977
7. T.B. Massalski, Binary alloy phase diagrams, vol.2, American Society for Metals, Ohio, 1986
8. W. Kurz, D.J. Fischer, Fundamentals of Solidification, Trans Tech Publications, 1984
9. M.C. Flemings, Solidification Processing, Materials Science and Engineering Series, 1974
10. A.S. Nowick and B.S. Berry, Anelastic relaxation in crystalline solids, Materials science series, 1972
11. S. Timoshenko, Résistance des matériaux, Librairie polytechnique Béranges, Paris, 1963
12. G. Gremaud, The Hysteretic Damping Mechanisms Related to Dislocation Motion, J. Phys., Tome 48, C8 15-30, 1987
13. X. Zhou, R. Fougères and A. Vincent, Internal damping effects due to the thermal expansion mismatch between aluminium and silicon in an Al 11.8%Si alloy, J. Phys., 2185-2201, 1992

# INTERFACE STUDY OF COMPOSITE BANDS FORMED BY POWDER PLATING AND ROLLING (PPR)

Sun Yong<sup>1</sup>, Zhang Shuhong<sup>1</sup>, Zhang Daiming<sup>1</sup>, Qian Tiancai<sup>2</sup>, Gao Yun<sup>2</sup>, Li Bin<sup>2</sup>

<sup>1</sup> *Department of materials, Kunming University of Science and Technology,  
Kunming 650093, Yunnan, P.R.China*

<sup>2</sup> *Yunnan Analytic & Testing Centre, Kunming 650051, Yunnan, P.R.China*

**SUMMARY:** Different kinds of metal powder have been plated on a band of mild steel and then both of them rolled together. With this new method, some composite bands such as Cu-steel, Al-steel, Sn-steel, etc., have been made. TEM, EPMA, XPS and XRD are used to study the interface among powder particles, the boundary of grains inside powder particles and the interface between composite-layered and matrix. The metal powders are deformed by force and their surface areas increase two or three times. There exist some pieces of oxidation film at the interface between powder particles, and there is a lot of dislocation-substructures in the grain inside powder particles. The SADP changes into multiple spots or small arcs, and take on a form of a discontinuous ring distribution. After annealing, a diffusion phenomenon can be observed at the interface among powder particles and between composite-layer and matrix. Three conclusions are given.

**KEYWORDS:** metals composite, surface coating, powder processing, multi-layers interfaces, laminar materials

## INTRODUCTION

It is well known that there are many methods for forming composite [1-3]. There also has been a lot of research focused on the structures and properties of composite [4-6]. PPR (Powder Plating and Rolling) is a new method for forming composite bands [7]. With PPR, which has been patented, metal powders (chosen as composite-layered metal) are plated onto the other metal band (chosen as the matrix) and then both of them are rolled together to obtain a composite band. In consideration of the difference of the presently reported technology from others, i.e. the composite-layered metal is not a sheet but powder, the interfaces of composite band formed by PPR are different from those of composites formed by other methods. In this paper, the main purpose is to study the interface among powder particles, the boundary of grain inside powder particles and the interface between the composite-layer and matrix. The effect of annealing temperature on the interface and microstructure of composite bands is also discussed. These will provide useful information for controlling the properties of composite in real production.

## EXPERIMENT

Plating a mild-steel band with different kinds of metal powder, and then rolling them together, a system of composite bands, such as Cu-steel, Al-steel, Sn-steel can be prepared. For different metal powder, a variant of annealing temperatures are employed in a vacuum furnace. Cutting out the composite bands into pieces, the samples for observing microstructure of composite bands are ready.

By rubbing the matrix off the sample, transforming the composite-lamella into thin foils. The thin foils are prepared by the electrochemistry-polishing method and examined in TEM of 2000-EX with accelerating voltage of 200 kv.

Samples for observing in EPMA are prepared by the way the same with the sample for observing in OM and then the samples are examined in EPMA of EPMA505. Some samples are analyzed by using XPS and XRD.

## RESULTS AND DISCUSSION

### Interfaces Among Powder Particles

Different from traditional composite materials, surface composite layer is an even substance formed of a multitude of metal powder particles that are elongated in all directions, one on the top of another in the deforming process. Therefore, there exist a large number of interfaces among particles. The binding at the interfaces is of importance. Before being pressed tight, powder particles with bigger diameter will begin to undergo a deformation while powder particles with smaller diameter will slide themselves into the gaps among the particles

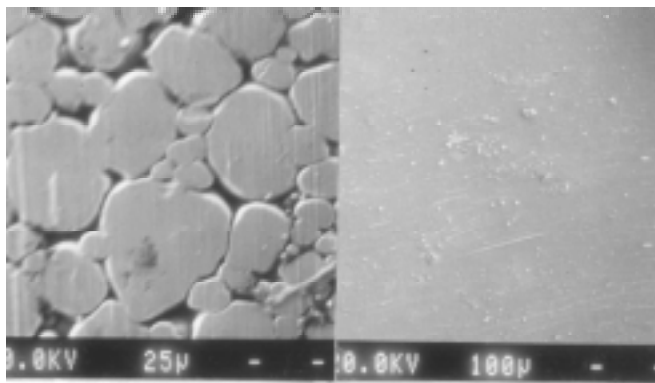


*Fig.1: Deforming process of metal powder particles*     *Fig. 2: TEM picture of the interfaces of aluminum powder particles*

with bigger diameter. With deforming pressure increasing, powder particles will gradually flatten out, close to each other, the gaps becoming smaller and smaller (See Fig.1a). Finally, the powder particles overlap each other and combine into continuous lamella. The appearance shows that metal particles have been cold welded into an even and continuous thin layer covering the surface of the matrix metal (See Fig.1b). An analysis finds that the surface areas of metal powder particles expand two or three times after undergoing deformation. The oxidation film wrapping the metal powder particles bursts, exposing a lot of clean and non-



oxidation surfaces. It is these clean non-oxidation surfaces that enable the metal particles to weld together closely. Table 1 presents the statistics of the deformation of metal powder particles.

Fig.2 shows that the broken fragments of aluminum oxide film can be observed at the interfaces of aluminum powder particles.

*Table 1: Statistics of the deformation of the metal powder particles*

metal powder	original diameter (mm)	thickness after deformation (mm)	average diameter after deformation (mm)	average elongation rate (%)	increase rate of surface areas (%)
Al	0.079	0.01	0.185	134	174
Cu	0.055	0.005	0.149	170	267
Sn	0.055	0.005	0.152	176	282

**Boundary of Grain Inside Powder Particle**

It can know from the above analysis that metal powder particles undergo a considerably big deformation in the composite processing with PPR. During the composite processing, the grains inside powder particle undergo a considerably big deformation too. The result of XRD examination shows that the grain's size inside a powder particles is about 1200--1400 Å before deformation while the size becomes about 240--280Å after deformation. This shows that deformation affects a strong crushing function on metal grains. An observance reveals that there exist concentrated dislocation groups (See Fig.3a) inside grains. These dislocation lines tangle together, forming dislocation-substructures. The results of SADP can

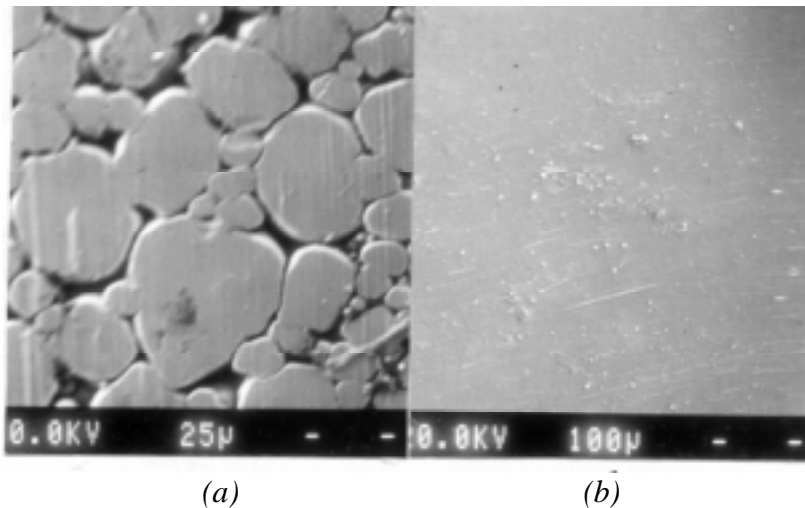


*Fig. 3: Dislocation line and SADP inside grains of copper powder particle*

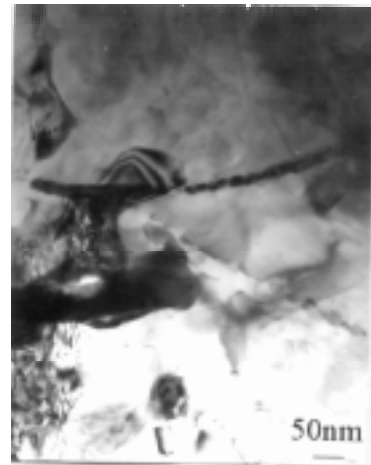


*Fig. 4: Dislocation outcrop copper powder particle etched tanks at the interface of the dislocation-substructure inside grain*

be seen in Fig.3(b), in which the diffraction spots change into multiple spots or small arcs, and take on a form of a discontinuous ring distribution. This means that the crystals inside the grains are crushed and been super-fineness under the large deformation forces, and these dislocation-substructures are of small phase difference in selected area. Fig.4 clearly shows the dislocation outcrop etched tanks at the interface of the dislocation-substructure inside the grain. After recrystallization annealing treatment, the original grain boundaries and dislocation line are hard to find under TEM. The substructure inside grain is replaced by annealing twin crystals or normal crystals (See Fig. 5 and Fig. 6).

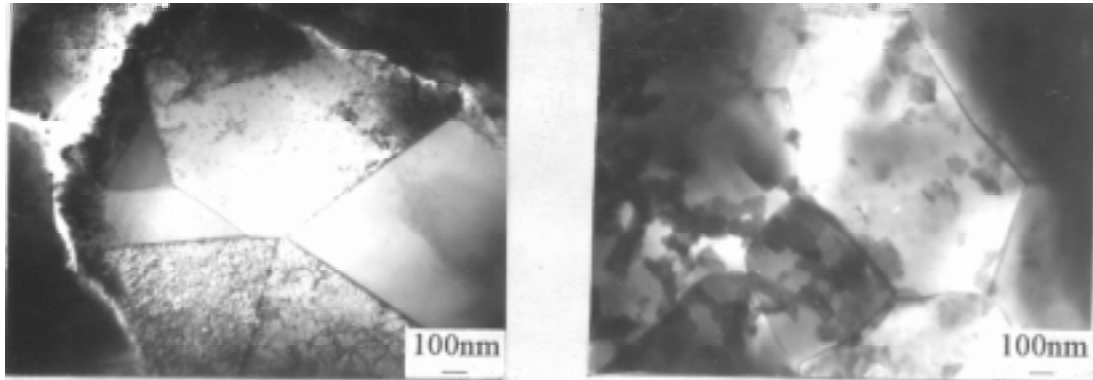


*Fig. 5: Texture of copper grains after annealing Fig. 6: Texture of tin grains after annealing*

### **Binding Interface Between Composite-Layer and Matrix Metal**

By using XPS, the characteristic binding energy peaks of Cu and Al can be found at the binding surface of the steel matrix (See Fig.7 and Fig.8). The analysis results show that under a strong external force the powder particles and the matrix are made to be close to each other to atomic size, producing a metallic bond binding between them.

The observation about the composite bands which has undergone diffusion annealing with EPMA also reveals that the composite layer metal is closely bond with the matrix and the metal atoms on the both sides of the interface can cross the interface between powder composite layer and matrix by means of diffusion to form a diffusion bonding. Fig.9 and Fig.10 present the second electronic images of the Al-steel, Cu-steel composite bands by using EPMA. The results of a linear scanning show that there is a clear component gradient changes at the binding interface, which shows clearly that there is a diffusion occurring at the interface between the composite layer and the matrix under the diffusion annealing temperature but no metal compound is formed. An examination of the bonding strength of the interface also reveals the good bonding.

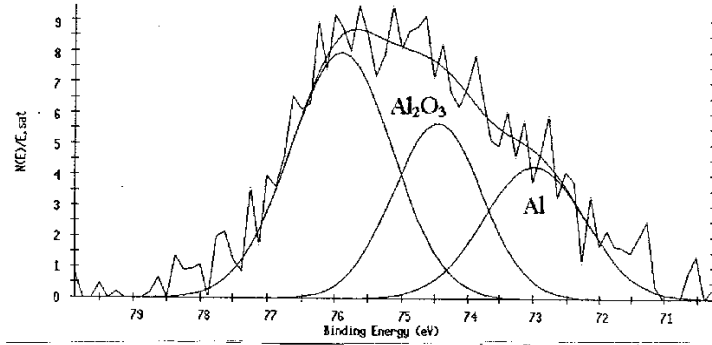


Fig. 7: XPS analytical spectrum line at the bonding surface of the steel matrix of aluminum-steel composite band

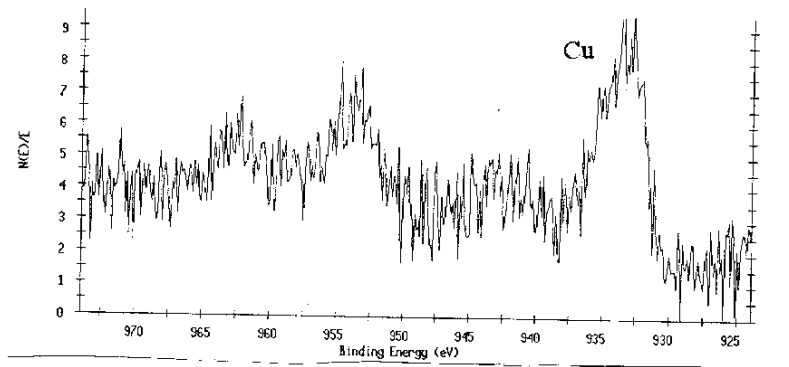


Fig. 8: XPS analytical spectrum line at the binding surface of the steel matrix of copper-steel composite band

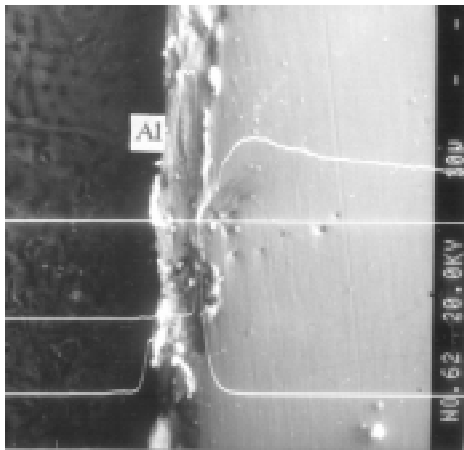


Fig. 9 Binding interface of aluminum-steel band

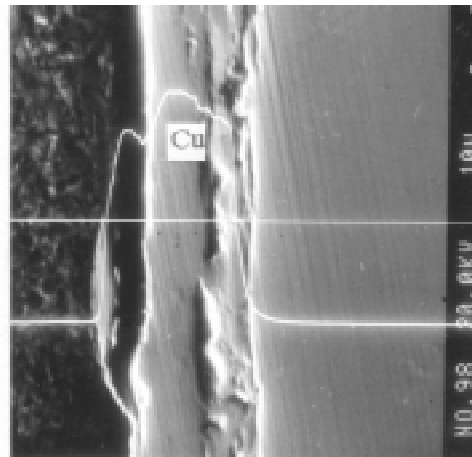


Fig. 10: Binding interface of copper-steel composite band.

## CONCLUSIONS

(1) In the preparation of PPR, the surface areas of metal powder particles increase two or three times, which makes the oxidation film of powder particles burst and fall down, exposing a lot clean and non-oxidation surface. It is these clean non-oxidation surfaces that ensure a bind among metal particles and between grain composite layer and matrix.

(2) After deformation, there exist much interfaces of powder particle inside composite layer and there exist much boundary inside grain in every powder particle. Therefore, it is important a good bind among the interfaces of powder particles and the boundaries of grains.

(3) A proper annealing treatment can make atoms spread cross the interface, thus causing the disappearance of the interfaces of powder particles which have overlapped each other, form an even continuous metal thin layer by recrystallizing. The dislocation-substructures inside grains is replaced by normal crystals. A diffusion bonding is formed at the interfaces between composite-layer and matrix through atomic diffusion.

## ACKNOWLEDGEMENT

This project is supported by the National Natural Science Foundation of China

## REFERENCES

1. M. M. Michorius, Chemical vapor deposition finds more and more uses, *Proces. Technologie*, 6(9), 1990, pp.18-21
2. A.Kelly, Novel forming methods for composites, *Inst. Phys. Conf. Ser.*,111,1990, pp.5-12
3. Kang xiancheng, The forming methods and using for metals composite sheets, *Guowaikeji*, 10, 1990, pp.1-4
4. A. Lawley, Characterization of microstructure in metallic and composite materials, *Dep. Mater. Eng., Drexel Univ., Philadelphia, USA*, Report 1987
5. W. Wlosinski, Bonded multi-layer materials-the materials of the future, *Trans. JWRI*, 17(1), 1988, pp.263-72
6. Shi Q. N., Sun, Y., Zhang D. M., Zhang S. H., A Study of Rolling Force in Composite Rolling Process with Metallic Powder and Metallic Sheets, *MSMM'96*, Beijing,1996.
7. Sun Y., Shi Q. N., Zhang S. H., Zhang D. M., The Microstructure of Composite Bands Formed by Powder Plating and Rolling ( PPR ), *Journal of Materials Processing Technology*, Vol. 63, Nos. 1-3, 1997, pp.438-441.

# MECHANICAL PERFORMANCE OF COMPRESSION MOLDED AND INJECTION MOLDED BLENDS OF LARC POLYIMIDE WITH POLYETHERIMIDE (PEI)

David Olivero<sup>1</sup>, Donald Radford<sup>1</sup>, Sarah Hummel<sup>1</sup>, Charles Smith<sup>2</sup> and Betty Tung<sup>3</sup>

1. *Composite Materials, Manufacture and Structures Laboratory (CMMS), Department of Mechanical Engineering, Colorado State University, Fort Collins, CO 80523*

2. *Department of Industrial Science, Colorado State University, Fort Collins, CO 80523*

3. *IMITEC, Inc., 1990 Maxon Rd., Schenectady, NY, 12308*

**SUMMARY:** Two high temperature polyimides from NASA-Langley, LaRC-SI and LaRC-IAX, were injection molded into tensile coupon shapes. A custom injection die was developed with built-in electric heaters to generate the required die temperatures. LaRC-SI and LaRC-IAX tensile coupons were produced by both injection molding and compression molding for performance comparison. Compression molding and injection molding yielded similar mechanical performance. However, non-optimal processing conditions and contamination reduced strength and strain to failure in some specimens. To evaluate trade-offs in blending LaRC-SI and LaRC-IAX with lower cost thermoplastics, PEI blends were studied, prepared by both compression and injection molding. Overall, mechanical properties followed a rule of mixtures relationship, with variations resulting from non-optimal processing rather than blending. Preliminary thermal analysis highlighted extremely different blending related to process conditions. Compression molding resulted in a binary polymeric system while injection molding resulted in a single, completely mixed phase.

**KEYWORDS:** LaRC-SI, LaRC-IAX, PEI, polyimide thermoplastic, injection molding

## INTRODUCTION

Two high temperature thermoplastics, LaRC-SI and LaRC-IAX, have recently been developed by NASA-Langley. These aromatic polyimides exhibit high strength and a high glass transition temperature (240°C), and have been identified for use as adhesives, films and composite matrix material [1]. Composite processing has already been demonstrated, particularly in prepregs of IM7 [2,3] Additional features of both LaRC-SI and LaRC-IAX include good chemical and oxidation resistance and high dielectric strength.

Thus far, LaRC-SI and LaRC-IAX, in powder form, have been successfully compression molded. However, compression molding can be a limiting and high cost manufacturing process. This fact, plus the high cost of LaRC-SI and LaRC-IAX limits the materials' applicability. Injection molding of these polyimides is thus of interest as a significant improvement in manufacturing potential. This paper discusses the results of preliminary injection molding trials with LaRC polyimides from pelletized stock.

To further increase the viability of this material, both LaRC-SI and LaRC-IAX have been blended with ULTEM 1000, an amorphous polyetherimide (PEI) with a glass transition temperature of 212°C. PEI is currently much less expensive than LaRC, yet with comparable

physical properties and only slightly reduced mechanical performance. Blending of these thermoplastics has therefore been investigated as a way to increase the economy of LaRC-SI and LaRC-IAX.

Tensile tests were undertaken to investigate the effects of both processing method and PEI blend ratio on the mechanical performance of LaRC-SI and LaRC-IAX. To investigate the presence of any thermal degradation, as well as the degree of mixing of PEI with each LaRC polyimide, differential scanning calorimetry (DSC) traces of specimens produced by both compression and injection molding are presented.

## **EXPERIMENTAL**

### **Compression Molding of LaRC-SI, LaRC-IAX and Blends with PEI**

Compression molding of LaRC-SI/PEI and LaRC-IAX/PEI blends was carried out with a 20 ton hot press. Powders of LaRC-SI and LaRC-IAX were used to produce all compression molded specimens. At the time of this study, PEI was not available as a powder. Sheets of PEI were therefore milled into small flakes, and dry blends of the thermoplastics were well mixed. Unfortunately, this process of milling PEI introduced impurities which, after molding, resulted in stress concentrating defects in some tensile coupons.

Compression molding of all blends was carried using process parameters obtained with past experience compression molding LaRC-SI. To produce blends with good consolidation and no thermal degradation, a processing temperature of 320°C was used. An aluminum die with a 63.5 mm x 177.8 mm x 25.4 mm cavity was used to prepare all specimens. The resulting 63.5 mm x 177.8 mm sample was subsequently machined into three separate ASTM D-638 type #1 tensile coupons. Machined specimen edges were sanded to eliminate machining induced surface flaws.

### **Injection Molding of LaRC-SI, LaRC-IAX and Blends with PEI**

A two-ton injection molder was used to investigate the injection molding potential for LaRC-SI and LaRC-IAX. The molder, pictured in figure 1, was a screw injector with individual temperature control of the hopper, preheat, screw, nozzle and mold zones.



*Figure 1: Two-ton injection molder at CSU*

All process zones in the molder are capable of temperatures approaching 400°C, which were found to be necessary to mold these high temperature thermoplastics, except for the water heated mold, which has a maximum temperature near 100°C. To prevent freezing at the mold,

a steel die was custom modified with electric cartridge heaters to enable mold temperatures above 220°C. The geometry of the die cavity was milled to ASTM D-638-89 type #1 tensile coupon specifications, with the exception of a draft angle milled into the cavity walls to facilitate part ejection.

As moisture absorption is an ongoing concern in injection molding plastics, all pellet blends were dried in a recycling desiccant hopper at 140°C for at least 15 hours just prior to injection molding. A given blend ratio was determined to be successfully molded once 20 specimens with good quality, consistency and reasonable absence of contaminants were continuously produced. This procedure allowed the investigation of a variety of blend ratios, from 0% polyimide to 100% polyimide (by volume) in 25% increments, with the limited quantity of LaRC-SI and LaRC-IAX at hand. A portion of the over 200 tensile coupons test coupons produced are pictured in figure 2. Three specimens were produced for each material, blend ratio and processing method combination. That is, a given blend specimen was produced by both compression molding and injection molding for process comparison.

### Tensile Testing

Tensile tests were performed at room temperature (25°C) with an ATS universal tester fitted with wedge lock grips. In some cases the grip sections of the tensile coupons were roughened to prevent slippage in the grips. A load rate of 5 mm/min was used in all tests, as per ASTM standard D-638. A clip gage extensometer with a 25.4 mm gage length was used to measure strain. Stress and stiffness for each coupon were calculated based upon the average gage thickness, which generally varied less than 0.05 mm across a given gage section.



*Figure 2: LaRC-SI and LaRC-IAX tensile test specimens*

### Differential Scanning Calorimetry (DSC)

Of great interest is the effect of processing method and conditions on the resulting blend of PEI with LaRC-SI or LaRC-IAX. In particular, the degree of mixing of the two constituents, investigated by looking at changes in glass transition temperature, gives an initial indication of blend quality. To investigate processing effects, two samples were prepared and tested with a Seiko DSC 220C analyzer, one sample taken from an injection molded sample and one from a compression molded sample. Each sample was scraped with a razor blade from the grip section of a 50% LaRC-SI, 50% PEI coupon after tensile testing.

## RESULTS AND DISCUSSION

Both LaRC-IAX and LaRC-SI, as well as blends with PEI, were successfully injection molded. Further, blends were found to retain the strength of the neat polymers, indicating the miscibility of the two constituents. A significant amount of data scatter was obtained, however, and is attributed to premature failures in some of the specimens. Typical problems in injection molded specimens included splay marks, white streaks and incomplete cavity fill. These problems can be related to the inability to fully optimize processing parameters such as temperature and pressure with the limited material at hand. Compression molded specimens were far more consistent in their quality, due to extensive processing experience with LaRC polyimides. Contamination was a significant problem for both processing methods, however, and was generally intermittent and unpredictable.

LaRC-SI blends exhibited greater ductility and toughness than LaRC-IAX blends. LaRC-SI blends were characterized by plastic flow associated with neck down, while LaRC-IAX blends were almost exclusively brittle in their fracture behavior. For the process parameters employed, the stress-strain behaviors observed in these materials are shown in figure 3 (a and b), which can be considered representative of mechanical behavior of LaRC-SI and LaRC-IAX.

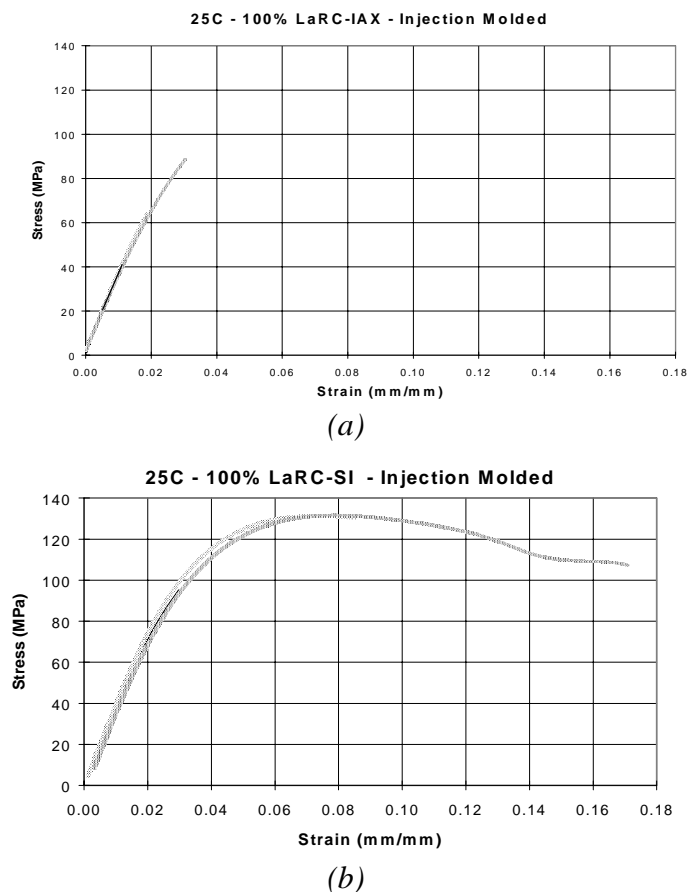


Figure 3 (a & b): Relative stress-strain performance of LaRC-SI and LaRC-IAX

Higher failure strengths were usually obtained with LaRC-SI than with LaRC-IAX. The highest ultimate tensile stresses obtained with LaRC-IAX blends were 110-115 MPa, while in LaRC-SI blends was 135 MPa. However, as seen in figure 3, the failure strength of



LaRC-IAX is similar to the yield point of LaRC-SI. LaRC-SI blends thus appear to be roughly 10-20% stronger, although this reduction may originate from reduced flaw sensitivity.

### LaRC-SI/PEI Blend Tensile Tests

Figure 4 relates the elastic modulus and ultimate tensile strength of LaRC-SI blends with PEI to the blend composition. Based on investigations of specimen failure mode, it was observed that low strength specimens failed prematurely at a point defect or impurity. Figure 4 thus shows the best performance obtained for each blend ratio, as these results are considered the most accurate assessment of the material.

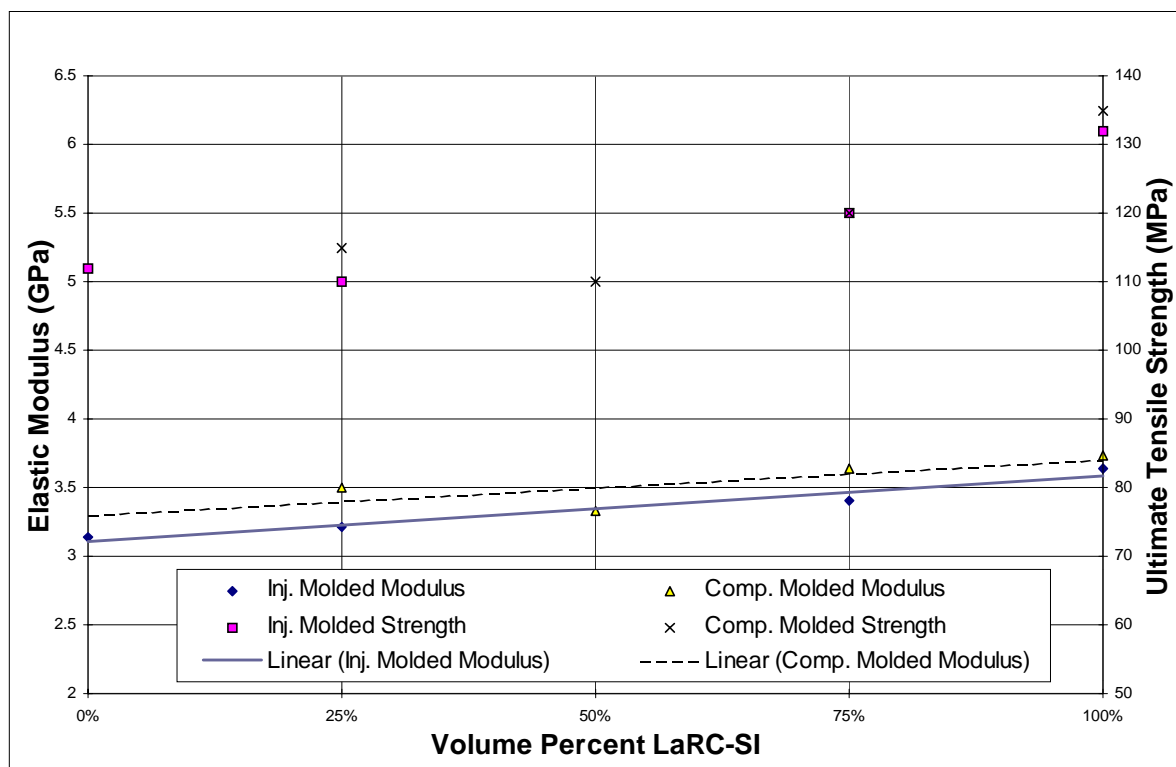


Figure 4: Elastic modulus and ultimate tensile strength vs. blend ratio for LaRC-SI/PEI

The strength of injection molded and compression molded LaRC-SI blends are very similar, indicating no strength tradeoff with injection molding. For each processing method, as the volume percent of LaRC-SI increases, the ultimate tensile strength increases in a linear fashion, from 110 MPa to over 130 MPa. Injection molded specimen modulus is consistently lower than the corresponding modulus of compression molded specimens. The origin of this difference is unclear, although it is less than 10% in most cases.

### LaRC-IAX/PEI Blend Tensile Tests

Figure 5 relates the elastic modulus and ultimate tensile strength in LaRC-IAX blends with PEI to blend composition in the same manner as figure 4. No clear trend in ultimate tensile strength is apparent with respect to blend composition in either compression or injection molded LaRC-IAX specimens. Blends of LaRC-IAX failed in a predominantly brittle fashion (recall figure 3a), and impurities had a significant effect on the ultimate strength due to flaw sensitivity. It should also be noted that the semi-crystalline nature of LaRC-IAX may have

played a role in making the generation of consistent blends more difficult than with LaRC-SI, which is amorphous. Further, the injection molding process was not as well optimized as with LaRC-SI, and so specimens of acceptable quality were more difficult to achieve.

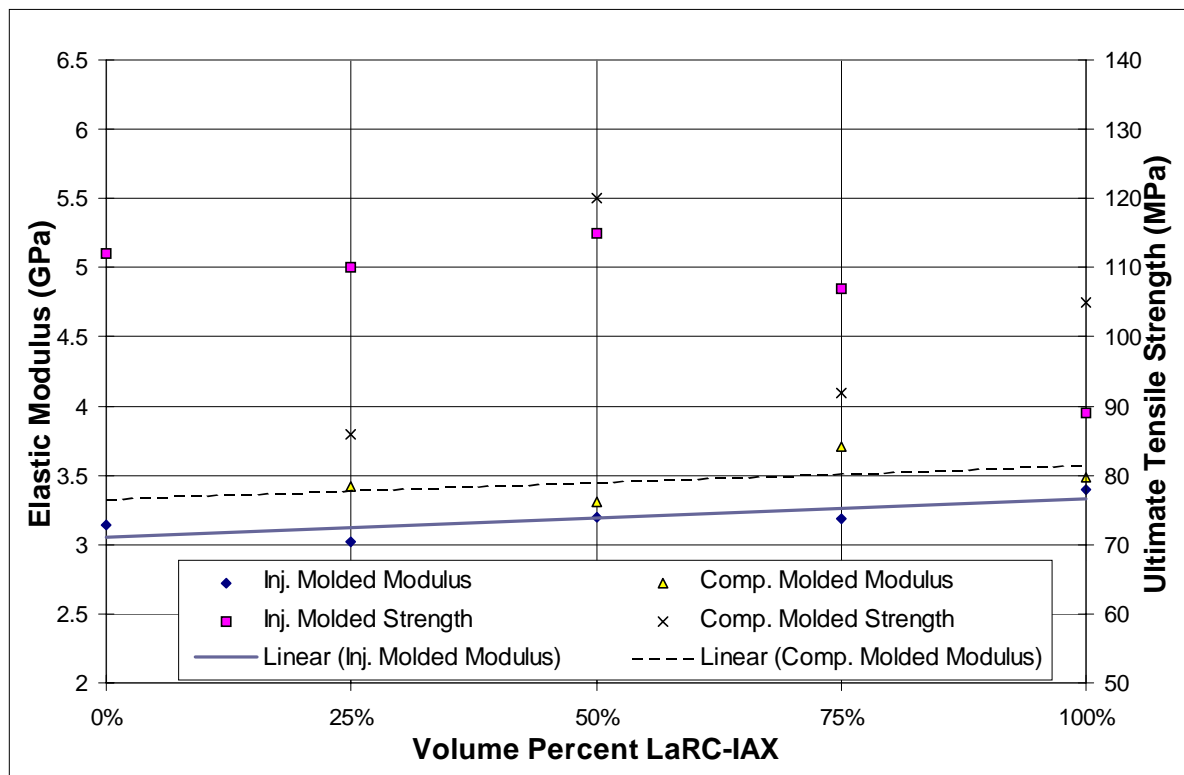


Figure 5: Elastic modulus and ultimate tensile strength vs. blend ratio for LaRC-IAX/PEI

Injection molded specimen modulus, shown in figure 5, is consistently lower than the corresponding modulus of compression molded specimens, just as in figure 4. The difference between the two processing methods is again less than 10% in most cases. The general trend is a slight increase in modulus as the amount of LaRC-IAX is increased. Data roughly follow a rule of mixtures relationship, with no significant deviations.

### Differences Between Compression Molded and Injection Molded Specimens

Compression and injection molding processes resulted in blends with similar yet highly scattered mechanical performance. Failures outside the gage section (indicating brittleness and high flaw sensitivity) were more prevalent in compression molded specimens. This is related to the presence of contaminants in the milled PEI prior to processing, which introduced defects and provides an explanation for the increased number of failures outside the gage length. Some injection molded specimens failed in this fashion, also at point defects related to contaminants. An example of an out-of-gage failure is seen in figure 6, a cross sectional micrograph of an internal flaw generated fracture surface in a 25% LaRC-IAX, 75% PEI injection molded part. The flaw is located at the center of the image.

All samples were observed to have elastic moduli in the range 3.2-3.7 GPa. Changes in modulus did not correlate with ultimate tensile strength. Failure strain, however, was clearly observed to increase with strength, as one would intuitively expect based on a Hookean relationship between stress and strain, given a more or less constant modulus.

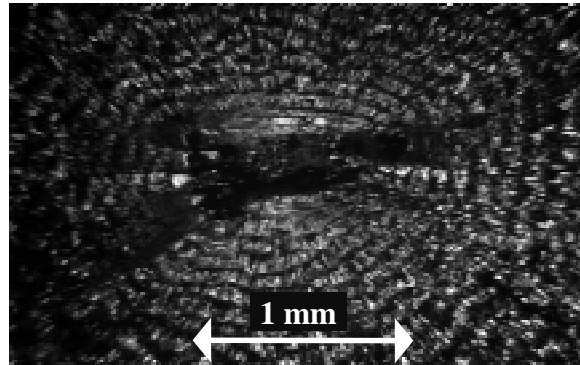


Figure 6: Cross-section micrograph of brittle fracture surface generated by internal flow outside gage section. Specimen is 25% LaRC-IAX, 75% PEI, injection molded.

### Differential Scanning Calorimetry (DSC)

Figure 7 and 8 show traces generated by DSC analysis of compression and injection molded specimens, respectively. Figure 7 shows two distinct "dips" in the DSC trace, one located at the  $T_g$  of PEI (212°C) and one at the  $T_g$  of LaRC-SI (239°C). The sample thus contains both polymer species, as separate phases rather than an actual blend. Note in figure 8, however, that in the injection molded specimen there is only one intermediate glass transition occurring, at 225°C. This indicates complete mixing of the two species, and the creation of a miscible blend of PEI and LaRC-SI. Thus, the compression and injection molding processes seem to produce blends that are fundamentally different. This difference may be due to the increased mixing, as well as the higher temperature and pressure of injection molding.

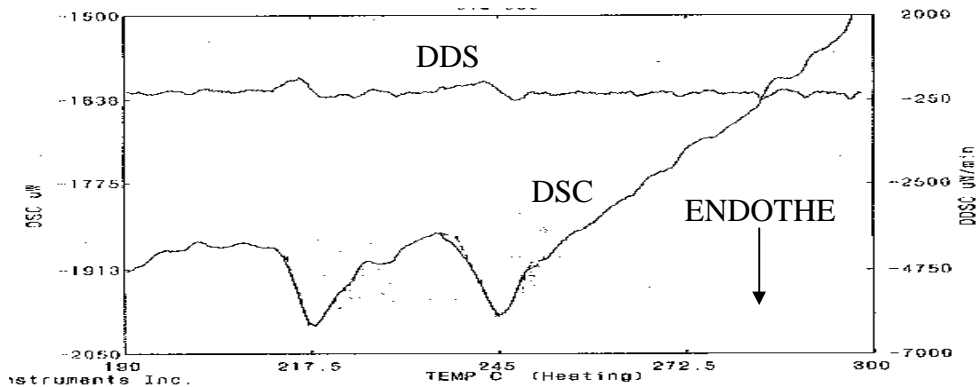


Figure 7: DSC trace of 50% LaRC-SI, 50% PEI compression molded specimen

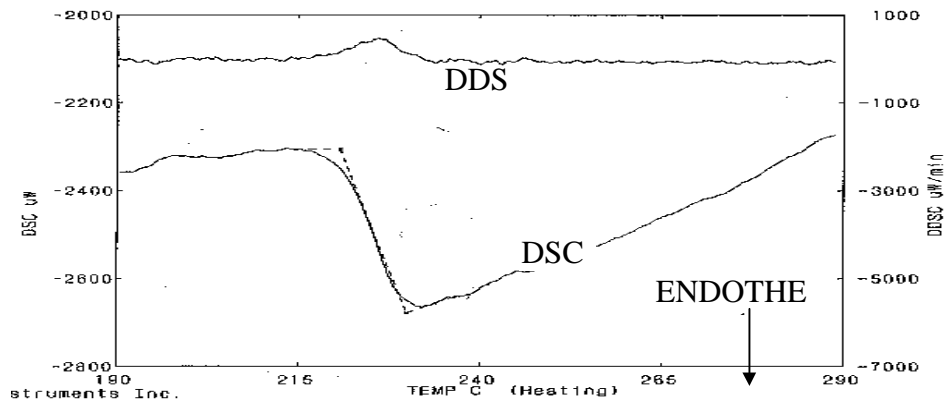


Figure 8: DSC trace of 50% LaRC-SI, 50% PEI injection molded specimen

## CONCLUSIONS

Both LaRC-SI and LaRC-IAX polyimides have been successfully injection molded into ASTM type #1 tensile coupons. Mechanical performance of these injection molded coupons compares favorably to compression molded specimens of LaRC-SI and LaRC-IAX. The polyimides have also been successfully blended with PEI and found to retain mechanical properties while significantly reducing the quantity of the thermoplastic polyimide.

Contamination and non-optimized processing have limited the mechanical performance observed in all blends. These conditions contributed to premature failures of a number of specimens during tensile testing. Further, it was found with differential scanning calorimetry that the compression molding parameters resulted in specimens which were essentially two phase materials, while injection molded specimens were completely blended.

Future efforts involving LaRC-SI/PEI and LaRC-IAX/PEI blends should involve commercial PEI powders to eliminate contamination, and optimization of injection molding parameters. Also, in-depth thermal analysis is planned to evaluate the various blends and changing process conditions. Finally, testing of non-mechanical performance of such blends is also necessary since one of the principal strengths of the high temperature thermoplastic polyimides is chemical resistance.

## ACKNOWLEDGMENTS

Appreciation is extended to Mr. Brent Sigmon for his invaluable assistance with injection molding. This work was supported by IMITEC, Inc. of Schenectady, NY.

## REFERENCES

1. D. Progar and T. St. Clair, "LARC-IA: A Flexible Backbone Polyimide," NASA TM-102586, 1990.
2. T. Hou et al., "Processing and Properties of IM7/LARC-IAX2 Polyimide Composites," *Journal of Advanced Materials*, Vol. 27, No. 2, 1996, pp. 11-18.
3. M. Rommel, L. Konopka and P. Hergenrother, "Process Development and Mechanical Properties of IM7/LaRC PETI-5 Composites," *28th Int. SAMPE Technical Conference: Technology Transfer in a Global Community*, 1996, pp. 1-13.

# ENGINEERING COMPOSITE ELECTRE MATERIALS

L.S. Pinchuk<sup>1</sup>, V.A. Goldade<sup>1</sup>, I.M. Vertyachikh<sup>1</sup> and V.N. Kestelman<sup>2</sup>.

<sup>1</sup> *Metal-Polymer Research Institute of Belarussian Academy of Sciences  
32a Kirov Str., 246652 Gomel, Republic of Belarus*

<sup>2</sup> *KVN International, 632 Jamie Circle, King of Prussia, PA 19406, USA.*

**SUMMARY:** Modification of polymer materials by electric fields is now part of advanced materials science. Polymer electrets are efficient means of rising serviceability of joints with small clearances between conjugated parts. Electret field makes it possible to regulate wetting and spreading, sorption and diffusion, as well as capillary permeation of liquids. Electrets in machines protect metal-polymer joints against corrosion, increase adhesion of composite components and articles, improve strength, enhance technological effectiveness of composite formation, improve tribological characteristics of friction joints. Electret plastics bear mechanical loads in machines and are the source of electric field. Electrets as materials of a new generation respond to the latest trends in technology for simultaneous increase in serviceability and reduction in machine size and mass.

**KEYWORDS:** electrets and materials, polarization, metal-polymer electrets, wetting and spreading, strength and adhesion, corrosion protection, tribological characteristics

## INTRODUCTION

Electric polarization is intrinsic physical state of the polymers being dielectrics in their majority. Polarization-retaining dielectrics, i.e. electrets or electric analogues of magnets are characterized by ability to generate a constant electric field.

The electrets are traditionally used in gas filters, microphones, systems of electronic focusing [1]. Electrets were not used in joints contributing much into machine serviceability, including bearings, seals, anti-corrosion systems. Nevertheless, experience in different technologies showed that electrets could improve working capacity of machine joints with a small clearance between conjugated parts [2,3]. The processes of lubrication, capillary permeation, spread of liquids, etc. (where surface phenomena are very important) can be controlled using a relatively weak electret field.

Technologists are usually not paying attention to the fact that electric fields always generate polarization in dielectrics. Polarization emerges even when electric field is used to solve some mechanical or physic-chemical problems to match dielectric components at composites forming.

More attention has been recently paid to ecological, environment protection problems. The problems arise from the growing industry, which environmental effect is commensurable with the natural processes. The former leads to changes in water, soil, air, violates equilibrium in nature. Application of electrets can influence some aspects of the problem. Use of electric field source in machines is ecologically pure. An experience has been attained in efficient

purification of industrial wastes and ejections, rise of combustion effectiveness, reduction of hostile media leakage by transfer of materials into the electret state.

Electrets perform two functions in machines: 1. the mechanical load carrier and 2. electric field source. Their application responds to the recent technological trends and permits to rise serviceability, reduce dimensions and material consumption in machines. These materials are fairly competitive, their composition and technology are new and patented.

The object of the present paper is to describe new perspectives of electret composite materials production and efficient use in machine joints governing serviceability of equipment.

## **RESULTS AND DISCUSSION**

### **Polarization Methods**

Methods of polymer composite electric polarization realize mostly the technology of thermo- and corona-electrets. In principle, they can be performed at any stage of article production [4].

It has been found out that polymer composites can be polarized by charged fillers [5]. Polyvinylbutyral (PVB) impregnation with corona-discharged oxide powders results in a maximal characteristic of the electret charge (Fig.1) during thermally stimulated depolarization (TSD) of the filled films. Space charge of the film and sheet materials can be formed without sources of electric voltage.

It has been shown earlier that a stable electret state emerges when the polymer layer between short-circuited electrodes of unlike metals in “metal 1-polymer-metal 2” systems undergoes thermal treatment [2,6-8]. The new type of electret state was called metal-polymer electret (MPE). It has also been established that during their formation and operation MPE can display and realize functional potentialities of composites, in particular, strength, corrosion resistance, as well as frictional, electric and other characteristics [9].

The use of fillers influences electric polarization of polymer composites. PVB samples were thermally treated under 393 K in contact with short-circuited copper and aluminum electrodes. Due to conductive or electret fillers graphs (Fig. 2) fall into two groups. The first group fillers (curves 1-3) features high charge density (up to  $10^{-3}$  C/cm<sup>2</sup>). The conducting filler particle bears, presumably, the function of auxiliary electrodes at polarization and the amount of charge carriers transmitted from the electrode into polymer matrix increases too. The second group (4,5) is characterized by the drop of charge with increasing content of dielectric filler. The latter does not participate in electric conductivity at sample polarization. The degree polarization current and TSD charge decrease with increase of filling degree.

The dependencies (Fig. 2) have a maximum at about 1 mass% of the filler content. Small quantities of foreign impurities contribute to formation of a more perfect permolecular structure in polymer binders and to electret charge formation. Further increase in filling degree causes disordering of permolecular structures accompanied by TSD charge reduction.

When  $C > 1\%$  (1-3) the charge grows and then reduces due to reduced quantity of polarized polymer. The described process is most prominent when the sample is filled with dielectrics (4,5).

### Wetting and Spreading

Liquid wetting and spreading over polymer surface can be regulated by the latter polarizing.

Pentaplast (PPI) films were transferred into electret state by heating between steel electrodes under  $150\text{ }^\circ\text{C}$  and electric field of  $E = 10^4\text{-}10^6\text{ V/m}$  (thermo-electrets) during 1 h or by corona discharge (corona-electrets). The technique of measuring liquid spreading over the sample surface is described in [10].

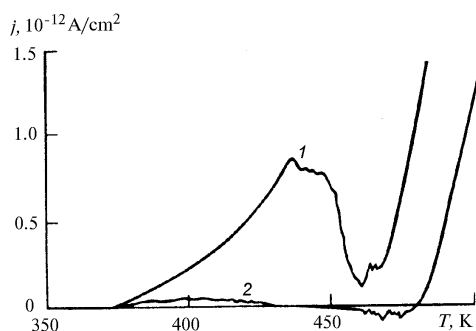


Fig. 1. TSD currents in  $\text{SiO}_2$ -filled PVB (up to 20 mass%) versus temperature and filler charge: 1 - corona-discharged, 2 - original

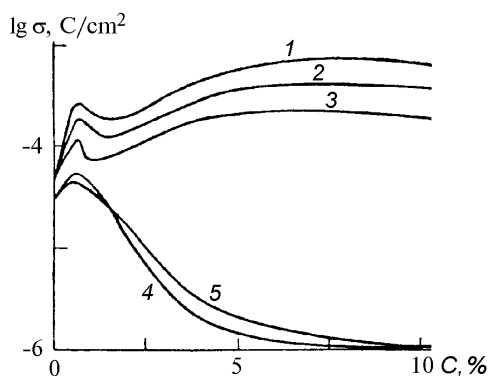


Fig. 2. TSD charge density in PVB samples depending on filler content: 1 — carbon fabric, 3 — Al and Cu powders, 4 — basalt fiber, 5 — fiber glass

The increase of sample polarization and electret charge reduces the initial velocity of the liquid spread (Table 1) and the actual contact area between the drop and sample (Fig. 3). The polarizing charge creates energy barrier in experimental conditions. To overcome this barrier the motive force of spreading is spent.

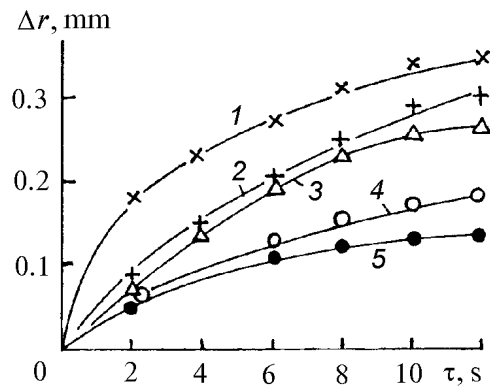


Fig. 3. Increase in diethylene glycole drop radius  $\Delta r$  spreading over pentaplast sample surface as related to time  $t$  when the drop was placed on the sample and electret charge density ( $C/m^2$ ): 1 - 0, 2 -  $10^{-5}$ , 3 - 0.003, 4 - 0.36, 5 - 0.58.  $\Delta r = r - r_0$ , where  $r$  and  $r_0$  are the radius in moments  $t$  and 0.

Table 1. The initial velocity  $v$  of DEG spreading over PPI versus sample surface charge density  $\sigma$ .

Sample	$\sigma, C/m^2$	$v, 10^{-4} \text{ mm/sec}$
Reference	0	2.8
Thermo-electret	$4.96 \cdot 10^{-6}$	1.4
	$2.78 \cdot 10^{-3}$	0.6
Corona-electret	0.36	0.4

The experimental dependence of edge wetting angle on the polarizing charge density is described by the Eqn 1:

$$\cos \Theta = \cos \Theta_0 - 1.4 \cdot 10^4 \sigma - 2 \cdot 10^{-9} \sigma^2 \quad (1)$$

where  $\Theta$  and  $\Theta_0$  are the liquid equilibrium edge wetting angles for, correspondingly, electret and nonpolarized samples;  $\sigma$  is the sample surface charge density.

Figure 4 shows the scheme for a device to investigate capillary motion of a liquid in contact gaps between steel sample 7 and polymer electret coating 6 on the substrate 4. The liquid flows over to the studied joint from a glass tube 1 where its level reduces by a value  $\Delta h$ . Capillary pressure of the liquid penetrated into the joint and that of the column of the height  $\Delta h$  in tube 1 are equal. Based on the above procedure an Eqn 2 has been derived [3]

$$\Delta h = \frac{2}{dS\rho g} - \frac{W - \sigma_{12}}{\cos \Theta} \quad (2)$$

where  $S$  is tube 1 cross section,  $\rho$  - liquid density,  $g$  - gravity force acceleration,  $W$  is the work to be spent for the liquid to separate from the coating,  $\sigma_{12}$  - surface tension at the liquid gas surface.



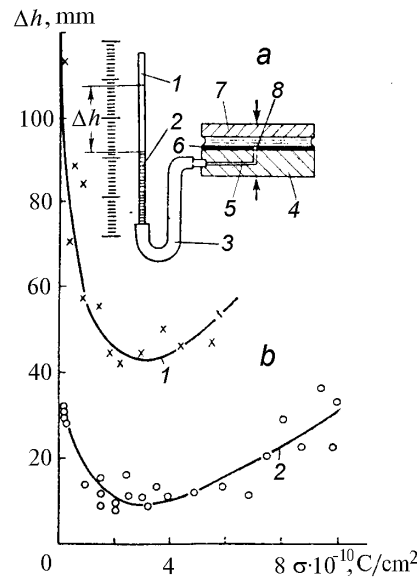


Fig. 4. Measurement diagram (a) of liquid capillary permeation into clearance between solids and dependence (b) of liquid level  $\Delta h$  variation in measured capillary on the sample charge surface density  $\sigma$ : a) 1 - glass tube, 2 - water, 3 - connecting tube, 4 - substrate, 5 - conduit, 6 - coating, 7 - sample, 8 - punch in the coating; b) 1 - polymethyl methacrylate (PMMA), 2 - fluoroplast-3 (F-3).

Nonmonotonous character of curves 1 and 2 in Fig. 4 is the result of superimposed reduction velocities  $W$  and  $\cos \Theta$  when the electret charge grows. On the initial inclining portion of the curves, the reduction of  $W$  dominates. At the same time physical adsorption of liquid molecules is intensified, which rises the double electric layer on the electret surface. When the layer is fully formed,  $W$  values stabilize. This corresponds to the minimum of  $\Delta h = f(\sigma)$  dependence. The ascending portion of the curves is the result of  $\cos \Theta$  reduction under constant  $W$ .

Curves 1 and 2 correspond to difference in parameters of PMMA and hydrophobic F-3 wetting with water.

### Sorption and Diffusion

The theory of diffusion based on the mechanism of diffusing particles jumping over the solid vacancies [11] suggests the following Eqn 3:

$$D = \frac{a^2}{\tau_0} \exp(-W / kT) \quad (3)$$

where  $D$  is diffusion coefficient,  $a$  is the solid lattice constant,  $\tau_0$  about  $10^{-13}$  s is the particle oscillation period,  $W$  - energy of diffusion activation,  $k$  - gas constant,  $T$  - absolute temperature. If diffusion proceeds in a solid dielectric possessing a polarized charge, then  $W = U + E + E_e$ , where  $U$  is the energy of vacancy formation,  $E$  is energy barrier height,  $E_e$  - energy acquired by a particle in the electret field. Diffusion proceeds in the electret faster or slower as compared to the polarized dielectric depending on  $E_e$  sign.

The polarized charge influences first of all the diffusing substance sorption by the electret. This influence behavior is conditioned by formation of the double electric layer in vicinity of

the electret surface. Sorption of organic solvent vapors was studied using PVB films thermally treated in contact with shorted copper and aluminum electrodes. The sample polarized charge density determined by the TSD method was about  $10^{-5}$  C/cm<sup>2</sup>. Both polarized and reference (thermally treated in contact with aluminum electrodes) samples were endured in diethylene glycole (DEG) and benzene vapors under  $T_1 = 303$  K and  $T_2 = 323$  K ( $T_2$  is about  $T_C$  of PVB). The experimental technique is described in [12].

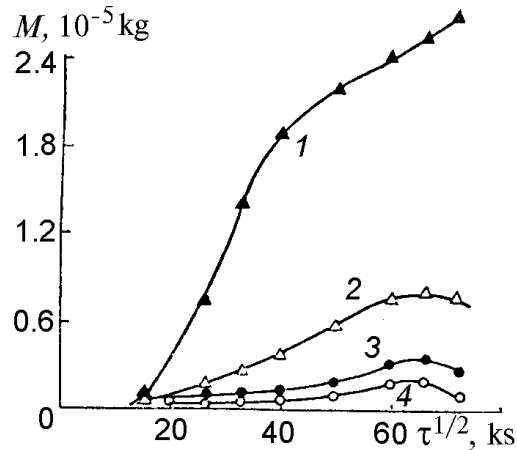


Fig. 5. Mass ( $M$ ) of PVB samples versus endurance time ( $t$ ) in DEG vapors. Temperature, K: 1, 2 -323, 3, 4 - 303. Samples: 1, 3 - reference, 2 and 4 - electret.

In Fig. 5 it is seen that DEG sorption by the electret under  $T_2$  (curve 2) is much less than in [1]. When  $T_1 < T_c$  the difference in sorption is not large (3 and 4). The similar results were obtained for the samples treated in benzene vapors (Table 2).

Table 2. Increase of PVB sample mass ( $M$ ) depending on time ( $t$ ) of endurance in benzene vapors under 323 K.

$t, 10^3$ s	M, 10 <sup>-2</sup> g for the samples	
	reference	electret
4.5	0.55	0
6.4	1.10	0
7.3	1.30	0.01
10.7	1.50	0.05
13.9	1.66	0.14
15.2	1.73	0.24

When  $T < T_c$ , the reduction in segmental mobility of macromolecules bounds sorption due to lower velocity of conformation transformations. This probably levels the difference in sorption of solvent vapors by electret and nonelectret films (curves 3 and 4 in Fig. 5). Upon the formation of the double electric layer from oriented dipoles near the electret surface, an equilibrium concentration of the solvent is established in the sample. The film permolecular structure in the process of electric polarization spurs sorption reduction in both polar (DEG) and nonpolar (molecular dipole moment equals zero) solvents. It appears that benzene

nonpolar molecules acquire the dipole moment in the electret field and interact with the electret following the described mechanism. Difference in DEG and benzene diffusion is attributed to DEG stronger solution capacity as compared to PVB.

### Adhesion

The effect of polarized charge on polymer adhesion to metals was first studied in the metal-polymer-metal systems [13]. Strength of splice adhesion was determined by lamination method. Strength increased 1.5-2 times when the adhesive joint formation was accompanied with the polymer transformation into MPE. Adhesion increase is much effected by activated in electric field diffusion of the metal-polymer contact reaction products into the polymer.

A model of a composite material is suggested. The composite incorporates a thermoplastic polymer binder and dispersed particles of metal oxides which differ by the value of the standard electrochemical potentials [14]. Fuming-oxides (FO) were used as the filler. They are a by-product of lead-zinc production and contain Zn, Pb, Mg, Cu and other oxides. During material formation FO reduction to metals is proceeding. The reduction of the sample ohmic resistance at heating, as well as the results of X-ray diffraction analysis are the proof of it. It was observed that with increasing time of treatment the intensity of peaks characterizing the oxide crystalline structure reduced, while the intensity of peaks corresponding to pure metal increased.

When a certain concentration of the conducting filler is reached, the formation of conducting bridges is probable in the composite and the contact between particles is unnecessary for the polarizing current to run. Microcircuits metal 1-polymer-metal 2 are formed between both the filler particles in the polymer matrix bulk and between a separate particle and metal electrode contacting the sample. Thus, electrochemical interaction of the composite components is realized in the process of thermal treatment which increases adhesion (Fig. 6).

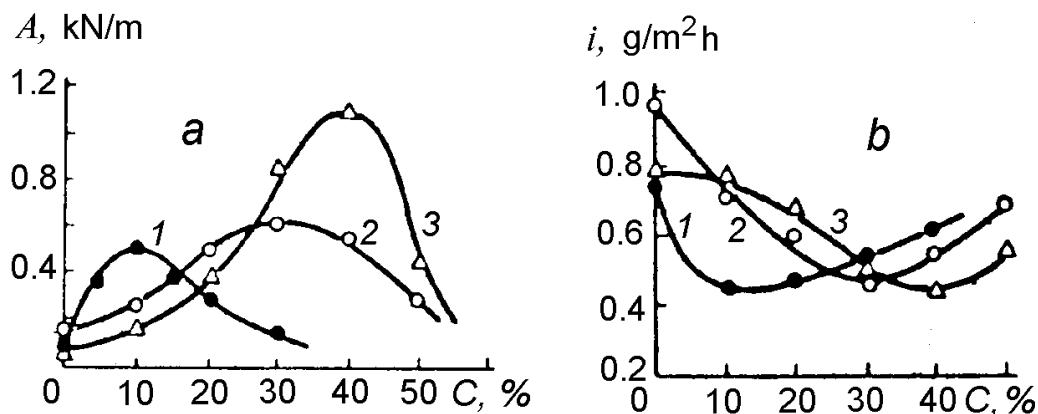


Fig. 6. Strength of adhesive joints (a) and protective capability (corrosion rate, b) from FO containing polymer composites with Al foil versus FO content and filler type: 1 - PE, 2 - PVB, 3 - PPI.

Rearrangement in the polymer permolecular structure accompanying polarization causes, as a rule, improvement of their strength and impairment of deformation characteristics. So, thermally electrified polycarbonate and PTFE samples show an increased by 15-60% breaking tensile stress and several times relaxation time of mechanical stress [4].

Strengthening of polymer composites by transferring their components into electret state has been verified experimentally [5]. Breaking tensile stress of composites (PE, PA, PVC, PPI, PTFE matrices; reinforcing elements - basalt, phenylone, glass, Dacron fibers) increases 1.6-2.5 times due to filler and matrix electric polarization. Adhesion of polymer binder to filler exerts a substantial effect on composite strength. Force of fiber glass peeling off from PVC-based fiber glass plastic increases at binder polarization from 3.4 to 4.4. kN/m. For PPI it increases from 1.7 to 2.6. kN/m .

### Protection against Corrosion

One of crucial factors for the polymer-based rustproof systems is the barrier action of polymer elements insulating metal from environment. It is believed that, when a structural polymer barrier is disturbed, it does not influence metal corrosion in electrolytes. Nevertheless, the polymer electret field effect on both barrier characteristics of polymers and kinetics of electrochemical processes in metal-polymer systems should be taken into account. The polarized charge effects the kinetics of liquid spreading over polymer electrets and sorption of liquid media.

Diffusion of liquids into MPE coating g on metals has been studied. If liquid concentration  $C_0$  on the coating surface is supposed to be constant during diffusion, then the amount of liquid sorbed by MPE to the moment  $t$  is [15]

$$Q = \frac{2C_0}{\pi} \sqrt{Dt} \exp(-\alpha\sigma) \quad (4)$$

where  $D$  diffusion coefficient of nonpolarized polymer;  $\sigma$ -MPE surface charge density determined by TSD. The parameter  $\alpha \sim 3 \cdot 10^4$  is determined experimentally for each polymer-liquid combination. The equation describes satisfactorily diffusion into MPE with  $\sigma > 5 \cdot 10^{-7} \text{ C/cm}^2$ . Probable reduction of coating diffusion permeability using polarization is limited by the ultimate charge density of MPE  $\sigma \leq 10^{-5} \text{ C/cm}^2$  due to electrodes blocked by products of metal-polymer reaction [16].

The initial corrosion of protected by polymer coating metal is penetration of corrosive medium along the coating-metal interface leading to the coating peeling off. Peeling is accompanied by the electrode metal potential bias to the negative domain. This evidences that under the coating there occurs either retardation of cathodic oxidation or acceleration of metal ionization. Both processes can be controlled using electret coatings.

Table 3 demonstrates test results of polymer coatings on steel with a through punch in the protecting film reaching the substrate. Coatings of group A were formed following the classical vibro-vortex method. Melting of group B coatings was accomplished in electric field of  $E = 20 \text{ kV/cm}$  strength by connecting upper electrode with the positive pole of a high-voltage source and the substrate with the ground. When melting group C coatings, the polymer layer was covered by a copper foil closed in the steel substrate. After cooling the foil was peeled off.

Table 3. The coating peeling area  $S$  and change of the substrate electrode potential  $\Delta U$  depending on endurance time  $t$  in a strong NaCl solution.

Coating Group	Coating material	$S$ (cm <sup>2</sup> ) during $t$ (days)					$\Delta U$ (V) 5 days
		1 day	2	3	4	5	
A	PPI	0.25	0.74	2.03	2.76	3.97	0.24
	PVB	3.03	6.24	10.32	—	—	—
B	PPI	0	0.01	0.02	0.02	0.04	0
	PVB	0.01	0.02	0.04	0.07	0.08	0.02
C	PPI	0	0.01	0.02	0.02	0.03	0
	PVB	0.01	0.02	0.05	0.07	0.08	0.02

It is obvious that Group B thermo-electrets which contact the substrate by the negatively charged surface peel off slower and their substrate unrefining is less as compared to nonelectret ones (group A). Similar results showed MPE-based coatings (C) formed without outer electric source.

### Triboengineering Characteristics

Among phenomena accompanying polymer friction, those of electrical nature are the least studied, though their influence is not of minor importance.

Crucial factors governing friction and wear of polymers being either a polarized body or electric field source are the following. Electrization potential  $U$  of the polymer element in a metal-polymer friction pair succeeds to saturate rather quickly (in a few seconds). Change of  $U$  sign during initial friction can be attributed to loss of moisture by the element surface layers. Air humidity and the presence of a liquid film on the friction surface exerts a considerable effect on  $U$ . Polymer in the field of electrization charge transfers under frictional heating into tribological electret state [7]. It determines the kinetics and intensity of physicochemical processes in the friction zone. Most important experimentally recorded parameters of triboelectret state are the efficient surface density of charge  $q$  and TSD current spectrum. The latter helps to estimate the correlation between homo- and heterocharge in the triboelectret, as well as activation energy of the charge formation and declining, time of relaxation, etc.

MPE wear was examined by removing from the friction surface the layers which contacted during polarization Cu and Al electrodes. The experimental technique is described in [18]. MPE charge is concentrated mainly in the surface layer (20-60  $\mu\text{m}$ ). It was recorded by TSD that  $q$  near the copper electrode is higher than near the aluminum one. Wear of the friction surface contacted Al at polarization is lower than that contacted Cu (Fig. 7). Obviously MPE wear proceeds more intensively with  $q$  growth. Such a regularity is violated only with thin (15-20  $\mu\text{m}$ ) surface layers displaying elevated concentration of chemical structural defects. This is also typical, though to a less degree, of nonelectret samples.

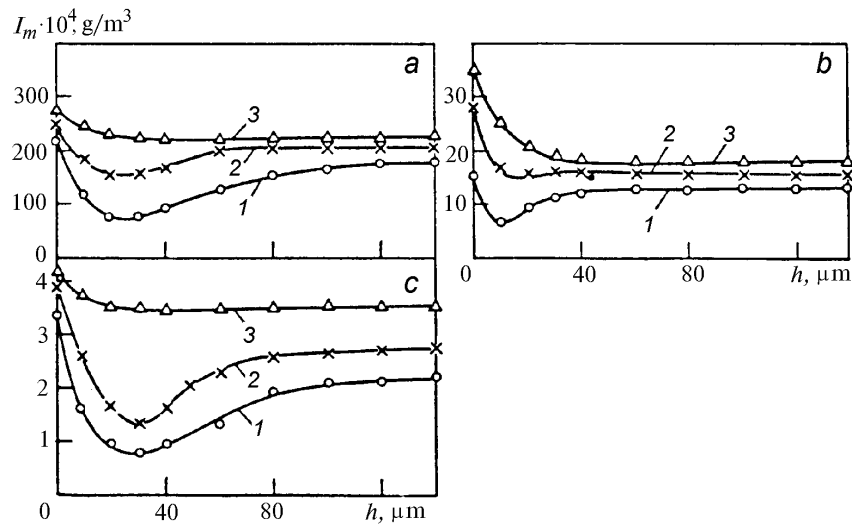


Fig. 7: The dependence of MPE wear rate on the thickness of the layer removed from the sample surface contacting Al (1) and Cu (2) at polarization. 3 - reference sample. Sample materials: a - PVB, b - PPI, c - PA.

Variation of MPE tribological characteristics are due to space charge formation accompanied by structural rearrangement of the near-electrode layer. Rise in degree of nonpolarized PPI samples crystallinity constitutes 4% from the copper electrode side and 6% from the aluminum one. Upon removal of 80-100  $\mu\text{m}$  thick layer the polarized and nonpolarized samples do not differ in crystallinity degree. It may be so that space charge generated in the near-electrode regions during crystallization hamper macromolecule packing. Therefore, the larger charge value localized near copper electrode corresponds to a smaller degree of crystallinity.

Novel triboengineering materials and friction joints have been developed [19-20]. They incorporate MPE as electric field generator to improve friction and wear parameters.

## CONCLUSIONS

Polymer electrets are used to regulate technological processes of composite material formation. They involve sorption, diffusion, wetting, spreading, saturation and etc. Electret composites contribute to protecting machine parts against corrosion, raise of components adhesion, material hardening and improvement of friction joint tribological characteristics.

Electret composites are the new materials effecting the engineering developments.

## ACKNOWLEDGEMENTS

The authors are grateful to Dr. Yu.I. Voronezhnev for experiments with MPE and discussion of results.

## REFERENCES

1. Electrets, Ed. by Sessler G.M., Springer-Verlag, Berlin, 1987.
2. Goldade V.A. and Pinchuk L.S., Electret Plastics: Physics and Materials Science, Nauka i Tekhnika, Minsk, 1987.
3. Pinchuk L.S., Hermetology, Nauka i Tekhnika, Minsk, 1992.
4. Voronezhnev Yu. I., Goldade V.A., Pinchuk L.S. and Snezhkov V.V., Electric and Magnetic Fields in Technology of Polymer Composites, Nauka i Tekhnika, Minsk, 1990.
5. Vertyachikh I.M., The Development of Engineering Polymer Composite Materials with Electret Components, Ph.D. Thesis, Gomel, 1990.
6. Goldade V.A., Pinchuk L.S. and Voronezhnev Yu.I., Electric Polarization of Polymers in Metal-Dielectric- Metal Systems, Proc. ISE-6 Conf., IEEE, New York, 1988, pp.419-423.
7. Goldade V.A., Voronezhnev Yu.I. and Pinchuk L.S., On Mechanism of Polymer Polarization in Metal 1-Polymer- Metal 2 Systems, Proc. Intern. Conf. Plastko- 90, Ostrava, 1990, pp. 76-80.
8. Goldade V.A. and Pinchuk L.S., New technology of Electrically Polarized Polymers Creation during Heat Treatment in Contact with Different Metals, Proc. Polymer Process. Soc., Stuttgart, 1995, pp. 6-9.
9. Goldade V.A. and Pinchuk L.S., New Spheres of Metal- Polymer Electrets Technical Application, Proc. ISE-9, IEEE, Shanghai, 1996, pp. 1079-1080.
10. Plevachuk V.G., Vertyachikh I.M., Goldade V.A. and Pinchuk L.S., Effect of the Charge of a Polymer Electret on the Spreading of Liquids, Polymer Science, A, Vol. 37, No. 10, pp. 1071-1074.
11. Frenkel Ya. I., Kinetic Theory of Liquids, USSR Acad. of Sci., Moscow, 1945.
12. Vertyachikh I.M., Goldade V.A., Neverov A.S. and Pinchuk L.S., The Effect of Polymer Electret Electric Field on Sorption of Organic Solvent Vapors, High-Mol. Comp., 1982, Vol. 24B, No. 9, pp. 683-687.
13. Belyi V.A., Goldade V.A., Neverov A.S. and Pinchuk L.S., Polymer Strength in Splices of Unlike Metals, Polymer Mechanics, 1977, No. 4, pp. 740-742.
14. Goldade V.A., On Adhesive Strength and Protective Capacity of Polymer Composite Coatings, Mechanics of Composite Materials, 1981, No. 5, pp. 842-845.
15. Voronezhnev Yu.I., Effect of Polymer Coating Electric Polarization on its Diffusion Permeability, Trans. of BSSR Acad. of Sci., Phys. Techn. Sci., 1986, No.4, pp. 42-44.
16. Goldade V.A., Voronezhnev Yu. I. and Pinchuk L.S., On Some Peculiarities of Polymer Electric Polarization in Metal 1-Polymer-Metal 2 Systems, High-Mol. Comp., 1988, Vol.30B, No. 6, pp. 427-431.
17. Klimovich A.F. and Guzenkov S.I., Electric Phenomena at Polymer Friction. III, Regularities of Electret State Formation, Soviet Friction and Wear, 1989, Vol. 10, No. 5, pp. 779-785.
18. Voronezhnev Yu.I., Goldade V.A., Pinchuk L.S. and Rechits G.V., Influence of Charge Distribution on Friction Characteristics of Polymer Electret, Soviet J. of Friction and Wear, 1984, Vol. 5, No. 11, pp. 110- 113.
19. USSR Patent No. 1165588, B29C, Device to Manufacture Articles from Polymer Bulk Materials, 1985.
20. USSR Patent No. 1055913, F16C, Sliding-Contact Bearing, 1983.

# MULTI-AXIAL WARP KNITTED LAYERS - A TEXTILE FOR REINFORCING CONCRETE

Dr.-Ing. Gerd Franzke<sup>1</sup>, Prof. Dr.-Ing. habil. Peter Offermann<sup>1</sup>, Dipl.-Ing. Thomas Bischoff<sup>2</sup>, Prof. Dr.-Ing. Burkhard Wulfhorst<sup>2</sup>

<sup>1</sup> Institut für Textil- und Bekleidungstechnik der TU Dresden,  
Mommßenstraße 13, 01069 Dresden, Germany.

<sup>2</sup> Institut für Textiltechnik der RWTH Aachen,  
Eilfschornsteinstraße 18, 52062 Aachen, Germany.

**SUMMARY:** The aims described before will be achieved by presenting the historical propagation in civil engineering from asbestos to glass fibres respectively alkaline resistant glass fibres. A short summary of existing technologies for processing short fibres with concrete matrices will show today's state of the art. Both aspects will be compared with the historical development of fibre reinforced plastics technologies. Derived from this comparison the necessary technology transfer from plastics to concretes will be obvious. Following this idea it will be presented how a new composite material has been born by reinforcing concrete with textiles. The results of a project including production of multiaxial layer fabrics, matrix optimization, production of test specimen and determination of mechanical properties will prove the technical and economical qualification of the new composite material in comparison with short fibre reinforcement.

**KEYWORDS:** textile reinforced concrete, alkali-resistant glass fibre, fibre tests, warp knitted multi-axial layer fabric WIMAG, stitch-bonded variable layer fabric NVG,

## INTRODUCTION

The reinforcement of mineral matrix systems using fibres has long been a state-of-the-art technique. The best known and quantitatively most widespread are asbestos fibres and building components reinforced with these. The need to find a substitute for asbestos fibres worldwide resulted in a shift of interest to, among other substances, glass fibres. In order to use these in a concrete matrix it was essential that the fibres be resistant to the alkaline environment if they were to retain their very good mechanical qualities for a sufficient duration. The development, 25 years ago, of alkali-resistant glass fibres enabled glass fibres in the form of short strands to be used for reinforcing concrete matrices, a technique which has become firmly established in the construction sector and is applied in a wide variety of ways. Some improvement is needed if optimal advantage is to be taken of these fibres, particularly in view of the short length of the fibres and the fact that their orientation is not always appropriate for achieving the bearing capacity required. The effectiveness of the fibres is to be improved by using glass filament yarns and orienting them in accordance with the function of the particular building component in



question. A technological variant is the production of textile fabrics that meet these requirements. At present knitting technology with its variable stitch-bonding techniques is ideal for the manufacture of such structures. Initial tests have been carried out at the Institute for Textiles and Clothing Technology, TU Dresden, and at the Institute for Textile Technology, RWTH Aachen, as a part of AiF project no. 9272/B [1]. The results of these tests form the basis for this talk.

### **FIBRE TESTS**

Reinforcement materials in a concrete building component are subject to media influences right from the start of the manufacturing process until the end of their service life. These include the alkaline influence from the concrete matrix and the acidic influence of rainwater seepage at defective points. In Germany, very high demands have to be met proving the durability of new building materials before their introduction in the construction industry. Tests concerning the influence of the above-mentioned media on the qualities of the reinforcement materials are therefore of particular interest.

This research project made use of the special glass fibres NEG AR H-340V, 650 tex produced by Nippon Electric Glass. These fibres have a raised zirconium content ( $ZrO_2$ ), providing good resistance in fine concrete. These fibres are referred to as alkali-resistant (AR) glass fibres. The yarns produced by Nippon Electric Glass are the only such fibres suited treatment as textiles and they were selected for these tests for this reason [1,2].

The experiments testing resistance to artificial rainwater (pH 6) and to sodium hydroxide (pH 12,1), which corresponds to the pH value of a special concrete matrix, were conducted according to the established norms. The fibre material was taken from a spool and laid out in test groups in developing trays which were subsequently filled with the solutions. The trays were then covered to prevent evaporation, thus ensuring constant pH values.

The test materials were then stored in a climatic chamber. After 24 hours, 7 days and 28 days they were removed, air-dried for three hours and then subjected to bending pressure. The force: bending ratio was determined in accordance with bending pressure test DIN 53834, part 1. Figure 1 shows the specific tensile strength of the AR glass fibre yarns in relation to duration of storage and the medium applied.

The results show that with the specimens stored in normal climate conditions only minor changes in durability are recorded, so that comparisons can be made between these and the specimens exposed to the special conditions as described above. After drying, the samples stored in the solutions have a slightly adhesive structure. The fibre lengths stored in rainwater, in particular, lead to higher degrees of durability as a result of these adhesive qualities which have the effect of bonding fibre and matrix together.

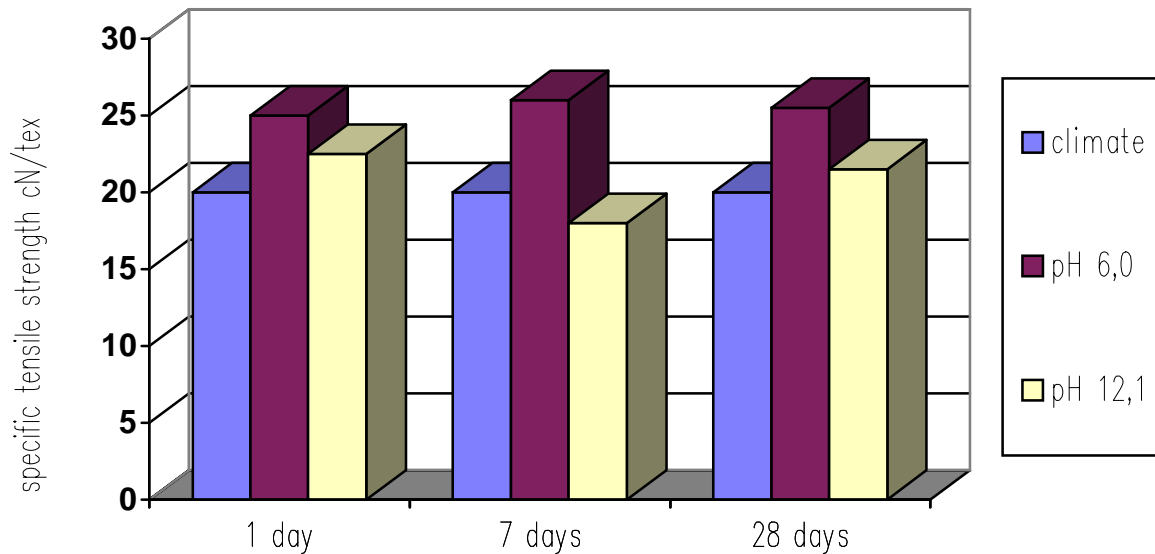


*Fig. 1: Specific tensile strength of AR glass filament yarns under the influence of media and duration of exposure*

The fibre lengths stored in sodium hydroxide solution show only minor changes in durability, thus confirming their good resistance to alkaline media.

## **PRODUCTION OF MULTI-AXIAL LAYER FABRICS FOR REINFORCEMENT OF CONCRETE**

Two multi-axial types of textiles will be manufactured for the initial basic tests on the suitability of long-fibre from AR-glass reinforcements in concrete matrices. The two manufacturing techniques which will be compared are MALIMO stitch bonding, with the stitch-bonded variable layer fabric (NVG) manufactured applying this technique, and the LIBA technique, together with its product, the warp knitted multi-axial layer fabric (WIMAG).

### **Production Of Warp Knitted-Multi-Axial Layer Fabrics (Wimag)**

The warp knitted multi-axial layer fabrics are used successfully in the field of plastic composites technology. This is due to the cost-effective production and excellent mechanical properties of WIMAG. Depending on the size of the machine, the textile (cf. Fig. 2) may comprise up to 8 layers of fibres and an additional 2 covering layers of fibre mats, which are fixed in place by warp knitted mesh threads.

Fig. 2 also illustrates the warp knitting machine (LIBA system) with its four weft insertion systems, as has been used at the Department of Textile technology of the Technical University of Aachen (ITA) for manufacturing WIMAG.

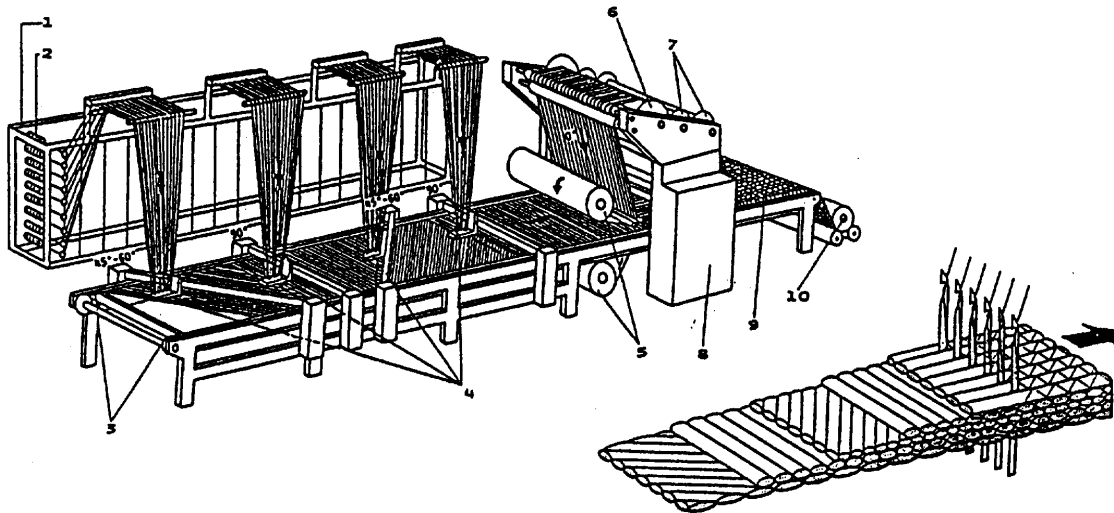


*Fig. 2: Warp Knitted Multi-Axial Layer Fabrics (LIBA-Technique)*

Here the reinforcing threads (2) are drawn off the warping creel (1) and inserted by the weft inserting systems in the required directions. The weft inserting systems oscillate between the needle transport chains (3), which fix the deposited fibres to the machine during transportation.

The weft inserting systems can be mounted in a fixed position ( $90^\circ$ ) or variably ( $30^\circ$  to  $60^\circ$ ) or ( $-30^\circ$  to  $-60^\circ$ ) to the direction of production.  $0^\circ$  threads can be fed directly from warp beams (6). It is also possible to supply non-woven fabrics or fibre mats as covering layers via rollers (5).

The warp knitted multi-axial layer fabric, designed in this manner, is fixed in place in the knitting unit (8). The warp knitting threads are removed from the warp beams (7). The finished WIMAG (9) is wound on at the end onto a cloth beam (10).

### **PRODUCTION OF STITCH-BONDED VARIABLE LAYER FABRICS (NVG)**

During the manufacture of stitch-bonded materials (cf. Fig. 3), a parallel weft yarn sheet is first of all laid with the aid of a weft guiding carriage. The continuous advance feed of the transport chain during laying causes this yarn sheet to be inserted at an angle of about  $88^\circ$ , and not precisely at  $90^\circ$ .

Using two variable thread guiding systems (V1 and V2), parallel yarn sheets can be inserted at an angle of between  $0^\circ$  and about  $80^\circ$ , and in addition, the distance between the threads can be altered. This allows the reinforcing textile to be reinforced locally in certain zones, which lie within the subsequent building component, for example in the zones where force is applied.

The weft thread sheet is fed to the knitting elements, together with the other thread layers. The reinforcing threads are fixed in place with the aid of a sewing yarn system which creates knitted meshes. Thus, this procedure combines elements of sewing (passing through and combining thread layers) and of knitting (creating knitted meshes from a large number of individual threads at the same time).

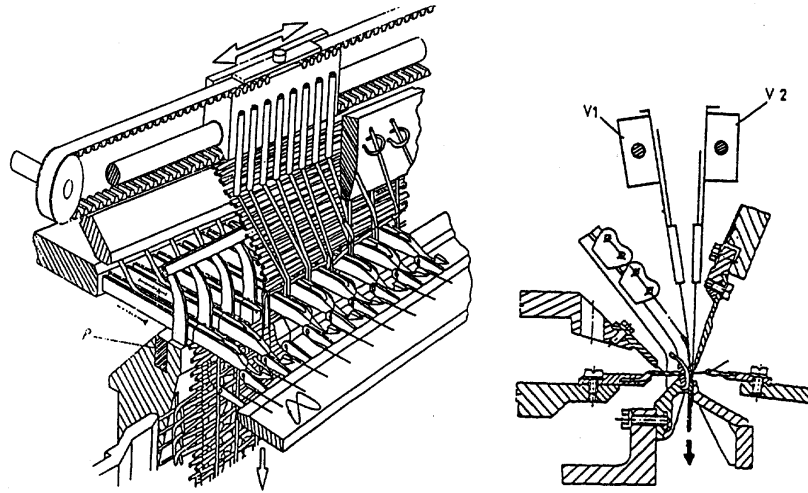


*Fig. 3: Malimo stitch-bonding technique*

The Malimo stitch-bonding technique is applied at the Institute of Textile and clothing Technology at the Technical University of Dresden (ITB).

### **TESTS ON THE TEXTILE PROPERTIES OF THE REINFORCEMENT**

The physical tests show that the processing of the reinforcement fibres into a net-shaped structure has been done satisfactorily, although the meshes sometimes have rather irregular thread patterns. With 90° oriented rovings the WIMAG fabrics were found to have somewhat better properties than the NVG fabrics (cf. Fig. 4). With 45° orientation hardly any difference was found in the test values for the two types of fabric [2].

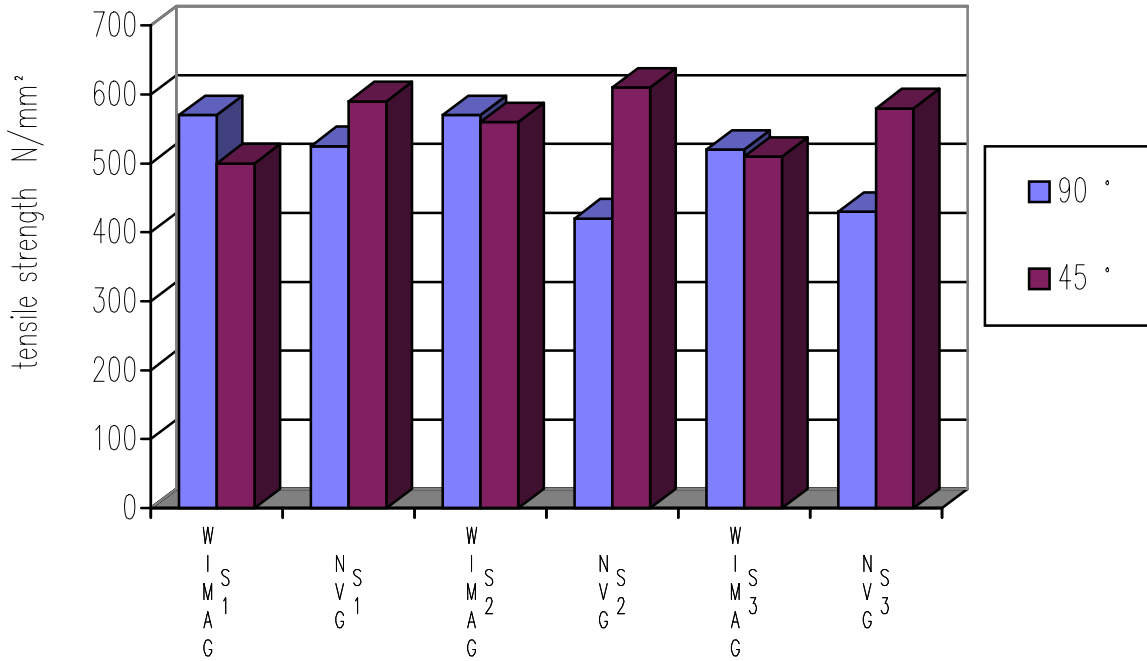


Fig. 4: Comparison of maximum tensile strength of the reinforcement textiles

Since working with these substances as textiles is not without its difficulties, the fabrics achieve a yarn strength of only 43% (as cited by the Manufacturer). Causes of this include the slightly wavy formation of yarn resulting from the open structure and from defects in the material used.

### THE COMPOSITE ELEMENTS

Three different net-shaped structures (S1, S2, S3) with 90° and +/- 45° oriented reinforcing fibres, made from AR fibre glass, is manufactured from the two types of textiles described above; the different fabric types can be compared. Net-shaped structures have been selected in order to ensure that the textile is impregnated by the relatively high viscous concrete.

A special-purpose matrix material has been developed on the basis of experience derived using types of short-staple reinforced concrete; this material attacks fibre glass less by forming a medium which is less alkaline around the fibre glass. These cement matrices are based on Portland cement with highly efficient alkali binding components. This type of cement was therefore selected for trials with the following additives (weights), on the recommendation of industry [3]:

Cement	1	part
Sand	1	part
Water	0,42 to 0,48	parts
Liquefier	0,22 to 0,04	parts
LP 1-87 Addiment	0,003	parts

## THE PRODUCTION OF THE TEST SPECIMENS

The test pieces are manufactured with aid of a positioning unit which allows the reinforcing textiles to be guided into the mould tool in a defined manner (cf. Fig. 5).

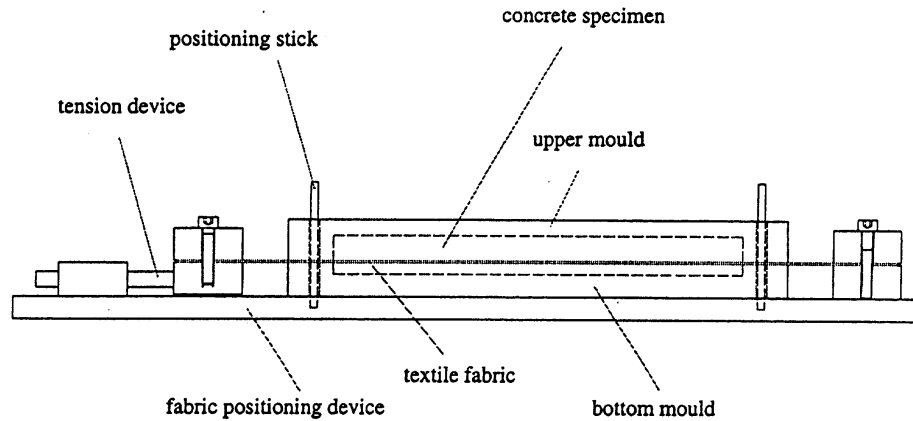


*Fig. 5: Production of Test Specimens*

The divisible mould tools are fixed in place above the positioning rods. Once the bottom halves of the mould tools have been positioned and filled, the reinforcing composite is fixed in place with the aid of clamping elements. The tension applied merely serves to ensure that the textile is laid evenly; in other words, no elastic deformation of the reinforcing textile is generated.

Once the composite has been fixed in place, the top and bottom of the mould tool are screwed together and filled with concrete. The complete mould tool can now be raised from the positioning unit and placed in a climatic chamber to be stored for 28 days.

## RESULTS OF THE MECHANICAL TESTS

The first series of tests, in which the two more open glass structures were tested, proves that the concrete with 0.42 parts by weight of water and 0,035 parts by weight of cement liquefier can withstand the highest maximum bending pressure. The specimens were tested after only 10 days curing time. At this stage the composite material still does not possess its ultimate properties. Nevertheless, the calculated bending tensions should only be viewed initially for the purpose of comparison in order to determine the ideal make-up of the concrete. In this series of trials, the concrete samples with the WIMAG glass reinforcing of greater density possess a maximum bending strength of 9.1 N/mm<sup>2</sup>, as opposed to 5.08 N/mm<sup>2</sup> in the case of non-reinforced concrete.

The optimised aggregate parts were used in the actual final of trials. The test pieces, which were produced applying the same process, were now stored for 28 days. The results of 4-point bending test are illustrated in Fig. 6.

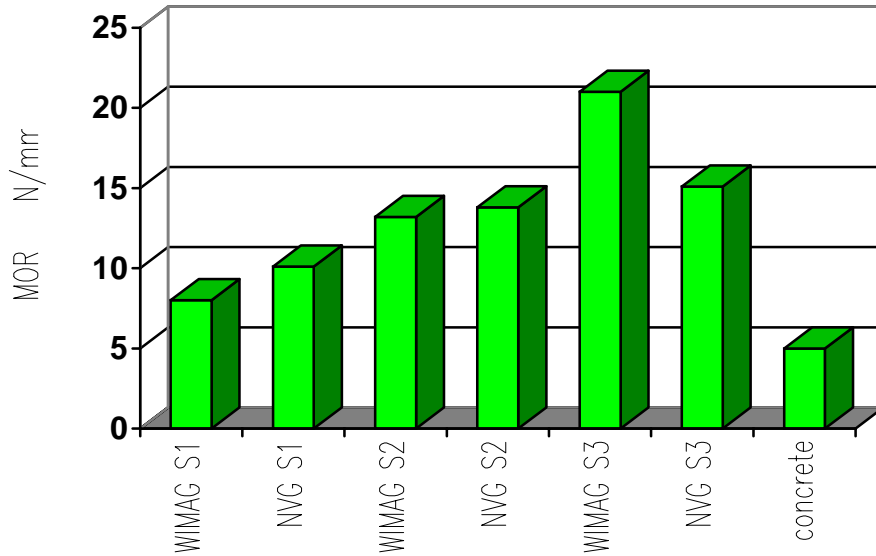


*Fig. 6: Results of the 4-Point-Bending Test*

It is clear that the modulus of rupture (MOR) of the textile reinforced concrete specimens (21.0 N/mm<sup>2</sup>) is up to four times higher than of non-reinforced concrete (5.1 N/mm<sup>2</sup>). This maximum value was achieved using the WIMAG AR glass structures of greatest density (WGS3). The more open (S2 or S1) or NVG structures lie somewhat below the maximum values.

### **THE PRODUCTION OF A DEMONSTRATOR COMPONENT**

For demonstration purposes, a girder used a window lintel, geometrically measuring 700 mm x 140 mm x 140 mm. In order to minimise its weight, the building component is built as a hollow concrete profile with a styrodur core measuring 700 mm x 100 mm x 100 mm. The girders were made by the Institute of Supporting Frameworks and Building Materials at the Technical University of Dresden, using the optimised concrete composition and with the aid of double moulds (cf. Fig. 7).



*Fig. 7: Production of a Window Lintel*

The reinforcing structures are first impregnated separately with the concrete matrix in a tray, before then being inserted in the mould and evenly aligned with a 2 kg weight at either end. The matrix material is fed into the bottom of the mould, and the styrodur core is then inserted; it is centred using U-shaped spacer pieces at either end of the mould. The remaining hollow spaces are then filled, and air pockets are removed by compressing the matrix. After curing, the girders are removed from the mould, impregnated in the water bath and stored for 28 days at climatic conditions of 20 °C and 55 % relative humidity.

Following the storage of the window lintels, the sides which were facing up during manufacture are ground. The girders are then tested in 4-point bending tests, conforming to DIN 51300 and DIN 51302. The breaking load, deformation and extension of the girders are ascertained.

The suitability of the different types of composites for reinforcing concrete building components can be judged taking the modulus of rupture (MOR) as an example (cf. Fig. 8). It clearly has a greater bearing capacity than concrete which is either non-reinforced or else only reinforced using chopped strands. The extension and deformation values of the reinforced windows lintels are also calculated as being clearly higher than the comparable values for the girders which were either non-reinforced or else only short-staple reinforced. The final appraisal of the results of the trials will have to be carried out following completion of the final trials [4].



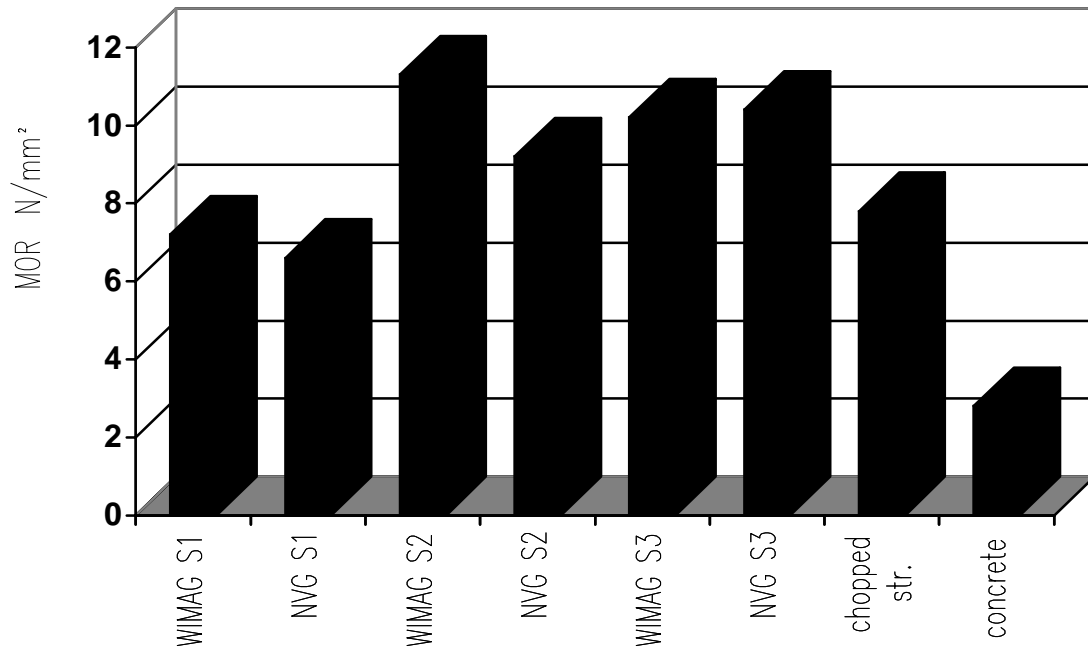


Fig. 8: Results of the Mechanical Testing of the Demonstrator Components

### CONCLUSION AND PROGNOSIS

The results of this research project show that sheets made up of AR glass fibre threads applied as reinforcements for concrete components can lead to better use of materials and hence reduce costs. A proportion of glass amounting to 1% by volume applied in this way produces the same durability as a 3-5% proportion applied as short-staple glass fibres. By orienting the yarns in accordance with the demand to be placed on the building component in question, a higher degree of efficiency is achieved in the reinforcement material. The results also show however, that there is still more room for improvement in the properties of the fabric sheets as regards their ability to be treated as textiles. Improvements in this sphere would lead to further enhancement of the properties of building components with respect to durability and the minimisation of weight.

More highly developed alkali-resistant glass filament yarns are currently being tested by Nippon Electric Glass with regard to their textile properties and as reinforcement materials for very thin concrete elements. In the future it is intended to establish rules on the dimensions of reinforcing sheets made of alkali-resistant glass fibre threads.

In order to solve the problems regarding the textile properties of these products, such as improvement of their processing potential, enhancement of fibre/matrix adhesion, and development of reinforcement structures appropriate to loading and processing demands, it is essential that there be intensive cooperation between manufacturers of fibres, textile machine

producers, the textile industry, and research institutions, always bearing in mind, of course, the needs of the end consumer, the construction industry.

We should like to express our thanks to the “Gesamttextil” Research Committee for its support of the work presented here (AiF-No. 9272 B) and other on-going research. This support is in the form of a research grant awarded by the Working Group of Industrial Research Associations from funds provided by the Federal Ministry of Trade and Commerce.

### REFERENCES

1. Wulfhorst, B., Bischoff, Th., Offermann, P., Franzke, G.: “Verwirkte Verstärkungsgelege für das textile Bauen”; Abschlußbericht zum AiF-Forschungsvorhaben Nr. 9272, RWTH Aachen und TU Dresden, 1996
2. Franzke, G., Bischoff, Th.: “Textilarmierung für mineralische Baustoffe”; Vortrag zur 3. Dresdner Textiltagung 1996, Dresden
3. Weiser, W.: Internal Information of the Fachvereinigung Faserbeton e. V. Düsseldorf, Germany, Juli 1994
4. Bischoff, Th., Franzke, G.: “Multi-Axial Warp Knitted Layers a Textile for Reinforcing Concrete” Strasbourg, France, International Congress GRC 95, 9-11 October 1995

# PROCESSING AND ELECTRICAL PROPERTIES OF PTCR COMPOSITE MATERIALS

Z. X. Xiong and K. Z. Baba-Kishi

*Department of Applied Physics, The Hong Kong Polytechnic University, Hong Kong*

**SUMMARY:** This paper reports the processing and electrical properties of a new type of PTCR composite materials, which has been made into electric heating cable and plate used in industrial and domestic area. The additives of carbon black and semiconductive ceramic powders were mixed with the matrix of polyethylene powder or epoxy resin. The SEM micrographs of the composites displayed that CB, SBT and silver powders were randomly distributed in the PE or ER matrix. A conducting model of the composite is proposed and its equivalent parallel-series electric circuit is schematically shown, to explain the mechanism of the PTCR effect of the composite.

**KEYWORDS:** processing, electrical property, PTCR composite and SEM

## INTRODUCTION

Polymer matrix composite materials not only exhibit PTCR (Positive Temperature Coefficient of Resistivity) effect but also behave perfect flexibility [1,2]. A new type of PTCR composite materials was reported here, which has been made into electric heating cable and plate used in industrial and domestic areas.

The PTCR effect of this kind of composite appears when a volume fraction of conductive additive was so large that the percolation threshold of conduction can take place [3,4], usually about 20 - 50 weight percentage of carbon-black is enough. The resistivity of the composite at room temperature is mostly equal to  $10^2$  to  $10^5 \Omega \cdot m$ .

## EXPERIMENTAL

As conductive and semiconductive additives, commercial carbon black (CB) powder, silver (S) powder or/and  $(Sr_{0.2}Ba_{0.8})(Ti_{0.999}Nb_{0.001})O_3$  ceramic (SBT) powder were mixed into polyethylene (PE) powder or epoxy resin (ER) by roll-milling at 150 ~ 180 °C for 30 minutes. The samples were then pressed by a hydropress at 100 ~ 130 °C for 5 minutes. Ga-In solution electrodes were applied. The samples were irradiated in an electron accelerator, 2 MeV for energy, with different irradiation dose. The resistivity of the samples was measured by a multimeter as a function of temperature with a heating speed of 1 °C/minute. The microstructure of the composite materials was observed with a scanning electron microscope (SEM).

## RESULTS AND DISCUSSION

Cooled down to room temperature at a slow speed, sample 1B exhibited lower resistivity at room temperature ( $R_r$ ) and behaved stronger PTCR effect than that of sample 1G that was cooled at a high speed (Fig. 1). However, there was little difference between sample 1B1 and 1G1 in which a special reagent was added. Partially substituting the CB powder with SBT powders uncoated and coated with a thin nickel layer, the authors produced samples 1B2 and 1G2. The later showed lower  $R_r$  and better PTCR effect; moreover, it took short time to reach a thermostatic temperature.

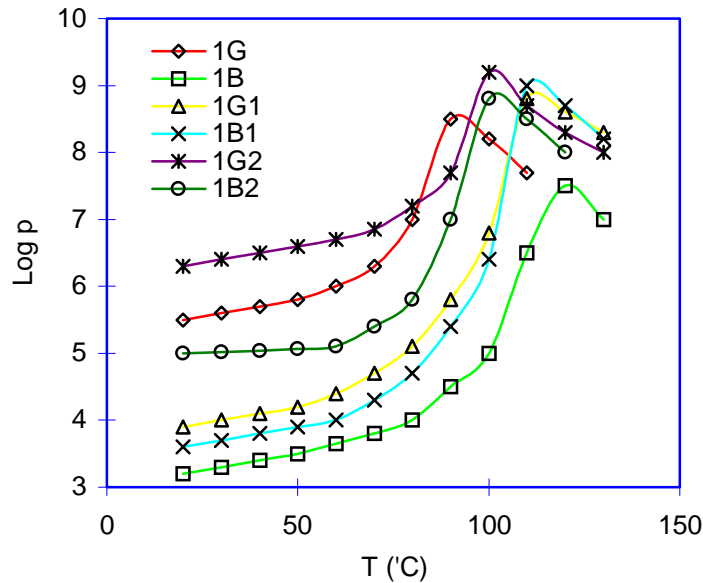


Fig. 1 Temperature dependence of resistivity of the composites

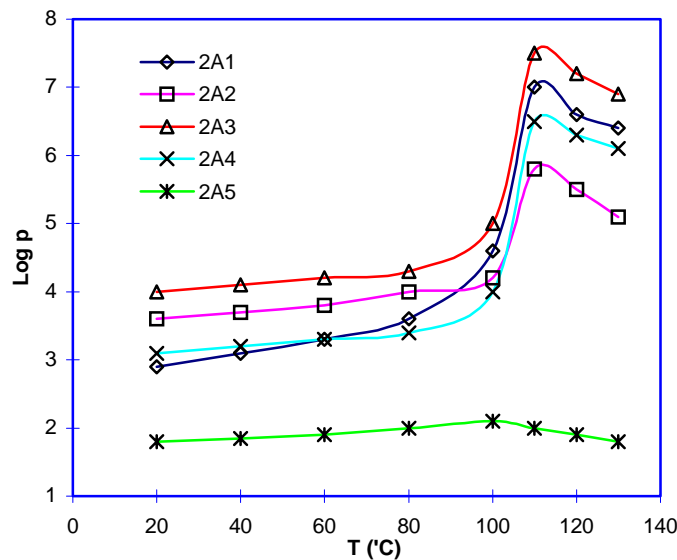


Fig. 2 Effect of additive content on PTCR curve of the composites

The PTCR effect of the samples was also dependent on the cross-linking degree or crystallinity of the PE matrix (Fig. 2). Sample 2A1 in which about 60 % PE matrix was cross-linked revealed stronger PTCR effect than sample 2A2 in which the PE matrix was free of cross-linking. Though influencing  $R_r$ , the CB content did not evidently change the PTCR effect of samples 2A3 and 2A4, in which 30 wt % and 50 wt % CB powders has been mixed with the ER matrix, respectively. Nevertheless, the PTCR effect of sample 2A5, which consisted of 30 wt % CB powder and 10 wt % silver powder in the ER matrix, was obviously weakened by the addition of the silver powder; meanwhile, the sample 2A5 behaved remarkably low resistivity within a wide temperature range. The PTCR effect of the material was influenced by the dose of electron irradiation when its degree of cross-linking was relatively low, as sample A1 (Fig. 3) with a, b, c and d representing irradiation dose of 2.0, 1.5, 1.0 and 0 x 10<sup>5</sup> Gy, respectively.

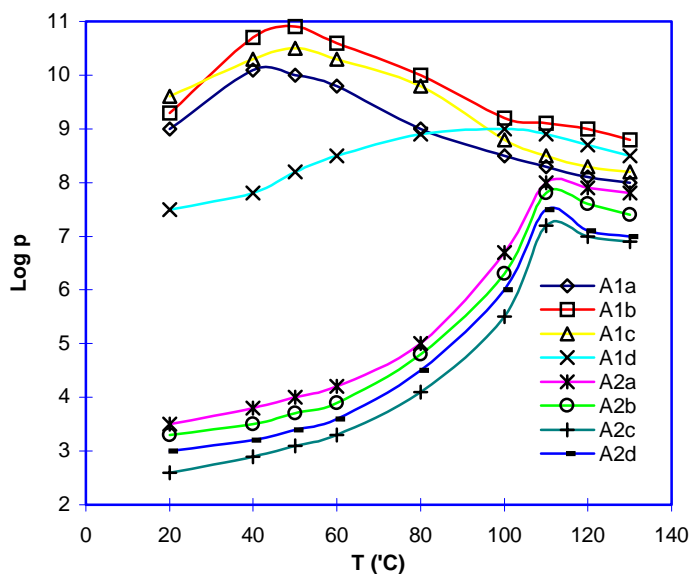


Fig. 3 Effect of electron irradiation dose on PTCR curve of the composites

The micrographs of the composites displayed that CB, SBT and silver powders were randomly distributed in the PE or ER matrix as shown in Fig. 4.

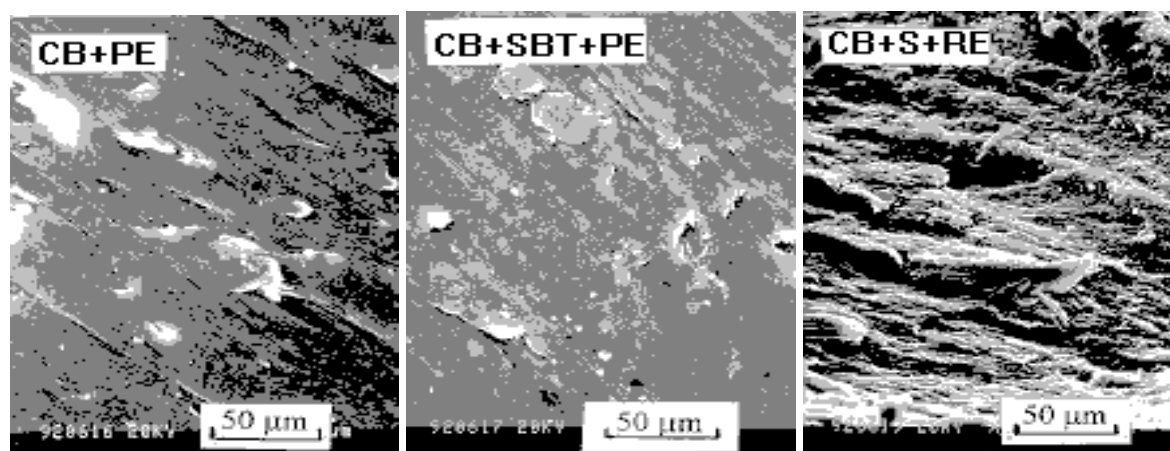


Fig. 4 SEM images of the PTCR composites

## CONDUCTING MODEL AND EQUIVALENT CIRCUIT

Based on the experimental results, a conducting model of the sample is proposed (Fig. 5) and a parallel-series equivalent electric circuit is schematically shown in Fig. 6. Since the

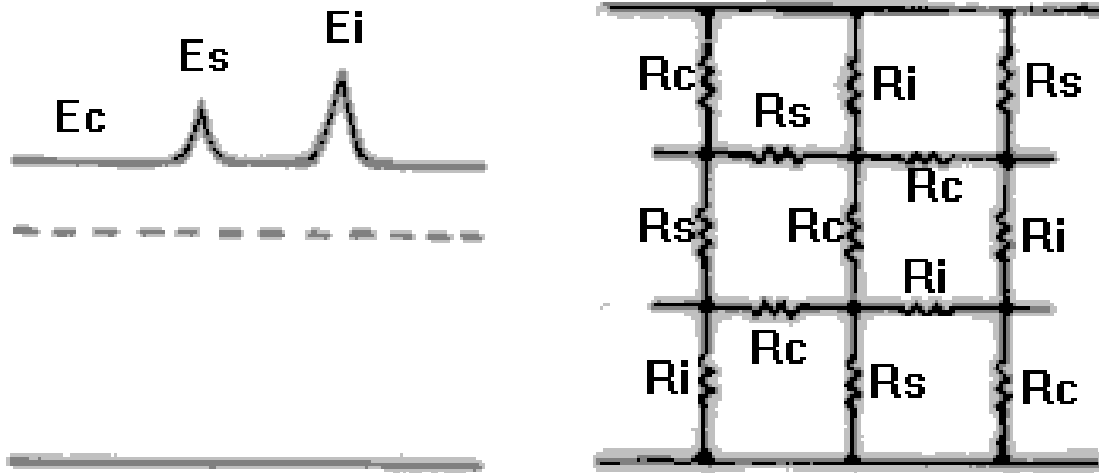


Fig.5 A conducting model of the sample Fig.6 A equivalent electric circuit of the sample

composite contained three phases: insulating polymer, semiconductive ceramics and conducting carbon-black, the conduction band of the composite with 0-3 connectivity are thus characterized by three parameters: the barrier height of the insulating polymer,  $E_i$ , the barrier height of the semiconductive ceramics,  $E_s$ , and the conduction level of the carbon-black,  $E_c$ . Therefore, the total resistance of the composite,  $R_t$ , results from three kinds of resistance: resistance of the polymer,  $R_i$ , resistance of the semiconductive ceramics,  $R_s$ , and, resistance of the carbon-black,  $R_c$ . The heights and widths of the barriers vary, in fact, at different micro-regions in the composite. The resistivity should be calculated by integration within the whole material to obtain more accurate results.

The temperature dependence of the resistivity can be roughly divided into three segments corresponding to three temperature regions. At room temperature the resistivity of the composite was usually small, which might be due to the relatively close distance between the conductive powders of the carbon-black or the semiconductive ceramics. The powders distributed randomly in the matrix of the polymer act as conducting bridges or network in the insulating polymer matrix. Moreover, the tunnel effect might also take place within a thin enough layer of the polymer at relatively low temperature when an electric field is applied. As the temperature is increased, however, the polymer matrix is expanded faster than that of the additives. The numbers of the conducting paths of the network are decreased, and the resistivity is thus increased sharply. So the PTCR effect appears within this temperature range. At a higher temperature, usually above the glass transition point of the polymer, the polymer matrix begins to melt. The concentration of conduction carriers is increased quickly at high temperature, and thus, the resistivity is decreased.

## CONCLUSION

A new type of PTCR composites consisting of conductive carbon-black and semiconductive ceramic powders in the matrix of PE or epoxy resin has been developed, which has been made into electric heating cable and plate used in industrial and domestic areas. The amounts of constituents and the processing parameters have effects on the electric properties of the composite materials.

## REFERENCES

1. J. Meyer, *Polym. Eng. Sci.*, 14 (1974) 706.
2. D. S. McLachlan, et al., *J. Am. Ceram. Soc.*, 73 (1990) 2187.
3. M. Sahimi, *Application of Percolation Theory*, Taylor & Francis Publishers, London, 1994.
4. D. Stauffer and A. Aharony, *Introduction to Percolation Theory*, Taylor & Francis Publishers, London, 1991.

## SUBJECT INDEX

3D woven structure	658	compression after impact	27, 503
Al <sub>2</sub> O <sub>3</sub>	769	compression loading	438
acrylonitrile / butadiene copolymers	254	compressive modulus	785
adhesion	859	conservation laws	522
alkali-resistant glass fibre	870	continuous fibre	775
aluminum-fiber	301	corrosion protection	859
anisotropic damage	682	coupling effect	103
anisotropic properties	785	crack	342, 431
aramid fiber reinforced epoxy matrix composite	503	crack growth	332
arc-melting	603	crack growth rate	215
artificial inserts	438	crack propagation	234
artificial viscosity	397	crack tip element	665
AS-4/PEEK	177	crack tip stress singularity	387
asymptotic expansion method	453	crease	312
		creep strength	167
		cyclic loading	682
		cylindrical bending	94
B <sub>4</sub> C-SiC composite	603		
B <sub>4</sub> C-TiB <sub>2</sub> composite	603	damage	203, 342, 374, 513, 638
ballistic damages	485	damage mechanics	364
ballistic impact	532, 542	damage mechanisms	114
ballistic limit velocity	522	damage tolerance	10, 17, 397, 513, 562
B-C system solid solution	603	damping capacity	833
beam end constraint	103	debonding	312
biomimetic composite	10	delaminated composite plates	47
bismaleimide	185	delamination	1, 36, 234, 290, 353, 415, 431, 438 503, 532, 573, 665
bolt	156	delamination onset	185
boron-rich boride	603	delamination resistance	244, 254
braking	638	delamination tests	322
brittle composite	203	design	474, 562
broken ellipsoidal inhomogeneity	364	discontinuous plies	353
buckling	1, 438, 573	discrete stiffener theory	84
		dislocations	833
C/C composite	630, 759	dynamic plate behavior	47
carbon	775		
carbon fibre	301, 342, 658, 759, 769	electrets and materials	859
carbon magnesium composite	804	electrical property	881
carbon/epoxy	225	electrophoresis	593
carbon-carbon	638	energy release rate	215
ceramic matrix composites	621, 658, 675, 682, 694 709	epoxy	342
cermet	709	equivalent inclusion method	364
CF/PEEK composite	114, 503	eutectic reaction	603
cluster polymetallo-carbosilanes	741	experimental design	27
coating	630	experiments	1
colloidal	775	extreme value theory	254
combined strength and toughness	785		
commingled prepreg	114	fabric orientation	447
complex frequency equations	94	fabrics	542
compliance	194	failure behavior	301
composite armor	464	failure criteria	156
composite laminates	583	failure mechanism	225, 630
composite layered plate analytical modeling	522	fatigue	124, 135, 156, 185
composite plate	36	fatigue behaviour	114, 145, 177
composite progressive failure	397	fatigue crack growth	194
composites processing	593	fatigue damage	211
compression	638		



fatigue life model	203	injection molding	851
fatigue strength	167	interface	613, 709, 759, 775, 845
fiber orientation distribution	10	interface coating	741
fiber pull-out and push-out	387	interfacial constitutive laws	47
fiber reinforced plastics	167	interfacial crack	387
fibre breakage	532	interferometry	438
fibre orientation	415	interlaminar delamination toughness	322
fibre pull-out	646	interlaminar shear stress	185
fibre reinforced composites	273		
fibre tests	870	laminar materials	845
fibre-reinforced polymer-matrix laminated composites	145	laminar laminate	55, 431
fibres	613	laminated composite	552
finite element analysis	1, 353	laminated composite beam	103
finite element method	290, 583, 759	LaRC-IAX	851
finite element modelling	397	LaRC-SI	851
fractography	225, 573	large deflection	74
fracture	10, 342, 387, 665, 694	lateral loading	74
fracture mechanics	353	liquid phase sintering	613
fracture mechanism	312	load carrying capacity	364
fracture mirror	646	load frequency	124
fracture toughness	215, 234, 424, 431, 447, 675	loading rate	215
free vibration	36, 55	local	438
free-edge effects	453	low velocity impact	513
friction	387	low-energy impact	177
fusion bonding	1		
		magnesium	833
glass fabric	447	magnesium alloy	424
glass fibre	244, 342	manufacturing	794
glass matrix composites	593	manufacturing defects	322
glass/polyester composite	135	marine	244, 415
global	438	material surface law	453
gradient design concept	464	matrix	775
graphite	759	matrix cracking	621
graphitic foams	825	maximum stress failure criterion	495
		mean field theory	364
hardness	638	mechanical properties	312, 658, 703, 775, 794, 804
heterogeneous materials	332	mechanical strength	833
hierarchical model	552	metallic fibre reinforcement	593
high speed testing	405	metal-matrix composite	211
high temperature	215, 301	metal-polymer electrets	859
high velocity impact	522	metals composite	845
higher-order shear deformation theory	55	method of cells	47
homogenisation	374	microcracking	682
homogenisation approach	552	micromechanics	785
hot-pressing	593, 613	micromechanics	47, 332, 364
hybrid element	290	microstructural characterisation	646
hybrid matrix composite	769	microstructure	703, 833
hybrid short-fiber	301	mixed mode	665
hypervelocity impact damage	474	MMC	804
hysteresis loop	124	mode I	215, 234
		modelling	342, 562, 813
impact	1, 74, 495, 562, 573	modulus	813
impact damage	17, 583	Moiré	438
impact loading	503	molybdenum disilicide	741
impact perforation	522	mullite	775
impact strength	234	multi-layers	845
indentation test	759		
inelastic strains	682	natural fibre	794
initial defect	353	natural frequency	36, 103
		nondestructive inspection	503

non-linear dynamic response	64	sandwich beam	495
notch	301	sandwich plates	513
notched sample	10	scanning acoustic microscope	503
		self reinforce	703
oblique reinforcement	694	SEM	881
off-axis loading	552	shaping	735
open-cell foams	825	shear	225
orbital debris	474	shear modulus	785
orientation influence	804	sheet molding compounds	194
oxide film	630	shock-wave propagation	552
oxygenless ceramic polymer precursors	741	SiC	769, 775
		SiC particles	424
PAEK resin	301	SiC/Si <sub>3</sub> N <sub>4</sub> ceramic	735
parallelism	374	SiC/SiC	646
particle or short-fiber reinforced composites	364	Si-C-N nanometer particles	675
particle size	312	silicon carbide	613
particulate composites	751	silicon carbide fiber	211
particulate filled polypropylene	312	silicon nitride	675, 703
PEI	851	single leg bending	665
perforation	542	singular element	290
phase separation	229	singular interlaminar stresses	453
pin	156	sintering	593, 735
plain weave	84	skin-stringer	573
plastic flow	312	slot	301
plastic zone	353	small arms body armor	464
plate	55	S-N curve	177
ply orientation	103	sol-gel	769
polarization	859	specific damping capacity	94
polyamide composites	405	spider silk	785
polycarbonate	452	static strength	167
polyethylene	542	statistical model	332
polyimide thermoplastic	851	stick-slip phenomenon	234
pores	322	stiffness degradation	495
post failure	532	stiffness loss	203
post-failure behavior	495	stitch-bonded variable layer fabric NVG	870
post-impact fatigue	17	stochastic process modelling and analysis	145
potential energy release rate	290	strain energy release rate	353, 387
powder metallurgical technique	424	strain rate dependence	405
powder processing	845	strength	859
power law equation	194	strength criteria	273
precursor	735, 769	strength ratio	10
precursor pyrolysis	658	stress redistribution	621
<i>p</i> -Ritz method	55	stress singularity	290
processing	27, 825, 881	stress transfer	813
progressive modeling	156	stress/strain	646
PTCR composite	881	structural foams	825
pultruded tubing	74	structures	573
pyrolysis	735	subdomain decomposition techniques	374
		subsurface	638
quality	27	surface coating	845
quasi-static modeling	74	survivability	485
random fiber composites	194	T300/976	177
rate effect	234	temperature influence	804
rectangular cutout	84	tensile behaviour	405
reinforcement cracking	364	tensile modulus	785
residual strength	135	tensile test	646
residual velocity	522	tension-tension fatigue	114
resin transfer molding	27	test data evaluation	273
ring stiffened composite cylindrical shell	84	testing	562

tetragonal zirconia polycrystals	751	unstable fracture	234
tetravinylsilane	741	variational principle	290
textile reinforced concrete	870	vibration damping	94
thermal effect	124	vibratory and fatigue characteristics	485
thermal stability	804	vinyl ester	244, 254
thermoelasticity	374	viscoelasticity	94, 215
thermoelectric property	262, 612	viscoplasticity	47, 215
thermoplastic	1, 124, 794	voids	322
thermoset	415		
thick annular composite plates	64	wall effect	453
through thickness stress	353	warp knitted multi-axial layer fabric WIMAG	870
time-temperature superposition principle	167	water absorption	503
Timoshenko beam theory	103	wear	638
tip mass	103	Weibull distribution	177
toughening	675	wetting and spreading	859
toughness	387, 415	wood composites	813
transition behavior law	453	woven fabric composite	447, 804
transmission electron microscopy	759	woven fibre reinforcement	593
tribological characteristics	859	woven glass fibres	415
tungsten carbides	751	woven glass roving reinforcement	254
		woven preform	769
ultrasonic C-Scan	1	woven roving	244
unidirectional	244, 775	YAG (yttrium aluminium garnet)	613
unidirectional fibres	833	Young's modulus	759
unidirectional laminates	453		
unsaturated curing organosilicons	741		

## AUTHOR INDEX

ABACHI, P.	424	FARYNA, Marek	751
ABE, Kenichi	522	FLORINA, E.K.	741
ADDESSIO, Frank L.	47	FRANZKE, Gerd	870
AL-HMOUZ, I.	124	GANESAN, R.	145
ALLEN, D.H.	94	GAO, Yun	845
ANDERSON, David P.	825	GARKHAIL, S.	794
ANDERSONS, J.	135	GERLIVANOV, V.G.	741
ANSART, Thierry	27	GESHURY, Amotz J.	464
ARENDTS, F.J.	438	GOLADE, V. A.	859
ASP, Leif E.	322	GOTO, Takashi	603
ATODARIA, D.R.	194	GREENHALGH, Emile	573
BABA-KISHI, K. Z.	881	GUBIN, S.P.	741
BAO, Xiaoheng	735	HABERKO, Krzysztof	751
BASTE, Stéphane	682	HABOUSSI, Mohamed	453
BEAUMONT, P.W.R.	342	HAHN, H. Thomas	17
BÉGUELIN, Ph.	405	HAUSMANN, C.	804
BERTHET, Florentin	27	HEIJENRATH, R.	794
BILLÖET, Jean Louis	453	HEYNE, T.	804
BISCHOFF, Thomas	870	HILD, Francois	621
BOCCACCINI, Aldo R.	593	HIRAI, Toshio	603
BOEIJSMA, J.	709	HIROKAWA, Tetsuro	646
BOLDUC, M.	532	HOA, S.V.	145
BONORA, N.	203	HOJO, Masaki	234
BOS, H.	794	HUANG, C.L.D.	64
BRANDT, Fredrik	322	HUGHES, Derke R.	513
BRUNET, Louis J.	74	HUMMEL, Sarah	851
BURCHILL, Peter J.	244, 254	INOUE, Mari	785
BURR, Alain	621	ISHIGURO, Takeshi	167
CARDEW-HALL, M.	94	ISHII, Hitoshi	364
CARMAN, Greg P.	17	ISHIKAWA, Takashi	1, 646
CHANG, Fu-Kuo	397	JAMES, Peter F.	775
CHEN, C.C.	55	JAR, P.-Y.B.	244, 415
CHEN, Zhaohui	658, 675, 735	JIANG, Dazhi	583, 658, 769
	769	JING, X.T.	447
CHENG, Haifeng	735	JONES, F.R.	775
CHENG, Laifei	630	JUN, Xiao	431
CHO, Young-Tae	364	KAINER, K.U.	424
COMPSTON, P.	244, 415	KALYANASUNDARAM, S.	94, 225
CRAFT, William J.	513	KAMIYA, Akira	717
CRASTO, Allan S.	185	KASANO, Hideaki	522
CUNTZE, Ralf G.	273	KAUSCH, H.H.	405
CZARNECKI, Gregory J.	263	KAWABATA, Sueo	785
DAI, Jin	332	KEARNS, Kristen M.	825
DAVIDSON, Barry D.	665	KELKAR, Ajit D.	513
DAVIES, Ian J.	646	KERN, Heinrich	593
DAVIES, P.	415	KESTELMANN, V. N.	859
DEVOS, Pierre	27	KIM, Patrick	10
DEVRIES, F.	374	KIM, Ran Y.	185
DIAO, Xiaoxue	114	KIM, Young-Wann	84
DIMANT, R.A.	342	KITIPORNCHAI, S.	55
DU, Shanyi	332	KO, Frank K.	464, 785
DUBNIKOVA, I.L.	312	KOHYAMA, A.	759
DUMONTET, H�el�ene	453	KOLSTER, B.H.	709
EL-KARMALAWY, M.	145	KOMAI, Kenjiro	503
FARRIES, Pamela M.	613	KOMATSU, H.	542

KONDO, Kyohei	290	PUTATUNDA, S.K.	194
KORSGAARD, J.	135	QIAN, Tiancai	845
KUROKAWA, Tomoaki	234	QIAN, W.	387
KUSAKA, Takayuki	234	RADFORD, Donald	851
L'HOSTIS, G.	374	RAŠUO, Boško	785
LAI, Ren-Cheng	36	REMOND, Yves	638
LECKIE, Frederick A.	621	RESNYANSKY, A.D.	552
LEE, Ya-Jung	495	ROBERTS, Donald	573
LEE, Young-Shin	84	ROMENSKY, E.I.	552
LÉNÉ, F.	374	SATO, S.	759
LESSARD, Larry B.	156	SCHÄFF, W.	804
Li, Bin	845	SCHALLER, Robert	833
LI, Fengmei	703	SCHMITT-THOMAS, Kh. G.	301
LI, Jianhui	603	SCZEPANIK-WEINMANN, M.	438
LI, Shujie	709	SELVARATHINAM, Alex S.	694
LI, Shunling	431	SERIZAWA, H.	759
LI, Yongqing	735	SHEN, Wei	583
LI, Yuping	709	SHERCLIFF, H.R.	342
LIEW, K.M.	55	SHERWOOD, Tor W.	665
LIM, C.W.	55	SHIBUYA, Masaki	646
LIN, Bor-Horng	725	SHOKRIEH, Mahmood M.	156
LITYNSKA, Lidia	751	SHORTLIFFE, G.D.	474
LIU, Fengrong	658, 769	SHYU, Yau	495
LIU, Hsien-Kuang	725	SIMPSON, Gary J.	244, 254
LOWE, Adrian E.	94, 225	SINGER, R.F.	804
MAAS, J.H.	709	SINGH, Sunil	573
MAI, Y.-W.	114	SMITH, Charles	851
MALKE, R.	301	SONG, John W.	464, 785
MALLICK, P.K.	194	SOULAT, D.	374
MATSUSHIMA, Masamichi	1	STOLL, U.	438
MAYENCOURT, Christine	833	STRAZNICKY, P.V.	532
MINOSHIMA, Kohji	503	SUN, C.T.	387
MITROVIC, Milan	17	SUN, Yong	845
MIYANO, Yasushi	167	SUN, Y.Q.	447
MORDIKE, B.L.	424	TAI, Nyan-Hwa	177
MORVAN, Jean-Marie	682	TAKAHASHI, K.	405, 542
MUCHA, Herbert	717	TAKAO, Y.	215
MURAVIN, D.K.	312	TANAKA, Kazuto	503
NAKADA, Masayuki	167	TANIMOTO, T.	10
NEMES, James A.	74	TAO, Jie	431
NEWAZ, G.M.	203	TENNYSON, R.C.	474
NIWA, Masako	785	TODO, M.	405
NWOSU, Sylvanus N.	263	TOHGO, Keiichiro	364
OCHIAI, Shojiro	234	TRINH, Khanh	397
OFFERMANN, Peter	870	TSENG, Chih-Ming	177
OLIVERO, David	851	TSIRLIN, A.M.	741
OSHYMYAN, V.G.	312	TSUNAKAWA, H.	759
ÖTTINGER, O.	804	TUNG, Betty	851
PAN, Jin	211	TYLKO, S.	532
PATER, R.H.	215	UBELS, L.C.	562
PATON, Rowan	813	VAN DER OEVER, M.	794
PEDZICH, Zbigniew	751	VAN HOOFF, J.	532
PEIJS, T.	794	VERTYACHIKH, I. M.	859
PETROSSIAN, Z.	353	VEYRET, Jean-Bernard	613
PINCHUK, L. S.	859	WAGNER, Christiane	638
POLAHA, Jonathon J.	665	WAN, Hong	211
POPOVA, N.A.	741	WANG, Biao	332
POTTER, B.D.	215	WANG, J.B.	447
PRONIN, Yu E.	741	WANG, W.X.	215

WANG, Xingye	658, 769	YANG, Zhen-Guo	301
WANG, Xing-Ye	583	YE, L.	114
WEILAGE, Bernhard	717	YEH, Meng-Kao	36
WEITSMAN, Y.J.	694	YIP, Ming-Chuen	177
WIGGENRAAD, J.F.M.	562	YOKOYAMA, T.	103
WILLIAMS, Todd O.	47	YONG, Li	431
WINKLER, Volker	593	YU, Hui-Chia	177
WISNOM, Michael R.	353	YUAN, F.G.	215
WORSWICK, M.J.	532	ZHANG, Changrui	675, 735
WU, Jiali	775	ZHANG, Daiming	845
WULFHORST, Burkhard	870	ZHANG, Litong	630
XIAO, Jiayu	658, 769	ZHANG, Shuhong	845
XIAO, X.R.	124	ZHANG, S.	145
XIE, Kai	675	ZHENG, S.R.	447
XIONG, Z. X.	881	ZHENG, Wen-Wei	658, 769
XU, Yongdong	630	ZHOU, Anchen	675, 735
YAGI, Kazuhiro	290	ZHOU, Xingui	675
YANG, Deming	211	ZHUO, Yue	211
YANG, Z.M.	103		